

**Realistic LOCA Evaluation
Methodology Applied to the
Full Spectrum of Break Sizes
(FULL SPECTRUM LOCA
Methodology)**

**Volume II
WCOBRA/TRAC-TF2
Assessment**

Book 2 of 3

16 HORIZONTAL STRATIFIED FLOW AND WAVY-DISPERSED FLOW

16.1 INTRODUCTION

In general, the predicted performance of a pressurized water reactor (PWR) during a small break Loss-of-Coolant Accident (LOCA) transient is, to some extent, determined by the two-phase flow regime present in the horizontal pipes of the reactor coolant system (RCS). The duration of the []^{a,c}

regime(s) in the []^{a,c} are a consequence of the flow []^{a,c} respectively.

In the WCOBRA/TRAC-TF2 computer code, a hybrid transition criterion combining []

[]^{a,c} is utilized to define the horizontal stratified flow regime. At the relatively low flow rates associated with the break size range of a small break LOCA, the horizontal two-phase flow is expected to be in the horizontal stratified or wavy-dispersed flow regimes most of the time. Once the flow regime is identified to be horizontal stratified or wavy-dispersed, the appropriate closure relations are selected for the interfacial area, the interfacial drag and the interfacial heat transfer. The interfacial drag and interfacial heat transfer, particularly condensation in the cold leg (Section 6, Volume 1), for the horizontal stratified and wavy-dispersed flow are the basic processes that are directly related to the high-ranked items in the LOCA PIRT. In addition, the offtake phenomenon (Section 5.13, Volume 1) affects the inlet boundary conditions (quality) at the inlet of the break flow. The offtake model in Section 5.13, Volume 1 is considered when the cold leg node connected to the break is calculated to be in the horizontal stratified flow regime or wavy-dispersed flow regime.

The selection criterion for either the horizontal stratified or wavy-dispersed flow regimes is discussed in Section 4, Volume 1, while Sections 5 (interfacial and wall drag) and 6 (interfacial heat transfer) of Volume 1 provide the closure relationships associated with these flow regimes. Scaling and applicability of those models were also discussed in these sections.

The objective of this section is to compare the void fraction prediction for horizontal stratified flow with relevant test data to assess the stratified flow interfacial drag model, wall drag model, and influence of inlet and outlet boundaries.

16.2 KEY PHYSICAL PROCESSES

The capability of the code in predicting the transition from the horizontal stratified or wavy-dispersed regimes to other intermittent flow regimes (bubbly slug, churn, and annular-mist) or interpolation region is very important because interface characteristics (interfacial drag and interfacial heat transfer) change by several orders of magnitude. This is an important mechanism because it affects the venting capability of the vessel from the upper plenum to the cold legs and finally to the break.

[The transition criterion from stratified to non-stratified regimes in Section 4, Volume 1 is affected by the predicted void fraction, or water level, in a stratified pipe with the given liquid and gas superficial velocities. From the mass and momentum equations for the stratified flow in Section 5, Volume 1, the void fraction is determined by the interfacial drag, wall drag, and boundary condition (via gravitational water head term) for a horizontal pipe.]

]^{a,c}

[The wavy-dispersed flow regime is a special horizontal stratified flow regime, which prevents intermittent flow in the high pressure conditions of a Small Break LOCA (SBLOCA) scenario. The relevance of the wavy-dispersed flow regime was discussed in Section 4, Volume 1. The wavy-dispersed regime is established [

]^{a,c}. Under these circumstances, [

]^{a,c}. The wavy-dispersed flow regime will prevent the formation of slug flow and departure from the separated flow regimes.

The four other processes in LOCA which are affected by the horizontal stratified flow regime are:

[

[

[

]^{a,c}

I

2

] a,c

In WCOBRA/TRAC-TF2 the transition criterion for stratification is a hybrid model based on [

^{a,c} The accuracy of the hybrid transition criterion was assessed against experimental data at various pressures, pipe diameters, and void fractions and an uncertainty range for the transition criterion was quantified. The adoption of a transition criterion as a function of $|J|$

J^{a,c}. In this section, the assessment focuses on the accuracy of void fraction prediction by WCOBRA/TRAC-TF2.

The prediction of void fraction is controlled by the wall drag, the interfacial drag and the gravitational water head. The applicability of the wall drag model for stratified flow was addressed in Section 5, Volume 1. The gravitational water head term was implemented in the momentum equations as discussed in Section 3, Volume 1. Therefore, the assessment of this section focuses on the interfacial drag model together with the influence of the inlet and outlet boundaries.

The assessment is made against Two-Phase Flow Test Facility (TPTF) stratified flow data. TPTF is a Japan Atomic Energy Research Institute (JAERI) steam-water stratified flow test with a large scale pipe diameter, high pressure, and broad range of flow rates and void fractions. These characteristics render TPTF tests to be excellent benchmark tests for the stratification in small break LOCA. The interfacial and wall drag models for the stratified flow in WCOBRA/TRAC-TF2 are assessed via comparison between the measured void fraction and the predicted void fraction.

The wavy-dispersed flow regime was first reported by TPTF researchers as a relevant flow regime for SBLOCA (see Section 4, Volume 1). |

1a,c

16.3 TEST FACILITY DESCRIPTION

TPTF (Nakamura et al., 1983) was designed and built by JAERI to study the nature of SBLOCA. This facility was designed to perform various steam/water two-phase flow and heat transfer experiments at steady state and at pressures up to 12.8 MPa. These experiments were characterized by a high system pressure (3~12 MPa), a large test section diameter (0.18 m) and a wide range of mass flux (40 to 1000 kg/m²-s) obtained in the test section for concurrent saturated two-phase flow. The test also simulated the pump effect at inlet, and the water level effect at outlet. These characteristics render TPTF to be an ideal test to assess SBLOCA safety evaluation codes.

Figure 16-1 shows the flow loop used in the TPTF, which consisted of an electrically heated boiler, separate pumps for steam and water lines, a mixer and a 10 m long, 180 mm inner diameter (ID) horizontal test section. The demineralized water was heated in the boiler to saturation conditions at a desired system pressure. Saturated steam was pumped from the top of the boiler through an orifice meter and into the mixer located at the entrance of the test section. The steam pump was a blower-type pump that was specially designed and manufactured for use at high pressure. The steam flowed through a demister located at the top of the boiler and became slightly superheated at the exit of the pump. Saturated liquid was drawn from the bottom of the boiler and similarly pumped through an orifice meter into the mixer. The piping for both the steam and liquid lines was well-insulated to minimize heat loss and prevented steam condensation or liquid subcooling.

The mixer was T-shaped and was connected to the steam and water lines such that steam was introduced horizontally and liquid from the bottom of the tee. There were two types of T shaped mixers used in TPTF experiments as schematically shown in Figure 16-2. Early series of tests used a “bubbly flow” type of mixer. The steam was introduced horizontally into a bundle of tubes and was forced out through numerous holes drilled along the side of each tube. Liquid introduced from the bottom of the tee flowed on the outside of the tube bundle, where the steam and liquid mixed with each other. A nearly homogeneous mixture of liquid and vapor was expected to enter the test section. This homogeneous mixture is similar to the two-phase flow condition in the cold leg after a rotating reactor coolant pump (RCP). The data of Kawaji et al. (1987) came from this “bubbly flow” type mixer. However, because of the homogeneous flow type inlet, the flow was far away from the equilibrium state horizontal stratified flow. The void fraction tended to be larger than the equilibrium state flow and the relative gas-liquid speed was lower than the relative speed in equilibrium state stratified flow. Thus, the non-equilibrium stratified flow due to the homogeneous flow inlet tended to be stable according to the horizontal stratification model. The length of cold leg pipe ($L/D=56$) was not long enough to allow flow to reach equilibrium state from the homogeneous mixture. Another problem associated with a “bubbly flow” mixer is that the entrained bubbles cannot be released rapidly from liquid if the speed of liquid is large. Those factors led to the observation that the separated to slug flow transition never appeared in the tests with a “bubbly-flow” mixer.

The later TPTF tests used a “separated-flow” type mixer, which contained a horizontal flat plate. Due to this flat plate, the two phases entered the test section as a separated two-phase flow. The height of the separator plate was either 0.3 or 0.7 in height-to-diameter ratio. Thus, there was essentially no bubble entrainment and the flow was not far away from the equilibrium state horizontal stratified flow. All the TPTF flow regime transition data by JAERI were obtained with a “separated flow” type mixer (Anoda et al., 1989). The TPTF data from the “separated-flow” mixer was utilized to verify the stratification transition criteria in Section 4, Volume 1. In this section, the data from the “bubbly-flow” mixer are applied to assess the interfacial drag and the prediction of void fraction.

The water level at the exit of the test section was controlled by the water level in the boiler. There were two water levels in the TPTF tests. In the case of high water level, the water level in the boiler was 0.4 m higher than the center of the test section pipe. In the case of low water level, the water level in the boiler was 0.4 m lower than the center of the test section pipe. The purpose of high or low water level was to simulate the effect of downcomer. The effect of full or empty downcomer was simulated in TPTF test.

The test section consisted of five sections of 180 mm ID stainless-steel piping, each 2 m long and joined by Grayloc connectors. The overall length was 10.0 m and the length-to-diameter ratio (L/D) was 56. The volumetric flow rates of vapor and liquid entering the test section were changed independently by adjusting the flow control valves and the pump speed. The maximum volumetric flow rates were 0.194 m³/s for steam and 0.047 m³/s for liquid. For the 180 mm ID test section, the maximum superficial liquid and vapor velocities were 1.9 and 7.6 m/s, respectively.

The horizontal test section was equipped with various two-phase flow instruments (Figure 16-3). In order to obtain detailed information about the flow structure, several of the instruments were attached to traversing devices which enabled measurement of mass and momentum distributions across the pipe cross section. To measure density (or void) distribution, two of the γ -densitometers with vertically-shot γ -ray beams were traversed across the pipe cross section horizontally, yielding a horizontal distribution of vertical chord-average void fractions at locations near the inlet (L/D=17) and outlet (L/D=48) of the test section. The third densitometer with a horizontal beam was traversed vertically across the pipe cross section at L/D=21, yielding a vertical distribution of horizontal chord-average void fractions. The fourth was a three-beam densitometer fixed to the pipe. To measure momentum flux, a water-purged Pitot tube was used. The Pitot tube was attached to a driving mechanism which moved the probe vertically along the centerline of the pipe at a speed of 0.22 mm/s to measure the momentum flux distribution. To further aid in flow pattern identification, five conductivity probes specially developed for use in high-temperature and high-pressure steam/water environments were attached to a rod which was situated along the vertical centerline of the test section.

A large matrix of tests was conducted by JAERI during 1980s. Part of the data is available in public literature (Kawaji et al., 1987). That data were digitized and provides the applicability for the validation of the flow regime and interfacial drag closure relation in WCOPRA/TRAC-TF2.

In summary, TPTF data are selected as the primary data source for the assessment because of the following reasons:

[

[

[

[

[

]^{a,c}

16.3.1 Test Selection and Basis

A large matrix of tests was conducted by JAERI during the 1980s. Part of data is available in the public literatures (Kawaji et al., 1987). TPTF experiment data are listed in Tables 2, 3, 4, and 5 in Kawaji et al. (1987). The void fraction information of the data in Table 2 (Kawaji et al., 1987) is missing, and thus could not be used here. The void fraction data in Table 5 (Kawaji et al., 1987) are in contradiction with Figure 11 in Kawaji et al. (1987). There is no other resource to verify those data, so data in Table 5 (Kawaji et al., 1987) are also excluded from the assessment. The remaining data in Tables 3 and 4 (Kawaji et al., 1987) are selected for the assessment. The data are reproduced in Table 16-1 for convenience. According to Kawaji et al. (1987), all those data were in the stratified flow regime based on visual inspections during experiments. The data points are also presented in the WCOPRA/TRAC-TF2 flow regime map in Figure 16-4. There is a substantial amount of data points beyond the horizontal stratification transition boundary of WCOPRA/TRAC-TF2. The discrepancy between the WCOPRA/TRAC-TF2 flow regime map and the observed stratified flow regime in the experiment is likely attributed to [

]^{a,c}.

Nevertheless, the data with the homogenous inlet mixer are still applicable to assess the interfacial drag and the prediction of void fraction.

It is noted that the selected data are limited to the pressure range from 7.4 MPa to 8.0 MPa. []^{a,c}

There are two main aspects that are critical for an accurate prediction of the flow regime: a) the transition from stratified to non-stratified flow regimes; and b) the predicted void fraction in the stratified flow regime.

The adequacy of the transition criterion was discussed in Section 4, Volume 1. Here the focus is on the accuracy of the prediction of void fraction (level) in the pipe. The main objectives of the assessment are the following:

1. Confirm the capability of the code in predicting the transition from stratified flow to non-stratified flow.
2. Assess the interfacial drag model together with the effect of boundary conditions.
3. Identify the controlling parameters and associated biases and uncertainties.

16.4 WCOBRA/TRAC-TF2 MODEL DESCRIPTION

The WCOBRA/TRAC-TF2 model includes the TPTF pipe from the location of first void fraction measurement point ($L/D=17$) to the exit to the water tank. The pipe from the homogeneous mixer to the first void fraction measurement point at $L/D=17$ is neglected. The influence of the homogenous inlet mixer is removed to better assess the interfacial drag model and wall drag model for horizontal stratified flow. The inlet of the pipe is modeled with flow boundary conditions (FILL component) by providing the specific j_g and j_l for each test run. The []^{a,c} is used to evaluate the gas phase velocity and the liquid phase velocity for the FILL component. The water level in the tank is simulated by []^{a,c}

[]^{a,c}

The noding diagram is shown in Figure 16-5. The cold leg in the TPTF test section is intended to represent the PWR's cold leg. However, the L/D of the TPTF pipe is longer than the L/D of the PWR's cold leg, but not long enough to develop an equilibrium state stratified flow. The boundary conditions of the TPTF tests have been incorporated into the input model. Thus, the non-equilibrium state stratified flow, as well as the influence from the boundary condition, is part of the simulation.

The diameter of the TPTF pipe is similar to that of the ROSA Integral Effects Test (Section 21) cold leg, but the L/D is much larger than that of ROSA. To preserve the []^{a,c}

is adopted. The node length (DX) and the hydraulic diameter (HD) of the cold leg node in the ROSA IET are []^{a,c}, respectively. The HD of the pipe in TPTF is 0.18 m (Figure 16-3). []^{a,c}

[]^{a,c}

[]
] ^{a,c}

] ^{a,c}

16.5 ASSESSMENT RESULTS

The simulation is carried out until a steady-state condition is reached. A typical void fraction profile in the pipe is shown in Figure 16-6 together with the flow regime numbers for TPTF Test 722. Per Table 16-1, Run 722 was a low mass flux case with a high water level in the boiler. The weighting factors W_{st} of the two measurement points in Run 722 were calculated as 1.0 and 0.95 using Equation 4-117 in Section 4.4.5, Volume 1. The parameters C_{stfru} and C_{hs_slug} default to [] ^{a,c}, respectively.

The weighting factors $W_{st}=1$ indicates stratified flow, while $W_{st}=0$ indicates a non-stratified flow in the basic flow regime map. In the interpolation region, $0 < W_{st} < 1$. The weighting factors indicate the flow in TPTF Test 722 is [] ^{a,c} per the WCOBRA/TRAC-TF2 flow regime map.

The code-predicted flow regime number of each node is marked with “N”. A summary of flow regime numbers in a 1D component is given in Table 4.4-1. It is seen that the flow regime numbers are [] ^{a,c} in the nodes of the PIPE component, except []

] ^{a,c}

The WCOBRA/TRAC-TF2 predicted void profile is shown with the solid line in Figure 16-6. The squares represent the measured void fractions at $L/D=17$ and $L/D=48$. []

[] ^{a,c} The dashed line represents the theoretical void fraction that would be obtained assuming the steady-state equilibrium in an infinitely long pipe [] ^{a,c}. Obviously in this case, []

] ^{a,c}

Figure 16-7 presents the void fraction distribution and the flow regime numbers for TPTF Test 845, which was a high mass flux case with a low water level in the boiler. The flow is []

] ^{a,c}

The measured void fractions and weighting factors at L/D=17 and L/D=48, together with the predicted void fractions and flow regime numbers at node 1 (L/D=18) and node 13 (L/D=48) are collected in Table 16-2. It is noted that the FILL component is a boundary node, so the flow regime is not evaluated by the code. Instead, []^{a,c}.

The weighting factors in Table 16-2 confirm that []^{a,c}.

[]^{a,c}.

Figure 16-8 compares the predicted void fraction at node 13 (L/D=48) with the measured void fraction at L/D=48 for the runs []^{a,c}.

[]^{a,c}

16.6 CONCLUSIONS

An improved horizontal flow regime map is included in the 1D module of WCOBRA/TRAC-TF2 to expand the applicability of the code to small break LOCA scenarios. The 1D module is based on the TRAC-P []^{a,c} formulation. TRAC-P []^{a,c} shortcomings are identified and corrected with a revised model which better describes the conditions expected in a PWR during postulated LOCA scenarios.

The improved model includes a hybrid transition criterion for the transition from horizontal stratified flow to non-horizontal stratified flow, []^{a,c}.

A wavy-dispersed model, []^{a,c} which is applied generically regardless of the orientation of the pipe. A detailed discussion on the flow regime, transition criteria and applicability can be found in Section 4, Volume 1.

The purpose of this section is to assess the void fraction prediction for the horizontal stratified flow against relevant test data. []^{a,c}

16.7 REFERENCES

1. Anoda, Y., Kukita, Y., Nakamura, N., and Tasaka, K., 1989, "Flow Regime Transition in High-Pressure Large-Diameter Horizontal Two-Phase Flow," *Proc. of 26th ASME/AICHE/ANS National Heat Transfer Conference*, pp. 61-68, Philadelphia.
2. Asaka, H., Kukita, Y., Anoda, Y., Nakamura, H., and Tasaka, K., 1991, "Improvement of TRAC-PF1 Interfacial Drag Model for Analysis of High-Pressure Horizontally – Stratified Two-Phase Flow," *Journal of Nuclear Science and Technology*, Vol. 28, No. 1, pp. 33-44.
3. Barnea, D., and Taitel, Y., 1993, "Stability criteria for stratified flow: viscous versus non-viscous (Inviscid) approaches," *Int. J. Multiphase Flow*, Vol. 19, No. 4, pp. 639-649.
4. Crowley, C. J., Wallis, G. B., and Barry, J. J., 1992, "Validation of one-dimensional wave model for the stratified to slug flow regime transition with consequences for wave growth and slug frequency," *Int. J. Multiphase Flow*, Vol. 18, No. 2, pp. 249-271.
5. Kawaji, K., Anoda, Y., Nakamura, H., and Tasaka, T., 1987, "Phase and Velocity Distributions and Holdup in High-Pressure Steam/Water Stratified Flow in a Large Diameter Horizontal Pipe," *Int. J. Multiphase Flow*, Vol. 13, No. 2, pp. 145-159.
6. Kukita, Y., Asaka, H., Mimura, Y., Anoda, Y., Ishiguro, M., Nemoto, T., Tasaka, K., 1990, "Developmental Assessment of RELAP5/MOD3 Code Against ROSA-IV TPTF Horizontal Two-Phase Experiments," JAERI-M-90-053.
7. Nakamura, H., Tanaka, M., Tasaka, T., Koizumi, Y., and Murata, H., 1983, "System Description for ROSA IV Two Phase Flow Test Facility (TPTF)," JAERI-M-83-042.
8. Taitel, Y., and Dukler, A.E., 1976, "A Model for Predicting Flow Regime Transitions in Horizontal and Near Horizontal Gas-Liquid Flow," *AICHE Journal*, Vol. 22, No. 1, pp. 47-55.
9. Wallis, G. B., and Dobson, J.E., 1973, "The Onset of Slugging in Horizontal Stratified Air-Water Flow," *Int. J. Multiphase Flow*, Vol. 1, pp. 173-193.

Table 16-1 Selected TPTF Test Data from Kawaji et al. (1987)

Run	P(MPa)	Water Level ⁽¹⁾	G (kg/m ² s)	x (-) ; quality	j _l (m/s)	j _g (m/s)	Void Fraction	
							L/D=17	L/D=48
857	7.4	Low	1016	0.2	1.12	5.15	0.67	0.64
855	7.4	Low	1020	0.104	1.26	2.69	0.51	0.47
853	7.4	Low	1025	0.06	1.33	1.55	0.35	0.33
851	7.4	Low	1015	0.02	1.37	0.52	0.17	0.17
849	7.4	Low	1015	0.011	1.38	0.28	0.08	0.10
845	7.4	Low	440	0.374	0.38	4.17	0.76	0.77
843	7.4	Low	442	0.122	0.54	1.37	0.42	0.42
847	7.4	Low	426	0.022	0.57	0.23	0.16	0.22
836	7.5	Low	114	0.81	0.03	2.33	0.89	0.91
838	7.4	Low	112	0.634	0.056	1.79	0.83	0.87
1561	7.6	Low	116	0.153	0.14	0.45	0.67	0.68
1563	7.6	Low	114	0.093	0.14	0.27	0.65	0.66
1565	7.6	Low	115	0.052	0.15	0.15	0.64	0.65
1567	7.7	Low	116	0.038	0.16	0.11	0.64	0.67
834	7.5	Low	42.6	0.575	0.025	0.62	0.82	0.88
1555	8	Low	45.2	0.378	0.041	0.42	0.87	0.83
1557	7.8	Low	43.5	0.209	0.049	0.23	0.83	0.79
1559	7.7	Low	42.8	0.122	0.053	0.13	0.79	0.82
779	7.3	High	1011	0.003	1.38	0.085	0.06	0.09
781	7.3	High	1013	0.005	1.37	0.13	0.09	0.13
775	7.3	High	1010	0.01	1.37	0.26	0.13	0.15
751	7.4	High	1007	0.019	1.35	0.51	0.19	0.15
749	7.4	High	1004	0.048	1.31	1.28	0.38	0.29
747	7.4	High	1001	0.077	1.27	2.02	0.48	0.41
773	7.3	High	1010	0.101	1.24	2.58	0.57	0.50
743	7.4	High	1000	0.195	1.1	5.1	0.73	0.69
732	7.4	High	400	0.391	0.33	4.1	0.84	0.81
730	7.3	High	402	0.196	0.44	2.06	0.66	0.64
783	7.3	High	414	0.106	0.51	1.11	0.43	0.47

Table 16-1 Selected TPTF Test Data from Kawaji et al. (1987)
 (cont.)

Run	P(MPa)	Water Level⁽¹⁾	G (kg/m²s)	x (-) ; quality	j_l (m/s)	j_g (m/s)	Void Fraction	
							L/D=17	L/D=48
785	7.3	High	410	0.039	0.54	0.41	0.26	0.27
755	7.4	High	407	0.019	0.55	0.21	0.13	0.13
757	7.4	High	383	0.01	0.52	0.1	0.16	0.12
759	7.4	High	381	0.005	0.52	0.05	0.08	0.06
761	7.4	High	380	0.003	0.52	0.031	0.06	0.04
726	7.4	High	99.1	0.794	0.028	2.06	0.97	0.83
728	7.3	High	100	0.596	0.055	1.57	0.91	0.69
708	7.3	High	99.4	0.293	0.1	0.76	0.65	0.53
710	7.3	High	99.5	0.391	0.083	1.02	0.76	0.61
1545	7.4	High	106	0.164	0.12	0.44	0.32	0.31
1547	7.4	High	103	0.098	0.13	0.26	0.2	0.20
1549	7.4	High	105	0.05	0.14	0.13	0.12	0.11
763	7.4	High	102	0.01	0.14	0.027	0.05	0.04
720	7.3	High	39.6	0.691	0.017	0.72	0.63	0.48
722	7.3	High	39.7	0.59	0.022	0.61	0.57	0.44
712	7.3	High	39.9	0.392	0.033	0.41	0.48	0.38
714	7.3	High	40.2	0.196	0.044	0.21	0.31	0.24

Note:

1. High water level: water level in boiler is about 0.4 m above center of test section pipe. Low water level: water level in boiler is below center of test section pipe.

Table 16-2

J^{a,c}

a,c

Table 16-2
(cont.)

1

J^{a,c}

a,c

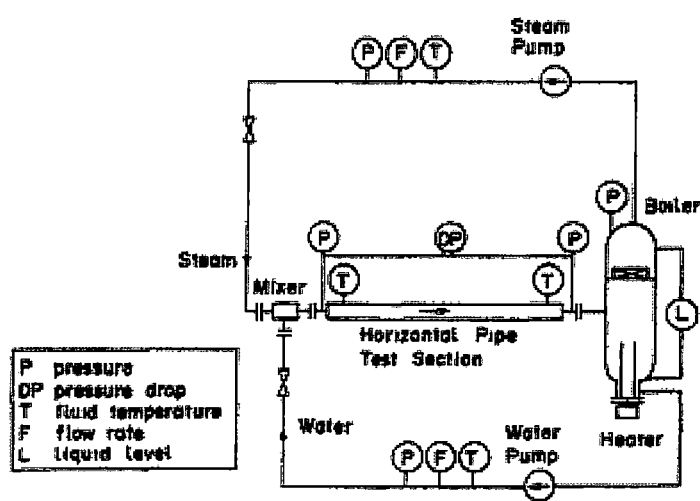
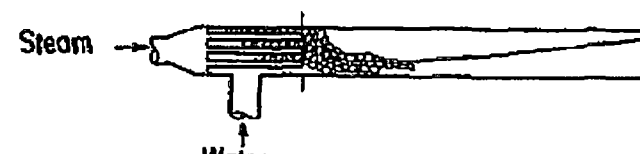
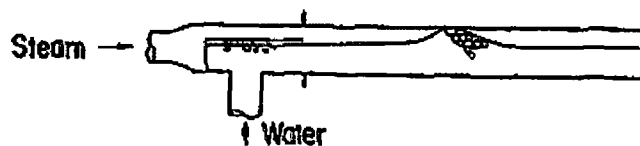


Figure 16-1 The Schematic of the TPTF Facility (Nakamura et al., 1983)



(a) "Bubbly-flow" type mixer



(b) "Separated-flow" type mixer

Figure 16-2 T Shaped Mixers used in TPTF (Anoda et al., 1989)

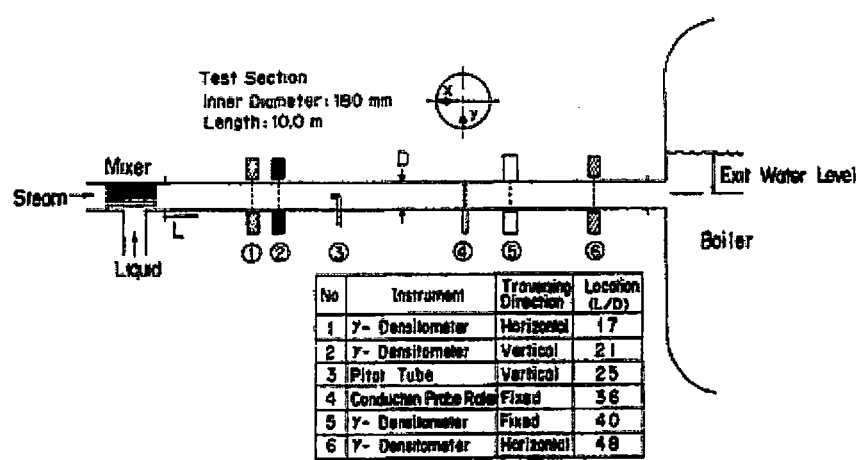


Figure 16-3 Test Section and Measurement Instruments (Kawaji et al., 1987)

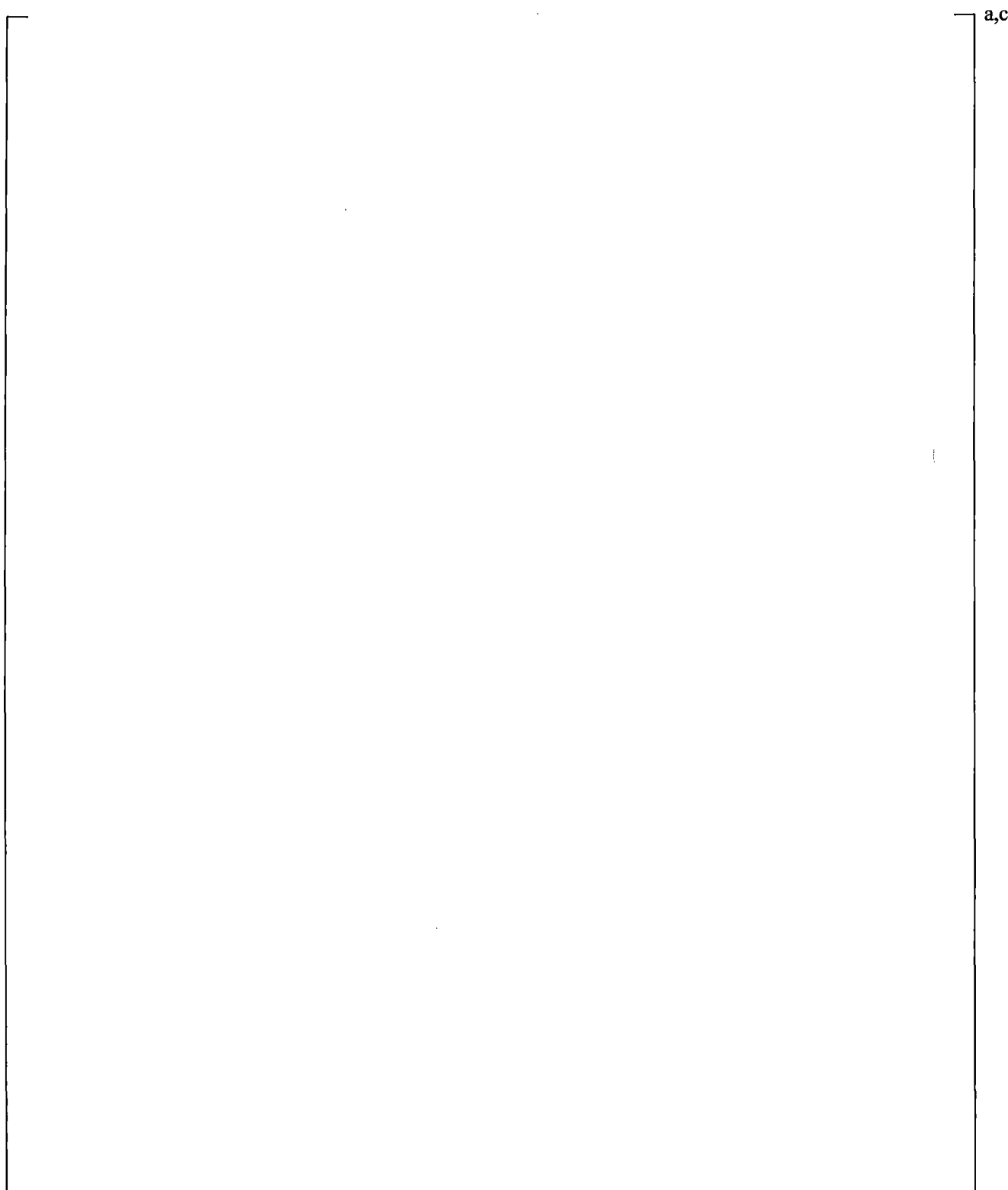


Figure 16-4 TPTF Test Data on WCOBRA/TRAC-TF2 Flow Regime Map

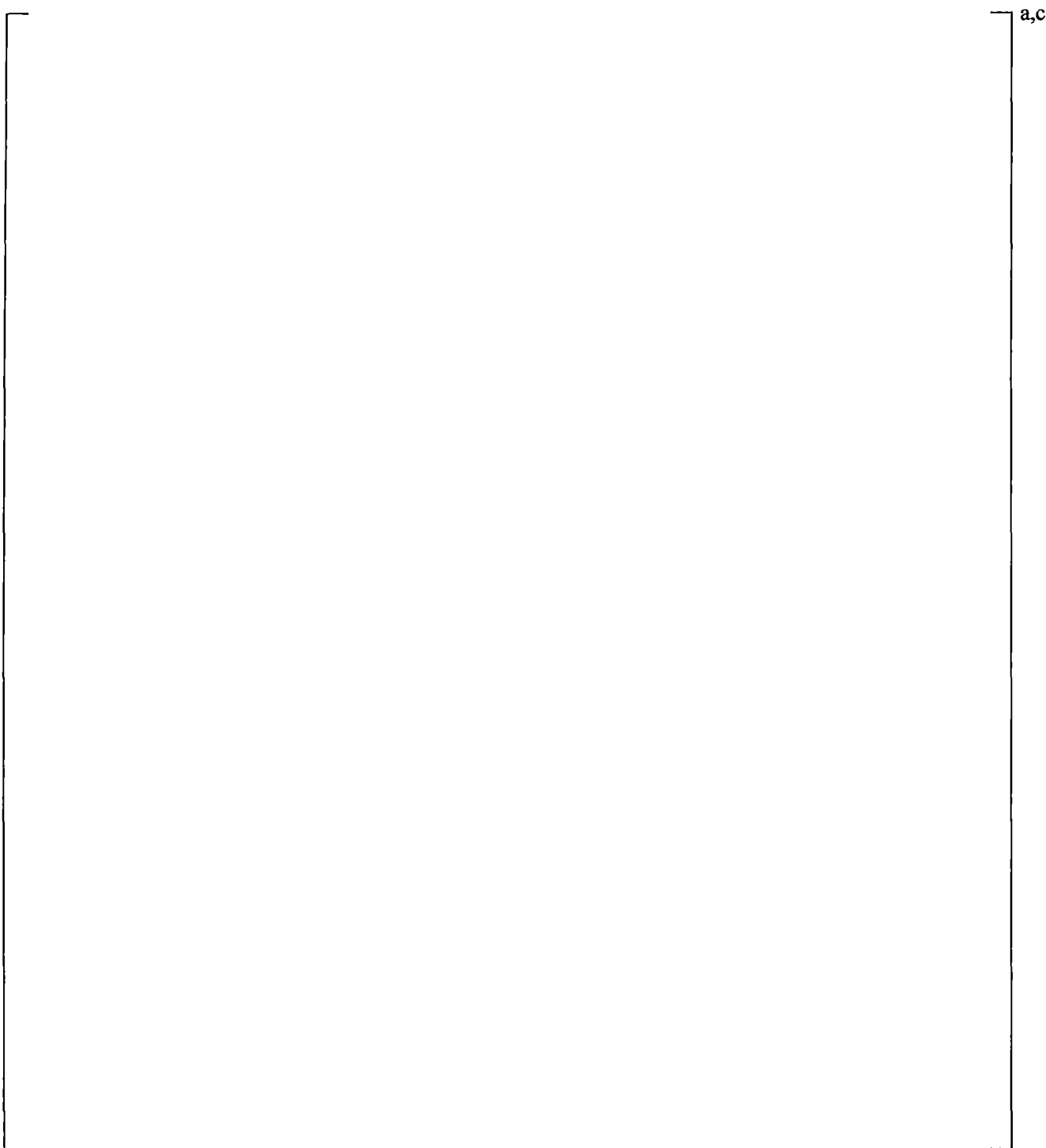
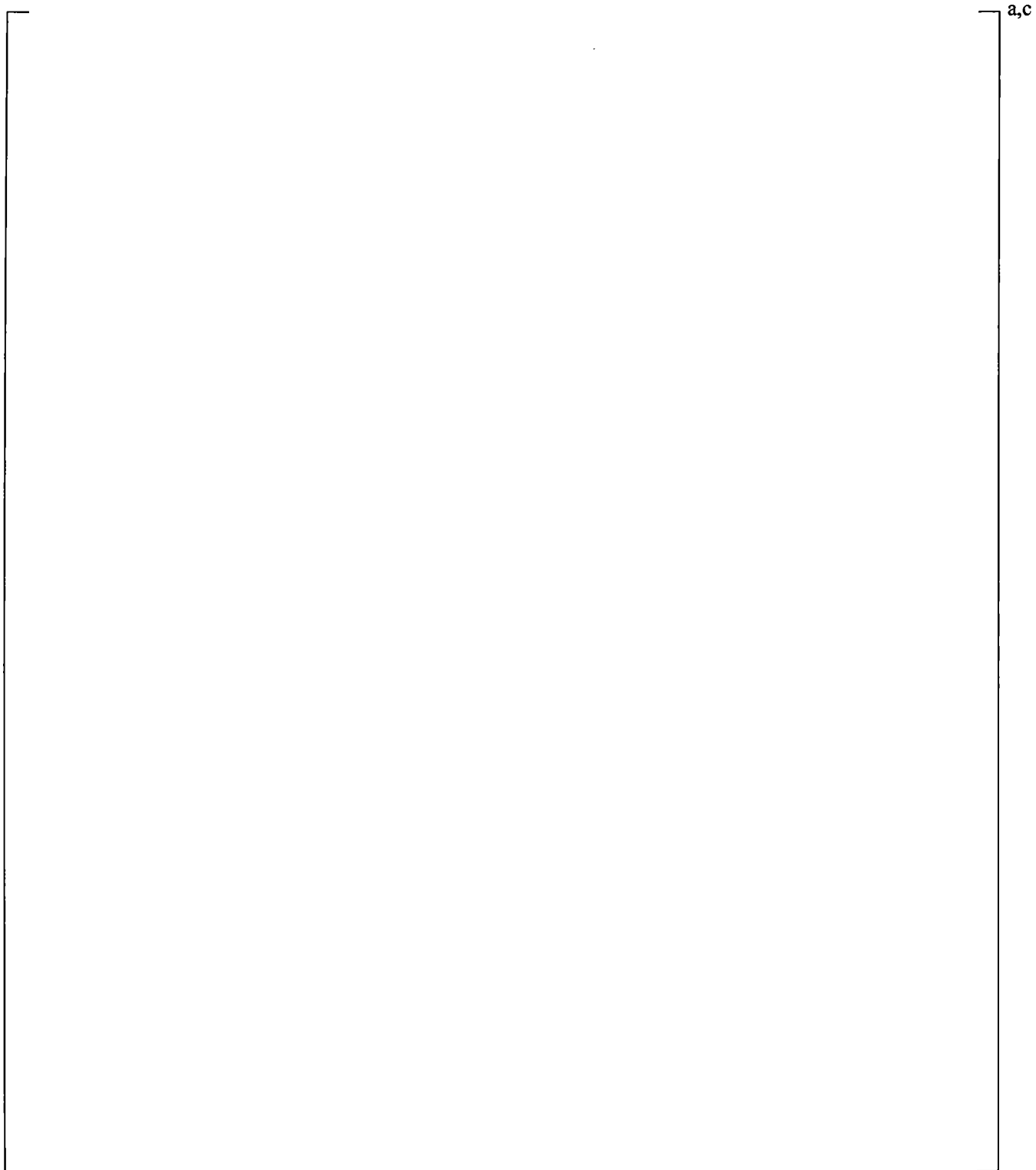
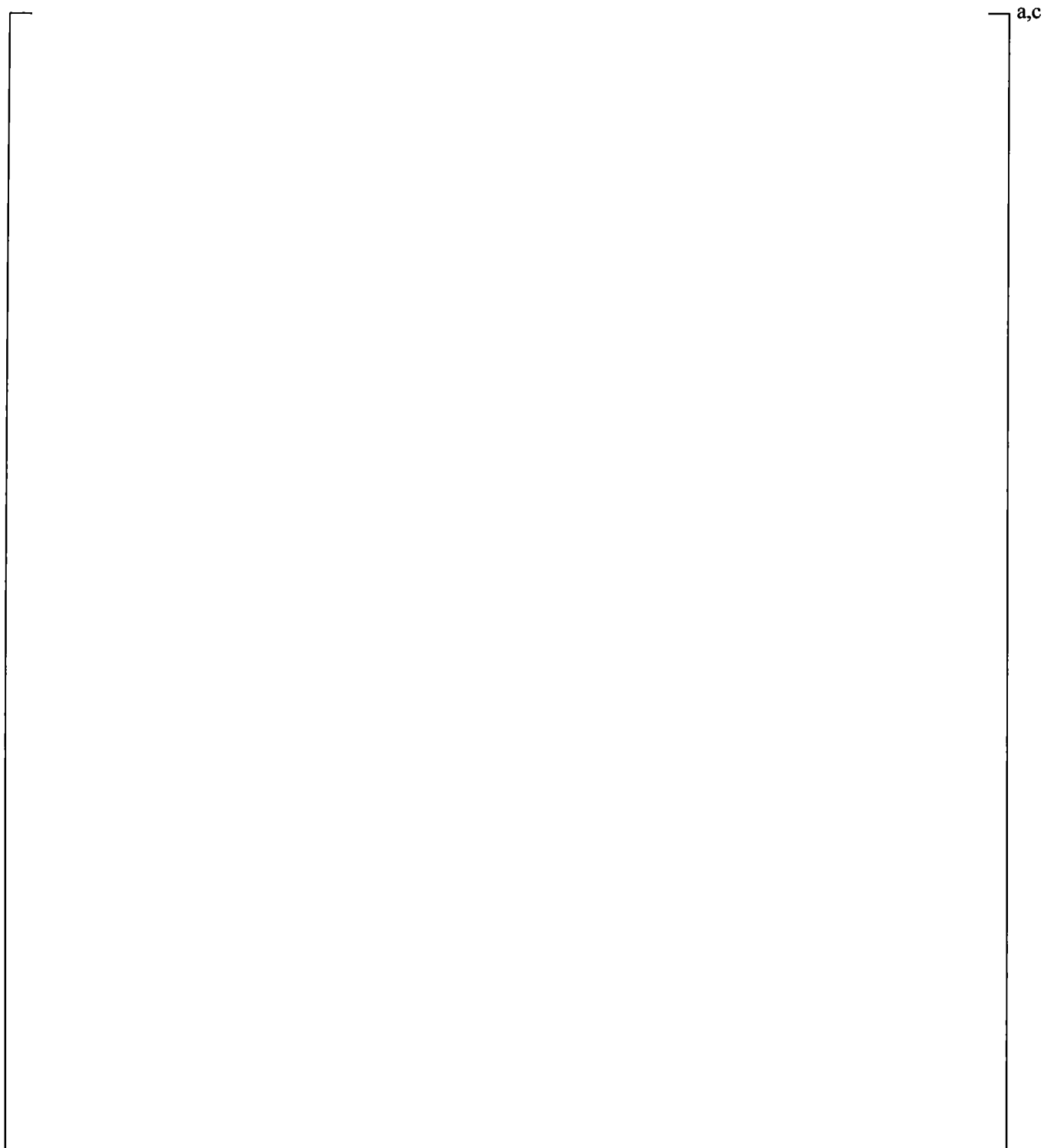


Figure 16-5 WCOBRA/TRAC-TF2 Input Models for TPTF. The Fill Component Corresponds to the Location of L/D=17 in the TPTF Facility



**Figure 16-6 Comparison Between Measured Void Fraction in
TPTF Run 722 and Predicted Void Fraction**



**Figure 16-7 Comparison Between Measured Void Fraction in
TPTF Run 845 and Predicted Void Fraction**

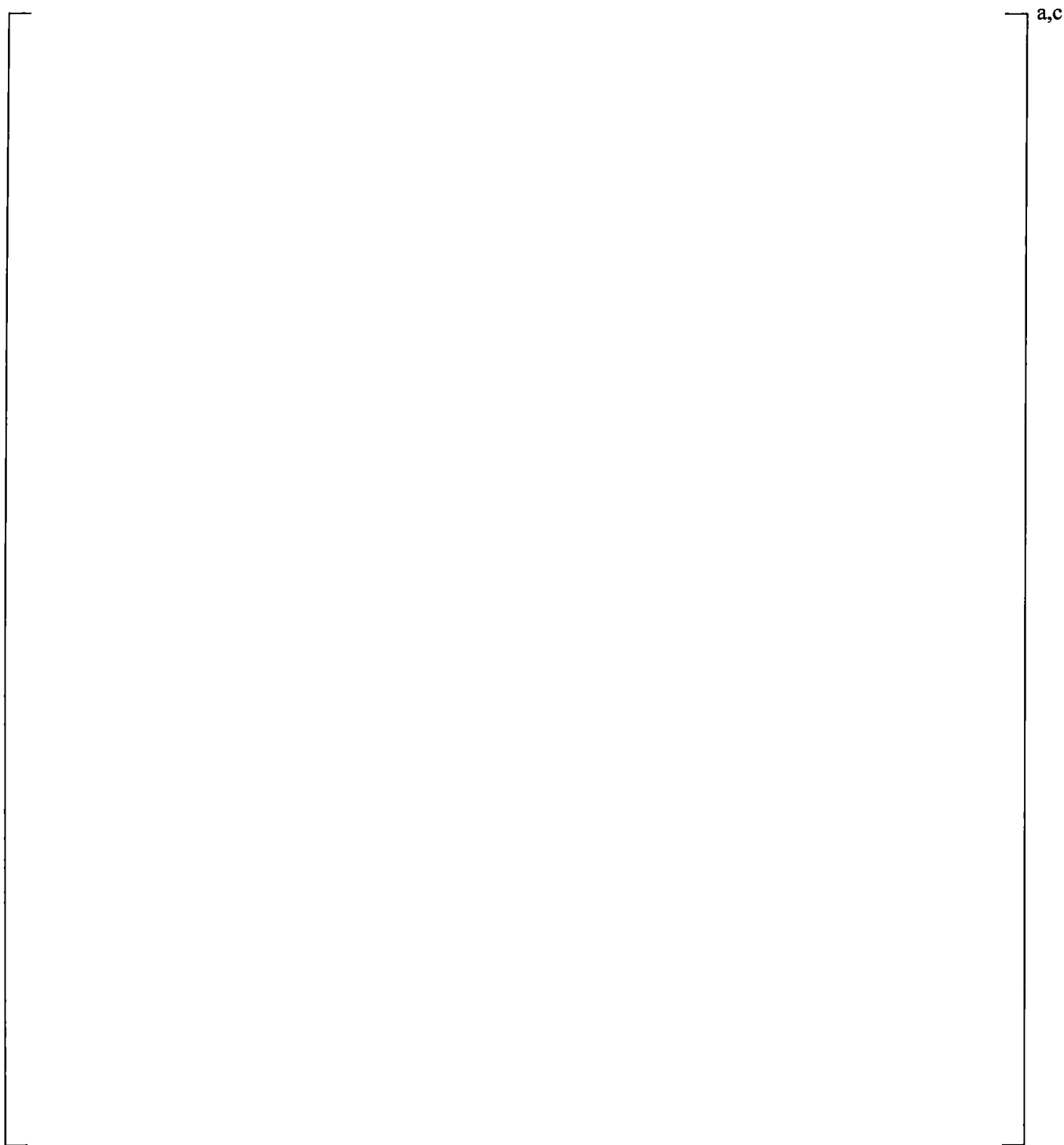


Figure 16-8 [

]^{a,c}

17 COLD LEG CONDENSATION: COSI EXPERIMENTS, ROSA-IV SB-CL-05 EXPERIMENT, AND UPTF 8A EXPERIMENT

17.1 INTRODUCTION

The condensation of steam by the cold liquid injected from the emergency core cooling system (ECCS) by sources such as the accumulator (ACC), safety injection (SI), and residual heat removal (RHR) injection (also called low head safety injection (LHSI)) into the cold leg is an important phenomenon during both small and large break loss-of-coolant accidents (LOCAs) (see Phenomena Identification and Ranking Table (PIRT) in Section 2, Volume 1). Cold leg condensation is ranked high (H) during the boiloff period and the recovery period of a small break LOCA. During these periods, the flow in the cold leg is stratified flow which would lead to negligible condensation due to low interfacial heat transfer. However, the impingement of the SI jet into the layer of liquid in the cold leg enhances condensation greatly. As the break size increases, the effect of the accumulator injection and of the higher pumped SI flow rates leads to an increased importance of condensation in the jet region. For a large break LOCA (LBLOCA), the cold leg condensation is the highest (H) ranked phenomenon during the refill period when the condensation process in the cold leg helps to reduce bypass flow at the top of downcomer, promoting emergency core cooling (ECC) penetration. The condensation effects are reduced during the reflood period as the accumulators end their injection and the low head safety injection continues, but condensation still impacts the break flow rate, the downcomer and core water inventory, and the liquid subcooling in the downcomer. Thus, a ranking of medium (M) was assigned for the cold leg condensation in the reflood stage of a LBLOCA. For intermediate breaks, the cold leg condensation is ranked high (H) for both the accumulator injection period and (low head) safety injection period. More details on the cold leg direct contact condensation processes were also discussed in Section 6.3.6, Volume 1.

As discussed in Section 6.3.6 of Volume 1, a special cold leg condensation model was developed and implemented in WCORBA/TRAC-TF2 to calculate the condensation heat transfer rate from cold water injection into the cold leg when the cold leg is expected to be in the horizontal stratified flow regime, wavy-dispersed flow regime, or annular-mist flow regime. The model basis, development and applicability are discussed in Section 6.3.6, Volume 1. The purpose of this section is to describe the assessment of the model against an independent dataset. The model is applied whenever the flow regime in the cold leg is predicted to be horizontal stratified, wavy-dispersed, or annular-mist, regardless of the break size or pressure. Therefore, it is important to assess the model performance, not only under conditions for which the model was developed (COSI experiments), but also under conditions at lower pressures and higher flow rates, more typical of intermediate and large break LOCA.

The assessments of small break LOCA and large break LOCA are given in Section 17.2 and Section 17.3, respectively. Section 17.2 covers condensation experiments designed for small break LOCA, such as Condensation On Safety Injection (COSI) and Rig-of-Safety Assessment Number 4 (ROSA-IV) SB-CL-05, which are high pressure and medium scale experiments, while Section 17.3 gives an assessment of the condensation in Upper Plenum Test Facility (UPTF) 8A experiments designed for large break LOCA (low pressure, full-scale experiments).

The focus of this section is to assess the WCOBRA/TRAC-TF2 performance in the analysis of condensation in the cold leg. Additional assessment of the condensation process, especially relative to condensation in the downcomer during the ECC bypass period of larger breaks, is provided in Section 19.

The cold leg condensation model uncertainty will be addressed in Section 29.1.6, Volume 3.

17.2 SMALL BREAK LOCA EXPERIMENTS – COSI AND ROSA SB-CL-05

To investigate the ability of the WCOBRA/TRAC-TF2 code to correctly predict condensation phenomena under conditions representative of small break scenarios, three different test facilities have been considered.

The Westinghouse COSI facility (Shimeck, 1988) is an approximately 1:100 scale model of the cold leg and safety injection lines of a Westinghouse-type pressurized water reactor (PWR), constructed specifically for investigating the interaction of steam and cold SI water in a prototypical PWR configuration and at typical PWR fluid conditions encountered during a small break LOCA.

The cold leg condensation correlation used in WCOBRA/TRAC-TF2 was fitted against a subset of Westinghouse COSI data. Therefore, an independent dataset is needed for the code assessment. The following tests were selected for this purpose.

1. The Westinghouse horizontal injection COSI experiment []^{a,c}

The diameter of []^{a,c}

[]^{a,c} The assessment of the Westinghouse horizontal injection COSI tests provides information on the capability of the WCOBRA/TRAC-TF2 code with the SI pipe running partially full.

2. The Framatome COSI experiments, which compared with the Westinghouse COSI experiments were performed at a lower pressure []^{a,c}, higher SI water temperature []^{a,c}, and with a []^{a,c} condition.
3. ROSA is an integral effects test (IET). The facility had volumes scaled at 1/48 of a typical Westinghouse 4-loop plant. Its layout was a 2-loop test facility. The diameter of the cold leg was 0.207 m. An extensive assessment of the ROSA integral effects test results is provided in Section 21. In this section, we are interested in the analysis of ROSA SB-CL-05 (Kawaji, M., et al., 1986), a 5% side break in the cold leg with high head safety injection, with respect to the assessment of the condensation process in the cold leg. In the assessment, only the []^{a,c} were modeled in the WCOBRA/TRAC-TF2 input decks. This makes it a type of []^{a,c} and this ROSA SB-CL-05 SET provides an SI condensation experiment in a cold leg larger than the COSI experiment. The effect of superheated steam on the cold leg condensation model is also assessed by the ROSA SB-CL-05 cases.

17.2.1 Test Facilities and Tests Description

As discussed above, there are three test facilities serving as the basis for the assessment plan for small break LOCA. Those are the Westinghouse COSI facility, Framatome COSI facility, and ROSA-IV SB-CL-05 test facility. Both the Westinghouse COSI and Framatome COSI tests are separate effects tests. ROSA-IV SB-CL-05 is an integral effects test, however separate effects test data was extracted for the purpose of the assessment of the condensation rate in the cold leg. The facilities are introduced separately in the following sections.

Westinghouse COSI Facility

In the 1980's, the COSI experiments were performed as a four party venture between Westinghouse, Framatome, the French Atomic Energy Commission (CEA), and Électricité de France (EDF). The objective of these experiments was to characterize the condensation phenomenon and develop an accurate condensation model which could be used to evaluate the condensation heat transfer in a PWR during a LOCA.

The Westinghouse COSI facility is a 1:100 scale model of the cold leg and safety injection ports of a Westinghouse-type PWR. It is capable of operating at pressures []^{a,c} and at appropriately scaled flow rates to cover nearly the entire range of injection conditions expected in a PWR small break transient, during which condensation on the safety injection water phenomenon was judged important. The main scaling philosophy followed in designing the system was to maintain similar []^{a,c} in the cold leg as would be encountered in a small break LOCA.

The main loop of the test facility []^{a,c}

A removable weir with a height []^{a,c} was incorporated into a spool piece at the outlet end of the main pipe to allow for varying of the water level retained within the cold leg pipe. Measurements were available for the steam and liquid flow rates in and out of the test

assembly, the temperature of fluid entering and exiting the test section, and the system pressure and differential pressures. Within the test section, a series of thermocouple rakes provided the temperature profile and the information concerning stratification of the liquid. Significant amounts of temperature stratification were observed and combined with examination of the actual temperatures the conclusion was that the overall behavior depicted in Figure 17-3 was taking place. Fluid temperatures upstream and downstream of the injection point were stable and indicated that a counter-current flow pattern was in place on the upstream side. On the downstream side, the flow pattern was co-current or counter-current depending on the steam flow configuration, but again stratification was noted. In the immediate vicinity of the injection port, the thermocouple measurements exhibited significant temperature oscillations, indicating turbulent conditions. The downward impingement of the safety injection jet, combined with the significant influx of steam to this point, supported a turbulent jet mixing zone, with rather complex flow and heat transfer patterns. The conclusion from analysis of the data was that most of the condensation mechanism occurs in the proximity of the jet mixing zone. The Westinghouse cold leg condensation model in Section 6.3.6 of Volume 1 was developed based on the assumption that the majority of condensation occurs near the safety injection point.

A large matrix of tests was conducted over the course of the program by both Westinghouse and Framatome (Gros d'Aillon, 1987), and some reconfigurations of the facility test section were performed with regard to the length of the main pipe in the test assembly and the angle and size of the injection piping. A core series of 15 tests, with 75 individual data, from Westinghouse configuration was conducted.

The COSI experimental data report only gives boiler power and heat loss for the entire test loop. The net condensation heat transfer rate Q_{cond} in the cold leg is calculated [

$$\left[\quad \right]^{a,c} \quad (17-1)$$

[]

$$]^{a,c}$$

The condensation heat transfer rate in the downcomer Q_{DC} is estimated by [

$$]^{a,c}$$

[]

$$]^{a,c}$$

The process of the data reduction is listed below for the Westinghouse COSI tests.

1. The net condensation heat transfer rate, Q_{net} , in the test section (including downcomer) is []^{a,c}
 2. The net condensation efficiency is calculated using Equation 17-2,
- $$\eta_{net} = \frac{Q_{net}}{m_{SI}(h_f - h_{SI})} \quad (17-2)$$
- where Q_{net} is net condensation heat transfer in the test section, m_{SI} is the SI flow rate and h_f and h_{SI} are the enthalpy of saturated water and the SI water (at the test pressure and SI temperature).
3. The net condensation efficiency is []^{a,c} in several runs, for which the test report did not provide an explanation. In this data reduction process, the net condensation in those cases is []^{a,c}.
 4. The condensation heat transfer rate in the test section is split into two portions, the condensation in the cold leg (Q_{cond}) and the condensation in the downcomer (Q_{DC}). The condensation heat transfer rate in the downcomer is evaluated using 3 pairs of tests with the only differences being the []^{a,c}. There are 3 pairs of tests identified for different pressures, []^{a,c}. All 5 runs in each pair are used to establish the downcomer condensation efficiency at the particular pressure. The []^{a,c} is the nominal condensation efficiency at the pressure and the maximum and minimum values provide the uncertainty of the downcomer condensation efficiency.
 5. The net condensation efficiency minus the efficiency caused by downcomer condensation is the cold leg condensation efficiency. []^{a,c}

6. The cold leg condensation heat transfer rate is evaluated using the cold leg condensation efficiency and the condensation potential with Equation 17-3.

$$Q_{cond} = \eta_{cond} m_{SI} (h_f - h_{SI}) \quad (17-3)$$

There were two types of Westinghouse COSI tests based on their SI angle relative to the direction of the cold leg. The tests with []^{a,c} are called "vertical" COSI test, and the tests with []^{a,c} injection angle are called "horizontal" COSI test. Section 6.3.6 in Volume 1 describes in detail how the vertical injection tests have been used to define the cold leg condensation model implemented in

WCOBRA/TRAC-TF2. The vertical injection COSI tests also serve as a part of the assessment documented in this section because the data will be used to validate the WCOBRA/TRAC-TF2 code with the cold leg condensation model, not only the cold leg condensation correlation itself. The Westinghouse vertical COSI data, which were utilized to define the safety injection condensation correlation, are listed in Table 17-1.

Compared with the vertical COSI tests, the horizontal COSI tests have a []^{a,c}

Test data from the Westinghouse horizontal COSI tests are shown in Table 17-2.

Framatome COSI Facility

The Framatome COSI facility is similar to the Westinghouse COSI facility. The loop structure shown in Figure 17-1 is the same for the Framatome COSI facility, but the Westinghouse test section in Figure 17-2 was replaced with the Framatome test section, which is shown in Figure 17-5. The cold leg diameter of both test sections is 0.118 m, but the length of the Framatome test section (cold leg) is only []^{a,c}

[]^{a,c} in the Westinghouse test section. Compared to the Westinghouse setup, this shorter test section is more appropriate from a scaling standpoint.

The Framatome test section had two injection points (Boileau, 1988). One injection was []^{a,c}

The diameter of this injection port was []^{a,c}. Another injection port was located in the horizontal plane with a diameter of []^{a,c}. Since there is no data reported for the larger horizontal pipe, that flow configuration is not considered in this report.

Another difference between the Westinghouse test section and the Framatome test section is steam flow.

[]^{a,c}

[]^{a,c}

The Framatome test section had two weir heights, []^{a,c} cold leg diameters, and a case without a weir. In contrast to the two downcomer water levels []^{a,c} used in the Westinghouse COSI tests, the water level in the downcomer was consistently set to []^{a,c} relative to the cold leg. In the Framatome test, the water level in downcomer was always in the high position []^{a,c}

The system pressure in the Framatome COSI tests was either []^{a,c}. The pressure of []^{a,c} is lower than the lowest system pressure []^{a,c} in the Westinghouse COSI tests.

The range of SI water temperature in the Framatome COSI tests was []^{a,c}, while the SI water temperature in the Westinghouse COSI tests was almost constant []^{a,c}. High SI

water temperature is possible during the later stages of a SBLOCA in some PWRs, when the SI water comes from the sump instead of the RWST and is not cooled by the component cooling water.

The calculation for the heat loss, downcomer condensation, and upper and lower bound of the Q_{cond} follows the same procedure used for the Westinghouse COSI data reduction.

The condensation in the downcomer is a function of the downcomer water level and the SI water mass flow rate. Both the Westinghouse and Framatome COSI experiments used the same downcomer (a structural difference only exists at the cold leg). The downcomer water level in the Framatome COSI tests was []^{a,c}. Therefore, the downcomer condensation can be evaluated using the same equation for the Westinghouse COSI test with a downcomer water level of []^{a,c}. However, it is noted that [

] ^{a,c}. Thus, the downcomer condensation efficiency of [

] ^{a,c}. It is also noted that the SI injection rate in the Framatome COSI tests is generally higher than those in the Westinghouse COSI tests. However, the downcomer condensation efficiencies []^{a,c}.

The Framatome COSI experiments include both []^{a,c}. It is noted that the cold leg condensation model does not depend on the []^{a,c} flow configuration. The cold leg condensation model predicts the same condensation heat transfer rate if all the parameters in the correlation are the same. To validate the cold leg condensation model against the possible []^{a,c} in the broken cold leg, the Framatome inverse COSI tests are included in the assessment plan.

[

] ^{a,c}

The qualified Framatome COSI test data with zero break flow are shown in the Table 17-3.

JAERI ROSA-IV/LSTF Facility

The ROSA-IV Large Scale Test Facility (LSTF) is a 1/48 volumetrically scaled facility discussed in Section 21. In this section, only the ROSA-IV SB-CL-05 test is considered. []^{a,c}

Table 17-4 provides the major dimensions and scaling factors of the ROSA facility in comparison to the COSI facilities and typical PWR dimensions. While the detailed ROSA-IV LSTF system description is

discussed in Section 21, some key features, specifically relative to the cold leg and SI injection, are reviewed here.

[

|

|

|

]^{a,c}

The test facility was very well instrumented and this allowed for the extraction of separate effects test data. The test SB-CL-05 was considered for the purpose of analyzing the cold leg condensation in detail. The cold leg condensation in the cold leg was in a slow transient state. However an accurate evaluation of the cold leg condensation was possible by assuming a quasi-steady state progression of the transient.

[

|

|

]^{a,c} in ROSA is modeled and simulated in the separate effects test.

[

]^{a,c}

[]
 $I^{a,c}$

To set up the steady state separate effects test, several instantaneous flow conditions in the cold leg are captured. []

[]
 $I^{a,c}$ The flow conditions are given in Table 17-5.

In summary, the following key considerations are applied to select the tests for the assessment:

- The Westinghouse vertical injection COSI experiment (i.e., with injection angle of 90°) has been used, as documented in detail in Section 6.3.6, Volume 1 to define the cold leg condensation model implemented in WCOBRA/TRAC-TF2. The assessment of the vertical injection COSI tests is provided here to verify the WCOBRA/TRAC-TF2 code with the cold leg condensation model described in Section 6.3.6 of Volume 1, thus to confirm the correct code implementation of the model documented in Section 6.3.6, Volume 1.
- The Westinghouse horizontal injection COSI experiment had a []^{a,c} injection angle in the flow direction, different than the vertical injection experiments. The diameter of the horizontal injection port was larger than the diameters in vertical experiment. This larger diameter and the 45° injection angle cause the water to []^{a,c}. The assessment of WCOBRA/TRAC-TF2 against the Westinghouse horizontal injection serves the purpose of validating the cold leg condensation model.
- The Framatome COSI experiment provides the assessment of the code at lower pressure []^{a,c} and at higher SI water temperature []^{a,c} than the Westinghouse experiments.
- The ROSA SB-CL-05 separate effects test provides an SI condensation experiment with a larger diameter cold leg. The effect of superheated steam on the cold leg condensation model is also assessed by simulating ROSA SB-CL-05 cases.

17.2.2 Description of WCOBRA/TRAC-TF2 Models

Figure 17-9 shows the component layout of the WCOBRA/TRAC-TF2 model of the Westinghouse vertical COSI facility. []

[]
 $I^{a,c}$

[]^{a,c}

The cold leg condensation model is applied only []^{a,c}.
As discussed in Section 6.3.6 of Volume 1, []^{a,c}.

[]^{a,c} The condensed water flows to the BREAK component. It is noted that the physical location of the vertical SI injection is not at the center of the cold leg in the Westinghouse COSI test facility. Only the scaled part of the cold leg (Figure 17-2) is simulated. The injection port is at the junction of the TEE component. This logic is applied to both the Westinghouse horizontal COSI and Framatome COSI test facilities.

The layouts of the Westinghouse horizontal COSI and Framatome COSI test facilities are similar to that of the Westinghouse vertical COSI facility. The major differences are the diameter of SI line and the angle of the SI line, which is []^{a,c} for the horizontal COSI.

The nodding diagram for the ROSA SB-CL-05 safety injection tests is similar to that of the Westinghouse vertical COSI facility, which is given in Figure 17-9. However, the diameters and lengths of the cold leg and SI line are different, as are the system pressure, steam flow rate, and SI flow rate. The []^{a,c} of the ROSA facility is also simulated.

The nodding diagram for the Framatome counter-current (Inverse) COSI tests is shown in Figure 17-10. []^{a,c}

[]^{a,c}

17.2.3 WCOBRA/TRAC-TF2 Results

The condensation heat transfer rate is calculated from the heat transfer rate of the liquid, which is given as:

$$q_{il} = h_{il} A_i (T_{sat} - T_l) \quad (17-4)$$

where q_{il} is the heat transfer rate from the liquid to the gas-liquid interface, h_{il} is the heat transfer coefficient from the liquid to the interface, and A_i is the gas-liquid interfacial area. Because the cold leg condensation model is only applied to the junction cell of the TEE component, the heat transfer comparison is only on the junction cell. []^{a,c}

[]
] ^{a,c}

The comparison between the calculated condensation heat transfer rate and the measured heat transfer rate for the Westinghouse COSI tests is shown in Figure 17-11a. [

] ^{a,c}

There are differences between the vertical COSI and horizontal COSI. [

] ^{a,c}

The comparison between the calculated condensation heat transfer rate and the measured heat transfer rate for Framatome COSI tests is shown in Figure 17-12. The test series at [

] ^{a,c}

The comparison between the calculated condensation heat transfer rate and the measured heat transfer rate for the ROSA SB-CL-05 cold leg condensation tests is shown in Figure 17-13. [

] ^{a,c}

The steam temperatures in the cold leg for ROSA SB-CL-05 are shown in Figures 17-14 to 17-17. Steam superheating is constant upstream of the safety injection. The steam superheating gradually decreases downstream of the safety injection. [

]^{a,c}

17.2.4 Small Break LOCA Experiments Conclusions

WCOBRA/TRAC-TF2 models for three test facilities (Westinghouse COSI, Framatome COSI, and ROSA SB-CL-05) are developed to assess the cold leg condensation model with focus on the small break LOCA scenario.

The overall assessment of code predictions against data from Westinghouse COSI, Framatome COSI, and ROSA-IV SB-CL-05 is summarized in Figure 17-18. [

]^{a,c}

The uncertainty range of the cold leg condensation model will be assessed in Section 29, Volume 3.

17.3 LARGE BREAK LOCA EXPERIMENTS: UPTF TEST 8A

17.3.1 Introduction

In Section 17.2, the assessment of the condensation process in the cold leg was focused on the small break LOCA scenario. For the large breaks, condensation is of the highest relative importance during the refill period. When the ECC water is no longer bypassed in the refill period, the condensation process at the top of the downcomer helps to induce downflow through the core, promoting cooling. In this scenario, the thermal hydraulic conditions are different from those analyzed in the previous sections, and the effect of the accumulator injection and the low head safety injection flow rates needs to be assessed.

[

]^{a,c}

As part of the UPTF test matrix, two cold leg flow regime separate effects tests, Tests 8 and 25, were run to investigate steam/water flow phenomena in the cold legs during the refill/reflood phase of a large break LOCA. These phenomena include steam condensation on subcooled ECC at different flow regimes (e.g., plug flow, stratified flow) in the cold leg. Test 8A (2D/3D Program Report, 1988) focused on the effect of ECC flow rate on cold leg flow phenomena. Test 25A (2D/3D Program Report, 1990) investigated the effects of steam flow rate and steam superheating. UPTF Test 25A provides the assessment basis for different hydrodynamic phenomena and is discussed in Section 19, but the

implication to the cold leg condensation model will be addressed in this section. The integral UPTF Test 8A model with the VESSEL and the loop structure is developed and assessed in Section 19. In this section, the UPTF Test 8A is modeled as a single TEE as discussed in Section 17.3.2.

UPTF Test 8A was performed to investigate the flow regimes that might arise in the intact cold legs of a PWR during a postulated LBLOCA, when subcooled ECC liquid mixes with superheated steam. During the blowdown and refill phases, the flow of accumulator water is of sufficient magnitude to theoretically condense all the steam flowing into the cold leg. During reflood the low head safety injection flow (LHSI/RHR), at its minimum levels, is typically insufficient to condense all the steam flowing into the cold leg.

Cold leg liquid slug formation and oscillations may occur when the subcooled injected ECC liquid causes condensation of the steam flowing in the cold leg. A liquid slug is a region in which the cold leg is completely filled with liquid. Steam flowing through the cold leg from the pump towards the downcomer condenses when in contact with subcooled injected ECC liquid. A liquid slug in the region between the injection point and the downcomer can form when the liquid subcooling and the interfacial heat transfer are sufficient to completely condense the flow of steam.

Once the liquid slug forms, further condensation of steam results in a reduction of pressure upstream of the liquid slug. A local reduction in pressure at the condensation point causes the slug to move back towards the ECC injection point. The movement may be expected to continue until the liquid slug completely covers the injection point.

Eventually, the pressure increase, due to the steam entering the cold leg, is sufficient to move the liquid slug towards the downcomer again. These conditions were experienced in UPTF Test 8.

17.3.2 WCOBRA/TRAC-TF2 Model Description

The WCOBRA/TRAC-TF2 model of UPTF Test 8A is documented in Section 19.3.7 with the full structure of the loop and the vessel. The single TEE model in this section serves as the base model for validating the cold leg condensation model and performing sensitivity studies. Unlike the integral UPTF Test 8A model in Section 19.3.7, which represents the entire facility, the TEE model only represents

[^{a,c}] The advantage of the single TEE model is that [^{a,c}]

[^{a,c}]. The single TEE model development includes the following cases:

1. Base Model – [^{a,c}]

2. Sensitivity Study on ECC Injection Angle – [^{a,c}]

3. Sensitivity Study on Cold Leg Noding – []^{a,c}
4. Sensitivity Study on ECC Injection Node – []^{a,c}
5. Sensitivity Study on Ranging Cold Leg Condensation Rate Multiplier (KCOSI) – []^{a,c}
6. Sensitivity Study on Ranging Horizontal Stratification Criteria (HS_SLUG) – []^{a,c}

The noding diagram is shown in Figure 17-20. []^{a,c}

17.3.3 WCOBRA/TRAC-TF2 Results: Base Model

The WCOBRA/TRAC-TF2 simulation of UPTF Test 8A was run for the first 200 seconds of the test, which covered the period where flow was injected into the Loop 2 intact cold leg. The as-measured injection steam and ECC flow rates were used as boundary conditions in the WCOBRA/TRAC-TF2 model. The BREAK component was maintained at a constant pressure of 390 kPa (57 psia).

In Section 19, it is demonstrated that the WCOBRA/TRAC-TF2 simulation of UPTF Test 8A with the full vessel model and loop structure shows []^{a,c}.

The TEE model for UPTF Test 8A provides additional validation on the cold leg condensation model with a fixed boundary condition. []^{a,c}

The measured and predicted temperatures in the Loop 2 cold leg are compared in Figures 17-21 through 17-24. At the pump exit (Figure 17-21), the single TEE model predicts a lower degree of oscillation with a shorter time period at the beginning of stage 1 than the integral model does (Figure 19.3-156). []^{a,c}

The single TEE model predicted the water temperature near the injection point is shown in Figure 17-22.

[

]^{a,c}

Figure 17-23 shows the comparison between the measured temperature and the WCOBRA/TRAC-TF2 predicted water temperature at the downstream injection point. [

]^{a,c}

Figure 17-24 shows the comparison between the measured temperature and the WCOBRA/TRAC-TF2 predicted water temperature at the cold leg near the vessel inlet. The overall effect of the cold leg condensation is shown in this figure. [

]^{a,c}

17.3.4 WCOBRA/TRAC-TF2 Results: Sensitivity Studies

Sensitivity Study on ECC Injection Angle

This case studies the impact of the ECC injection angle on the cold leg condensation. [

]^{a,c}

[

]^{a,c}

[

]^{a,c}**Sensitivity Study on Cold Leg Noding**

Figure 17-28 shows the noding size sensitivity on the predicted water temperatures at the injection cell of the cold leg. The predicted temperatures are different from stage 3 to stage 6. Figures 17-29 and 17-30 show the same comparison downstream of the injection cell and at the outlet of the cold leg, respectively.

[

]^{a,c}**Sensitivity Study on ECC Injection Node**

This is a sensitivity study on the junction node to which ECC water is injected. [

]^{a,c}

Sensitivity Study on Cold Leg Condensation Rate Multiplier (KCOSI)

The uncertainty of the cold leg condensation model is ranged using the cold leg condensation rate multiplier, KCOSI. [

]^{a,c}

Sensitivity Study on Horizontal Stratification Criteria

The cold leg condensation model requires the flow regime to be horizontal stratified flow, wavy-dispersed flow, or annular-mist flow. The transition from horizontal stratified flow to non-stratified flow is ranged by the multiplier HS_SLUG. [

]^{a,c}]^{a,c}

]^{a,c}

17.3.5 Large Break LOCA Experiments Conclusions

UPTF Test 8A is utilized to assess the applicability of the cold leg condensation model in a large break LOCA. The simulation of UPTF Test 8A with the full vessel and loop structure in Section 19 shows

[]^{a,c}. The single TEE models for the UPTF Test 8A experiment were assessed in this section. []^{a,c}

The sensitivity studies give the following conclusions:

[]

]^{a,c}

UPTF Test 25A is another cold leg condensation test for the reflood stage of LBLOCA characterized with a variable steam flow rate and a substantial steam superheating. The simulation and results of UPTF Test 25A are discussed in Section 19.3.

17.4 OVERALL CONCLUSIONS

WCOBRA/TRAC-TF2 models for four test facilities (Westinghouse COSI, Framatome-COSI, ROSA SB-CL-05, and UPTF Test 8A) are developed to assess the cold leg condensation model over conditions representative of both small and large break LOCA scenarios.

The overall assessment documented in Sections 17.2 and 17.3, together with the LBLOCA assessment in Section 19, is summarized in Sections 17.2.4 and 17.3.5 for small and large break LOCA conditions, respectively. The comparison with experimental results shows that the WCOBRA/TRAC-TF2 code is able to predict condensation within a reasonable range of uncertainty. The WCOBRA/TRAC-TF2 predictions are judged to be acceptable for the purpose of analyzing a full spectrum of break sizes in a PWR LOCA.

Sensitivity analyses to key parameters using a single TEE model of UPTF Test 8A cold leg and ECC lines are also performed. The sensitivities consider the ECC branch line orientation relative to the cold leg, the nodding size selected for modeling the cold leg, the condensation rate multiplier (KCOSI) and the horizontal stratified flow regime transition criterion (HS_SLUG). Results of the sensitivity studies are summarized in Section 17.3.5 to support methodology decisions for the purpose of modeling a PWR.

Additional validation of the cold leg condensation model is provided by the simulation of UPTF Test 25A in Section 19.3.

17.5 REFERENCES

1. 2D/3D Program Upper Plenum Test Facility Experimental Data Report, 1990, "Test No. 25, Downcomer/Cold Leg Steam/Water Interaction Test," E314/90/11, KWU.
2. 2D/3D Program Upper Plenum Test Facility Experimental Data Report, 1988, "Test No. 8, Cold/Hot Leg Flow Pattern Test," U9 316/88/12, KWU.
3. Boileau, H., 1988, "Condensation on Safety Injection, FRAMATOME Analysis Report," EP/TA/DC.0771.
4. Emmerling, R., et al., 1988, "UPTF: Program and System Description," Siemens U9 414/88/023.
5. Gros d'Aillon, M., 1987, "Essais De Condensation En Regime Permanent," (COSI Report), SETh/LET/87-45.
6. Kawaji, M., et al., 1986, "ROSA-IV/LSTF 5% Cold Leg Break LOCA Experiment Data Report, Run SB-CL-05," JAERI-memo 61-056.

7. The ROSA IV Group, 1985, "ROSA-IV Large Scale Test Facility (LSTF) System Description," JAERI-M 84-237.
8. Shimeck, D. J., 1988, "COSI SI/Steam Condensation Experiment Analysis," WCAP-11767.

Table 17-1 Westinghouse Vertical COSI Tests Data

Table 17-1 Westinghouse Vertical COSI Tests Data

a,c

**Table 17-1 Westinghouse Vertical COSI Tests Data
(cont.)**

a,c

Table 17-2 Westinghouse Horizontal COSI Tests Data

a,c

Table 17-3 Selected Framatome COSI Tests Data and Calculation for Qcond

a,c

Table 17-4 Comparison of Facilities for Cold Leg Condensation Assessment

a,c

Table 17-5 ROSA SB-CL-05 SI Condensation Test Data for SETs

a,c

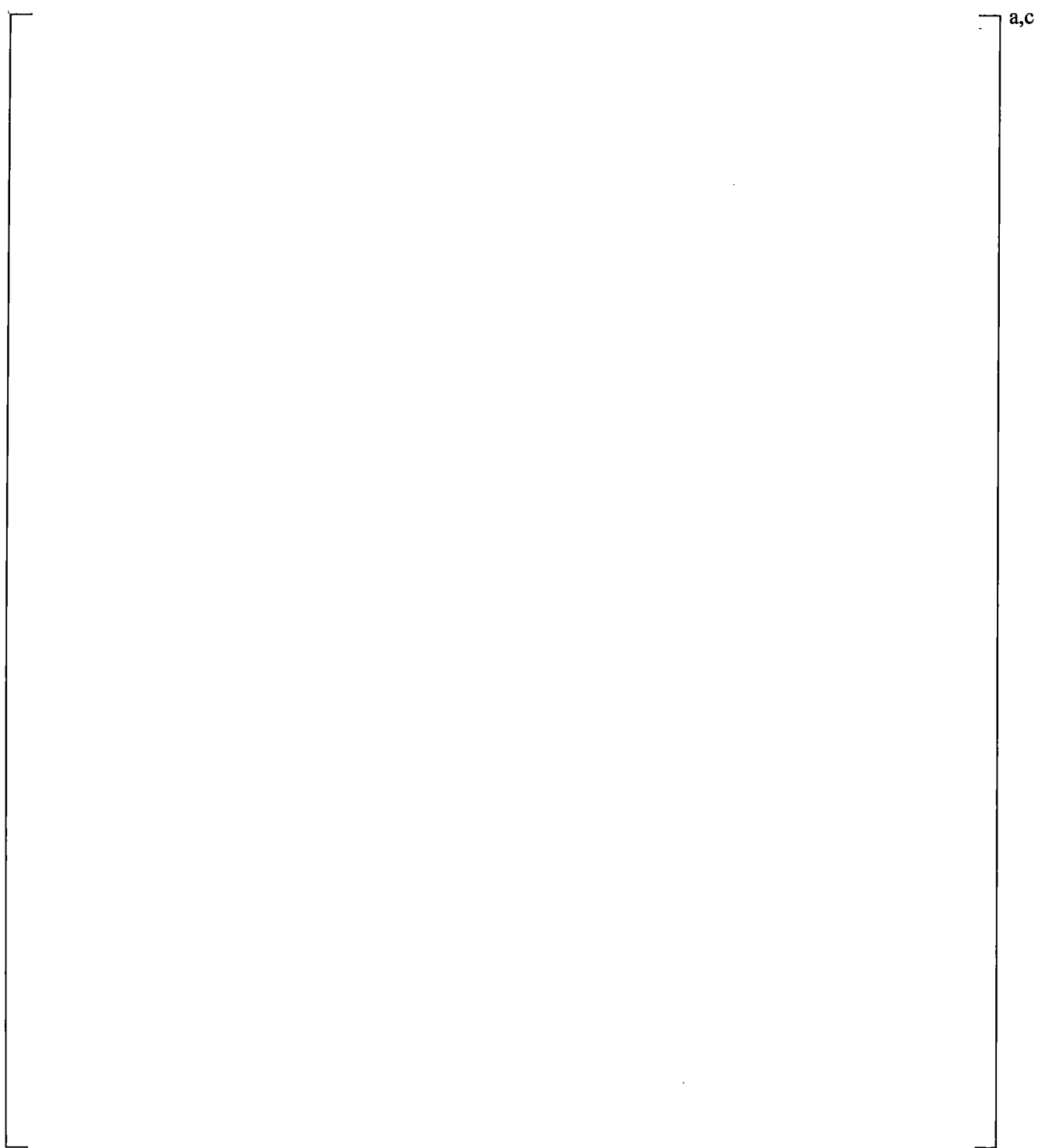


Figure 17-1 COSI Facility Arrangement

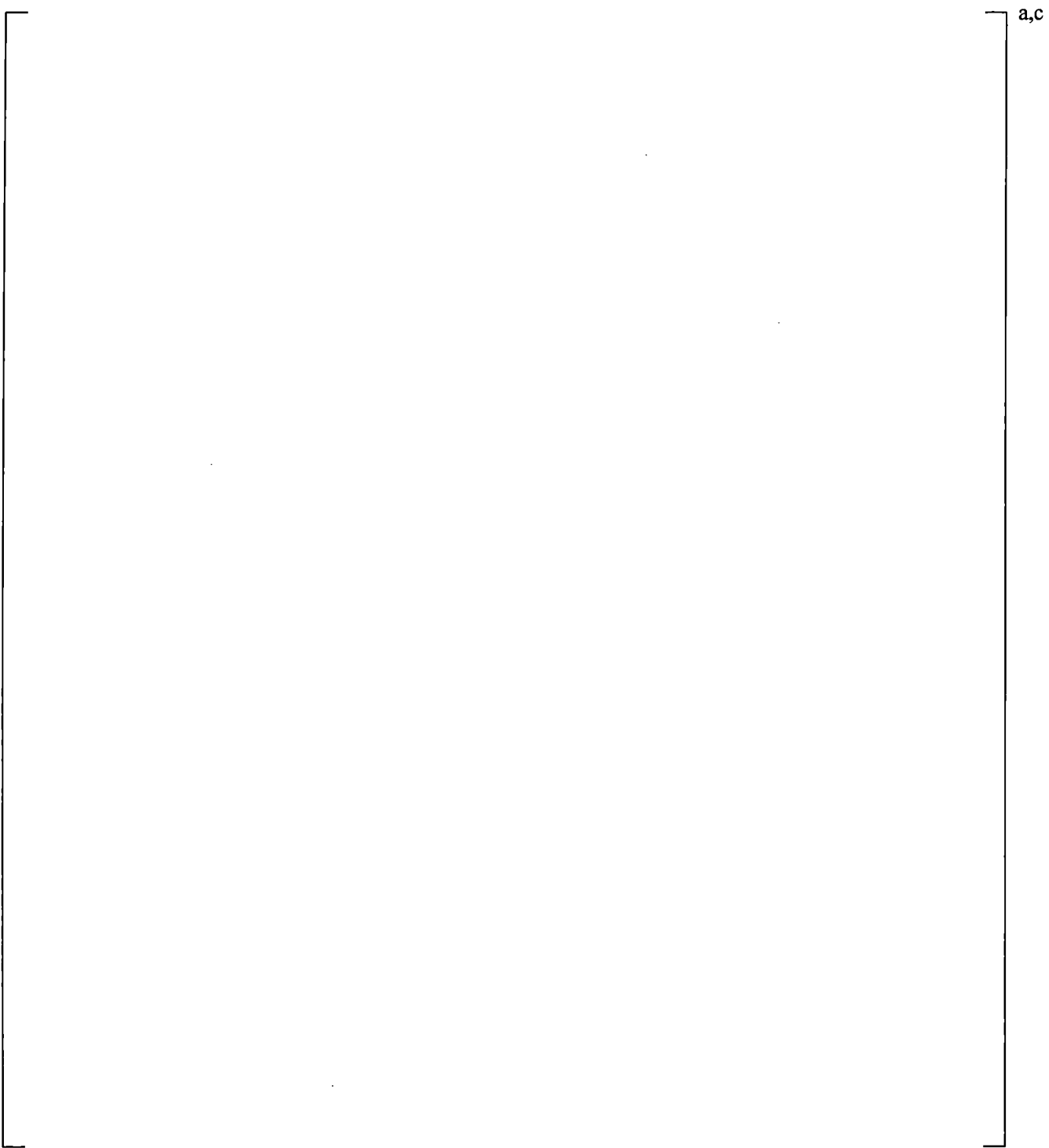


Figure 17-2 Westinghouse COSI Test Section Arrangement

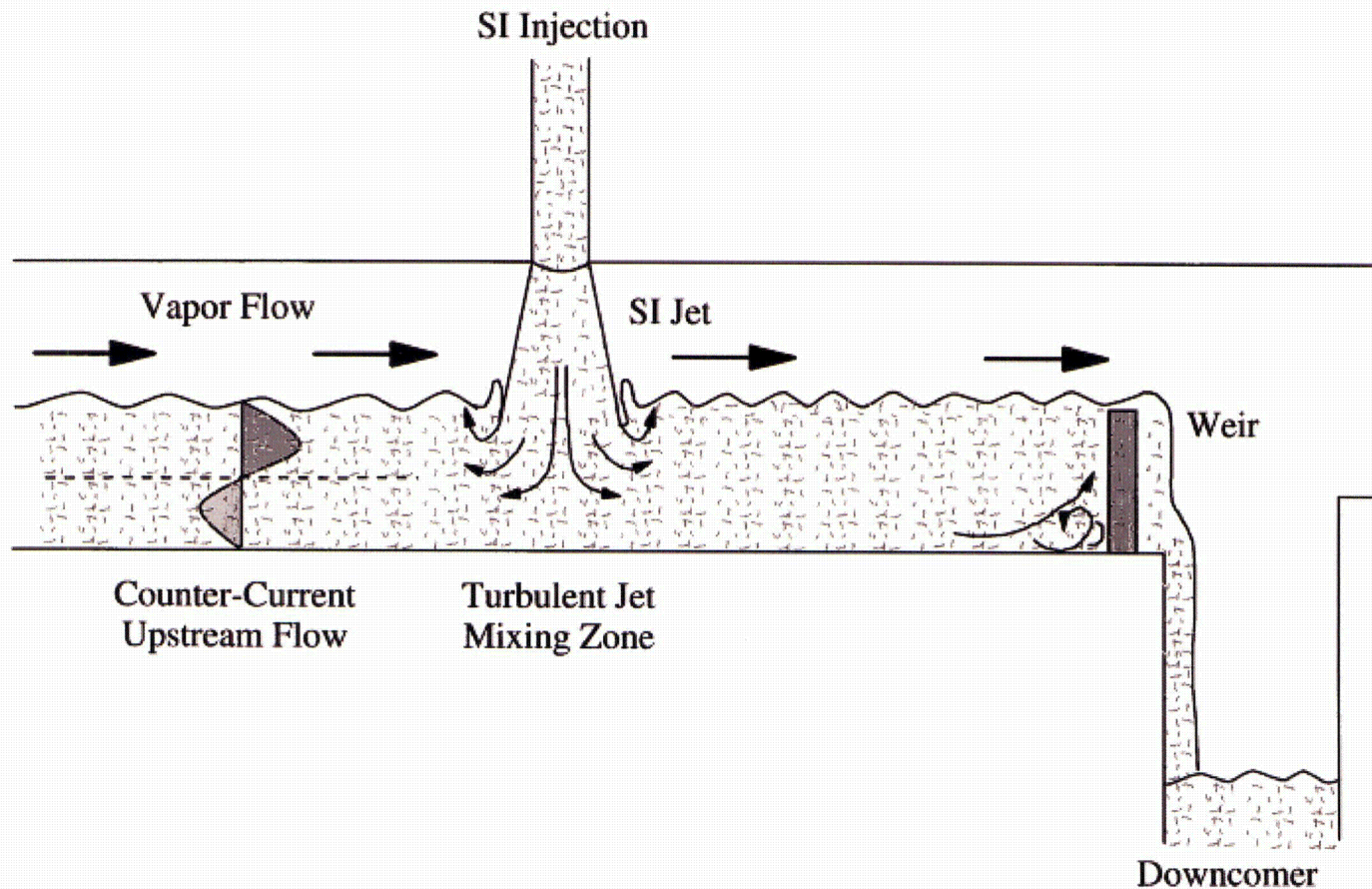


Figure 17-3 Depiction of Flow Patterns in the Test Section as Deduced from Data

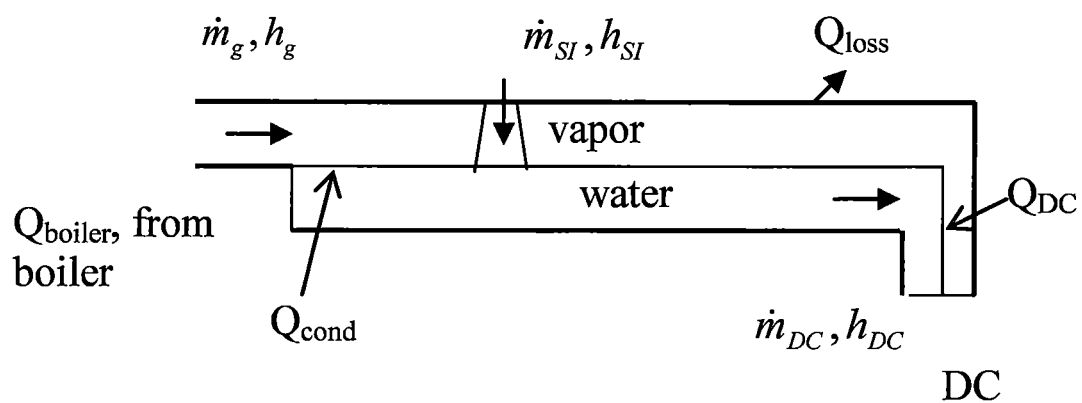


Figure 17-4 Illustration of Condensation in COSI Test Section

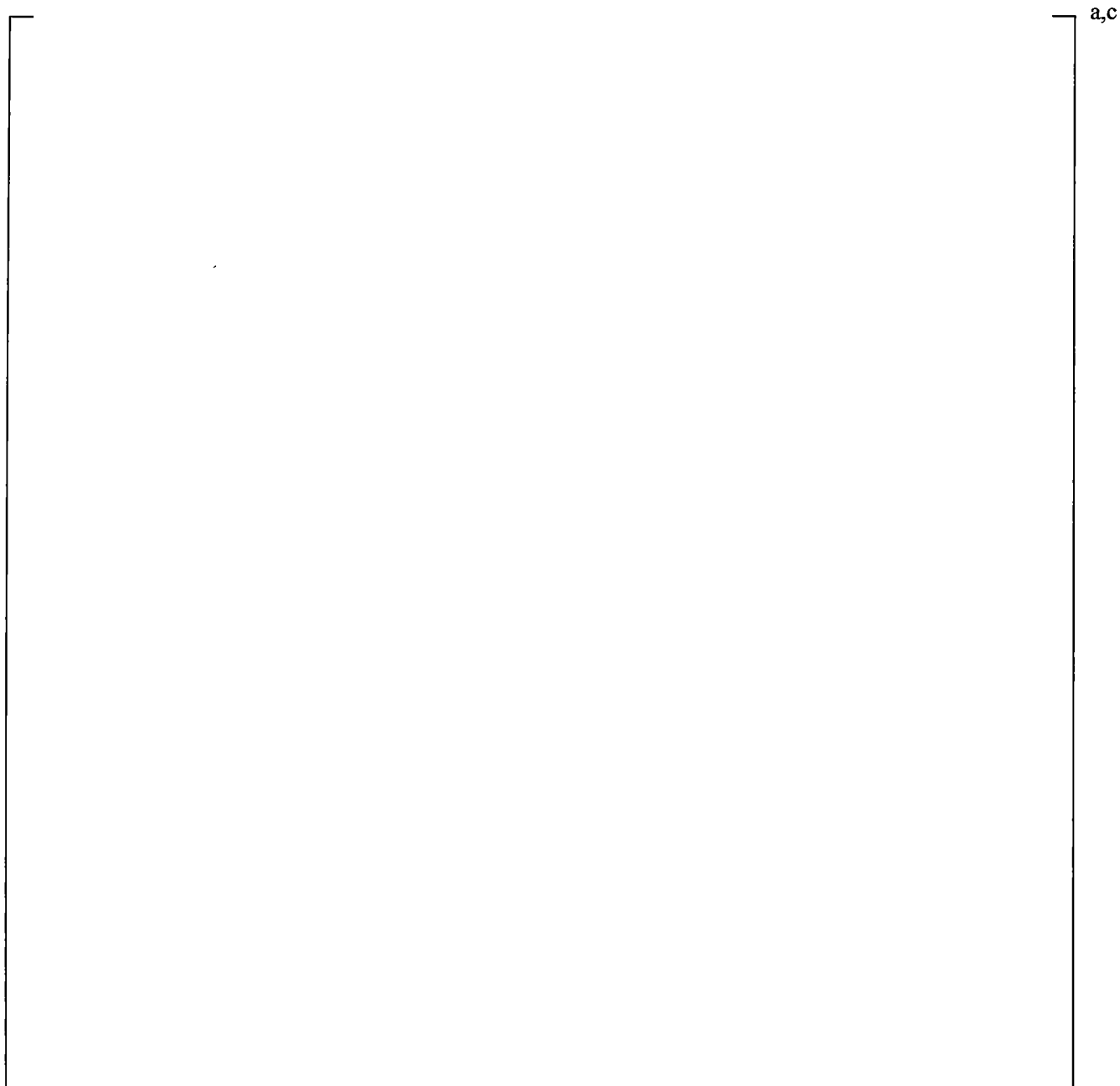


Figure 17-5 [

]^{a,c}



Figure 17-6 Comparison of Westinghouse Test Section and Framatome Test Section in Cross Section of Cold Leg



Figure 17-7 General Structure of Cold Leg from Crossover Leg to Downcomer in the ROSA Facility



Figure 17-8 Schematics of ECCS Configuration in ROSA-IV SB-CL-05



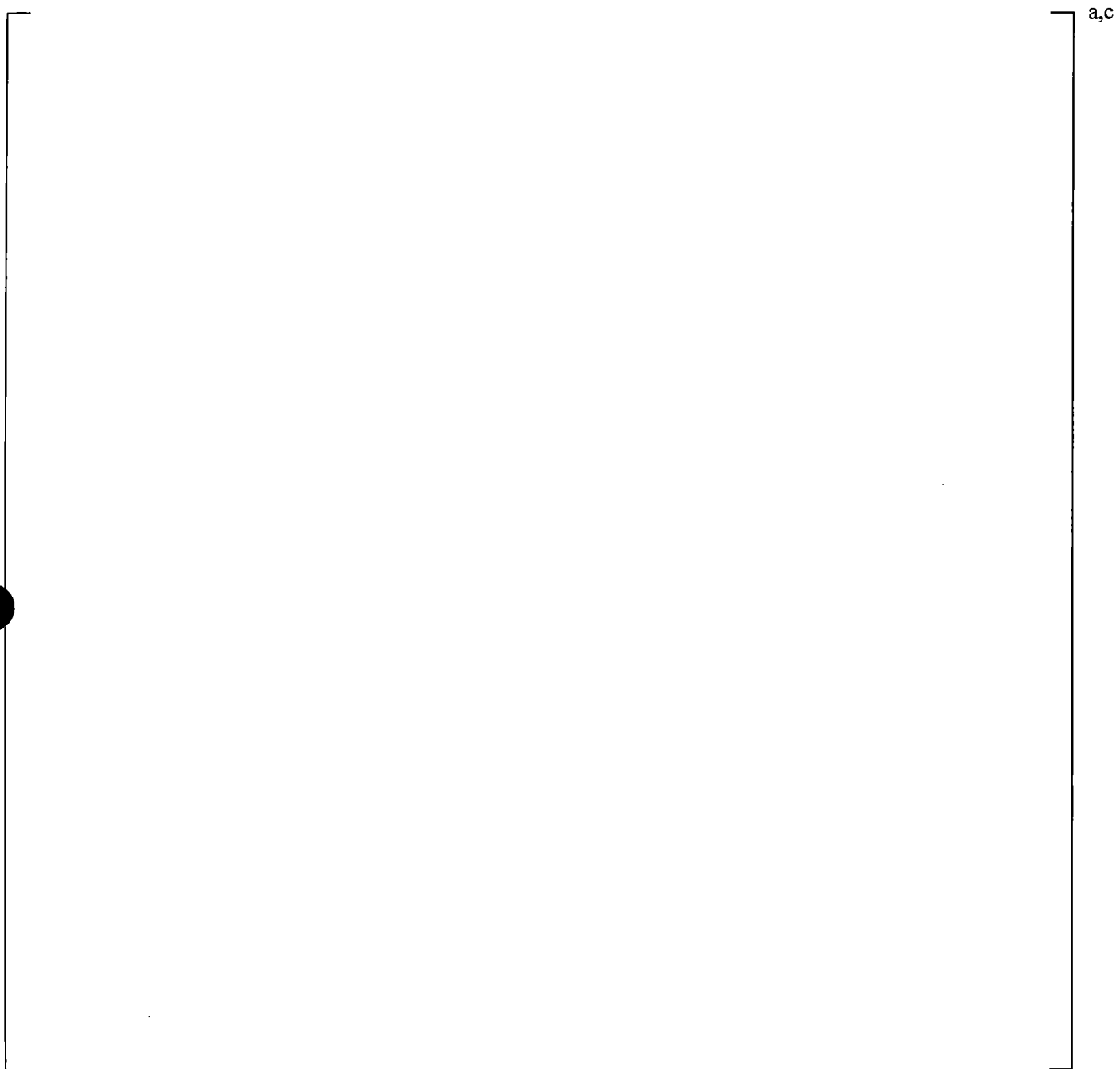
Figure 17-9 WCOBRA/TRAC-TF2 Single TEE Noding Diagram for Westinghouse Vertical COSI, Framatome COSI, and ROSA-IV SB-CL-05; for Westinghouse Vertical COSI, the Inclination angle of SI Line is 45°



Figure 17-10 WCOBRA/TRAC-TF2 Two-TEE Noding Diagram for Framatome Inverse COSI Tests



Figure 17-11a Comparison between Measured Westinghouse COSI Condensation Heat Transfer Rate and WCOBRA/TRAC-TF2 Predicted Condensation Heat Transfer Rate



**Figure 17-11b Predicted Heat Transfer Rate for Westinghouse COSI
(TEE Junction Cell is Number 4)**

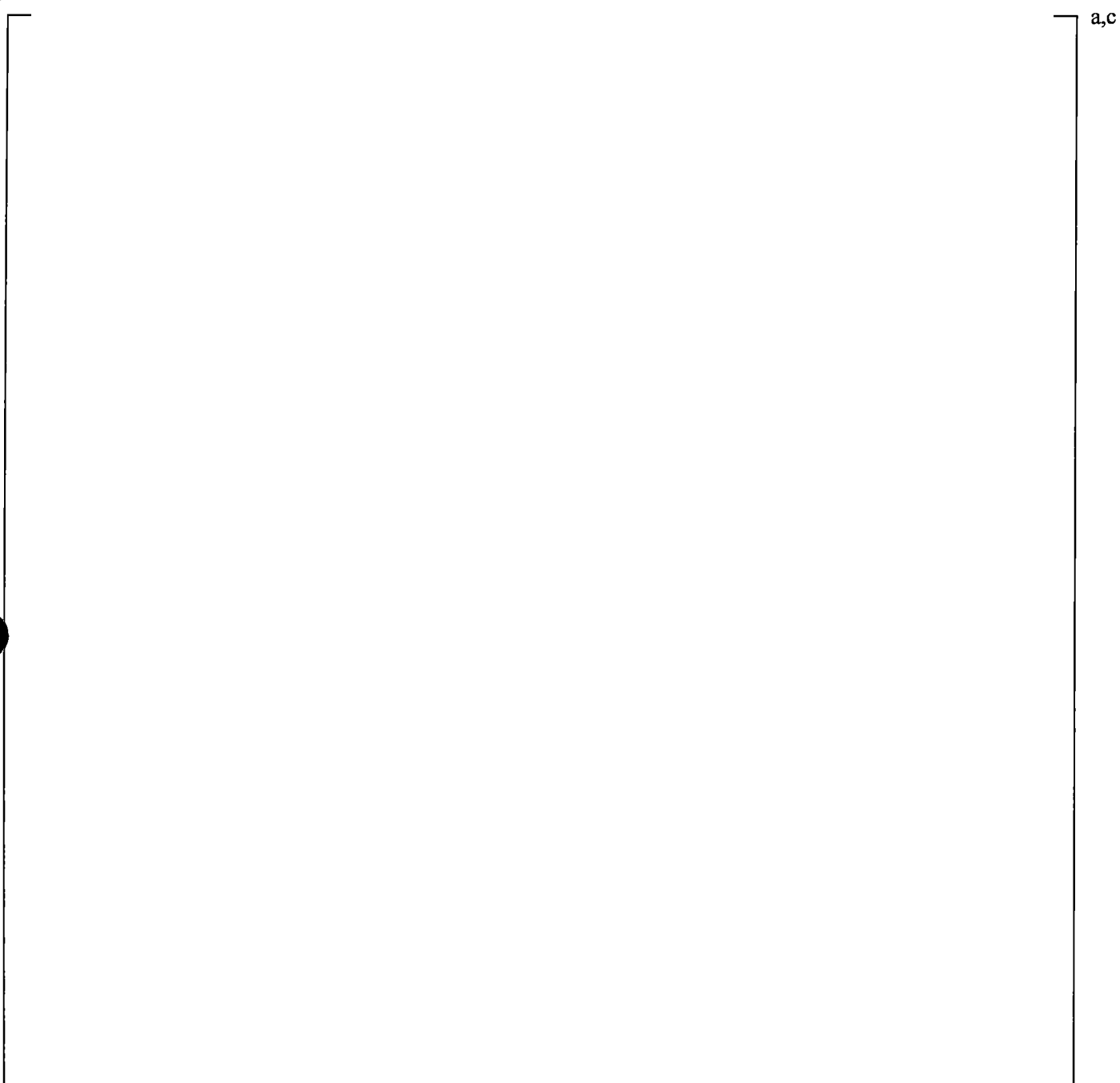


Figure 17-12 Comparison between Measured Framatome COSI Condensation Heat Transfer Rate and WCOBRA/TRAC-TF2 Predicted Condensation Heat Transfer Rate. Data in Circles are Tests with High SI Temperature (~80C)



Figure 17-13 Comparison between Measured ROSA SB-CL-05 SI Condensation Heat Transfer Rate and WCOBRA/TRAC-TF2 Predicted Condensation Heat Transfer Rate

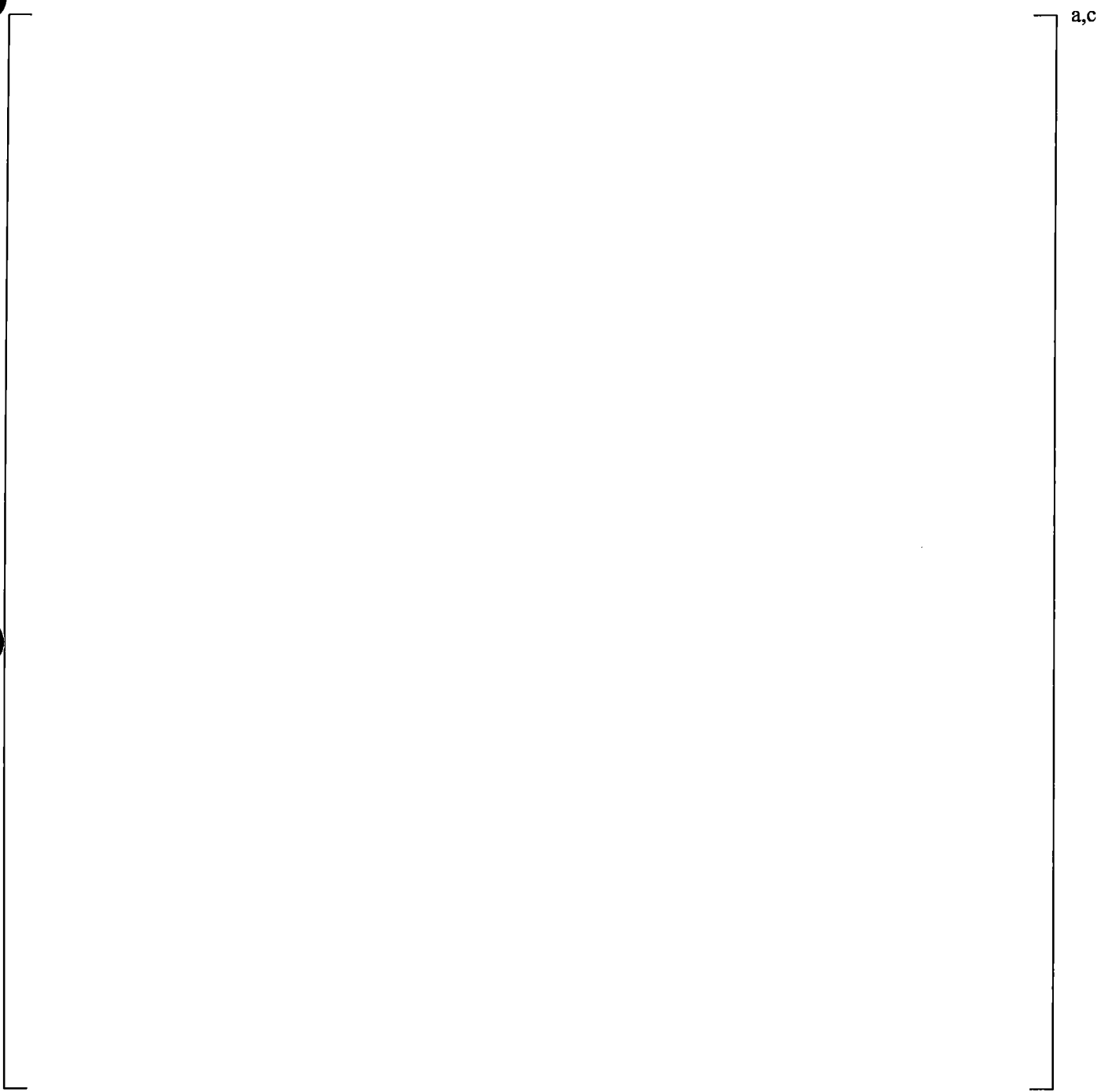


Figure 17-14 Steam Temperature Profile in Cold Leg in ROSA Test No. 1

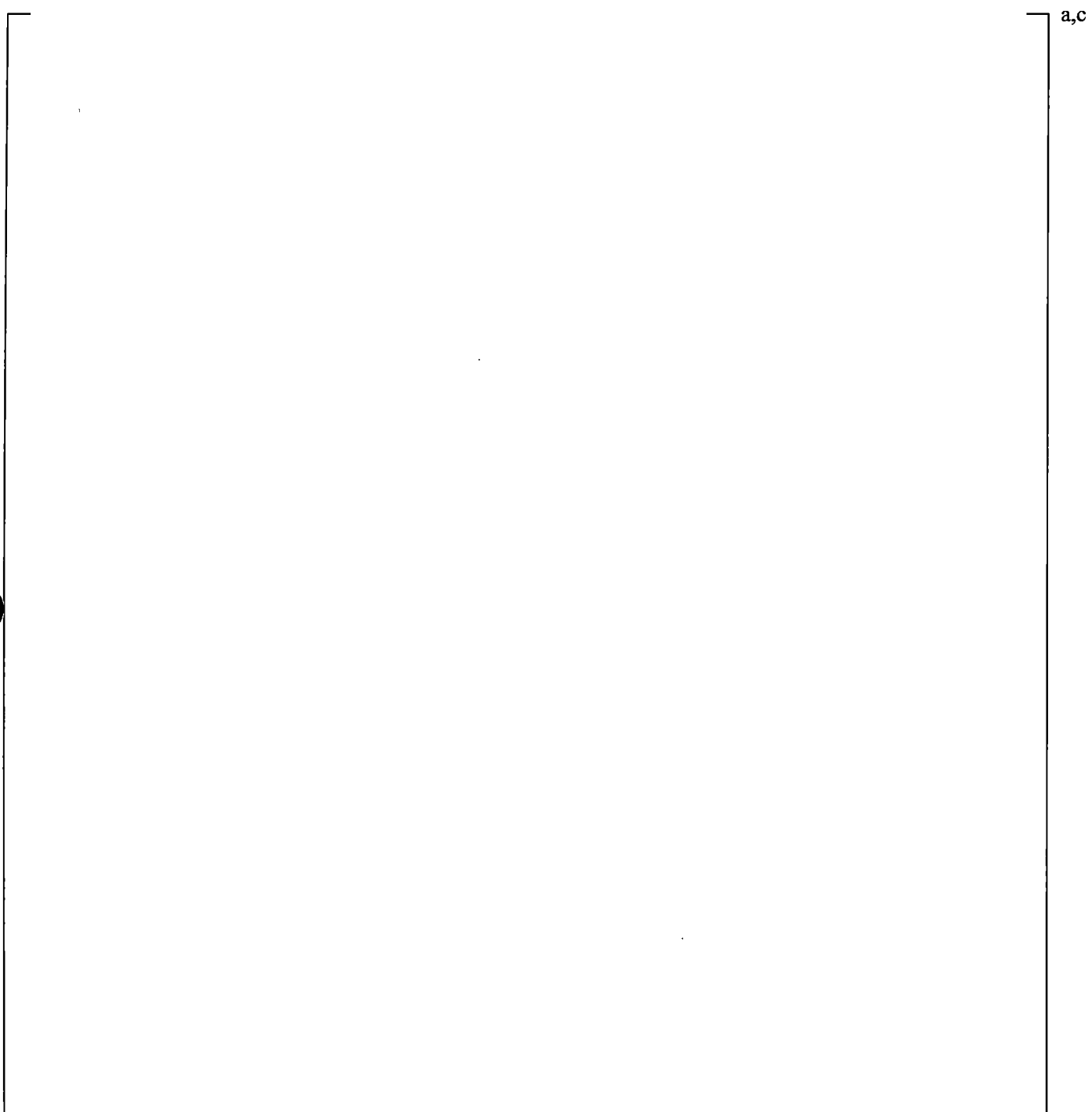


Figure 17-15 Steam Temperature Profile in Cold Leg in ROSA Test No. 2

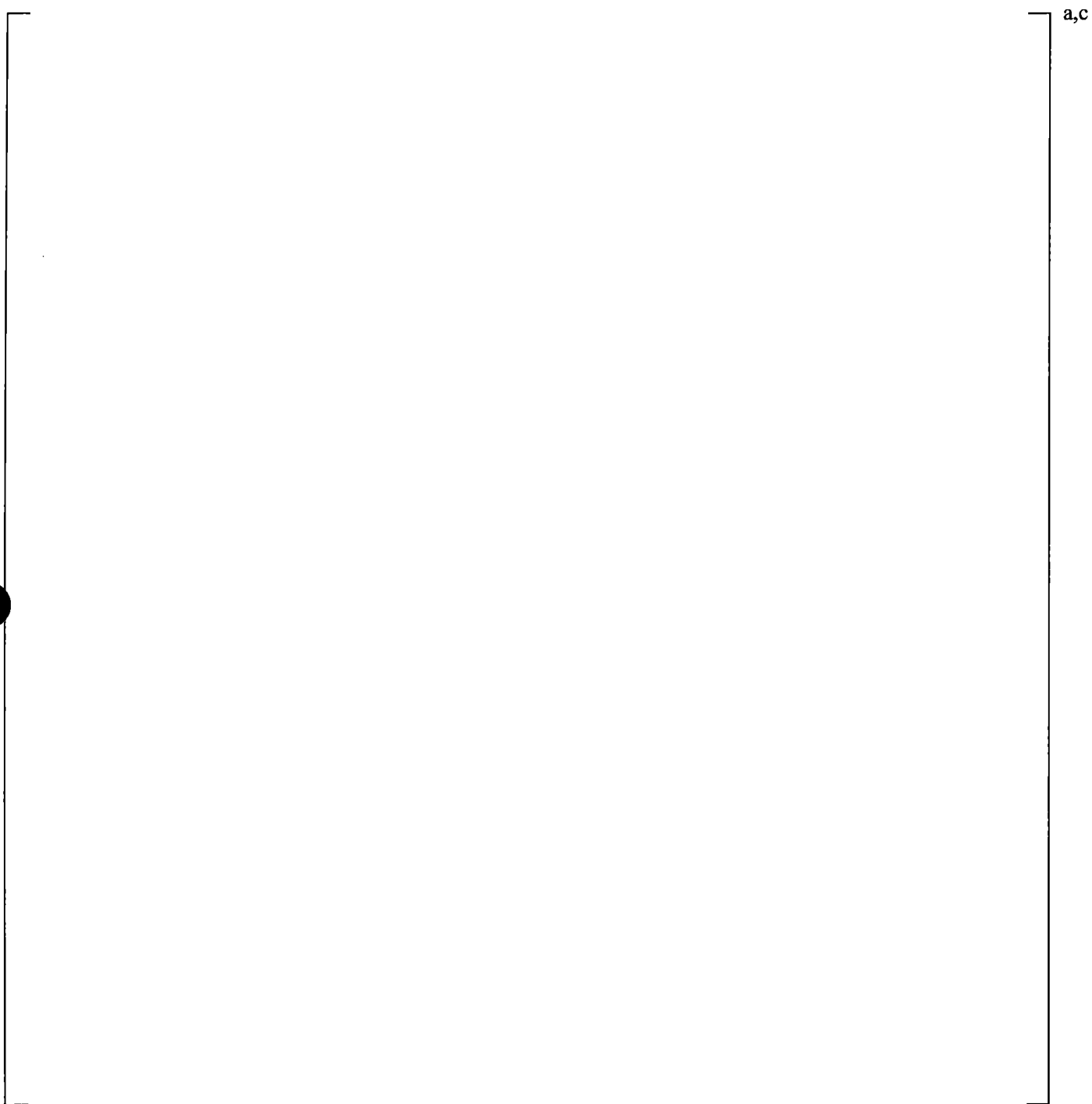


Figure 17-16 Steam Temperature Profile in Cold Leg in ROSA Test No. 3

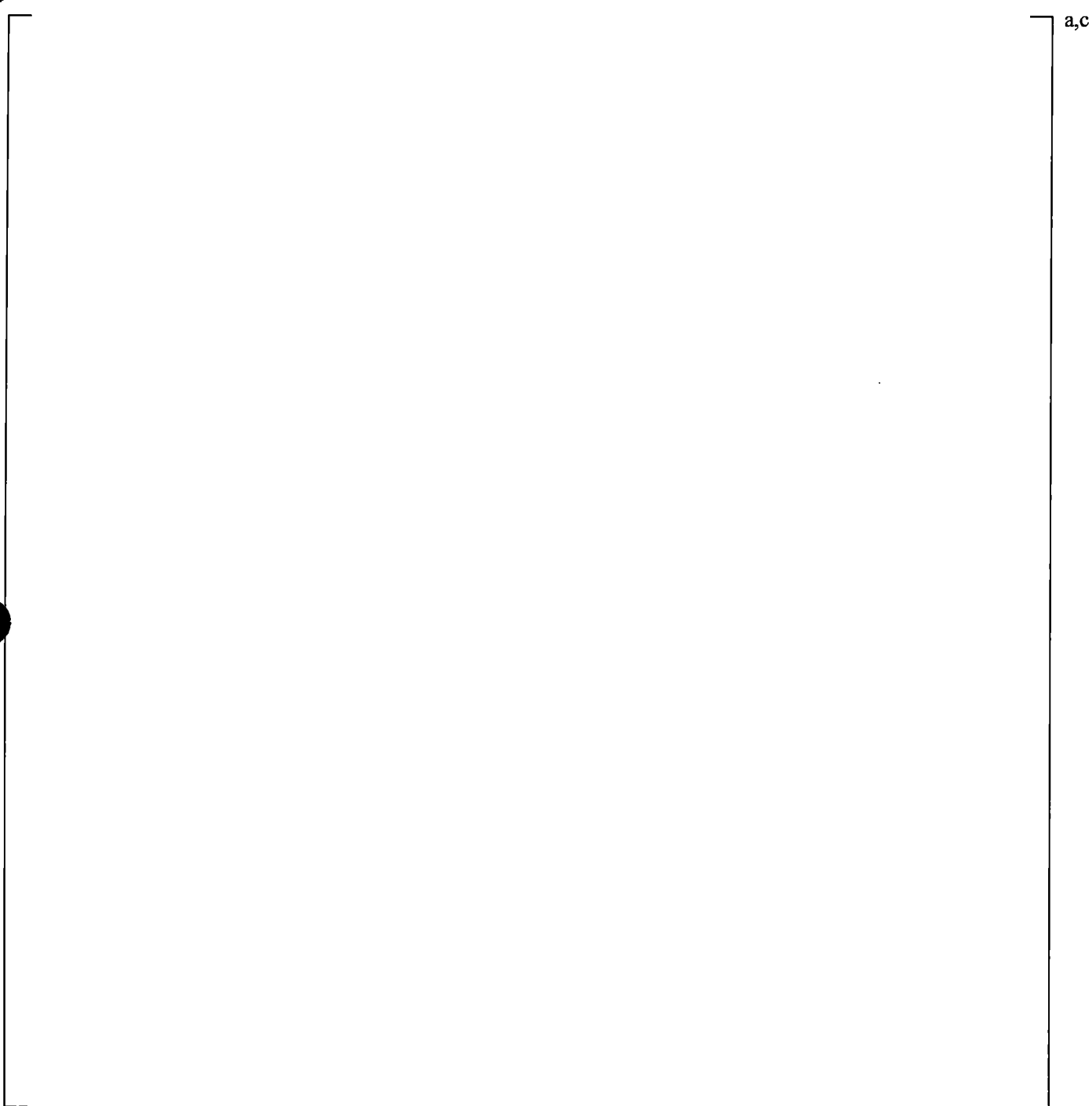
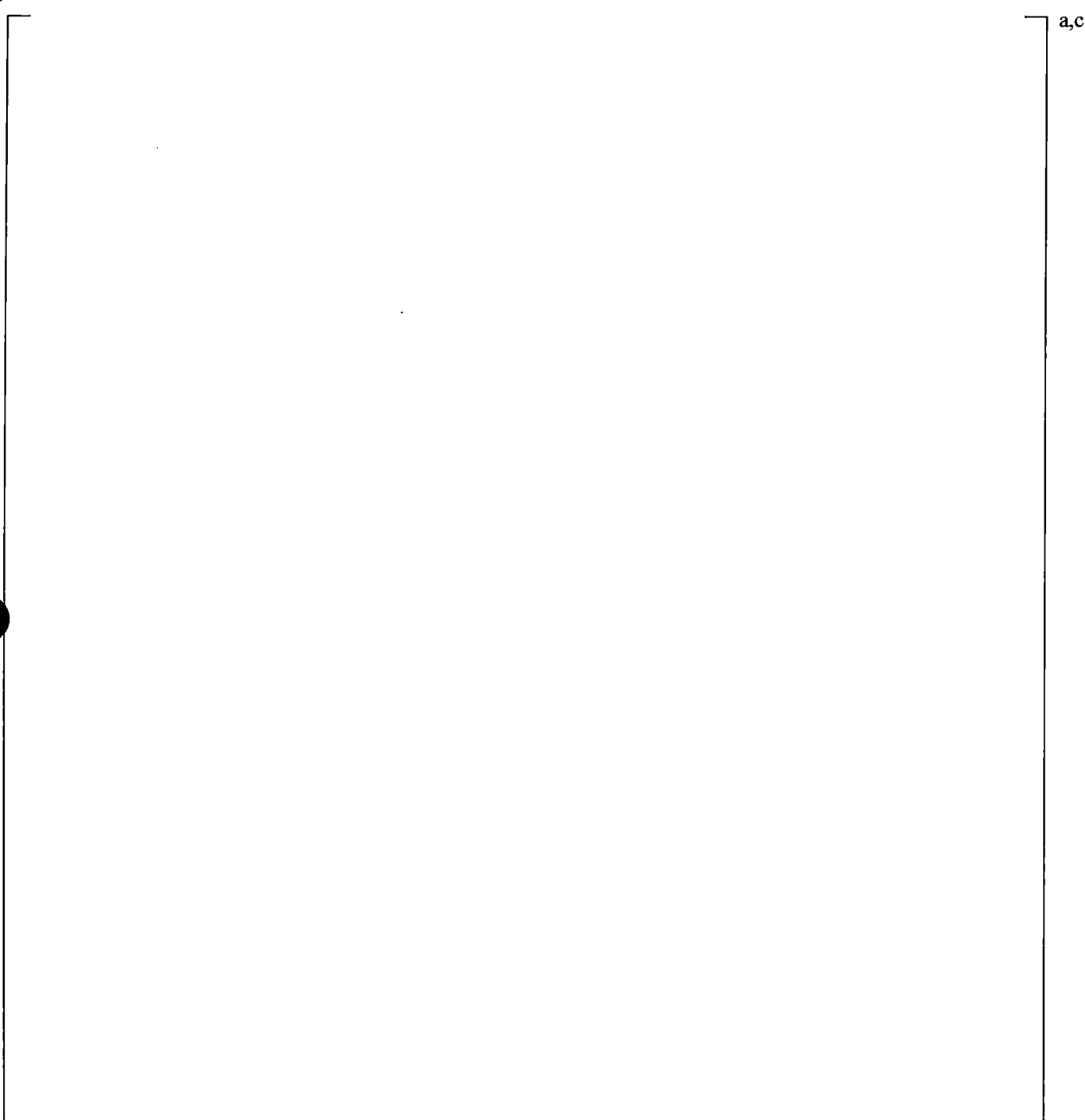


Figure 17-17 Steam Temperature Profile in Cold Leg in ROSA Test No. 4



**Figure 17-18 Comparison between Measured Condensation Heat Transfer Rate and
WCOBRA/TRAC-TF2 Predicted Condensation Heat Transfer Rate for
All Validation Cases**

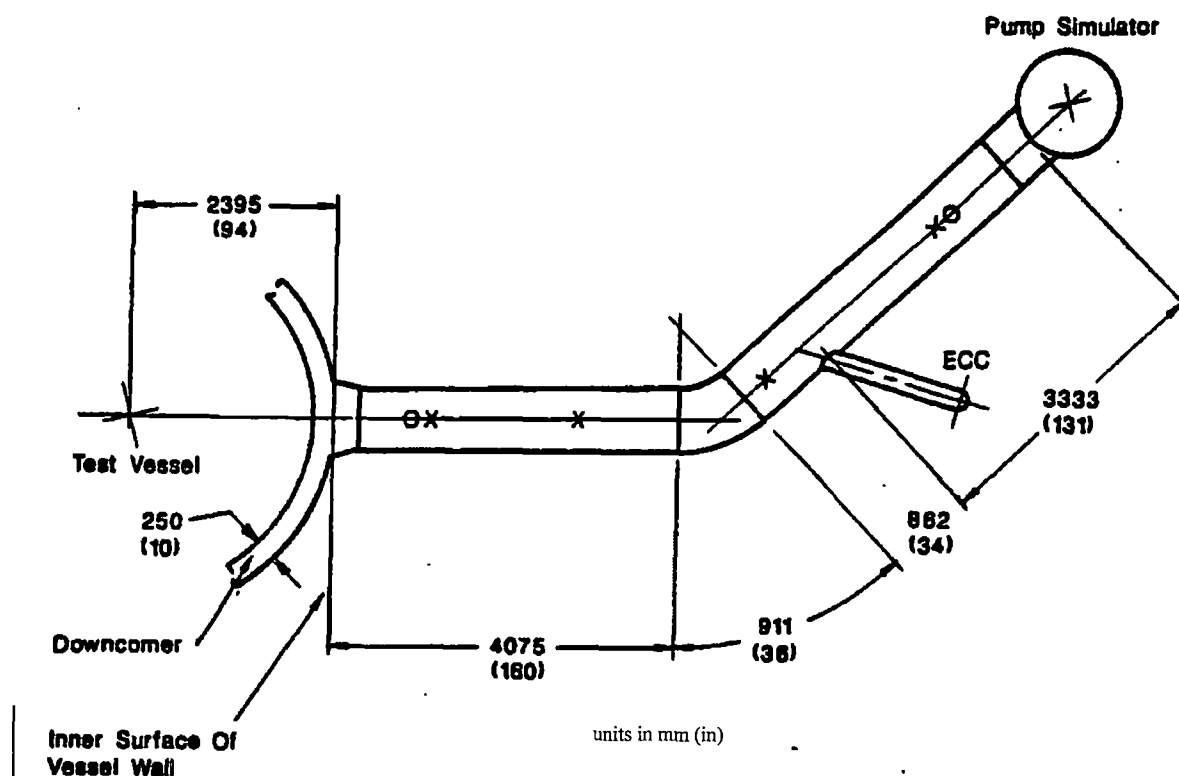


Figure 17-19 Cold Leg Piping Region of UPTF Test Facility

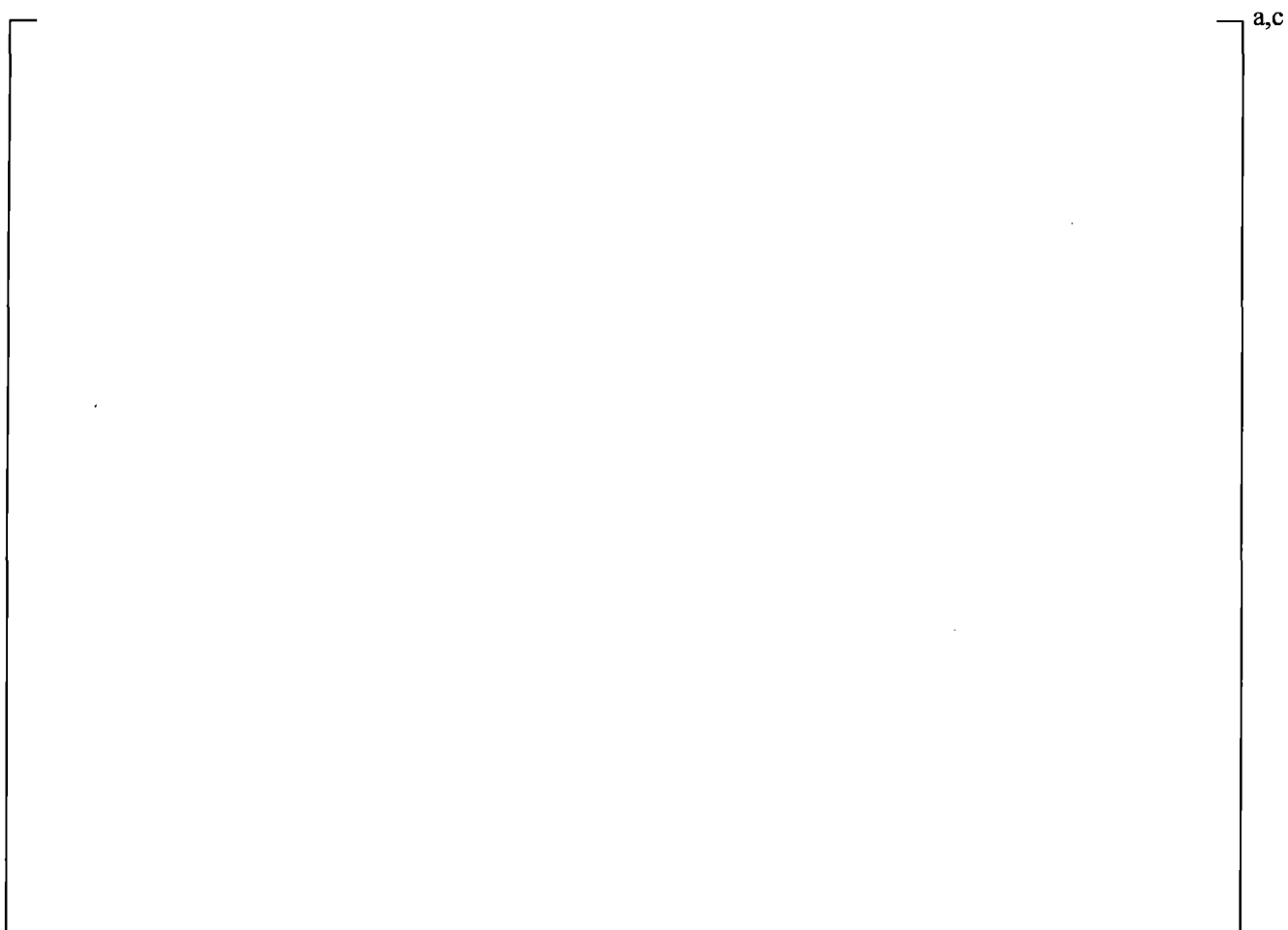


Figure 17-20 WCOBRA/TRAC-TF2 Single TEE Model for UPTF 8A

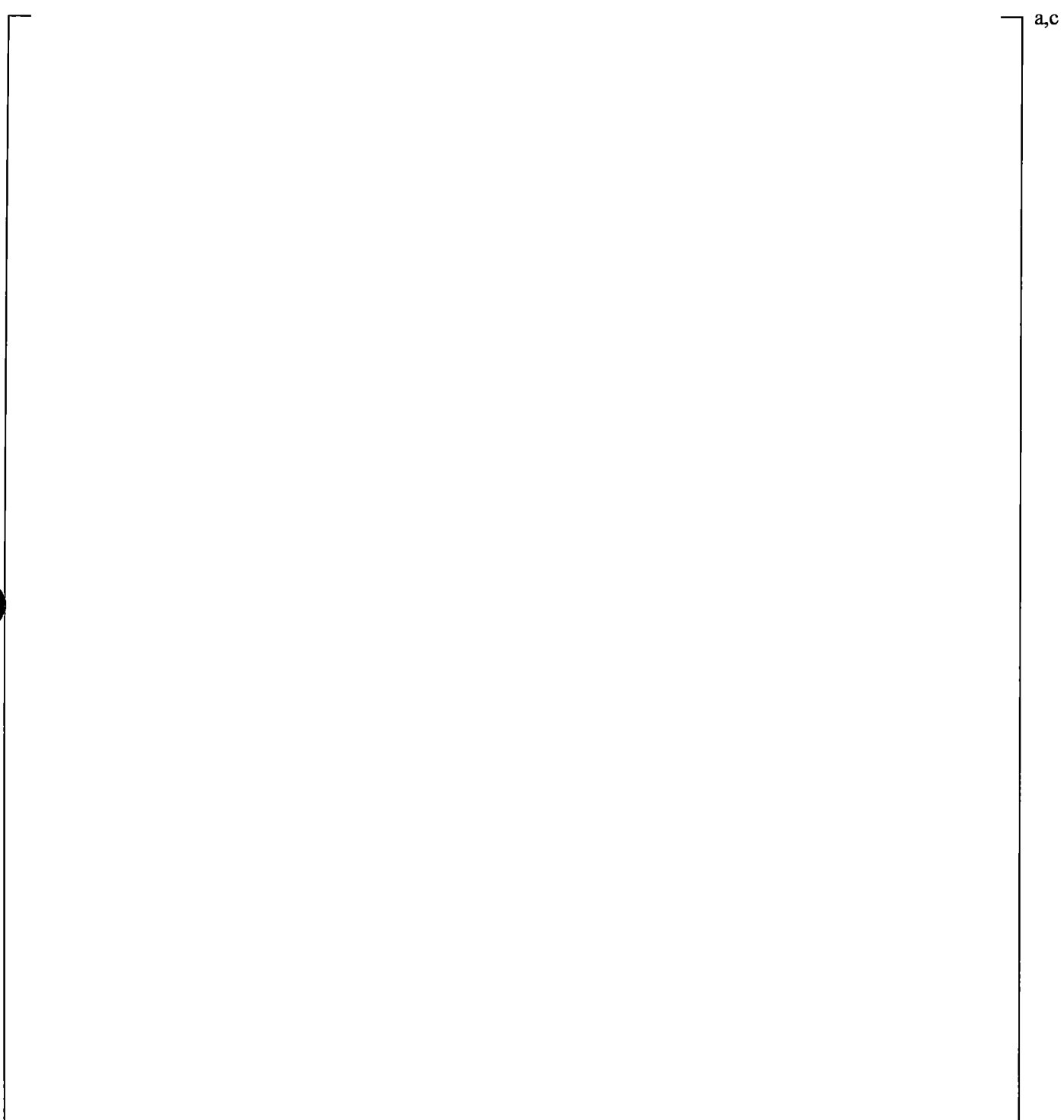


Figure 17-21 Comparison between Measured Fluid Temperature and WCOBRA/TRAC-TF2 Predicted Water Temperature at Pump Exit

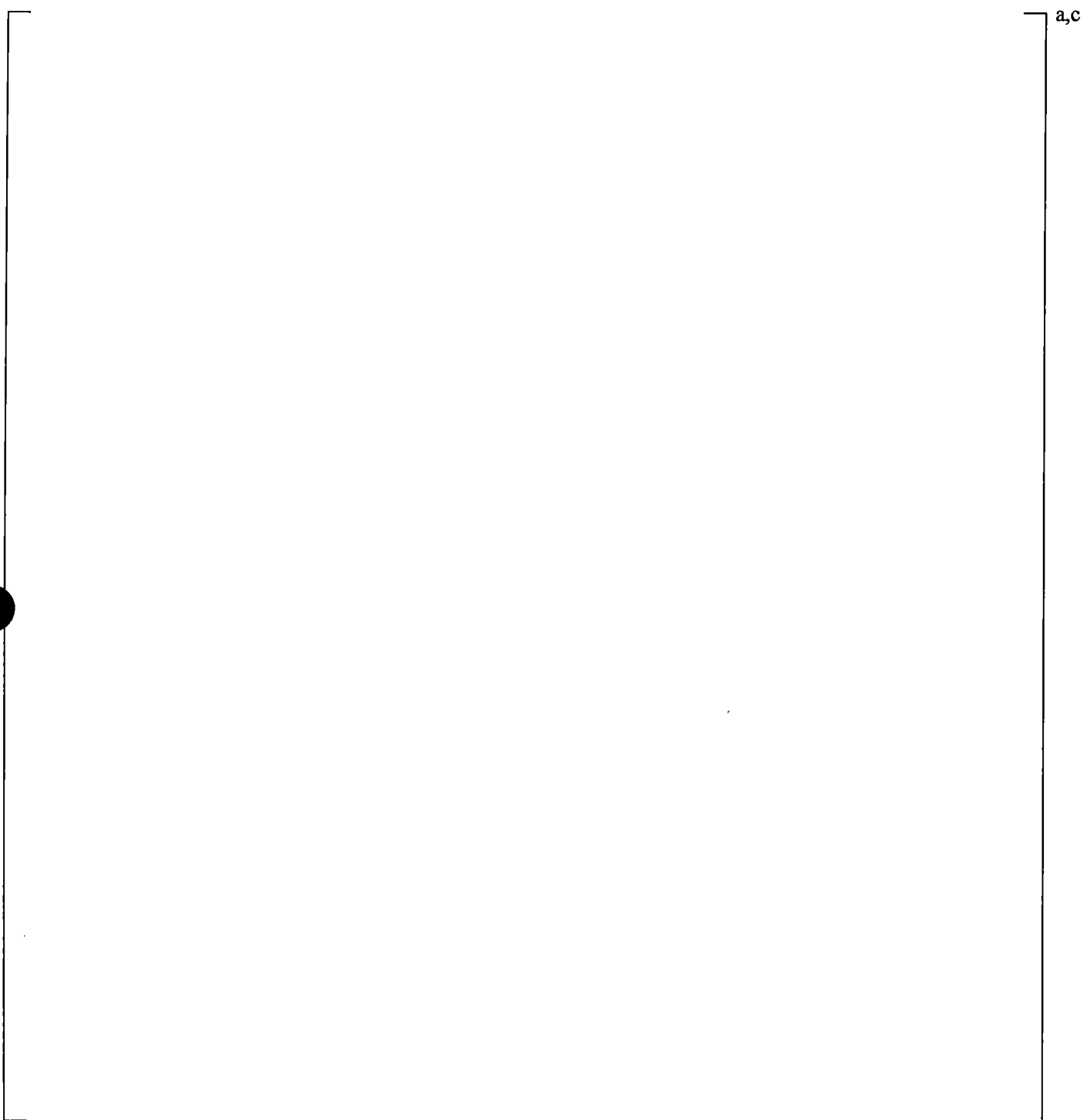


Figure 17-22 Comparison between Measured Fluid Temperature and WCOBRA/TRAC-TF2 Predicted Water Temperature near Injection Point

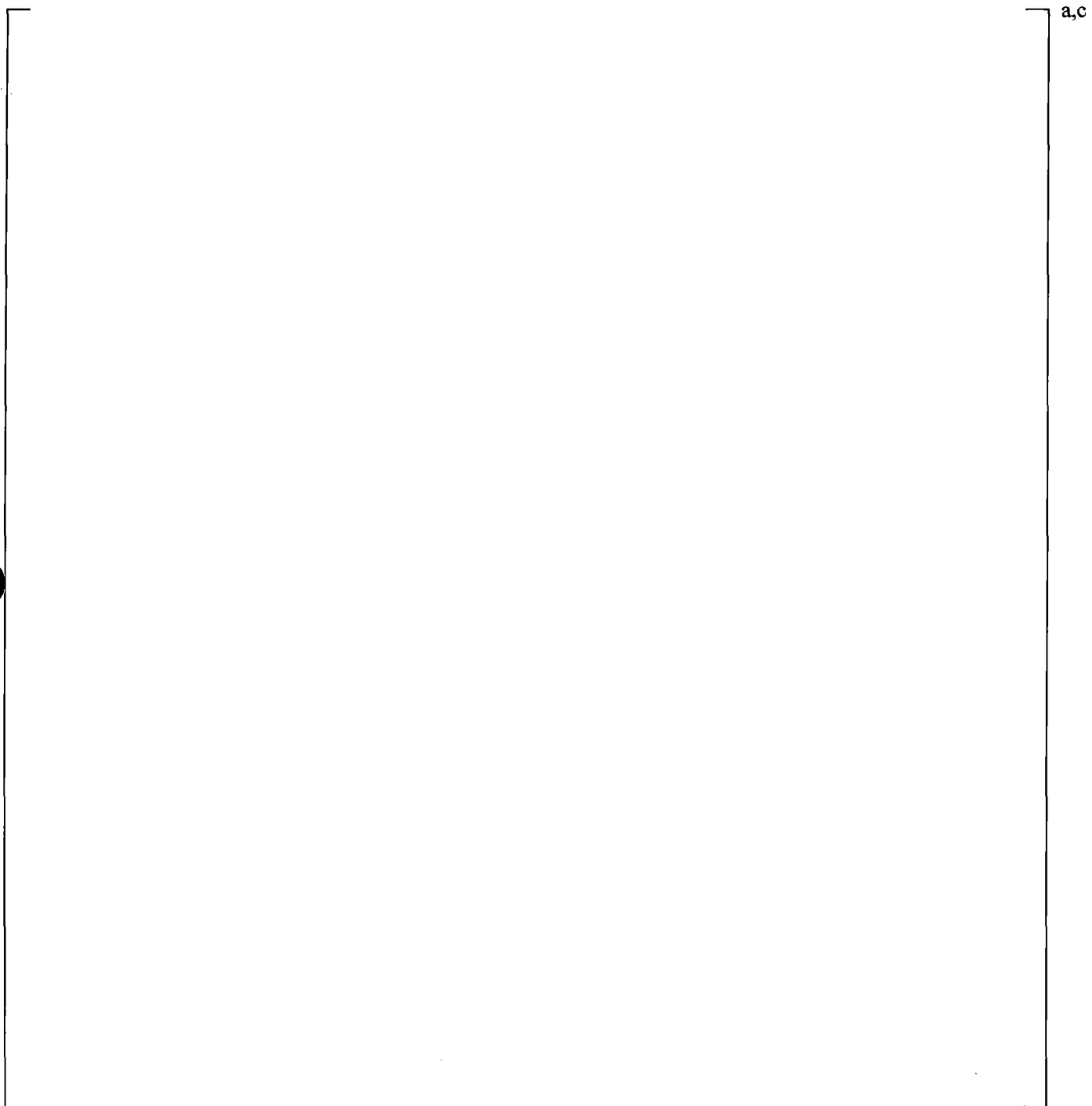


Figure 17-23 Comparison between Measured Fluid Temperature and WCOBRA/TRAC-TF2 Predicted Water Temperature at Downstream of Injection Point

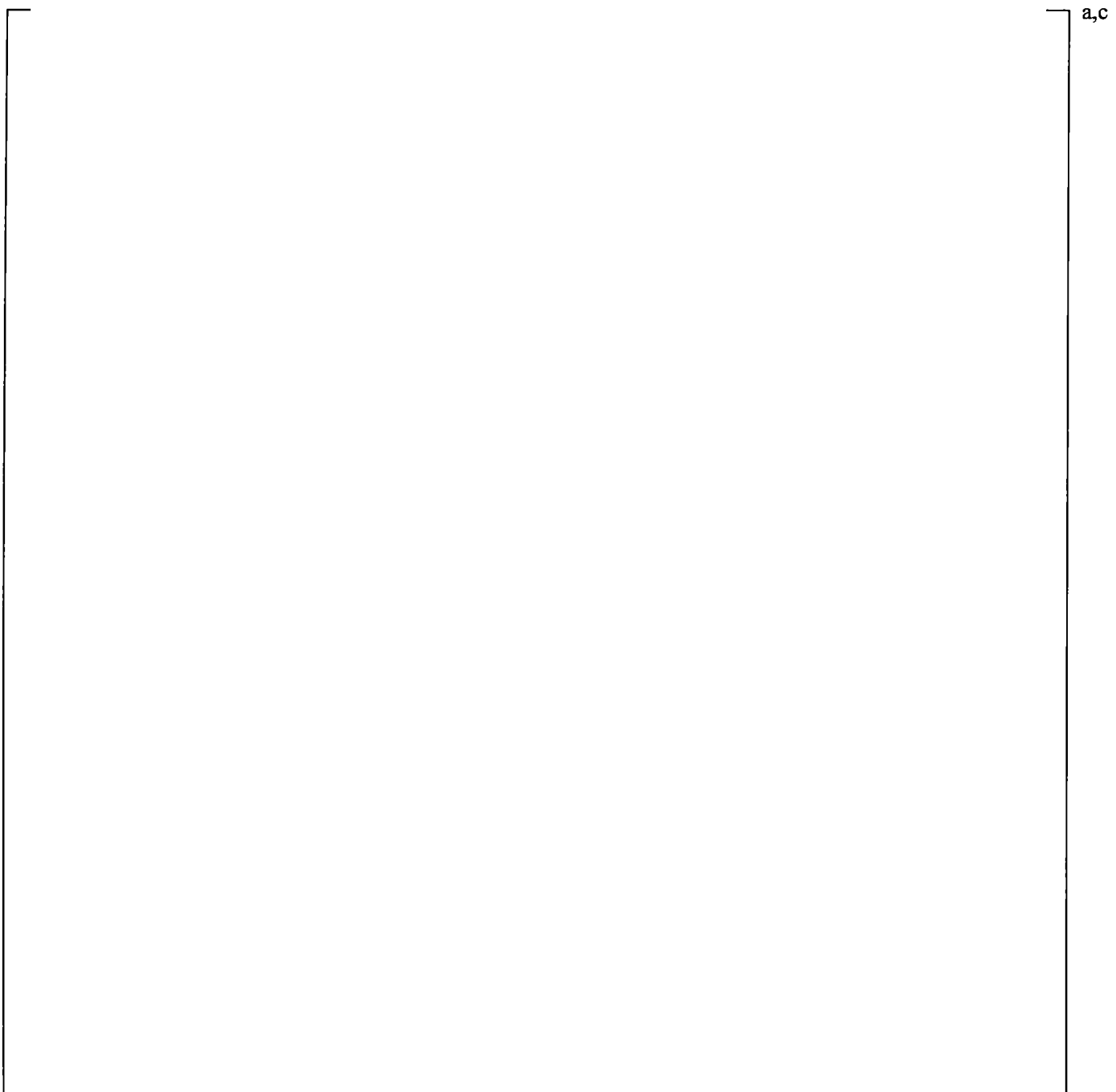


Figure 17-24 Comparison between Measured Fluid Temperature and WCOBRA/TRAC-TF2 Predicted Water Temperature at Outlet of Cold Leg

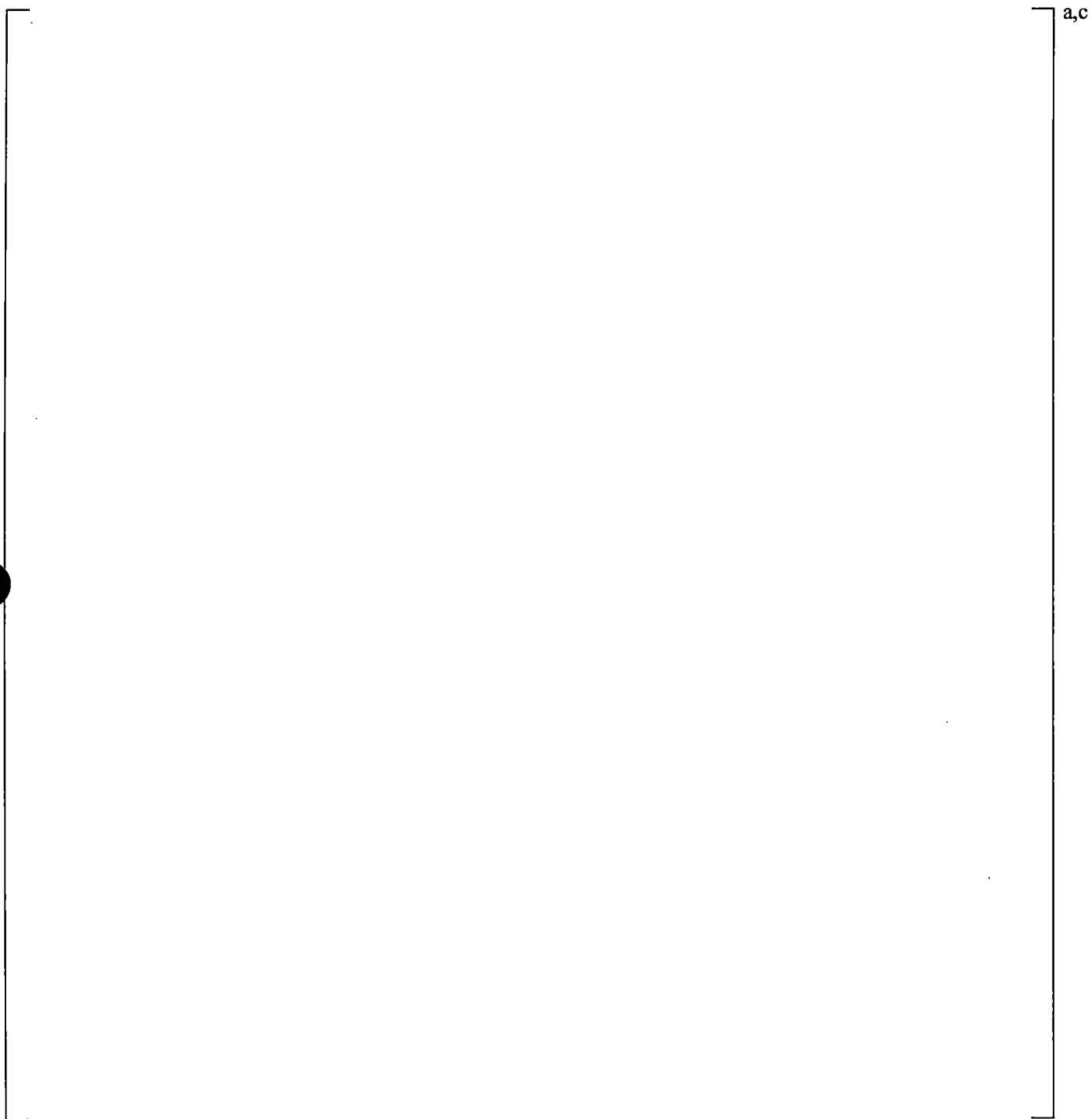


Figure 17-25 Comparison between the Predicted Water Temperatures at Injection Cell of Cold Leg in ECC Injection Angle Sensitivity Study

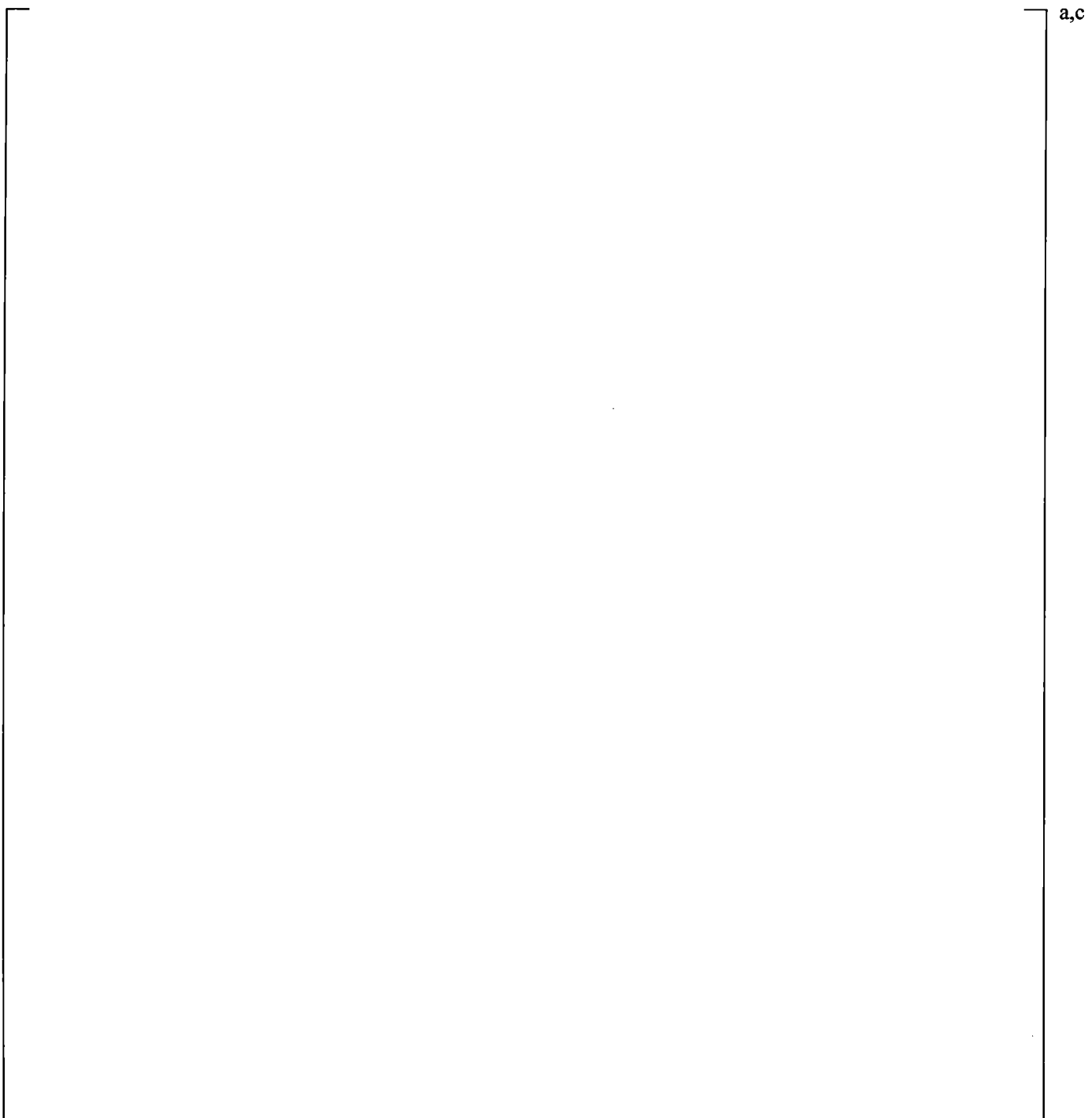
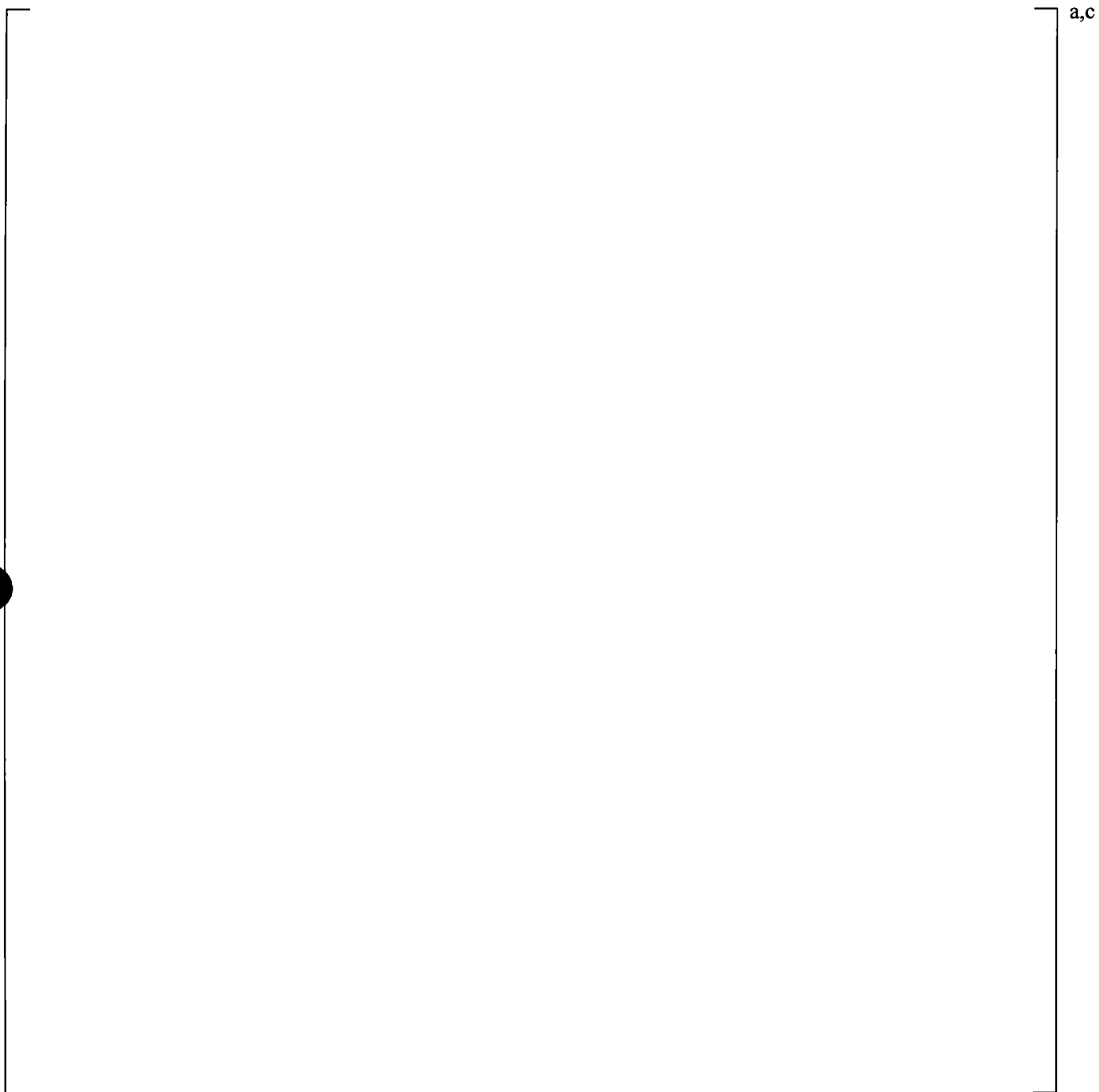


Figure 17-26 Comparison between the Predicted Water Temperatures at Downstream Cell of Cold Leg in ECC Injection Angle Sensitivity Study



**Figure 17-27 Comparison between the Predicted Water Temperatures at Outlet of Cold Leg
in ECC Injection Angle Sensitivity Study**

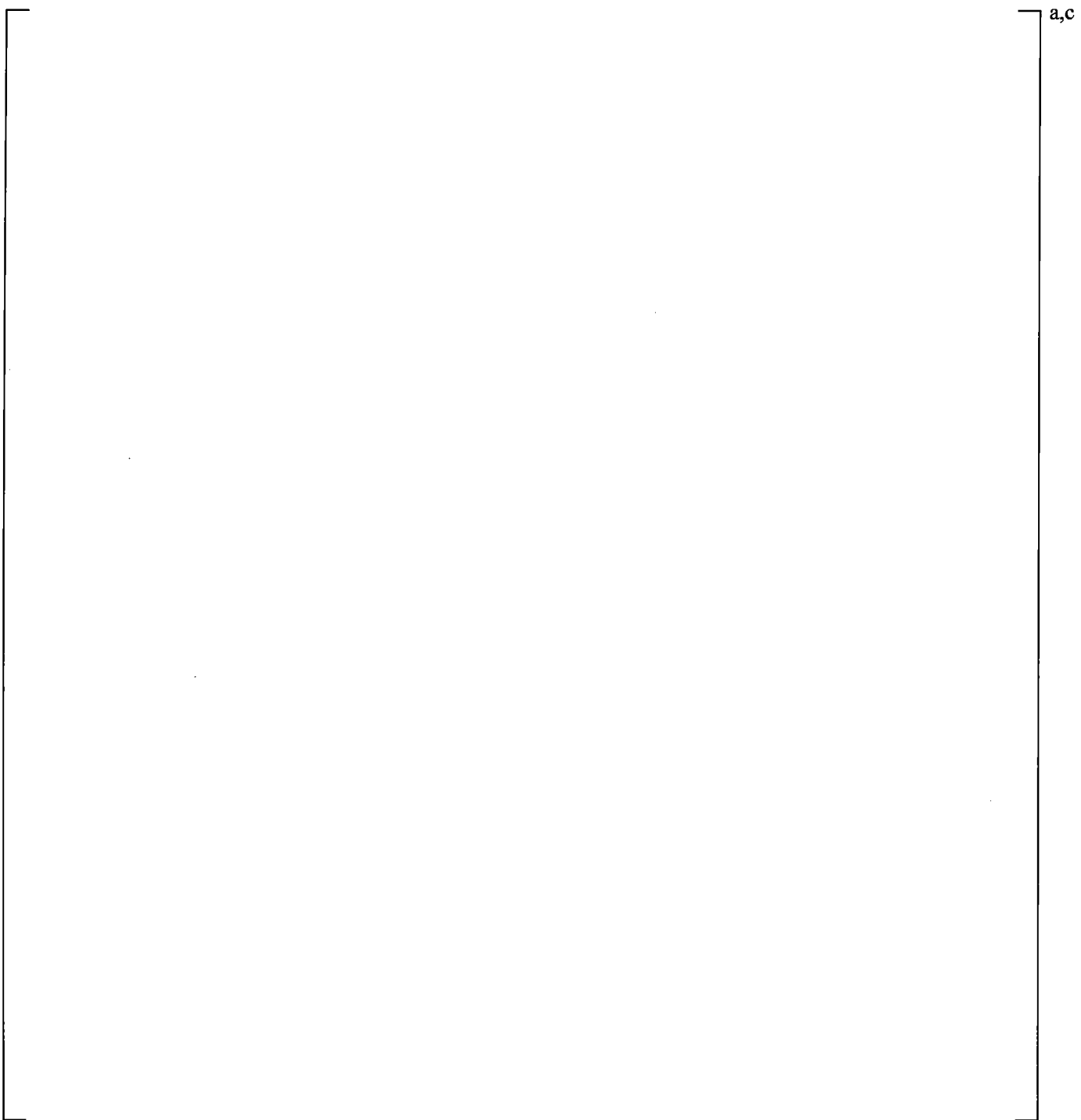


Figure 17-28 Comparison between the Predicted Water Temperatures at Injection Cell of Cold Leg in Cold Leg Noding Sensitivity Study

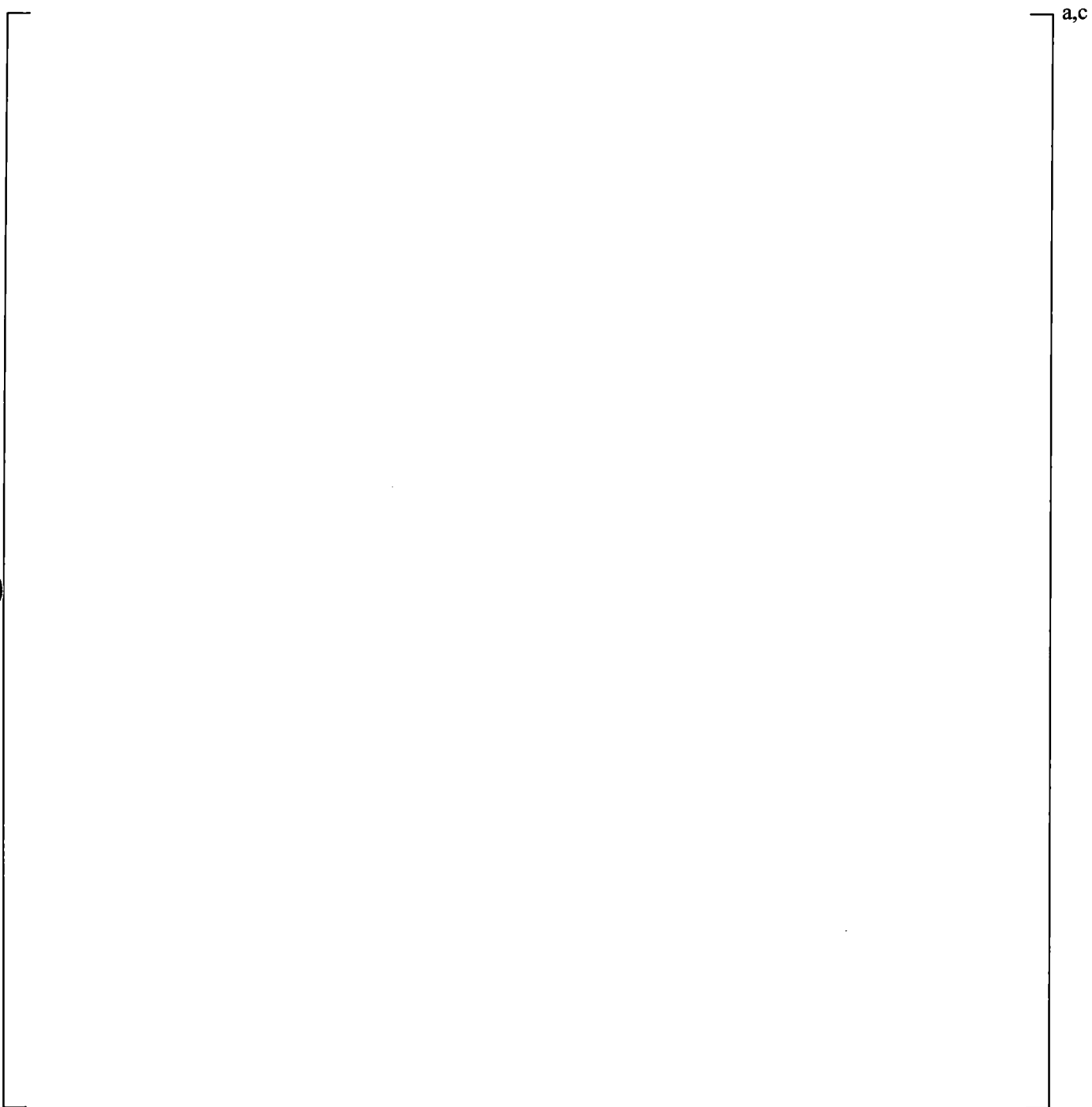


Figure 17-29 Comparison between the Predicted Water Temperatures at Downstream of Injection Cell in Cold Leg in Cold Leg Noding Sensitivity Study

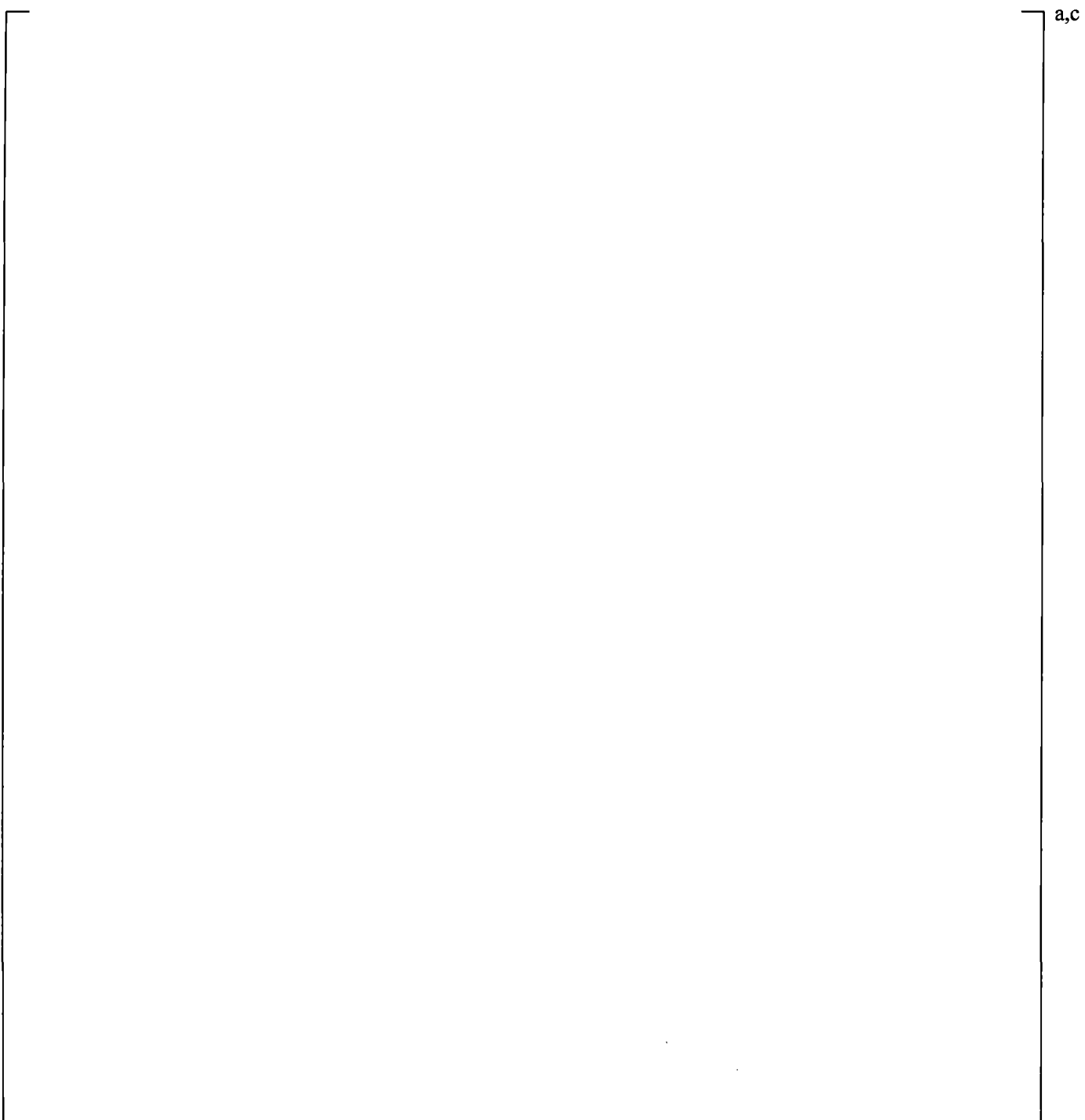


Figure 17-30 Comparison between the Predicted Water Temperatures at Outlet of Cold Leg in Cold Leg Noding Sensitivity Study

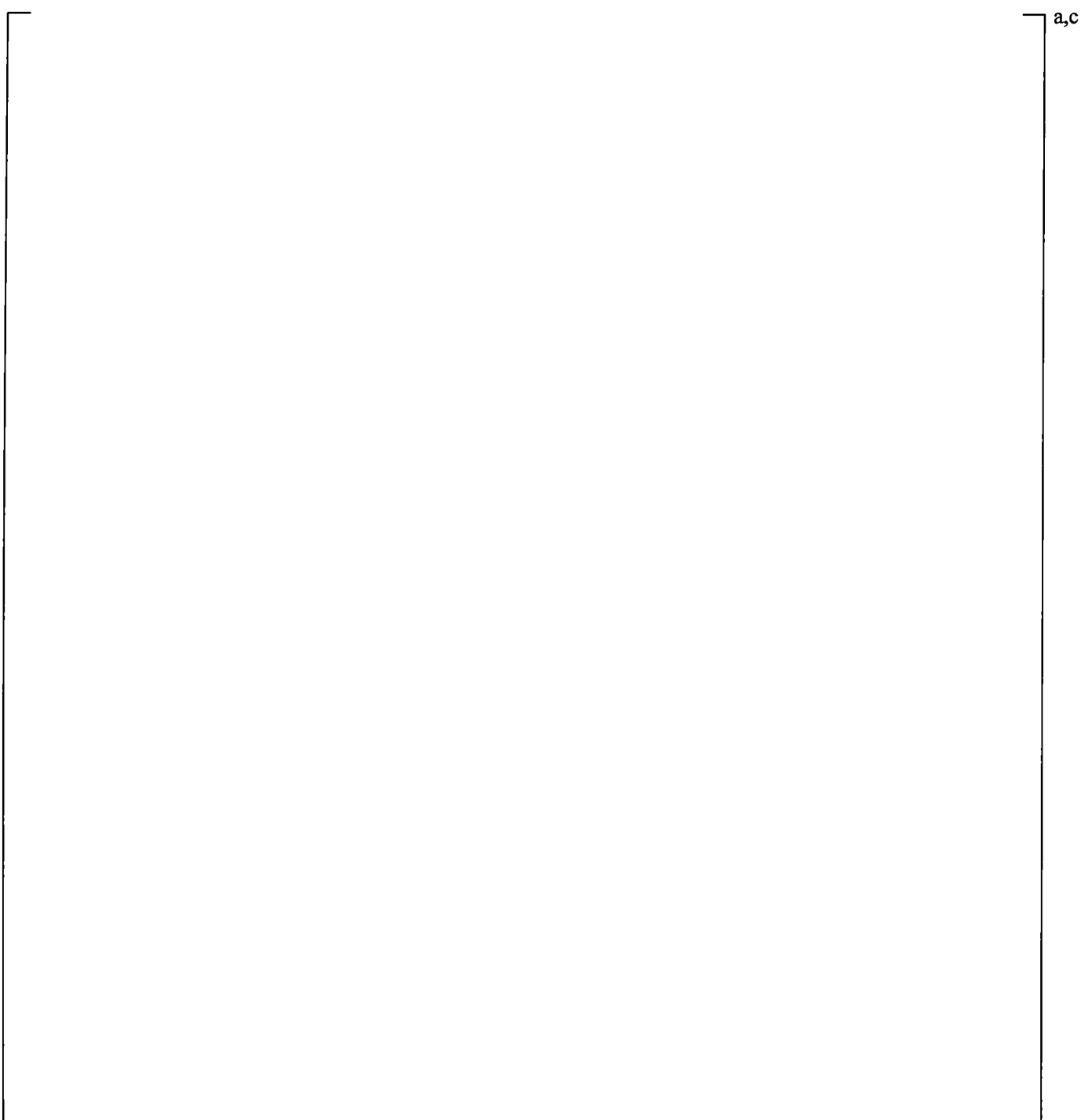


Figure 17-31 [

]^{a,c}

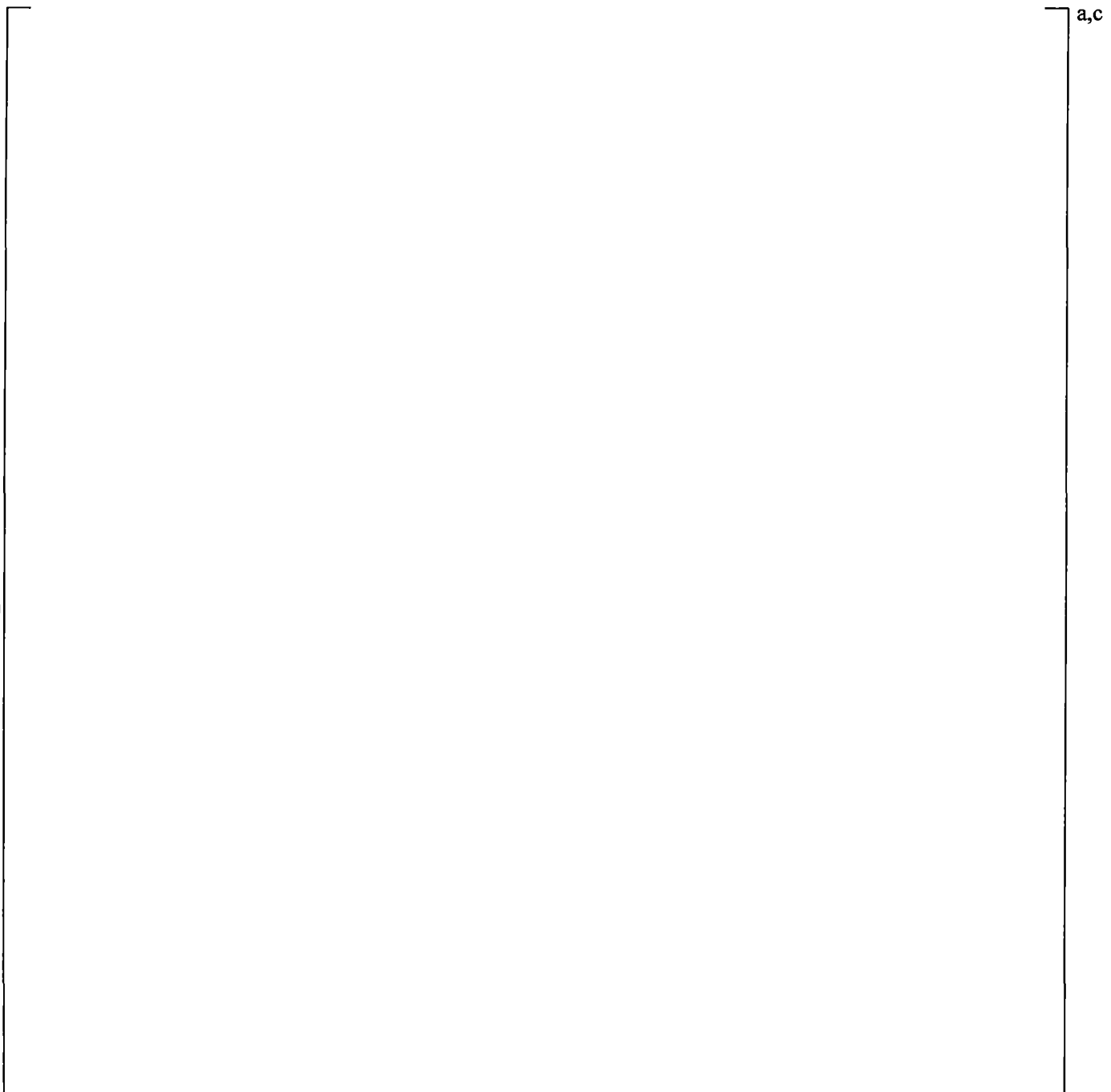


Figure 17-32 [

]^{a,c}

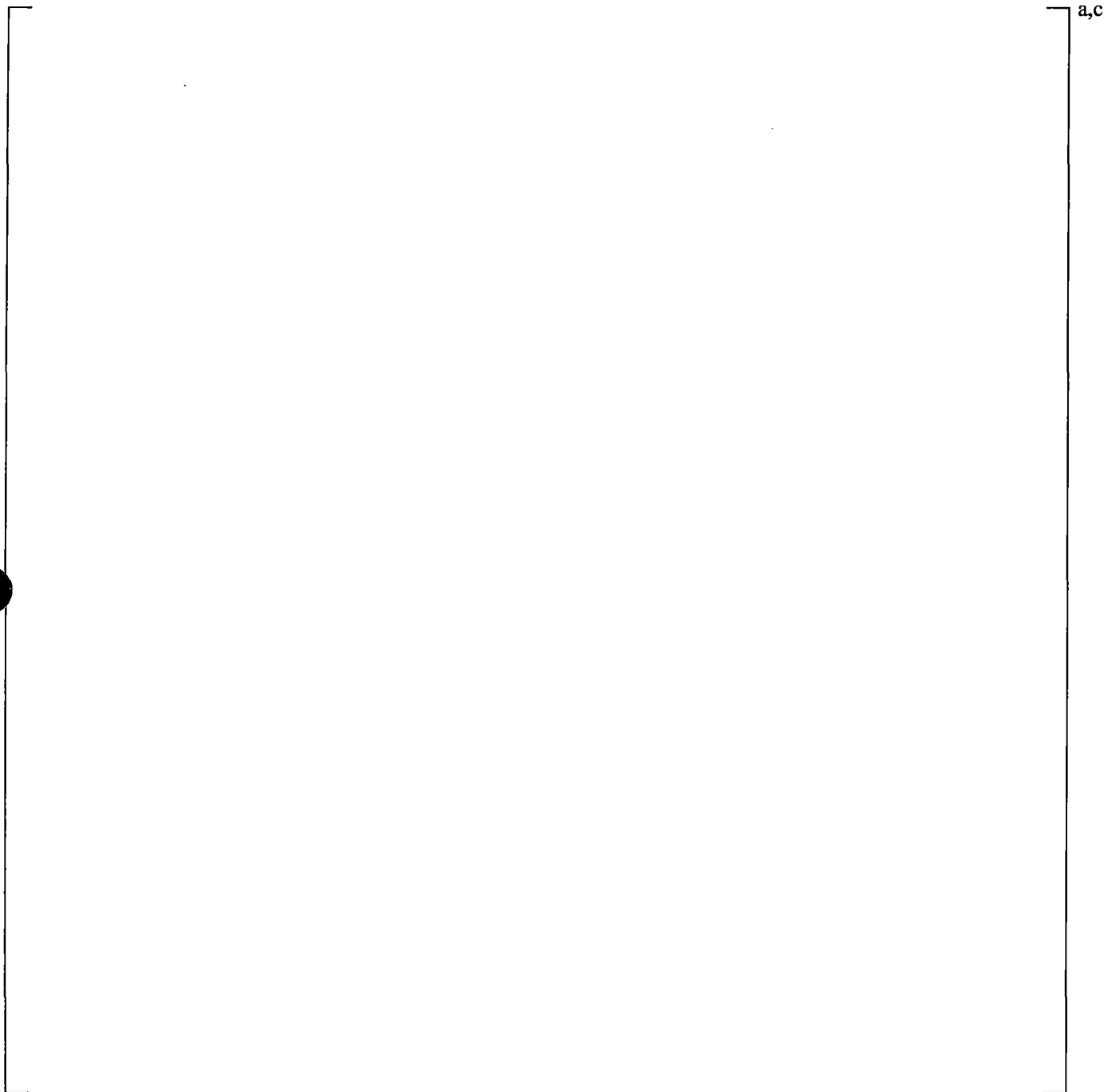


Figure 17-33 [

]^{a,c}

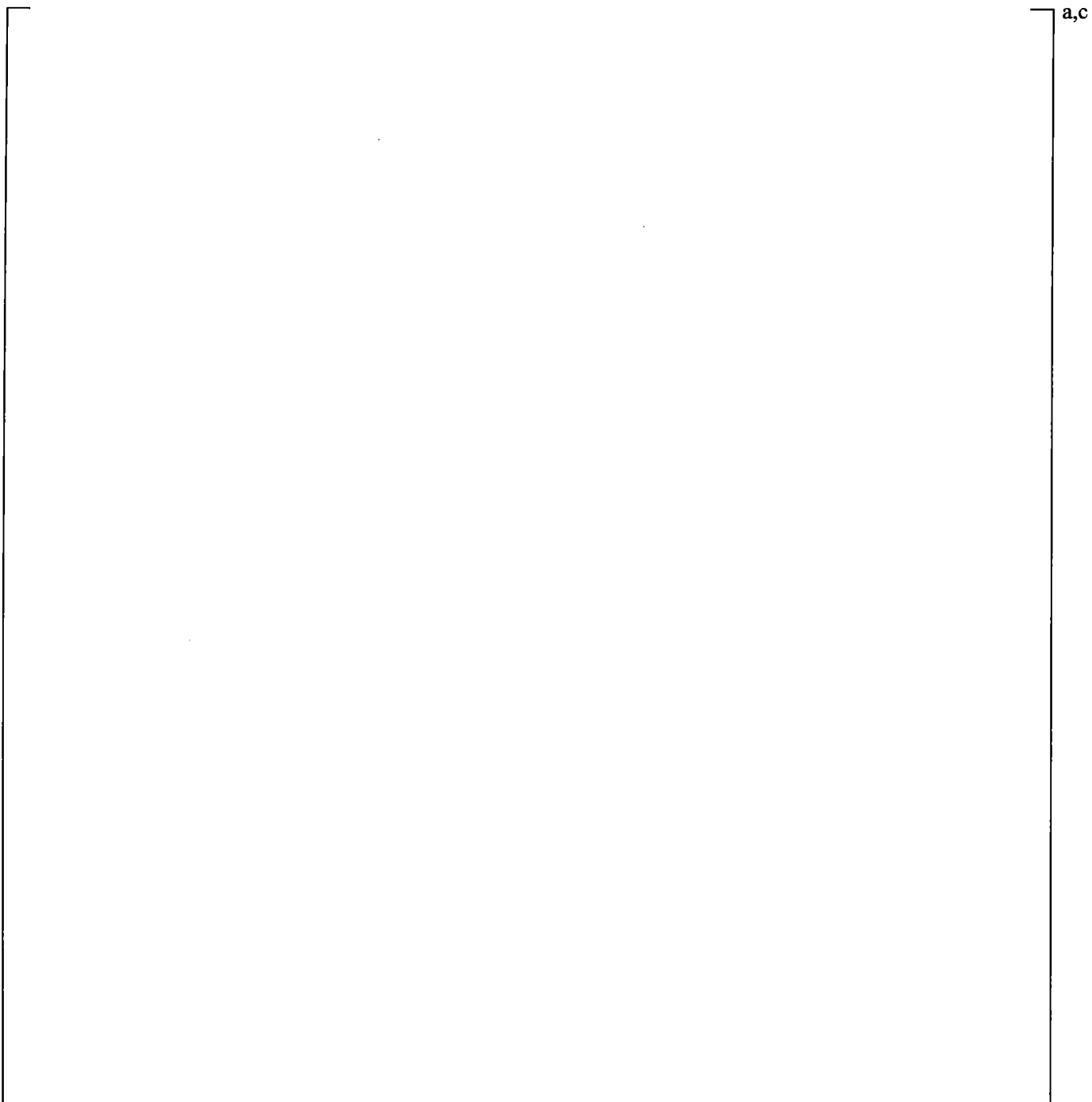


Figure 17-34 [

]^{a,c}

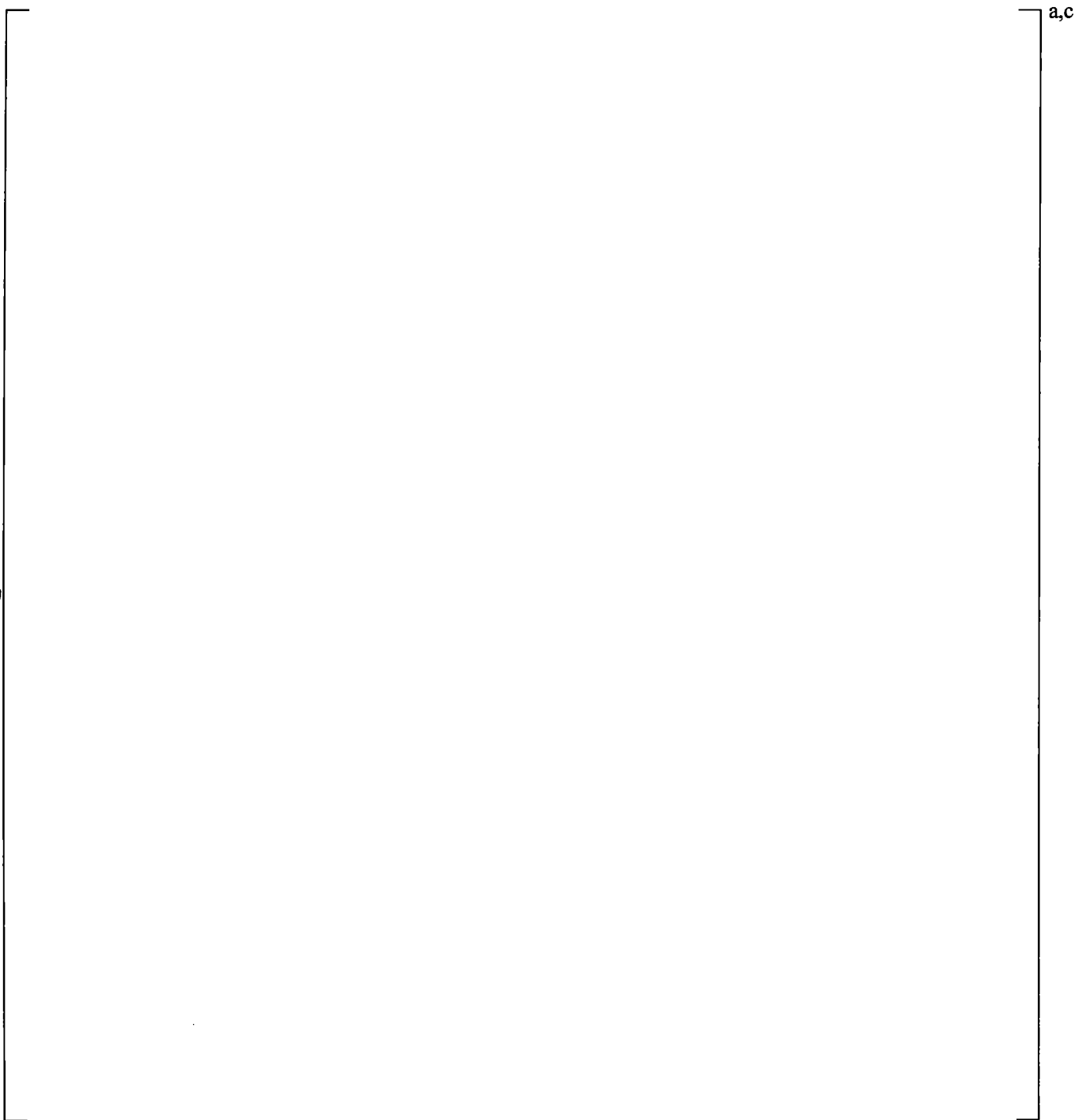


Figure 17-35 [

]^{a,c}

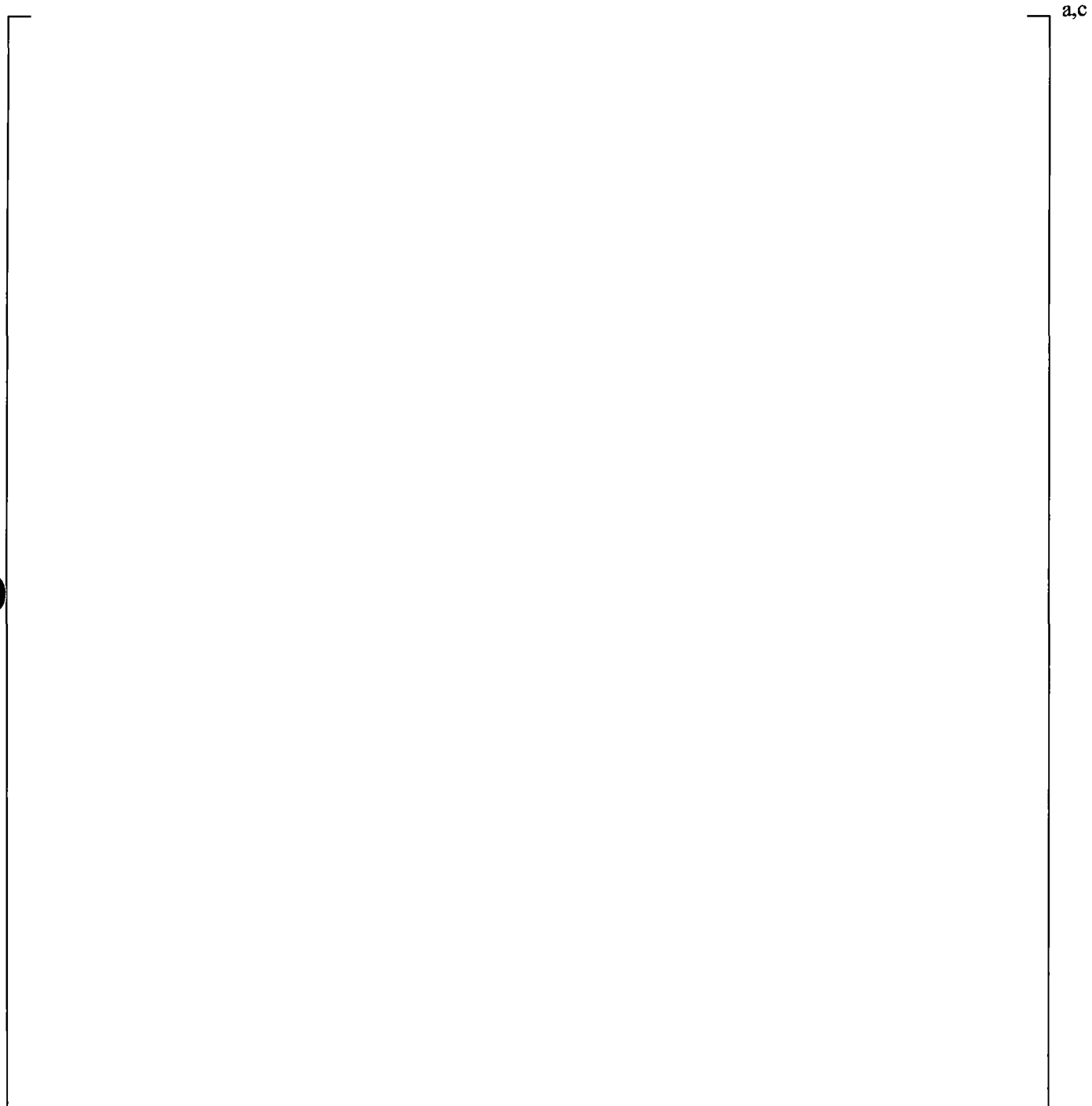


Figure 17-36 [

]^{a,c}

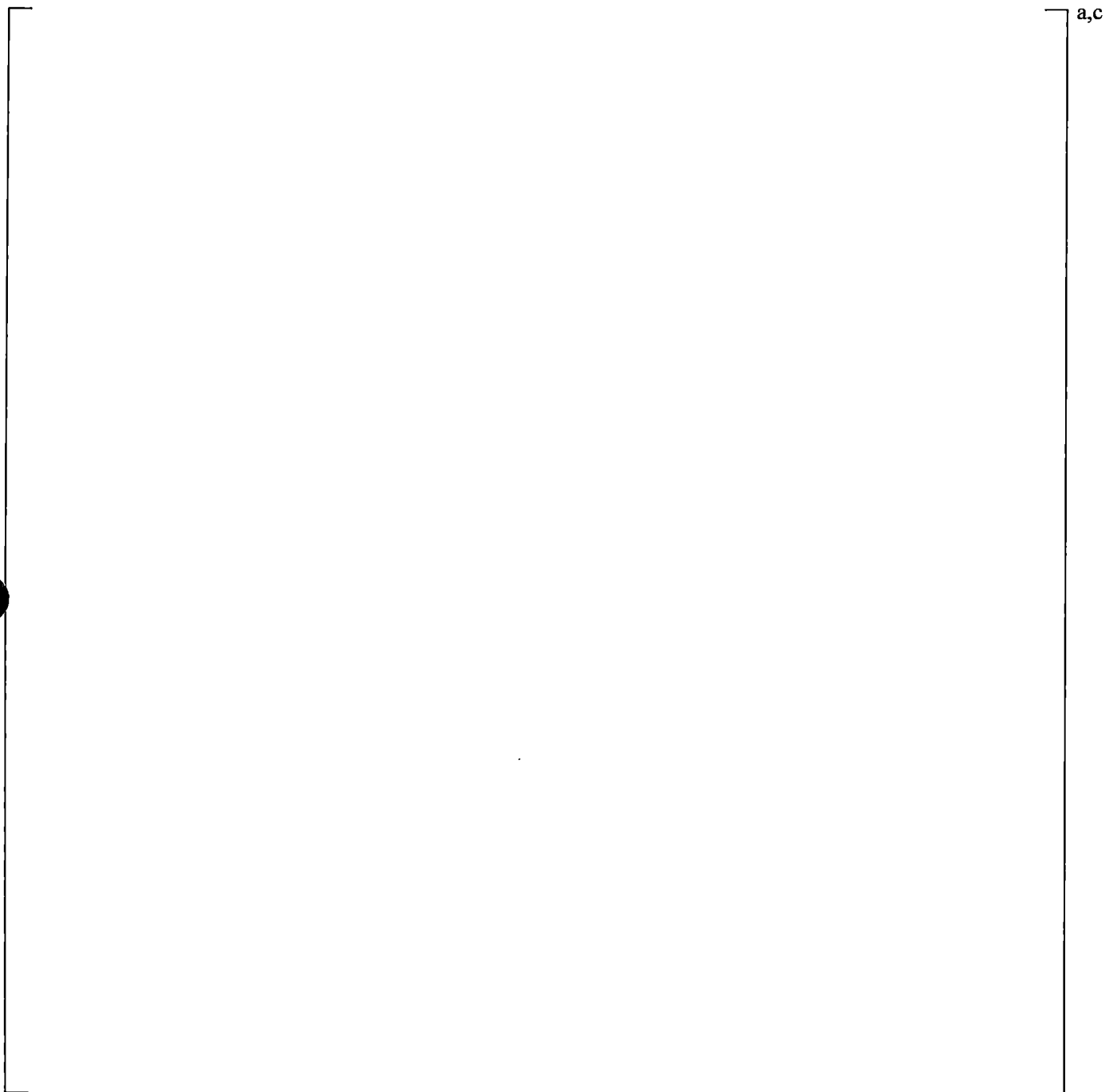


Figure 17-37 [

]^{a,c}

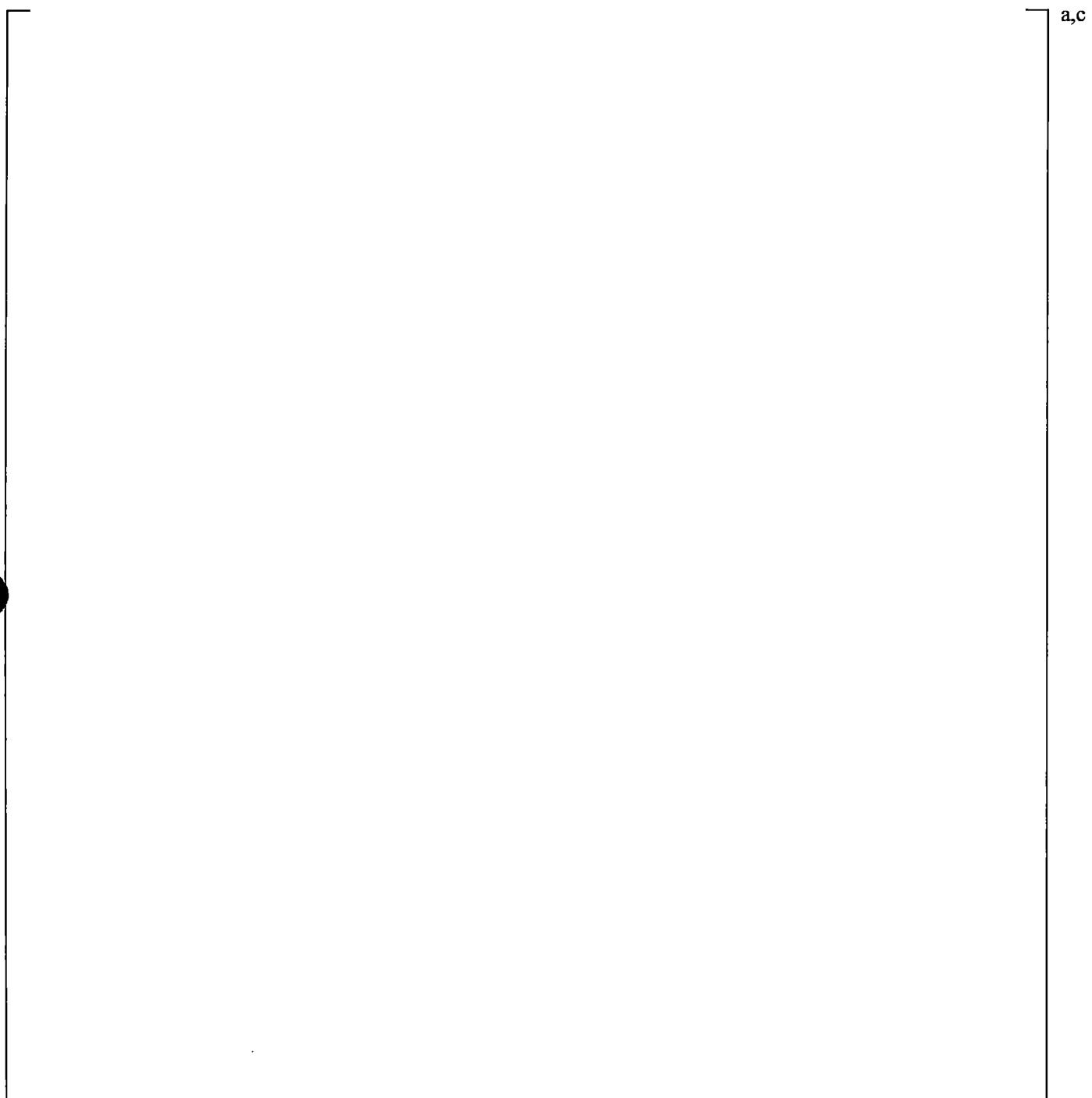


Figure 17-38 [

]^{a,c}

18 LOOP SEAL CLEARANCE

18.1 INTRODUCTION

The FULL SPECTRUM LOCA (FSLOCA) methodology Phenomena Identification and Ranking Table (PIRT) in Section 2.3, Volume 1 of this document identifies the loop seal behavior as an important process affecting the evolution of a small break Loss-of-Coolant Accident (LOCA) transient. This component and its effect on the transient are discussed in more detail below. The following sections identify the important phenomena occurring in the loop seal and the available experiments to assess the performance of WCOBRA/TRAC-TF2 in predicting such phenomena.

During a small break LOCA, mass is slowly depleted from the system. Early in the transient, the pumps continue to run and the flow through the pump suction piping remains single-phase. After generation of a reactor trip signal, the reactor trips and subsequently the pumps trip either due to loss of offsite power or operator action. The system then enters a natural circulation phase. Pressures have fallen sufficiently to cause boiling in the fluid entering the hot leg, but the steam generator acts as a heat sink, and the fluid entering the pump suction pipe is still nearly single-phase. Any bubbles that enter the pump suction pipe are carried through by natural circulation as illustrated in Figure 18.1-1a.

When the primary pressure approaches the secondary pressure, voids remain in the fluid as it enters the steam generator. As the loop mass flow rate decreases further, liquid begins to drain down both the uphill and downhill sides of the steam generator tubes. Natural circulation is terminated, and mixture levels form on both the uphill and downhill sides of the tubes. The levels then move downward as liquid drains and vapor rises as shown in Figure 18.1-1b.

Because there is no escape path for the steam generated in the core, except for some small bypass paths such as the upper head, the pressure in the region above the core (the upper plenum, the hot legs, and the steam generator tubes) rises and depresses the level in both the core and the downhill sides of the pump suction pipe. Eventually, the downhill side level reaches the top of the horizontal portion of the pump suction pipe, as shown in Figure 18.1-1c, and vapor begins to escape into the pump and flow toward the break.

At the onset of clearing, the fluid pressure in the downhill leg of the loop seal is higher than on the uphill side, due to the column of liquid from the horizontal leg to the pump outlet as shown in Figure 18.1-1c. Because the volume of steam at this pressure is significant in the steam generator tubes, hot legs, vessel upper plenum and upper head, the steam flowing through the pump suction becomes significantly greater than the core steam generation rate for a period of time (Kukita, 1990). This causes the loop seal to clear completely, not resealing until much later in the transient.

As the steam flows through the pump suction, the flow regime is first a slug regime with significant amounts of liquid being entrained from the pump suction pipe as seen in Figure 18.1-2 and described by (Tuomisto and Kajanto, 1988). Eventually, a residual level of liquid will remain in the pump suction pipe.

As the pressure in the system is relieved, the steam flow decreases to the core steam generation level. If this steam flow is low enough, liquid in the cold leg may begin to drain back through the pump and begin to fill the pump suction again as shown in Figure 18.1-1d. Another potential source of loop seal refilling is the draining of condensed steam from the downhill side of the steam generators. Because there is no pressure driving force, the steam flow through the loop seal is quickly terminated when the liquid level reaches the top of the horizontal section and plugs the loop seal. The system pressure increases, and core and loop seal levels change once again as the loop seal plugging and clearing cycle is repeated (Kukita, 1990).

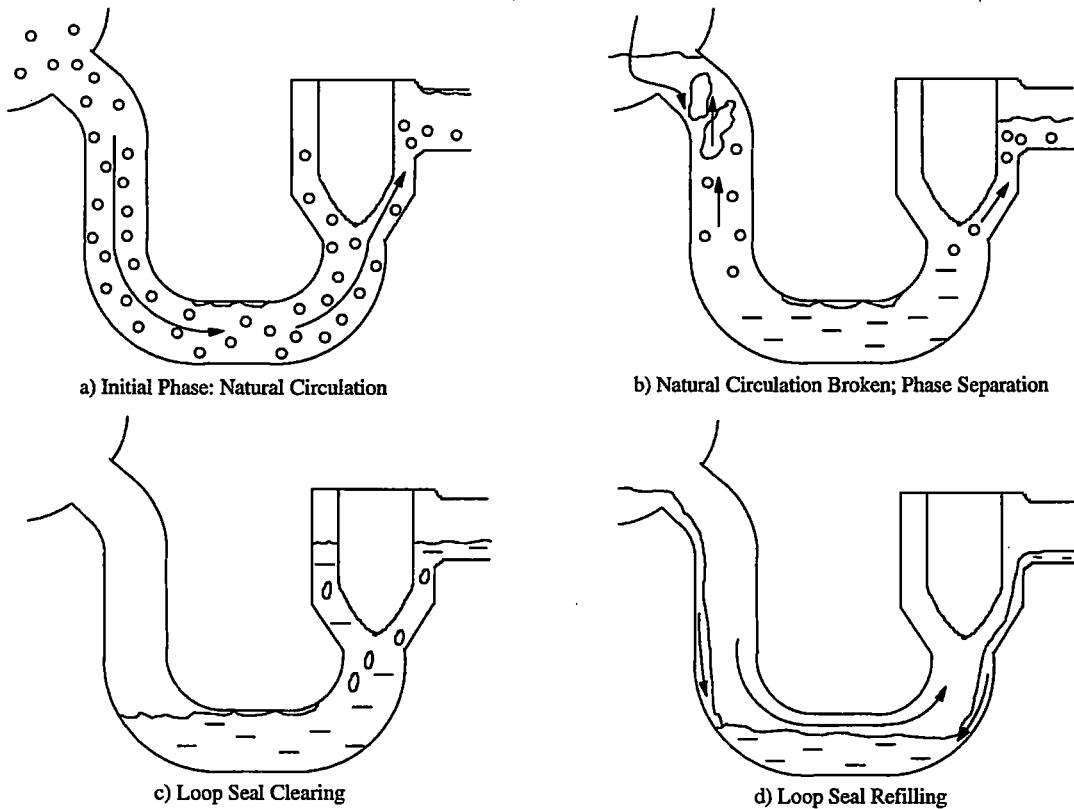


Figure 18.1-1 Loop Seal Clearing and Refilling

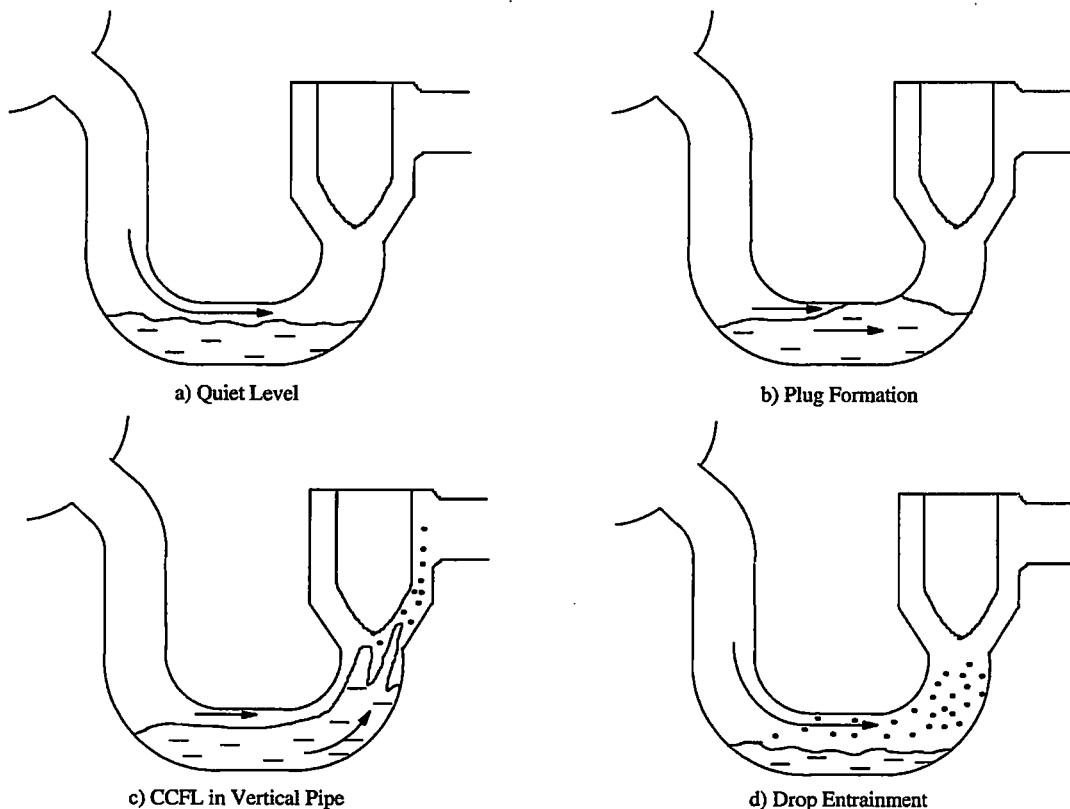


Figure 18.1-2 Loop Seal Clearing Process

18.2 IMPORTANT PHYSICAL PROCESSES AND SCALING LAWS

The onset of loop seal clearing is a function of the pressure difference across the loop seal, which depresses the level to the bottom of the loop seal and depends on the following factors:

- Core steam generation rate
- Bypass steam flow rate through vent paths
- Rate of accumulation of liquid in the pump suction pipe

These factors are the result of processes that occur elsewhere in the system and are accounted for in other components (for example, the core steam generation rate is accounted for by sampling the core power which directly influences the steam generation).

The loop seal clearing and refilling process is a function of the interfacial drag between the vapor and the liquid. The initial steam flow surge and the interfacial drag determine the rate at which liquid is expelled. The steam flow rate, in turn, depends on the loop pressure drop, of which the loop seal is a part. This determines how quickly the venting process takes place and the final liquid level in the horizontal section. The residual liquid and degree to which liquid is held up by steam flowing out of the pump suction pipe determine the rate at which the pump suction refills and replugs. Based on these considerations, the following factors are considered to be important in the assessment of predictions of loop seal behavior:

- Overall loop seal pressure drop as a function of steam flow
- Liquid distribution in the loop seal as a function of steam flow

Various experiments have shown that the basic physical process is controlled by two factors: the extent to which a stratified flow regime can be maintained in the horizontal leg of the loop seal, and the degree to which liquid pushed into the downstream vertical leg can be entrained out of the loop seal. Figure 18.1-2 illustrates these processes.

First, the Rig-of-Safety Assessment (ROSA) 5% and 10% break integral tests are examined for loop seal behavior. Then, scaled loop seal experiments are discussed in the following section to gain a better understanding of the loop seal behavior. These tests are used to highlight important physical and scaling features. The time period of interest is the steady-state, post clearing portion. Next, the scaled tests are compared with larger scale tests to confirm the indicated scaling trends. Finally, the larger scale tests are simulated using WCOBRA/TRAC-TF2 to assess the models and correlations in the code.

18.2.1 ROSA

Loop seal clearing behavior can be observed from the ROSA 5% and 10% break integral tests (Kumamaru, et al., 1989 and Koizumi and Tasaka, 1988; see Section 21 for test facility description). Figures 18.2.1-1a and 18.2.1-1b show the loop seal differential pressure behavior of the broken loop for the 5% and 10% breaks, respectively. As observed in the figures, [

]^{a,c}.



Figure 18.2.1-1a Measured Pressure Drop in Broken Loop of ROSA 5% Break (Kumamaru, et al., 1989)

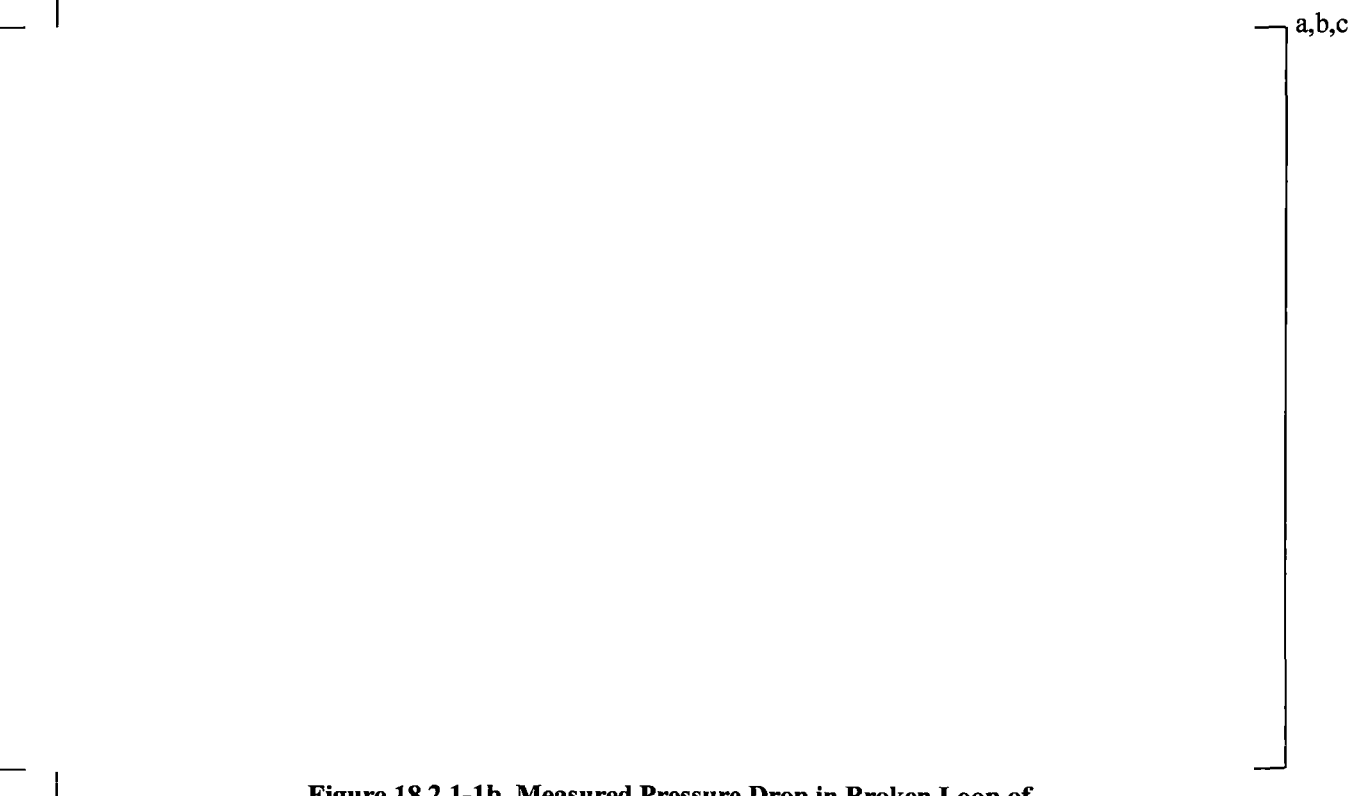


Figure 18.2.1-1b Measured Pressure Drop in Broken Loop of ROSA 10% Break (Koizumi and Tasaka, 1988)

PWS 2.3 Loop Seal Tests

Scaled U-tube experiments designed to examine the hydraulic behavior of a U-tube under conditions similar to those encountered during a small break LOCA were performed as part of the ECTHOR (an acronym from French “Ecoulements dans des Tuyauteries Horizontales en Eau-Air” which stands for Air-Water Flow in Horizontal Pipes) Program (Boileau and Bourteele, 1985). The vapor flow required to clear the U-tube was a specific focus of the tests.

18.2.1.1 Test Facility Description

The tests were run in a plexiglass facility with air and water at atmospheric pressure. The facility, illustrated schematically in Figure 18.2.2-1, consists of a blower, a run of horizontal piping from the blower, a U-tube, and a catch tank.

The pipe diameter chosen for the facility was []^{a,c}. This corresponds to approximately []^{a,c} scale compared with a pressurized water reactor (PWR), which has a pipe diameter of 2.58 feet. The air and water flow rates were scaled so that approximate similitude was maintained for the Froude number, shown to define the flow regime transition from stratified to intermittent and annular flow by (Taitel and Dukler, 1976). Figure 18.2.2-2 shows the predicted flow regime transition using the Taitel and Dukler flow regime map for atmospheric pressure, []^{a,c} scale, compared with the transition for steam at 1000 psia, full-scale geometry. This figure indicates that the transition from stratified to annular flow occurs at a higher vapor flux in the air-water tests. While better similitude could have been obtained with a smaller pipe, the chosen diameter also assures that the vertical pipes of the U-tube are sufficiently large so that any countercurrent flow limits (CCFL) that occur will not be affected by the pipe diameter. According to (Richter, 1981), the critical vapor flux for CCFL in pipes larger than approximately 2 inches in diameter depends only on pressure, not on pipe diameter.

Pressure drop across the U-tube was measured. In the horizontal and in the downstream vertical sections, several independent measurements of void fraction were made using pressure drops, optical probes, and gamma densitometers.

18.2.1.2 Test Procedures

Several test series were performed, as described below:

- Limit Line Tests

These tests were designed to obtain the liquid level in the horizontal portion of the U-tube, which produces significant liquid entrainment for a given air flow rate. This is equivalent in some ways to the CCFL limit and is termed the U-tube limit line. The tests were performed as follows:

[]^{a,c}

[

]^{a,c}

- Within Limit Line Tests

These tests were performed at air and water flows inside the limit lines established in the first phase with little or no entrainment. The tests primarily examined the interaction, if any, between the gas and the liquid at non-limiting flows (i.e., no entrainment). The tests were run as follows:

[

]^{a,c}

- Optical Probe Tests

These tests were performed similar to the Within Limit Line Tests. Optical probes were used to measure the liquid level. These tests confirmed the differential pressure measurements later used to derive vapor fraction.

- Complementary Tests

In some of the tests with high initial liquid level, oscillatory flow was observed. These oscillations consisted of movements of water back and forth between the upstream and downstream elbows. Slugs of liquid momentarily filled the pipe, increasing the pressure drop across the U-tube. These slugs were then ejected from the U-tube. The tests were similar to the limit line tests except [

]^{a,c}.

- Gamma Densitometer Tests

These tests used a gamma densitometer to measure the mixture density inside the horizontal portion of the U-tube. The tests confirmed void fraction measurements based on differential pressure.

18.2.1.3 Analysis of PWS 2.3 Test Results

Figure 18.2.2-3 plots the normalized residual liquid level in the loop seal (H/D) as a function of the gas volumetric flux (j_g). The loop seal was completely cleared when gas velocities exceeded about []^{a,c}. At low gas flows [

[]^{a,c}

The residual liquid level is an indication of the overall liquid mass contained in the loop seal as a function of gas flow, but does not represent the liquid distribution within the U-tube during the tests. Figure 18.2.2-4 shows the average void fraction at the midpoint of the horizontal leg and in the downstream vertical leg during the test. At low gas flow rates, []^{a,c}

[]^{a,c}

Figure 18.2.2-6 shows the measured pressure difference between the upstream and downstream exits of the U-tube. As liquid collects in the downstream vertical leg for the low gas flows, the pressure difference increases.

The basic processes occurring during these tests can be explained in terms of several hydrodynamic limits applied to both the horizontal and vertical legs. Figure 18.2.2-7 shows the horizontal leg average void fraction as a function of j_g^* , defined as:

$$j_g^* = \frac{j_g}{\left[\frac{(\rho_l - \rho_g)gD}{\rho_g} \right]^{0.5}} \quad (18-1)$$

where,

D is the pipe diameter, j_g is gas superficial velocity, g acceleration due to gravity, and ρ_l and ρ_g are the liquid and gas densities, respectively.

Figure 18.2.2-8 shows the various flow regimes observed for the tests performed under the limit lines and that the liquid level in the horizontal leg was []^{a,c}.

The loop seal behavior can be explained in terms of three regimes, bounded by the limit lines shown in Figure 18.2.2-7. The three regimes are described in the following paragraphs.

[

|

|

|

|

I^{a,c}

|^{a,c}

[

]^{a,c}

18.2.1.4 Effect of Scale

An important question which must be answered is what distortions the scaled geometry and low pressure used in these tests have introduced relative to the PWR. Having explained the data in terms of the limit lines above, we can examine the effect of scale by seeing how these limit lines change with scale (Figure 18.2.2-10). [

|

|

|

]^{a,c}

]^{a,c}

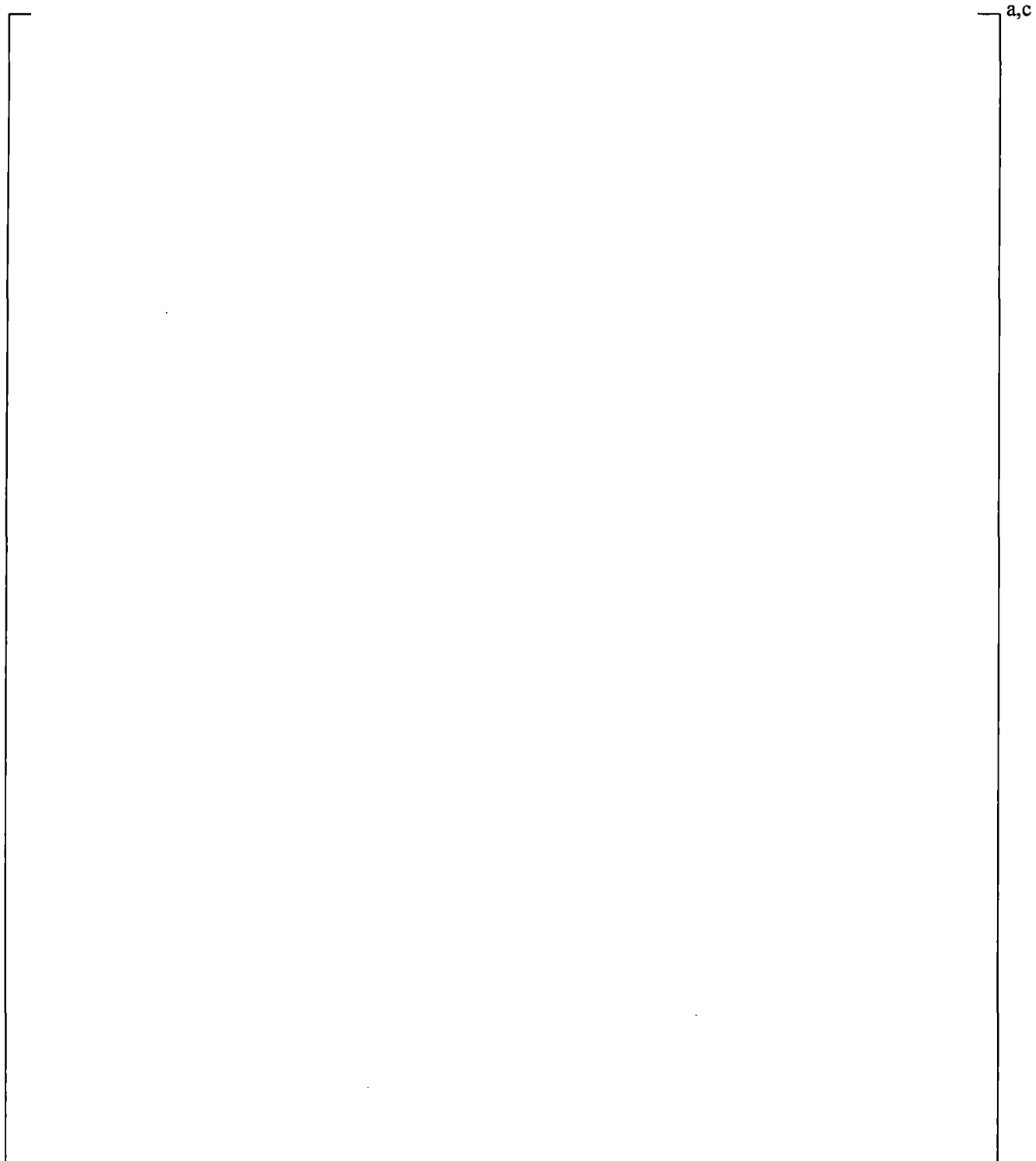
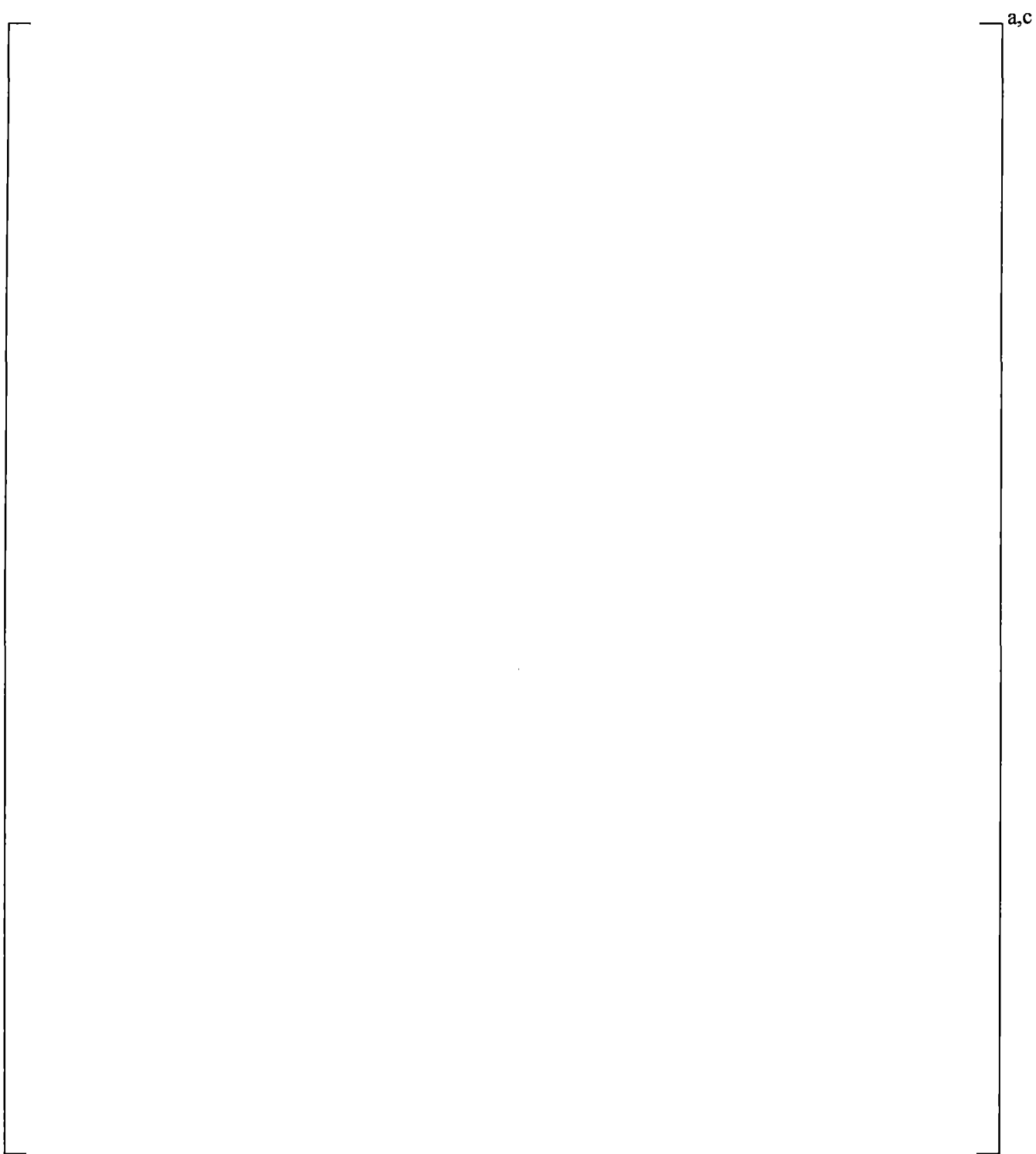
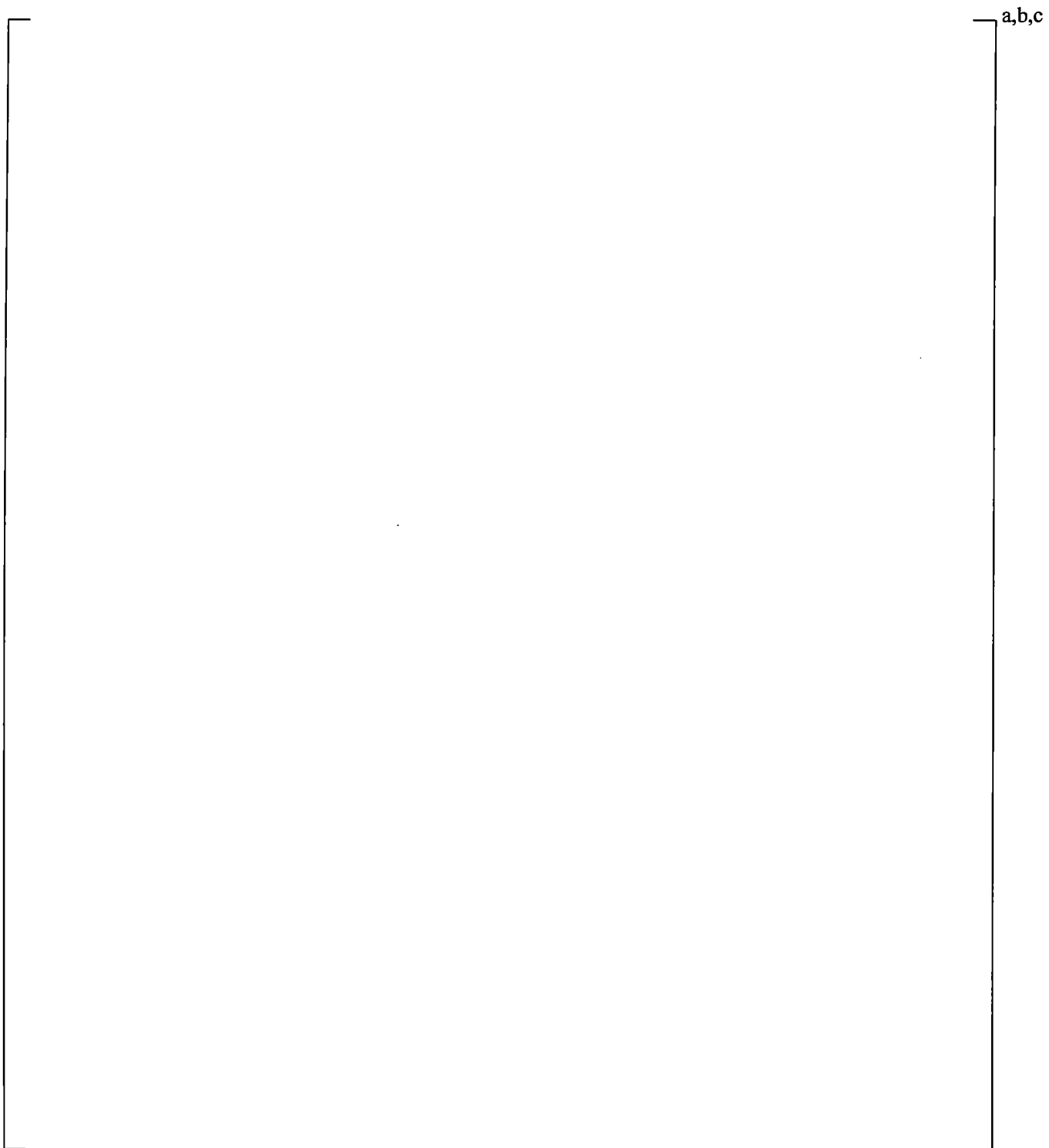


Figure 18.2.2-1 PWS 2.3 U-Tube Test Facility



**Figure 18.2.2-2 Taitel-Dukler Flow Regime Map, Comparing 1/3-Scale Pipe
at 14.7 psia and Full-Scale Pipe at 1000 psia**



**Figure 18.2.2-3 PWS 2.3 U-Tube Residual Liquid Level Remaining
After Test as a Function of Test Gas Flow Rate**

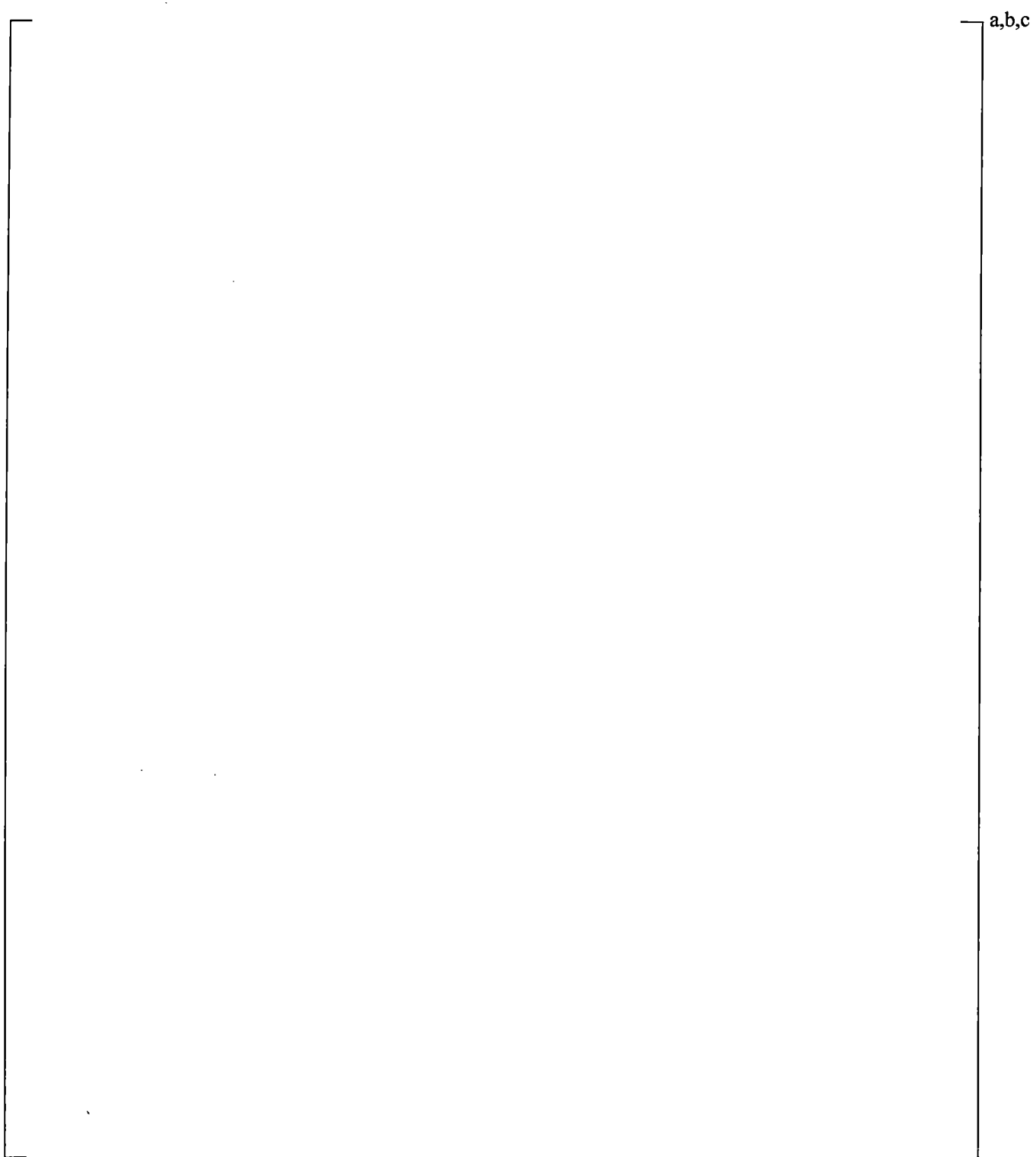
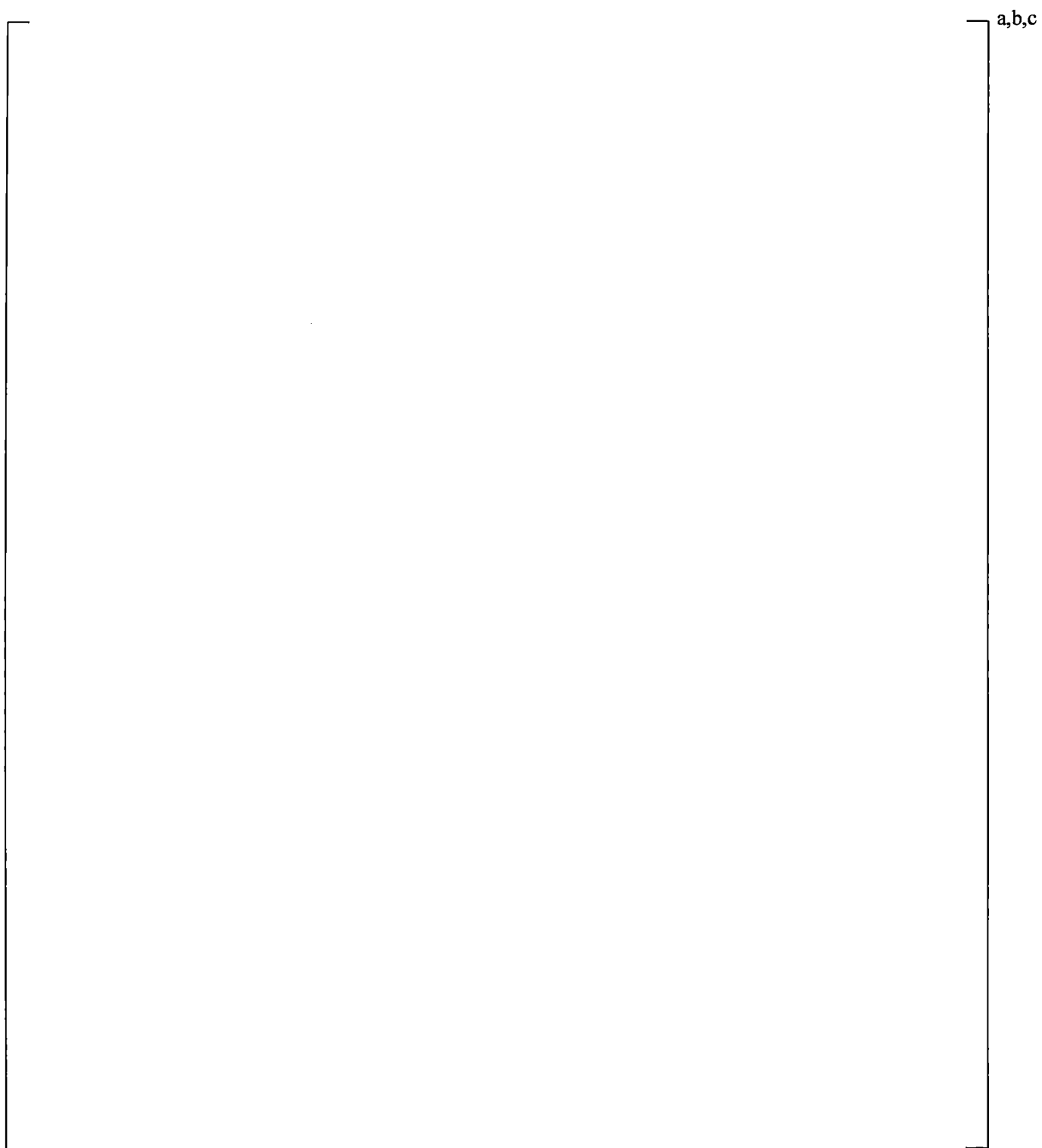


Figure 18.2.2-4 PWS 2.3 U-Tube Horizontal and Vertical Leg Average Void Fractions During Test



**Figure 18.2.2-5 PWS 2.3 U-Tube Horizontal Average Void Fraction During Test
Compared with Average Void Fraction after Test**

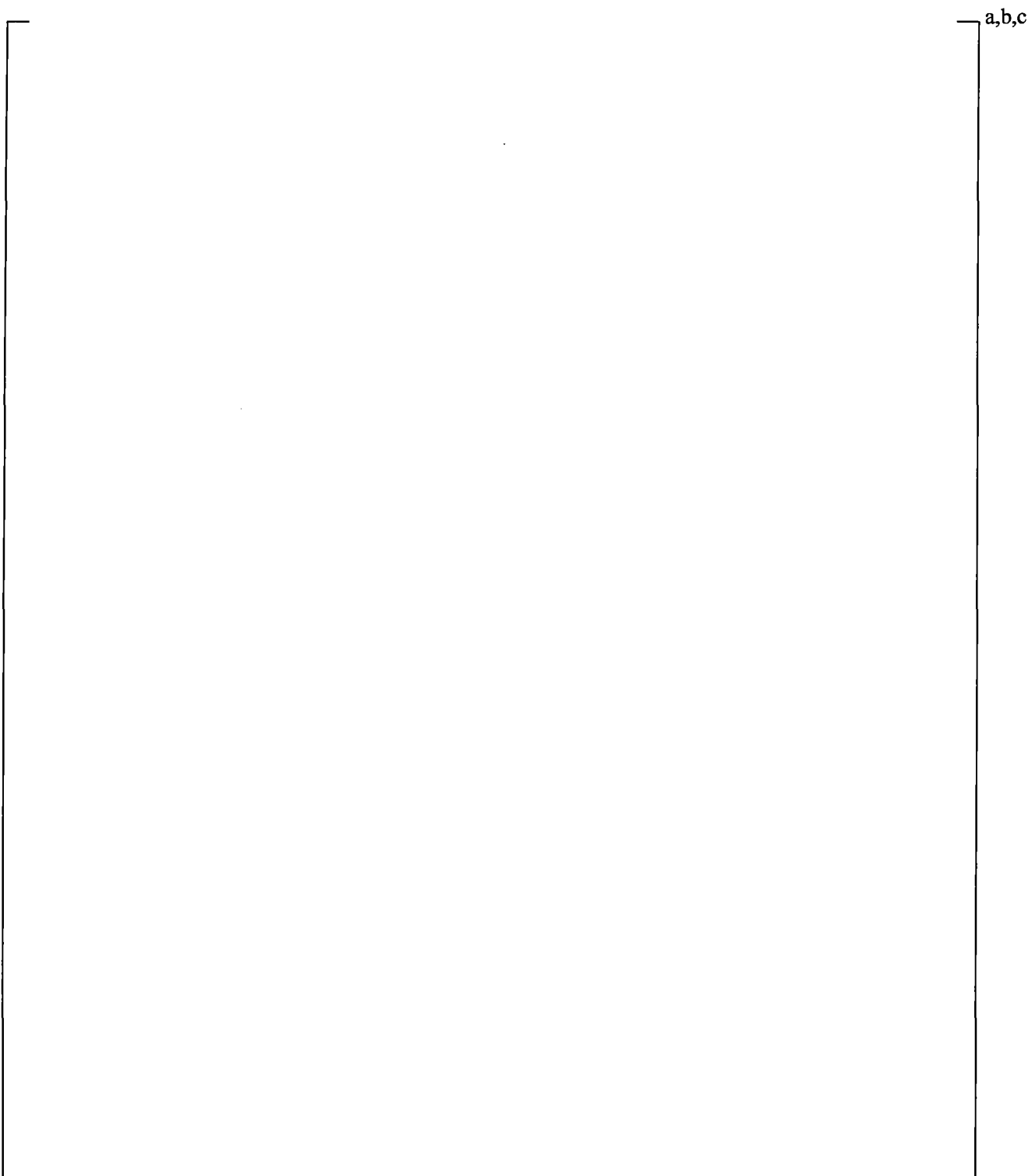


Figure 18.2.2-6 Pressure Difference Across the PWS 2.3 U-Tube

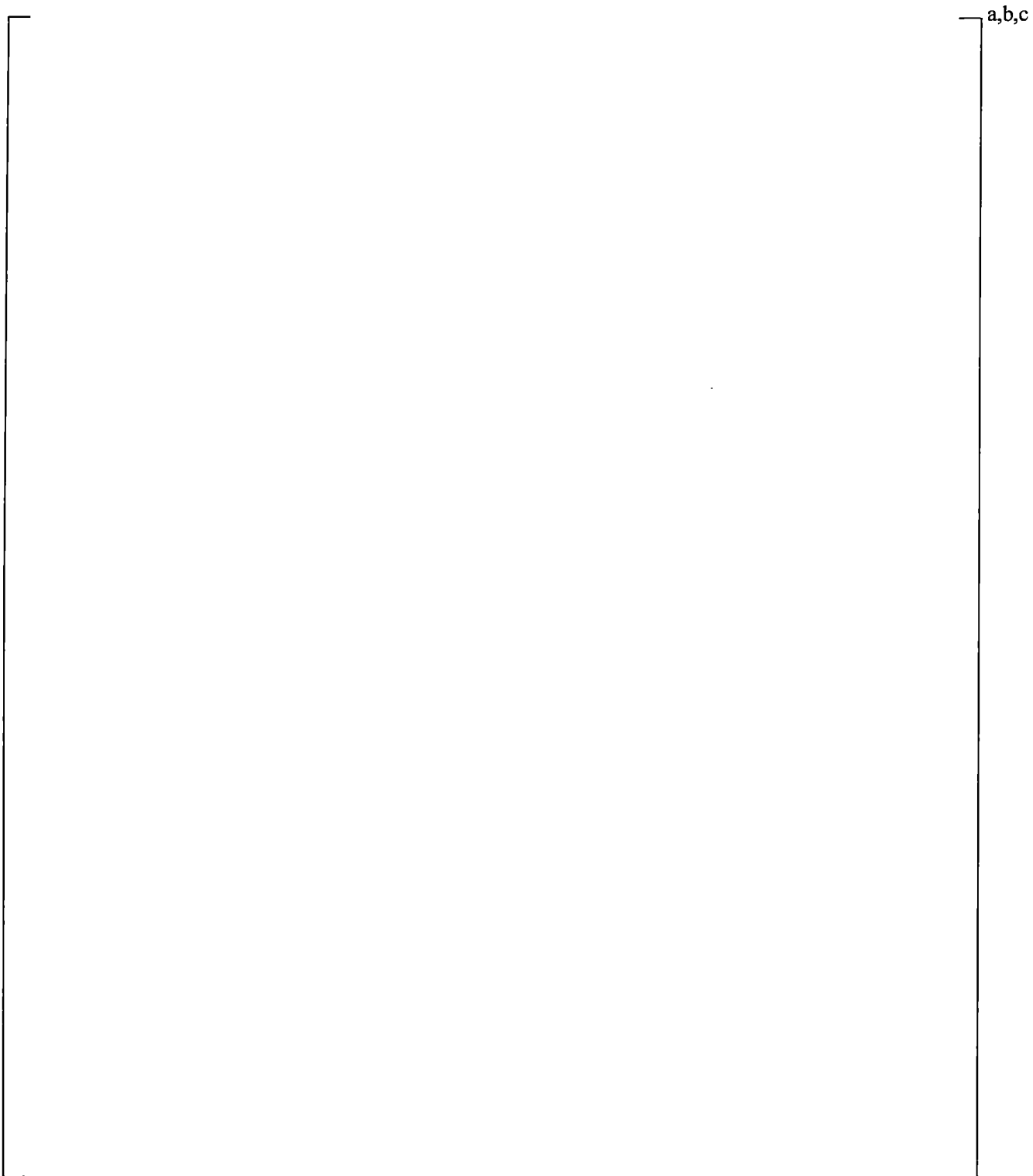


Figure 18.2.2-7 PWS 2.3 U-Tube Normalized Level and Limit Lines

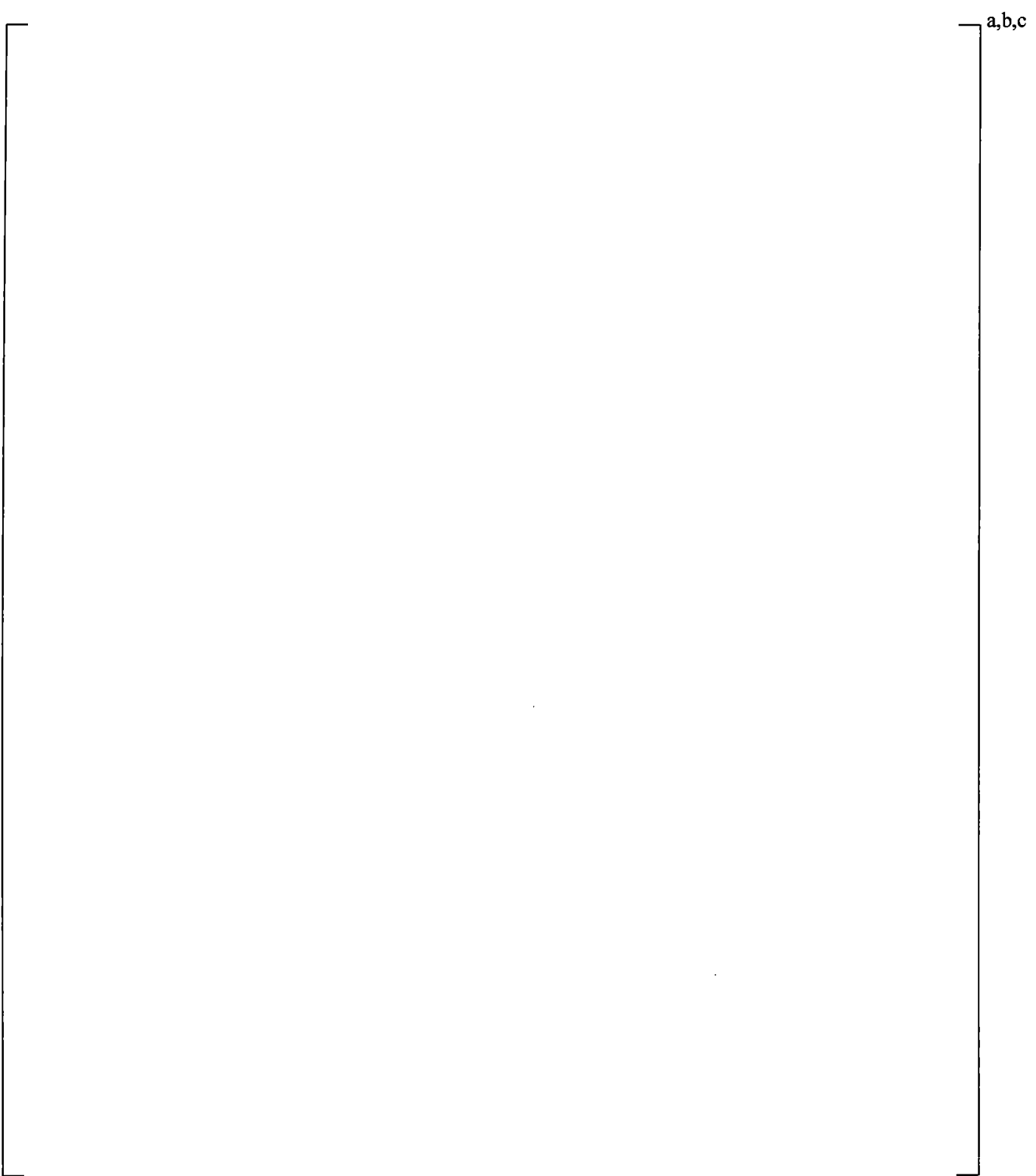


Figure 18.2.2-8 PWS 2.3 U-Tube Flow Regimes Observed Under the Limit Line

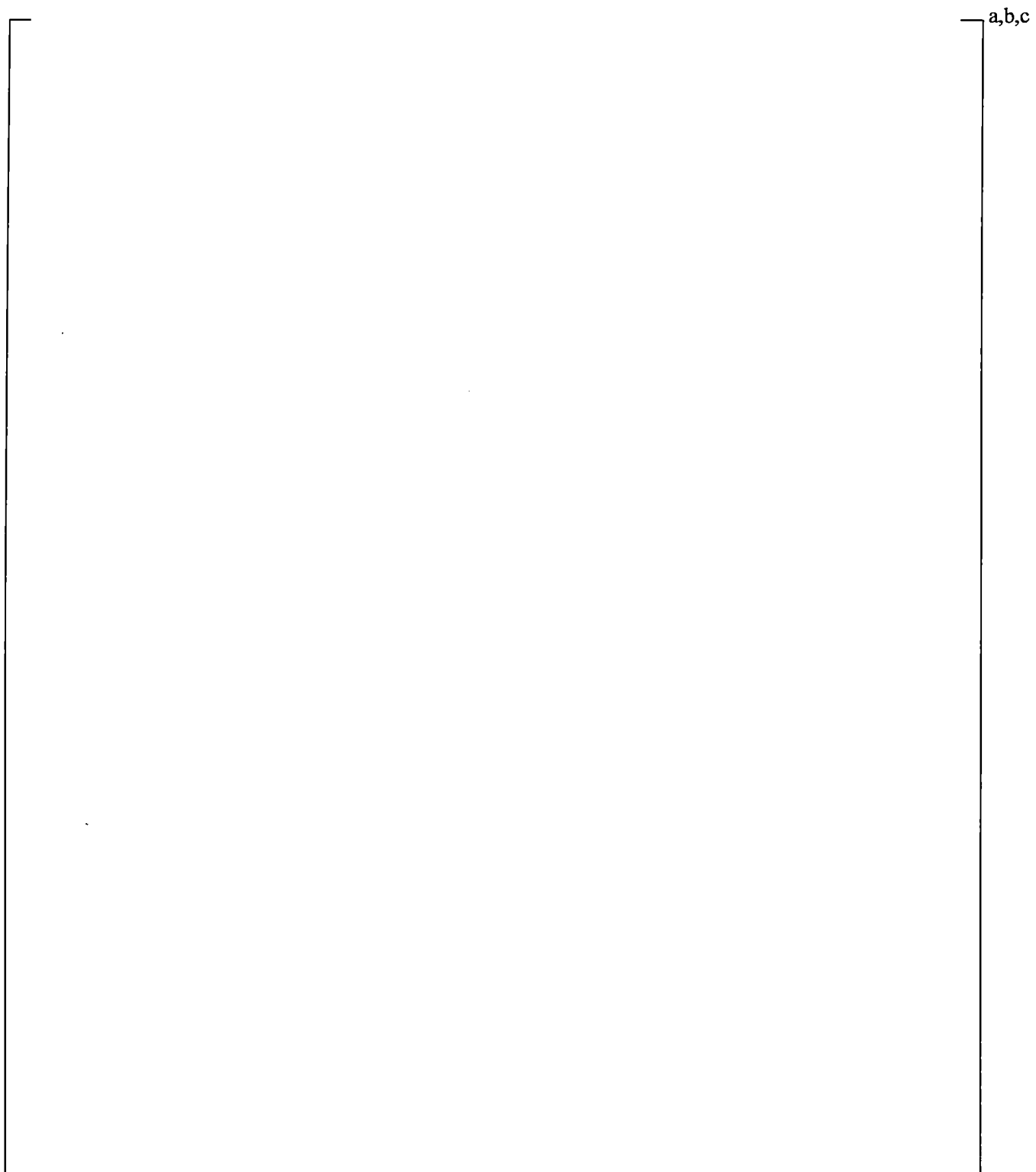


Figure 18.2.2-9 Hysteresis in Loop Seal Limit Line

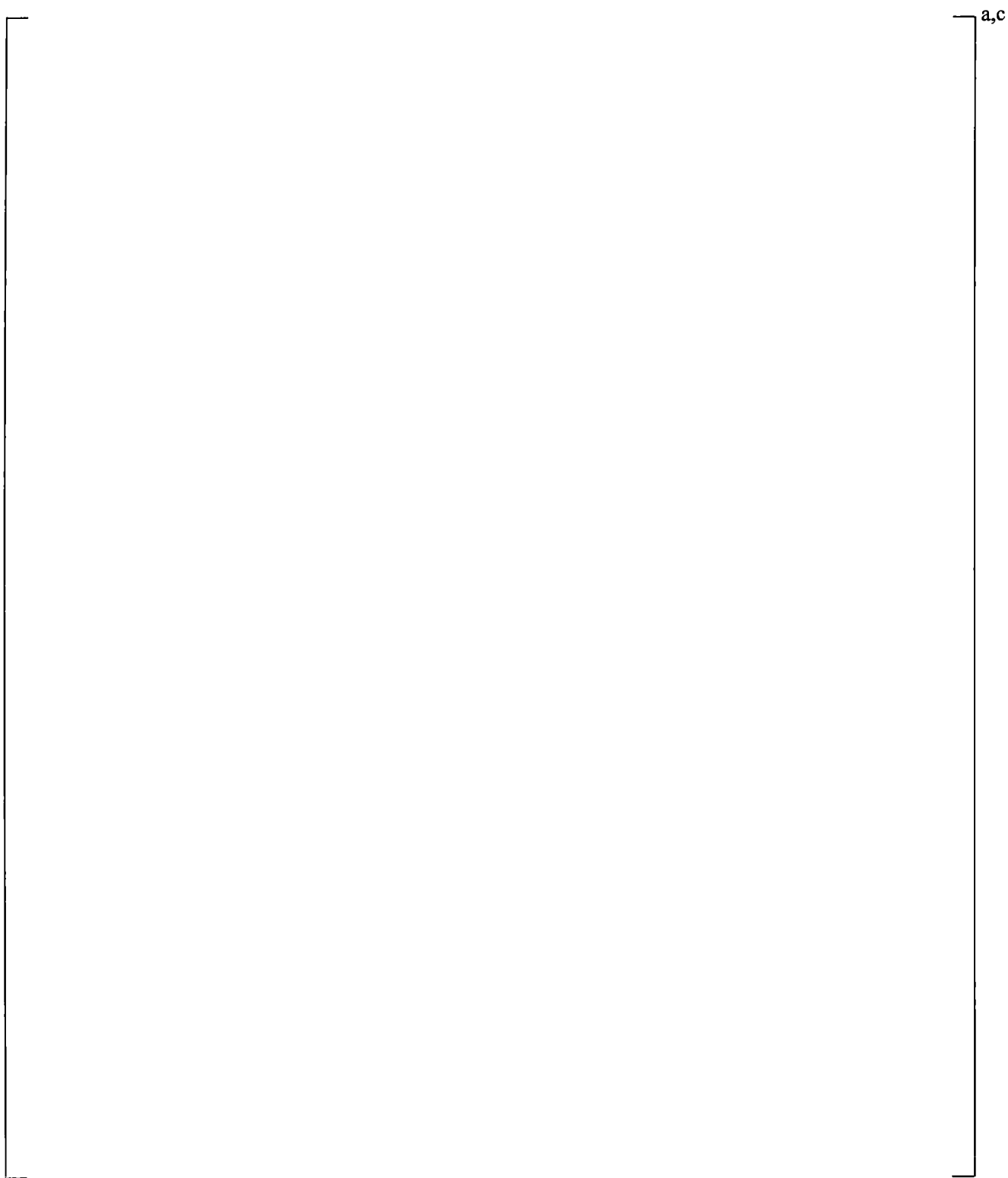


Figure 18.2.2-10 Effect of Increased Geometric Scale on Limit Lines

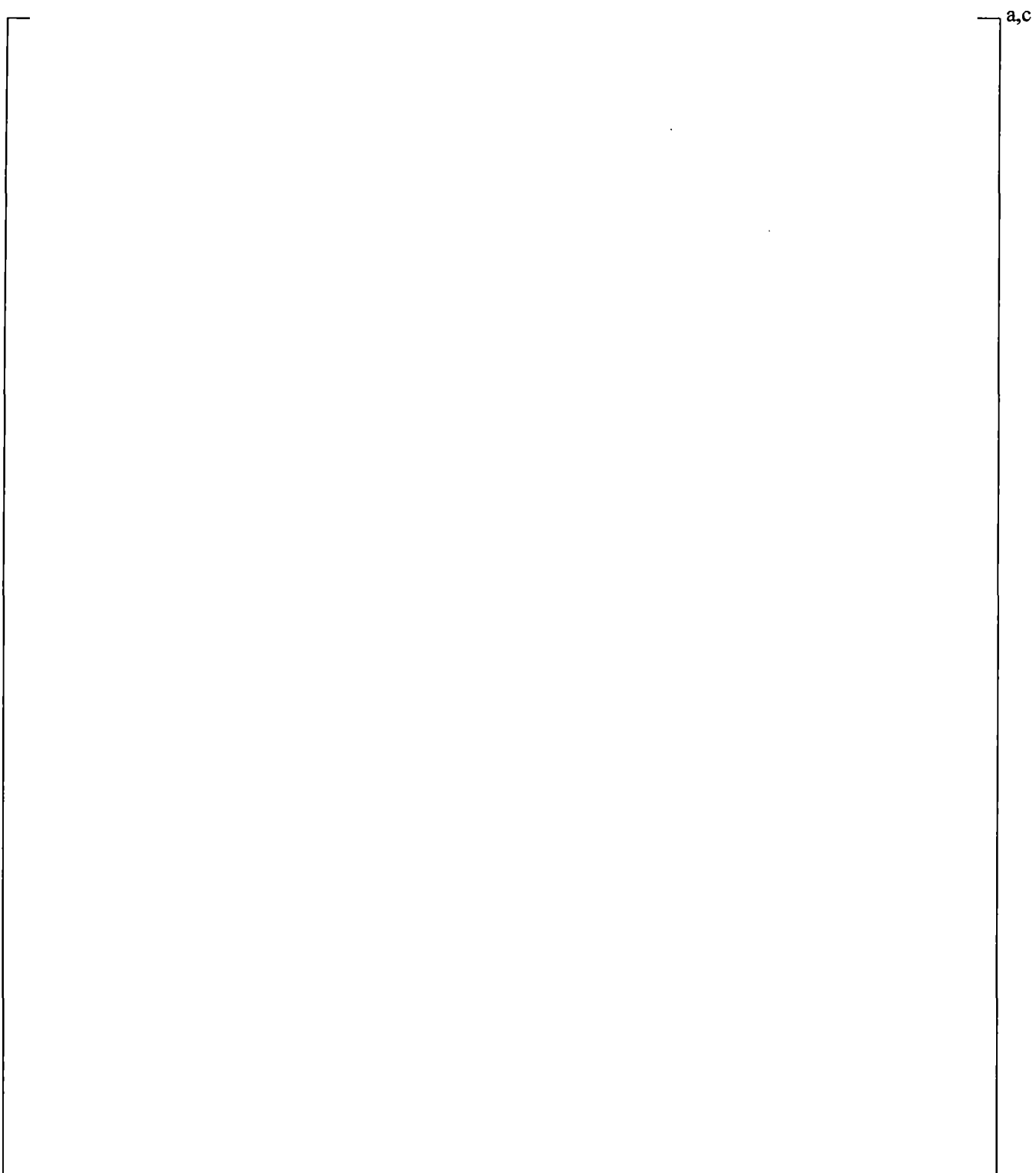


Figure 18.2.2-11 Effect of Increased Pressure and Scale on Limit Lines

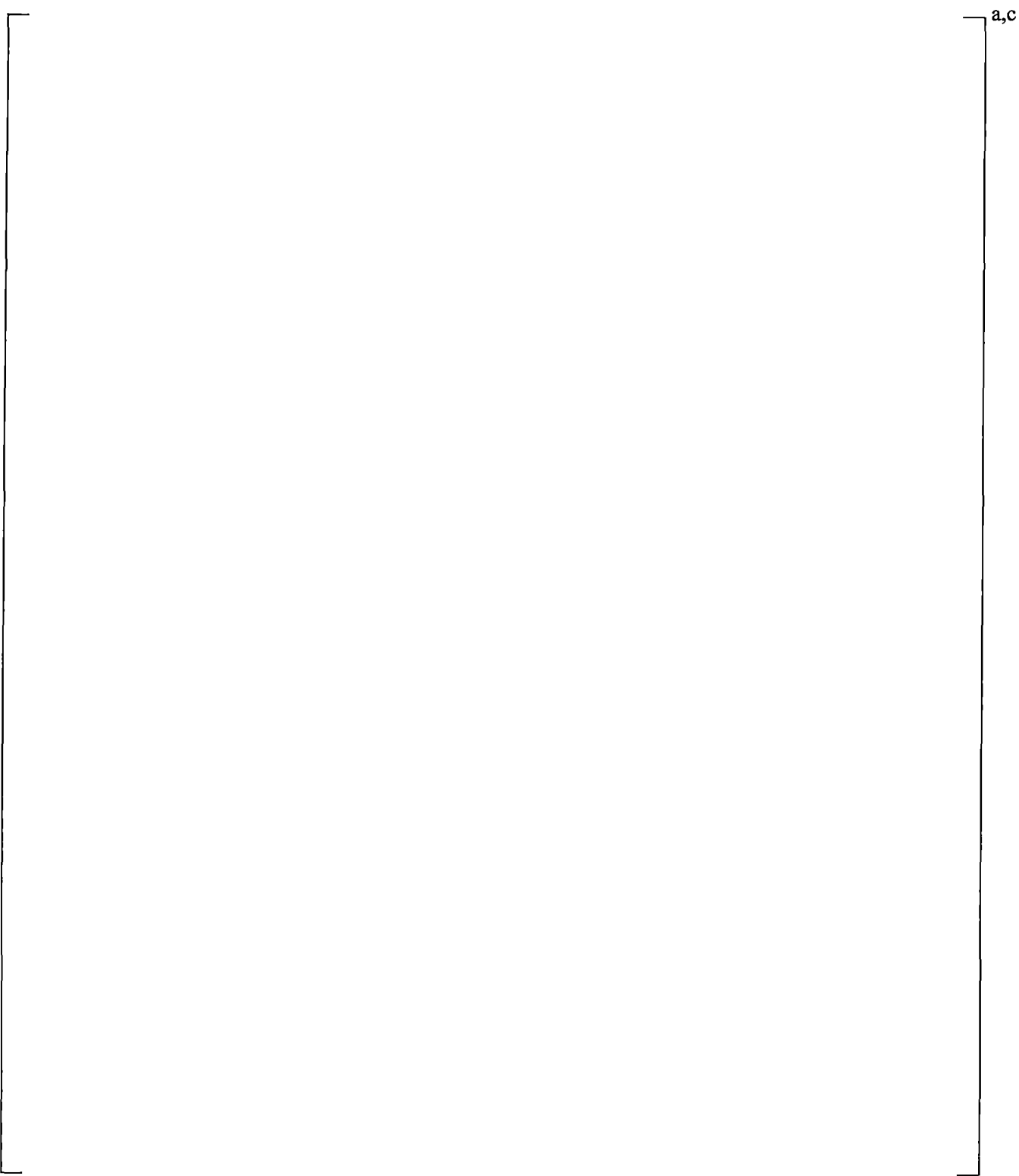


Figure 18.2.2-12 IVO Full-Scale Final Void Fraction and Limit Lines

18.2.2 Full-Scale Steam-Water Tests

Tests were performed at full-scale for a typical four-loop PWR in the Upper Plenum Test Facility (UPTF) at pressures of 3 bar (43.5 psia) and 15 bar (217.5 psia). The separate effects tests (Liebert and Emmerling, 1998) were conducted by blocking three of the four loops as seen in Figure 18.2.3-1, partially filling the loop seal in the open loop, injecting steam into the reactor vessel simulator, and measuring the residual level once entrainment had completed, but before the steam flow was terminated. The published data from the two test series are shown in Figure 18.2.3-2 (Liebert and Emmerling, 1998 and Ohvo, et al., 1998).

Lines are drawn through the data that represents a constant average gas velocity as seen in Figure 18.2.3-2. This velocity is the best-estimate of the minimum velocity at which entrainment from the liquid surface will take place within the horizontal section of the loop seal and is independent of the level in the horizontal run. Also shown is the Taitel-Dukler line for transition from slug to entrained flow. Liebert and Emmerling note that slugging was observed only at the lowest Froude number in each test series. Otherwise, the flow was observed to be stratified. The calculated critical gas velocities are 60 ft/s and 32 ft/s for the 3-bar and 15-bar test series, respectively.

Using the above critical velocities and calculated viscosity numbers and the critical velocity from the PWS 2.3 air-water tests (Figure 18.2.2-3), the results can be compared to Ishii's correlation as shown in Figure 18.2.3-3 (Ishii and Grolmes, 1975), where the Ishii parameter is calculated as:

$$Ish = \frac{w_g \mu_g}{\sigma} \left(\frac{\rho_g}{\rho_w} \right)^{0.5} \quad (18-7)$$

The UPTF and PWS 2.3 data (diamonds in the figure) lie []^{a,c} the database upon which Ishii's correlation was constructed (triangles in figure). While the UPTF data lie []^{a,c}. As shown in Figure 18.2.3-3, the UPTF data lie []^{a,c}.

[]^{a,c}

Using an Ishii number of 0.0033, a Reynolds number of approximately []^{a,c} is obtained from Equation 18-3. Recalling that this is the approximate Reynolds number for []^{a,c}

[]^{a,c}

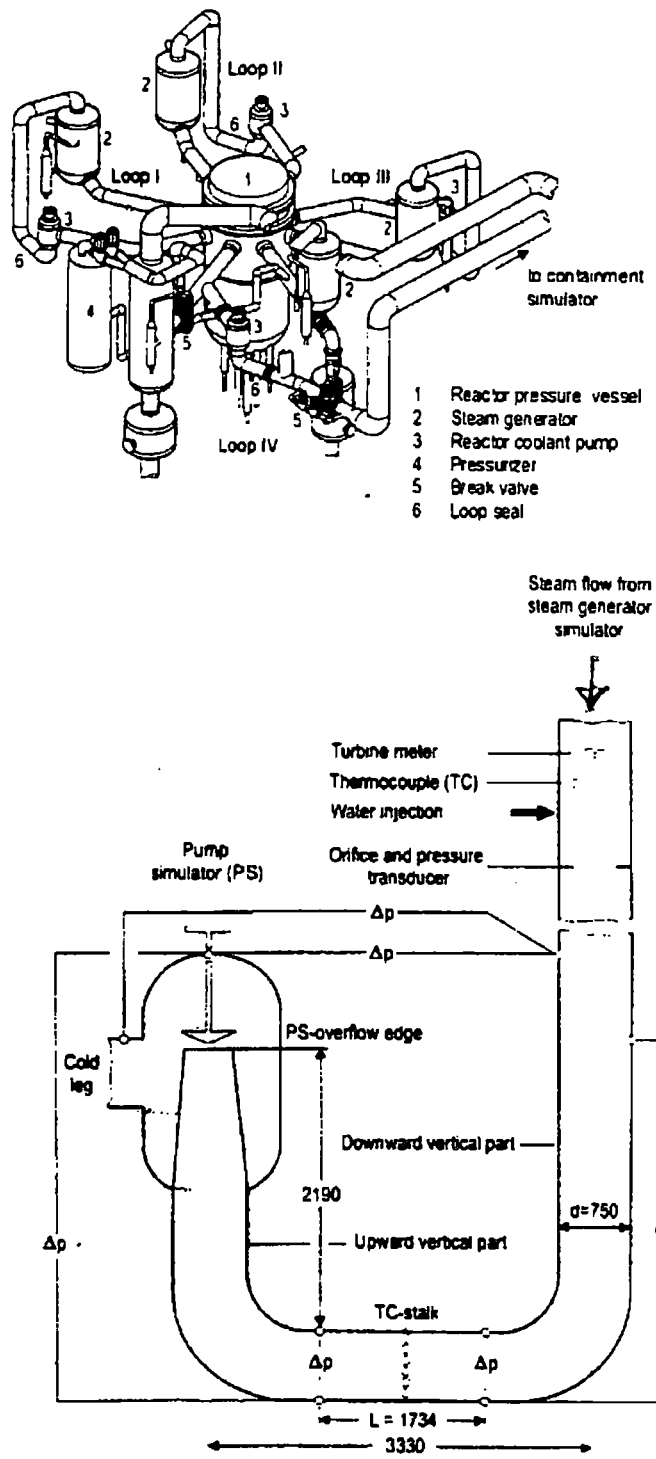
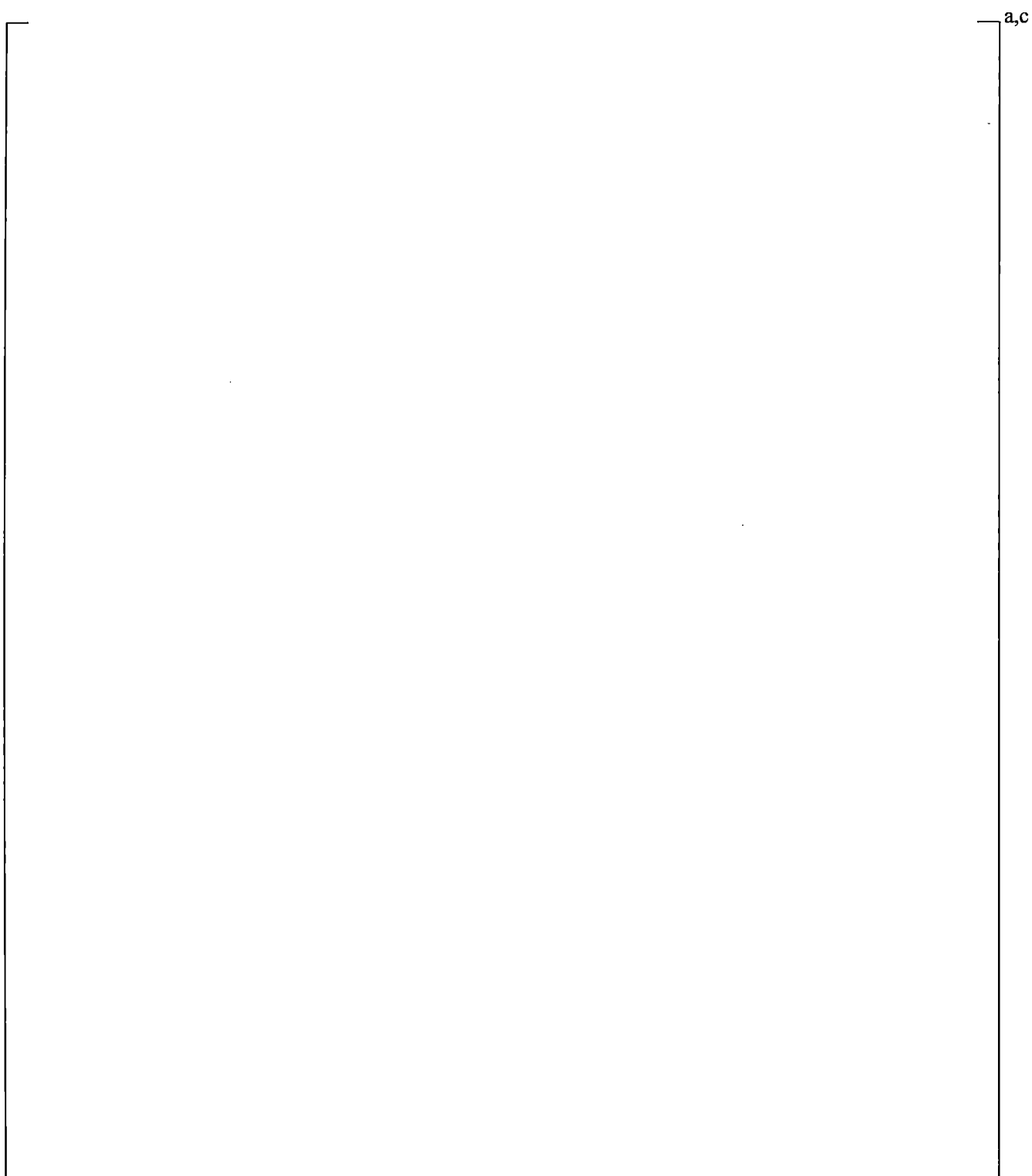


Figure 18.2.3-1 UPTF Facility and Single Loop Seal (Liebert and Emmerling, 1998)



**Figure 18.2.3-2 Lines of Constant Gas Velocity Compared to UPTF Data
for 3-Bar and 15-Bar Loop Seal Tests**

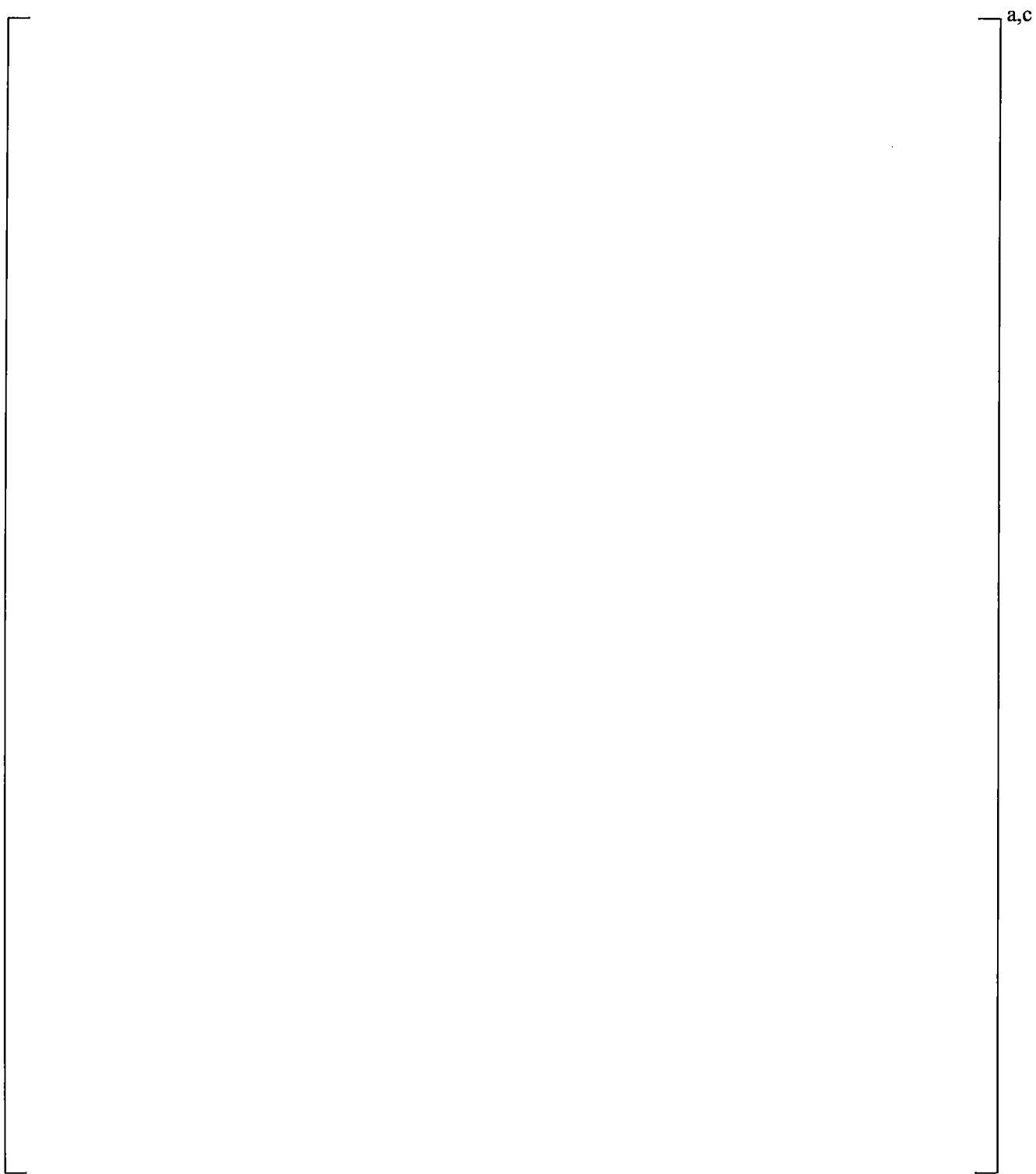


Figure 18.2.3-3 UPTF and PWS 2.3 Compared to the Ishii Correlation and Data Base

18.3 WCOBRA/TRAC-TF2 MODELING OF LOOP SEAL CLEARING PROCESS

The objective of this assessment is to confirm that WCOBRA/TRAC-TF2 adequately predicts the loop seal clearing phenomena for a PWR, namely, the residual liquid level in the loop seal and differential pressure across the loop seal post clearing. Discussions on the number of loop seals that clear and which loop seals clear are in Sections 28 and 31, Volume 3.

18.3.1 WCOBRA/TRAC-TF2 Simulation of the UPTF 3-Bar and 15-Bar Tests

The two UPTF full-scale steam-water tests were simulated with WCOBRA/TRAC-TF2. The separate effects tests were conducted by blocking three of the four loops and injecting steam into the reactor vessel simulator as shown in Figure 18.2.3-1 (Liebert and Emmerling, 1998). The WCOBRA/TRAC-TF2 model for the simulations has three components, as depicted in Figure 18.3-1; a FILL is used to supply the vapor; a PIPE is used to simulate loop 2 of the facility; and, a BREAK is used to maintain the test pressure. The PIPE has a total of []^{a,c} making up the actual loop seal. []^{a,c}

for simulation of the UPTF tests, and similar modeling (STRTX=1 at these cell faces) is expected to be used in the plant simulations.

The UPTF tests were run with a slightly superheated steam supply (Ohvo, et al., 1998). With the flow of superheated steam, liquid in the loop seal may be evaporated. However, it is expected that the amount of liquid evaporation is small compared to the amount of liquid lost due to slugs of liquid/entrained liquid being expelled out the loop seal. As such, the WCOBRA/TRAC-TF2 simulations were performed assuming []^{a,c}.

Although the initial liquid level was varied in the tests, the calculations are initialized []^{a,c}

[]^{a,c} Liebert noted that varying the initial level and liquid flow did not significantly affect the test results. For the 3-bar tests, the residual levels are lower for the cases with liquid injection for approximately the same Froude number. Thus, a set of initial conditions consistent with a hypothetical small break LOCA are used for the simulations.

Each of the test simulations is run separately, starting from the same initial conditions. The steam flow rate is increased from zero to the specified flow rate []^{a,c}

[]^{a,c}

The results of the 3-bar simulations are shown in Figure 18.3-2. WCOBRA/TRAC-TF2 generally []^{a,c}

[]^{a,c} Figure 18.3-3 shows the total mass in the system for the 3-bar and 15-bar cases with $j_g^* \approx 0.1$.

The predicted behavior for the 15-bar tests compared to the data is shown in Figure 18.3-4. WCORBA/TRAC-TF2 []^{a,c}.

Figure 18.3-5 shows a comparison of the predicted versus measured residual liquid levels for both tests. As observed in the figure, the []^{a,c} for both pressures.

Although no data are known to exist for full geometric and pressure scale, WCORBA/TRAC-TF2 calculations were performed using the UPTF model at 1000 psia. Based on the pressure-scaling discussion in Section 18.2.2.4, it is expected that []^{a,c}.

[]^{a,c}

Measured pressure drops across the UPTF loop seal are shown in Figure 18.3-7a. The highest pressure drops occur for $j_g^* < 0.1$ and then become approximately constant with increasing steam velocity. Also the magnitude of the observed differential pressure oscillations is significantly greater for $j_g^* < 0.1$. The pressure drop calculated by WCORBA/TRAC-TF2 is shown in Figure 18.3-7b. The calculated pressure drops shown in Figure 18.3-7b represent []^{a,c}.

[]^{a,c}

Figures 18.3-8a through 18.3-8c provide the pressure drop transient during the vapor injection period for three different 15-bar cases, which shows trends in pressure drop amplitude and frequency []^{a,c} (Figure 18.3-7a).

Figures 18.3-9a and 18.3-9b show smoothed pressure drop transients for the 3-bar and 15-bar $j_g^* \approx 0.05$ cases, respectively, and Figures 18.3-9c and 18.3-9d show smoothed pressure drop transients for the 3-bar and 15-bar $j_g^* \approx 0.22$ cases, respectively. For the 3-bar and 15-bar high vapor flow cases, []^{a,c}.

[]^{a,c}. For the 3-bar and 15-bar low vapor flow cases, []^{a,c}.

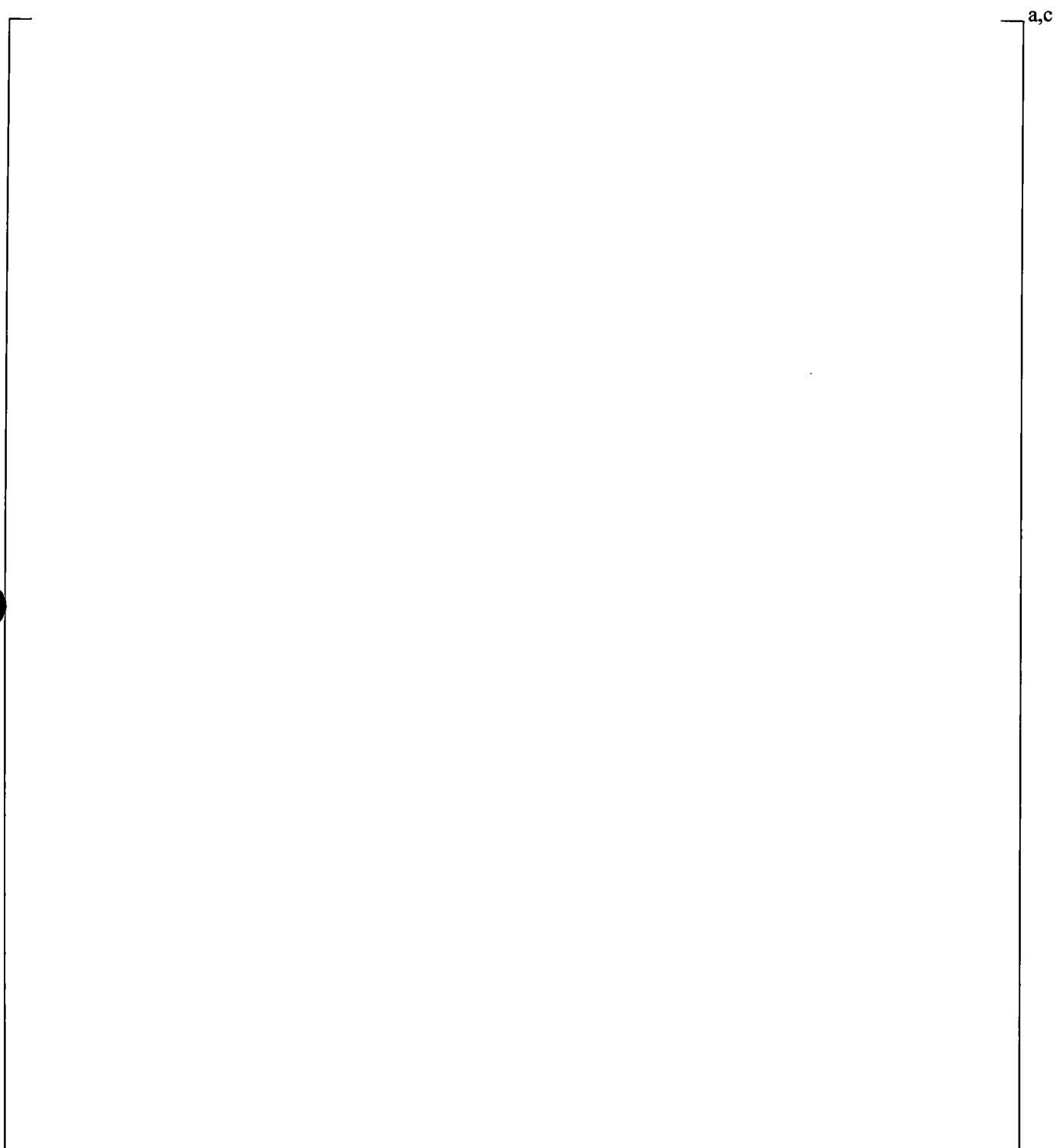


Figure 18.3-1 WCOBRA/TRAC-TF2 Model of the UPTF Separate Effects Loop Seal Clearing Tests



Figure 18.3-2 Comparison of WCOBRA/TRAC-TF2 Calculations and UPTF Data for the 3-Bar Tests



Figure 18.3-3 Comparison of WCOBRA/TRAC-TF2 Calculations Total System Mass for UPTF 3-bar and 15-bar $j_g^* \approx 0.1$ Cases

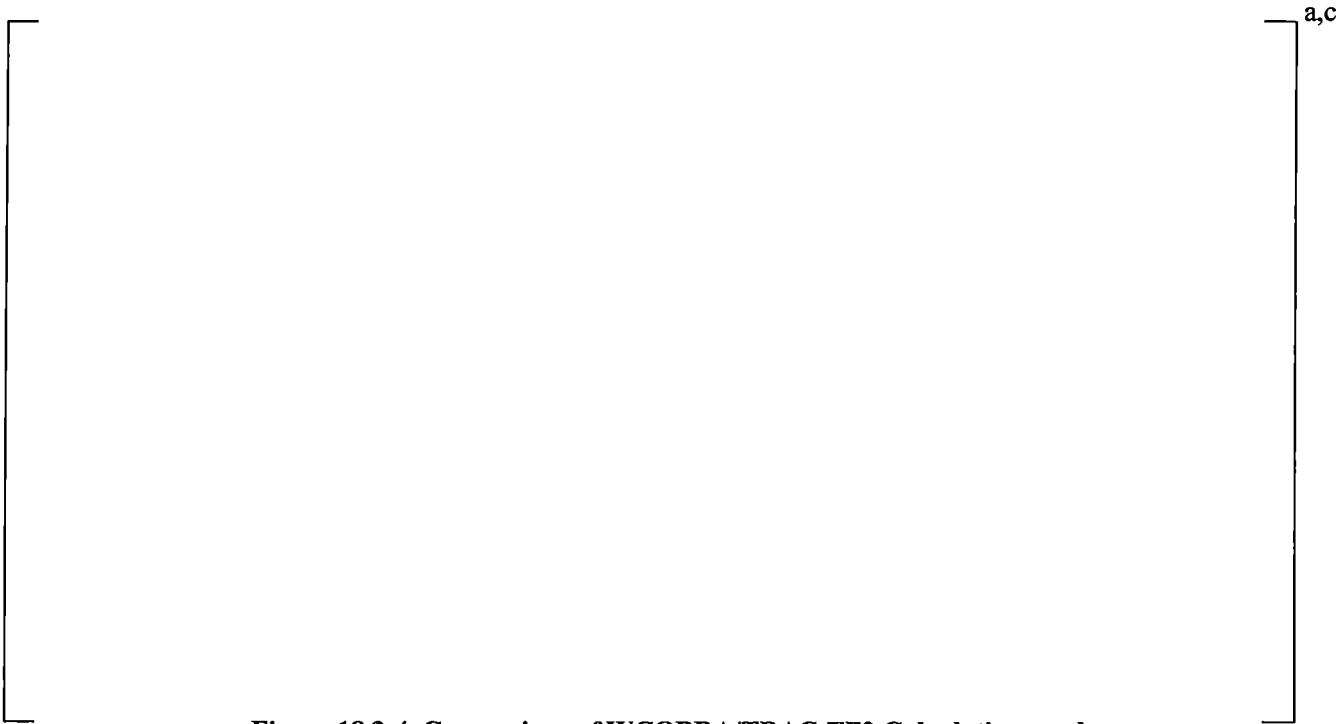


Figure 18.3-4 Comparison of WCOBRA/TRAC-TF2 Calculations and UPTF Data for the 15-Bar Tests



Figure 18.3-5 Comparison of Calculated vs. Measured Residual Liquid Levels

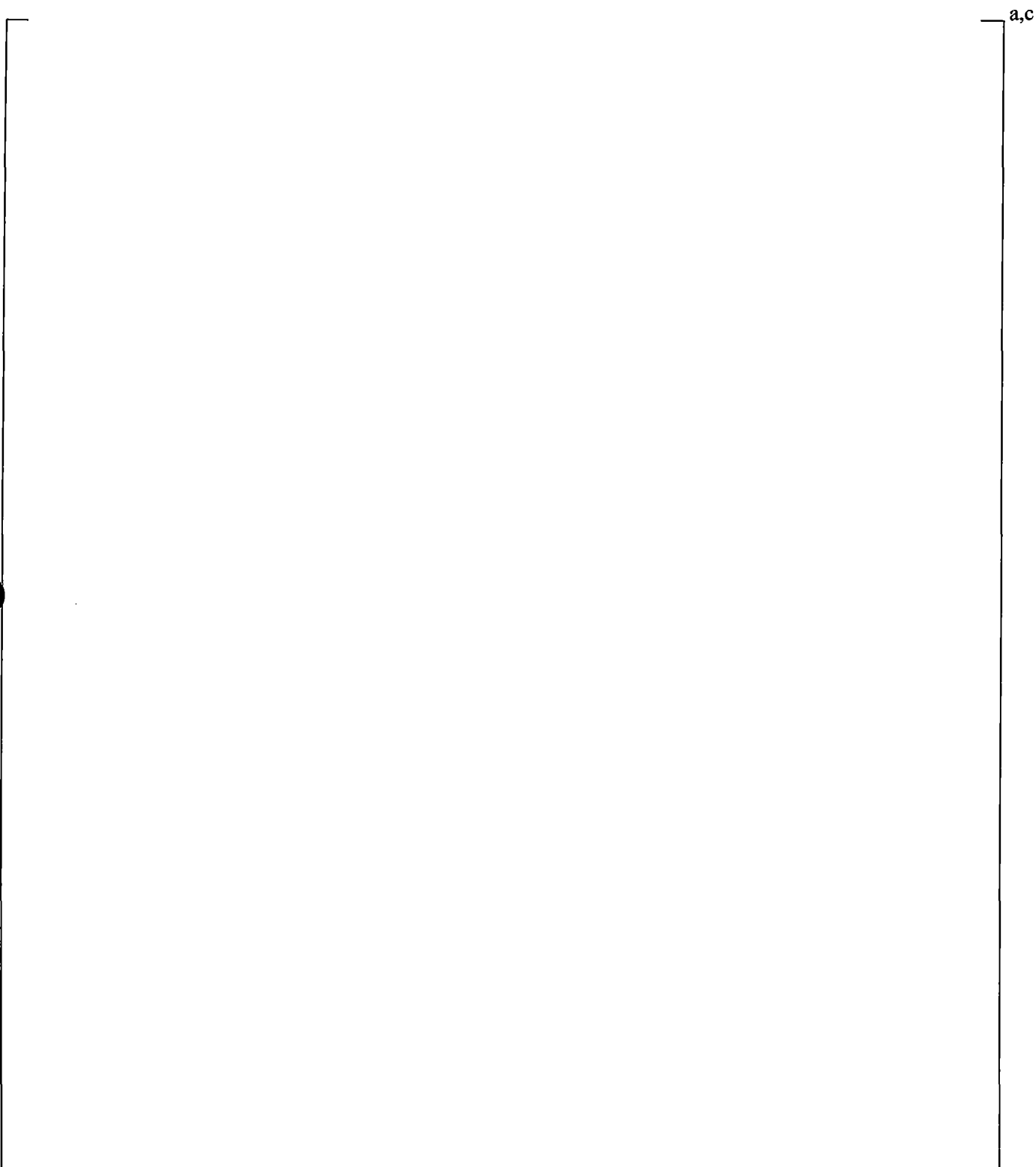


Figure 18.3-6 Calculated Residual Liquid Levels and CCFL Limit ($K_u = 3.2$) for 1000 psia

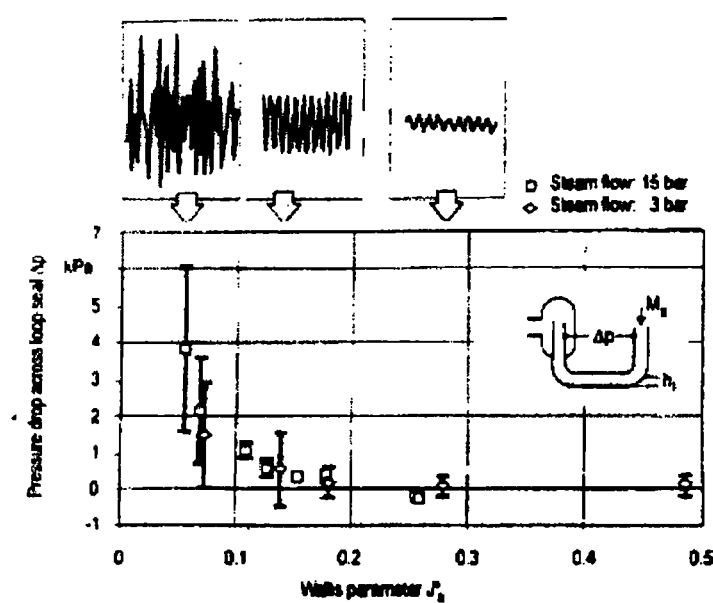


Figure 18.3-7a Measured Pressure Drop for UPTF 3-Bar and 15-Bar Loop Seal Tests (from Liebert and Emmerling, 1998)

Figure 18.3-7b Calculated Loop Seal Pressure Drop for 3-Bar, 15-Bar, and 1000 psia

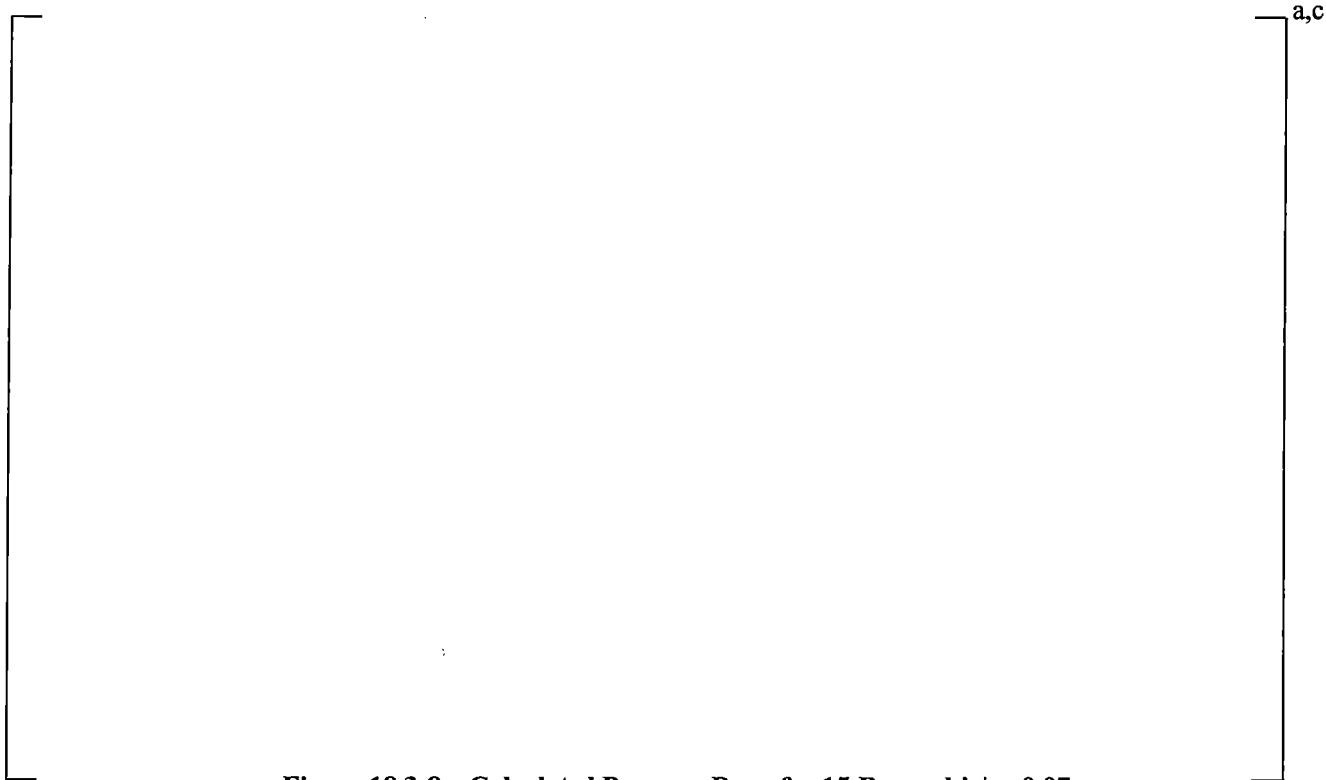


Figure 18.3-8a Calculated Pressure Drop for 15-Bar and $j_g^* \approx 0.07$

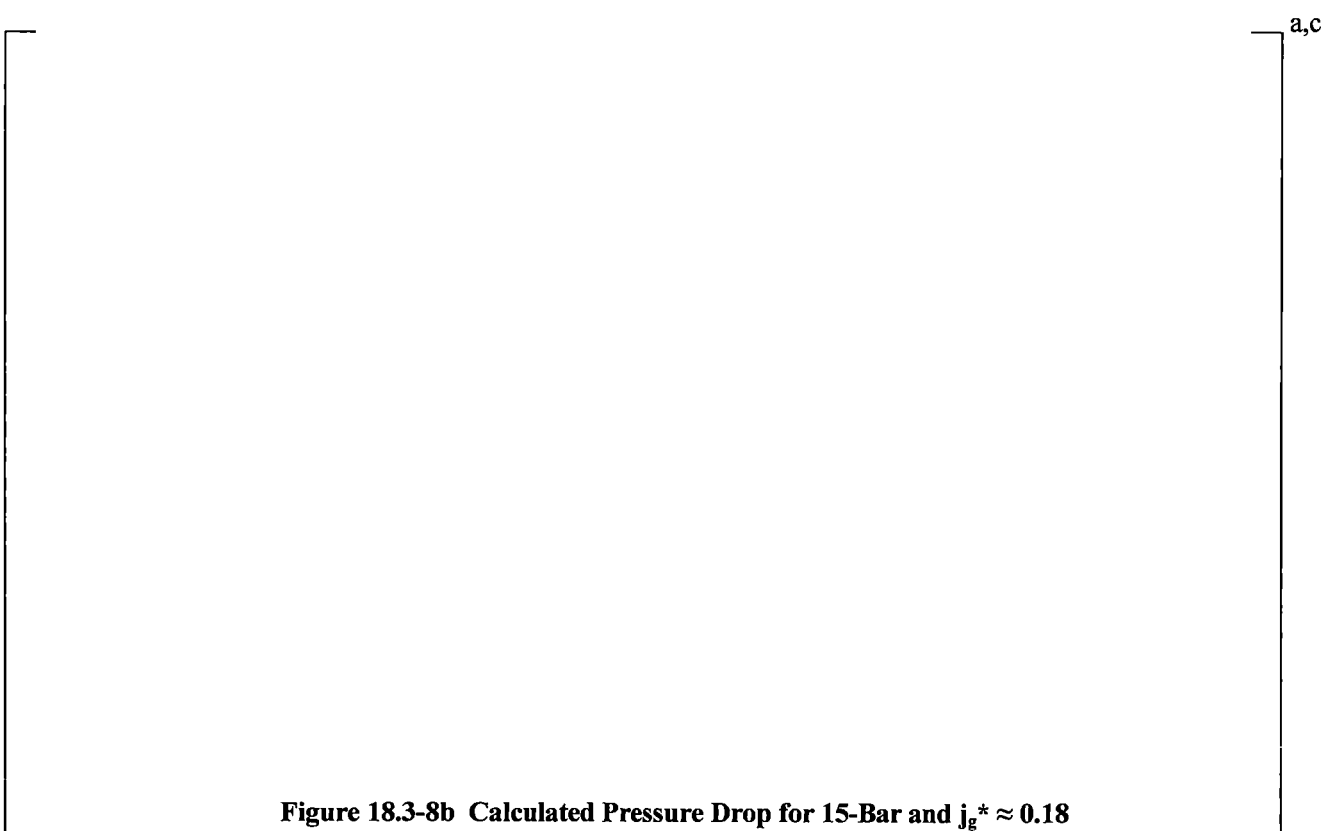


Figure 18.3-8b Calculated Pressure Drop for 15-Bar and $j_g^* \approx 0.18$

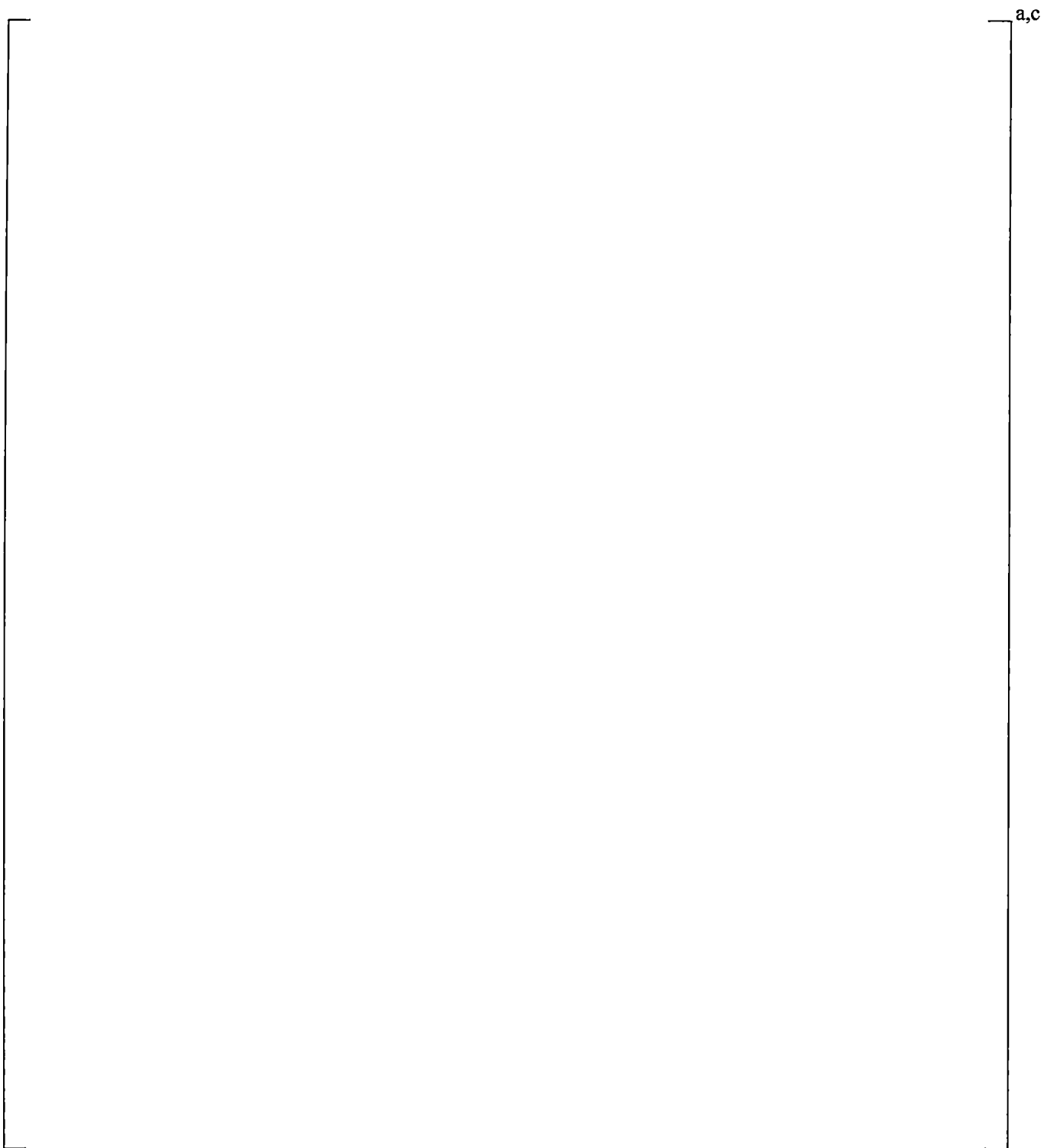


Figure 18.3-8c Calculated Pressure Drop for 15-Bar and $j_g^* \approx 0.32$

a,c

Figure 18.3-9a Comparison of Pressure Drop in Bends for $j_g^* \approx 0.05$ 3-bar Case

a,c

Figure 18.3-9b Comparison of Pressure Drop in Bends for $j_g^* \approx 0.05$ 15-bar Case



Figure 18.3-9c Comparison of Pressure Drop in Bends for $j_g^* \approx 0.22$ 3-bar Case

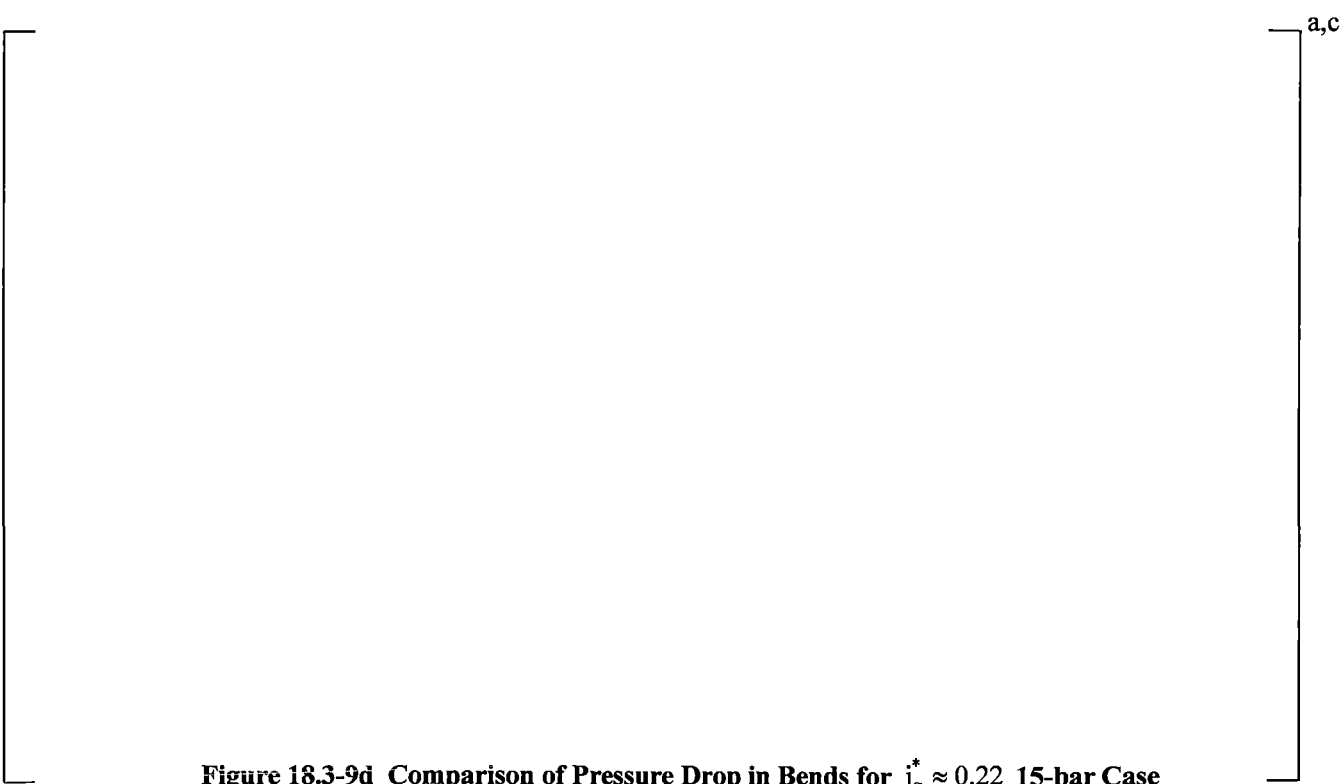


Figure 18.3-9d Comparison of Pressure Drop in Bends for $j_g^* \approx 0.22$ 15-bar Case

18.4 CONCLUSIONS

Assessment of the experimental data indicates the following:

[

]^{a,c}

Assessment of WCOBRA/TRAC-TF2 relative to the experiments indicates the following:

[

]^{a,c}

18.5 REFERENCES

1. Boileau, H., and Bourteele, J. P., 1985, "ECTHOR Program, PWS 2.3: Small Size Break, Final Report," EP/TA/DC 533.
2. Ishii, M. and Grolmes, M. A., 1975, "Inception Criteria for Droplet Entrainment in Two-Phase Concurrent Film Flow," *AICHE J.*, Vol. 21, No 2.
3. Koizumi, and Tasaka, K., 1988, "Quick Look Report for ROSA-IV/LSTF 10% Cold Leg Break LOCA Test, SB-CL-14," []^b
4. Kukita, Y. et al., 1990, "Loop Seal Clearing and Refilling During a PWR Small Break LOCA," *Nuclear Eng. and Design*, 121, 431-440.
5. Kumamaru, H. et al., 1989, "ROSA-IV/LSTF 5% Cold Leg Break LOCA Experiment Run SB-CL-18 Data Report," JAERI-M 89-027.
6. Liebert, J. and Emmerling, R., 1998, "UPTF Experiment Flow Phenomena During Full-Scale Loop Seal Clearing of a PWR," *Nuclear Engineering and Design*, Vol. 179, pp. 51-64.
7. Ohvo, J., et al., 1998, "Simulation of Full-Scale UPTF Loop Seal Experiments with APROS, CATHARE and RELAP," 6th International Conference on Nuclear Engineering, ICONE6-6090.
8. Pushkina, O. L. and Sorokin, Y. L., 1969, "Breakdown of Liquid Film Motion in Vertical Tubes," *Heat Transfer-Soviet Research*, Vol. 1, No. 5.
9. Richter, H. J., 1981, "Flooding in Tubes and Annuli," *Int. J. Multiphase Flow*, Vol. 7, No. 6, pp. 647-658.
10. Taitel, Y. and Dukler, A. E., 1976, "A Model for Predicting Flow Regime Transitions in Horizontal and Near Horizontal Gas-Liquid Flow," *AICHE J.*, Vol. 22, No 1.
11. Tuomisto, H. and Kajanto, P., 1988, "Two Phase Flow in a Full Scale Loop Seal Facility," *Nuclear Eng. and Design*, 107, 295-305.

19 ADDITIONAL LOCA HYDRODYNAMIC ASSESSMENT AGAINST LARGE SCALE EXPERIMENTS

19.1 INTRODUCTION

The phenomena identification and ranking table (PIRT) documented in Section 2, Volume 1 identified highly important hydrodynamic phenomena that occur during the Loss-of-Coolant Accident (LOCA) sub-scenarios. The objective of this section is to complete the assessment of specific WCOBRA/TRAC-TF2 models that were not addressed with the Separate Effects Test (SET) or Integral Effects Test (IET) evaluation presented in the other sections. The phenomena considered here are associated in particular with the Large Break LOCA (LBLOCA) scenario.

For previous WCOBRA/TRAC evaluation models, an extensive assessment was performed, and has been documented in Sections 14 and 15 of the Code Qualification Document, CQD (Bajorek et al., 1998). The most critical elements of this original assessment are repeated here to validate the performance of the new WCOBRA/TRAC-TF2 code, and confirm that the conclusions in terms of biases remain consistent with the already validated versions. The rational for the selection of the tests used in this assessment is discussed in Section 2, Volume 1.

The PIRT identified the following critical hydrodynamic models that can occur during a postulated LOCA transient.

Counter-Current Flow Limitation

The Counter-Current Flow Limitation (CCFL) is associated with the process of restricting liquid flow by counter-flowing vapor, due to interfacial drag forces. For example, liquid downflow in a pipe under the influence of gravity becomes unstable with increasing vapor upflow and eventually flows together with the vapor. Thus, stable counter-current conditions can exist only within a certain range. The boundary of this range is recognized as the CCFL.

CCFL can occur in several locations in a pressurized water reactor (PWR) during a LOCA. Emergency Core Cooling (ECC) bypass during the blow-down phase of a Large Break LOCA is an example of exceeding CCFL conditions in the downcomer annulus. CCFL is possible in other locations in the vessel. Liquid in the upper plenum may be held up at the upper core plate or tie plate by an upflow of steam from the core. Note, the upper core plate is the most flow restrictive area between the core and upper plenum. For Westinghouse PWRs, the tie plate corresponds to the fuel assembly top nozzle region. CCFL may also occur in the loops during some LOCA scenarios. CCFL may occur in the U-tubes of a steam generator or in the hot leg bend during a Small Break LOCA (SBLOCA) transient, affecting the depressurization of the system, and therefore, the overall progression of the transient. For larger breaks, the flow in the hot leg tends to stratify, and liquid is intermittently swept into the plenum of the steam generator. Any liquid swept into the steam generator tubes will tend to be evaporated, Section 1-3-3-3 of (Bajorek et al., 1998).

The predictive capability of WCOBRA/TRAC-TF2 for CCFL phenomena is assessed for different conditions, as follows:

1. CCFL in a Downcomer Annulus – [

]^{a,c}

2. CCFL in a Perforated Plate – [

]^{a,c}

3. CCFL in the Steam Generators – [

]^{a,c}

4. CCFL in the Hot Leg Bend – CCFL in the hot leg was [

]^{a,c}

Entrainment and De-Entrainment

Entrainment from liquid films and de-entrainment on structures are important processes that determine the mass distribution in the Reactor Coolant System (RCS) during a LOCA. Droplets leaving the core can be de-entrained by the upper plenum structures, forming a pool above the upper core plate. The de-entrainment and liquid accumulation in the upper plenum has two competing effects on the core flooding rate. Liquid that de-entraains in the upper plenum does not carryover into the steam generators and forms a pool in the upper plenum. The pool in the upper plenum creates a static pressure head that could decrease the flooding rate by some amount. A beneficial effect of the upper plenum pooling is the potential for draining of water into the core in the low power regions, where the steam flow is insufficient to prevent counter-current flow conditions. Liquid draining from the upper plenum can contribute to cooling by replenishing the core liquid inventory and providing topdown cooling. The entrained droplets that leave the upper plenum can be brought to the steam generator and evaporate inside the steam generator U-tubes, if the secondary side temperature is higher than the primary side temperature. The steam acceleration and the high speed of steam result in a large pressure drop in the steam generators. This high pressure loss in the steam generator caused by the evaporation of droplets, which is called steam binding effect, further contributes to additional pressure increase in the upper plenum.

[

]^{a,c}

Entrainment at the quench front has a strong effect on the net reflood rate and on the downstream heat transfer. Droplets entrained at the quench front readily evaporate, de-superheating the vapor, and can under certain conditions, impact on the fuel rods (though direct contact heat transfer is not modeled as discussed in Section 7.2.7, Volume 1). Lower downstream vapor temperatures and direct contact heat transfer increases the rate of heat transfer far ahead of the quench front, decreasing the peak cladding temperatures. [

]^{a,c}

Entrainment also occurs in the lower plenum during blowdown and the early part of refill. Droplets can be entrained from the liquid pool at the bottom of the vessel. During blowdown, these droplets are swept out of the vessel to the break through the voided downcomer. In the refill period, some of the droplets may enter the core and contribute to cooling, while most de-entrain on the lower core plate and remain in the lower plenum. [

]^{a,c}

Finally, entrainment/de-entrainment occurs in the downcomer during reflood. As the water level in the downcomer approaches the loop level, high steam or non-condensable flow from the intact loops may cause some water entrainment out the break. [

]^{a,c}

Therefore, the predictive capability of WCOBRA/TRAC-TF2 for entrainment and de-entrainment phenomena needs to be assessed for different conditions, as follows:[

]^{a,c}

Entrainment/de-entrainment models are relevant in various regions of plant analyzed. The capability of the code to model these processes together with the interaction with other process (e.g., the heat transfer) is a potential source of compensating errors. Section 24 provides an in-depth analysis of such compensating errors and the assessment presented in this section is the basis of such analysis.

Condensation

Condensation of steam by subcooled water will be initiated during a Large Break LOCA when accumulator water begins to flow into the cold leg piping. High head safety injection (HHSI) may begin earlier, but the flow rate is much lower than the accumulator (ACC) or low head safety injection (LHSI), and is therefore relevant only for the smaller breaks, where the time before accumulator or low head safety injection could be significant. Condensation of steam is of critical importance for both small and larger breaks, but the physical conditions differ significantly, and the Westinghouse cold leg condensation models introduced in Section 6 must be robust and generic enough to adequately address these different conditions. It is noted that the high head safety injection and low head safety injection are named as safety injection (SI) and residual heat removal (RHR) in Section 26, respectively.

For large breaks, the subcooled Emergency Core Cooling System (ECCS) water will flow from the cold legs into the upper downcomer and, later in the transient, into the lower plenum and core. During late blowdown and refill, the flow of accumulator water is of sufficient magnitude to theoretically condense all the steam flowing into the cold leg. During the reflood phase, the low head safety injection flow, at its minimum levels, is typically insufficient to condense all the steam flowing into the cold leg.

Condensation of steam in the downcomer has been observed to strongly affect the counter-current flow behavior in the downcomer as ECCS water penetrates into the lower plenum. As discussed above, ECCS bypass and Counter-Current Flow are basic processes, of which the accurate prediction is a fundamental requirement for a best-estimate LOCA code.

Also, steam condensation affects steam velocity in the downcomer and as a result the sweep-out, entrainment of liquid toward the break. The higher steam flow rate, in turn, may entrain more water from the downcomer to the break, and may increase the pressure drop through the broken cold leg nozzle.

Condensation of steam by ECCS water was also observed to produce flow and pressure oscillations of sufficient magnitude to affect the flow through the intact loops during reflood. This led initially to a concern that condensation phenomena would induce resistance in the intact cold legs and impede the flow of steam from the core during reflood. Tests in which the injection of ECCS water into the cold leg was simulated indicated that, while the hydrodynamic behavior was highly oscillatory, the induced resistance was relatively small.

The degree to which condensation of steam occurs in the cold leg, usually indicated by the condensation efficiency, is also important in determining the steam flow rate and temperature of the water flowing into the vessel during reflood. If the condensation efficiency is high, the steam flow will be reduced, and the water temperature will be increased. The condensed water, if it is still subcooled, will reach saturation after it enters the vessel and begin to boil sooner in the downcomer and core. The lower steam flow may entrain less water from the downcomer out the break, and leads to more vessel inventory. It also may result in a smaller pressure drop across the broken cold leg nozzle. If the condensation efficiency is low, the colder water will contribute to maintain the subcooling of the water in the downcomer.

Condensation is known to be strongly affected by the presence of non-condensable gases. As the accumulator empties, nitrogen is discharged in the system and results in pressurization of the downcomer as well as reduction in steam condensation rate. During reflood, a large volume of nitrogen is injected into the cold legs when the accumulator runs out of water. During refill, the RCS pressure may momentarily drop below containment pressure because of condensation, allowing containment gases to flow into the RCS via the broken cold leg.

For larger breaks, the primary side system experiences a rapid depressurization so that most of the condensation phenomena take place at low pressure. For smaller breaks however, the system pressure transient is slower, as discussed in Section 2. In this case, condensation in the cold leg at the high head safety injection is of significant importance, as condensation of the steam from the cold high head safety injection can significantly impact the transient pressure and vessel inventory. The assessment of the cold leg condensation for the Small Break LOCA is addressed in Section 17, while this section focuses on the Large Break LOCA.

Therefore, the predictive capability of WCOBRA/TRAC-TF2 for the condensation phenomenon needs to be assessed for different conditions, as follows:^[1]

[1]^{a,c}

The rest of this section discusses the performance of the models and correlations in WCOBRA/TRAC-TF2 used to simulate the processes discussed above.

The assessment roadmap is presented in Section 19.2. WCOBRA/TRAC-TF2 assessments are then documented in detail in Sections 19.3 through 19.6. Finally, Section 19.7 provides overall conclusions of the assessments documented in this Section.

19.2 HYDRODYNAMIC MODELS ASSESSMENT

Counter-Current Flow Limitation

Section 5.4 discusses the interfacial drag models that determine the existence of CCFL conditions in the vessel, Section 5.7 describes the corresponding interfacial drag models used for 1D components, and Section 5.15 describes the models available to enforce CCFL in the vessel and 1D components. As discussed in the previous Section 19.1, the predictive capability of WCOBRA/TRAC-TF2 for CCFL phenomena needs to be assessed for the following conditions:

1. CCFL in a Downcomer Annulus – CCFL/ECC bypass in the downcomer annulus of the full-scale Upper Plenum Test Facility (UPTF) is evaluated in Section 19.3, where WCOBRA/TRAC-TF2 results are compared to experimental data for the UPTF 6 tests.
2. CCFL in a Perforated Plate – CCFL could occur above the core at the top nozzle (tie plate) or upper core plate elevations. CCFL is []^{a,c}

^{a,c} WCOBRA/TRAC-TF2 predictions of CCFL at a perforated plate are evaluated with saturated liquid and steam at 1000 psia, 35 psia, and 14.7 psia, and results are compared with Northwestern test data in air-water at atmospheric conditions (Hsieh et al., 1980) in Section 19.4. The geometry of the plate (perforation ratio and thickness) simulates, at small scale, a perforated plate in a PWR. []^{a,c}

3. CCFL in the Steam Generators – CCFL is []^{a,c}

^{a,c} The CCFL in steam generator U-tubes is evaluated based on simulations of the Rig-of-Safety Assessment (ROSA) experiments in Section 21.10. []^{a,c}

4. CCFL in the Hot Leg Bend – CCFL is []^{a,c}

^{a,c} The CCFL in the hot leg bend is also evaluated based on simulations of the ROSA experiments in Section 21.10. CCFL in the hot leg was []^{a,c}

CCFL is not enforced in the pump suction piping since any draining of liquid into the loop seal region would tend to increase the resistance to steam venting.

Entrainment and De-Entrainment

Section 5.6 of Volume 1 described the models and correlations in WCOBRA/TRAC-TF2 that are used to calculate the entrainment and de-entrainment processes. A summary of the applicable models in WCOBRA/TRAC-TF2 is provided for reader convenience in Section 19.2.1 herein.

As discussed in the previous Section 19.1, the predictive capability of WCOBRA/TRAC-TF2 for entrainment and de-entrainment phenomena needs to be assessed for the following conditions:

1. Upper Plenum Entrainment and Carryover – WCOBRA/TRAC-TF2 simulations were performed for tests that provided information on the net effects of entrainment/de-entrainment and carryover in the upper plenum. Applicable simulations include UPTF Test 29B, Cylindrical Core Test Facility (CCTF) 62 and Loss-of-Fluid Test (LOFT) experiments (LOFT analysis is presented in Section 22). UPTF Test 29B simulated the conditions in the upper plenum during reflood, and provided measurements of liquid level above the upper core plate. The UPTF upper plenum was full-scale in both height and cross section. The main purpose of Test 29B was to determine the amount of upper plenum de-entrainment and carryover. The WCOBRA/TRAC-TF2 simulation of this test is described in Section 19.3.
2. Downcomer Entrainment, during ECC Bypass Period and During Reflood – During the latter part of blowdown, ECC fluid injected into the cold legs begins to penetrate and fall into the downcomer. Partial penetration may occur, as liquid falls part way down the downcomer but is then swept back to the broken cold leg. As the steam flow rates in the downcomer decrease, liquid can eventually reach the lower plenum. Evaluations by Siemens of UPTF bypass tests showed that the ECC delivery to the lower plenum is multi-dimensional in nature. The fraction of ECC liquid reaching the lower plenum depended not only on the steam flow rate, but also on the relative location of the ECC downcomer entry point to the broken loop (Glaeser, 1992). In addition to determining the downcomer flooding limit, the five subphases of UPTF Test 6 are selected to evaluate the ability of WCOBRA/TRAC-TF2 to predict entrainment and de-entrainment phenomena that occur in a downcomer during the blowdown and early refill periods of a LOCA. These tests and the WCOBRA/TRAC-TF2 simulations of them are described in Section 19.3.

Downcomer entrainment is also an important process during the reflood phase. During reflood, the liquid level in the downcomer can oscillate and reach up to the level of the bottom of the cold legs. Liquid can be swept from the downcomer out of the break during these oscillations. While the liquid level is below the cold legs, drops can be entrained from the liquid pool and carried out the break if high steam flows occur around the downcomer. UPTF Test 25A was conducted in order to investigate entrainment and downcomer level behavior during the reflood phase of a Large Break LOCA. The simulation of UPTF 25A using WCOBRA/TRAC-TF2 is described in Section 19.3.

3. Entrainment in the Core During Bottom Reflood – The correlation used to determine the entrainment rate at a quench front is described in Section 5.6 of Volume 1. The model is consistent with the work of Kataoka and Ishii (1983) and assumes the entrainment is due to vapor bubbling through a pool of liquid. The Full-Length Emergency Core Heat Transfer (FLECHT)

reflood test simulations provide a means of examining the performance of the entrainment model for bottom reflood. Mass balances were calculated from the test data so that carryout fraction and mass retention in the test bundle could be estimated. Section 19.5 compares the WCOBRA/TRAC-TF2 predictions of carryout fraction, total bundle mass, steam exit flow, and liquid outflow to estimates derived from the FLECHT test data. The comparisons provide a means of assessing the bottom reflood entrainment model.

Condensation

Section 6 of Volume 1 described the models and correlations in WCOBRA/TRAC-TF2 that are used to calculate the condensation processes (interfacial heat and mass transfer models). Section 6.2 describes the treatment of interfacial heat and mass transfer in the vessel component, while Section 6.3 addresses 1D components. The effect of non-condensable is described in Sections 6.2.11 and 6.3.7 for the respective vessel component and 1D components.

As discussed in the previous Section 19.1, the predictive capability of WCOBRA/TRAC-TF2 for condensation phenomena needs to be assessed for the following conditions:

1. Condensation in Downcomer Annulus – Condensation in the downcomer is an important contributor to the end of bypass/beginning of refill in a Large Break LOCA. Condensation in the downcomer of the full-scale UPTF is evaluated in Section 19.3, where WCOBRA/TRAC-TF2 results are compared to experimental data for the UPTF Test 6 series.
2. Condensation in Cold Legs, at both High and Low Pressure – Condensation in the cold legs was evaluated in Section 17. Condensation in the presence of safety injection at high pressures, representative of a Small Break LOCA, was assessed using data from the Westinghouse and Framatome Condensation on Safety Injection (COSI) configurations, and the ROSA facility. Condensation at low pressures, representative of a Large Break LOCA, was assessed using data from UPTF Test 8A. The effect of condensation in both the cold legs and downcomer is also examined with respect to the sweep-out phenomena during reflood by examining UPTF test 25A. The assessment of code predictions against UPTF 8A and UPTF 25A is presented in Section 19.3
3. Effect of Non-Condensable Gases on Condensation – Accumulator nitrogen injection was part of the LOFT and ACHILLES experiments, and the WCOBRA/TRAC-TF2 assessment results are discussed in Section 20. Additional assessment of the effect of non-condensables is provided via numerical “thought problems” in Section 23.

Integral Effects Assessment

CCTF is an integral effects test to evaluate the combined effect of CCFL in the tie plate, upper plenum de-entrainment, steam binding in steam generators, condensation in the cold leg and downcomer, entrainment/de-entrainment in the downcomer, and entrainment in the core, for the reflood phase of a Large Break LOCA. The modeling, simulation and assessment of CCTF 62 are presented in Section 19.6.

19.2.1 WCOBRA/TRAC-TF2 Models for Entrainment

Section 5.6 of Volume 1 described the models and correlations in WCOBRA/TRAC-TF2 that are used to calculate the entrainment and de-entrainment processes. Entrainment is the result of interfacial shear between vapor and liquid film. In WCOBRA/TRAC-TF2, liquid is moved from the continuous liquid field to the entrained field when the interfacial shear forces acting on the liquid are sufficient. In de-entrainment, liquid is moved from the entrained field to the continuous liquid field. A summary of the applicable models in WCOBRA/TRAC-TF2 is as follows:

1. Entrainment in Film Flow – WCOBRA/TRAC-TF2 determines film entrainment rates by comparing the entrainment rate based on a stable film flow to an empirical entrainment rate based on the work of Walley et al. (1973).
2. Entrainment in Bottom Reflood – The model for entrainment in the core near the quench front is based on a model by Kataoka and Ishii (1983) assuming vapor bubbling through a liquid pool.
3. Entrainment in Top Down Reflood – Models describing the transfer of liquid from the continuous liquid to the entrained drop field is described in Section 5.6.4 of Volume 1. The models account for the entrainment of liquid draining from pools and the entrainment of films from the rods at a top down quench front.
4. De-Entrainment in Film Flow – The model to estimate the de-entrainment of entrained drops into the continuous liquid field uses an empirical model by Cousins et al. (1965).
5. Crossflow De-Entrainment – Entrained liquid in the upper plenum can de-entrain on structures there as the two-phase mixture flows from the vessel into the hot legs. WCOBRA/TRAC-TF2 uses a model based on experiments by Dallman and Kirchner (1980) to determine the amount of de-entrainment in the upper plenum and other regions of the reactor vessel.
6. De-Entrainment at Area Changes – De-entrainment occurs as a two-phase mixture encounters a flow restriction such as a tie plate. WCOBRA/TRAC-TF2 uses a simple area ratio to de-entrain a fraction of the droplet field where an area reduction occurs in the reactor vessel.
7. De-Entrainment at Solid Surfaces and Liquid Pools – Drops are assumed to de-entrain when the drops flow into a cell with a solid surface at the opposite face, or when the drops flow into a cell which is in a bubbly flow regime.

19.3 UPPER PLENUM TEST FACILITY TESTS

19.3.1 Introduction

The UPTF was designed to obtain experimental data relative to the multi-dimensional flows expected in a PWR during a LOCA. The UPTF was the German contribution to the 2D/3D program established by the United States Nuclear Regulatory Commission (NRC), the Japan Atomic Energy Research Institute (JAERI) and the Federal Republic of Germany (BMFT). Tests conducted in the UPTF gave special consideration to:

1. Entrainment and de-entrainment in the upper plenum,
2. Co-current and counter-current two-phase flow in the upper core plate and tie plate region,
3. Co-current and counter-current flow and bypass in the downcomer, and
4. Condensation and steam/water mixing processes caused by ECC injection in the cold legs.

This section describes the modeling and simulation of several of the UPTF experiments using WCOBRA/TRAC-TF2. The simulations used were Tests 6 (to evaluate the ability of the code to predict ECC bypass), Test 25A (to evaluate entrainment of liquid out of the downcomer due to steam flow during reflood and condensation in cold leg and downcomer), Test 8A (to evaluate the models and correlations for condensation in the cold leg), and Test 29B (to validate the models for calculating de-entrainment in the upper plenum).

An overall facility description is provided in Section 19.3.2. The ECC bypass and entrainment/de-entrainment in downcomer and the simulations of UPTF 6 are described in Sections 19.3.3 to 19.3.5, while the cold leg condensation and the simulation of UPTF 8A are described in Sections 19.3.6 to 19.3.8. The downcomer entrainment/de-entrainment and cold leg condensation in UPTF 25A is described and simulated in Sections 19.3.9 to 19.3.11, and the upper plenum de-entrainment in UPTF 29B is described in Sections 19.3.12 to 19.3.14.

19.3.2 UPTF Facility Description

The UPTF simulated a full-scale 3900 MWt German PWR. The facility had four loops, each with a steam/water separator to simulate a steam generator and a variable resistance to simulate a reactor coolant pump. The upper plenum contained full size internals in an arrangement typical of a KWU PWR. Figures 19.3-1 and 19.3-2 show an overall diagram of the UPTF.

The upper plenum test facility was designed to investigate:

1. Water entrainment and separation processes in the upper plenum,
2. Co-current and counter-current steam/water flow phenomena in the upper core plate or tie plate region including water break-through into the core,
3. Co-current and counter-current steam/water flow in the downcomer and possible bypass of the ECC water injected into the cold legs of the loops to the break nozzle,

4. Condensation and mixing processes in the hot and cold legs of the loops, in the upper plenum and in the downcomer as a result of the injection of cold ECC water and,
5. Loop behavior with regard to possible water plug formation and oscillations in the hot and cold legs of the loops with ECC injection.

This range of investigation was achieved by varying the configuration of the facility. Full details of the facility and its instrumentation are given in Emmerling et al. (1988).

There were three intact loops and one loop with a break in the cold leg. The loop break was represented by gate valves and orifice plates to control the flow and a containment simulator gave the desired back pressure. The broken loop cold leg contained a water separator to prevent water from entering the containment simulator. The steam generators were simulated by four steam/water separators and adjustable passive resistances were used to simulate the four reactor coolant pumps. The facility did not contain a heated core, but the internals at the top of the core and in the upper plenum were full-scale replicas. The core itself was simulated by a steam/water injection system to set up the appropriate flow conditions in the vessel. The tubes that deliver the fluid to the core came up through the lower plenum.

The reactor vessel is shown in Figure 19.3-3. The upper plenum contained sixty-one guide tubes, eight support columns above the simulated fuel assemblies and eight support columns outside the periphery of the core (Figure 19.3-4). The downcomer gap width was 0.25 meters (9.8 inches) and the vessel internal diameter was 4.87 meters (191.7 inches).

The UPTF simulated the upflow of steam and droplets through the core during reflood by injection of steam and water into dummy fuel rods. The dummy fuel rods represented the upper quarter of a core with 193 assemblies of 16x16 array of fuel rods. Sixty-one of the assemblies were below guide tubes and had control rod spider simulators (Figure 19.3-5). The remaining assemblies were below flow restrictors in the upper core plate. The water and steam injection nozzles are shown in Figure 19.3-6. There were seventeen independently controlled injectors which divided to provide a separate nozzle for each dummy fuel rod assembly.

The dummy control rods terminated at the bottom of the guide tubes which were sealed to prevent flow from the upper plenum to the upper head. The upper head was thereby isolated from the rest of the vessel and had no effect on the facility.

The UPTF cold legs had an inner diameter of 750 millimeters. The ECC injection was at an angle of 60° to the cold leg centerline in UPTF and was 5822 millimeters (19.1 feet) from the inside wall of the vessel.

The steam generator simulators for the intact and broken loops and the broken cold leg water separator are shown in Figure 19.3-7. Flow entered an inlet plenum, which had the same volume as a PWR steam generator, and rose through cyclone tubes. The cyclones separated the water from the steam and the water was removed from the loop. The steam flowed through the steam generator upper plenum and returned to the cold leg.

The water drainage system removed the large quantities of water that accumulated during a test. Generally these quantities were found in the test vessel, the steam generator simulators, the broken cold leg water separator, and in the drainage vessels of the broken loops.

The raw data produced from the instrumentation was continuously recorded throughout a test, some of which was post-processed to give computed parameters. An example of a computed parameter derived from raw data is liquid level, which is derived from the measurement of differential pressure.

The downcomer was instrumented with fluid distribution grids, turbine meters, differential and absolute pressure transducers, and fluid and wall thermocouples. The lower plenum and core regions were instrumented with optical liquid level detectors, differential pressure transducers, and fluid and wall thermocouples. The instrumentation in the upper plenum included:

1. Wall and fluid thermocouples,
2. Fluid thermocouples in end boxes and below the tie plate,
3. Differential pressure transducers across the tie plate,
4. Differential pressure transducers and capacity liquid level detectors in upper plenum,
5. Optical liquid level detectors and fluid distribution grids,
6. Video probes in upper plenum,
7. Break-through detectors below tie plate,
8. Tie plate drag bodies in end boxes and,
9. Turbine meters in end boxes and in upper plenum.

19.3.2.1 Scaling Consideration and Applicability to PWR

The cold leg and the test vessel upper plenum, the lower plenum, and the downcomer of the UPTF are geometrically similar to a PWR. Table 19.3-1 compares the major dimensions of UPTF with a typical Westinghouse 4-loop PWR, which is referred to as typical PWR in the following discussions.

Comparisons of the primary system components are summarized below.

Downcomer

The downcomer dimensions below the cold legs (e.g., gap, diameter, length, and flow area) are basically the same for UPTF and the typical PWR. The vessel wall of the UPTF is thinner than that of a typical PWR.

Cold Leg

The cold leg piping diameters are fairly similar between UPTF and the typical PWR (0.75 m vs. 0.70 m). The UPTF cold leg flow area is only 15% larger than that for the typical PWR. The distance from the ECC nozzle to the downcomer at UPTF is 30% longer than that at the typical PWR. A longer mixing region in the cold leg may result in more condensation at UPTF than at a PWR. The ECC nozzle diameters are comparable between UPTF and the typical PWR. For a PWR, the ECC nozzles are typically located on top of the cold leg with an injection angle of 90°. In UPTF, the nozzle lies in a horizontal plane at an angle of 60° from the cold leg piping.

Reactor Core

UPTF did not have an active core, but there were 193 16x16 dummy fuel assemblies on top of the core, which is similar to the core of a typical PWR (193 15x15 fuel assemblies). As for flow area, UPTF has a core flow area of 1.05 times the core flow area of a typical PWR.

Upper Plenum

The ratio of the UPTF upper plenum flow area to that of typical PWRs is around 1.2. It should be noted that the exact configuration and arrangement of the upper plenum structures are plant specific. The height of the upper plenum in the UPTF is only about 0.67 of that in a typical PWR because of the shorter distance from the hot leg nozzle to the upper support plate in UPTF. The height difference is not expected to be important for the assessment of the entrainment/de-entrainment in the upper plenum.

Hot Leg

The hot leg diameter at UPTF is slightly larger than that at typical PWRs, while the flow area of an UPTF hot leg is less than the flow area of a typical PWR hot leg. This is because the flow area of the UPTF hot leg is reduced by an internal ECC injection pipe (called Hutze in UPTF). The difference of the hot leg between UPTF and a typical PWR is judged inconsequential for the assessment.

UPTF 6, UPTF 8A, UPTF 25A, and UPTF 29B are utilized for the assessment in this section. The test conditions and the applicability of the test are analyzed below.

UPTF 6

[

|

|

|

]^{a,c}

UPTF 25A

[

|

|

|

]^{a,c}

UPTF 8A

[

|

|

]^{a,c}

UPTF 29B

[

|

|

]^{a,c}

]^{a,c}

19.3.3 UPTF 6 ECC Bypass and Downcomer Counter-Current Flow Test Descriptions

During the blowdown phase of a large cold leg break LOCA, the reactor vessel rapidly depressurizes, causing most of the liquid inventory to flash into steam. This steam and entrained water flow up the downcomer and out the broken cold leg. After the system has partially depressurized, ECC is injected into the intact cold legs. The resulting counter-current steam/water flow in the downcomer is important since it affects how quickly the reactor vessel refills. As the pressure in the reactor vessel begins to reach an equilibrium state with the containment pressure, the steam flow is reduced and the ECC starts to fill the vessel and reflood the core. The objective of UPTF Test 6 was to investigate ECC penetration and counter-current flow phenomena in the downcomer of a PWR during the end of blowdown and refill portions of a LOCA. In addition to determining the downcomer flooding limit, simulation of these tests also evaluates the ability of WCOBRA/TRAC-TF2 to predict entrainment and de-entrainment phenomena in a downcomer during blowdown and early refill. The assessment of the condensation efficiency in the downcomer is also part of the objective of UPTF 6 simulations.

The system configuration of UPTF Test 6 is shown in Figure 19.3-8; the pump simulators were closed and only the cold leg break valve was opened. Steam was injected in the core simulator and steam generator simulator. Because flow paths to the intact cold leg and broken hot leg were blocked, the steam was forced to flow downward through the lower plenum, up the downcomer, and out the vessel through the broken cold leg. ECC water was injected to each intact cold leg.

A summary of test boundary conditions for UPTF 6 is given in Table 19.3-2. In UPTF Test 6, five steady-state runs were conducted with steam flows of 102, 203, 295, 396, and 439 kg/s to establish points on a flooding curve for UPTF. Steam injection was to both the core and steam generator simulators except for the low steam flow run during which injection was only to the core. ECC water was injected at approximately 500 kg/s to each of the three intact cold legs. The subcooling of ECC water varied from 28 to 65 °C. The containment pressure was maintained around 2.5 bar except Test 135, where pressure was 3.4 bar.

19.3.4 WCOBRA/TRAC-TF2 Model for UPTF Test 6

The WCOBRA/TRAC-TF2 model VESSEL component for the calculations to compare to UPTF Test 6 simulations is shown in Figures 19.3-9 through 19.3-13. [

]^{a,c}

The WCOBRA/TRAC-TF2 loop model used for the UPTF Test 6 transient calculations is shown in Figure 19.3-14. In the test facility, the broken loop is a piping system leading from the vessel to a steam water separator and then to the containment simulator (Figure 19.3-1). A simplified model was used to simulate UPTF Test 6. [

]^{a,c}

The intact cold legs were represented by PIPE components, and the ECC was modeled as a boundary condition applied through the FILL components. The broken loop was represented by one PIPE component. The pressure at the broken loop flowmeter was specified by a BREAK component.

19.3.5 Simulation of UPTF Test 6

UPTF Test 6 was run in five separate sub-phases, each sub-phase with a different combination of liquid and steam injection rates. The intact loops were blocked at the pump simulators, forcing all steam down through the lower plenum and up the downcomer to the broken cold leg.

The results of the five tests UPTF 6-131, 132, 133, 135, and 136 are presented in the following sections. As discussed in Section 19.2, the UPTF 6 simulation with WCOBRA/TRAC-TF2 is used specifically to assess the code capability with regards to three specific processes: (1) ECC Bypass in the downcomer (CCFL); (2) entrainment and de-entrainment in the downcomer during ECC Bypass and (3) condensation in the downcomer. The discussion of CCFL during ECC bypass, entrainment and de-entrainment during ECC bypass, and condensation efficiency in the UPTF 6 tests is also given in this section.

19.3.5.1 UPTF 6-131

The total core steam injection flow for Run 131 is shown in Figure 19.3-15, and the steam generator injection flows is shown in Figure 19.3-16. The ECC injection to each of the intact cold legs is shown in Figure 19.3-17. These as-measured injection flow rates were used as boundary conditions in the WCOBRA/TRAC-TF2 model for Run 131. The measured pressure at the pipe flow meter was applied to the BREAK component as the boundary condition.

The WCOBRA/TRAC-TF2 simulation was run for 100 seconds, which corresponds to the test time period of 30 to 130 seconds for Run 131. [

]^{a,c}

I^{a,c}

19.3.5.2 UPTF 6-132

The total core steam injection flow for Run 132 is shown in Figure 19.3-33, and the steam generator injection flows in Figure 19.3-34. The ECC injection to each of the intact cold legs is shown in Figure 19.3-35. These as-measured injection flow rates were used as boundary conditions in the WCOBRA/TRAC-TF2 model for Run 132. The measured pressure at the pipe flow meter was applied to the BREAK component as the boundary condition.

The WCOBRA/TRAC-TF2 simulation was run for 100 seconds, which corresponds to the test time period of 31 to 131 seconds for Run 132. I^{a,c}

I^{a,c}

]^{a,c}

19.3.5.3 UPTF 6-133

The total core steam injection flow for Run 133 is shown in Figure 19.3-51, and the steam generator injection flows in Figure 19.3-52. The ECC injection to each of the intact cold legs is shown in Figure 19.3-53. These as-measured injection flow rates were used as boundary conditions in the WCOBRA/TRAC-TF2 model for Run 133. The measured pressure at the pipe flow meter was applied to the BREAK component as the boundary condition.

The WCOBRA/TRAC-TF2 simulation was run for 100 seconds, which corresponds to the test time period of 30 to 130 seconds for Run 133. [

]^{a,c}

J^{a,c}

19.3.5.4 UPTF 6-135

The total core steam injection flow for Run 135 is shown in Figure 19.3-69, and the steam generator injection flows in Figure 19.3-70. The ECC injection to each of the intact cold legs is shown in Figure 19.3-71. These as-measured injection flow rates were used as boundary conditions in the WCOBRA/TRAC-TF2 model for Run 135. The measured pressure at the pipe flow meter was applied to the BREAK component as the boundary condition.

The WCOBRA/TRAC-TF2 simulation was run for 100 seconds, which corresponds to the test time period of 30 to 130 seconds for Run 135. [

J a,c

[

]^{a,c}

19.3.5.5 UPTF 6-136

The total core steam injection flow for Run 136 is shown in Figure 19.3-87. The ECC injection to each of the intact cold legs is shown in Figure 19.3-88. No steam was injected through the steam generator simulators in this run. These as-measured injection flow rates were used as boundary conditions in the WCOBRA/TRAC-TF2 model for Run 136. The measured pressure at the pipe flow meter was applied to the BREAK component as the boundary condition.

The WCOBRA/TRAC-TF2 simulation was run for 100 seconds, which corresponds to the test time period of 30 to 130 seconds for Run 136. [

|

|

|

]^{a,c}

19.3.5.6 ECC Bypass in UPTF 6: CCFL in Downcomer Annulus

The amount of ECC water which penetrated into the lower plenum during the UPTF 6 tests was obtained by converting a pressure difference to the lower plenum inventory (2D/3D, 1989) or performing a mass balance on the lower plenum (2D/3D, 1989) or the vessel (MPR-1163, 1990a). Three different methods have been used to estimate the test ECC penetration flow rate:

- Method 1: Lower plenum refill rate converted from measured pressure difference between the bottom of lower plenum and the top of lower plenum (direct way), as determined by Siemens (2D/3D, 1989).
- Method 2: Lower plenum refill rate estimated from a mass balance (indirect way), as determined by Siemens (2D/3D, 1989).
- Method 3: Vessel refill rates estimated from vessel liquid accumulation (direct way) and mass balance (indirect way), as determined by MPR (MPR-1163, 1990a).

The ECC penetration rate was estimated for a certain period of time during the test, called the evaluation time period. The evaluation time period over which the pressure measurement or mass balance was taken extended from the point where full steam and water flow were established in the test, to the point where the lower plenum filled with liquid. The ECC penetration rate was then calculated as the average accumulation rate over this time period.

The evaluation period and refill rate of Method 1 are obtained from Table 4 in the UPTF 6 test report (2D/3D, 1989), and the lower plenum inventory of Runs 131, 132, 133, 135, and 136 are obtained from Tables 5, 6, 7, 8, 9, and 10 of the UPTF 6 test report (2D/3D, 1989), respectively. The evaluation period, lower plenum inventory, and refill rate of Method 1 are summarized in Table 19.3-3.

The evaluation period of Method 2 is the same as that of Method 1, and the refill rate of Method 2 is also obtained from Table 4 of the UPTF 6 test report (2D/3D, 1989). The evaluation period, lower plenum inventory, and refill rate of Method 2 are summarized in Table 19.3-4. It is noted that no refill rate of Method 2 is available for Run 135. There is no record of lower plenum inventory from Method 2. Instead, the lower plenum inventory at the beginning of the evaluation period is assumed the same as that from Method 1. The lower plenum inventory at the end of the evaluation period is evaluated from the inventory at the beginning, the length of the evaluation period, and the refill rate.

The difference between Method 1 and Method 2 is an indication that such estimates are affected by a large uncertainty.

The MPR report (MPR-1163, 1990a) gives estimated vessel inventories from both measured pressure difference (direct way) and mass balance (indirect way) using Method 3. For estimation of the ECC penetration rate, the lower plenum inventory and the lower plenum refill rate are clearer indicators than the vessel inventory, which includes the downcomer inventory. Therefore, this report focuses on the comparison between the lower plenum refill rate from Method 1 and Method 2 and the WCOBRA/TRAC-TF2 prediction.

I^{a,c}

The CCFL behavior calculated by WCOBRA/TRAC-TF2 for UPTF Test 6 was evaluated by comparing the scaled Kutateladze number (UPTF scale) to the published data (Glaeser, 1992) and the following CCFL flooding curve suggested for UPTF (Glaeser, 1992):

$$\sqrt{K_g^*} + m\sqrt{K_\ell^*} = C \quad (19.3-1)$$

where K_g^* is the UPTF-scaled Kutateladze number $K_g^* = \frac{K_g v_g^{2/3}}{g^{1/3} \left(\frac{l_2 + l_3}{2} \right)}$, $m=0.011$ and $C=0.0245$.

The Kutateladze numbers are expressed as:

$$K_g = \frac{\dot{m}_s}{\sqrt{\rho_g} A_{DC} (g\sigma(\rho_\ell - \rho_g))^{1/4}} \quad (19.3-2)$$

$$K_\ell = \frac{\dot{m}_\ell}{\sqrt{\rho_\ell} A_{DC} (g\sigma(\rho_\ell - \rho_g))^{1/4}} \quad (19.3-3)$$

The symbols \dot{m}_s and \dot{m}_ℓ are the steam mass flow rate and liquid mass flow rate, respectively, the phasic density is ρ , the surface tension is σ , and g is the gravitational acceleration. The value A_{DC} , l_2 , and l_3 are geometry information of UPTF.

Table 19.3-7 presents the results of the calculation of Kutateladze numbers for both the experimental data and the WCOBRA/TRAC-TF2 prediction. The steam flow rates in Table 19.3-7 are the actual steam flow rates of the UPTF 6 tests in Table 19.3-5. The actual steam flow rate also served as the boundary condition for the prediction. Therefore, the Kutateladze number of the steam flow is the same for both the experiment and the prediction.

[

]^{a,c}

19.3.5.7 Entrainment and De-Entrainment in the Downcomer During ECC Bypass

In the previous discussion, the lower plenum mass inventory was analyzed to assess the prediction of CCFL in a downcomer annulus during ECC bypass. In the following discussion, comparisons of the estimated and predicted mass distributions in the UPTF Test 6 series are used to assess the prediction of net entrainment/de-entrainment effects. The correctness of the prediction of net entrainment/de-entrainment requires the correct prediction of the vessel mass, and the correct prediction of the mass flow rate to the broken loop, with the condition of the same total ECC injection and steam injection.

In Run 131, steam was injected into the core simulators and the steam generator simulators at a combined initial rate of nearly 400 kg/sec. ECC was injected into each intact cold leg at a rate of 482 kg/sec. Figure 19.3-112 shows the estimated mass distribution for Run 131. Shortly after the start of ECC injection, fluid mass began to collect in the vessel. Later in time, after about 60 seconds, the rate of mass retention in the vessel increased. The vessel inventory leveled off, until after 65 seconds, when it began to increase more rapidly indicating that CCFL breakdown occurred. Figure 19.3-113 shows the WCOBRA/TRAC-TF2 prediction of the mass distribution during Run 131. For Run 131,

[

]^{a,c}

In Run 132, the steam was injected into the core simulators and the steam generator simulators at a combined initial rate of nearly 300 kg/sec. The ECC was injected into each intact cold leg at a rate of 490 kg/sec. Figure 19.3-114 shows the estimated mass distribution for Run 132. Shortly after the start of ECC injection, the fluid mass began to slowly collect in the vessel. Later in time, between 60 and 67 seconds, the rate of mass retention in the vessel increased but then leveled off through 80 seconds into the test. Figure 19.3-115 shows the WCOBRA/TRAC-TF2 prediction of the mass distribution during Run 132. [

]^{a,c}

Figures 19.3-116 and 19.3-117 compare the estimated and predicted mass distributions in Run 133. In this run, the steam was injected into the core simulators and the steam generator simulators at a combined initial rate of 203 kg/sec. ECC was injected into each intact cold leg at a rate of 491 kg/sec. [

]^{a,c}

The estimated and predicted mass distributions for Run 135 are shown in Figures 19.3-118 and 19.3-119, respectively. Shortly after the start of ECC injection, the fluid mass began to collect rapidly in the vessel in the experiment. The estimated vessel mass became erratic for a brief period, actually decreasing near 55 seconds. [

]^{a,c}

Figures 19.3-120 and 19.3-121 compare the estimated and predicted mass distributions in Run 136. In this subphase, steam was injected into the core simulator at an initial rate of 102 kg/sec. This was the lowest steam injection rate of the five runs. ECC was injected into each intact cold leg at a rate of 490 kg/sec. After 50 seconds, the vessel inventory was estimated to have increased steadily for the rest of the test.

[

]^{a,c}

19.3.5.8 Condensation Efficiency in UPTF 6

The UPTF Test 6 series also gave consideration to the steam-water interaction in the downcomer. The steam-water interaction calculation with WCOBRA/TRAC-TF2 is reflected by the condensation efficiency calculation.

- | Condensation efficiencies (f_c) were estimated by MPR (MPR-1163, 1990a) for the UPTF flooding test series using two methods. The condensation efficiency was calculated in two ways. In Method 1, the efficiency is defined as [

$J^{a,c}$

$$\left[\quad \quad \right]^{a,c} \quad (19.3-4)$$

- | [

$J^{a,c}$

The second method measured [

$$J^{a,c} \quad \left[\quad \quad \right]^{a,c} \quad (19.3-5)$$

[

$J^{a,c}$

[
]
]^{a,c}

The WCOBRA/TRAC-TF2 predicted condensation efficiencies for UPTF 6 Runs 131 to 136 were obtained from Equation 19.3-5, [
]
]
]

[
]
]
]^{a,c}

19.3.5.9 DTMAX Sensitivity Study for UPTF 6

]^{a,c}

19.3.5.10 Cold Leg Nozzle Loss Coefficient of UPTF 6

]^{a,c}

A detailed analysis of the pressure drops in the broken cold leg from CCTF tests was performed, and a nozzle loss coefficient of 0.5 was estimated (Akimoto et al., 1984). UPTF ECC bypass (Test 6) data were examined here in more detail to determine whether they could be used to better define the value to be used in the PWR. A short period of single-phase steam flow exists in UPTF before the ECC is injected into the cold legs. Using the measured steam flow, pressure, temperature, and measured differential pressure, a cold leg nozzle unrecoverable loss can be calculated from the extended Bernoulli Equation for a number of run points from UPTF Test 6.

19.3.5.10.1 Data Reduction for the Cold Leg Nozzle Loss Coefficient

The calculation approach used in this analysis was to write the extended Bernoulli Equation between the pressure taps for pressure cell []^{a,c} which is shown on Figure 19.3-131. This cell spans the broken cold leg nozzle from the upper downcomer region to a point []^{a,c} down the broken cold leg.

The extended Bernoulli Equation (or Mechanical Energy Equation) is written as:

$$\frac{P_2 - P_1}{\rho} + \frac{U_2^2 - U_1^2}{2g_c} + \frac{fL}{D} \frac{U_2^2}{2g_c} + k_N \frac{U_2^2}{2g_c} + \frac{(Z_2 - Z_1)g}{g_c} = 0 \quad (19.3-6)$$

The first term is the static pressure change, the second term represents the kinetic energy change, the third term is the frictional drop in the cold leg, the fourth term represents the unrecoverable loss of the nozzle, both contraction and turning loss. The last term represents the potential energy change, and is set to zero since the flow is horizontal. Equation 19.3-6 assumes the flow to be incompressible, which is a reasonable approximation for the purpose of this analysis.

The steam flow, pressure drop, steam temperature, and absolute pressure were taken directly from the data, and were averaged over the single-phase period. The friction factor was taken from the Moody chart for smooth pipes using the cold leg Reynolds number (Figure 19.3-132). The single-phase friction was used over the length of the cold leg up to the pressure tap.

Solving Equation 19.3-6 for the nozzle cold leg loss coefficient, where state 2 is the cold leg (CL) and state 1 is the downcomer (DC) annulus, results in:

$$K_N = - \frac{\left[\left(\frac{P_{CL} - P_{DC}}{\rho} \right) + \frac{U_{CL}^2 - U_{DC}^2}{2g_c} + \frac{fL_{CL}}{D_{CL}} \frac{U_{CL}^2}{2g_c} \right]}{\frac{U_{CL}^2}{2g_c}} \quad (19.3-7)$$

The data for the steam mass flow rate, downcomer pressure, and steam temperature were taken from the UPTF data report (2D/3D, 1989). The selected values of the measured parameters are given in Tables 19.3-12 and 19.3-13. The data which was used to obtain these values are shown in Figures 19.3-133 to 19.3-142, and the selected values are indicated on the figures. []^{a,c}

The steam mass flow values reflect the sum of the steam flow injected from the core simulator as well as the steam generator simulators. The measured broken cold leg steam flow was the measurement used to calculate the cold leg velocity in this analysis. The cold leg steam temperatures and the downcomer pressure minus one-half the pressure drop were used to calculate the effective density which was used in Equation 19.3-7.

Table 19.3-14 gives calculated thermal-hydraulic values for the different runs of Test 6. The broken cold leg velocity was calculated using the average density in Table 19.3-14 and the cold leg inside diameter $D_{CL}=750$ mm (2.46 ft). That is:

$$U_{CL} = \frac{\dot{m}}{\rho A_{CL}} = \frac{\dot{m}}{\rho \left(\frac{\pi D_{CL}^2}{4} \right)} \quad (19.3-8)$$

where,

\dot{m} is the steam mass flow rate and the cold leg area is:

$$A_{CL} = \frac{\pi D_{CL}^2}{4} \quad (19.3-9)$$

The cold leg Reynolds number was calculated from the cold leg velocity, cold leg diameter and the average steam density and viscosity as:

$$Re_{CL} = \frac{U_{CL} \bar{\rho} D_{CL}}{\mu_{CL}} \quad (19.3-10)$$

The cold leg Mach number was then calculated using the following value for the speed of sound,

$$C_{CL} = \sqrt{\gamma R (\bar{T}_{CL} + 460^\circ R)} \quad (19.3-11)$$

where,

\bar{T}_{CL} is cold leg steam temperature

$\gamma = 1.25$ for steam

$R = 85.7 \frac{\text{ft} \cdot \text{lbf}}{\text{lbm} \cdot \text{R}}$ for steam

the Mach number is then:

$$M_{CL} = \frac{V_{CL}}{C_{CL}} \quad (19.3-12)$$

The cold leg friction factor was taken from the Moody chart shown in Figure 19.3-132. A value of roughness for commercial pipe ($\epsilon = 0.00015$ ft) was used. The ϵ/D value for the UPTF cold leg is then:

$$\left[\quad \quad \right]^{a,c}$$

The steam density values calculated using the average pressure between the cold leg and the downcomer, and the cold leg temperature were found to agree with the cold leg density values presented in the UPTF report (2D/3D, 1989).

The results of these calculations are summarized in Table 19.3-15. [

$J^{a,c}$ The average loss coefficient is recommended for the broken cold leg nozzle of IETs, SETs and plant models (unless a more appropriate value is determined due to geometrical differences). The uncertainty of cold leg nozzle loss coefficient (KN) for plant models is discussed in Section 29.1.2.1, Volume 3.

19.3.5.10.2 Nozzle Loss Assessment

The estimated average loss coefficient 0.54 has been applied to the broken cold leg nozzle in UPTF 6 input models in Section 19.3.4. Next, the predicted pressure loss across the broken cold leg nozzle is compared with the measured pressure loss. [

$J^{a,c}$

In summary, an average broken cold leg nozzle loss coefficient of 0.54 is generated from UPTF 6 test data. The average loss coefficient 0.54 is applied to the broken cold leg nozzle in the UPTF 6 input models. [

$J^{a,c}$

19.3.6 UPTF 8A Cold Leg Condensation Test Descriptions

- | The UPTF test facility is discussed in detail in Section 19.3.2. The components relevant to condensation in the cold leg are discussed in more detail below.
- | The cold leg flow regime tests (2D/3D, 1988) focused on behavior in the cold legs in the region of ECC injection. This region is bounded by the reactor coolant pump simulator and the test vessel downcomer as shown in Figure 19.3-149. The cold leg piping has an internal diameter of 750 mm (29.5 inches) and each loop is 9181 mm (30.1 feet) long from the reactor coolant pump simulator outlet to the inner surface of the test vessel wall at the downcomer. The diameter of safety injection line is 222.5 mm.

The distance from the ECC nozzle to the downcomer is 30% longer at UPTF than at typical PWRs. The ECC nozzle diameters are comparable with the UPTF nozzle diameter slightly smaller (by no more than 16%). The most significant difference is that UPTF uses side injection whereas typical PWRs, generally use top injection.

Test Conditions

For UPTF Test 8A steam was injected only in the core simulator and flowed through the loops. ECC was injected into the cold leg of Loop 2. The steam injection rate was relatively constant while the ECC flow rate was decreased in steps. Each ECC flow rate was maintained for about 30 seconds to allow steady-state conditions to be established. The ECC flow rates covered the range of flows expected in a PWR during a Large Break LOCA. Test 8A had two phases with essentially the same conditions; the difference being that the pump simulator K-factor in Loop 2 was higher for Phase B than Phase A. This condition resulted in a slightly lower Loop 2 steam flow in Phase B compared to Phase A.

The steam flow in Loop 2 was held approximately constant due to Loop 3 being open to maintain a constant differential pressure across the reactor coolant loops. Loop 2 steam flow was maintained between 31 and 38 kg/sec throughout the test.

UPTF Test 8A was conducted in two major phases, each with two parts. In the first part of each phase ECC was injected to the Loop 2 cold leg, and in the second part the ECC injection went to the hot leg. Since there is not hot leg ECC injection to typical PWRs, and since the boundary conditions for Phase A (Run 112) and Phase B (Run 111) are similar, only the first part of Phase A was simulated with WCOBRA/TRAC-TF2. Figure 19.3-150 shows the system configuration for UPTF 8A. The configurations of specific components are as follows:

- A water seal was maintained in the lower plenum of the test vessel to ensure the steam from the core simulator flows through the loops.
- Steam was injected through the test vessel core simulator.
- Loop 1 was blocked at the pump simulator.
- The Loop 2 pump simulator was set to provide a K factor of 10 based on a pipe diameter of 750 mm (29.5 inches).
- The Loop 3 pump simulator was set to provide a K factor of 18 based on a pipe diameter of 750 mm (29.5 inches).
- ECC was injected into the Loop 2 cold leg. No nitrogen was injected into the ECC water.
- The broken loop hot leg and broken loop cold leg were open to the containment simulator. The broken loop hot leg break valve was set to provide a K factor of 18.2 based on a pipe diameter of 750 mm (29.5 inches).

A summary of test boundary conditions for UPTF 8A is given in Table 19.3-16.

Summary of Experimental Results

- | An observation on the temperature distribution in the cold leg in UPTF 8A is given in Figure 19.3-151. The flow regime and temperature stratification are clearly shown in Figure 19.3-151. The results of the UPTF cold leg flow regime separate effects tests indicate that plug flow only occurred when the condensation of the ECC exceeded the steam supply. At low steam flows, plug flow was unstable because the momentum of the steam flow was not sufficient to maintain the plug. The cyclic formation and decay of water plugs in unstable plug flow resulted in large pressure and flow oscillations. The test results also indicate that stratified flow always occurred when the steam supply exceeded the ECC condensation potential. In some cases, thermal stratification of the water layer in the bottom of the cold leg limited condensation to less than its maximum value and prevented total consumption of the steam.

The loop steam flow was completely condensed for plug conditions and only partially condensed for stratified flow conditions. The condensation efficiency (the ratio of condensation heat transfer rate to the condensation rate that would bring liquid to saturation temperature), during stratified flow conditions ranged from 80 to 100%. The efficiency was higher as ECC flow decreased or as steam flow increased.

19.3.7 WCOBRA/TRAC-TF2 Model for UPTF 8A

The validations against UPTF Test 8A serve as a separate effect test for the condensation in cold leg and downcomer during refill period and reflood period. The test is also part of validation for the cold leg condensation model discussed in Section 17. Two UPTF 8A models are developed. An integral UPTF 8A input model includes both vessel and loop structure of the UPTF. A simplified (separate effects) UPTF 8A TEE model documented in Section 17 only simulates the cold leg and the ECC line in UPTF 8A test. The UPTF 8A TEE model presented in Section 17 also serves as a base model for the sensitivity studies on the ECC line injection angle, the cold leg noding, the uncertainty of the cold leg condensation model and the uncertainty of the horizontal stratification model.

The integral UPTF 8A model presented here [

]^{a,c}

]^{a,c}

19.3.8 Simulation of UPTF 8A

The WCOBRA/TRAC-TF2 simulation of UPTF Test 8A was run for the first 200 seconds of the test, which covered the period where flow was injected into the loop 2 intact cold leg. The as-measured injection flow rates were used as boundary conditions in the WCOBRA/TRAC-TF2 model. The containment simulator was maintained at a constant pressure of 400 kPa (58 psia).

Since most of ECC injections were turned-off for Test 8A, the condensation only exists in the intact loop 2. The WCOBRA/TRAC-TF2 simulation of Phase A (Run 112) modeled only the cold leg injection phase, so results after 200 seconds are not considered. The following comparison of WCOBRA/TRAC-TF2 results and UPTF Test 8A data considers the overall performance of the code and modeling of the facility. Note, the simulation of 200 seconds covers periods 1 through 6 in Table 19.3-16. The stage 7 is insignificant for the assessment because the ECC flow rate was too low related to the typical RHR flow.

]^{a,c}

[

|

|

|

|

|

|

|

|

|

]^{a,c}

J^{a,c}

19.3.9 UPTF 25A Downcomer Entrainment/De-Entrainment and Cold Leg Condensation Test Descriptions

UPTF Test 25A (2D/3D, 1990a) was a quasi-steady state experiment to investigate entrainment/de-entrainment in the downcomer and condensation in the cold leg and downcomer during the reflood phase of a PWR LBLOCA. The UPTF test facility is discussed in detail in Section 19.3.2. Figure 19.3-164 shows the system configuration of UPTF Test 25A.

The configurations of specific components are as follows:[

J^{a,c}

] ^{a,c}

| UPTF Test 25 Phase A simulated conditions expected during the reflood phase of a Large Break LOCA. ECC was injected to the cold legs, while the steam flow through the UPTF was established by injecting steam in the steam generator simulators. UPTF 25 Phase B was similar to Phase A, but the vessel walls were not superheated and there was no waiting period between phases. Since UPTF 25A is more representative for the reflood period of a LBLOCA, only Phase A was simulated using WCOBRA/TRAC-TF2.

Table 19.3-17 lists the conditions for each Phase A sub-phase of Test 25.

19.3.10 WCOBRA/TRAC-TF2 Model for UPTF Test 25A

The vessel model for UPTF 25A is also similar to the vessel model for UPTF 6. [

] ^{a,c}

19.3.11 **Simulation of UPTF Test 25A**

The WCOBRA/TRAC-TF2 calculated transient corresponding to the UPTF Test 25A simulation is run for nearly the entire 900 seconds of the test. [

] ^{a,c}

The downcomer fluid temperatures at Level 28 are compared in Figures 19.3-170 and 19.3-171, while the downcomer fluid temperatures at Level 24 are compared in Figures 19.3-172 and 19.3-173. [

12, C

Figure 19.3-175 shows the measured and predicted axial differential pressure from the bottom of the lower plenum to the middle of the downcomer [Pa] and the axial differential pressure from the bottom of the lower plenum to the top of the downcomer [Pa] for UTRI-25 Phase A. The axial pressure difference is an indicator of the water level in the downcomer.

1

1 a,c

The measured and predicted axial differential pressures in the downcomer between the bottom of downcomer and the cold leg nozzle elevation are compared in Figure 19.3-176. In Figure 19.3-176, four WCORBA/TRAC-TF2 curves are shown. Each curve represents the level in a different quadrant of the downcomer, each being adjacent to a loop connection. In the measured levels, the level was highest in the downcomer quadrant below the broken cold leg. [

J^{a,c}

]^{a,c}

Figures 19.3-177 and 19.3-178 provide the steam and water flow rates to the broken loop. The vapor flow to the broken loop is shown in Figure 19.3-177. Figure 19.3-177 demonstrates that the vapor flow rate changes during each sub-phase with the change in steam injection rate. [

]^{a,c}

One additional parameter of interest is the void height in the downcomer as a function of the steam flow rate. The void height is the distance from the average collapsed downcomer liquid level to the bottom of the cold leg nozzles. The distance from the bottom of the downcomer to the bottom of the cold leg nozzle is []^{a,c}. The WCORBA/TRAC-TF2 calculated downcomer void height is determined for each of the four sub-phases, and then plotted against test data and estimates provided by MPR Associates (MPR-1346, 1993) in Figure 19.3-179.

]^{a,c}

The measured and predicted fluid temperatures in the Loop 2 cold leg are compared in Figures 19.3-180 through 19.3-182. Figure 19.3-180 shows the comparison between the measured temperature and the WCORBA/TRAC-TF2 predicted water temperature at the ECC injection point. The measured temperature profiles from the top of the cold leg to the bottom of the cold leg indicate a stratified flow pattern in all sub-phases, with superheated steam at the top and subcooled water at the bottom. The fluid temperature drops from sub-phase I to sub-phase IV as the steam flow rate reduces in a stepwise manner.

[
]^{a,c}

Figure 19.3-181 shows the comparison between the measured temperature and the WCORBA/TRAC-TF2 predicted water temperature downstream of the injection point. Thermocouples were wetted by the liquid during the experiment and showed saturated or subcooled temperature. The measured liquid temperature at the bottom of the cold leg increased substantially from measured temperature at the ECC injection point, which implies further condensation downstream of the ECC injection point.

]^{a,c}

Figure 19.3-182 shows the comparison between the measured temperature and the WCORBA/TRAC-TF2 predicted water temperature at the cold leg near the vessel inlet. It is shown that the water temperature rose further for all four sub-phases.

[
]^{a,c}

Sensitivity Study with []^{a,c}

[

[

[

[

[

]^{a,c}

Sensitivity Study with []^{a,c}

[

[

]^{a,c}

] ^{a,c}

19.3.12 UPTF 29B Upper Plenum Entrainment/De-Entrainment Test Descriptions

During the reflood phase of a LBLOCA, water rises through the core. The hot fuel rods cause the water to boil and the steam produced entrains droplets which are carried through the core into the upper plenum. The droplets either fall back into the core, de-entrain on the internals in the upper plenum, or pass through into the hot legs towards the steam generators. The entrained droplets which enter the hot steam generator tubes are vaporized, causing an increase in loop pressure, which inhibits core reflood. This phenomenon is known as steam binding.

UPTF Test 29B (2D/3D, 1990b) was a quasi-steady state experiment to investigate upper plenum entrainment and steam binding during the reflood phase a PWR LBLOCA. The UPTF test facility is discussed in detail in Section 19.3.2. Figure 19.3-193 shows the system configuration of UPTF Test 29B.

] ^{a,c}

A summary of test boundary conditions for UPTF 29B (Run 212) is given in Table 19.3-19.

19.3.13 WCORBA/TRAC-TF2 Model for UPTF Test 29B

The vessel model used in the simulation of the UPTF 29B is shown in Figure 19.3-195. Compared to the vessel models employed in the simulation of the UPTF 6, 8A, 25A tests, this model is more detailed above the tie plate and in the upper plenum region. The vessel model for the upper plenum tests used a coarser noding in the downcomer and the lower plenum regions because in these tests the flows into the downcomer were not significant. At the start of the tests, a liquid level was established in the bottom of the vessel to prevent the steam flow from the core to the downcomer through the lower plenum.

I

|

|

|

|

|

|

|

|

|

|

|

|

I^{a,c}

19.3.14 Simulation of UPTF Test 29B

Test 29B was performed to determine the amount of upper plenum de-entrainment and carryover. This test consists of six sub-phases. Each sub-phase consists of a period of steady core simulator injection followed by a “rest” period. During the “rest” period, water suspended in the upper plenum was allowed to drain back into the vessel. Table 19.3-19 lists the core simulator injection rates for Test 29B.

Phase B of Test 29 is simulated using WCOBRA/TRAC-TF2 over the entire 900 seconds of the test. For each phase of UPTF Test 29B, a mass balance is performed based on test measurements by MPR Associates (MPR-1213, 1990b), and the mass distribution estimated.

Figure 19.3-199 compares the estimated and predicted upper plenum water mass in sub-phase 1 of UPTF Test 29B. [

]^{a,c}

The estimated and predicted upper plenum mass for sub-phase 2 of UPTF Test 29B is shown in Figure 19.3-200. [

]^{a,c}

Figure 19.3-201 compares the estimated and predicted upper plenum mass for sub-phase 3. [

]^{a,c}

The estimated and predicted upper plenum mass for sub-phase 5 of Test 29B are compared in Figure 19.3-203. [

]^{a,c}

Finally, Figure 19.3-204 compares the estimated and predicted upper plenum mass for sub-phase 6. In this case, [

]^{a,c}

[

]^{a,c}

Table 19.3-1

1a,c

a,c

Table 19.3-3

12,c

Table 19.3-4

J^{a,c}

a,c

a,c

a,c

Table 19.3-8 []^{a,c}

a,c

Table 19.3-9

a,c

Table 19.3-10 [

J^{a,c}

Table 19.3-11 [

J^{a,c}

Table 19.3-12 Steam Mass Flows in UPTF Test 6 (all Values are in kg/sec)

a,c

Table 19.3-13 Selected Test Conditions from UPTF Test 6 (Single-Phase Steam Portion)

a,c

Table 19.3-14 Calculated Parameters for UPTF Test 6

a,c

Table 19.3-15 Calculated Cold Leg Nozzle K, $U_{DC}=0$

a,c

Table 19.3-16 UPTF Test 8 Phase A Conditions

Conditions	Subphase						
	1	2	3	4	5	6	7
Pressure (kPa)	405						
Saturation Temperature (°C)	144						
Core Simulator Steam Flow (kg/s)	110						
Loop Steam Flow Rate (kg/s)	31~38 ⁽¹⁾						
Steam Temperature (°C)	145 ⁽²⁾						
ECC Flow (Parts 1-7) (kg/s)	600	400	250	200	150	90	15
ECC Subcooling (°C)	110						

Notes:

1. Estimated steam flow rate in loop 2.
2. This steam temperature is cold leg inlet steam temperature. The nominal temperature of steam injection to core simulator is 201°C.

Table 19.3-17 [**]^{a,c}**

a,c

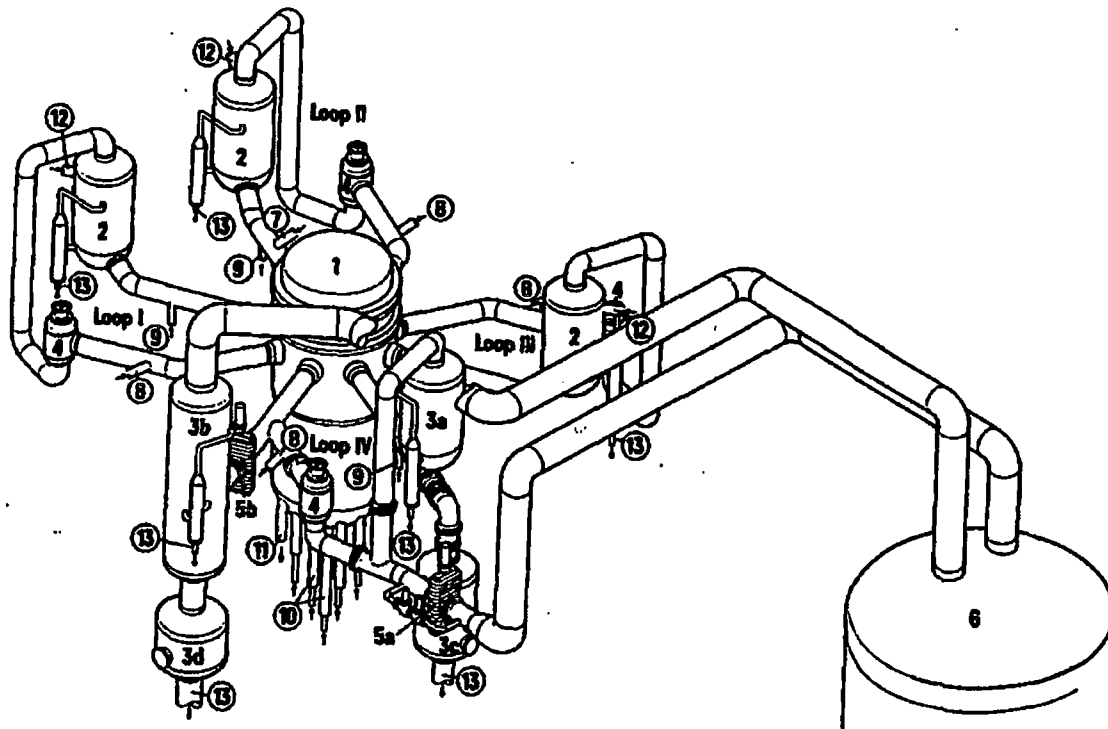
Table 19.3-18 [$J^{a,c}$

a,c

Table 19.3-19 [$J^{a,c}$

a,c

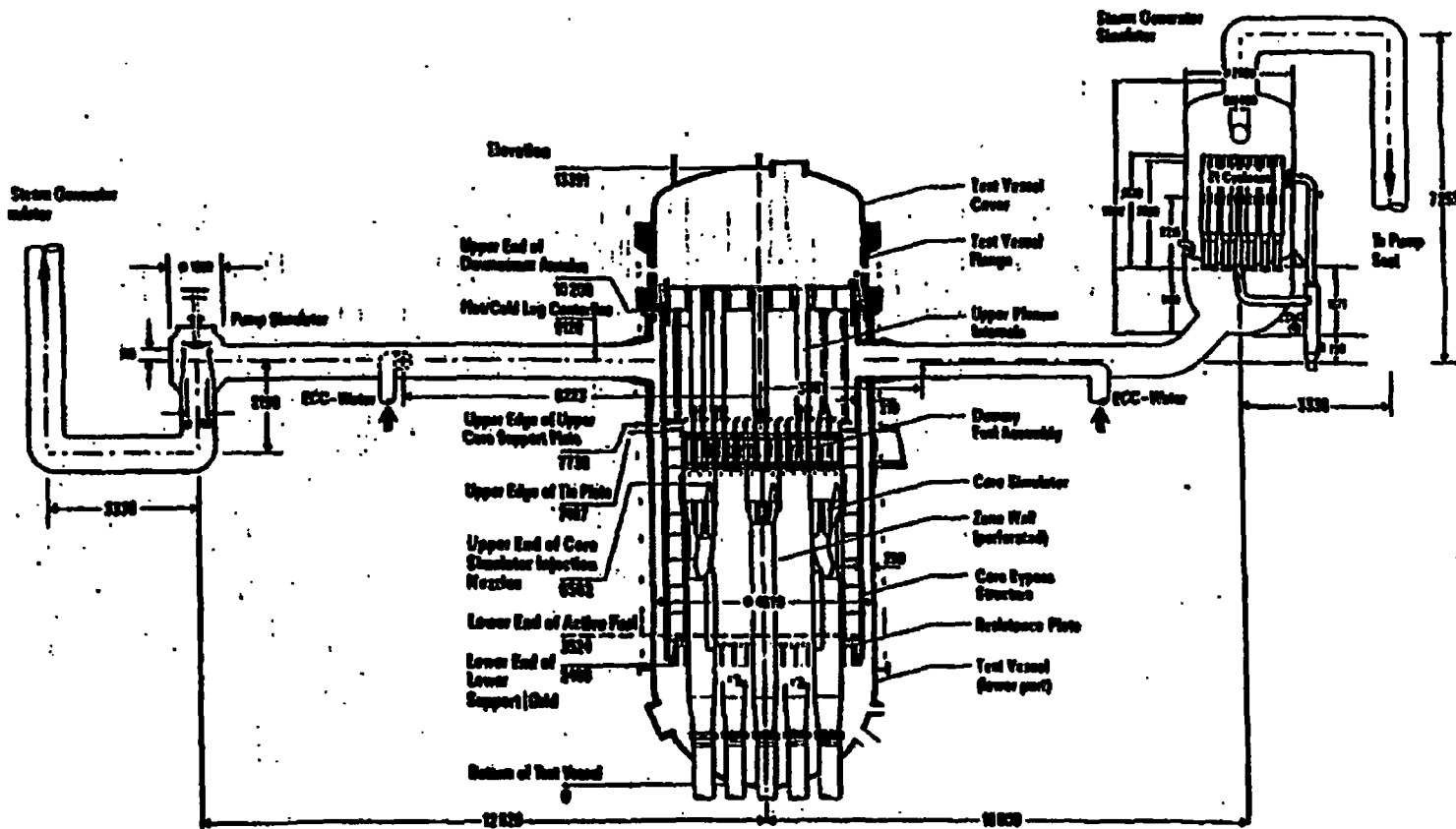
Figure 19.3-1 UPTF Plan View



- 2 Steam Generator Simulator (Intact Loop)
- 3a Steam Generator Simulator/ Water Separator (Broken Loop Hot Leg)
- 3b Water Separator (Broken Loop Cold Leg)
- 3c Drainage Vessel for Hot Leg
- 3d Drainage Vessel for Cold Leg
- 4 Pump Simulator
- 5a Break Valve (Hot Leg)
- 5b Break Valve (Cold Leg)
- 6 Containment Simulator

- 7 Surge-line-Nozzle
- 8 ECC-Injection Nozzles (Cold Leg)
- 9 ECC-Injection Nozzles (Hot Leg)
- 10 Core Simulator Injection Nozzle
- 11 TV-Drainage Nozzle
- 12 Steam Injection Nozzle
- 13 Drainage Nozzle

Figure 19.3-2 UPTF Test Vessel and Primary Loop



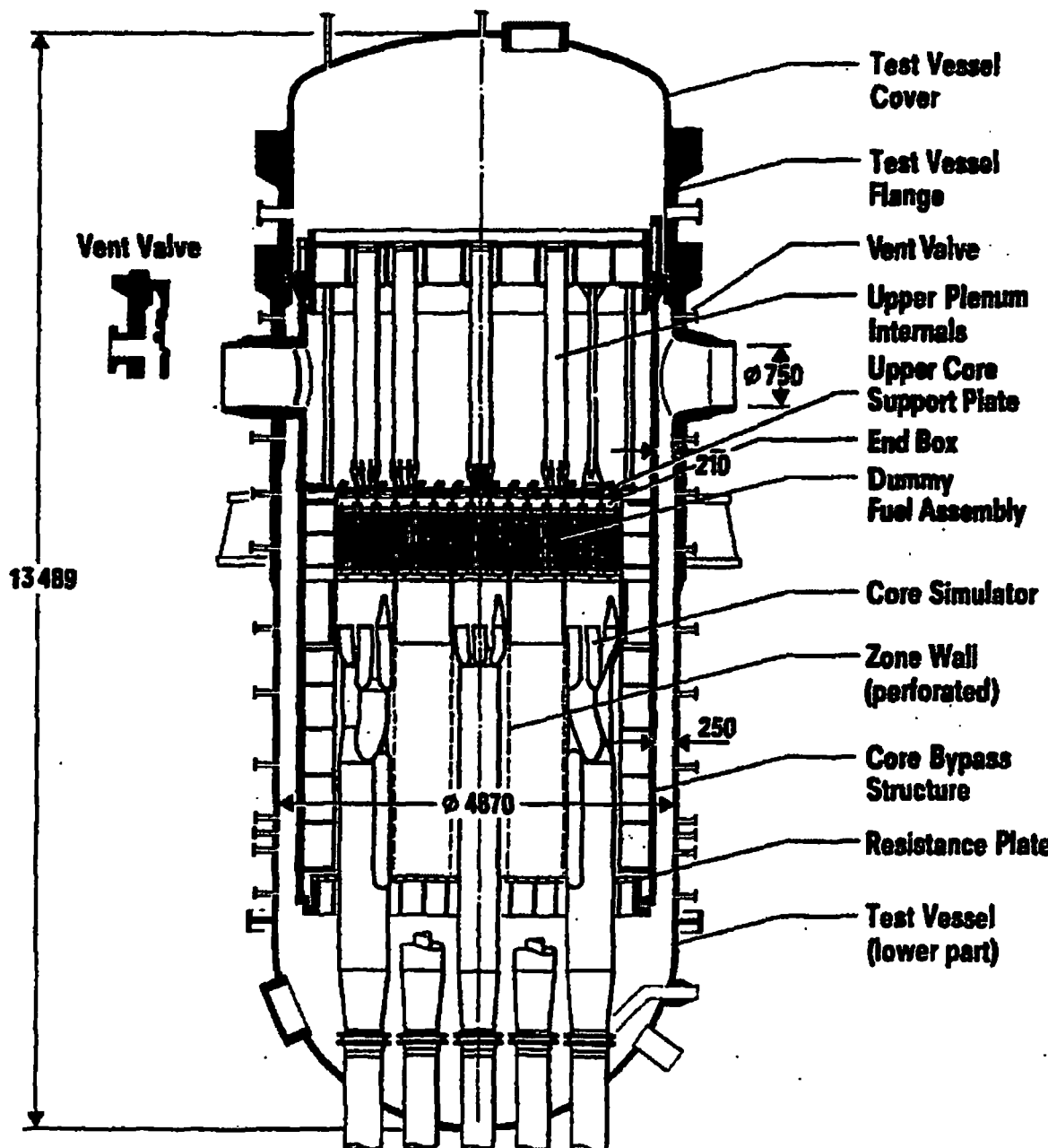


Figure 19.3-3 UPTF Reactor Vessel

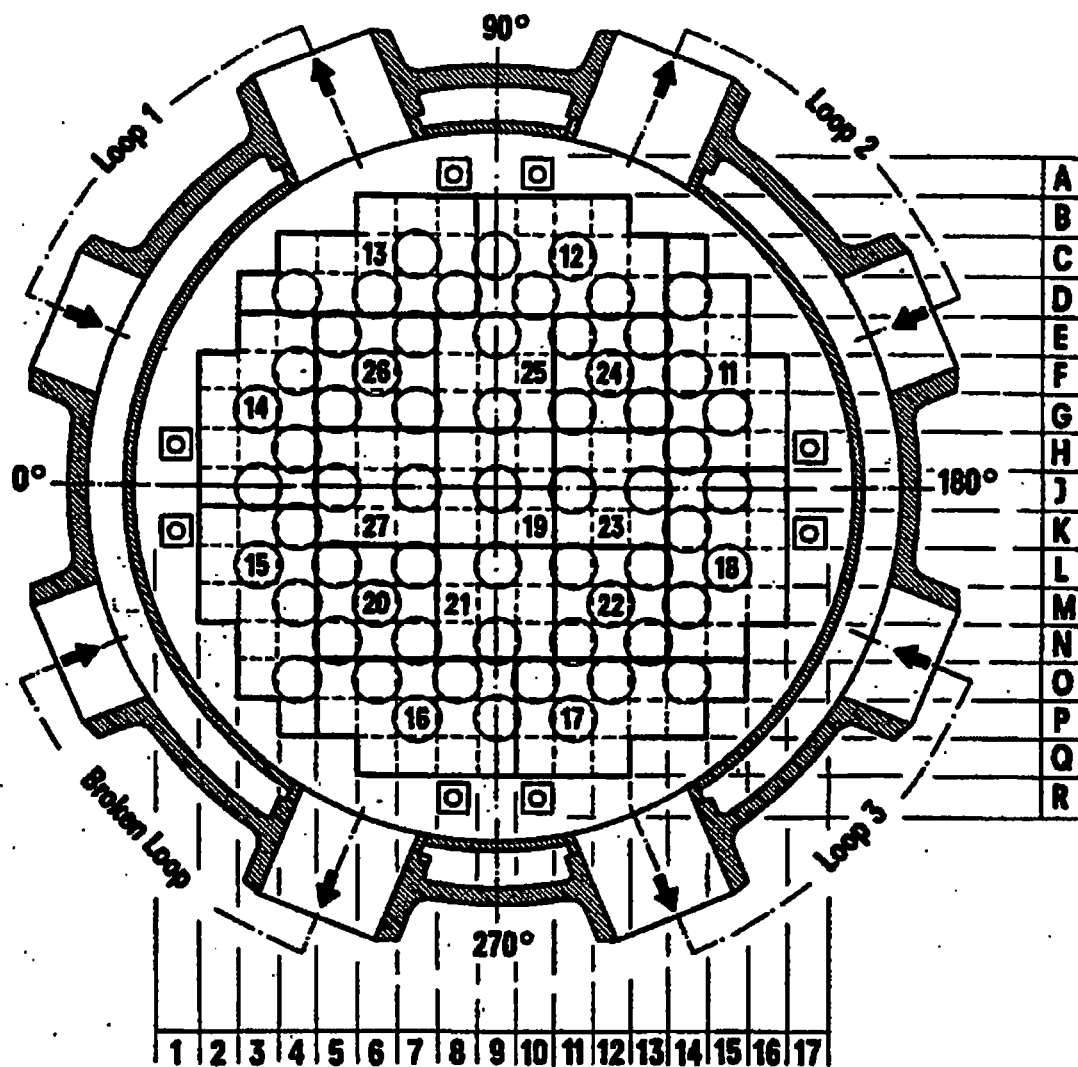
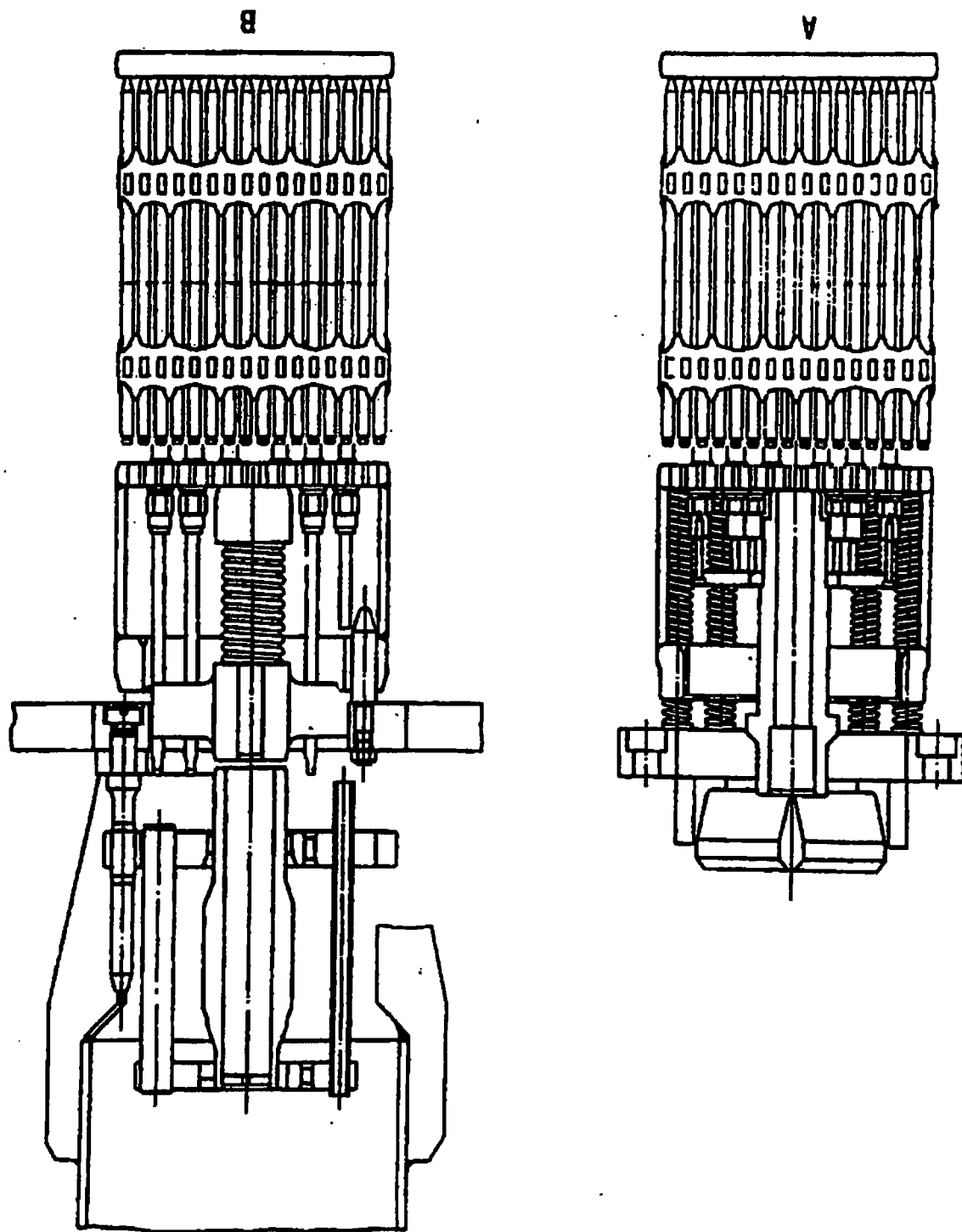


Figure 19.3-4 UPTF Upper Plenum Structures

Figure 19.3-5 Dummy Fuel Assembly and End Box with Flow Restrictor (A) or Spider (B)



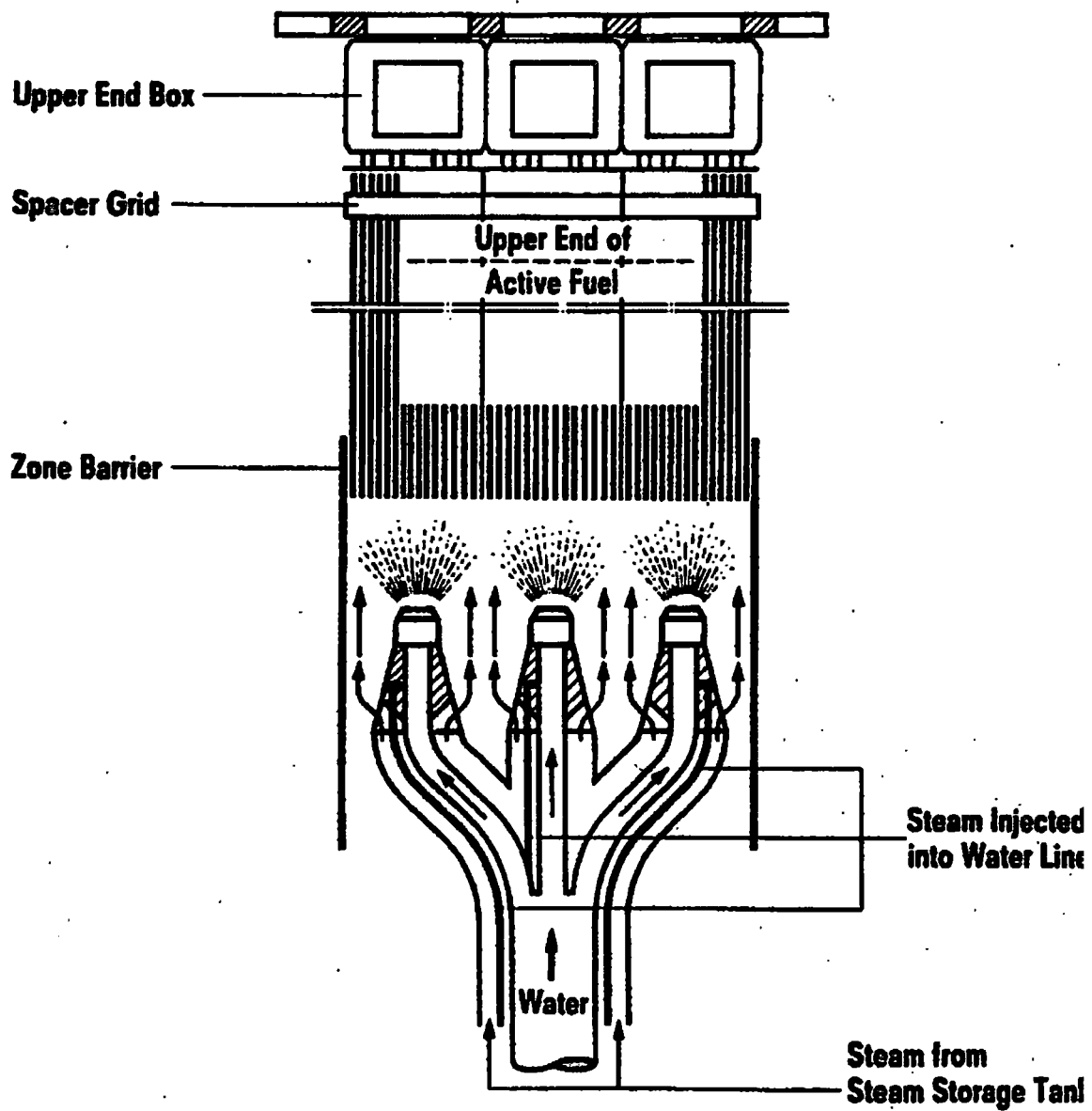
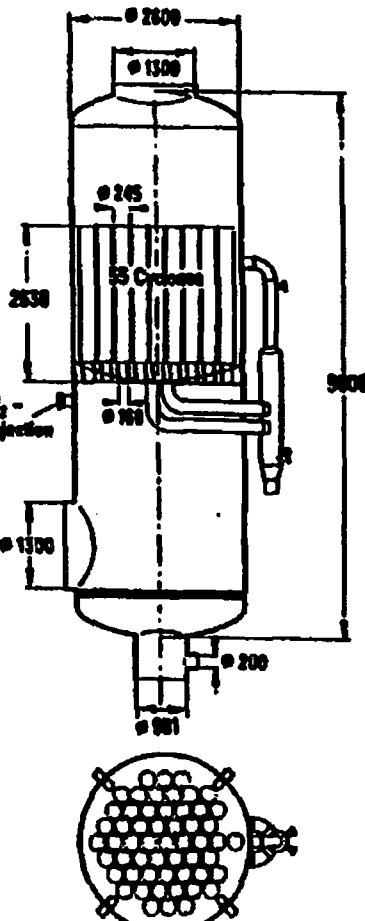
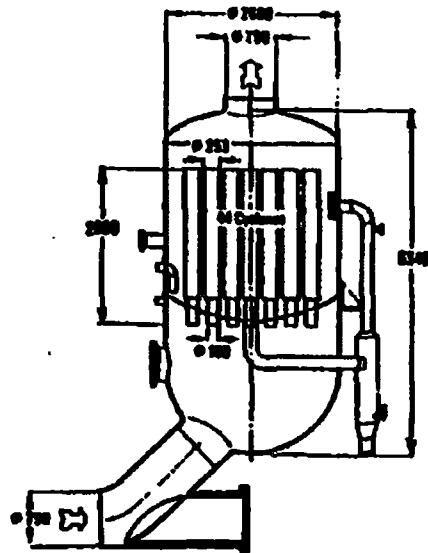


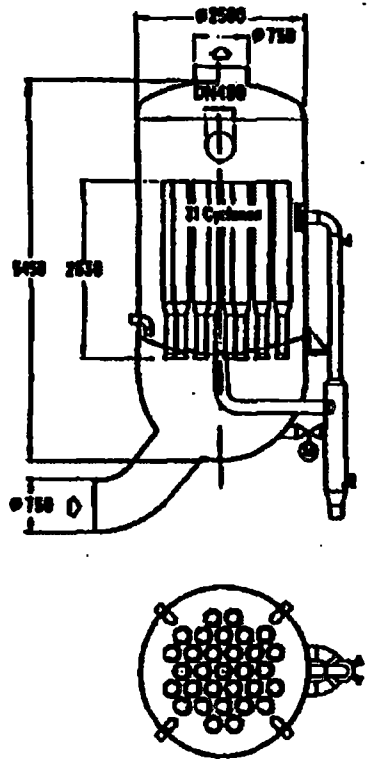
Figure 19.3-6 UPTF Core Simulator Injection Assembly



**Water Separator of
Broken Loop Cold Leg**



**Steam Generator Simulator
(Water Separator) of
Broken Loop Hot Leg**



**Steam Generator Simulator
of Intact Loop**

Figure 19.3-7 UPTF Steam Generator Simulators and Water Separators

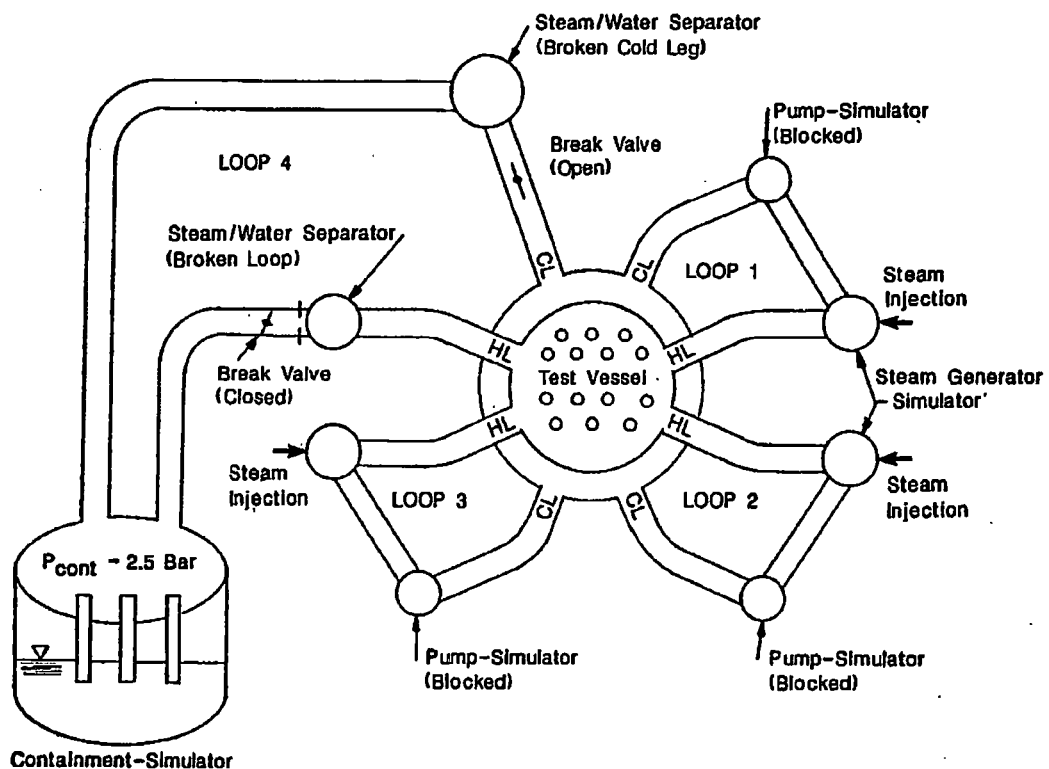


Figure 19.3-8 UPTF System Configuration for Test 6 (MPR-1163, 1990a)

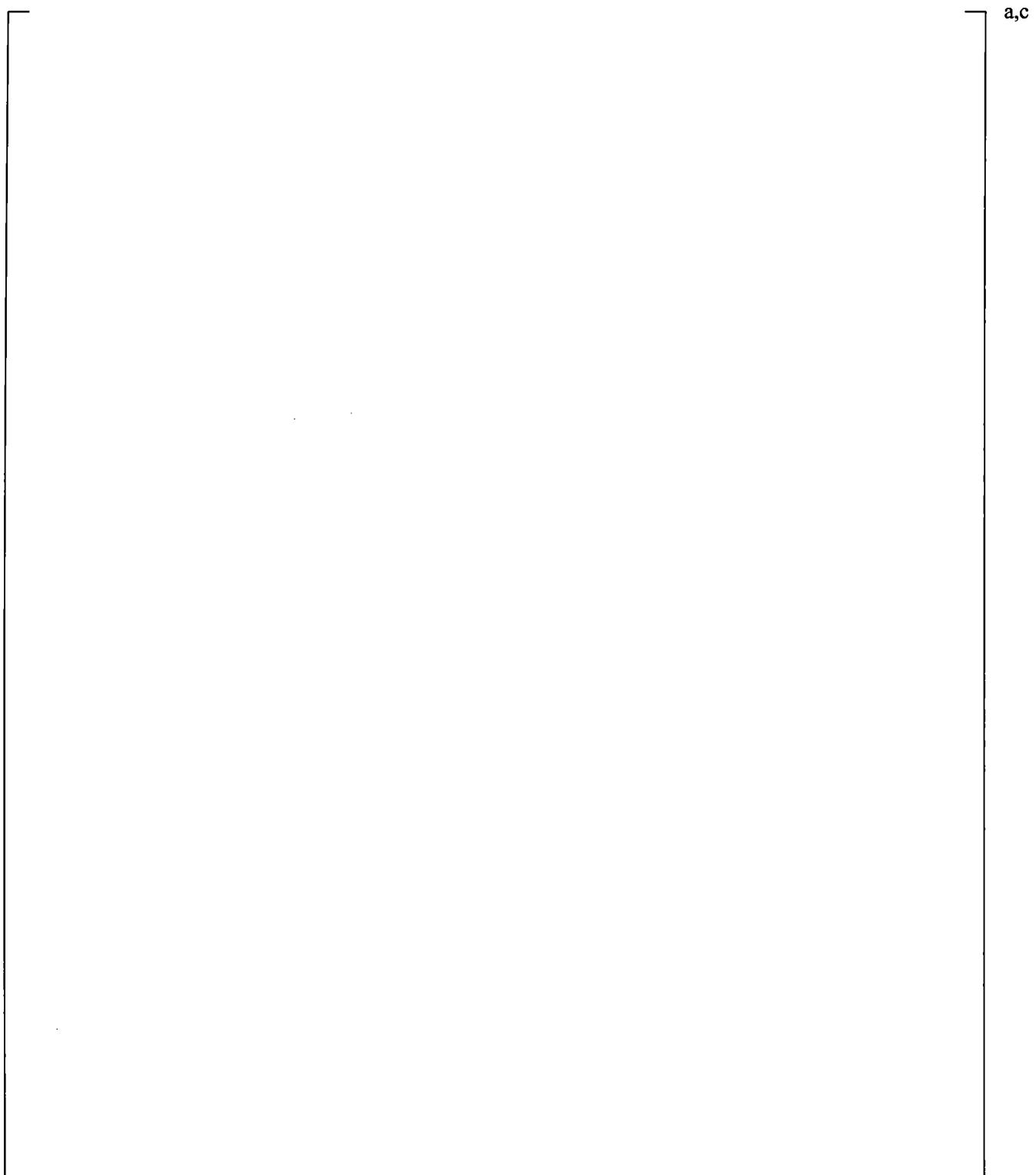
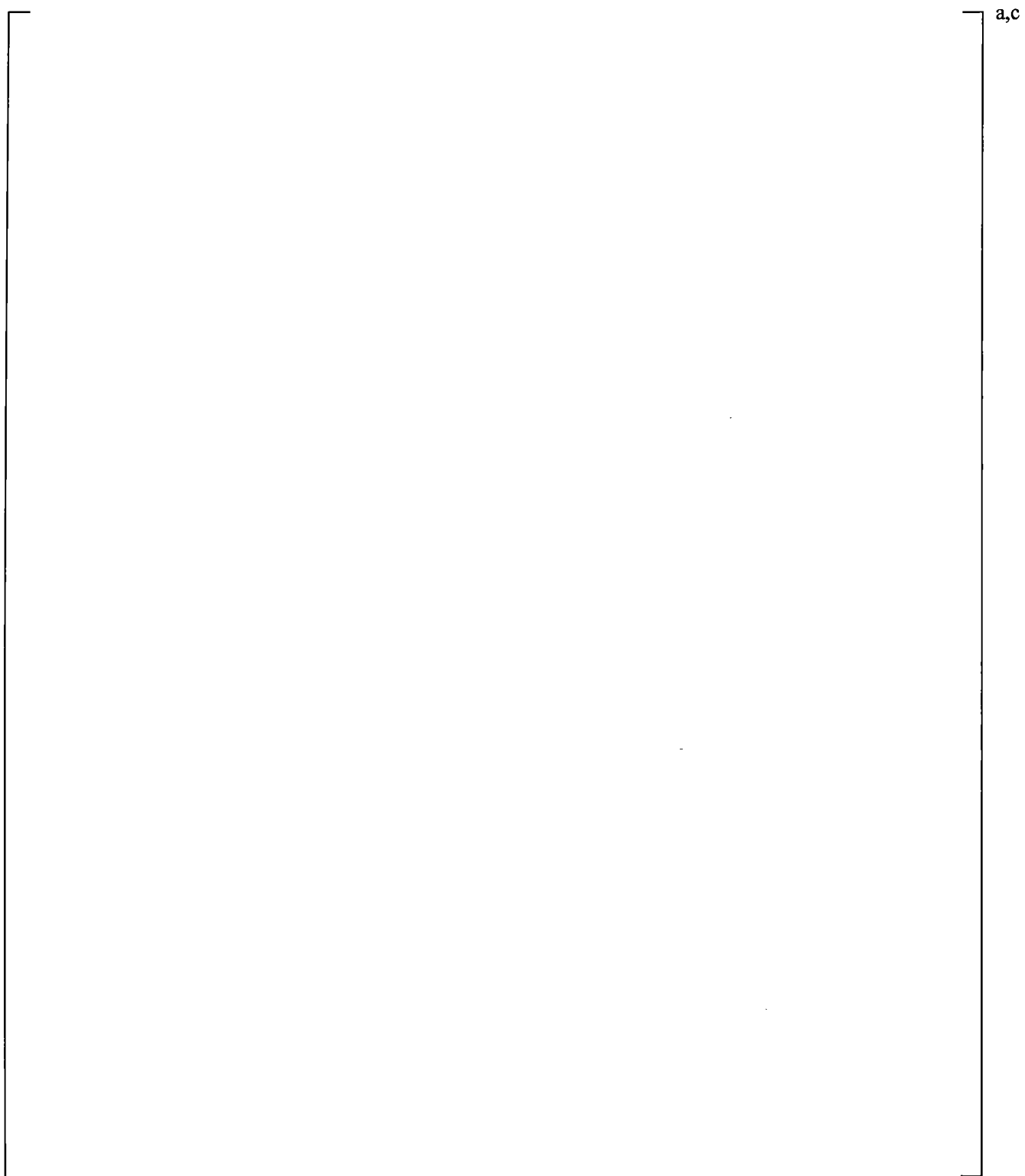


Figure 19.3-9 WCOBRA/TRAC-TF2 VESSEL Component Axial View for UPTF Bypass Tests



**Figure 19.3-10 WCOBRA/TRAC-TF2 VESSEL Component Sections 1 and 2 for
UPTF Bypass Tests**

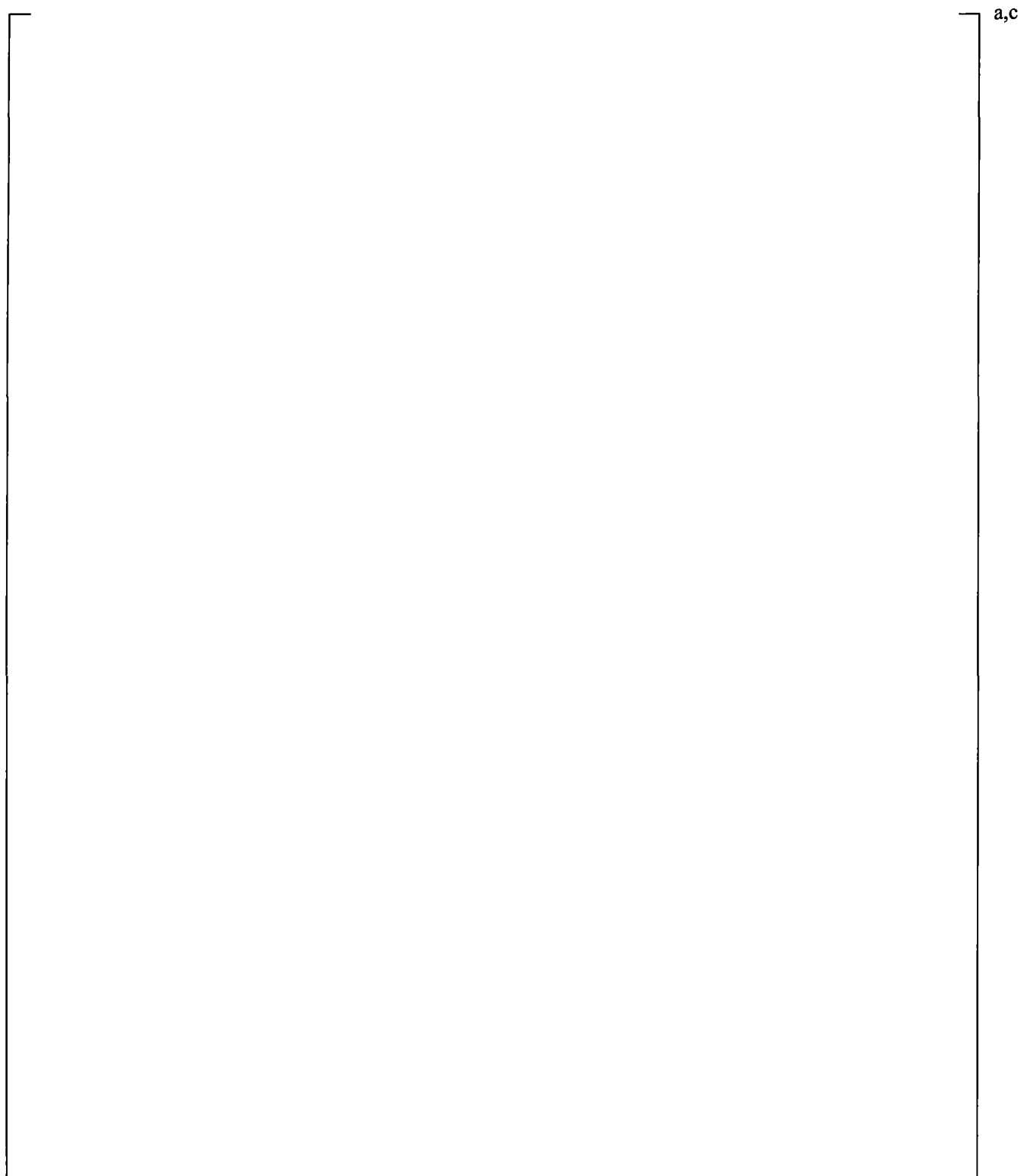


Figure 19.3-11 WCOBRA/TRAC-TF2 VESSEL Component Sections 3 and 4 for UPTF Bypass Tests

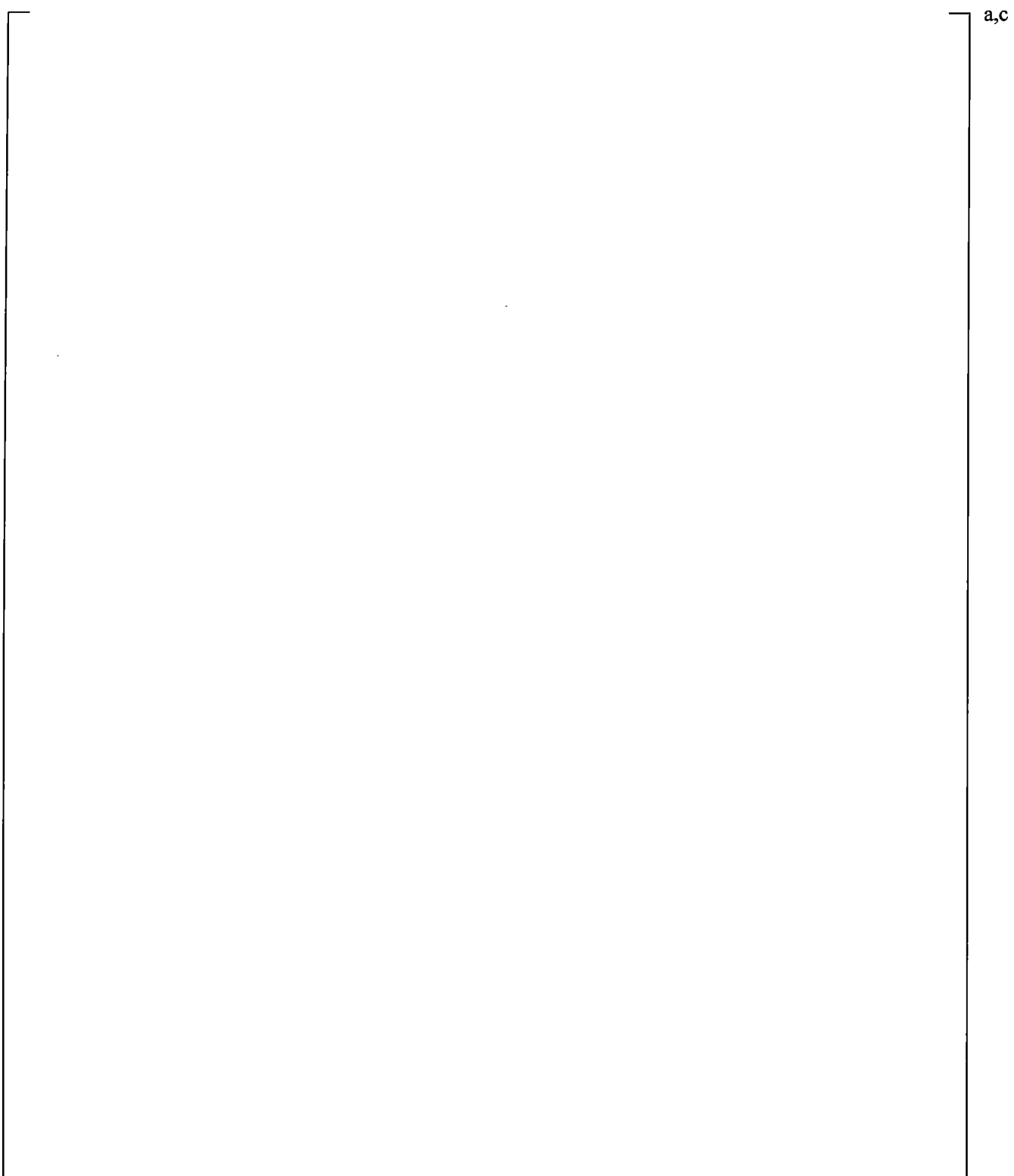


Figure 19.3-12 WCOBRA/TRAC-TF2 VESSEL Component Sections 5 and 6 for UPTF Bypass Tests

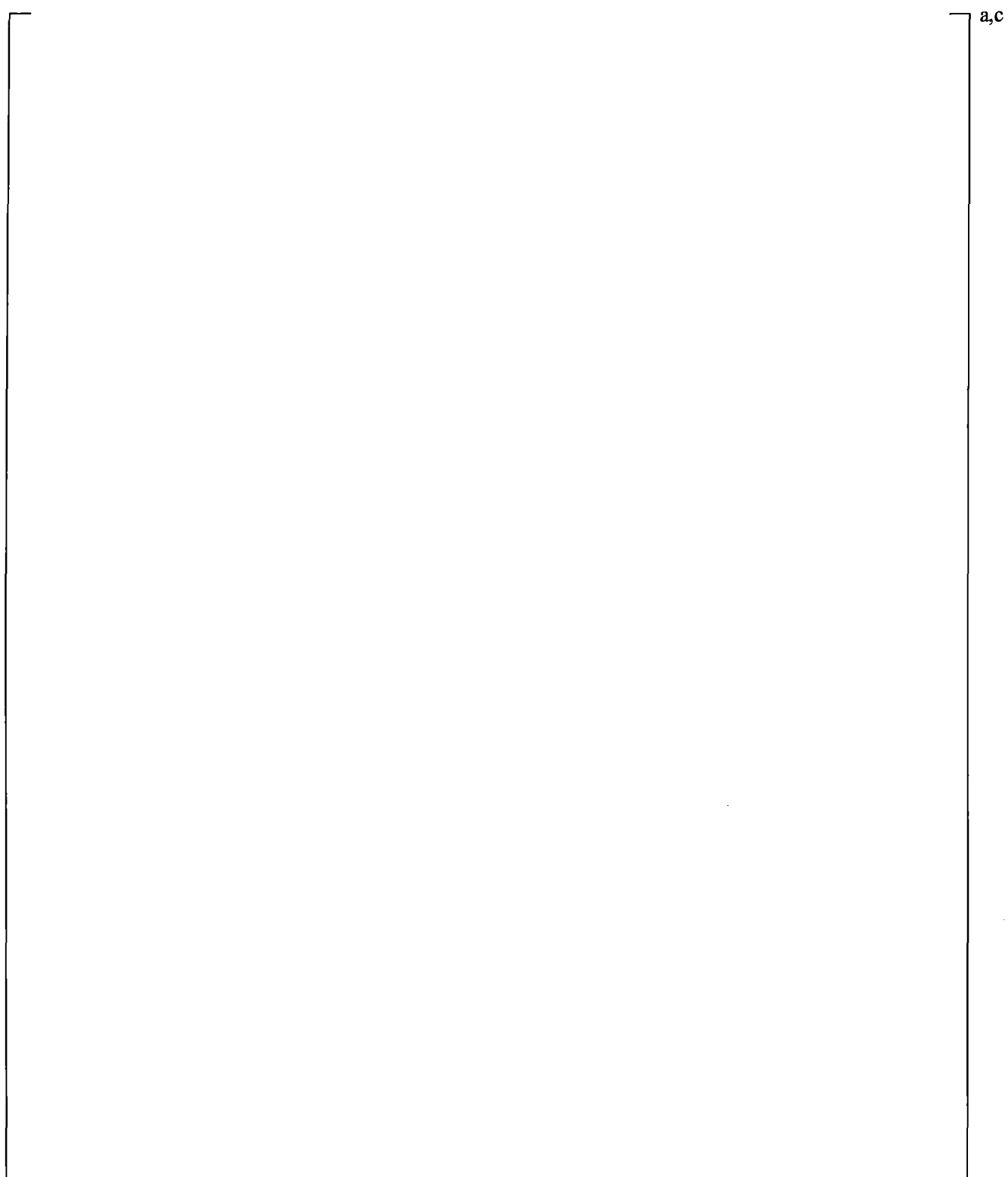


Figure 19.3-13 WCOBRA/TRAC-TF2 VESSEL Component Sections 7 and 8 for UPTF Bypass Tests

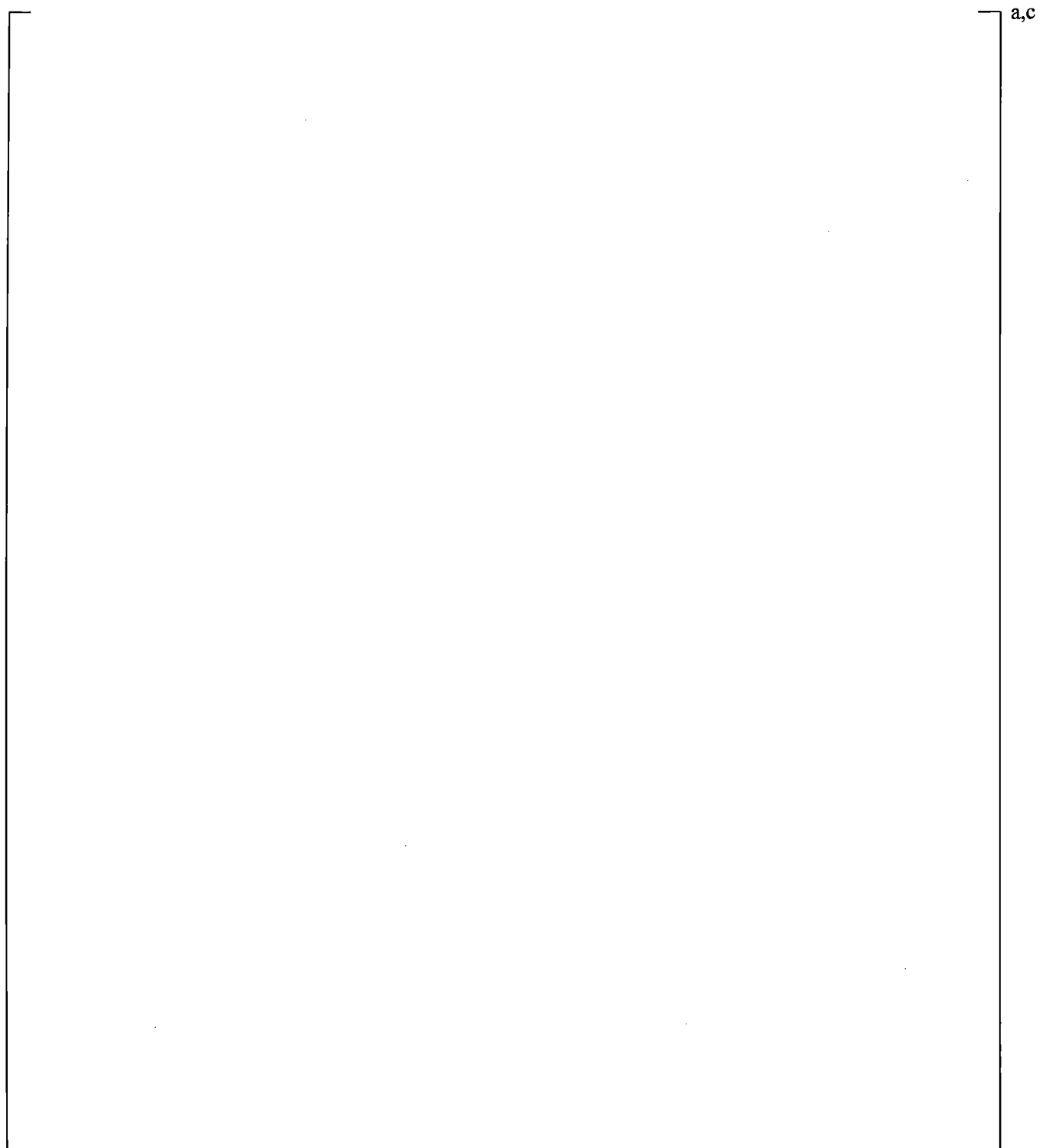


Figure 19.3-14 WCOBRA/TRAC-TF2 One-Dimensional Component Model for UPTF Test 6

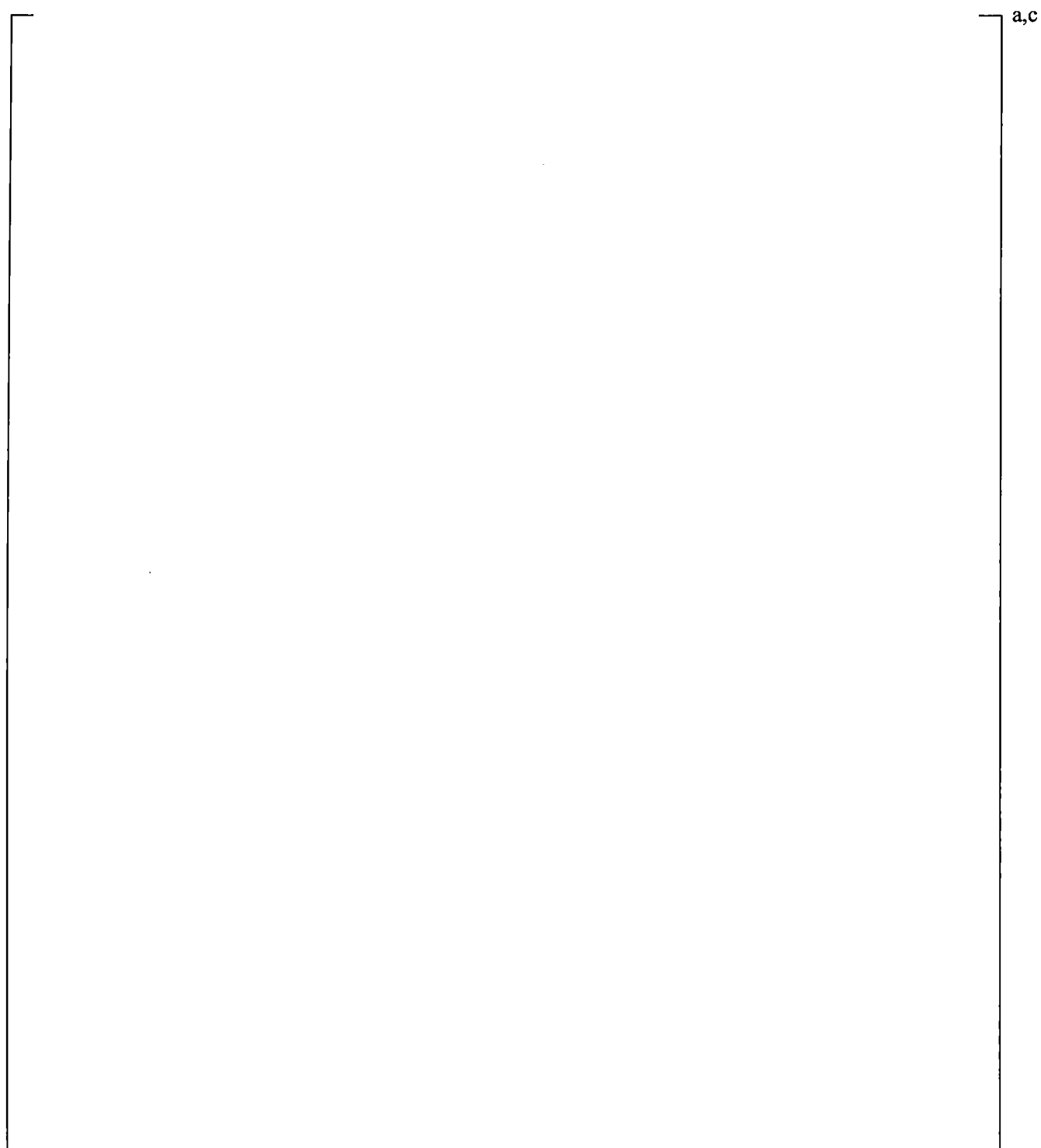


Figure 19.3-15 Total Core Steam Injection, UPTF Test 6 – Run 131

a,c

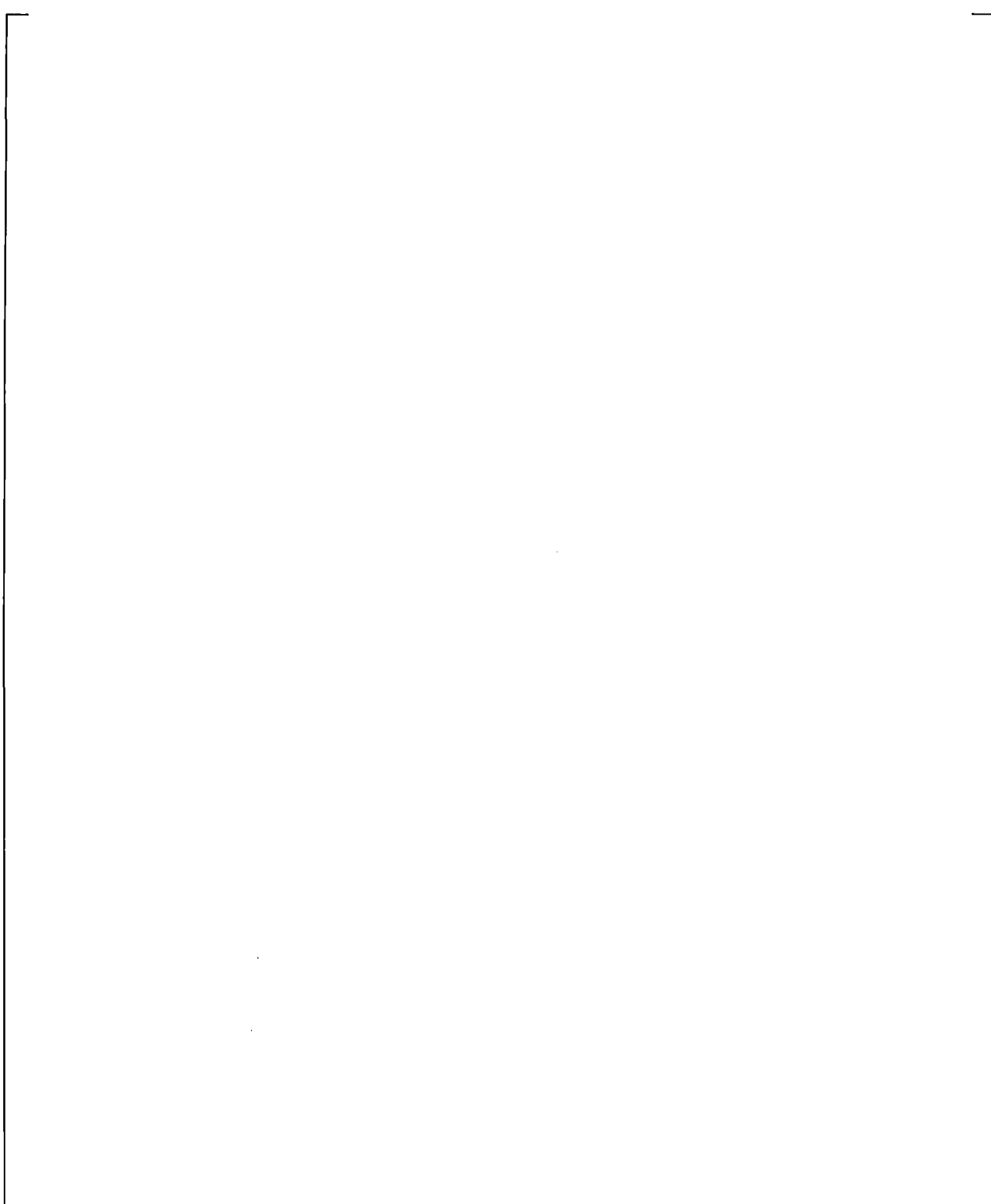


Figure 19.3-16 Steam Generator Simulator Steam Injection, UPTF Test 6 – Run 131

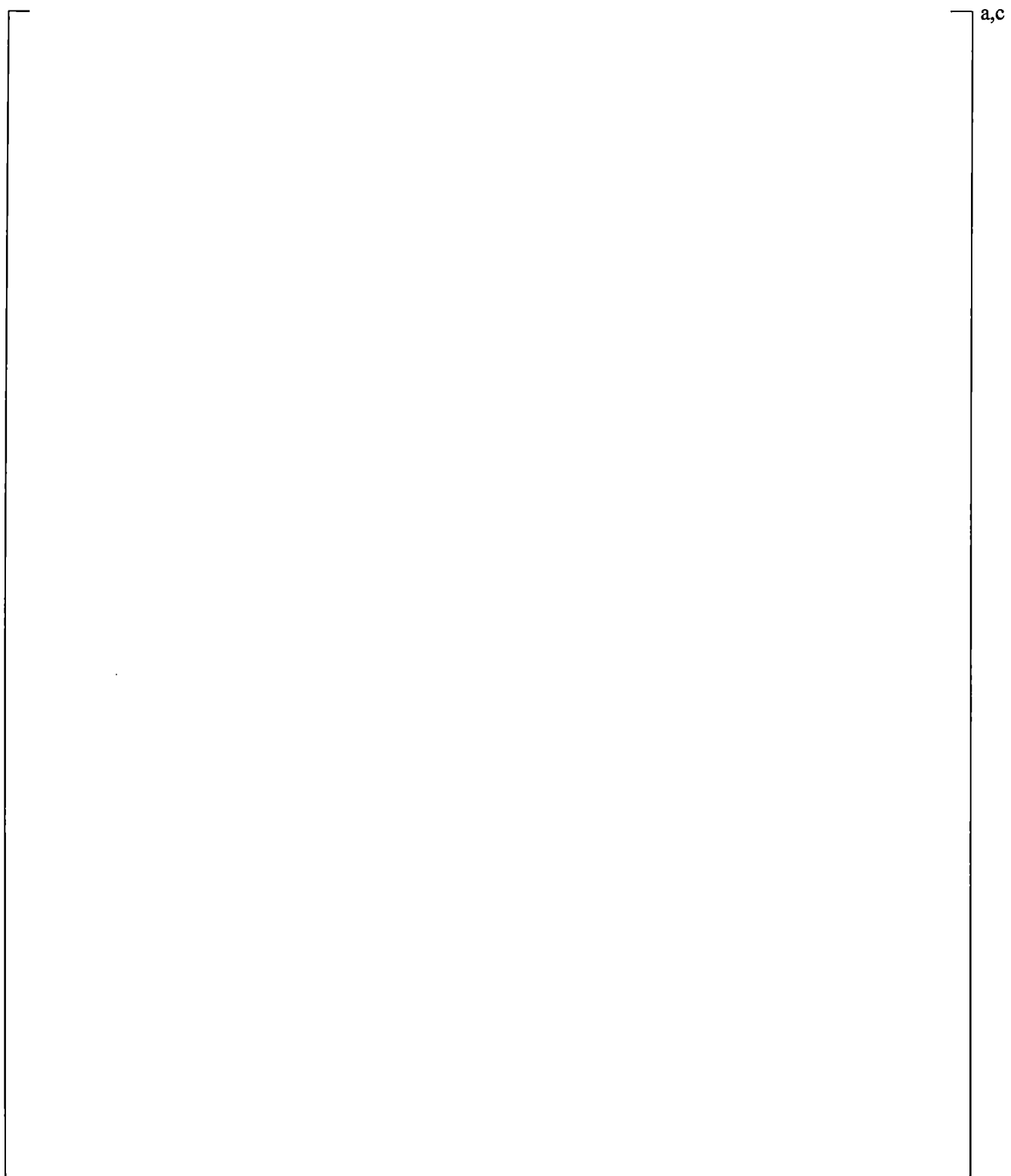


Figure 19.3-17 Intact Loop ECC Injection, UPTF Test 6 – Run 131



Figure 19.3-18 Measured Absolute Pressures in the Upper Plenum and Downcomer, UPTF Test 6 – Run 131



Figure 19.3-19 Predicted Absolute Pressures in the Upper Plenum and Downcomer, UPTF Test 6 – Run 131



Figure 19.3-20 Measured Downcomer Fluid Temperature at Level 21, UPTF Test 6 – Run 131



Figure 19.3-21 Predicted Downcomer Fluid Temperature at Level 21, UPTF Test 6 – Run 131



Figure 19.3-22 Measured Downcomer Fluid Temperature at Level 01, UPTF Test 6 – Run 131



Figure 19.3-23 Predicted Downcomer Fluid Temperature at Level 01, UPTF Test 6 – Run 131

a,c

**Figure 19.3-24 Predicted Liquid Flow at Bottom of the Downcomer in Intact Side, UPTF
Test 6 – Run 131**

a,c

**Figure 19.3-25 Predicted Liquid Flow at Bottom of the Downcomer in Broken Side, UPTF
Test 6 – Run 131**

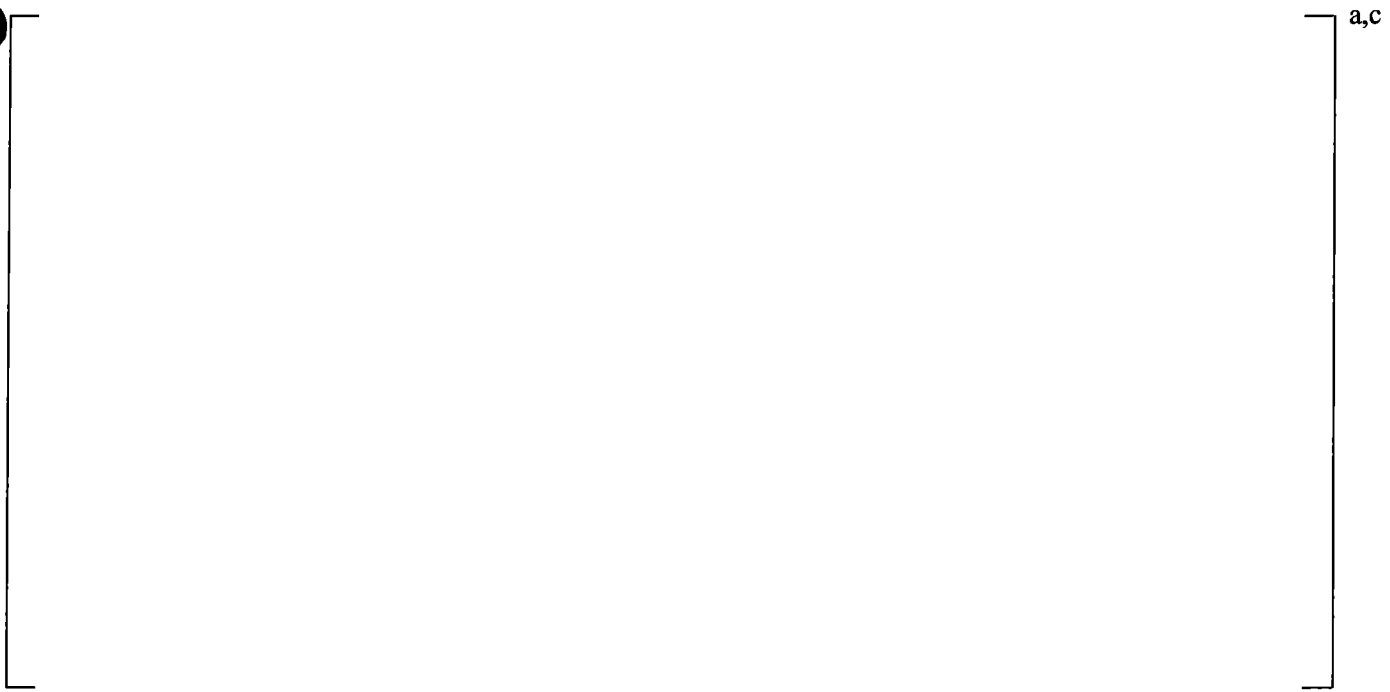


Figure 19.3-26 Measured Axial Differential Pressures in Downcomer, UPTF Test 6 – Run 131



Figure 19.3-27 Predicted Axial Differential Pressures in Downcomer, UPTF Test 6 – Run 131



**Figure 19.3-28 Measured Azimuthal Differential Pressures in Downcomer at Level 06,
UPTF Test 6 – Run 131**



**Figure 19.3-29 Predicted Azimuthal Differential Pressures in Downcomer at Level 06,
UPTF Test 6 – Run 131**



**Figure 19.3-30 Measured Azimuthal Differential Pressures in Downcomer at Level 22,
UPTF Test 6 – Run 131**

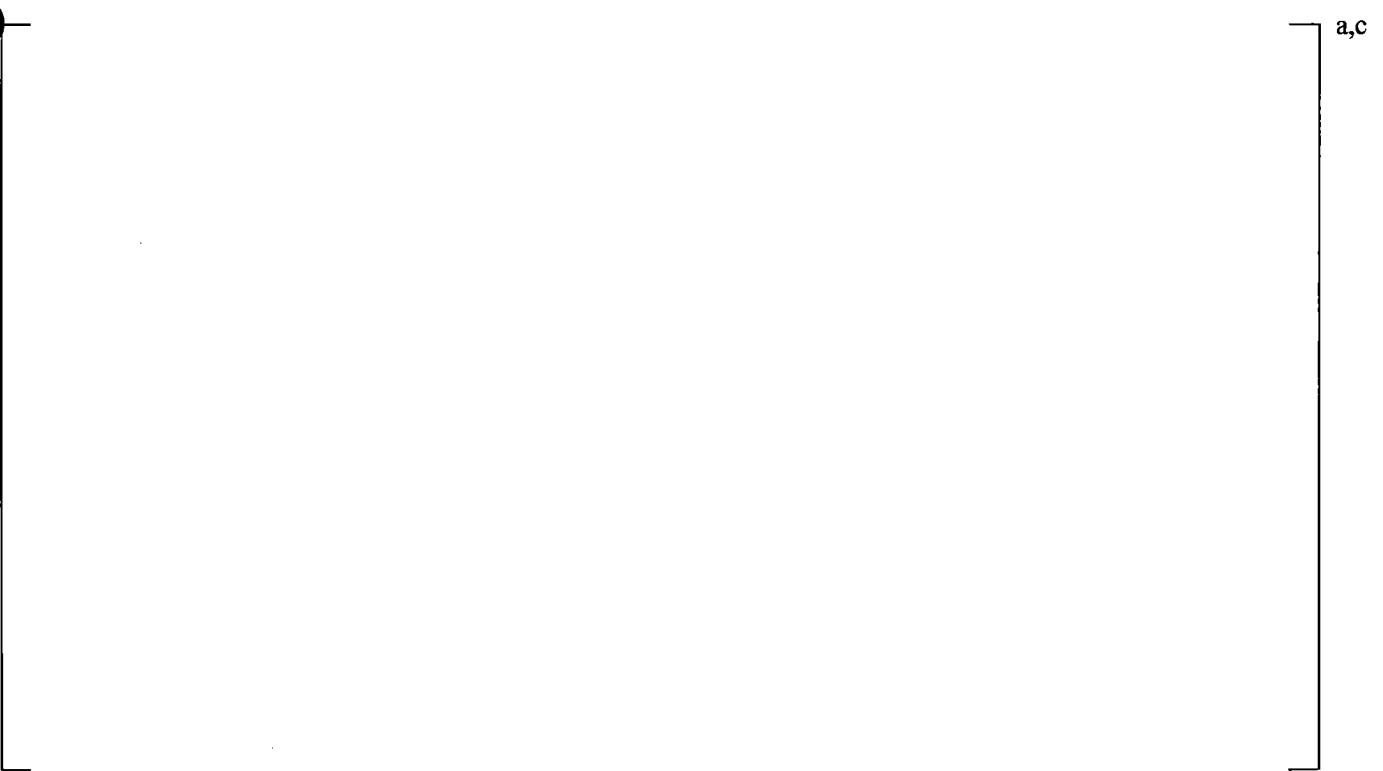


**Figure 19.3-31 Predicted Azimuthal Differential Pressures in Downcomer at Level 22,
UPTF Test 6 – Run 131**

a,c

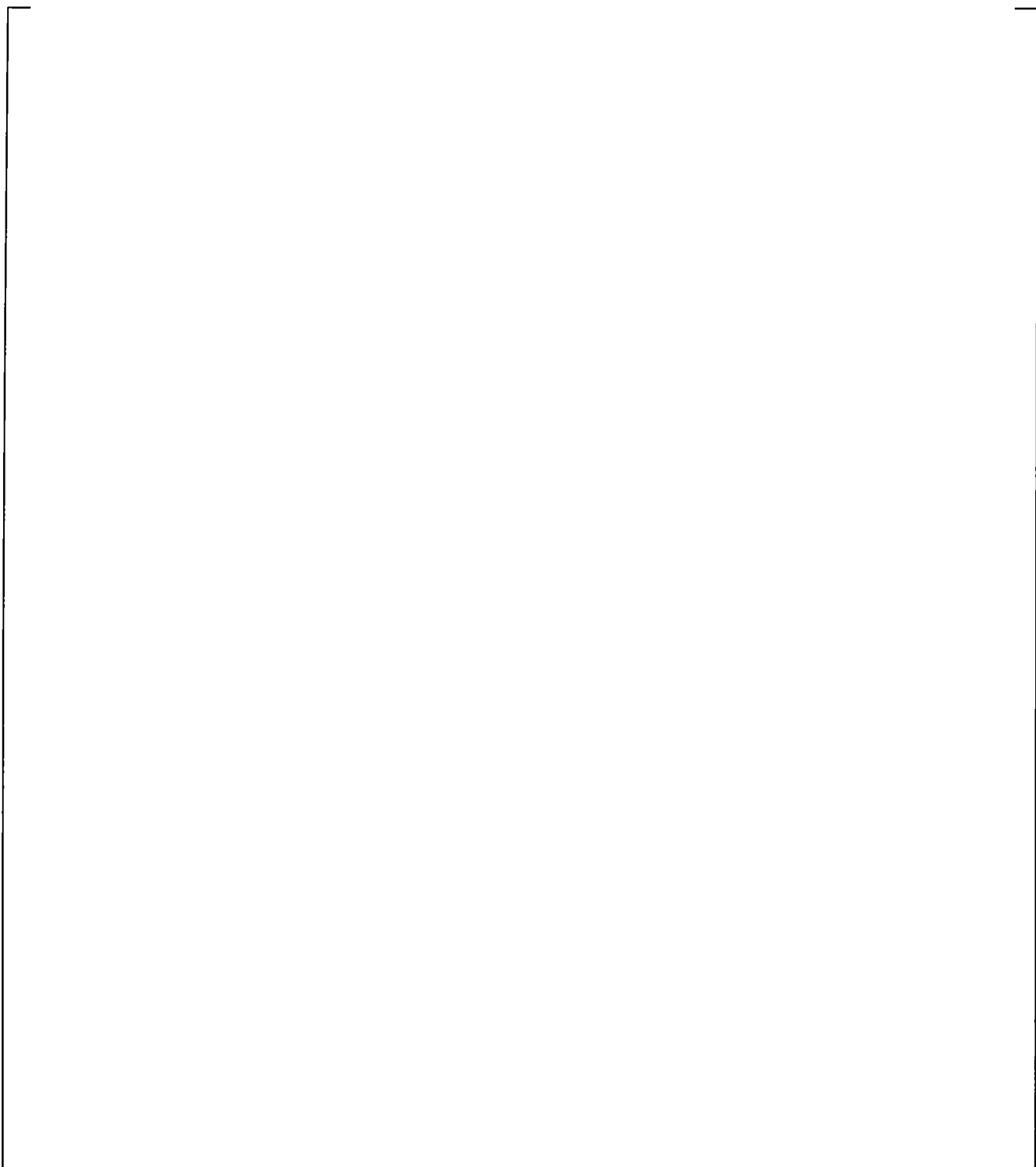


Figure 19.3-32 Comparison on Differential Pressure in Lower Plenum, UPTF Test 6 – Run 131

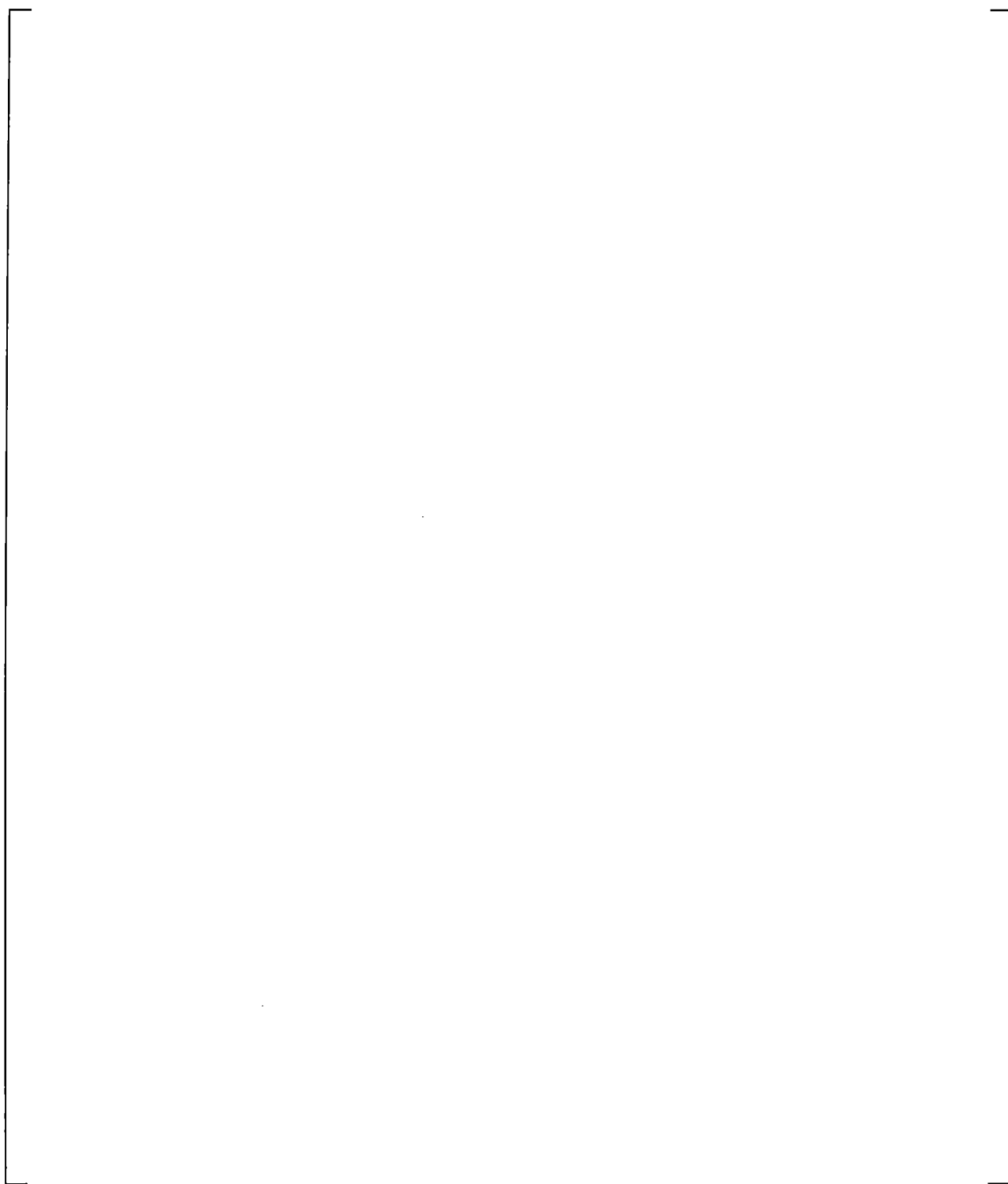


Figure 19.3-33 Total Core Steam Injection, UPTF Test 6 – Run 132

a,c



Figure 19.3-34 Steam Generator Simulator Steam Injection, UPTF Test 6 – Run 132

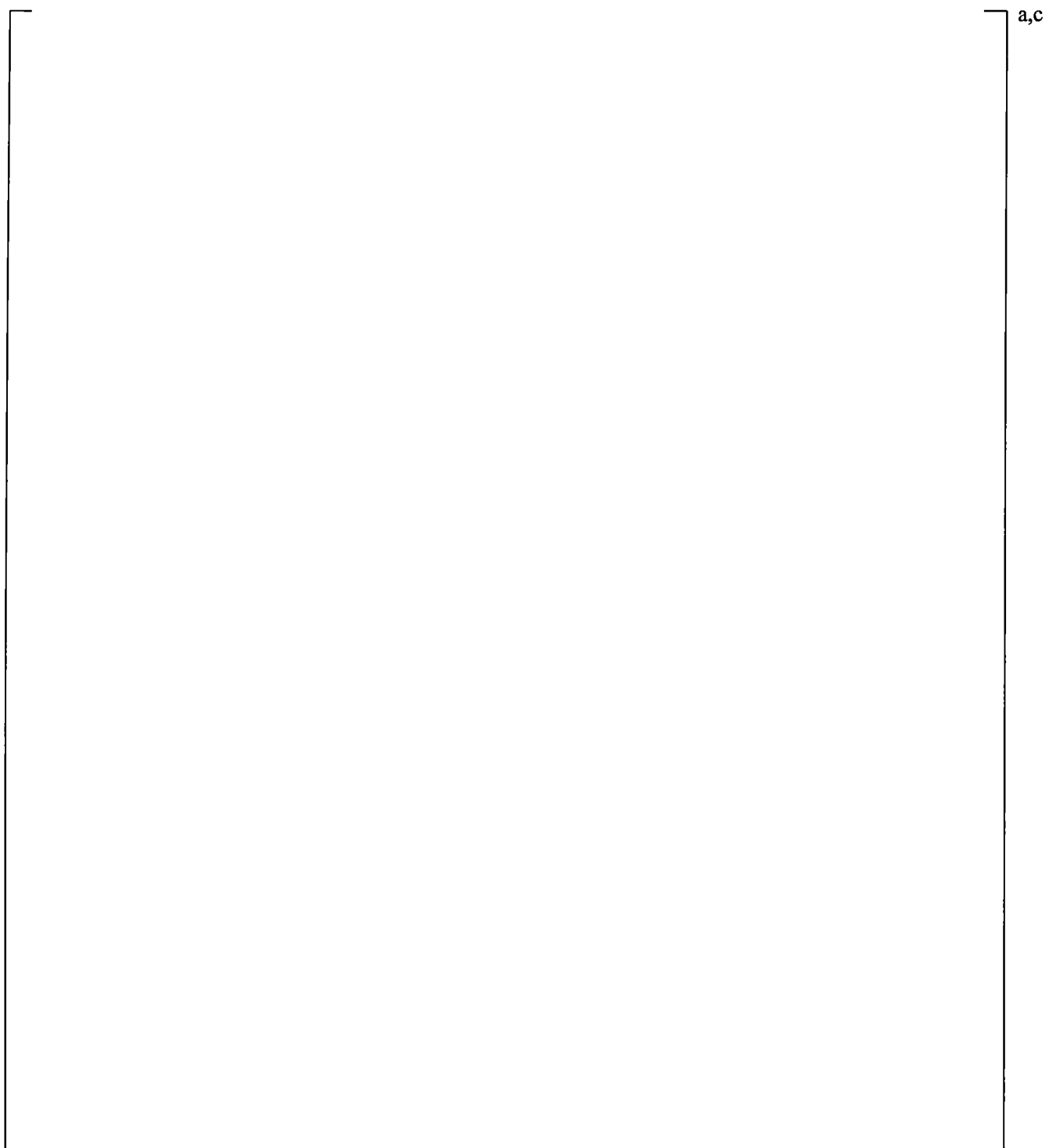
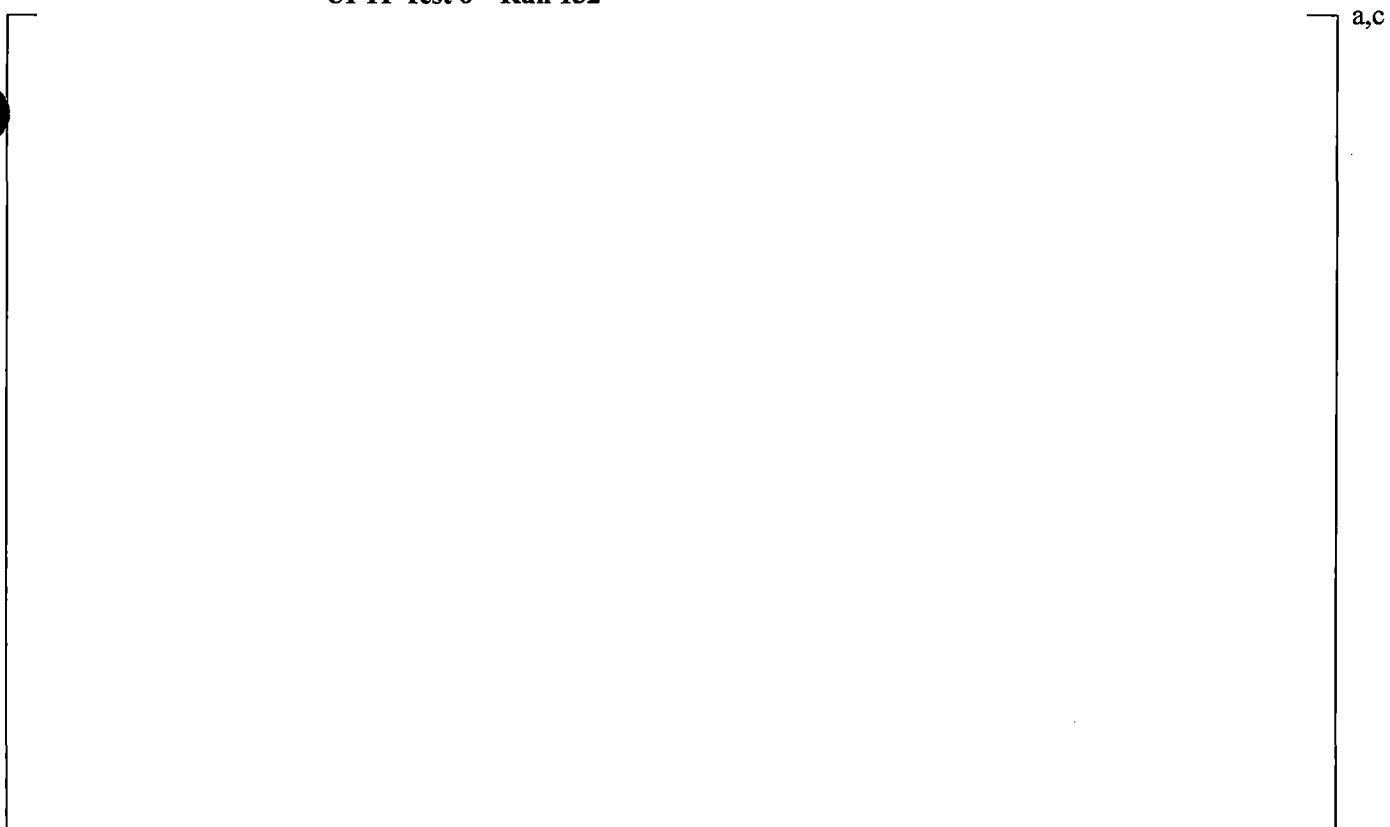


Figure 19.3-35 Intact Loop ECC Injection, UPTF Test 6 – Run 132



**Figure 19.3-36 Measured Absolute Pressures in the Upper Plenum and Downcomer,
UPTF Test 6 – Run 132**



**Figure 19.3-37 Predicted Absolute Pressures in the Upper Plenum and Downcomer,
UPTF Test 6 – Run 132**



Figure 19.3-38 Measured Downcomer Fluid Temperature at Level 21, UPTF Test 6 – Run 132



Figure 19.3-39 Predicted Downcomer Fluid Temperature at Level 21, UPTF Test 6 – Run 132



Figure 19.3-40 Measured Downcomer Fluid Temperature at Level 01, UPTF Test 6 – Run 132



Figure 19.3-41 Predicted Downcomer Fluid Temperature at Level 01, UPTF Test 6 – Run 132



**Figure 19.3-42 Predicted Liquid Flow at Bottom of the Downcomer in Intact Side,
UPTF Test 6 – Run 132**



**Figure 19.3-43 Predicted Liquid Flow at Bottom of the Downcomer in Broken Side,
UPTF Test 6 – Run 132**



Figure 19.3-44 Measured Axial Differential Pressures in Downcomer, UPTF Test 6 – Run 132



Figure 19.3-45 Predicted Axial Differential Pressures in Downcomer, UPTF Test 6 – Run 132



**Figure 19.3-46 Measured Azimuthal Differential Pressures in Downcomer at Level 06,
UPTF Test 6 – Run 132**



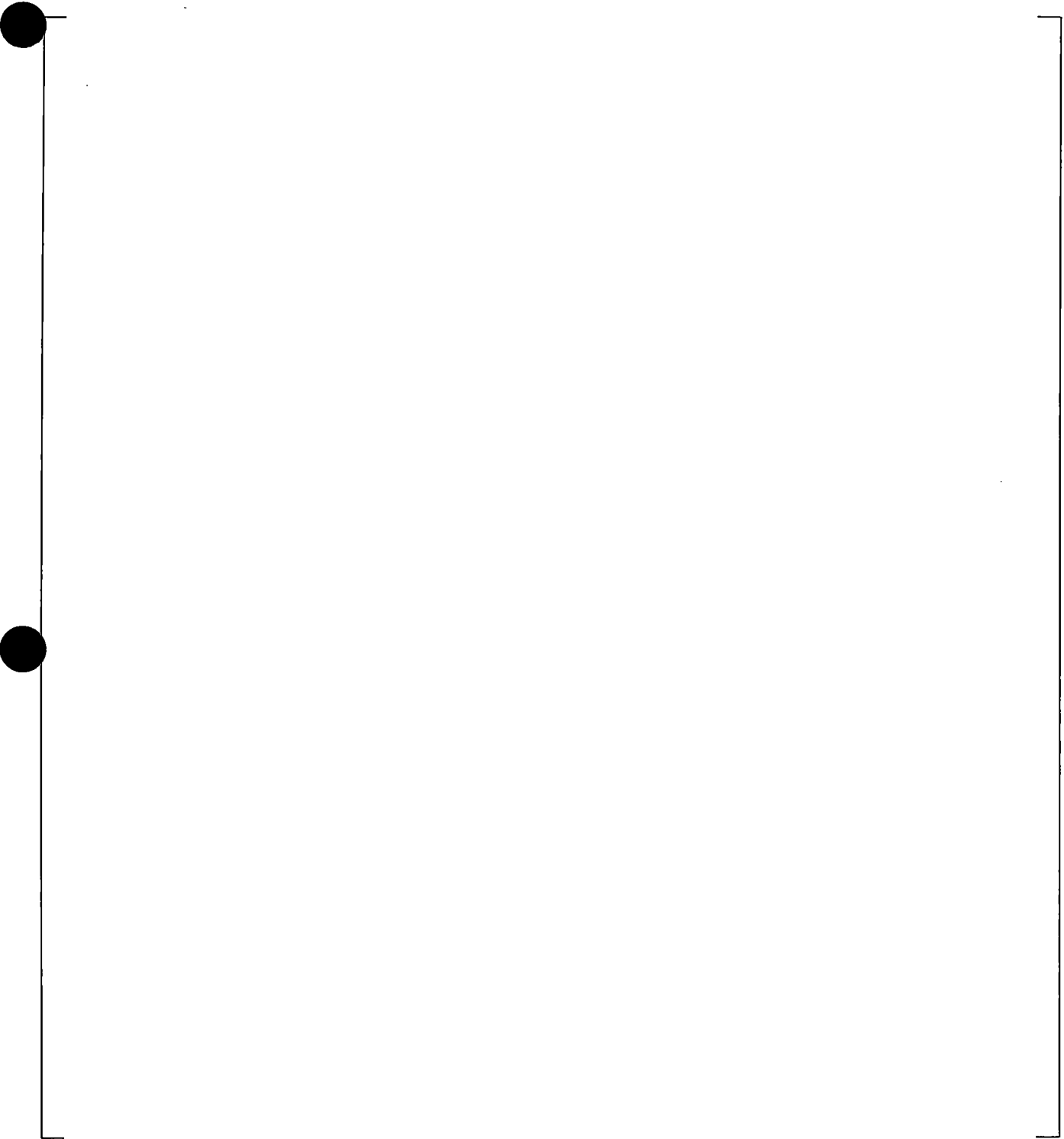
**Figure 19.3-47 Predicted Azimuthal Differential Pressures in Downcomer at Level 06,
UPTF Test 6 – Run 132**



**Figure 19.3-48 Measured Azimuthal Differential Pressures in Downcomer at Level 22,
UPTF Test 6 – Run 132**



**Figure 19.3-49 Predicted Azimuthal Differential Pressures in Downcomer at Level 22,
UPTF Test 6 – Run 132**



a,c

Figure 19.3-50 Comparison on Differential Pressure in Lower Plenum, UPTF Test 6 – Run 132

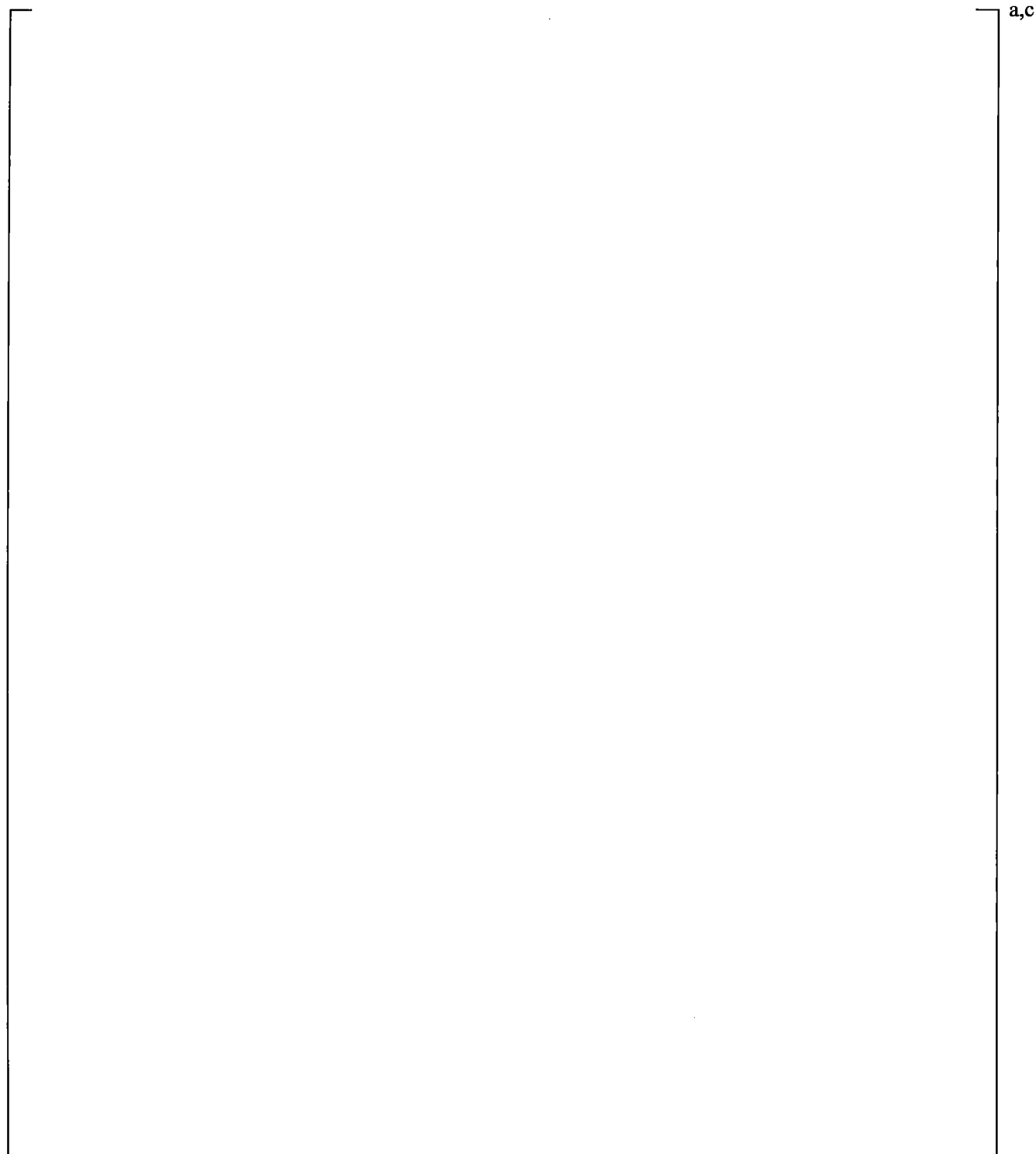


Figure 19.3-51 Total Core Steam Injection, UPTF Test 6 – Run 133

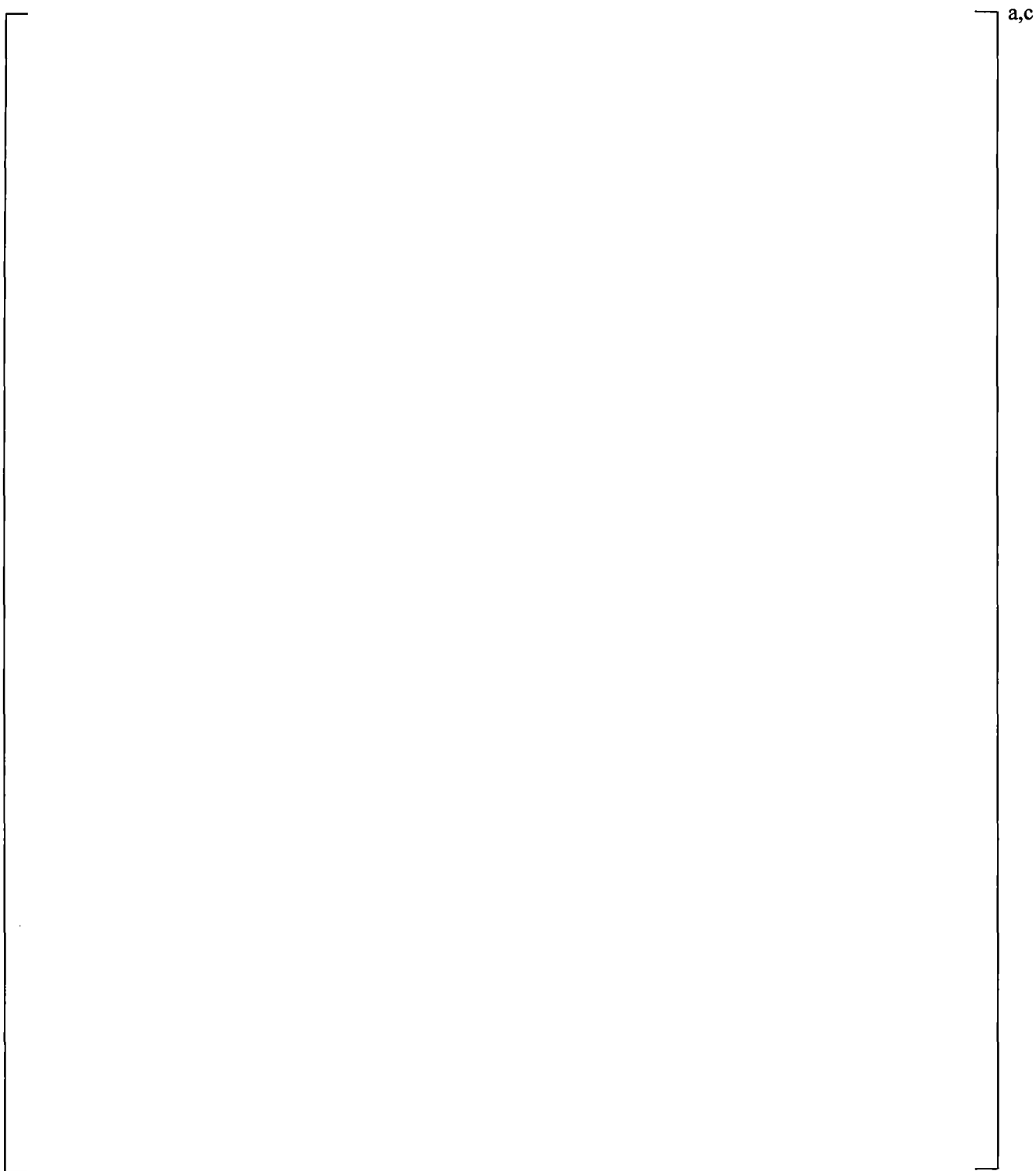


Figure 19.3-52 Steam Generator Simulator Steam Injection, UPTF Test 6 – Run 133

a,c



Figure 19.3-53 Intact Loop ECC Injection, UPTF Test 6 – Run 133



**Figure 19.3-54 Measured Absolute Pressures in the Upper Plenum and Downcomer,
UPTF Test 6 – Run 133**



**Figure 19.3-55 Predicted Absolute Pressures in the Upper Plenum and Downcomer,
UPTF Test 6 – Run 133**



Figure 19.3-56 Measured Downcomer Fluid Temperature at Level 21, UPTF Test 6 – Run 133



Figure 19.3-57 Predicted Downcomer Fluid Temperature at Level 21, UPTF Test 6 – Run 133



Figure 19.3-58 Measured Downcomer Fluid Temperature at Level 01, UPTF Test 6 – Run 133



Figure 19.3-59 Predicted Downcomer Fluid Temperature at Level 01, UPTF Test 6 – Run 133



a,c

**Figure 19.3-60 Predicted Liquid Flow at Bottom of the Downcomer in Intact Side,
UPTF Test 6 – Run 133**

a,c

**Figure 19.3-61 Predicted Liquid Flow at Bottom of the Downcomer in Broken Side,
UPTF Test 6 – Run 133**



Figure 19.3-62 Measured Axial Differential Pressures in Downcomer, UPTF Test 6 – Run 133



Figure 19.3-63 Predicted Axial Differential Pressures in Downcomer, UPTF Test 6 – Run 133



**Figure 19.3-64 Measured Azimuthal Differential Pressures in Downcomer at Level 06, UPTF
Test 6 – Run 133**



**Figure 19.3-65 Predicted Azimuthal Differential Pressures in Downcomer at Level 06, UPTF
Test 6 – Run 133**

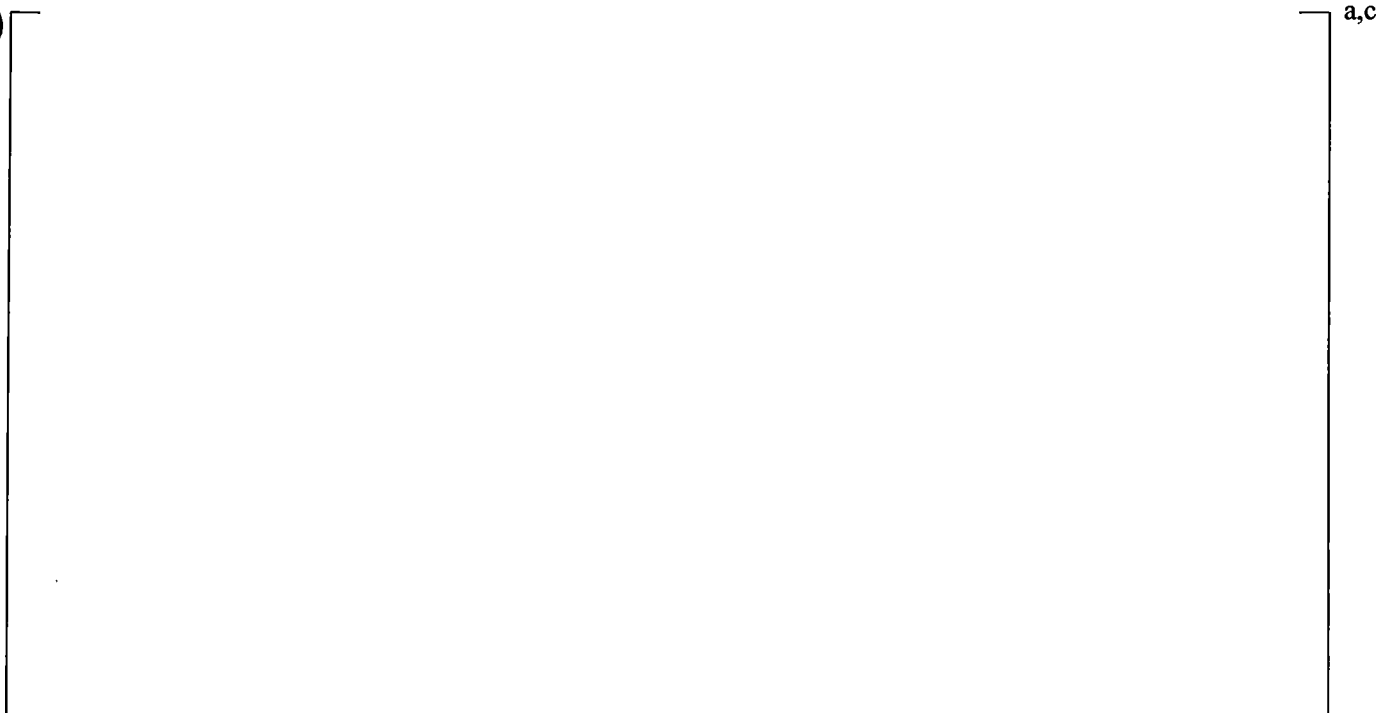


**Figure 19.3-66 Measured Azimuthal Differential Pressures in Downcomer at Level 22,
UPTF Test 6 – Run 133**



**Figure 19.3-67 Predicted Azimuthal Differential Pressures in Downcomer at Level 22,
UPTF Test 6 – Run 133**

Figure 19.3-68 Comparison on Differential Pressure in Lower Plenum, UPTF Test 6 – Run 133

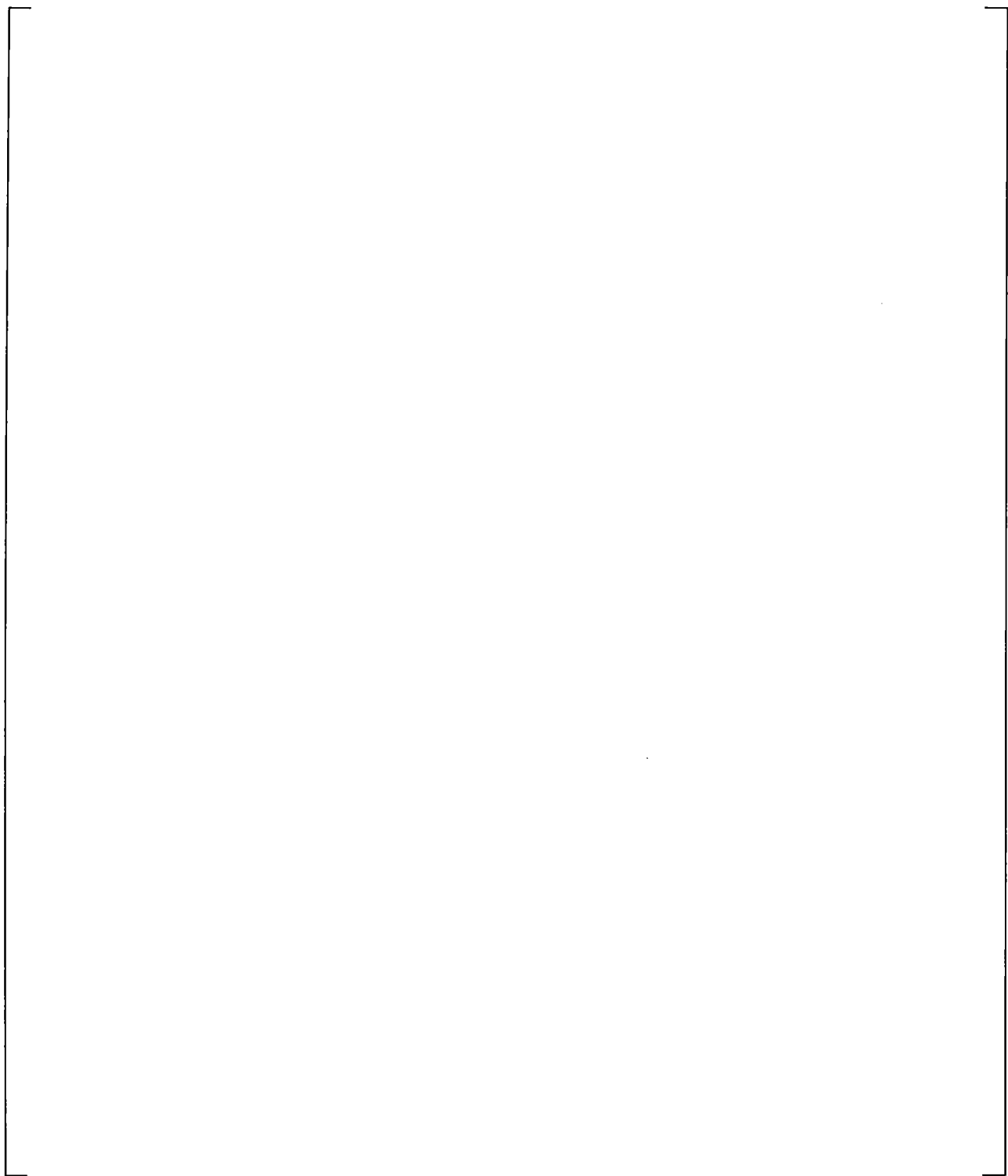


Figure 19.3-69 Total Core Steam Injection, UPTF Test 6 – Run 135

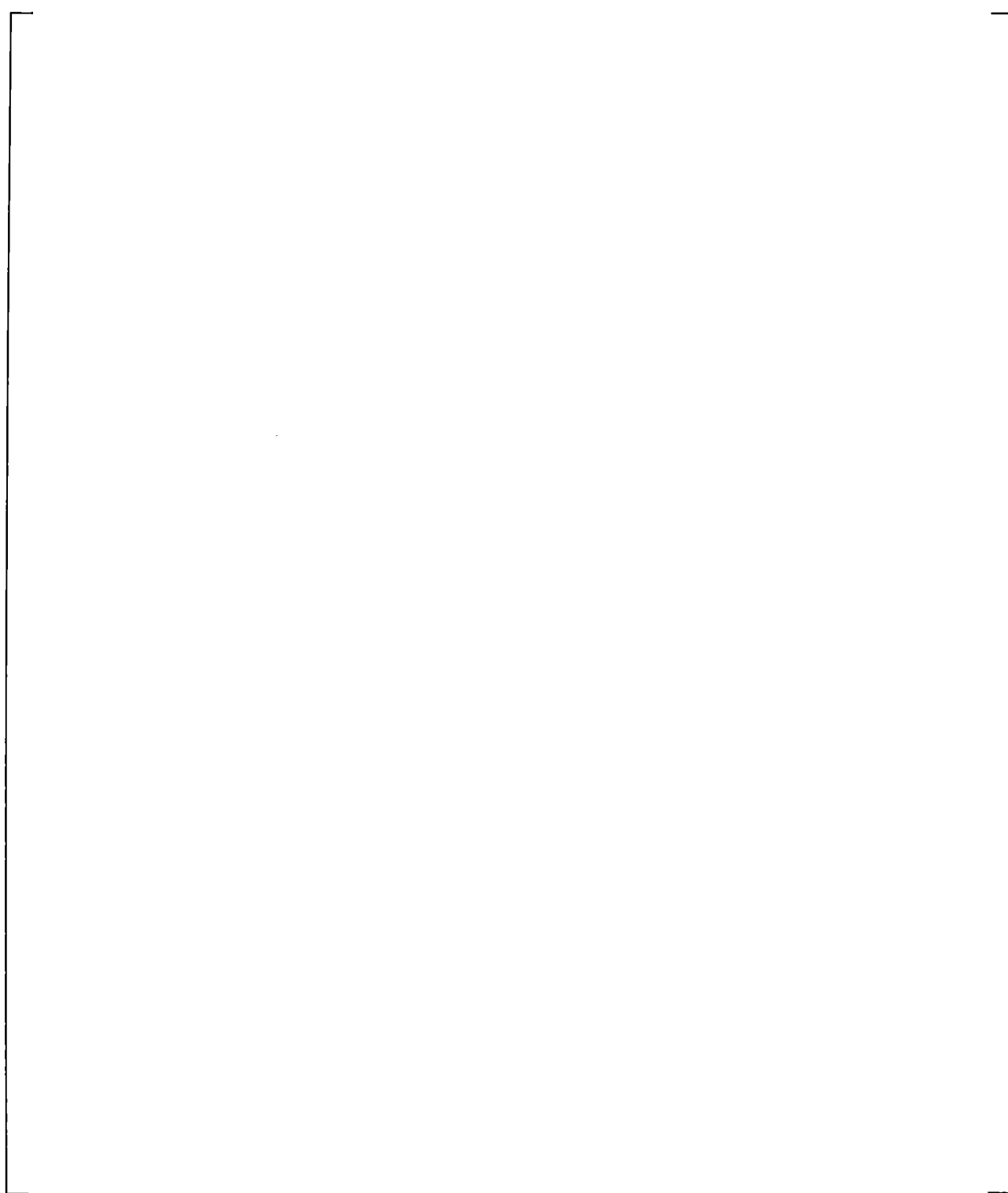


Figure 19.3-70 Steam Generator Simulator Steam Injection, UPTF Test 6 – Run 135

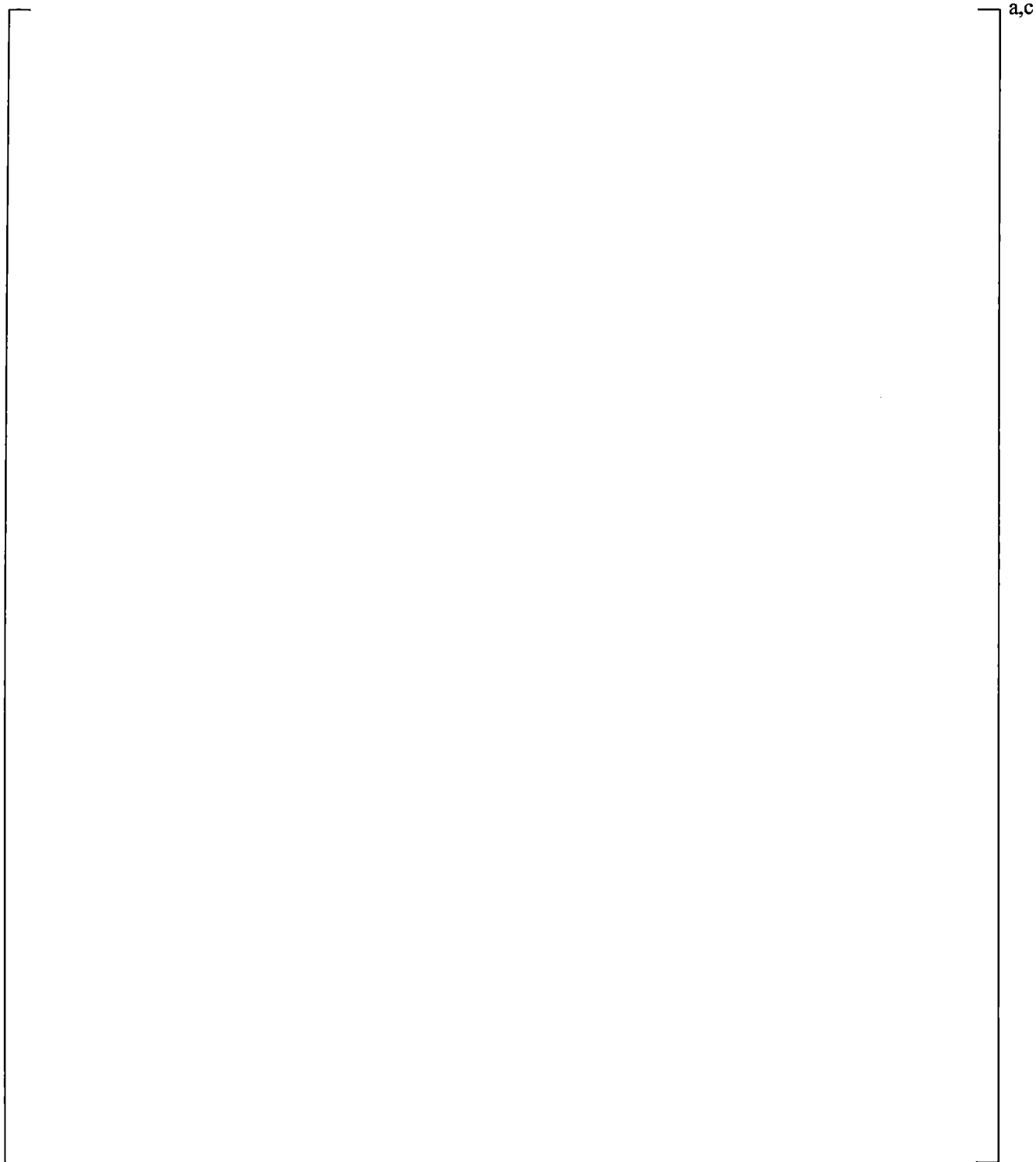


Figure 19.3-71 Intact Loop ECC Injection, UPTF Test 6 – Run 135

a,c



**Figure 19.3-72 Measured Absolute Pressures in the Upper Plenum and Downcomer,
UPTF Test 6 – Run 135**

a,c



**Figure 19.3-73 Predicted Absolute Pressures in the Upper Plenum and Downcomer,
UPTF Test 6 – Run 135**



Figure 19.3-74 Measured Downcomer Fluid Temperature at Level 21, UPTF Test 6 – Run 135



Figure 19.3-75 Predicted Downcomer Fluid Temperature at Level 21, UPTF Test 6 – Run 135



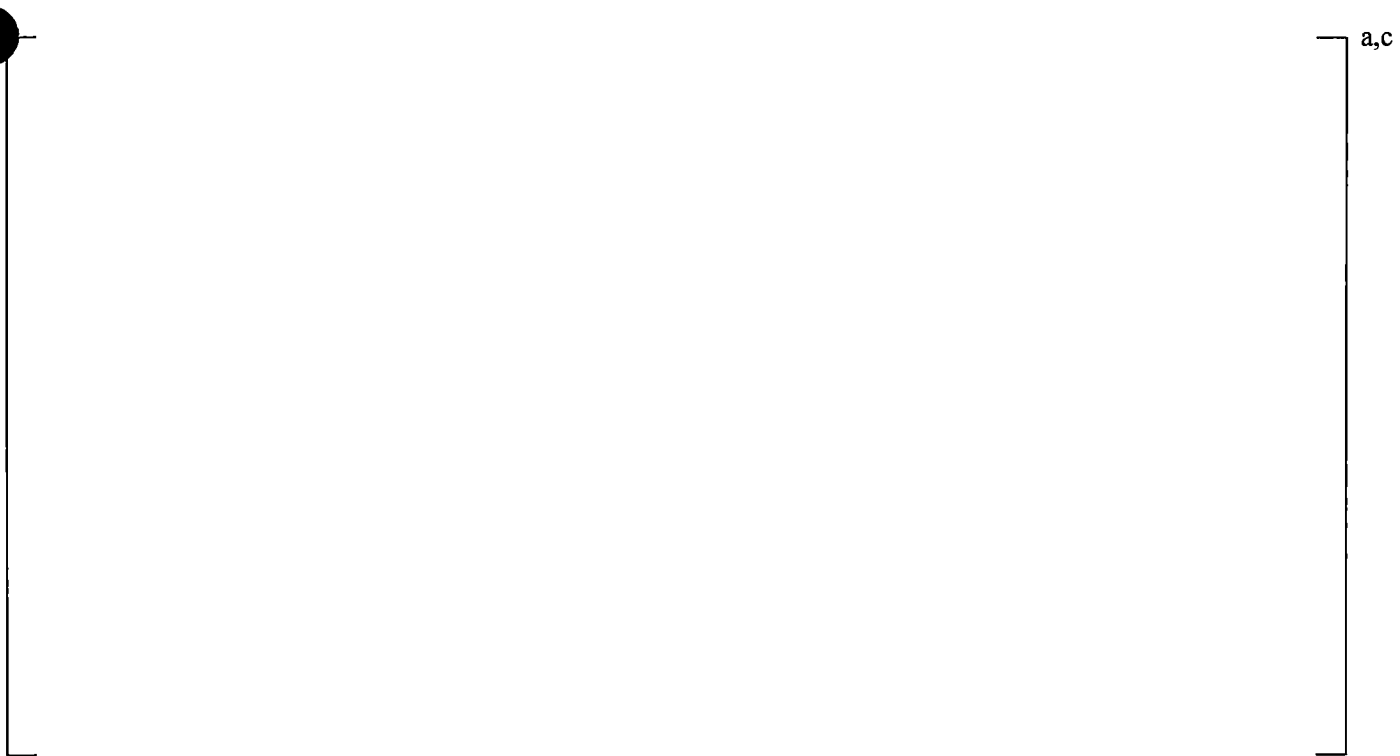
Figure 19.3-76 Measured Downcomer Fluid Temperature at Level 01, UPTF Test 6 – Run 135



Figure 19.3-77 Predicted Downcomer Fluid Temperature at Level 01, UPTF Test 6 – Run 135



**Figure 19.3-78 Predicted Liquid Flow at Bottom of the Downcomer in Intact Side,
UPTF Test 6 – Run 135**



**Figure 19.3-79 Predicted Liquid Flow at Bottom of the Downcomer in Broken Side,
UPTF Test 6 – Run 135**



Figure 19.3-80 Measured Axial Differential Pressures in Downcomer, UPTF Test 6 – Run 135



Figure 19.3-81 Predicted Axial Differential Pressures in Downcomer, UPTF Test 6 – Run 135



**Figure 19.3-82 Measured Azimuthal Differential Pressures in Downcomer at Level 06, UPTF
Test 6 – Run 135**



**Figure 19.3-83 Predicted Azimuthal Differential Pressures in Downcomer at Level 06, UPTF
Test 6 – Run 135**



**Figure 19.3-84 Measured Azimuthal Differential Pressures in Downcomer at Level 22,
UPTF Test 6 – Run 135**



**Figure 19.3-85 Predicted Azimuthal Differential Pressures in Downcomer at Level 22,
UPTF Test 6 – Run 135**

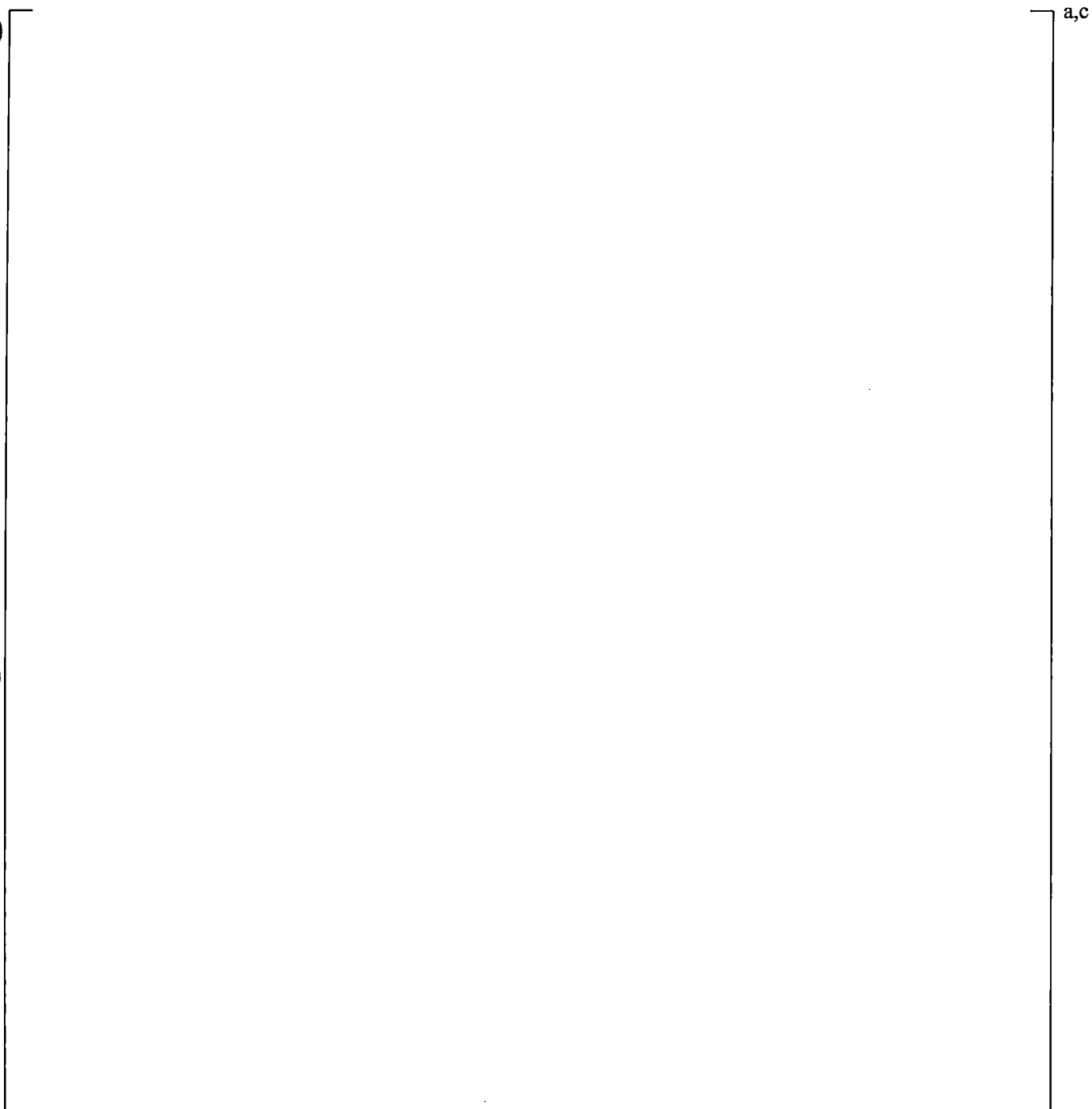


Figure 19.3-86 Comparison on Differential Pressure in Lower Plenum, UPTF Test 6 – Run 135

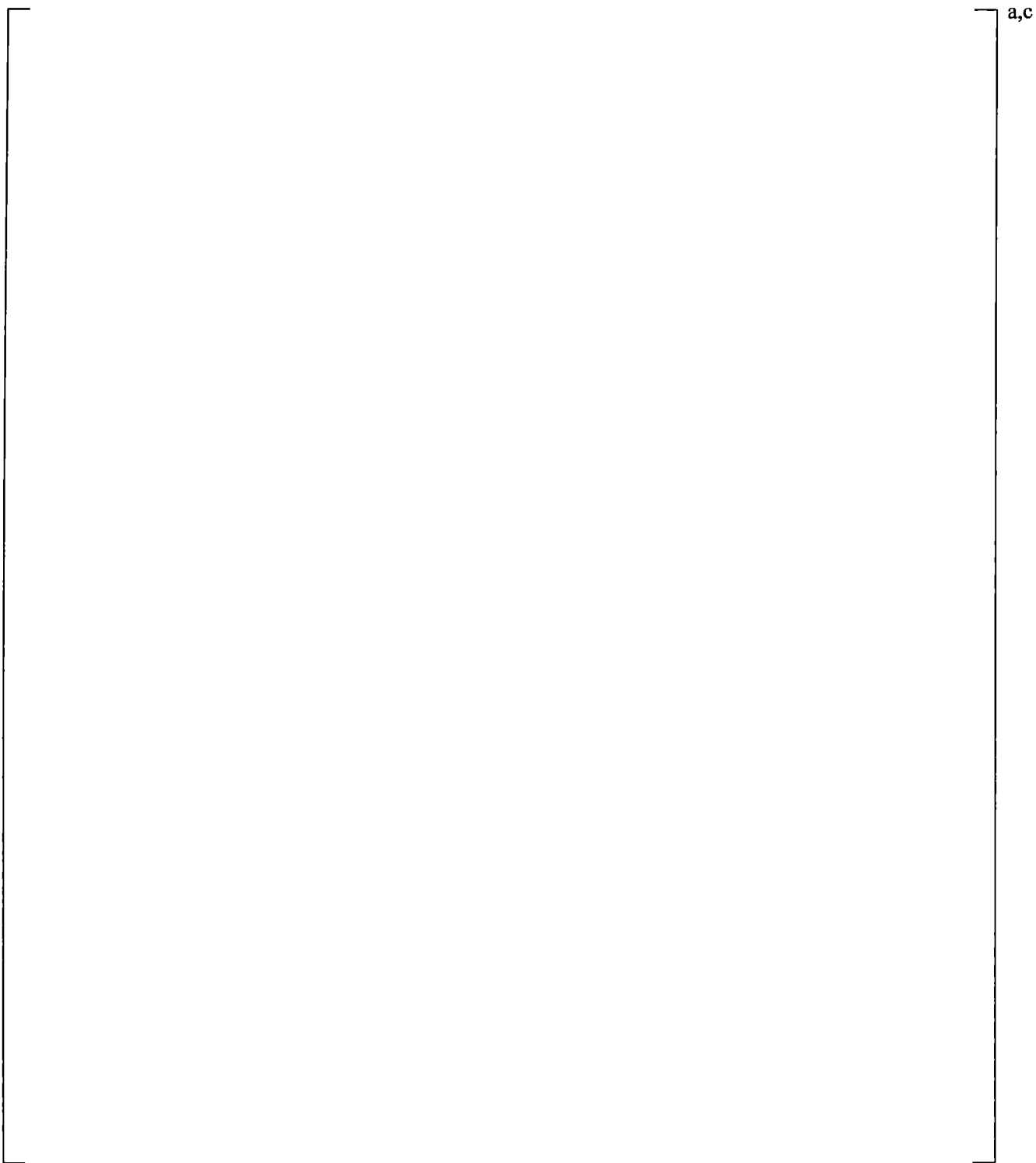


Figure 19.3-87 Total Core Steam Injection, UPTF Test 6 – Run 136

a,c

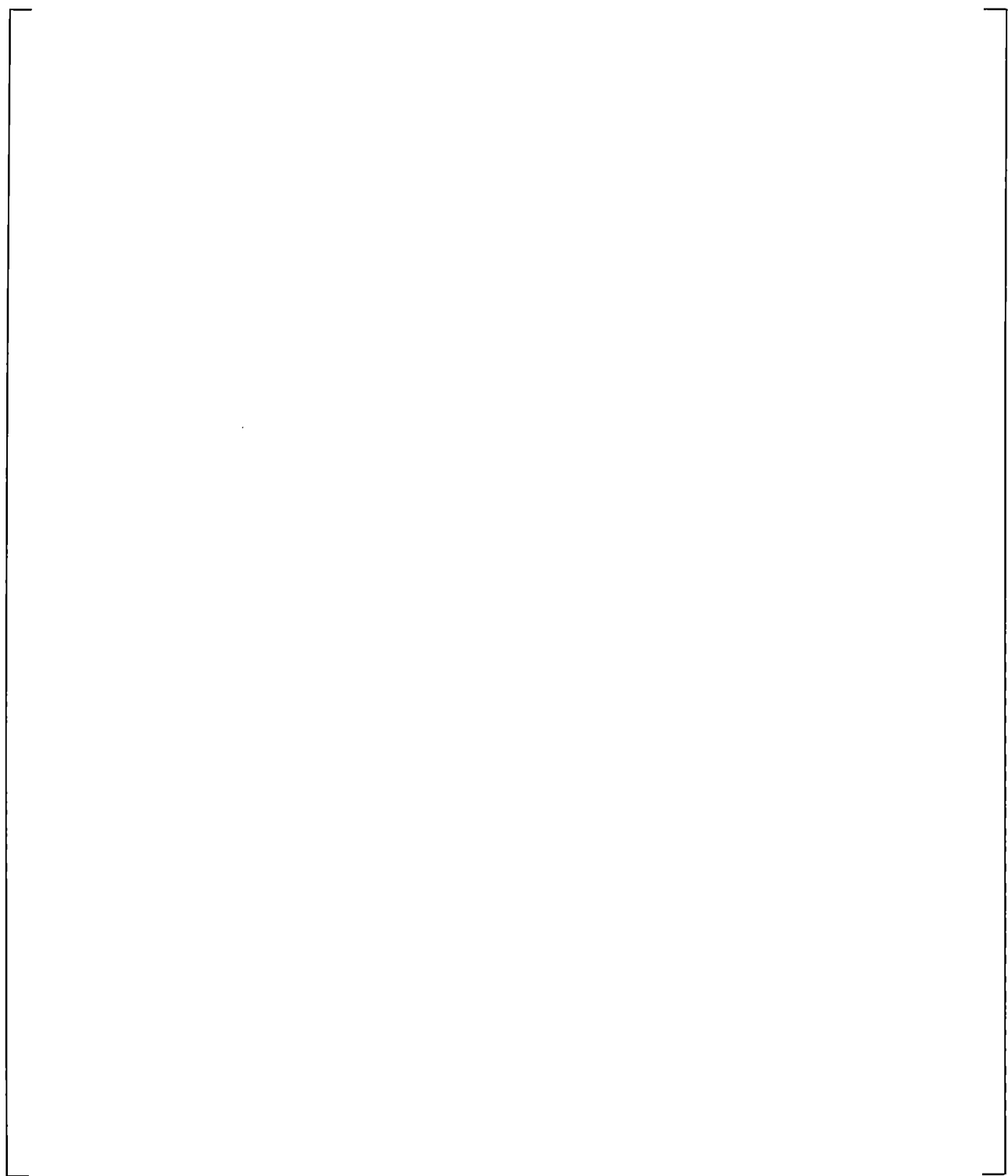


Figure 19.3-88 Intact Loop ECC Injection, UPTF Test 6 – Run 136



**Figure 19.3-89 Measured Absolute Pressures in the Upper Plenum and Downcomer,
UPTF Test 6 – Run 136**



**Figure 19.3-90 Predicted Absolute Pressures in the Upper Plenum and Downcomer,
UPTF Test 6 – Run 136**



Figure 19.3-91 Measured Downcomer Fluid Temperature at Level 21, UPTF Test 6 – Run 136



Figure 19.3-92 Predicted Downcomer Fluid Temperature at Level 21, UPTF Test 6 – Run 136



Figure 19.3-93 Measured Downcomer Fluid Temperature at Level 01, UPTF Test 6 – Run 136



Figure 19.3-94 Predicted Downcomer Fluid Temperature at Level 01, UPTF Test 6 – Run 136

a,c

**Figure 19.3-95 Predicted Liquid Flow at Bottom of the Downcomer in Intact Side,
UPTF Test 6 – Run 136**

a,c

**Figure 19.3-96 Predicted Liquid Flow at Bottom of the Downcomer in Broken Side,
UPTF Test 6 – Run 136**



Figure 19.3-97 Measured Axial Differential Pressures in Downcomer, UPTF Test 6 – Run 136



Figure 19.3-98 Predicted Axial Differential Pressures in Downcomer, UPTF Test 6 – Run 136



a,c

**Figure 19.3-99 Measured Azimuthal Differential Pressures in Downcomer at Level 06,
UPTF Test 6 – Run 136**

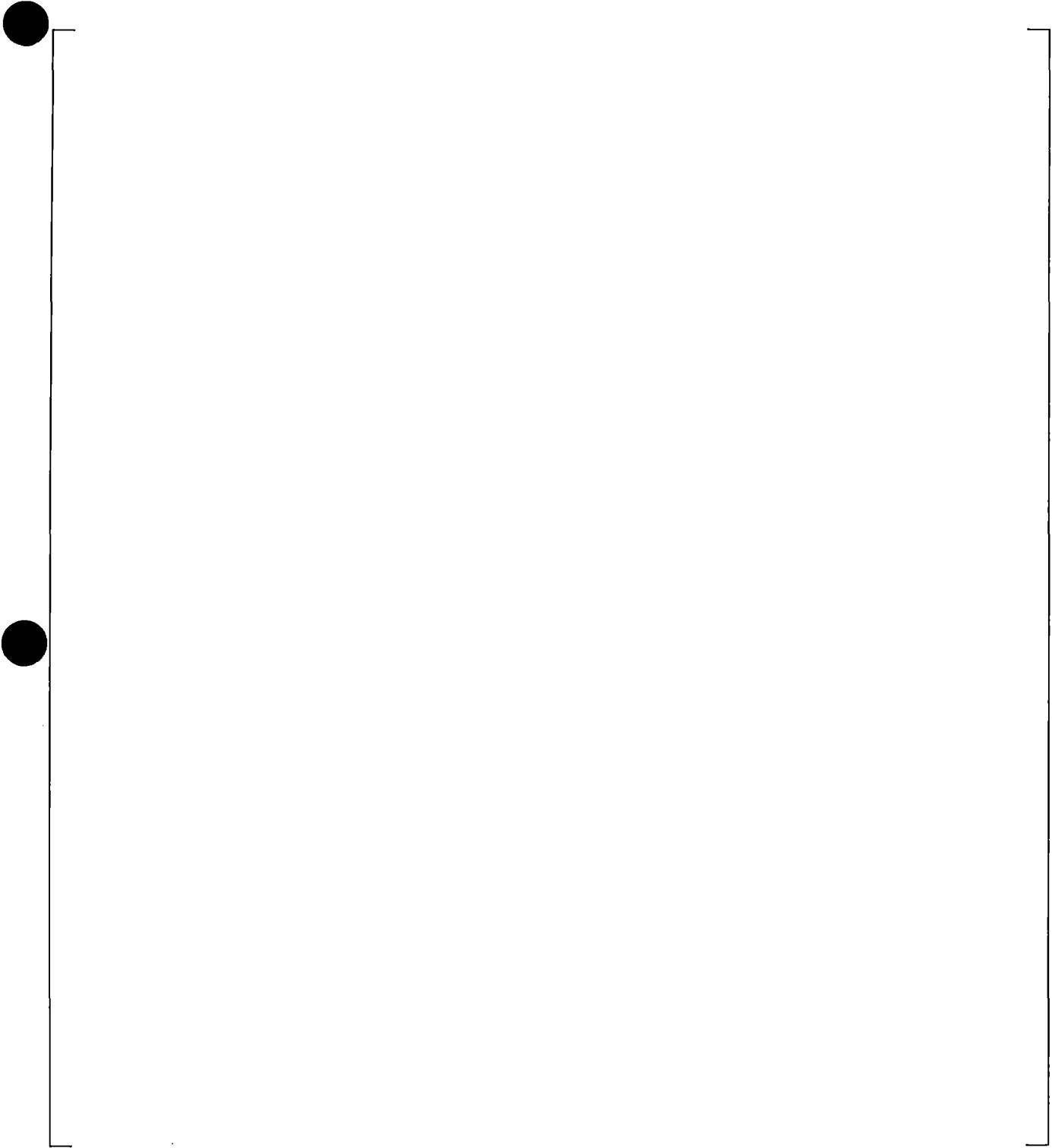
**Figure 19.3-100 Predicted Azimuthal Differential Pressures in Downcomer at Level 06,
UPTF Test 6 – Run 136**



**Figure 19.3-101 Measured Azimuthal Differential Pressures in Downcomer at Level 22,
UPTF Test 6 – Run 136**



**Figure 19.3-102 Predicted Azimuthal Differential Pressures in Downcomer at Level 22,
UPTF Test 6 – Run 136**



a,c

Figure 19.3-103 Comparison on Differential Pressure in Lower Plenum, UPTF Test 6 – Run 136

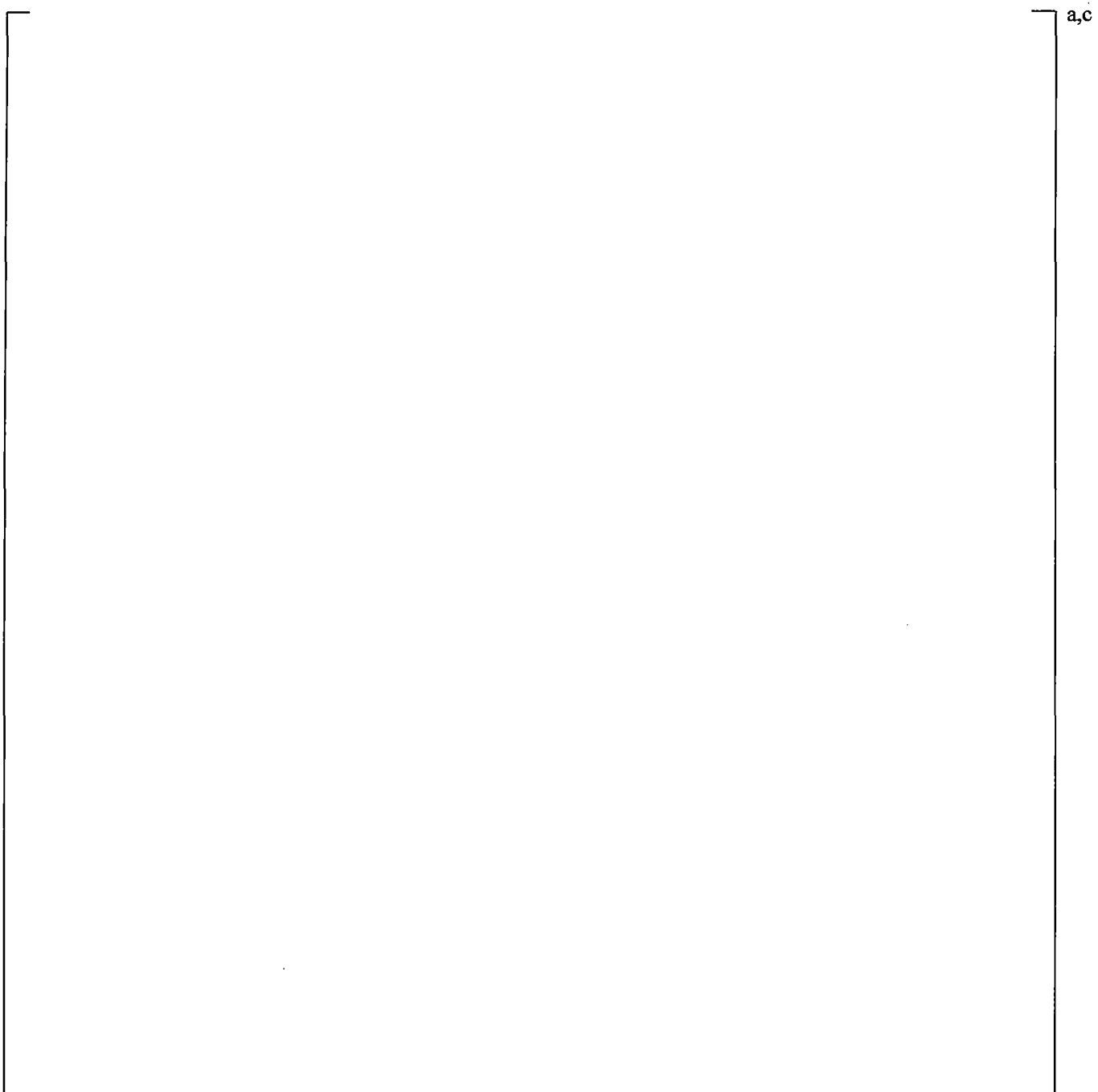


Figure 19.3-104 Lower Plenum Fluid Inventory, UPTF Test 6 – Run 131

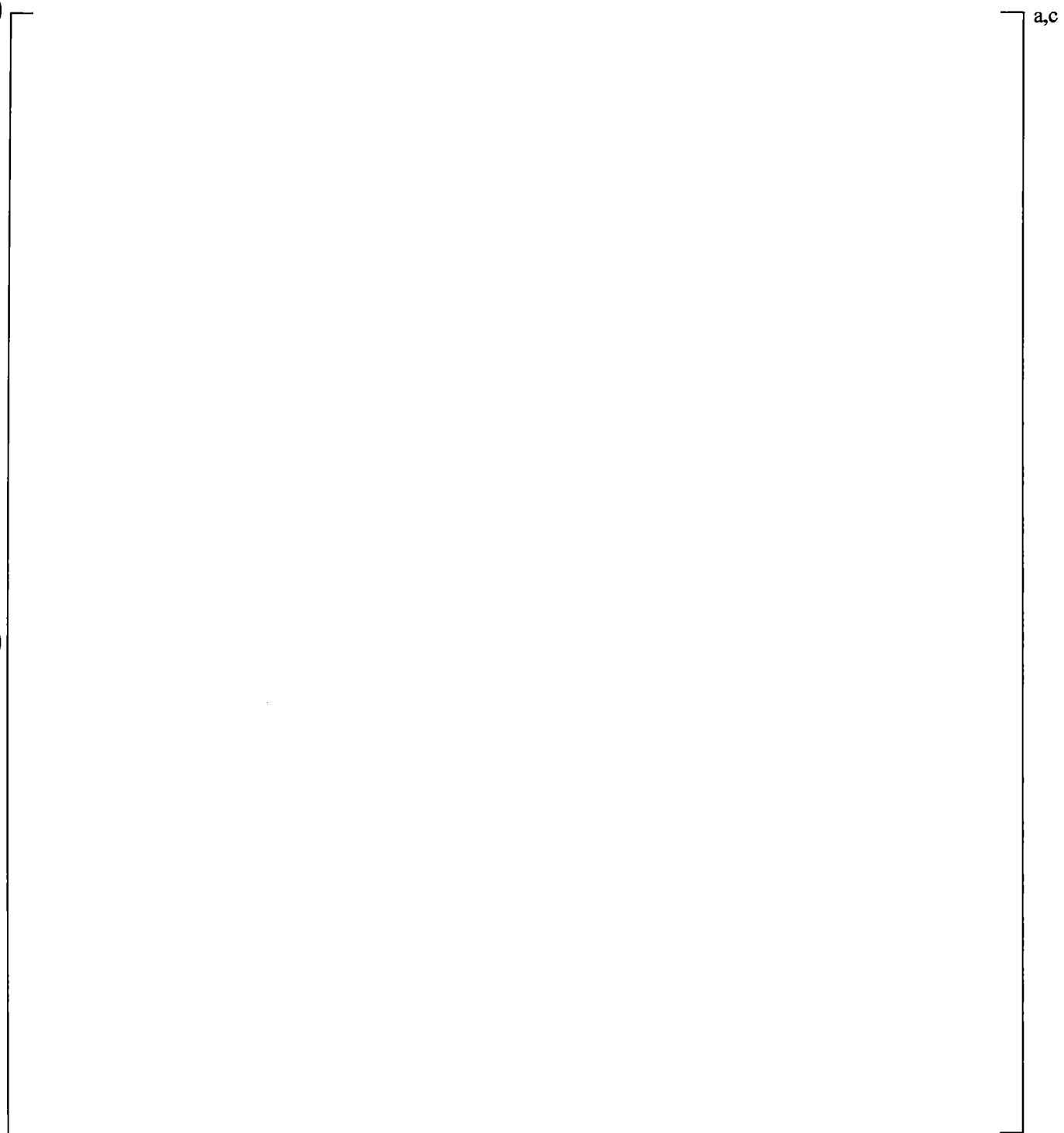


Figure 19.3-105 Lower Plenum Fluid Inventory, UPTF Test 6 – Run 132

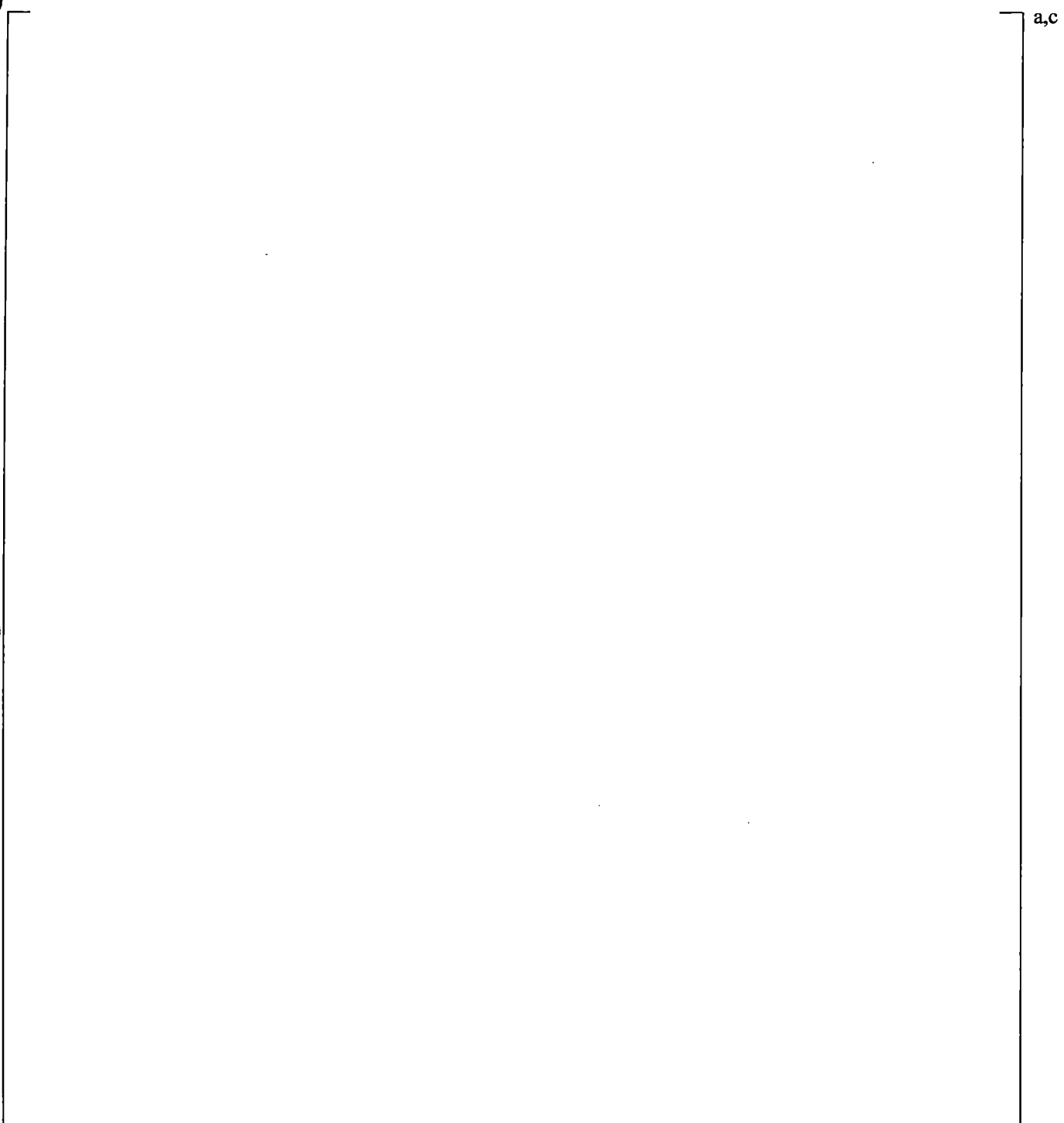


Figure 19.3-106 Lower Plenum Fluid Inventory, UPTF Test 6 – Run 133

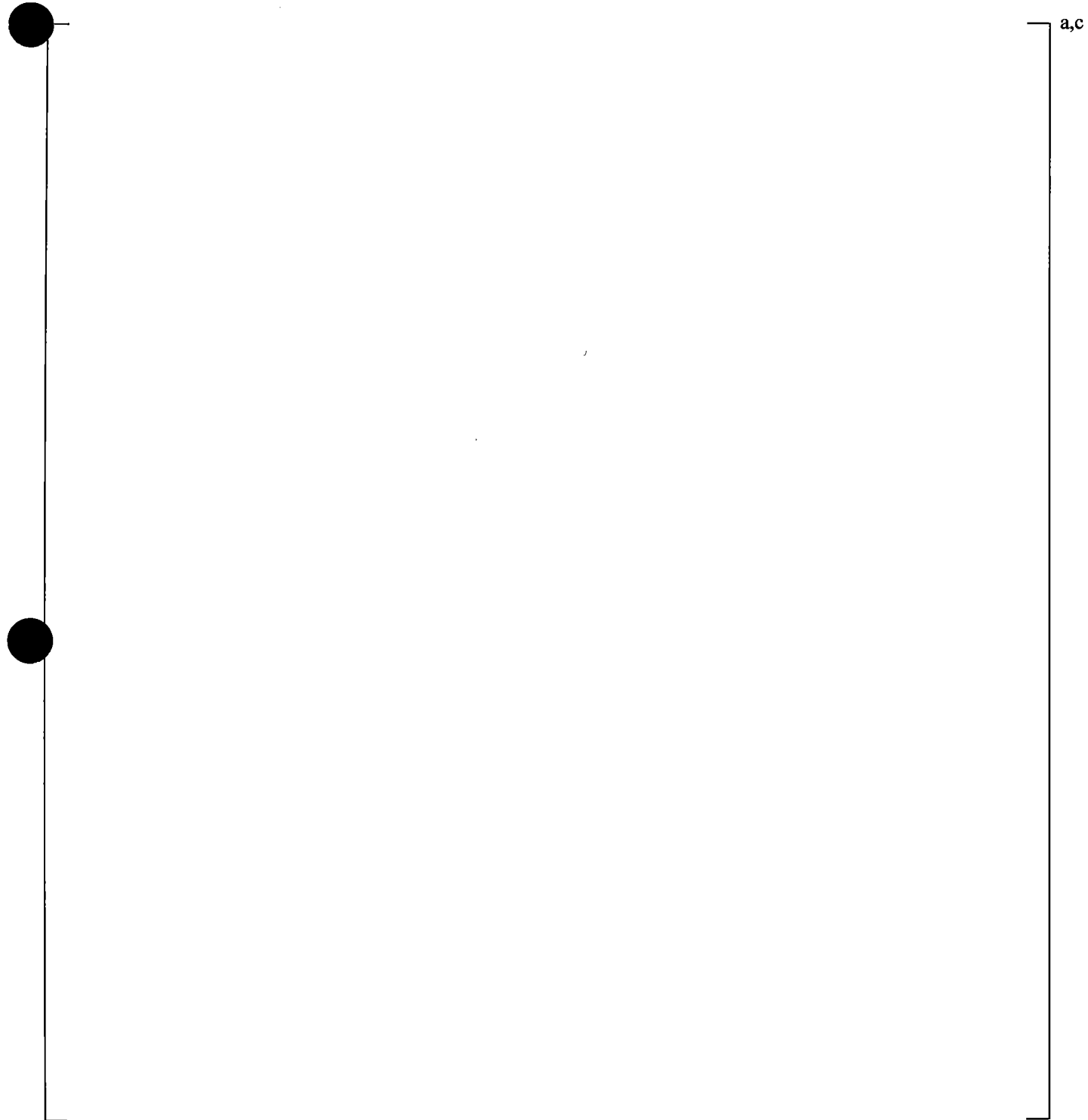


Figure 19.3-107 Lower Plenum Fluid Inventory, UPTF Test 6 – Run 135

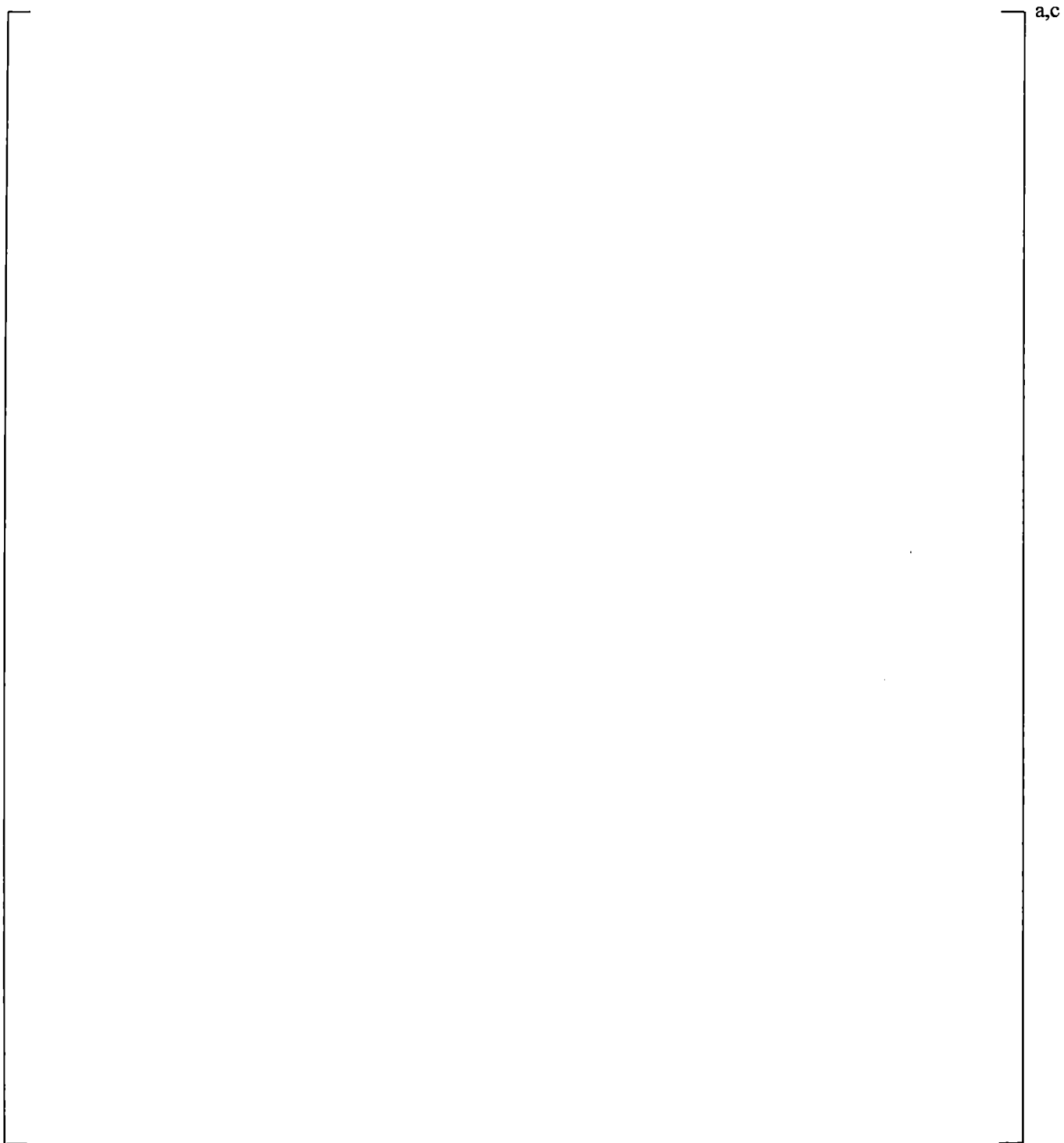


Figure 19.3-108 Lower Plenum Fluid Inventory, UPTF Test 6 – Run 136

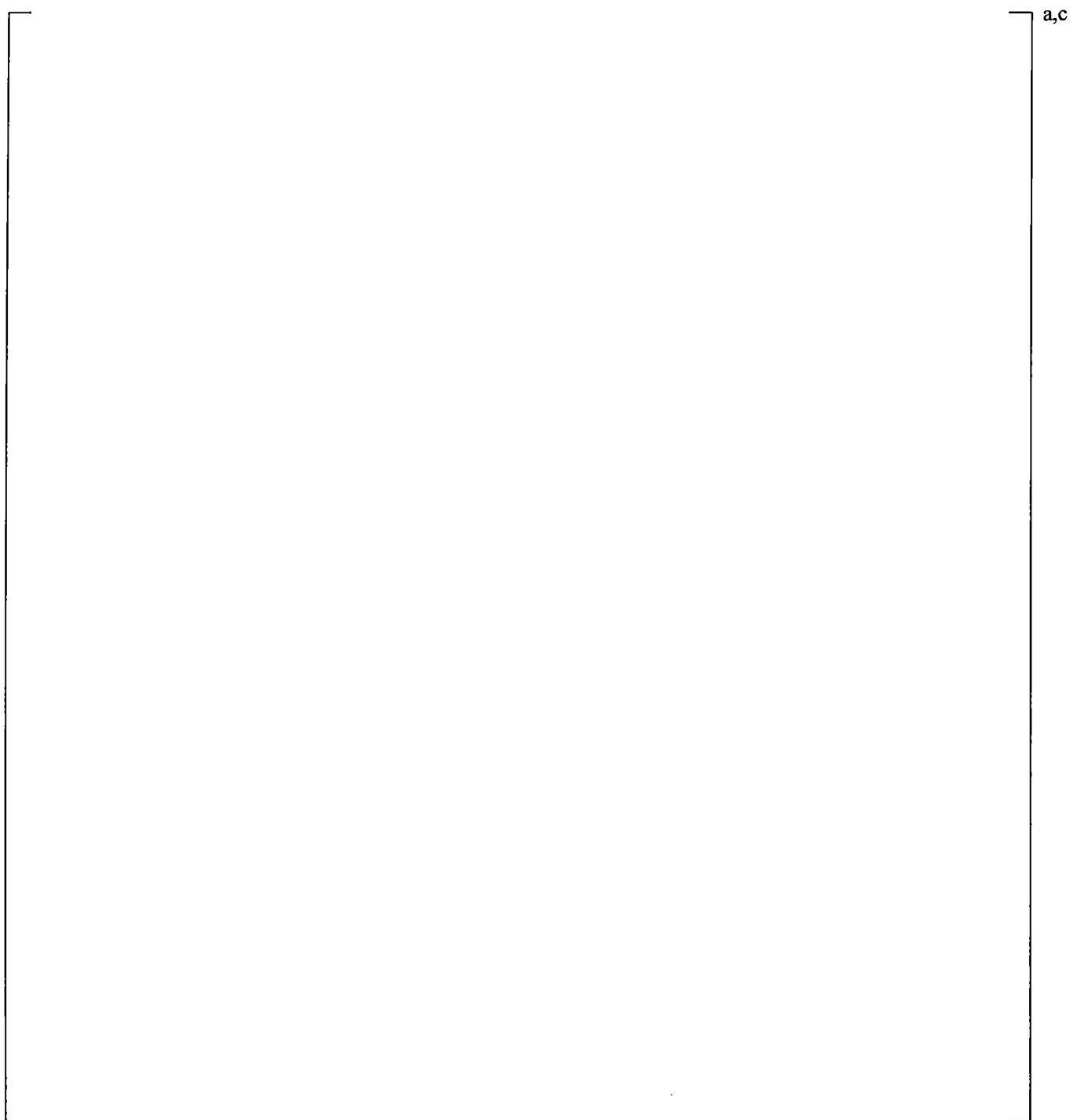


Figure 19.3-109 Comparison between Measured and Predicted Penetration Rates in UPTF Test 6

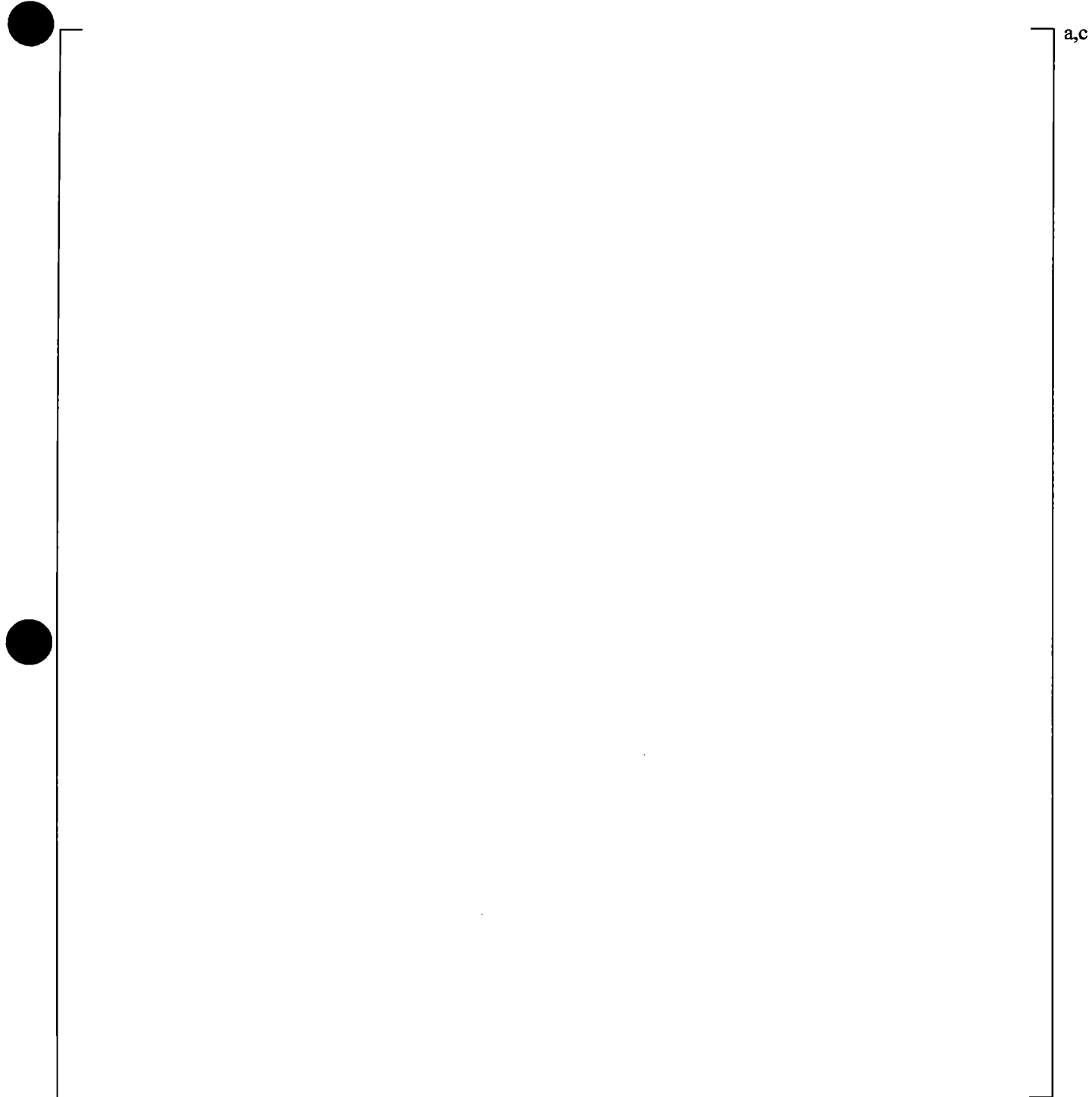


Figure 19.3-110 Comparison between Measured and Predicted Refill Periods versus Nominal Steam Flow Rate for Lower Plenum in UPTF Test 6

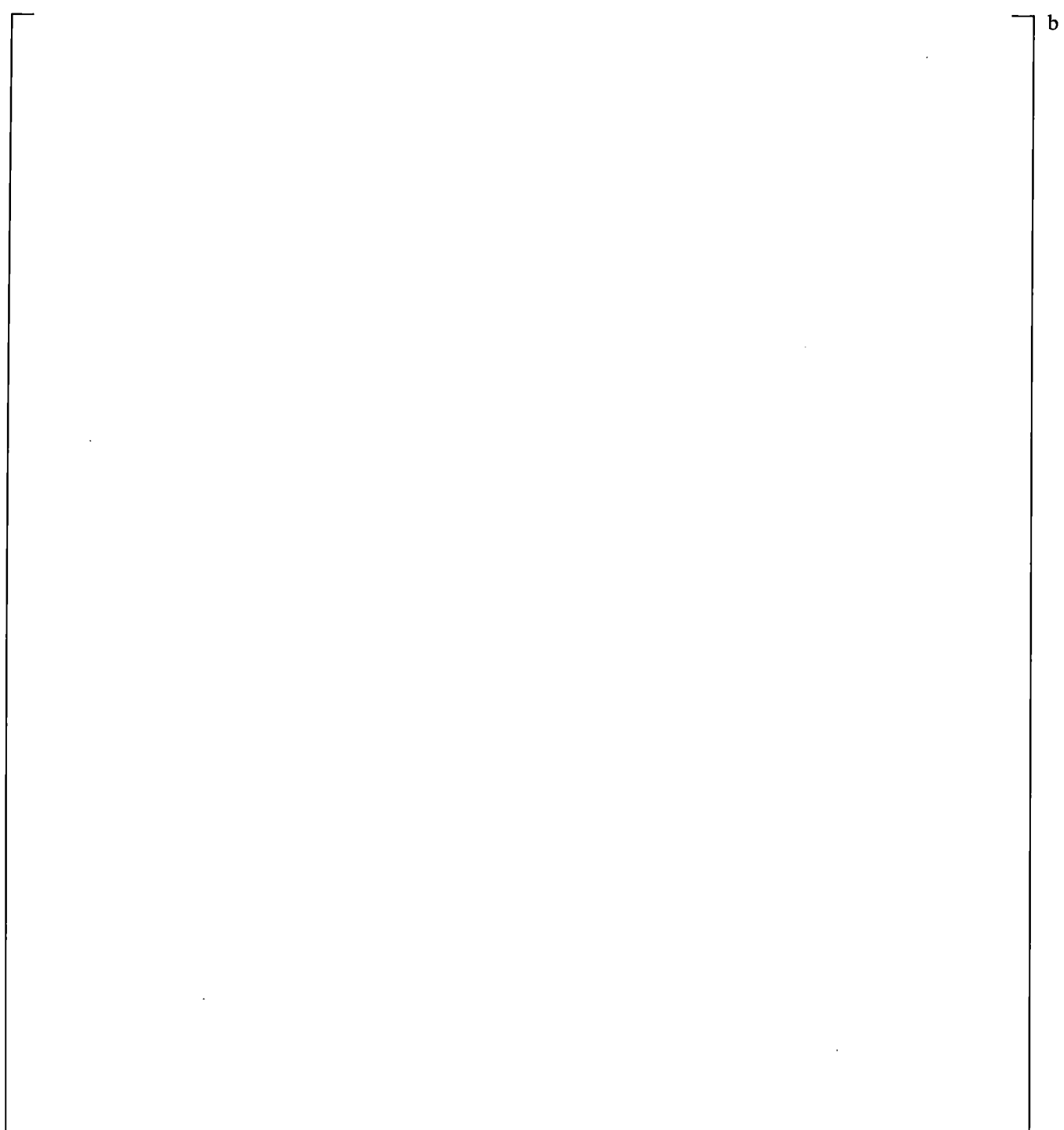


Figure 19.3-111 Downcomer CCFL Behavior for UPTF Test 6



Figure 19.3-112 Estimated Mass Distribution, UPTF Test 6 – Run 131



Figure 19.3-113 Predicted Mass Distribution, UPTF Test 6 – Run 131



Figure 19.3-114 Estimated Mass Distribution, UPTF Test 6 – Run 132



Figure 19.3-115 Predicted Mass Distribution, UPTF Test 6 – Run 132



Figure 19.3-116 Estimated Mass Distribution, UPTF Test 6 – Run 133



Figure 19.3-117 Predicted Mass Distribution, UPTF Test 6 – Run 133

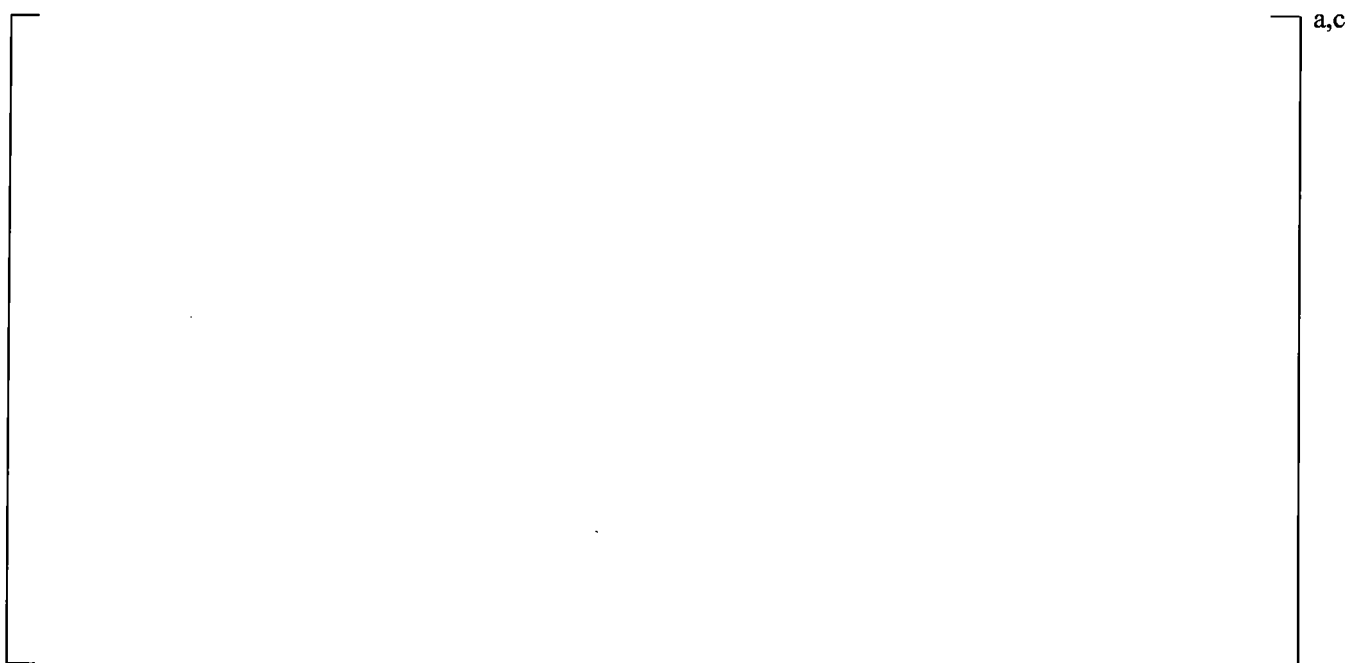


Figure 19.3-118 Estimated Mass Distribution, UPTF Test 6 – Run 135



Figure 19.3-119 Predicted Mass Distribution, UPTF Test 6 – Run 135



Figure 19.3-120 Estimated Mass Distribution, UPTF Test 6 – Run 136



Figure 19.3-121 Predicted Mass Distribution, UPTF Test 6 – Run 136

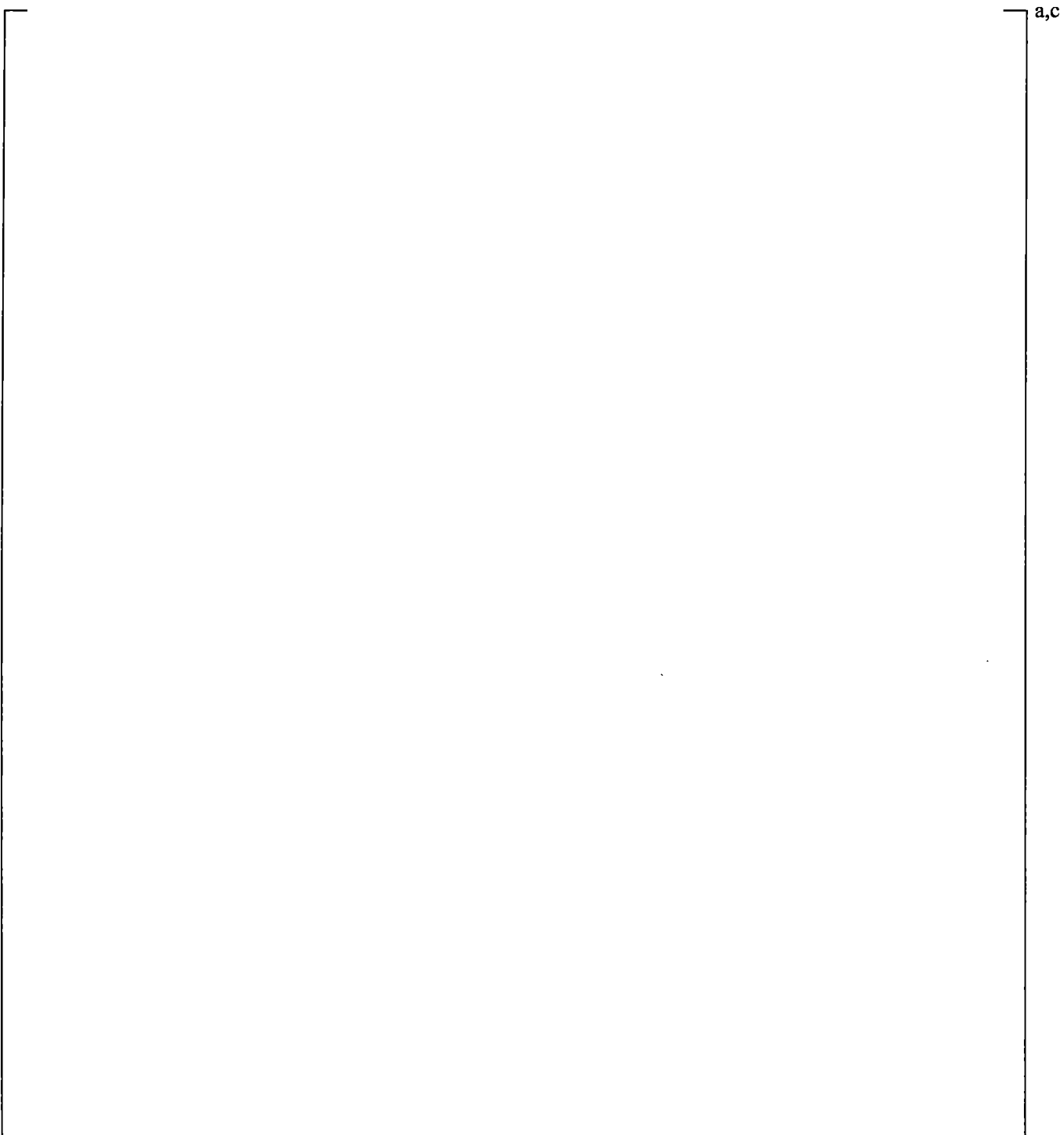


Figure 19.3-122 Vessel Condensation Efficiency, UPTF Test 6 – Run 131

a,c

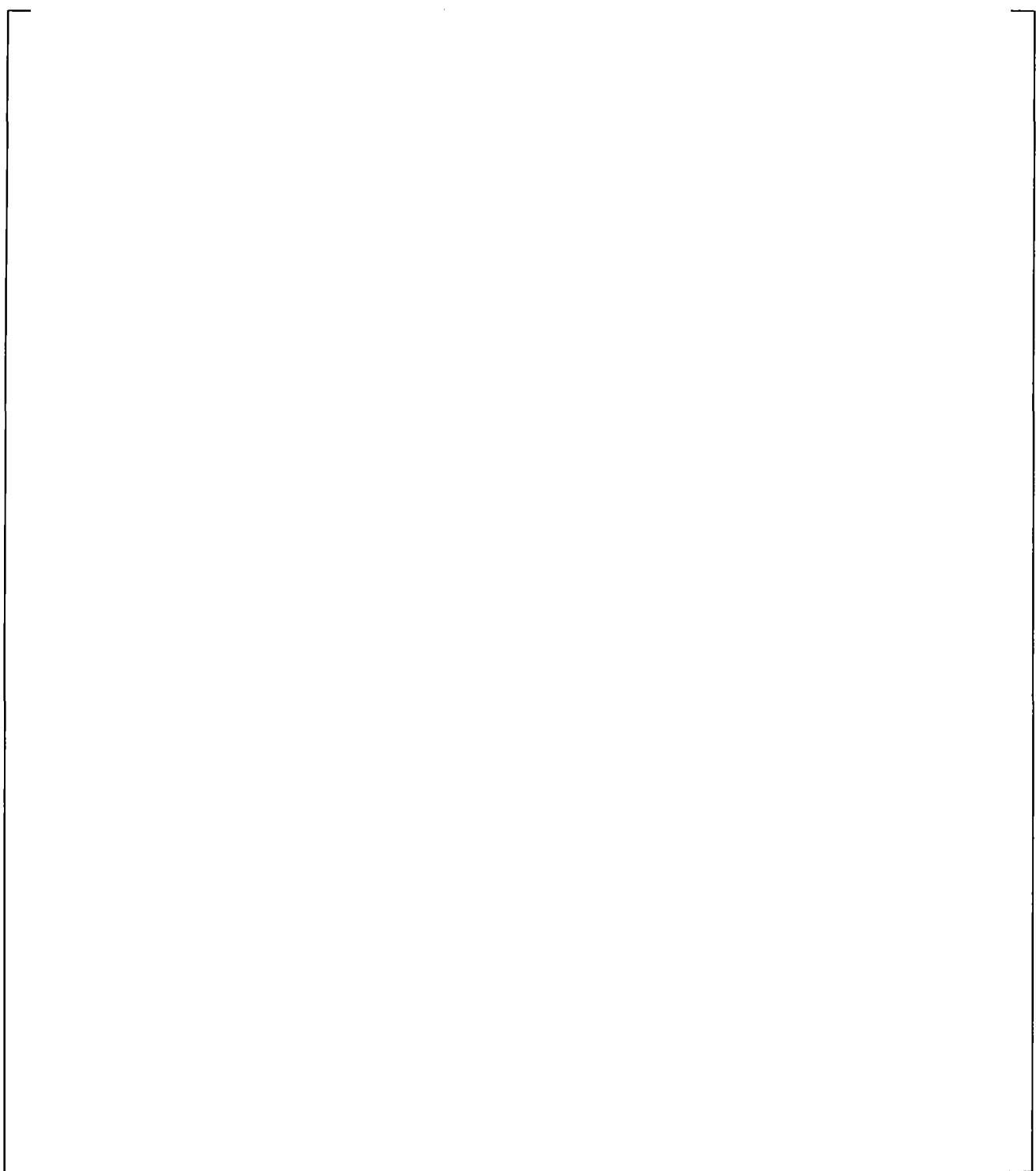
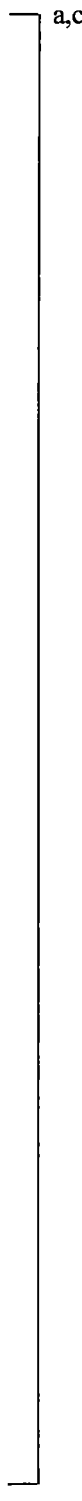


Figure 19.3-123 Vessel Condensation Efficiency, UPTF Test 6 – Run 132



a,c

Figure 19.3-124 Vessel Condensation Efficiency, UPTF Test 6 – Run 133

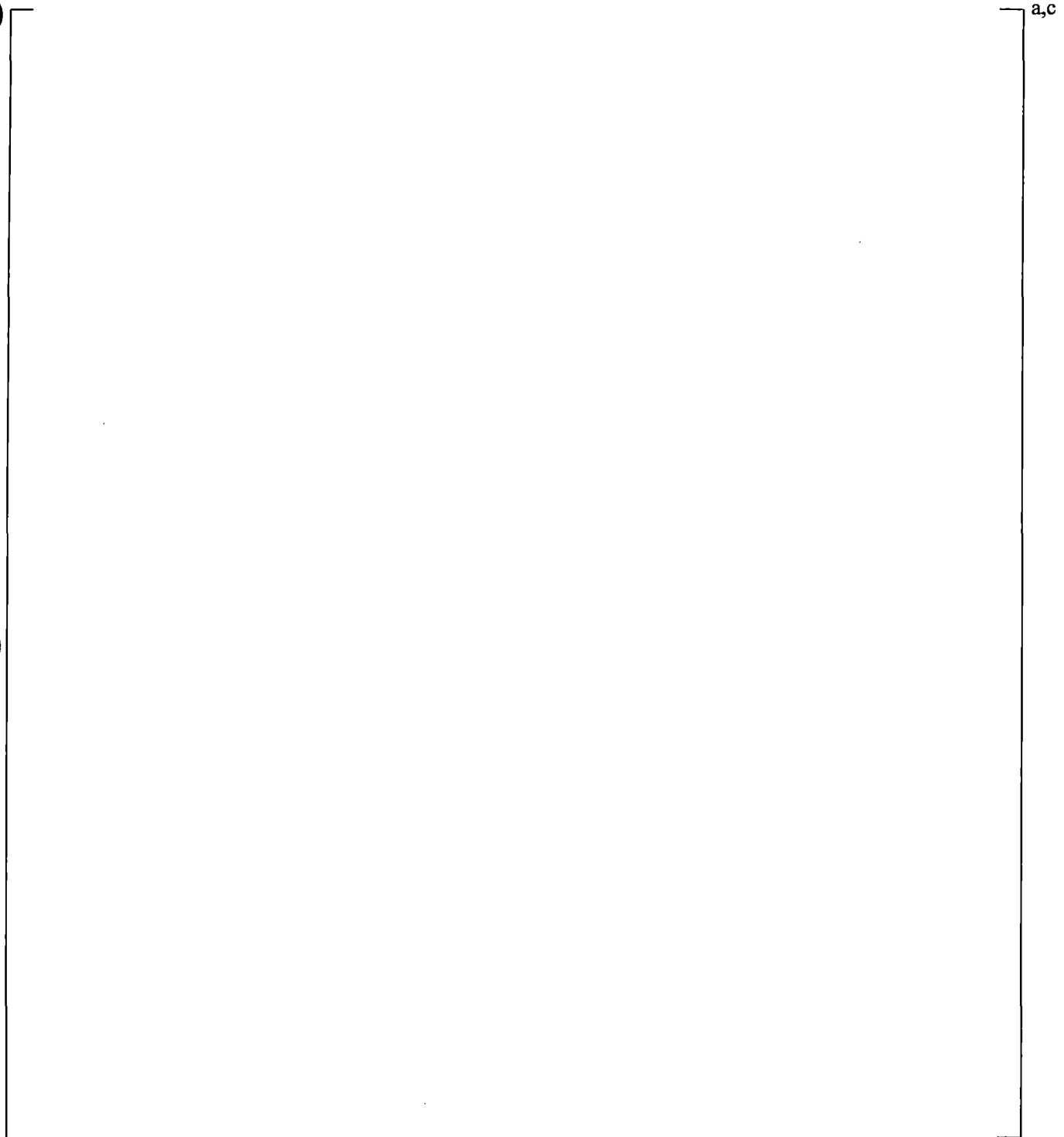


Figure 19.3-125 Vessel Condensation Efficiency, UPTF Test 6 – Run 135

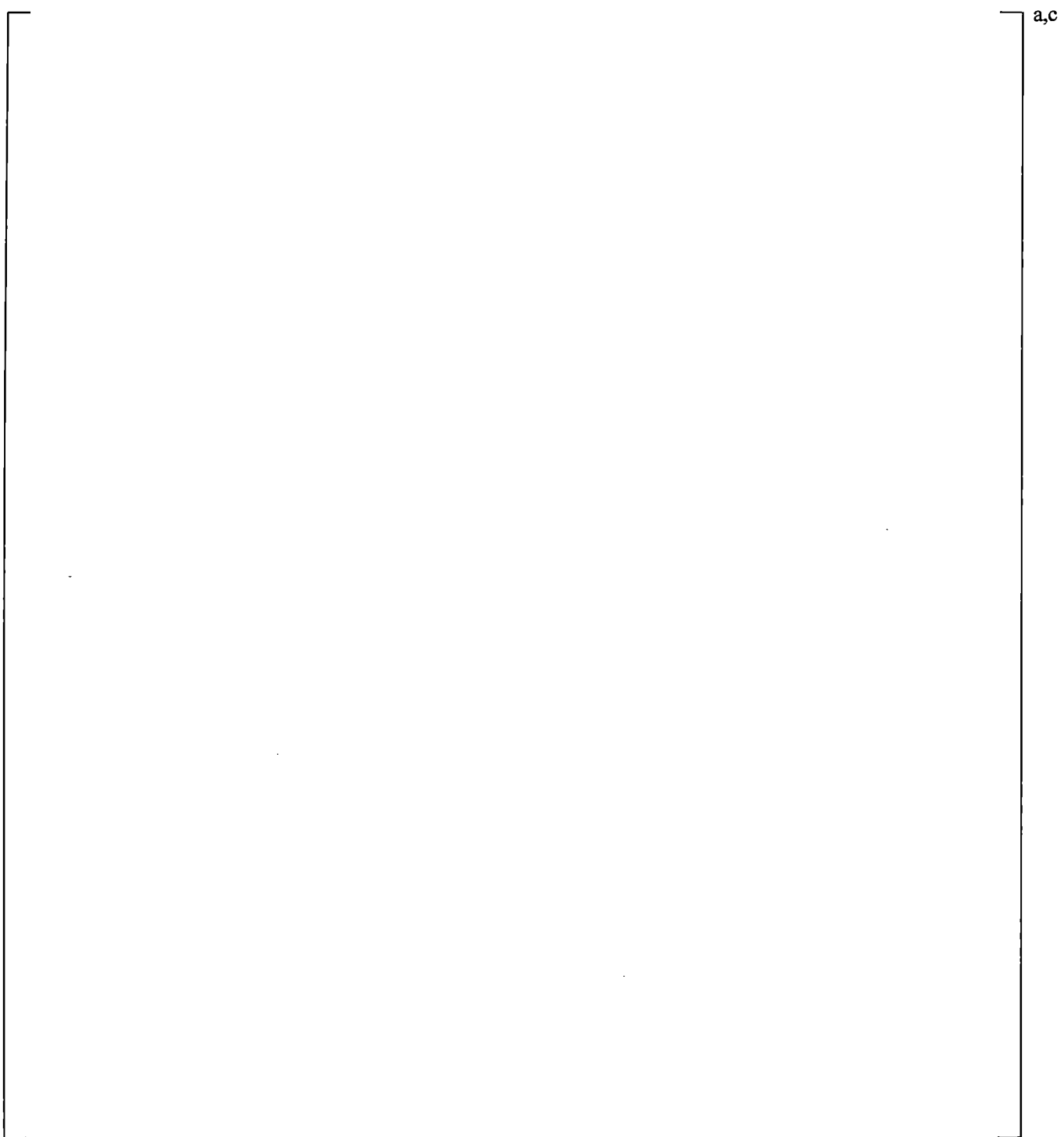
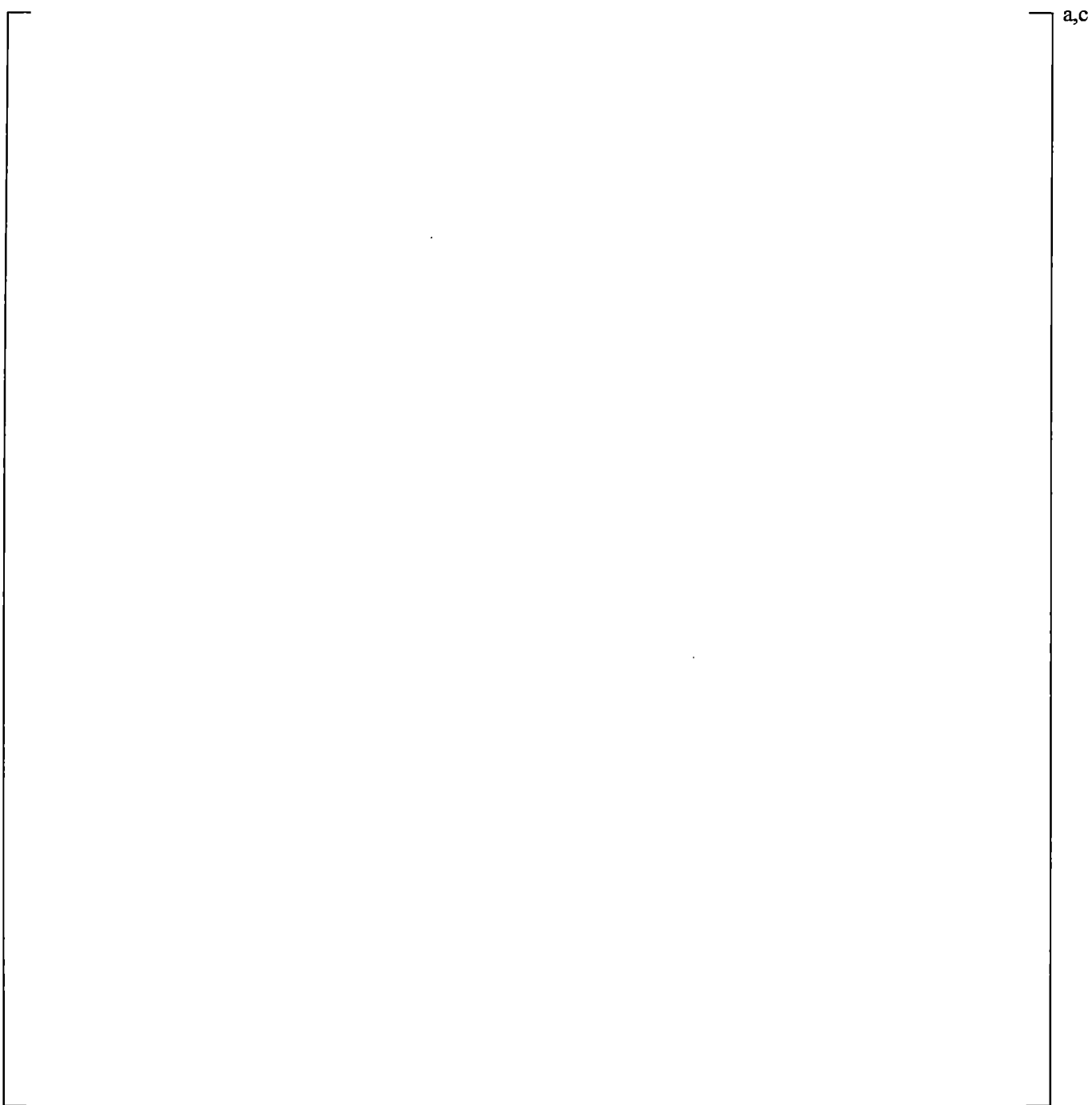


Figure 19.3-126 Vessel Condensation Efficiency, UPTF Test 6 – Run 136



**Figure 19.3-127 Comparison of Vessel Condensation Efficiency versus Nominal Steam Flow Rate,
UPTF Test 6; Experimental Condensation Efficiency is Estimated by MPR
(MPR-1163, 1990a); Predicted Condensation Efficiency is Evaluated Using Steam
Flow Rate at Break**

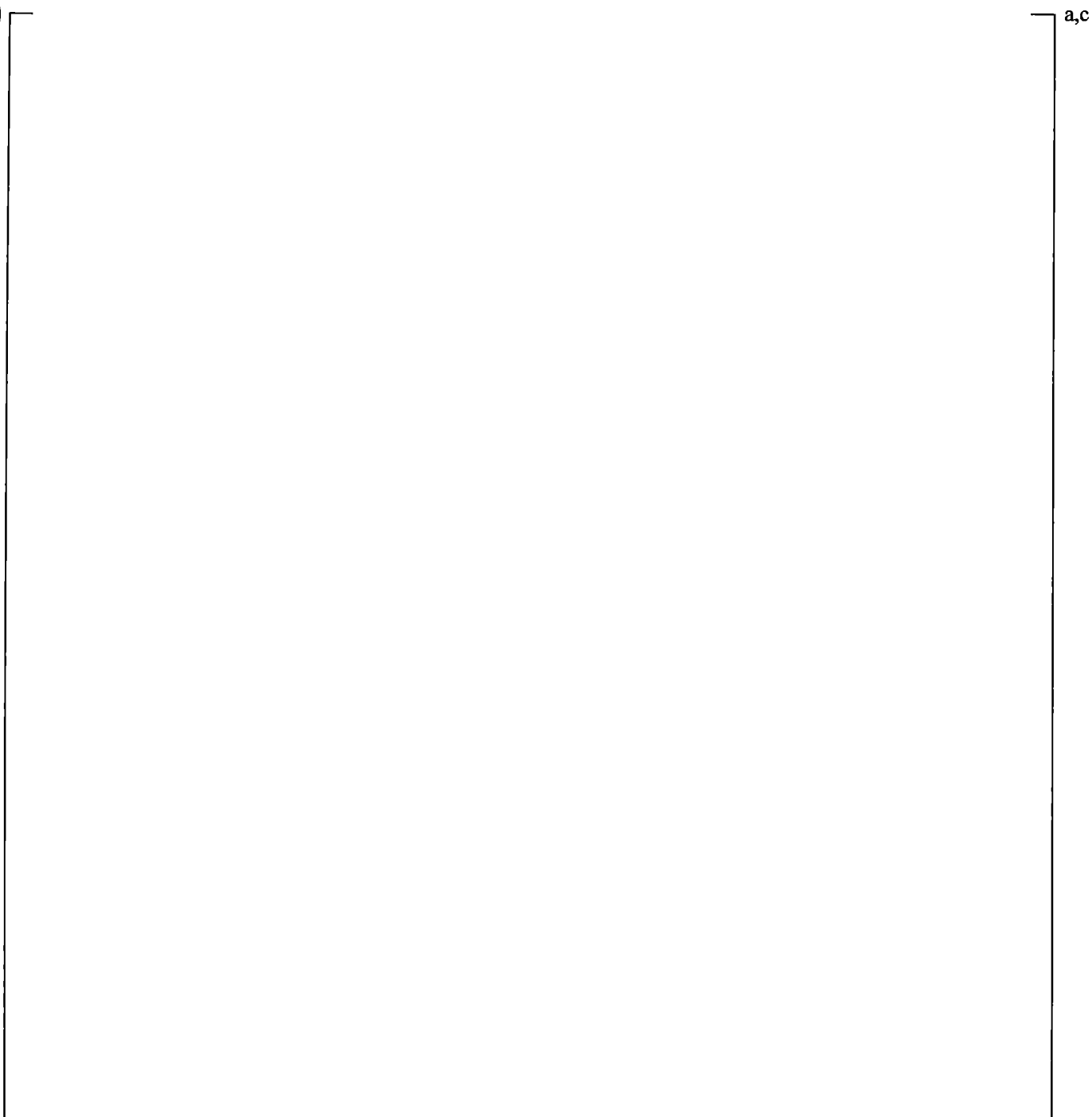


Figure 19.3-128 Comparison of Vessel Condensation Efficiency versus Nominal Steam Flow Rate with Various DC Condensation Multipliers, UPTF Test 6; Predicted Condensation Efficiency is Evaluated Using Steam Flow Rate at Inlet of Broken Cold Leg

a,c

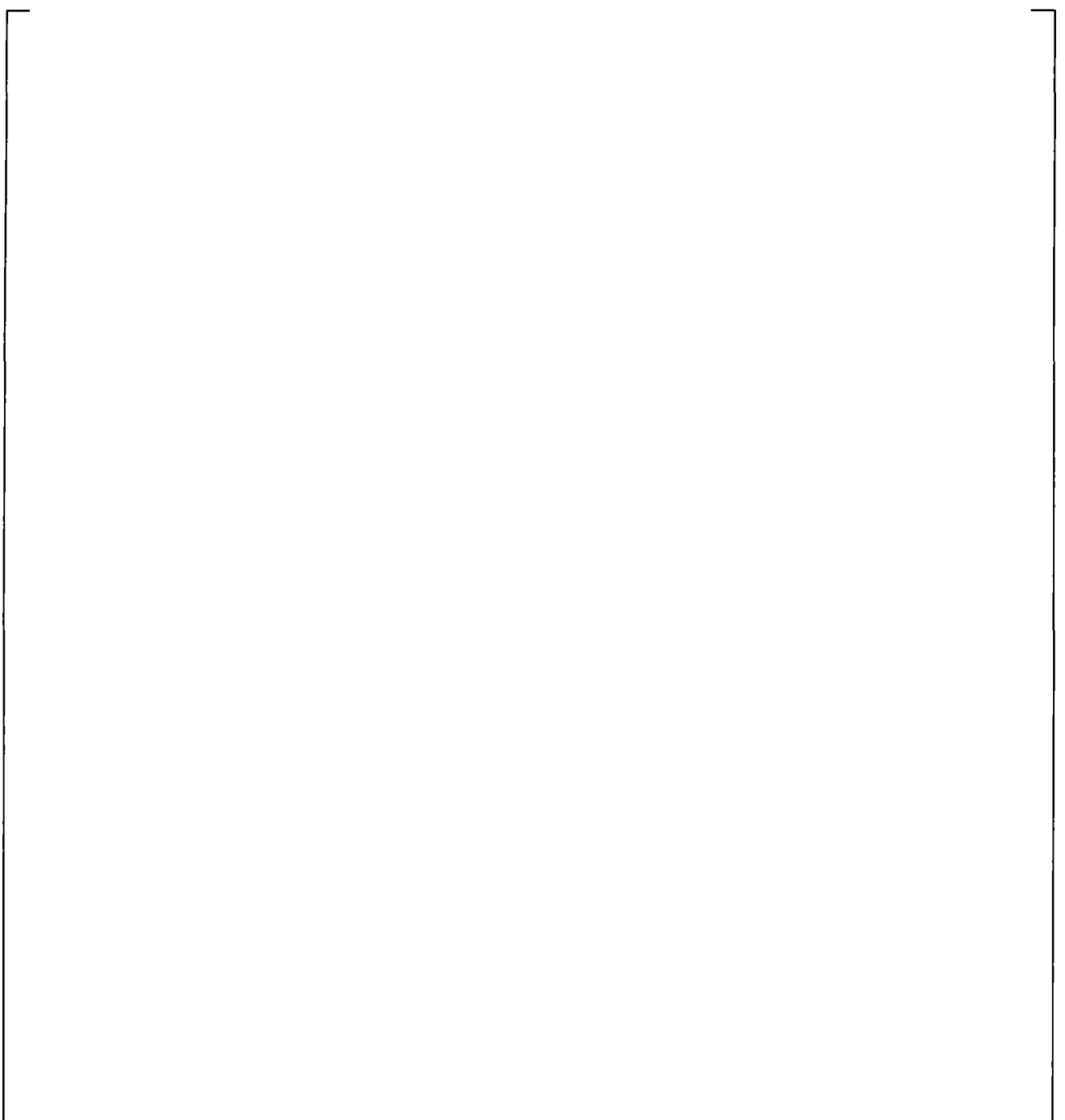


Figure 19.3-129 Comparison of Filling Period from Start of ECC Injection to End of Lower Plenum Filling with Various DC Condensation Multipliers versus Nominal Steam Flow Rate, UPTF Test 6. Note, Run 132 did not Fill the Lower Plenum at the End of the Calculation.

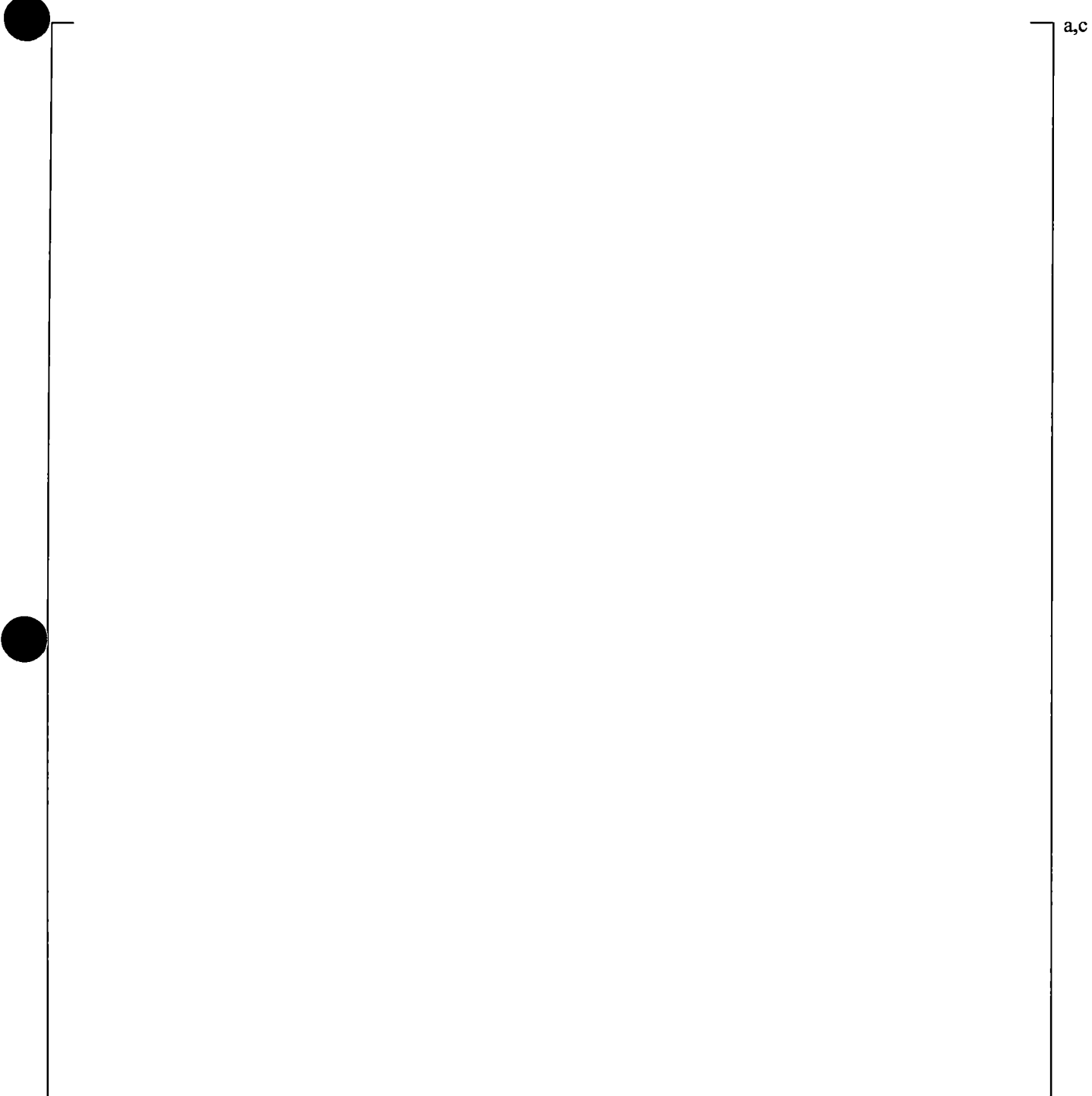
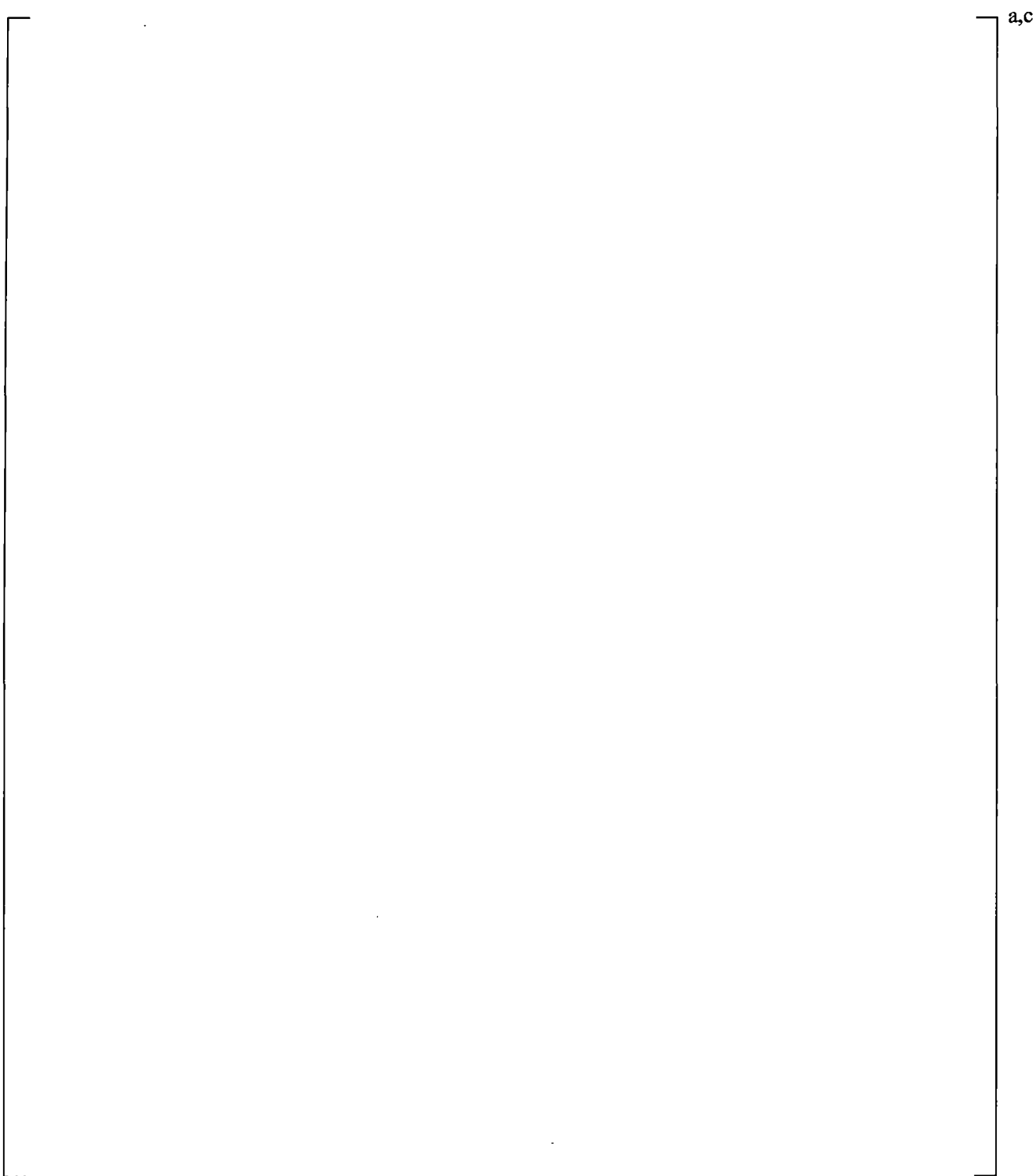


Figure 19.3-130 Comparison of Length of Refill Period from Start of ECC Injection to End of Lower Plenum Filling versus Nominal Steam Flow Rate with Various DTMAX, UPTF Test 6



**Figure 19.3-131 Location of Fluid Thermocouples, Differential and Absolute Pressure
Measurements in Broken Cold Leg of Loop 04**

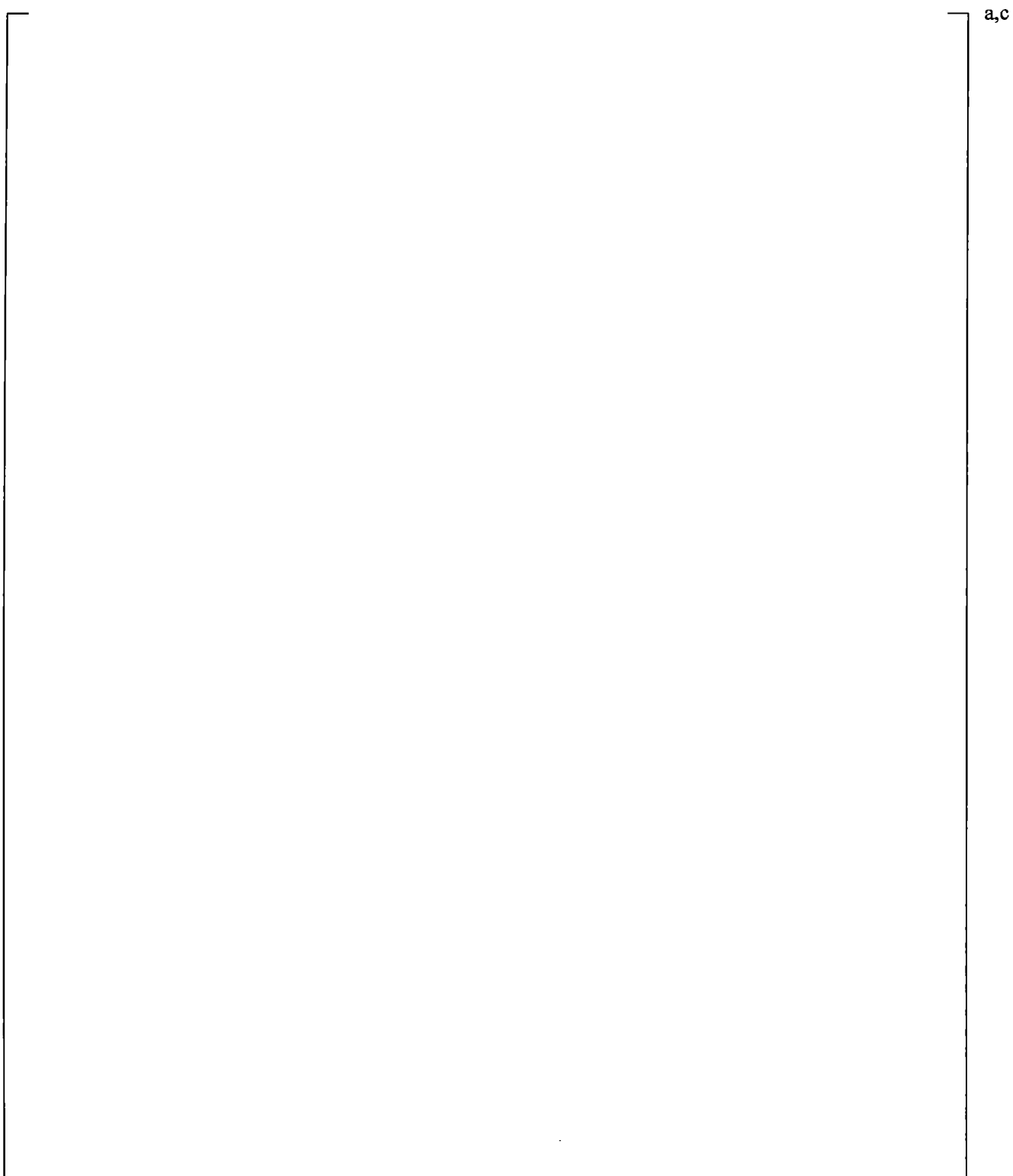


Figure 19.3-132 Moody Diagram

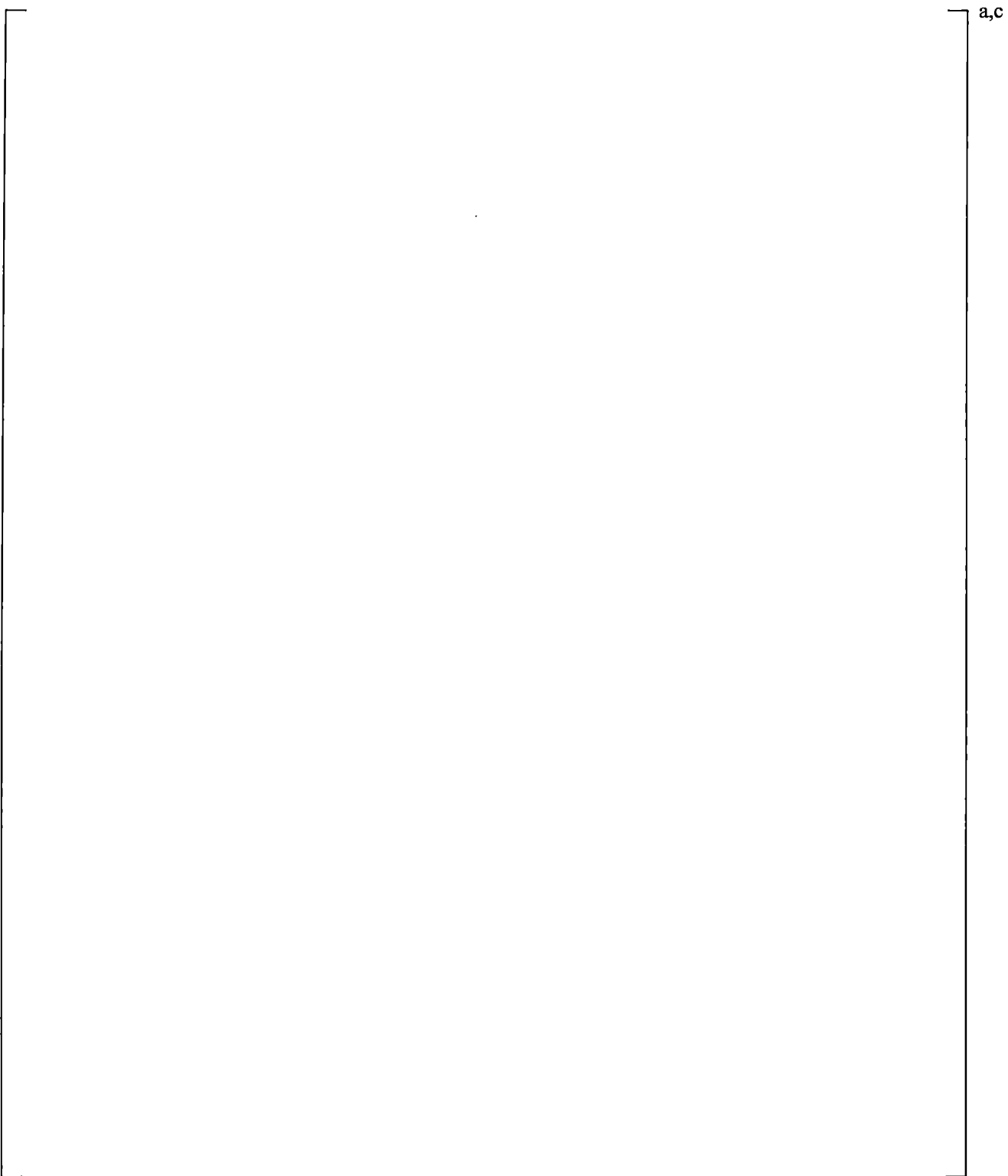


Figure 19.3-133 Cold Leg Steam Flow Rate (Top) and Downcomer Pressure (Bottom) for Test Run 131

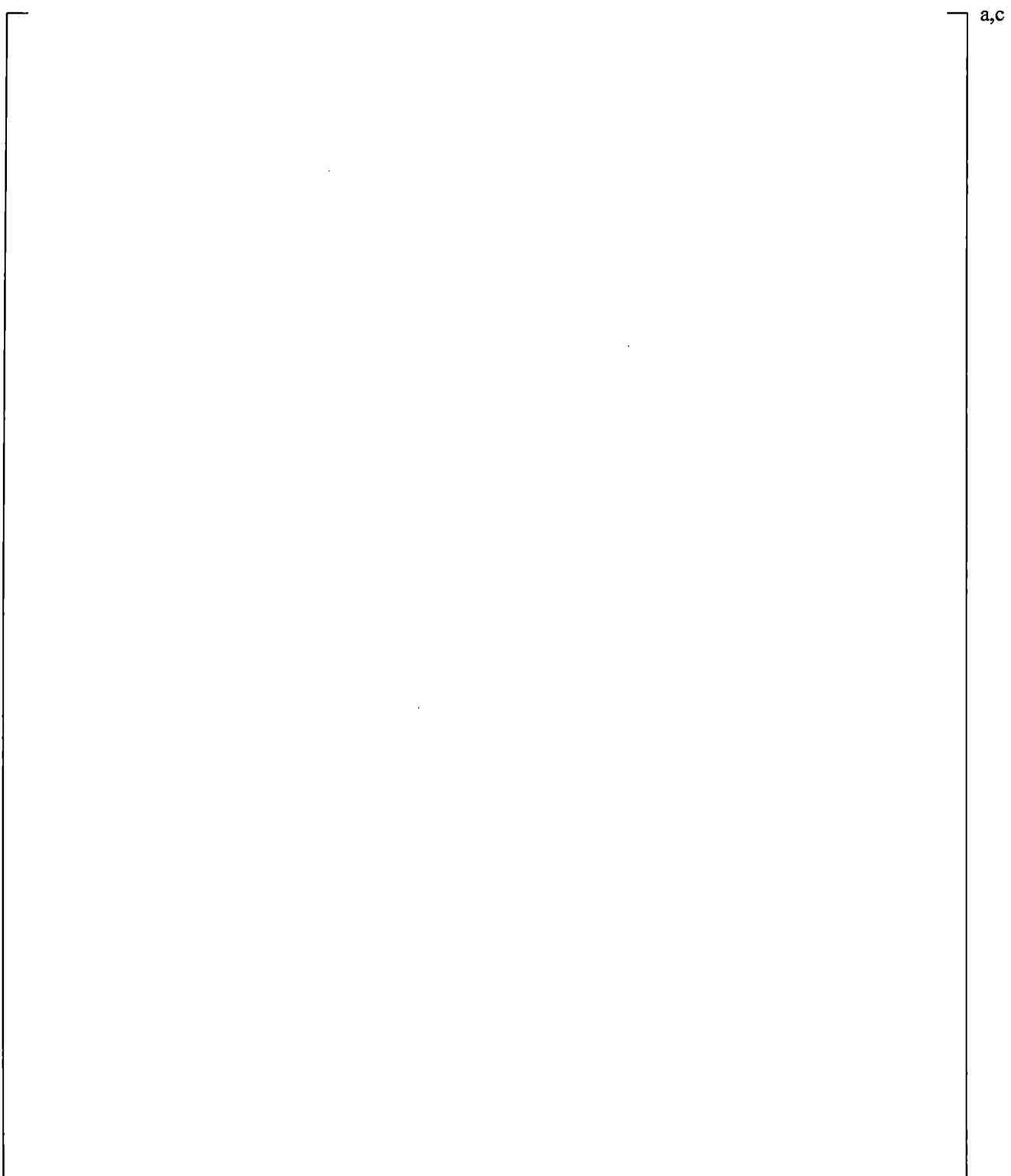


Figure 19.3-134 Cold Leg Fluid Temperature (Top) and Cold Leg to Downcomer Pressure Drop (Bottom) for Test Run 131

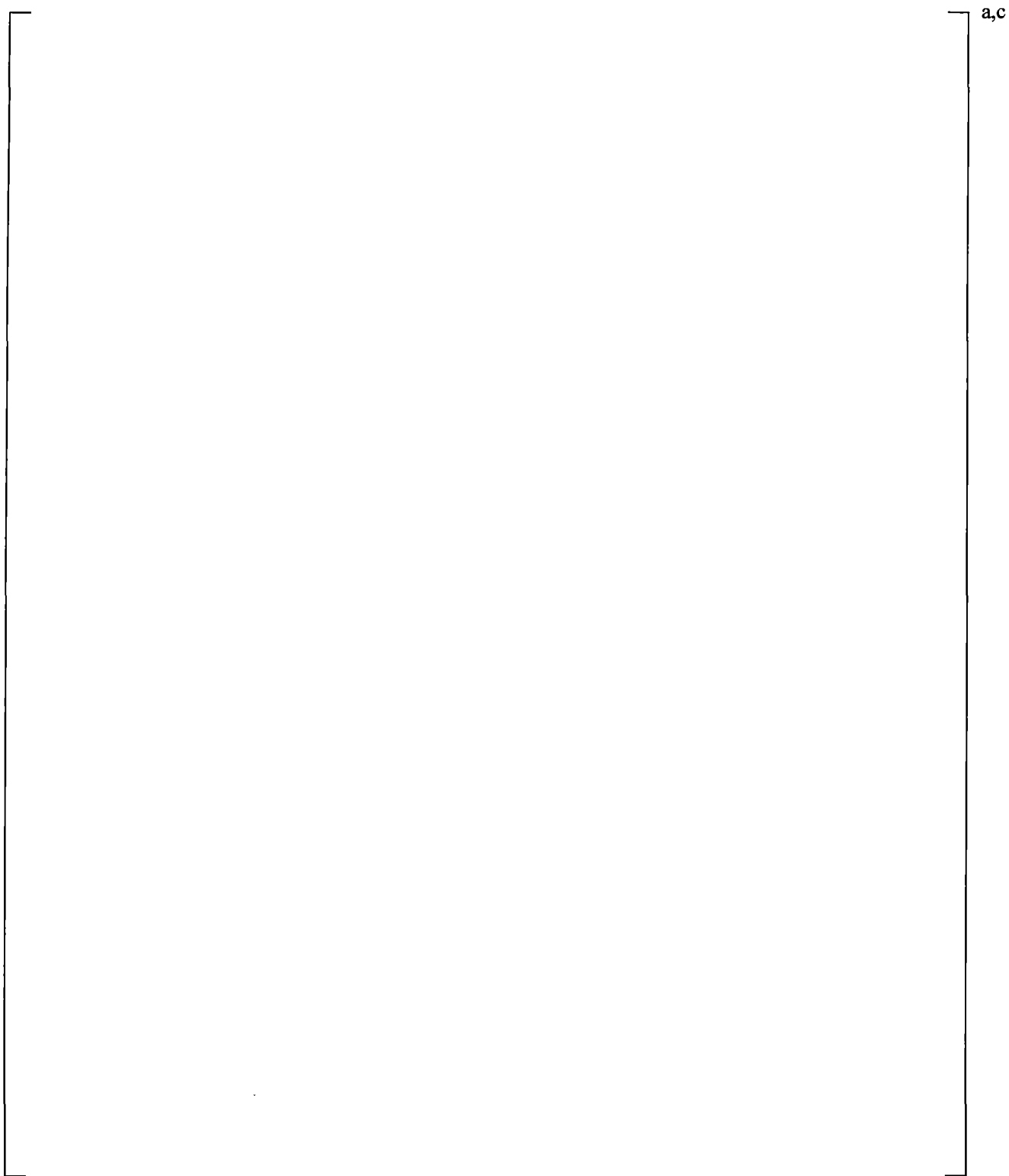


Figure 19.3-135 Cold Leg Steam Flow Rate (Top) and Downcomer Pressure (Bottom) for Test Run 132

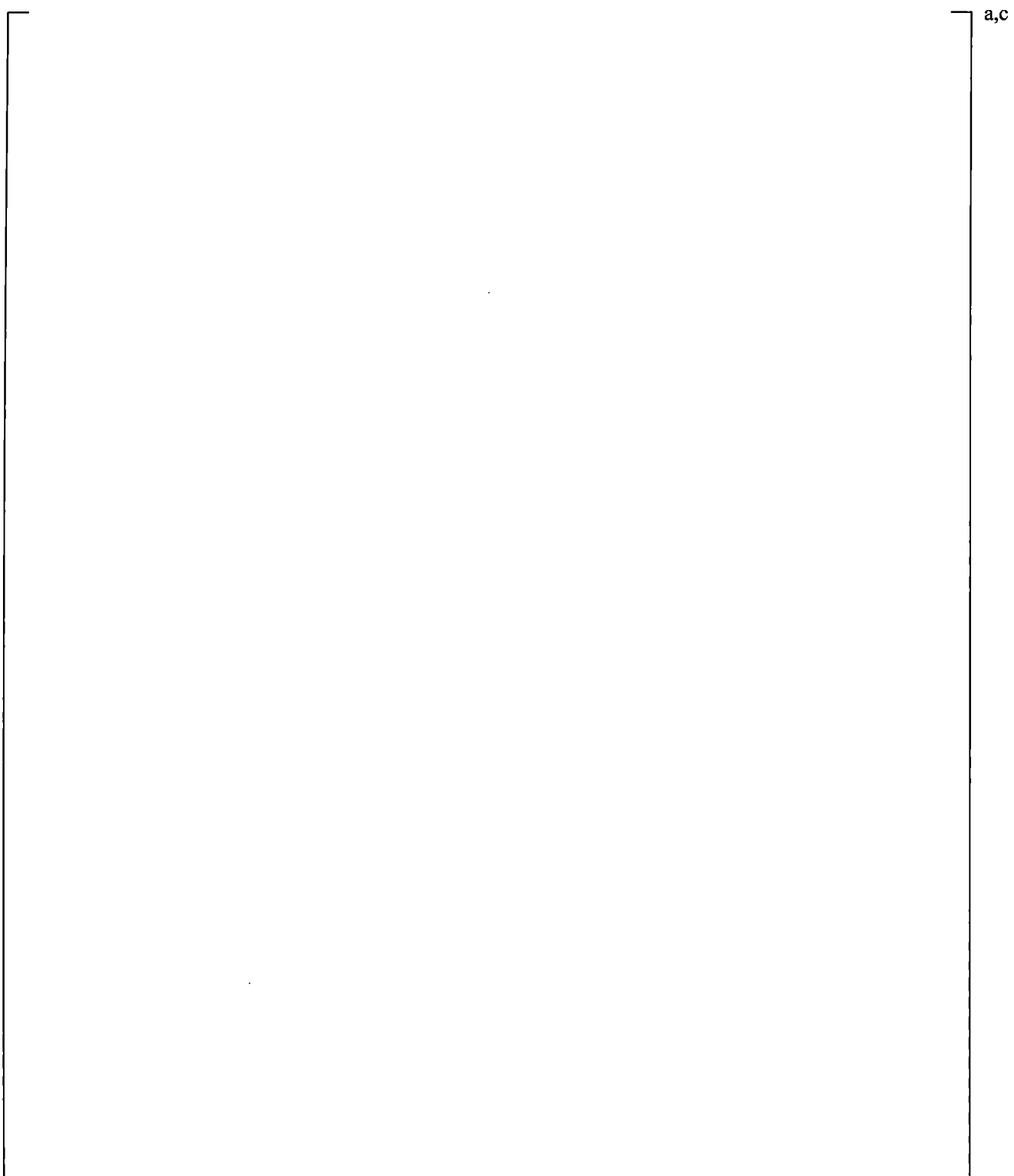


Figure 19.3-136 Cold Leg Fluid Temperature (Top) and Cold Leg to Downcomer Pressure Drop (Bottom) for Test Run 132

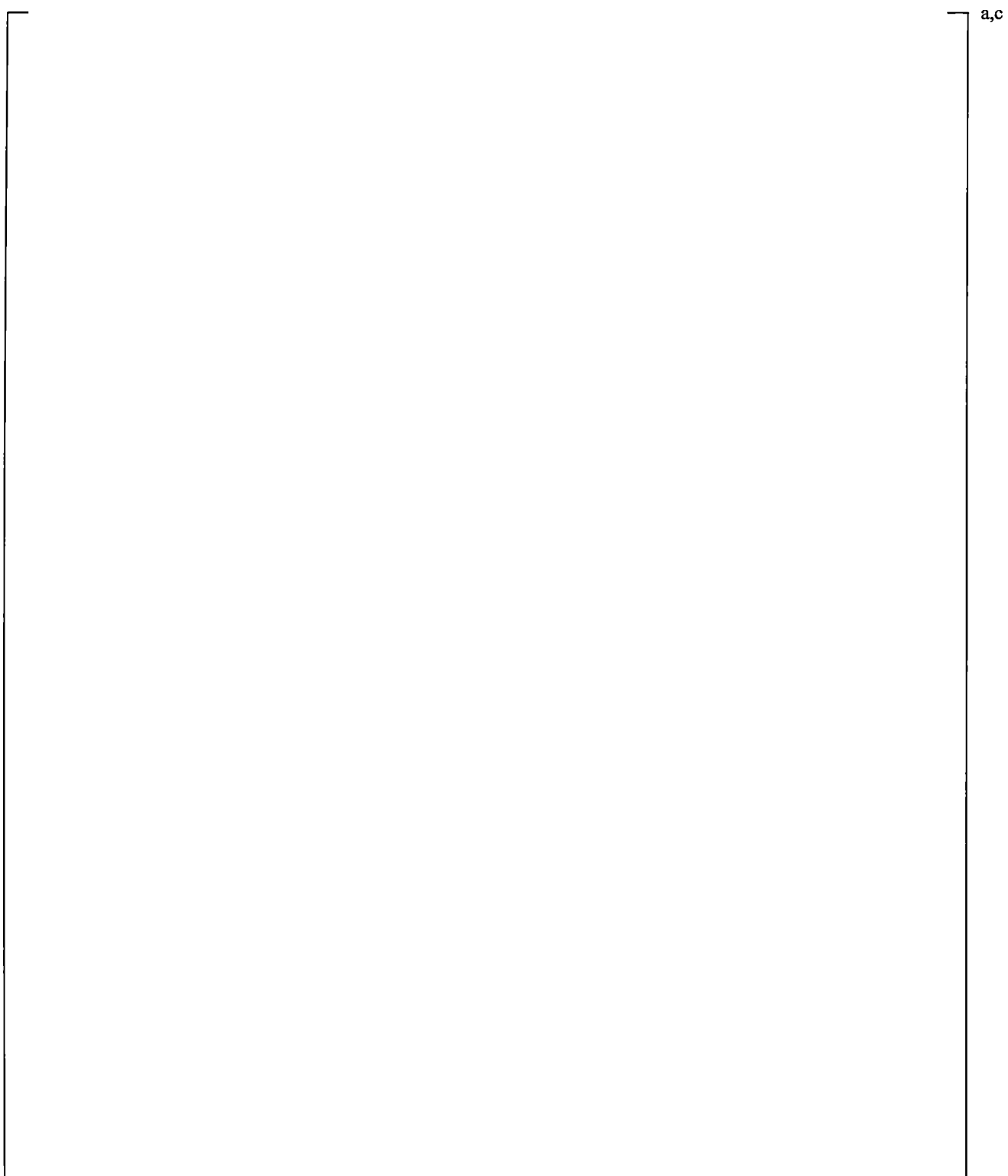


Figure 19.3-137 Cold Leg Steam Flow rate (Top) and Downcomer Pressure (Bottom) for Test Run 133

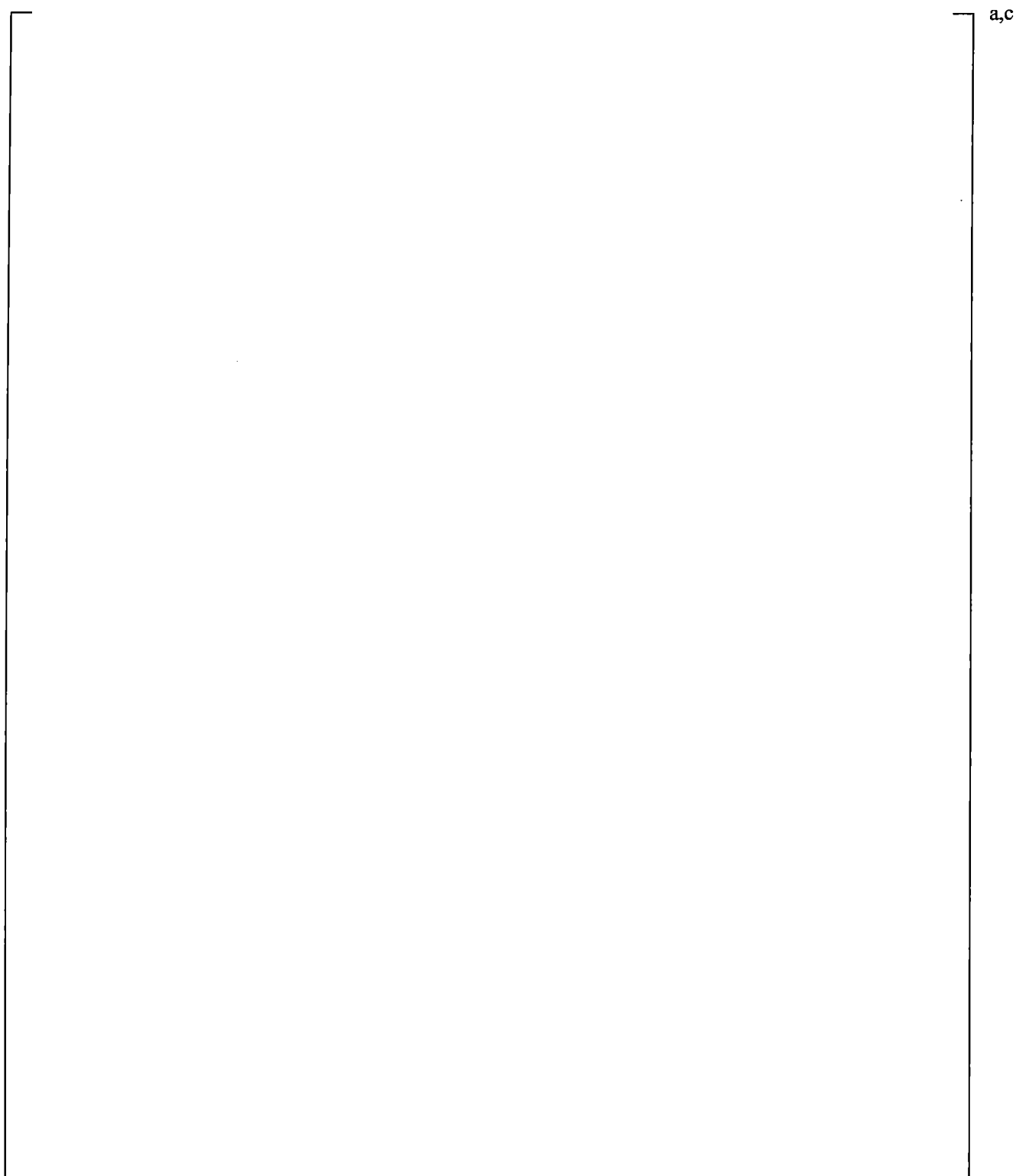


Figure 19.3-138 Cold Leg Fluid Temperature (Top) and Cold Leg to Downcomer Pressure Drop (Bottom) for Test Run 133

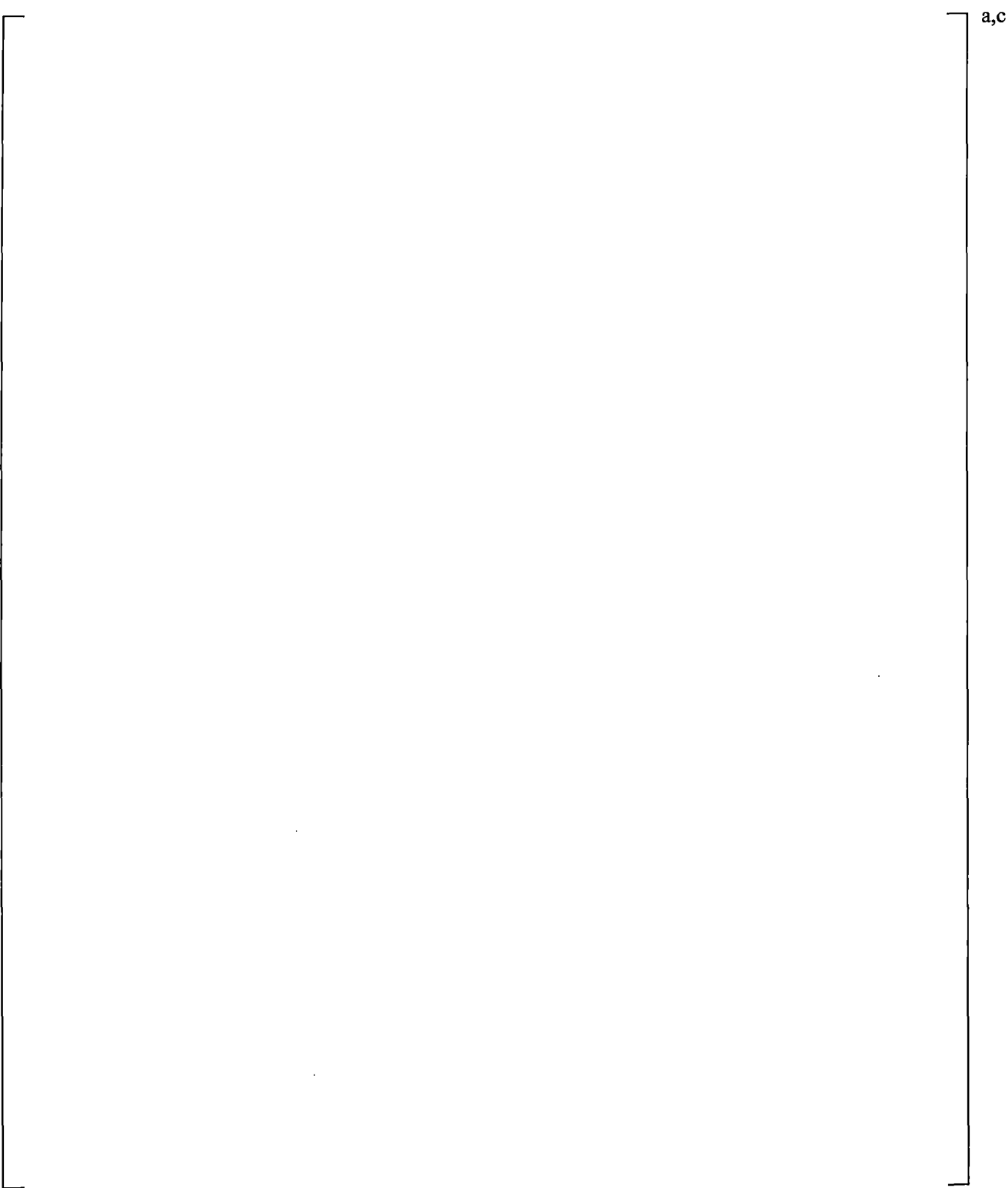


Figure 19.3-139 Cold Leg Steam Flow rate (Top) and Downcomer Pressure (Bottom) for Test Run 135

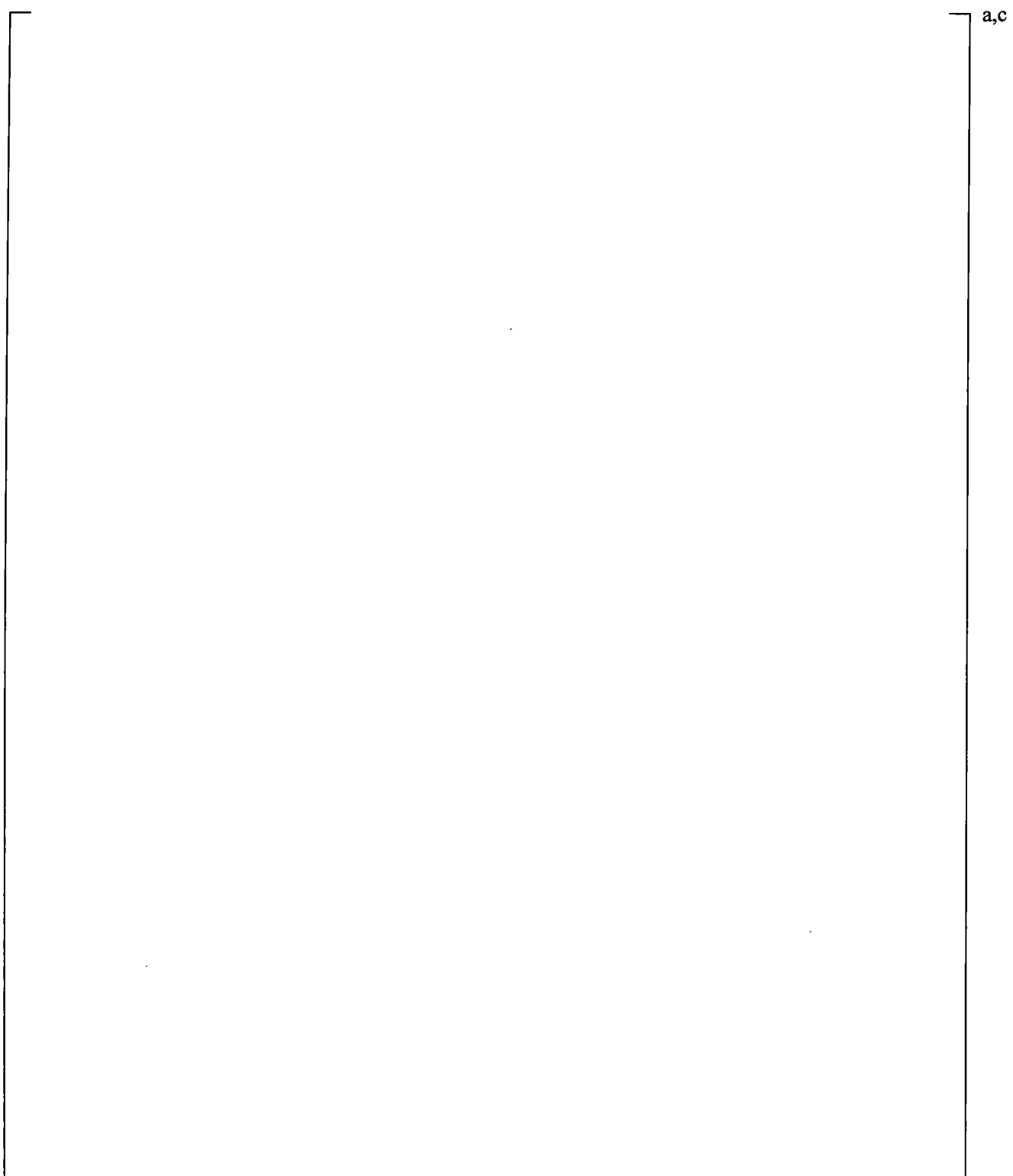


Figure 19.3-140 Cold Leg Fluid Temperature (Top) and Cold Leg to Downcomer Pressure Drop (Bottom) for Test Run 135

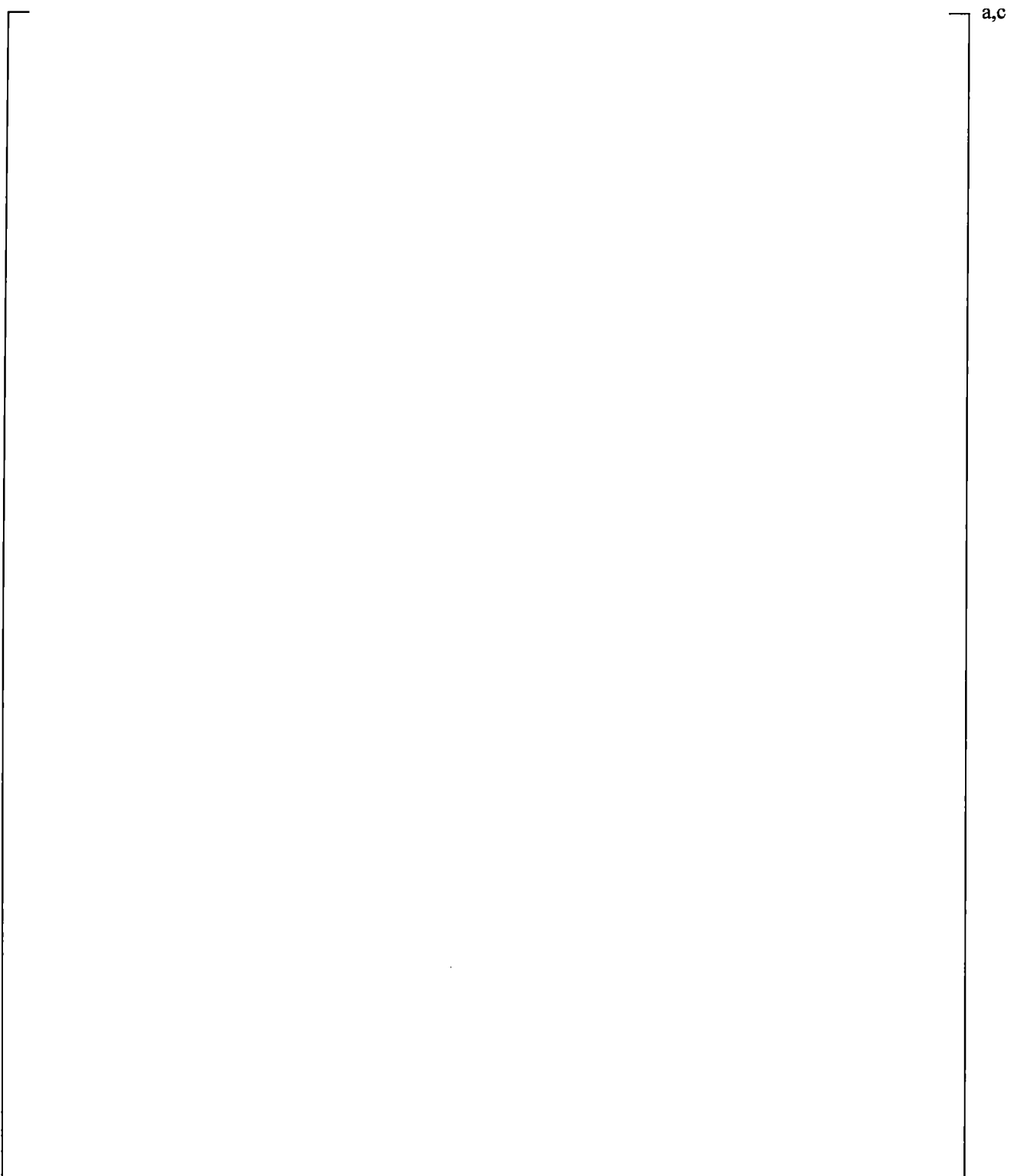


Figure 19.3-141 Cold Leg Steam Flow Rate (Top) and Downcomer Pressure (Bottom) for Test Run 136

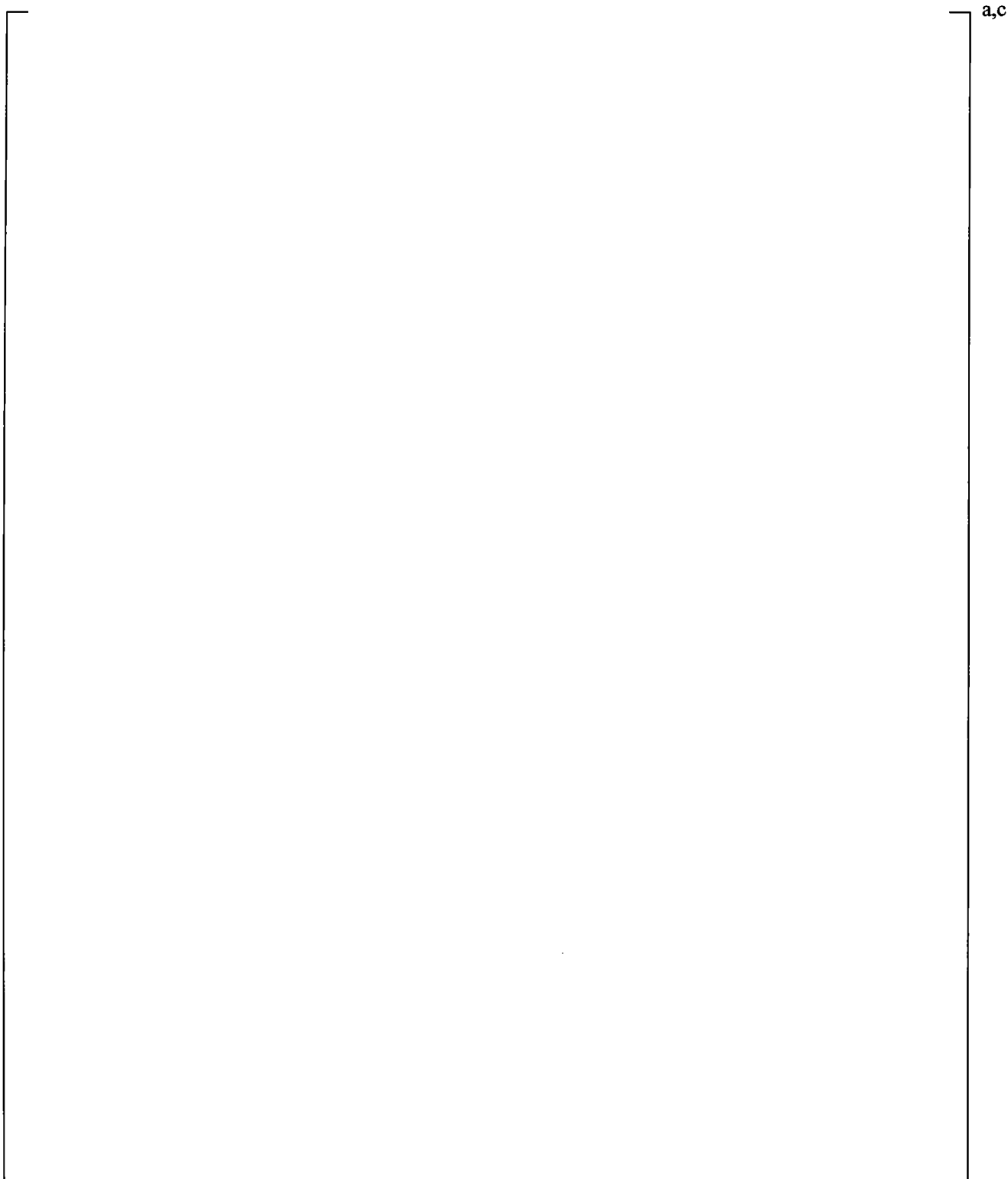


Figure 19.3-142 Cold Leg Fluid Temperature (Top) and Cold Leg to Downcomer Pressure Drop (Bottom) for Test Run 136

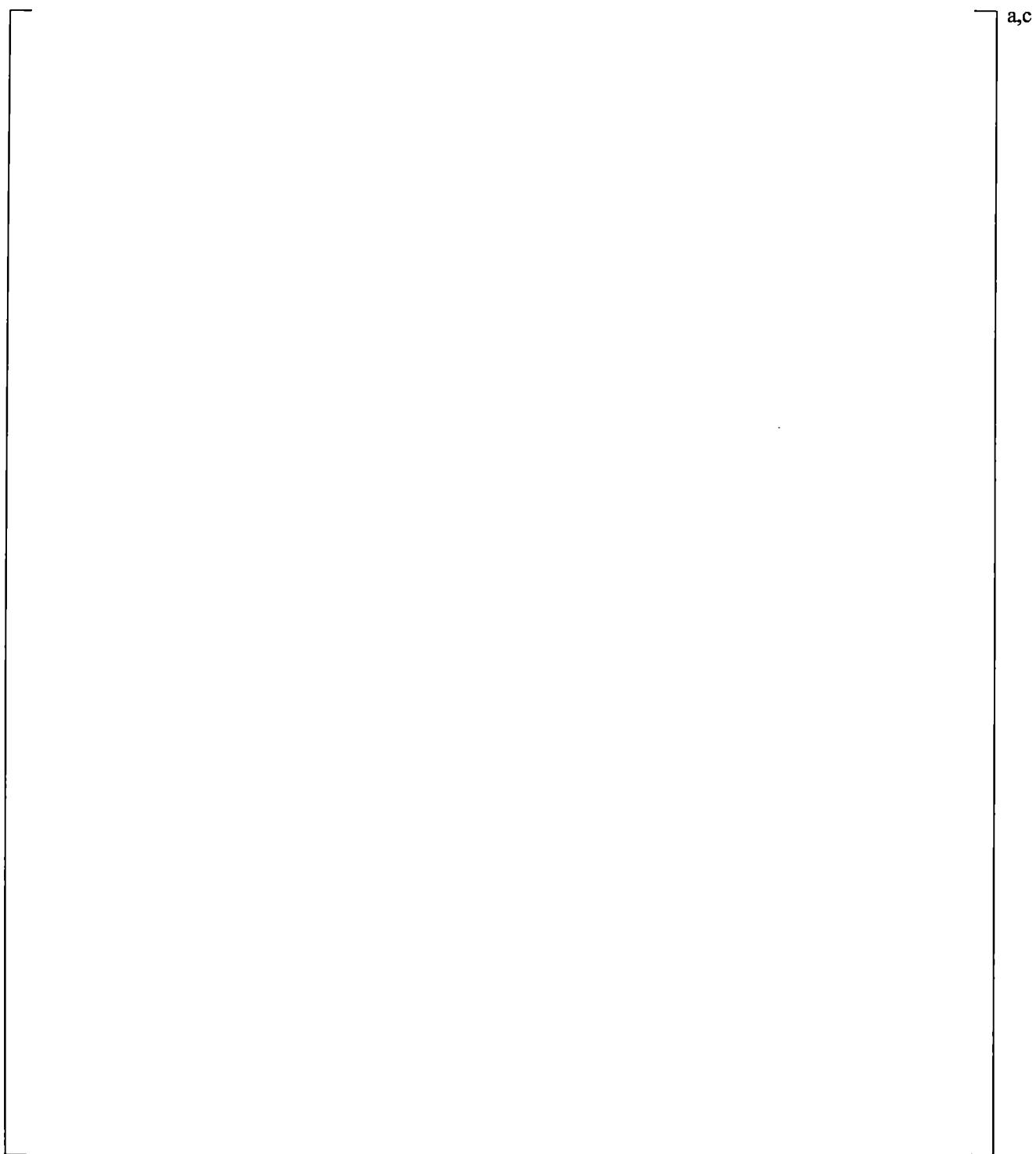


Figure 19.3-143 An Illustration of Downcomer and Broken Cold Leg Nozzle Noding

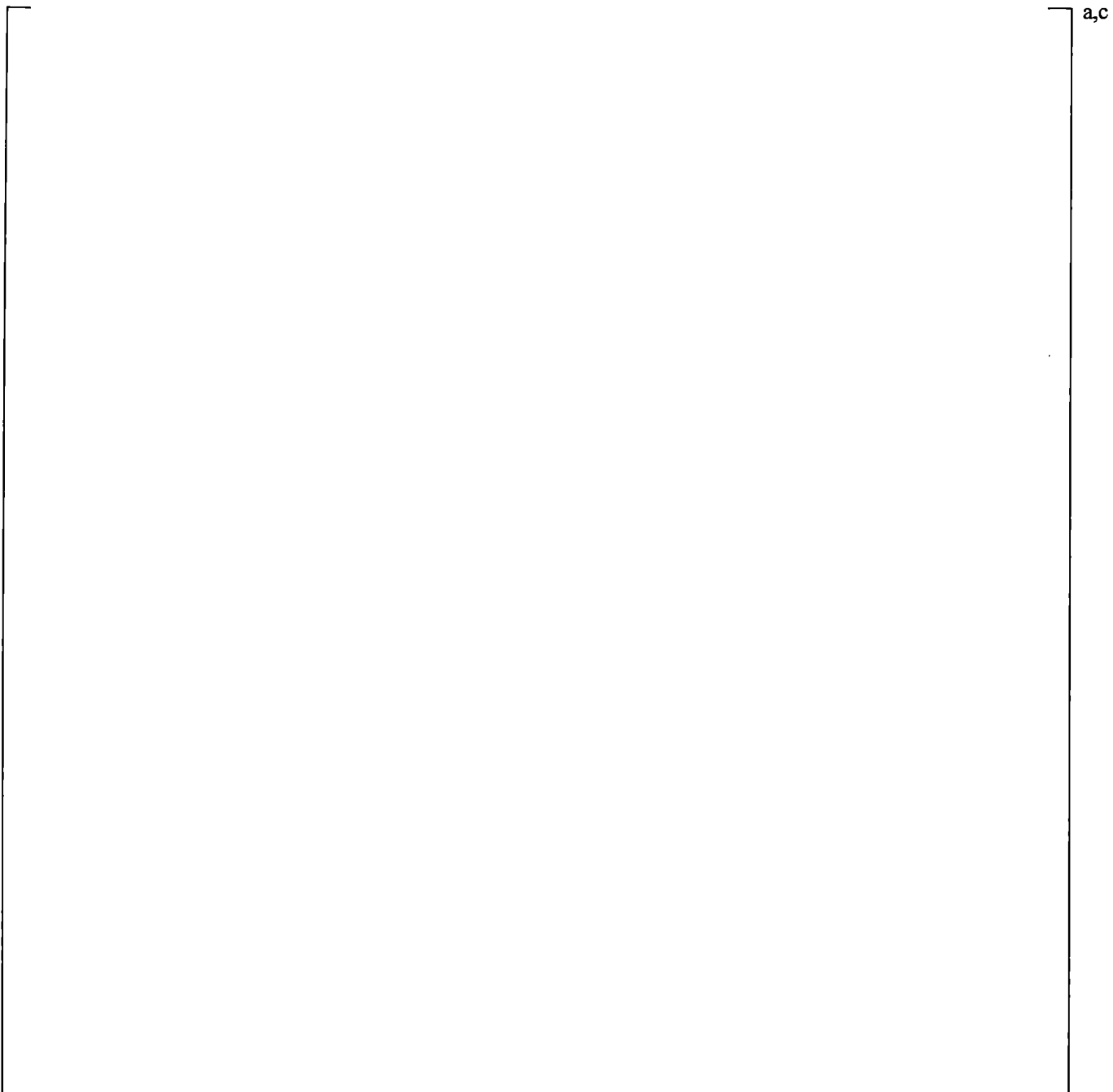


Figure 19.3-144 Comparison between Measured Pressure Loss and Predicted Pressure Loss across Broken Cold Leg Nozzle for UPTF 6-131

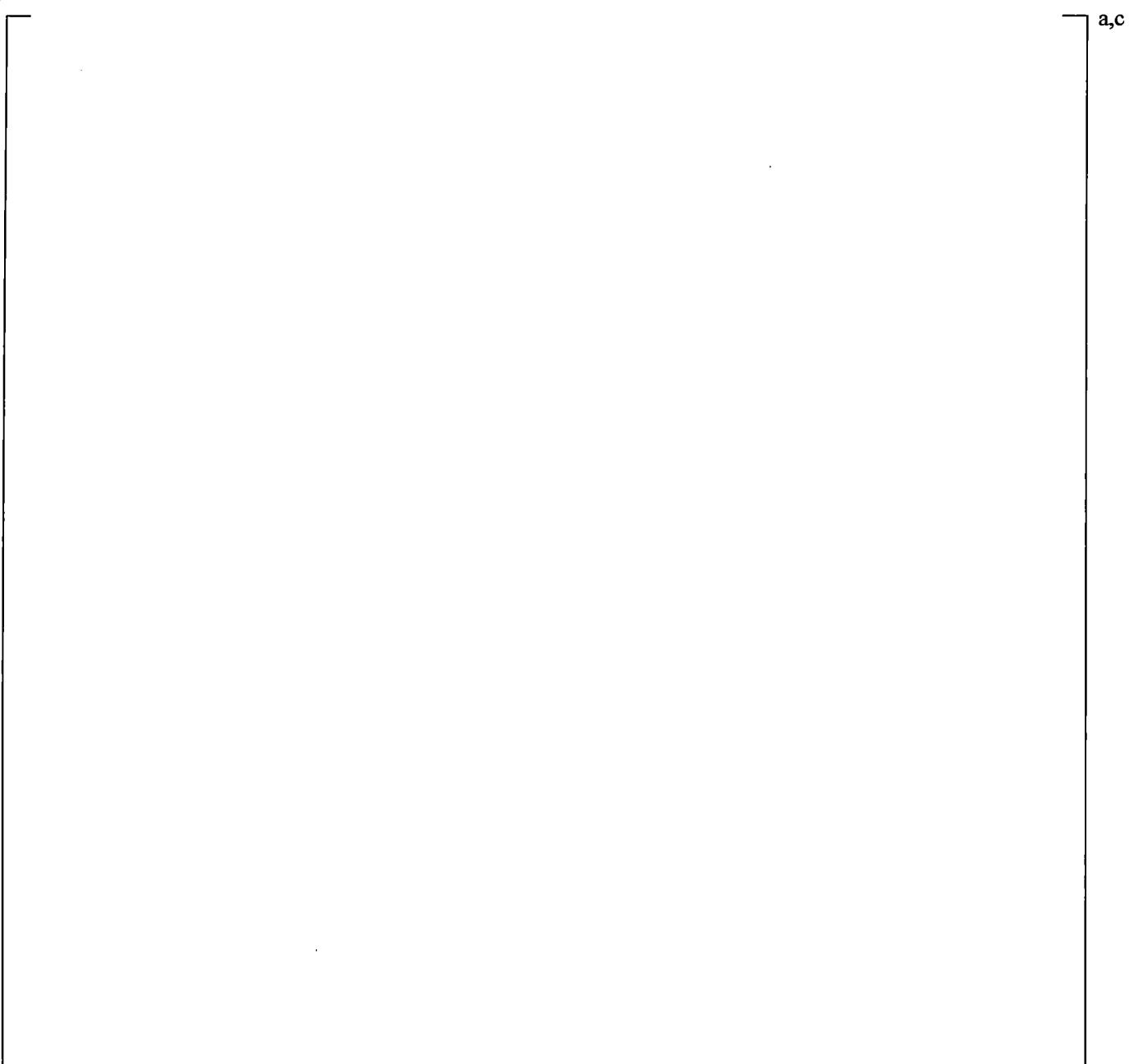


Figure 19.3-145 Comparison between Measured Pressure Loss and Predicted Pressure Loss across Broken Cold Leg Nozzle for UPTF 6-132

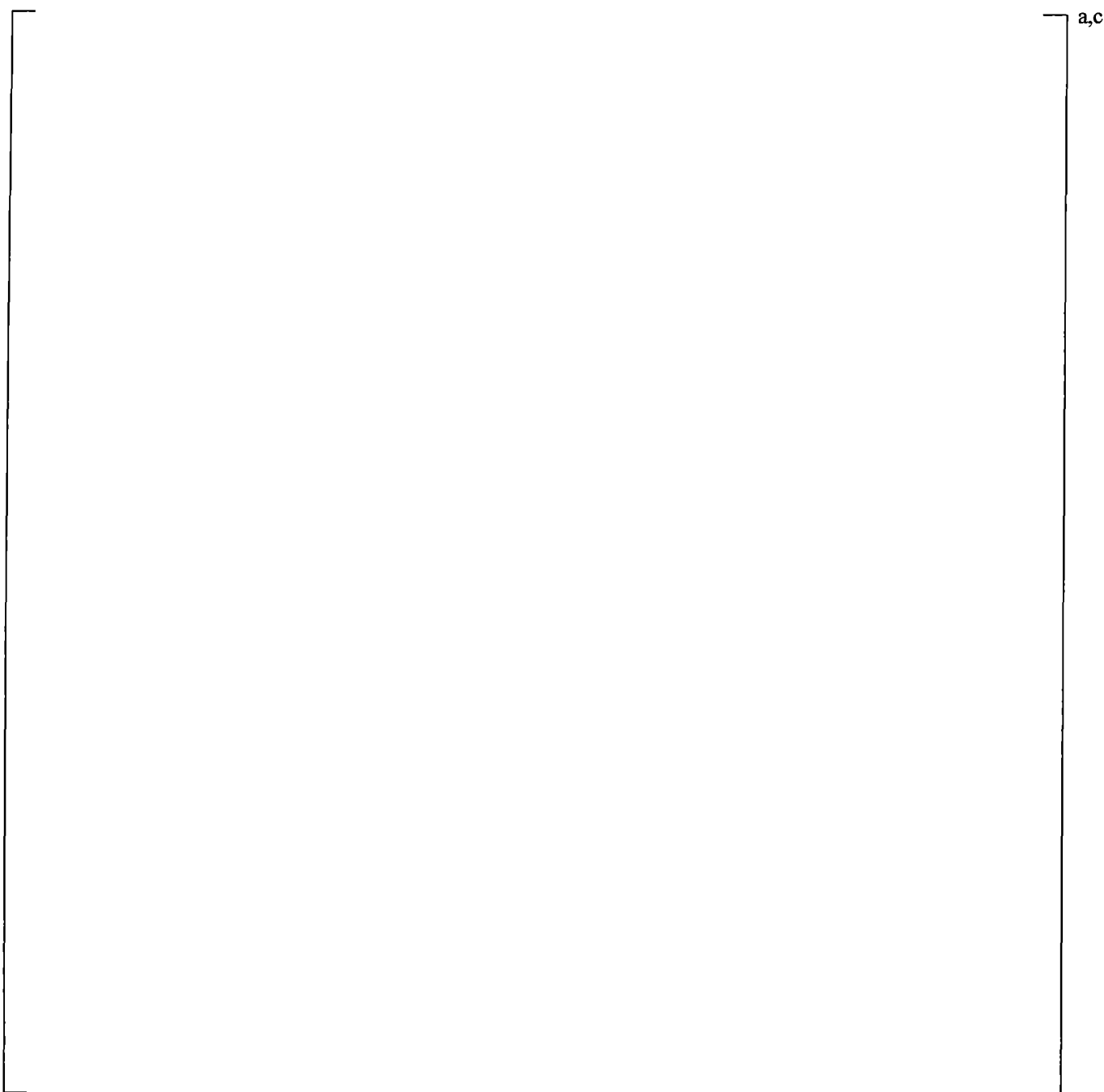


Figure 19.3-146 Comparison between Measured Pressure Loss and Predicted Pressure Loss across Broken Cold Leg Nozzle for UPTF 6-133

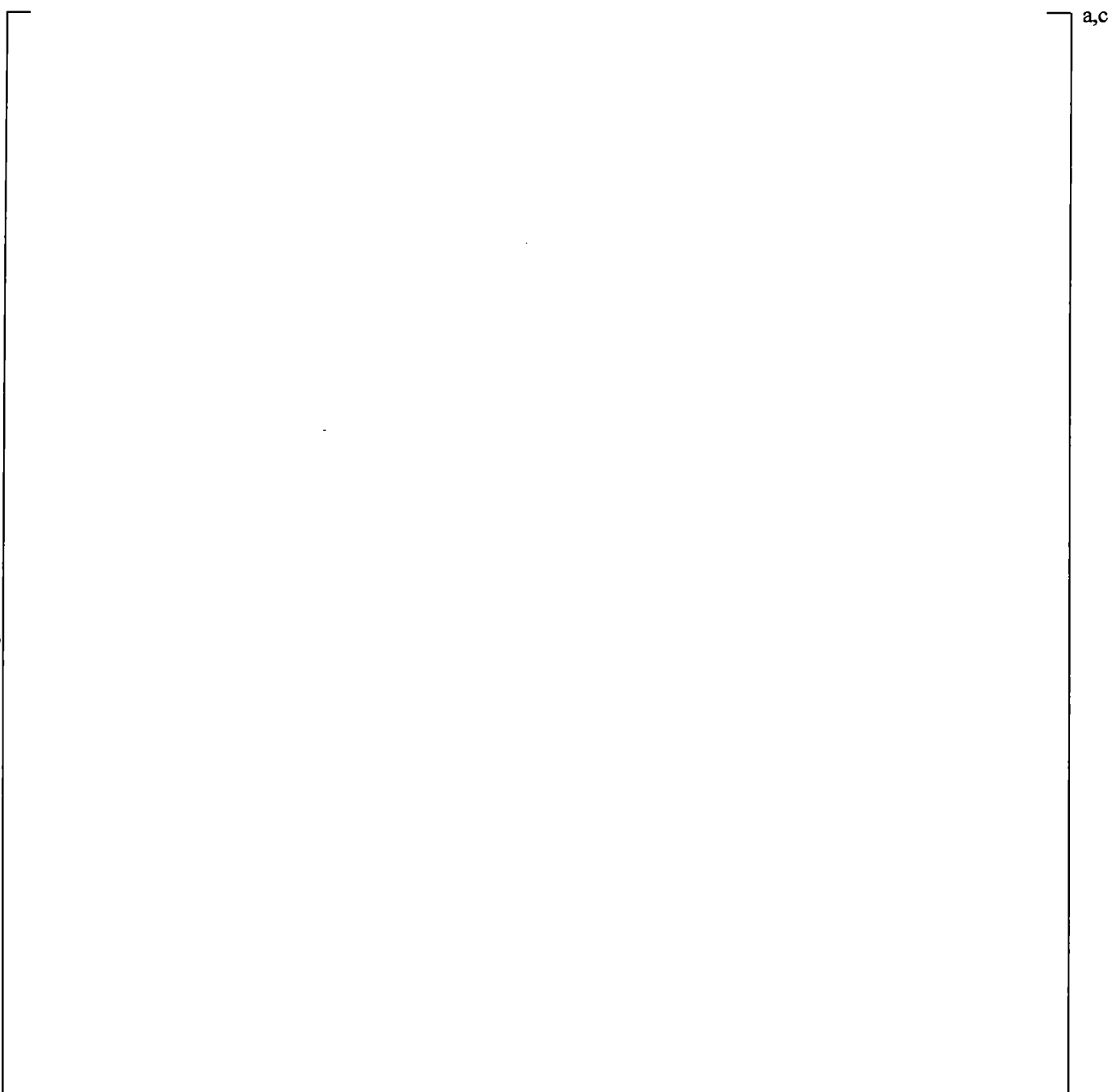


Figure 19.3-147 Comparison between Measured Pressure Loss and Predicted Pressure Loss across Broken Cold Leg Nozzle for UPTF 6-135

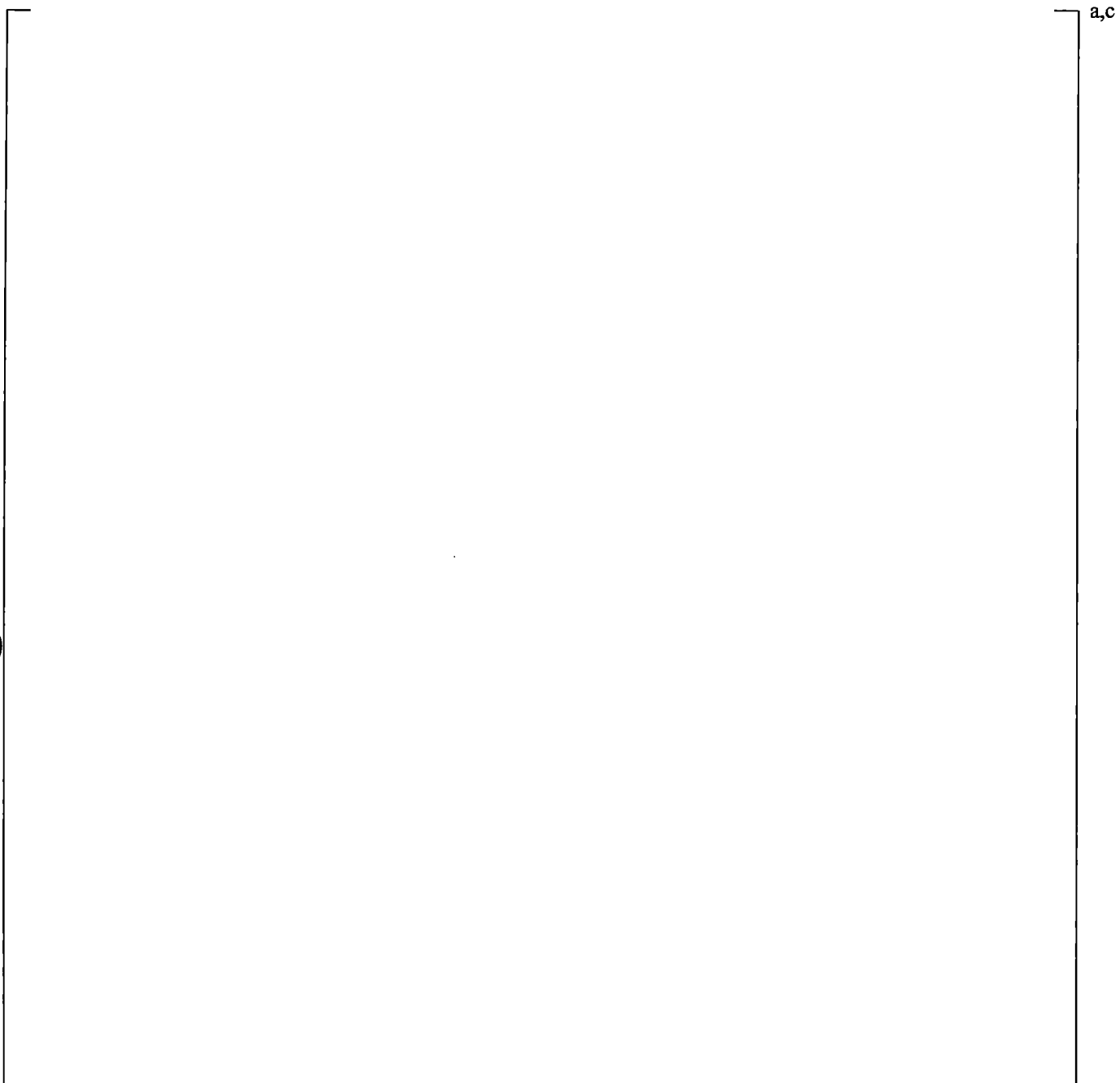


Figure 19.3-148 Comparison between Measured Pressure Loss and Predicted Pressure Loss across Broken Cold Leg Nozzle for UPTF 6-136

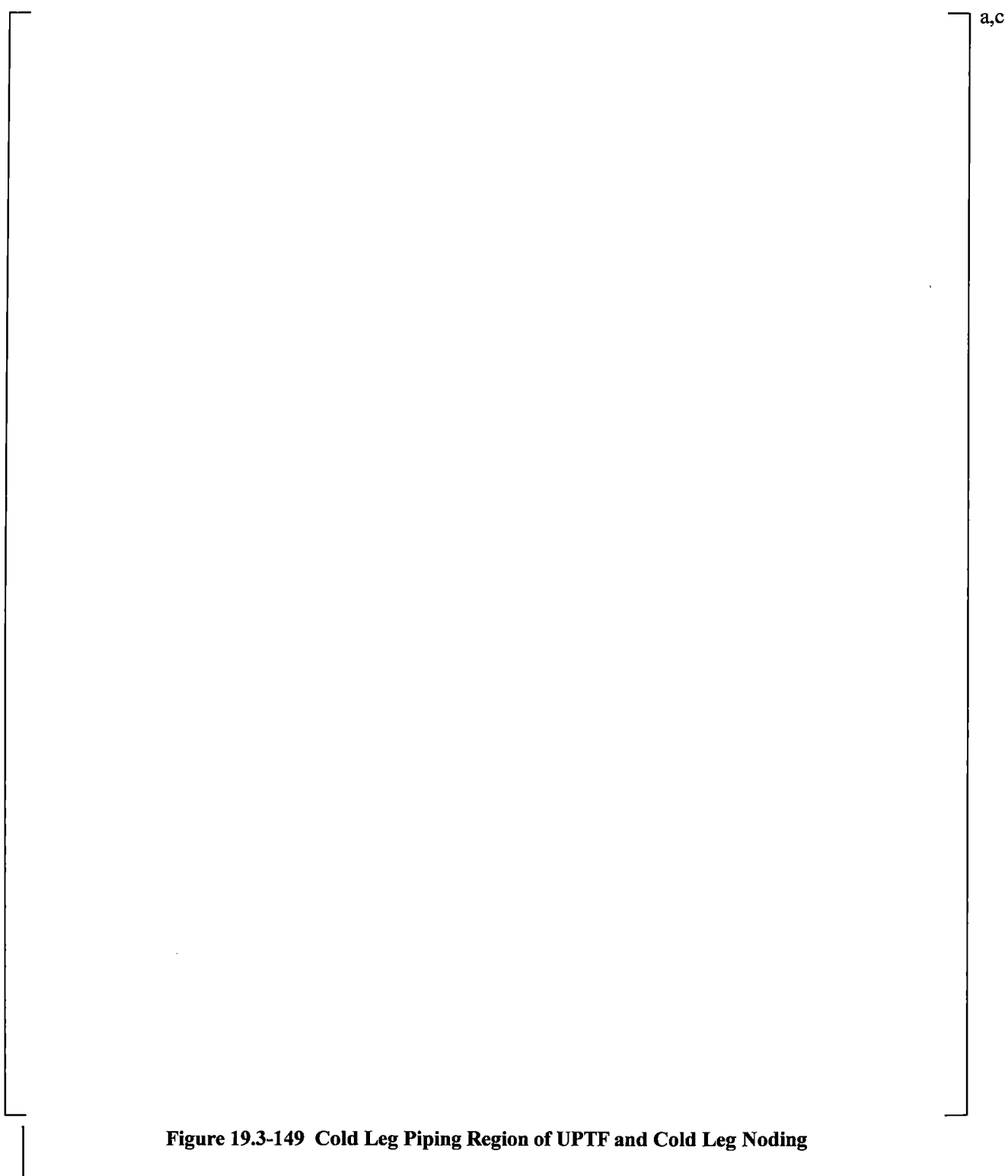


Figure 19.3-149 Cold Leg Piping Region of UPTF and Cold Leg Nodding

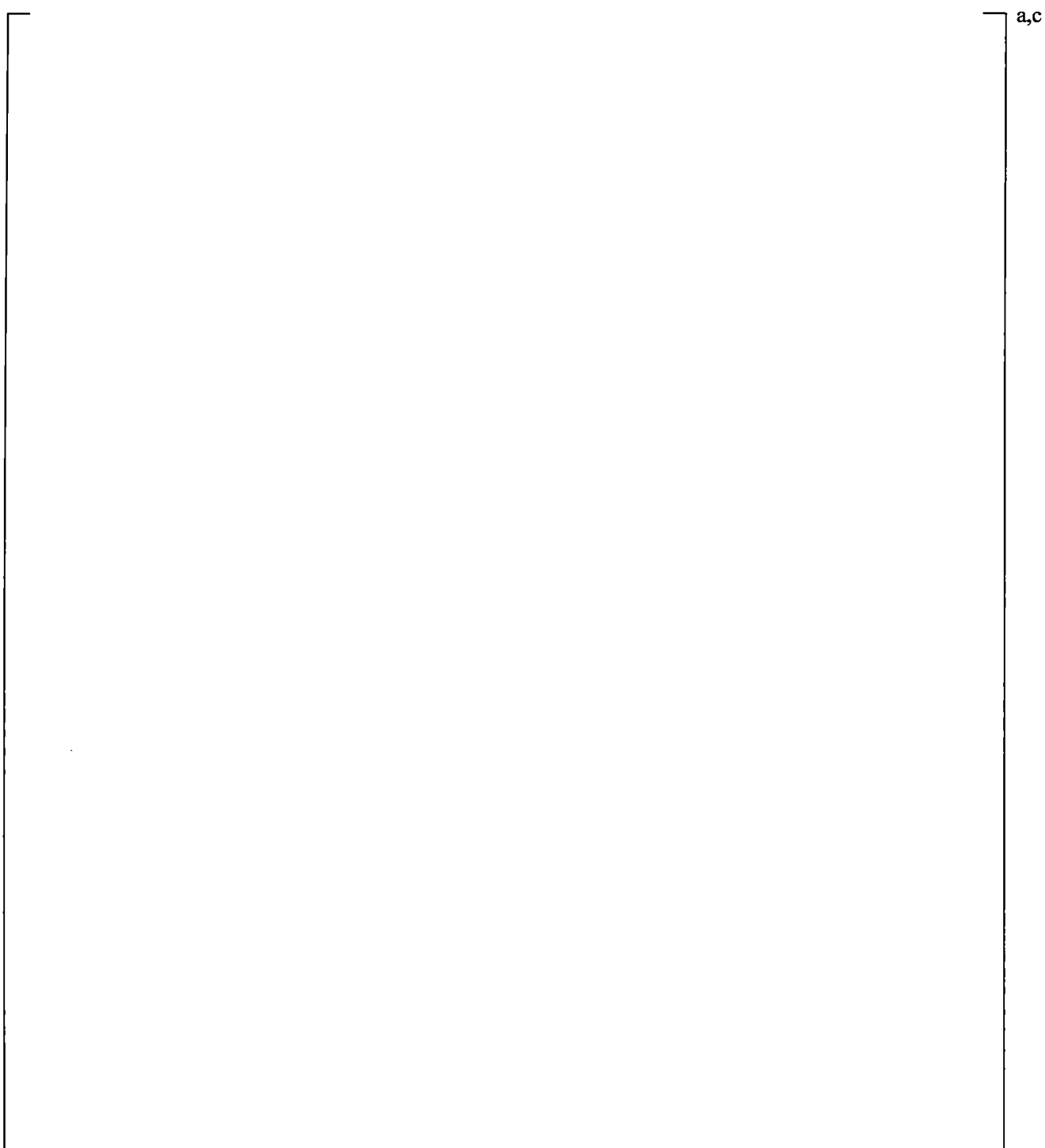
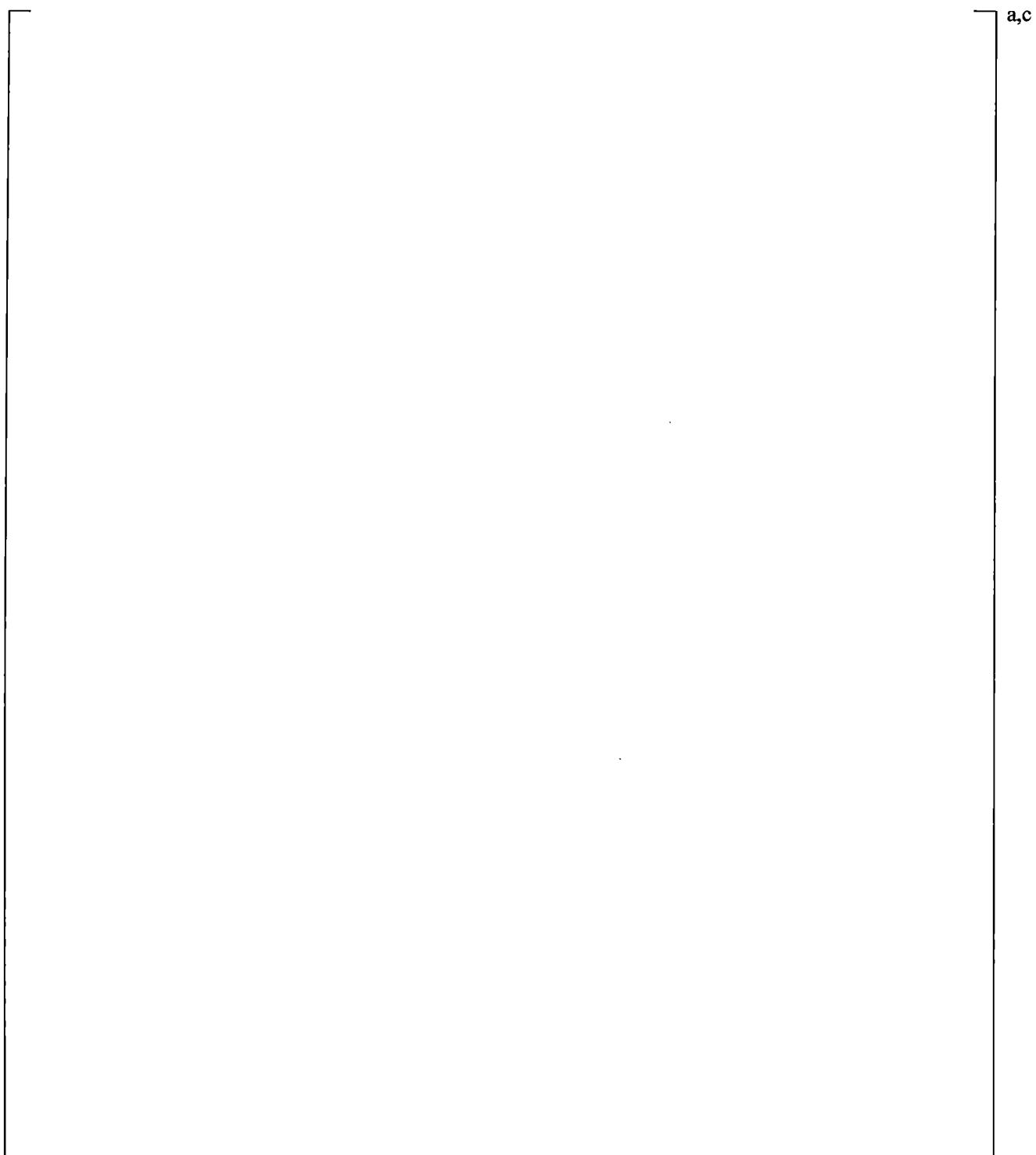


Figure 19.3-150 System Configuration for UPTF 8A



| **Figure 19.3-151 Observation on Temperature Distribution in UPTF 8A Experiments (MPR-1208, 1992) and Comparison with Predictions from WCOPRA/TRAC-TF2**

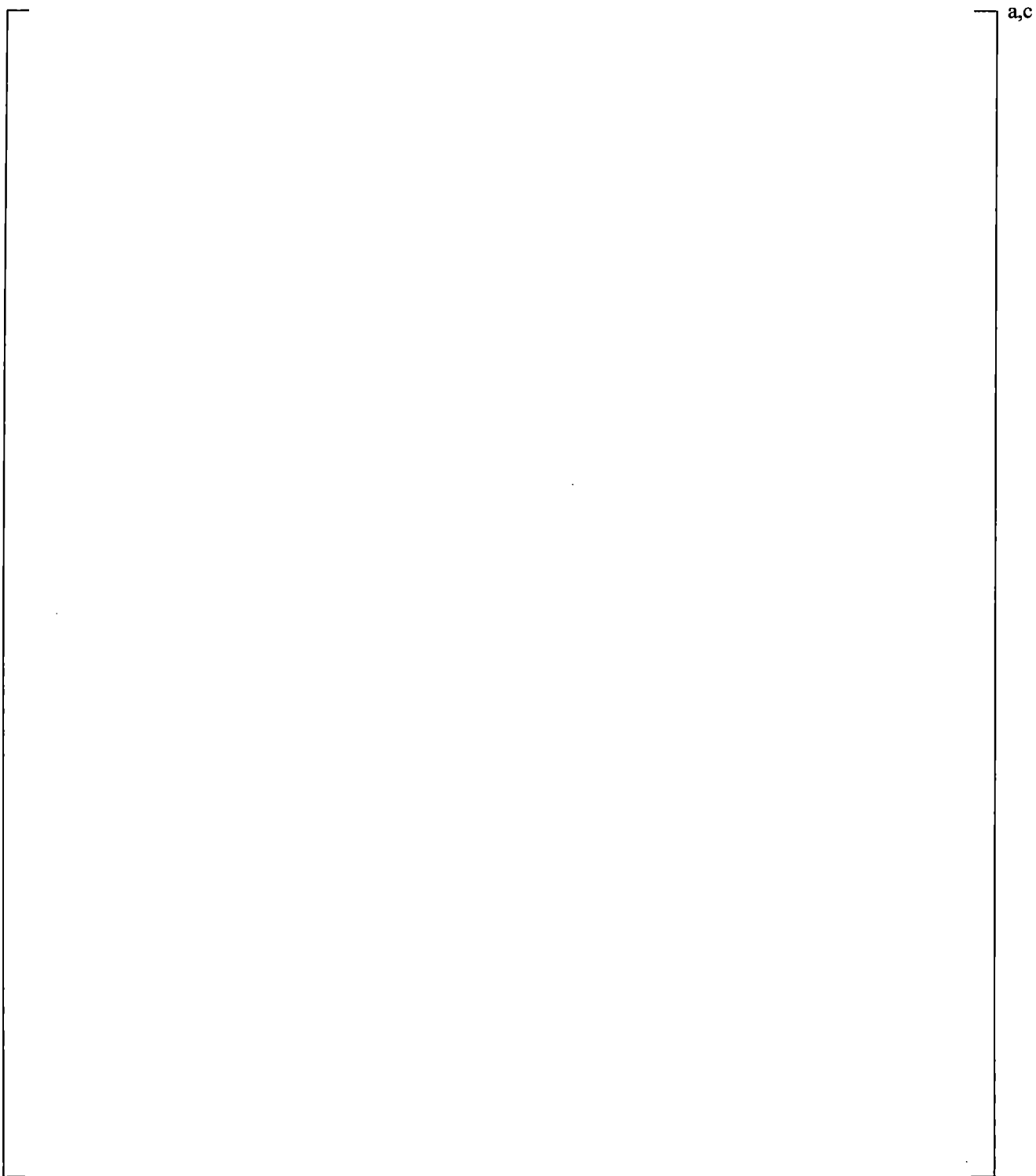


Figure 19.3-152 WCOBRA/TRAC-TF2 Vessel Model for UPTF Test 8A

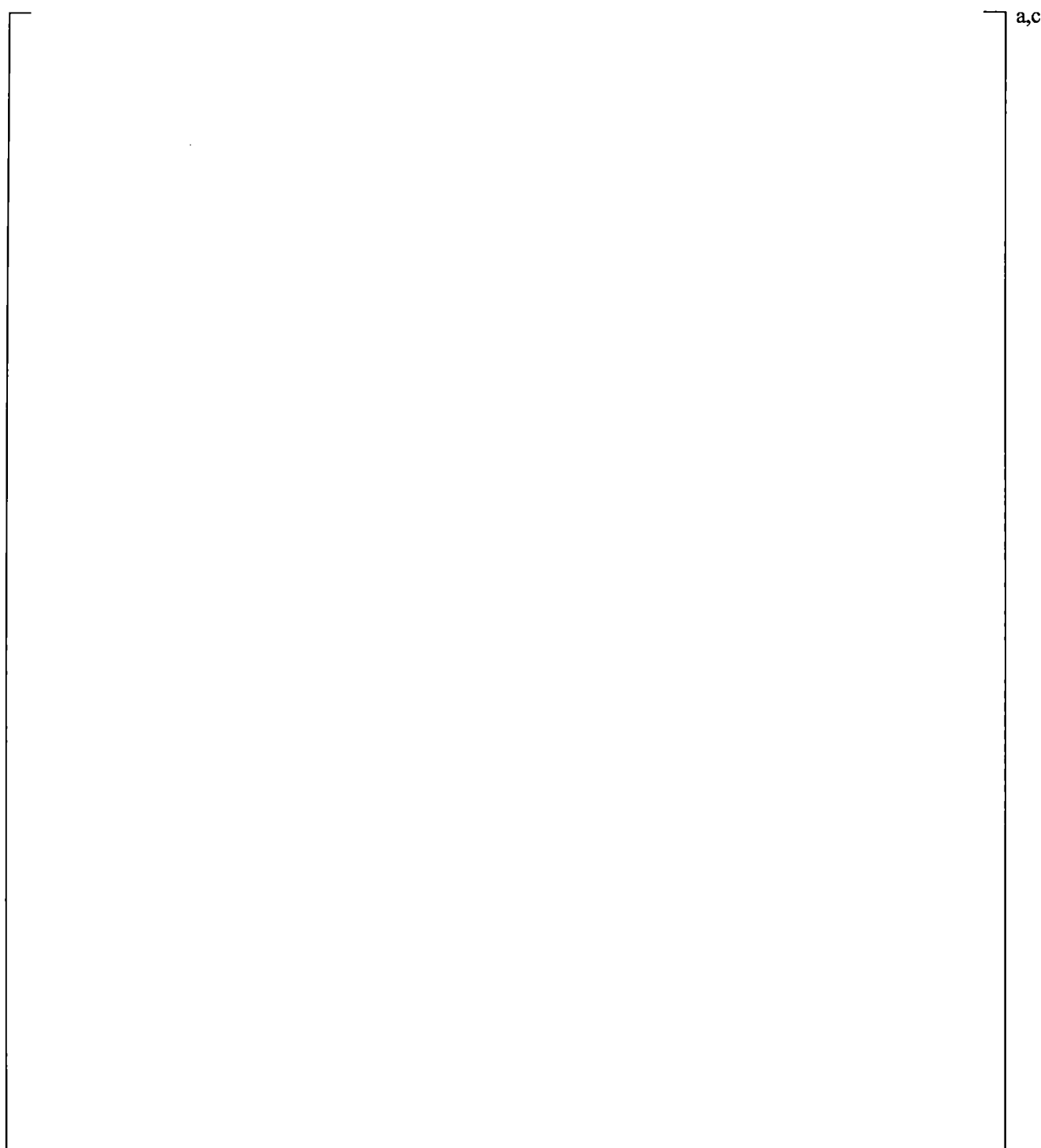
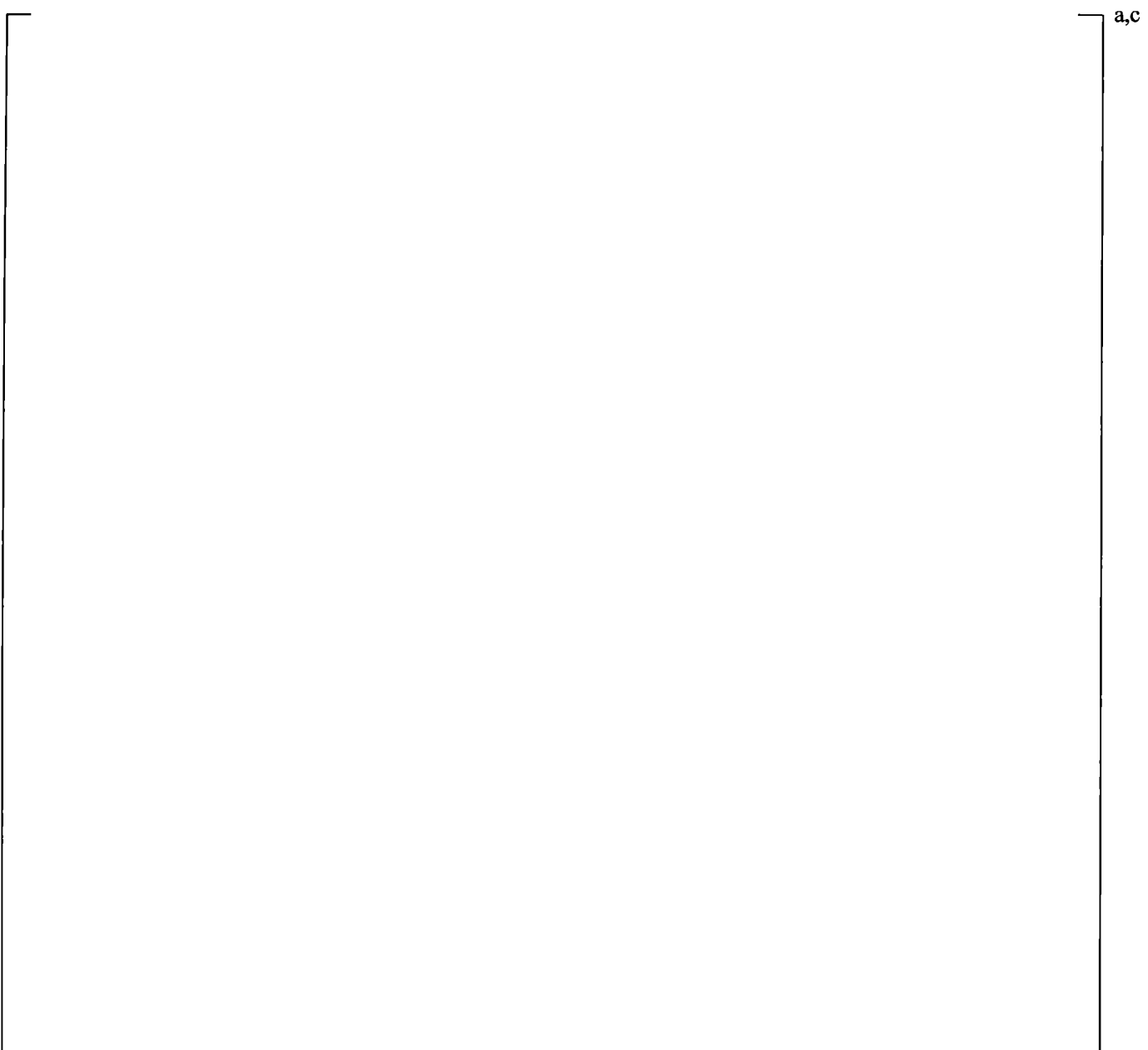


Figure 19.3-153 WCOBRA/TRAC-TF2 Loop Model for UPTF 8A



**Figure 19.3-154 Comparison between the Measured Steam Flow Rates and the
WCOBRA/TRAC-TF2 Predicted Steam Flow Rates in the Cold Leg of the
Loop 2**

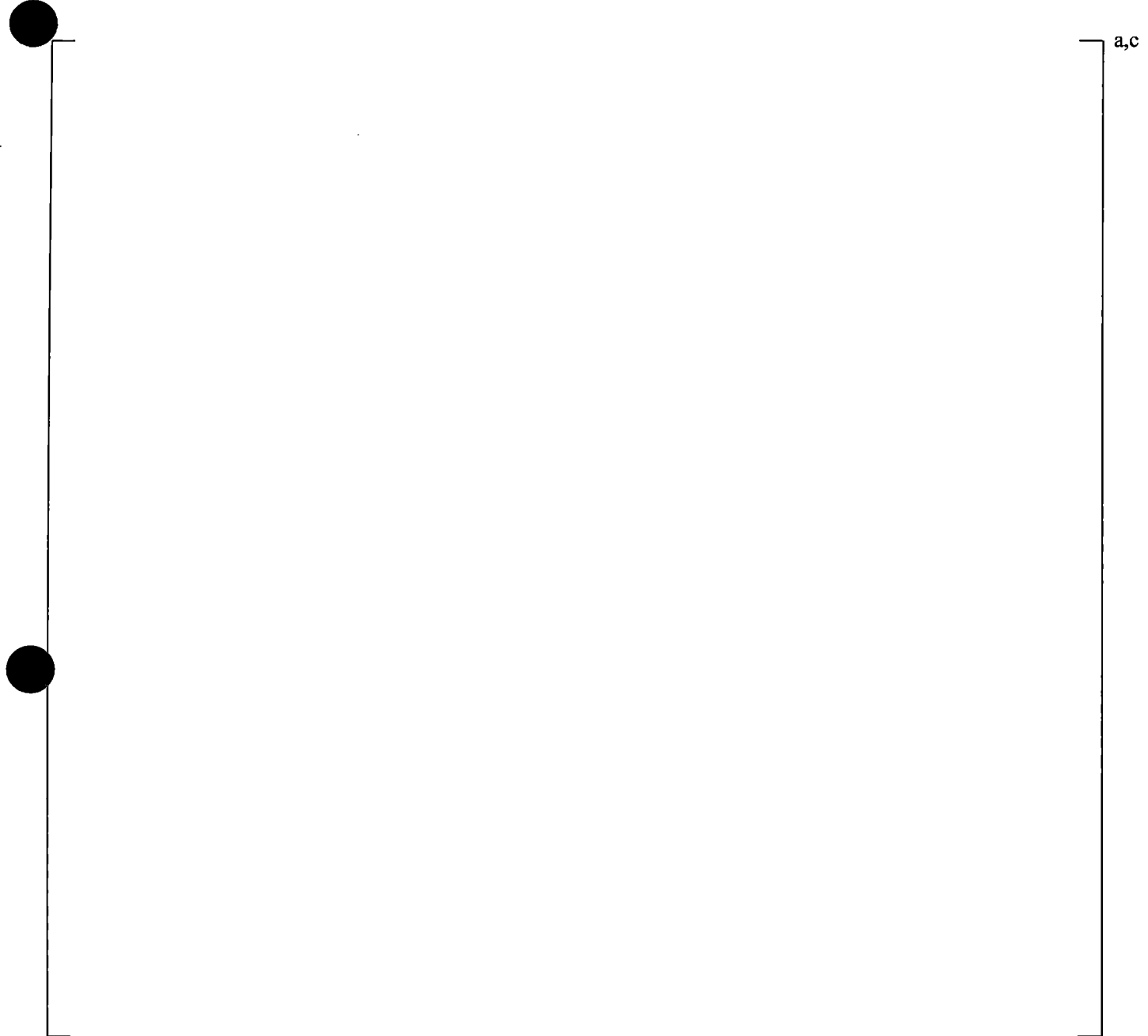


Figure 19.3-155 ECC Injection Flow Rate to Cold Leg in Loop 2

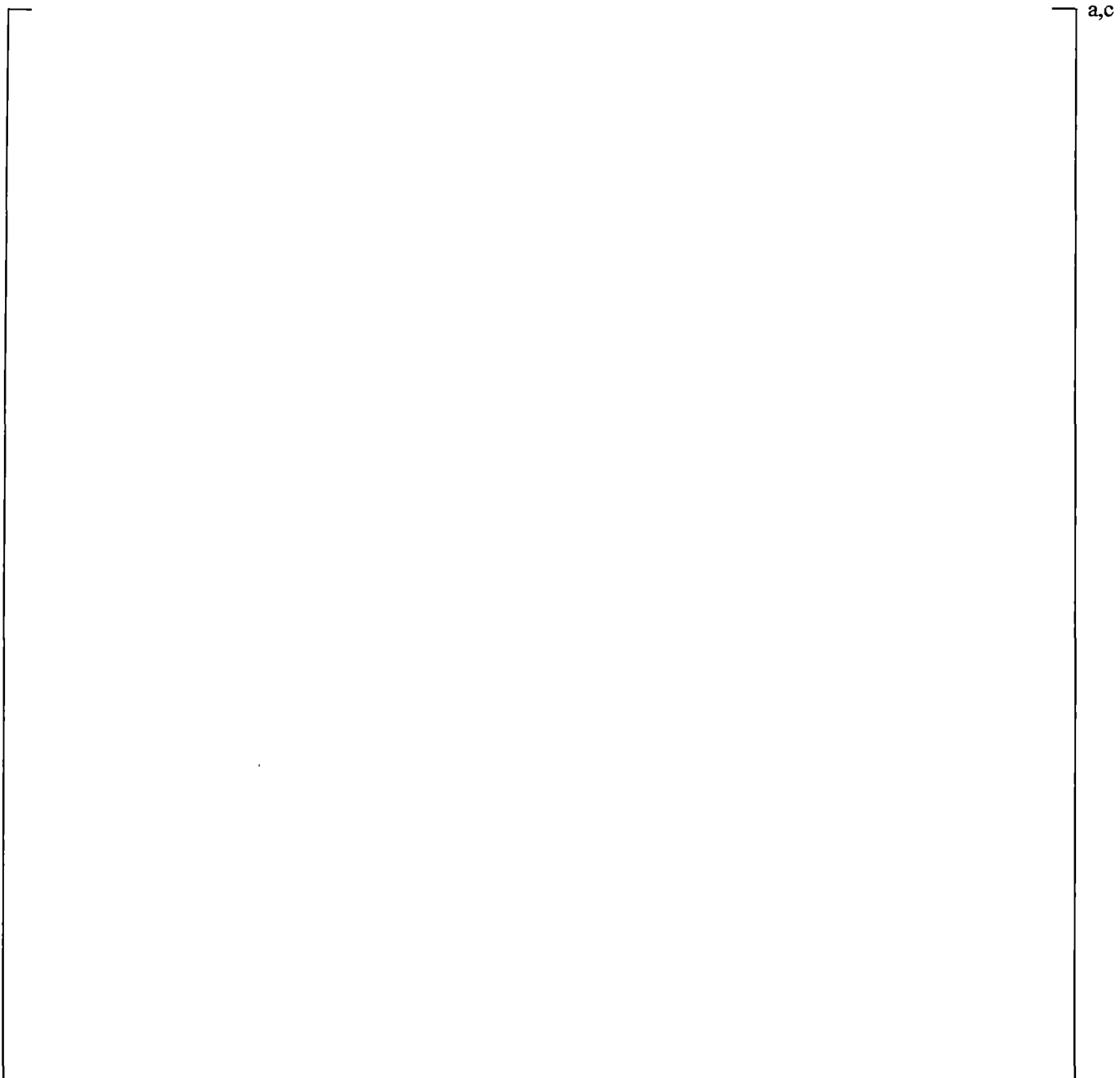


Figure 19.3-156 Comparison between Measured Fluid Temperature and WCOBRA/TRAC-TF2 Predicted Water Temperature at Pump Exit

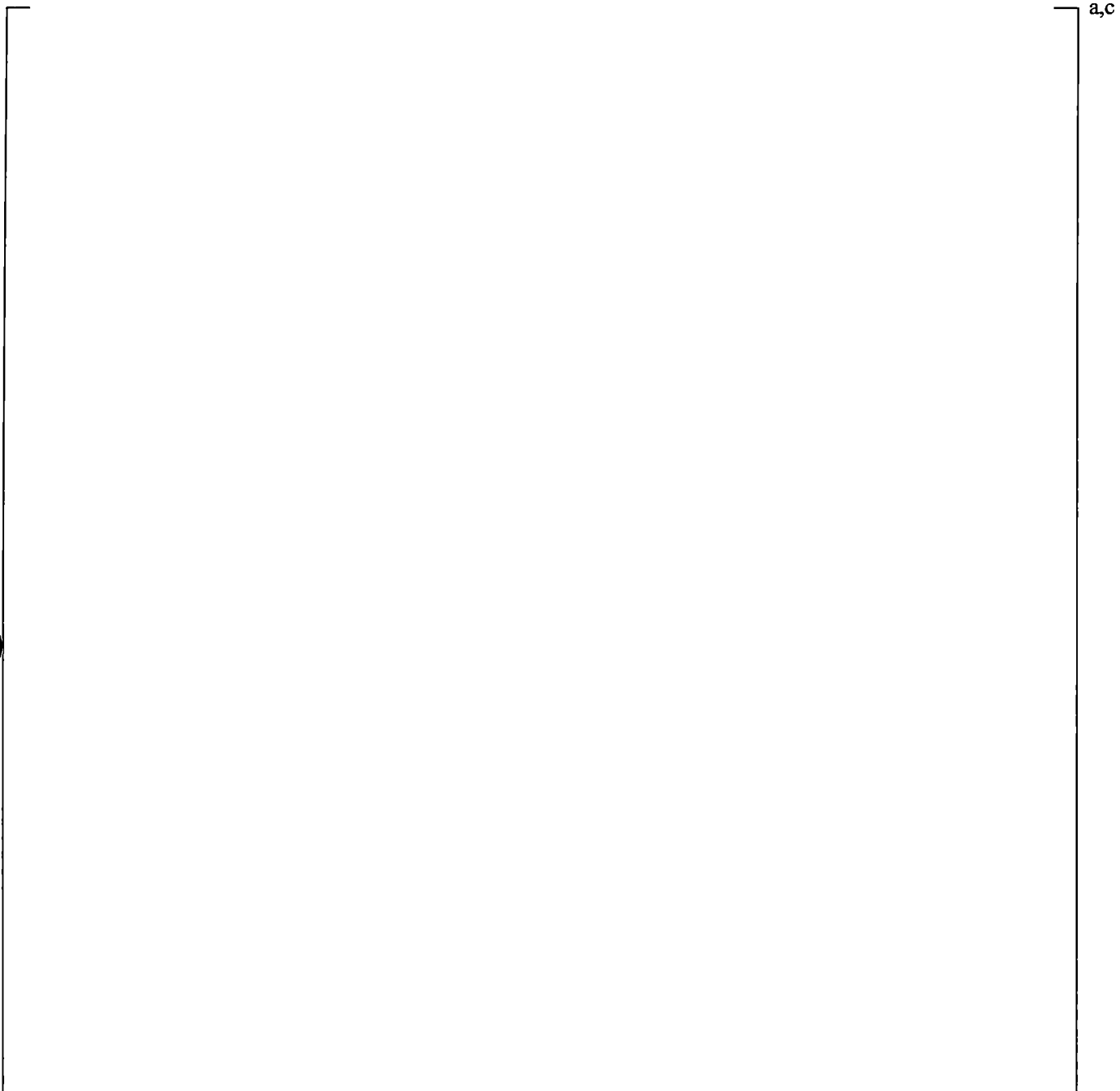


Figure 19.3-157 Comparison between Measured Fluid Temperature and WCOBRA/TRAC-TF2 Predicted Water Temperature near Injection Point

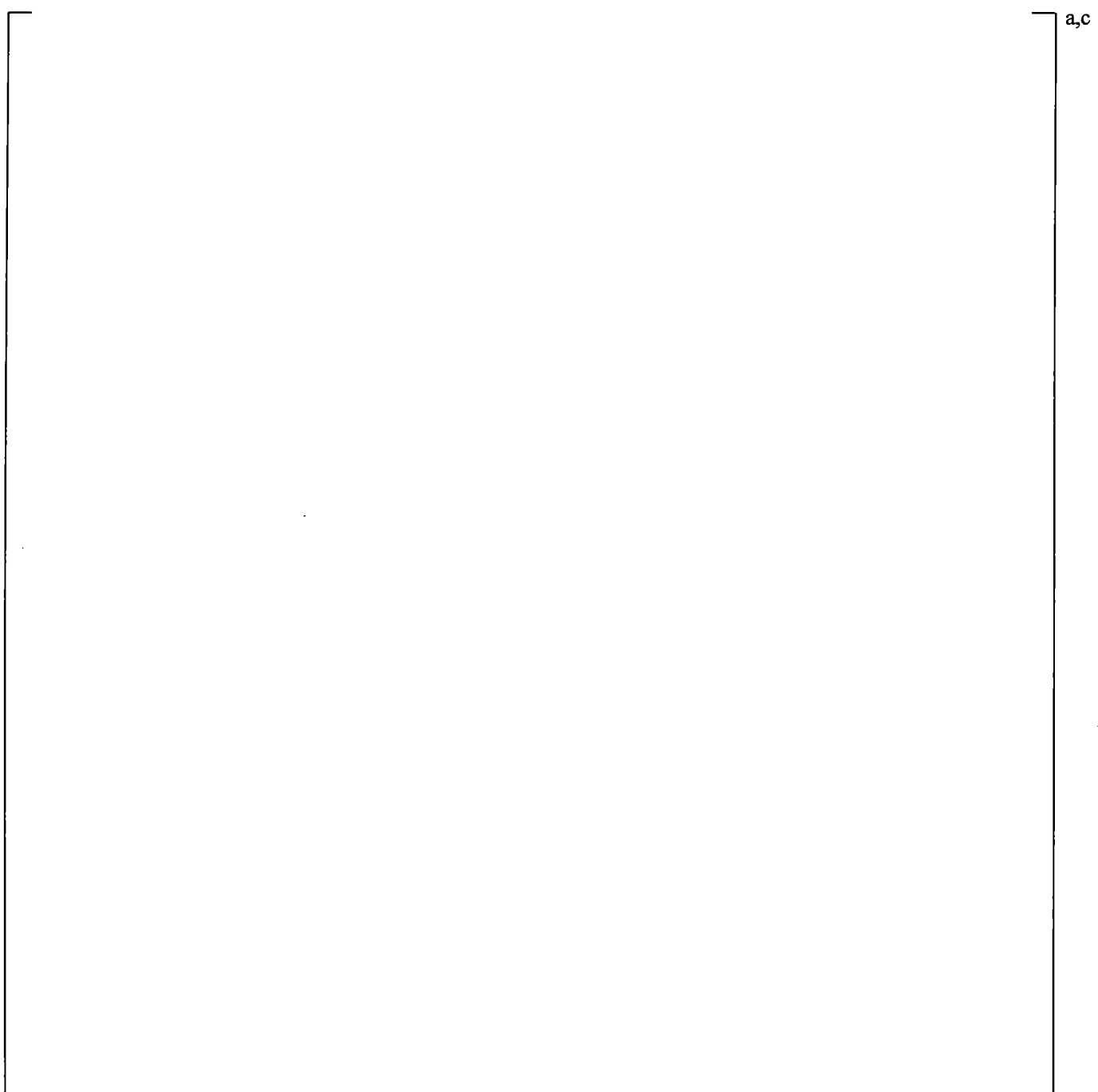


Figure 19.3-158 Comparison between Measured Fluid Temperature and WCOBRA/TRAC-TF2 Predicted Water Temperature at Downstream of Injection Point

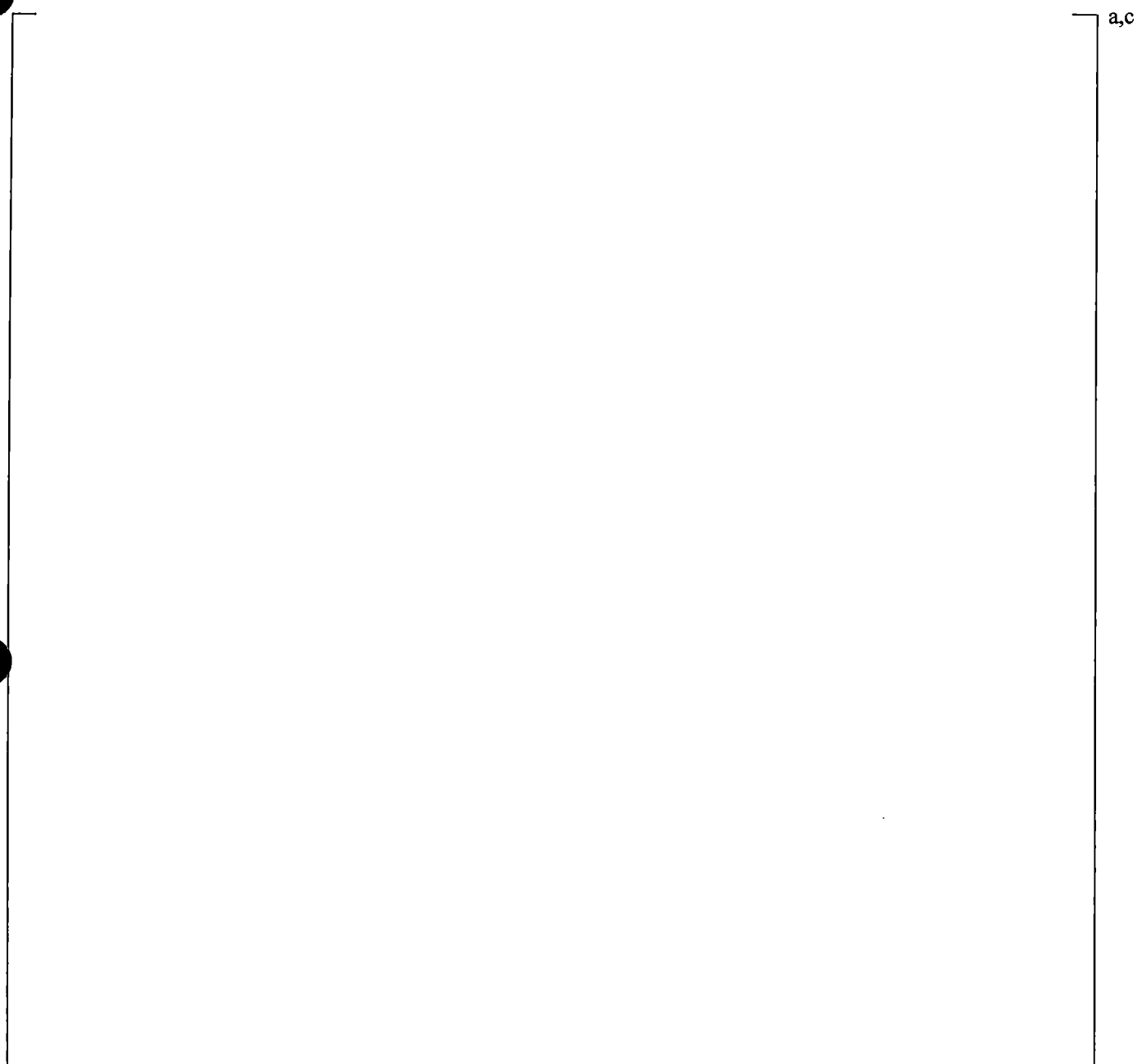


Figure 19.3-159 Comparison between Measured Fluid Temperature and WCOBRA/TRAC-TF2 Predicted Water Temperature at Outlet of Cold Leg

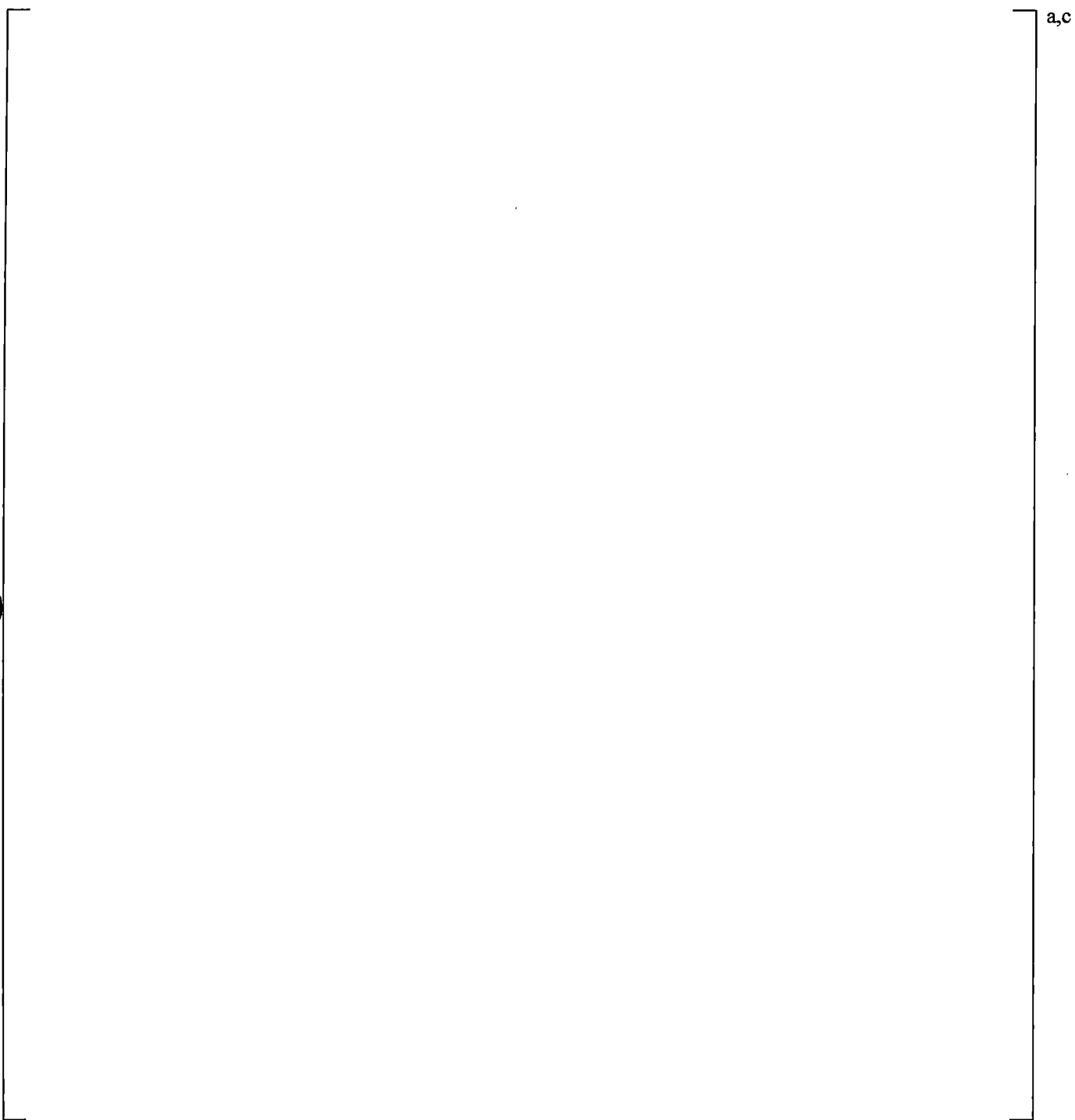


Figure 19.3-160 Predicted Flow Regime Number of Cell Face 4 of Cold Leg

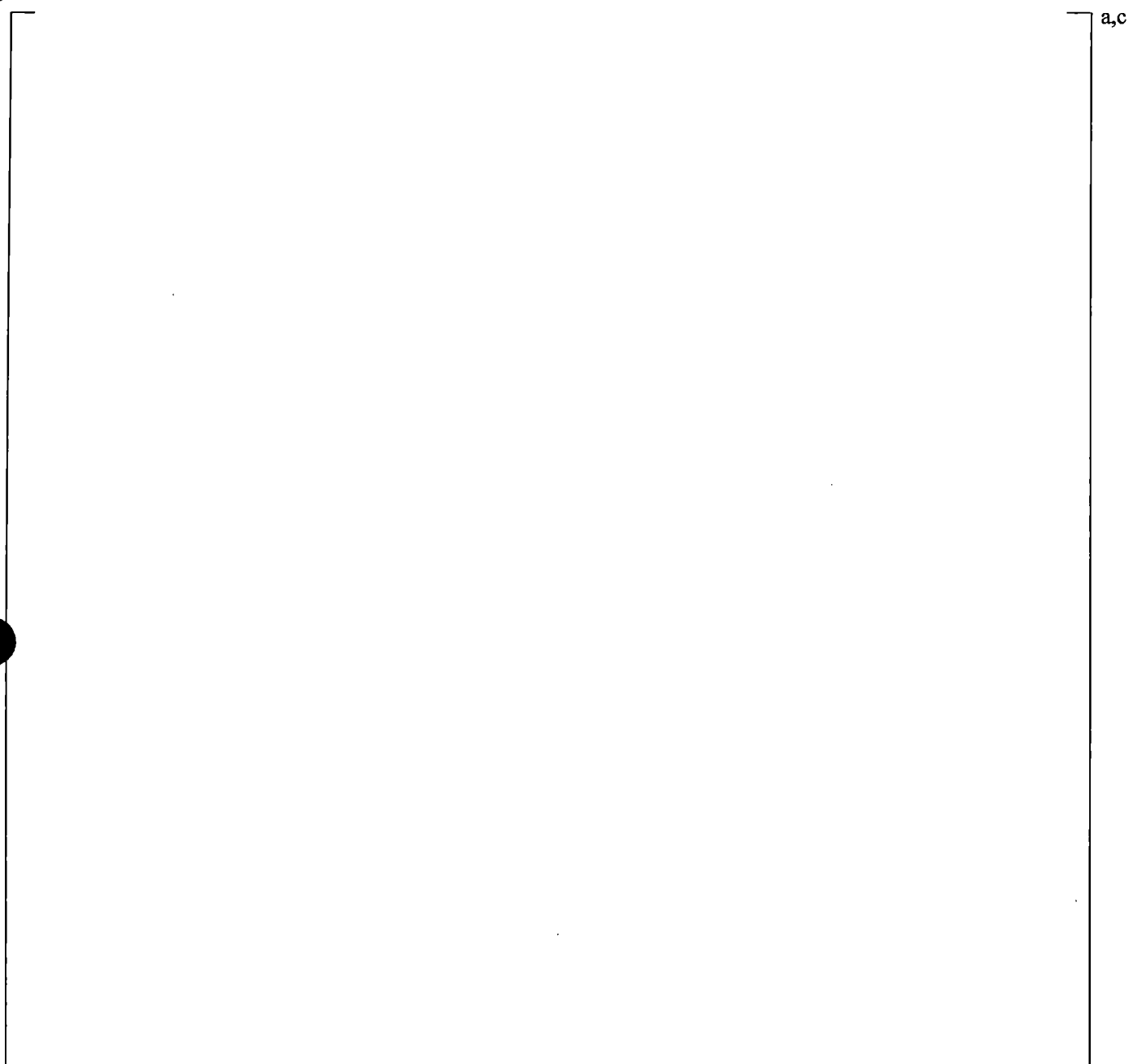


Figure 19.3-161 Predicted Flow Regime Number of Cell Face 5 of Cold Leg

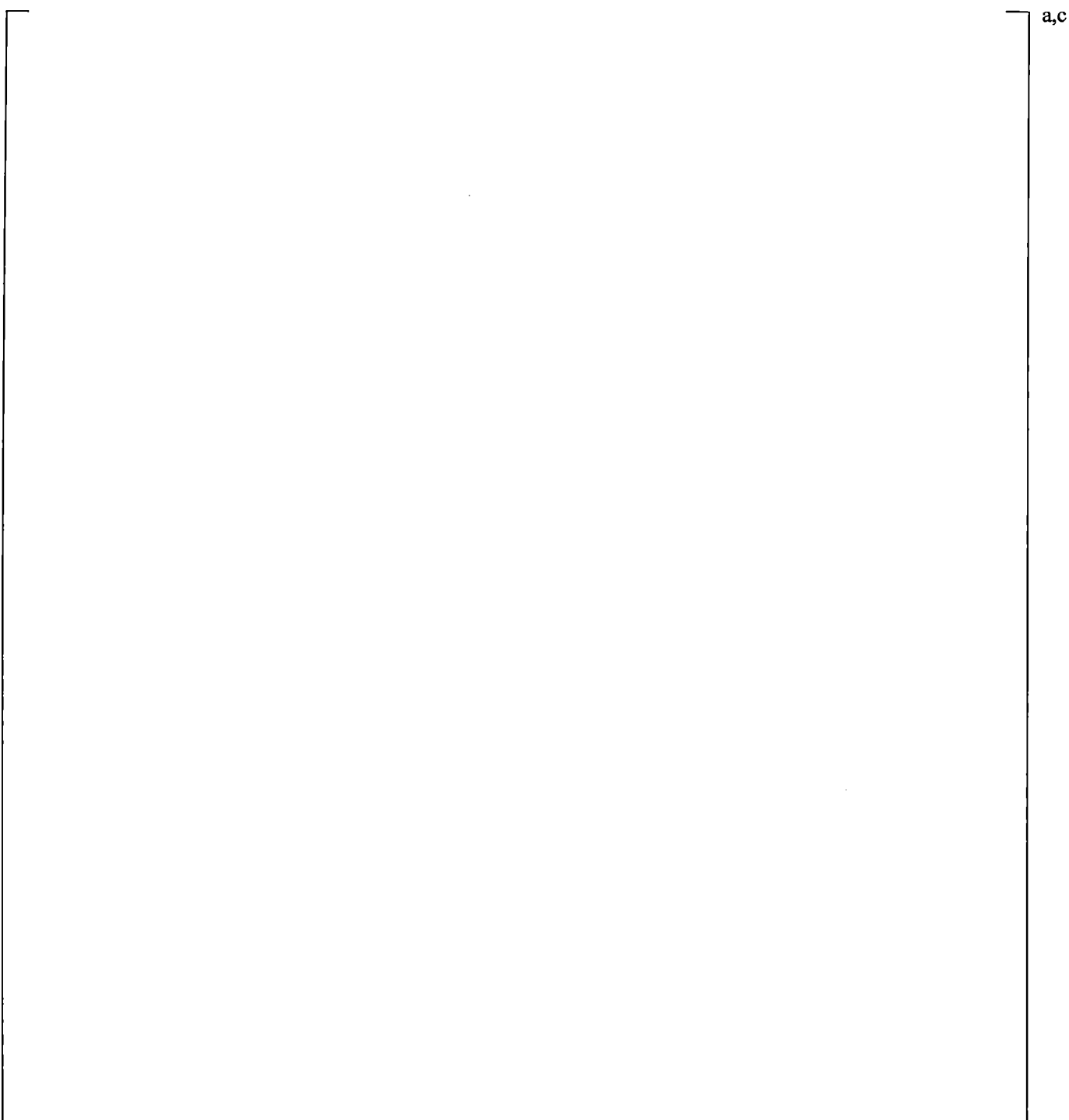


Figure 19.3-162 Predicted Flow Regime Number of Cell Face 6 of Cold Leg

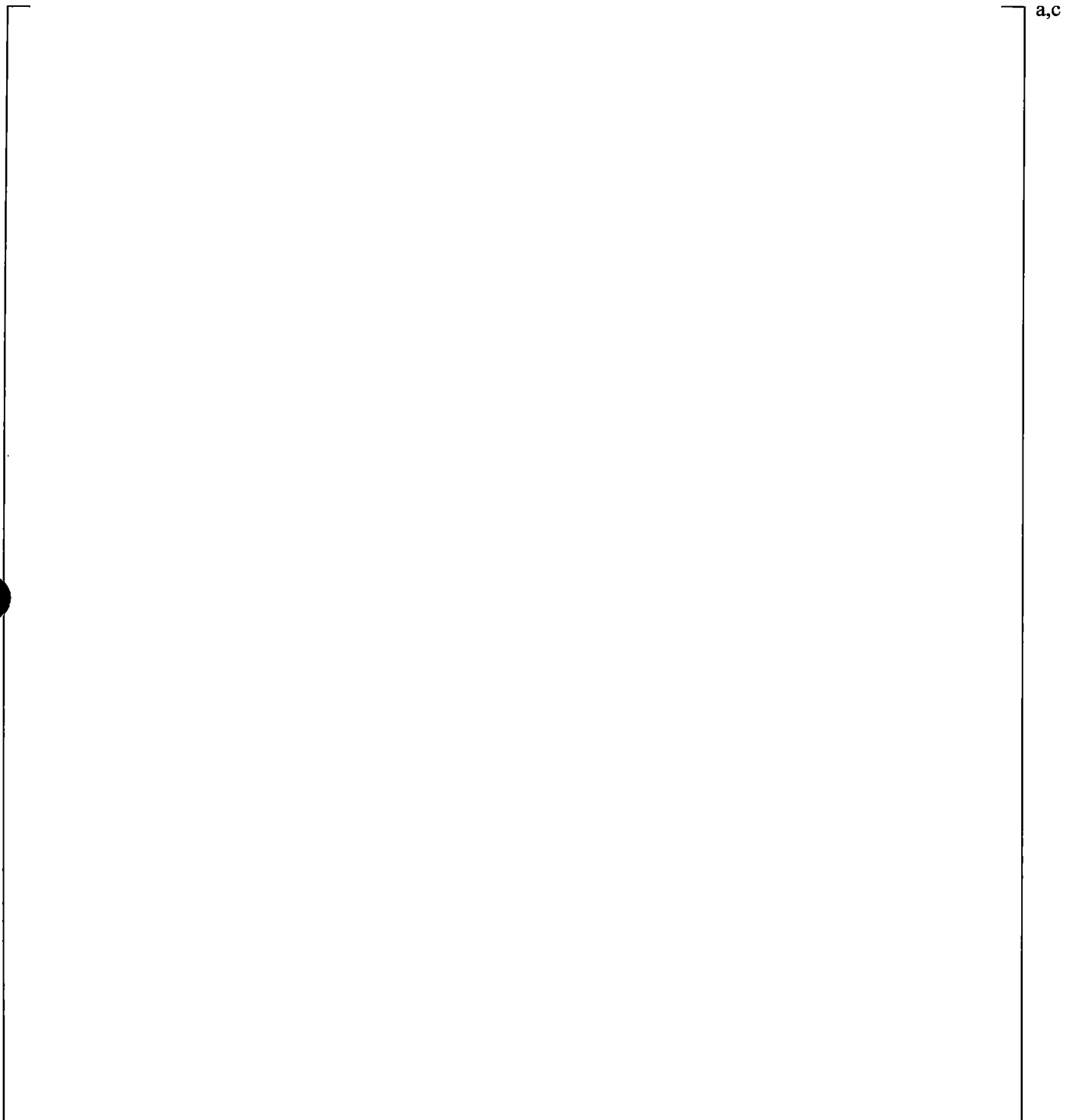


Figure 19.3-163 Predicted Flow Regime Number of Cell Face 7 of Cold Leg

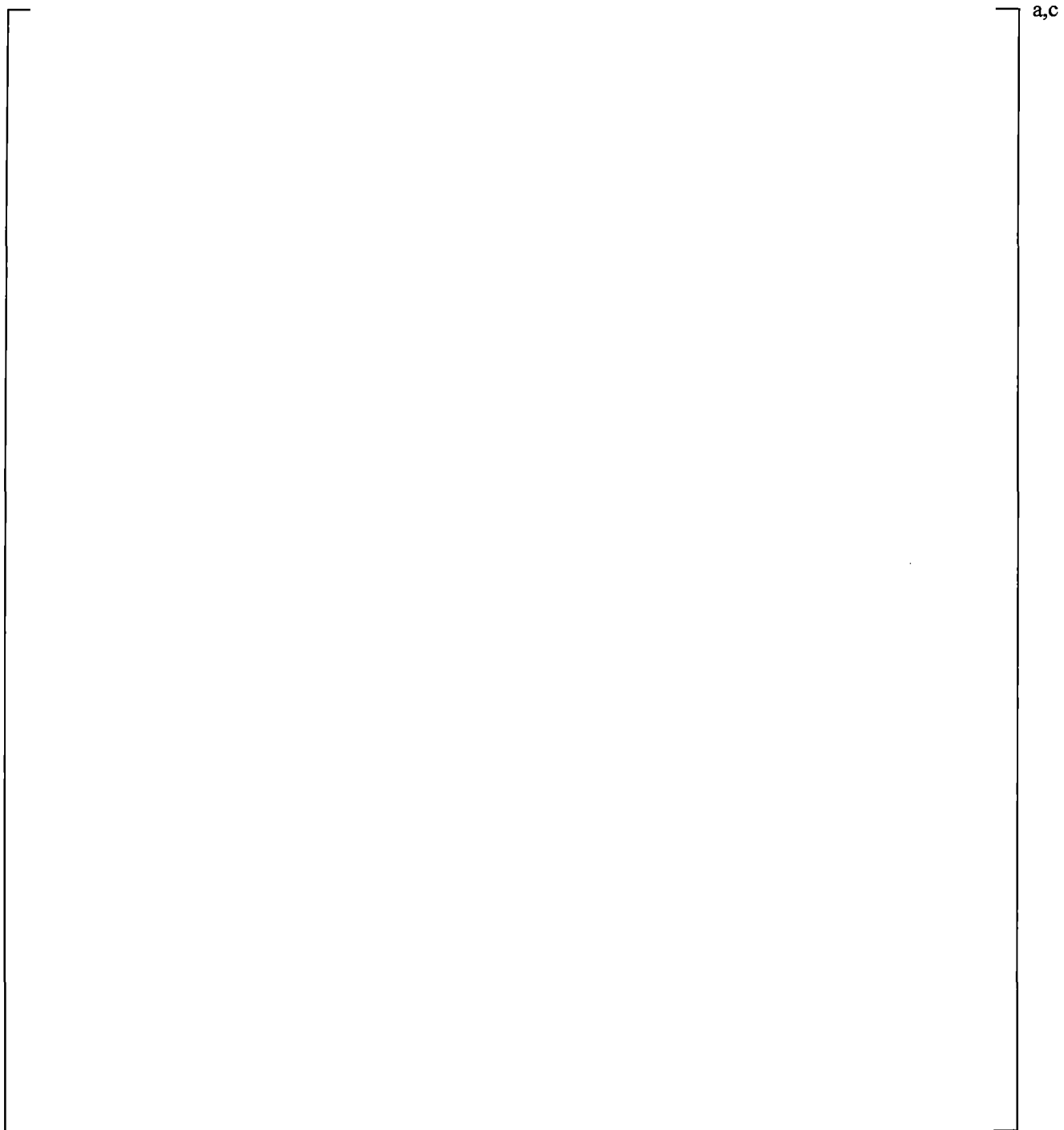


Figure 19.3-164 System Configuration for UPTF Test 25, Phase A (Run 242) and Phase B (Run 241)

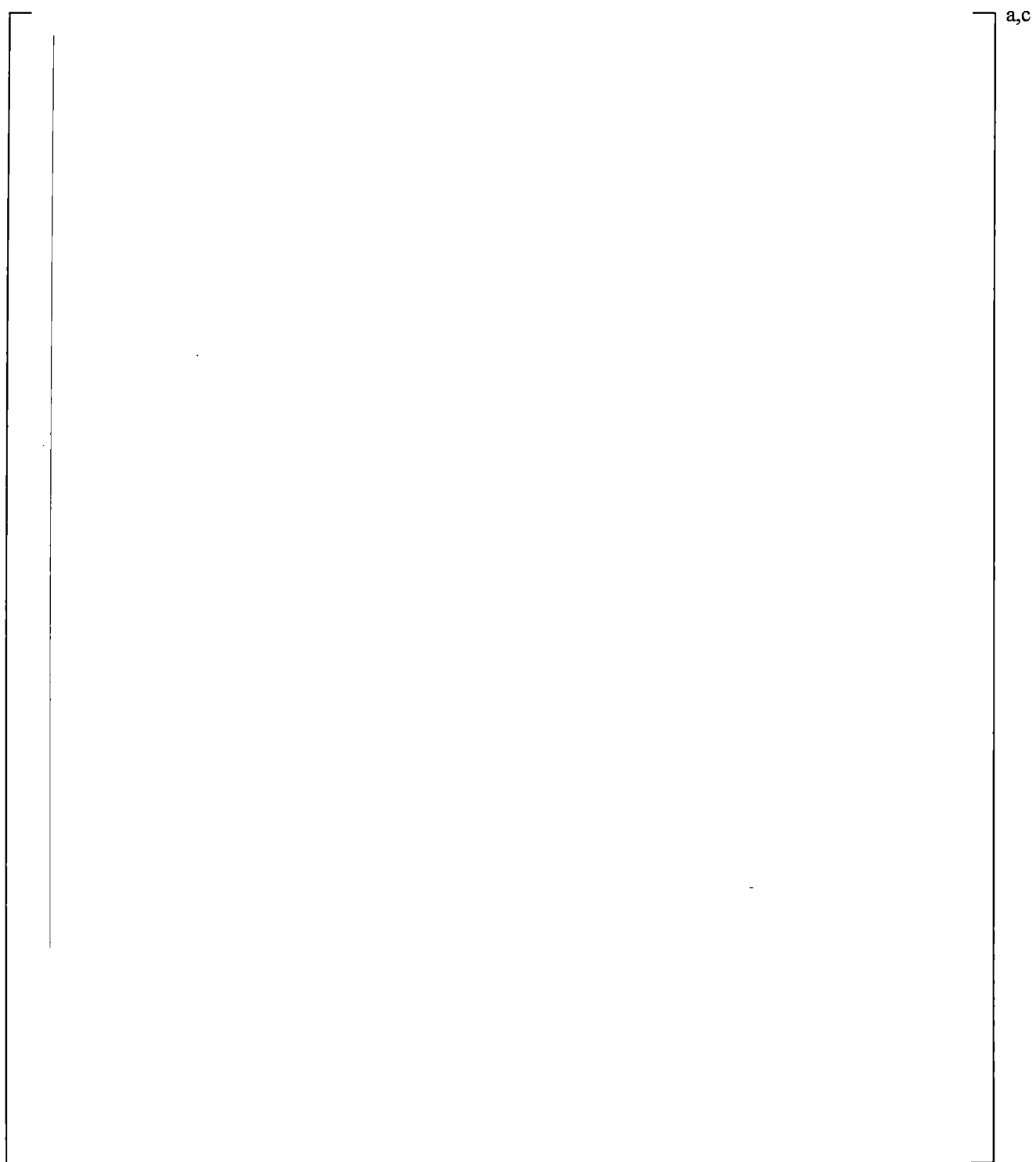


Figure 19.3-165 Steam Flow Rate for UPTF Test 25, Phase A (Run 242)

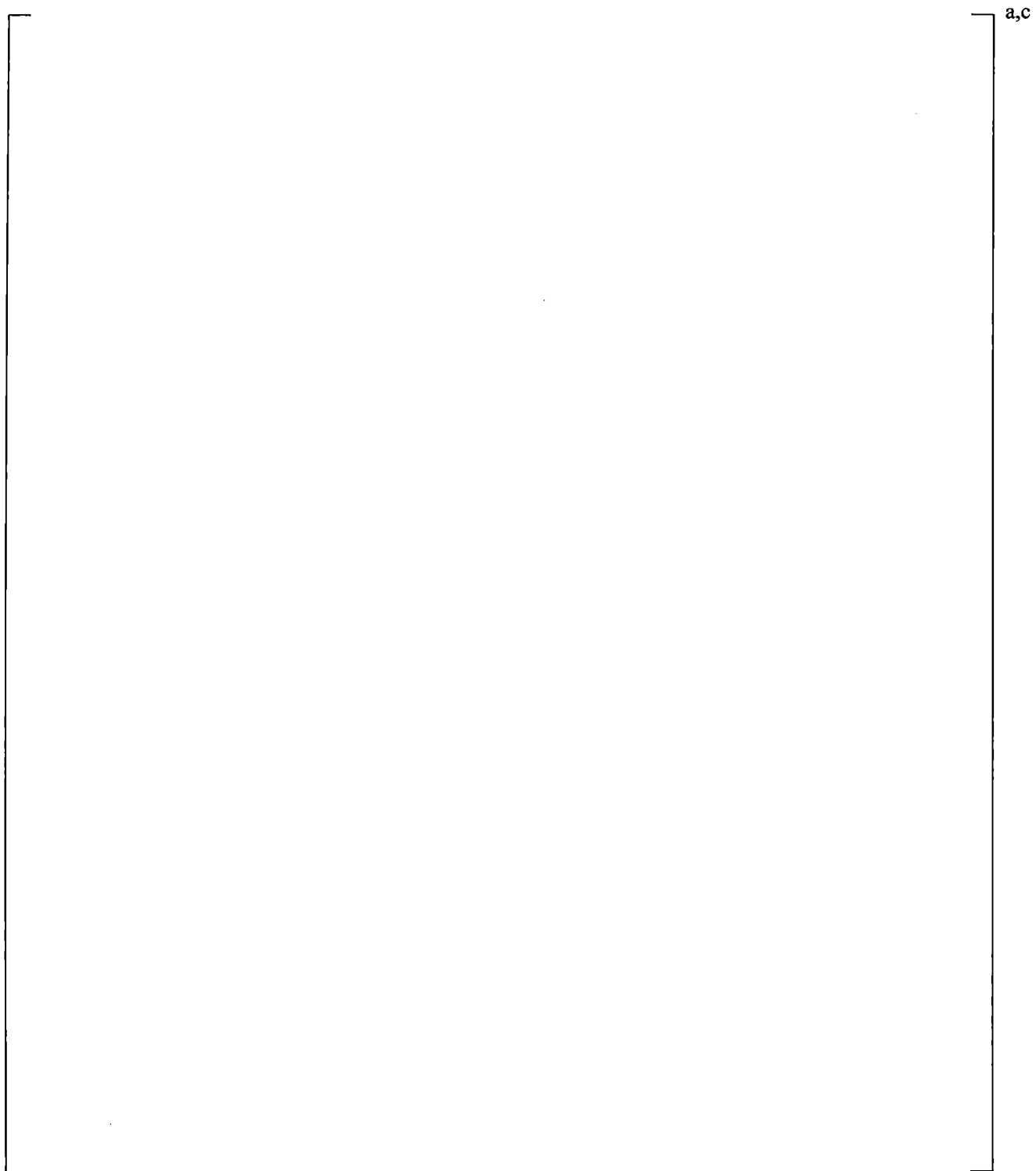


Figure 19.3-166 ECC Flow Rate for UPTF Test 25, Phase A (Run 242)

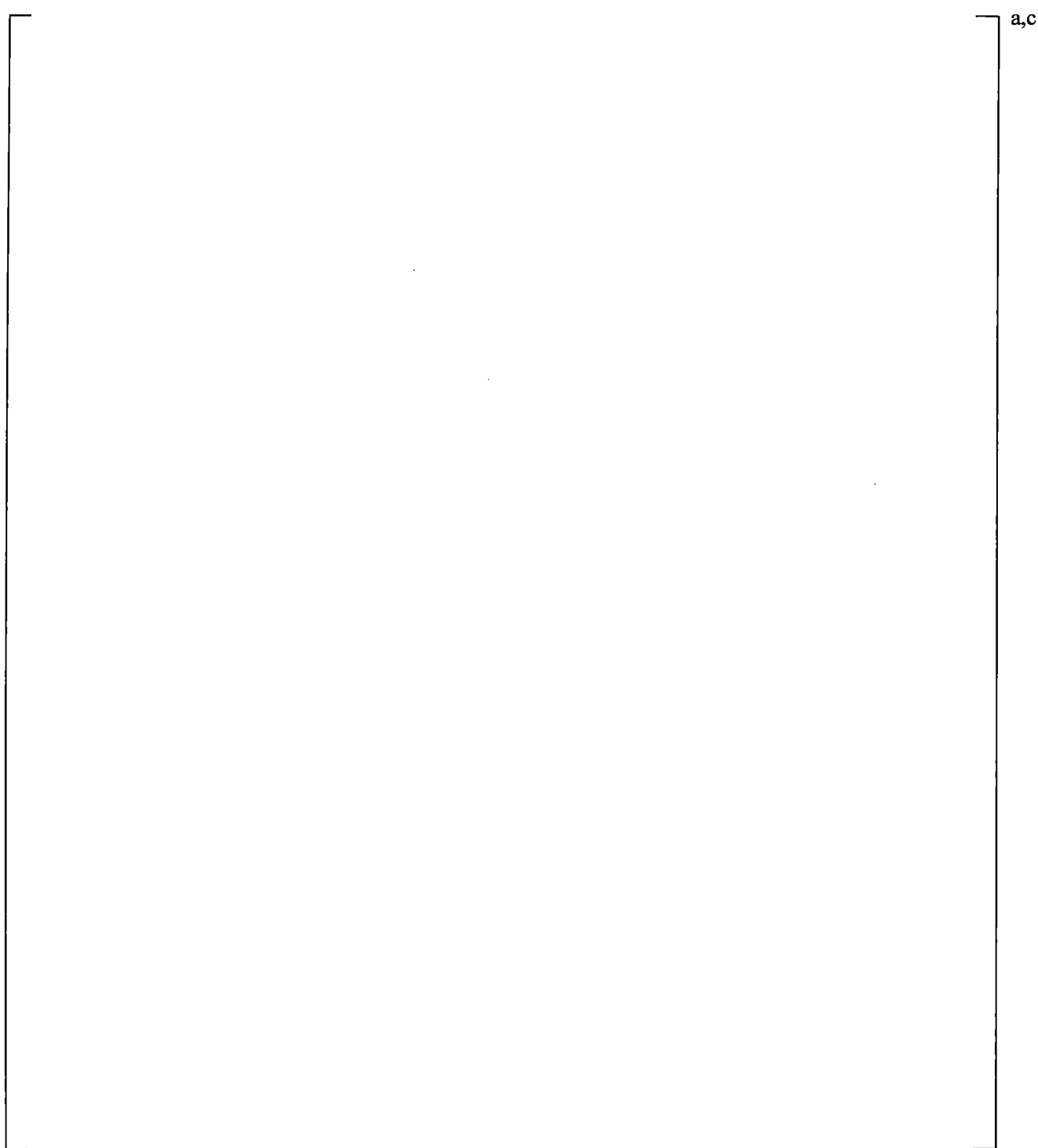


Figure 19.3-167 Drainage Flow Rate for UPTF Test 25, Phase A (Run 242)

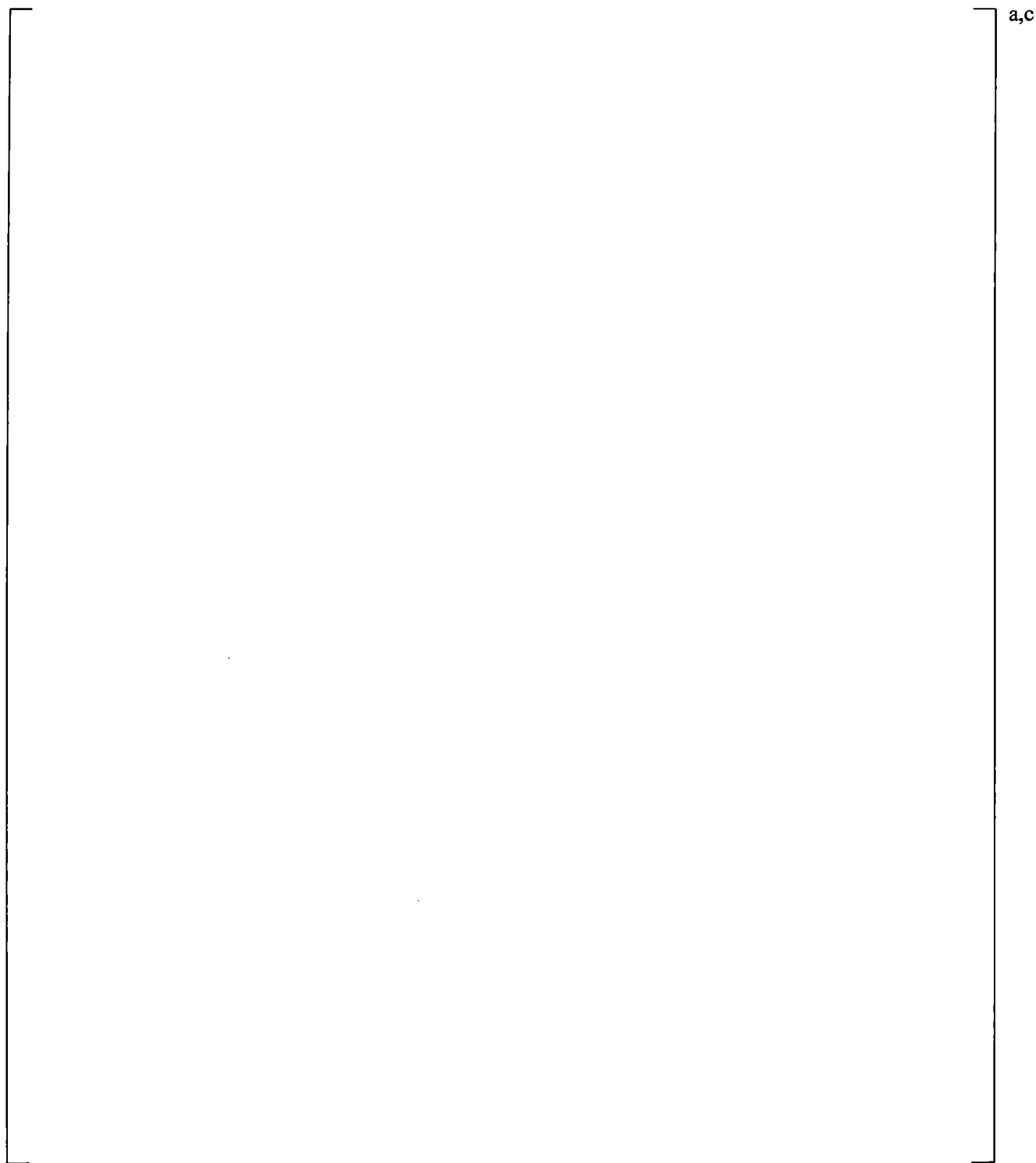


Figure 19.3-168 WCOBRA/TRAC-TF2 Loop Model for UPTF Test 25A

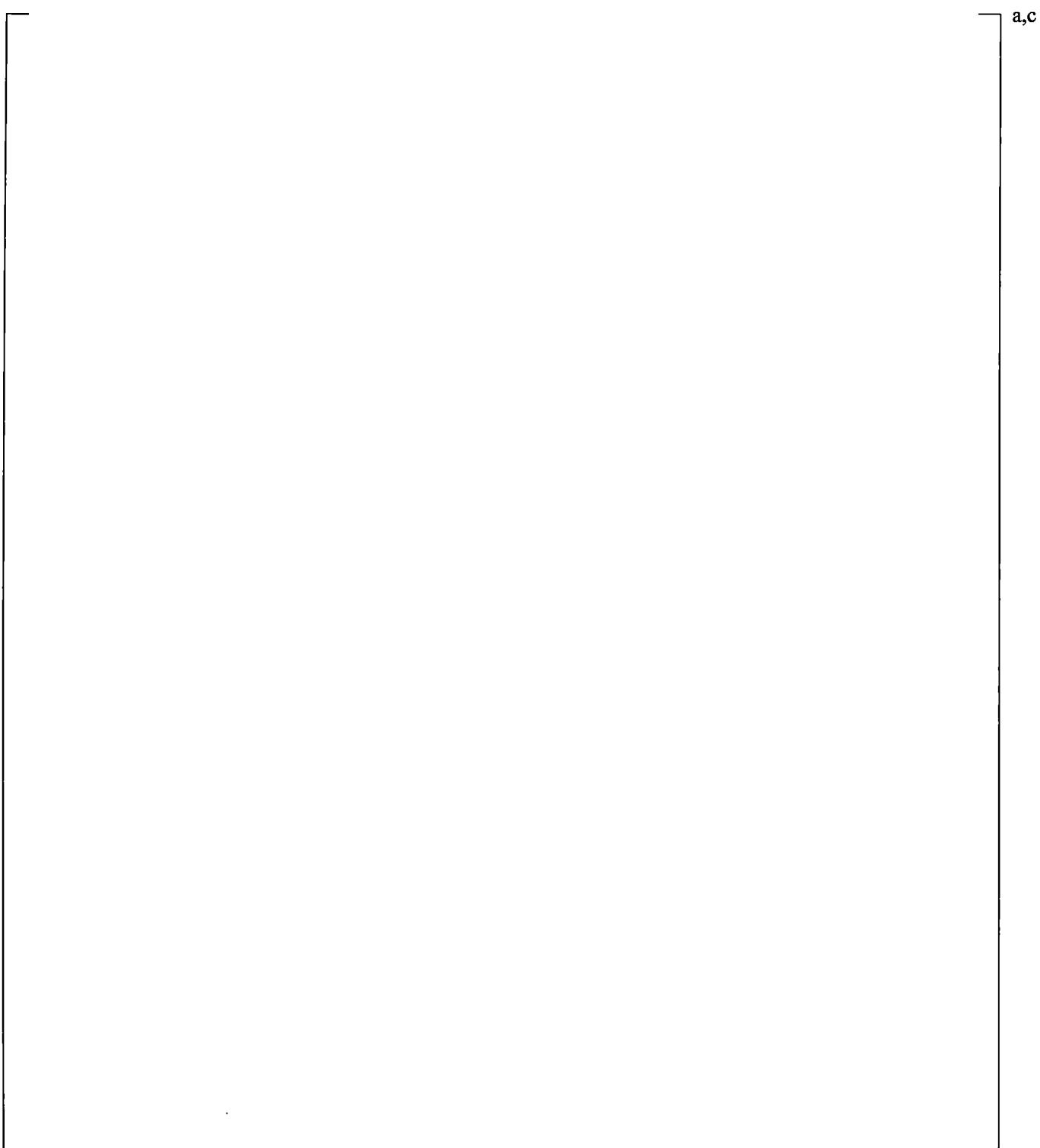


Figure 19.3-169 Absolute Pressure in the Upper Plenum and Downcomer for UPTF Test 25A

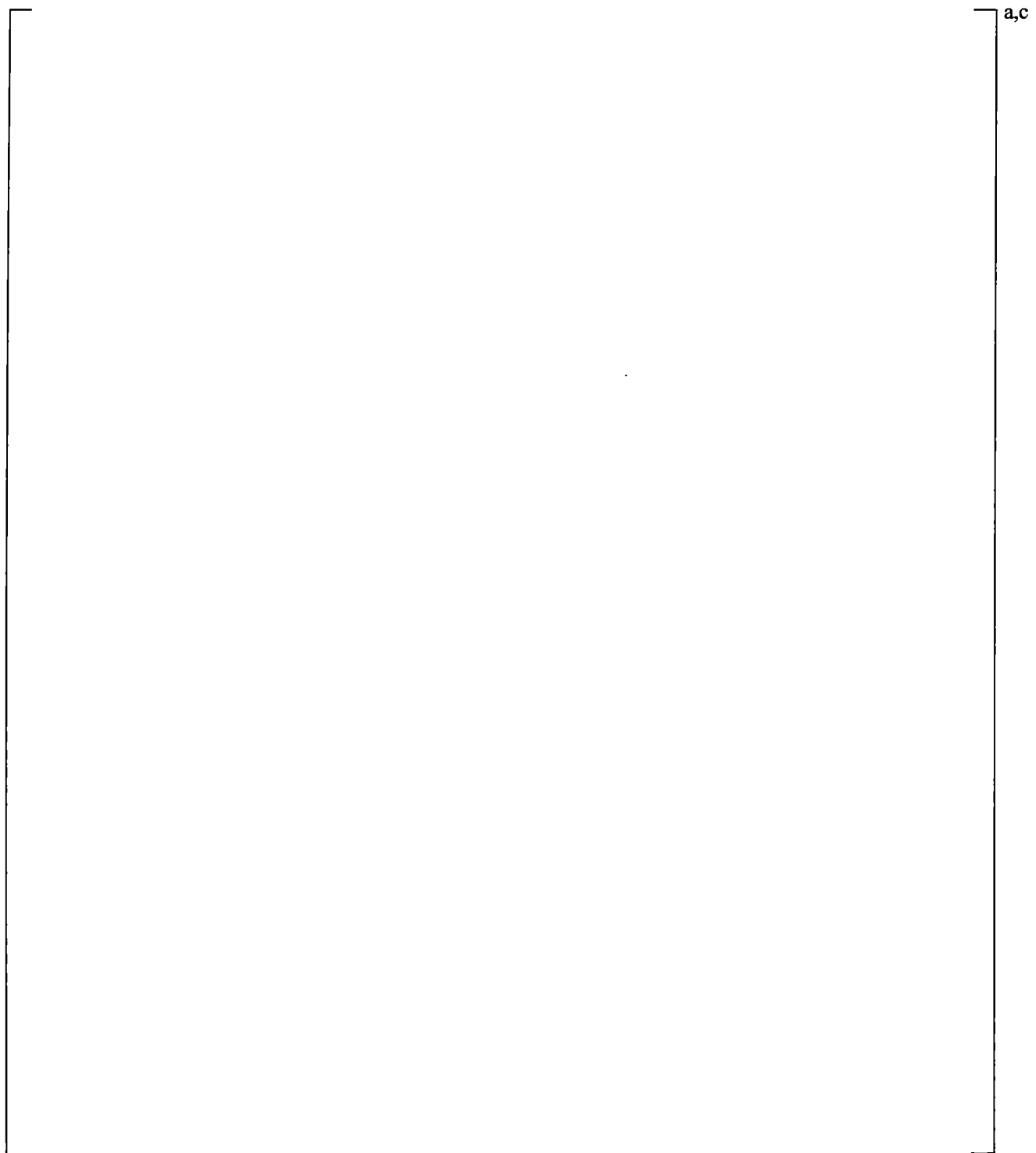


Figure 19.3-170 Measured Downcomer Fluid Temperature at Level 28 for UPTF Test 25A

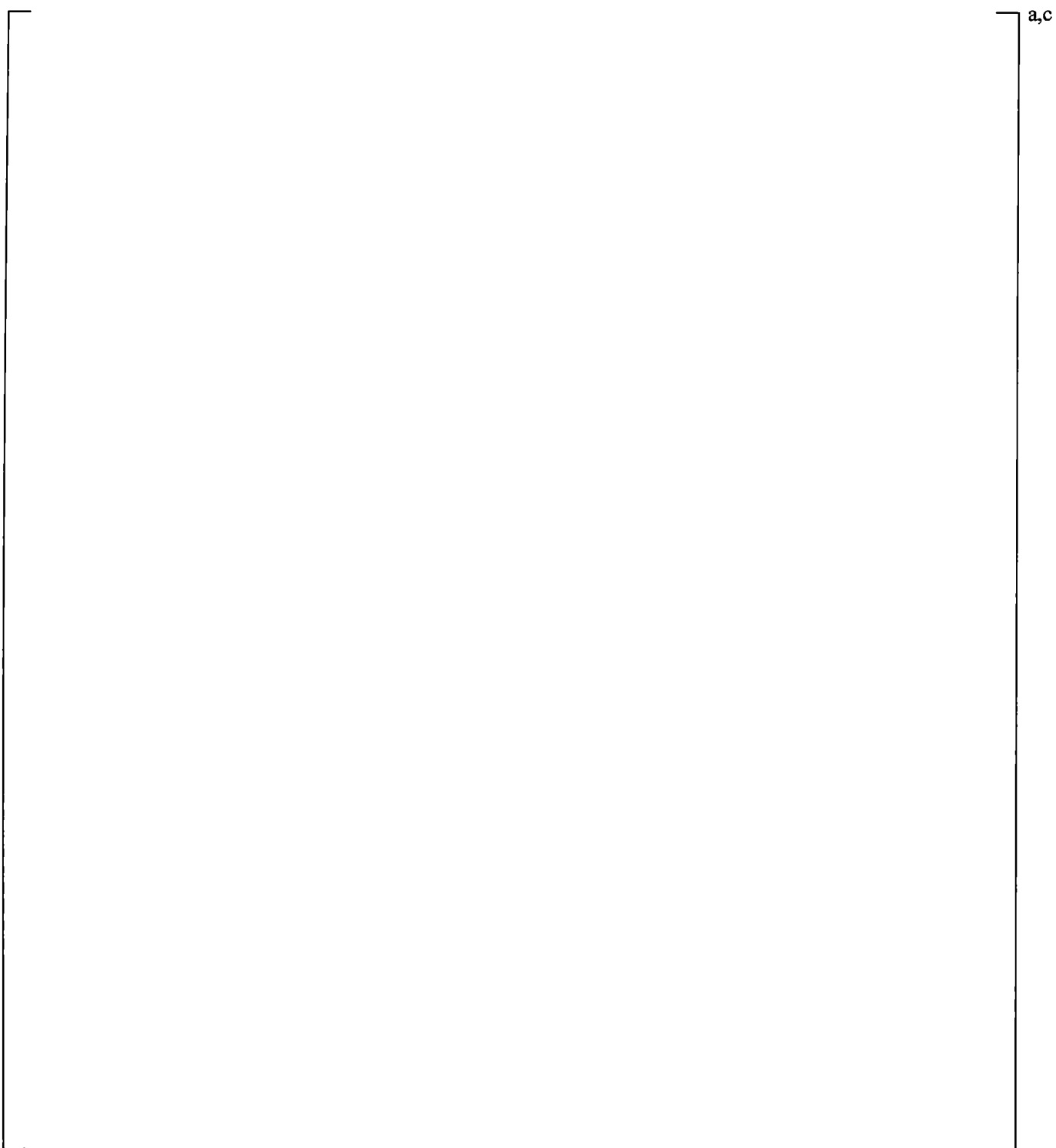


Figure 19.3-171 Predicted Downcomer Fluid (Vapor) Temperature at Level 28 for UPTF Test 25A



Figure 19.3-172 Measured Downcomer Fluid Temperature at Level 24 for UPTF Test 25A



Figure 19.3-173 Predicted Downcomer Fluid (Liquid) Temperature at Level 24 for UPTF Test 25A

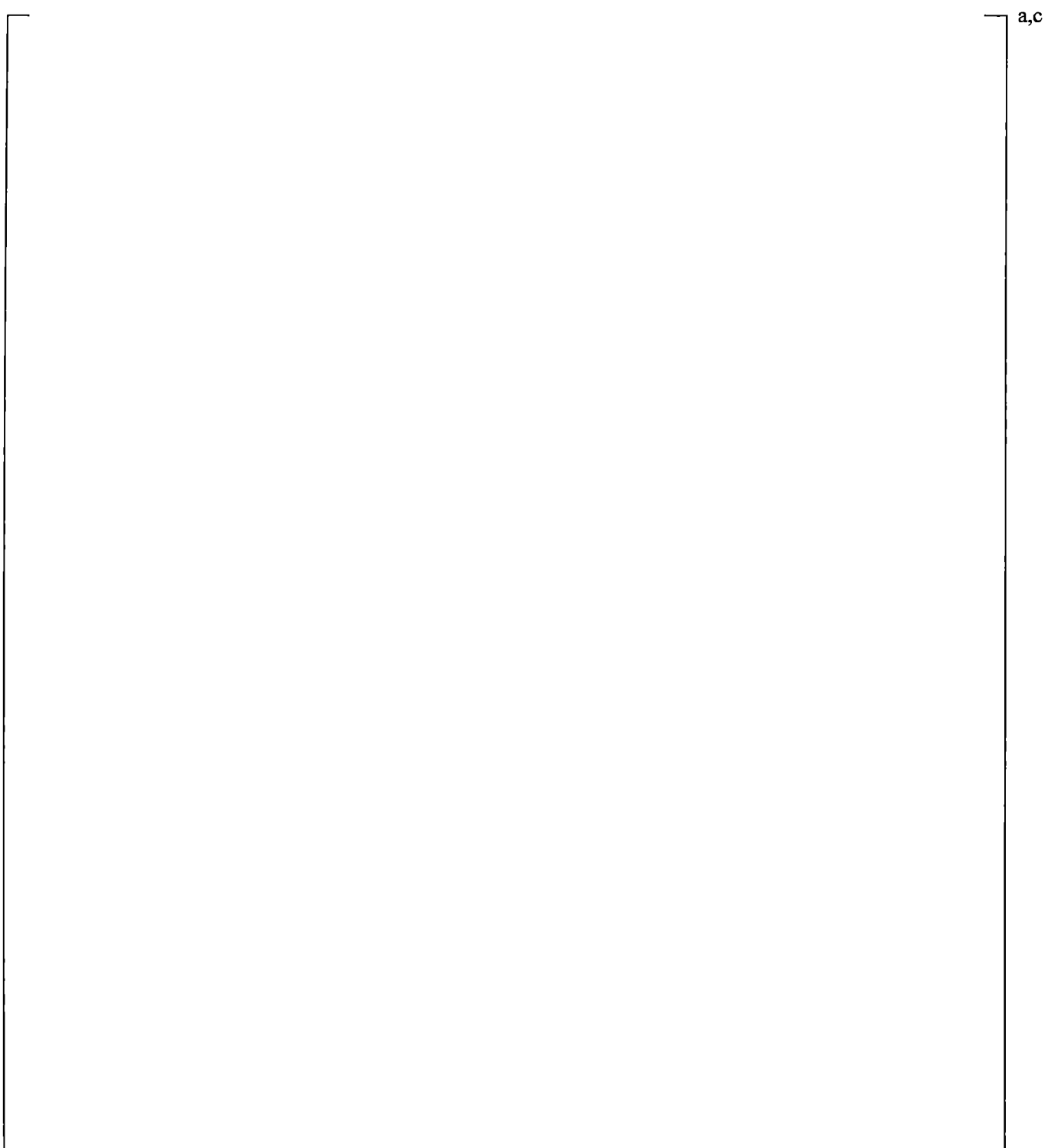


Figure 19.3-174 Differential Pressure between Upper Plenum and Downcomer for UPTF Test 25A

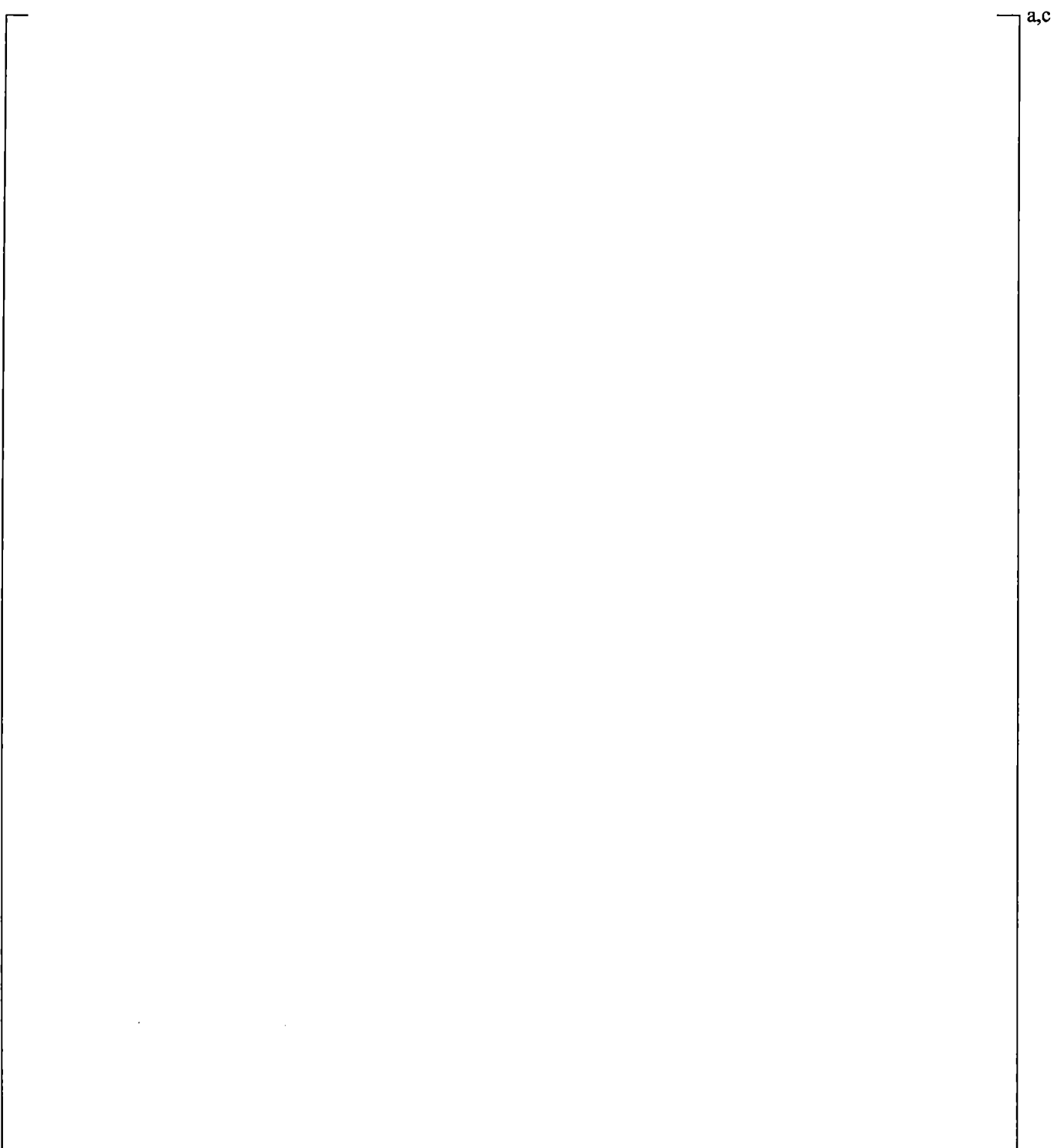


Figure 19.3-175 Axial Differential Pressure in Downcomer for UPTF Test 25A

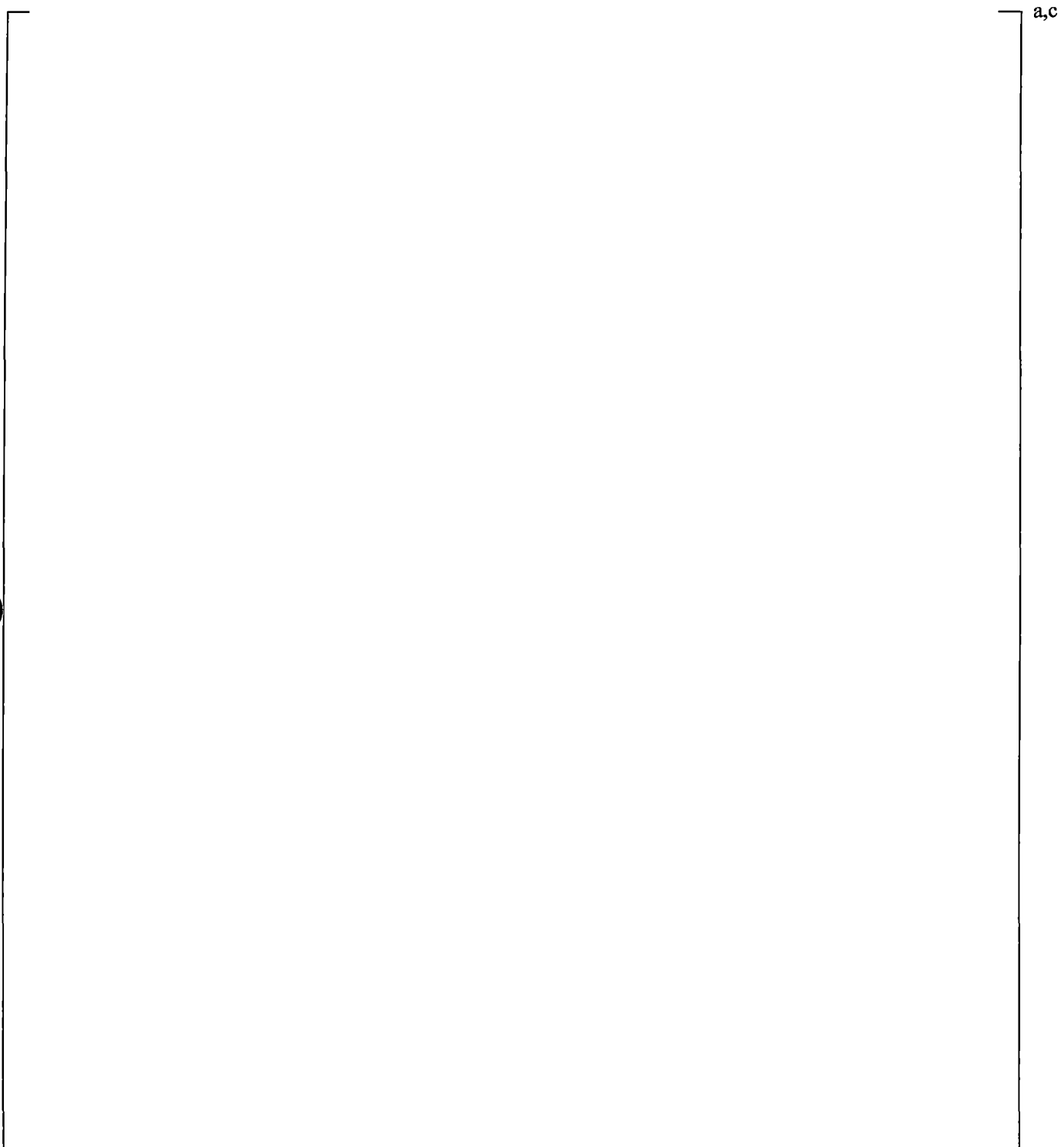


Figure 19.3-176 Axial Differential Pressures in Downcomer for UPTF Test 25A; Curve 2 is in Broken Quadrant and Curves 1, 3 and 4 are in Intact Quadrants

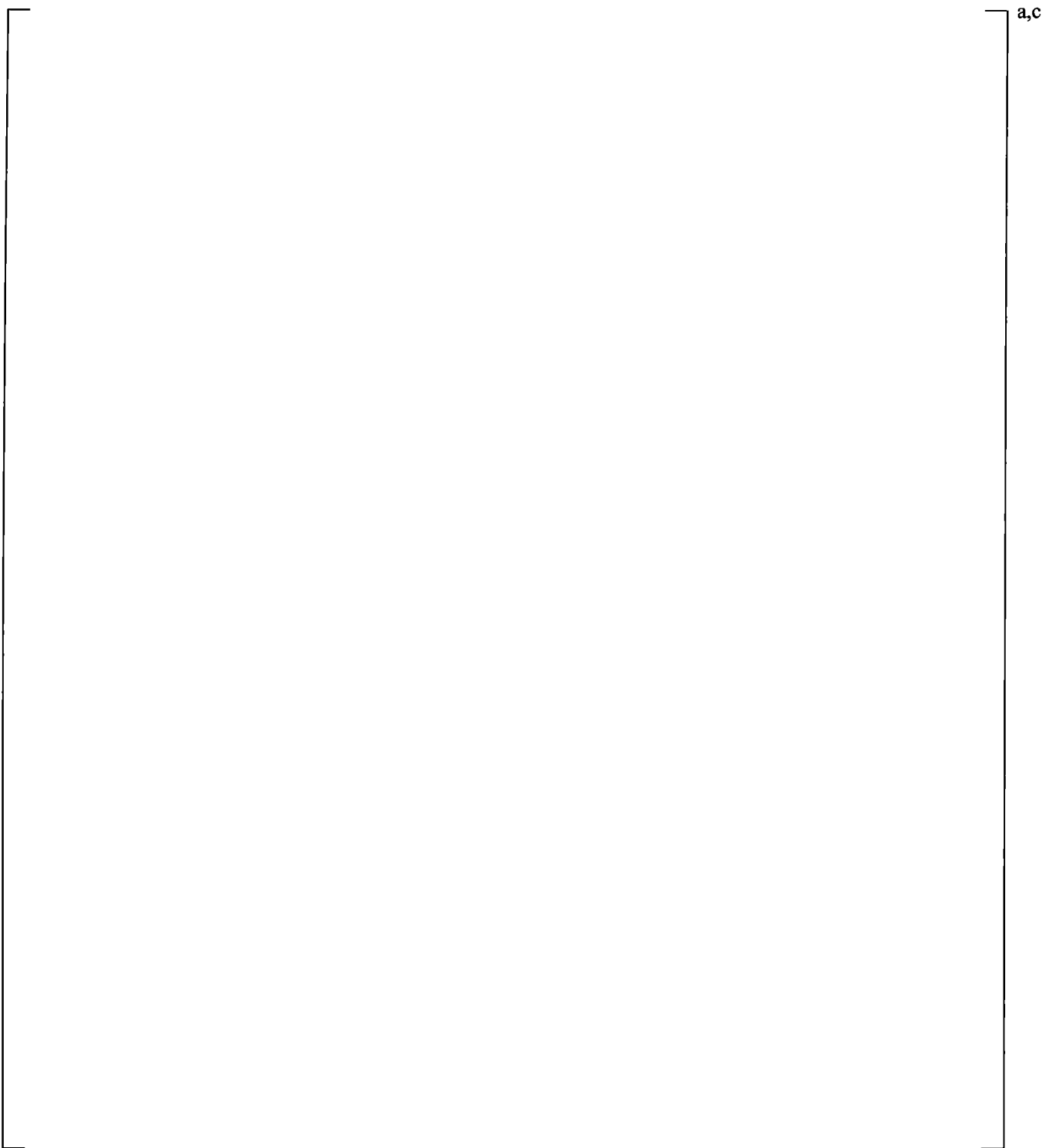


Figure 19.3-177 Broken Loop Steam Flow Rate for UPTF Test 25A

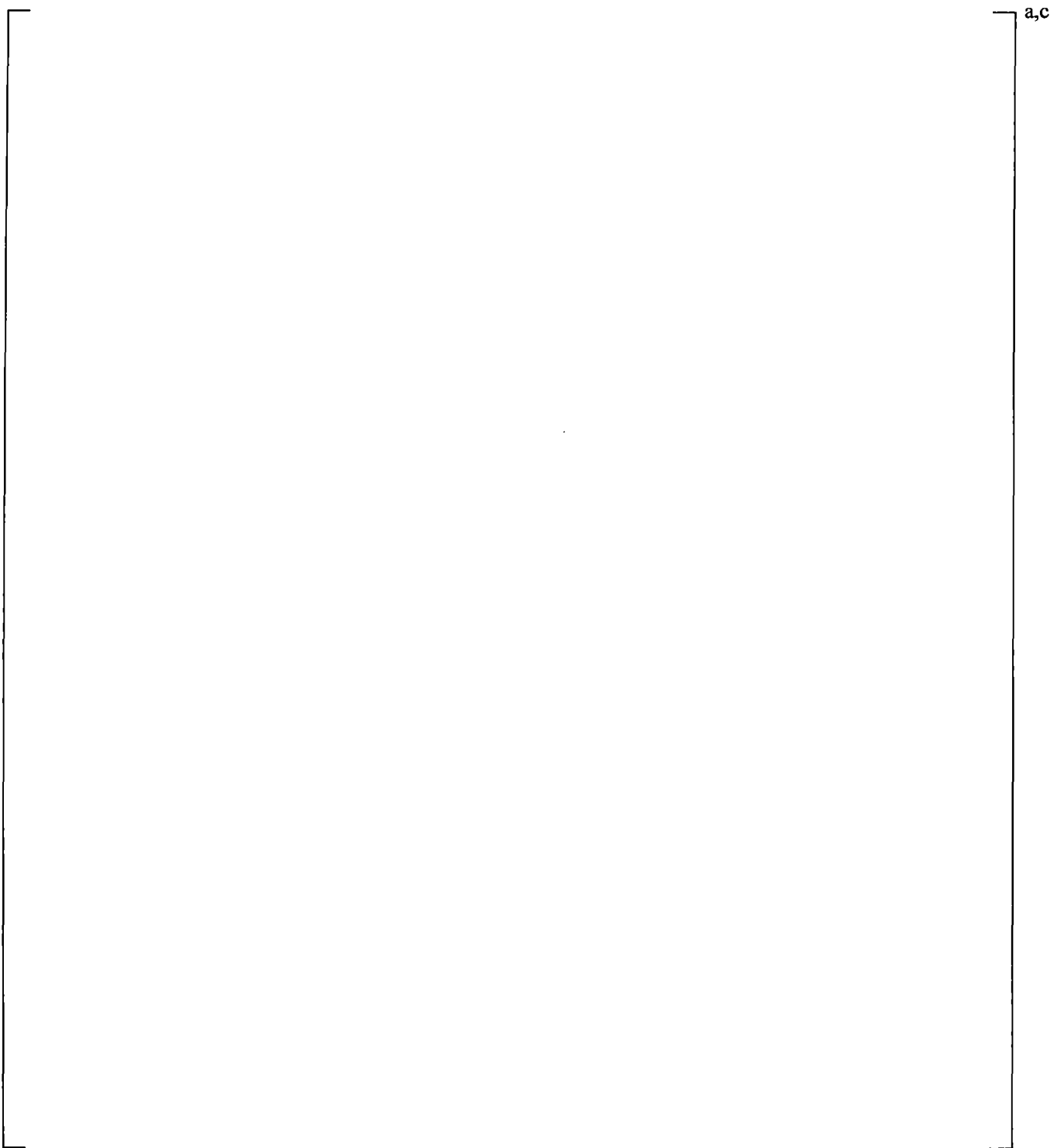


Figure 19.3-178 Broken Loop Liquid Flow Rate for UPTF Test 25A

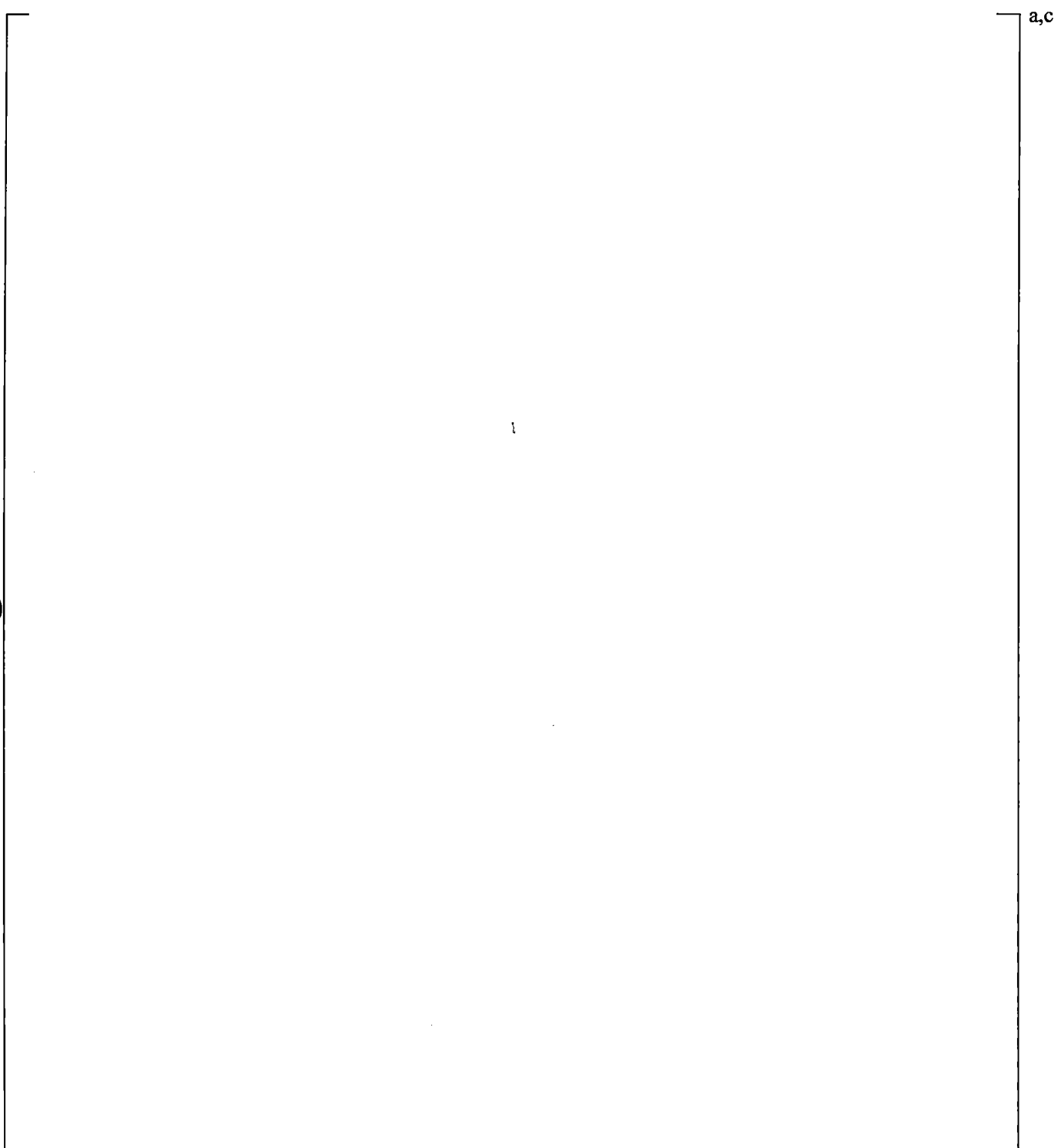


Figure 19.3-179 Void Height versus Steam Flow Rate for UPTF Test 25A

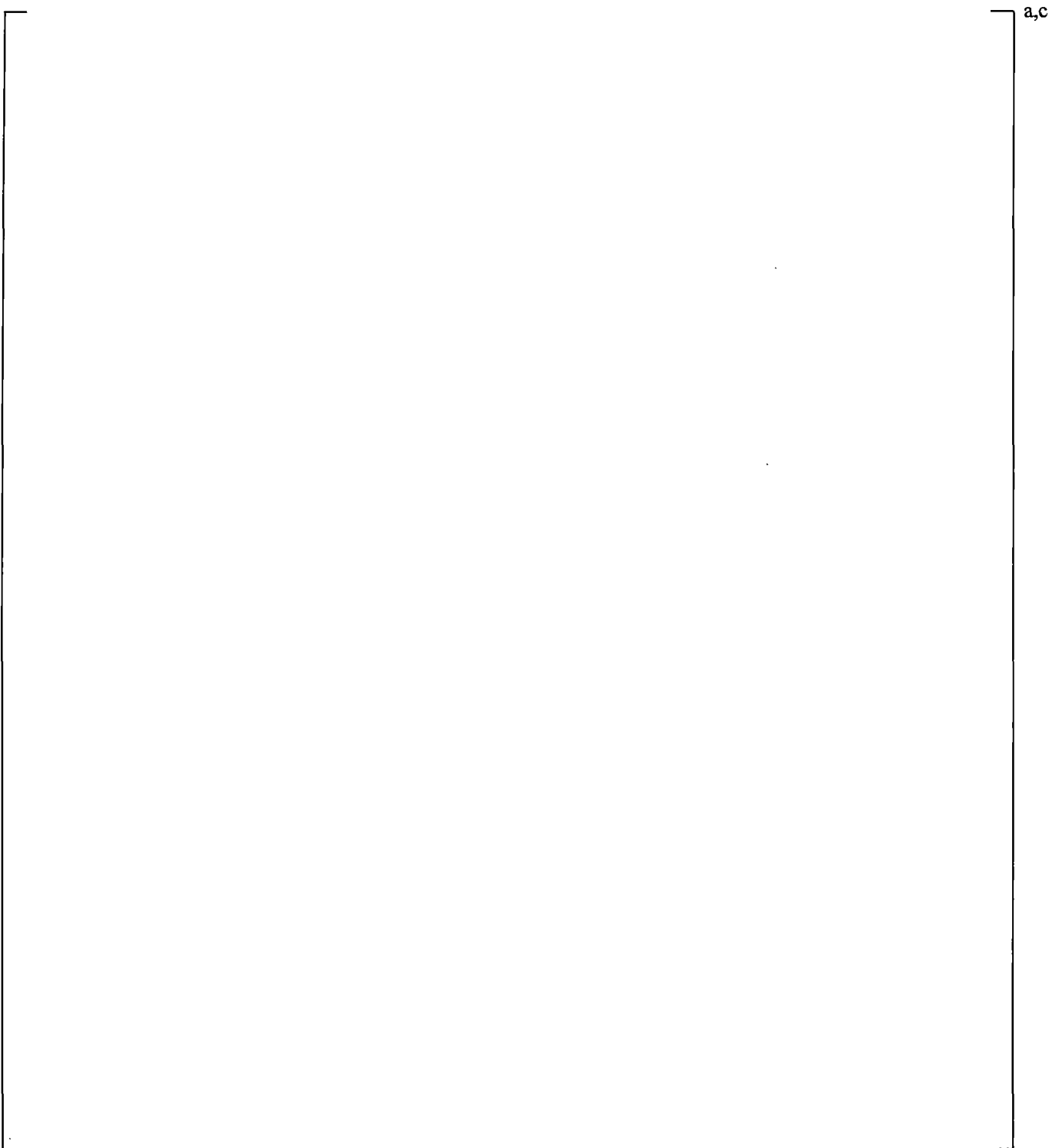


Figure 19.3-180 Cold Leg Temperature near ECC Injection for UPTF Test 25A

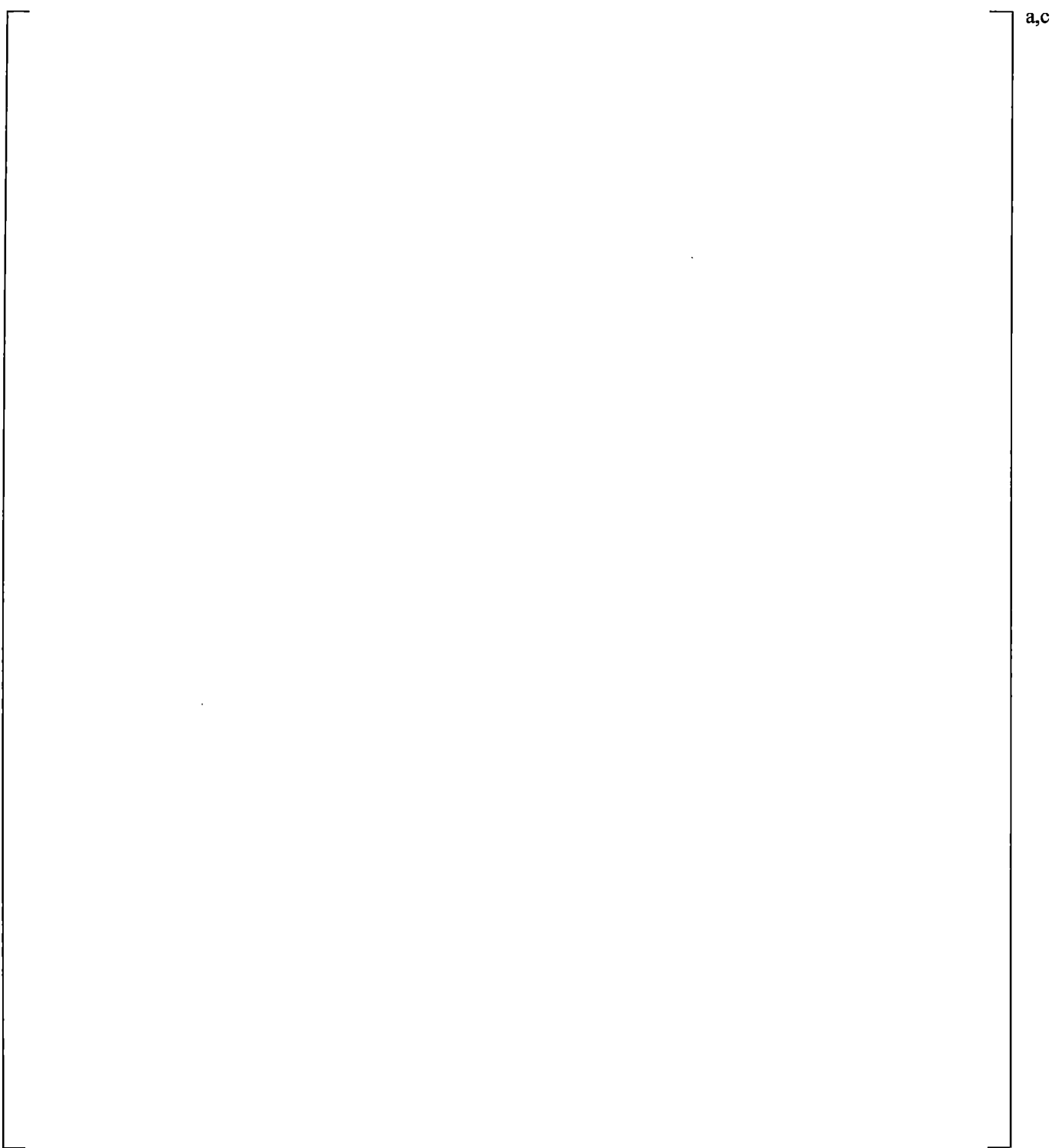


Figure 19.3-181 Cold Leg Temperature Downstream of ECC Injection for UPTF Test 25A

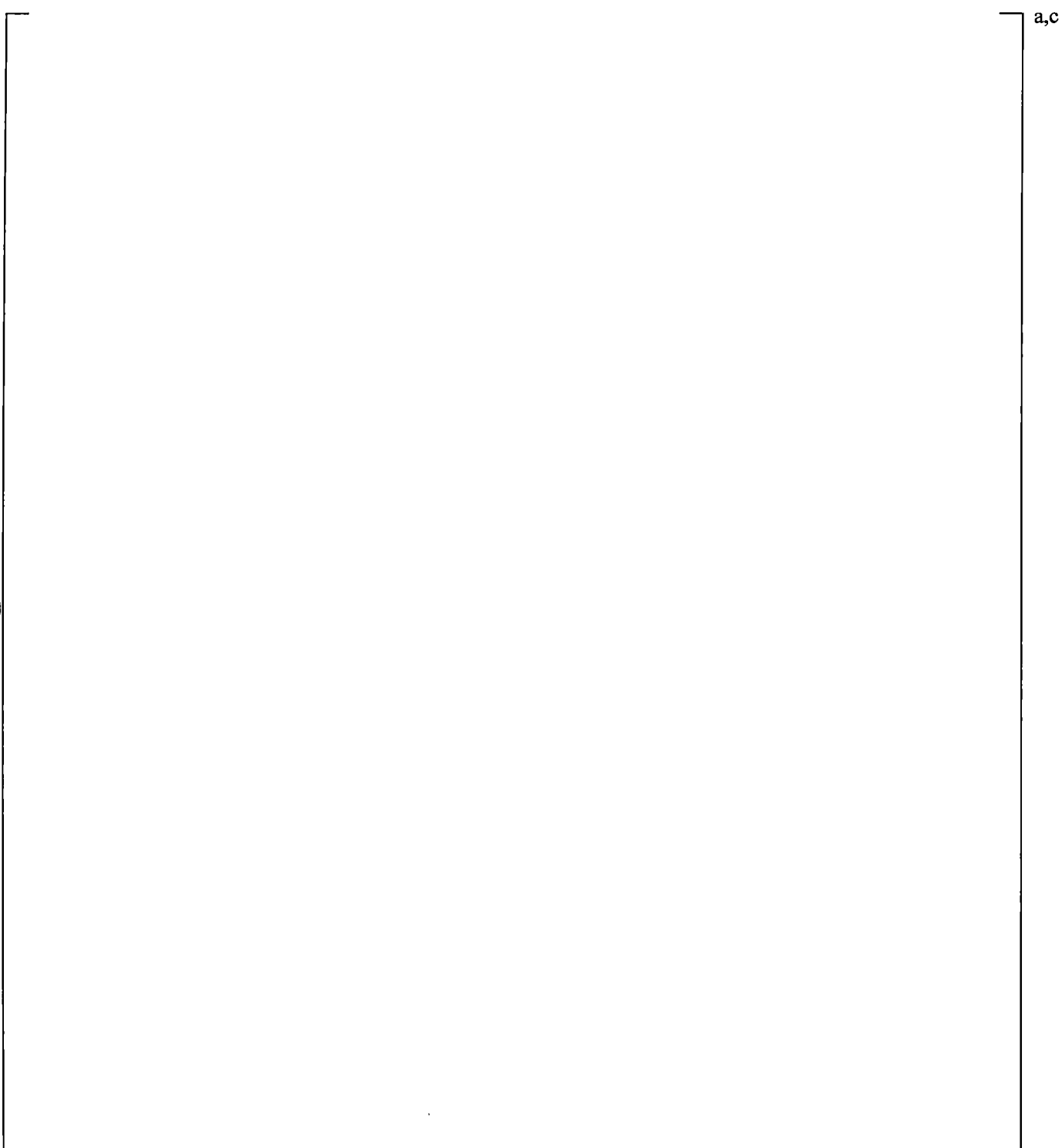


Figure 19.3-182 Cold Leg Temperature at Exit of Cold Leg for UPTF Test 25A

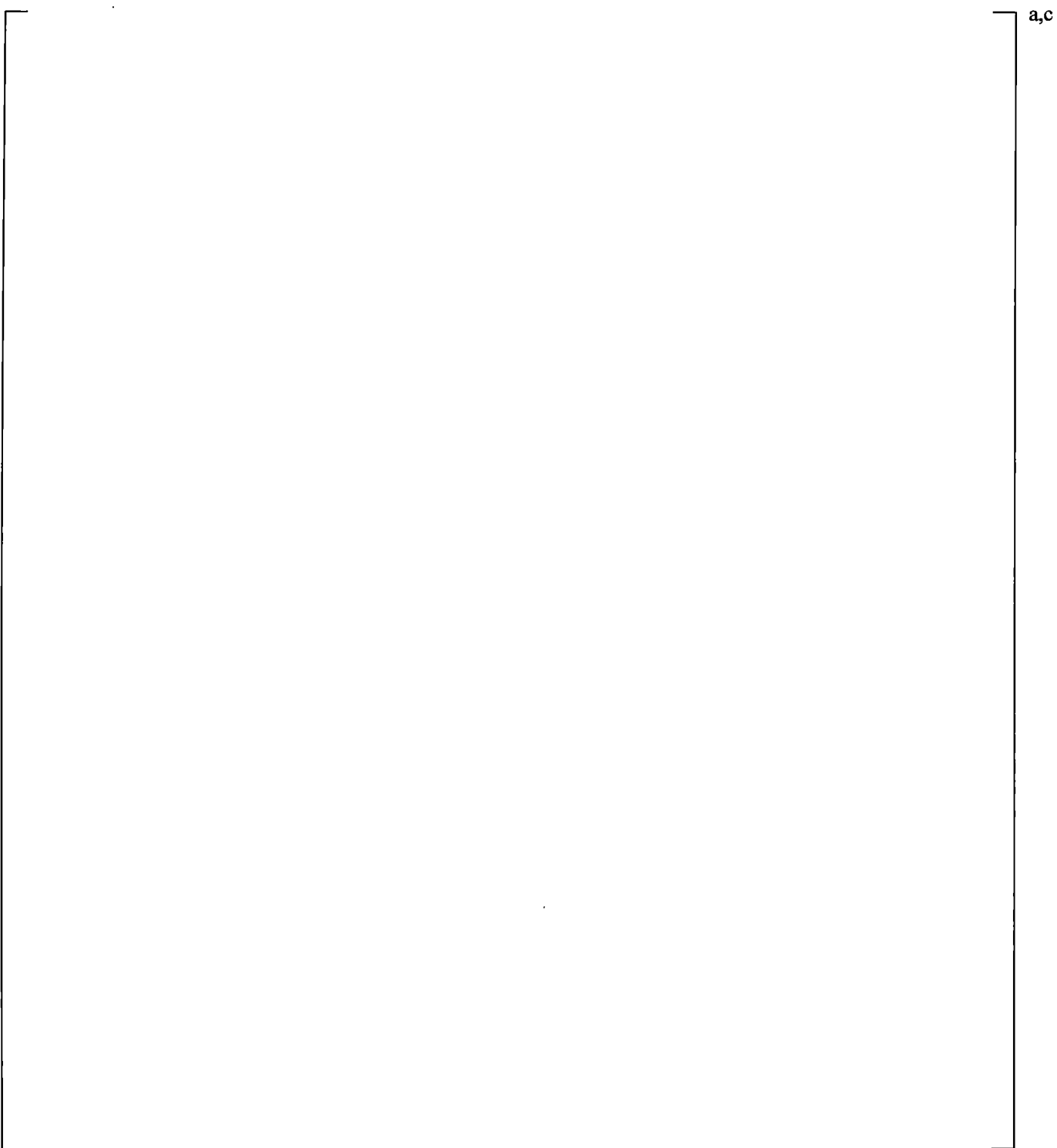


Figure 19.3-183 Cold Leg Temperature near ECC Injection for UPTF Test 25A with KCOSI=0.5

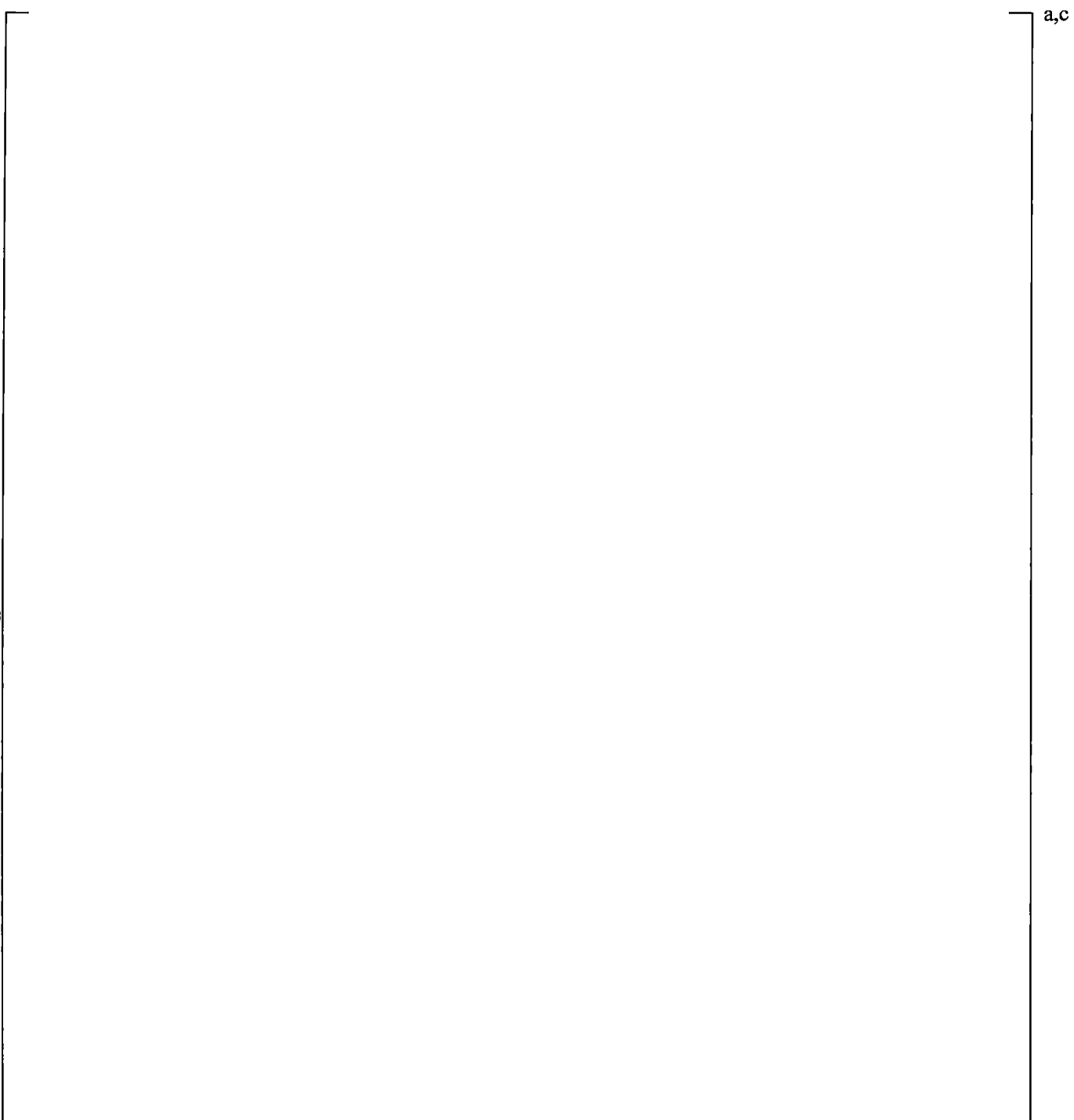


Figure 19.3-184 Cold Leg Temperature Downstream of ECC Injection for UPTF Test 25A with KCOSI=0.5

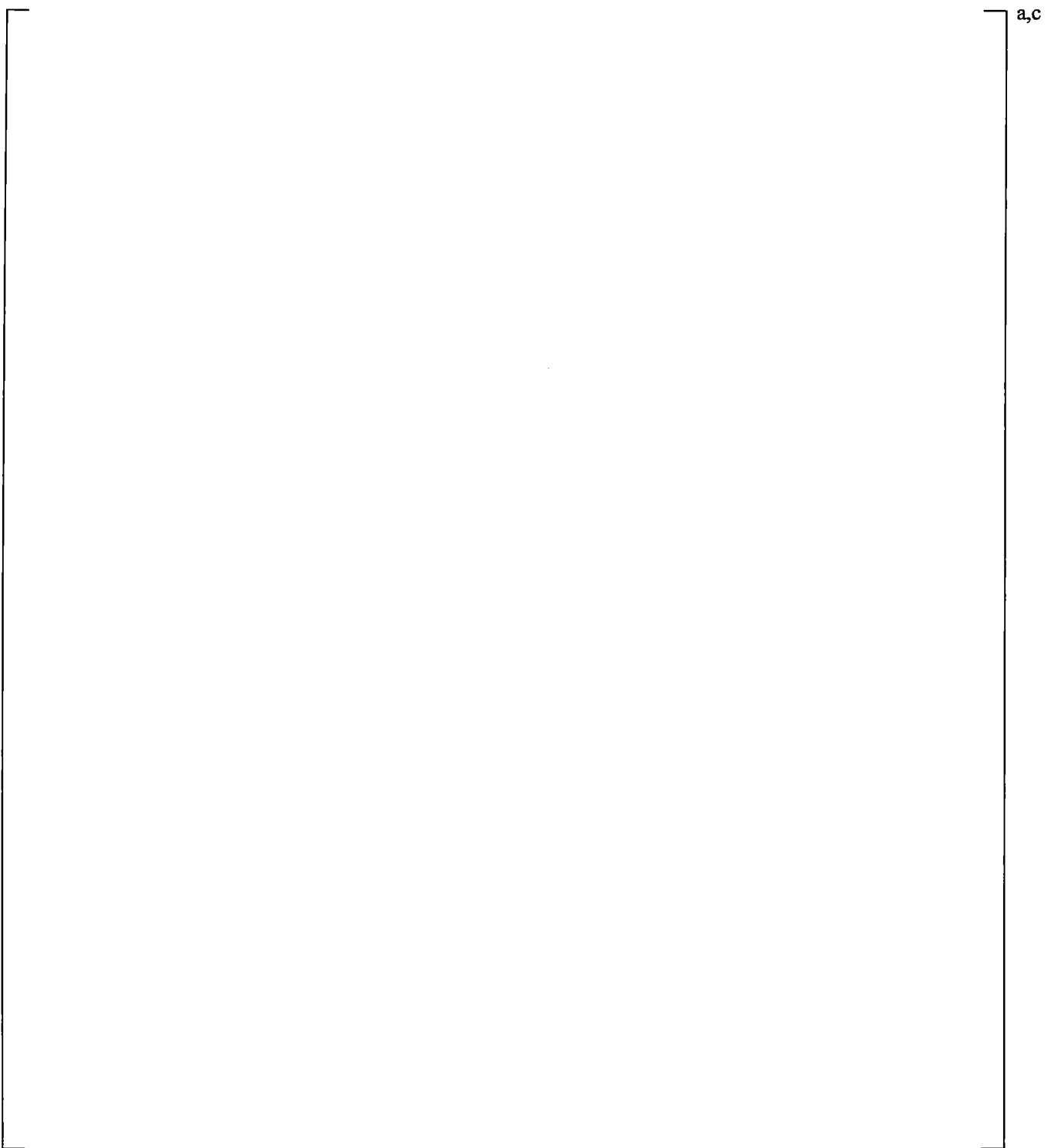


Figure 19.3-185 Cold Leg Temperature at Exit of Cold Leg for UPTF Test 25A with KCOSI=0.5

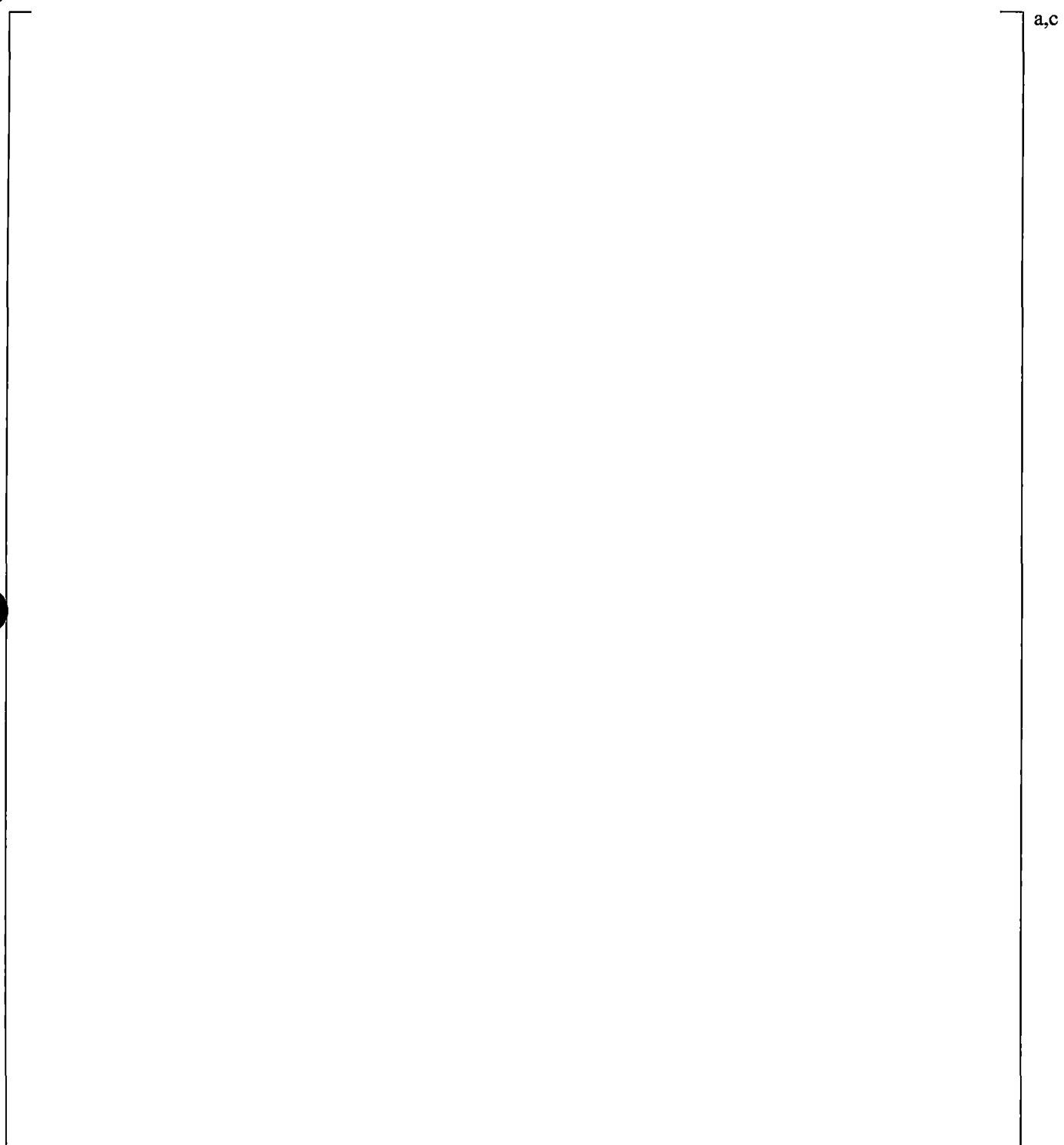


Figure 19.3-186 Axial Differential Pressures in Downcomer for UPTF Test 25A with KCOSI=0.5

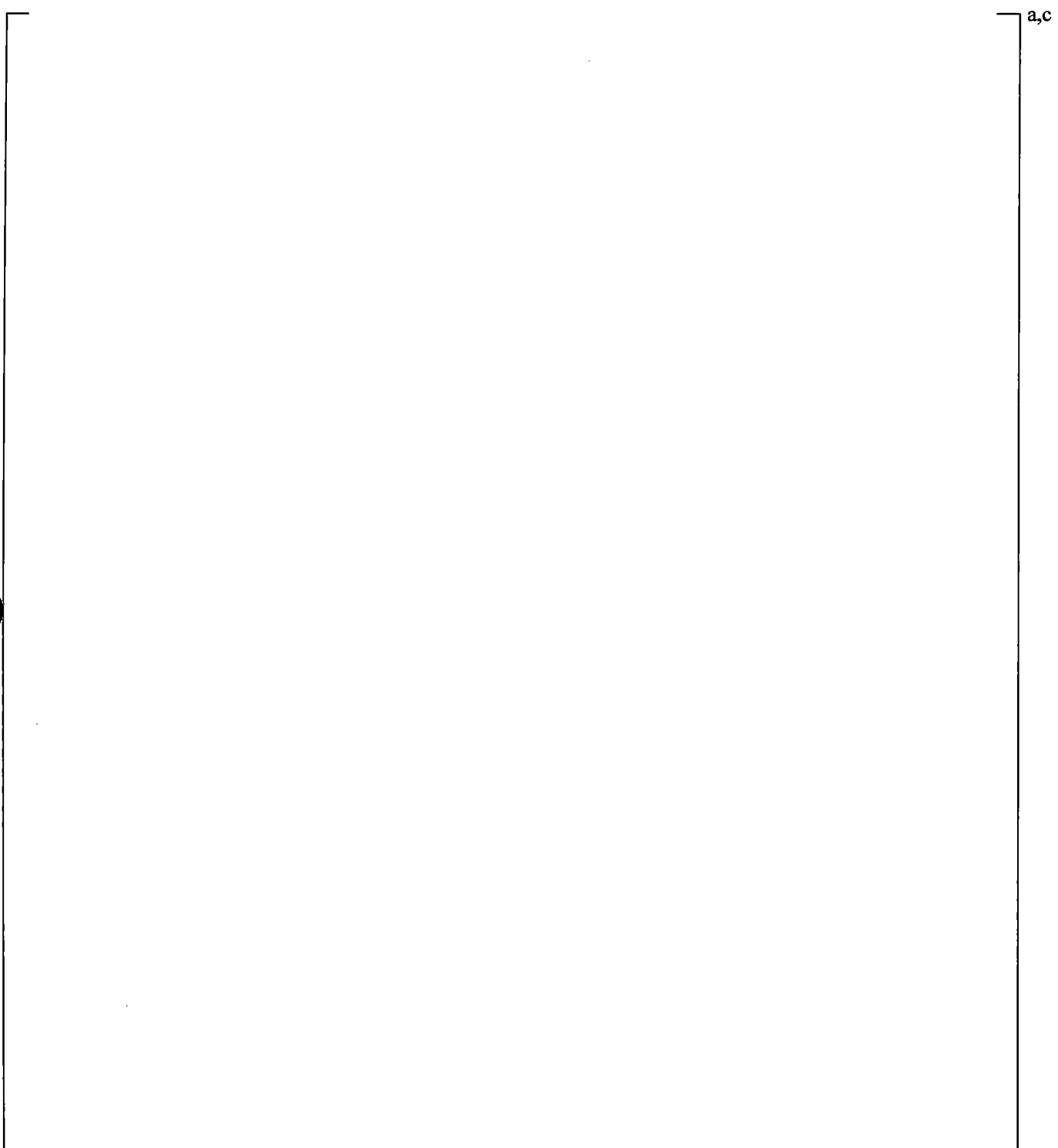


Figure 19.3-187 Broken Loop Steam Flow Rate for UPTF Test 25A with KCOSI=0.5

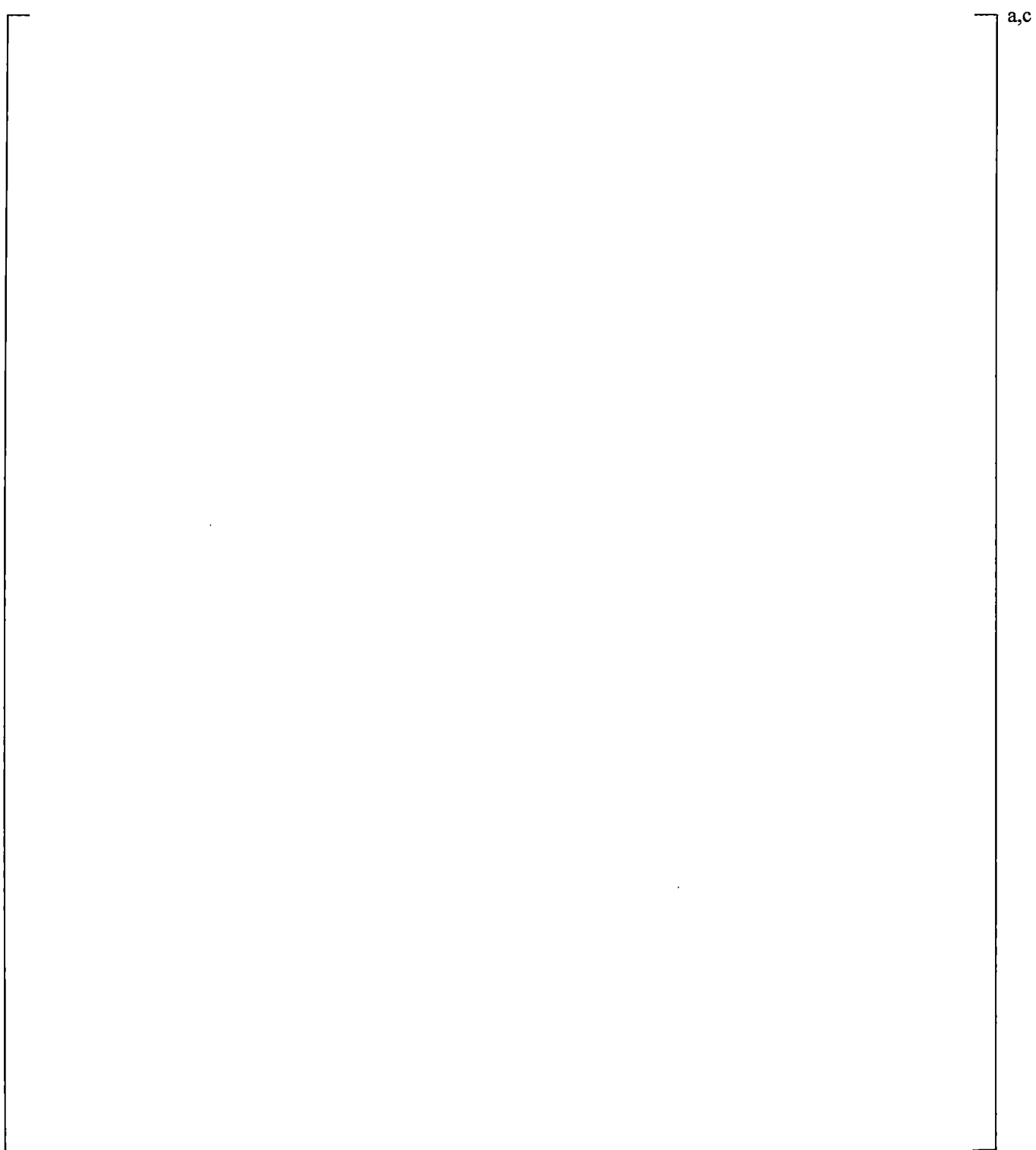
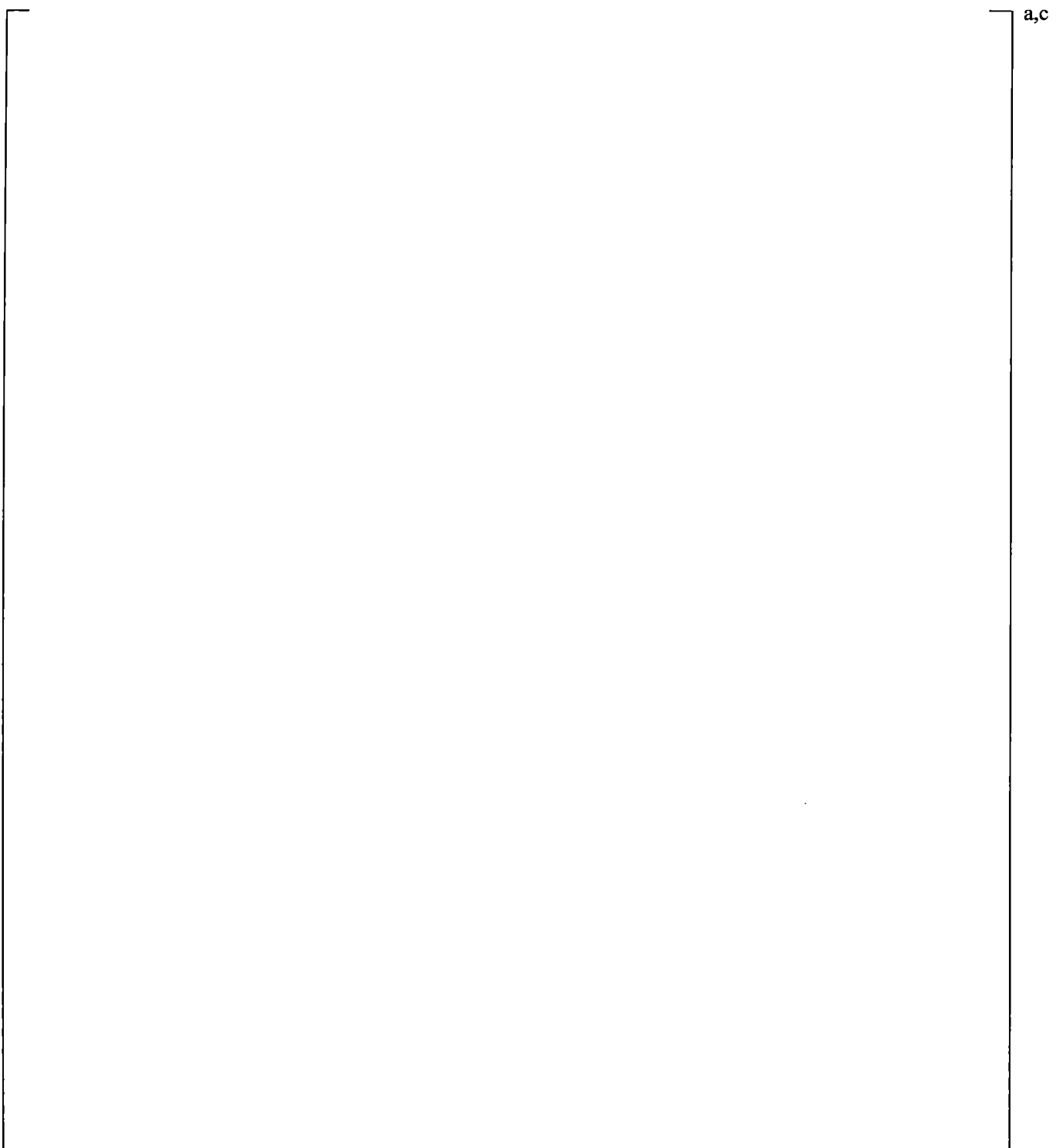


Figure 19.3-188 Broken Loop Liquid Flow Rate for UPTF Test 25A with KCOSI=0.5



**Figure 19.3-189 Differential Pressure between Upper Plenum and Downcomer for UPTF Test 25A
with XC=0.4**

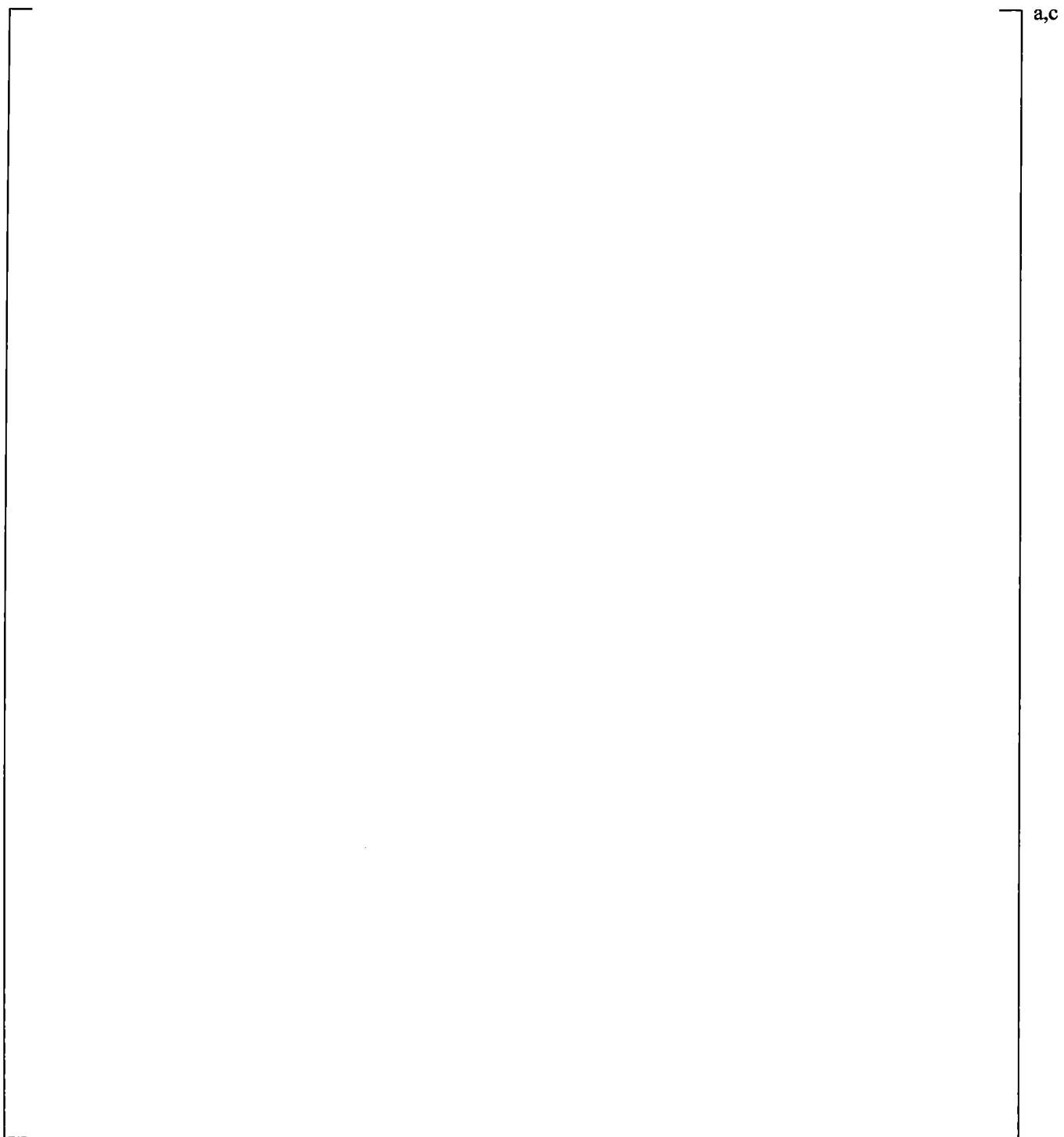


Figure 19.3-190 Axial Differential Pressure in Downcomer for UPTF Test 25A with XC=0.4

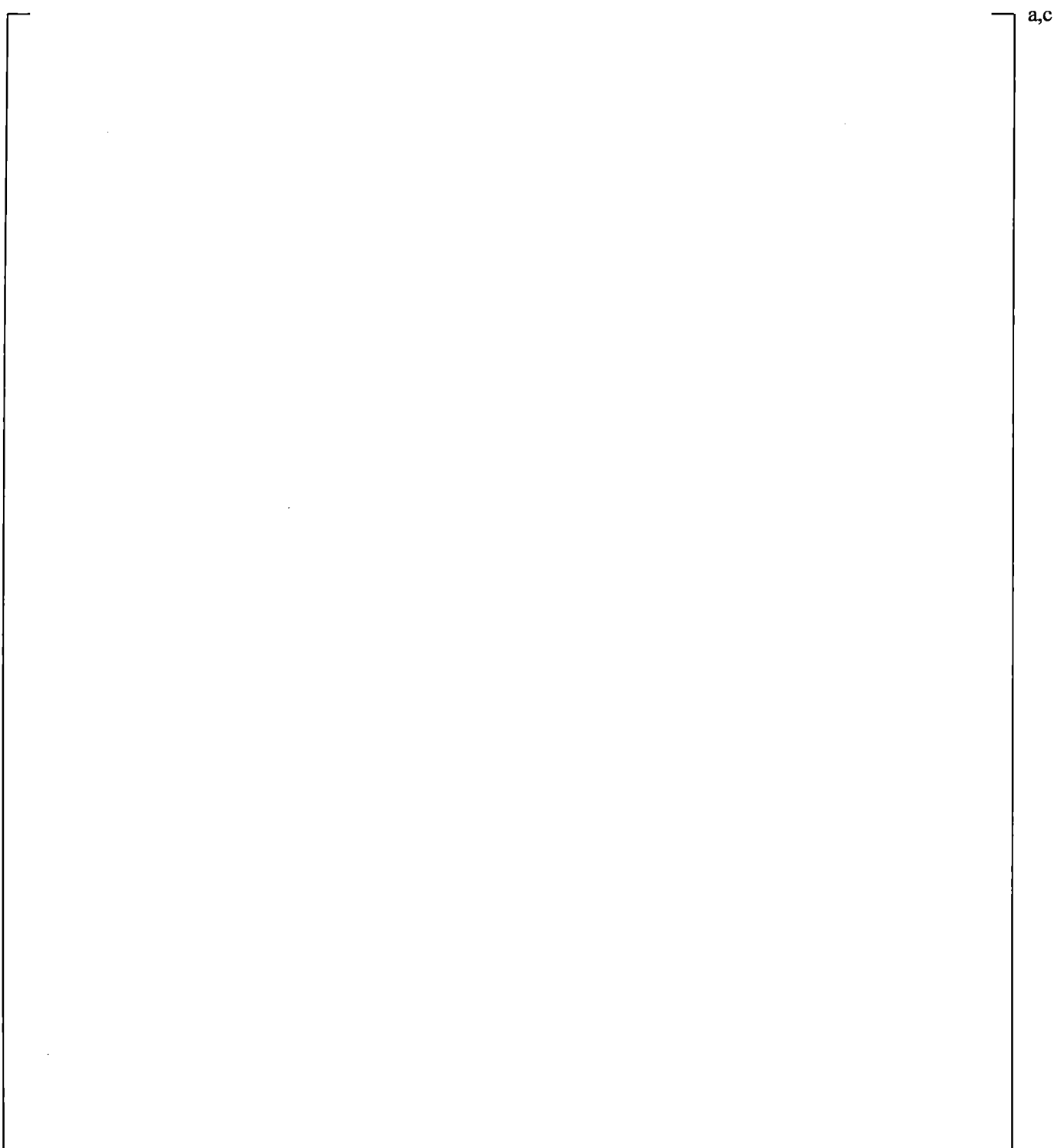


Figure 19.3-191 Axial Differential Pressures in Downcomer for UPTF Test 25A with XC=0.4

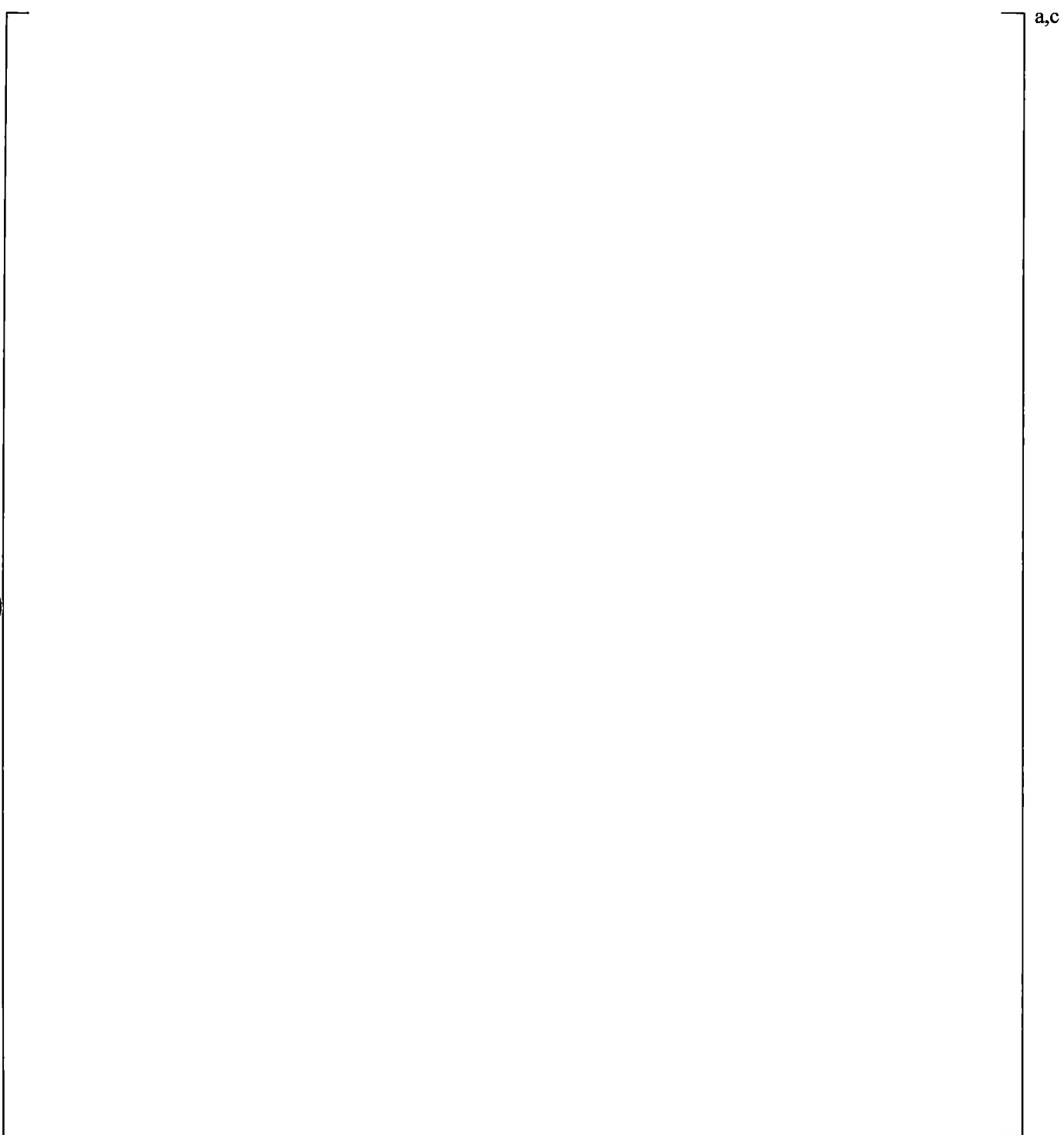


Figure 19.3-192 Void Height versus Steam Flow Rate for UPTF Test 25A with XC=0.4

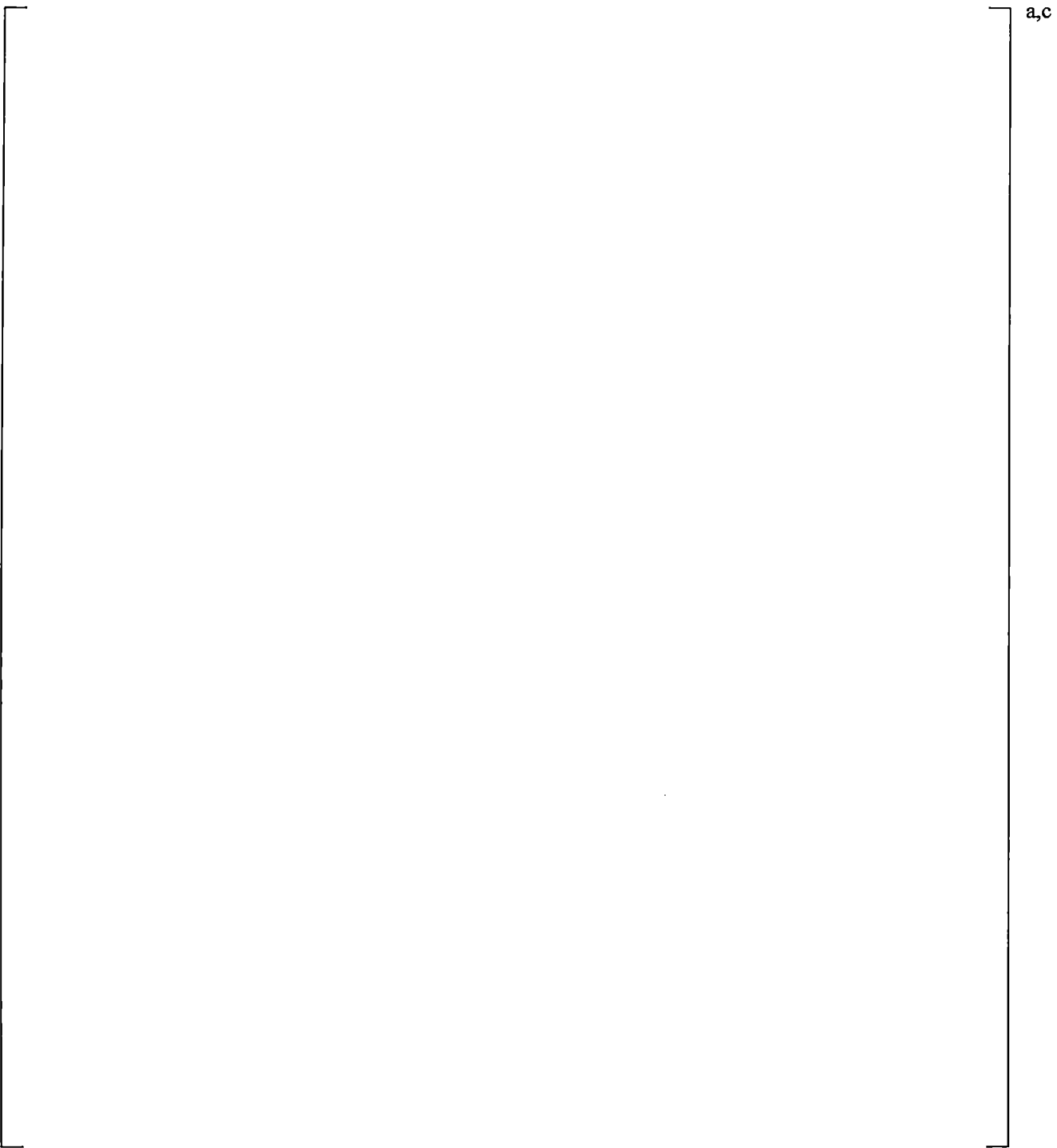


Figure 19.3-193 System Configuration for UPTF, Test 29 Phase B (Run 212) (MPR-1213, 1990b)

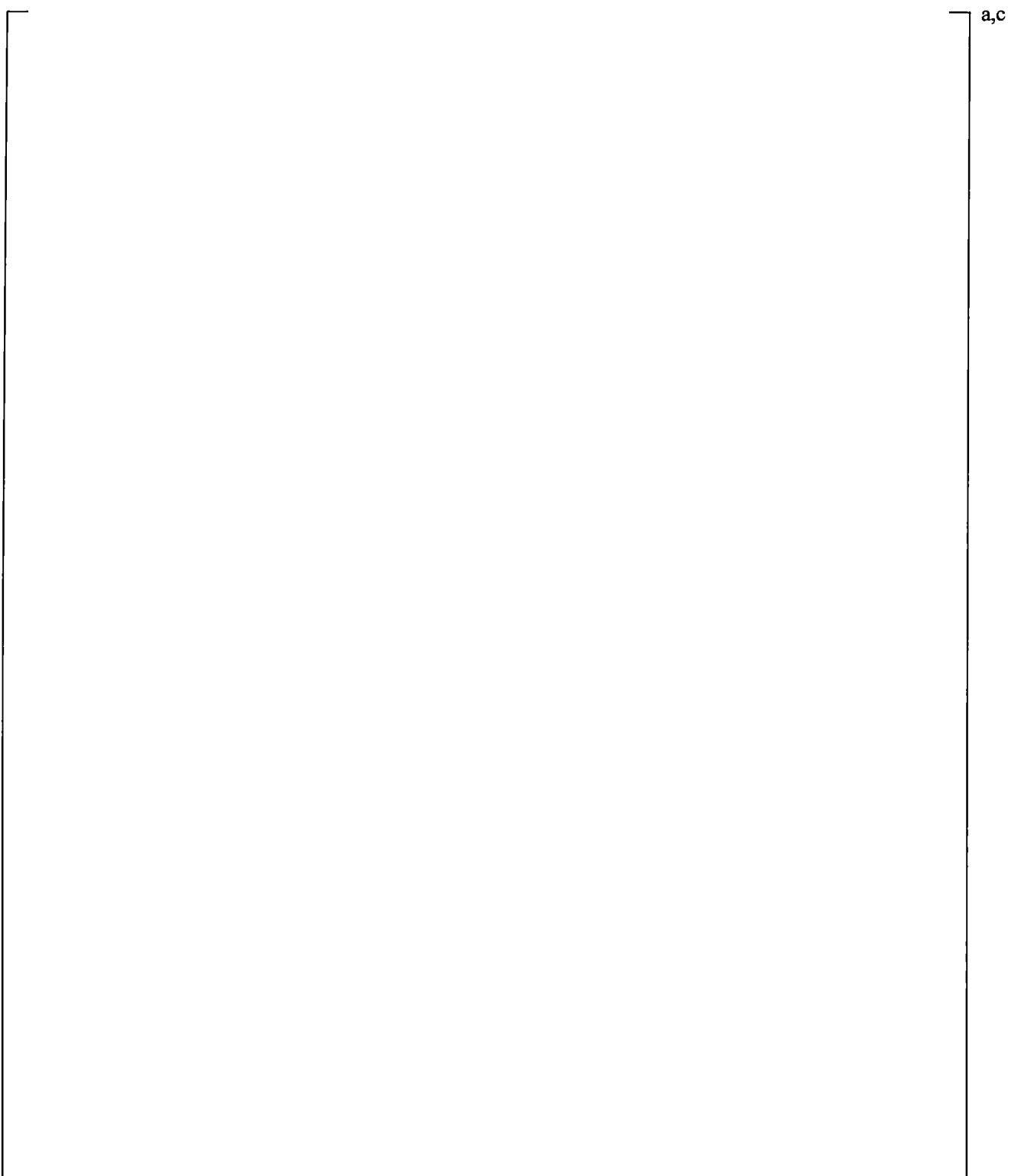


Figure 19.3-194 Injection Rates into Core Simulator, UPTF 29B

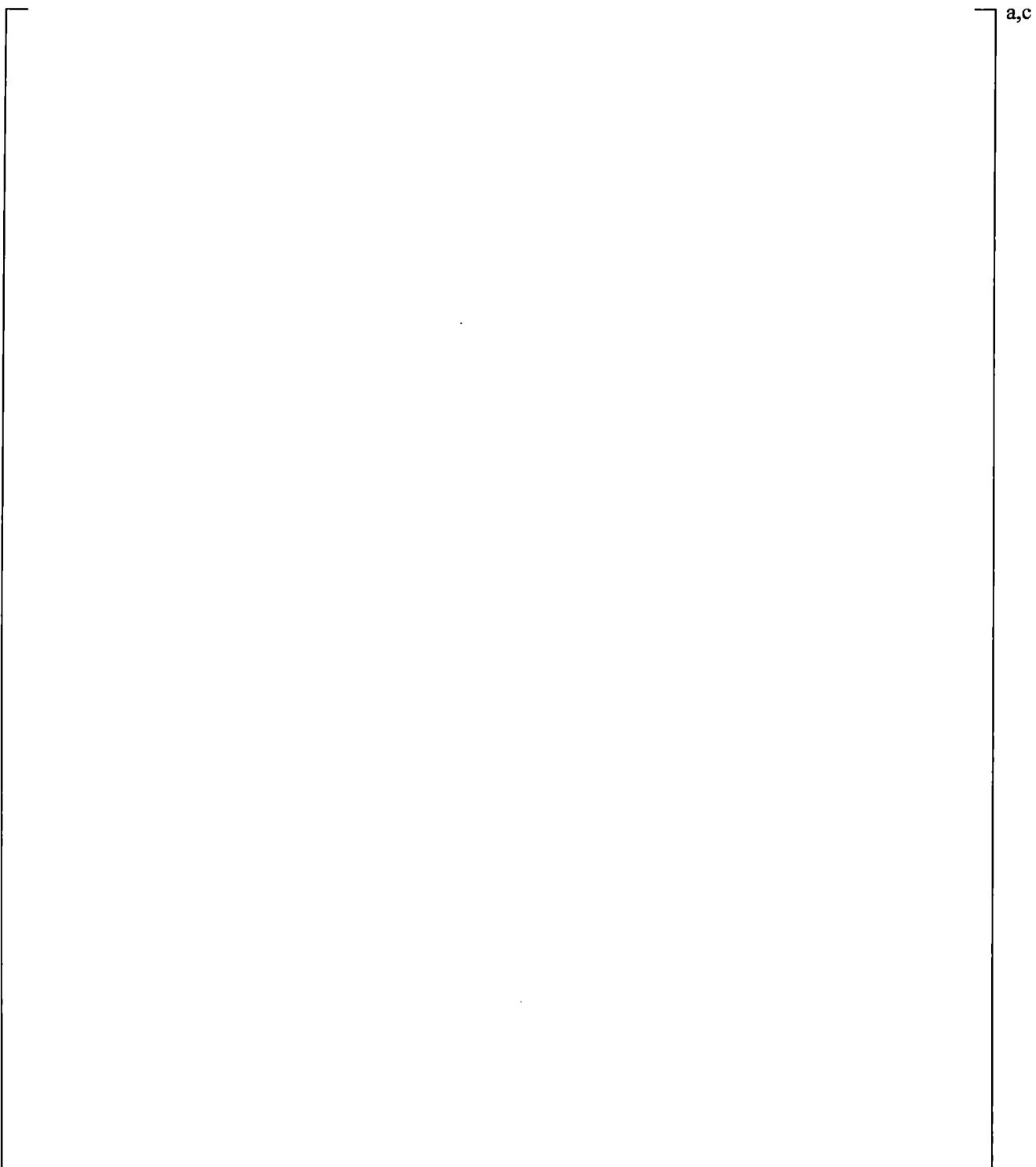


Figure 19.3-195 WCOBRA/TRAC-TF2 Vessel Component for UPTF Test 29B

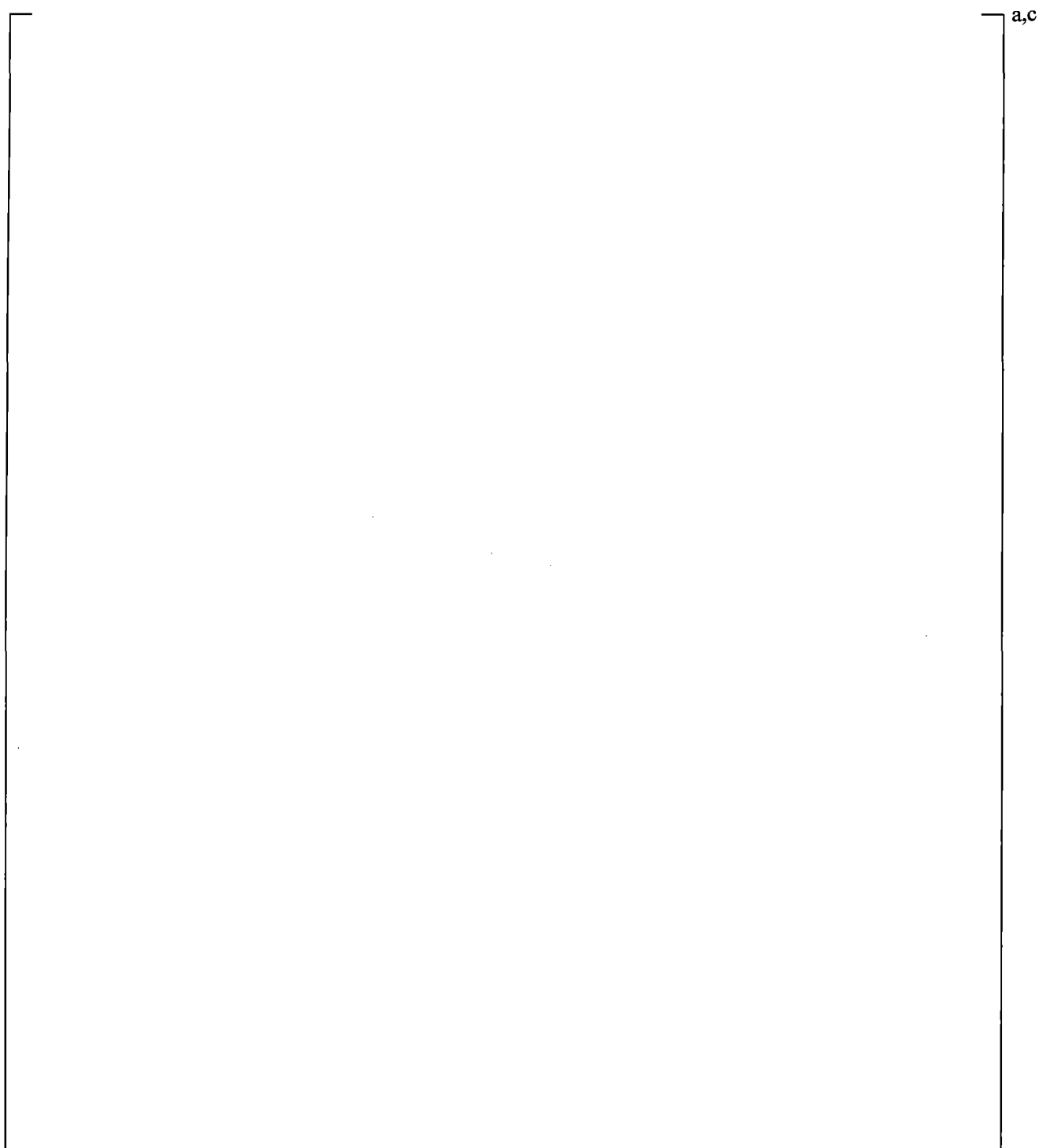


Figure 19.3-196 Illustration of Jet Channel and Global Channel in Upper Plenum

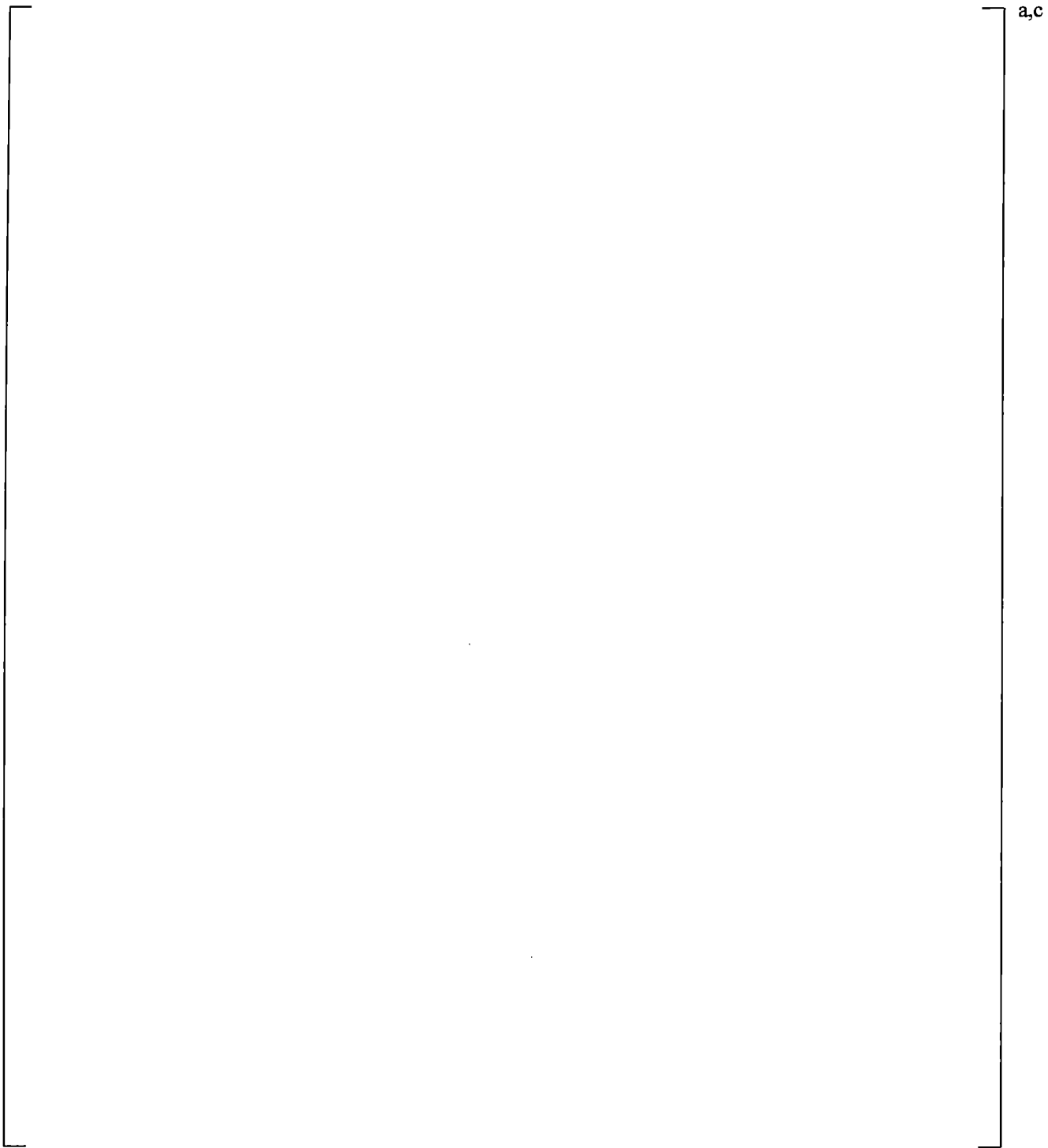


Figure 19.3-197 Section 5 of Upper Plenum Noding Model for UPTF Test 29B

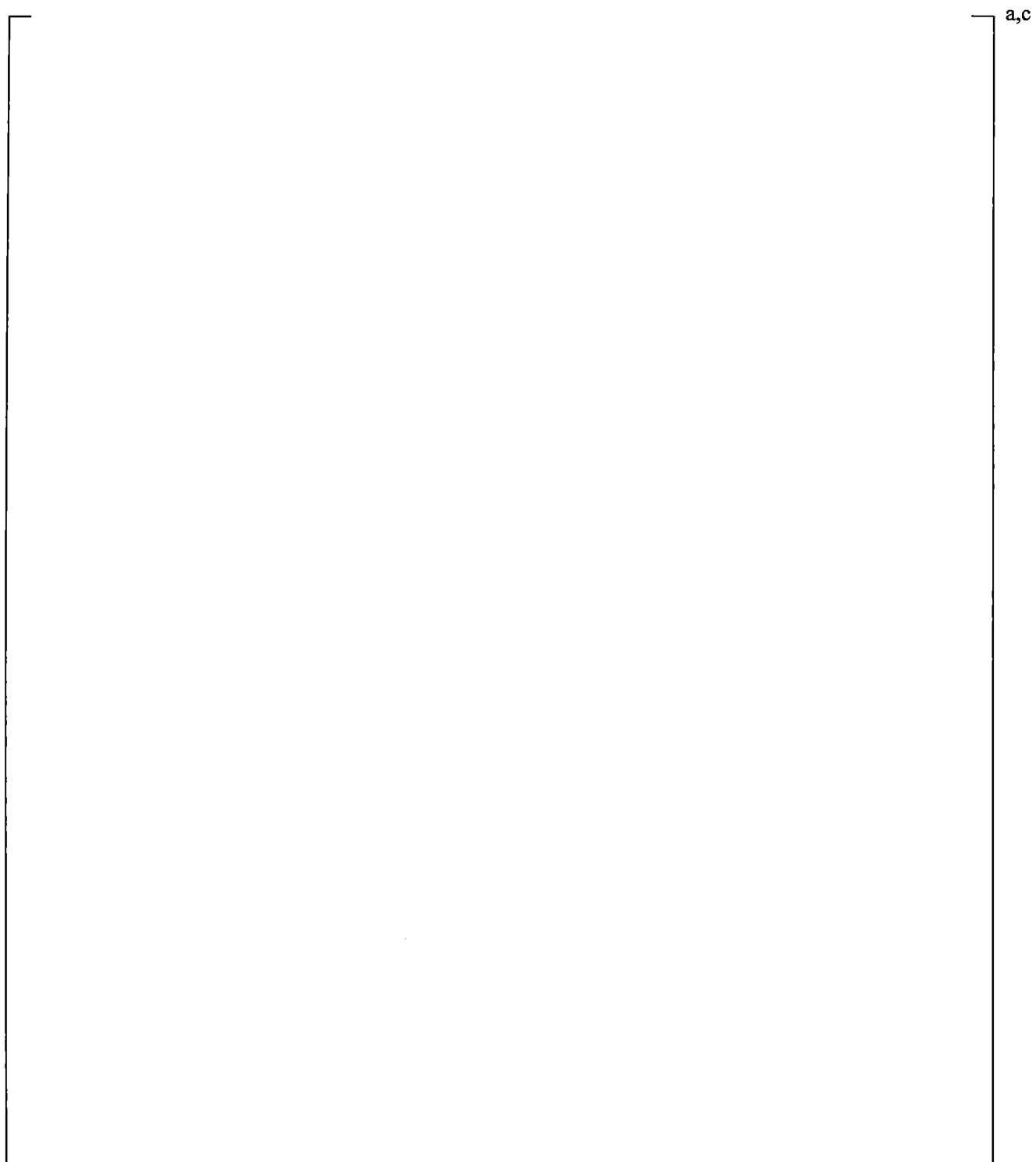


Figure 19.3-198 WCOBRA/TRAC-TF2 Loop Model for UPTF Upper Plenum Test

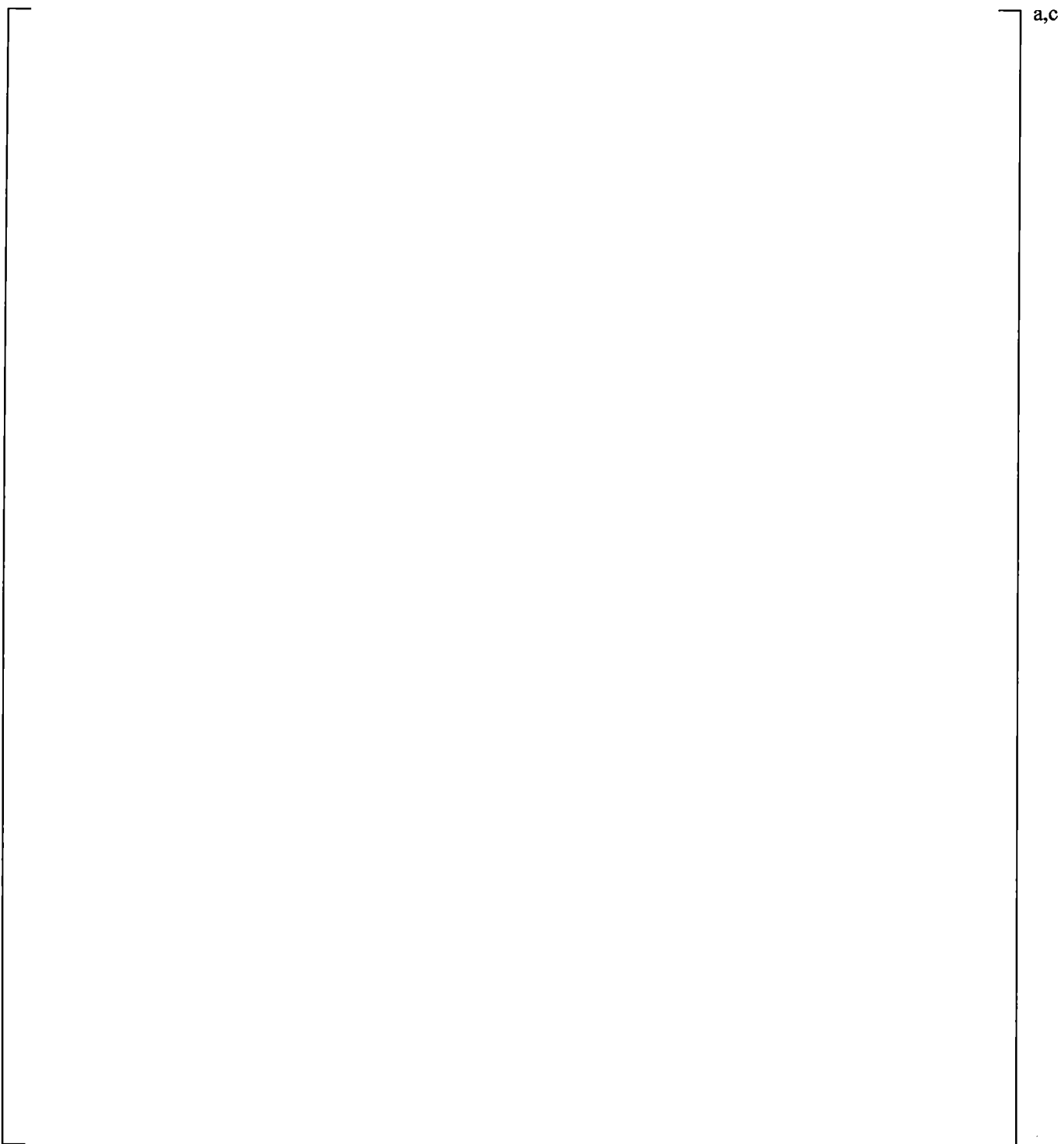


Figure 19.3-199 Quasi-Steady State Upper Plenum Mass for Phase I of UPTF Test 29B

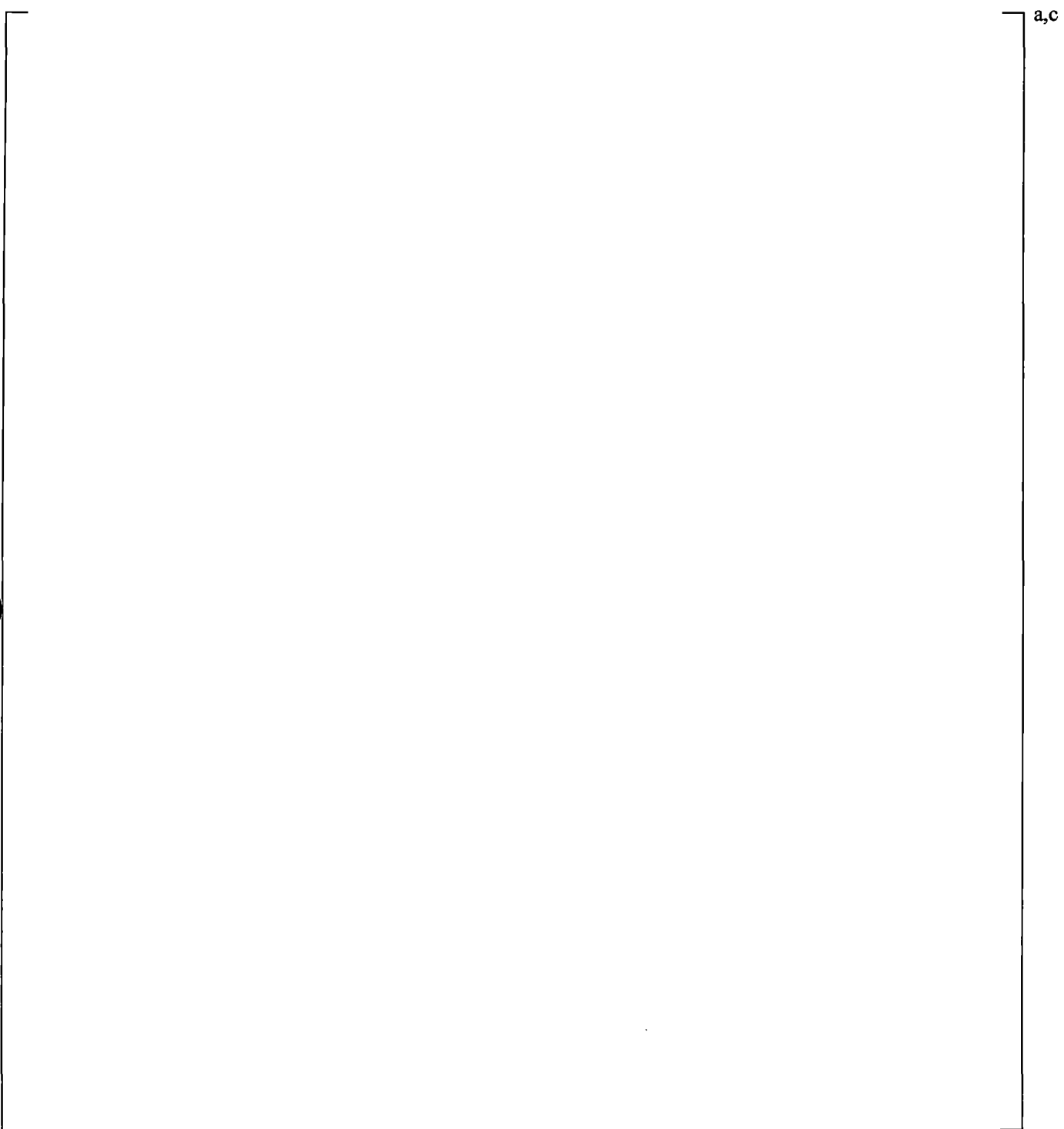


Figure 19.3-200 Quasi-Steady State Upper Plenum Mass for Phase II of UPTF Test 29B

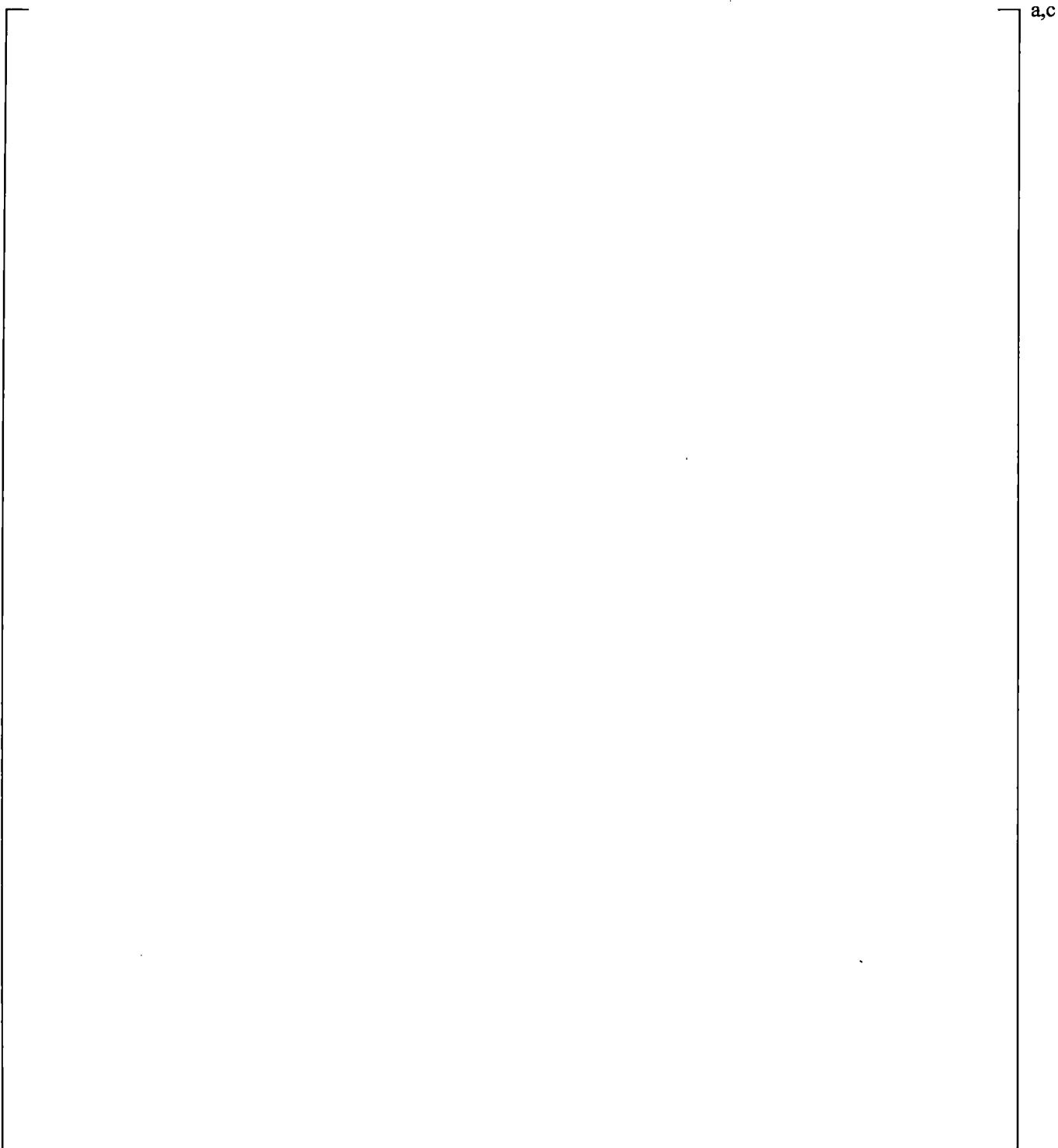


Figure 19.3-201 Quasi-Steady State Upper Plenum Mass for Phase III of UPTF Test 29B

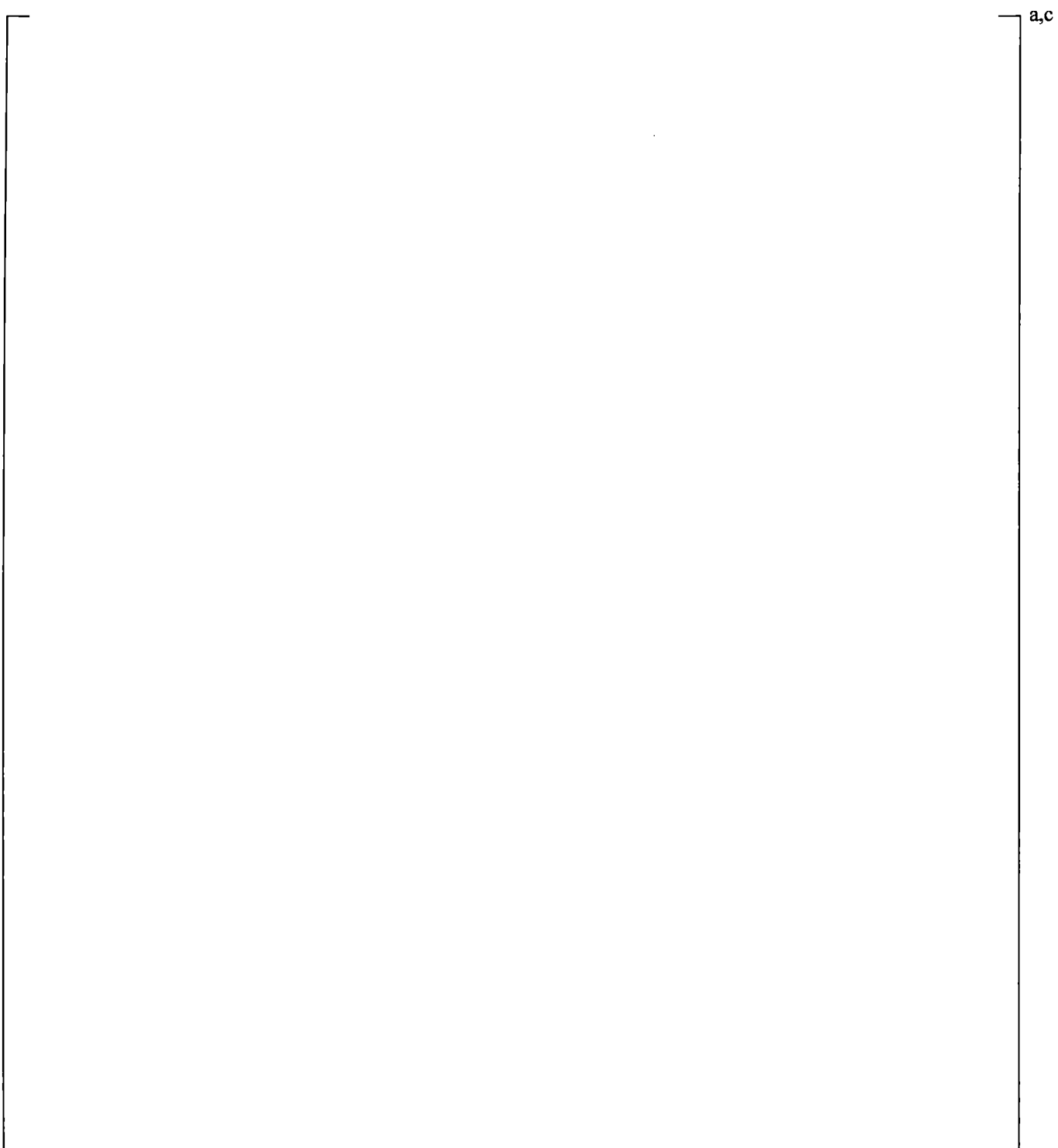


Figure 19.3-202 Quasi-Steady State Upper Plenum Mass for Phase IV of UPTF Test 29B

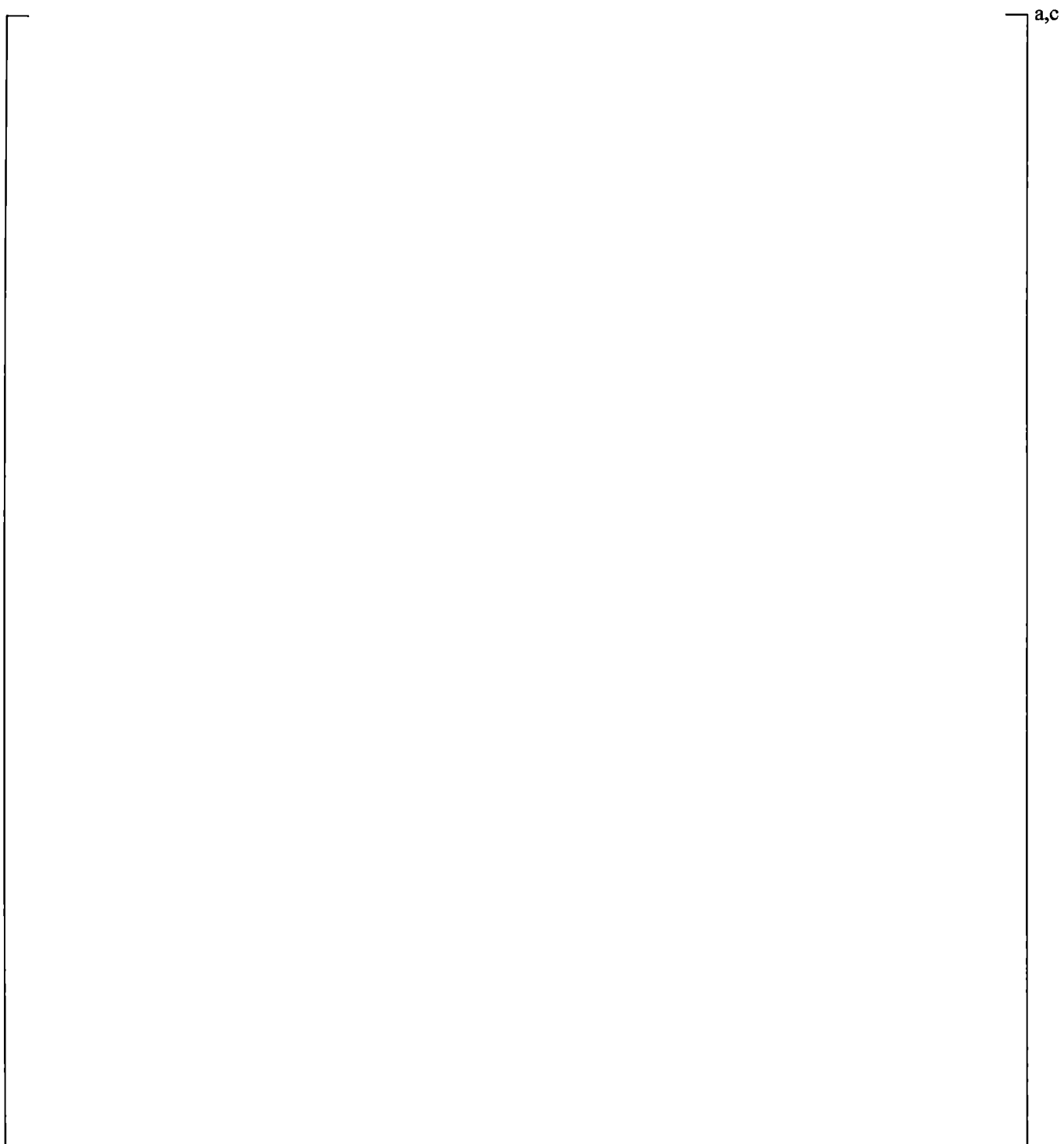


Figure 19.3-203 Quasi-Steady State Upper Plenum Mass for Phase V of UPTF Test 29B

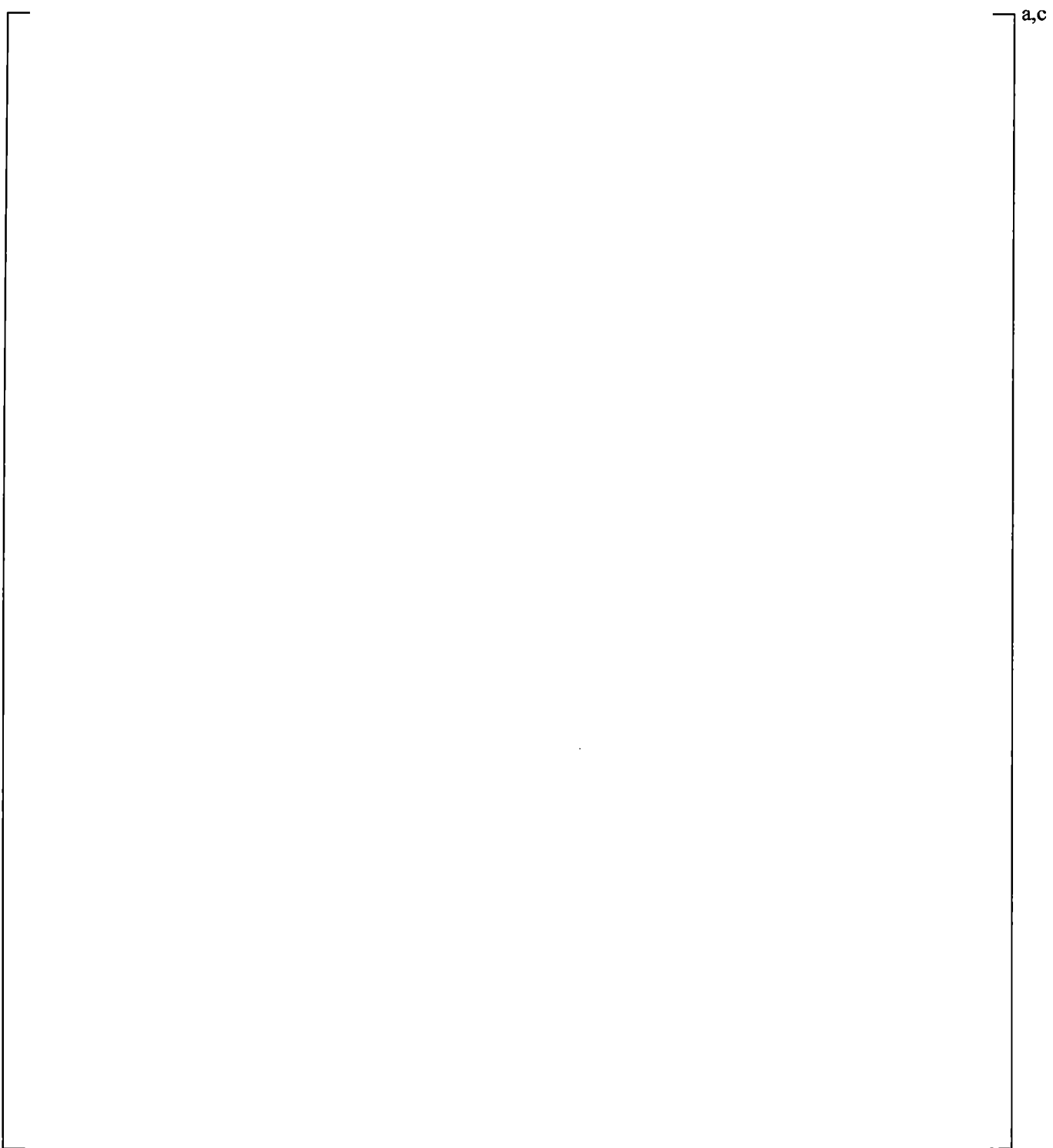


Figure 19.3-204 Quasi-Steady State Upper Plenum Mass for Phase VI of UPTF Test 29B

19.4 PERFORATED PLATE FLOODING ANALYSIS

CCFL in a perforated plate has been tested and analyzed by Hsieh et al. (1980). The tests were conducted with air/water and steam/water systems on perforated plates with different hole size and geometries.

The air/water experiment was designed to investigate the effects of geometric factors on the rate of weeping. The steam/water tests investigated subcooling effects on the CCFL. To assess the capability of

WCORBA/TRAC-TF2 on modeling the CCFL phenomenon, the air/water tests performed by Hsieh et al. (1980) on their 15-hole perforated plate is simulated. The 15-hole plate tests were selected due to its similar geometry to a PWR fuel assembly top nozzle (or tie plate). As the steam/cold water CCFL on a perforated plate is not encountered in the LOCA transients of a typical PWR except for the upper plenum injection (UPI) plant which is currently not included in the FSLOCA methodology, the steam/cold water CCFL tests reported by Hsieh et al. (1980) were not used to assess WCORBA/TRAC-TF2. Furthermore, the test data on the steam/water system are only limited to the boundaries of weeping and no-weeping and therefore insufficient to check the code on predicting the weeping liquid rate in the range between the ‘no-weeping’ and ‘dumping’ (all the inlet liquid falls down through the perforated plate). The obtained test data on the weeping rate in their air/water system are readily available to develop a test CCFL flooding limit which can then be checked against the applicable theoretical CCFL flooding limits based on the scaling factors developed, for example, by Hsieh et al. (1980) among others.

Based on the available and applicable test data, first, the air/water test with a 15-hole perforated plate was simulated by WCORBA/TRAC-TF2 using nitrogen/water to compare with the test and the CCFL curve based on the Northwestern scaling factor (Hsieh et al., 1980). The computed results of the nitrogen/water system are compared with the test data since the pertinent properties to CCFL of the air and nitrogen are within the appropriate range for the WCORBA/TRAC-TF2 assessment.

[

]^{a,c}

In Section 19.4.1, the different scaling factors used in the CCFL at a perforated plate are described.

The WCORBA/TRAC-TF2 input models for the perforated CCFL simulations are introduced in Section 19.4.2 for the nitrogen/water and high pressure and low pressure steam/water systems.

The comparisons of the computed CCFL are presented and summarized in Section 19.4.3; [

]^{a,c}.

19.4.1 Correlations and Scaling for CCFL in a Perforated Plate

The various flooding models available within the code were discussed in Section 5.15, Volume 1. The Northwestern scaling is compared to other scaling methods in this section.

Northwestern (H^*) Scaling

Hsieh et al. (1980) developed a scaling parameter similar to the one employed by Wallis (1969) to define a non-dimensional volumetric flux, which is referred to here as Northwestern scaling,

$$H_k^* = j_k \left[\frac{\rho_k}{gw(\rho_f - \rho_g)} \right]^{1/2} \quad (19.4-1)$$

$$w = d_h^{1-\alpha} L^\alpha \quad (19.4-2)$$

$$\alpha = \tanh(r \cdot k_c \cdot d_h) \quad (19.4-3)$$

where,

subscript k	= g, f for gas and liquid phase, respectively
j_k	= the superficial velocity of phase k
ρ_k	= the density of phase k
d_h	= the hole diameter
L	= the Laplace capillary constant
r	= A_h/A_T (hole area divided by total plate area)
k_c	= the wave number defined by:

$$k_c = \frac{2\pi}{t_p} \quad (19.4-4)$$

in which t_p is the thickness of the plate.

With these dimensionless volumetric fluxes, the test data for CCFL in the perforated plates was correlated by Hsieh et al. (1980) to yield:

$$H_g^{*1/2} + H_f^{*1/2} = C \quad (19.4-5a)$$

where,

$$C = \min \begin{cases} 1.07 + 4.32 \times 10^{-3} L^* \\ 2.0 \end{cases} \quad (19.4-5b)$$

$$L^* = n\pi d_h \left[\frac{g(\rho_f - \rho_g)}{\sigma} \right]^{1/2} \quad (19.4-5c)$$

and n is the number of holes. One way to examine Northwestern scaling is to compare it to other scaling methods as discussed below.

Wallis (J^*) Scaling

$$j_k^* = j_k \left[\frac{\rho_k}{g d_h (\rho_f - \rho_g)} \right]^{1/2} \quad (19.4-6)$$

Kutateladze (K^*) Scaling

$$K_k^* = j_k \left[\frac{\rho_k}{g \left[\frac{\sigma}{g(\rho_f - \rho_g)} \right]^{1/2} (\rho_f - \rho_g)} \right]^{1/2} = j_k \left[\frac{\rho_k^2}{g \sigma (\rho_f - \rho_g)} \right]^{1/4} \quad (19.4-7)$$

or

$$K_k^* = j_k^* (D^*)^{1/2}$$

where use has been made of the dimensionless diameter,

$$D^* = d_h \left[\frac{g(\rho_f - \rho_g)}{\sigma} \right]^{1/2} \quad (19.4-8)$$

For a given plate thickness (t), the Northwestern scaling approaches the following limits:

For $d_h \rightarrow 0$, it approaches the Wallis number,

$$H_k^* \rightarrow j_k^*, \quad k = g, f \quad (19.4-9)$$

For $d_h \rightarrow \infty$, on the other hand,

$$H_k^* \rightarrow K_k^*, \quad k = g, f \quad (19.4-10)$$

19.4.2 WCOBRA/TRAC-TF2 Model

For WCOBRA/TRAC-TF2 analyses of the test data, the test case with the 15-hole plate that approximates the typical dimensions in a PWR or LOFT fuel assembly top nozzle (tie plate) is selected. The 15-hole plate has the following dimensions:

$$\begin{aligned} d_h &= 0.413 \text{ in} \\ t_p &= 0.787 \text{ in} \\ A_T &= 4.754 \text{ in}^2 \\ A_h &= 2.013 \text{ in}^2 \\ r = A_h/A_T &= 0.4260 \end{aligned}$$

With these dimensions, the C in Equation (19.4-5) is calculated to be 1.9 and 2.0 using Equations (19.4-5b) and (19.4-5c) for the nitrogen/water and steam/water systems, respectively. The WCOBRA/TRAC-TF2 model used to predict the CCFL for the perforated plate is shown in Figure 19.4-1.

]^{a,c}

For the steam/water or nitrogen/water system, the computational experiment is performed in the following manner. [

]^{a,c}

]^{a,c}

$$\left[\quad \right]^{a,c}$$

[

]^{a,c}

19.4.3 WCOBRA/TRAC-TF2 Simulation

The predicted nitrogen/water system CCFL by WCOBRA/TRAC-TF2 is compared with the air/water test data in Figure 19.4-2, covering the range of liquid flow rate tested in the experiment. The nitrogen/water and air/water systems at the room temperature and pressure are considered to be comparable with regard to the concerns of the CCFL phenomena. The Northwestern flooding limit is also shown in the comparison in Figure 19.4-2 [

]^{a,c}

Figures 19.4-3 and 19.4-4 show the predicted steam/water system flooding curve under the system

[

]^{a,c}

For a higher [

]^{a,c}

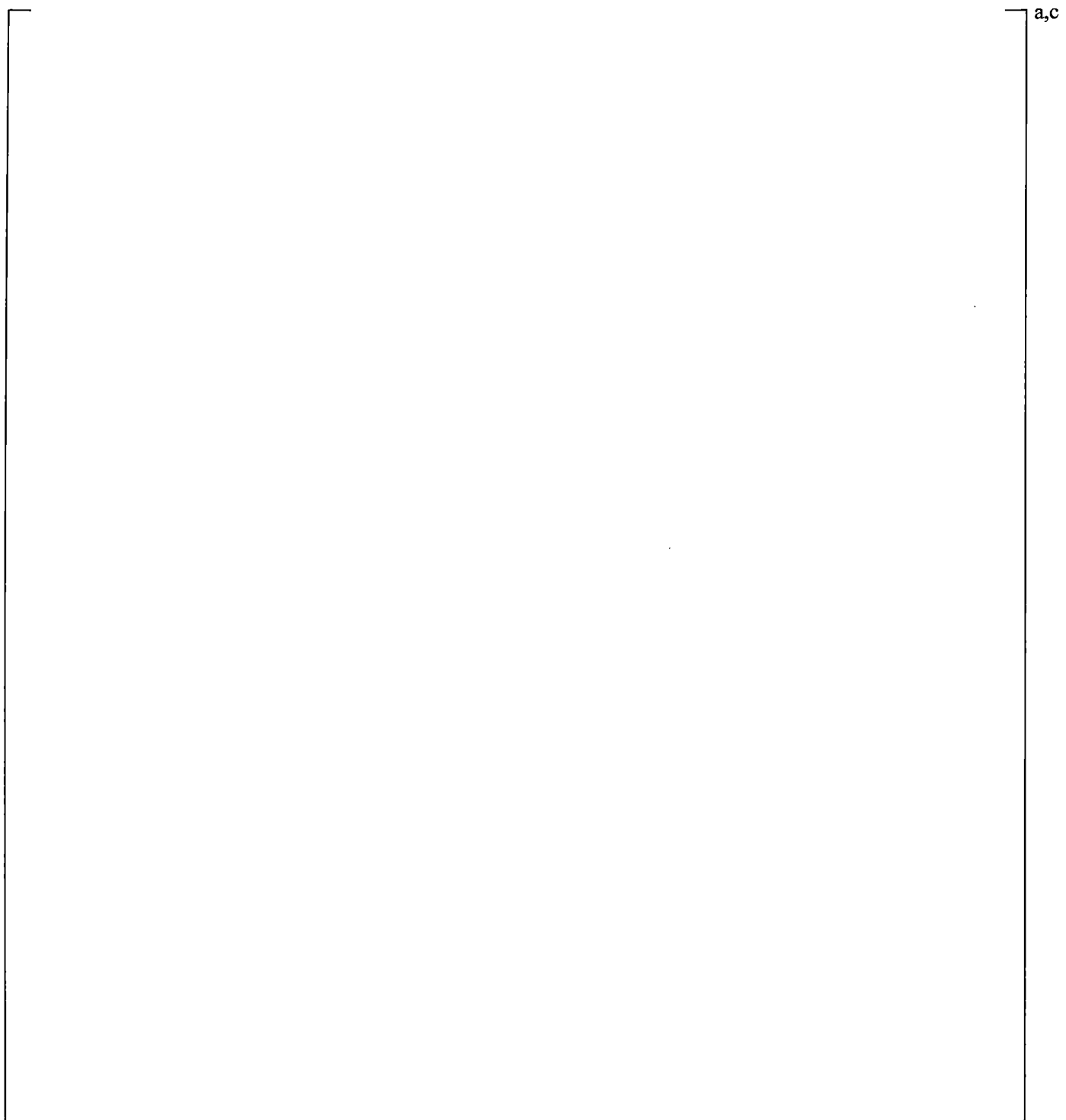


Figure 19.4-1 Flooding Model for a Perforated Plate

**Figure 19.4-2 Flooding Velocities for the Nitrogen/Water System at []^{a,c}
Compared with the Air/Water Test (Hsieh et al., 1980) and Northwestern Flooding
Limit**

a,c

Figure 19.4-3 Flooding Velocities for Saturated Liquid and Vapor at [Northwestern Flooding Limit (WCOPRA/TRAC-TF2)

]^{a,c} Compared with

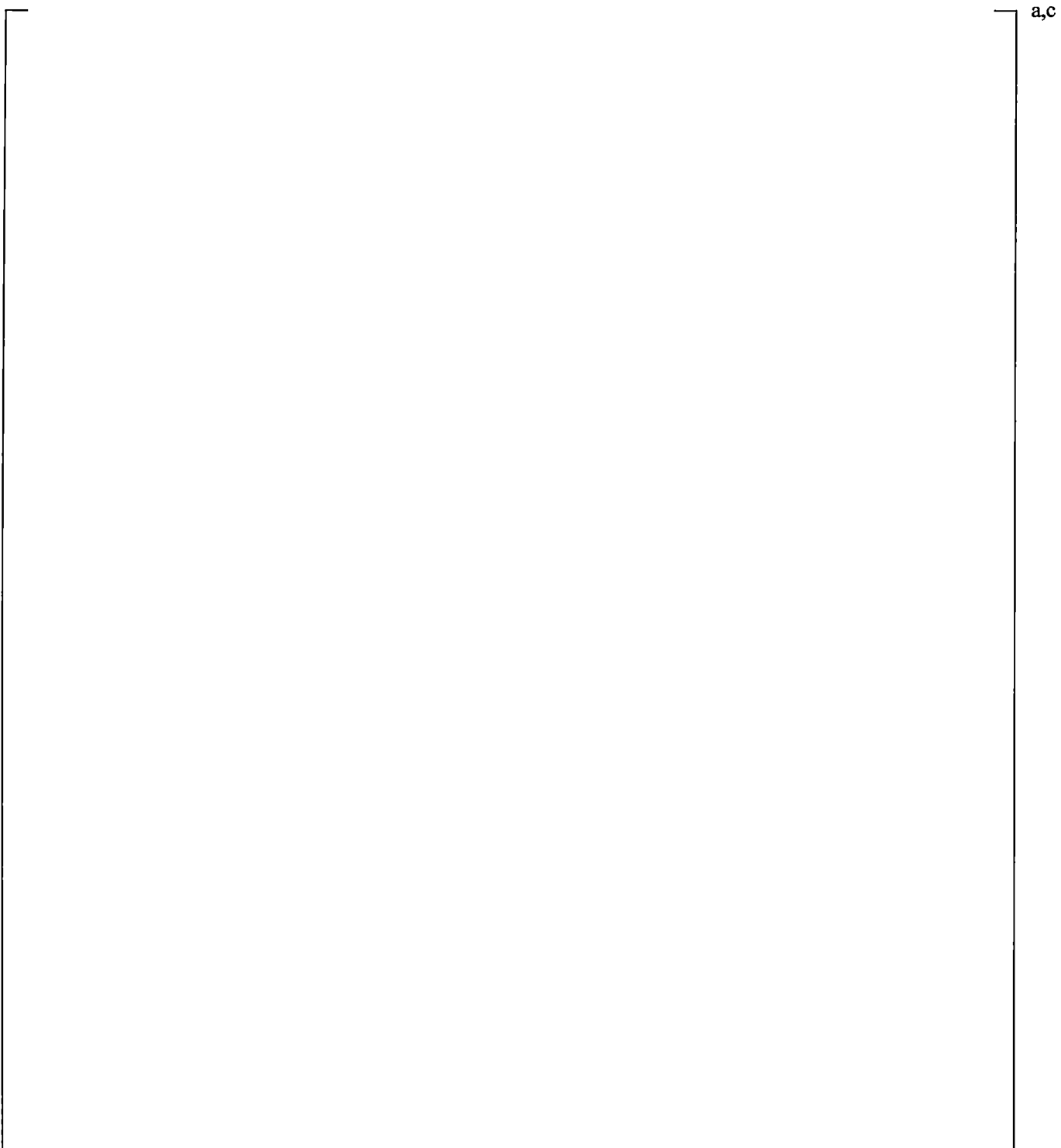
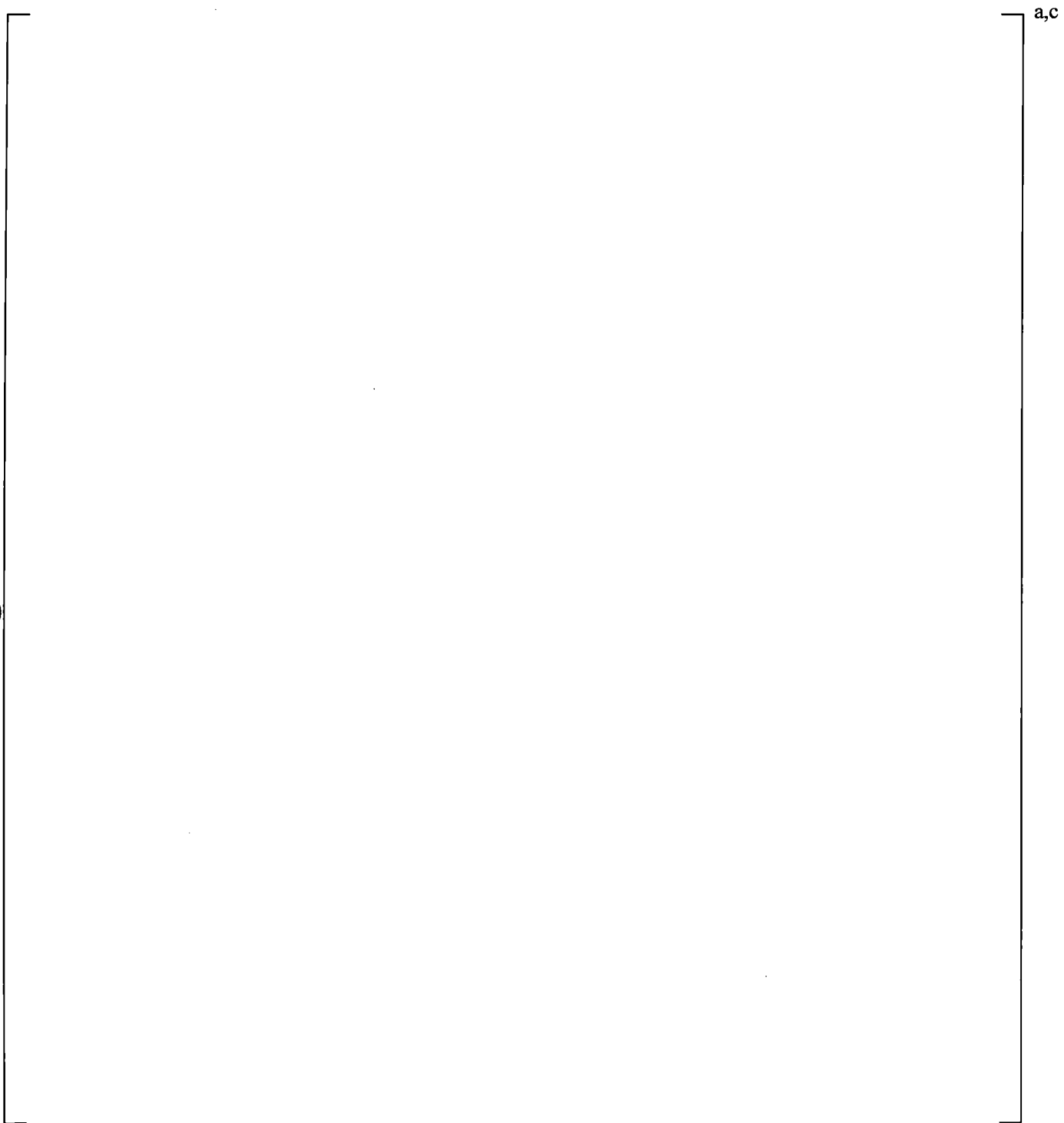
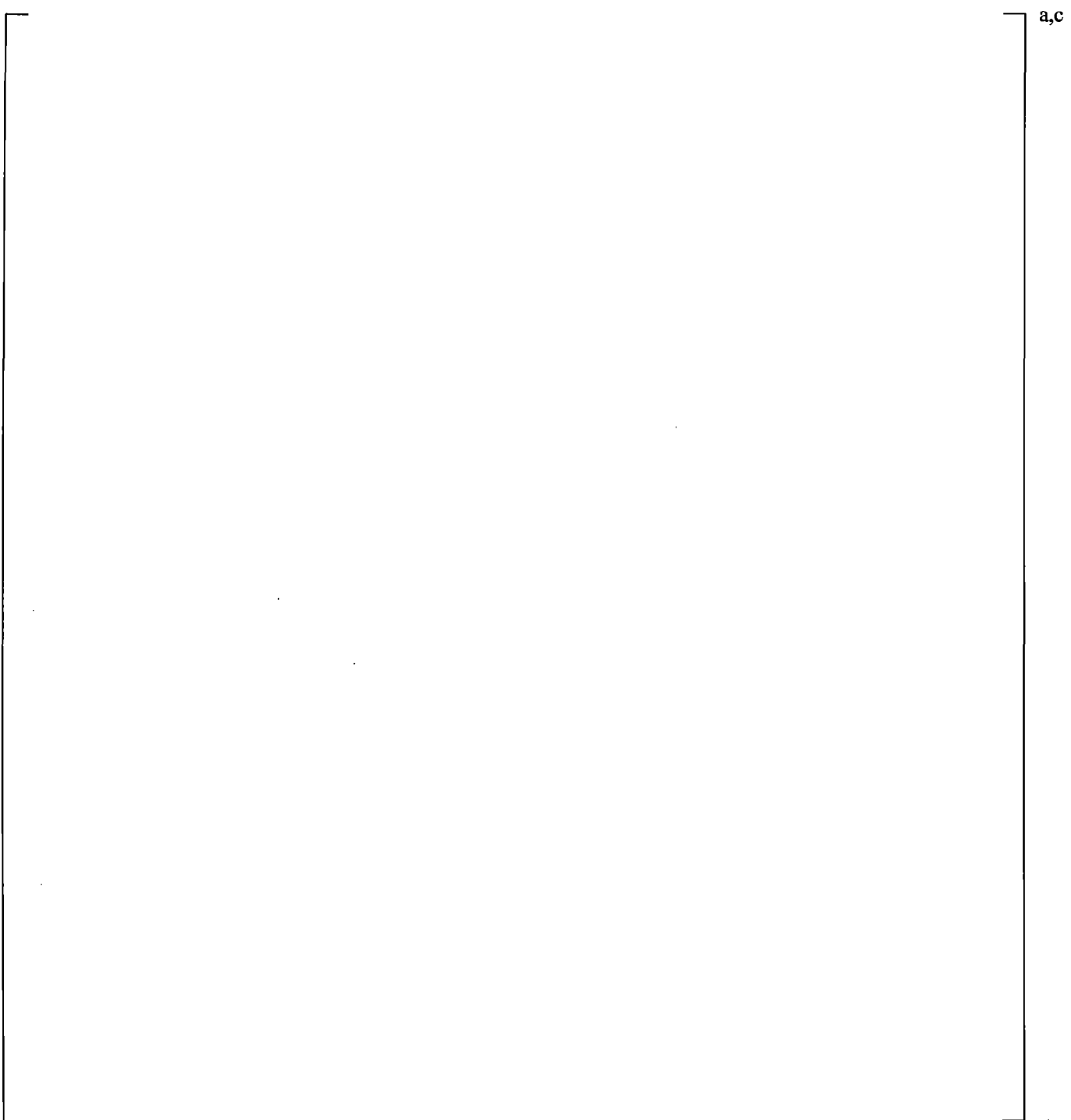


Figure 19.4-4 Flooding Velocities for Saturated Liquid and Vapor at []^{a,c} Compared with Northwestern Flooding Limit (WCOBRA/TRAC-TF2)



**Figure 19.4-5 Liquid Mass Flow Rates through Perforated Plate at [
(WCOBRA/TRAC-TF2)**

]^{a,c}



**Figure 19.4-6 Vapor/Liquid Mass Flow Rates through Perforated Plate at [
]^{a,c} (WCOBRA/TRAC-TF2)**

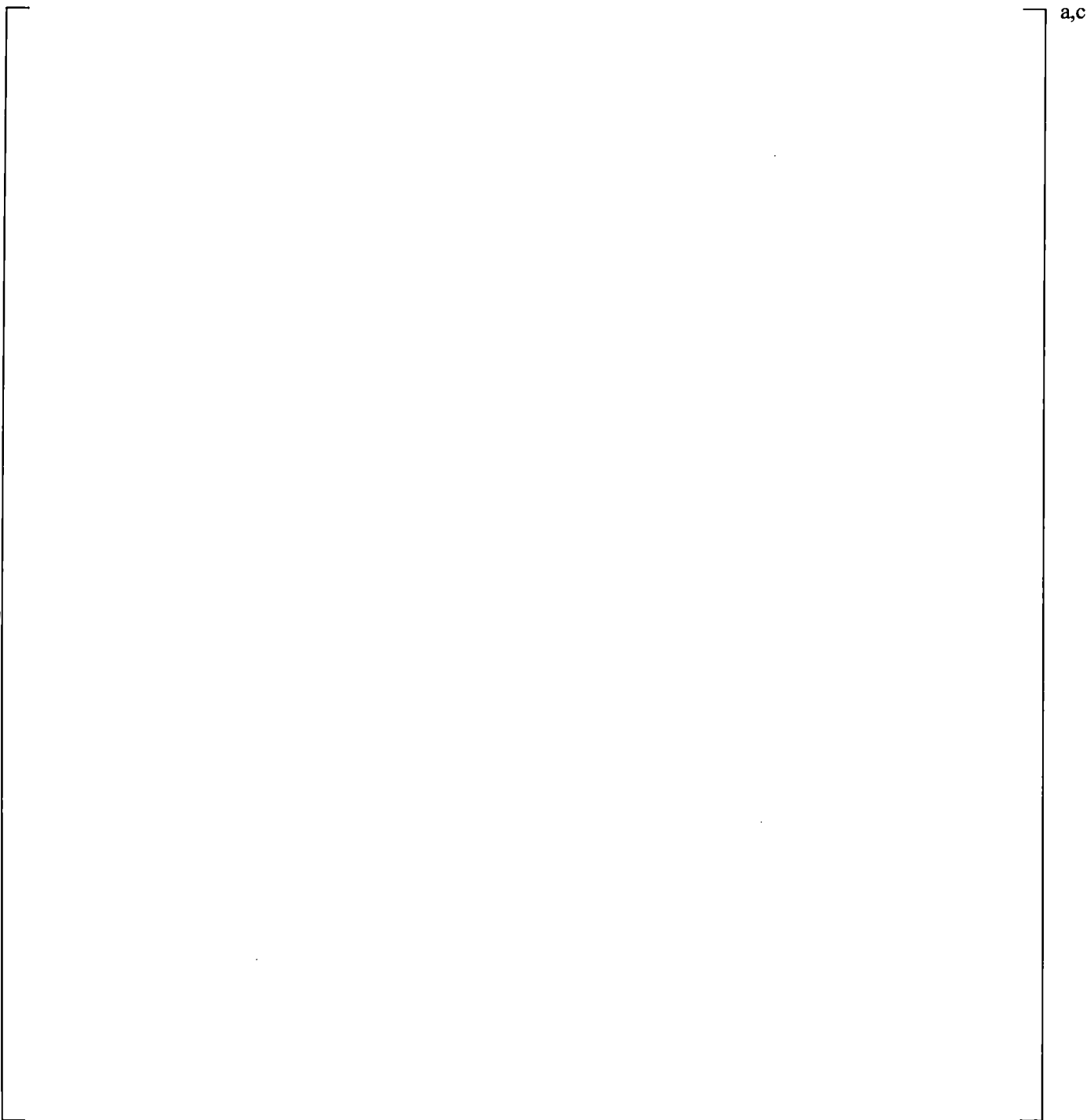


**Figure 19.4-7 Liquid Mass Flow rates through Perforated Plate at [
(WCOBRA/TRAC-TF2)**

$J^{a,c}$

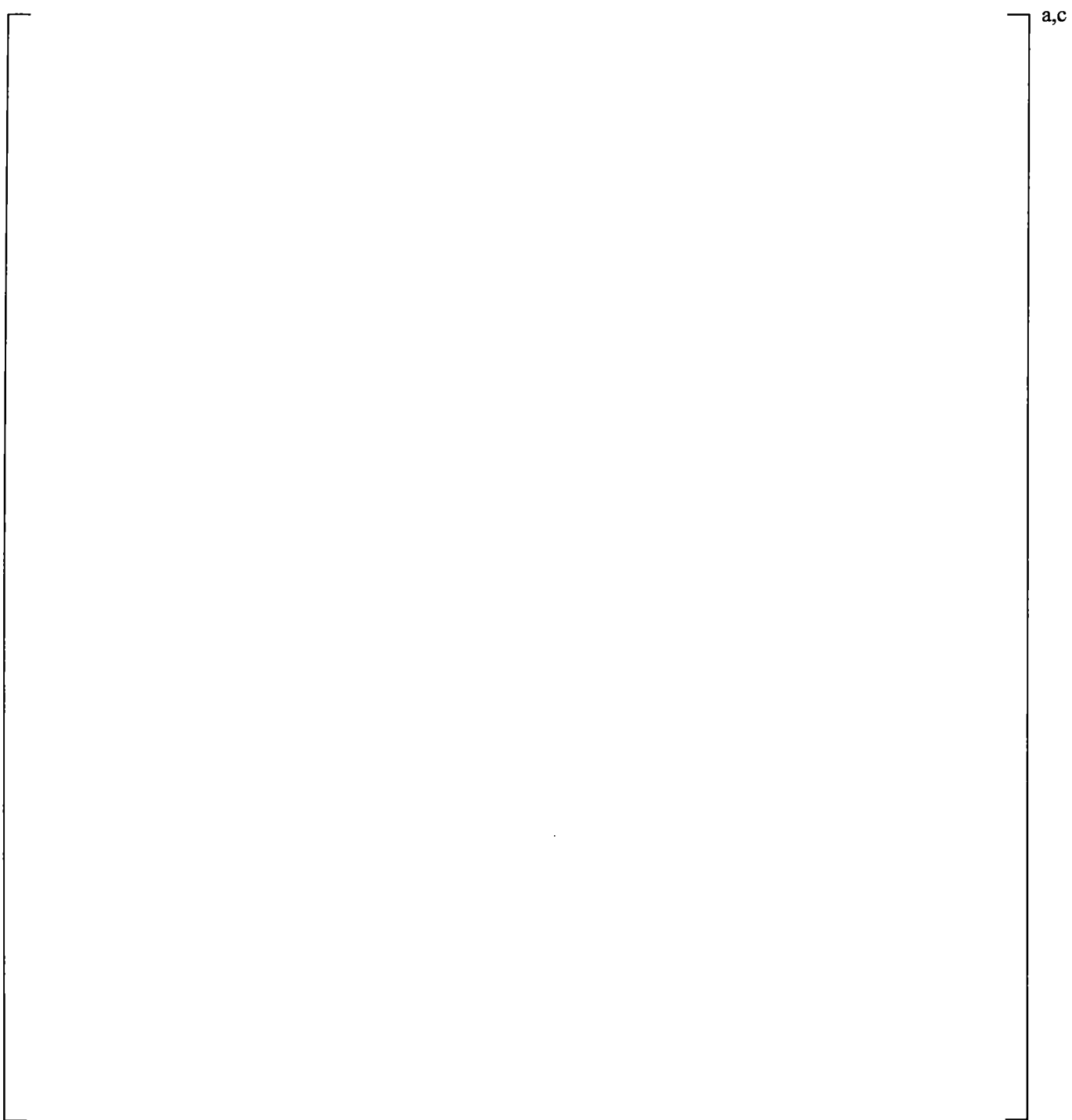


**Figure 19.4-8 Vapor/Liquid Mass Flow rates through Perforated Plate at [
]^{a,c} (WCOPRA/TRAC-TF2)**

19.5 FULL-LENGTH EMERGENCY COOLING/CORE HEAT TRANSFER

The correlation used to determine the entrainment rate at a quench front is described in Section 5.6, Volume 1. The model is consistent with the work of (Kataoka and Ishii, 1983) and assumes the entrainment is due to vapor bubbling through a pool of liquid.

The reflood test simulations provide a means of examining the performance of the entrainment model for bottom reflood. Mass balances were calculated from the test data so that carryover fraction and mass retention in the test bundle could be estimated. This section compares the WCOBRA/TRAC-TF2 predictions of carryover fraction, total bundle mass, steam exit flow, and liquid outflow to estimates derived from the test data. The comparisons provide a means of assessing the bottom reflood entrainment model.

19.5.1 FLECHT Test Facility

First, it is important to describe the data collection methods used to estimate carryover which are not discussed in Section 14 for the FLECHT facility. Figure 19.5-1 shows a schematic of the FLECHT facility, identifying mass collection and flow rate measurements. These measurements were used to determine the mass inventory in the bundle, and the carryover fraction. Each of the FLECHT facilities, FLECHT Separate-Effects and System-Effects Tests (SEASET) (Loftus et al., 1981), FLECHT Low Flooding Rate (Rosal et al., 1975), and FLECHT Top Skewed Power (Rosal et al., 1977), used the same type of collection system. The difference between the facilities was the design of the test bundle itself, and in the number of differential pressure (DP) cells used in the test bundle.

Liquid was injected into the test bundle from an accumulator. The mass lost from this accumulator was reported in the test data and used as a check on the overall mass balance. Liquid leaving the accumulator was regulated, and the flow rate into the bundle was measured by a turbine meter. DP cells in the test bundle were used to estimate the bundle mass. The measurements were corrected for frictional effects.

The steam/droplet mixture leaving the heated bundle entered an upper plenum. In this plenum, the steam and most droplets were separated. The liquid went to a “Carryover Tank,” where the total mass and its rate of change were determined from a DP cell.

After leaving the upper plenum, the steam went through another separator to remove any remaining droplets. The liquid removed at this second removal point went into a “Steam Separator Tank” and was measured. In general, this amount of liquid was small compared to the mass retained in the Carryover Tank.

Finally steam, now assumed to be “dry,” was vented to the atmosphere through an exhaust orifice. The exhaust orifice provided the flow rate of steam from the facility. The data evaluation provided both the dry steam effluence rate, and the total mass of steam that exited the facility.

The instantaneous carryover fraction (CO) is defined as:

$$CO(t) = \frac{\dot{m}_{out}(t)}{\dot{m}_{inj}(t)} \quad (19.5-1)$$

where $\dot{m}_{out}(t)$ and $\dot{m}_{inj}(t)$ are the flow rate out of and into the bundle, respectively. Note that for forced injection reflood tests such as FLECHT-SEASET, the flow rate into the bundle is essentially constant.

The instrumentation in the facility allowed the carryover fraction to be determined in two different ways; from mass stored in the bundle and from mass flows exiting the bundle. The following forms were calculated:

1. From mass stored in the test bundle,

$$CO_1 = 1 - \frac{m_{ts}(t)}{\int \dot{m}_{inj}(t) dt} \quad (19.5-2)$$

2. From the (instantaneous) rate of storage in the test bundle,

$$CO_2 = 1 - \frac{\dot{m}_{ts}(t)}{\dot{m}_{inj}(t)} \quad (19.5-3)$$

3. From the total mass that exited the test section and was stored in the separator tanks or exited as dry steam,

$$CO_3 = \frac{m_{CO}(t) + m_{ss}(t) + \int \dot{m}_{steam}(t) dt}{\int \dot{m}_{inj}(t) dt} \quad (19.5-4)$$

4. From the rate of change of mass in the separator tanks and the exhaust orifice flow rate,

$$CO_4 = \frac{\dot{m}_{CO}(t) + \dot{m}_{ss}(t) + \dot{m}_{steam}(t)}{\dot{m}_{inj}(t)} \quad (19.5-5)$$

(Nomenclature is indicated in Figure 19.5-1.)

The carryover fractions CO_1 and CO_3 are essentially the instantaneous carryover fraction integrated over time period "t" and then averaged over that same time period (this is true for the FLECHT tests, since the tests are at a constant flooding rate), while CO_2 and CO_4 are based entirely on instantaneous measurements. Both instantaneous and averaged forms show the amount of carryover. [

]^{a,c}

The carryover fraction and bundle mass were calculated using WCOBRA/TRAC-TF2 predictions of several forced reflood tests. The carryover fraction for the WCOBRA/TRAC-TF2 results is based on the total integrated vapor mass flow (FGM), continuous liquid mass flow (FLM), and entrained liquid mass flow (FEM) entering and leaving the bundle. (Recall from Figures 15.6.1-2, 15.6.2-2 and 15.6.3-2, the channels representing the bundle are Channels 2 and 3, and there are a total of []^{a,c} cells in the channels of the bundle region.) Since subcooled liquid was injected for all the tests, the inlet mass flow is taken to be only the liquid mass flow. So, the WCOBRA/TRAC-TF2 predictions are calculated as:

$$\left[\quad \right]^{a,c} \quad (19.5-6)$$

The carryover fraction thus calculated by Equation 19.5-6 is of integral form. The carryover fraction for the prediction CO_{WCT} , is equivalent to the CO_1 and CO_3 definitions in the data evaluation, since in the calculation there is no "lost mass" as there can be in the experiment due to measurement inaccuracy. This form for CO_{WCT} was chosen, because it provides a more clear comparison with the data. Instantaneous values are too oscillatory to provide a clear indication of the trends.

19.5.2 WCOBRA/TRAC-TF2 Simulation

The tests presented here are FLECHT-SEASET (Loftus et al., 1981) Tests 31805, 31701, and 31203; FLECHT Low Flooding Rate (Rosal et al., 1975) Tests 04641 and 05029; and, FLECHT Top Skewed (Rosal et al., 1977) Tests 15305, 13609, and 13812. Figures 19.5-2 through 19.5-9 show comparisons of predicted and measured carryover fraction. The most appropriate comparison to make in these figures is between the predicted carryover fraction and CO_1 . []^{a,c}

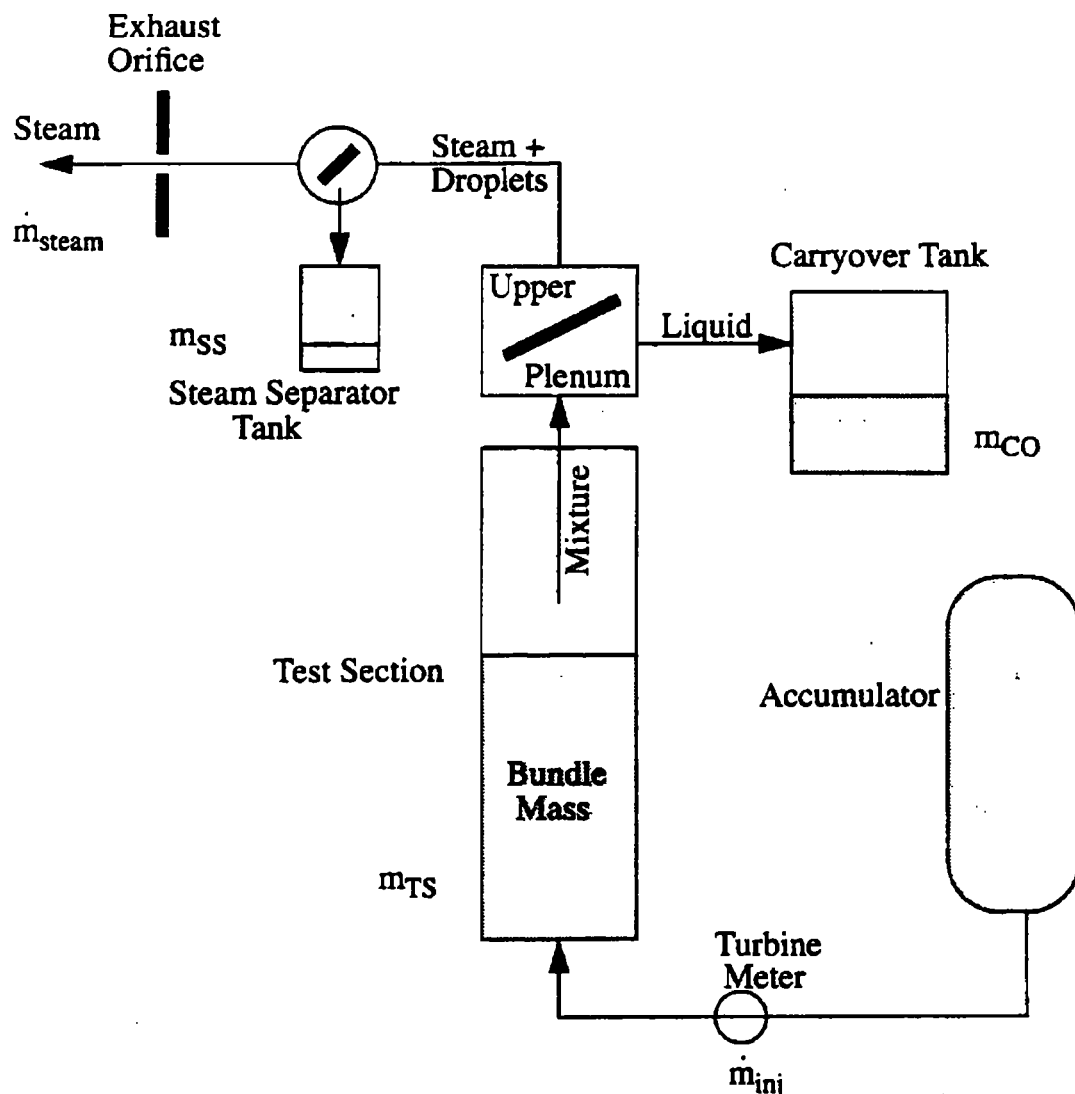


Figure 19.5-1 Mass Inventory Measurements in the FLECHT Facilities

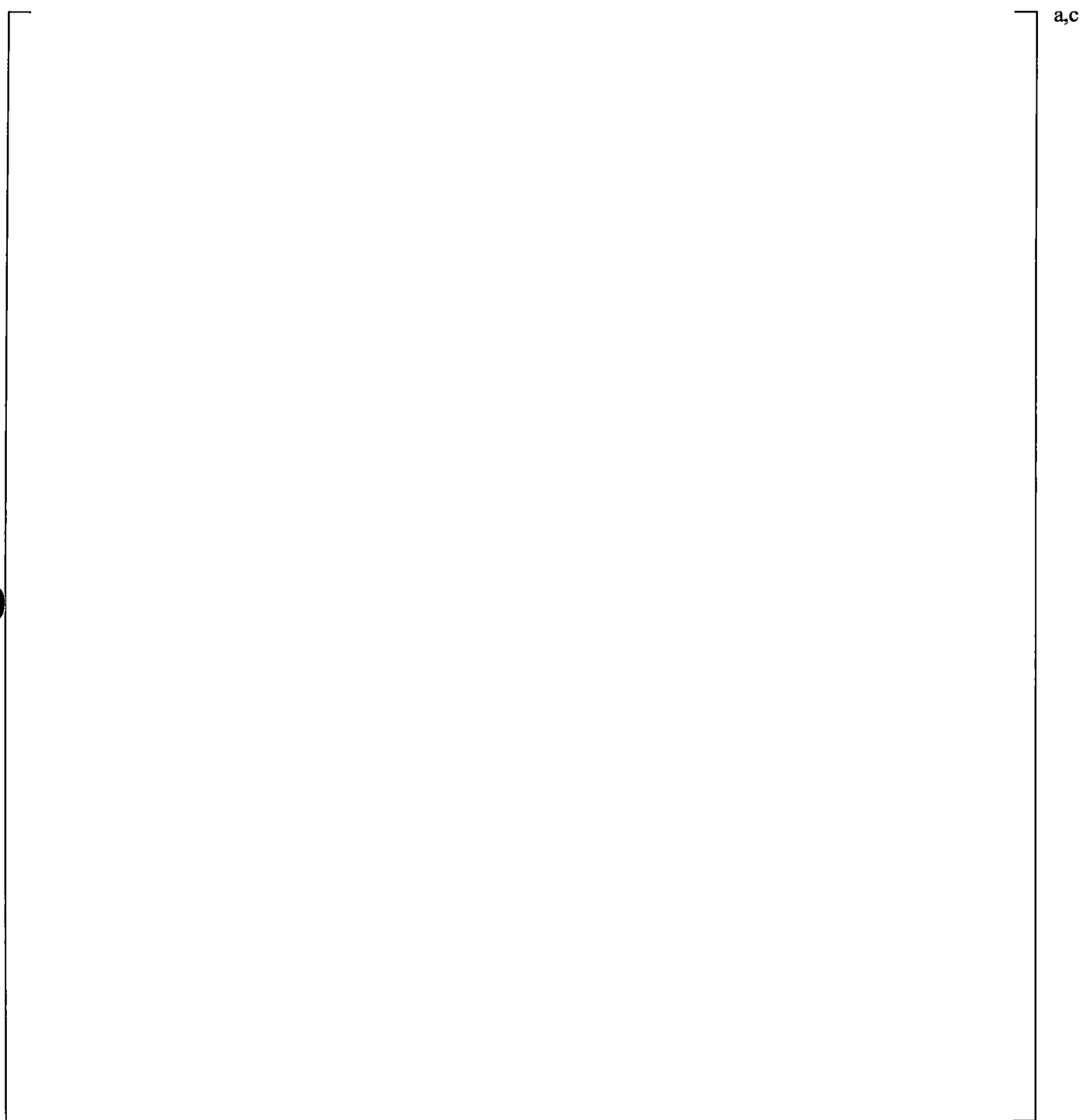


Figure 19.5-2 Predicted and Measured Carryover Fraction, FLECHT-SEASET Test 31805

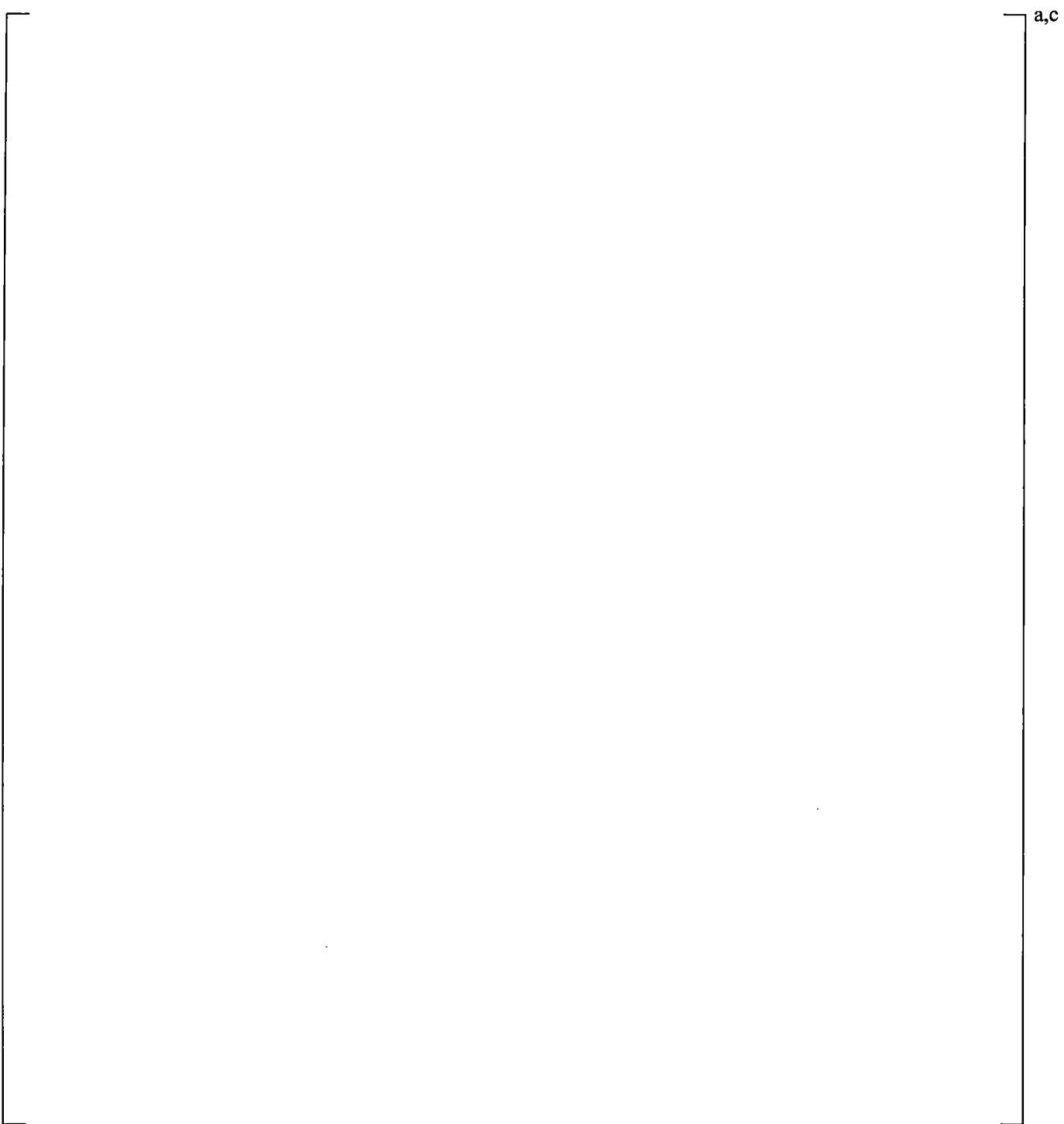


Figure 19.5-3 Predicted and Measured Carryover Fraction, FLECHT-SEASET Test 31701

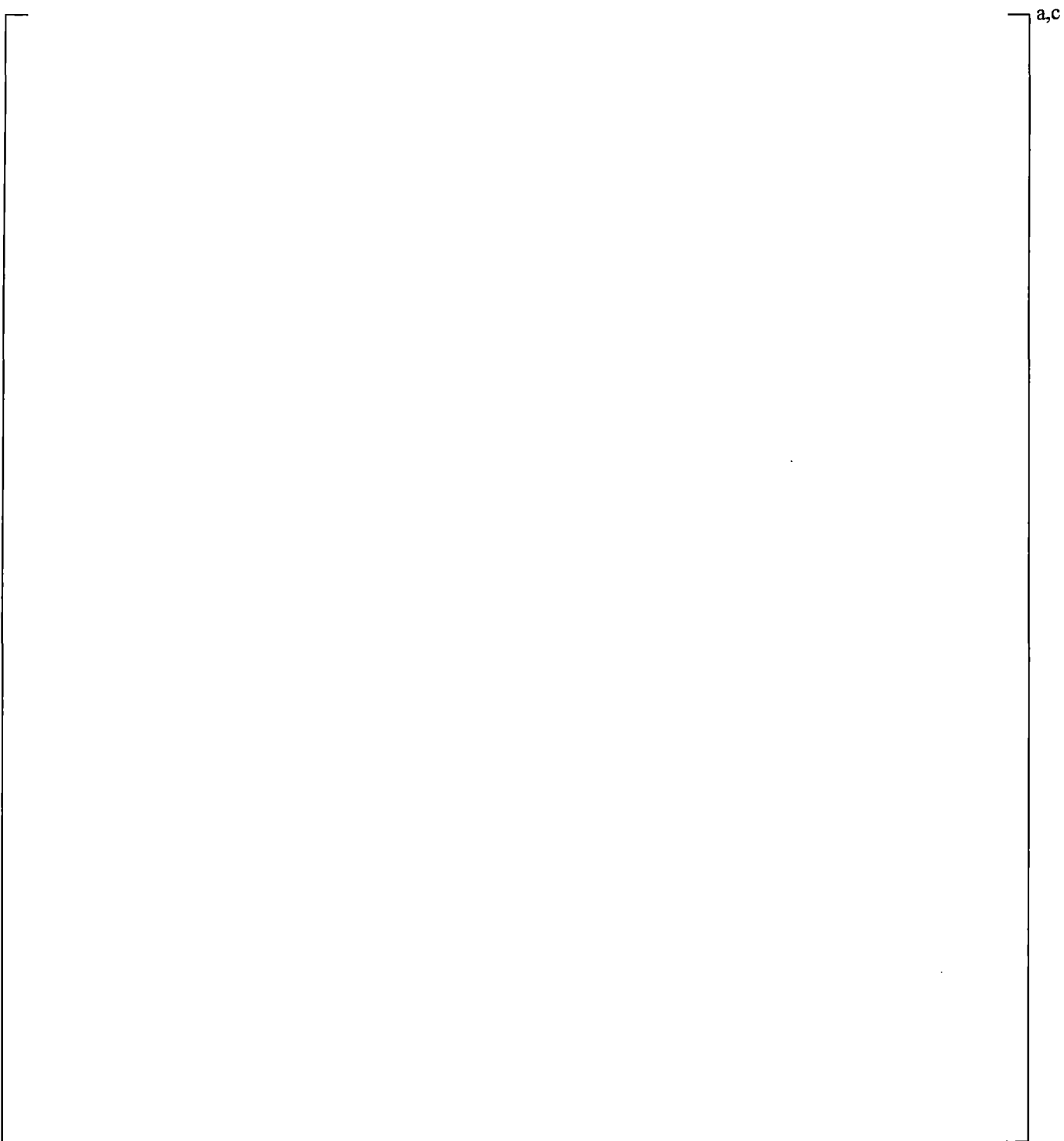


Figure 19.5-4 Predicted and Measured Carryover Fraction, FLECHT-SEASET Test 31203

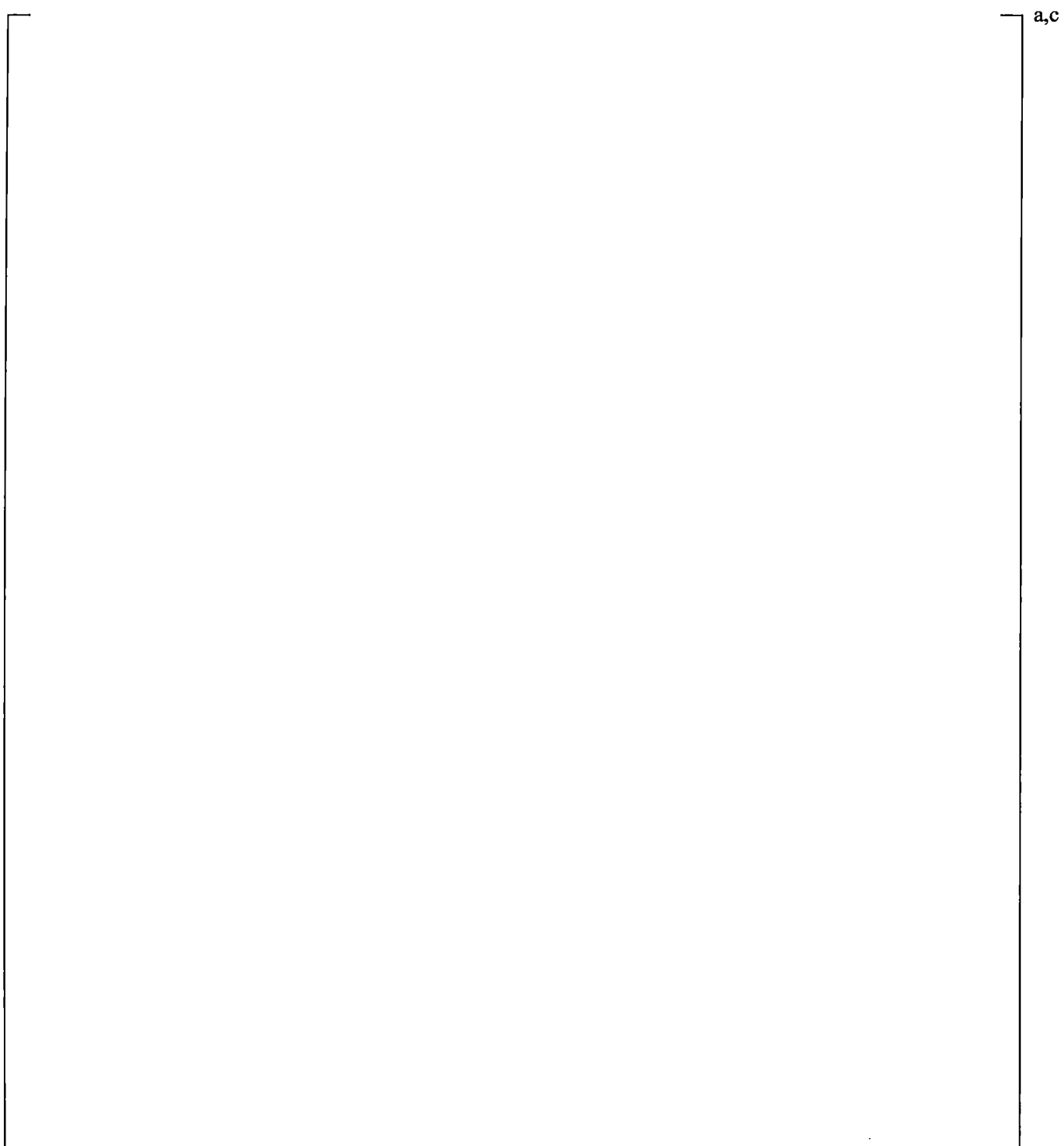


Figure 19.5-5 Predicted and Measured Carryover Fraction, FLECHT Test 04641

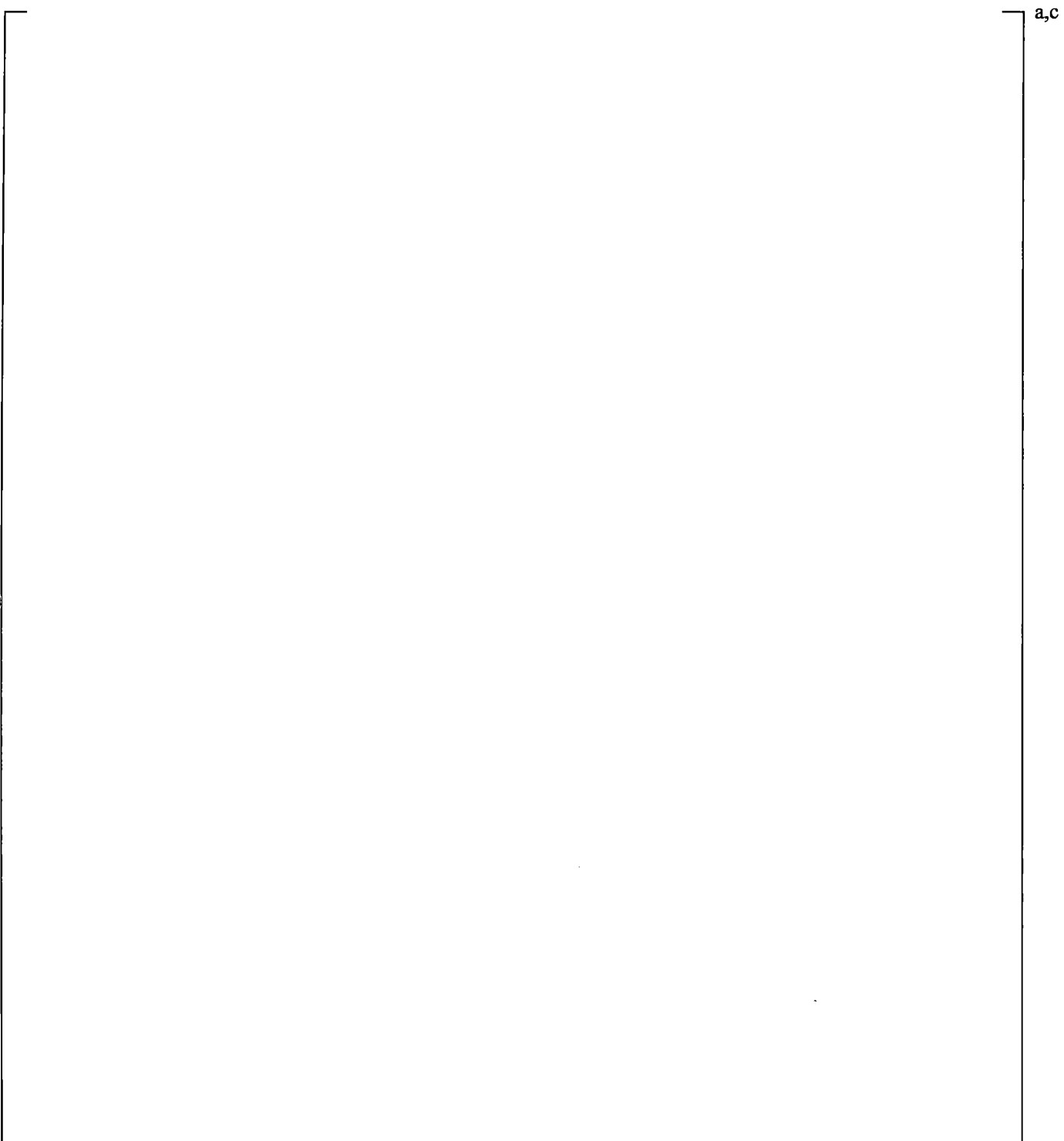


Figure 19.5-6 Predicted and Measured Carryover Fraction, FLECHT Test 05029

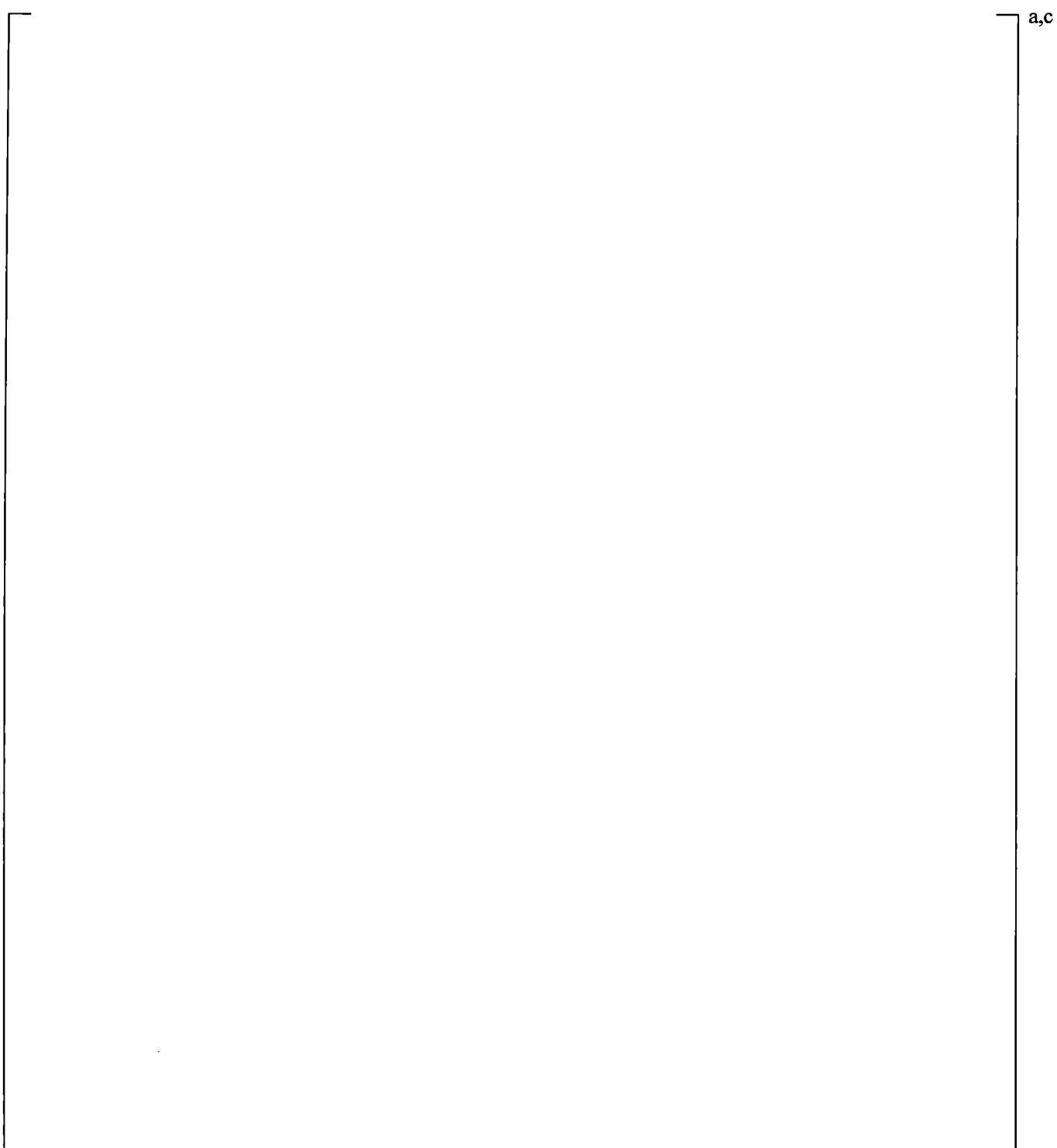


Figure 19.5-7 Predicted and Measured Carryover Fraction, FLECHT Top Skewed Test 15305

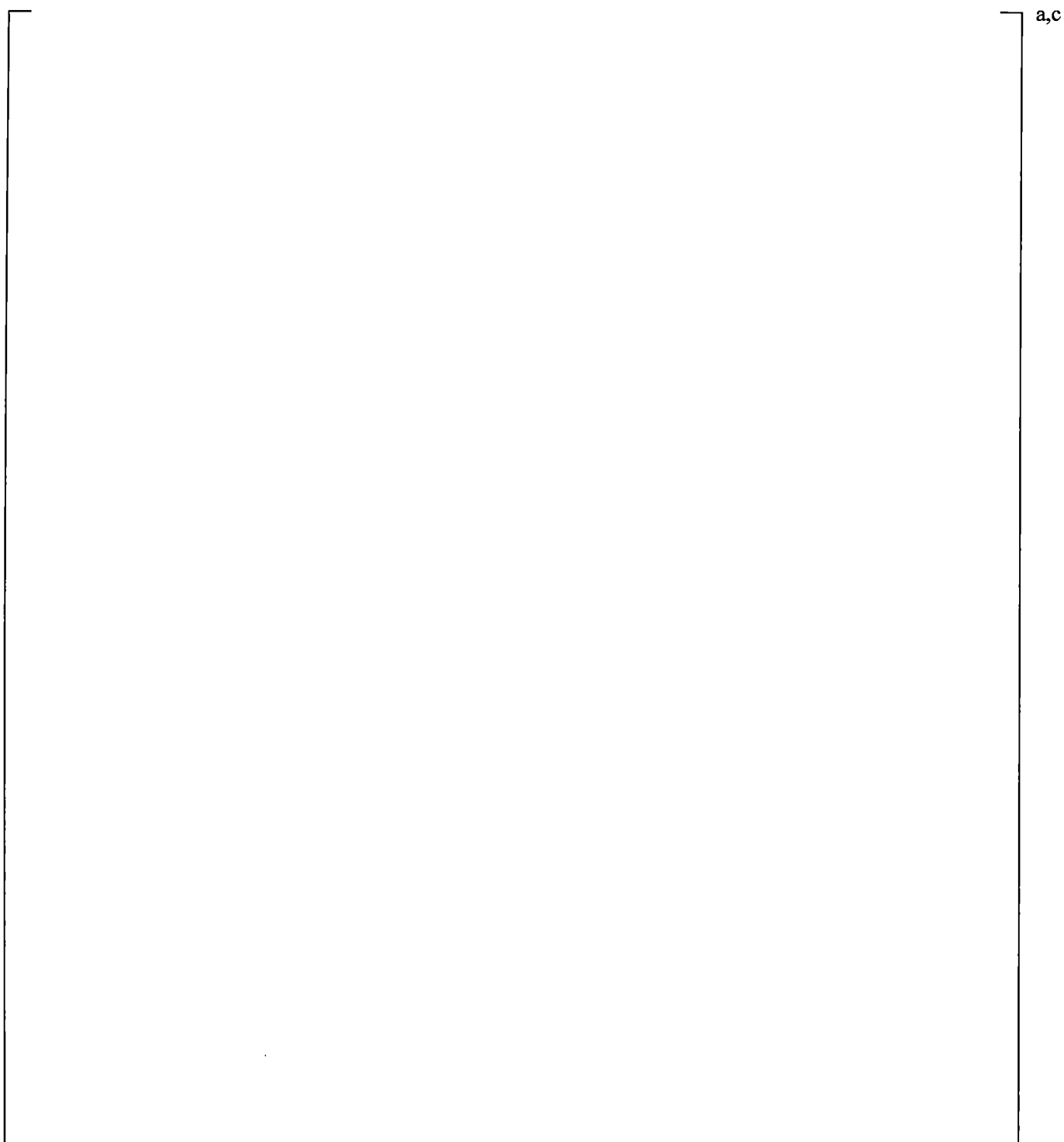


Figure 19.5-8 Predicted and Measured Carryover Fraction, FLECHT Top Skewed Test 13609

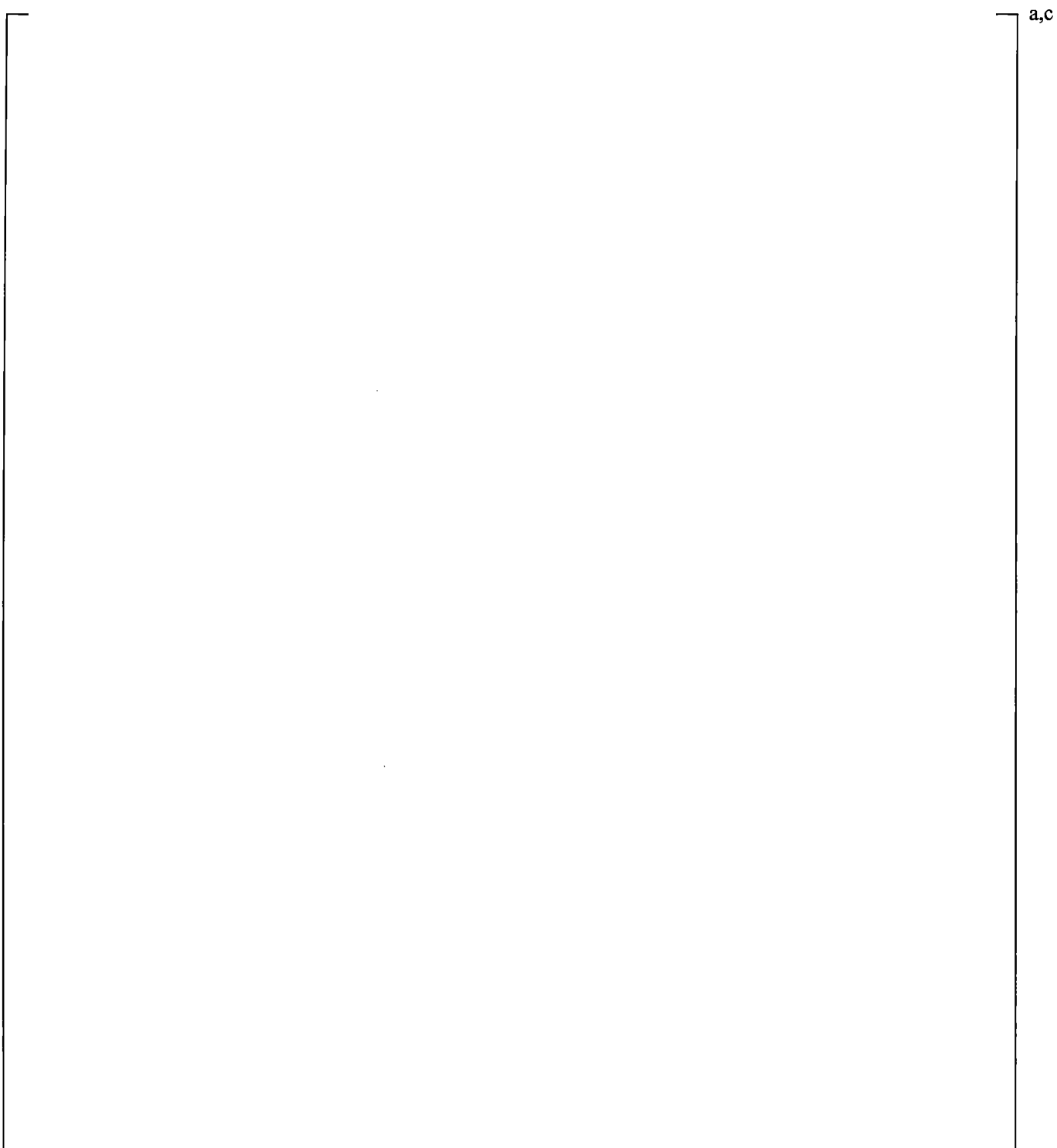


Figure 19.5-9 Predicted and Measured Carryover Fraction, FLECHT Top Skewed Test 13812

19.6 CYLINDRICAL CORE TEST FACILITY

To assess the capability of the WCOBRA/TRAC-TF2 computer code to predict the thermal-hydraulic core behavior in PWRs, specific code validation was performed using data from the Cylindrical Core Test Facility (Core II). The CCTF test program was conducted by JAERI and was used to investigate the thermal-hydraulic response of the plant during the refill and reflood phases associated with a postulated LBLOCA.

The objective of this section is to assess the ability of WCOBRA/TRAC-TF2 to predict the cladding temperature response, mass flows, and liquid distribution in CCTF. The important phenomena to be addressed by the CCTF 62 simulation are water accumulation in the upper plenum, the steam binding effect, and core quenching during gravity reflood. The facility and tests used for the prediction are summarized, the WCOBRA/TRAC-TF2 modeling is described in detail, and the predicted results are compared with data.

19.6.1 CCTF Tests

The CCTF tests are the largest scale integral tests available to investigate the phenomena important during the reflood phase of a PWR during a LBLOCA. CCTF has a flow area scaling of 1/21.4 of a four loop PWR. Their large scale makes them particularly suited as verification of the code's ability to handle the multi-dimensional thermal hydraulics in the core. In addition, the full-height scaling makes these tests important indicators on the extent to which core/downcomer oscillations affect the reflood transient.

The test chosen for simulation by WCOBRA/TRAC-TF2 is C2-4 (Run 62). Run 62 (Okubo et al., 1984) was taken as the reference test in the Code Qualification Document (Bajorek et al., 1998) CCTF Simulations; while other CCTF tests were examined in the CQD (63, 64, 67 and 75, as documented in Section 14-2-6-2 of the CQD), only this reference test is analyzed in detail herein.

The initial and boundary conditions for this test are given in Table 19.6-2. They are compared, where appropriate, with the range of conditions expected in a typical four-loop PWR at the beginning of reflood (scaled to CCTF).

19.6.2 CCTF Facility Description

The CCTF Core-II is a large scale experimental facility designed to study the system response of a typical four-loop PWR for loss-of-coolant transients (Figure 19.6-1). The facility is used to provide data on the thermal-hydraulic behavior in the primary system during the refill and reflood phases of a hypothetical LOCA in a PWR. Table 19.6-1 compares the scaled dimensions of the system components with those of a PWR.

The CCTF includes a full-height (12-foot heated length) core section with three intact loops, and a fourth loop simulating a full double-ended guillotine break. The test vessel includes a downcomer, lower plenum, core region, and upper plenum with associated internals (support columns and guide tubes). The dimensions for the vessel are shown in Figure 19.6-2. The configuration of the rods in the core and the upper plenum structure are shown in Figure 19.6-3. The core has 32 8x8 rod bundles each containing

57 electrically heated rods (0.421-inch OD) and 7 unheated/instrumented rods (0.543-inch OD). The rods have a pitch spacing of 0.563 inches. The geometry of these rods is equivalent to a typical PWR 15x15 fuel assembly. Each heated rod has a nichrome heating element and is packed with magnesium oxide and boron nitride. The sheath is made of Inconel-600. The rods are held together by six grids spaced at 26.18-inch intervals up the bundle.

The core is divided into the three main power zones: low, intermediate, and high. The lower power zone consists of 16 assemblies on the periphery of the core, as shown in Figure 19.6-3. The intermediate power zone consists of 12 assemblies, while the high power zone consists of the 4 central assemblies. Under guide tubes, there are 4 low power assemblies and 6 medium power assemblies. Under support columns, there are 8 low power assemblies and 2 high power assemblies. Under open holes, there are 4 low power assemblies, 6 medium power assemblies, and 2 high power assemblies. The axial power profile, along with the locations at the grid spacers, is shown in Figure 19.6-4.

The three intact loops and the broken loop each contain a steam generator and pump simulator. Flow from the broken loop enters two interconnected containment tanks via two blowdown valves, connected to each break. ECC water can be injected either from two accumulator tanks or by a low pressure coolant injection (LPCI) pump and its associated water storage tank. Water can be injected directly to injection ports positioned in the lower plenum or to the cold legs.

19.6.3 CCTF Test Procedure

The following is a general outline of the experimental test procedure. Figure 19.6-5 shows the sequence of events for the CCTF 62 test. The initial and boundary conditions for this test are given in Table 19.6-2. They are compared, where appropriate, with the range of conditions expected in a typical four-loop PWR at the beginning of reflood (scaled to CCTF).

The primary system was heated with pre-heaters to its specified temperatures and pressurized to a specified pressure using steam. The water in the LPCI tanks and accumulator tanks was heated to its specified temperature. LPCI water was circulated to ensure that the injection lines were at the same temperature. The accumulator tanks were pressurized with nitrogen to give sufficient head for the required injection flow. The steam generator secondary fluid was then heated and pressurized. The heaters were then turned off and the lower plenum was filled to the specified level with saturated water. When the initial conditions had been established, power was applied to the heater rods and data recording started (referred to as time zero.) The heater rods heated up under near adiabatic conditions until the cladding temperature reached a pre-specified value.

At this point accumulator injection to the lower plenum began. The containment tank pressure was maintained throughout the tests by controlling the outlet valve on the containment tanks. The heater rod power decay was initiated when the water reached the bottom of the heated length of the core (referred to as the BOCREC time). The water injection was changed from the lower plenum to the cold legs after a specified time. When the accumulator flow was coming to an end, LPCI flow was introduced to the cold legs and was maintained until the end of the test.

The generated steam and the entrained water flowed via broken and intact loops to the containment tanks. The steam was then vented to the atmosphere to maintain a constant pressure in the containment tanks. After all thermocouples on the surface of the heater rods indicated quench, the power supply to the heater rods and the ECC water injection were turned off. The recording system was then stopped, terminating the test.

19.6.4 WCOBRA/TRAC-TF2 CCTF Model

The WCOBRA/TRAC-TF2 model used for the CCTF simulations uses one-dimensional components for the intact loops (which models three CCTF loops) and for the broken loop, and employs a sub-channel formulated mesh for the vessel. First, the vessel component model is described. This is followed by a description of the loop model.

19.6.4.1 **Vessel Component Model**

The vessel component model is developed following the noding strategy in Section 26.1.1, Volume 3. A comparison between the CCTF and the PWR noding as presented in the FSLOCA methodology application is summarized in Table 19.6-3.

I^{a,c}

]^{a,c}

19.6.4.2 Loop Component Model

[

]^{a,c}

]^{a,c}

19.6.5 CCTF Run 62 Transient Calculation

In the following sections, the WCOBRA/TRAC-TF2 predictions are examined. Predicted cladding temperatures are compared with data averages of all instrumented rods within the channel (excluding obviously bad data channels). Predicted vapor fractions are compared with vapor fractions estimated from differential pressure (delta-p) measurements. In the core, the delta-p between several one-foot spans is available. Collapsed water levels and masses in various components are also estimated from the delta-p measurements. In CCTF, the liquid and vapor mass flows in the loops were measured at instrument spool pieces containing turbine meters and drag discs. The locations of these measurements in the system are shown in Figure 19.6-1.

The discussion provided here is intended to assess key variables and identify important differences between the predictions and the data. This run has the nominal test conditions which are summarized in Table 19.6-2. It is noted the simulation of CCTF 62 starts from BOCREC (bottom of core recovery) which is 94s after the test initialized, and the comparisons in this section are based on time of BOCREC.

In general, peak cladding temperatures (PCTs) and quench times in the CCTF tests tend to be []^{a,c} (Figures 19.6-20 to 19.6-22 and Table 19.6-5). [

]^{a,c}

There are two thermal couples at 6 ft. [

]^{a,c}

The core collapsed liquid level is shown in Figure 19.6-24. [

]^{a,c}

Figures 19.6-31 to 19.6-33 compare the predicted steam temperature rise and the measured temperature rise across the steam generators in 3 intact loops. [

]^{a,c}

Figures 19.6-34 and 19.6-35 compare the predicted and the measured total flow rates in the intact and broken hot legs. [

] a,c

The integrated core inlet mass flow rates are shown in Figure 19.6-36. [

12, c

For the CCTF Test C2-4 Run 62 simulation, the WCOBRA/TRAC-TF2 calculated clad temperature is []^{a,c} the experimental data considering the same elevations.

The results from the CCTF 62 test show the code giving reasonable prediction of the various phenomena involved. [

1a, 6

19.6.6 DTMAX Sensitivity Study for CCTF 62

To support the time step sensitivity study in Section 28.1.3, Volume 3, the sensitivity studies for DTMAX are carried out for the CCTF 62 test. |

Those time step sizes are consistent with those used in the plant model in Section 26, Volume 3. In this sensitivity study, the relative []^{a,c} time step sizes are chosen to show the effect of time step sensitivity. For the initial surge stage, the time step size is increased from []^{a,c}, while []^{a,c} are used for the remaining reflood period.

Figures 19.6.37 to 19.6.39 compare the predicted cladding temperatures at elevations of 6.0 ft, 8.0 ft, and 10.0 ft, respectively. []

]^{a,c}

In general, the time step sensitivity study shows the time step size effect is []^{a,c} for the CCTF 62 simulation, which covers the initial surge of the reflood period of a LBLOCA.

Table 19.6-1

12, C

a,c

Table 19.6-2 [

^{a,c}

a,c

Table 19.6-3

] a,c

a,c

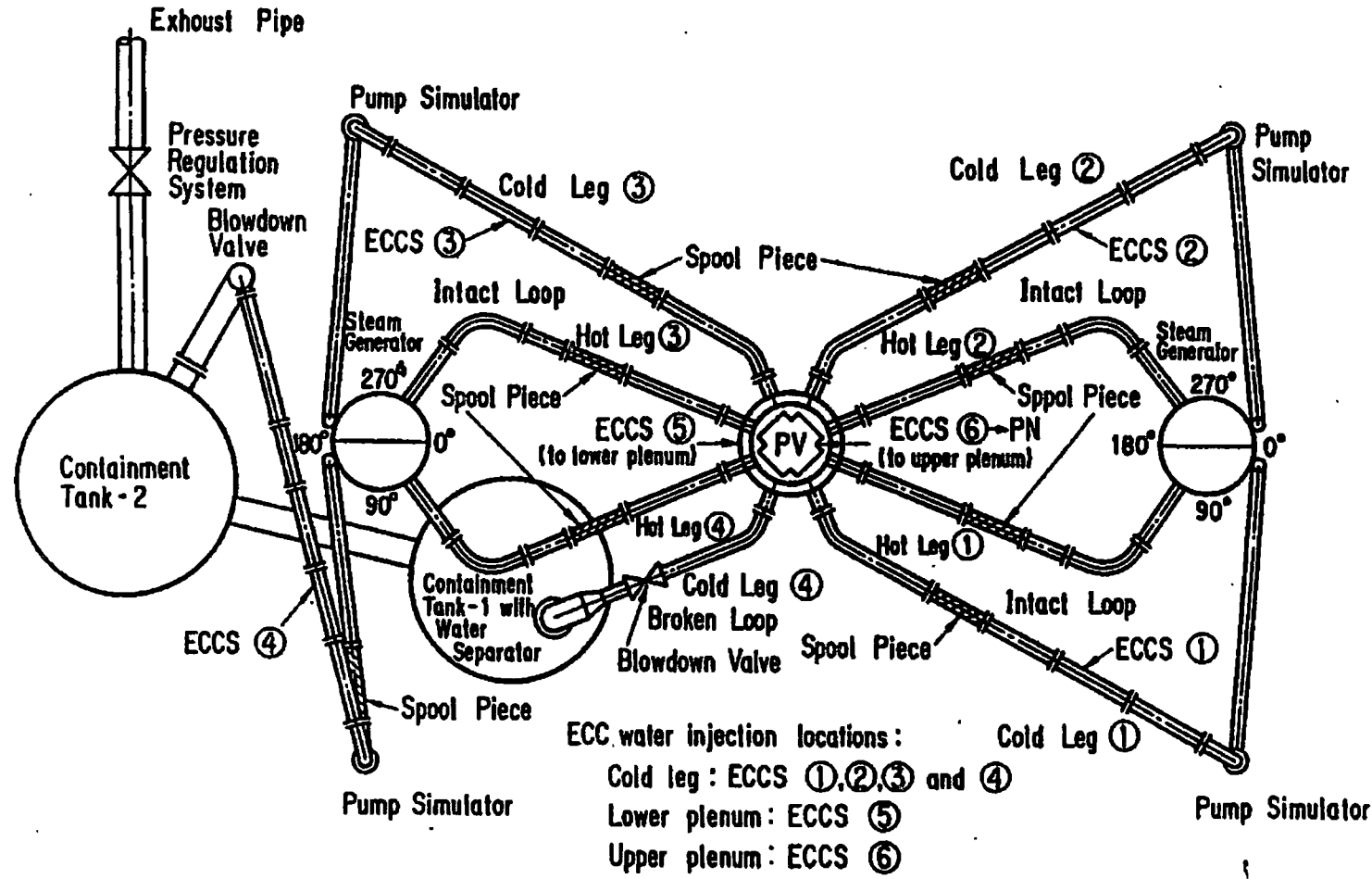
Table 19.6-4]^{a,c}

a,c

Table 19.6-5]^{a,c}

a,c

Figure 19.6-1 Top View of Primary Loop Piping



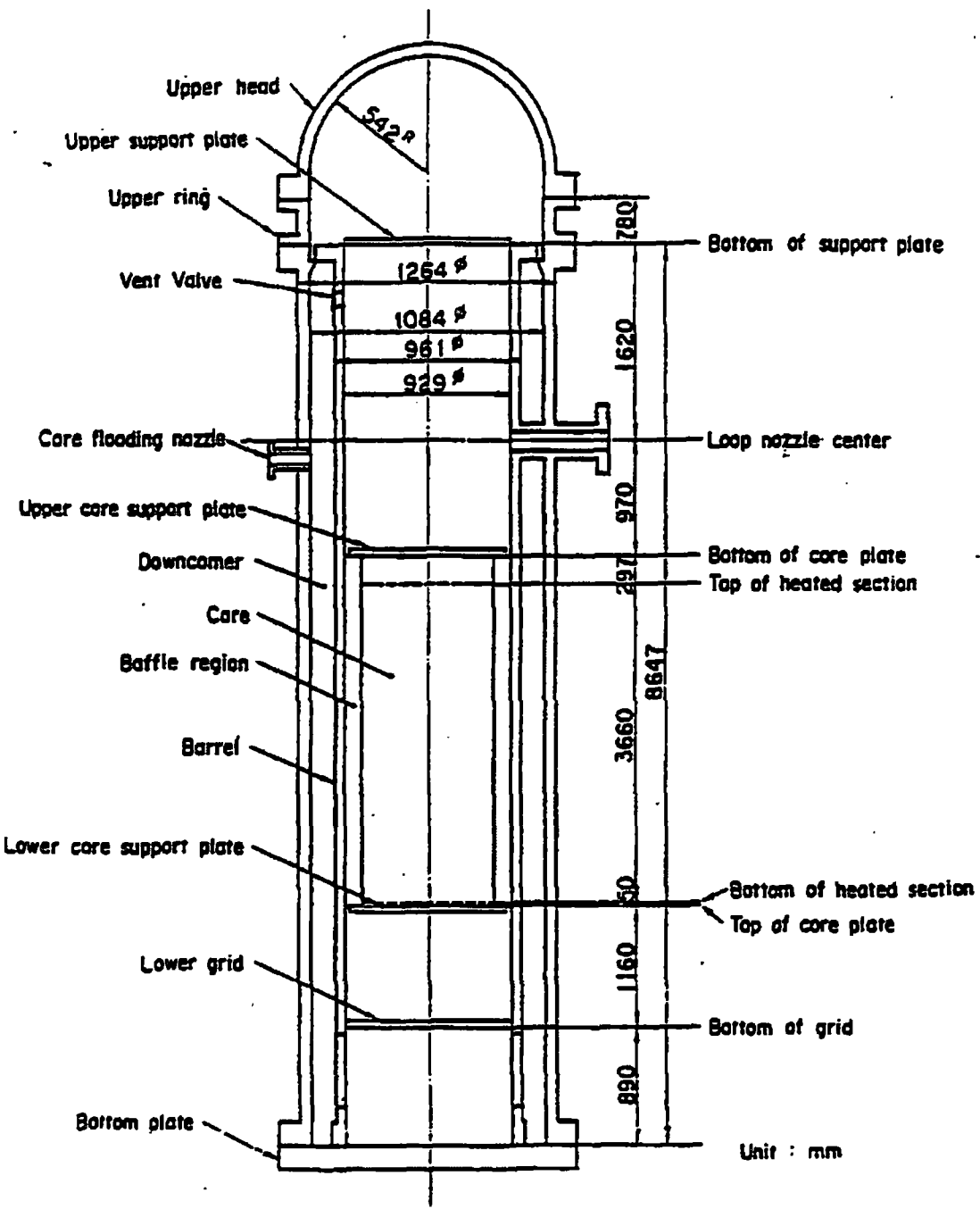


Figure 19.6-2 Diagram of CCTF Pressure Vessel

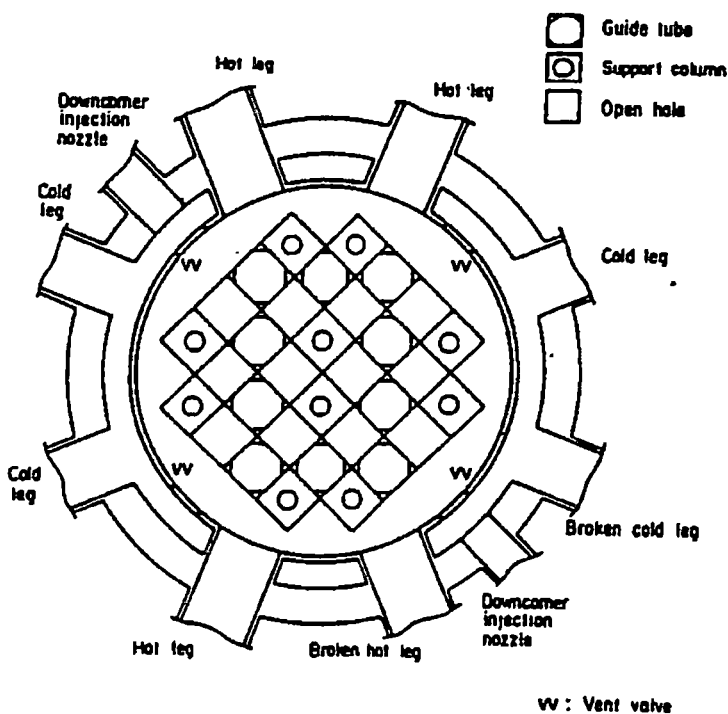
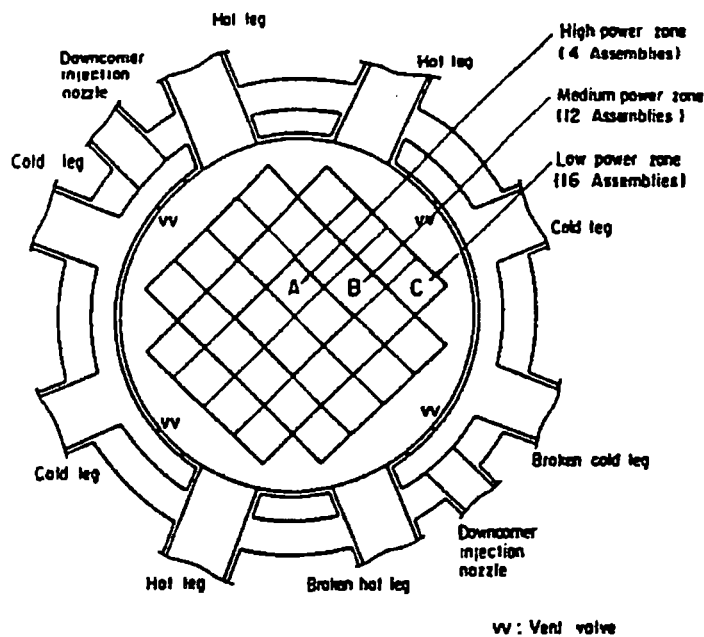


Figure 19.6-3 CCTF Cross Sections (a) Pressure Vessel (b) Upper Plenum Internals

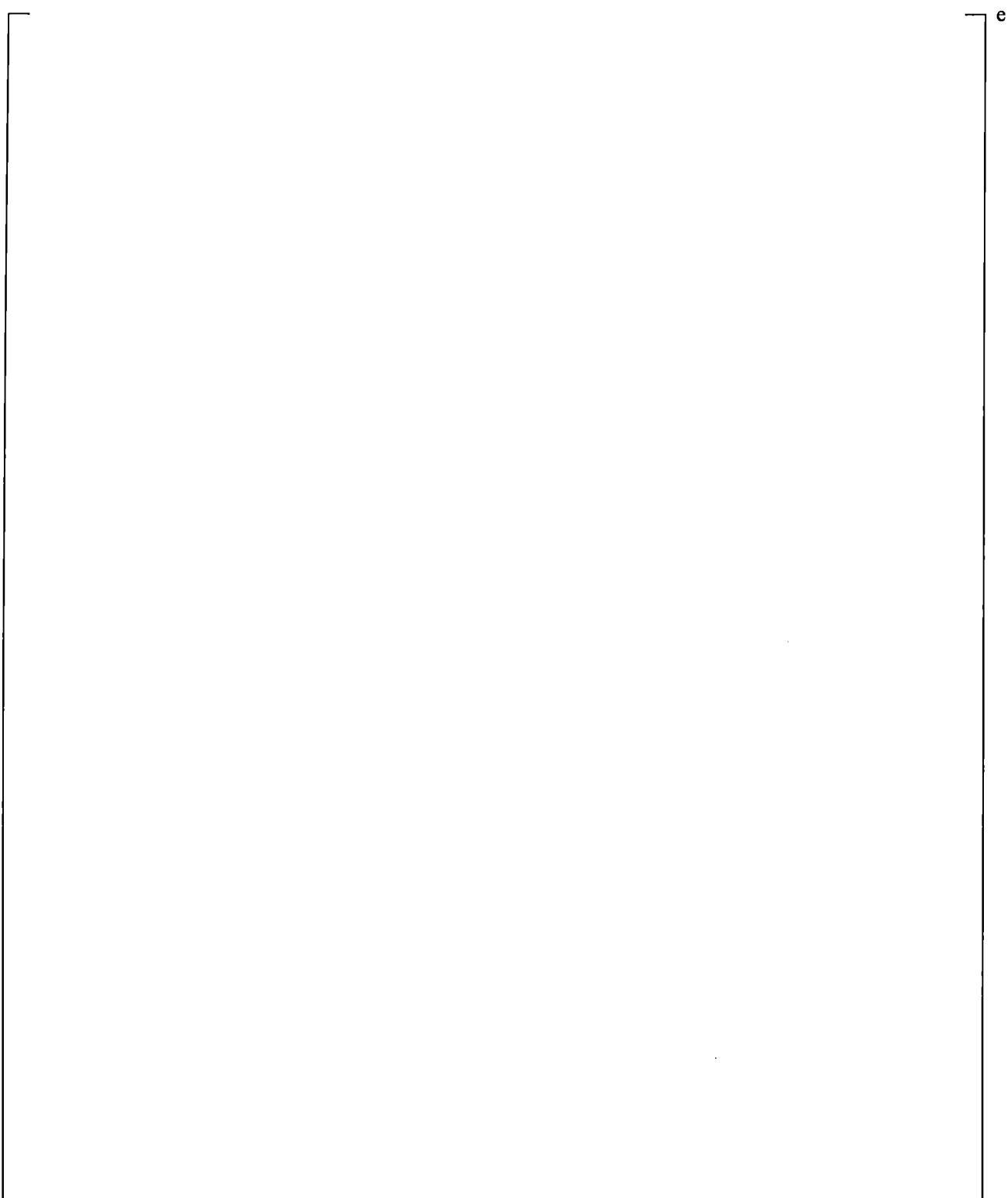


Figure 19.6-4 Axial Power Profile of Heated Rods in CCTF

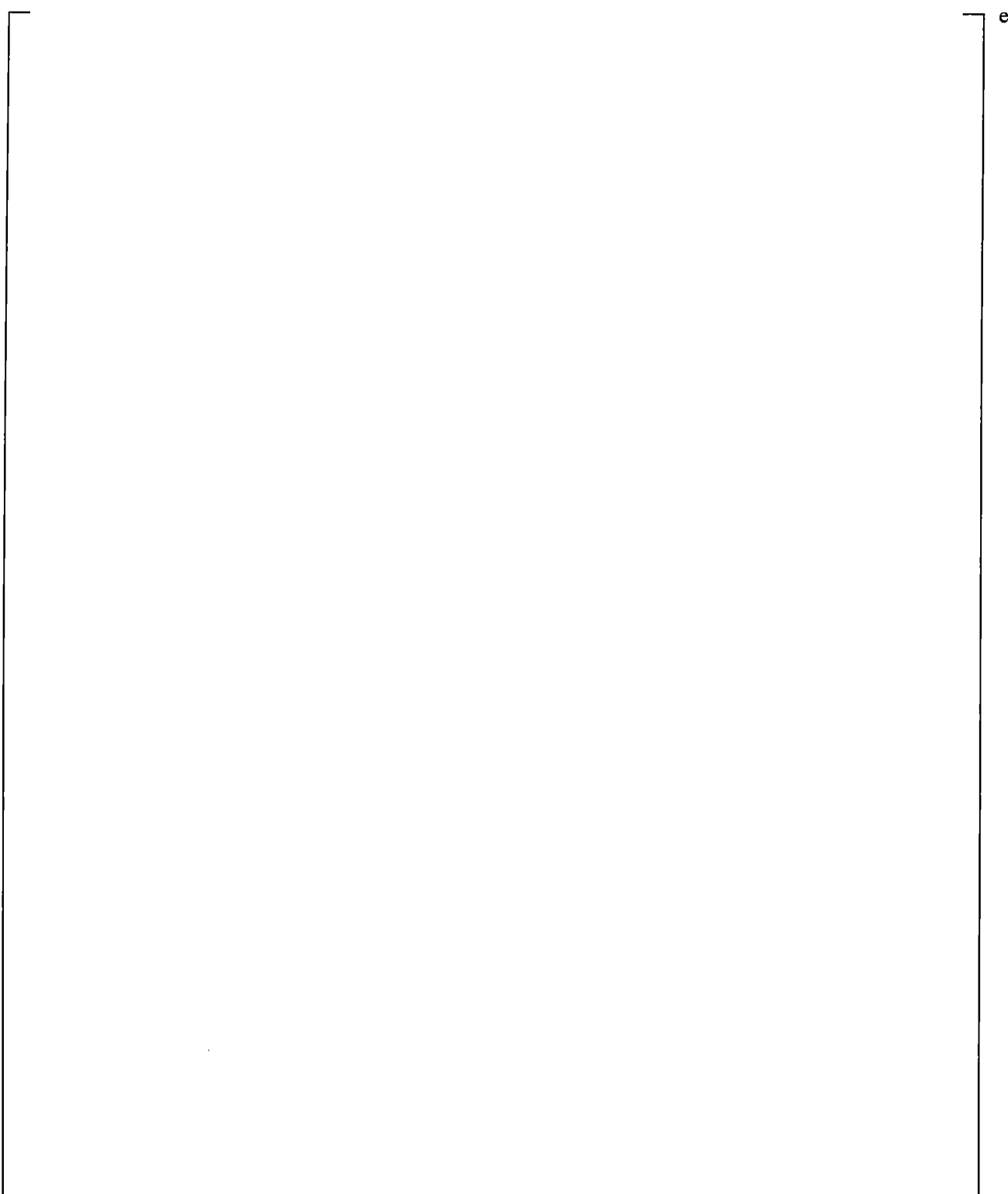


Figure 19.6-5 CCTF Test Sequence for Run 62



Figure 19.6-6 CCTF Vessel Noding Diagram

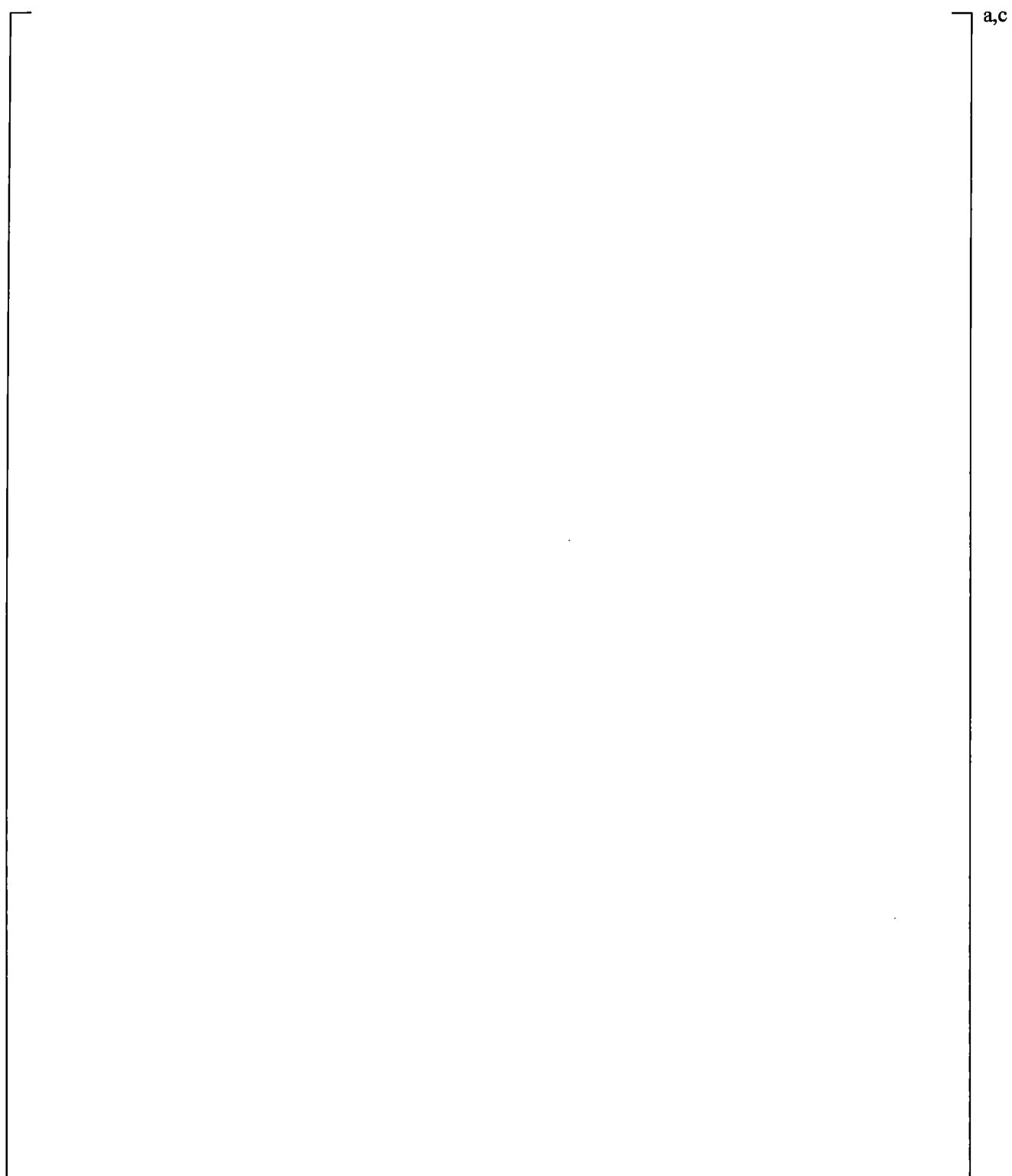


Figure 19.6-7 CCTF Section 1 Noding

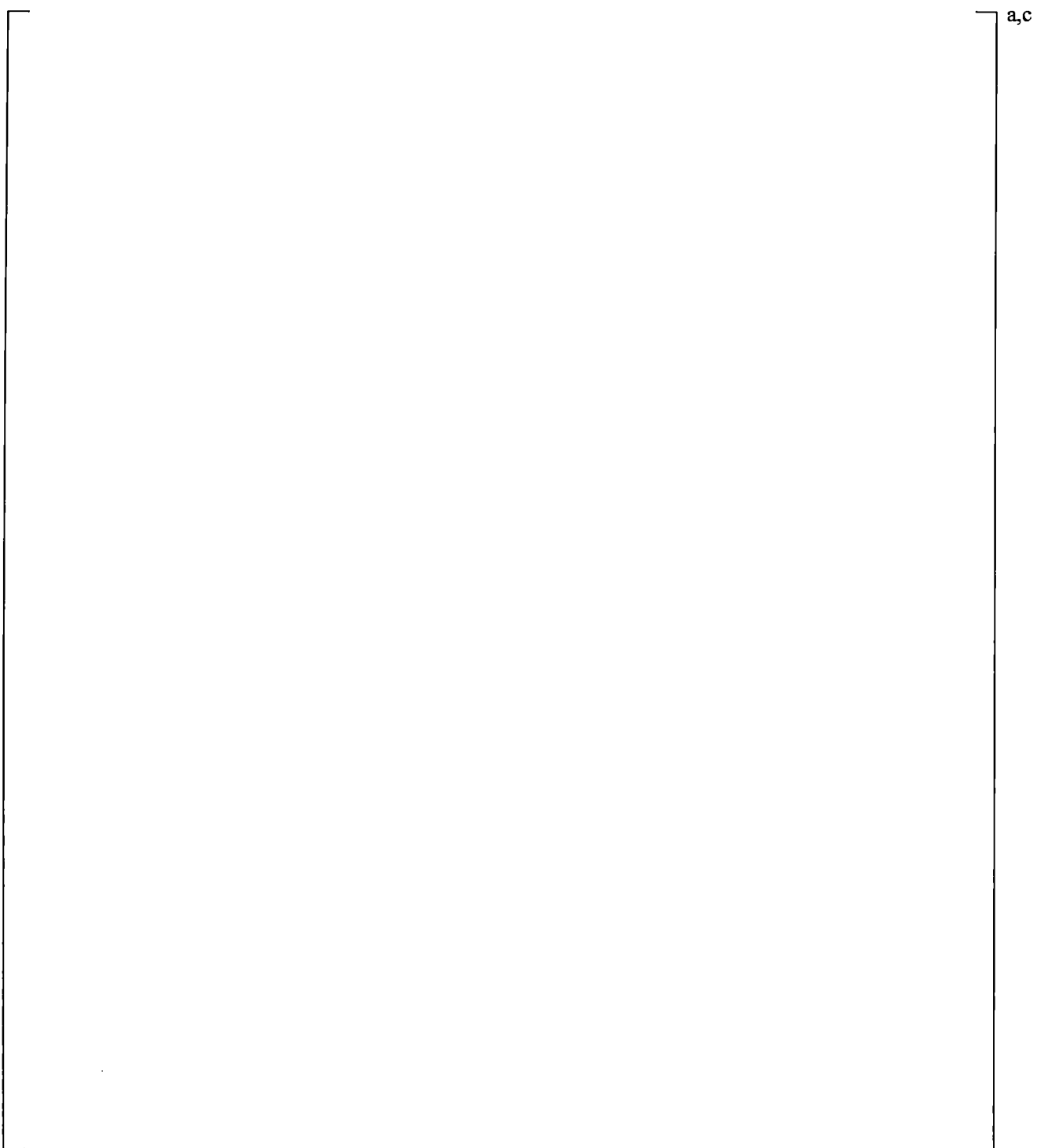


Figure 19.6-8 CCTF Section 2 Noding

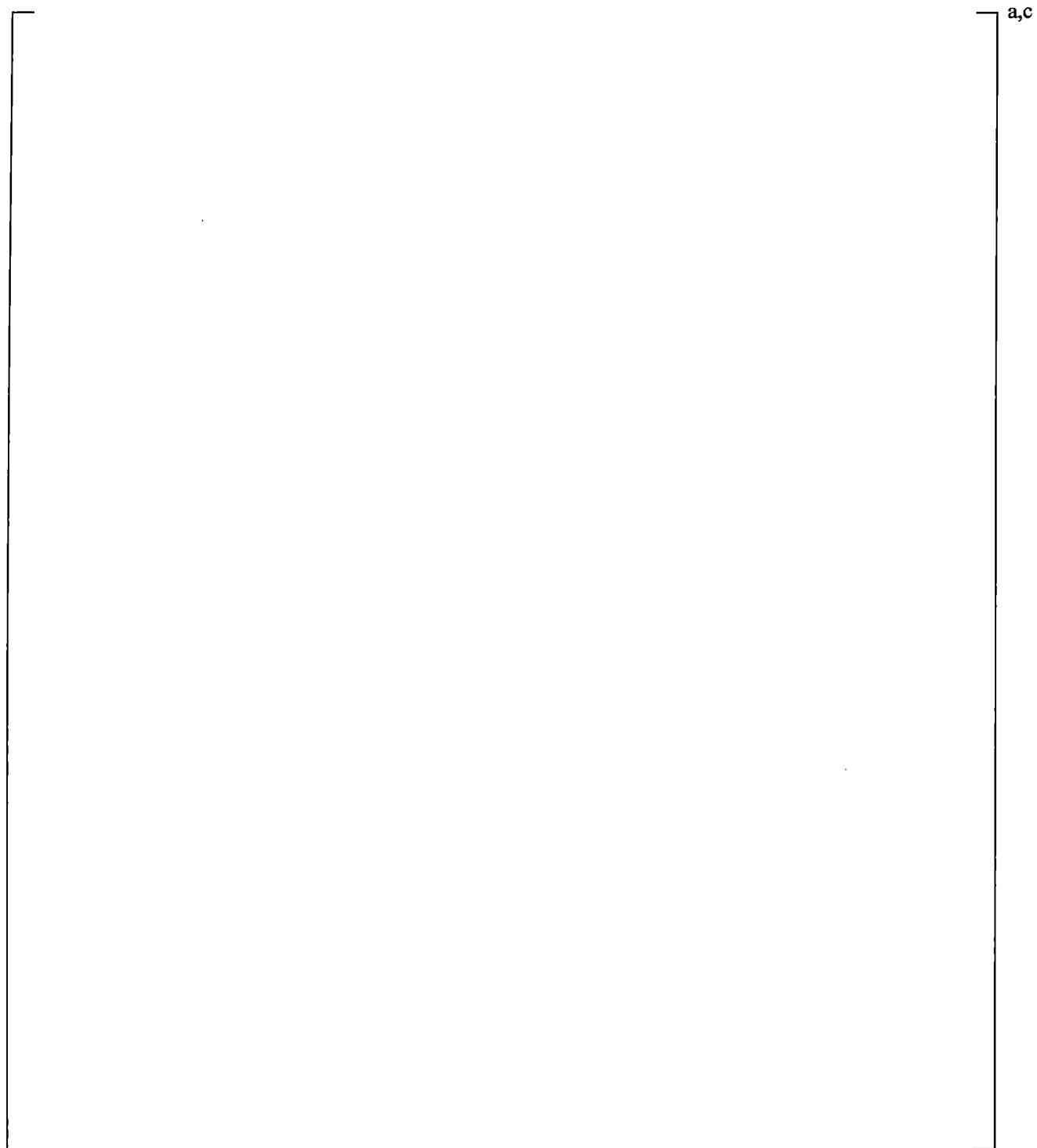


Figure 19.6-9 CCTF Section 3 Noding

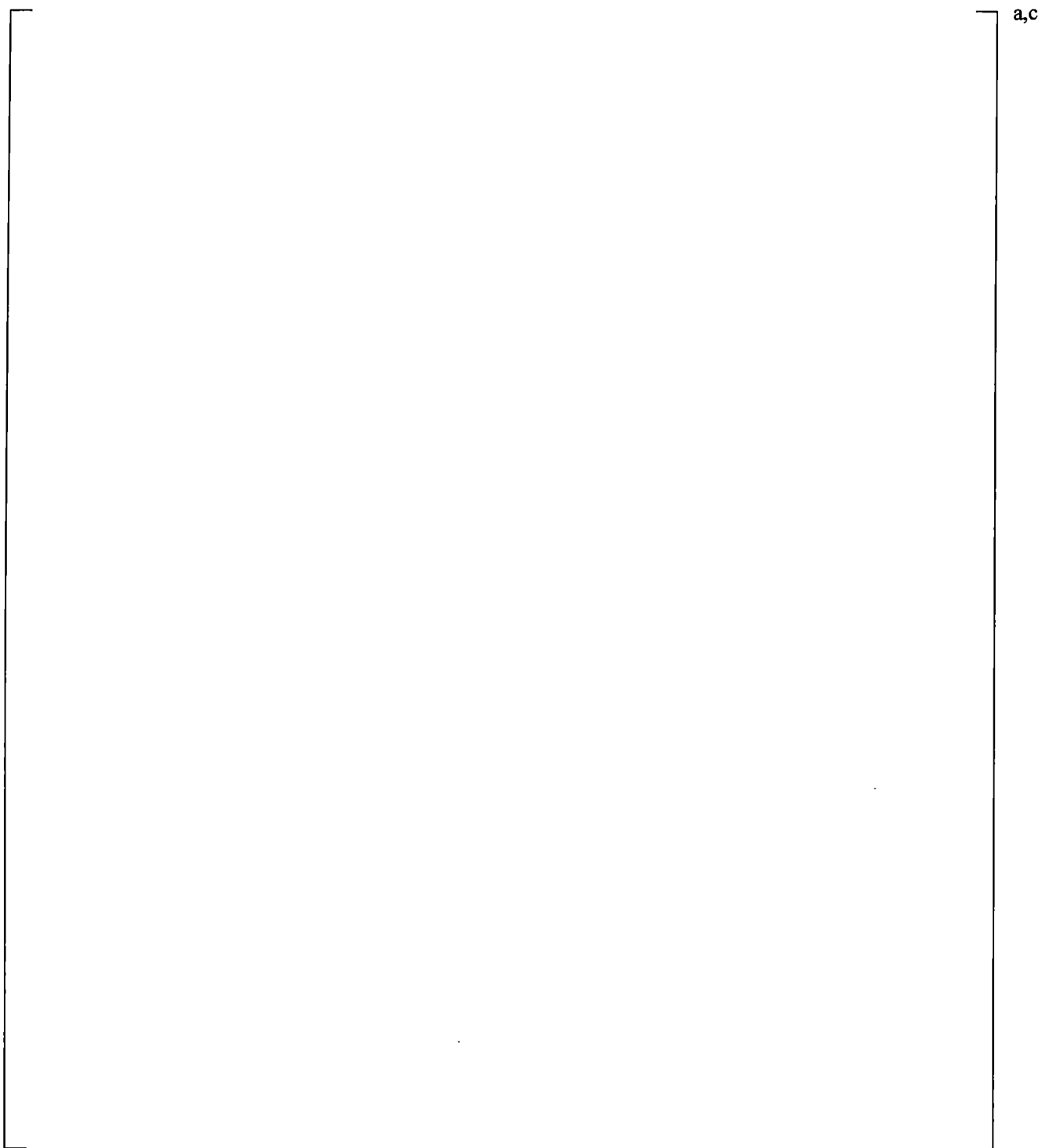


Figure 19.6-10 CCTF Section 4 Nodding

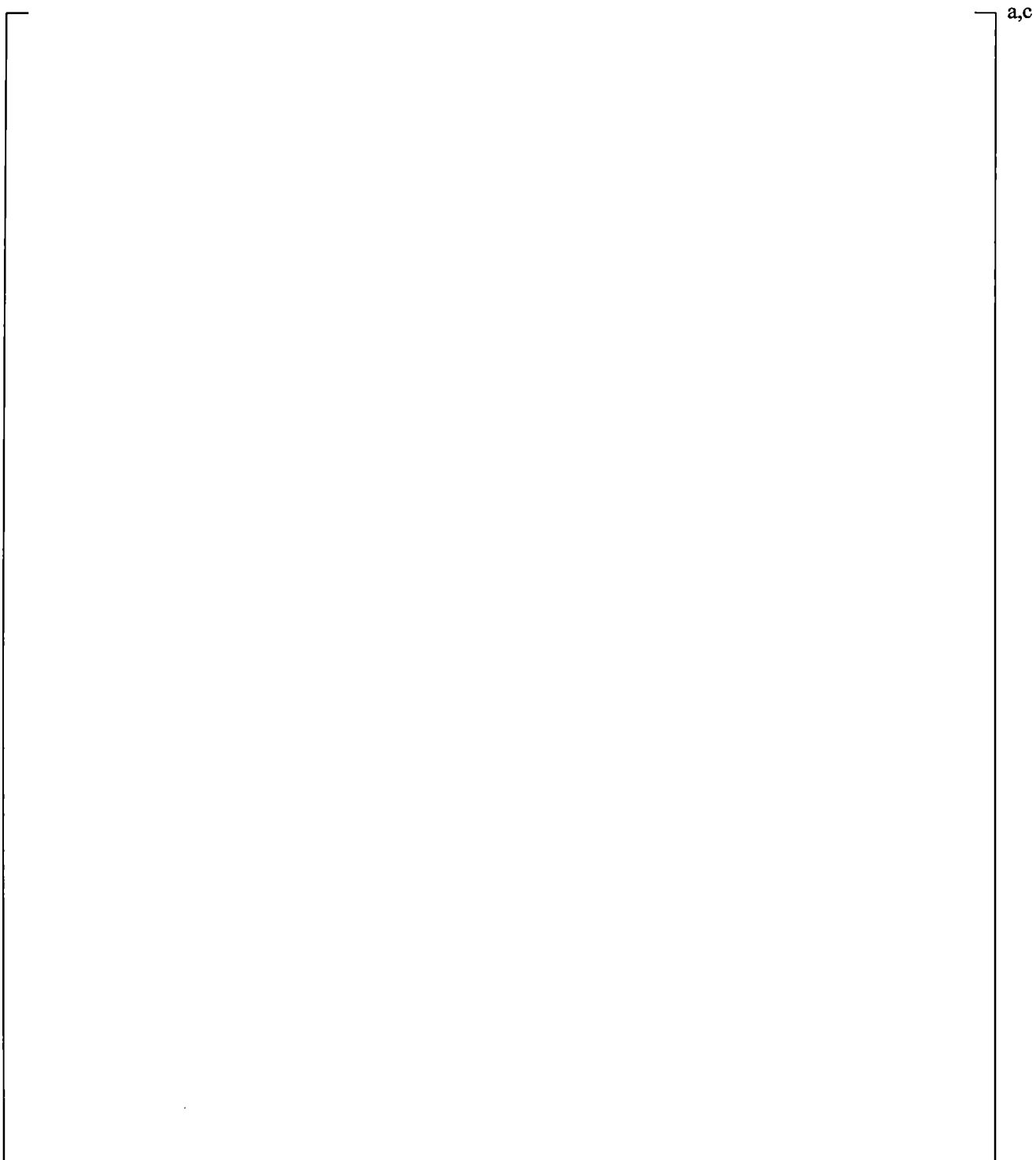


Figure 19.6-11 CCTF Section 5 Nodding

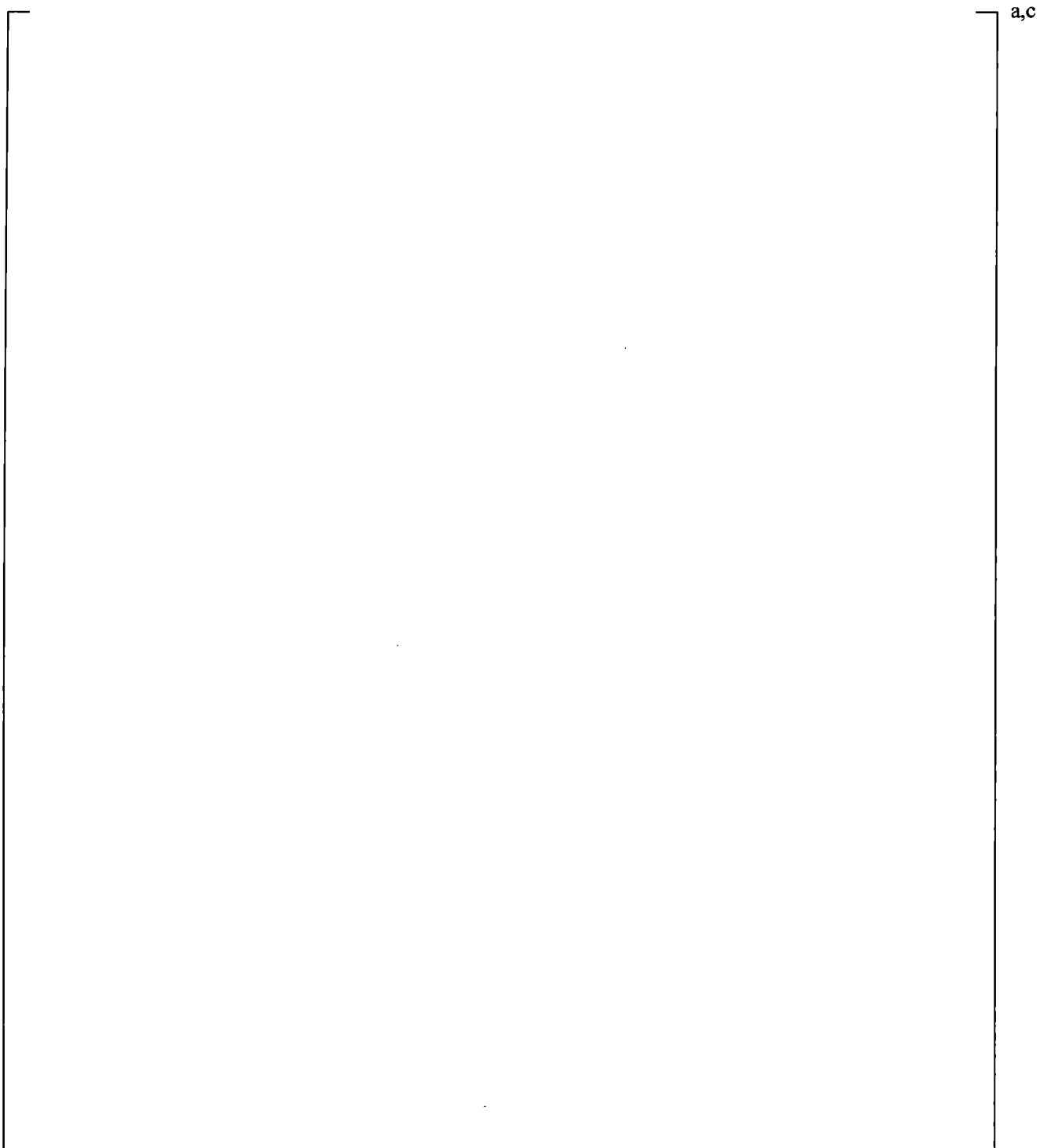


Figure 19.6-12 CCTF Section 6 Nodding

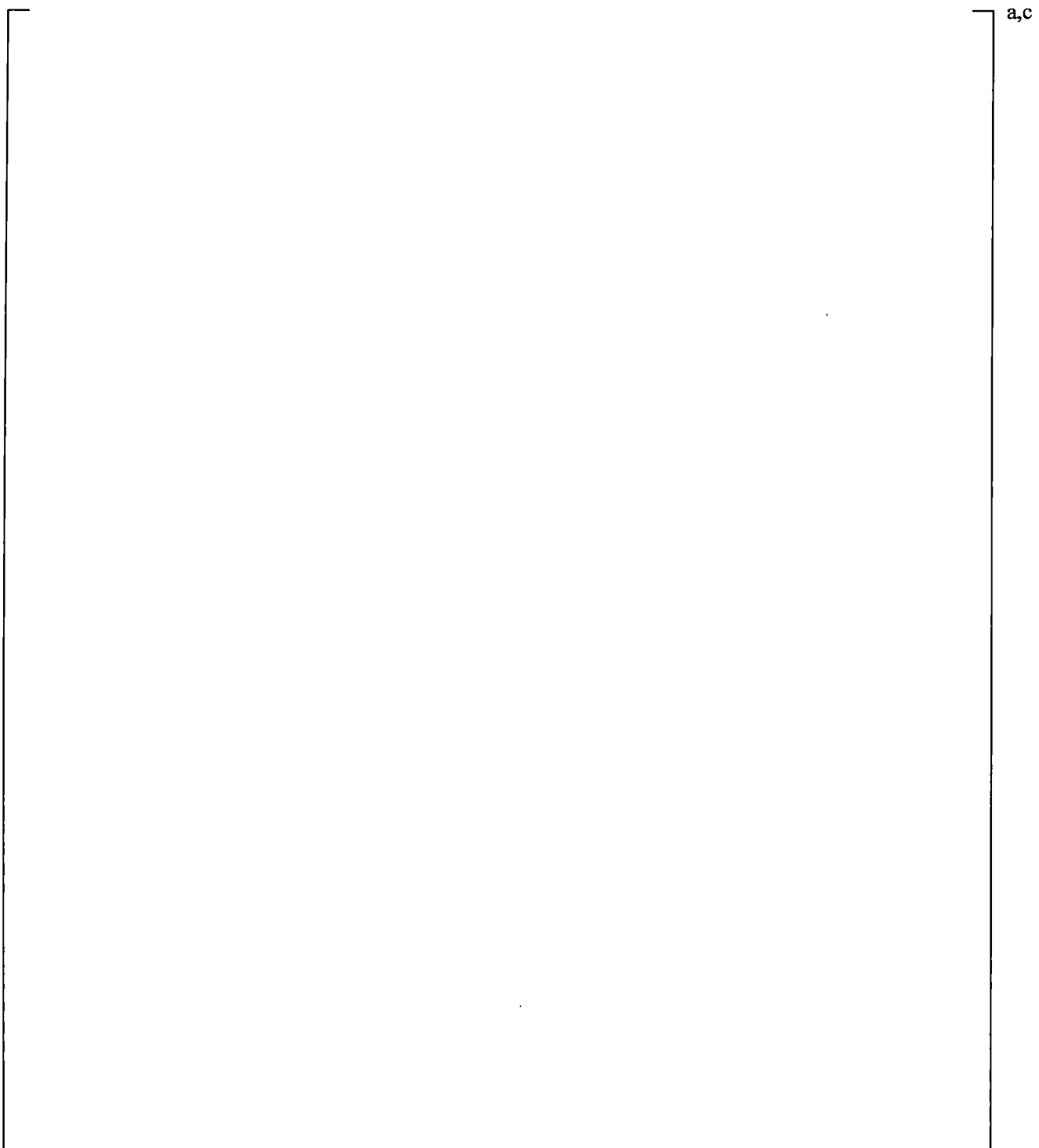


Figure 19.6-13 CCTF Section 7 Nodding

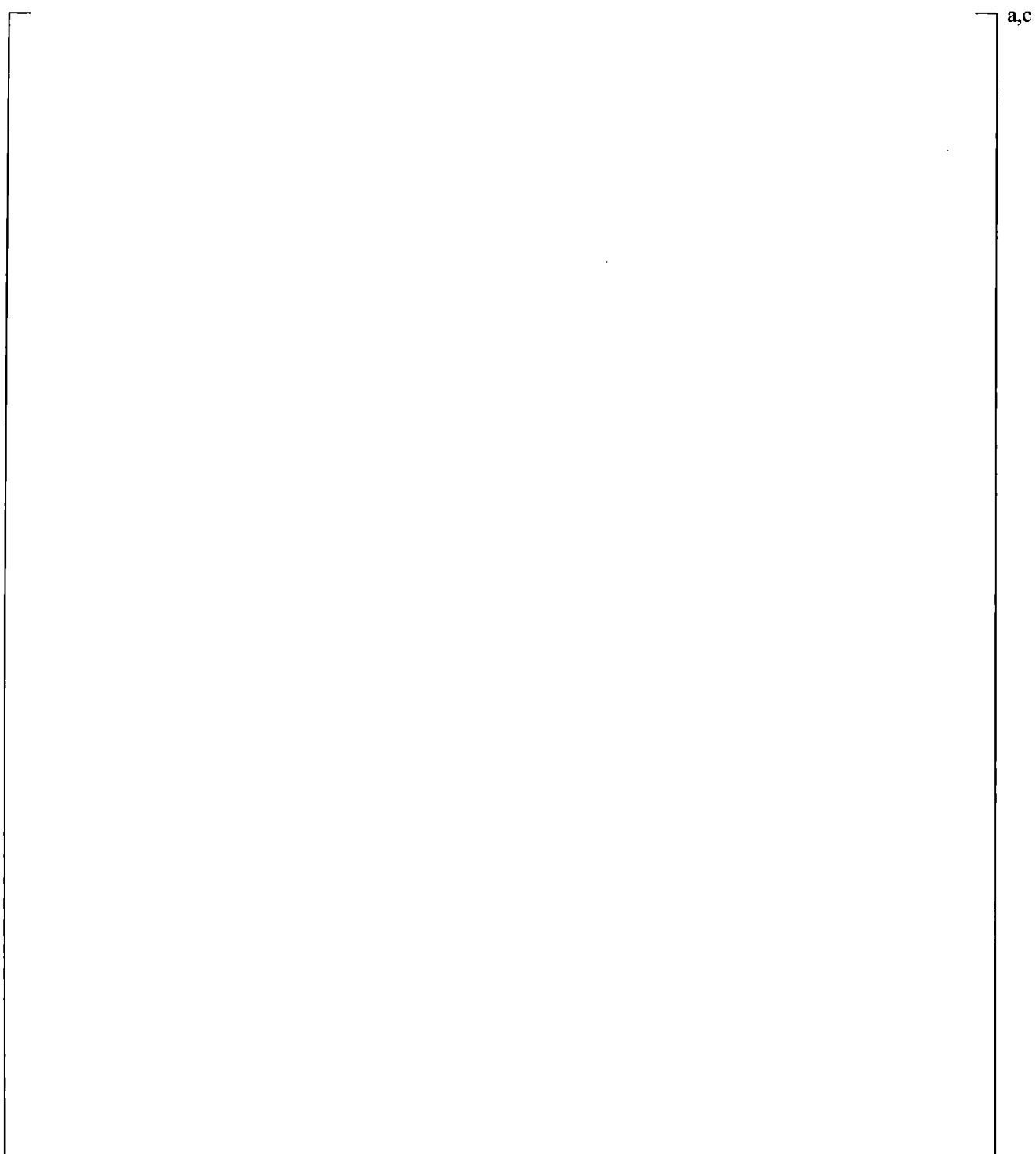


Figure 19.6-14 CCTF Loop Component Diagram

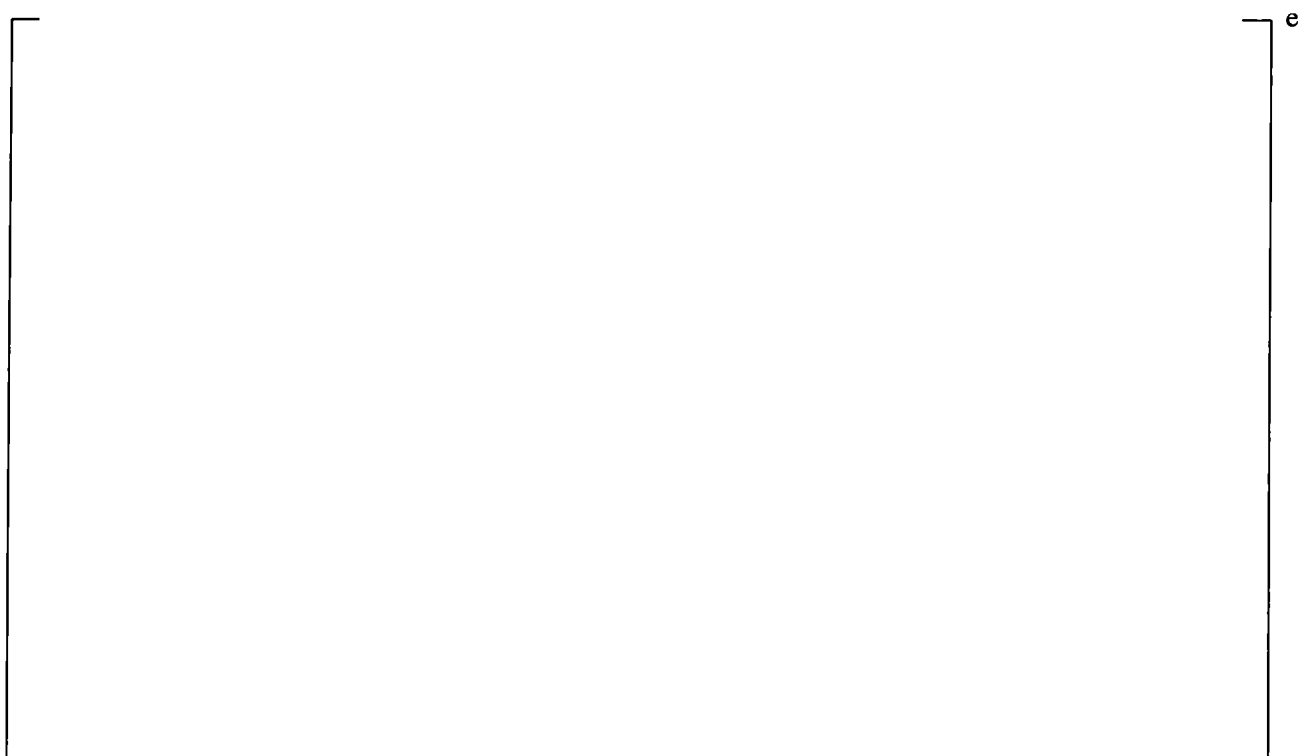


Figure 19.6-15 Dimensions of Hot Leg in CCTF

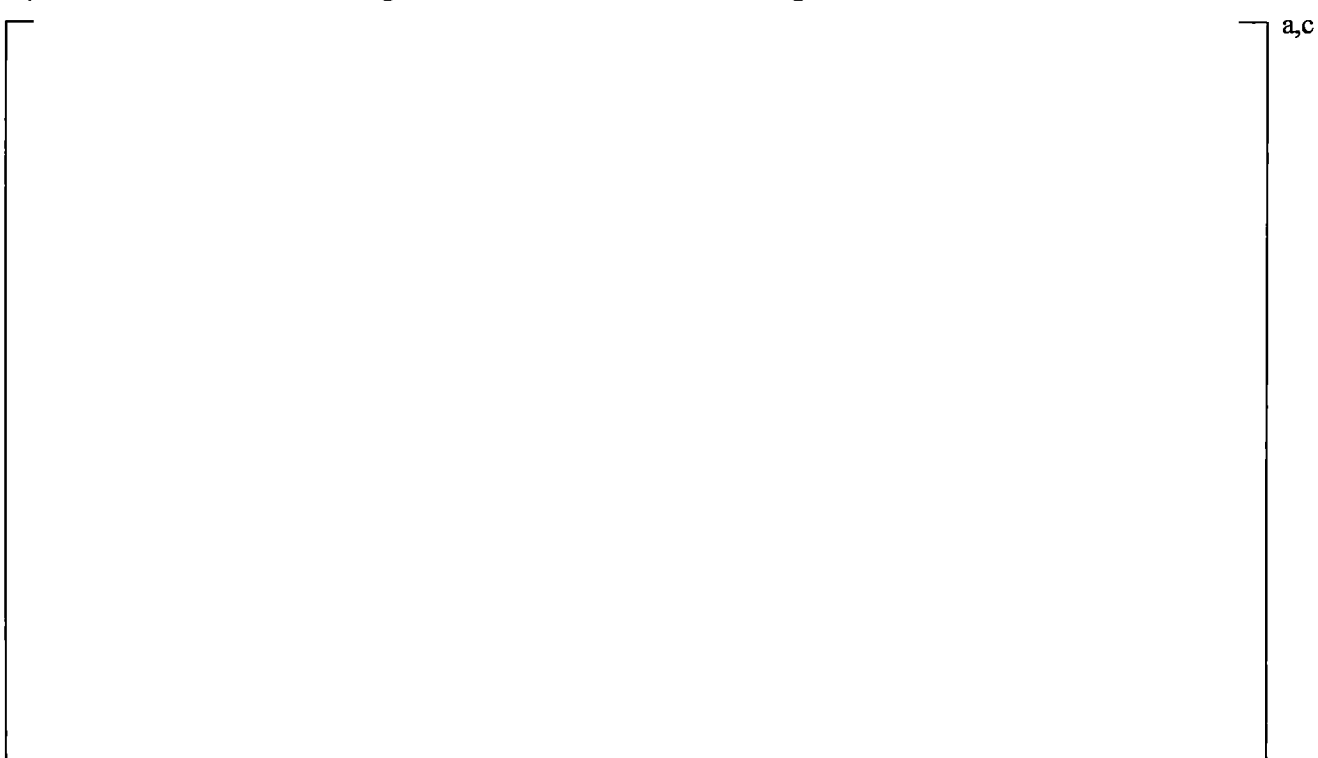


Figure 19.6-16 Noding Diagram of Hot Leg



Figure 19.6-17 Dimension of Crossover Leg, Pump Simulator, Cold Leg, and ECC Port in CCTF



Figure 19.6-18 Noding Diagram of Crossover Leg, Pump Simulator, Cold Leg, and ECC Port in Loop 1; Other Intact Loops are Identical to Loop 1

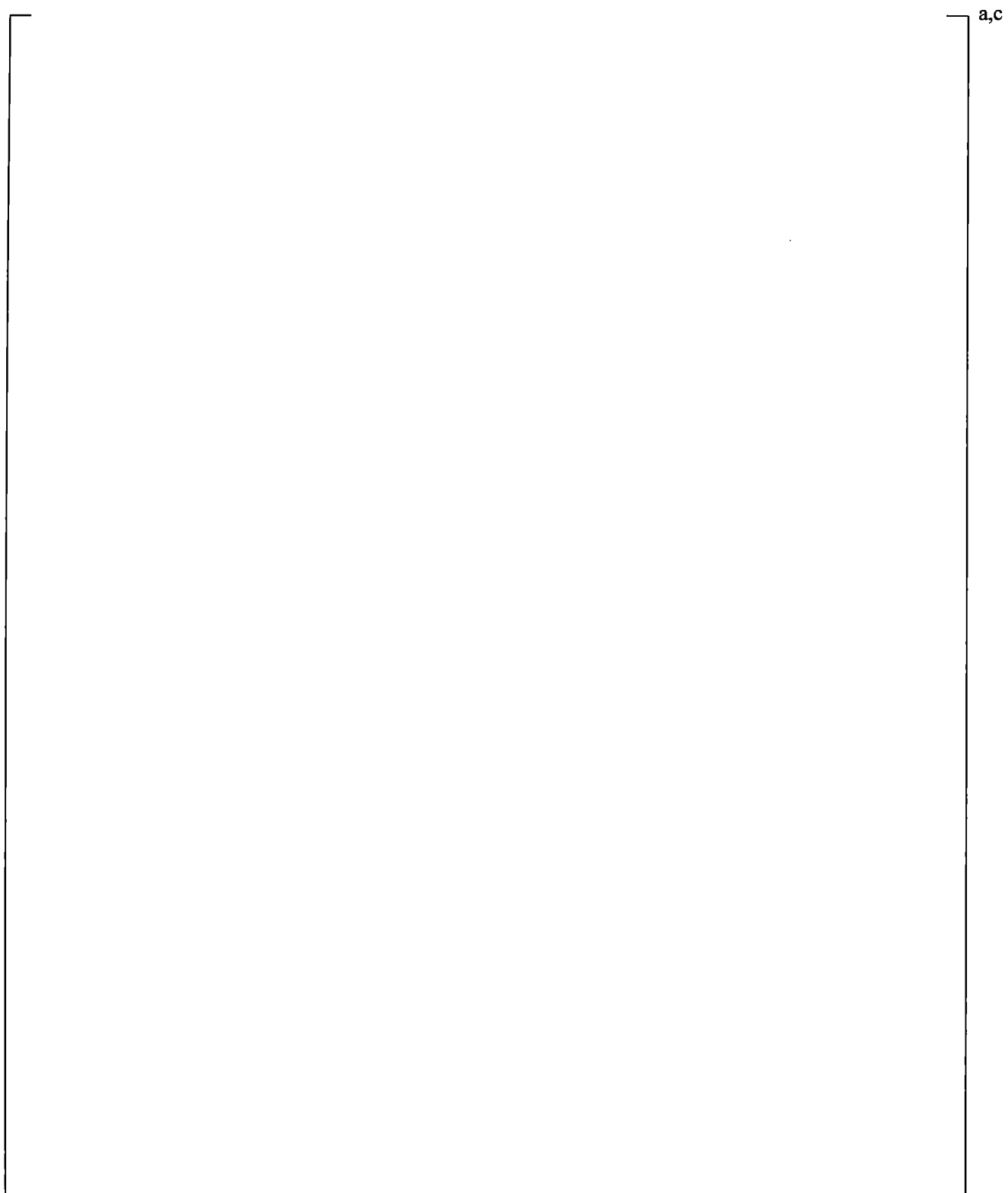


Figure 19.6-19 Steam Generator Component Diagram

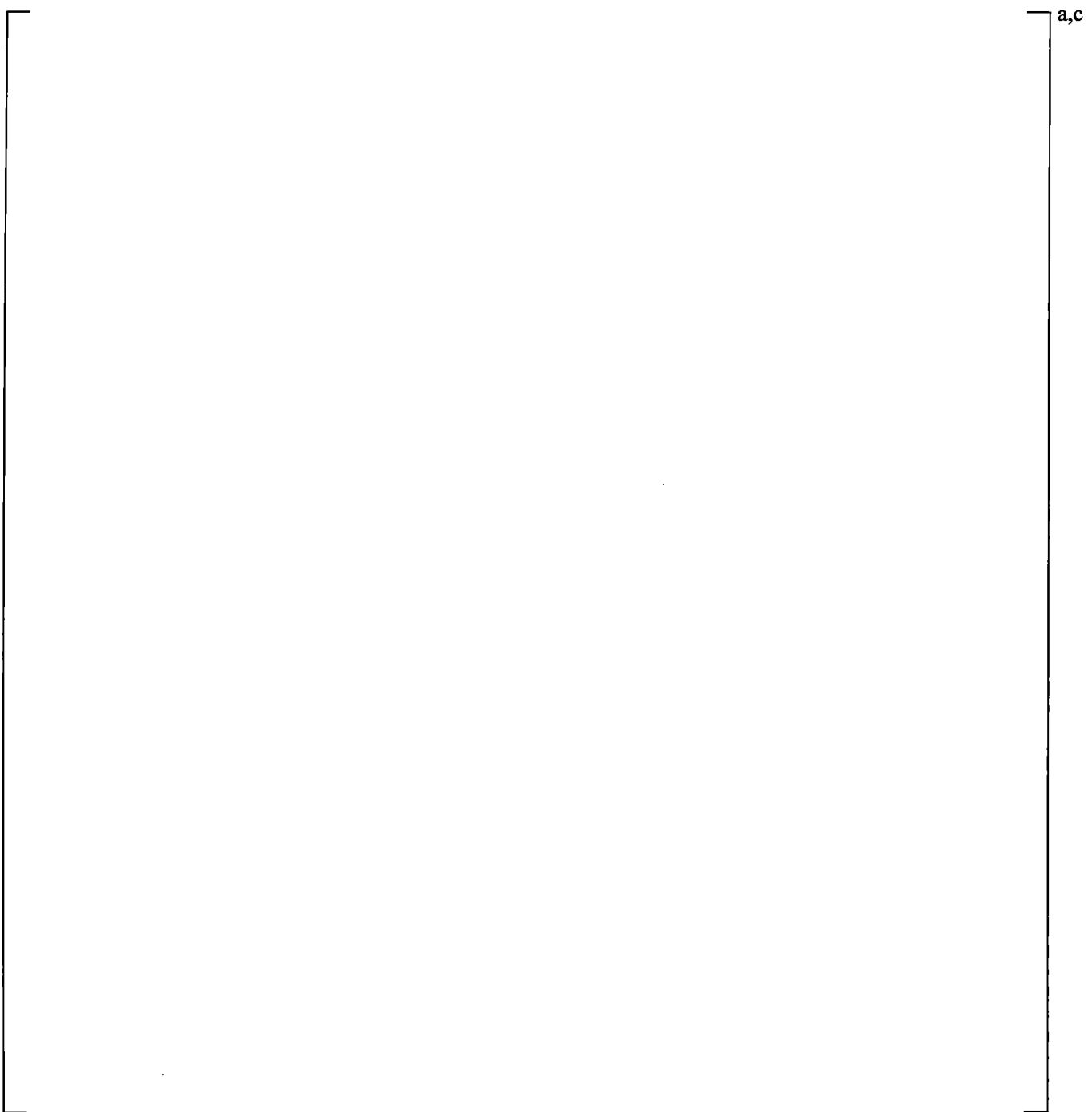


Figure 19.6-20 CCTF Run 62 Cladding Temperature at 6.0 ft for Channel 9 (Rod 6)

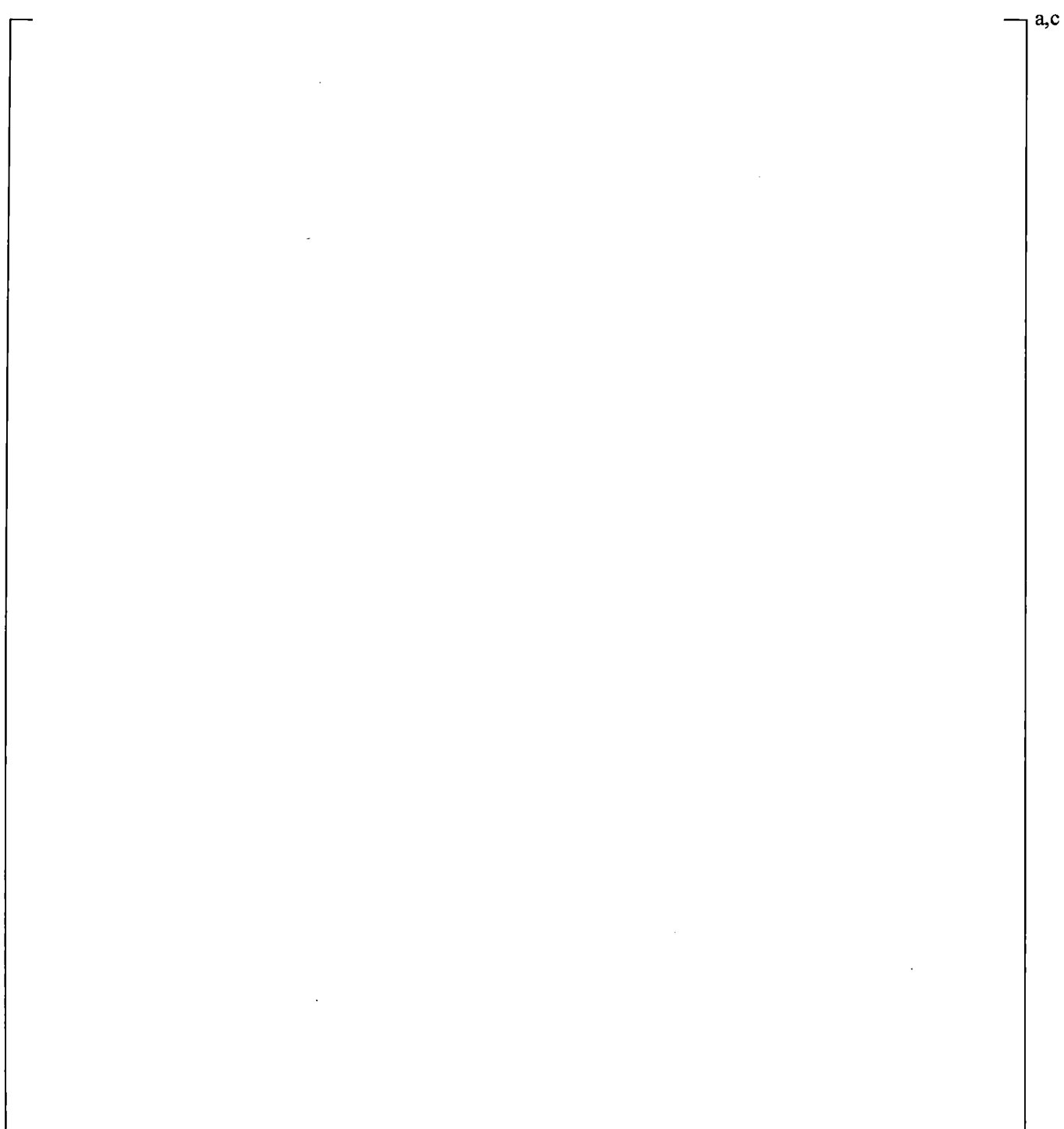


Figure 19.6-21 CCTF Run 62 Cladding Temperature at 8.0 ft for Channel 9 (Rod 6)

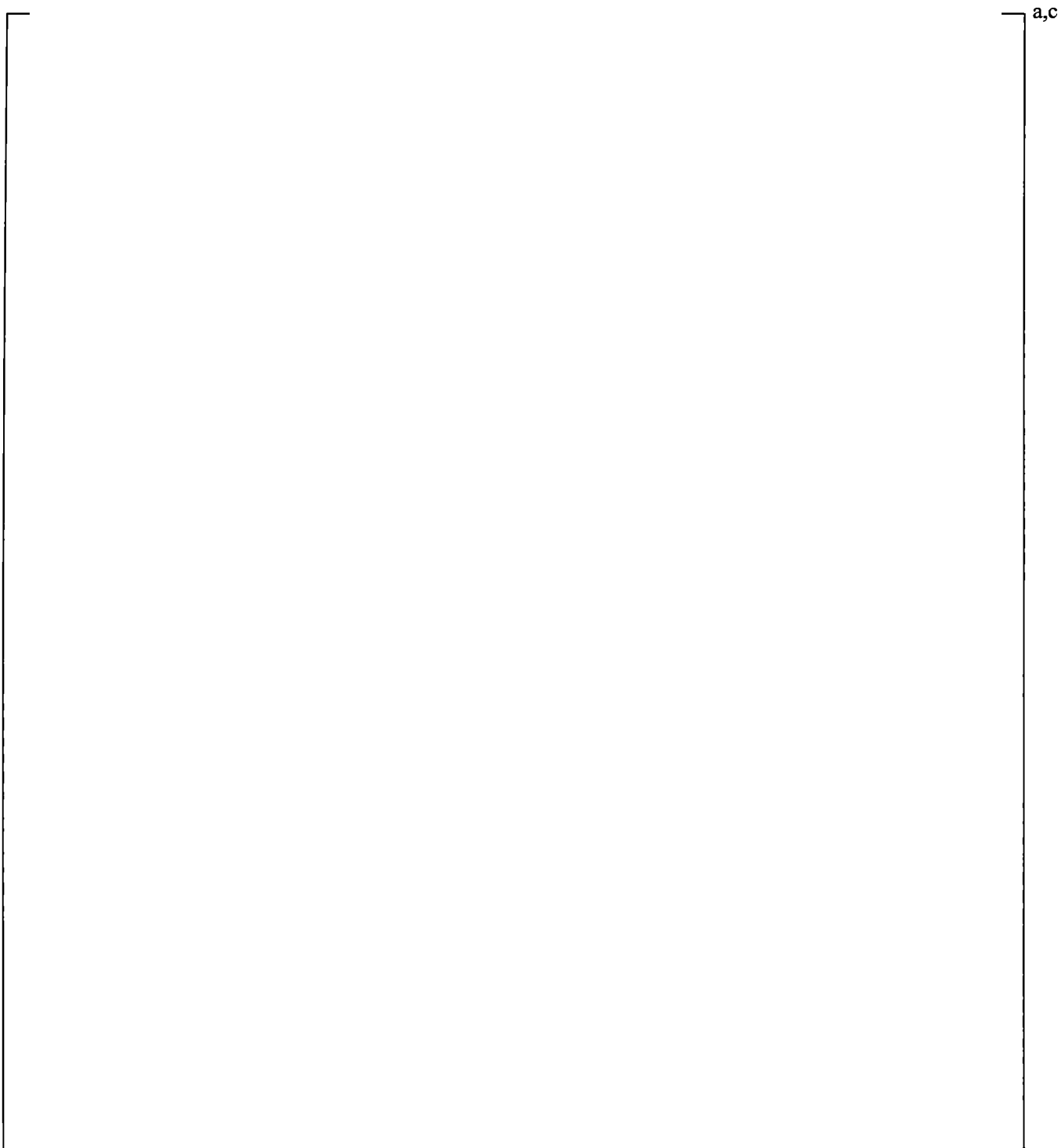


Figure 19.6-22 CCTF Run 62 Cladding Temperature at 10.0 ft for Channel 9 (Rod 6)

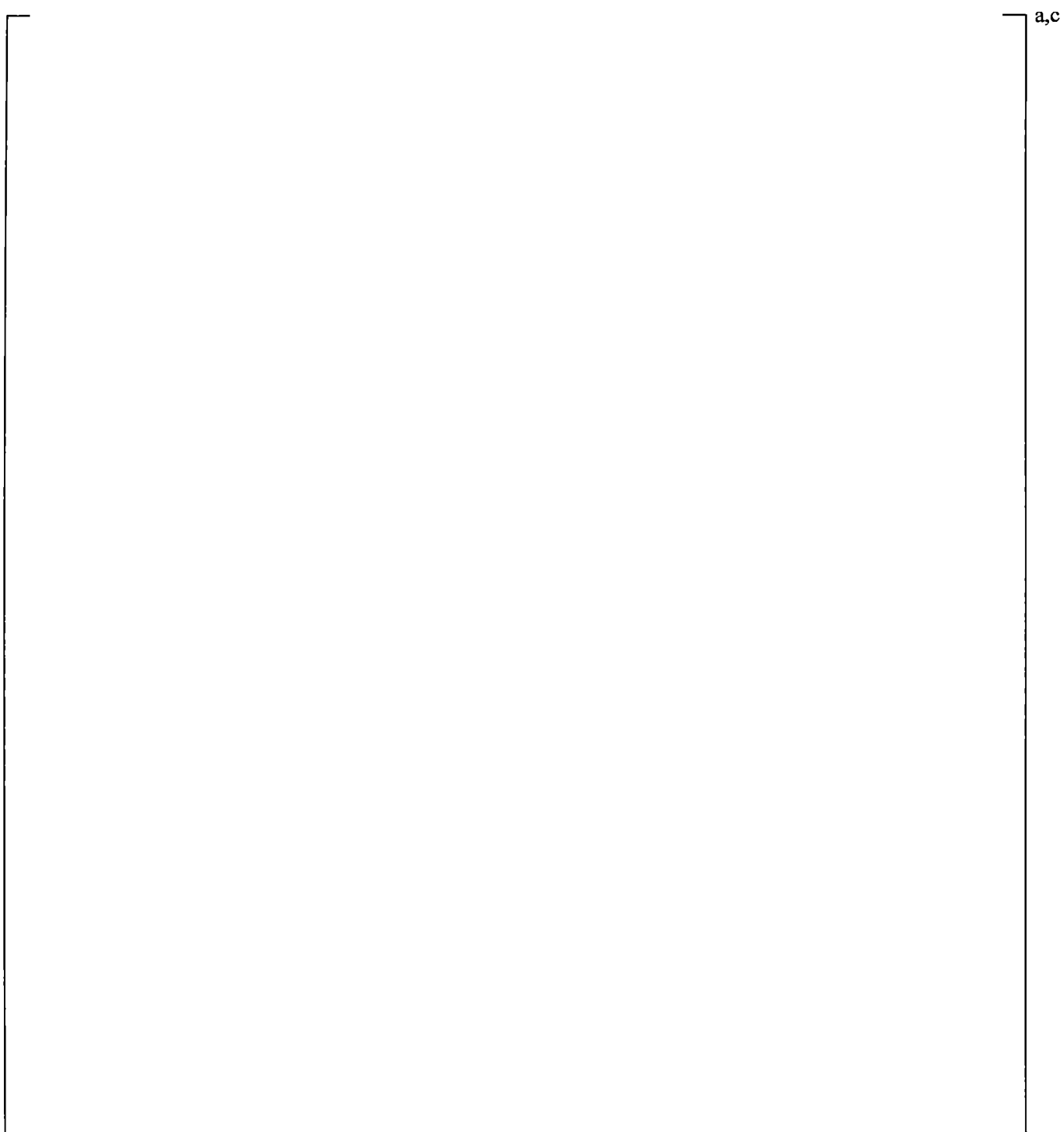


Figure 19.6-23 CCTF Run 62 Vapor Temperature at 6.0 ft for Channel 9

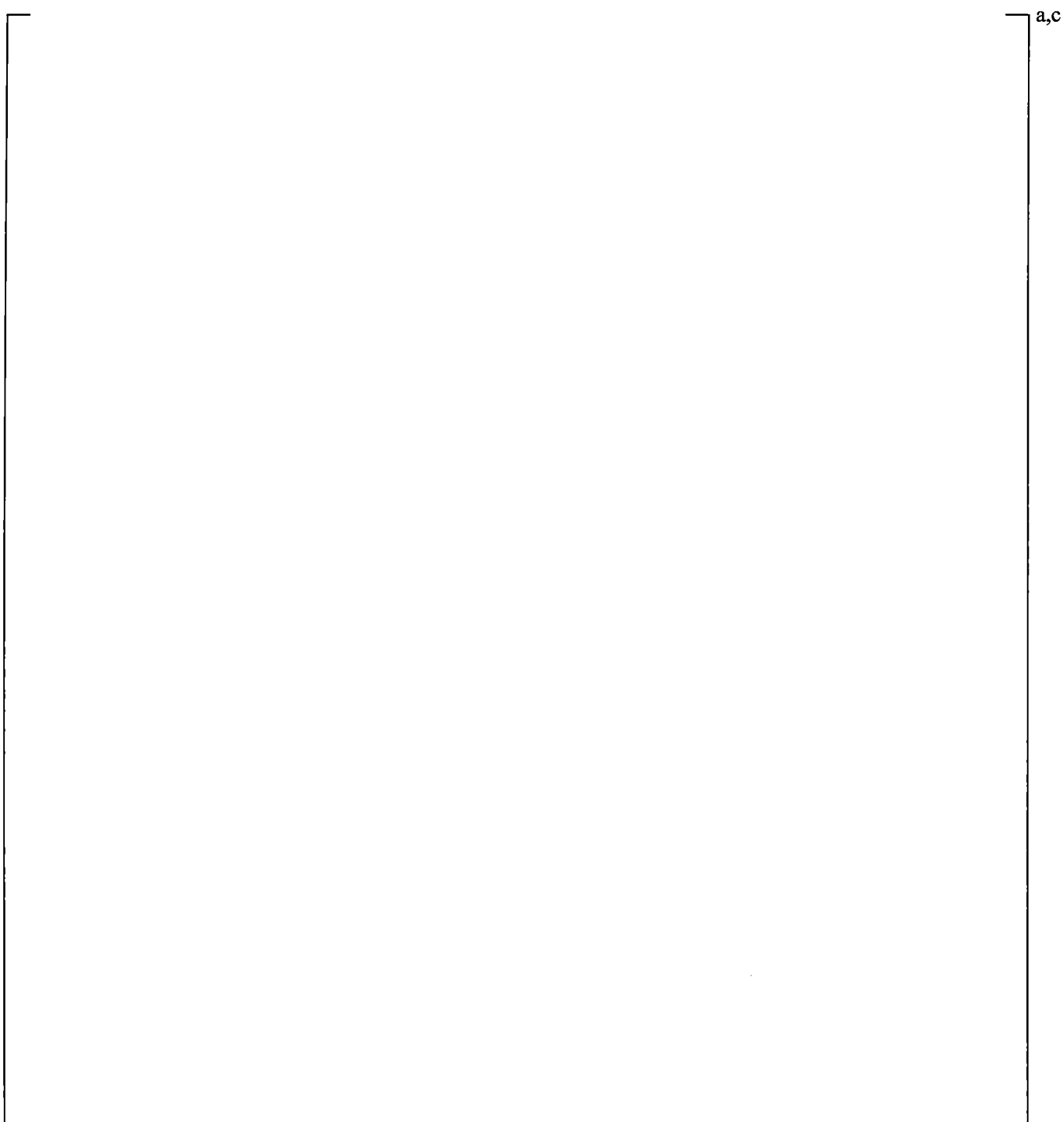


Figure 19.6-24 CCTF Run 62 Liquid Level in Core

a,c

Figure 19.6-25a CCTF Run 62 Void Fraction in End Box (CCFL Region)



Figure 19.6-25b CCTF Run 62 Liquid Level in Upper Plenum

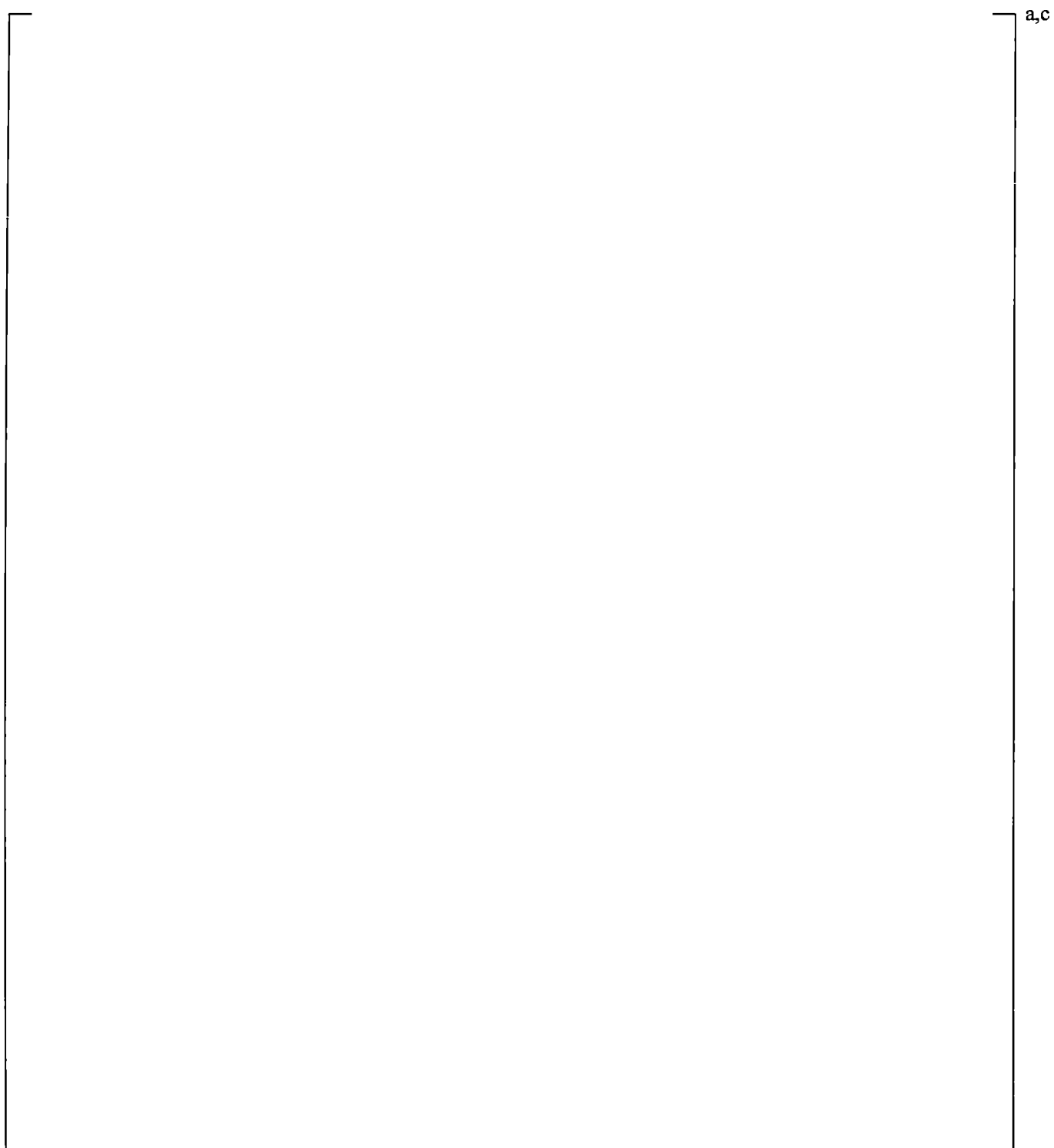


Figure 19.6-26 CCTF Run 62 Pressure Difference from Lower Plenum to Upper Plenum

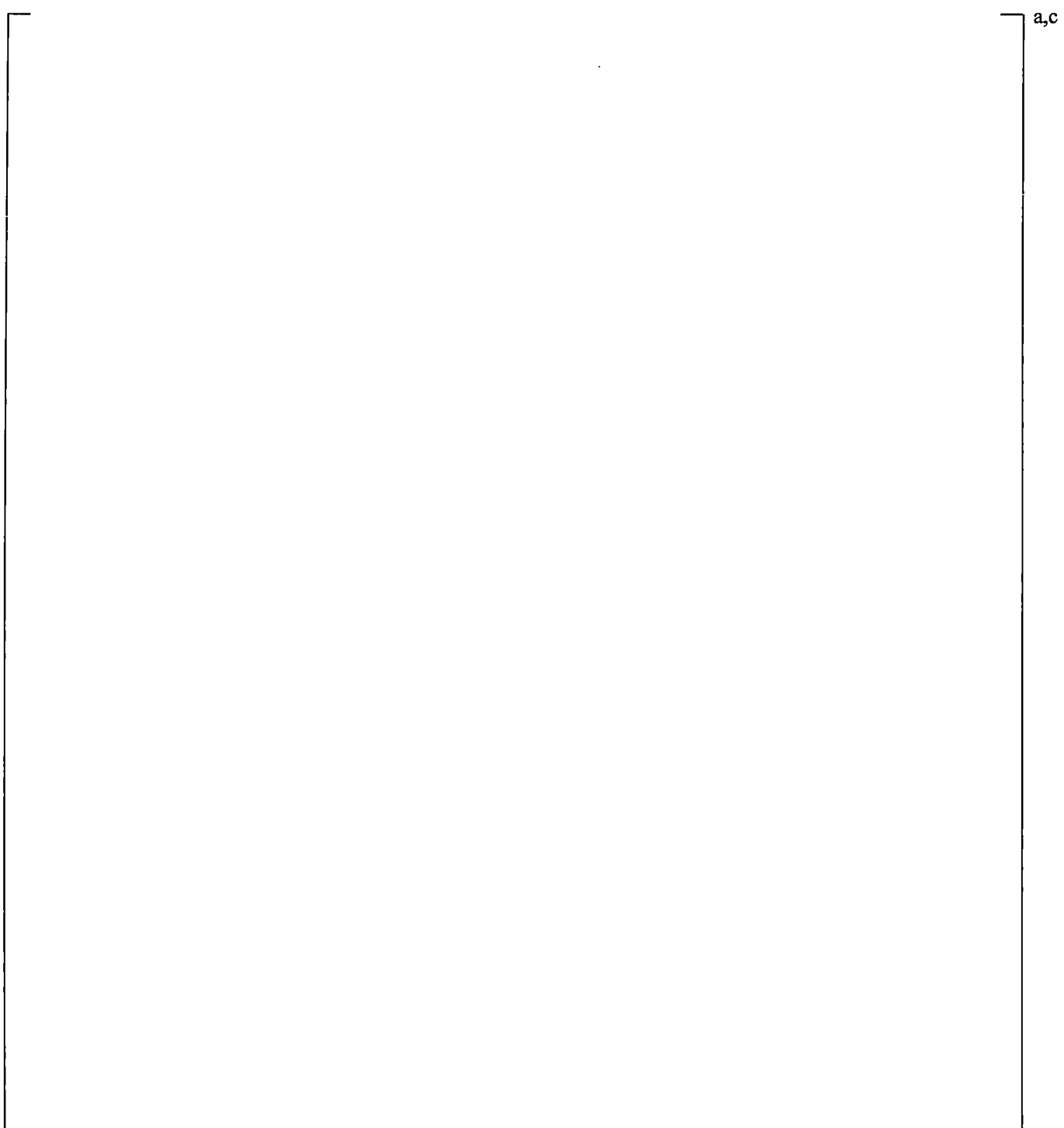


Figure 19.6-27 CCTF Run 62 Pressure Difference from Lower Plenum to Top of Downcomer

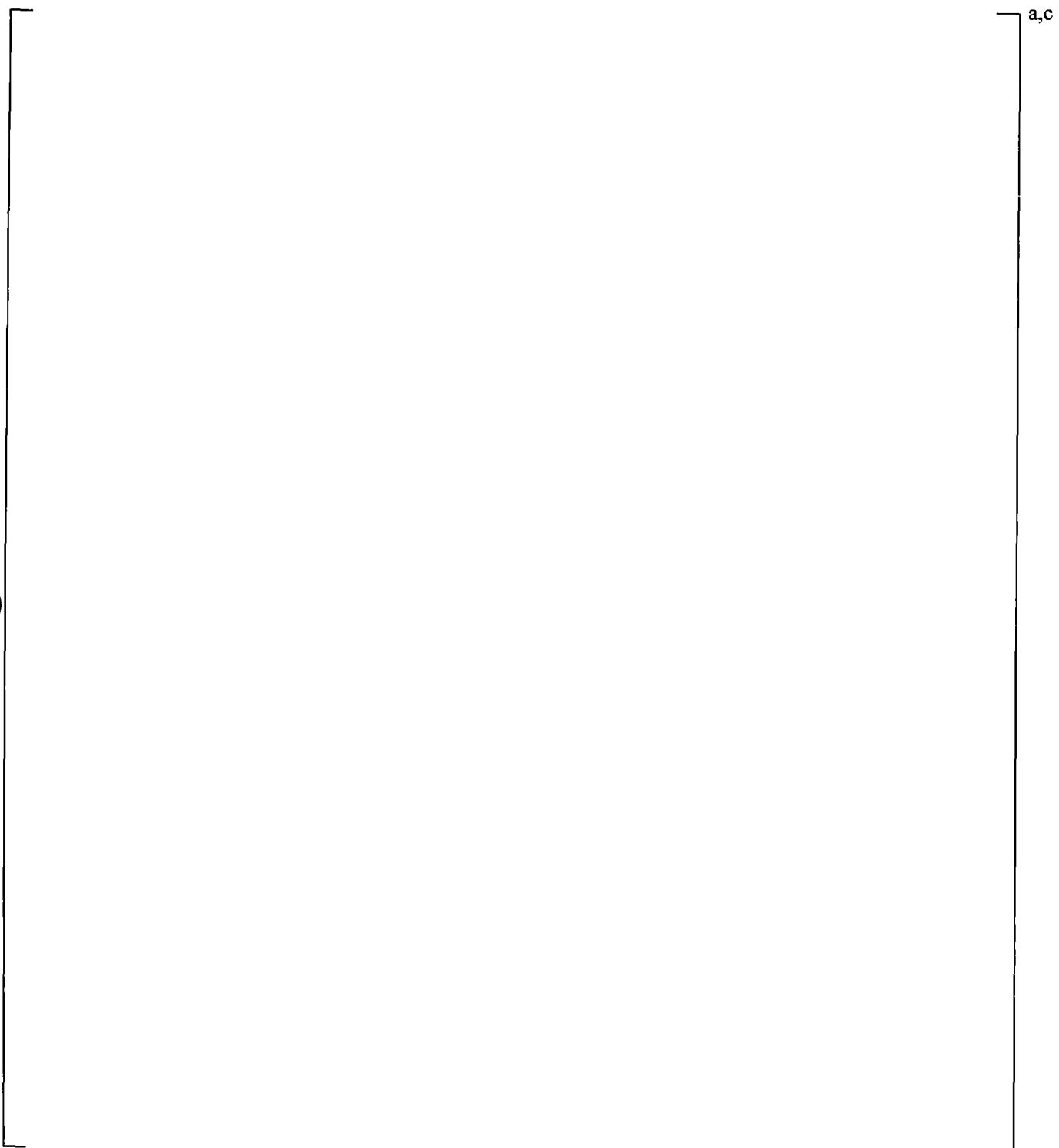


Figure 19.6-28 CCTF Run 62 Pressure Difference across Intact Loop

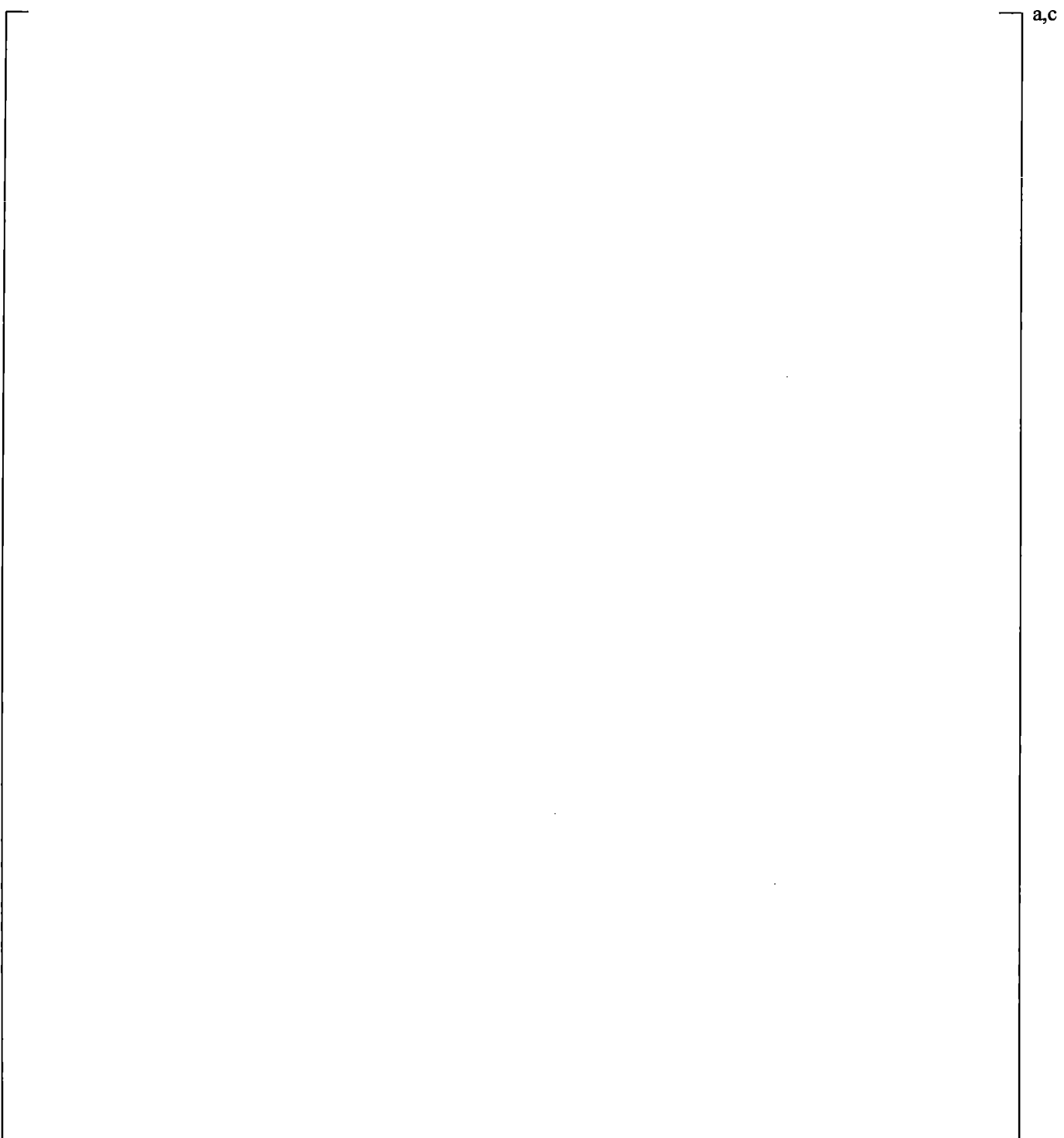


Figure 19.6-29 CCTF Run 62 Pressure Difference across Broken Loop

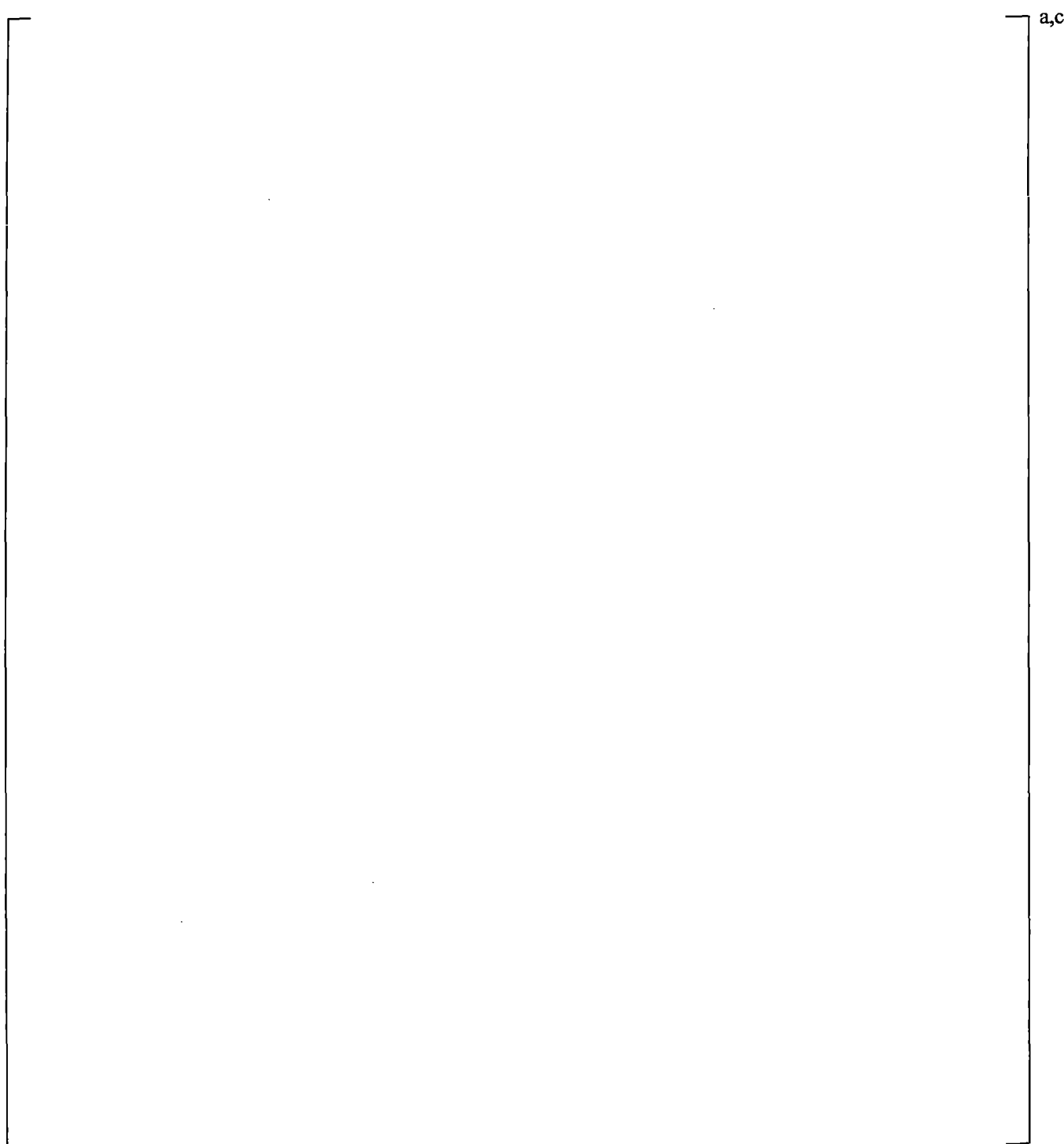


Figure 19.6-30 CCTF Run 62 Pressure Difference across Steam Generators; Averaged for 3 Intact Loops

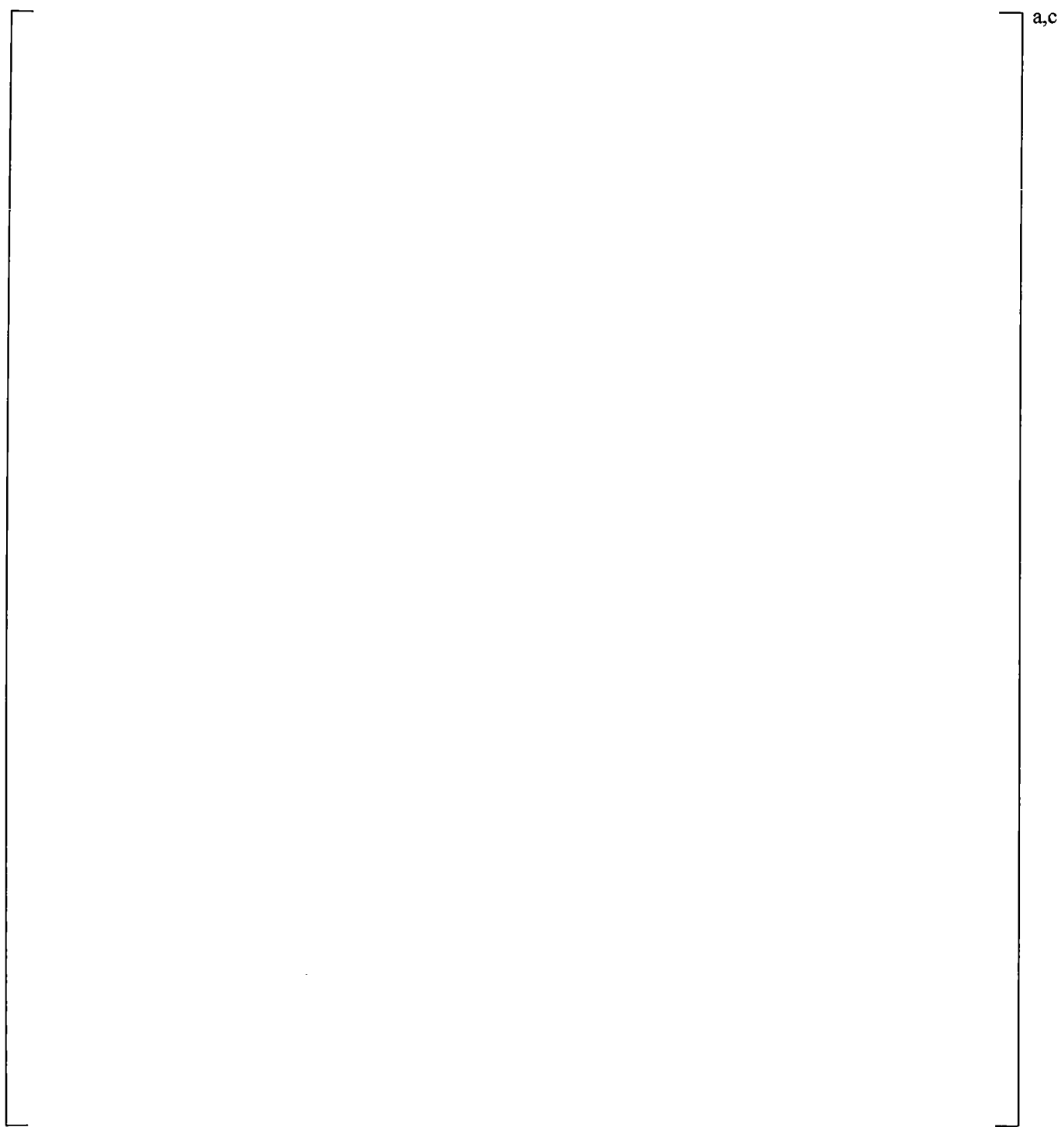


Figure 19.6-31 CCTF Run 62 Temperature Rise across Steam Generator of Loop 1

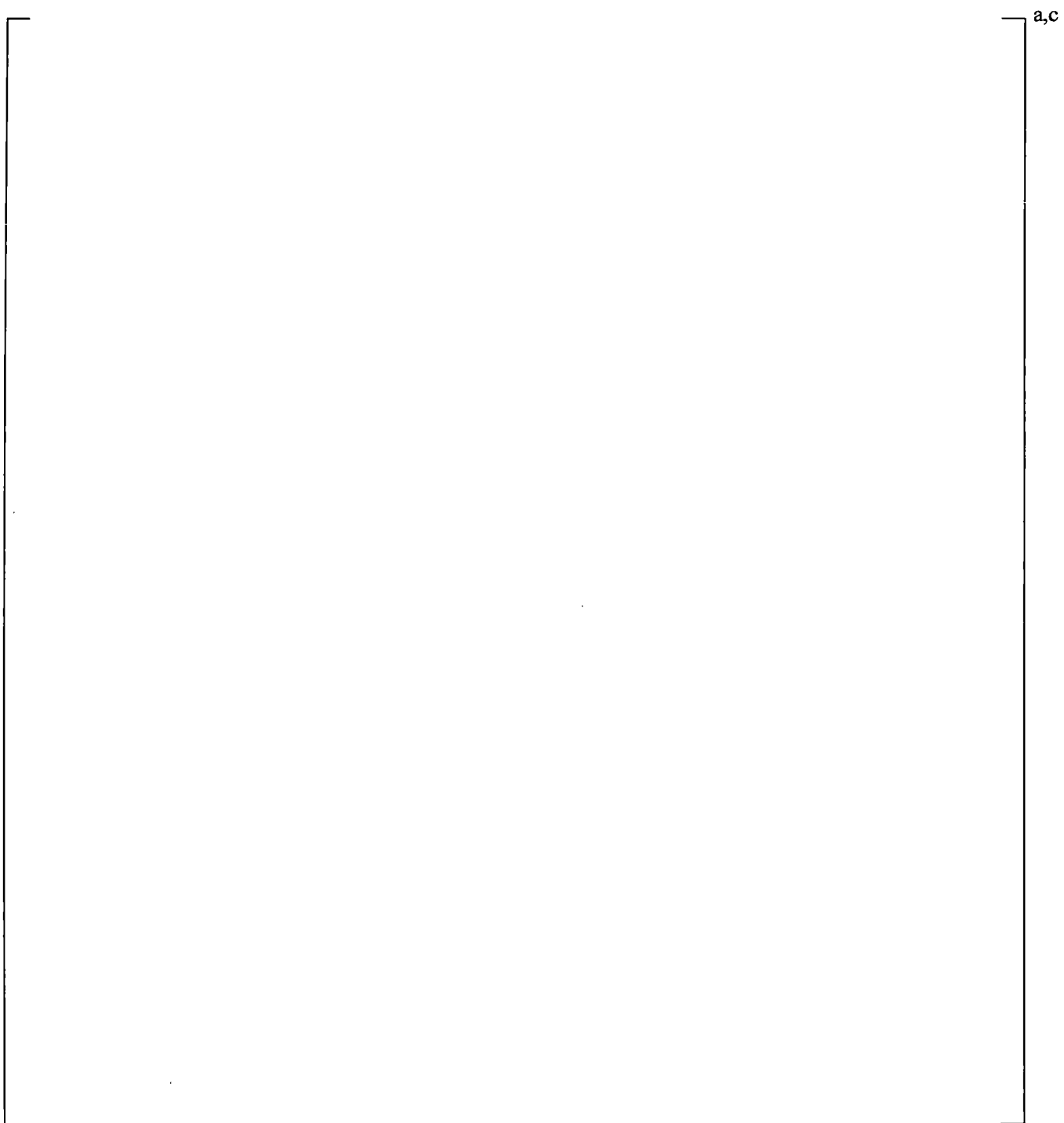


Figure 19.6-32 CCTF Run 62 Temperature Rise across Steam Generator of Loop 2

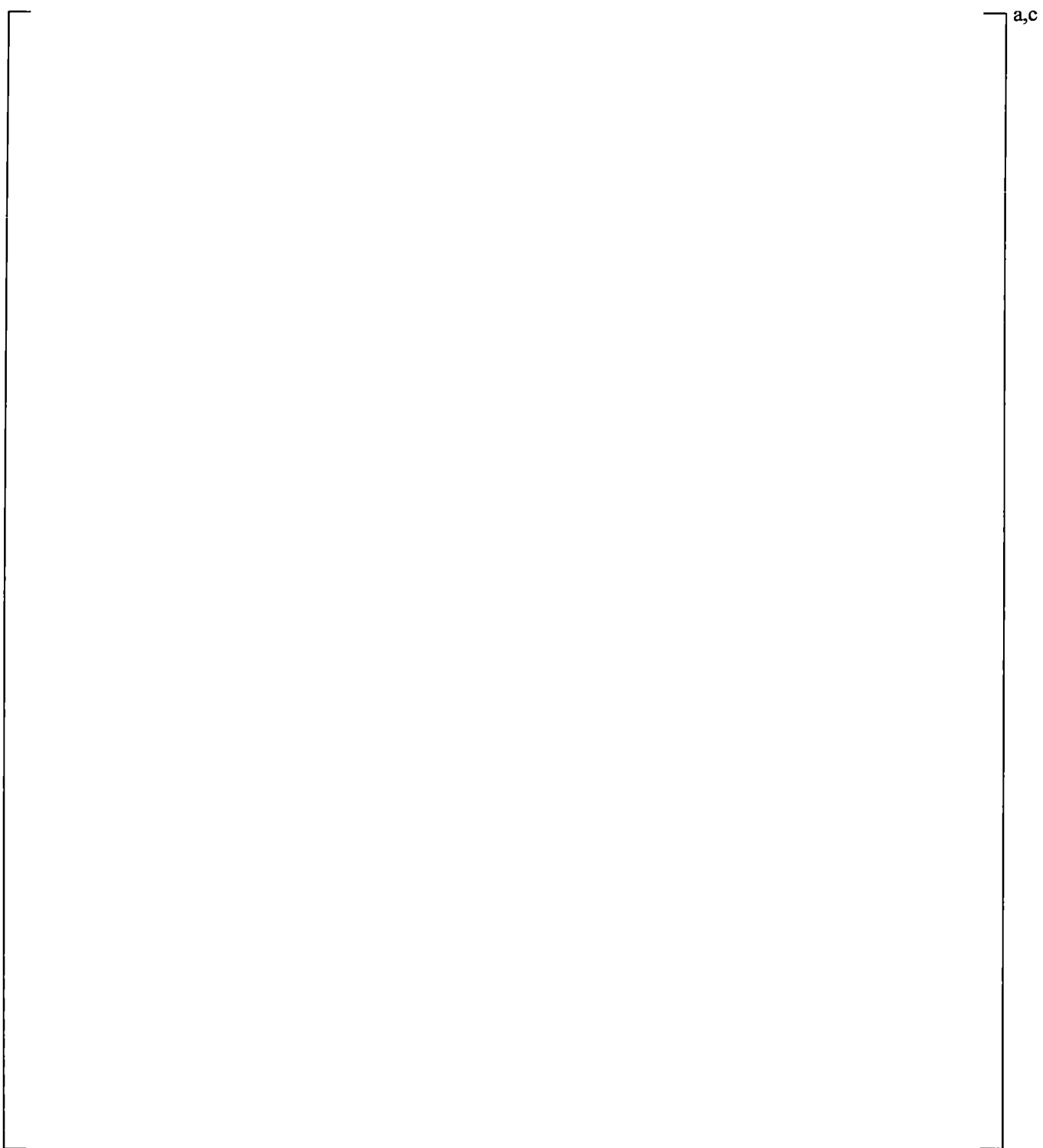


Figure 19.6-33 CCTF Run 62 Temperature Rise across Steam Generator of Loop 3

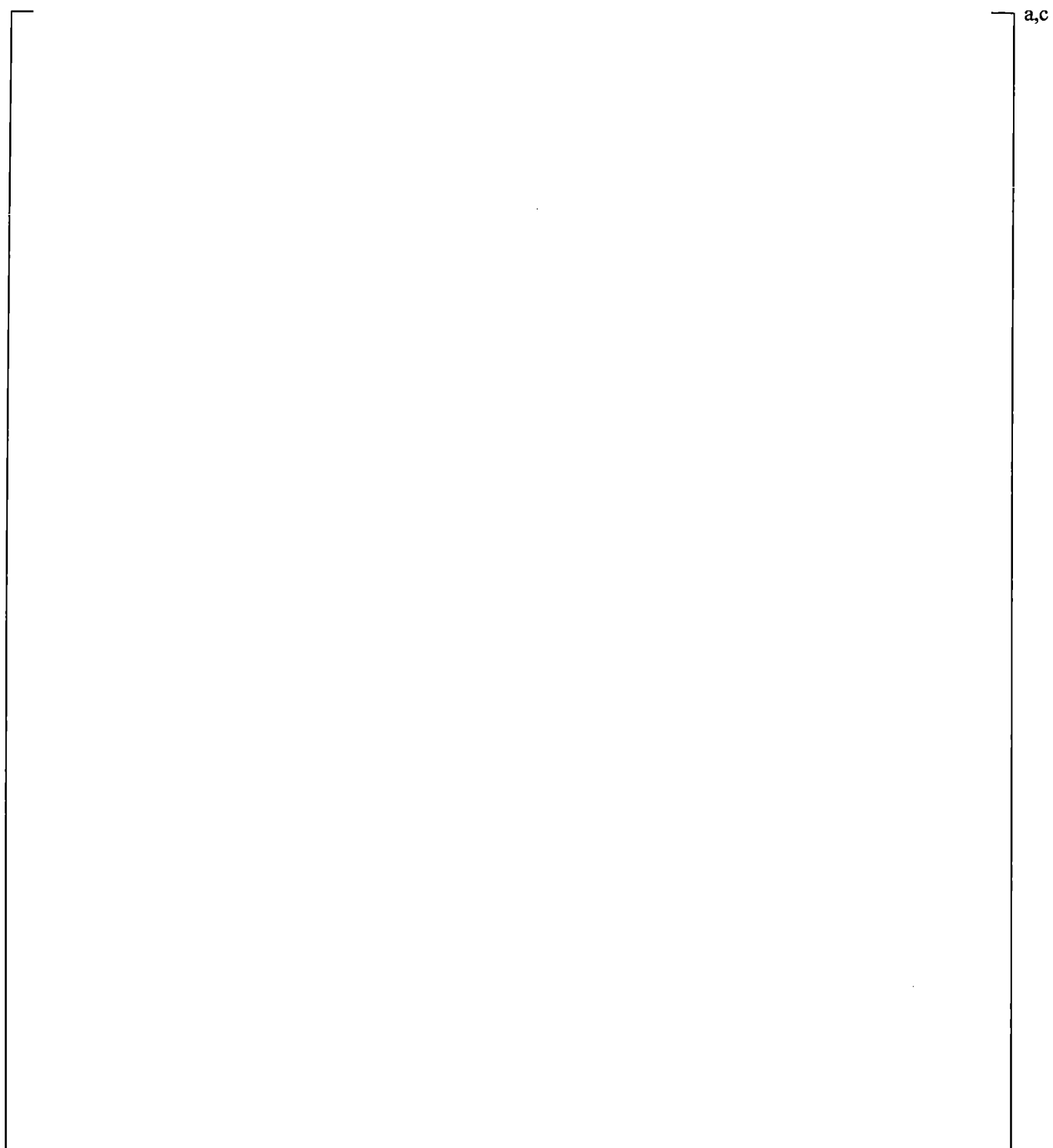


Figure 19.6-34 CCTF Run 62 Total (Liquid and Vapor) Mass Flow Rate in Intact Loop Hot Leg

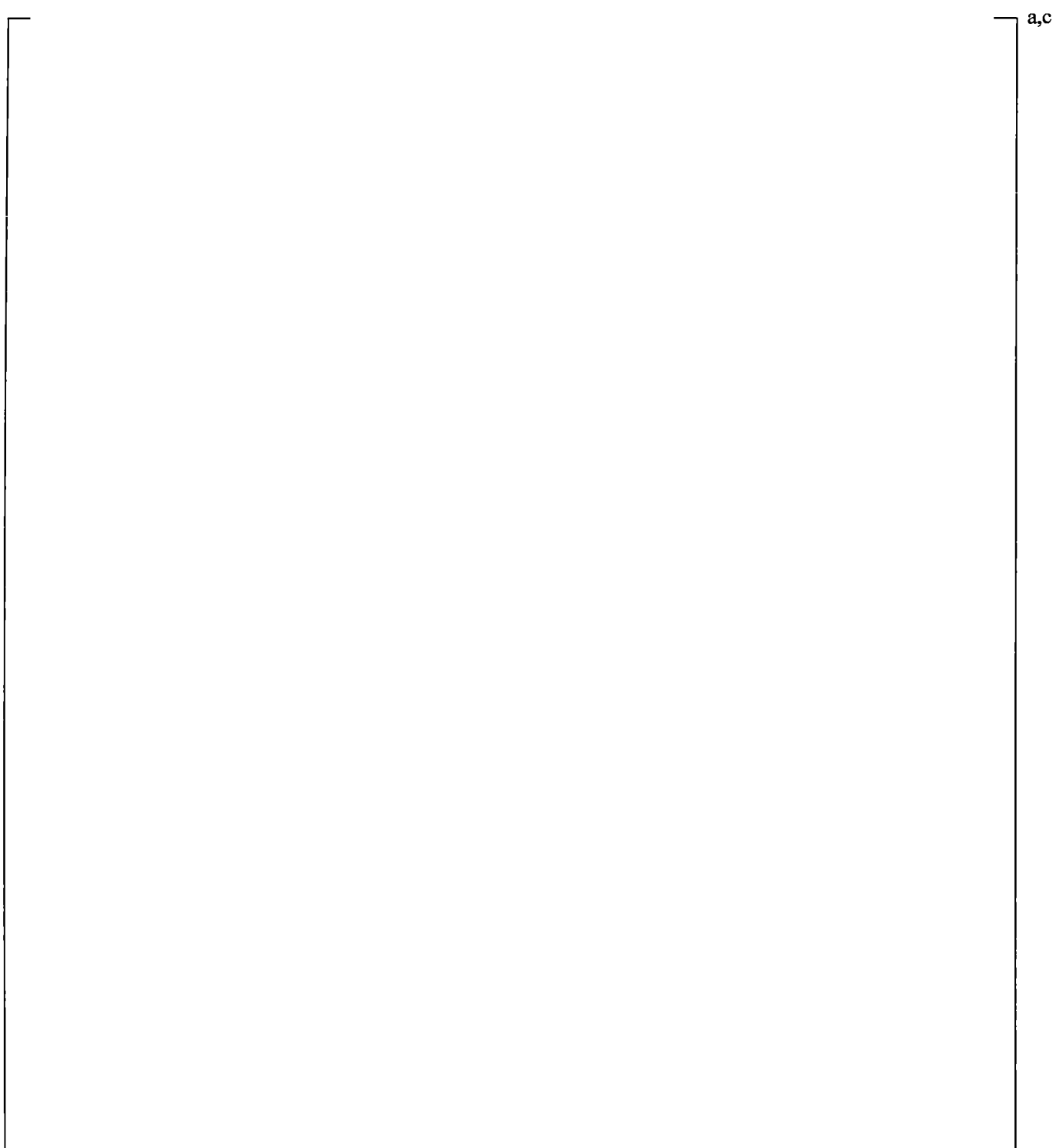


Figure 19.6-35 CCTF Run 62 Total (Liquid and Vapor) Mass Flow Rate in Broken Loop Hot Leg

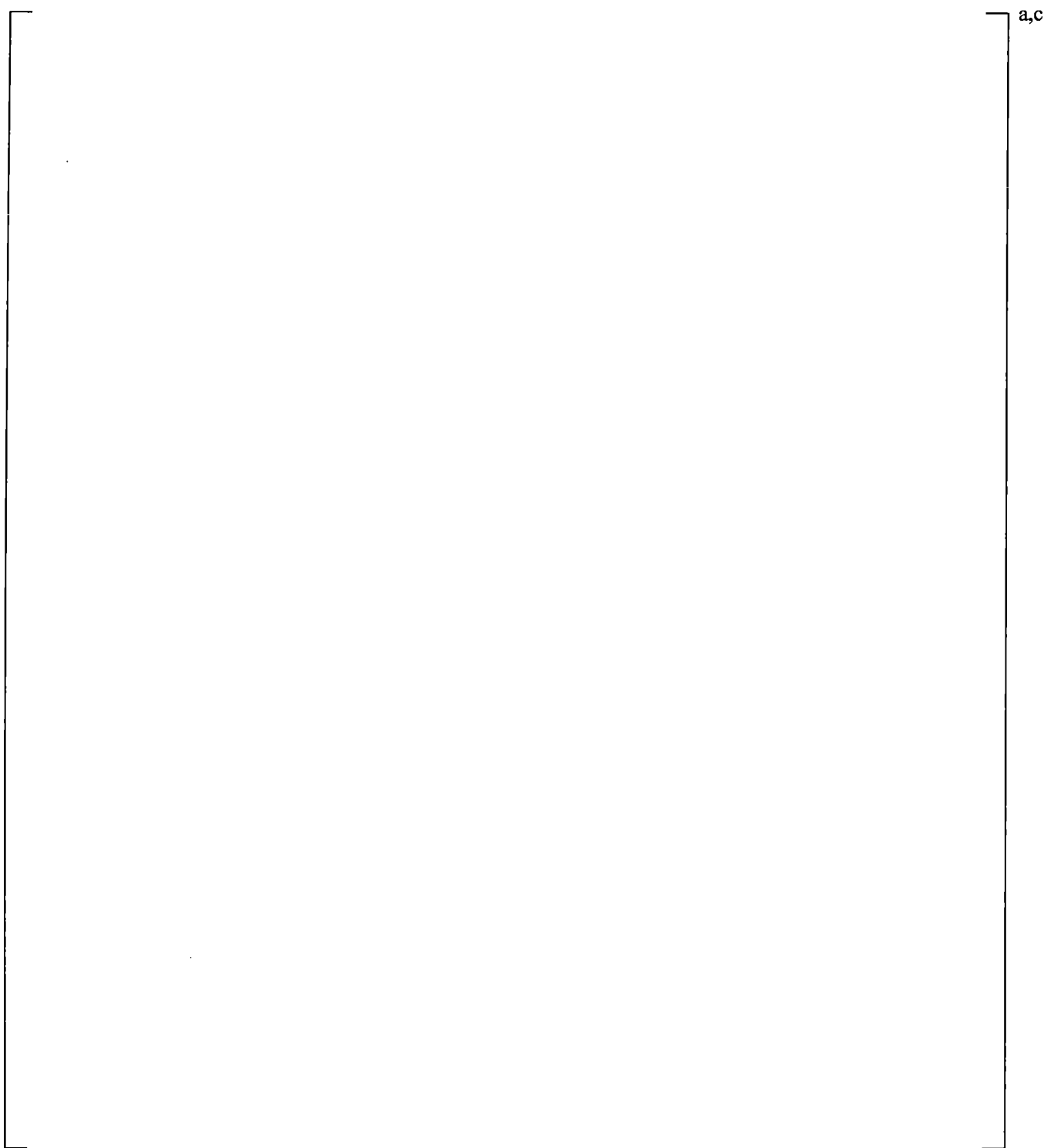


Figure 19.6-36 CCTF Run 62 Core Inlet Mass Flow Rate

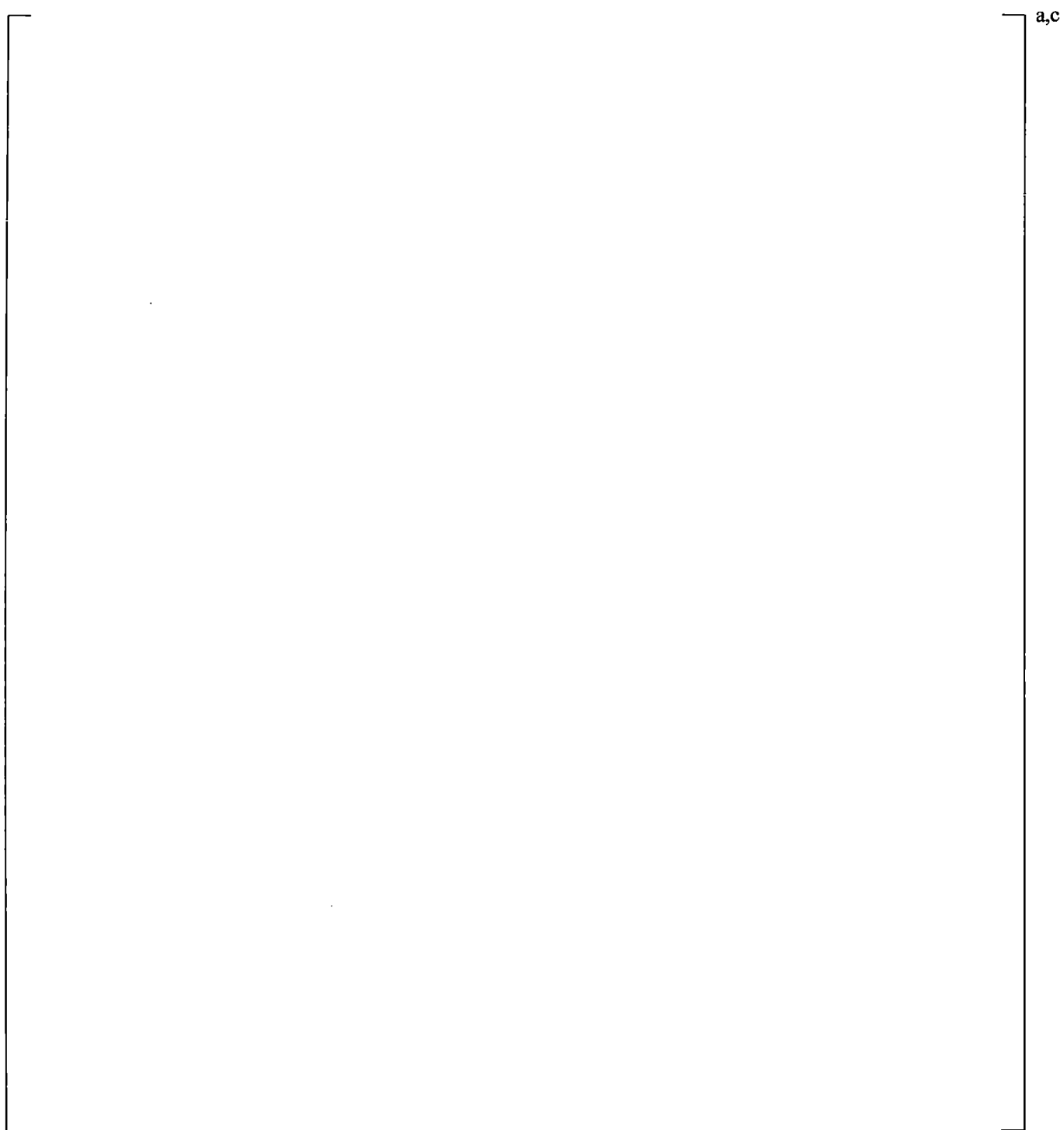


Figure 19.6-37 CCTF Run 62 Time Step Sensitivity Study: Cladding Temperature at 6.0 ft.

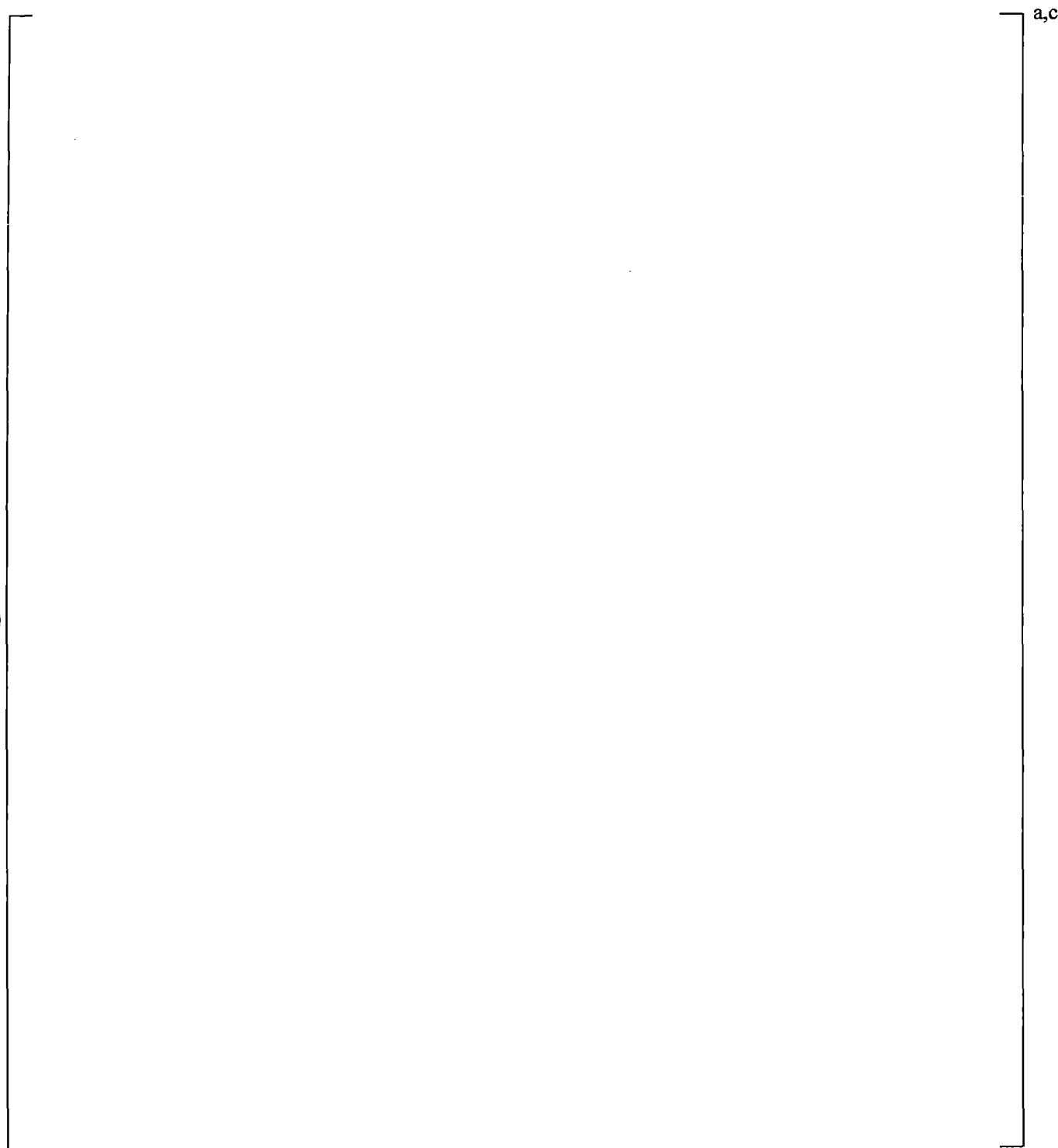


Figure 19.6-38 CCTF Run 62 Time Step Sensitivity Study: Cladding Temperature at 8.0 ft.

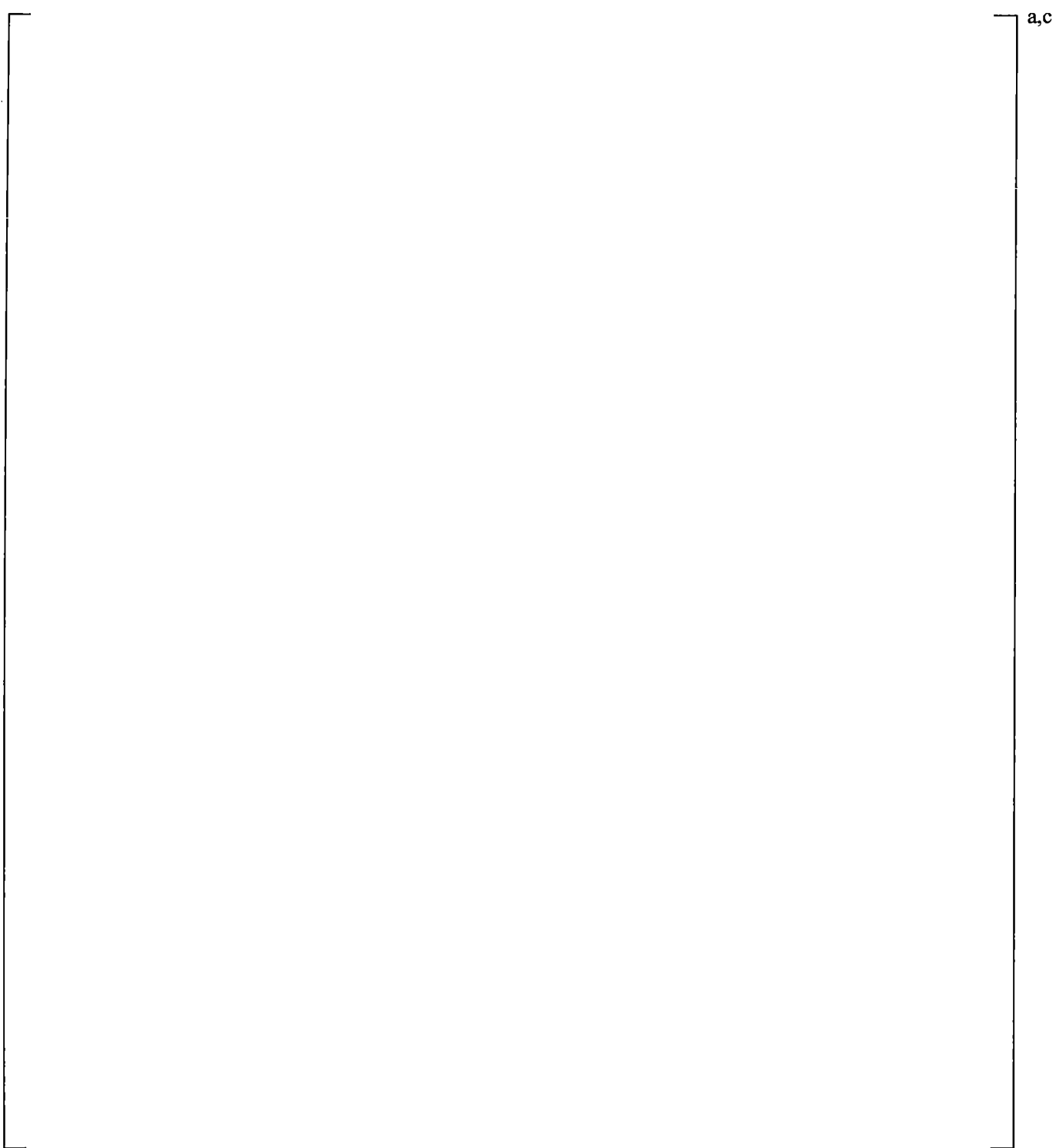


Figure 19.6-39 CCTF Run 62 Time Step Sensitivity Study: Cladding Temperature at 10.0 ft.

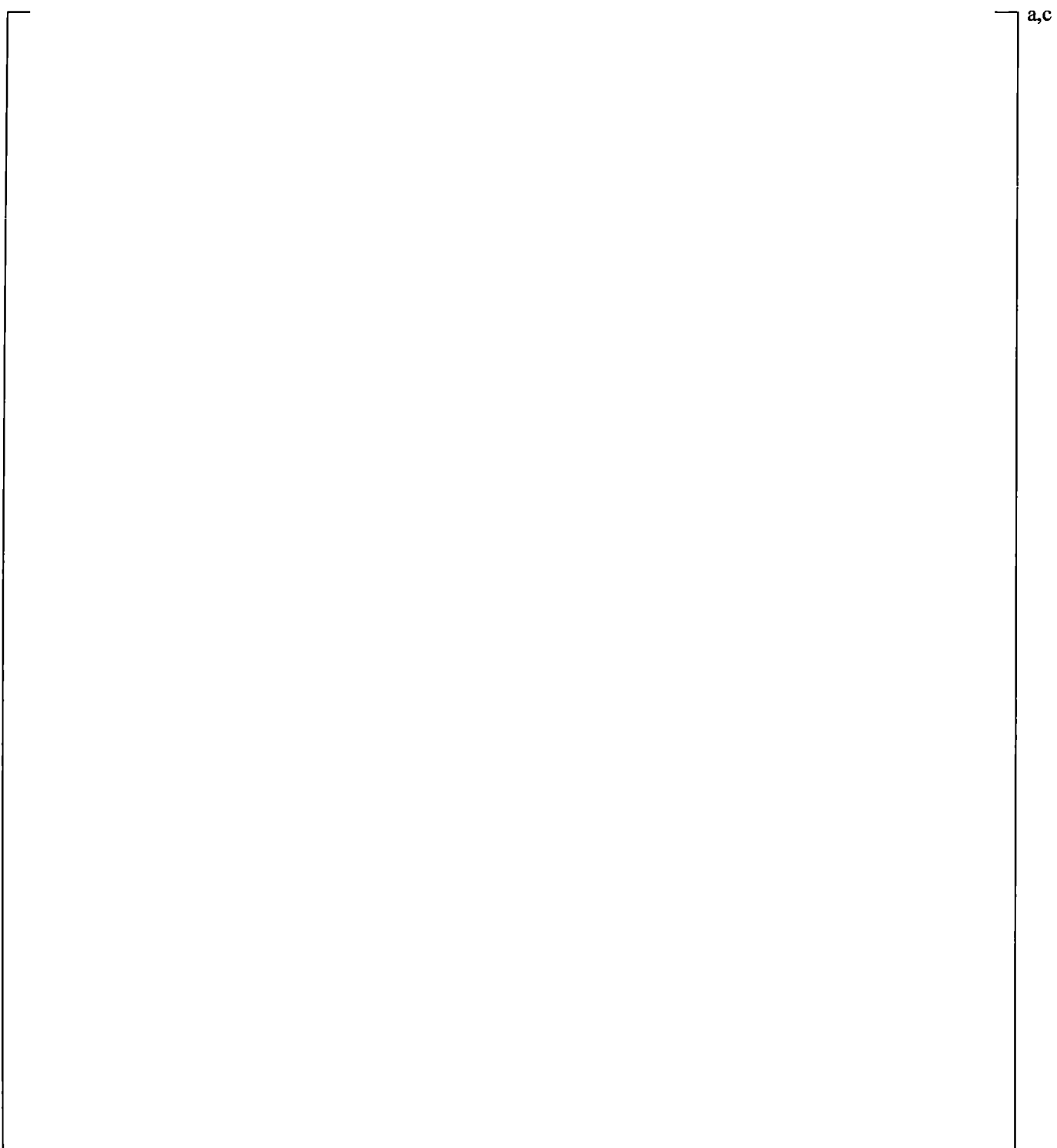


Figure 19.6-40 CCTF Run 62 Time Step Sensitivity Study: Collapsed Liquid Level in Core

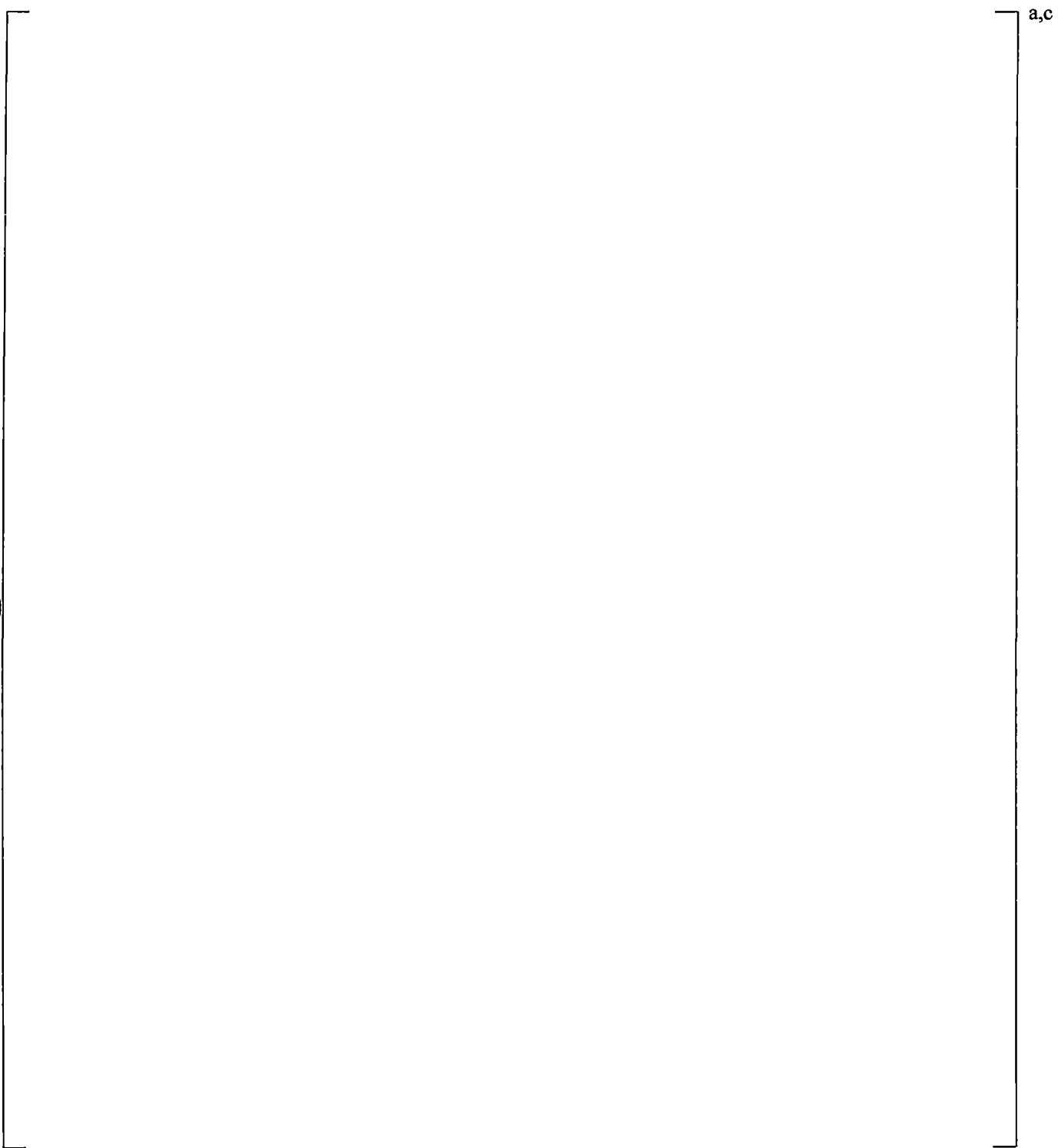


Figure 19.6-41 CCTF Run 62 Time Step Sensitivity Study: Collapsed Liquid Level in Upper Plenum

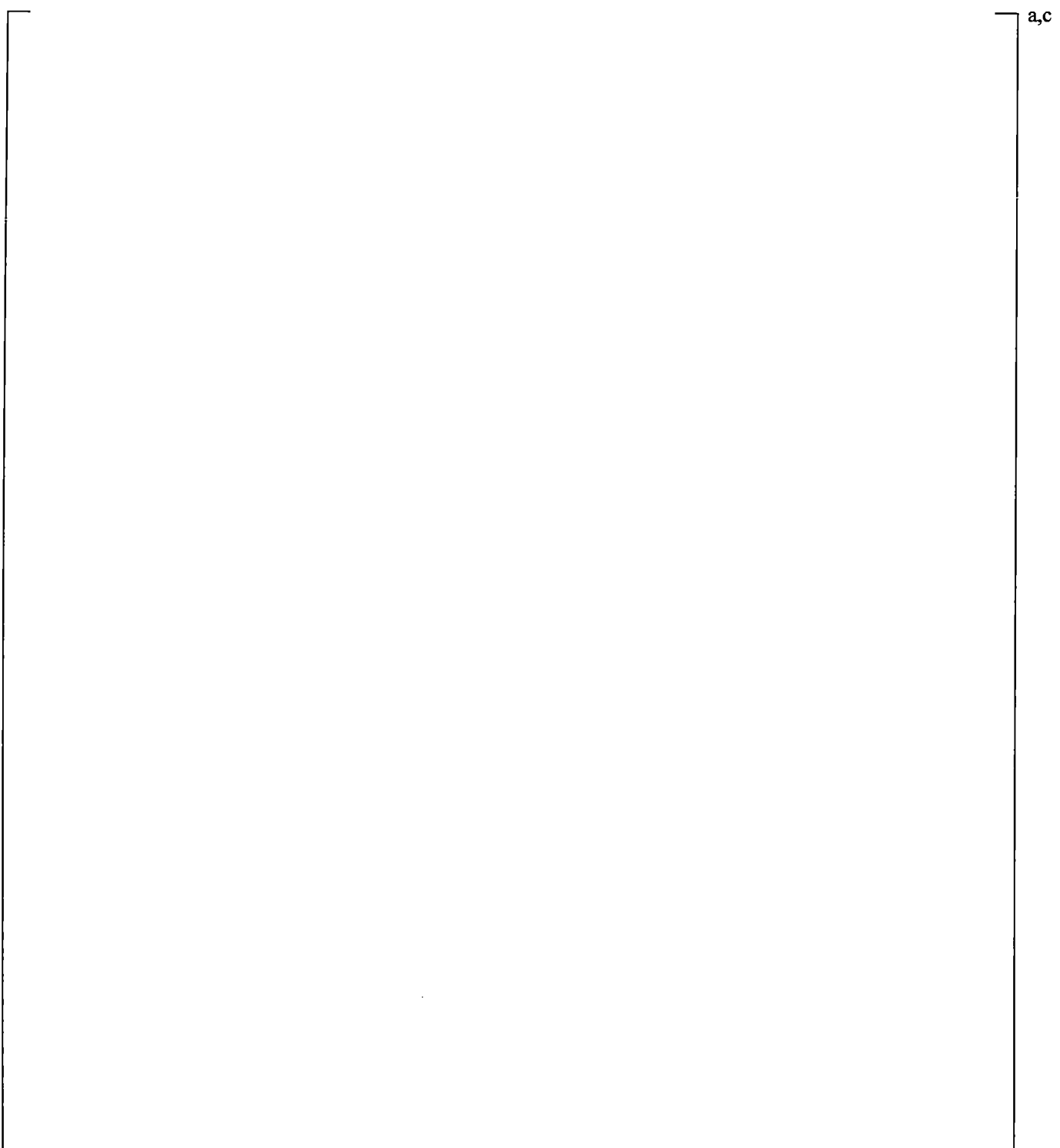


Figure 19.6-42 CCTF Run 62 Time Step Sensitivity Study: Pressure Difference from Lower Plenum to Upper Plenum

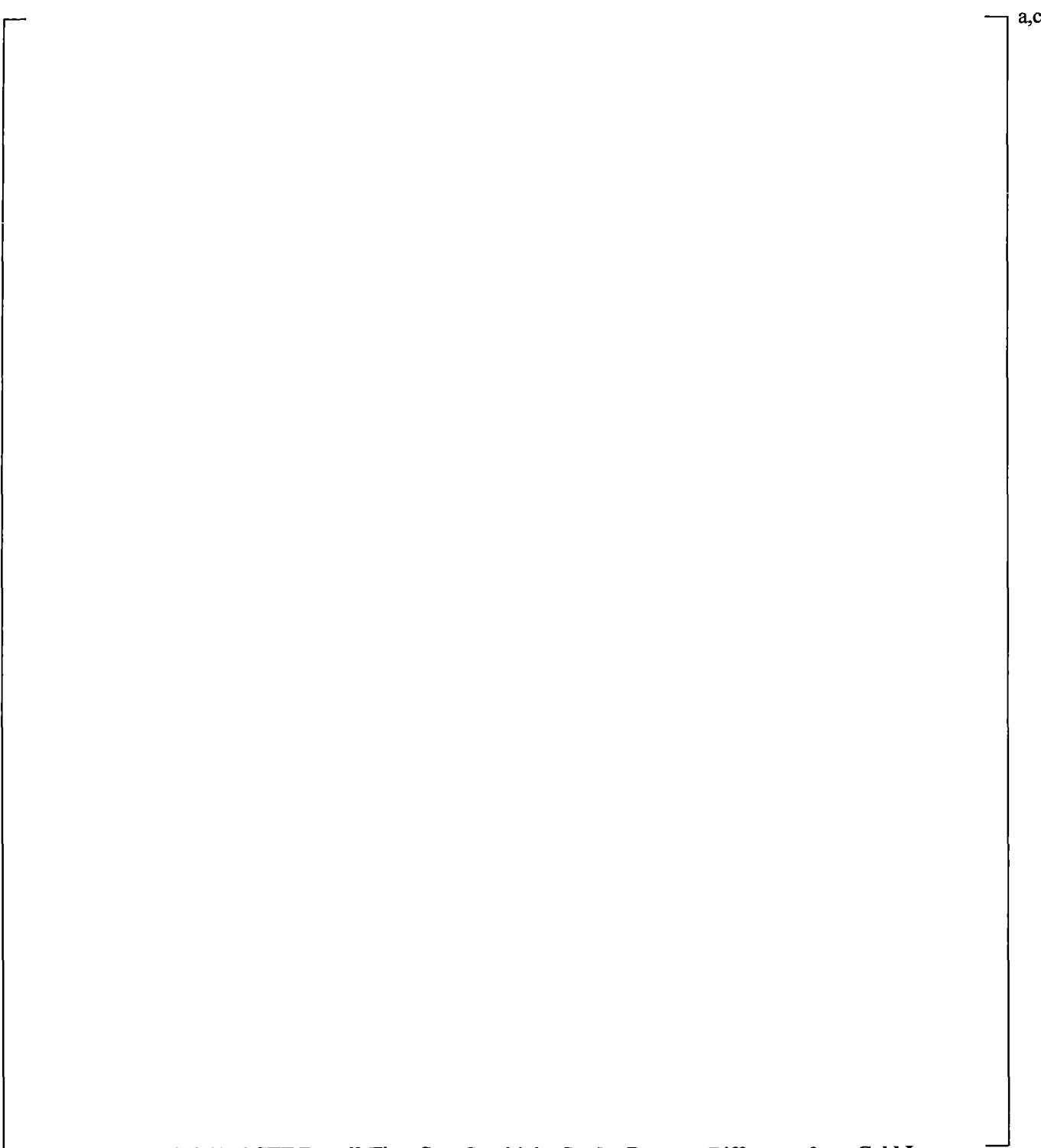


Figure 19.6-43 CCTF Run 62 Time Step Sensitivity Study: Pressure Difference from Cold Leg Nozzle to Upper Plenum

19.7 CONCLUSIONS

The results of the assessment of CCFL, entrainment and de-entrainment, and condensation documented in these sections are summarized as follows. The assessment includes Separate Effects Tests of UPTF 6, UPTF 8A, UPTF 25A, UPTF 29B, FLECHT, and perforated plate, and CCTF-62 Integral Effects Tests.

Counter-Current Flow Limitation

1. CCFL in a Downcomer Annulus – CCFL/ECC bypass in the downcomer annulus of the full-scale UPTF was evaluated in Section 19.3, where WCOBRA/TRAC-TF2 results were compared to experimental data for the UPTF 6 tests. [

]^{a,c}

2. CCFL in a Perforated Plate – The perforated plate analysis documented in Section 19.4 shows that the WCOBRA/TRAC-TF2 predictions [

]^{a,c}

3. CCFL in the Steam Generators – This is addressed in Section 21.10. [

]^{a,c}

4. CCFL in the Hot Leg Bend – This is addressed in Section 21.10. CCFL in the hot leg was [

]^{a,c}

Entrainment and De-Entrainment

As discussed in the previous Section 19.1, the predictive capability of WCOBRA/TRAC-TF2 for entrainment and de-entrainment phenomena needs to be assessed for the following conditions:

1. Upper Plenum Entrainment and Carryover – UPTF Test 29B has been simulated and the predicted upper plenum inventories were compared to test data in Section 19.3.14. [

]^{a,c}

2. Downcomer Entrainment, During ECC Bypass Period and During Reflood – UPTF Tests 6 and 25A were simulated and the results were used to examine the ability to model the entrainment process in the downcomer in Sections 19.3.5 and 19.3.11, respectively. [

]^{a,c}

3. Entrainment During Bottom Reflood – The ability of WCOBRA/TRAC-TF2 to calculate the entrainment rate at a quench front was evaluated by comparing the predicted bundle mass, carryout fraction and exit flows to experimental data from the FLECHT forced reflood facilities in Section 19.5, and by comparing the liquid distribution from the CCTF Run 62 simulation to the experimental data. [

]^{a,c}

Condensation

1. Condensation in Downcomer Annulus – Condensation, CCFL, and entrainment/de-entrainment in the downcomer are inter-related physical processes that affect the ability to predict end-of-bypass and beginning of reflood. [

]^{a,c}

2. Condensation in Cold Legs, at Low Pressure – [

]^{a,c}

3. Effect of Non-Condensable Gases on Condensation – Non-condensable effects on interfacial heat transfer in the 1D and 3D components were assessed in Section 20.

Integral Effects Assessment

The results from the CCTF 62 test show the code giving [$I^{a,c}$]. The comparisons between the prediction and the measurements show that WCOBRA/TRAC-TF2 predicts the overall thermal-hydraulics of a reflood transient properly. In particular, [

19.8 REFERENCES

1. 2D/3D Program Upper Plenum Test Facility Experimental Data Report, 1988, "Test No. 8, Cold/Hot Leg Flow Pattern Test," U9 316/88/12, KWU.
2. 2D/3D Program Upper Plenum Test Facility Quick Look Report, 1989, "Test No. 6; Downcomer Countercurrent Flow Test," Siemens/KWU U9 316/89/2.
3. 2D/3D Program Upper Plenum Test Facility Experimental Data Report, 1990a, "Test No. 25, Downcomer/Cold Leg Steam/Water Interaction Test," E314/90/11, KWU.
4. 2D/3D Program Upper Plenum Test Facility Experimental Data Report, 1990b, "Test No. 29, Entrainment/De-entrainment Test," E314/90/05, KWU.
5. Akimoto, H., et al., 1984, "Pressure Drop through Broken Cold Leg During Reflood Phase of Loss-of-Coolant Accident of PWR," *Journal of Nuclear Science and Technology*, 21 [6].
6. Bajorek, S. M., et al., 1998, "Code Qualification Document for Best Estimate LOCA Analysis," WCAP-12945-P-A, Volume 1, Revision 2, and Volumes 2 through 5, Revision 1, and WCAP-14747 (Non-Proprietary).
7. Cousins, L. B., et al., 1965, "Liquid Mass Transfer in Annular Two-Phase Flow," Paper C4 presented at the Symposium on Two-Phase Flow, Volume 2, Exeter, England, pp. 401-430.
8. Dallman, J. C., and Kirchner, W. L., 1980, Los Alamos Scientific Laboratory, "De-Entrainment Phenomena on Vertical Tubes in Droplet Cross Flow," USNRC Report, NUREG/CR-1421.
9. Emmerling, R., et al., 1988, "UPTF: Program and System Description," U9 414/88/023, KWU.
10. Glaeser, H., 1992, "Downcomer and Tie Plate Countercurrent Flow in the Upper Plenum Test Facility (UPTF)," *Nucl. Eng. Des.*, 133.
11. Glaeser, H. and Karwat, H., 1993, "The contribution of UPTF experiments to resolve some scale-up uncertainties in countercurrent two phase flow," *Nuclear Engineering and Design*, 145, pp. 63-84.

12. Hsieh, C., et al., 1980, "Countercurrent Air/Water and Steam/Water Flow above a Perforated Plate," NUREG/CR-1808.
13. Kataoka, I. and Ishii, M., 1983, "Mechanistic Modeling and Correlations for Pool Entrainment Phenomenon," Argonne National Laboratory Report ANL-83-37, NUREG/CR-3304.
14. Loftus, M. J. et al., 1981, "PWR FLECHT-SEASET Unblocked Bundle, Forced and Gravity Reflood Task Data Report," Volumes 1 and 2, NUREG/CR-1532, WCAP-9699.
15. MPR Associates, 1990a, "Summary of Results from the UPTF Downcomer Separate Effects Tests, Comparison to Previous Scaled Tests, and Application to U.S. PWRs," MPR-1163.
16. MPR Associates, 1990b, "Summary of Results from the UPTF Carryover/Steam Binding Separate Effects Tests, Comparison to Previous Scaled Tests, and Application to U.S. Pressurized Water Reactors," MPR-1213.
17. MPR Associates, 1992, "Summary of Results from the UPTF Cold Leg Flow Regime Separate Effects Tests, Comparison to Previous Scaled Tests, and Application to U.S. Pressurized Water Reactors," MPR-1208.
18. MPR Associates, 1993, "Reactor Safety Issues Resolved by the 2D/3D Program," MPR-1346.
19. Okubo, T., et al., 1984, "Data Report on Large Scale Reflood Test – 82 – CCTF CORE-II TEST C2-4 (RUN 062) –," Department of Nuclear Safety Research, Tokai Research Establishment, JAERI-memo 59-450.
20. Okubo, T., Iguchi, T., Okabe, K., Sugimoto, J., Akimoto, H., and Murao, Y., 1985, "Evaluation Report on CCTF Core-II Reflood Test C2-4 (Run 62)," JAERI-M 85-026.
21. Rosal, E. R., Hochreiter, L. E., McGuire, M. F., and Krepinevich, M. C., 1975, "FLECHT Low Flooding Rate Cosine Test Series Data Report," WCAP-8651.
22. Rosal, E. R., Conway, C. E., and Krepinevich, M. C., 1977, "FLECHT Low Flooding Rate Skewed Test Series Data Report," WCAP-9108.
23. USNRC, 1989, "Best-Estimate Calculations of Emergency Core Cooling System Performance," Regulatory Guide 1.157.
24. Walley, P. B., et al., 1973, "Experimental Wave and Entrainment Measurements in Vertical Annular Two-Phase Flow," AERE-R7521, Atomic Energy Research Establishment, Harwell, England.
25. Wallis, G. B., 1969, One-Dimensional Two-Phase Flow. McGraw-Hill Inc., NY

20 ADDITIONAL COMPONENT MODEL ASSESSMENTS

This section provides additional validation of components not individually addressed in previous sections. Section 20.1 examines the accumulator component, Section 20.2 examines the pump, and Section 20.3 presents a control-volume verification of mass and energy conservation at the 1D/3D junction. The momentum coupling treatment and assessment is discussed in Section 19.3.5.10 regarding the cold leg nozzle loss coefficient.

20.1 ACCUMULATOR COMPONENT

20.1.1 Introduction

The accumulator component model was described in Volume 1, Section 10.8. That section also described the phases of accumulator water injection, emptying, and accumulator nitrogen discharge.

The Phenomena Identification and Ranking Table (PIRT) identifies 3 highly ranked phenomena associated with the accumulator behavior during a loss-of-coolant (LOCA) transient:

1. Injection Flow Rate/Flow Resistance. The delivery flow rate of the accumulator is of high or medium importance for the whole spectrum of postulated LOCAs: for the smaller breaks, injection from the accumulator is responsible for terminating the transient and limiting the duration of clad heatup (medium rank). For intermediate and large breaks, injection from the accumulator is responsible for re-filling the downcomer and initiating reflood, and the flow rate/flow resistance is ranked high. The Indian Point Unit 2 (IPP) and Callaway Blowdown Tests, as described in Sections 20.1.2 and 20.1.3, document the capability of a simplified accumulator model in adequately predicting accumulator injection flow rate both under rapid discharge conditions (i.e., larger break scenarios) and gradual discharge conditions (i.e., smaller break scenarios). In addition to these separate effect tests, the accumulator discharge is analyzed in the Rig-of-Safety Assessment (ROSA) and Loss-of-Fluid Test (LOFT) integral effect tests, as documented in Sections 21 and 22. Finally, the accumulator discharge for the LOFT 2-5 and ACHILLES tests are documented in Section 20.1.4.
2. Nitrogen Discharge (Non-condensable effects). The accumulator nitrogen provides the main source of non-condensable gas in the system during the LOCA transient. While the potential effects of non-condensables are discussed elsewhere as applicable, it is recognized that the accumulator cover gas provides the main source of non-condensable gas in the system, and thus the discharge process and impact on the transient is discussed herein. In general, large amounts of non-condensable gas will be released from the accumulator only during the larger breaks (for the period of interest in the analysis), and thus the assessment is focused on these break sizes. The LOFT 2-5 and ACHILLES tests documented in Section 20.1.4 are used to assess the discharge of nitrogen from the accumulator and the effect on the pressurized water reactor (PWR) reflood transient.
3. Broken Loop Accumulator Treatment. The approach and justification for the treatment of the accumulator in the broken loop for different break sizes is discussed in Section 26.2.1.3 of Volume 3 and with plant scoping studies in Section 28.2.6, Volume 3.

| This overall assessment demonstrates the adequacy of the accumulator model documented in Volume 1, Section 10.8.

20.1.2 IPP Accumulator Test

| An accumulator blowdown test was performed at Indian Point Unit 2 in 1971 during startup testing. The initial gas pressure in the accumulator was about 100 psig, the gas volume was about 400 cubic feet and the water volume was 700 cubic feet. Test runs were performed at ambient temperature (80°F), with reactor coolant system (RCS) back pressure of 0 psig. The cold legs were empty and water level in the vessel was well below the cold leg nozzle elevation. The control valves used to initiate the test runs were set to open from 0 to 100 percent in 10 seconds. Test runs were performed for the four accumulators which had various accumulator line lengths. The test runs would terminate when the pressure in the accumulator reached approximately 20 psig while the accumulator line was still in single-phase liquid flow. The measured pressure responses of the four accumulators were all similar. Pressure response for one of the accumulators was selected for WCOBRA/TRAC-TF2 model verification. Figure 20.1-1 is a sketch showing the layout of the accumulator piping.

20.1.2.1 WCOBRA/TRAC-TF2 Model

A WCOBRA/TRAC-TF2 model was constructed to simulate the accumulator test. A typical PWR model of the accumulator and its piping consists of [

]^{a,c} as shown in Figure 20.1-2. [

]^{a,c} In this model, the RCS was simulated by a BREAK component, supplying a constant back pressure. The volume, length, and hydraulic diameter for the accumulator and the accumulator line were all preserved. [

]^{a,c} Section 28.1.5, Volume 3 presents a Large Break LOCA (LBLOCA) sensitivity study with an accumulator elevation varying [

]^{a,c}

The resistance in the accumulator line was simulated [

]^{a,c}. The initial and boundary conditions were the same as those used in the 1971 IPP test. Both the water and nitrogen cover gas were initially at 80°F. A steady-state run of 20 seconds was first performed, followed by a blowdown run initiated by opening a control valve in the accumulator line. The valve reached 100 percent opening within the first 10 seconds of the blowdown run.

20.1.2.2 WCOBRA/TRAC-TF2 Simulation Results

The accumulator pressure predicted by WCOBRA/TRAC-TF2 is compared to measured test data (the only data available) in Figure 20.1-3. It can be seen that WCOBRA/TRAC-TF2 prediction and test data are in good agreement [

]^{a,c}

20.1.3 Callaway Accumulator Test

In order to evaluate the Small Break LOCA (SBLOCA) emergency core cooling system (ECCS) model, Westinghouse, with the cooperation of the personnel of the Callaway Nuclear Plant, conducted a slow accumulator blowdown test at the plant in December 1982.

In order to simulate the accumulator discharge during a small break LOCA within constraints of the plant, the accumulators would discharge into an empty reactor vessel from normal pressure. The discharge was extended by using an orifice to restrict the flow so that the tank would empty at a prescribed time. An orifice plate was installed in the outlet nozzle of the accumulator. The [

]^{a,c} was calculated to result in a discharge time of approximately 15 minutes.

The test was conducted by opening the motor operated gate valve which would allow the tank to drain and the data to be recorded. The test was performed from an initial pressure of 600 psig and with initial water volume of 850 cubic feet.

The opening time of the accumulator isolation valve was 11 seconds. The time required for the water to discharge from the accumulator was 954 seconds.

20.1.3.1 WCOBRA/TRAC-TF2 Model

The Callaway small break accumulator blowdown was simulated [

]^{a,c}. Water and gas volumes, as well as the accumulator discharge nozzle diameter were preserved to accurately represent the test conditions. [

]^{a,c} Liquid and gas temperatures were set to 87°F, consistent with test data.

20.1.3.2 WCOBRA/TRAC-TF2 Simulation Results

Figure 20.1-6 shows a comparison of the accumulator pressure and the test data. [

]^{a,c}

20.1.4 Effect of Accumulator Nitrogen on PWR Reflood Transients

In Appendix K-based evaluation models, simple models were incorporated to simulate the effect of the nitrogen injecting from the accumulator into the cold legs and out the break for approximately 30 seconds during reflood. The effect of the nitrogen is to pressurize the downcomer and force water into the core, while promoting core cooling. Typically, the effect of nitrogen was ignored in these earlier evaluation models.

The previous Westinghouse Best-Estimate LOCA methodologies (Code Qualification Document (CQD) and Automated Statistical Treatment of Uncertainty Method (ASTRUM)) used experimental evidence to support the conclusion that the effect of accumulator nitrogen realistically improves reflood rates and heat transfer. A simplified method was developed for WCOBRA/TRAC MOD7A to treat the effects of accumulator discharge on the reflood transient, without considering an explicit transport of the non-condensable gases.

WCOBRA/TRAC-TF2 explicitly provides the capability of treating non-condensable gases, which allows more mechanistic treatment of the effects of the nitrogen discharge on the reflood transient, without the need of a simplified model. The experimental evidence that assesses the WCOBRA/TRAC-TF2 on modeling the effects of the nitrogen discharge on the reflood transient is discussed below.

20.1.4.1 LOFT Test L2-5

The description of the LOFT facility and tests are provided in Sections 22.2 and 22.3, and the WCOBRA/TRAC-TF2 input models and simulation results of the six simulated LOFT tests, including L2-5, are presented in Section 22.4.

The sequence of events for the LOFT large break Test L2-5 (Bayless et al., 1982) during the period of accumulator flow is similar to that calculated for a typical plant transient. The accumulator liquid flows down into the downcomer directly below the intact loop cold leg nozzle while steam and dispersed liquid flows up the opposite side and out of the cold leg break during the blowdown. Toward the end of the period of accumulator flow, the downcomer is partially full of subcooled liquid.

As the LOFT accumulator empties of liquid, the nitrogen contained in the accumulator begins to flow down the accumulator line and into the cold leg. Figures 20.1-10 and 20.1-11 show the accumulator liquid level and pressure for Test L2-5. From the density measurement in the intact loop cold leg, as shown in Figure 20.1-12, the nitrogen in the accumulator entered the RCS after the accumulator emptied at about 50 seconds (Figure 20.1-10).

It can be seen from the core bubble plot (Figure 20.1-13a) that there is an increase in core level beginning at about 43 seconds. By 60 seconds the core is completely covered. Figure 20.1-13b shows the cladding temperature in one of the central bundles at different elevations in the test, and indicates a progressive quenching at two lower elevations, 8 inches and 26 inches from the bottom of the core, from approximately 48 to 60 seconds, respectively. Therefore, the appearance of the nitrogen in the downcomer does not cause a simultaneous sudden quench at these two different elevations.

A more recent analysis of the LOFT Self-Power Neutron Detectors (SPNDs) (Mackley and Birchley, 1985) provides further qualitative evidence of the density of the fluid in the LOFT core. Figure 20.1-14 shows the fluid densities in the central fuel bundle for LOFT Test L2-5 at elevations of 27 and 44 inches above the bottom of the core, and the fuel clad temperature transients at the same elevations were also co-plotted with the fluid densities respectively. In this experiment, the peripheral low power regions of the core were quenched either during blowdown or by the liquid entering the core prior to 60 seconds, and the high power regions were quenched by 60 seconds.

Evidence of the effect of nitrogen on the downcomer pressure is shown in Figure 20.1-15. A sudden increase in pressure is observed in the suppression tank at 60 seconds, coincident with the time that nitrogen enters the cold leg from the accumulator.

20.1.4.2 WCOBRA/TRAC Prediction of LOFT Reflood Transient

In the simulation of the LOFT tests (Section 22.3), the accumulators were modeled as in a PWR, [

I^{a,c}

The simulation results show that the accumulator water is predicted to flow down into the downcomer after the check valve in its discharging line is opened by low RCS pressure and makes its way into the cold leg and vessel. [

I^{a,c}

20.1.4.3 ACHILLES Experiments

A series of reflood heat transfer experiments were conducted in the ACHILLES test facility, using boundary conditions based on best-estimate computer code calculations (Dore and Denham, 1990). Two types of tests were conducted; “forced” reflood experiments, in which the downcomer water was forced into the core by applying a high nitrogen overpressure, and “natural” reflood experiments, in which the nitrogen overpressure was created by nitrogen discharged from a scaled accumulator. In both types of tests, the initial surge of water resulted in significant cooling, and entrainment of water out of the top of the test bundle. This was followed by a period of poor cooling, until the downcomer driving head could be re-established by the continuation of pumped safety injection. However, the net result was a significant reduction in the maximum cladding temperatures attained, relative to comparable tests with no initial surge into the bundle.

20.1.4.4 WCOBRA/TRAC Prediction of ACHILLES International Standard Problem 25

Westinghouse has used WCOBRA/TRAC-TF2 to simulate International Standard Problem (ISP) number 25 (Holmes, 1991), an experiment which simulated the end of the accumulator discharge period in a postulated large break loss of coolant accident. The test was performed in the ACHILLES test facility at AEA Technology Winfrith. The test facility was described by Denham et al. (1989), and ISP 25 results were reported by Holmes (1991). The facility layout is shown in Figure 20.1-24.

The WCOBRA/TRAC-TF2 model of the ACHILLES test facility is shown in Figure 20.1-25.

[

]^{a,c}

The test section was modeled [

]^{a,c}

Comparisons of the WCOBRA/TRAC-TF2 simulation with the experimental data are shown in Figures 20.1-27 through 20.1-36. Figures 20.1-27 and 20.1-28 show the accumulator depressurization and mass flow rate through the injection line during the early part of the transient. [

]^{a,c}

The predicted pressure loss from the top of the downcomer to the break is compared with the measured pressure loss in Figure 20.1-30. [

]^{a,c} The predicted gas mass flow rates to the break are compared with the measured data in Figure 20.1-31. [

]^{a,c}

Downcomer and core collapsed liquid levels are shown in Figures 20.1-32 and 20.1-33. [

]^{a,c}

Figures 20.1-34 through 20.1-36 show the cladding temperature transients at 1.08m, 2.01m, and 2.65m.

[

|

I^{a,c}

Broken Pipe Pressure Loss Sensitivity Study

| [

|

|

|

I^{a,c}

In general, the ACHILLES test simulation shows that [

|

|

I^{a,c}

[

]^{a,c}

20.1.5 Conclusion

The accumulator model as used in the PWR, was assessed against both Separate Effect Tests (SETs) and Integral Effects Tests (IETs). The prediction of discharge of subcooled water into the RCS in both LBLOCA and SBLOCA conditions is [

]^{a,c} Therefore, based on the assessment it is concluded that the WCOBRA/TRAC-TF2 accumulator model [

]^{a,c}

20.1.6 References

1. Bayless, P. D., et al., 1982, "Experimental Data Report for LOFT Large-Break Loss-of-Coolant Experiment L2-5," NUREG/CR-2826, EGG-2210.
2. Denham, M. K., et al., 1989, "ACHILLES Unballooned Cluster Experiments Part 1: Description of the ACHILLES Rig, Test Section, and Experimental Procedures," AEEW-R2336.
3. Dore, P. and Denham, M. K., 1990, "ACHILLES Unballooned Cluster Experiments Part 5: Best Estimate Experiments," AEEW-R2412.
4. Holmes, B. J., 1991, "ISP 25 Comparison Report," AEA-TRS-1043.
5. Mackley, A. D. and Birchley, J. C., 1985, "Estimated Post-Scram Reactor Coolant Densities from Prompt Response Self Powered Neutron Detectors in Loss-of-Coolant Experiments," Instrumentation Society of America, 31st International Instrumentation Symposium, San Diego, California.

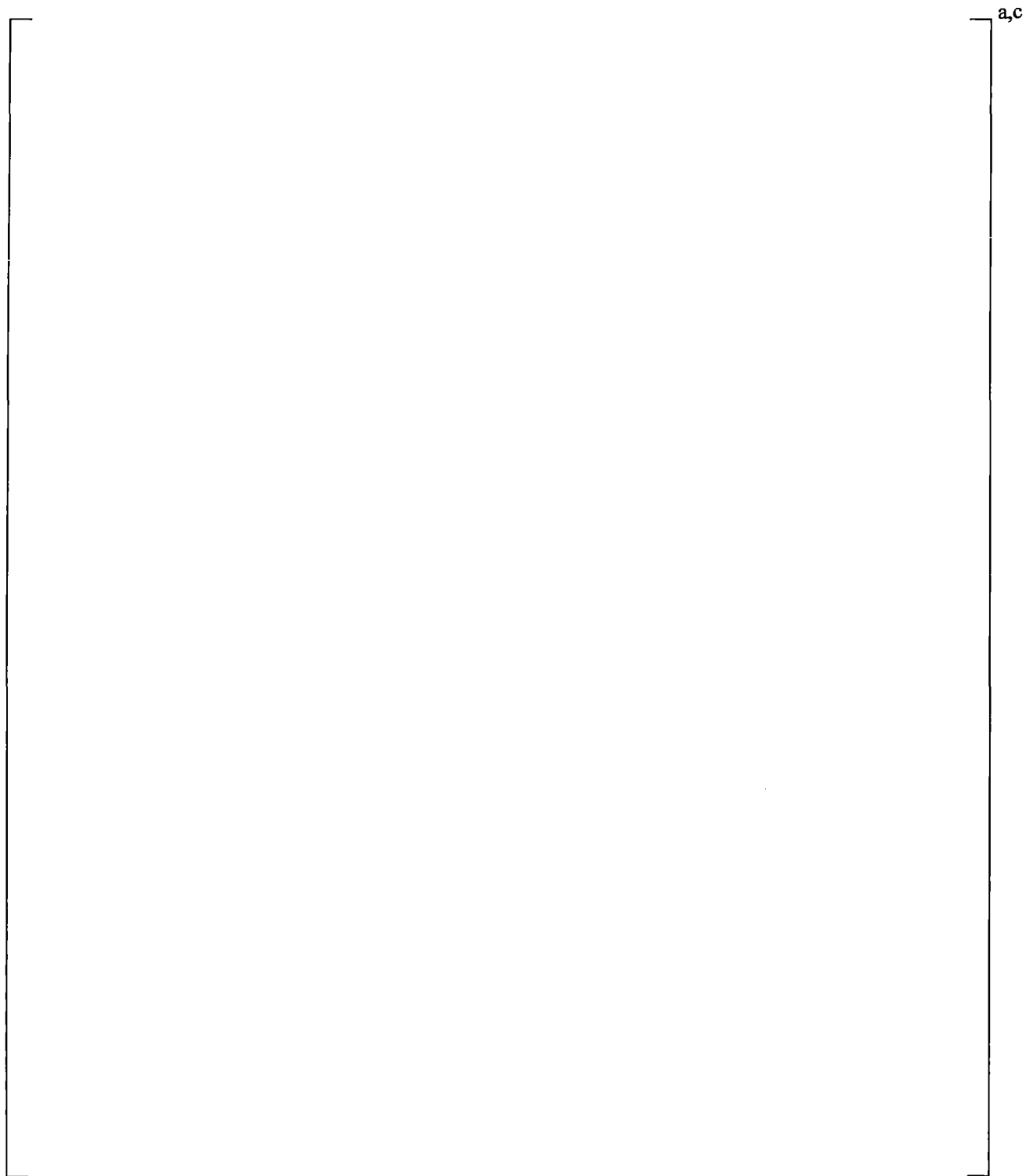
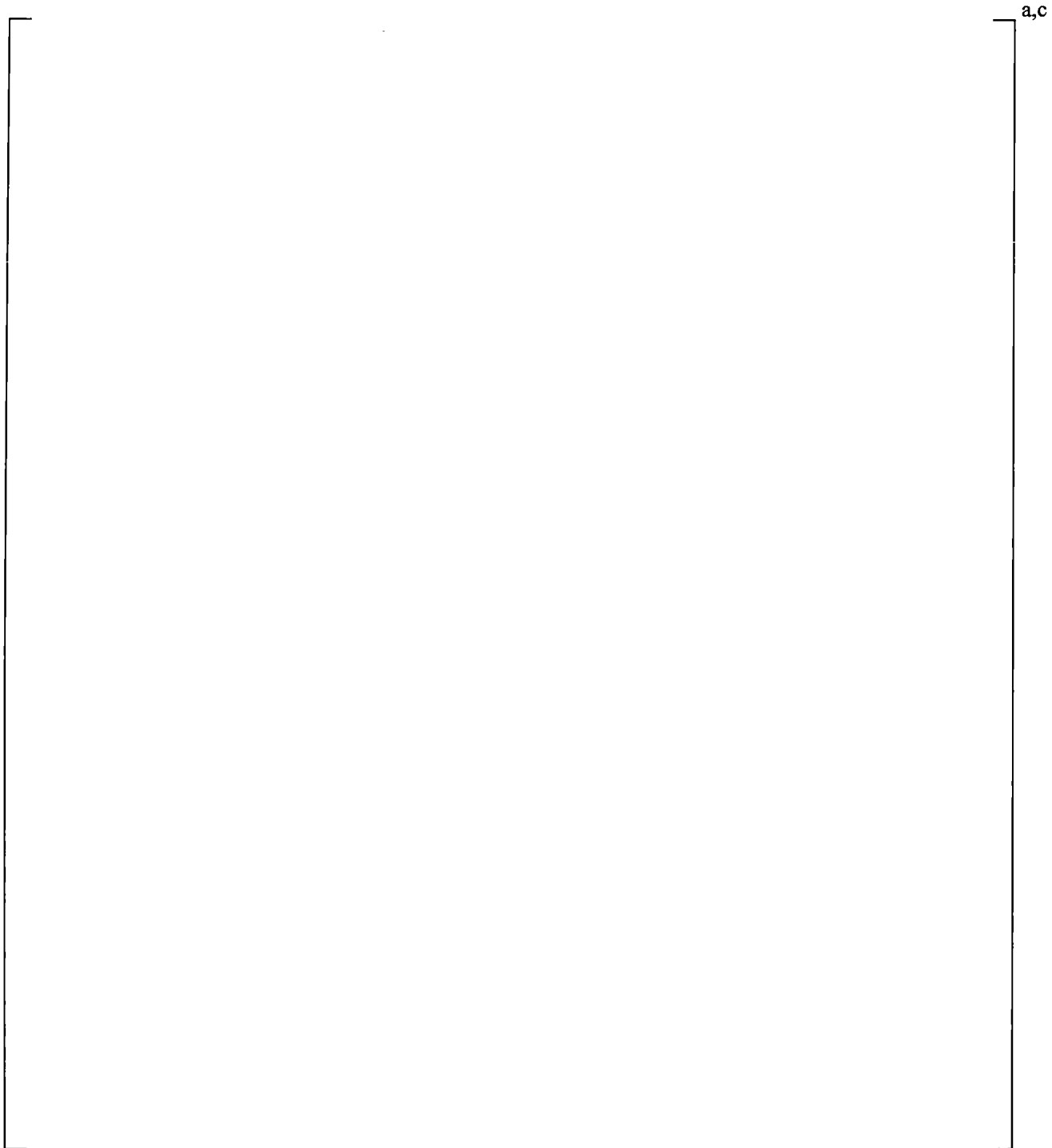
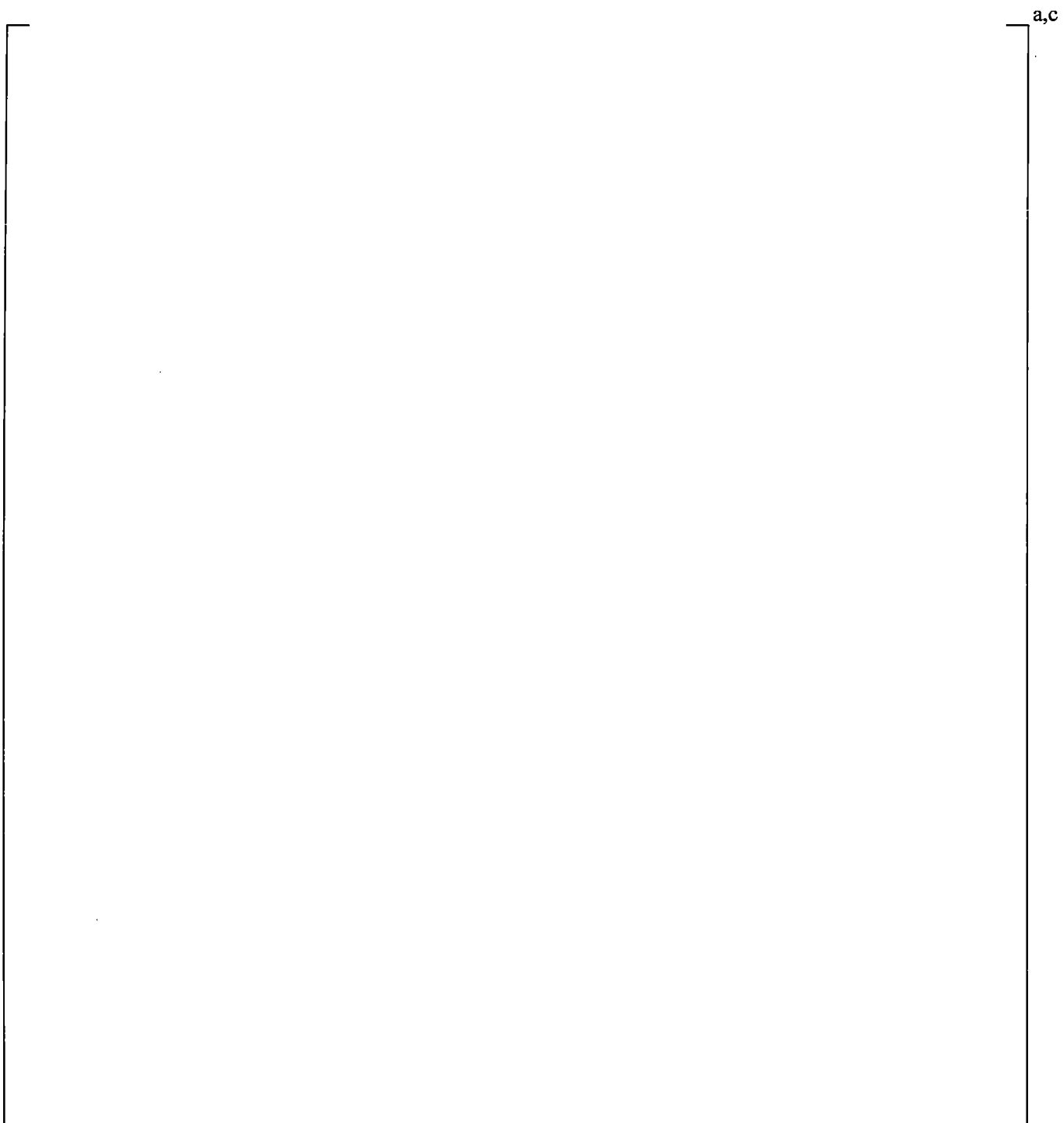


Figure 20.1-1 IPP Loop #2 Accumulator Line Schematic



**Figure 20.1-2 WCOBRA/TRAC-TF2 Model of Accumulator and
SI Line in IPP and Callaway Test Models**



**Figure 20.1-3 Predicted Accumulator Pressure (Solid Line) Compared with
Measured Test Data (Dashed Line)**

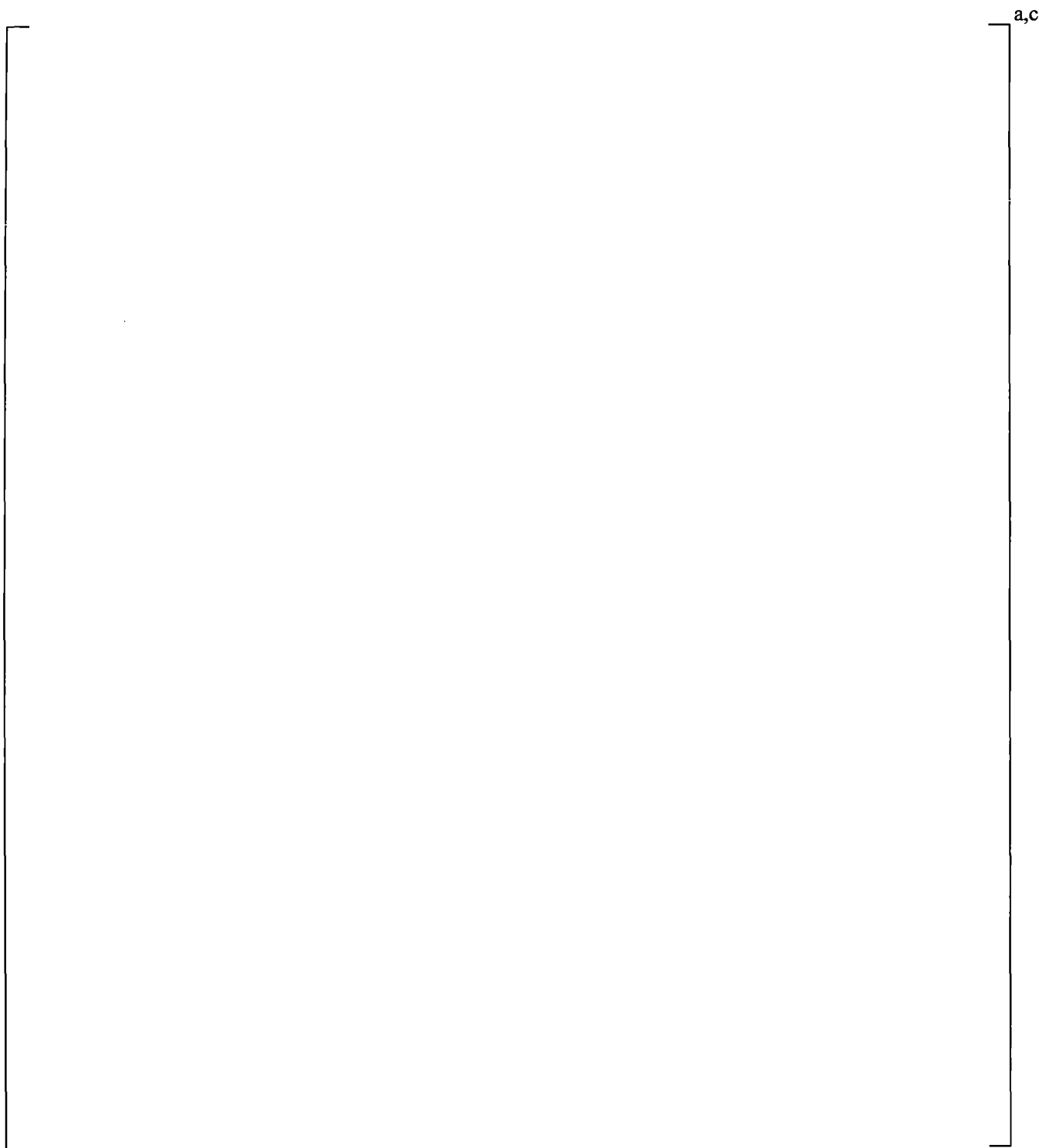


Figure 20.1-4 Predicted Accumulator Flow Rate

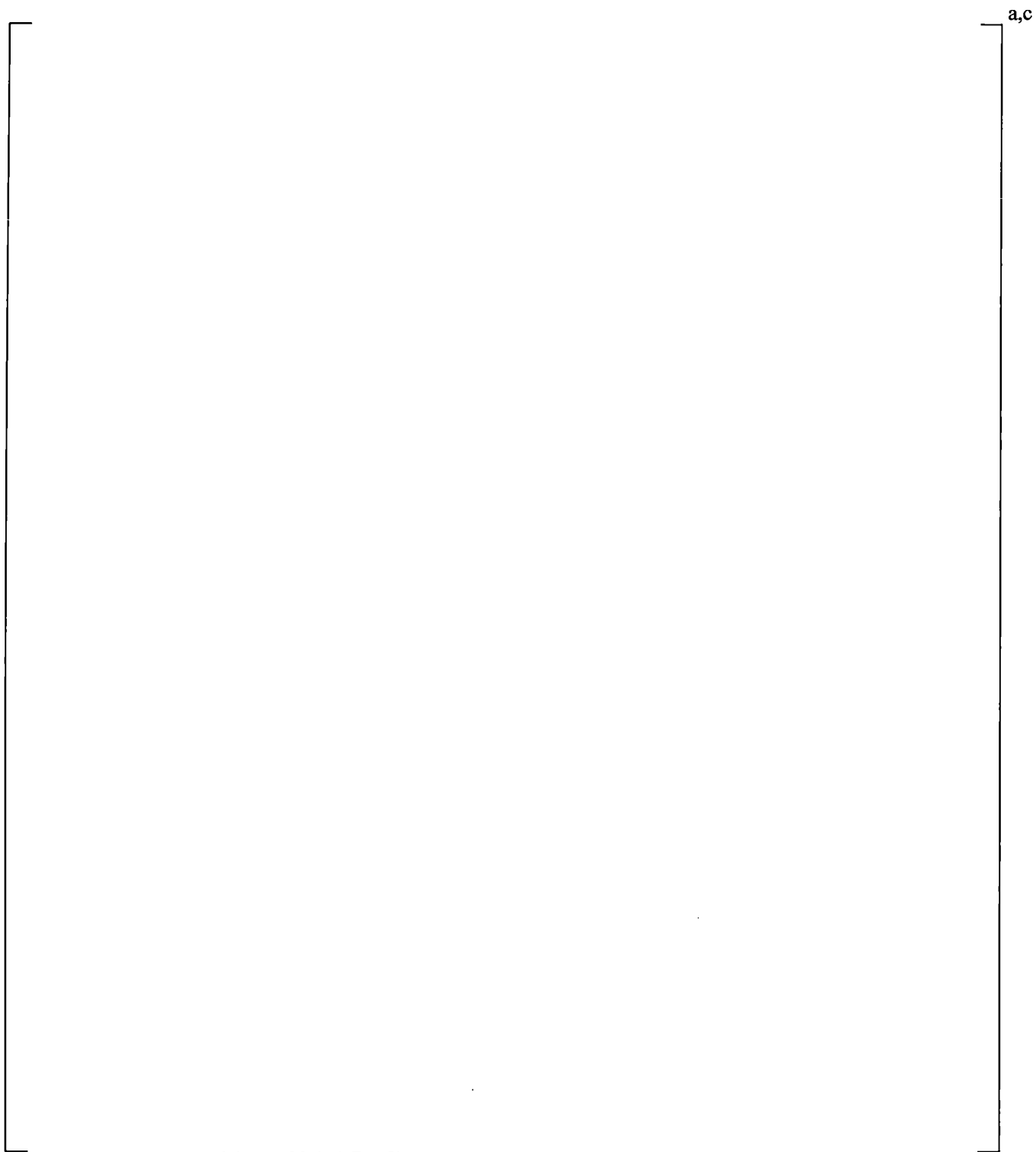
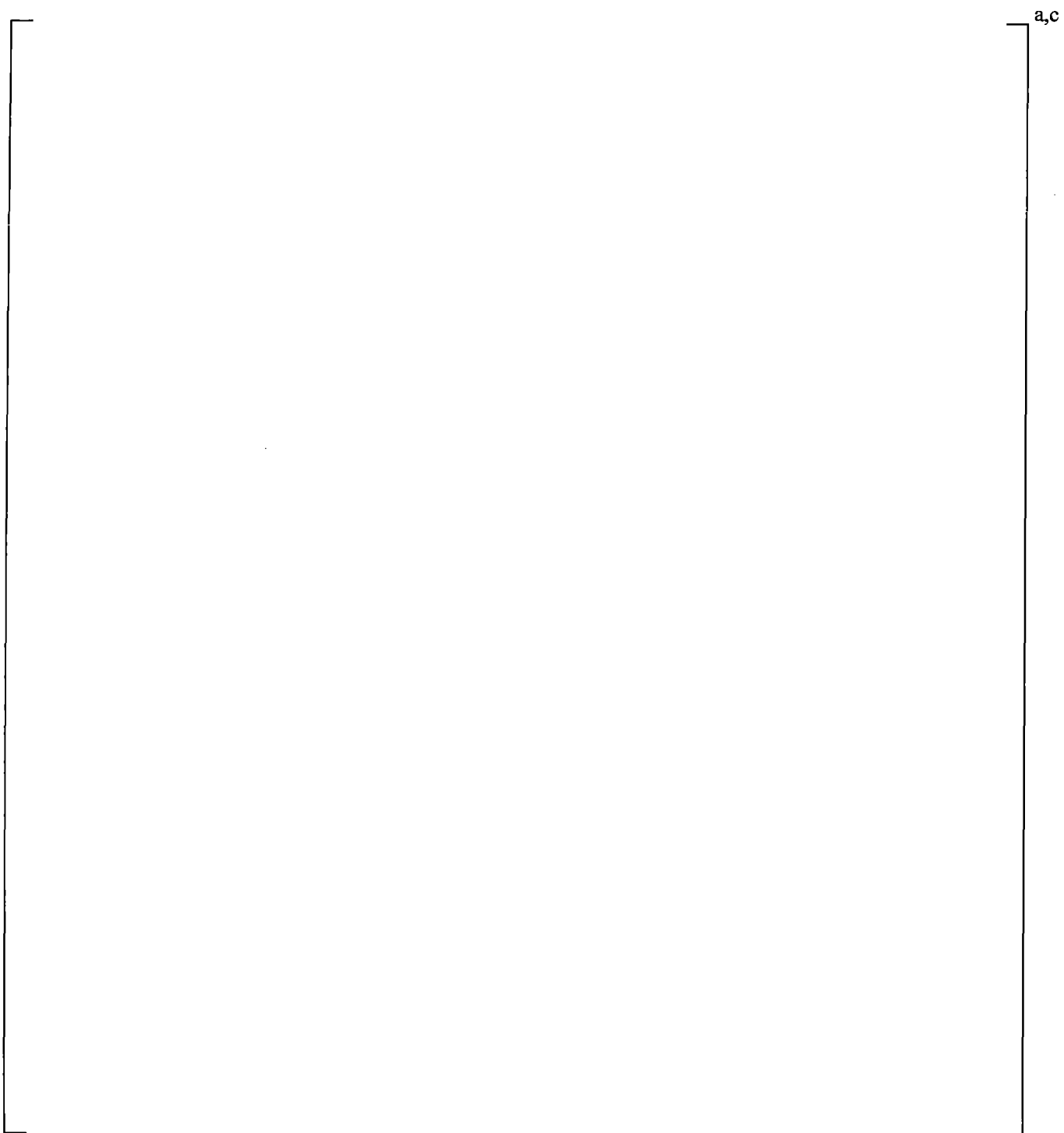
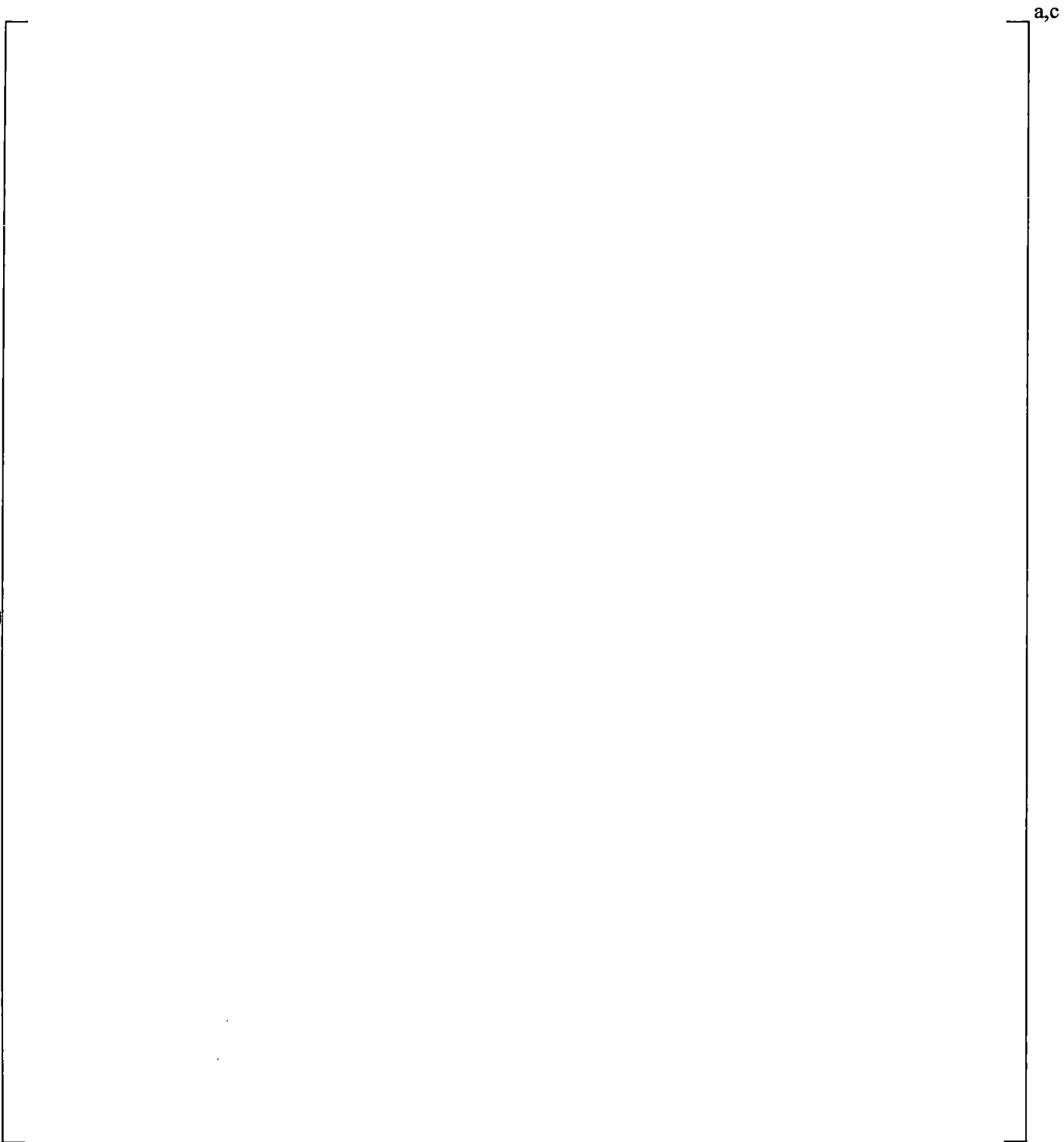


Figure 20.1-5 Predicted Gas Temperature at Top of Accumulator



**Figure 20.1-6 Comparison of Callaway Accumulator Blowdown Test Data and
WCOBRA/TRAC-TF2 Prediction of Accumulator Pressure**



**Figure 20.1-7 Comparison of Callaway Accumulator Blowdown Test Data and
WCOBRA/TRAC-TF2 Prediction of Accumulator Gas Volume**

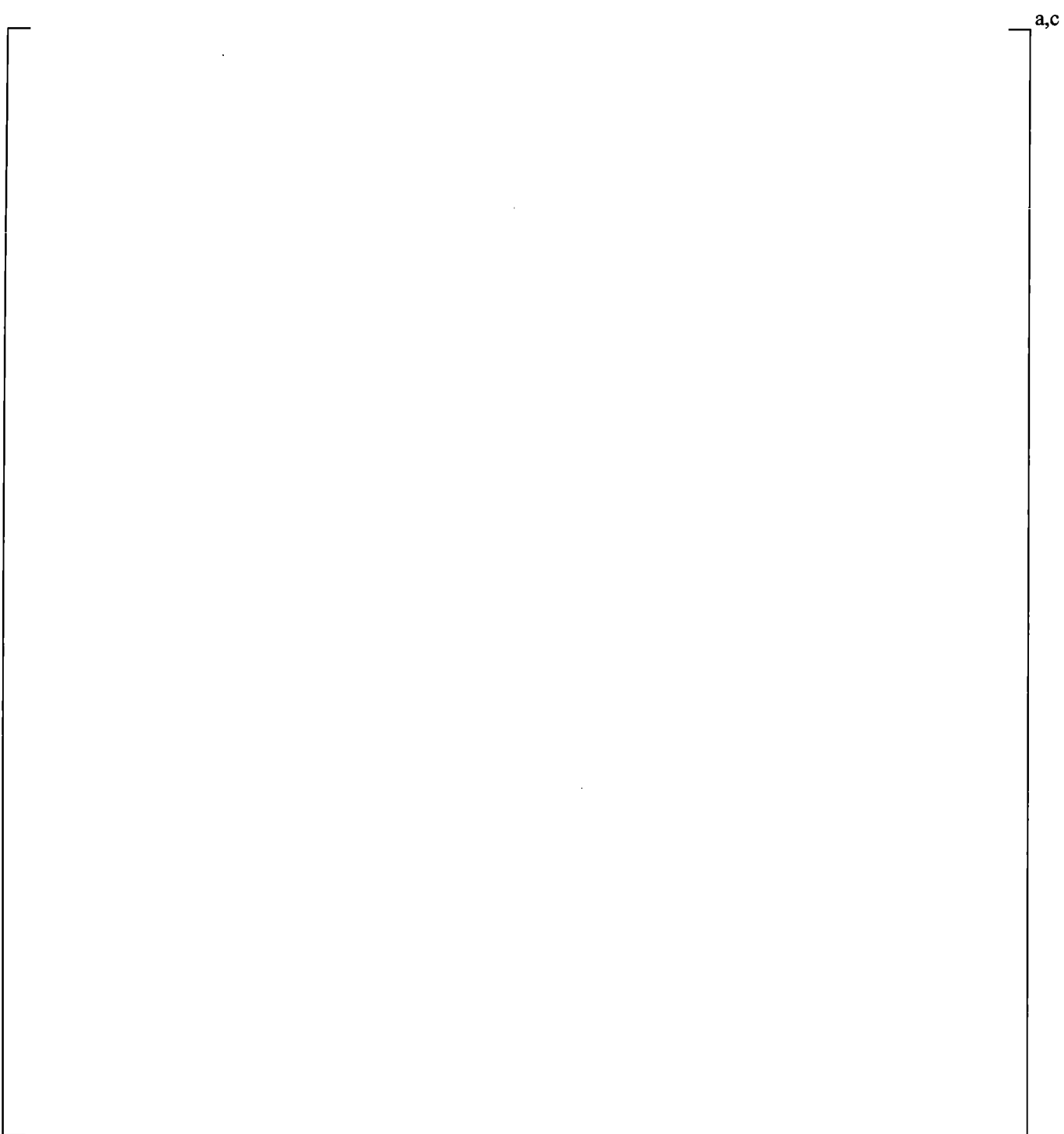


| **Figure 20.1-8 Comparison of Callaway Accumulator Blowdown Test Data and
WCOBRA/TRAC-TF2 Prediction of Accumulator Gas Temperature**

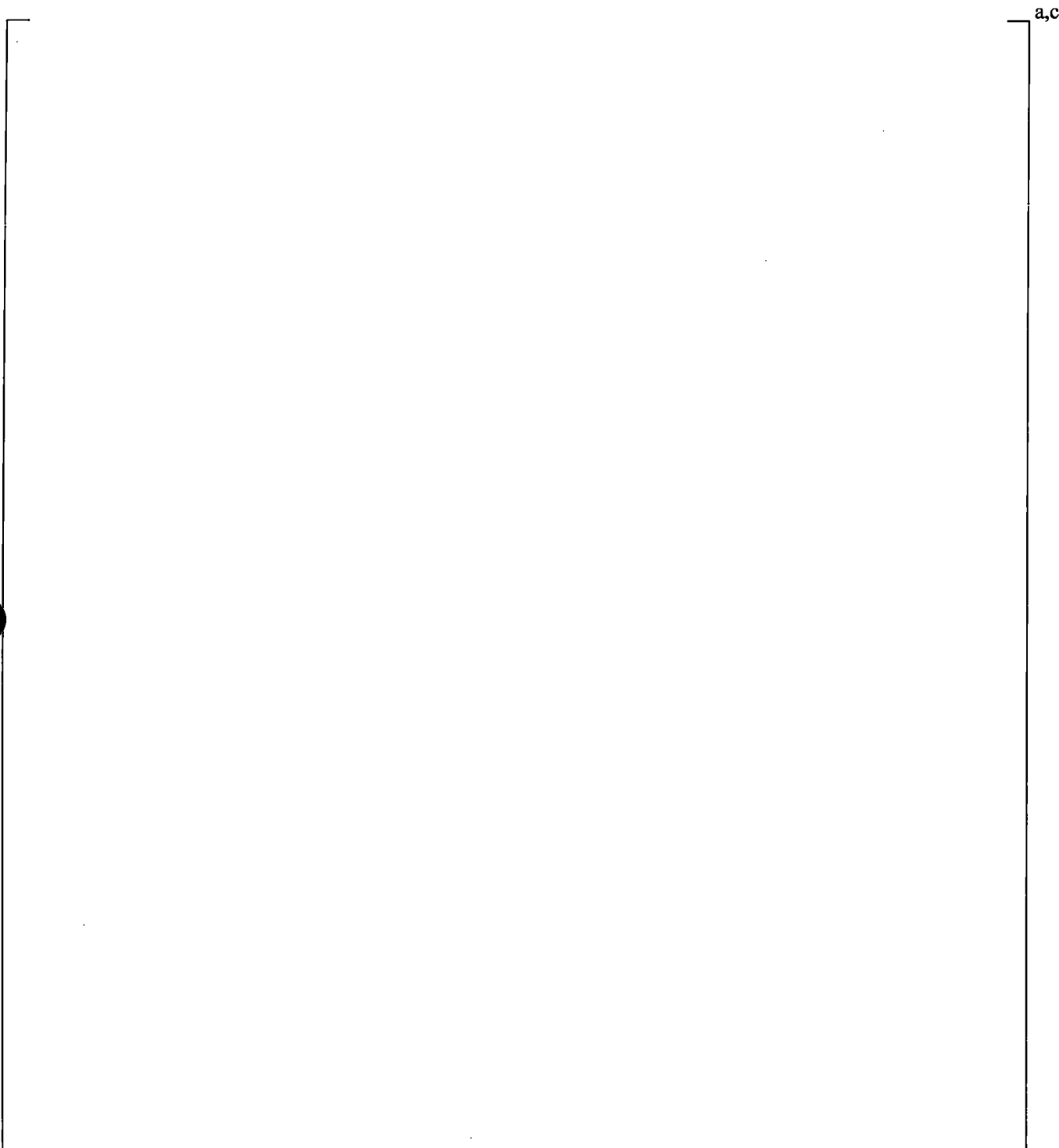


Figure 20.1-9 Best-fit Calculation of Polytropic Exponent from Callaway Accumulator Blowdown WCOBRA/TRAC-TF2 Prediction

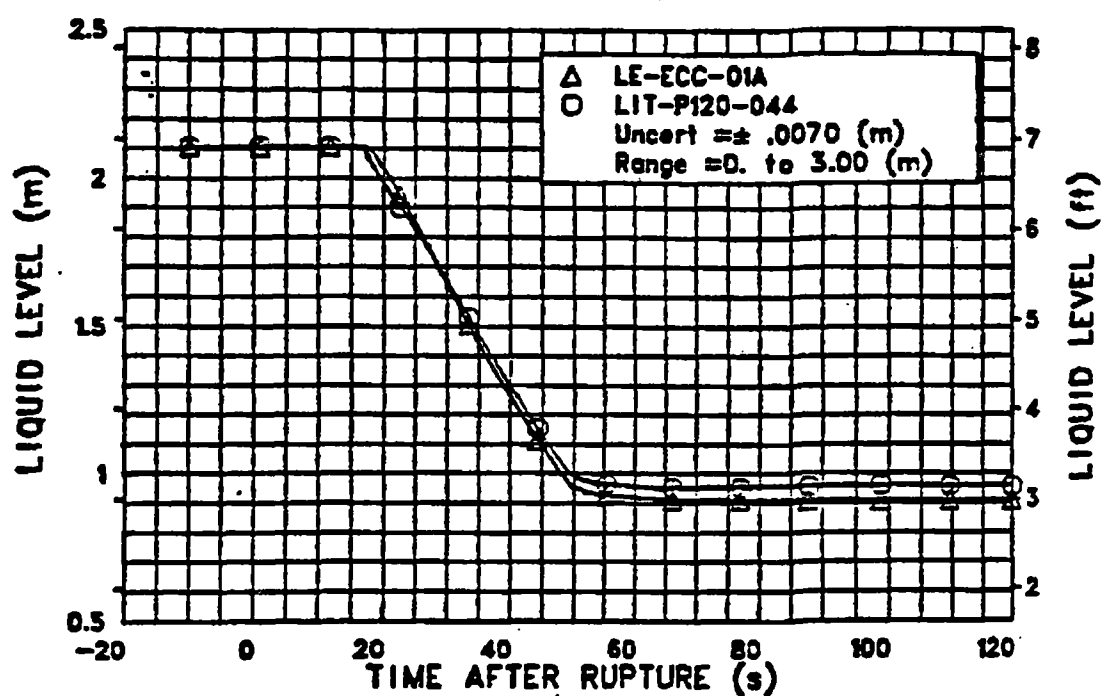


Figure 20.1-10 Accumulator Liquid Level for LOFT Test L2-5 (Bayless et al., 1982)

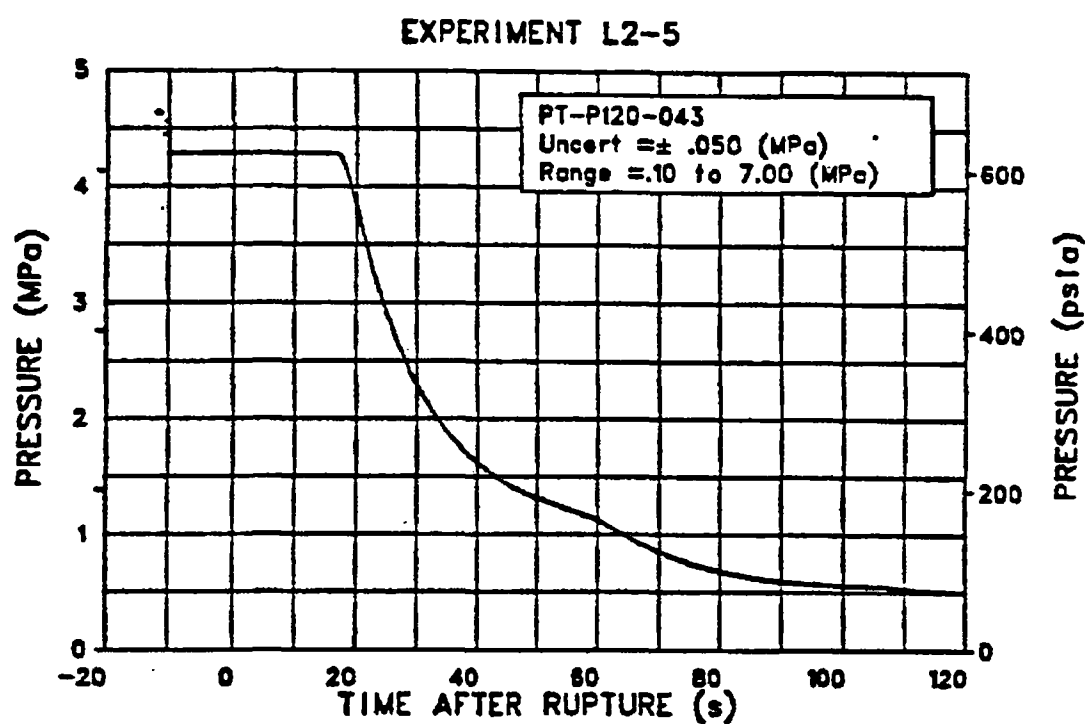


Figure 20.1-11 Accumulator Pressure for LOFT Test L2-5 (Bayless et al., 1982)

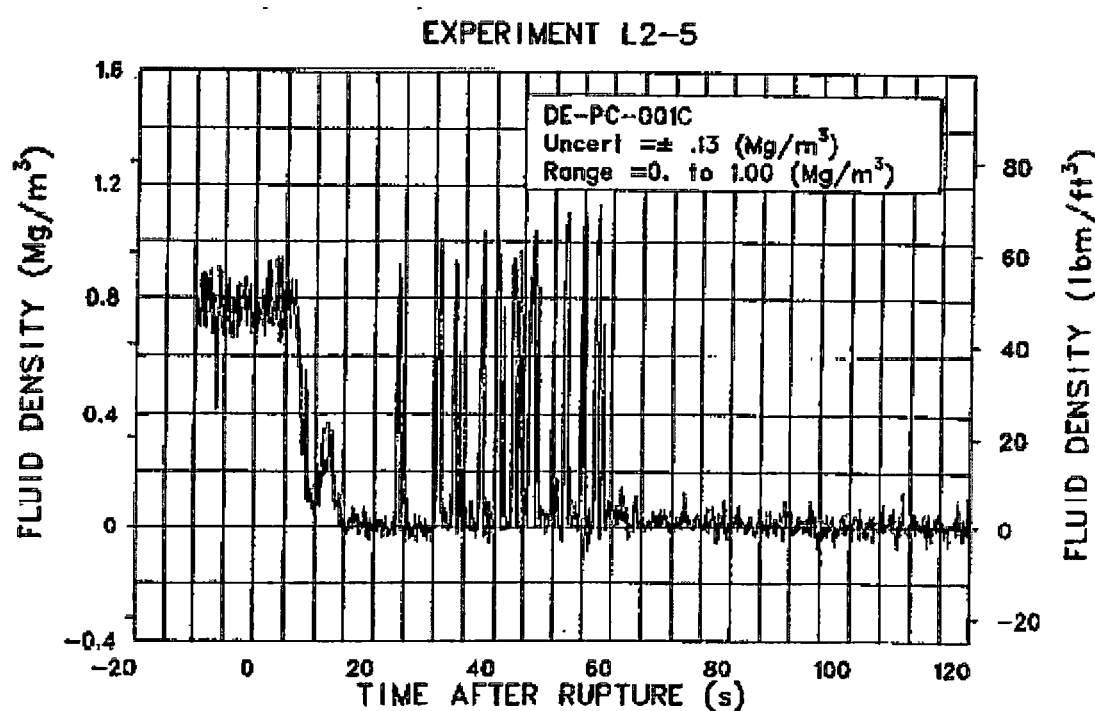
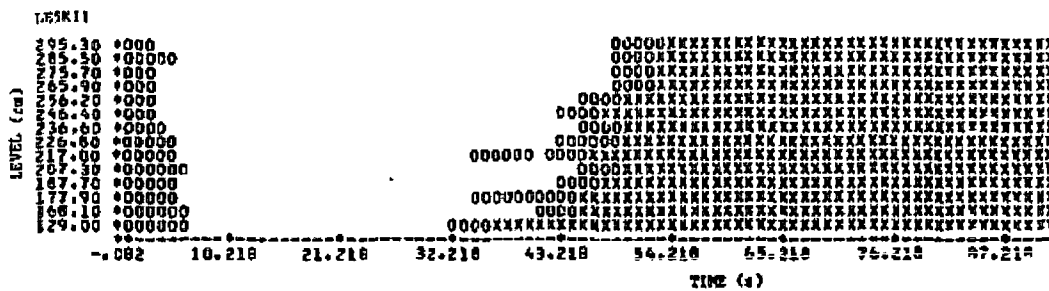
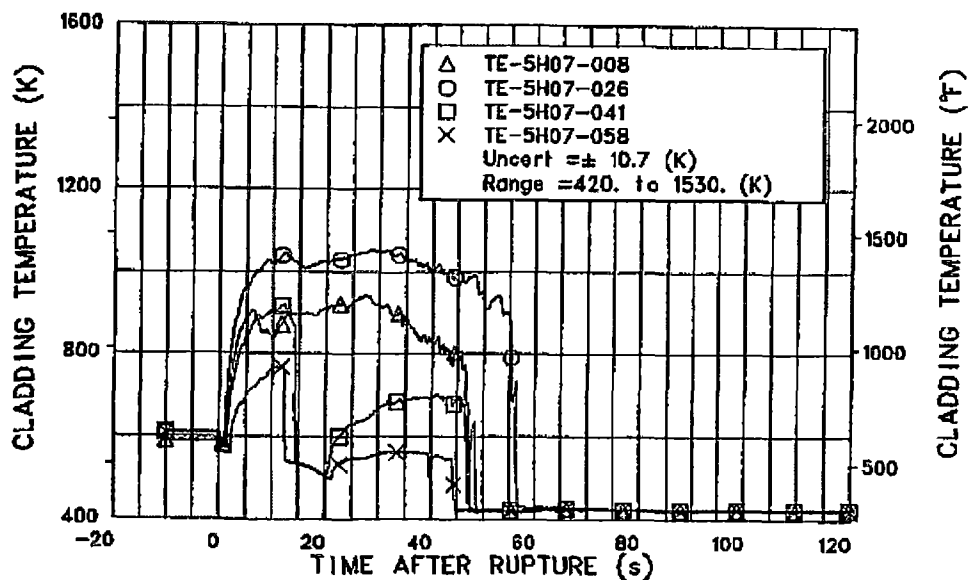


Figure 20.1-12 Intact Loop Cold Leg Density for LOFT Test L2-5 (Bayless et al., 1982)



(a)

- - HIGH VOID FRACTION
- 0 - INTERMEDIATE VOID FRACTION
- X - LOW VOID FRACTION



(b)

Figure 20.1-13 (a) Core Liquid Level Plots for LOFT Test L2-5 (Bayless et al., 1982)
(b) Fuel Rod Clad Temperatures (Bayless et al., 1982)

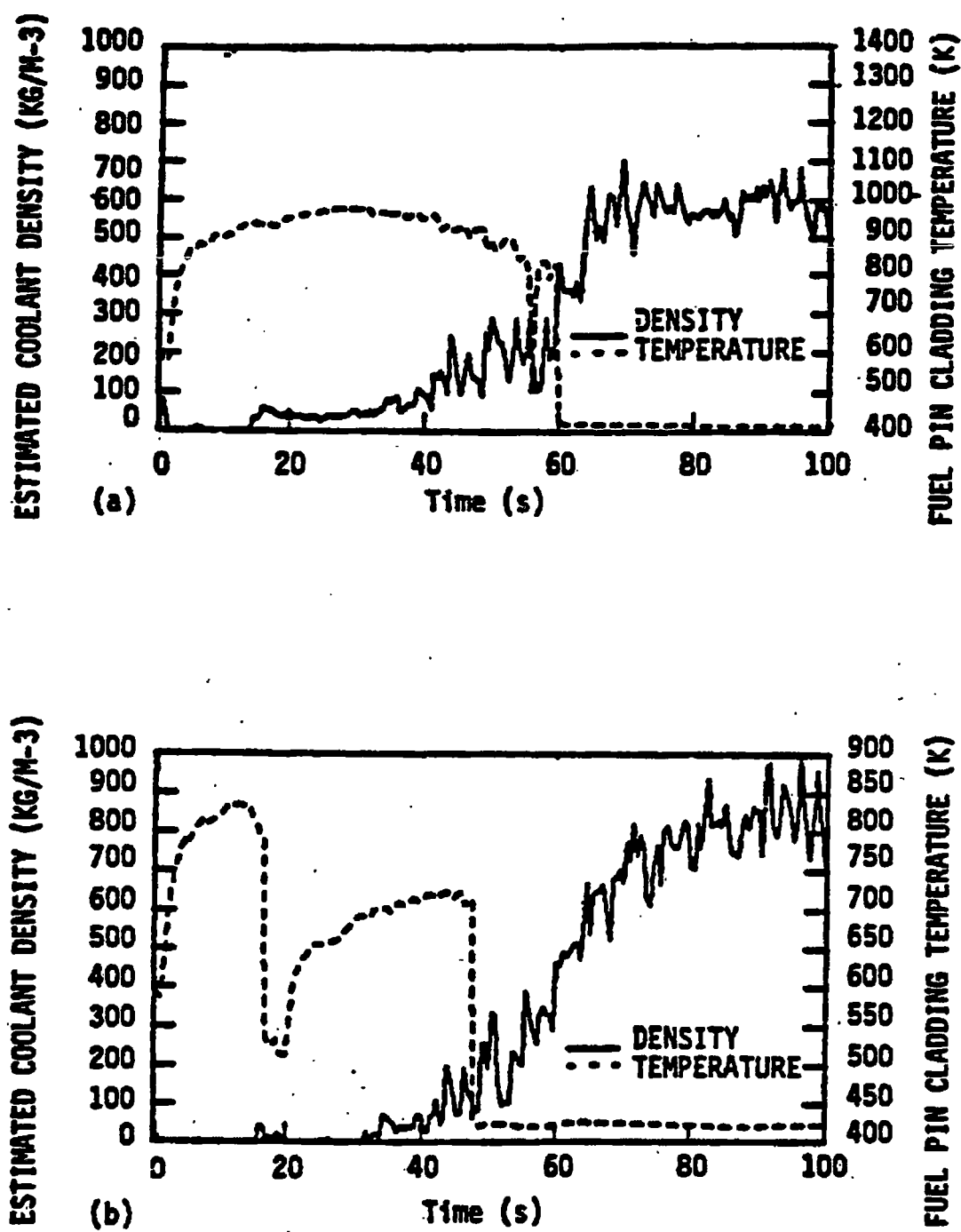


Figure 20.1-14 Fluid Density and Clad Temperature in Core at
 a) 27 inches,
 b) 44 inches Above Bottom of Core (Mackley and Birchley, 1985)

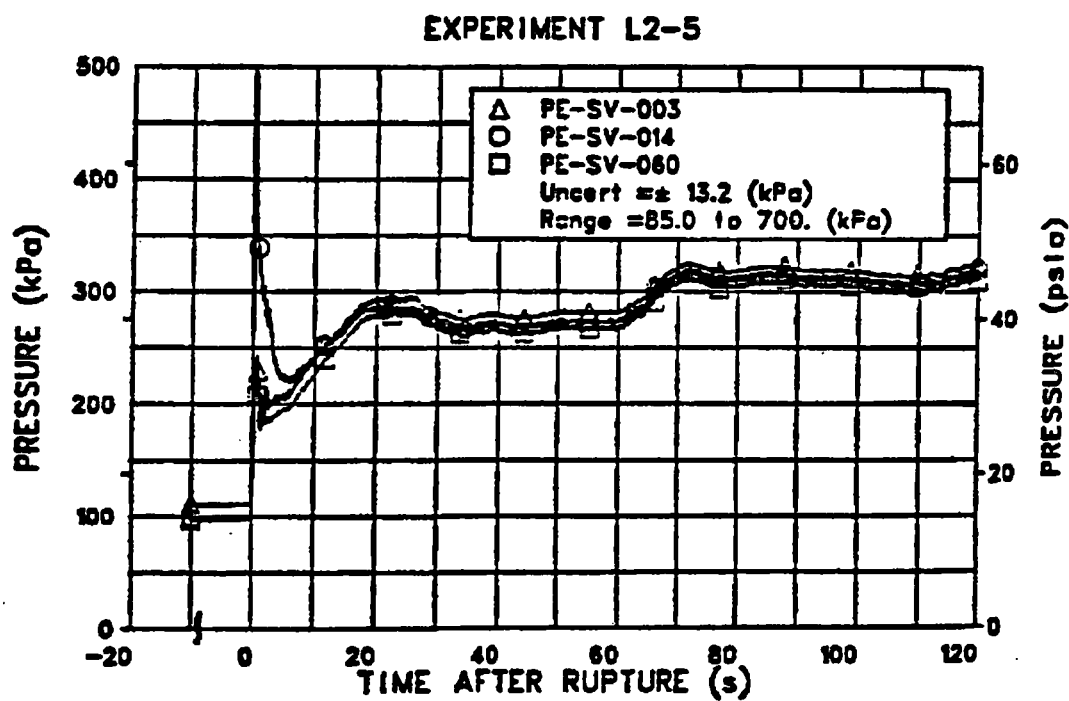


Figure 20.1-15 Suppression Tank Pressure for LOFT Test L2-5 (Bayless et al., 1982)

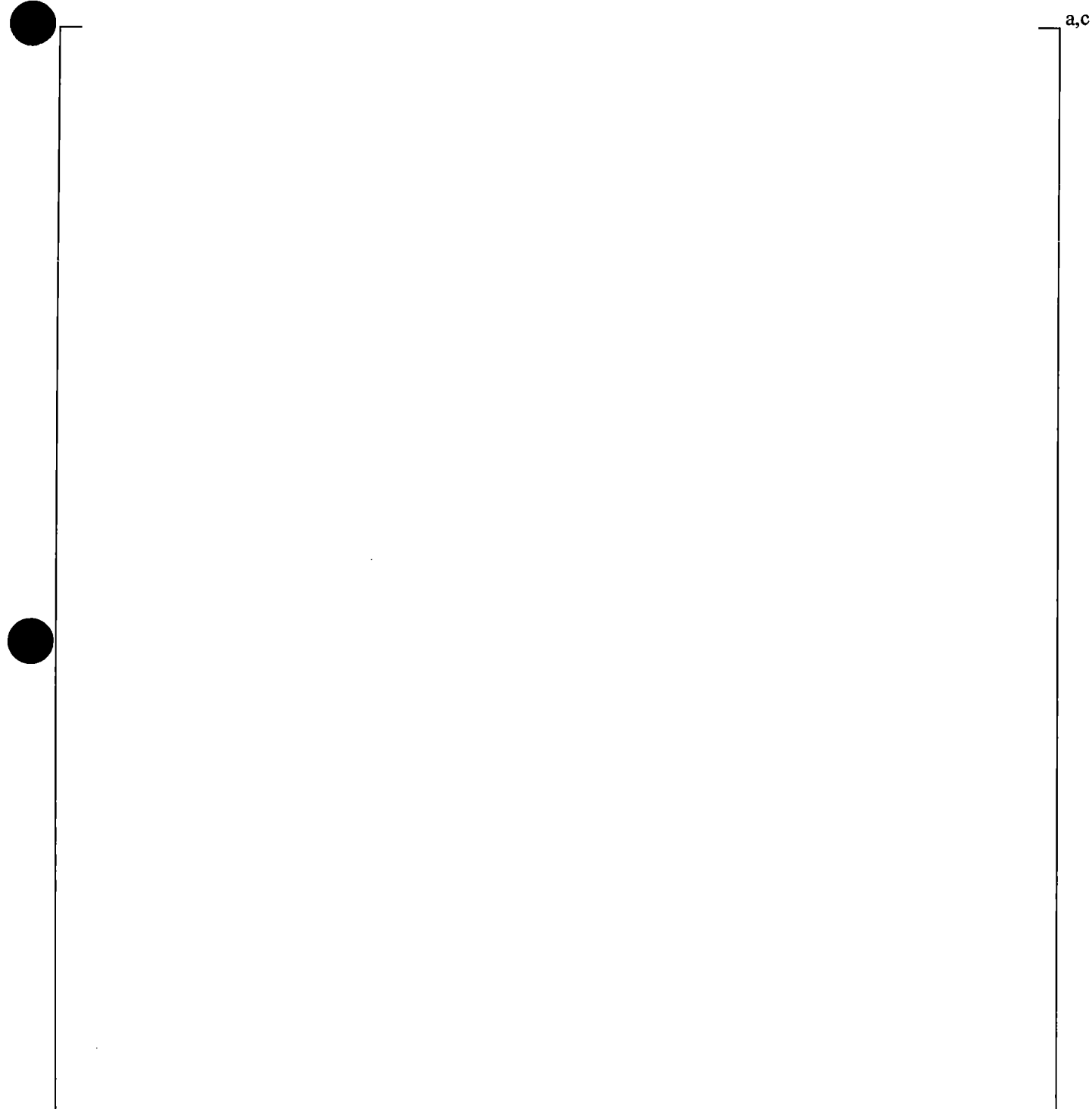


Figure 20.1-16 [

]^{a,c}

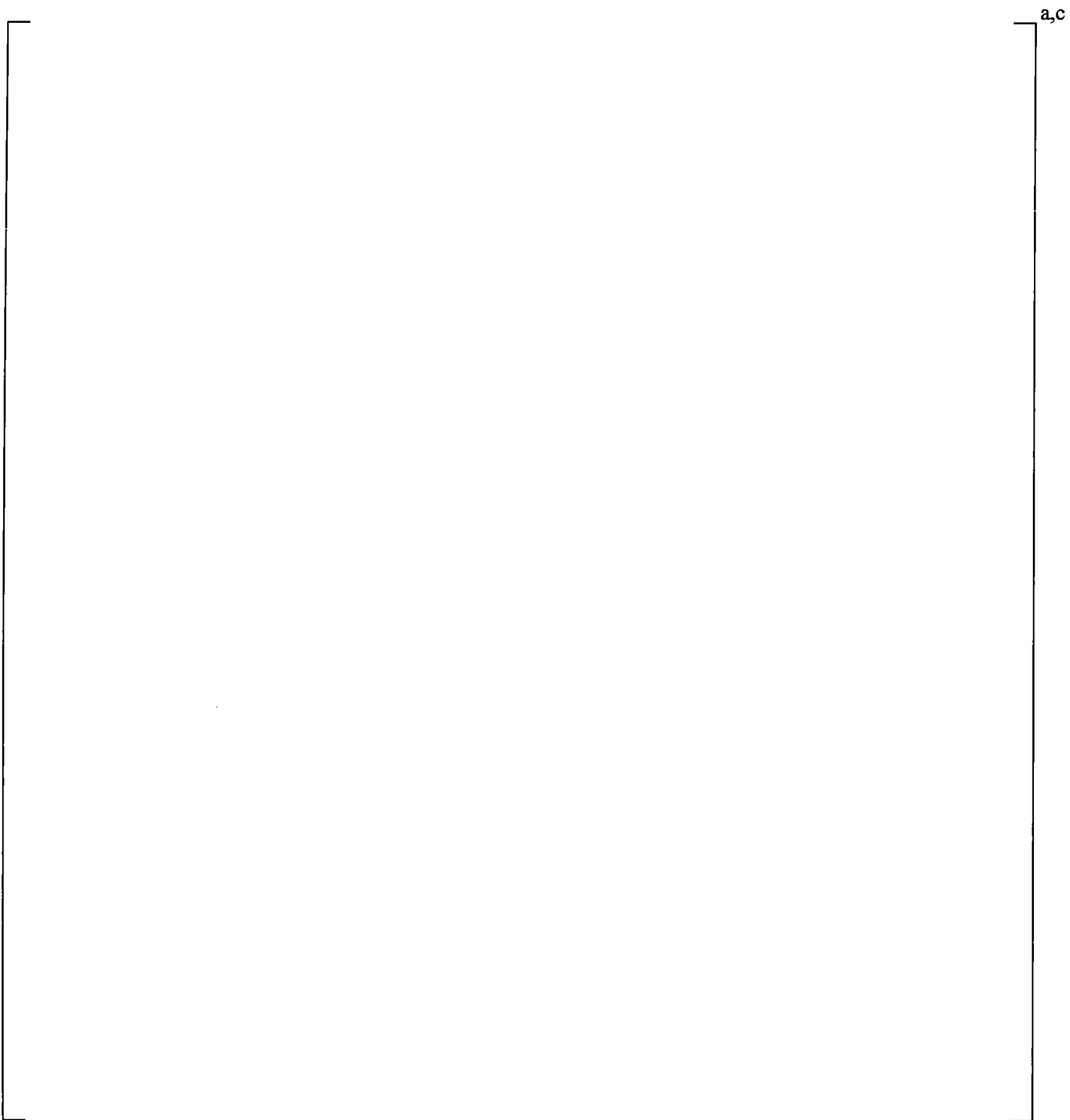


Figure 20.1-17 [

]^{a,c}

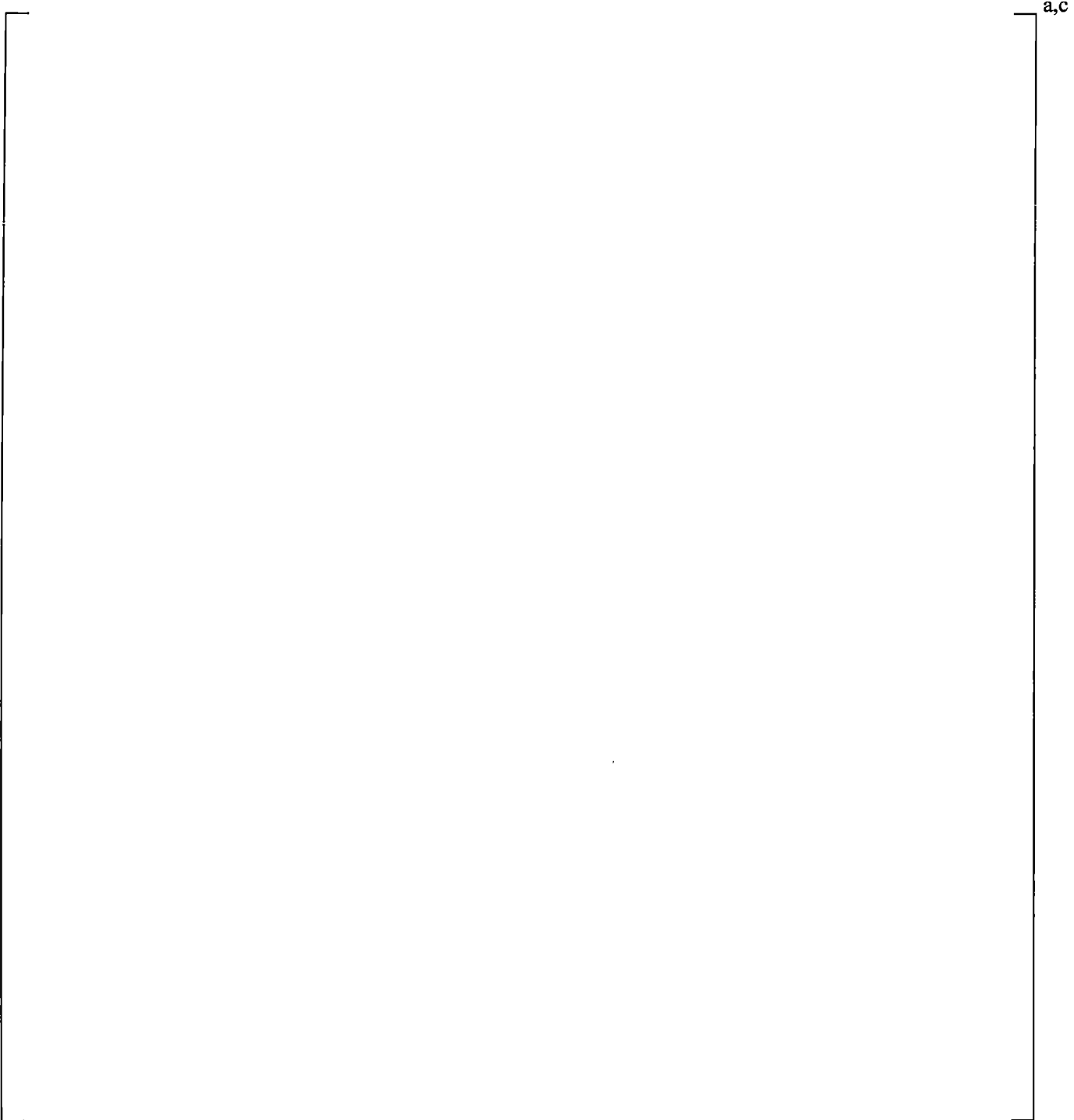


Figure 20.1-18 [

]^{a,c}

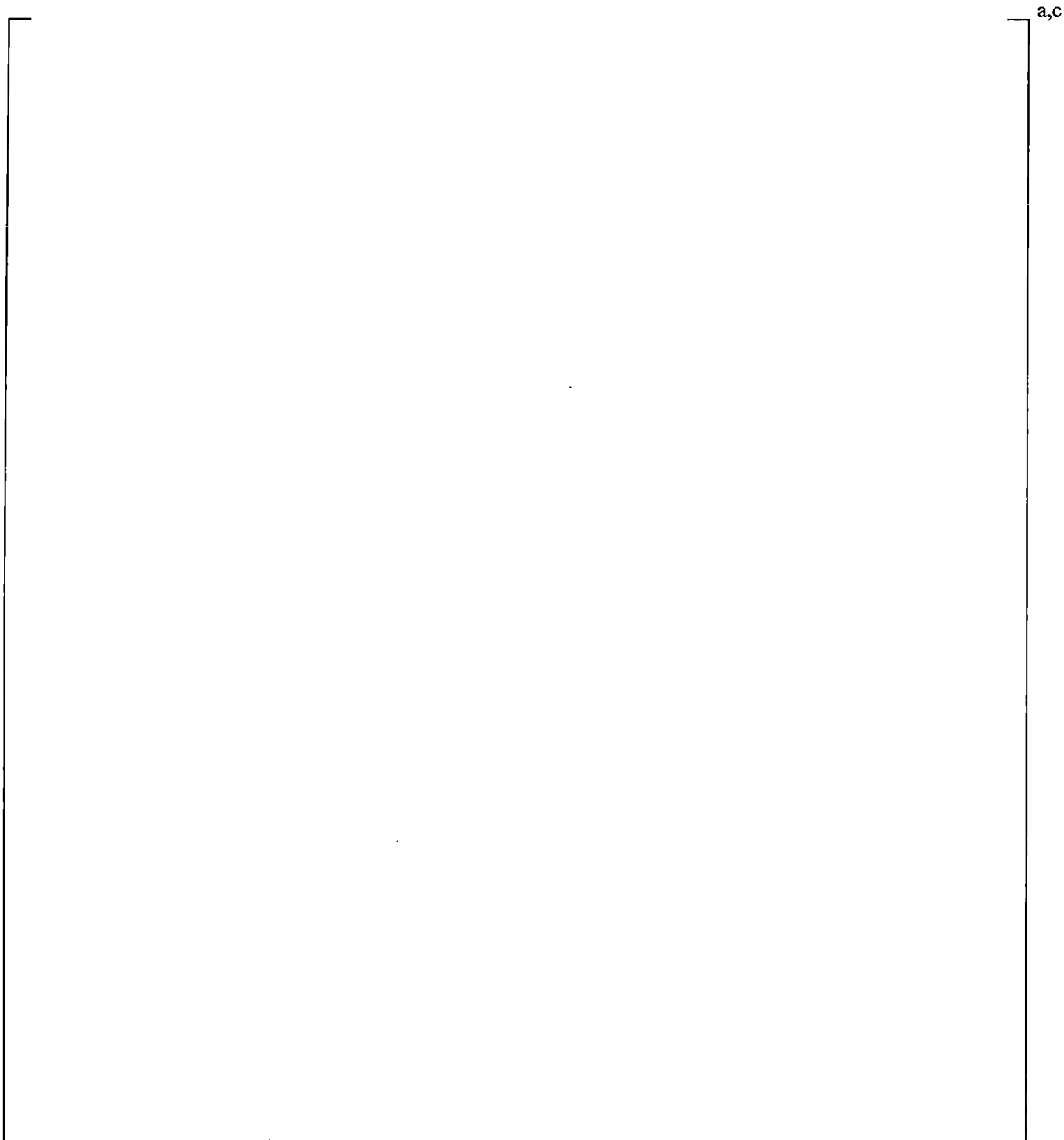


Figure 20.1-19 [

]^{a,c}

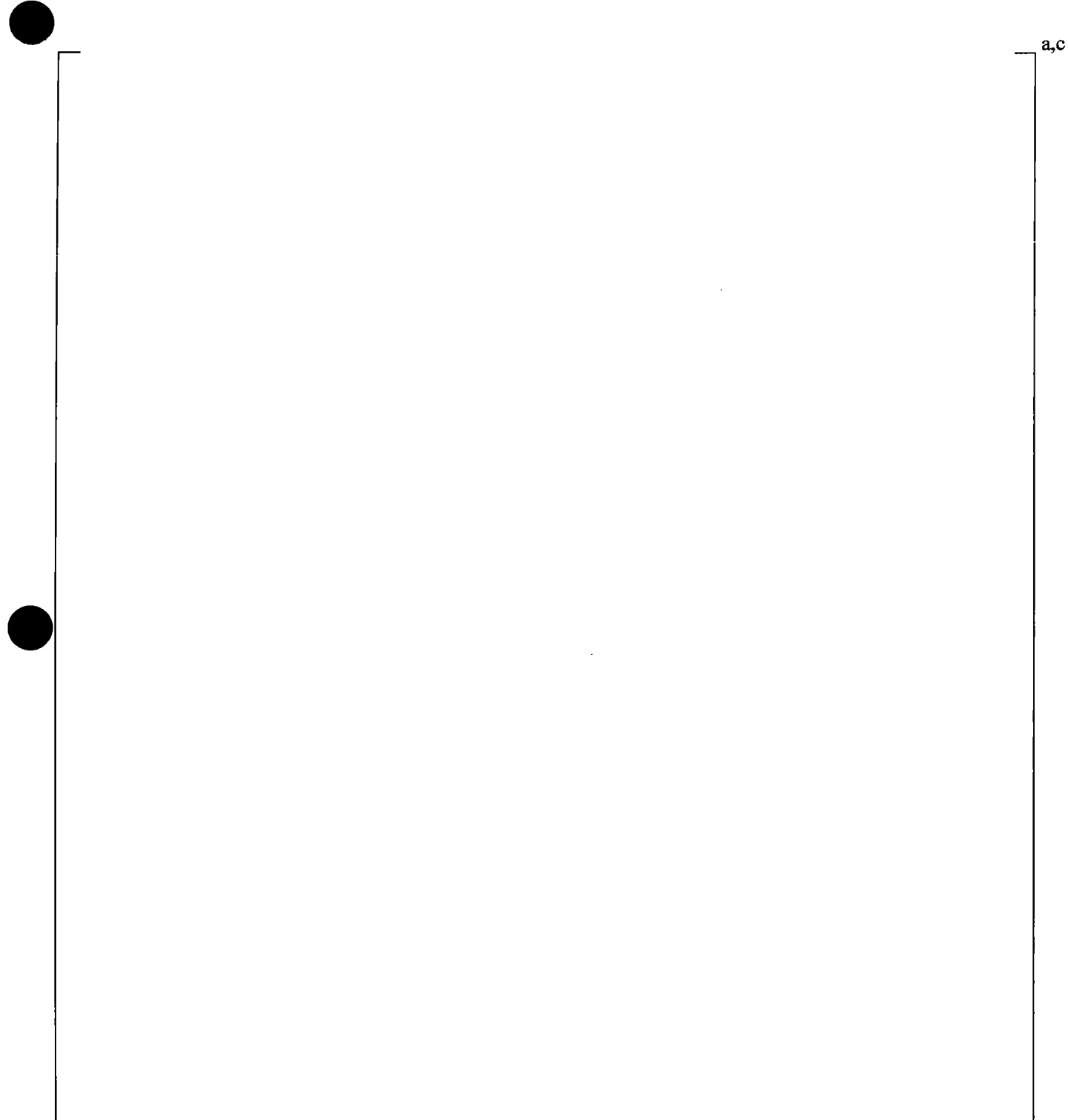


Figure 20.1-20 [

]^{a,c}

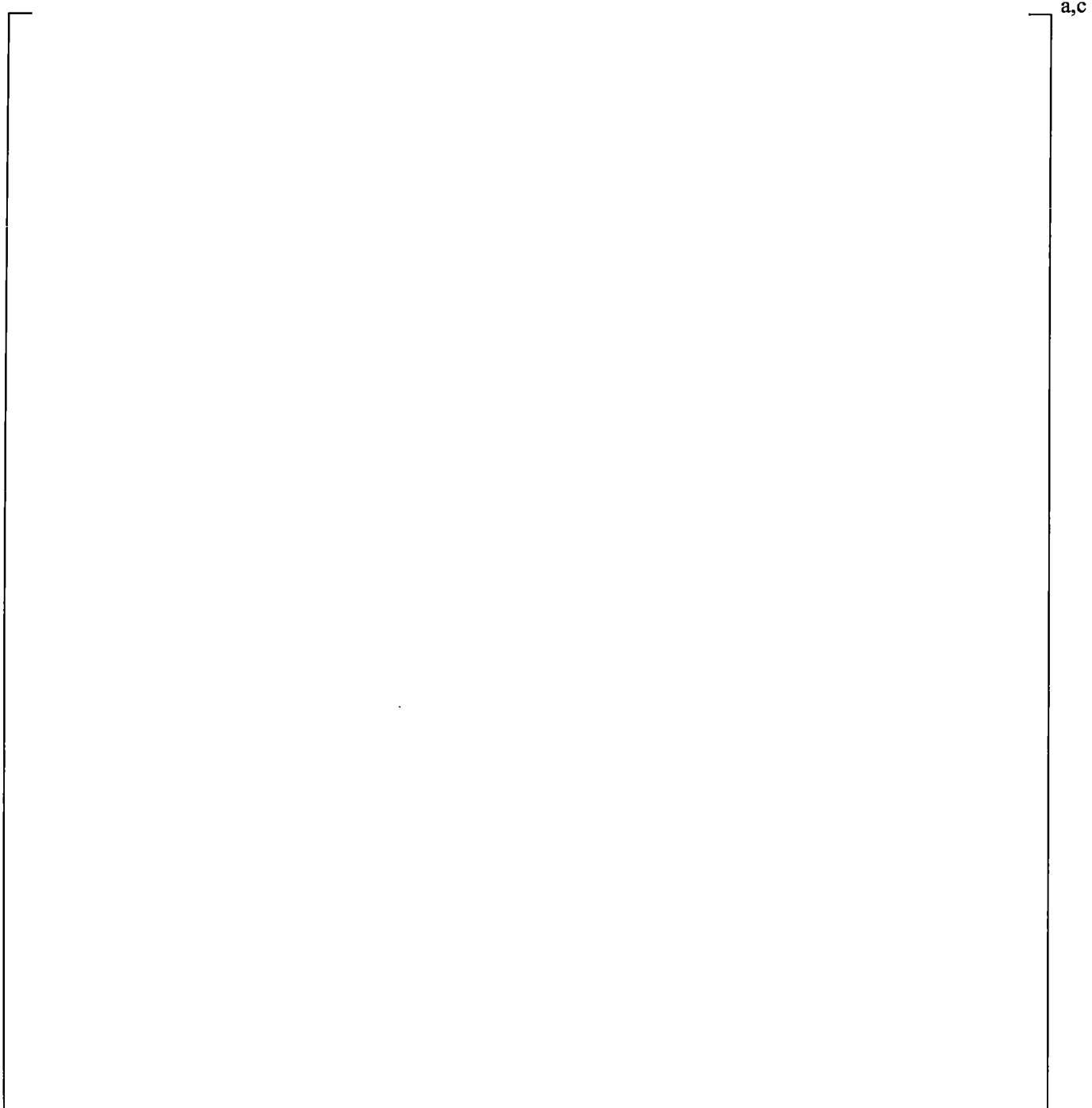


Figure 20.1-21 [

]^{a,c}

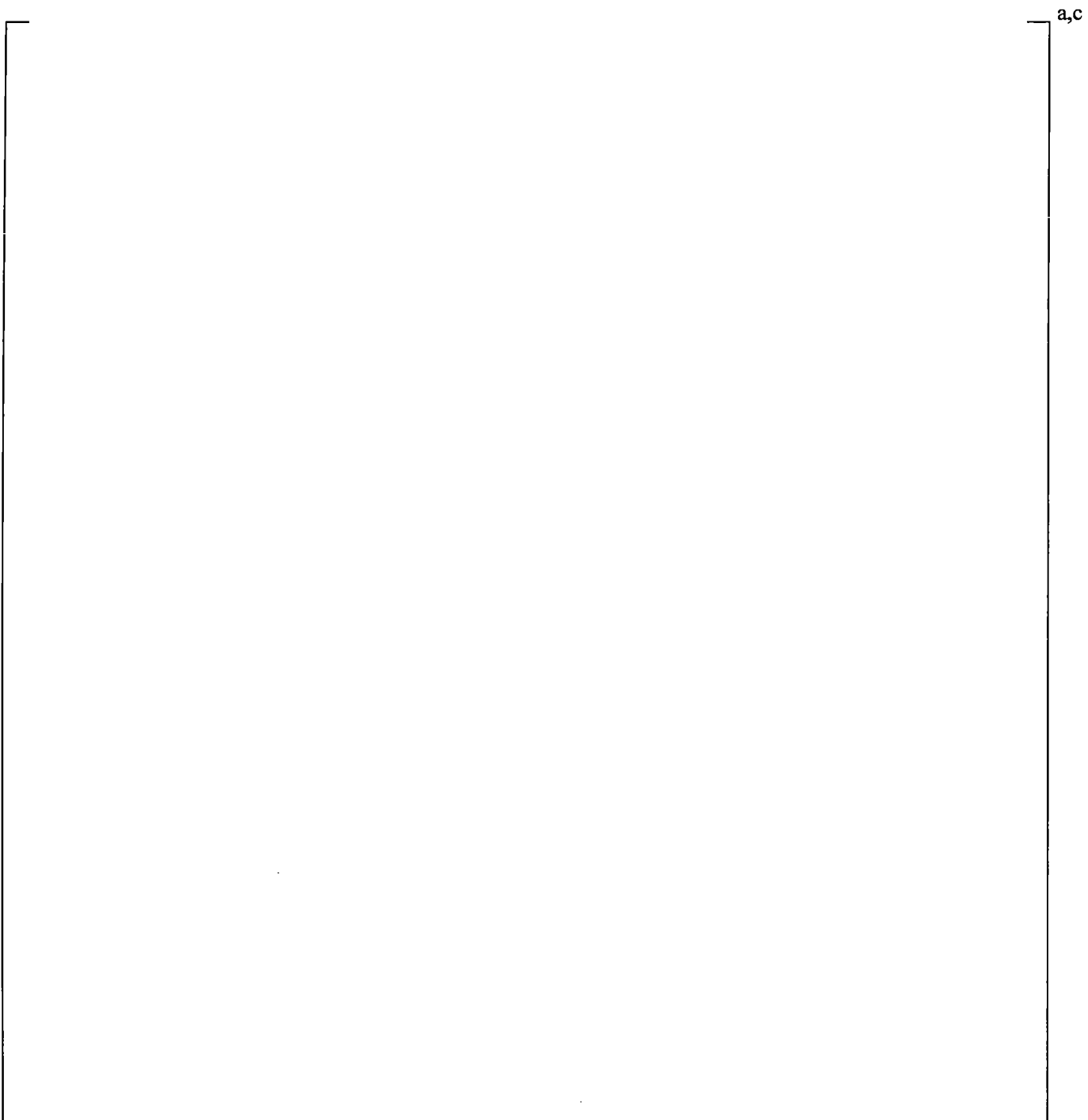


Figure 20.1-22 [

]^{a,c}

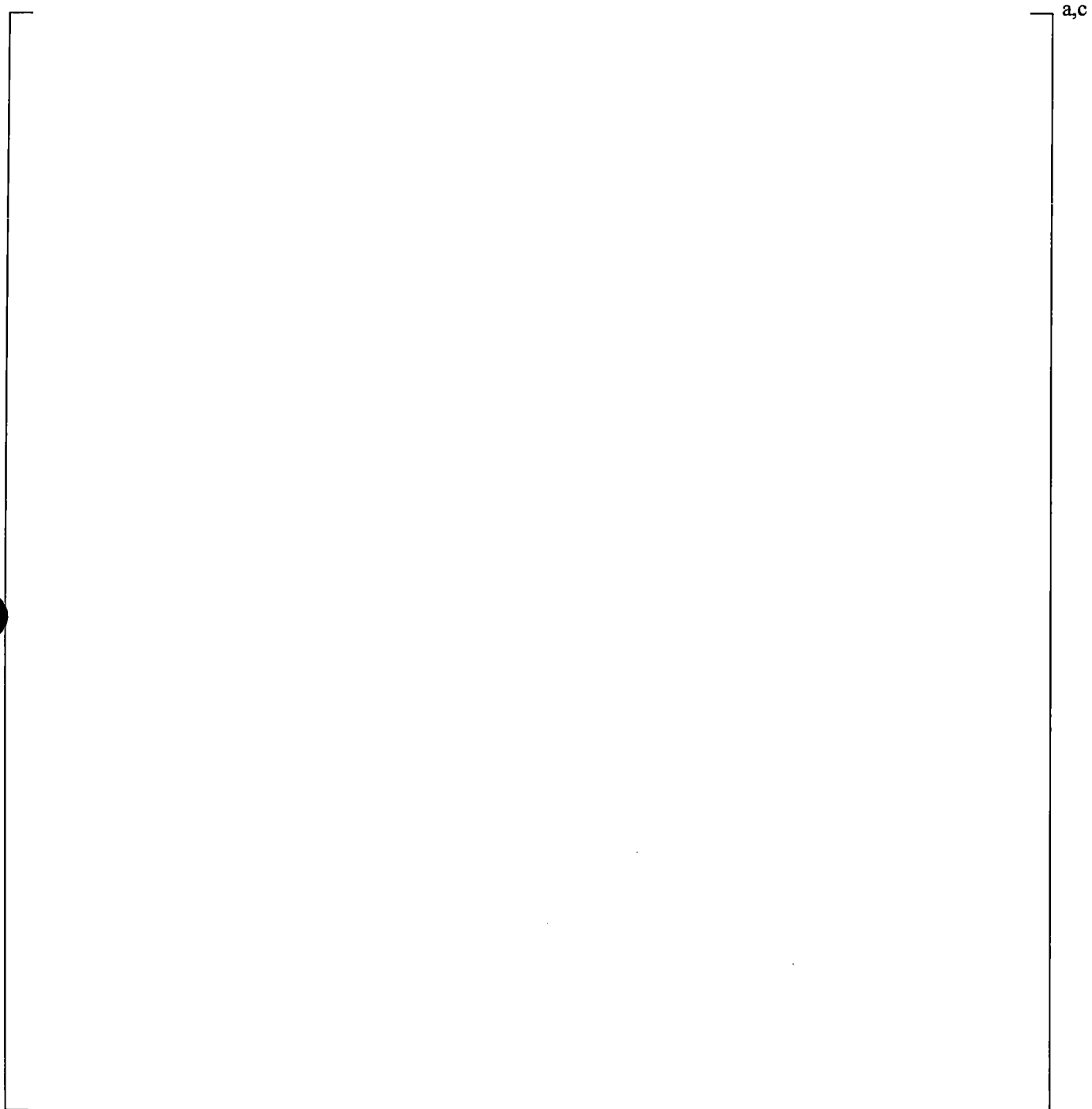


Figure 20.1-23 [

]^{a,c}

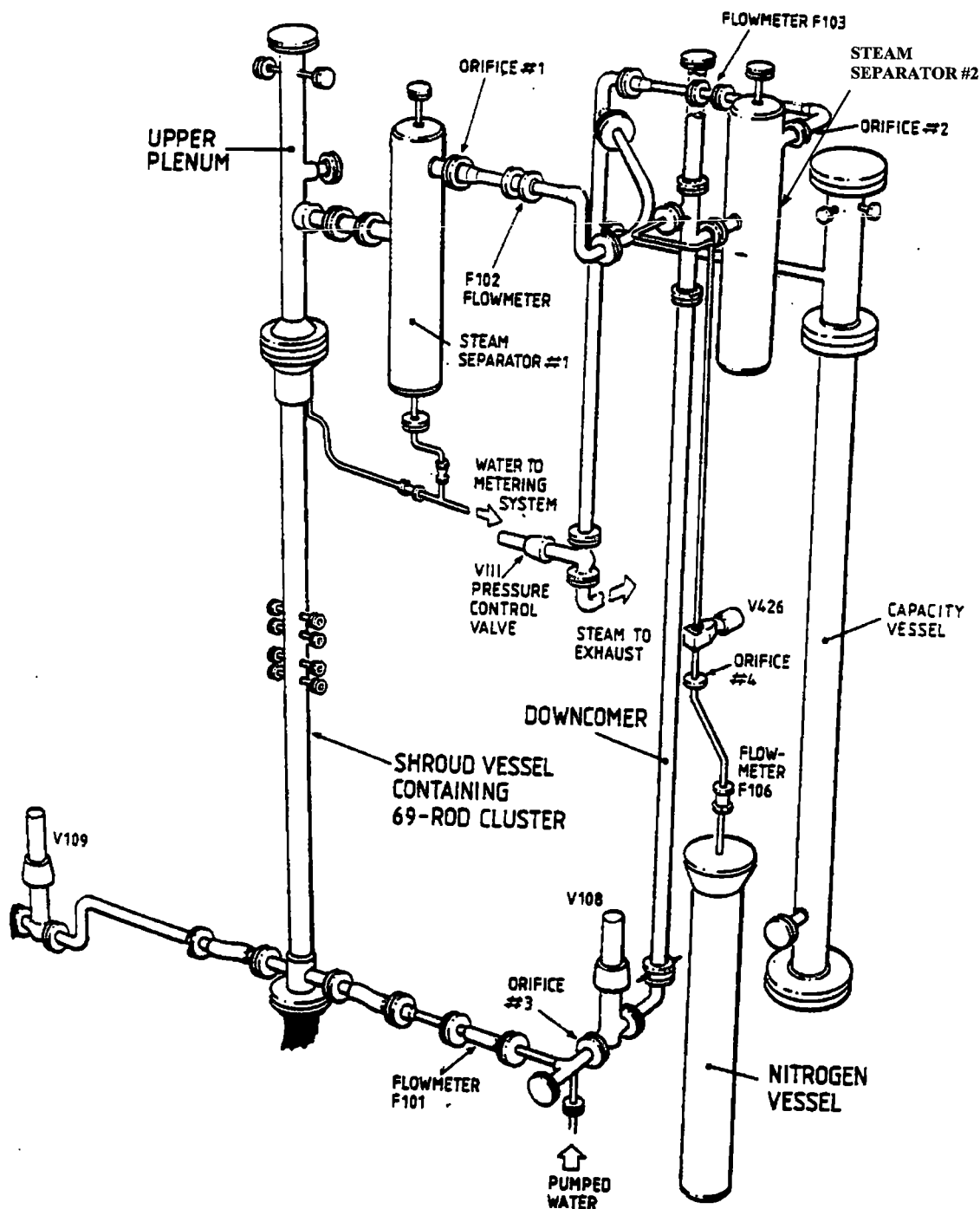


Figure 20.1-24 ACHILLES Rig Configured for Best-Estimate Transients

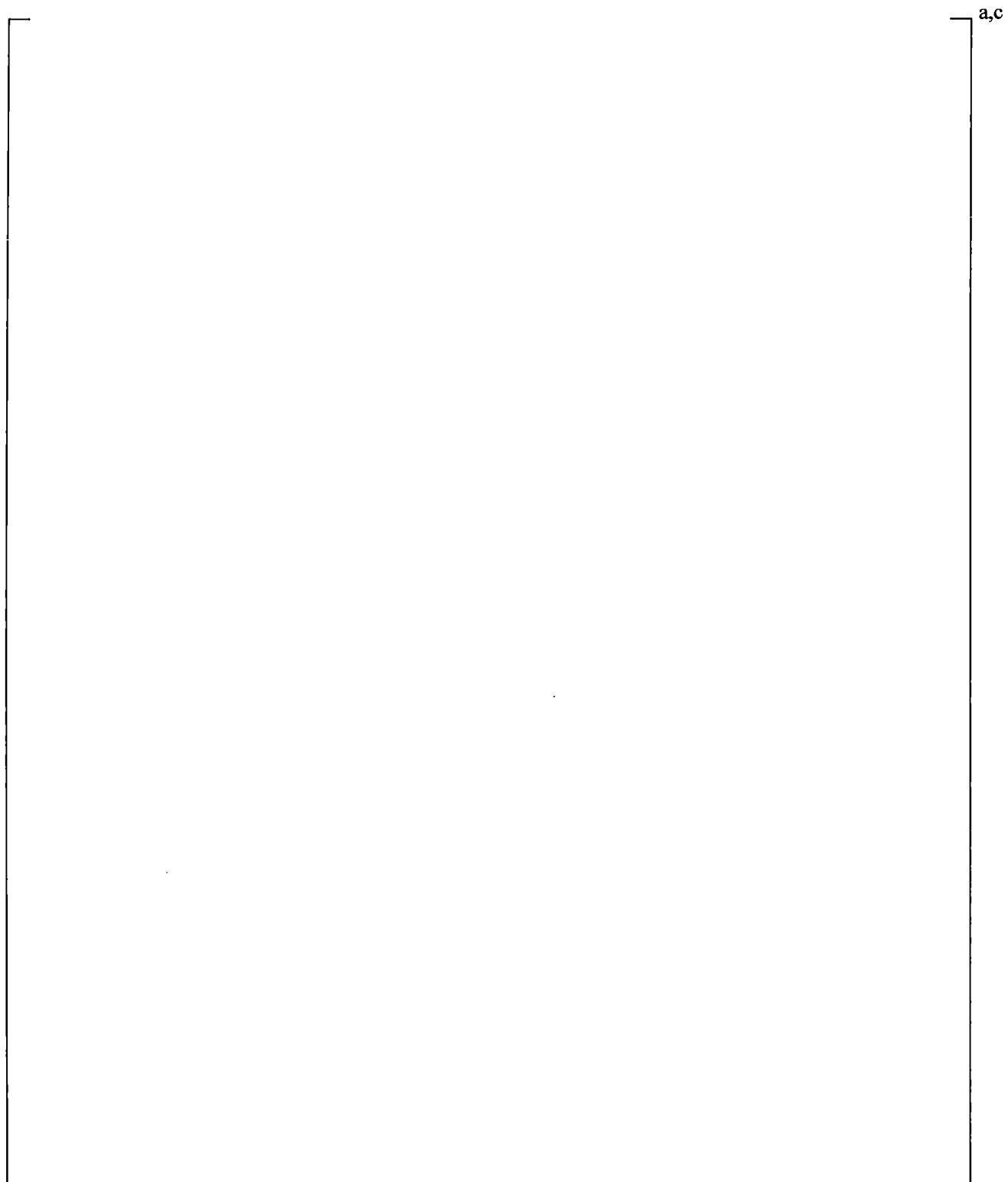


Figure 20.1-25 WCOBRA/TRAC-TF2 Model of ACHILLES Test

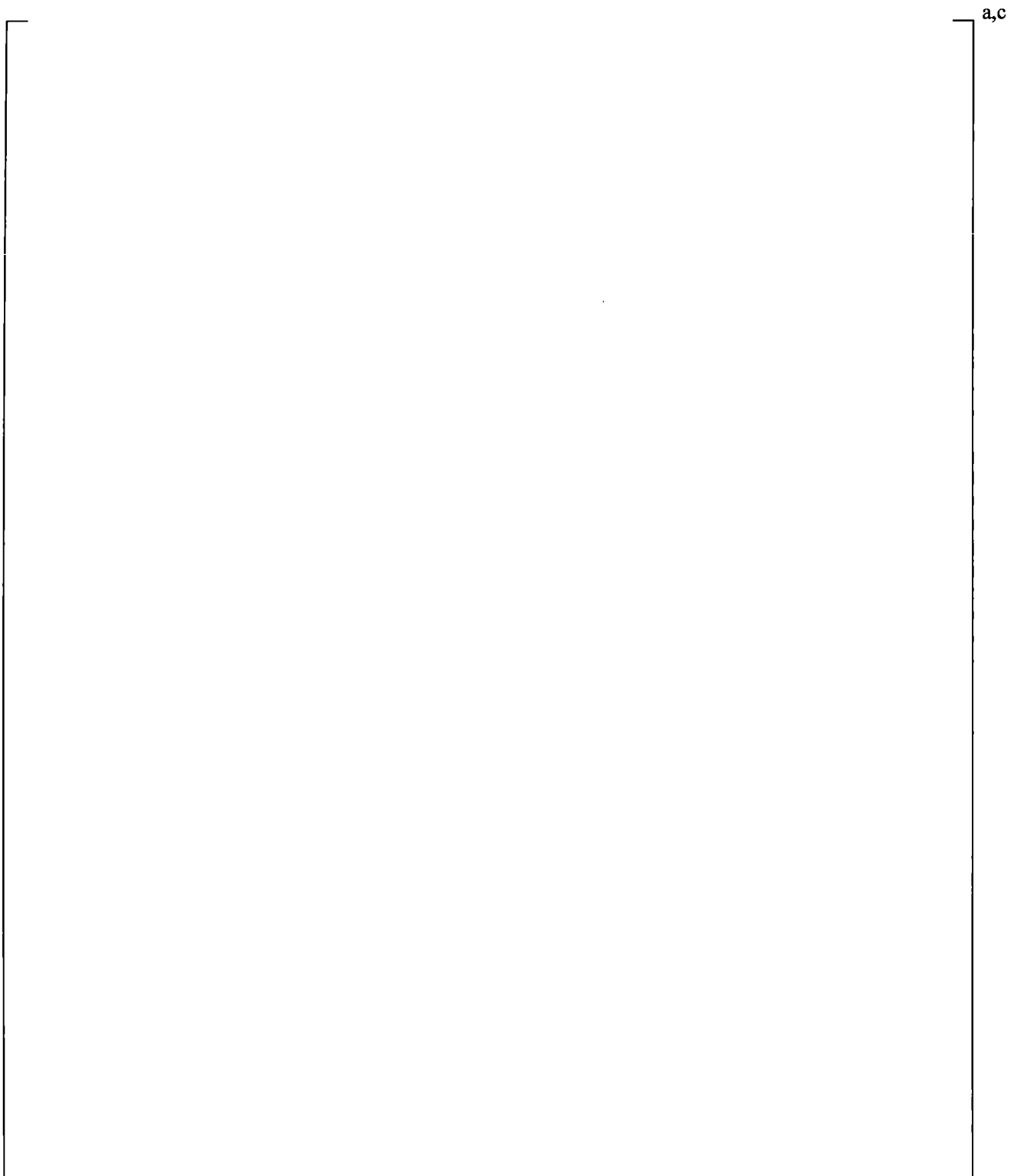


Figure 20.1-26 Cross Section of ACHILLES Cluster

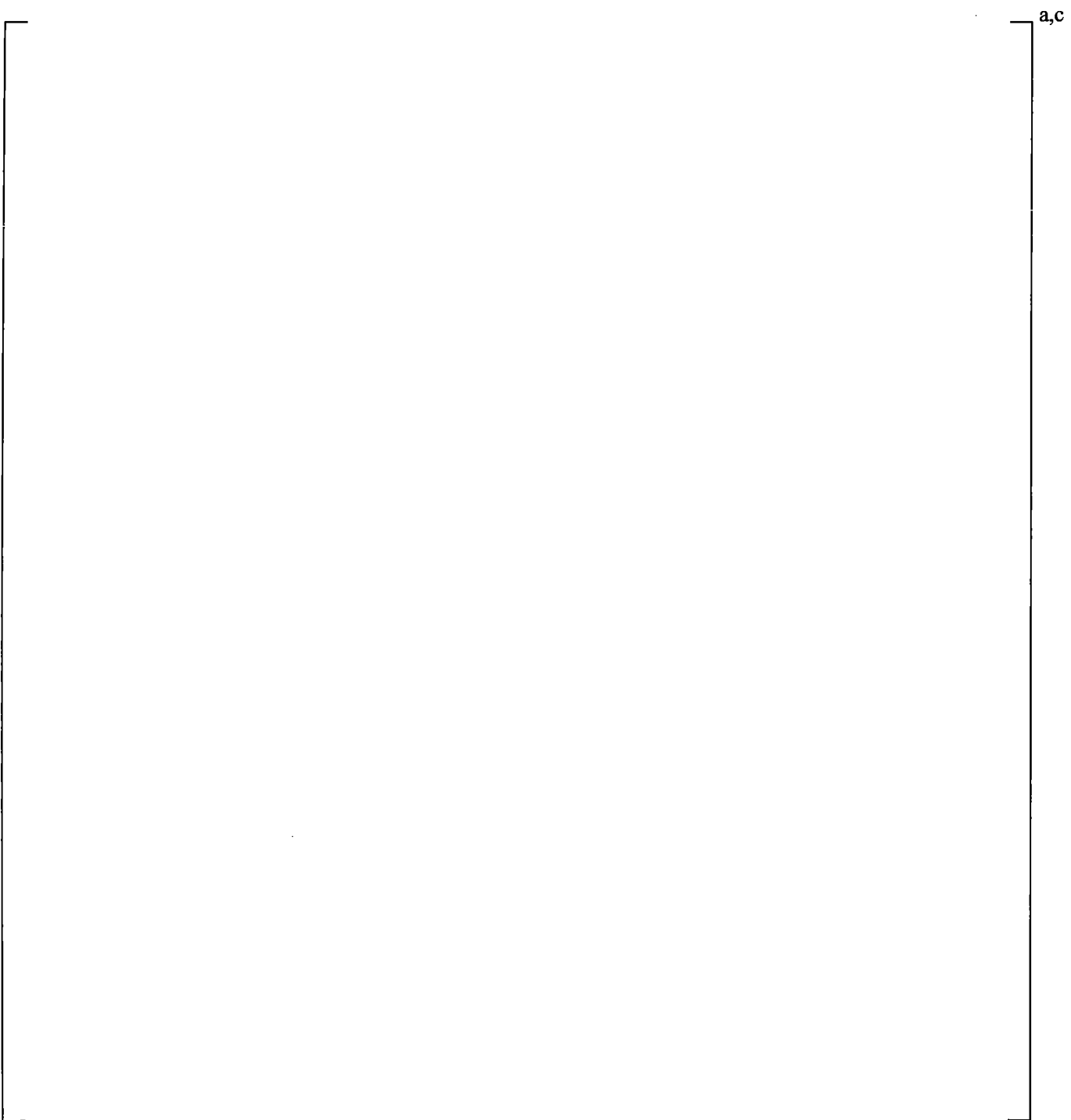


Figure 20.1-27 Measured and Predicted Accumulator Pressure

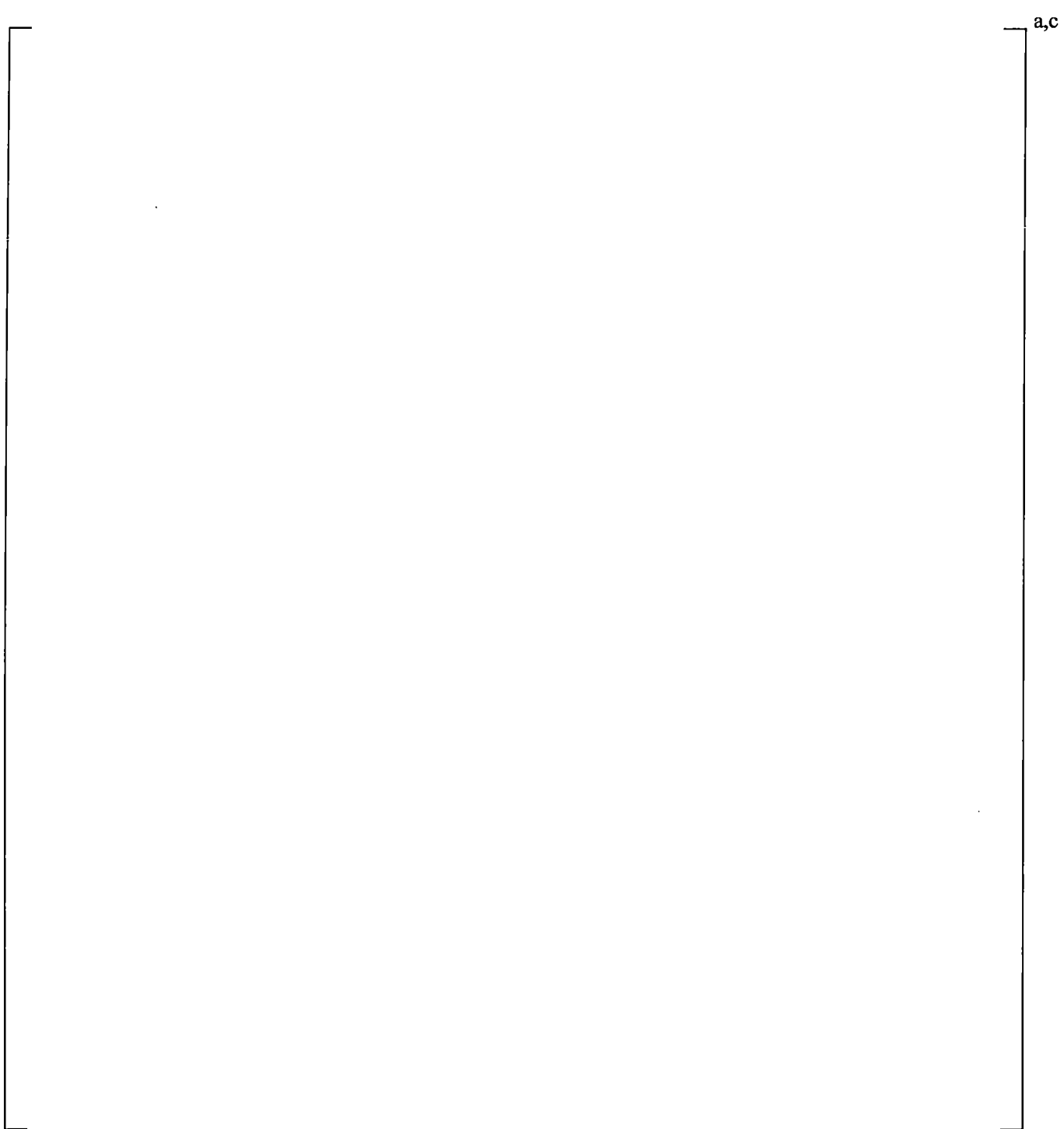


Figure 20.1-28 Measured and Predicted Accumulator Discharge Line Mass Flow Rate

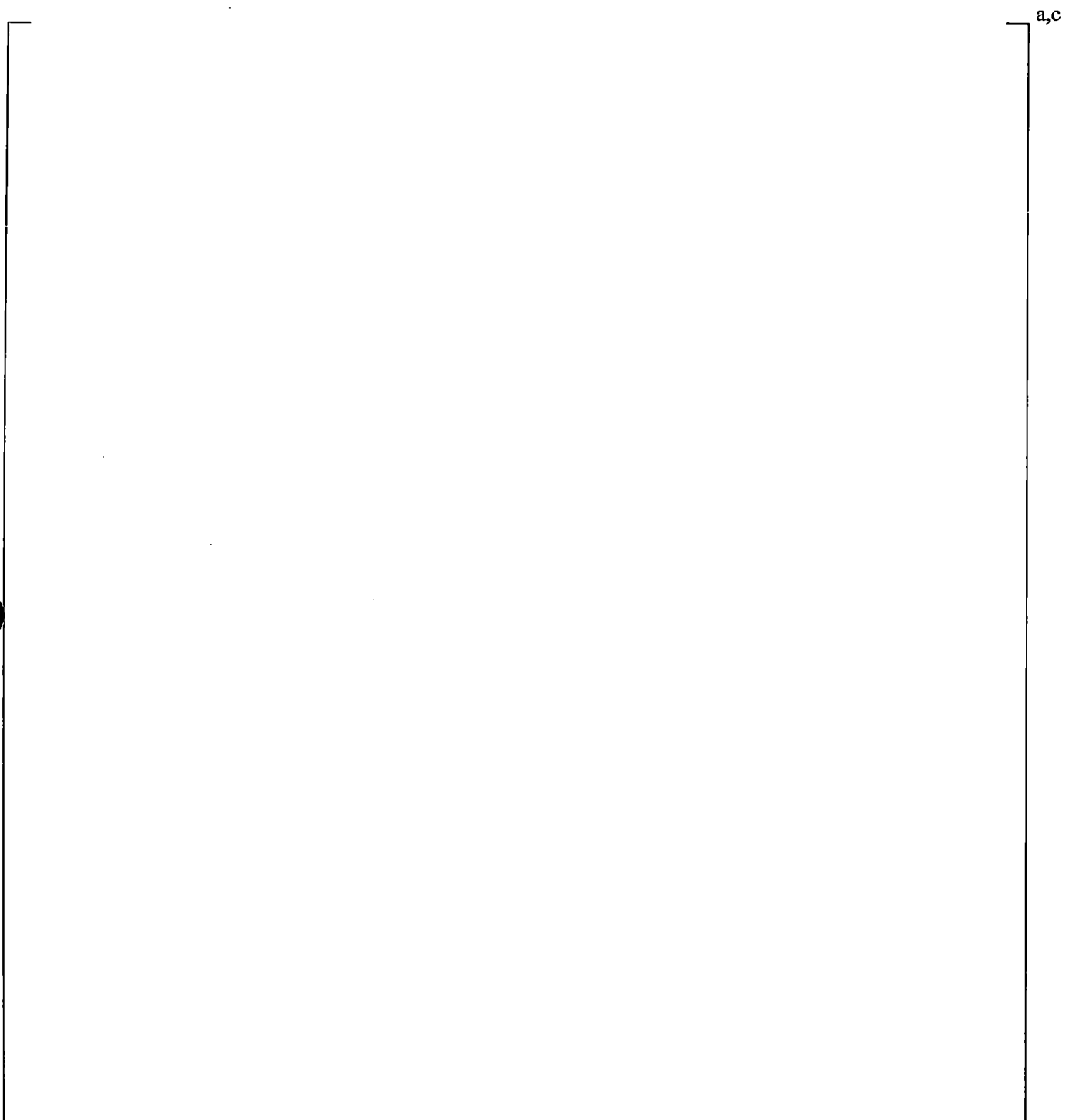


Figure 20.1-29 Measured and Predicted Pressure at Top of Downcomer

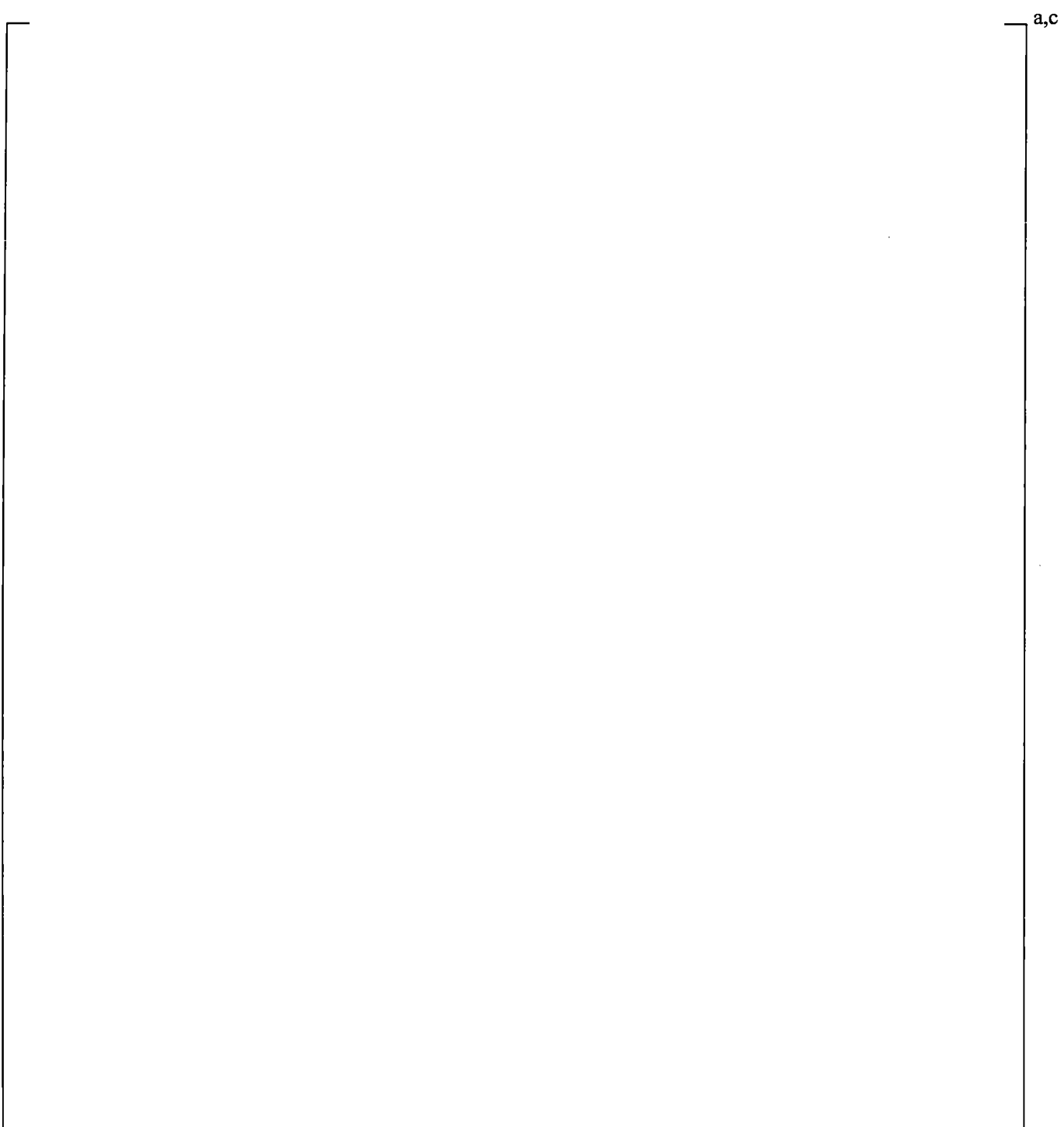


Figure 20.1-30 Measured and Predicted Pressure Loss from Top of Downcomer to Break

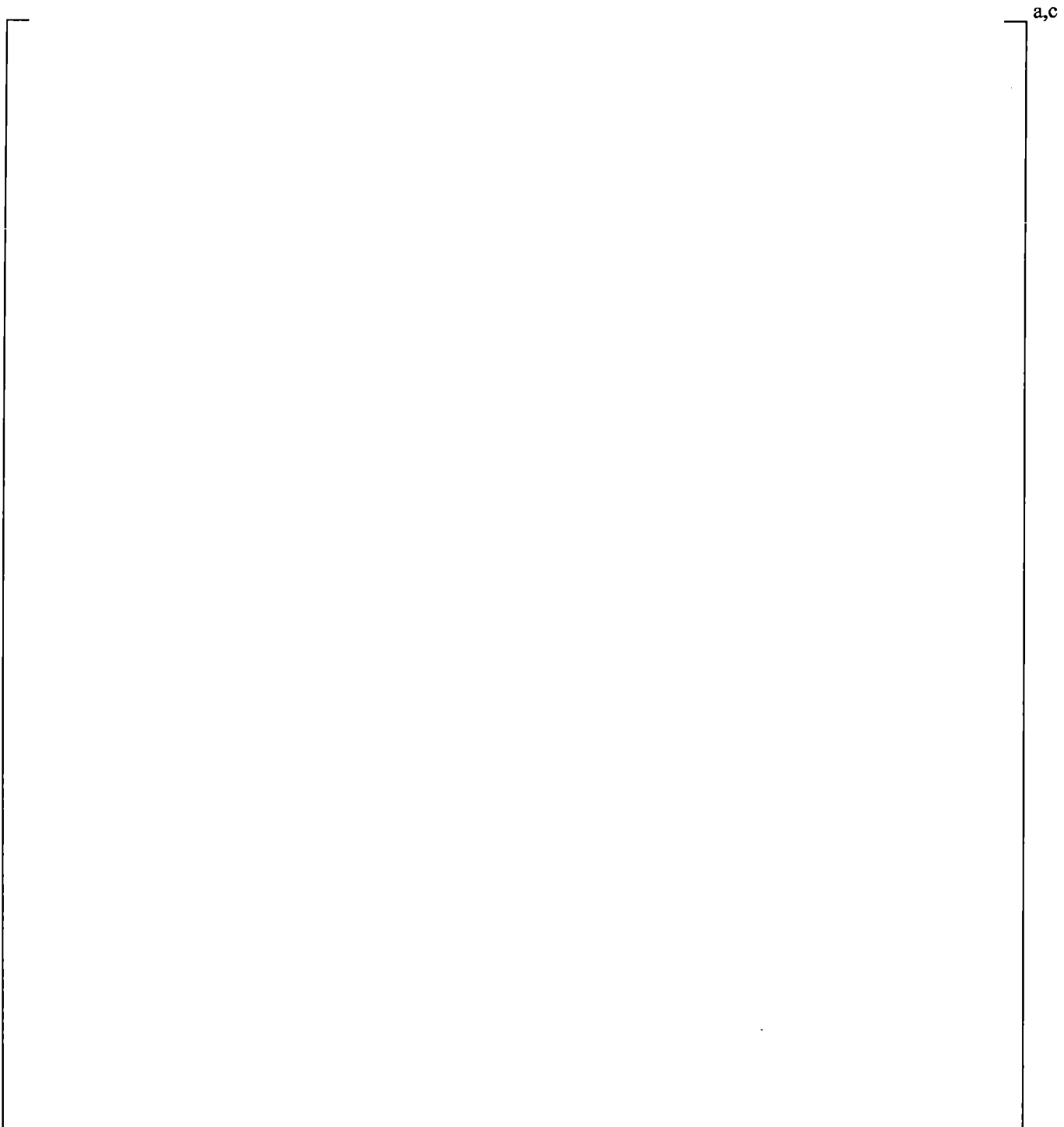


Figure 20.1-31 Measured and Predicted Gas Flow Rate from Top of Downcomer to Break

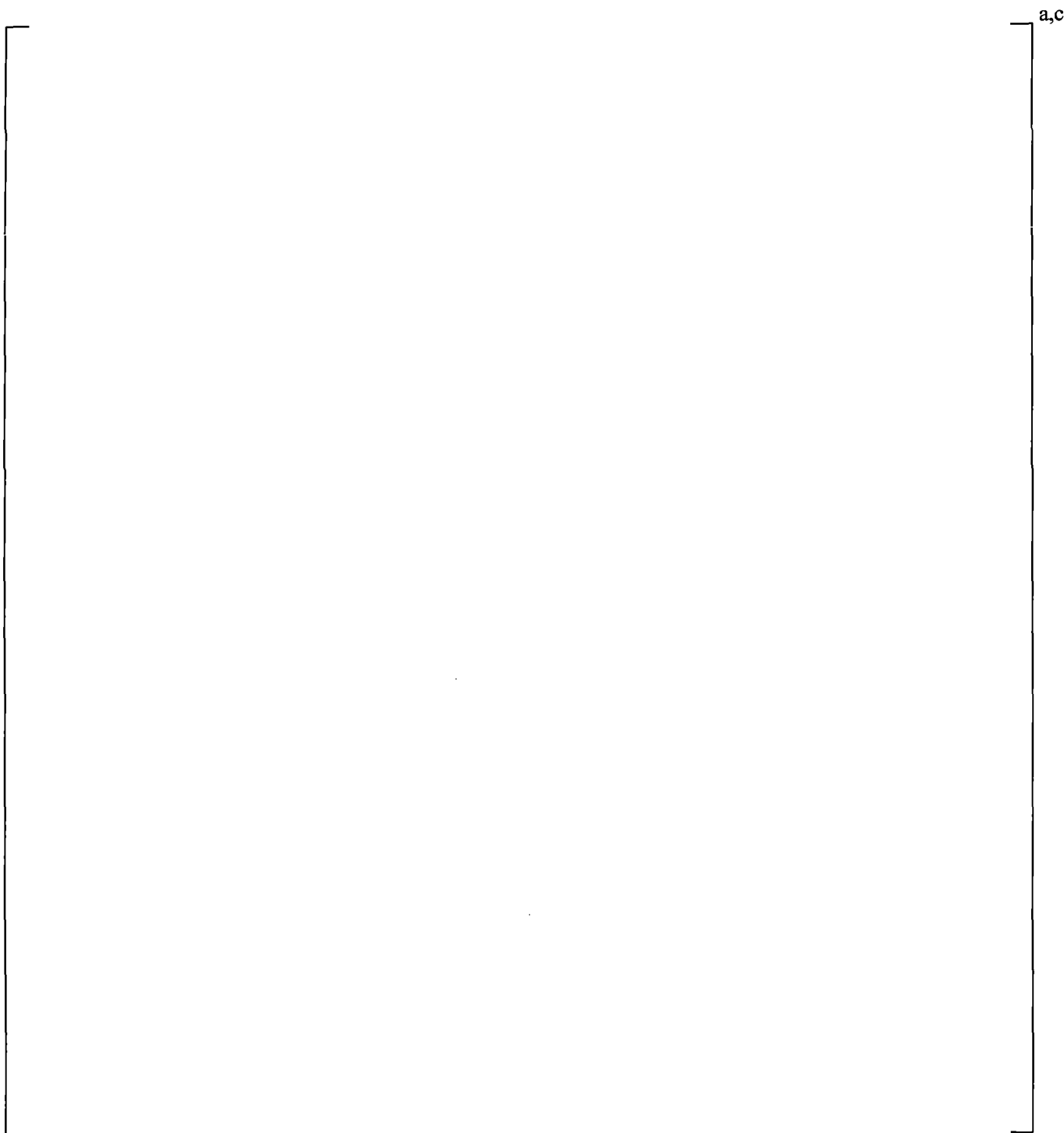


Figure 20.1-32 Measured and Predicted Downcomer Liquid Level

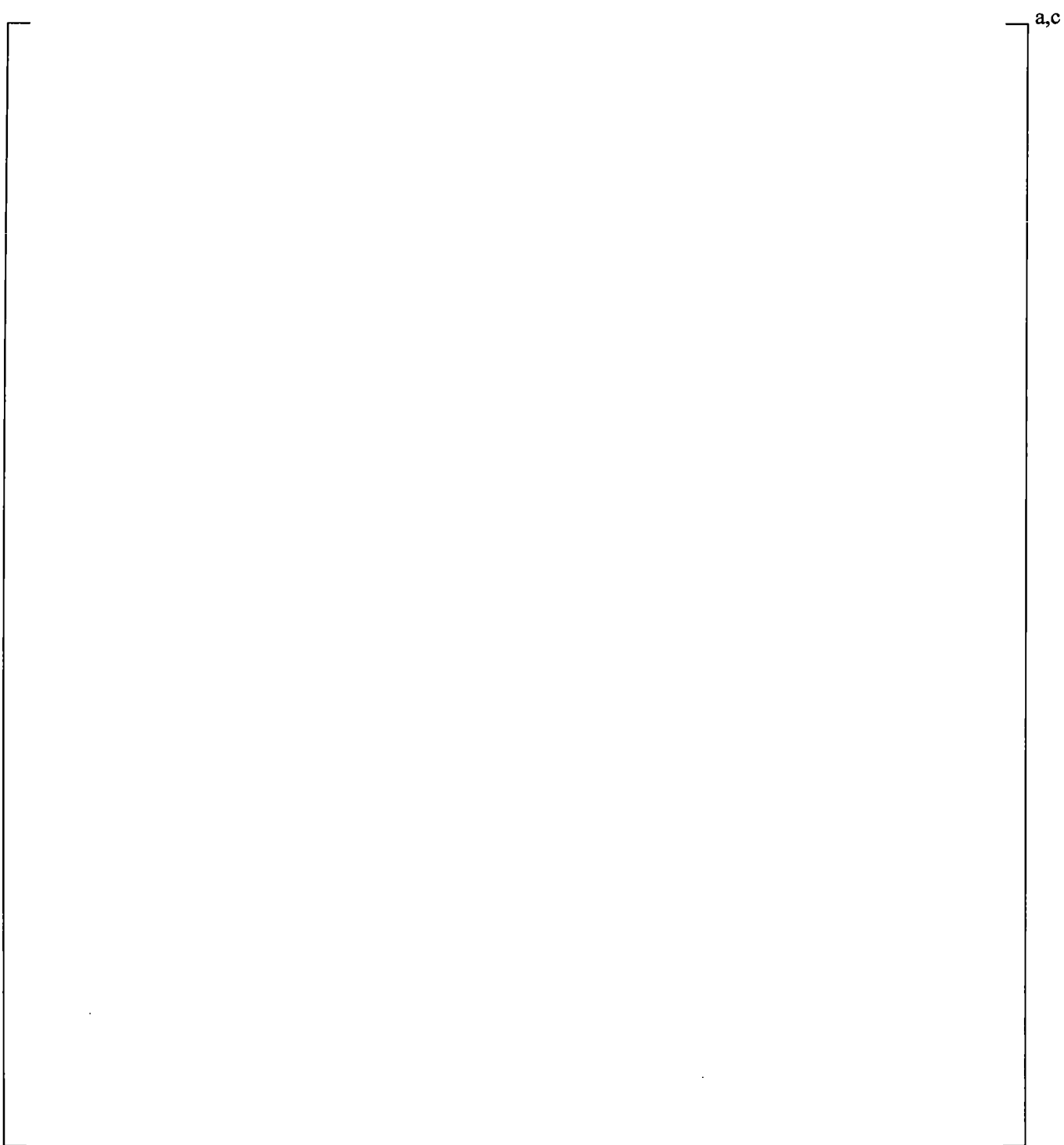


Figure 20.1-33 Measured and Predicted Test Section Liquid Level

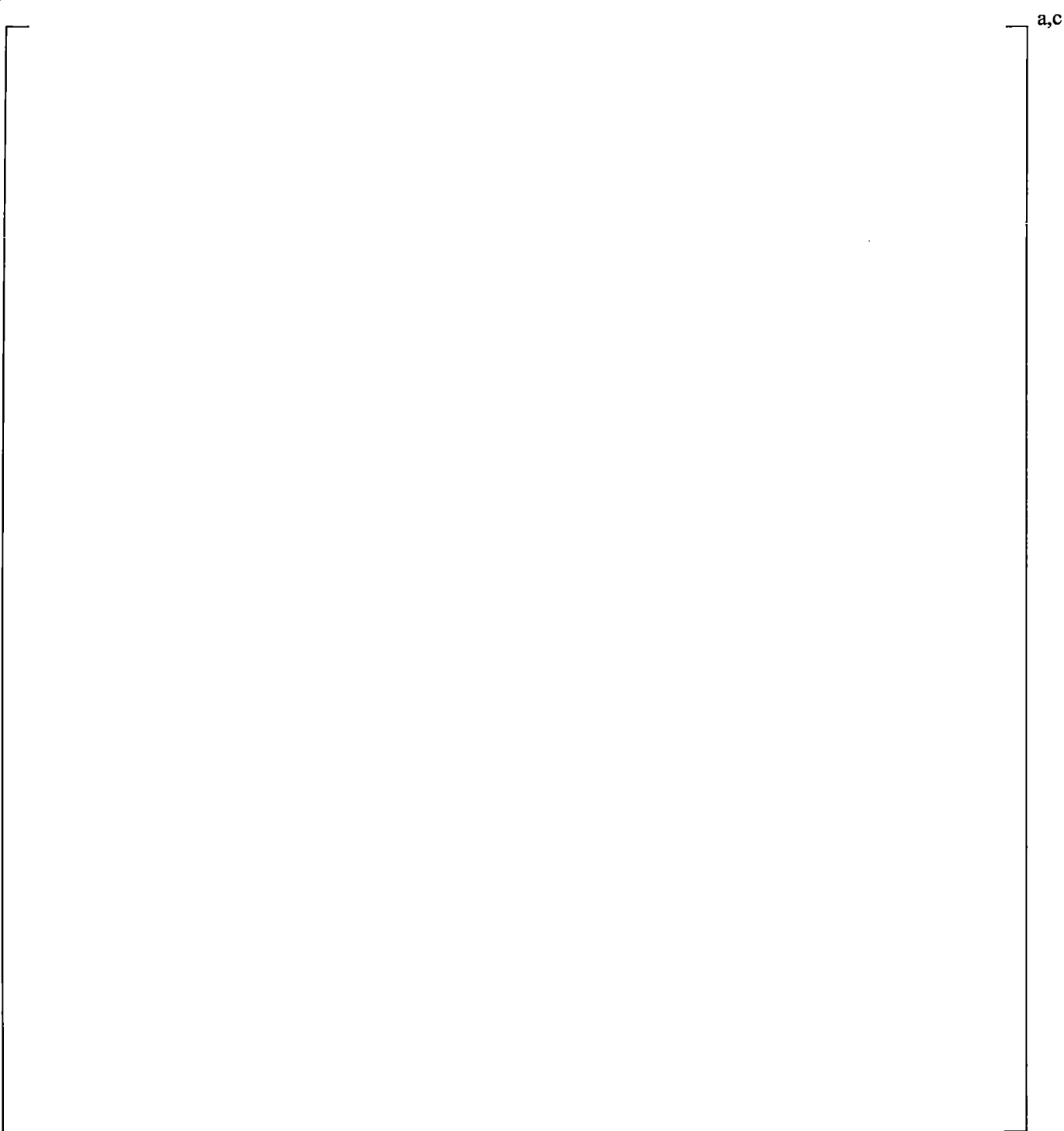


Figure 20.1-34 Measured and Predicted Cladding Temperature at 1.08m (3.54 ft)

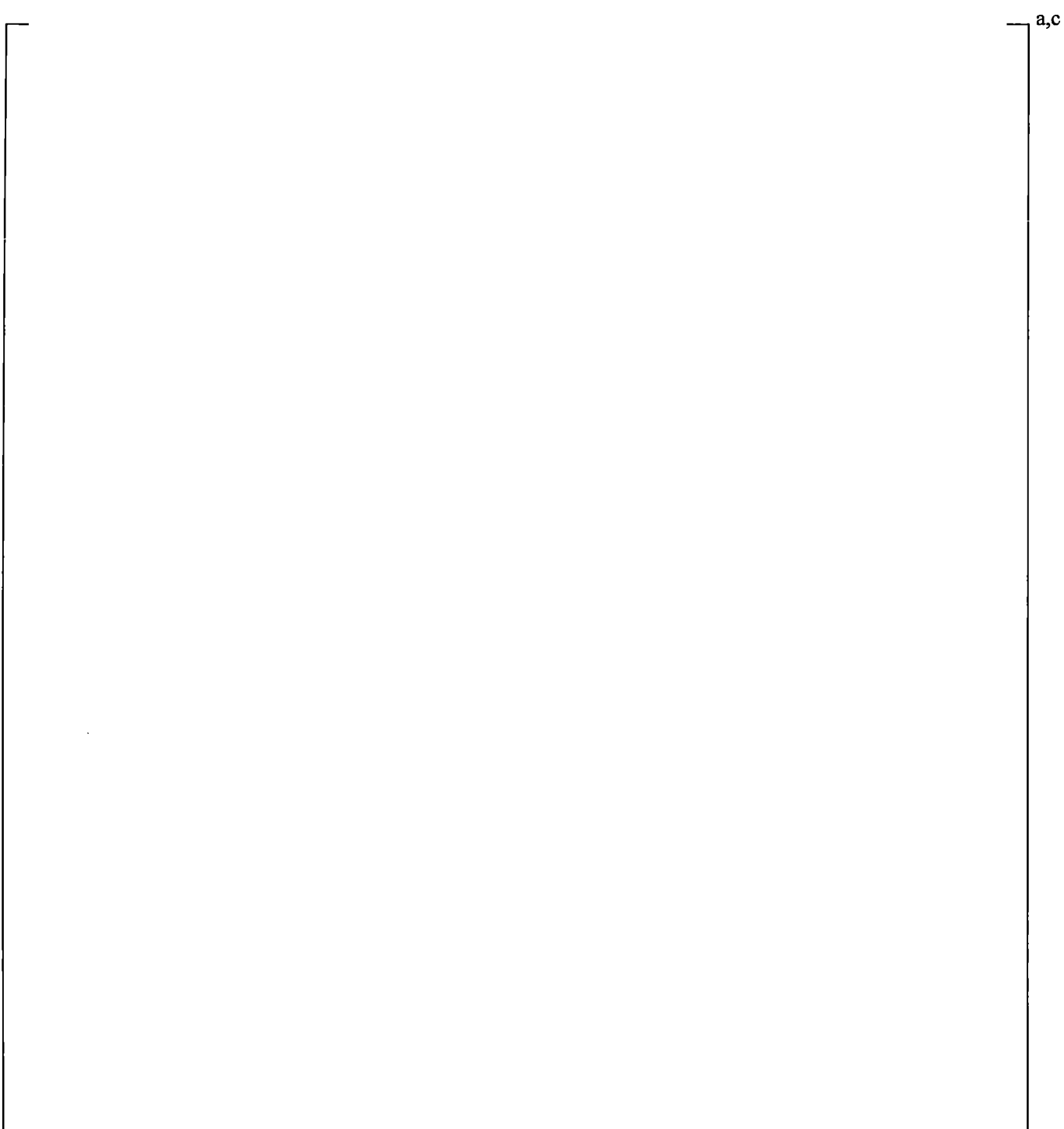


Figure 20.1-35 Measured and Predicted Cladding Temperature at 2.01m (6.59 ft)

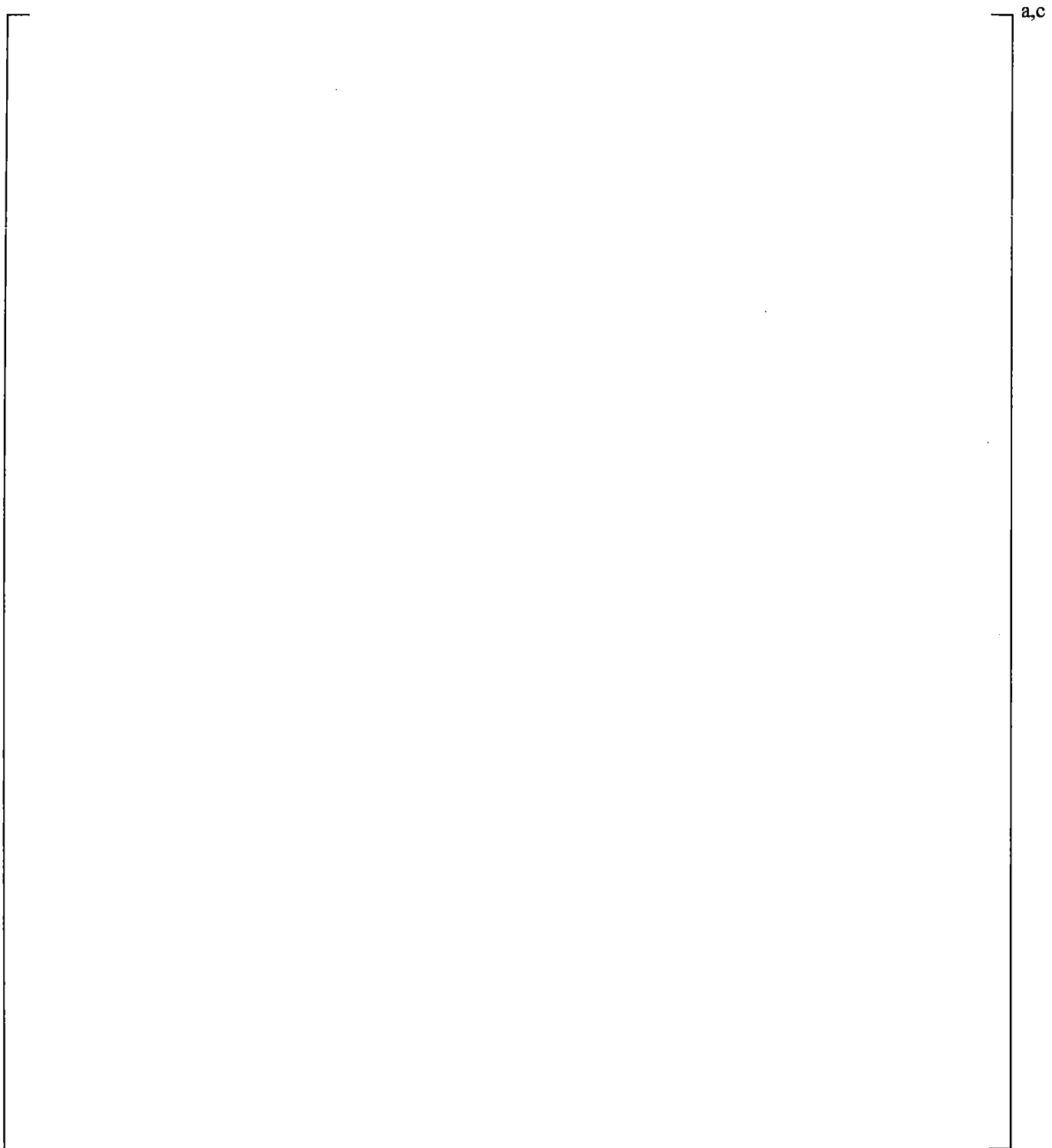
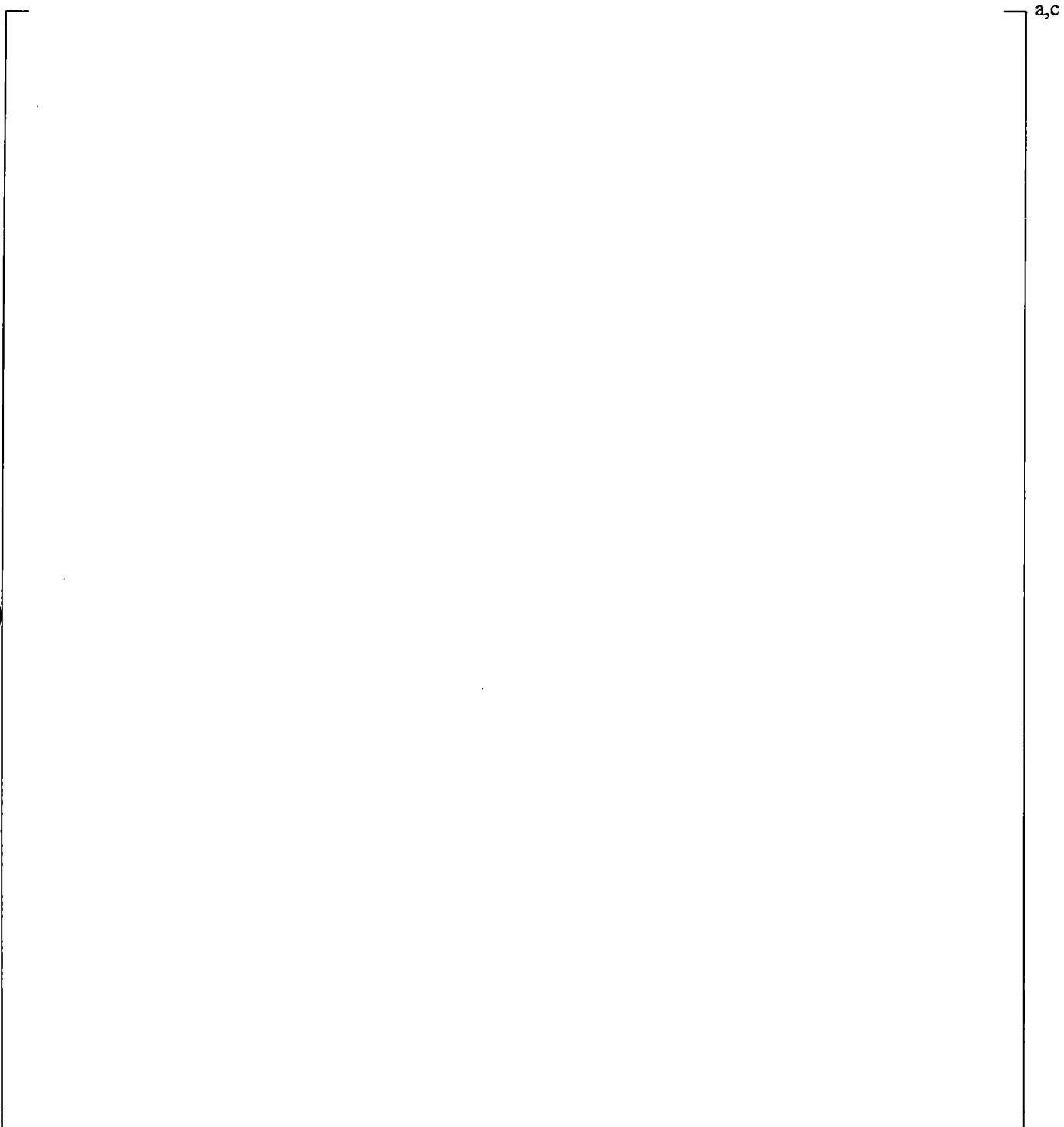
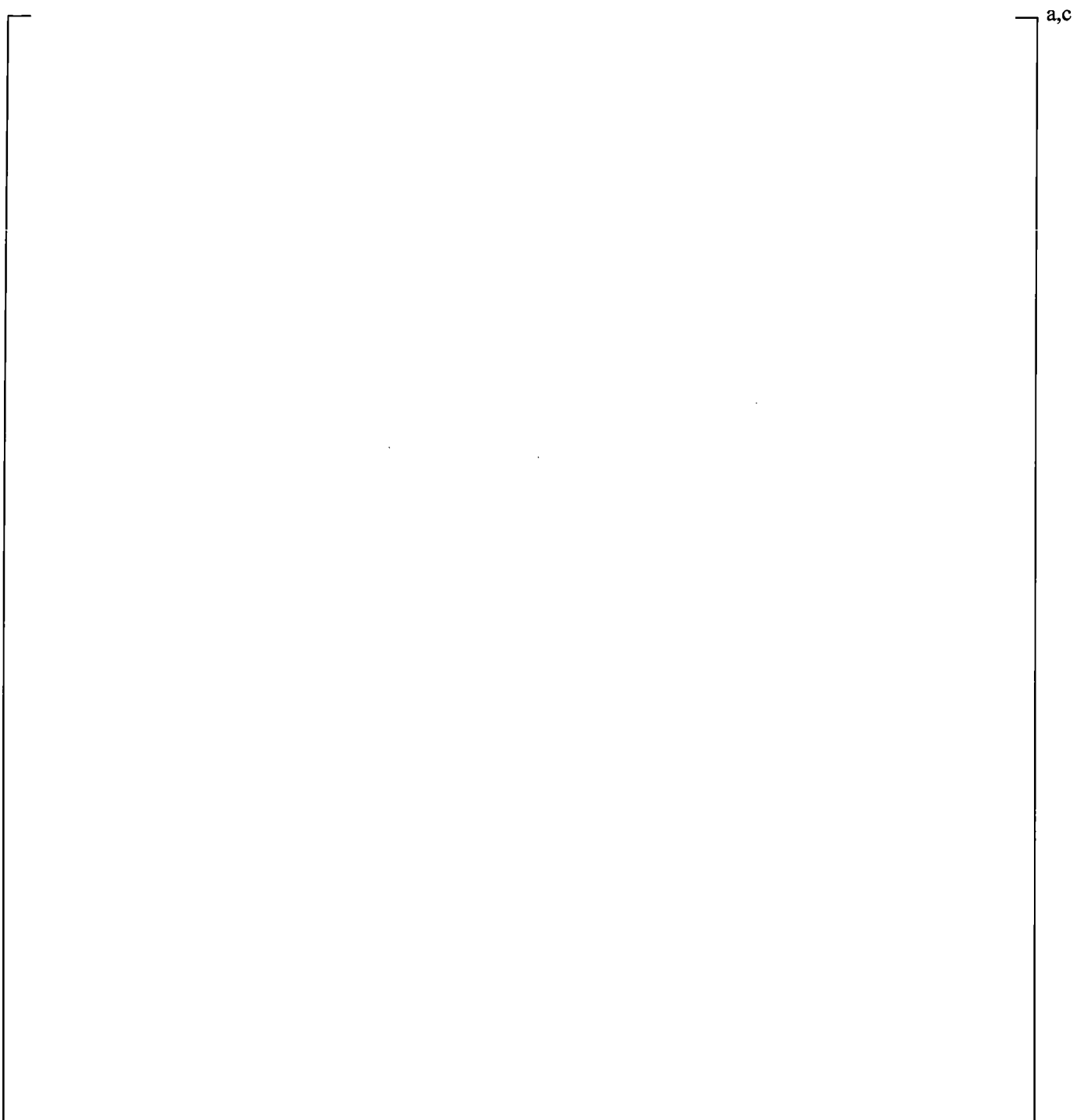


Figure 20.1-36 Measured and Predicted Cladding Temperature at 2.65m (8.69 ft)



**Figure 20.1-37 Measured and Predicted Accumulator Pressure
(Broken Pipe Pressure Loss Sensitivity Study)**



**Figure 20.1-38 Measured and Predicted Accumulator Discharge Line
Mass Flow Rate (Broken Pipe Pressure Loss Sensitivity Study)**

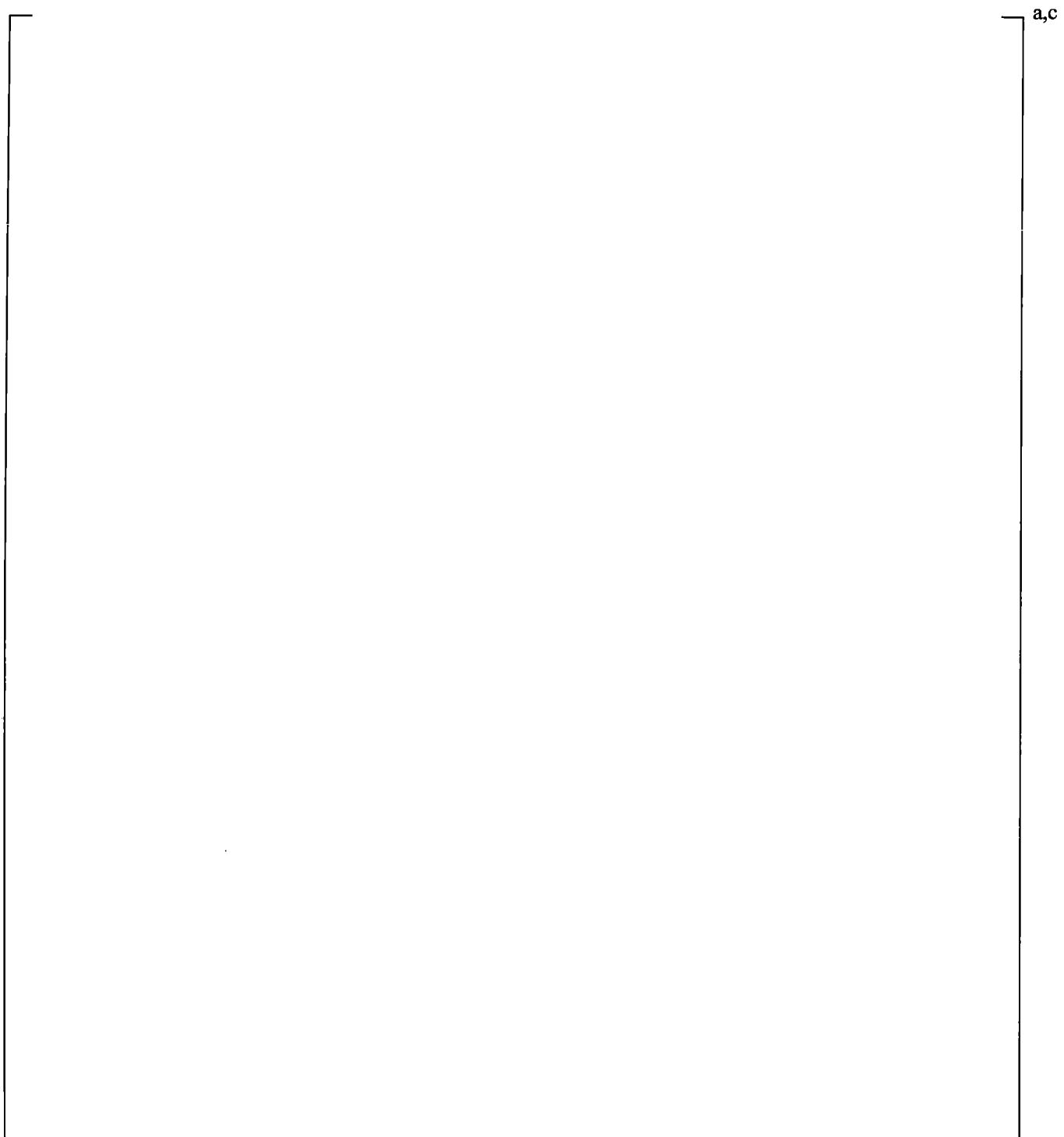


**Figure 20.1-39 Measured and Predicted Pressure at Top of Downcomer
(Broken Pipe Pressure Loss Sensitivity Study)**

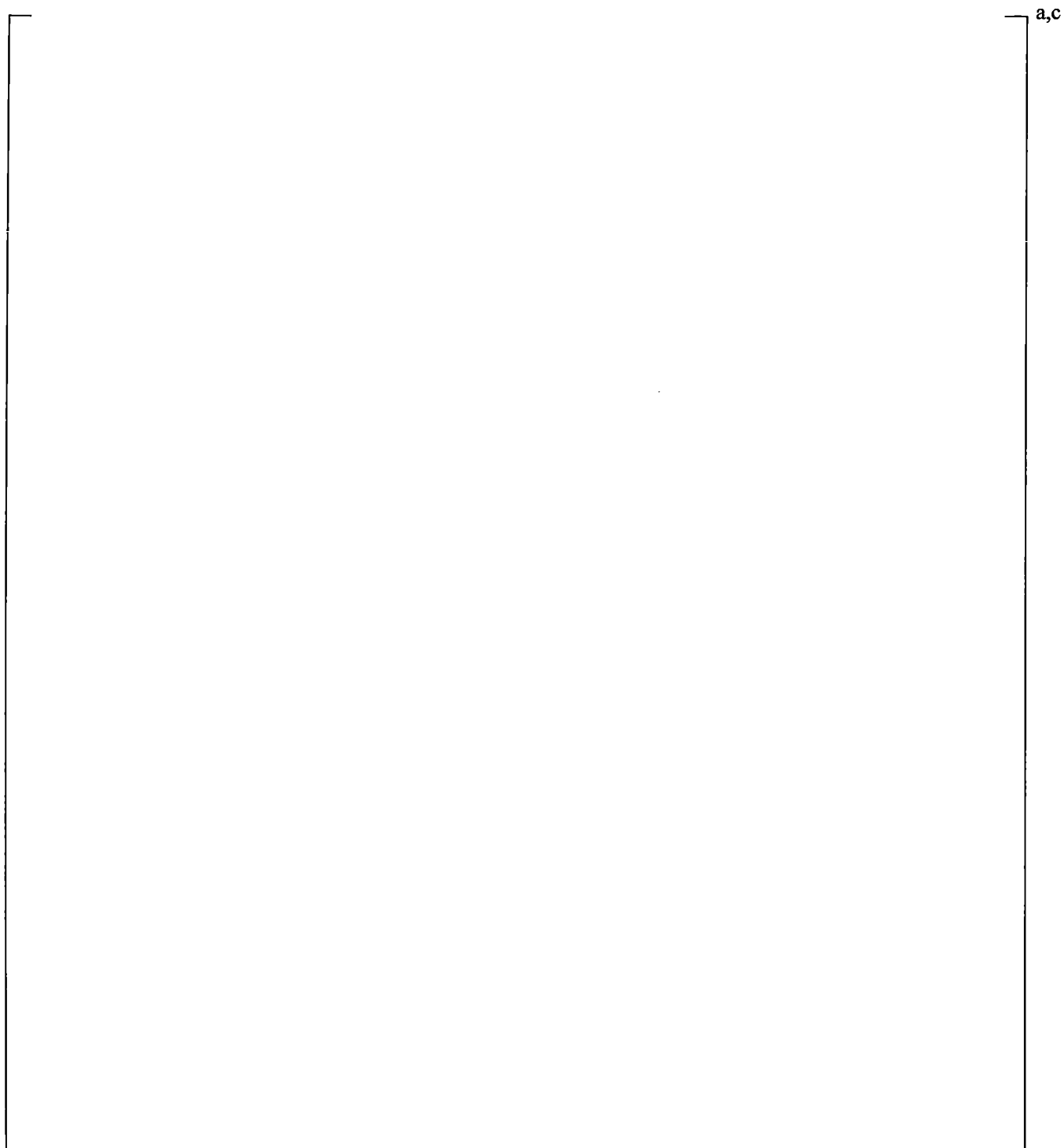


**Figure 20.1-40 Measured and Predicted Downcomer Liquid Level
(Broken Pipe Pressure Loss Sensitivity Study)**

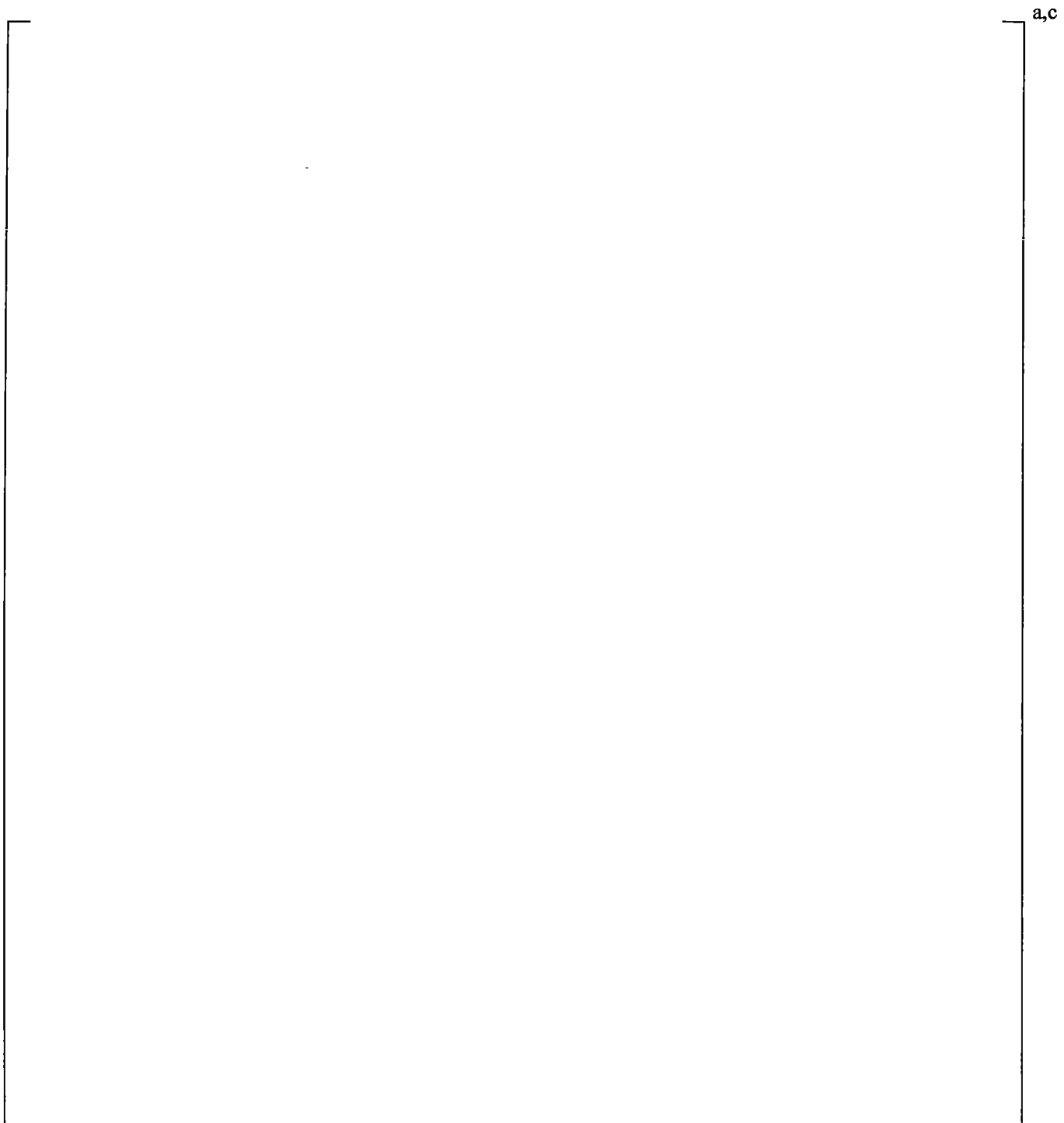


**Figure 20.1-41 Measured and Predicted Test Section Liquid Level
(Broken Pipe Pressure Loss Sensitivity Study)**

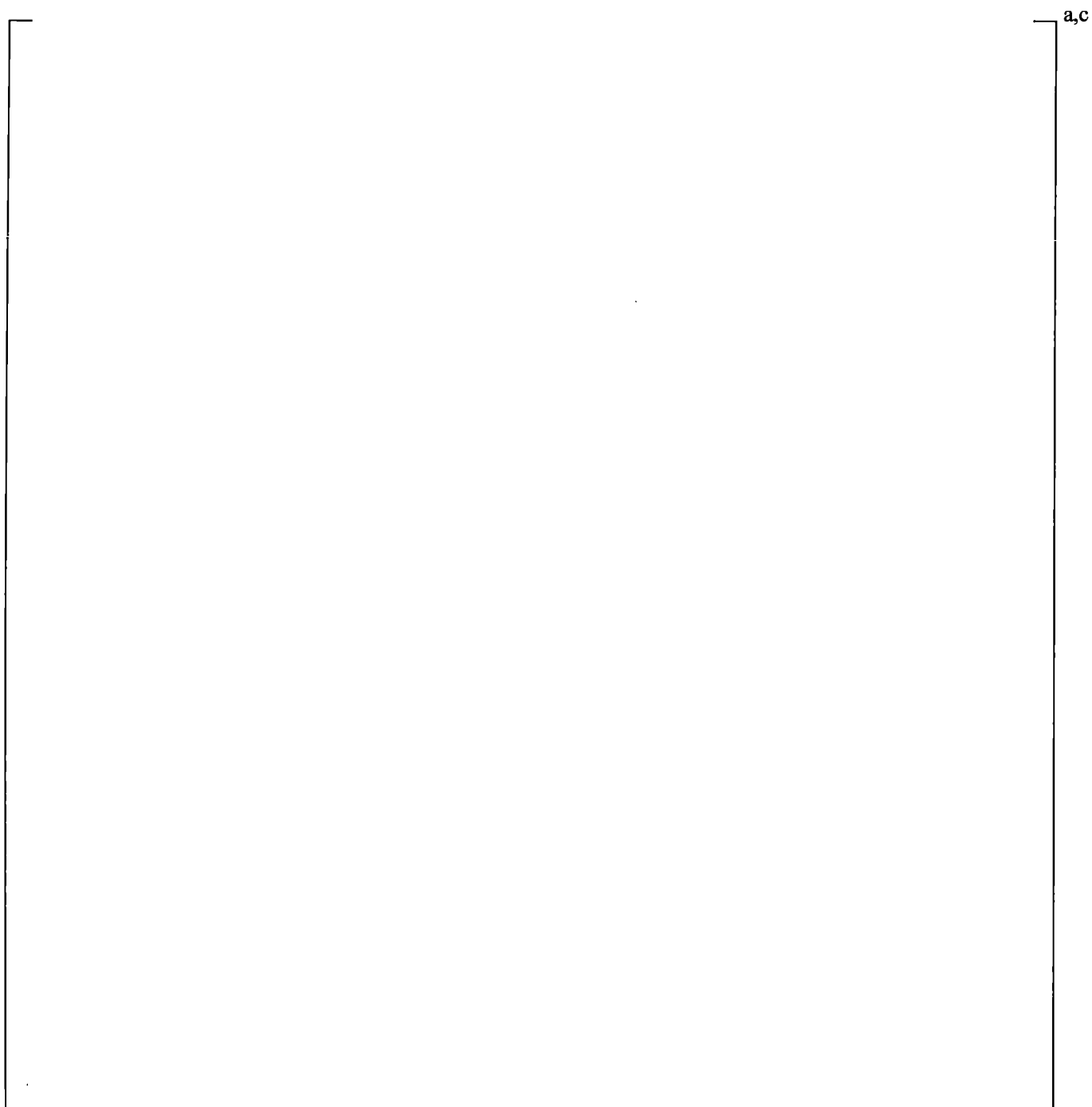


**Figure 20.1-42 Measured and Predicted Cladding Temperature at 1.08m (3.54 ft)
(Broken Pipe Pressure Loss Sensitivity Study)**

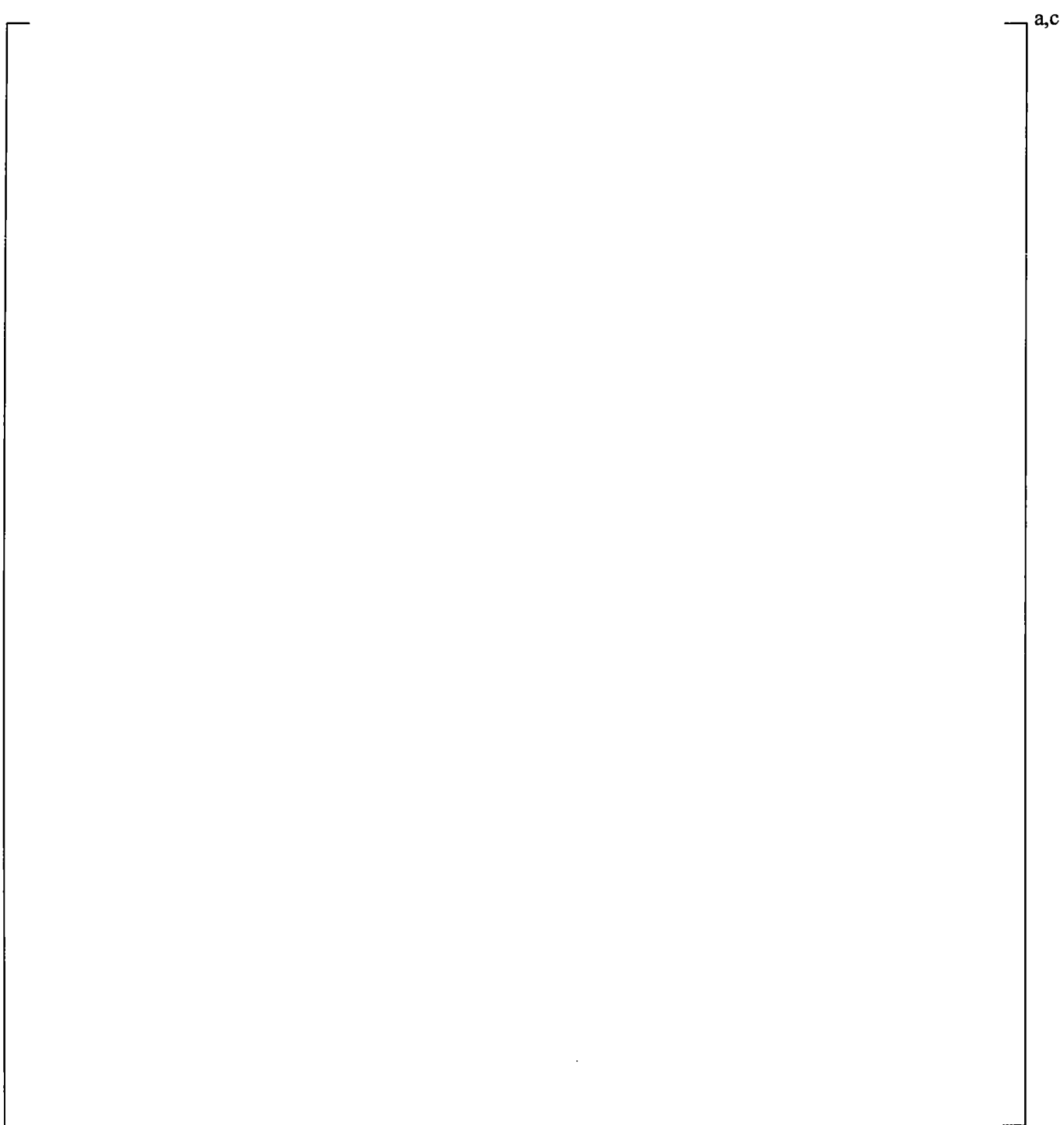


**Figure 20.1-43 Measured and Predicted Cladding Temperature at 2.01m (6.59 ft)
(Broken Pipe Pressure Loss Sensitivity Study)**

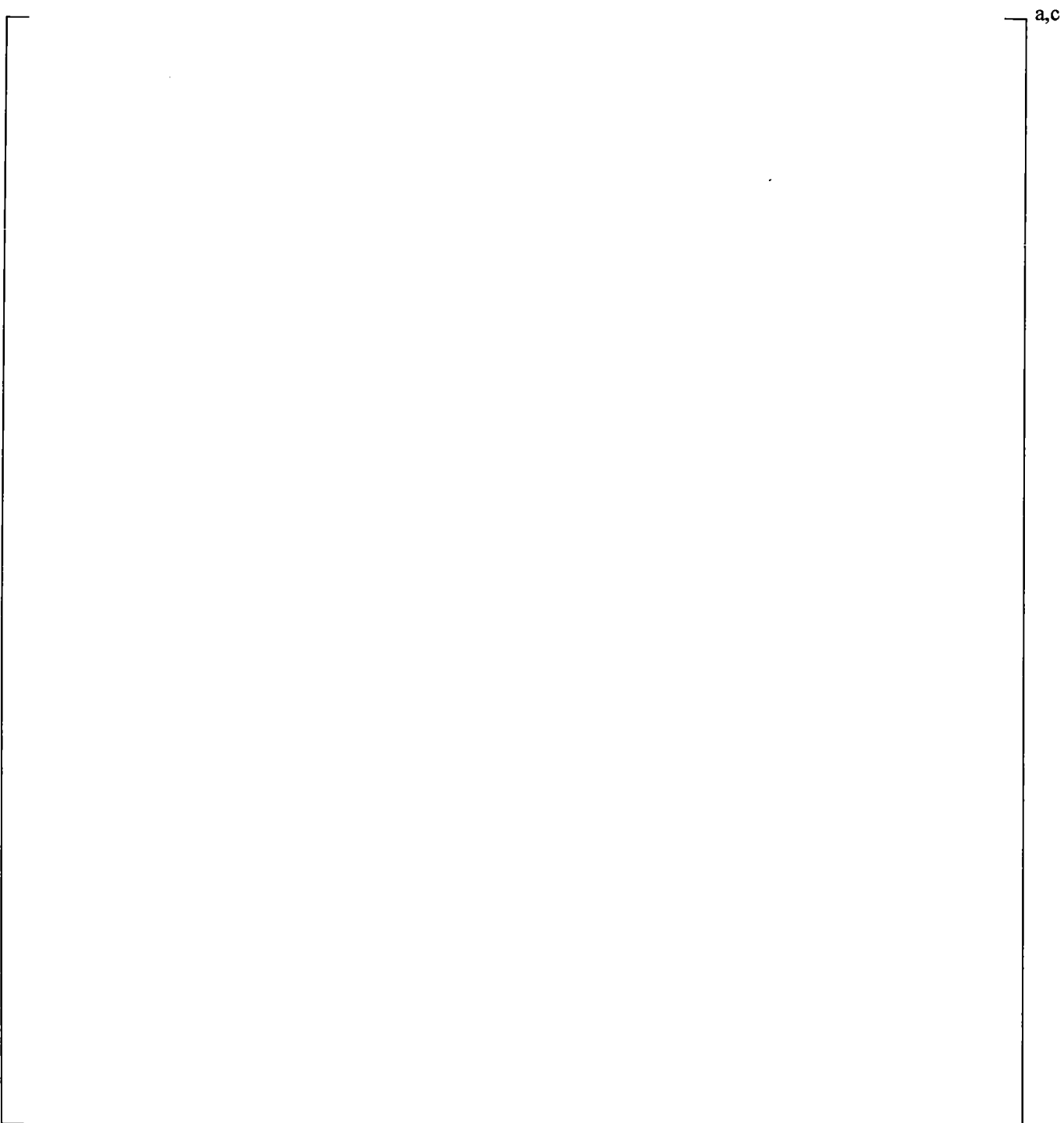


**Figure 20.1-44 Measured and Predicted Cladding Temperature at 2.65m (8.69 ft)
(Broken Pipe Pressure Loss Sensitivity Study)**

20.2 PUMP COMPONENT MODEL

The pump component model was described in Section 10.4 of Volume 1. It is an empirical model in which the pressure differential generated by the pump, and the corresponding torque applied to the pump during single- and two-phase flow, is derived from single- and two-phase flow data in scaled pumps. In particular, the pump head and torque during two-phase flow is assumed to vary as a function of void fraction from the single-phase value to a “fully degraded,” or minimum value which occurs at intermediate void fractions. For the pump head,

$$H = H_1 - M(\alpha) * (H_1 - H_2) \quad (20.2-1)$$

where,

H	=	pump head
H_1	=	single-phase pump head
H_2	=	fully degraded pump head
$M(\alpha)$	=	two-phase multiplier

A similar equation is used for the pump torque (Equation 10-9) with the multiplier defined as $N(\alpha)$.

This is clearly an approximate description of the actual variation of the pump head. As described by Rohatgi et al. (1989), the uncertainty associated with such a model is relatively large and needs to be considered in the code uncertainty. In Section 2.3.2.9 of Volume 1, the performance of the reactor coolant pump was included as part of the PIRT. For one- and two-phase performance, a medium (M) ranking was assigned during blowdown. Pump coastdown was ranked medium (M) during blowdown for intermediate breaks as well, and was ranked high (H) for large breaks. Flow resistance was ranked medium (M) for intermediate breaks and high (H) for large breaks during blowdown. The purpose of this section is to describe the basis for the empirical model used in the LOCA analysis of the PWR, establish the basis for its uncertainty, and relate it to the pump model used in LOFT. Comparisons with LOFT data of the predicted pump head then serve as validation that the empirical model adequately predicts pump head for both LOFT and a PWR.

20.2.1 Westinghouse Pump Data

The Westinghouse pump model is based on air/water data obtained from a scale model of a 93A model pump, designed to operate at a pump head of 92.6 feet, a flow of 7420 gpm, and an impeller speed of 1799 rpm. The scale model used to obtain single- and two-phase data is shown in Figure 20.2-1. It was designed to be geometrically similar to a full-scale Westinghouse model 93A pump, with an equivalent specific speed. The specific speed N_s of a centrifugal pump is defined as:

$$N_s = N Q^{1/2} / H^{3/4} \quad (20.2-2)$$

where,

N is in rpm
Q is in gpm

H is in feet of water

Specific speed has been found to be a convenient parameter distinguishing the performance characteristics of different pumps. The specific speeds of Westinghouse pumps range from approximately 5000 to 7000 rpm. In contrast, the specific speed of the LOFT pumps is 3300 rpm.

Single-Phase Data

Figures 20.2-2 and 20.2-3 show some of the test data used to determine the single-phase homologous curves for forward and reverse flow through the pump. The data consists of water data from the scale model of the 93A pump, as well as air data from the same scale model and test facility where two-phase data was obtained (Howland and Lamers, 1973). It can be seen that the air and water data agree well, indicating that the change in test fluid and test facility had little effect on the test results.

The uncertainty of the single-phase data was determined by evaluating two data sources. The first source was from the Westinghouse single-phase data cited above. A band can be drawn to bound the data in Figure 20.2-3 (the normalized head ratio h/v^2 data is plotted against the inverse of the normalized flow ratio v/α in this figure). [

]^{a,c}

The second source examined was from data developed by Cudlin (1977), where the normalized head ratio in the forward flow, dissipative quadrant for a 1/3-scale model pump is shown in Figure 20.2-4.

[

]^{a,c}

Two-Phase Data

The two-phase data were obtained by running air/water mixtures through the pump (Howland and Muench, 1975). The test facility is illustrated in Figure 20.2-5. Water was drawn from a large basin using a diesel powered pump, mixed with air in a mixing chamber, and pushed through the scale model pump. Inlet line venturi meters and orifices were used to measure inlet flow rates. Pump pressure differential, impeller speed, and impeller torque were also measured. The inlet void fraction was not measured but was inferred from the flow rates. A correlation was used to estimate the void fraction from the flow rates. In addition, a homogeneous void fraction was used. It was found that the basic nature of the data was not affected by the choice of void fraction. In the following discussion, the homogeneous (zero slip) void fraction is used.

Typically, homologous head data is plotted using two x-axes, normalized flow divided by normalized speed (v/α as in Figure 20.2-2), and normalized speed divided by normalized flow (α/v as in Figure 20.2-3). An alternative way to plot the head data is to show normalized head divided by normalized speed squared (h/α^2), versus normalized flow divided by normalized speed (v/α), for all forward flow conditions. This results in Figure 20.2-6, which more clearly shows the transition, as flow increases, from a positive head or pumping mode, to a negative head or energy dissipation mode. The intact loop pumps are operating in the pumping mode during the initial stages of a cold leg break LOCA, while the broken loop pump is operating in an energy dissipation mode during the entire transient. The two-phase data is also shown on this figure, and indicates that the pumping mode data shows relatively little scatter, while the dissipation mode data shows more scatter. The increased scatter may be due to the fact that, when the downstream pressure is lower, the upstream conditions are no longer as accurate a

representation of conditions within the pump. Also plotted on this figure are the single-phase head curve and a fully degraded head curve drawn through the lower bound data.

The method for determining the two-phase multiplier $M(\alpha)$ and $N(\alpha)$ in Equations 10-8 and 10-9 from the pump data is as follows:

1. Determine single-phase homologous head and torque. The pressure difference across the pump, and the torque applied to the pump impeller, are measured under a variety of flow conditions. Homologous head and torque curves are derived by dividing these data by the appropriate quantities (rated flow, rated speed, etc.). Each pump model (designated 93, 93A, 100, etc.) designed by Westinghouse has a set of homologous curves derived from scale model single-phase tests using both air and water.
2. Measure the pump pressure difference and torque under two-phase conditions over a range of void fractions. The lower boundary of the data, when converted to homologous form, is defined as the "fully degraded" homologous head and torque. These data were obtained from a 1/3-scale model pump with the same specific speed as the model 93A pump. The pump head data are shown in Figure 20.2-7, and the pump torque data in Figure 20.2-8. The single-phase and "fully degraded" curves constructed from these data are also shown (they are also shown in Figures 10-4 to 10-7). In Figure 20.2-7, HSP1 and HTP1 are the single- and fully degraded two-phase head (h/α^2) curves presented as a function of v/α , while HSP2 and HTP2 present the head (h/v^2) as a function of α/v . Note that the fully degraded curves are always drawn below the single-phase curves, and bound nearly all the data.

The two-phase data indicate that the amount of full degradation in head or torque is approximately a constant. That is, the fully degraded curve is offset from the single-phase curve by a constant. This is more easily seen in Figure 20.2-6. This observation allows the fully degraded curve to be extended into areas where data is sparse or lacking.

3. Assume that the homologous head and torque go from single-phase to fully degraded back to single-phase values as the pump inlet void fraction ranges from 0 to 1.0. Use Equation 20.2-1 in the following form to calculate $M(\alpha_i)$ for each pump head data point $H(\alpha_i)$:

$$M(\alpha_i) = \frac{H(\alpha_i) - H_1}{H_2 - H_1}$$

Use the $M(\alpha_i)$ data to define the appropriate shape of the $M(\alpha)$ function, as in Figures 20.2-9 and 20.2-10. Figure 20.2-9 includes only the pumping mode data, while Figure 20.2-10 includes all the data. Perform a similar exercise for the pump torque (Figure 20.2-11).

Data are lacking for void fractions greater than approximately 65 percent. [

]^{a,c} This assumption is supported by test data from other design pumps, for example, Figure 2.1 on page L-9 of the Code Scaling, Applicability, and Uncertainty (CSAU) report (Boyack et al., 1989).

The simple form of the $M(\alpha)$ function results in considerable scatter in the data in the dissipative, or turbine mode of pump operation. The effect of this uncertainty was examined by defining a new multiplier which was drawn below the lower bound of the data and was found to result in a relatively small effect for large breaks, due to the relatively short time that the pump is in the fully degraded low void fraction two-phase regime. This result is consistent with results obtained in the CSAU report (Boyack et al., 1989). For small breaks, the use of a multiplier representing the lower bound of the data has only a small effect when offsite power is available. In that case, because the pumps continue to rotate at fixed speed into the early portion of the natural circulation phase, differential pressure across the pumps is predicted differently when the flow is two-phase using the lower bound degradation curve. This effect subsides before loop seal clearance, however, so the effect on the transient is negligible. With a loss of offsite power, the effect on the small break transient is negligible due to the early coastdown of the pumps and the presence of primarily single phase flow in the loops.

[

]

]^{a,c}

20.2.2 Pump Model Comparison to Data

The only large break test which contains a powered pump is the LOFT test. Although the pumps in LOFT are of a different design than PWR pumps, they exhibit similar overall performance as can be seen from Figure 20.2-12. The pump model used in the LOFT simulations, described in Section 22 of this report, is the same as that used in the PWR, except that the homologous curves and the two-phase multiplier used were the LOFT specific curves, obtained from tests on the Semiscale pump (Reeder, 1978). Another difference was that the pump speed was input from the LOFT data, rather than calculated. This was done to examine specifically the pump head prediction, which will be shown later to be the more important parameter in the PWR calculation. The resulting prediction for LOFT Test L2-5 is shown in Figure 22-43.

These comparisons show that the predicted pressure difference across the pumps in the intact loops compares well with the measured pressure difference during blowdown.

The ROSA-IV test facility provides a means for comparison in the context of small breaks. Figure 21.5-2 shows that WCOBRA/TRAC-TF2 adequately predicts the pump speed throughout the SB-CL-05 test. Figure 21.6-1 shows the same for SB-CL-14. This, in conjunction with the reasonable prediction of pressures throughout the primary loops suggests that the pump model in WCOBRA/TRAC-TF2 is adequate.

These comparisons indicate that the relatively simple pump model in WCOBRA/TRAC adequately predicts pump behavior during LOCA. In addition, for the Westinghouse pump, the uncertainty in the data is most significant for a broken loop pump operating in the dissipative mode. Section 29.1.2.2, Volume 3 describes how this uncertainty will be treated in plant analyses.

20.2.3 References

1. Boyack, et al., 1989, "Quantifying Reactor Safety Margins," NUREG/CR-5249.
2. Cudlin, J. J., 1977, "1/3 Scale Air-Water Pump Program, Analytical Pump Performance Model," EPRI NP-160.
3. Howland, G. R. and Lamers, R. P., 1973, "Air Test Program to Establish the Complete Pump Characteristics of WEMD 93A Model Reactor Coolant Pump," Westinghouse Research Report 73-7E9-TAPSC-R1.
4. Howland, G. R. and Muench, R. A., 1975, "Air/Water Mixed Flow Testing of the WEMD 93A Model Reactor Coolant Pump," Westinghouse Research Report 75-7E9-CORCL-R1.
5. Reeder, D. L., 1978, "LOFT System and Test Description," NUREG/CR-0247.
6. Rohatgi, et al., 1989, "Quantifying Reactor Safety Margins," NUREG/CR-5249.

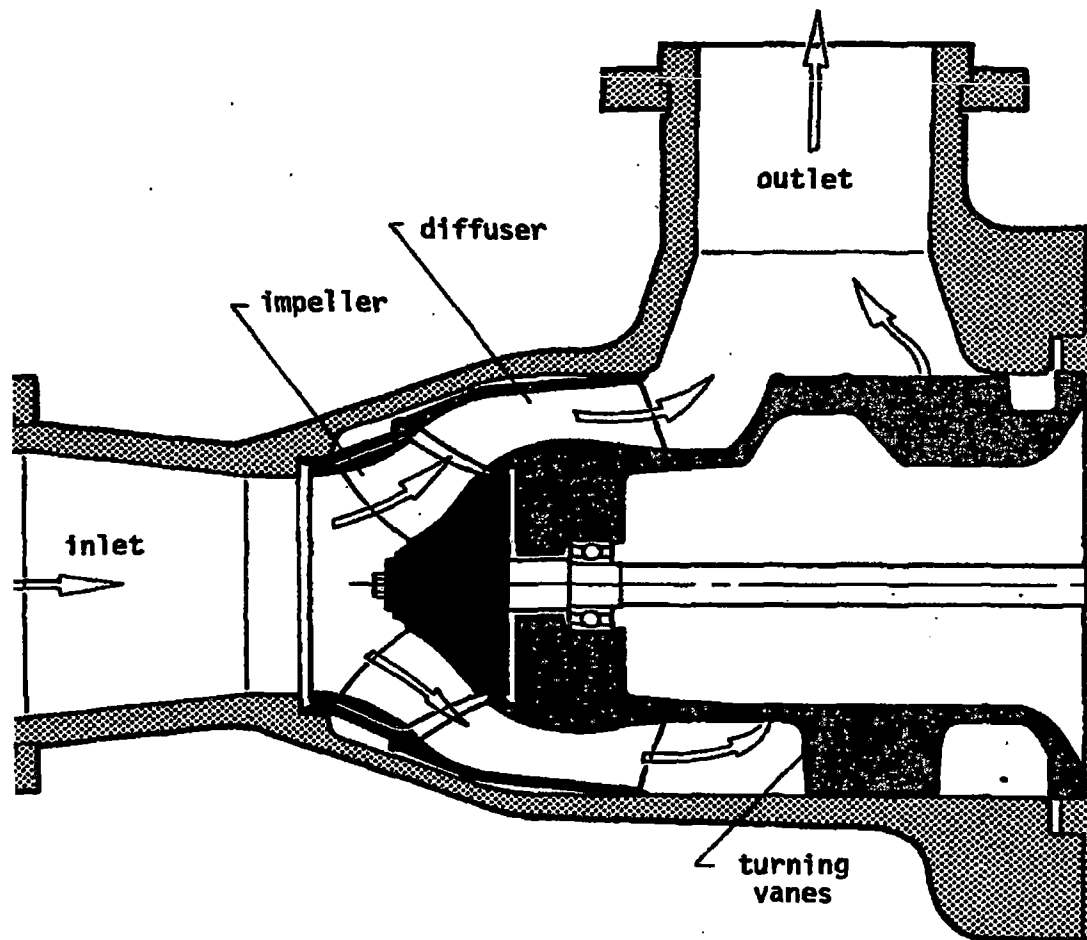


Figure 20.2-1 Cross-Sectional View of the Westinghouse Scale Model Pump

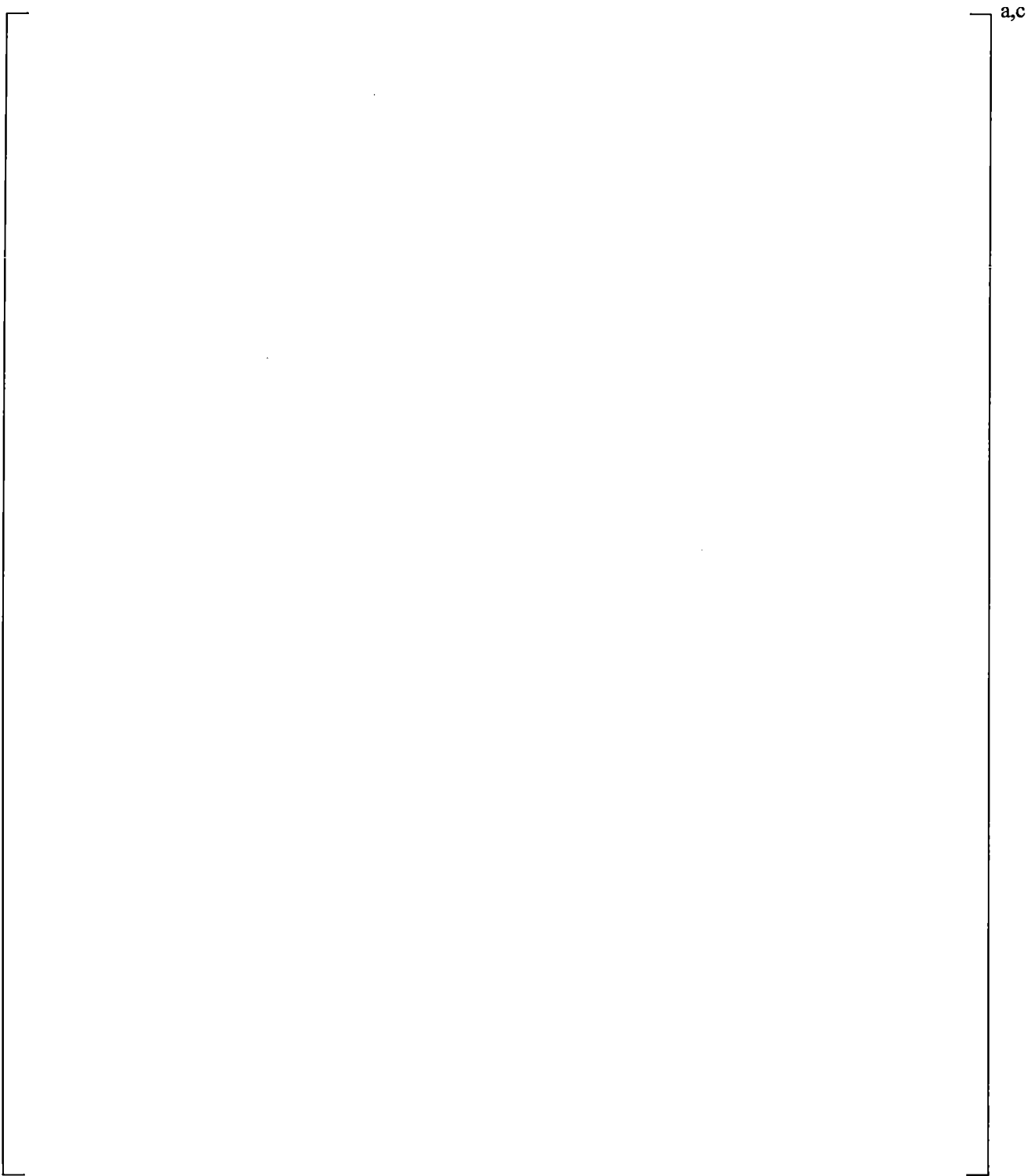
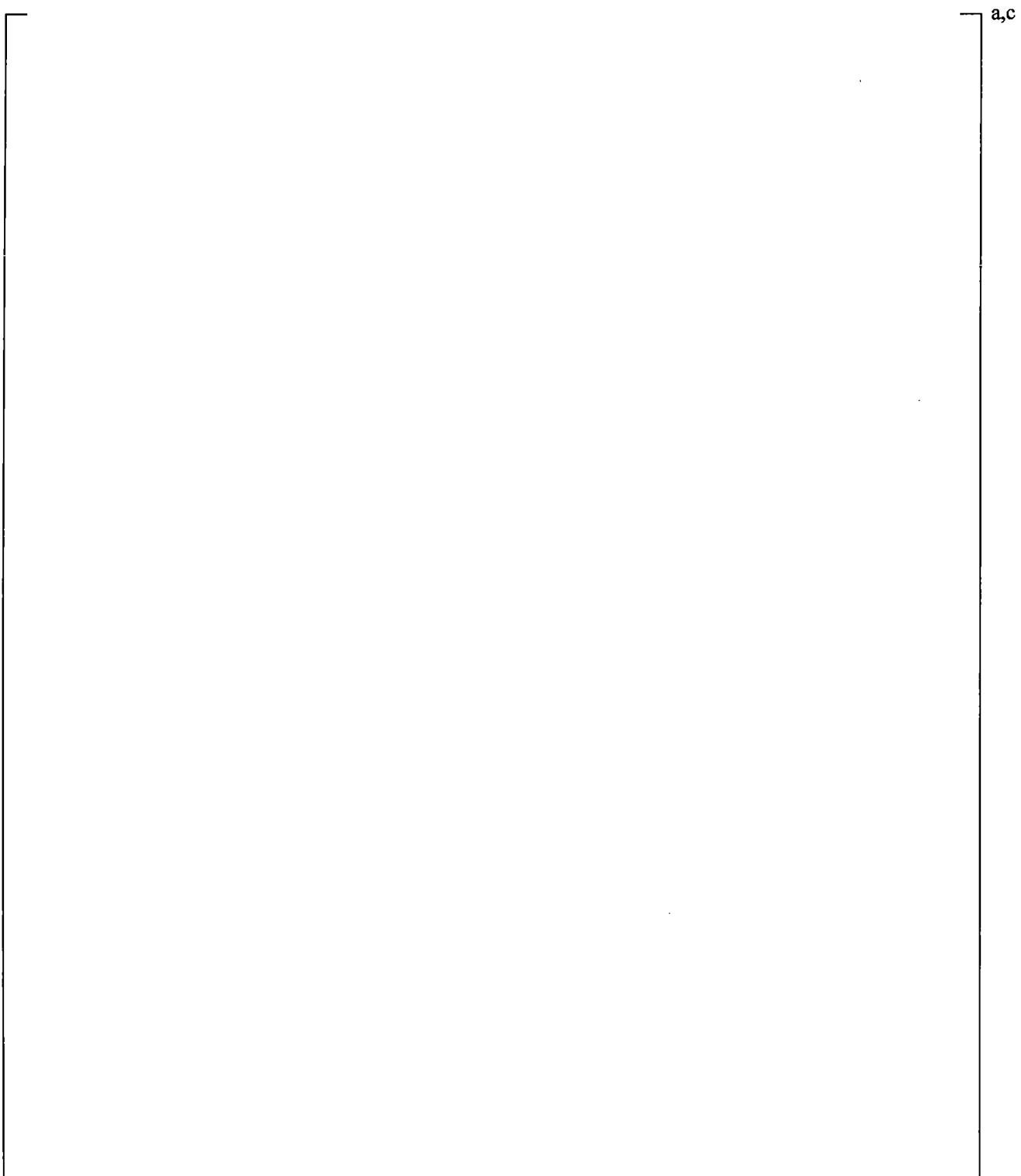


Figure 20.2-2 Scale Model Homologous Head Single-Phase Data in the Pumping Mode, Forward and Reverse Flow



**Figure 20.2-3 Scale Model Homologous Head Single-Phase Data
in the Dissipation Mode, Forward Flow**

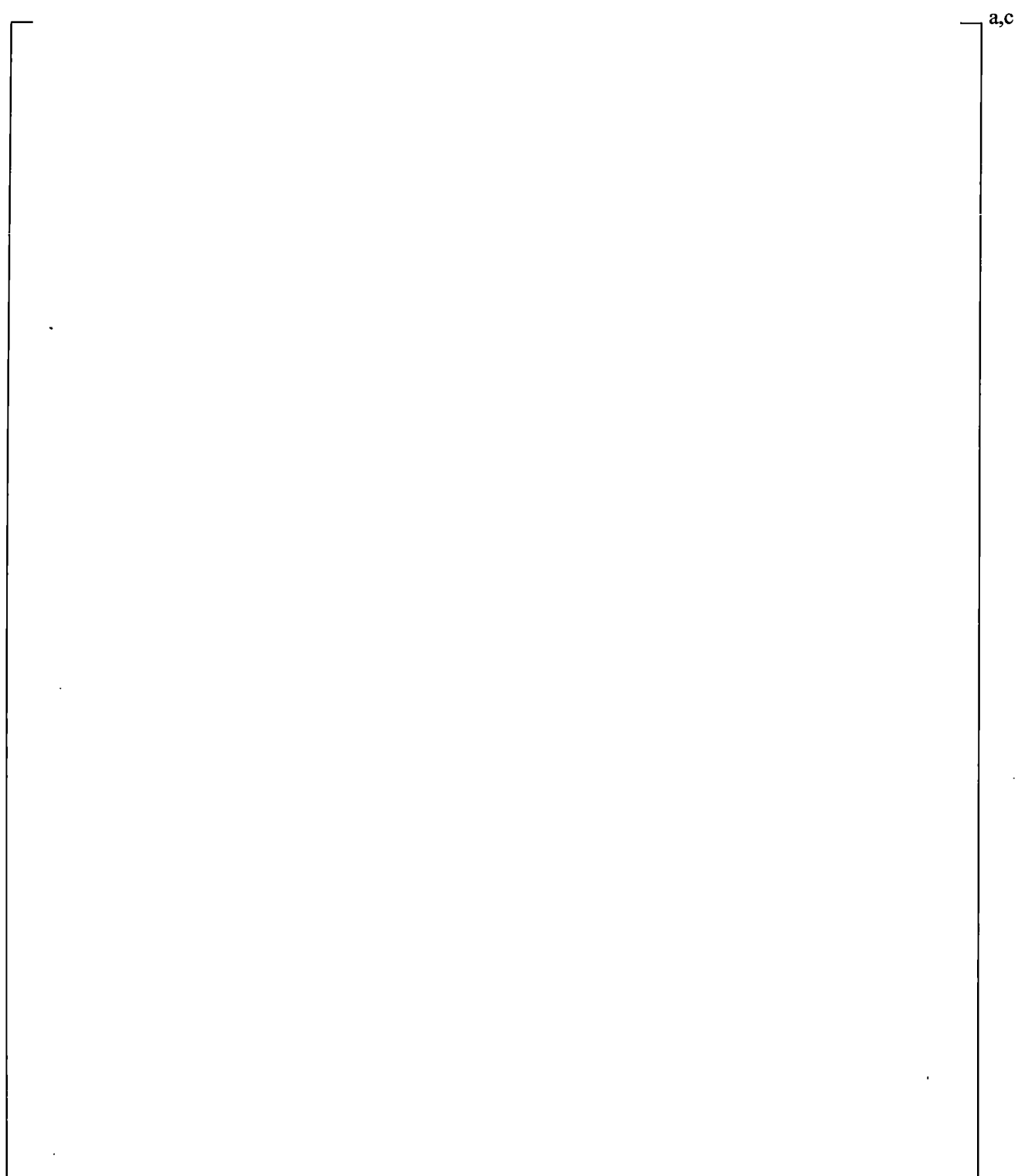


Figure 20.2-4 Data Scatter for Dissipative Mode 1/3-Scale Pump Data (Cudlin, 1977)

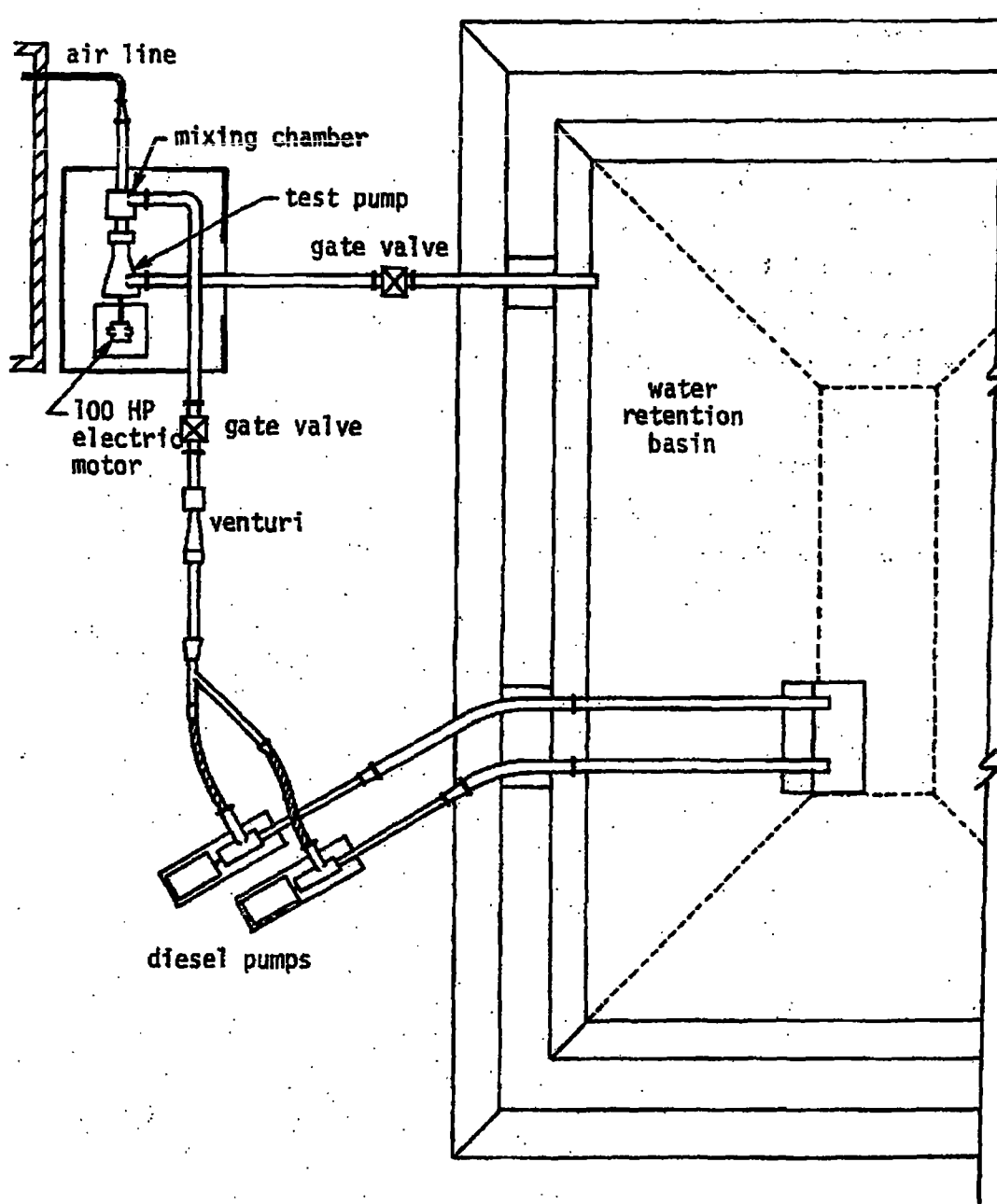


Figure 20.2-5 Schematic of the Air/Water Test Facility

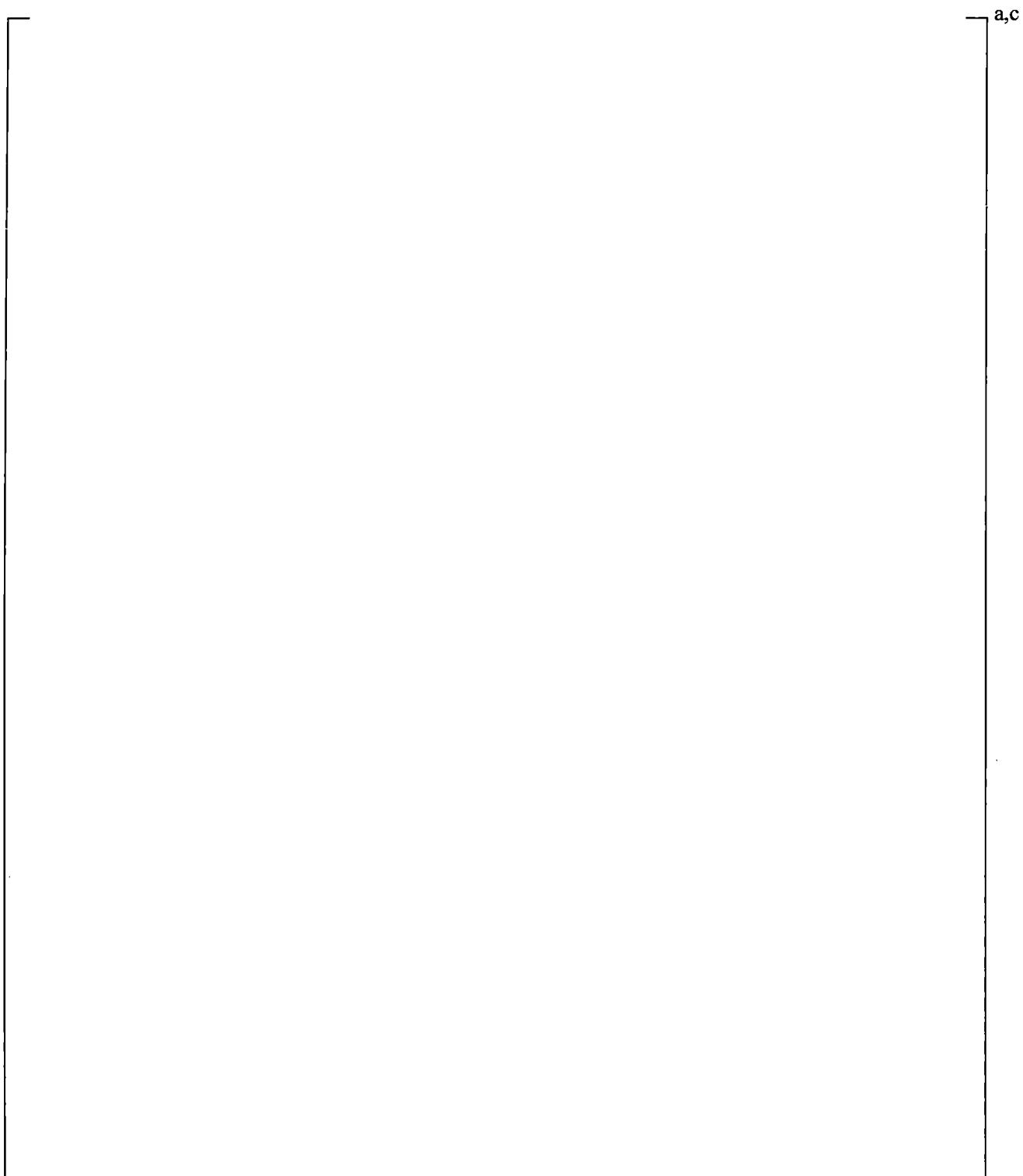
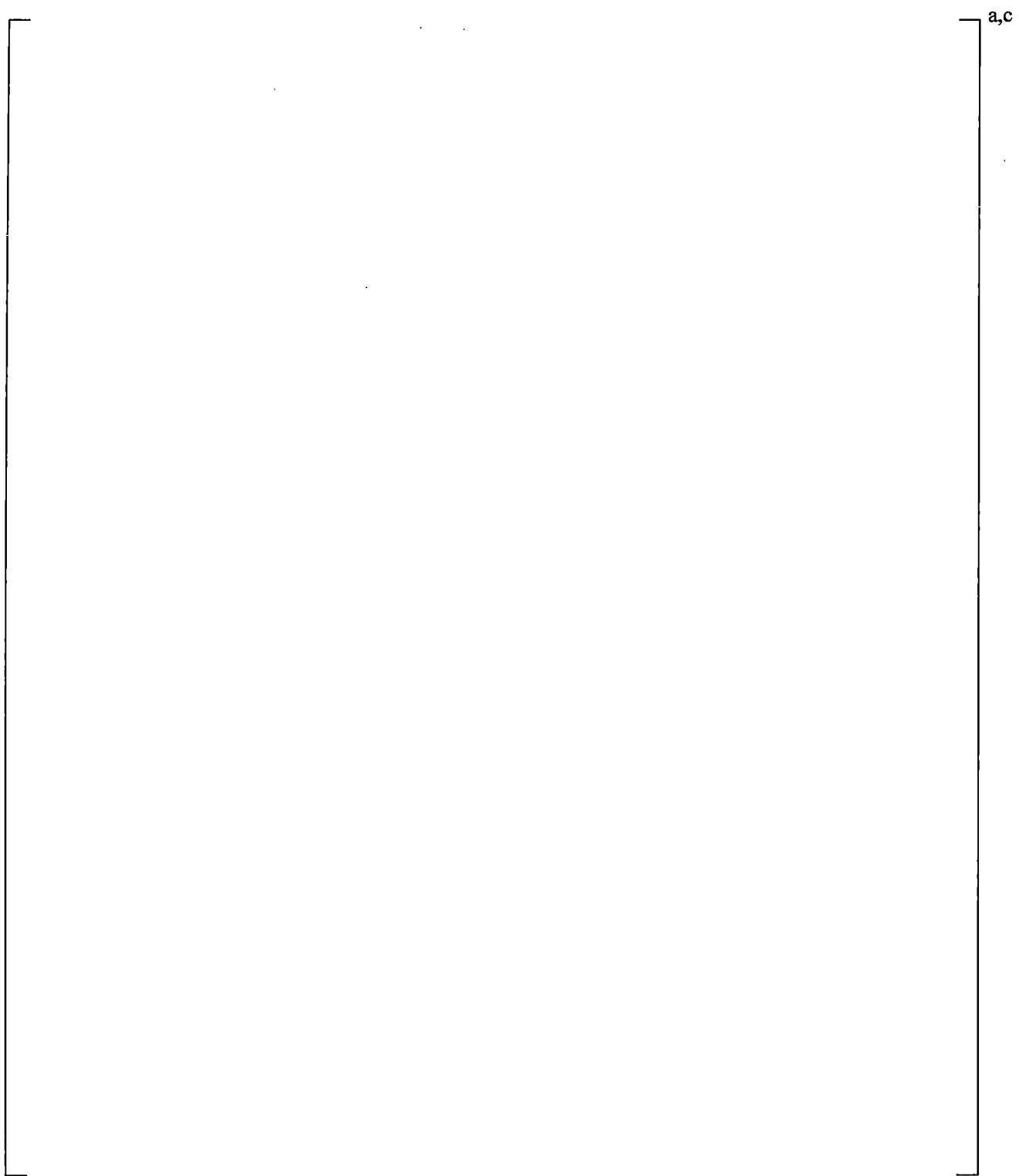
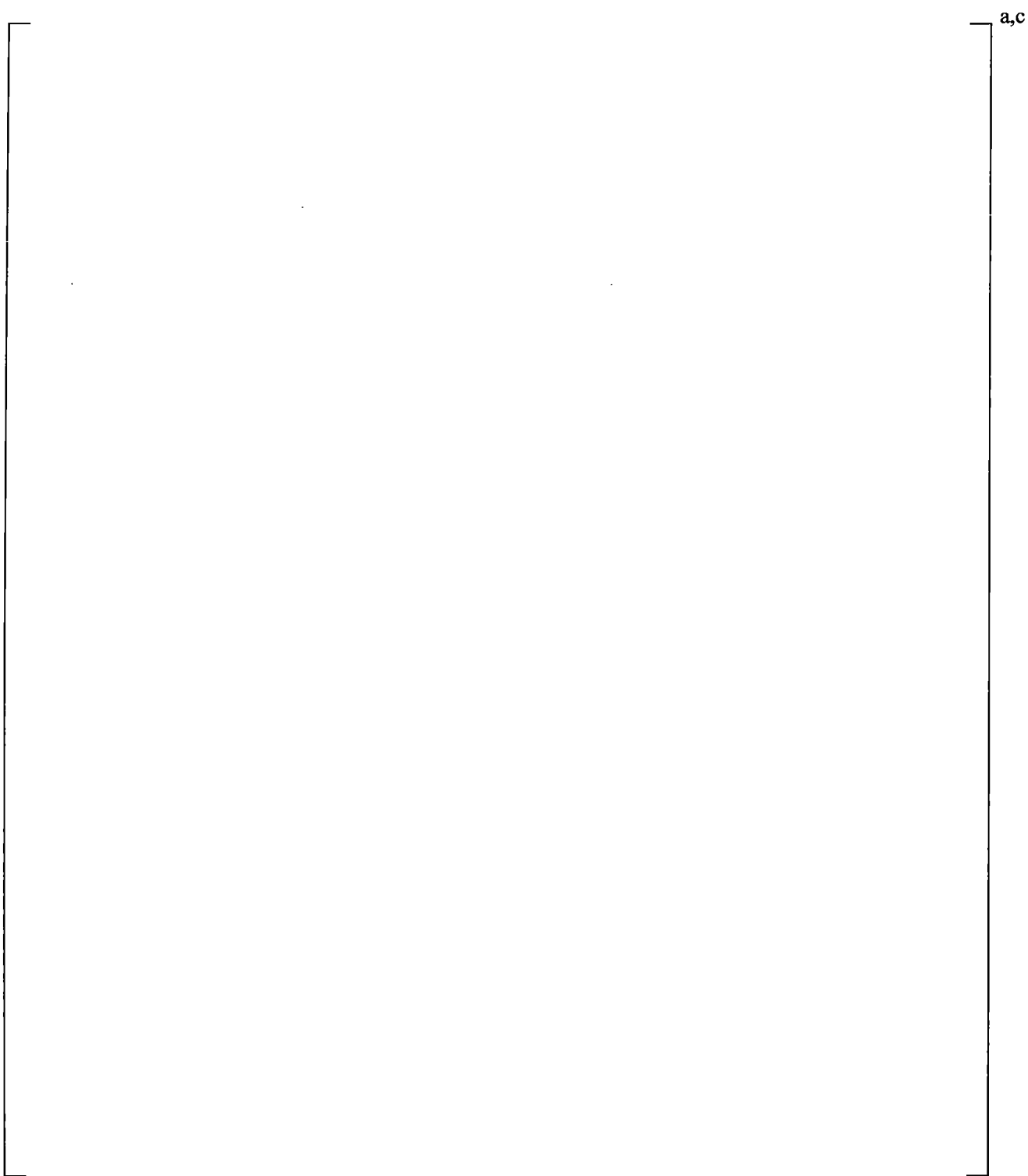


Figure 20.2-6 Homologous Head Curves and Westinghouse Air/Water Data



**Figure 20.2-7 Single-Phase and Fully Degraded Pump Head
Curves Compared With Two-Phase Data**



**Figure 20.2-8 Pump Single-Phase and Fully Degraded Torque Curves,
Compared With Two-Phase Data**

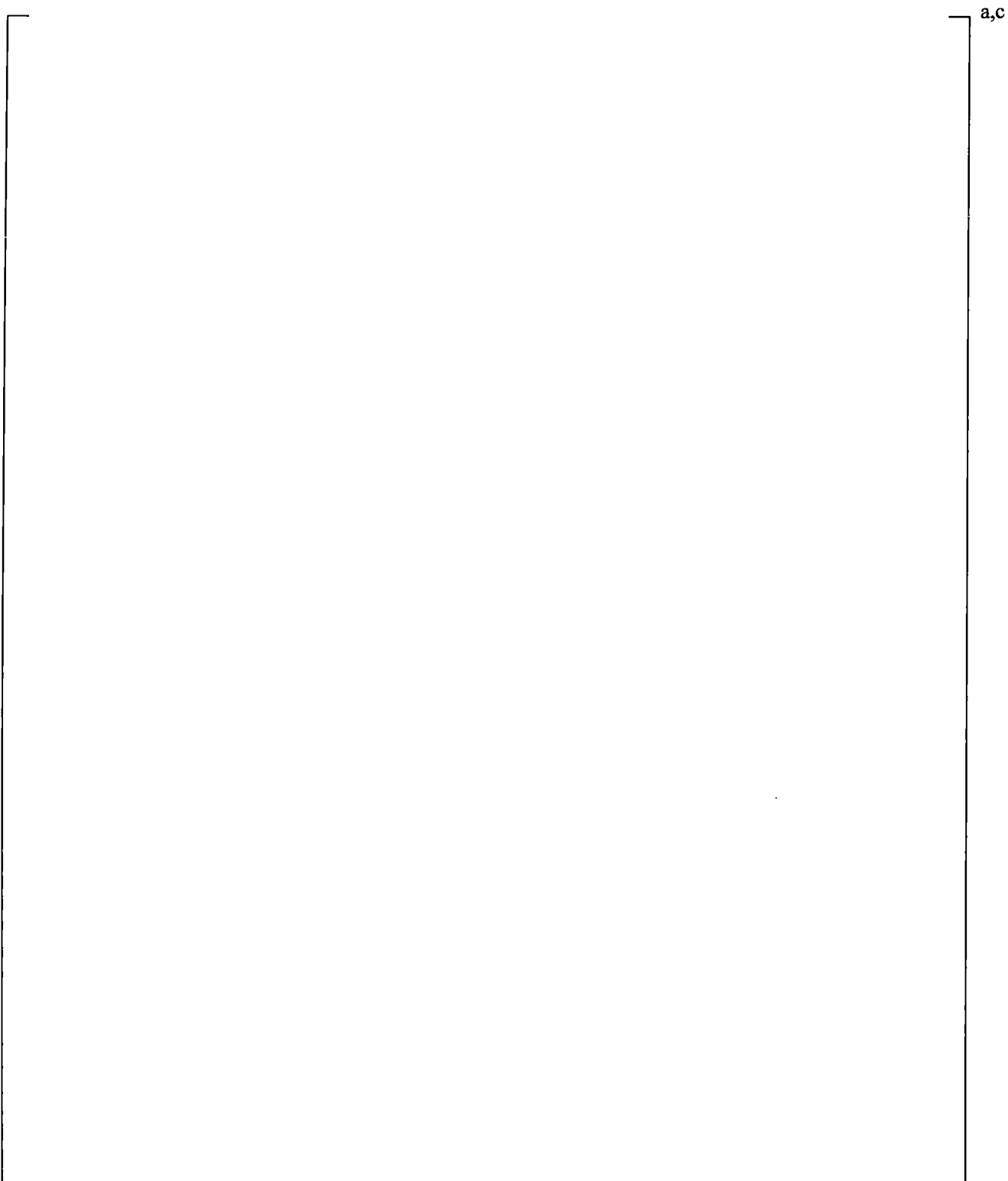


Figure 20.2-9 Two-Phase Multiplier and Pumping Mode Data

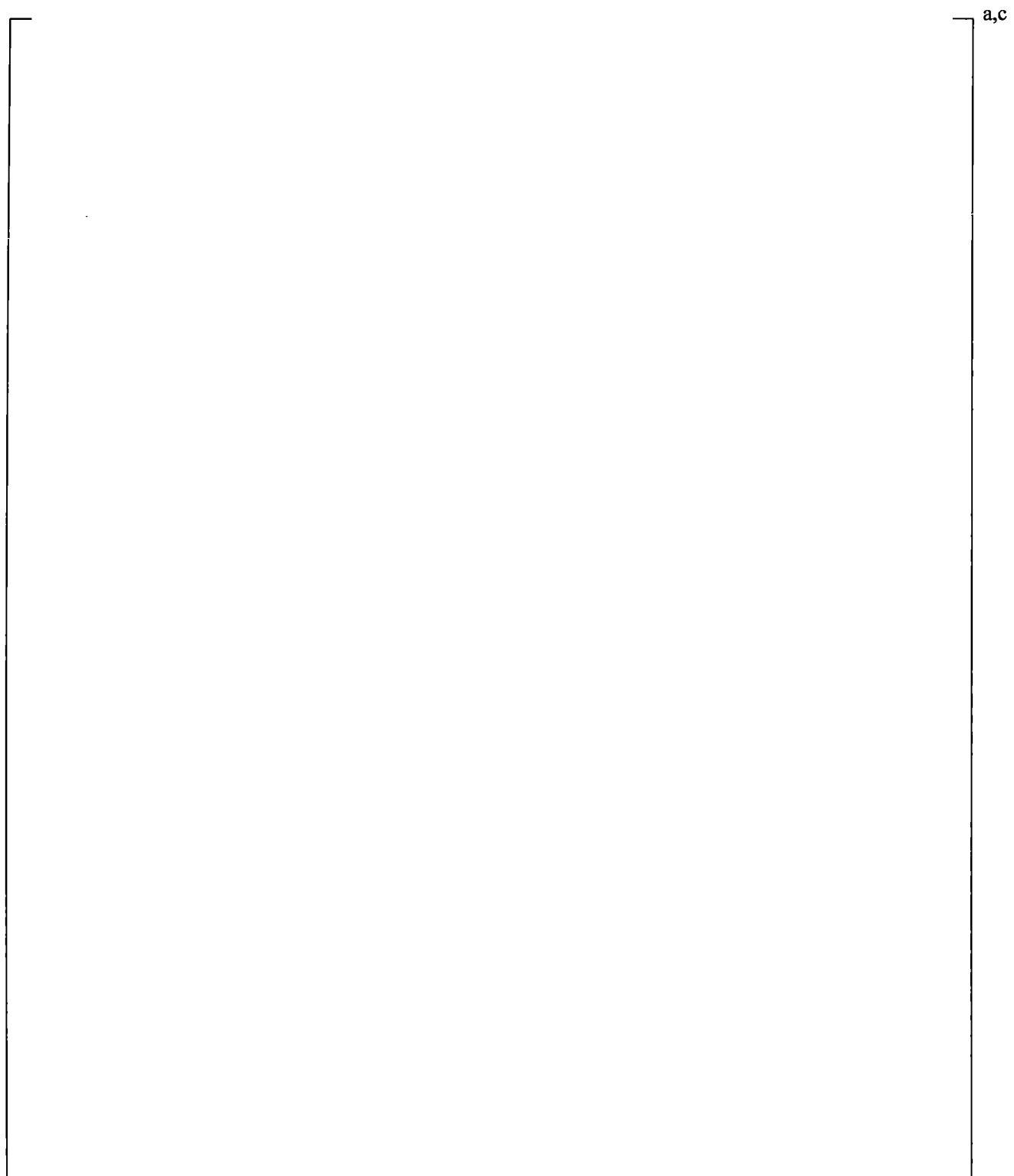


Figure 20.2-10 Two-Phase Multiplier and All Two-Phase Data

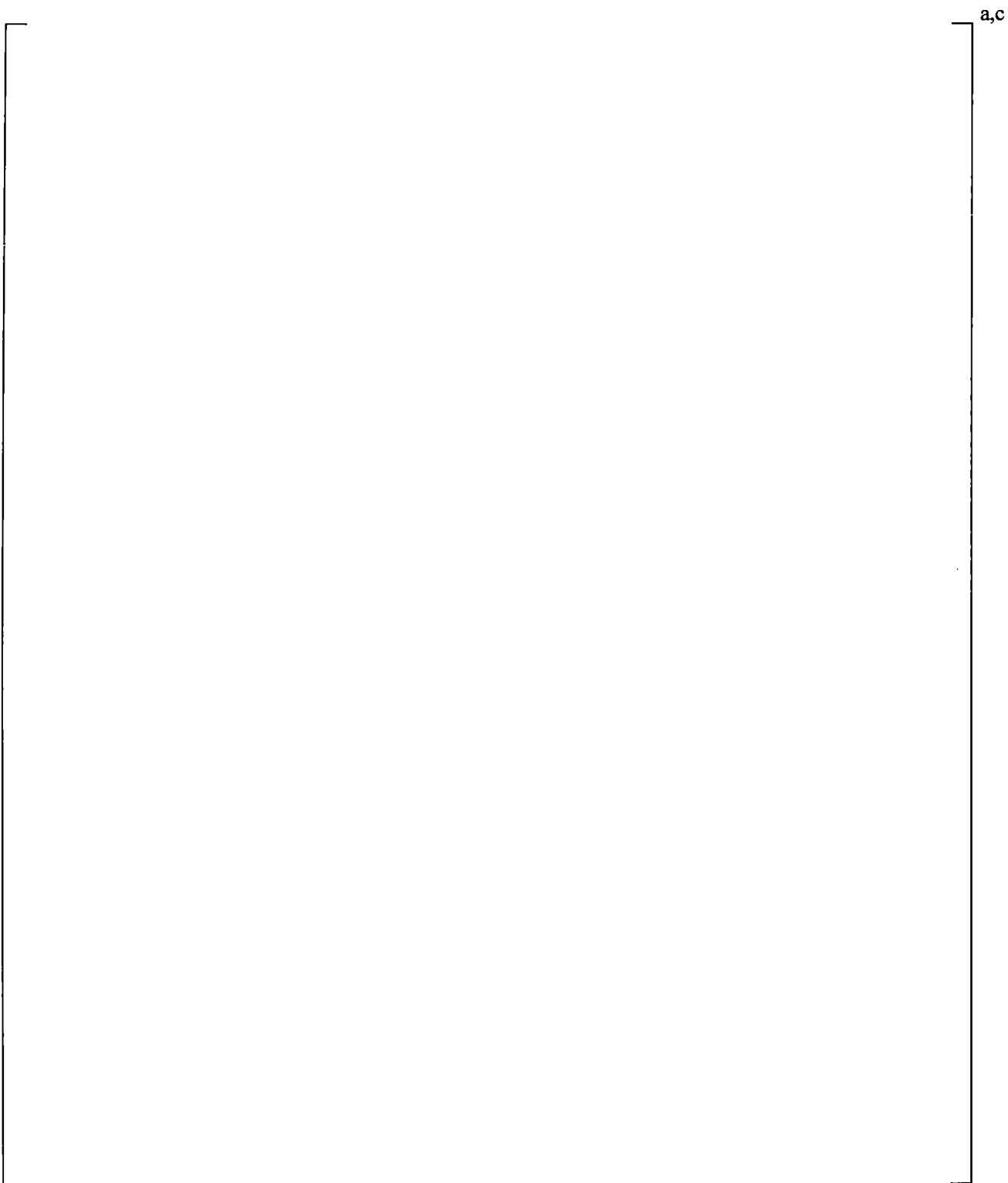


Figure 20.2-11 M(α) for Pump Torque (Referred to as N(α) in Equation 10-9)

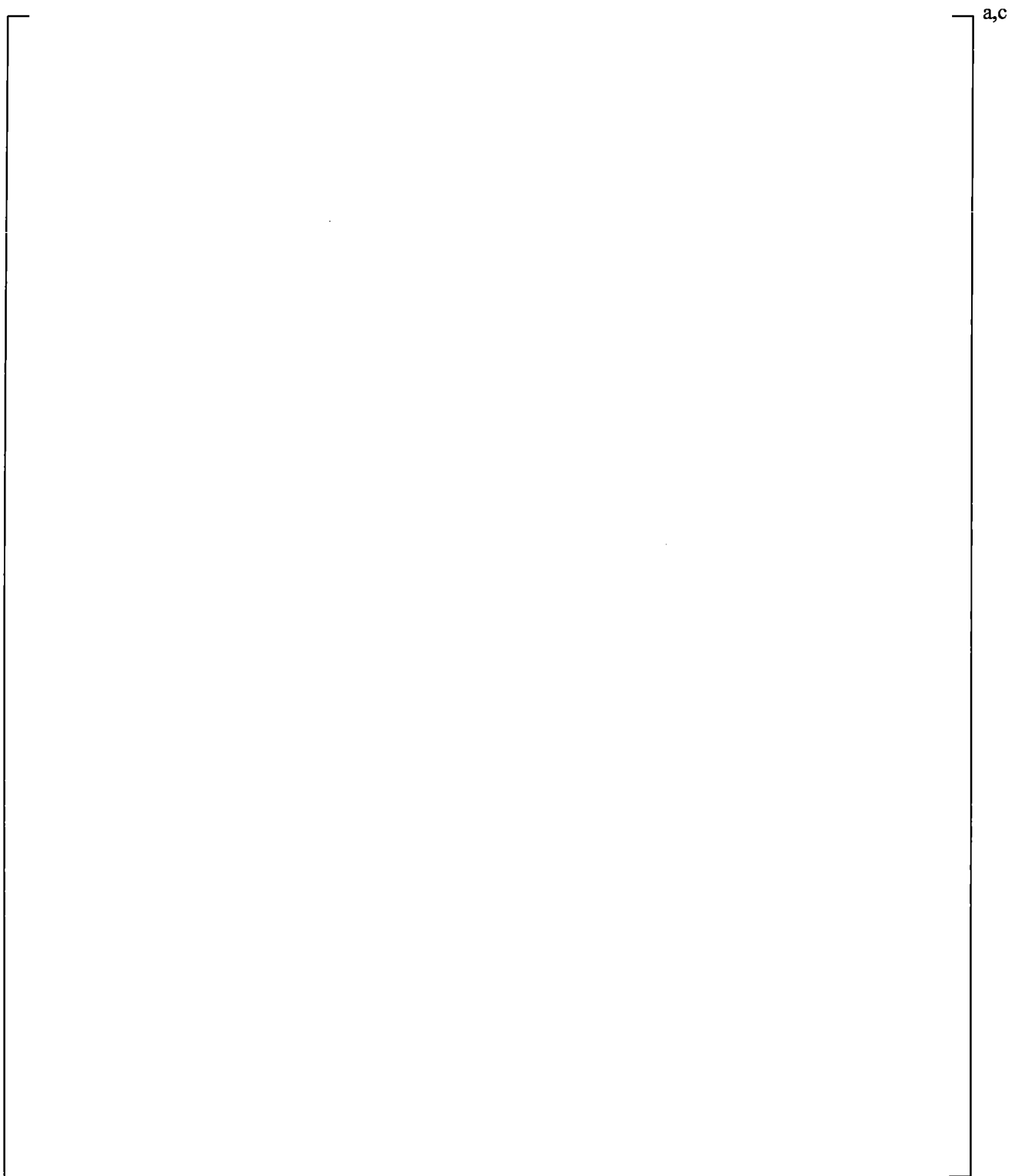


Figure 20.2-12 Westinghouse Pump Head Curves Compared With LOFT Pump Head Curves

20.3 MASS AND ENERGY CONSERVATION ACROSS 1D/3D JUNCTION

WCOBRA/TRAC-TF2, as described in Section 3 of Volume 1, is comprised of a two-fluid, three field representation of the vessel component (3D) and a two-phase, two-fluid representation for the one-dimensional components (1D). At the interfaces, such as cold and hot leg nozzles, are junctions coupling the numerical solution. This section serves to demonstrate the conservation of mass and energy across such a junction with the use of a simple numerical test problem. The momentum coupling treatment and assessment is discussed in Section 19.3.5.10 regarding the cold leg nozzle loss coefficient.

20.3.1 Scenario Description and **WCOBRA/TRAC-TF2** Model Description

A single channel, 10 node vessel (node height = 1.0 ft, node diameter = 2 in.) is connected to PIPE components at junctions at the bottom and top nodes (Figure 20.3-1). A third pipe is connected to node 5. Each PIPE has a diameter of 0.2 ft. A liquid velocity ramping up to 5 ft/s in the first 10s of the transient and to 10 ft/s within the first 50s is supplied with FILL components connected through junctions at the top and middle node. Zero axial flow boundary conditions are prescribed at the top and bottom of the vessel such that both inlet flows must exit the vessel at the 1D junction at the bottom node, where a 100 psia pressure boundary condition is prescribed with a BREAK component. The assumed temperature is 60°F.

The solution requires mass and energy to be conserved for the control volume. Given that the problem considers single phase, quasi-steady flow, and there is no net mass or energy accumulation in the vessel component, the following equations must be satisfied at the junctions:

$$\begin{aligned}\dot{m}_{in} &= \dot{m}_{out} \\ h_{in} \dot{m}_{in} &= h_{out} \dot{m}_{out}\end{aligned}$$

where,

h is the enthalpy of the mixture per unit mass and \dot{m} is the mixture mass flow rate.

20.3.2 Results and Conclusions

Figure 20.3-2 shows that throughout the transient as the velocity of each of the FILL components ramps to 10 ft/s, the mass flow entering the vessel equals the mass flow exiting the vessel. After 100 seconds, the mass flow rate error is []^{a,c}. Figure 20.3-3 shows that the energy (enthalpy) flow rate into the vessel equals the energy flow out of the vessel throughout the transient. After 100 seconds, the error is []^{a,c}.

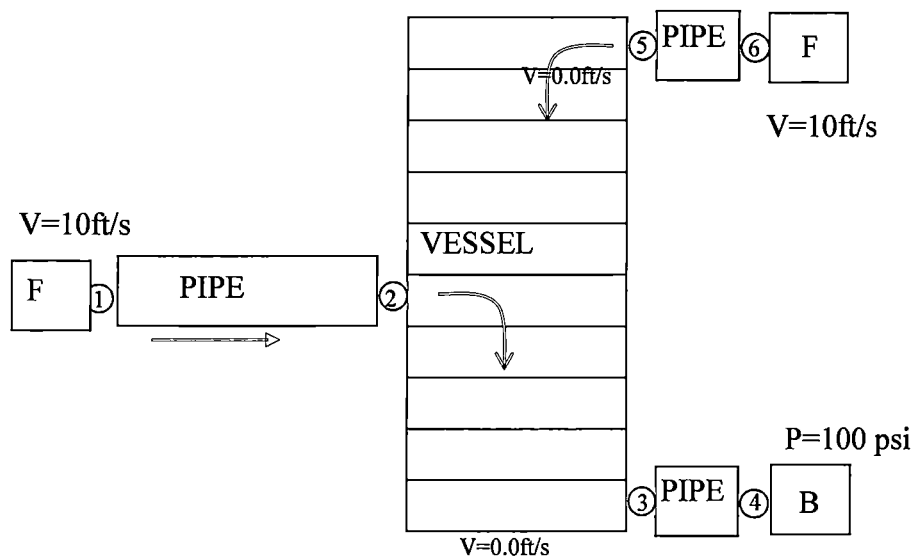


Figure 20.3-1 Scenario and Noding Diagram for 1D/3D Mass and Energy Test

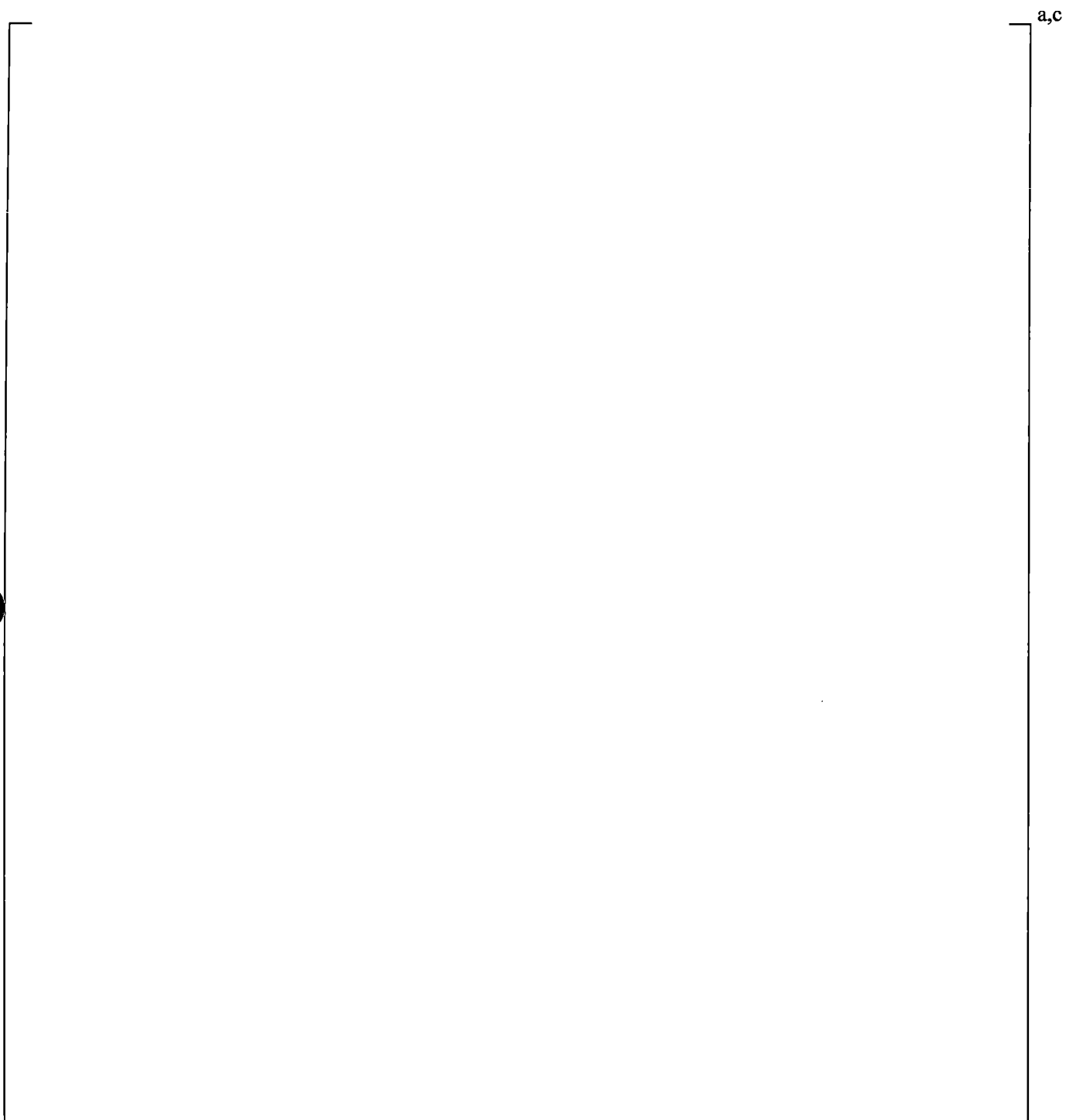


Figure 20.3-2 Mass Conservation for 1D/3D Mass and Energy Test

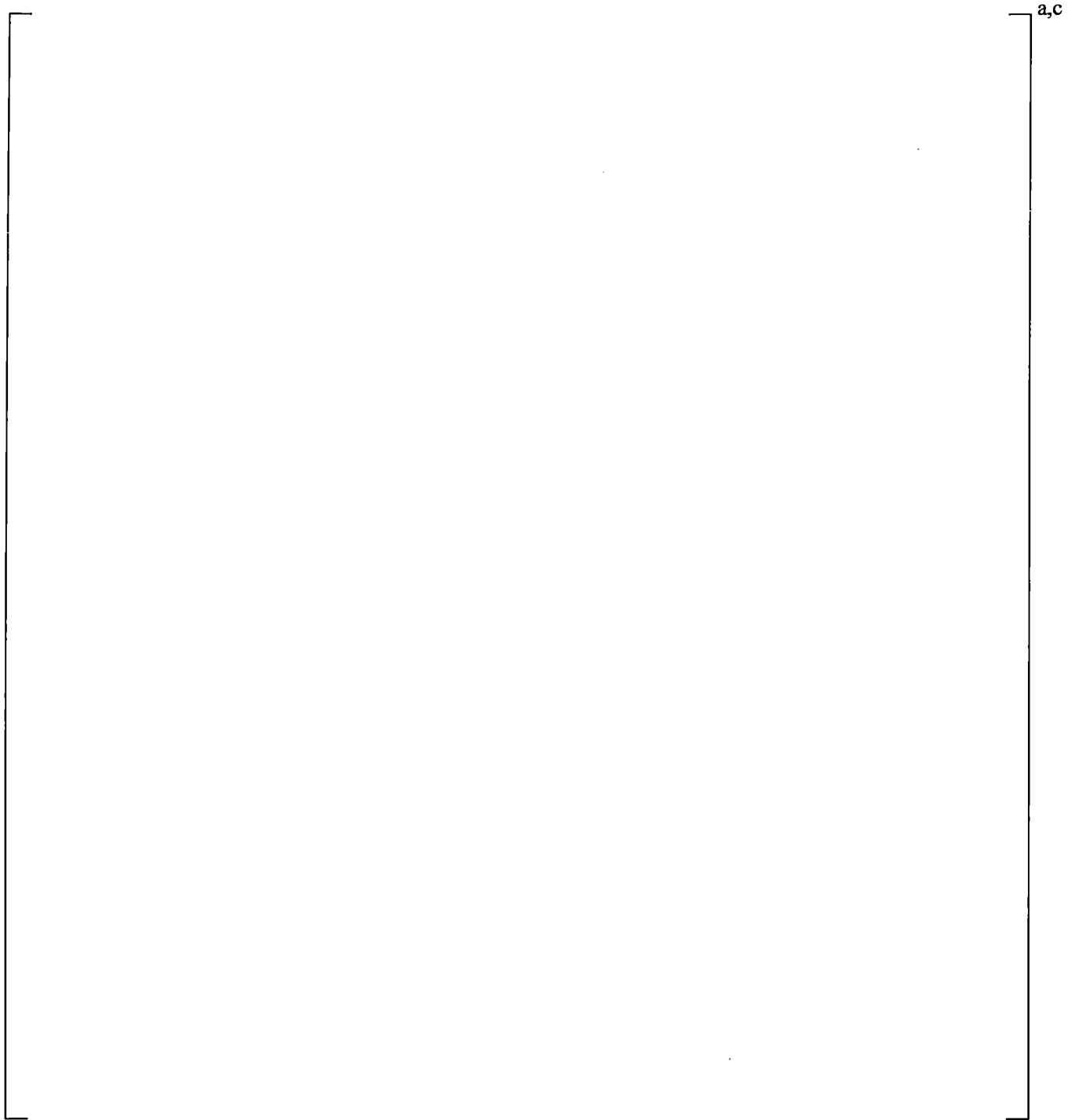


Figure 20.3-3 Energy Conservation for 1D/3D Mass and Energy Test

20.4 SUMMARY AND CONCLUSIONS

This section considered the WCOPRA/TRAC-TF2 component models that have special importance during the simulation of a LOCA in a PWR, and that have not been discussed in previous sections.

Section 20.1 documented the validation performed for the accumulator model. Accumulator blowdown tests performed at Indian Point Unit 2 and Callaway were modeled and simulated with WCOPRA/TRAC-TF2, and [

[^{a,c} Simulations of the LOFT experiments were made with accumulator modeling similar to that used in a PWR. The LOFT simulations showed that WCOPRA/TRAC-TF2 predicted [

]^{a,c}

The WCOPRA/TRAC-TF2 pump model was discussed in Section 20.2. The model was used in the simulation of the LOFT and ROSA tests, and the comparison of the predicted versus measured pressure difference across the pump was [

]^{a,c}

Finally, Section 20.3 provided [

]^{a,c}.

21 ROSA-IV TEST SIMULATIONS

21.1 INTRODUCTION

The Rig-of-Safety Assessment Number 4 (ROSA-IV) program conducted a series of experiments to investigate the thermal-hydraulic behavior of a Westinghouse-designed four-loop pressurized water reactor (PWR) during small break loss-of-coolant accidents (LOCAs) and operational transients using the Large Scale Test Facility (LSTF). A number of phenomena that are of interest to the FULL SPECTRUM LOCA (FSLOCA) Methodology were investigated in the ROSA-IV test facility. Tests were well documented and many test reports are available in open literature or via the library of the Japan Atomic Energy Agency (JAEA), former Japan Atomic Energy Research Institute (JAERI).

The ROSA-IV LSTF is discussed in Section 21.2, and the WCOBRA/TRAC-TF2 model of the facility used for analysis of the full spectrum of breaks considered is presented in Section 21.3.

Sections 21.4 through 21.9 describe the simulations of a number of ROSA tests using WCOBRA/TRAC-TF2. The following test series were selected for the assessment of the WCOBRA/TRAC-TF2 code and the FSLOCA methodology. SB-CL-01, SB-CL-02, SB-CL-03, SB-CL-05, SB-CL-14, SB-CL-12, SB-CL-15, SB-CL-16, SB-CL-18, and ST-NC-02. SB-CL-18 is a 5% cold leg break test which is considered to be the reference transient and is the Organization for Economic Cooperation and Development (OECD) international standard problem No. 26 (ISP-26) (Kukita et al., 1992). SB-CL-01, SB-CL-02, and SB-CL-03 are 2.5% cold leg break tests with the break located at the side, bottom and top. SB-CL-12, SB-CL-15, and SB-CL-16 studied the same break orientation effect but at 0.5% break size. SB-CL-14 is a 10% break test. SB-CL-12, SB-CL-01, SB-CL-18, and SB-CL-14 form a break size sensitivity study covering a break range of 0.5% to 10%. SB-CL-05 is another 5% cold leg break test and it is the only test with the high-head safety injection (SI) activated. Comparison of SB-CL-05 and SB-CL-18 investigated the impact of having the pumped SI throughout the transient. Finally, ST-NC-02 is the 2% power natural circulation test.

Table 21.1-1 shows the list of tests used for the validation work. It contains relevant reports and articles related to the ROSA-IV LSTF and the different tests considered herein.

The analysis of the different tests is presented as follows in Sections 21.4 through 21.9. First, the reference transient, SB-CL-18, is discussed in Section 21.4. Section 21.5 documents the simulation of another 5% break test (SB-CL-05) which was conducted with actuation of pumped safety injection. The results of the simulation of the 10% break test SB-CL-14 (intermediate break size) are documented in Section 21.6. The effect of break orientation is discussed in Section 21.7, using simulation results from the top/side/bottom 0.5% (SB-CL-16/12/15) and 2.5% (SB-CL-03/01/02) cold leg break tests. In Section 21.8, a break spectrum study is documented, using the simulation results of the 0.5% (SB-CL-12), 2.5% (SB-CL-01), 5% (SB-CL-18) and 10% (SB-CL-14) break tests. Finally, the simulation of ST-NC-02, a 2% power natural circulation test is documented in Section 21.9.

Section 21.10 discusses the capability of the code to calculate counter-current flow at the upper core plate (UCP), in the vicinity of the hot leg elbow and steam generator inlet nozzle, and the steam generator U-tube bundle. The results presented in that section are based on the code calculation of the different break tests, described in the previous Sections 21.4 through 21.9.

Section 21.11 contains results of various sensitivity calculations performed with selected ROSA-IV tests that are needed to support conclusions made in other sections of this Topical report.

Table 21.1-1 Selected ROSA-IV Test Series Description and Related Technical Reports

Run ID	Date	Break	Condition	JAERI-Report/Article
SB-CL-01	5/30/85	2.5% CL	Cold Leg w/o high-pressure injection (HPI), (Orifice in branch pipe)	(Koizumi et al., 1987), (Koizumi et al., 1988), (Osakabe et al., 1987)
SB-CL-05	6/26/85	5% CL	Cold Leg w/HPI, w/o auxiliary feed water (AFW), side break , (Orifice in branch pipe)	(Kawaji et al., 1986), (Osakabe et al., 1987), (Osakabe et al., 1988)
SB-CL-02	7/18/85	2.5% CL	Cold Leg w/o HPI, bottom break (orifice in branch pipe)	(Koizumi et al., 1987), (Koizumi et al., 1988)
SB-CL-03	8/8/85	2.5% CL	Cold Leg w/o HPI, top break (orifice in branch pipe)	(Koizumi et al., 1987), (Koizumi et al., 1988)
ST-NC/SG-02	12/4/85	2% power nat. circ.	Reflux to core uncover. Then stepwise secondary level drop.	(Tasaka et al., 1988), (Kukita et al., 1988), (Kukita et al., 1989), (Chauliac et al., 1988), (Stumpf et al., 1987), (Yonomoto, 2005)
SB-CL-14	8/28/86	10% CL	Cold Leg w/o HPI, side break , (orifice in branch pipe), realistic (low) power curve.	(Koizumi and Tasaka, 1988a)
SB-CL-12	7/29/87	0.5% CL	Cold leg w/o HPI, side break (orifice flush w/cold leg wall)	(Kukita et al., 1990a), (Kukita et al., 1990b)

Table 21.1-1 Selected ROSA-IV Test Series Description and Related Technical Reports (cont.)

Run ID	Date	Break	Condition	JAERI-Report/Article
SB-CL-15	1/26/88	0.5% CL	Cold leg w/o HPI, w/o AFW, bottom break , (orifice flush w/cold leg wall)	(Koizumi and Tasaka, 1988b), (Asaka et al., 1990)
SB-CL-16	3/2/88	0.5% CL	Cold leg w/o HPI, w/o AFW, top break , (orifice flush w/ cold leg wall)	(Koizumi and Tasaka, 1988b), (Asaka et al., 1990)
SB-CL-18	5/25/88	5% CL	Cold leg w/o HPI, w/o AFW, side break (orifice in branch pipe), repeat of SB-CL-08 with improved SG ΔP measurements. This is CSNI ISP-26.	(Kumamaru et al., 1989), (Kukita et al., 1992), (Glaeser et al., 2000)

21.2 TEST FACILITY DESCRIPTION

The LSTF is a 1/48 volume scale representation of a Westinghouse four-loop 3423 MWt PWR. Figure 21.2-1 is a schematic diagram of the facility. The LSTF consists of two equal volume loops, A and B, with a pressurizer attached to the hot leg of loop A. Table 21.2-1 compares the major design characteristics of the LSTF and the PWR. The core simulator contains 16 square 7x7 and 8 semi-crescent heater rod assemblies. The heater rods are 9.5 mm (0.374 inches) in diameter and 3.66 m (12 feet) in length. To simulate possible effects of non-uniform radial power distribution there are low, average and high power assemblies. The core utilizes chopped cosine axial power distribution.

The maximum power in the facility at steady state is 10 MW, which is equivalent to 14 percent of the scaled steady state core power of the reference PWR.

The secondary coolant system consists of two steam generators, main and auxiliary feed water pumps, and condensing system. The height of the LSTF steam generator is the same as in the reference PWR. The downcomer of each steam generator consists of four pipes located outside the steam generator vessel. The pipes are sized to provide a representative volume and width of a typical steam generator downcomer. Each steam generator contains 141 U-tubes with 19.6 mm (0.772 inches) inside diameter (ID) and 25.4 mm (1.0 inches) outside diameter (OD). Primary and secondary steam separators are included in each steam generator vessel.

The LSTF Emergency Core Cooling System (ECCS) consists of a high pressure charging system, a high pressure injection system, a low pressure injection system, an accumulator system, and a residual heat removal system.

The operational setpoints of the LSTF are detailed in Table 21.2-2. A detailed description of the facility is available in the JAERI documents (The ROSA-IV Group, 1985) and (The ROSA-IV Group, 1989).

21.2.1 Important Physical Phenomena and Scaling Considerations

The ROSA-IV LSTF is designed to conduct tests which provide important information regarding the behavior of a Westinghouse PWR during a small break LOCA transient. The scaling, relative to the typical 4-loop PWR, is such that the tests conducted can reproduce realistically the most important small break thermo-hydraulic phenomena. Since it is practically impossible to design a small test facility that can reproduce all aspects of the behavior of a complex system like a PWR, proper scaling can be achieved for only a few key small break LOCA phenomena.

The key scaling ratios of the ROSA-IV LSTF against a typical PWR are presented in Table 21.2-1.

At steady state conditions the core simulator power is 10 MW, which is 14% of the 1:48 scaled power of the reference PWR, resulting in a 1:342 power ratio at steady state conditions. The core flow ratio at steady state is 1:342 in order to achieve initial primary side temperatures representative of a PWR. Under these conditions the steady state power-to-volume (power density) ratio is approximately 1:7.

Preserving power-to-volume ratio of 1:1 assures that the time scale of the simulated transient phenomena is prototypical of the PWR. To achieve this ratio during the important phases of the small break LOCA transient, the power of the LSTF core simulator is actively controlled and follows a predefined power-vs-time curve which assures that beyond 30 seconds after reactor trip the simulated decay heat is scaled 1:48 to that of the representative PWR. In the small break tests, immediately after the break the pump speed is briefly increased and then follows a predefined coastdown curve, which assures that fluid velocities typical of a PWR are achieved during the initial phase of the transient.

Since the elevations of the major components of the LSTF are full-scale and match those of the real PWR the height scaling ratio is 1:1. Preserving the same height and characteristic elevations assures that the natural circulation phenomena important to core cooling and the general system behavior are adequately simulated in the tests. Preserving the bottom elevation of the cross-over legs is of great importance to observing the effects of a realistic depth of core uncover related to the loop seal clearance phenomenon.

Preservation of the same core height and fuel bundle geometry characteristics (square lattice, rod diameter, pitch, etc.) assures that important phenomena that might occur in the core during the different phases of the accident are simulated in a realistic manner. Some of these are void generation and distribution and related rod heatup during loop seal clearance, level swell and rod heatup during boiloff, etc.

With the height of key elevations preserved the same as the PWR, the scaling of each steam generator (volume and flow area ratios of 1:24 and U-tube surface area 1:25) assures that important thermo-hydraulic phenomena like primary-to-secondary heat transfer, natural circulation, reflux condensation and counter-current flow are simulated in a realistic manner. Note that one LSTF steam generator represents two PWR steam generators; therefore the total steam generator (SG) surface area scaling ratio is actually 1:48.

The diameter of the hot and cold leg pipes is large enough to allow the establishment of all possible flow regimes of significance that may develop in the real plant. This also allows investigating effects of break orientation on the small break LOCA (SBLOCA) transient.

The hot and cold legs, with a diameter of 207 mm (8.15 inches), are sized to conserve volume scaling and the ratio of length to the square root of the pipe diameter (L/\sqrt{D}) of the reference PWR. The (L/\sqrt{D}) ratio is in essence a Froude number and the 1:1 scaling relative to a PWR assures that flow regime transition would be manifested properly during the various tests, performed with the ROSA-IV LSTF.

The goal of preserving hot leg $L/\sqrt{D} = 1$ and volume ratio of 24 results in a hot leg flow area ratio of 12.68. Thus the flow area of the LSTF hot leg (and cold leg as well) is essentially twice the 1:24 scaled PWR hot leg area. This scaling distortion would create conditions where easier flow stratification in the hot and cold legs will be simulated during the tests compared to a real PWR small break transient.

As seen in Table 21.2-1, the scaling ratio of the upper core plate flow area is approximately 1:45, which is very close to the PWR/LSTF volume and power ratio of 1:48. This similarity creates the preconditions to simulate realistic fluid velocities and counter-current flow at the upper core plate during the SBLOCA tests.

Another phenomenon is the counter-current flow limitation (CCFL) that might occur at various locations of the primary system of a PWR. The importance of this phenomenon and its ranking with respect to its effect on the system behavior during the different phases of the LOCA transient have been discussed in Section 2.3.2, Volume 1. The design and scaling of the ROSA-IV LSTF allows for the effects of CCFL to be measured and observed at realistic PWR LOCA conditions. Detailed discussion of the CCFL considered at three key system locations (inlet of steam generator U-tubes, hot leg elbows and upper core plate) is provided in Section 21.10 and the ROSA-IV LSTF model described in Section 21.3.

Based on the discussion of the key scaling ratios presented above it is concluded that the tests conducted on the ROSA-IV LSTF can simulate the most important small break LOCA phenomena. Therefore, the available measurements and observations from various small break tests are appropriate for performing WCOBRA/TRAC-TF2 Model Assessments. Since the LSTF is a full height facility with exact representation of the key elevations of the individual PWR components, the modeling techniques developed, implemented and assessed in the LSTF test simulations can be adopted in the simulations of small break LOCA transients of the real PWR.

Table 21.2-1 Major Design Characteristics of LSTF and PWR

Characteristic	LSTF	PWR	PWR/LSTF
Pressure, MPa (psia)	15.5 (2250)	15.5 (2250)	1
Temperature, K ($^{\circ}$ F)	598 (617)	598 (617)	1
Number of fuel rods	1064	50,952	48
Core height, m (ft)	3.66 (12)	3.66 (12)	1
Total Primary Fluid volume, m^3 (ft^3)	7.23 (255.3)	374 (12,254.2)	48
Vessel Fluid Volume, m^3 (ft^3)	2.675 (94.47)	131.7 (4650.9)	49.24
Core Volume, m^3 (ft^3)	0.4078 (14.4)	17.5 (618.0)	42.91
Upper Plenum Volume (incl. end box), m^3 (ft^3)	0.5472 (19.32)	28.4 (1002.9)	51.9
Lower Plenum Volume, m^3 (ft^3)	0.5802 (20.49)	29.62 (1046.0)	51.05
Core power, MW	10	3423(t)	342 ⁽²⁾
Power density, kW/ m^3 (kW/ ft^3)	1383 (39.17)	9152.4 (279.33)	7.1
Core inlet flow, kg/sec (lbm/sec)	48.8 (97.6)	16700 (33,400)	342
Core Flow Area, m^2 (ft^2)	0.1134 (1.22)	4.75 (51.13) ⁽¹⁾	41.9
Upper Core Plate Area, m^2 (ft^2)	0.066 (0.71)	2.94 (31.65) ⁽¹⁾	44.5
Upper Plenum Area, m^2 (ft^2)	0.159 (1.71)	6.92 (74.48) ⁽¹⁾	43.5
Downcomer gap, m (in.)	0.053 (2.09)	0.26 (10.24)	4.9
Hot leg			
Diameter (D), m (ft)	0.207 (0.679)	0.737 (2.418)	3.56
Length (L), m (ft)	3.69 (12.1)	6.99 (22.93)	1.89
L/\sqrt{D} , $m^{1/2}$ ($ft^{1/2}$)	8.14 (14.68)	8.14 (14.68)	1.0
Volume $\left(\frac{\pi}{4} D^2 L\right)$, m^3 (ft^3)	0.124 (4.38)	2.98 (105.2)	24.0
Area $\left(\frac{\pi}{4} D^2\right)$, m^2 (ft^2)	0.03365 (0.362)	0.4266 (4.59)	12.68
Number of loops	2	4	2
Number of tubes in steam generator	141	3382	24.0
Total Inner Surface Area of U-tubes, m^2 (ft^2)	171 (1840.6)	4214 (45359.1)	25
Length of steam generator tube (average), m (ft)	20.2 (66.3)	20.2 (66.3)	1.0

a.c

Table 21.2-2 Standard Operational Setpoints of the ROSA-IV Large Scale Test Facility

Event	Setpoint
Reactor scram signal, MPa (psia)	12.97 (1881.1)
Initiation of pump coastdown	With reactor scram
Safety injection signal, MPa (psia)	12.27 (1779.6)
High pressure charging ⁽¹⁾	12 s after safety injection signal
Safety injection	17 s after safety injection signal
High pressure injection cutoff, MPa (psia) ⁽²⁾	10.7 (1551.9)
Low pressure injection cutoff, MPa (psia) ⁽³⁾	1.29 (187.1)
Accumulator injection, MPa (psia)	4.51 (654.1)
Main feedwater termination	With reactor scram
Turbine throttle valve closure	With reactor scram
Auxiliary feedwater initiation ⁽⁴⁾	28 s after reactor scram

Notes:

1. High-pressure charging was not actuated during the SB-Cl-18 and SB-CL-14.
2. High-pressure injection was not actuated during the SB-CL-18 test and SB-CL-14.
3. The SB-CL-18 test was terminated prior to the actuation of low-pressure injection.
4. Auxiliary feedwater was not actuated during the SB-CL-18 test.

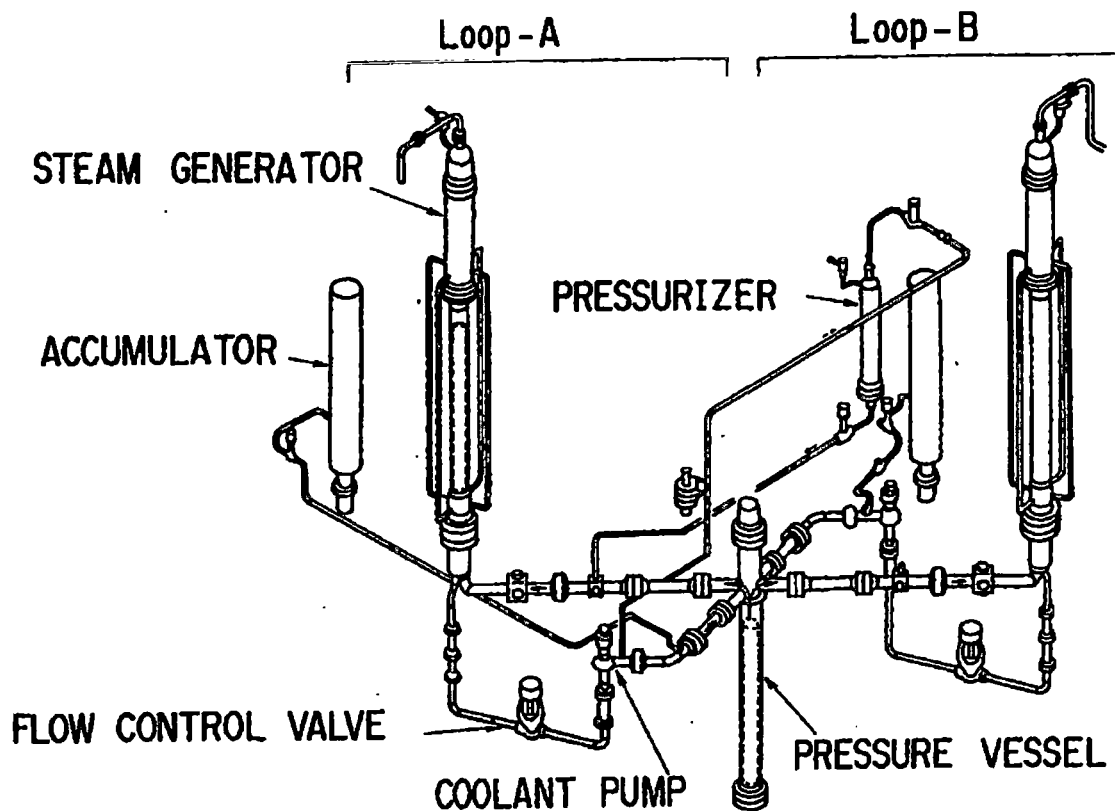


Figure 21.2-1 Schematic Diagram of LSTF

21.3 DESCRIPTION OF WCOBRA/TRAC-TF2 MODEL FOR ROSA/LSTF-IV

[

|

]^{a,c}

Vessel Model:

Figure 21.3-1 shows the WCOBRA/TRAC-TF2 noding of the LSTF pressure vessel. Figures 21.3-2 through 22.3-6 show the transverse channel connections in each of the vessel sections. Figure 21.3-7 shows the core simulator map of the LSTF. [

]^{a,c}

The upper plenum modeling of the LSTF facility includes [

]^{a,c}

]^{a,c}**Loop Model:**

The piping outside the LSTF pressure vessel is modeled by using 1-D components. Figure 21.3-8 shows the general 1-D loop noding diagram of the LSTF and Figure 21.3-9 provides more detail in the noding of the hot leg, steam generator and the loop seal regions.

Each hot leg, including the elbow at the inlet of the steam generator, is modeled [

]^{a,c}

As seen from Figure 21.3-8 and the more detailed Figure 21.3-9, primary flow enters the steam generator [

]^{a,c}

The steam generator secondary side includes sufficient detail to model recirculation in the downcomer and separation in the vapor dome region. [

]^{a,c}

During steady state simulation, and prior to reactor trip, steam leaving the generators passes through a TEE component and VALVE component to a constant pressure BREAK. At reactor trip, the main steam isolation valve (MSIV) is closed and flow goes through a VALVE component representing the main steam safety valve (MSSV) to a second BREAK component that provides a constant pressure boundary condition at the MSSV setpoint pressure.

Figure 21.3-9 shows the loop seal nodalization. Flow from the steam generator outlet passes through [

]^{a,c}

The safety injection system is shown in Figure 21.3-8. Combined high pressure safety injection plus charging flows to each loop are modeled [

]^{a,c} accumulator setpoint of 4.51 MPa (654.1 psia). VALVE Components 216 and 226 are isolation valves. The combined safety injections from the pumps and accumulators enter each of the cold legs through the side pipes of TEE Components 15 and 25 to loops A and B, respectively.

The cold leg condensation model, described in Section 6.3.6 of Volume 1, is [

]^{a,c}, consistent with the SI modeling approach and validation presented in Section 17.

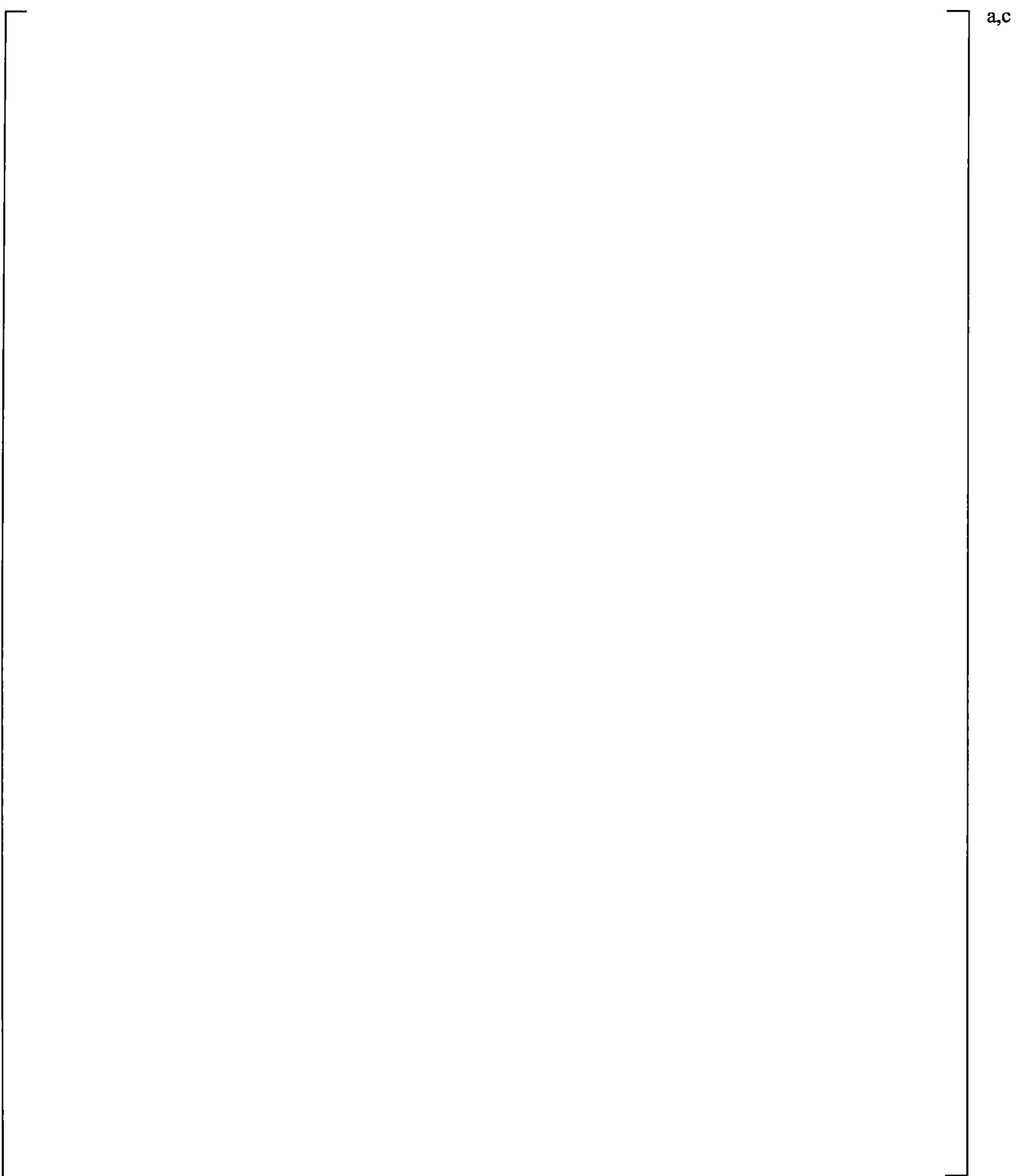


Figure 21.3-1 WCOBRA/TRAC-TF2 Model of LSTF Pressure Vessel

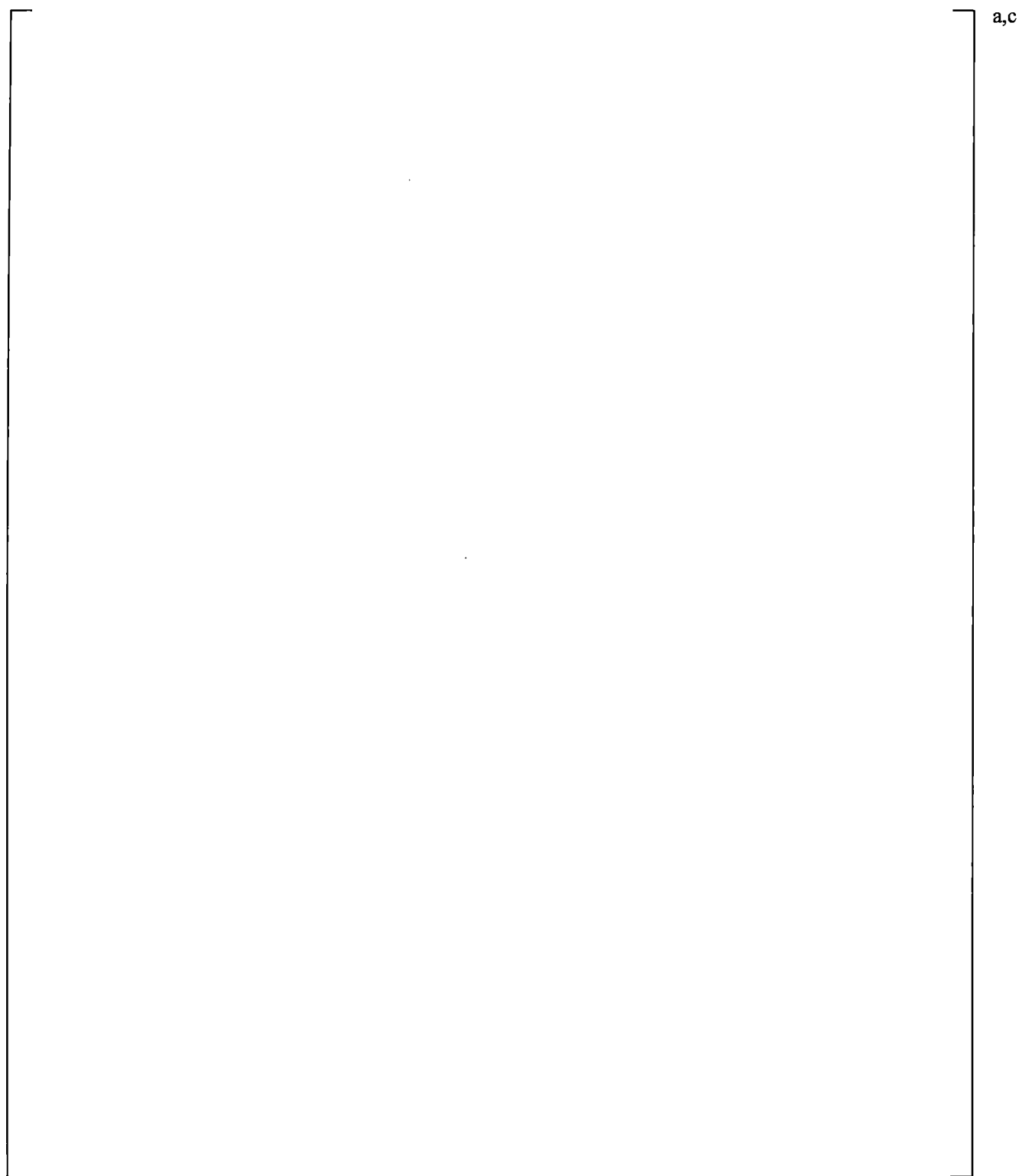


Figure 21.3-2 LSTF Pressure Vessel Sections 1 and 2

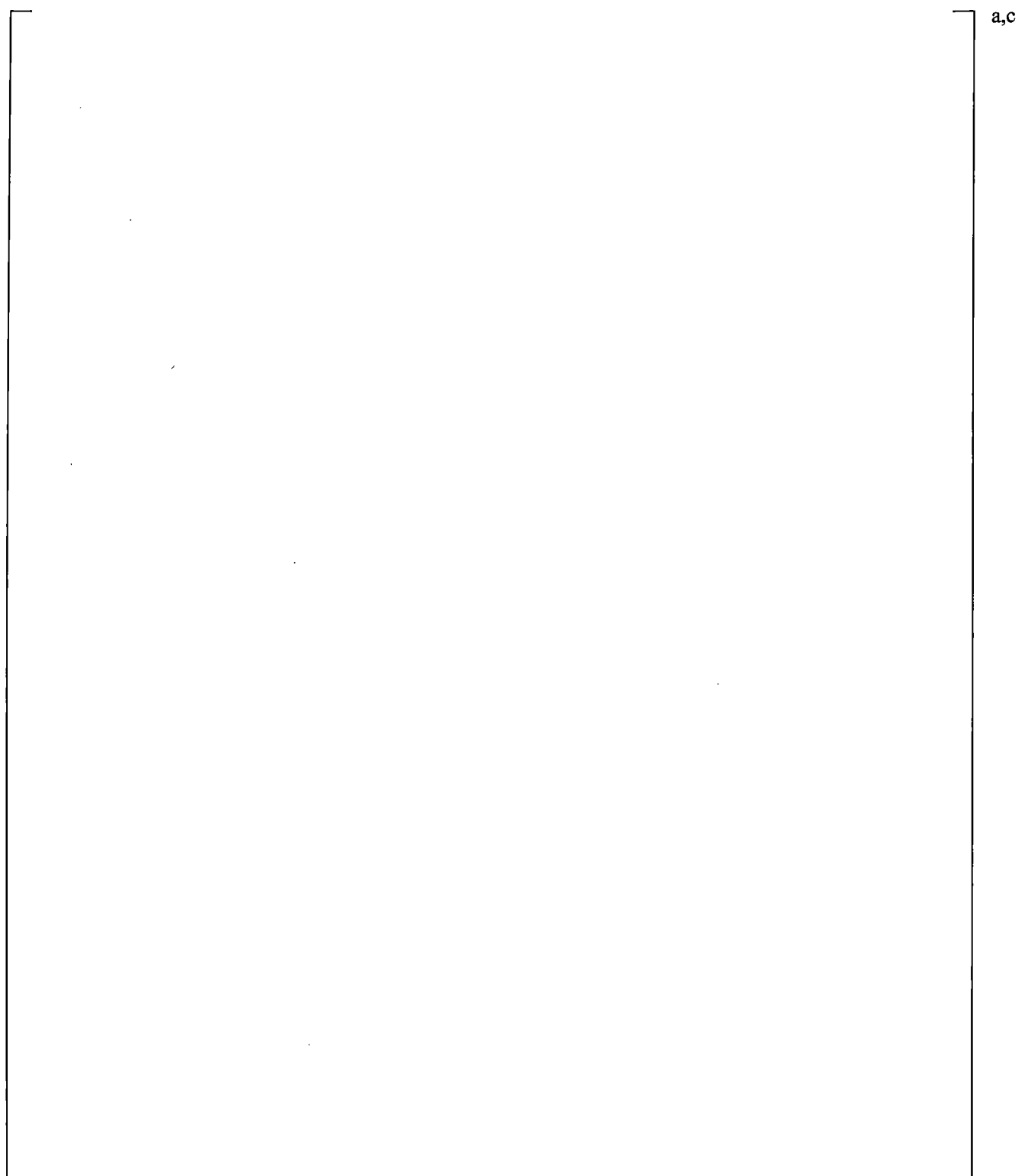


Figure 21.3-3 LSTF Pressure Vessel Sections 3 and 4

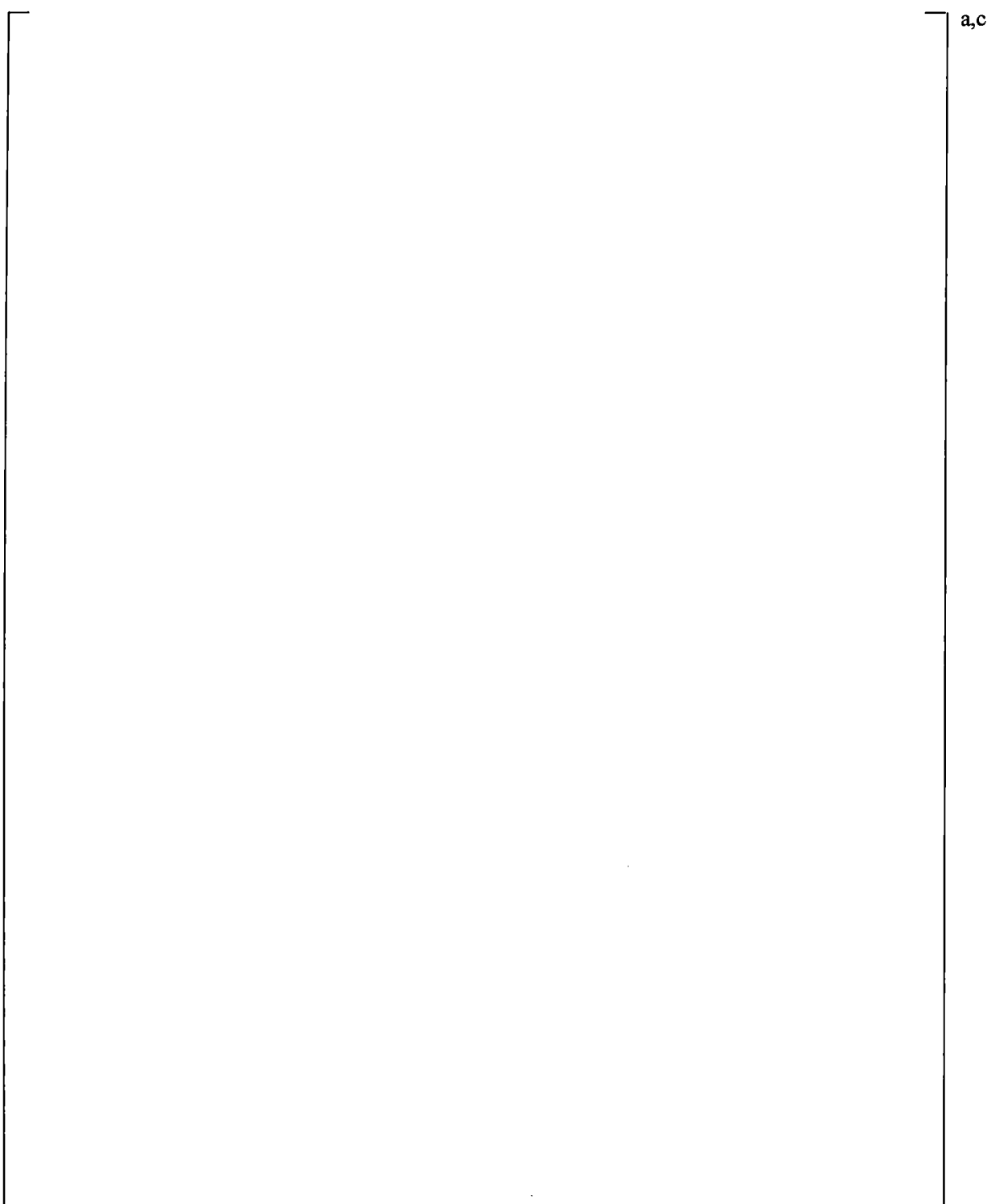


Figure 21.3-4 LSTF Pressure Vessel Sections 5 and 6

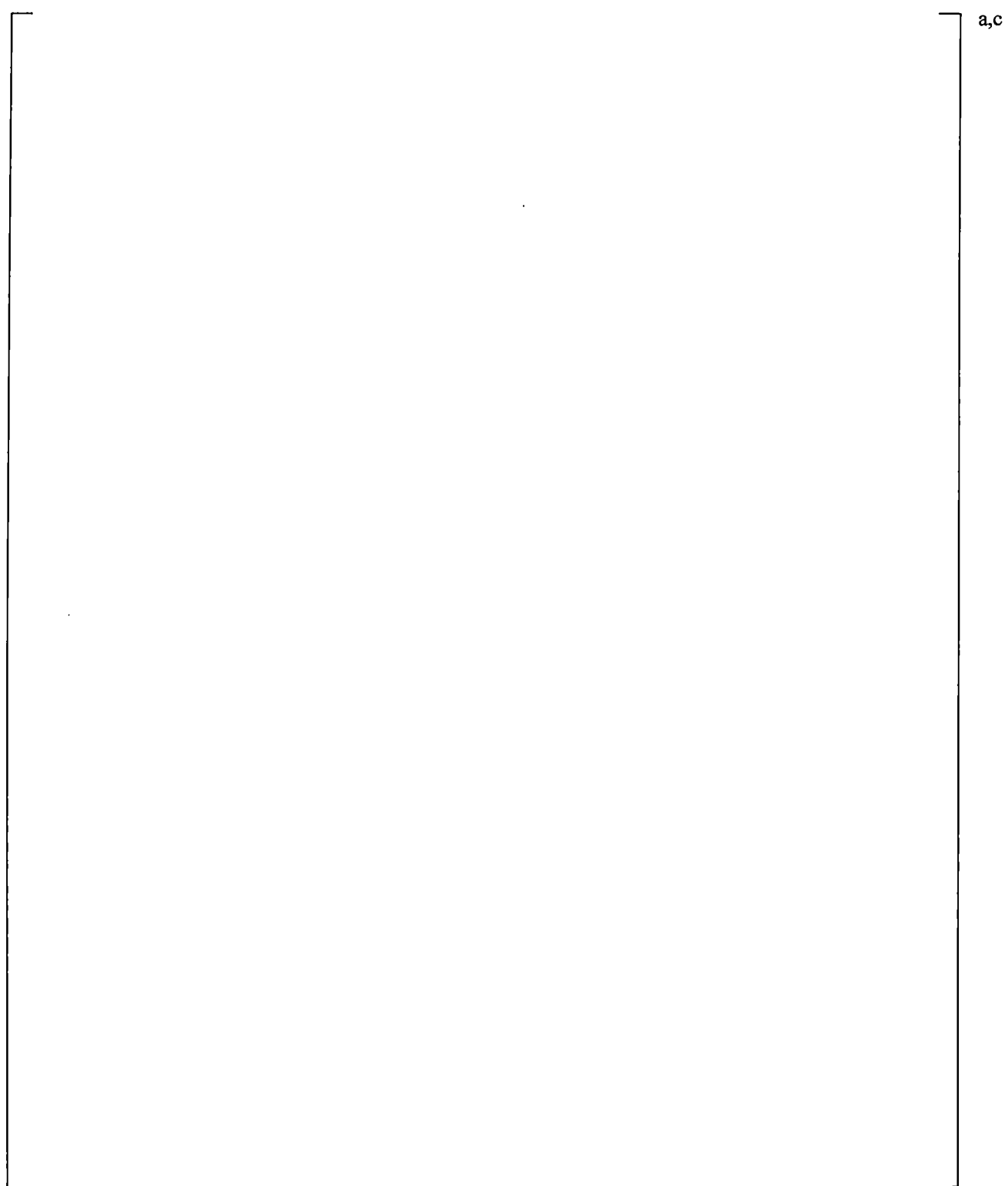


Figure 21.3-5 LSTF Pressure Vessel Sections 7 and 8

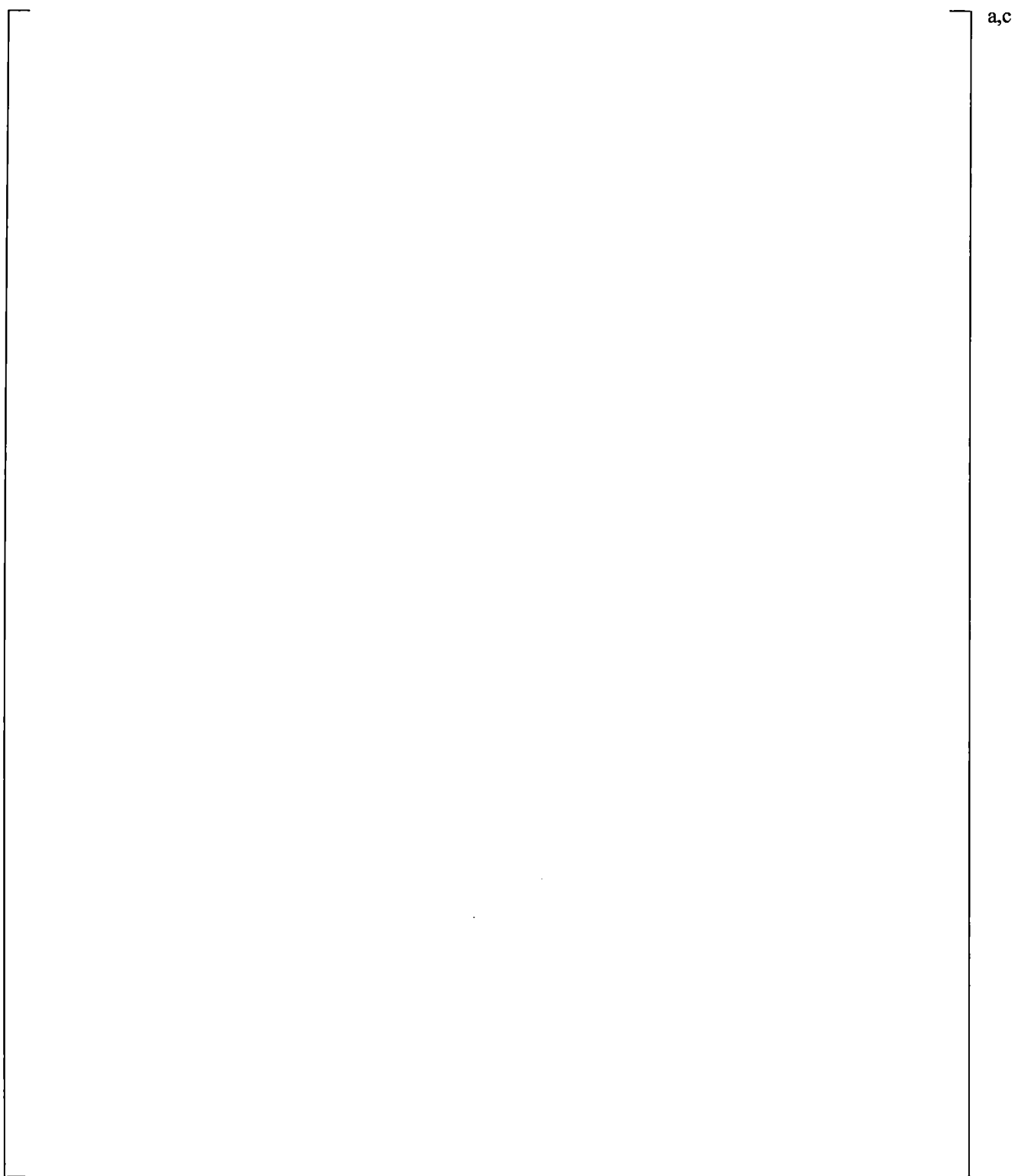


Figure 21.3-6 LSTF Pressure Vessel Sections 9 and 10

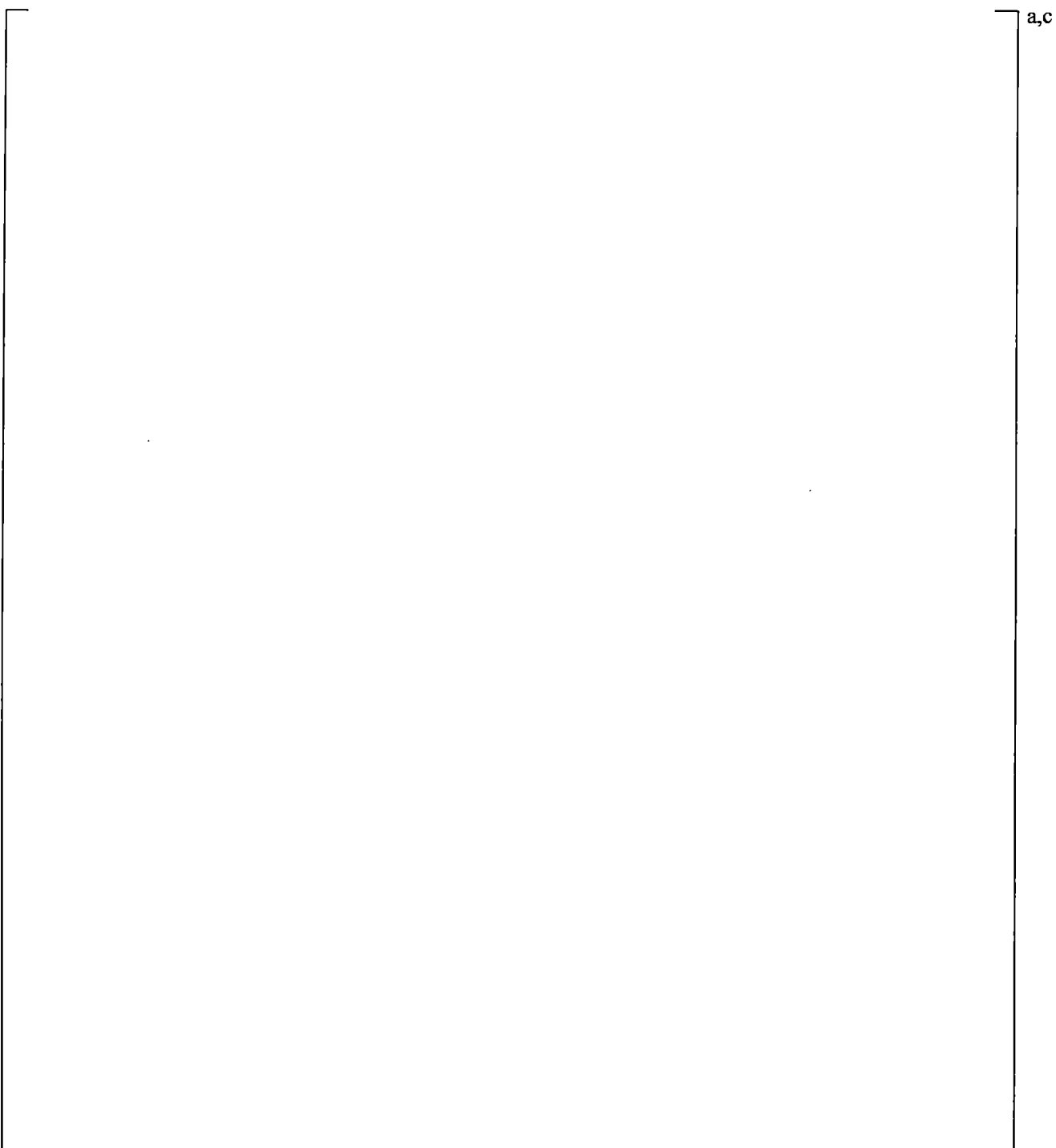


Figure 21.3-7 ROSA-IV LSTF Core Simulator Map

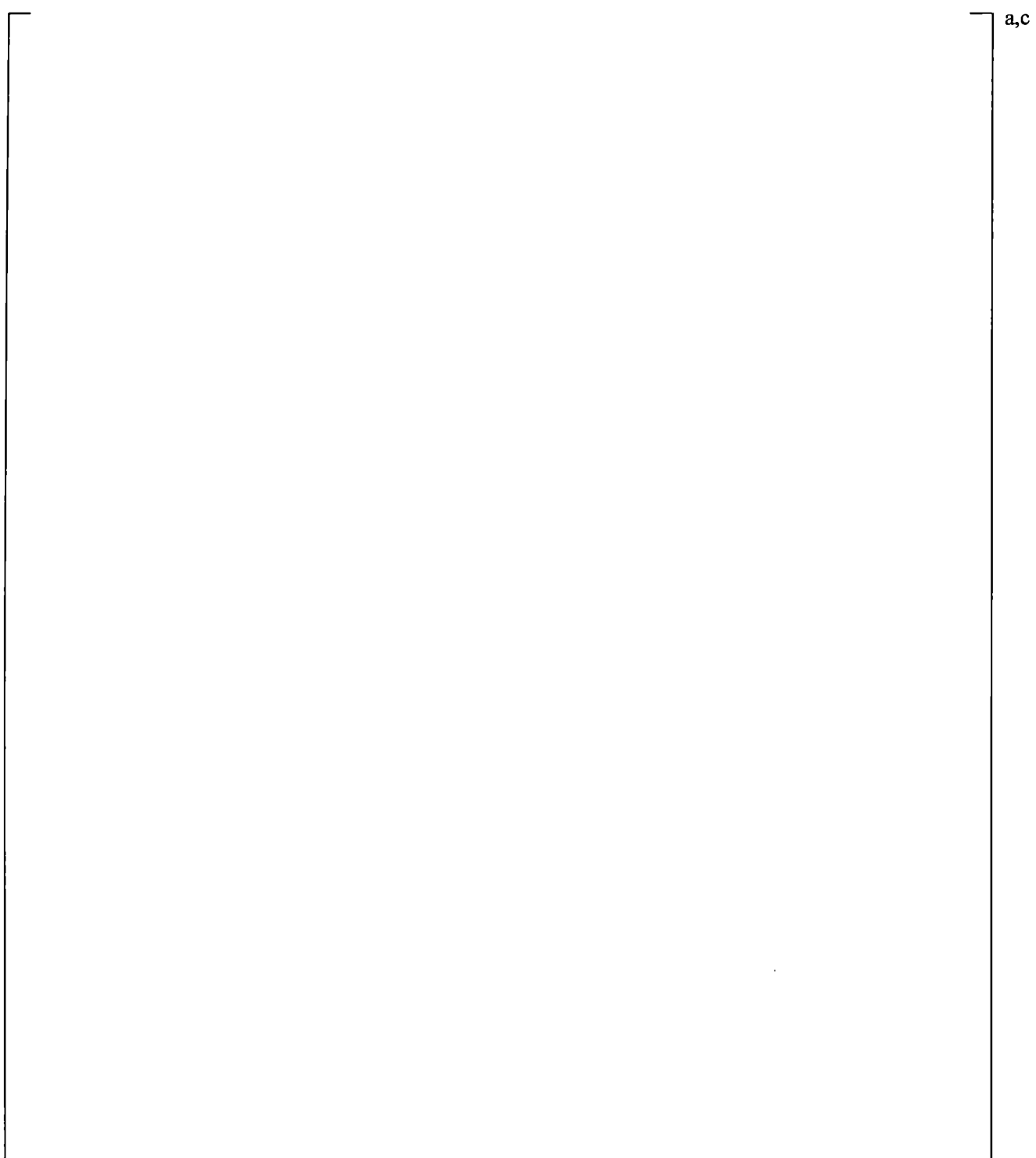


Figure 21.3-8 WCOBRA/TRAC-TF2 Loop Noding Diagram of LSTF

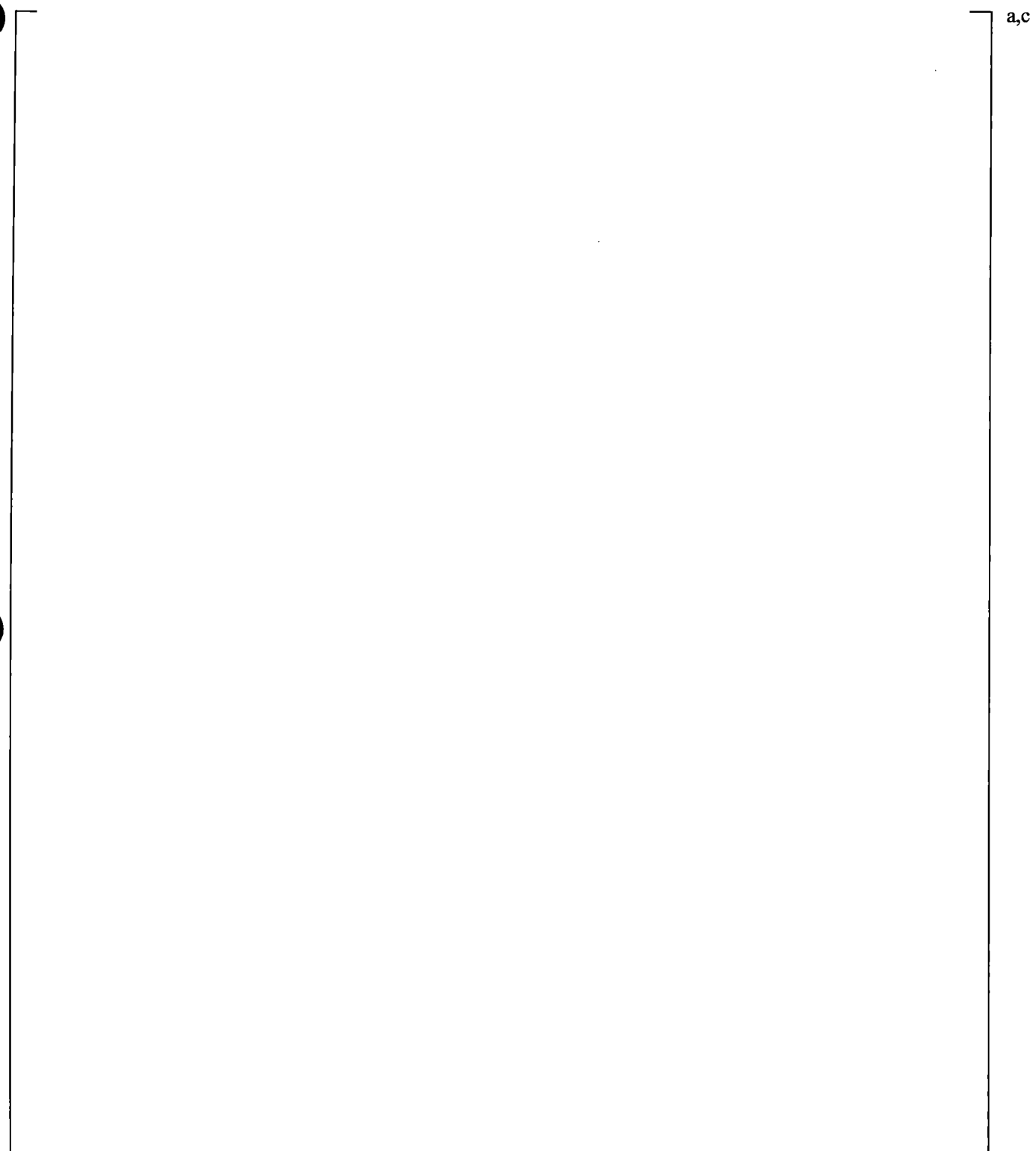


Figure 21.3-9 Hot Leg (Including Pressurizer), Steam Generator and Cross-Over Leg Noding

21.4 SIMULATION OF SB-CL-18, 5-PERCENT COLD LEG SIDE BREAK

21.4.1 Description of the SB-CL-18 Test Boundary and Initial Conditions

Experiments as part of ROSA-IV (LSTF-IV) were conducted for several different break areas.

Test SB-CL-18 simulated a 5-percent cold leg break, which corresponds to approximately a 6-inch break

in a PWR. The break was located in loop B and had a horizontal orientation. Unlike test SB-CL-05,

high-head safety injection (HHSI) and low-head safety injection (LHSI) were not modeled in this test.

The experimental results are available in the test data report JAERI-M 89-027 (Kumamaru et al., 1989).

This test is also known as OECD/NEA/CSNI International Standard Problem No. 26 (Kukita et al., 1992).

For each of the break test simulations, verification that the WCOBRA/TRAC-TF2 model of the LSTF-IV adequately represented the facility was accomplished through a full-power, 300-seconds steady state simulation. Table 21.4-1 summarizes initial conditions achieved for the SB-CL-18 test at the end of the 300 seconds steady state calculation. At the end of this 300-seconds simulation, predicted and measured system parameters were compared to ensure reasonably good agreement.

The operational setpoints for this test are the same as the standard set implemented for all ROSA-IV tests, provided in Table 21.2-2. As described in the test report (Kumamaru et al., 1989), the high-pressure charging and high-pressure injection were not actuated for this test, since they were assumed to fail. Low-pressure safety injection did not occur since the test was terminated before the cut-off pressure of 1.29 MPa was reached. Auxiliary feed water was not actuated as well.

The core power was scrammed once the primary pressure decreased below 12.97 MPa (1881 psia). The core decay heat was simulated following a pre-programmed curve, which accounts for actinides and delayed neutron effects and gives a slower decrease than the American Nuclear Society (ANS) standard. The decay heat curve implemented during the test and used in the SB-CL-18 simulations is provided in Table 21.4-2.

On the LSTF, the initial conditions prior to the initiation of the test are established at pump speeds (respectively fluid velocities) that are much lower than those existing at the PWR at steady state conditions. This was done so that, with the reduced core power at the LSTF, the initial cold leg and hot leg temperatures are preserved similar to a PWR. Immediately following the break, the pump speed was increased to achieve loop flow rates similar to the reference PWR. Loss of offsite power is assumed and the reactor coolant pumps are tripped to begin coastdown coincident with reactor scram. In the transient simulation, the pumps followed a coastdown curve consistent with the test. The main feed water was stopped, and the secondary sides of the two steam generators were isolated by closure of their MSIVs coincident with reactor trip.

21.4.2 Steady State Calibration and Transient Calculation Procedures

Steady State Calculation

In the SB-CL-18 test simulation first a steady state calculation is performed (in this case 300 seconds) in order to achieve the desired primary and secondary side conditions, according to those measured at the test. The initial steady state conditions achieved for the SB-CL-18 test are presented in Table 21.4-1.

Transient Calculation Procedure

The WCOBRA/TRAC-TF2 simulation of the LSTF-IV 5-percent cold leg break test SB-CL-18 is initiated by [

]^{a,c}

The transient calculation procedure described above is implemented for all ROSA LSTF-IV cold leg break test simulations presented in this section. Depending on the break size being simulated, the appropriate set of HRM1PM, HRM2PM and HRMOFD multipliers is used, in accordance with the break modeling described in Section 12.5.4.

Transient Acceptance Criteria

The primary acceptance criterion for the simulations of the ROSA-IV test documented herein is achieving the best possible consistency with the available test data. Particular attention is given to the accurate prediction of key transient phenomena like system depressurization, timing and magnitude of loop seal clearance, boiloff, etc. [

]^{a,c}

[

]^{a,c}

21.4.3 Results and Conclusions From the SB-CL-18 Simulations

This section presents the results of two SB-CL-18 test transient simulations. Both simulations were performed with break flow discharge coefficients []^{a,c}. One of the simulations was performed with CCFL enforced at the steam generator U-tubes []^{a,c}, the hot leg elbows []^{a,c} and upper core plate (Bankoff correlation). To illustrate the degree of conservatism of the adopted CCFL modeling approach, the other simulation was performed without any CCFL limits enforced. In the remainder of this section, similar pairs of simulations will commonly be referred to as “CCFL on” and “CCFL off” simulations, or simulations “with and without CCFL,” respectively. Note that CCFL may be predicted to occur even without enforcing the CCFL limits, as a result of the interfacial drag.

In this test, the primary system rapidly depressurized and equilibrated at a pressure slightly higher than the steam generator secondary pressure, at approximately 8.3 MPa (~1200 psia), Figure 21.4-1, until the loop seal cleared at about 140 seconds, (see DPE080-LSA in Figure 21.4-3 and DPE220-LSB in Figure 21.4-4).

After loop seal clearance, the break quality changed from a low quality mixture to primarily vapor and the primary system continued to depressurize.

As the primary system continued to drain, liquid is redistributed among the different regions; the core and downcomer, the upper plenum, hot legs and steam generator uphill and downhill side, and the uphill and downhill sides of the loop seal piping. A manometric (hydrostatic) balance is established between the liquid present in these regions during the transient. Prior to the loop seal clearance, the core collapsed level became depressed nearly to the bottom of the core, while liquid remained in the uphill side of the loop seal. At this time, the heater rods heated up rapidly. While most of the liquid had drained from the steam generator tubes, some of it remained in the steam generators’ inlet plenums and the bottom of the uphill side. After steam slipped through the loop seals, the core level recovered and most of the water was pushed out of both loop seals through the cold legs and into the downcomer.

Test SB-CL-18 had a core depression during loop seal clearance that was considerably below the elevation of the bottom of the loop seal piping. Osakabe (Osakabe et al., 1987) attributed this to a significant liquid holdup in the uphill side of steam generator tubes. During this core level depression, the peak rod cladding temperature at the test increased by approximately 190K (342°F) reaching a maximum of approximately 740K (872°F), Figure 21.4-6. After loop seal clearance, the core level recovered quickly and the rods were quenched.

Figures 21.4-1 through 21.4-20 compare predicted and measured results for the 5-percent cold leg break test SB-CL-18. Each of the figures shows SB-CL-18 simulation results with and without CCFL. Figures 21.4-21 through 21.4-24 present calculated CCFL conditions at key system locations (steam generator U-tube inlets, hot leg elbows and upper core plate) extracted from the SB-CL-18 simulations with and without CCFL enforced. Figures 21.4-25 through 21.4-27 show the calculated cladding temperatures at the 7.33-ft core elevation compared to the test data.

System Depressurization and Break Flow

Figure 21.4-1 compares predicted and measured primary system pressure. [

]^{a,c}

Break flow is compared in Figure 21.4-2. Early in the transient, flow out of the break is sub-cooled single-phase liquid. [

]^{a,c}

Loop Seal Clearance and Core Uncovery

Figures 21.4-3 and 21.4-4 show a comparison of the calculated and measured loop seal differential pressures. In the test, loop seal venting occurs at approximately 140 seconds. [

]^{a,c} The test data and calculations also show that after the loop seals clear, steam venting is established through both cross-over legs.

Before the loop seals vent, the collapsed liquid level in the core is depressed. Figure 21.4-5 compares calculated and measured inner vessel differential pressure, which is an indicator of the inner vessel collapsed level. [

]^{a,c}

Core heat-up occurs during the loop seal clearance period as the core is temporarily uncovered. Figure 21.4-6 compares the PCT predicted by WCOBRA/TRAC-TF2 to the maximum cladding heat-up observed in the data. [

]^{a,c}

The depth of core uncover during the loop seal clearance period depends upon the manometric balance between the core and downcomer, and the sum of pressure drops through the loop and uphill side of the loop seal piping. An important static head exists on the uphill side of the steam generator tubes, where water condensed in the tubes collects because of CCFL and flooding in the steam generator up-hill tubes. Figures 21.4-7 and 22.4-8 show a comparison of the predicted and measured differential pressures in the uphill steam generator tubes for SG-A and SG-B respectively. The calculation results in these two figures should be analyzed in conjunction with the calculated CCFL conditions at the steam generator U-tube inlets shown in Figures 21.4-21 and 21.4-22.

The calculated downcomer differential pressures, Figure 21.4-18, are in good agreement with the test.

Steam Generator U-tube and Inlet Plenum Draining

[

]^{a,c}

Figures 21.4-11 and 21.4-12 show a comparison of the calculated and measured differential pressures across the two steam generators. From those two figures, it is evident that during the loop seal clearance period ($t > 150$ sec) in both simulations the code calculates steam generator resistance [

]^{a,c}

Figures 21.4-13 and 21.4-14 show the calculated and measured collapsed liquid levels in the steam generator inlet plenums. [

]^{a,c}

[

]^{a,c}

Upper Plenum Draining

The upper plenum differential pressures (indicators of the liquid levels in the upper plenum) are shown in Figure 21.4-17. Until about 110 seconds the predictions are consistent with the test. Later on, the upper plenum level [

]^{a,c}

The almost complete draining of the upper plenum, observed at the test between 125 and 160 seconds, Figure 21.4-17, is related to the significant core uncover due to the loop seal clearance depression, Figure 21.4-5. The fast recovery of the upper plenum level between 160 and 170 seconds is caused by both the recovery of the core inventory and the draining of the steam generators, especially the draining surge from the steam generator inlet plenums, seen in Figures 21.4-13 and 21.4-14. Relatively constant liquid level is measured in the upper plenum until 330 seconds maintained by the gradual draining of the steam generator inlet plenums and the hot legs. As the system inventory is further depleted, due to the steam discharged through the break, the upper plenum drains completely by 400 seconds.

]^{a,c}

Rod Cladding Heatup

Figures 21.4-25 through 21.4-27 show a comparison of measured (TW curves) and calculated rod cladding temperatures (TCLAD curves) at the 7.33-ft elevation in the core; the TCLAD curves are from the SB-CL-18 simulation with CCFL enforced. The period of interest for this discussion is between 124 and 320 seconds; this is the period when counter-current flow conditions are predicted to occur at the UCP. The 7.33-ft elevation is selected since it is one of the locations where significant rod heatup was measured at the test during this period of interest due to loop seal core uncover.

Figure 21.4-25 shows the calculated and measured cladding temperatures of the low power rods. As seen in this figure, the test measurements show that only 4 out of 15 rods heated up briefly during the loop seal clearance period. The heatup of these (low power) rods was brief and the temperature increase did not exceed 50K. According to the measurements, the majority of the high-power rods heated up during the loop seal clearance period, Figure 21.4-26. Only 5 out of 13 rods in the inner average power region experienced heatup, according to Figure 21.4-27. In summary, the rod temperature measurements at the 7.33-ft elevation show that during the period of interest the peripheral (low power) region of the core simulator received and retained most of the fluid that was draining from the upper plenum. As a result, the inner average and high power regions tend to be depleted from coolant and experience more severe rod heatup.

]^{a,c}

Accumulator Injection

Figures 21.4-19 and 21.4-20 show the calculated and measured accumulator injection flows. The calculated initiation of the accumulator injection and the timing of the turn-around of the boil-off PCT, Figure 21.4-6, are consistent with those observed at the test. [

]^{a,c}

Summary

[

]^{a,c}

Table 21.4-1 Steady-State Parameter Checklist (Initial Conditions) for the SB-CL-18 Test

Parameter	Target (Measured)	a c
Pressurizer pressure, MPa (psia)	15.5 (2248)	
Hot leg fluid temperature, K (°F)	599 (619)	
Cold leg fluid temperature, K (°F)	564(555)	
Core power, MW (MBTU/hr)	10	
Core inlet flow rate, kg/sec (lbm/s)	48.7 (107.3)	
HL-to-DC Leakage Flow Rate, kg/sec (% core flow)	0.124 (0.25%)	
DC-to-UH Bypass Flow Rate, kg/sec/sec (% core flow)	0.146 (0.3%)	
Pressurizer water level, m (ft)	2.6 (8.5)	
Pump speed, rad/sec (rpm)		
For Pump A	80.5 (769)	
For Pump B	83.3 (796)	
Hot leg ΔP, kPa (psi)		
For Loop A	3.62 (0.53)	
For Loop B	3.50 (0.50)	
Steam generator inlet to outlet, kPa (psi)		
For Loop A	1.35 (0.19)	
For Loop B	1.46 (0.21)	
Cross-Over Leg Down ΔP, kPa (psi)		
For Loop A	-45.3 (-6.57)	
For Loop B	N/A	
Cross-Over Leg Up ΔP, kPa (psi)		
For Loop A	26.6 (3.86)	
For Loop B	26.6 (3.86)	
Downcomer ΔP, kPa (psi)	61.5 (8.92)	
Downcomer to upper plenum ΔP, kPa (psi)	2.65 (0.38)	
Lower Plenum ΔP, kPa (psi)	12.9 (1.87)	
Core ΔP (including lower core plate), kPa (psi)	33.2 (4.8)	
Upper Plenum ΔP, kPa (psi)	13.5 (1.96)	
Steam generator secondary pressure, MPa (psia)	7.35 (1066)	
Steam generator secondary level, m (ft)	10.6 (34.8)	
Steam generator feedwater temperature, K (°F)	494 (429.5)	
Steam generator feedwater flow rate, kg/sec (lbm/s)	2.7 (5.95)	
Steam generator secondary circulation flow, kg/sec (lbm/s)	16.5 (36.3)	

Table 21.4-2 Decay Heat Power Curve Used in the SB-CL-18 Test Simulation

Test Time sec	WC/T Time sec	Test Power MW	Normalized Power -
(1)	(2)	(3)	(4)
0	300.0	10.022	1.00000
46.6	346.6	10.025	1.00030
57.6	357.6	8.8175	0.87981
77.6	377.6	7.2675	0.72516
97.6	397.6	6.0925	0.60791
117.6	417.6	5.1775	0.51661
167.6	467.6	3.6325	0.36245
217.6	517.6	2.8650	0.28587
417.6	717.6	1.7925	0.17886
617.6	917.6	1.5800	0.15765
817.6	1117.6	1.5100	0.15067
899.6	1199.6	1.4750	0.14718

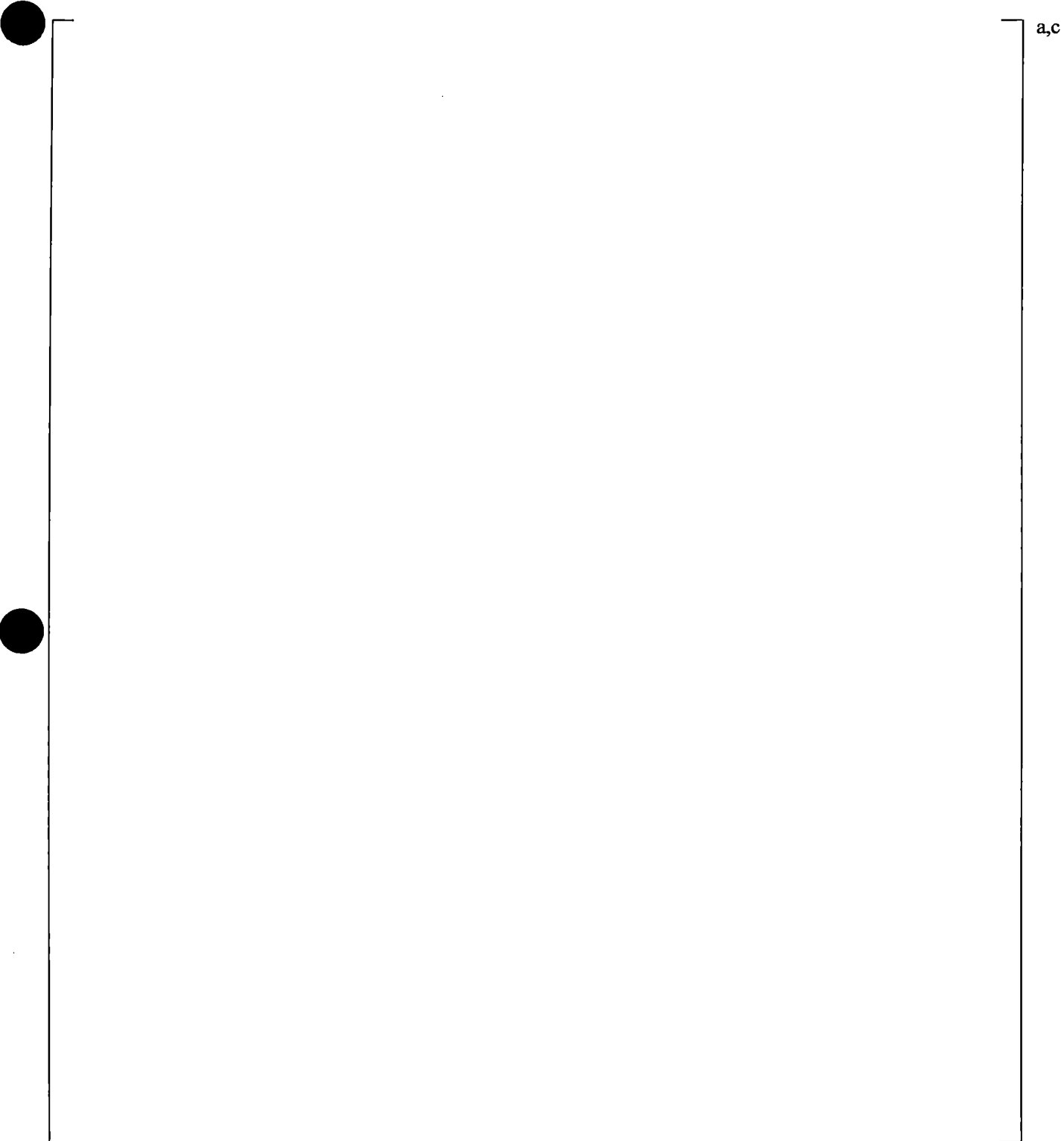


Figure 21.4-1 Pressurizer Pressure

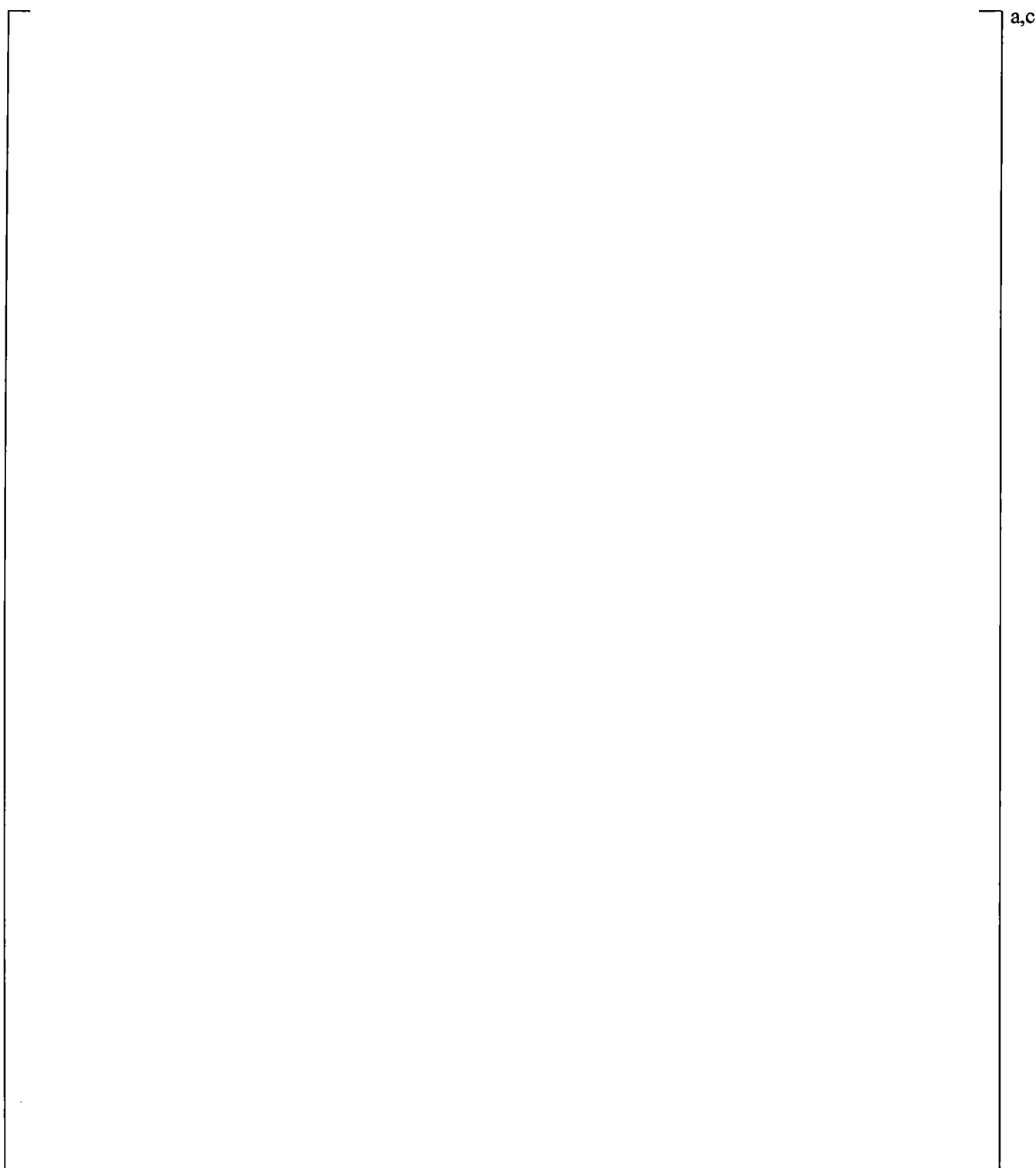


Figure 21.4-2 Break Flows

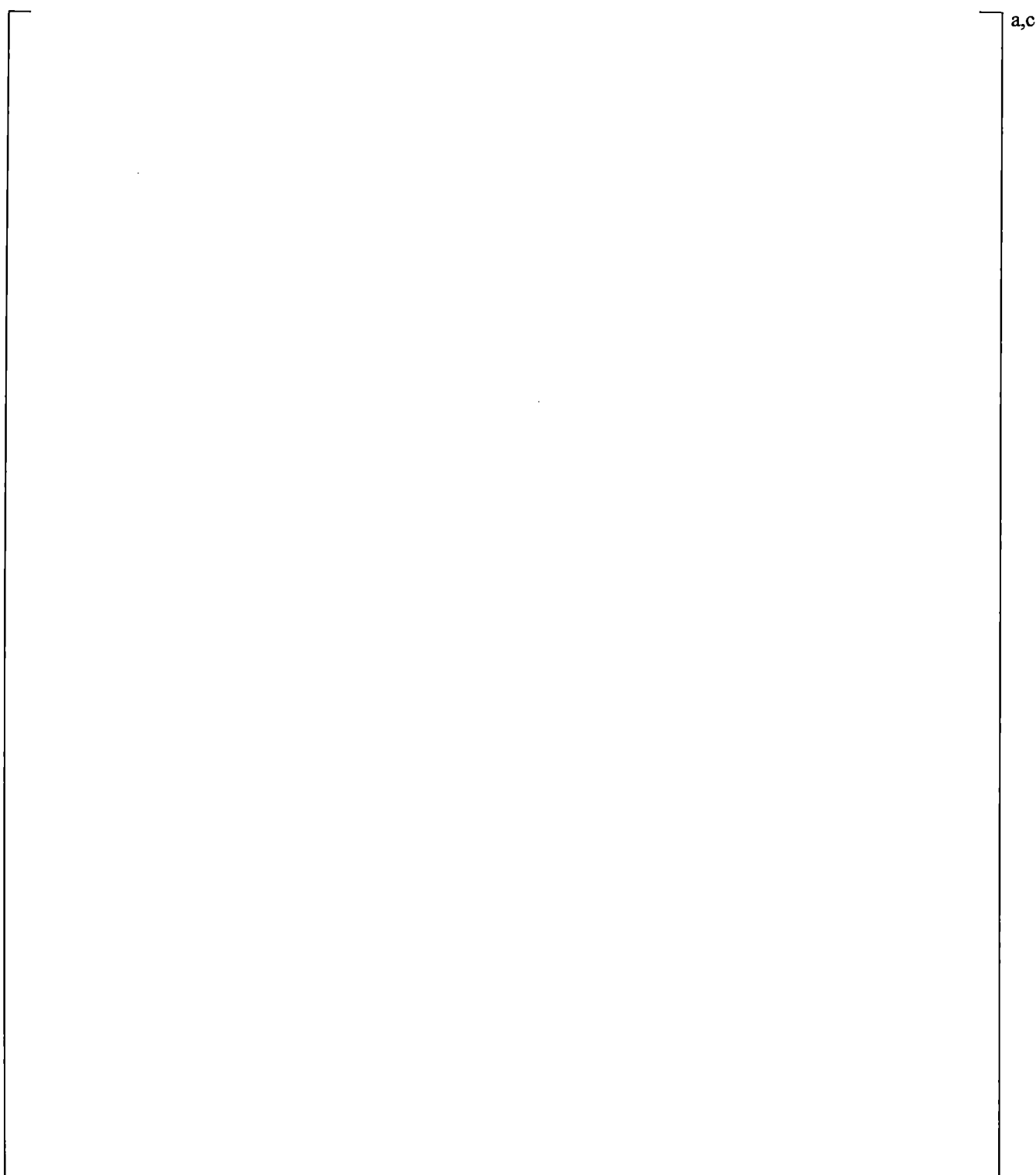


Figure 21.4-3 Cross-Over Leg A Differential Pressures

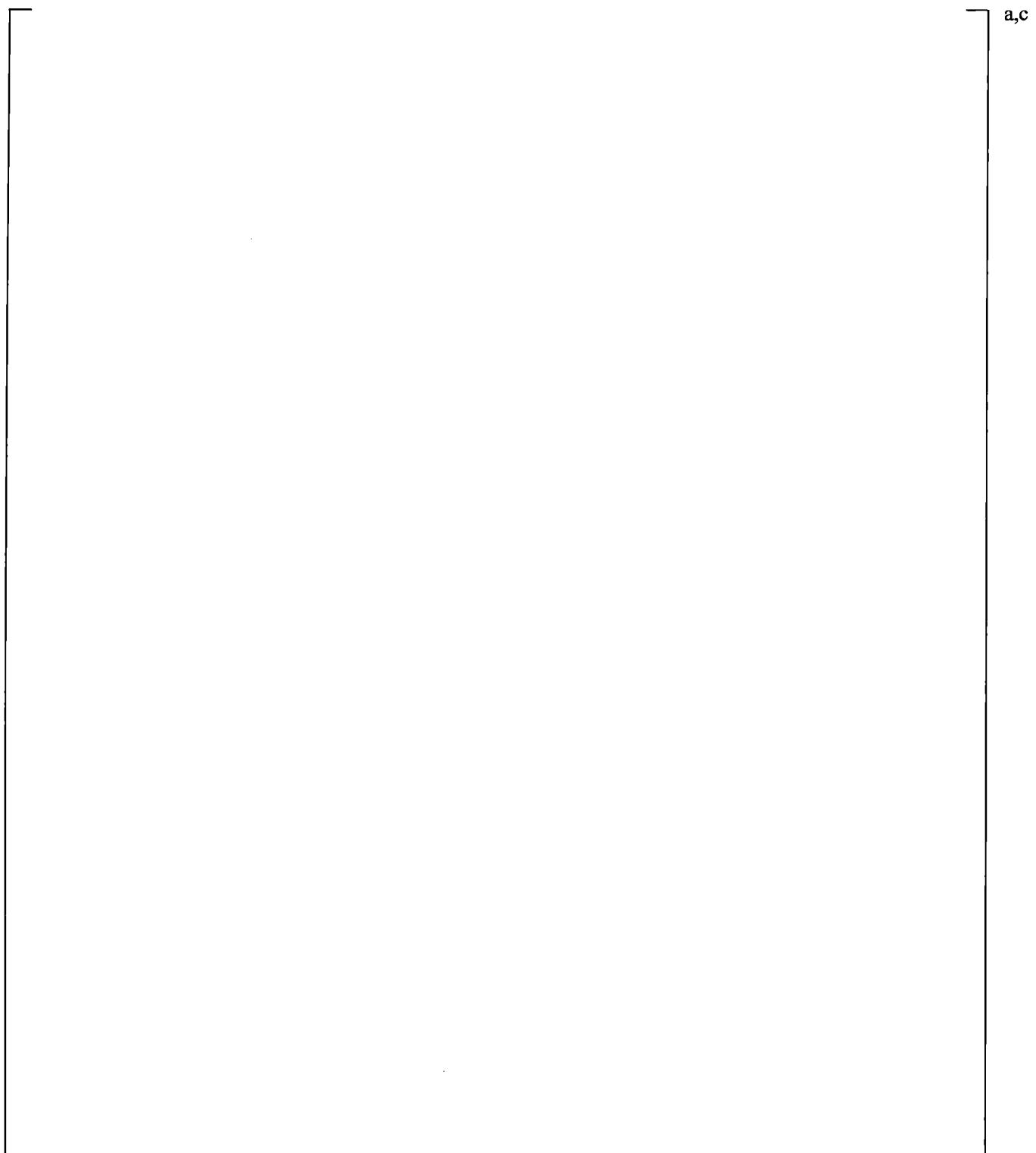


Figure 21.4-4 Cross-Over Leg B Differential Pressures

a,c

Figure 21.4-5 Inner Vessel Differential Pressures

a,c

Figure 21.4-6 Calculated and Measured Peak Cladding Temperatures



a,c

Figure 21.4-7 Steam Generator A U-tube Upflow Side Differential Pressures

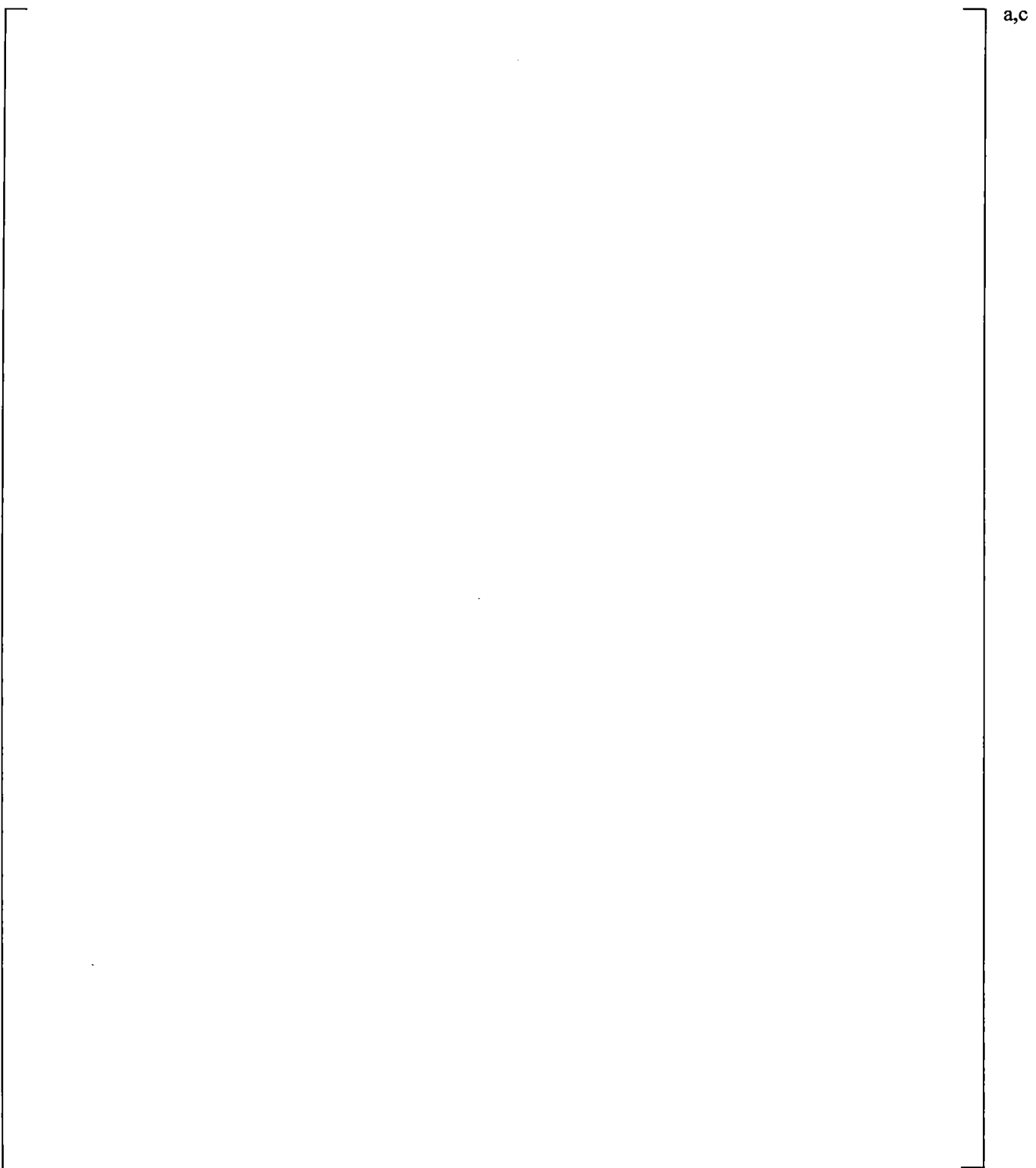
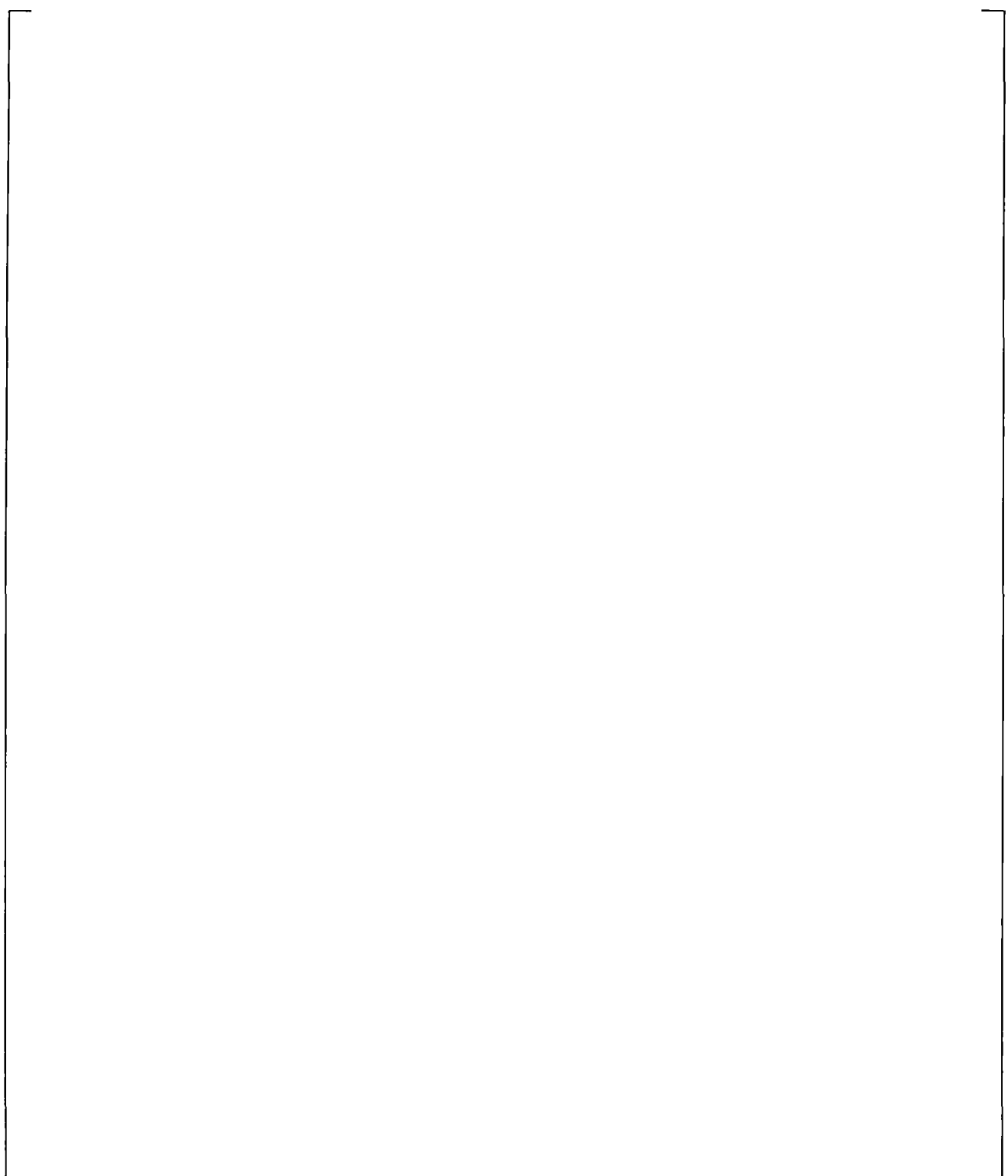


Figure 21.4-8 Steam Generator B U-tube Upflow Side Differential Pressures



a,c

Figure 21.4-9 Steam Generator A U-tube Downflow Side Differential Pressures

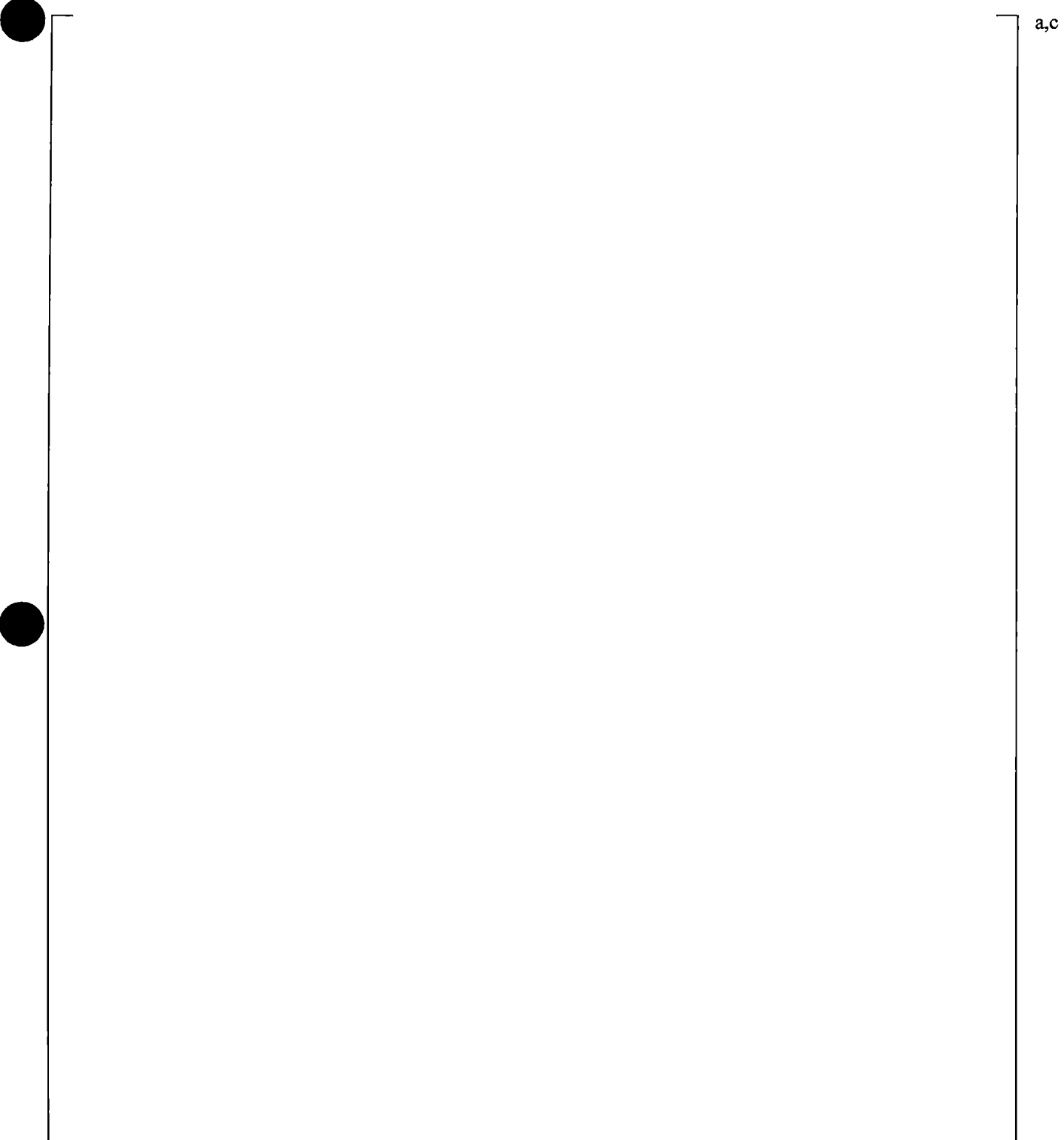
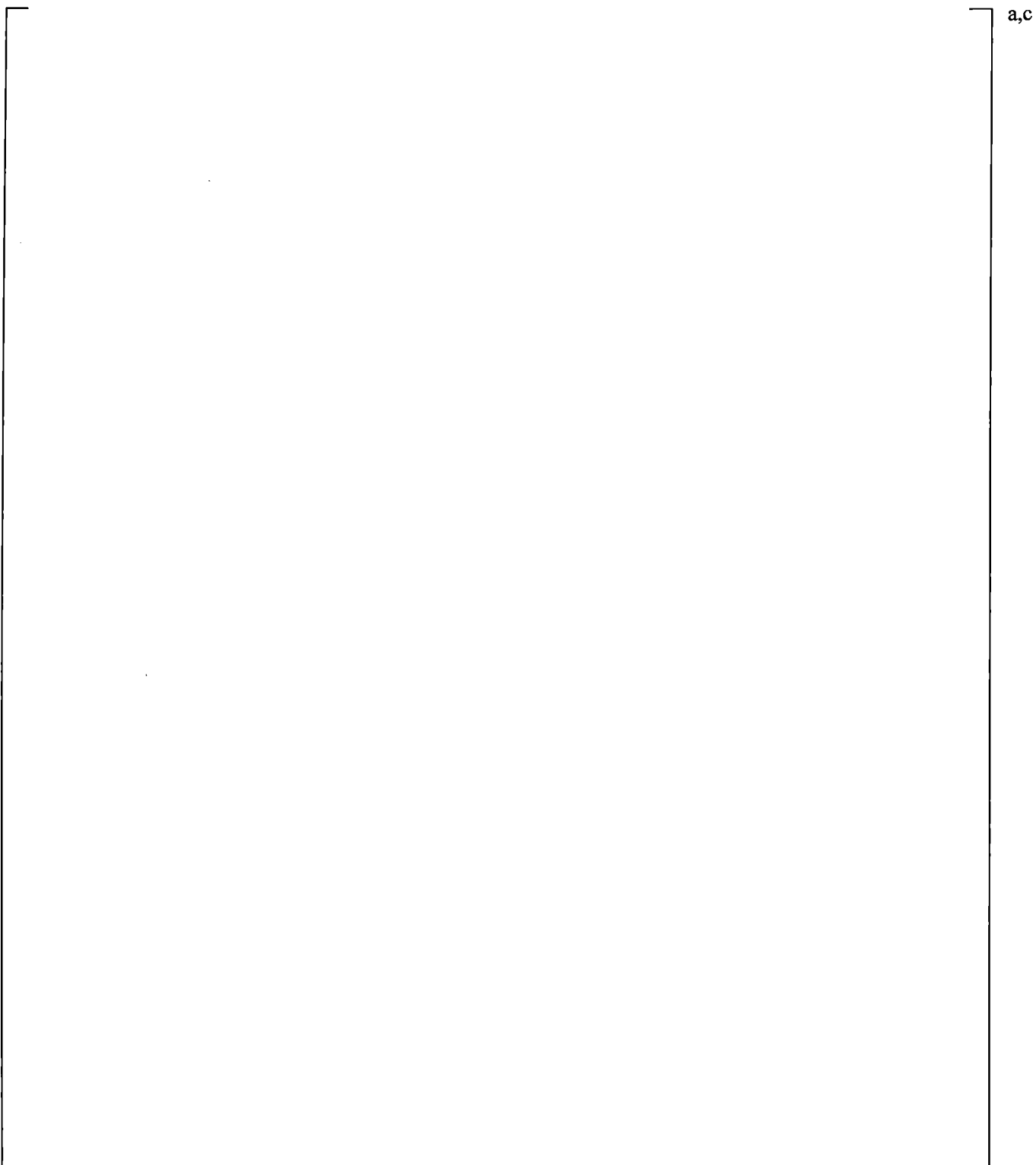
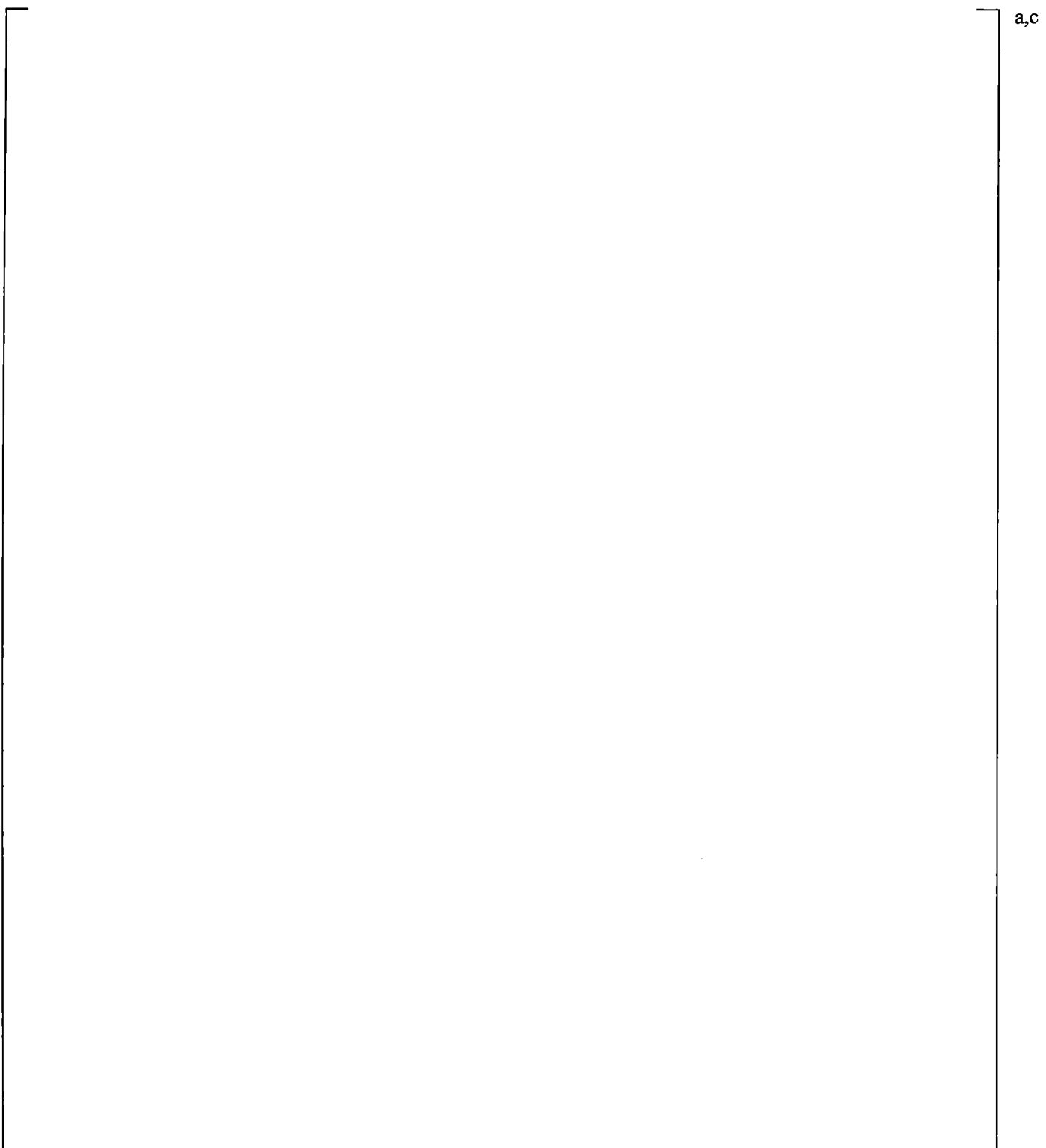


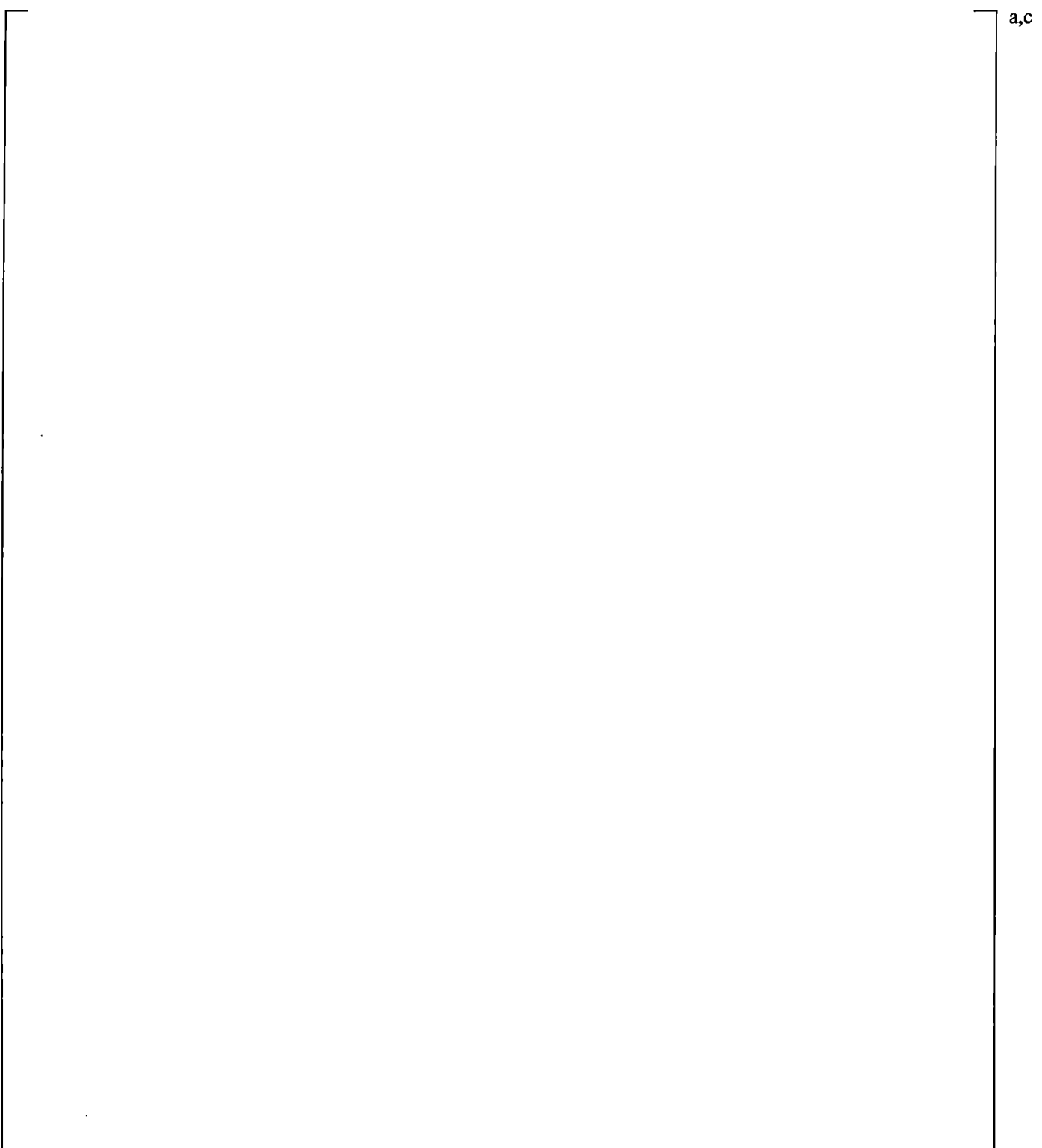
Figure 21.4-10 Steam Generator B U-tube Downflow Side Differential Pressures



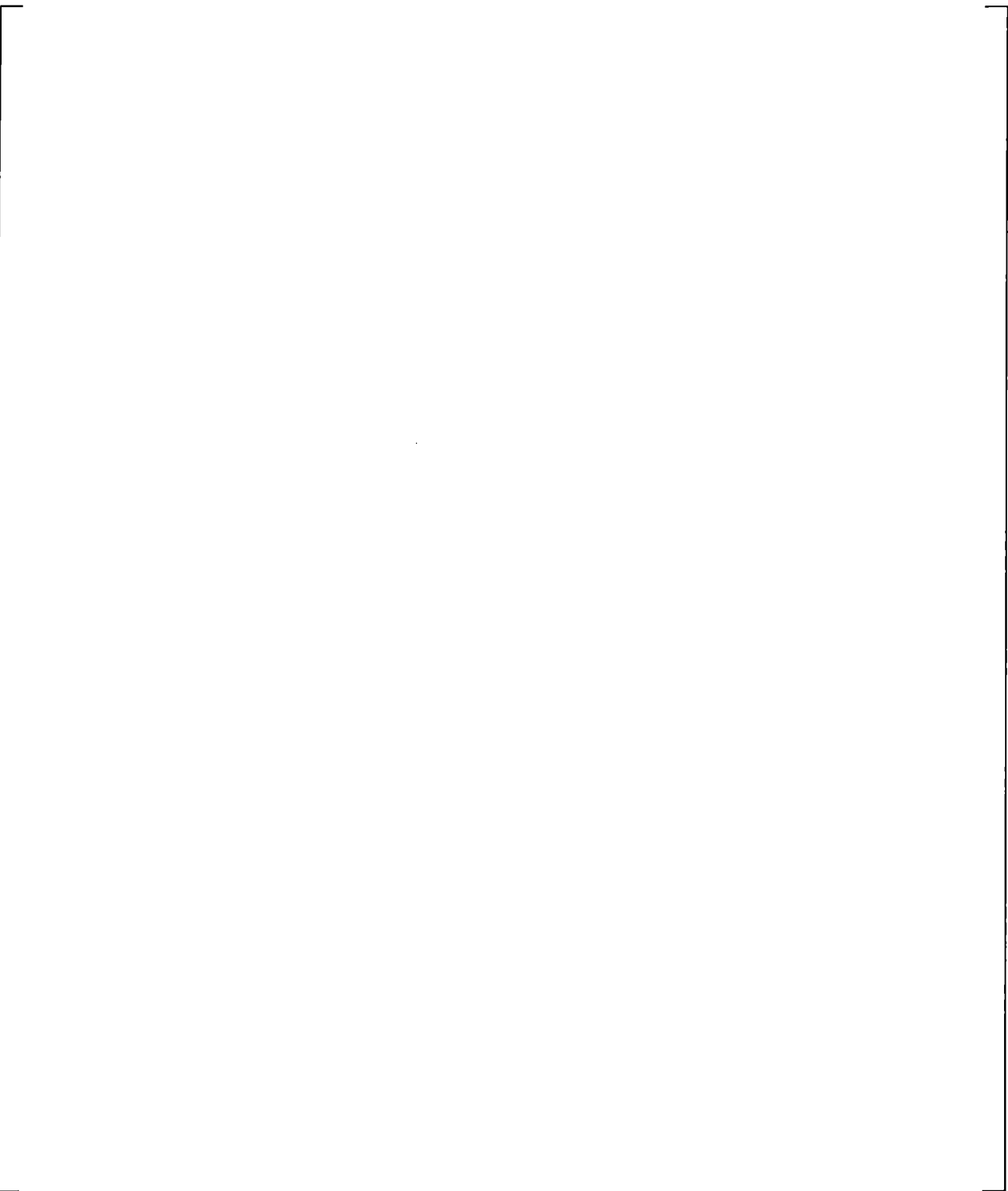
| **Figure 21.4-11 Steam Generator A Inlet-to-Outlet Differential Pressures**



| **Figure 21.4-12 Steam Generator B Inlet-to-Outlet Differential Pressures**

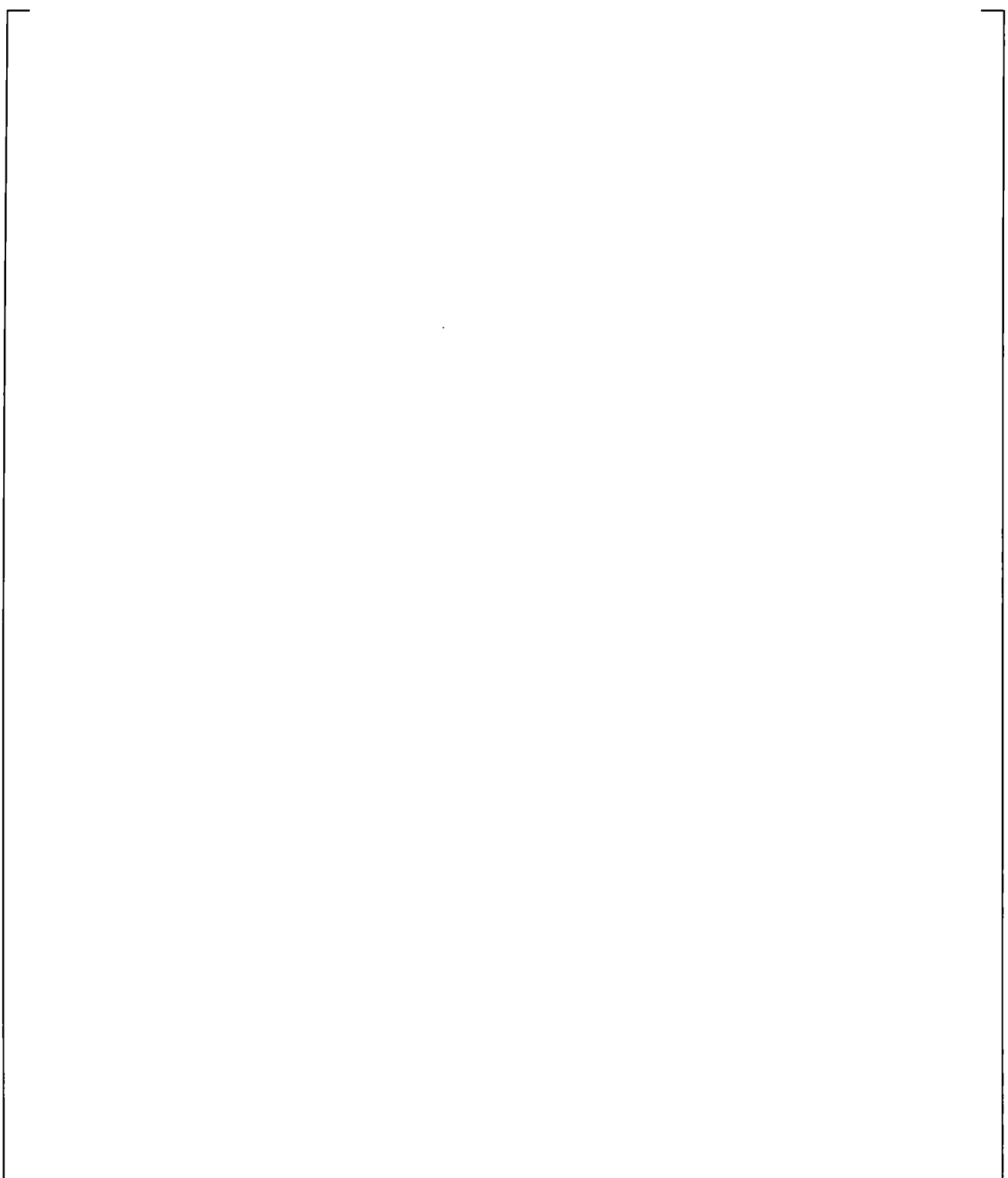


| **Figure 21.4-13 Steam Generator A Inlet Plenum Collapsed Liquid Levels**



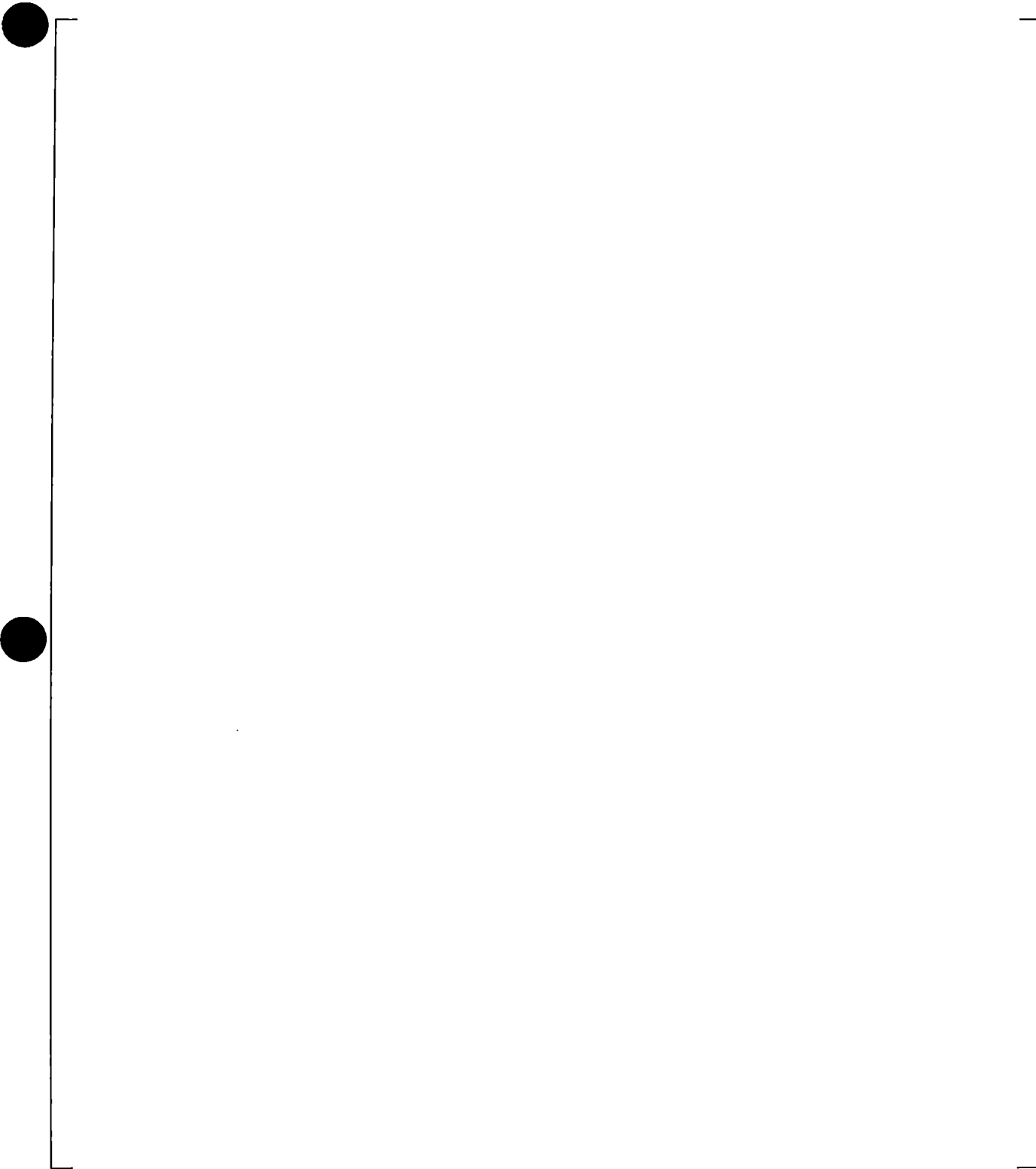
a,c

Figure 21.4-14 Steam Generator B Inlet Plenum Collapsed Liquid Levels



a,c

Figure 21.4-15 Upper Plenum to Steam Generator A Inlet Differential Pressures



a,c

| **Figure 21.4-16 Upper Plenum to Steam Generator B Inlet Differential Pressures**

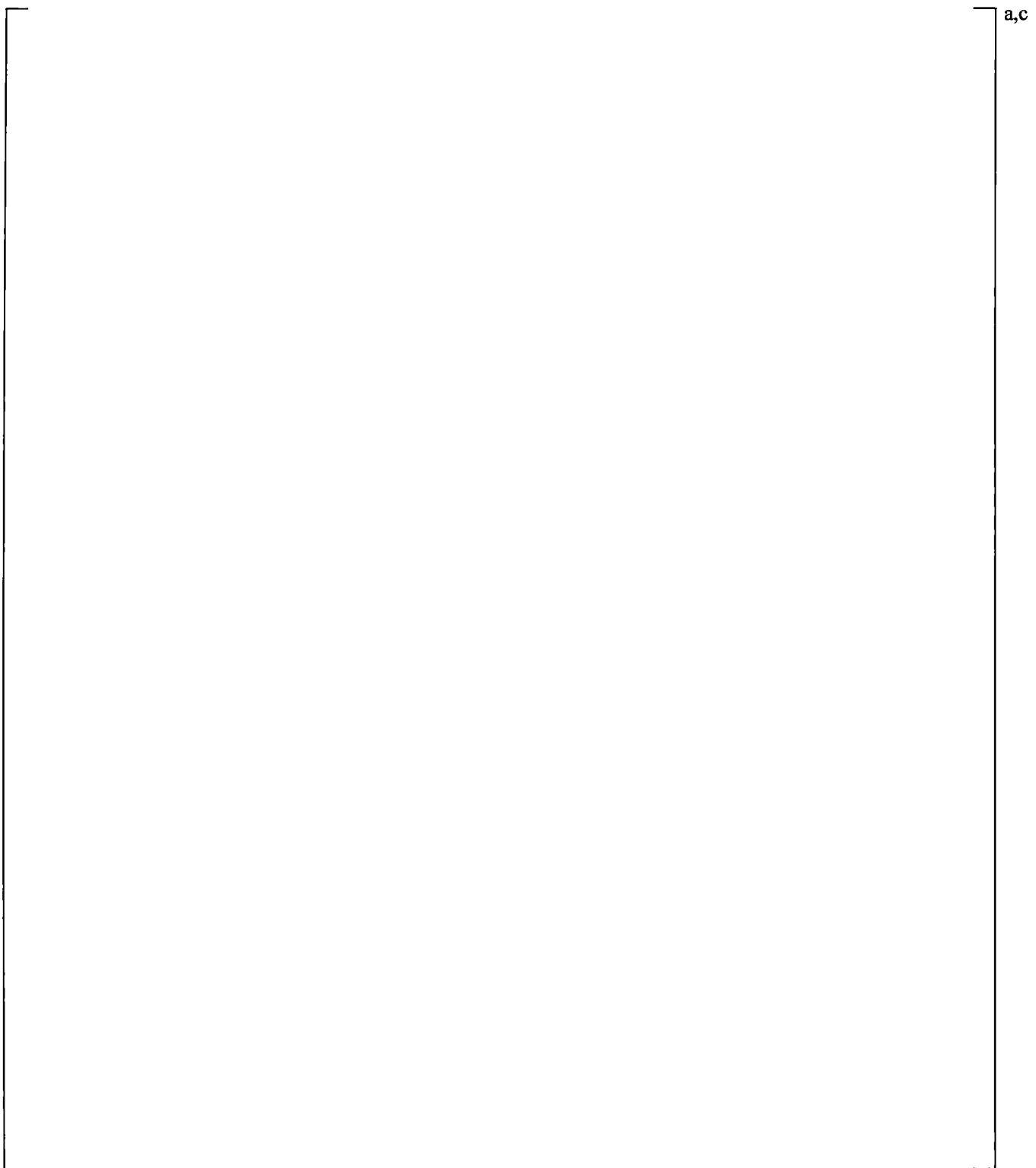


Figure 21.4-17 Upper Plenum Differential Pressures

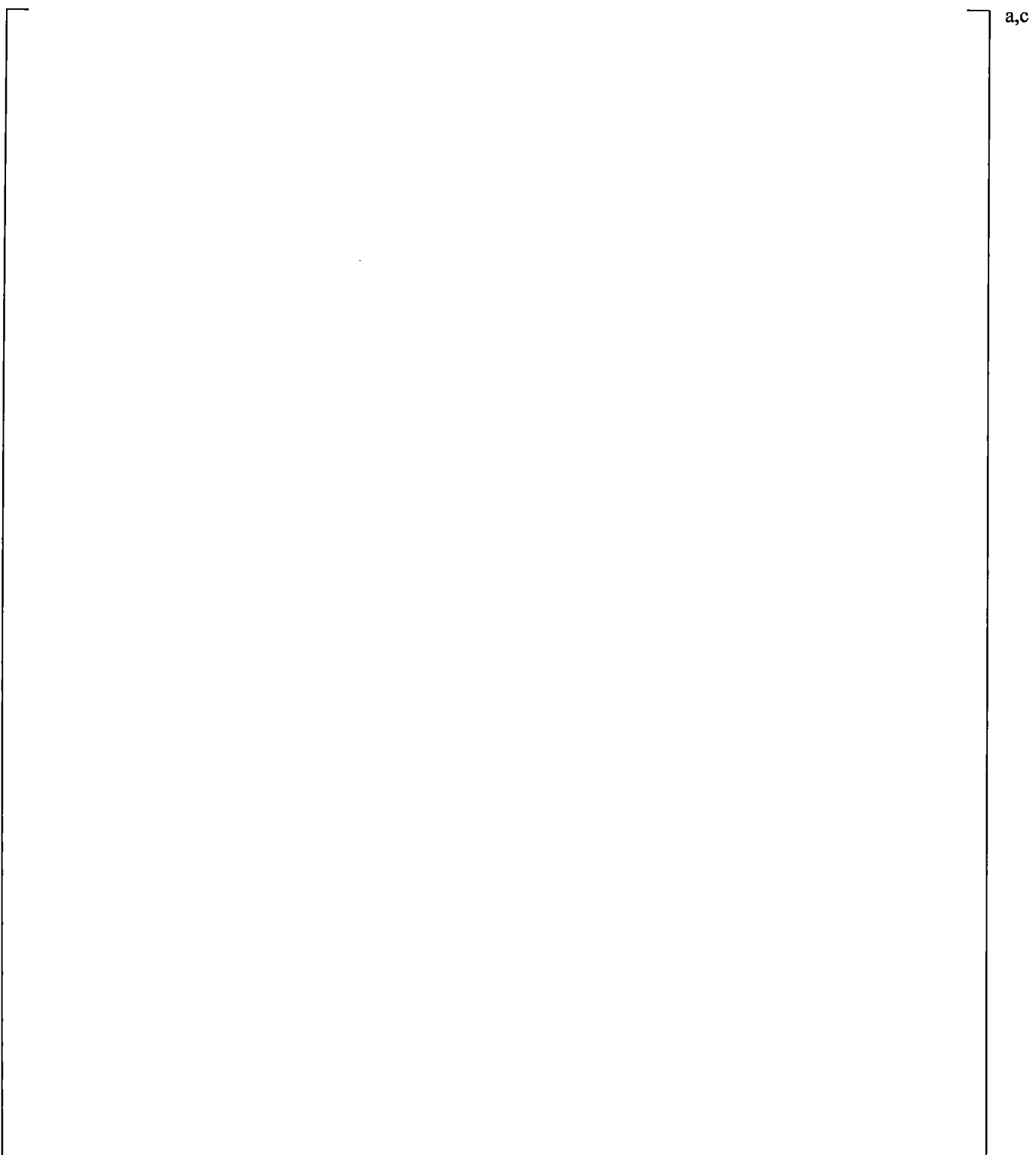


Figure 21.4-18 Downcomer Differential Pressures

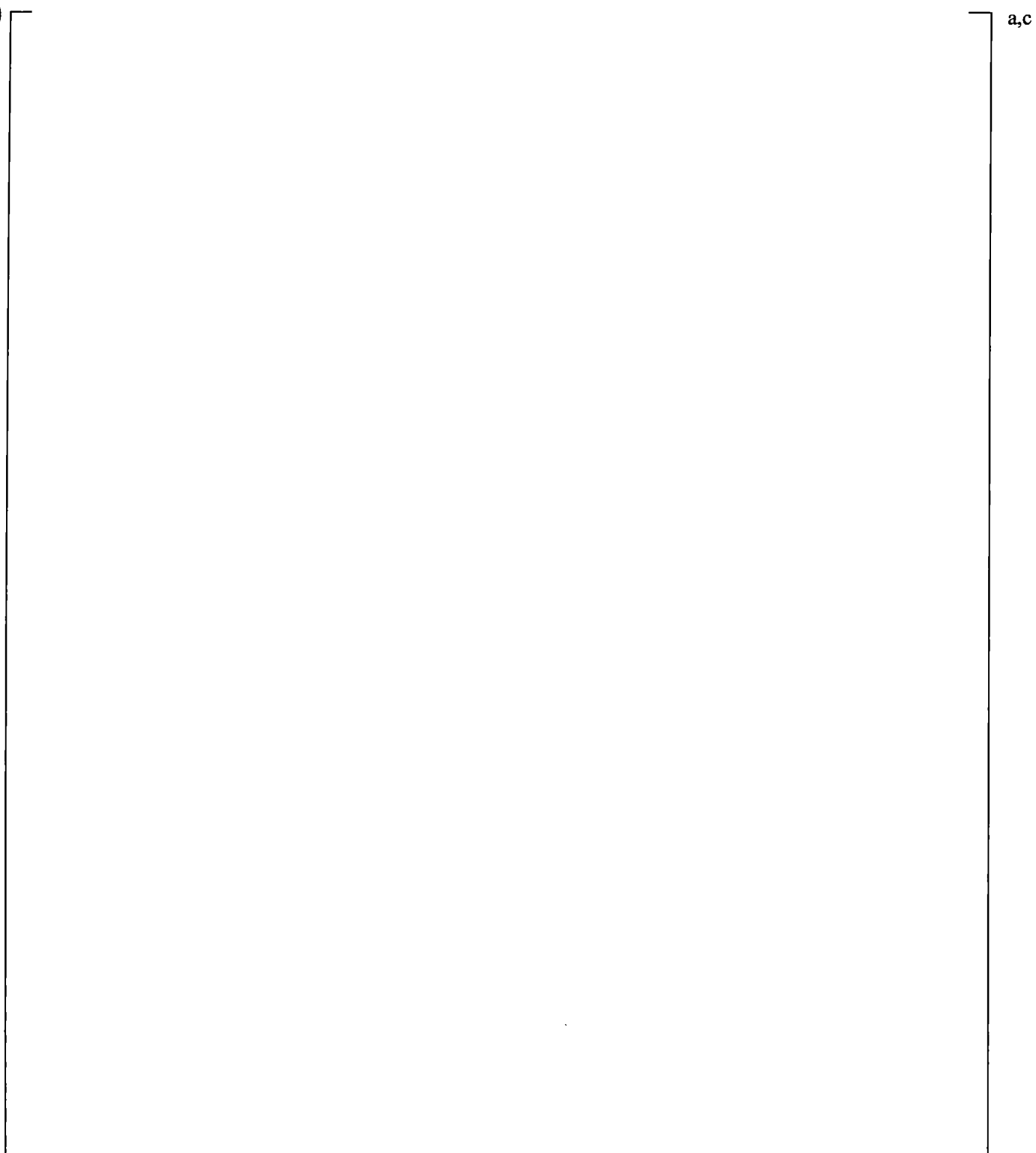


Figure 21.4-19 Comparison of Calculated and Measured Accumulator Injection Flows Loop A

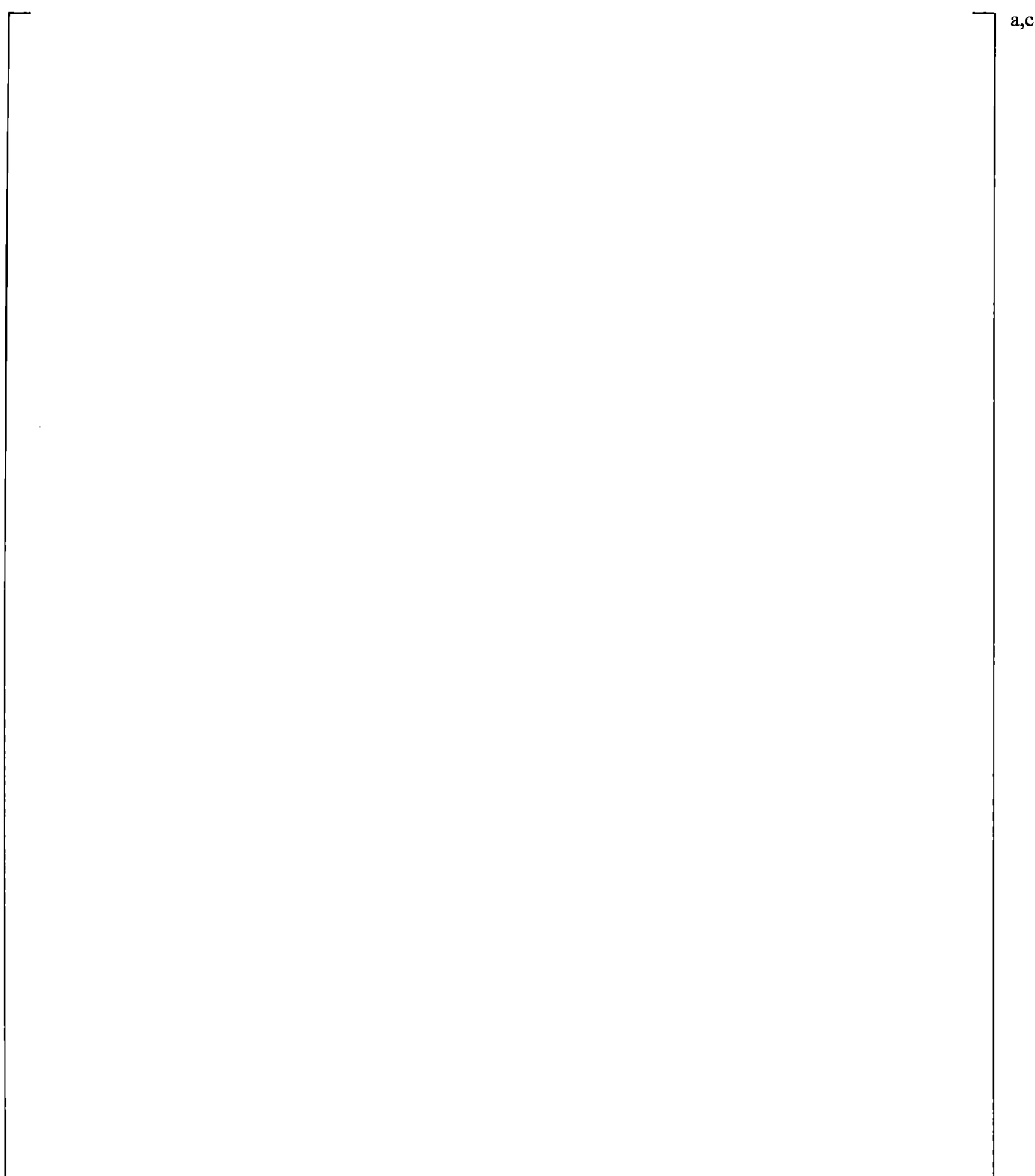


Figure 21.4-20 Comparison of Calculated and Measured Accumulator Injection Flows Loop B

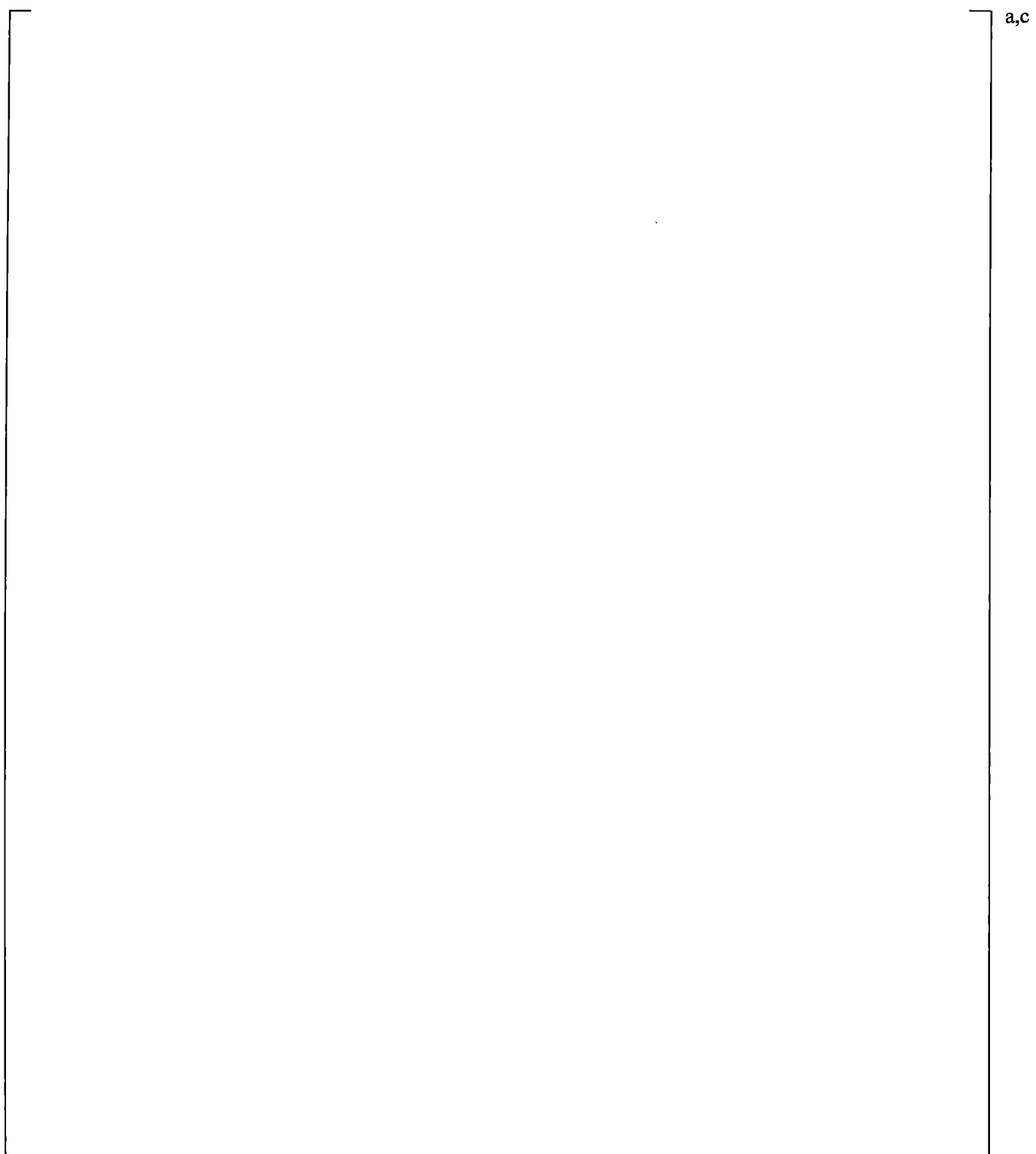
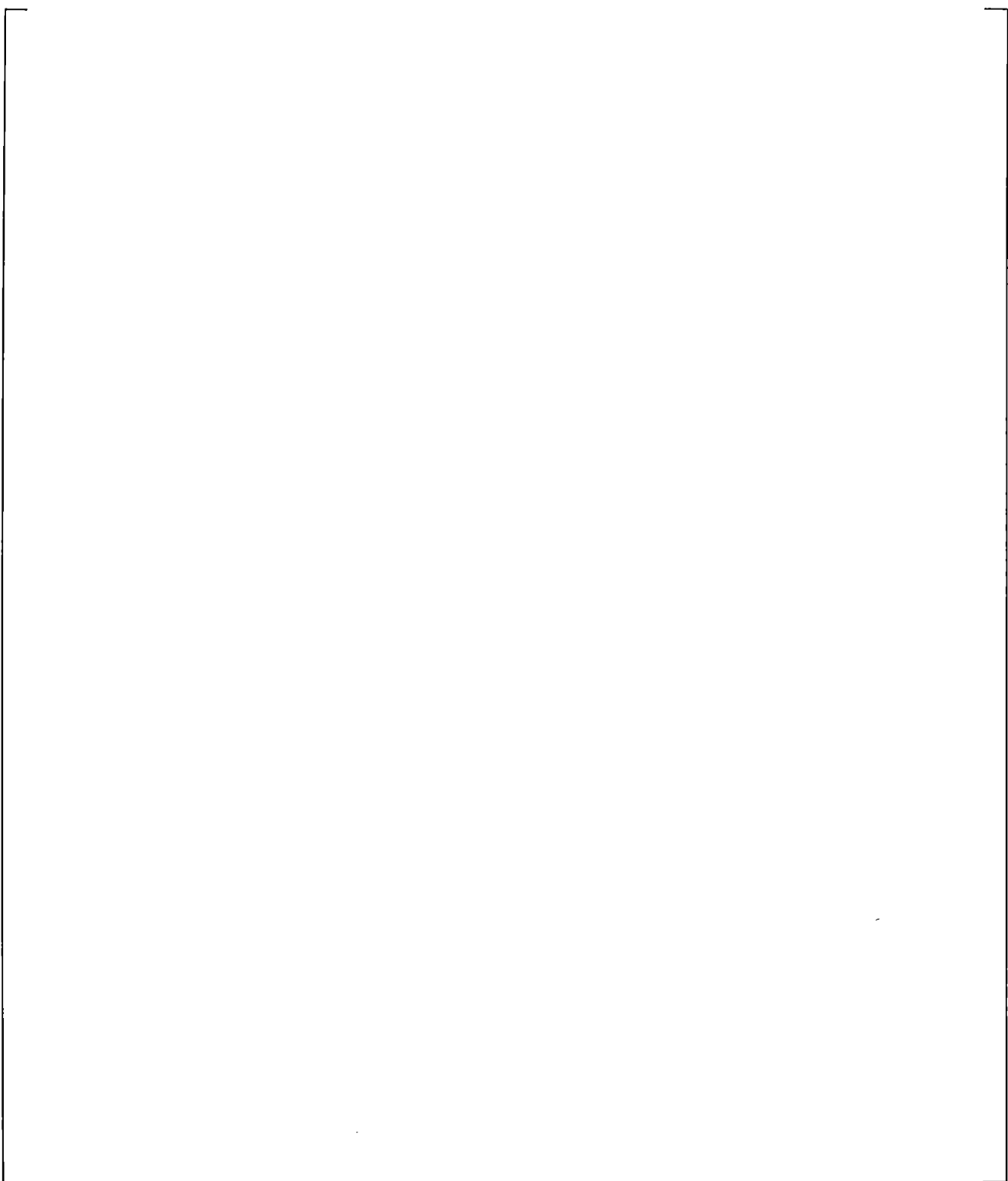


Figure 21.4-21 Calculated Counter-current Flow at Steam Generator A U-tube Inlet

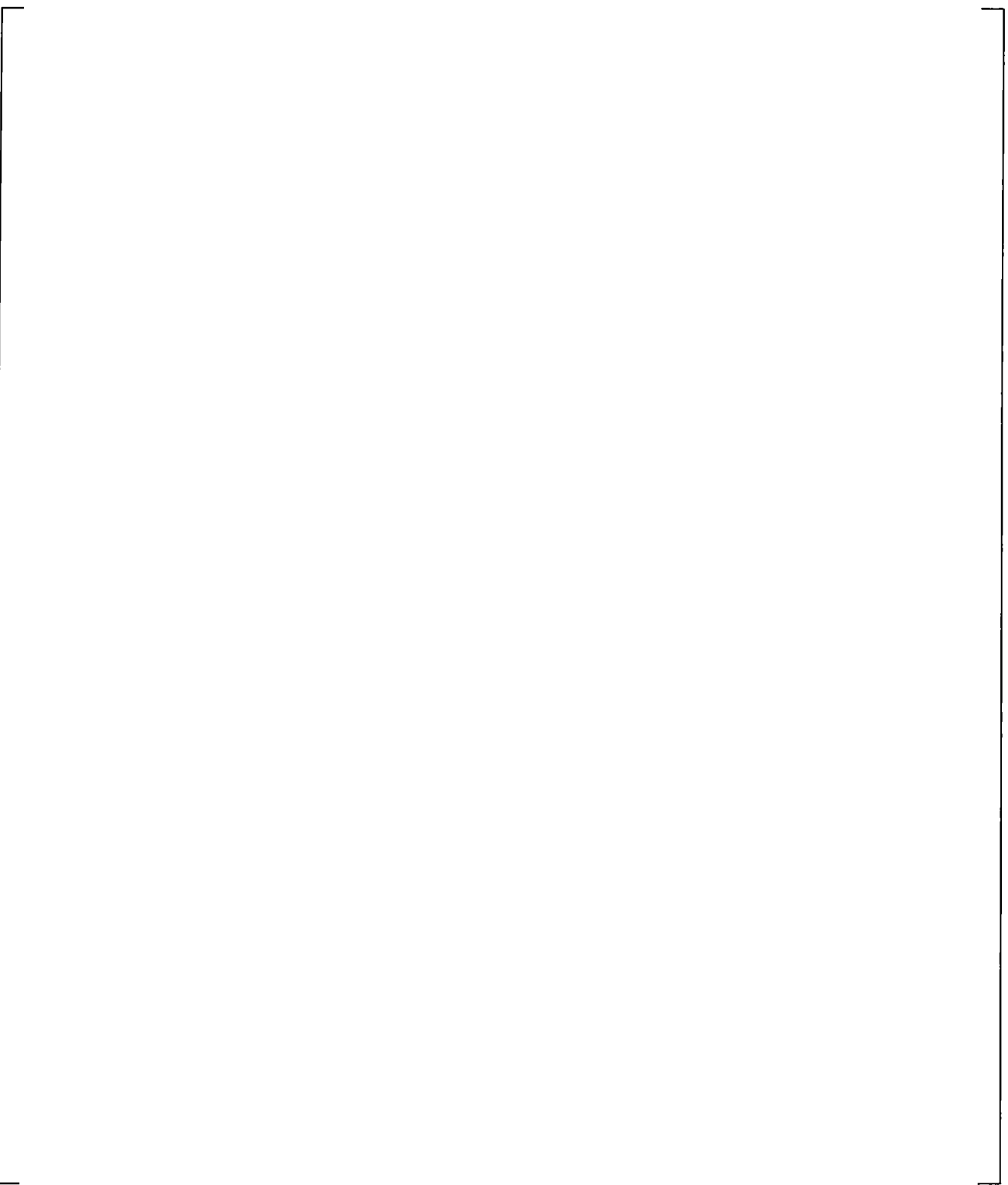


a,c

Figure 21.4-22 Calculated Counter-current Flow at Steam Generator B U-tube Inlet

a,c

Figure 21.4-23 Calculated Counter-current Flow at Elbow of Hot Leg A



a,c

Figure 21.4-24 Calculated Counter-current Flow at Elbow of Hot Leg B

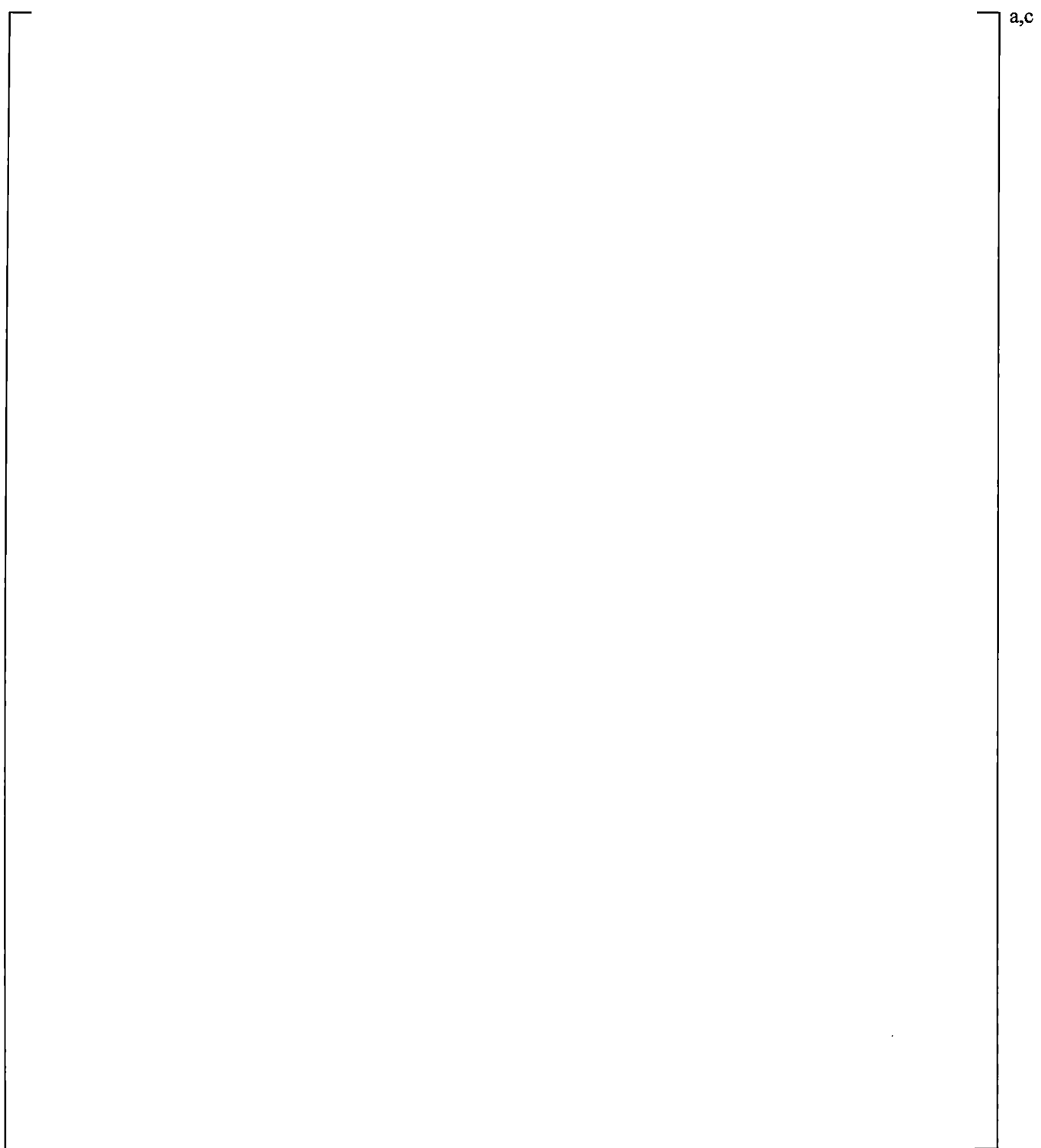


Figure 21.4-25 Calculated and Measured Cladding Temperatures of Low Power Rods at 7.33-ft Elevation

a,c

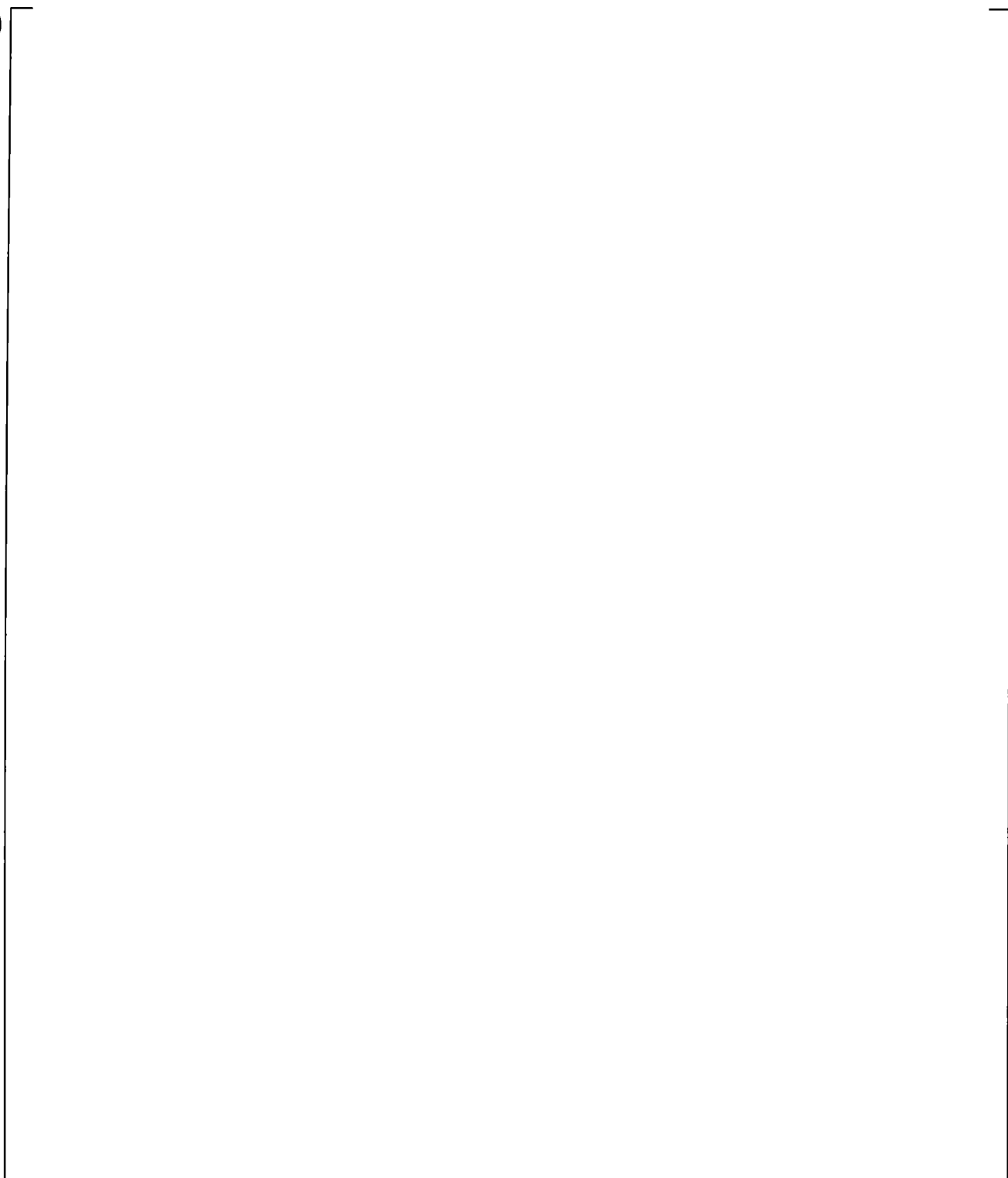


Figure 21.4-25 Calculated and Measured Cladding Temperatures of Low Power Rods at 7.33-ft Elevation

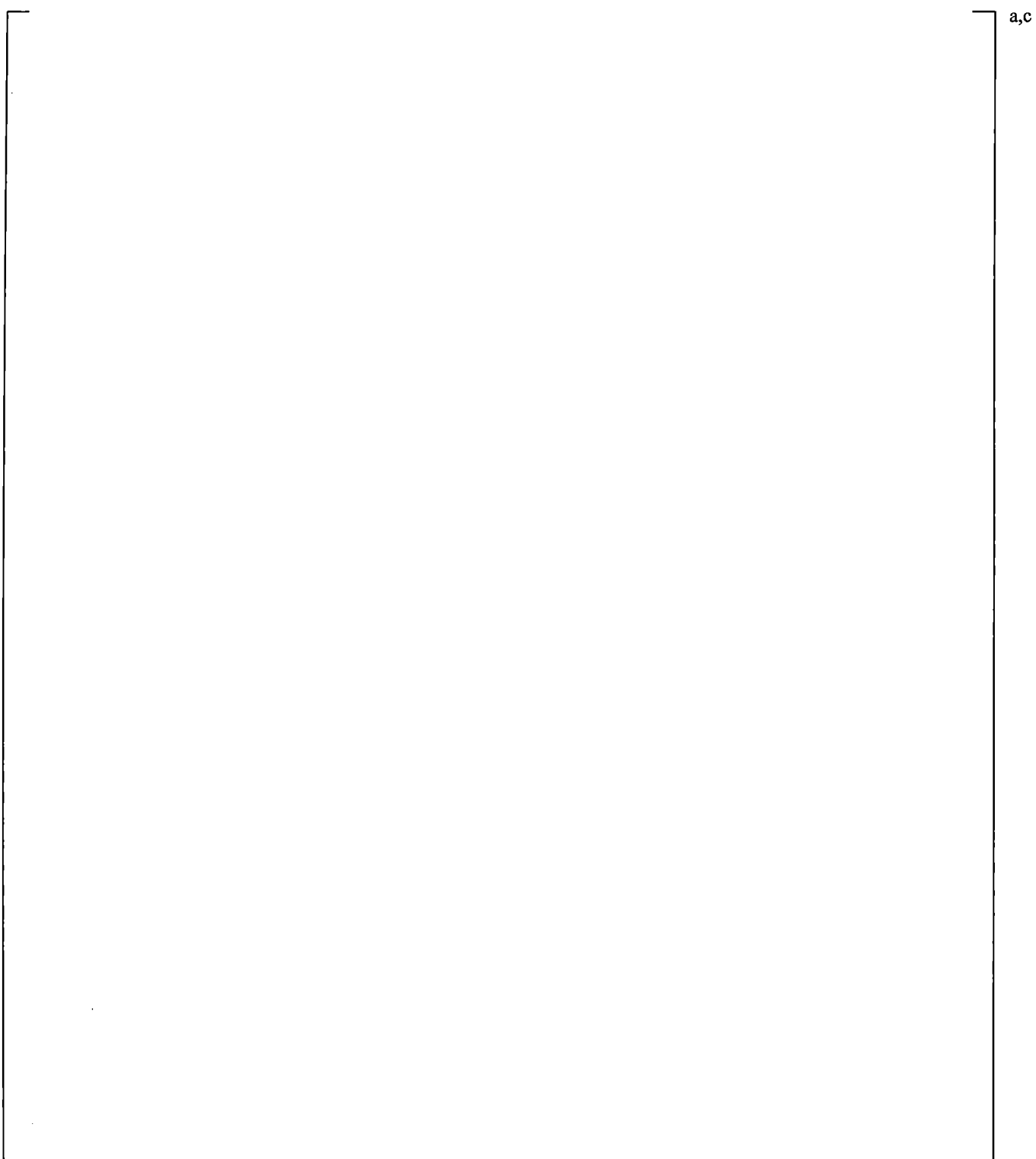


Figure 21.4-26 Calculated and Measured Cladding Temperatures of High Power Rods at 7.33-ft Elevation



a,c

Figure 21.4-26 Calculated and Measured Cladding Temperatures of High Power Rods at 7.33-ft Elevation

a,c

Figure 21.4-27 Calculated and Measured Cladding Temperatures of Average Power Rods at 7.33-ft Elevation

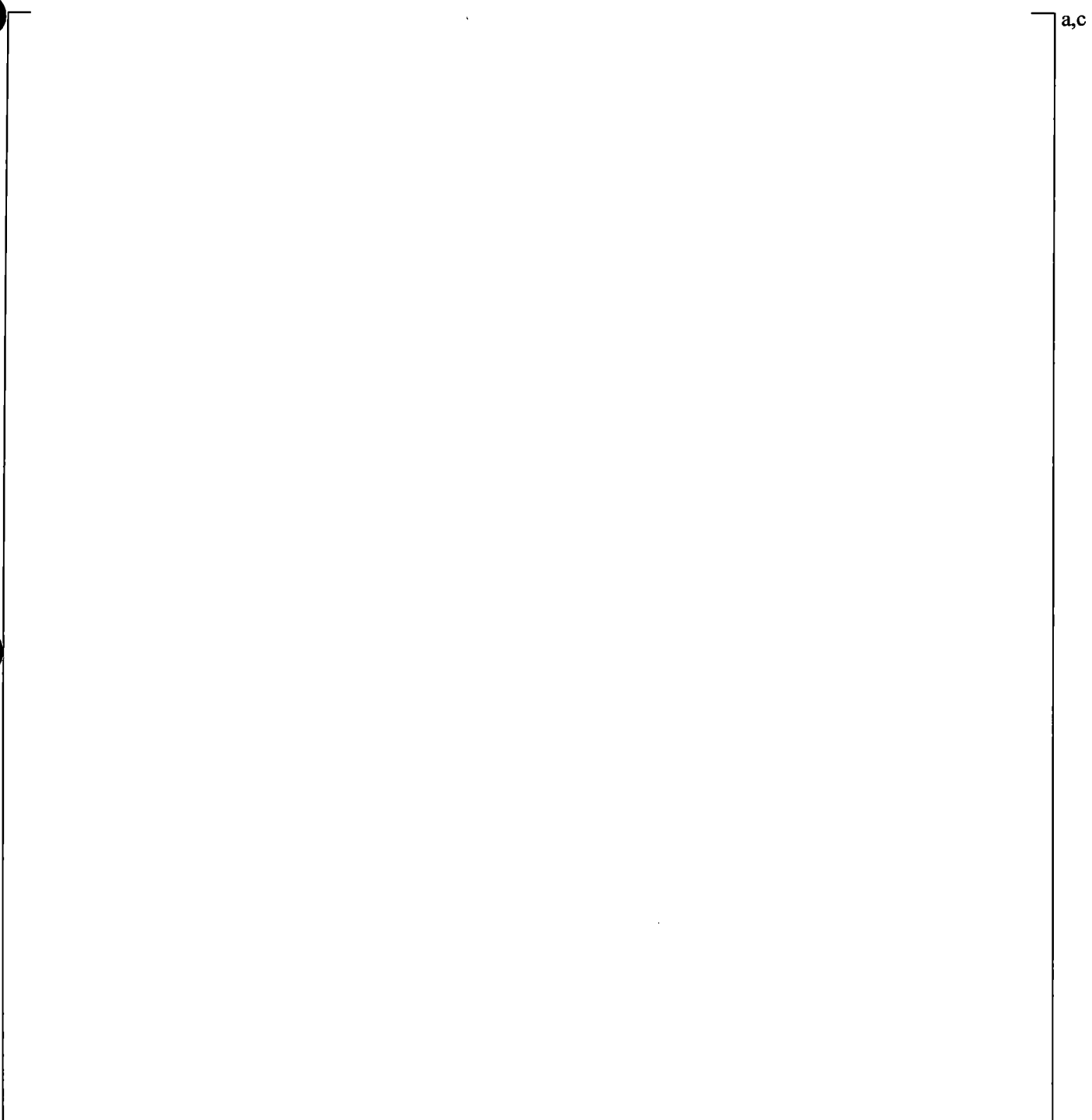


Figure 21.4-27 Calculated and Measured Cladding Temperatures of Average Power Rods at 7.33-ft Elevation

21.5 SI-INJECTION SENSITIVITY STUDY: SIMULATION OF SB-CL-05, 5-PERCENT COLD LEG SIDE BREAK

21.5.1 Description of the Boundary and Initial Conditions

Test SB-CL-05 simulated a 5-percent cold leg break (equivalent to a 6-inch break in a PWR). The test is one of the earliest of the ROSA-IV series. In terms of initial conditions, break size and decay heat curve this test is equivalent to the 5% break SB-CL-18, which is documented in the previous section. However, the SB-CL-05 test was conducted with charging and high-pressure injection available.

As in the SB-CL-18 test, the break was located in loop B and had a horizontal orientation. Safety injection flow rates corresponding to a single failure in the safety injection system were assumed. Experimental results are discussed by Kawaji (Kawaji et al., 1986) and Tasaka (Tasaka et al., 1988).

The operational setpoints for this test are the same as implemented in all ROSA-IV break tests, as listed in Table 21.2-2.

The core power was scrammed once the primary pressure decreased below 12.97 MPa (1881 psia). At scram, the primary coolant pumps began to coast down, the main feedwater was stopped, and the secondary sides of the two steam generators were isolated by closure of their main isolation valves.

In this test, the primary system rapidly depressurized to a pressure slightly higher than the secondary pressure, approximately 8 MPa (1160 psia), until the loop seal cleared at about 140 seconds.

After loop seal clearance, the break quality changed from a low quality mixture to primarily vapor and the primary system continued to depressurize. Primary pressure falls below secondary pressure at about 180 seconds after the break.

Test SB-CL-05 had a core depression during loop seal clearance that was considerably below the elevation of the bottom of the loop seal piping. Osakabe (Osakabe et al., 1987) attributed this to a large liquid holdup in the uphill steam generator tubes. During this core level depression, the cladding temperature increased by approximately 100K (180°F) reaching a maximum cladding temperature of approximately 720K (836°F). After loop seal clearance, the core level recovered quickly. Accumulator injection began at 417 seconds and prevented a second core uncover.

21.5.2 Results and Conclusions from the SB-CL-05 Simulation

Table 21.5-1 shows a summary of the key initial parameters measured at the SB-CL-05 test and achieved at the end of the steady-state calculation. Table 21.5-2 summarizes the observed (data) and predicted results for the SB-CL-05 test simulation.

The simulation of the SB-CL-05, presented herein, was performed with break discharge coefficients $I^{a,c}$ In addition, Wallis-type counter-current flow limits were enforced [

$J^{a,c}$ The results from the simulation are presented in the

following Figures 21.5-1 through 21.5-21. In these figures, the WCOBRA/TRAC-TF2 calculation results are compared to measured SB-CL-05 test parameters.

As intended, the core power (Figure 21.5-1) and pump speed (Figure 21.5-2) were modeled to be consistent with the measurements. [

]^{a,c}

Figure 21.5-4 shows the calculated break flow compared against that measured by the high-range flow meter (FE560A-BU).

The break flow prediction is similar to the one observed in the SB-CL-18 test simulations. Early in the transient, flow out of the break is sub-cooled, that is, single-phase liquid. [

]^{a,c}

Beyond 100 seconds the conditions at the break transition from single-phase liquid to single-phase steam. The observed disparity relative to the FE560A-BU measurement is explained by the fact that the test break flow is outside the measurement accuracy of the FE560A flow meter. [

]^{a,c}

The pressurizer pressure calculation is fairly consistent with the measured (Figure 21.5-6). Initially, there is a small discrepancy in the depressurization which appears to be consistent with the break flow mismatch trend. [

[

]^{a,c}

]^{a,c}

]^{a,c}

The agreement between the calculated pumped ECCS flows and the measured during the test is good, Figures 21.5-18 and 21.5-19.

The comparison of the calculated and measured accumulator levels indicate inconsistency between the code calculation and the test, Figure 21.5-20. The inconsistency is not investigated in further detail due to the fact that the timing and magnitude of accumulator injection does not appear to be a contributor to the lack of boil-off. As discussed earlier in Section 21.4, possible reason of the under-prediction of accumulator injection is that the code tends to calculate nitrogen gas expansion following a polytropic exponent of 1.225, compared to 1.118 estimated from the test measurements, as evident from the Callaway small break accumulator discharge presented in Section 20.1.3.2. Overall, the predicted accumulator discharge is conservative and adequate for the purpose of the FSLOCA methodology.

]^{a,c}

Table 21.5-1

a,c

Table 21.5-2

18

a,c



Figure 21.5-1 Core Power

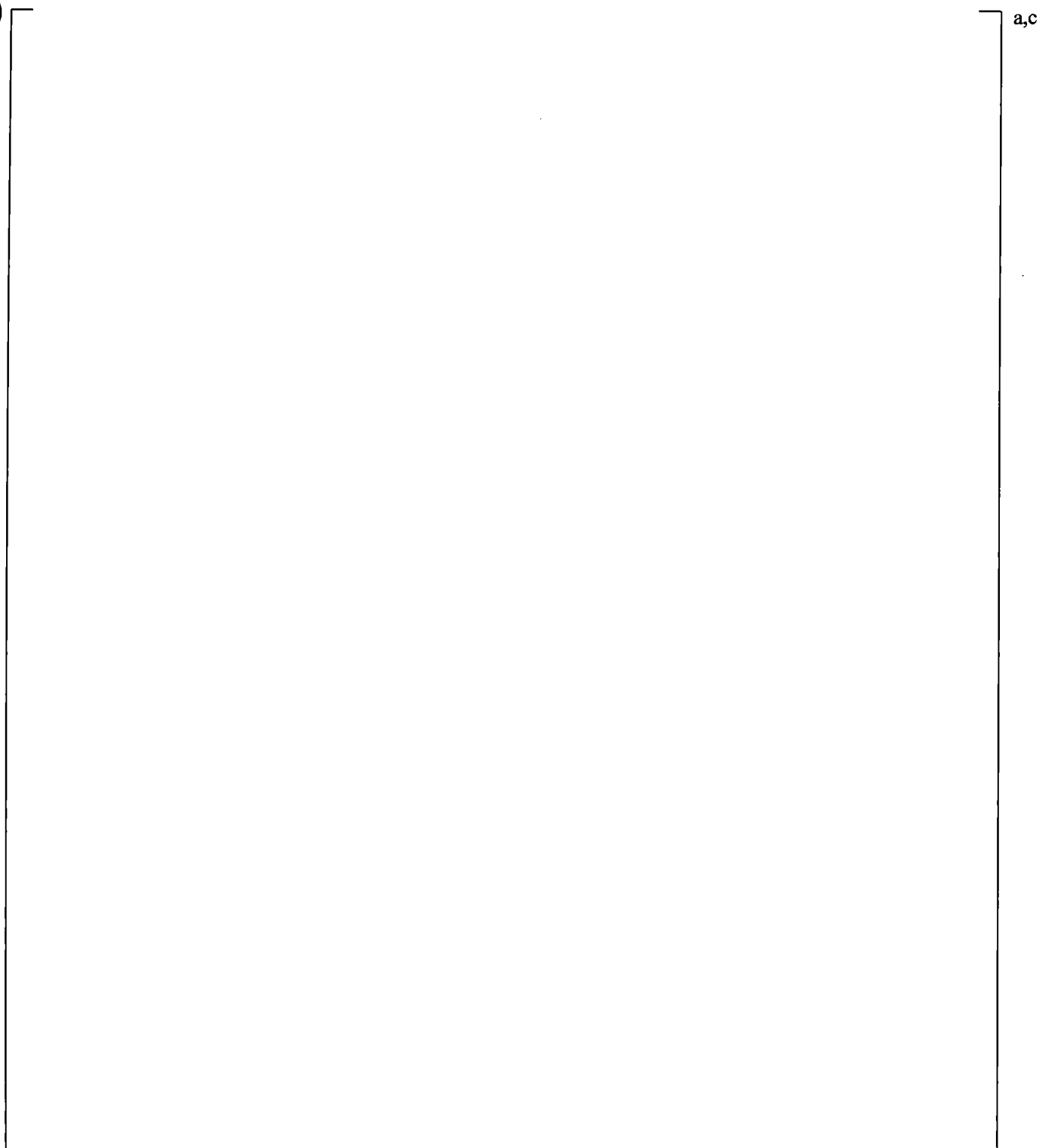


Figure 21.5-2 Pump Speed

a,c

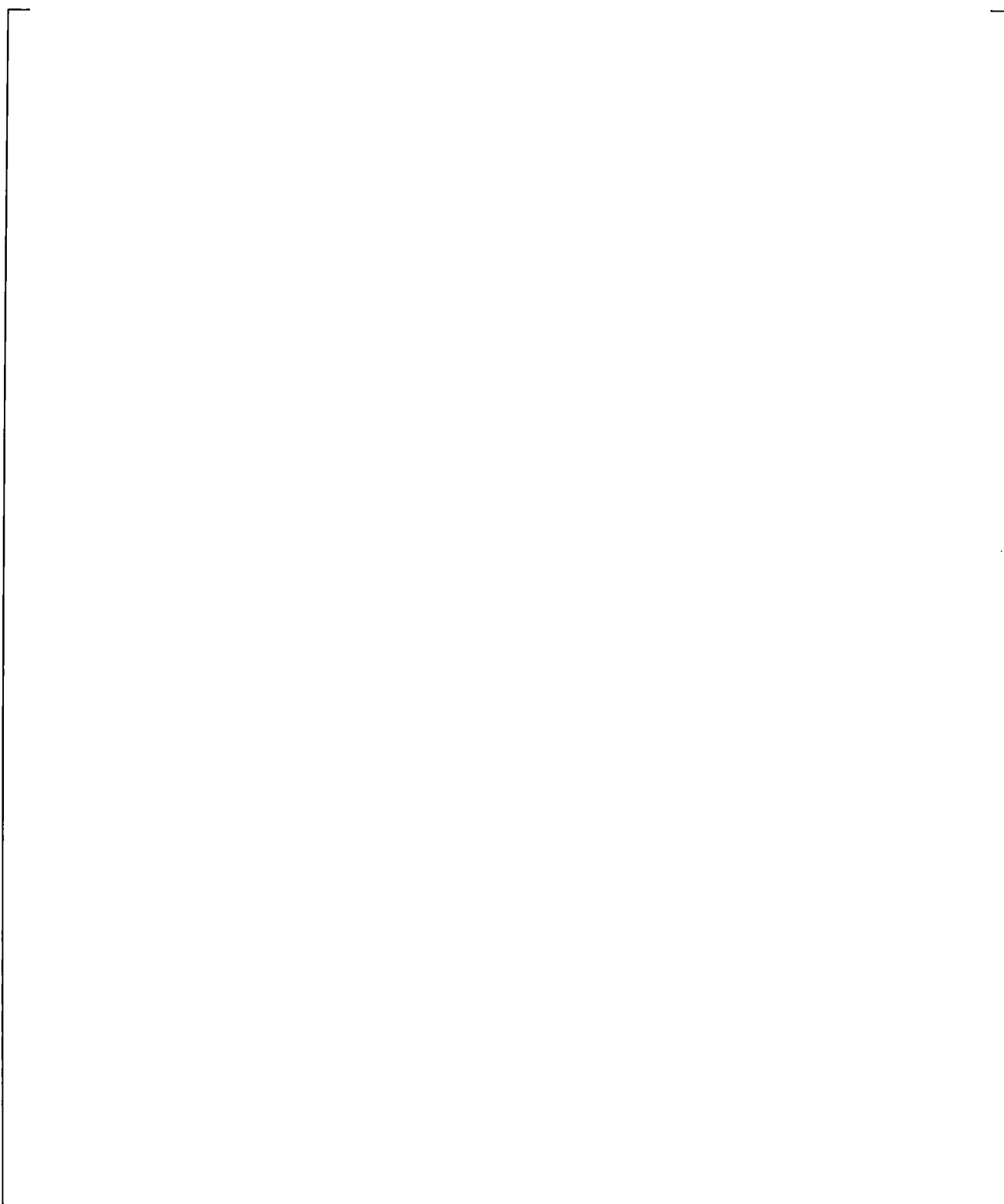


Figure 21.5-3 Loop Flow Rates

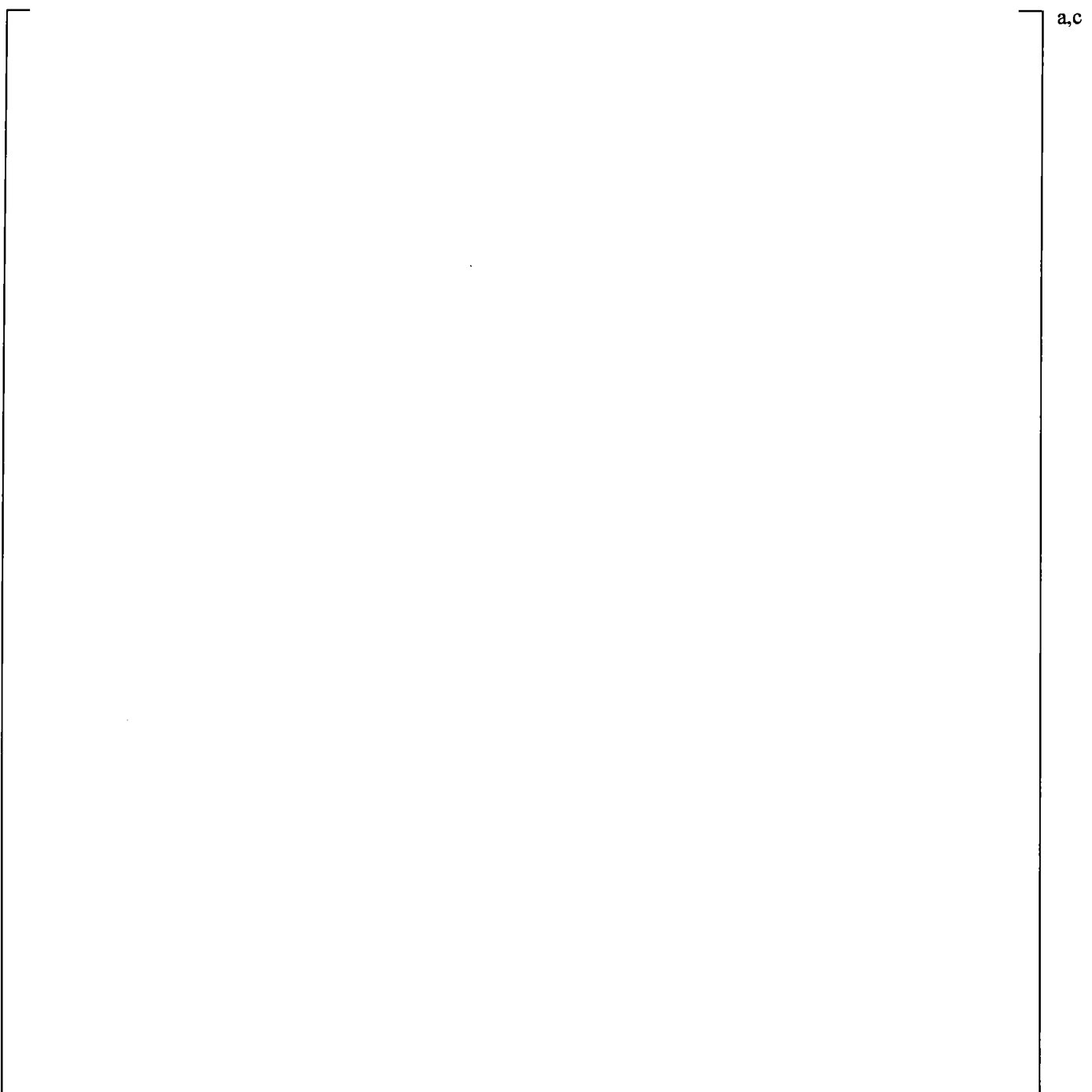


Figure 21.5-4 Break Flows

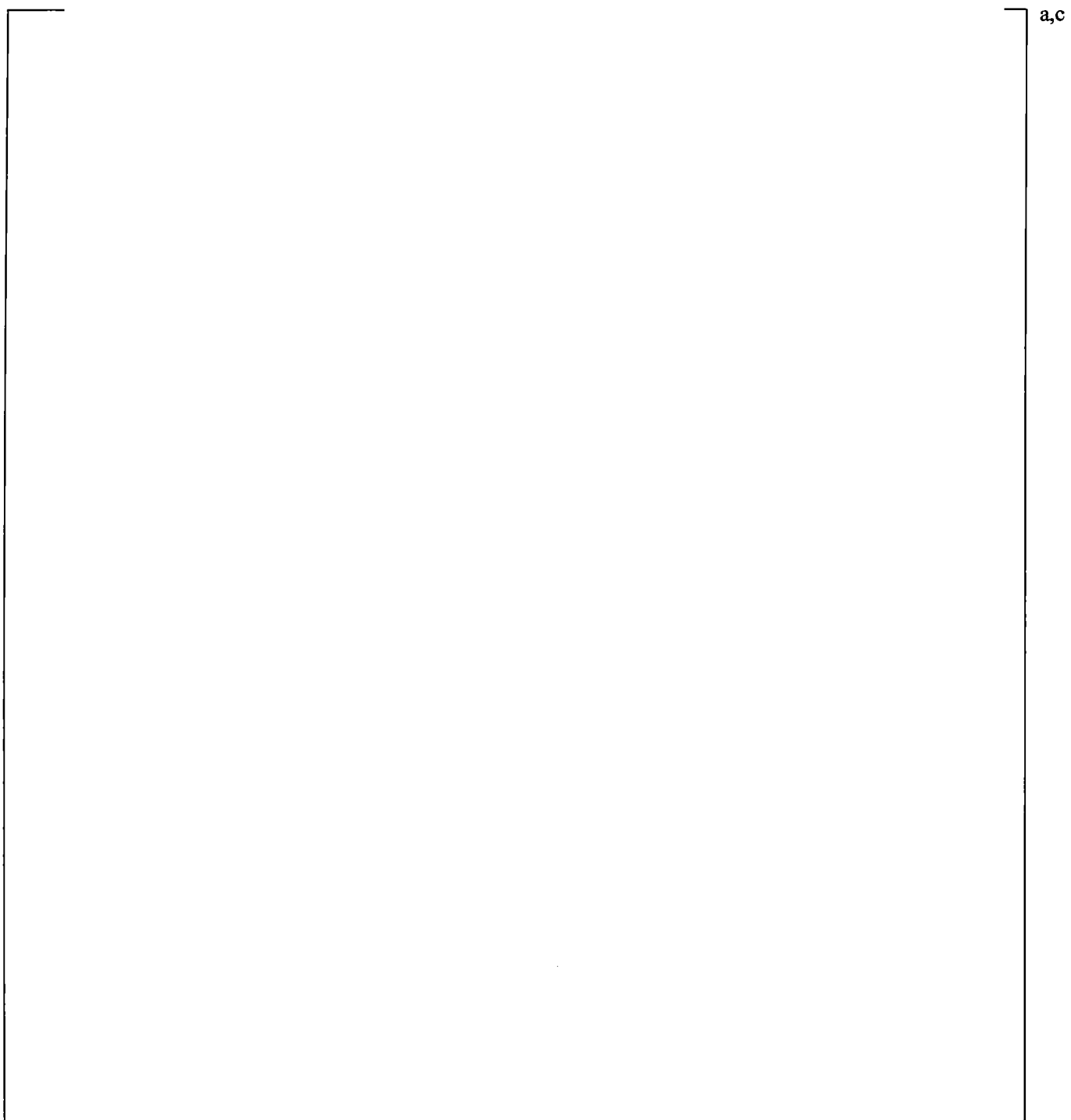


Figure 21.5-5 Calculated Break Spool Void Fraction

Note: This location is in the side pipe of the broken TEE#26, upstream of the break orifice location.

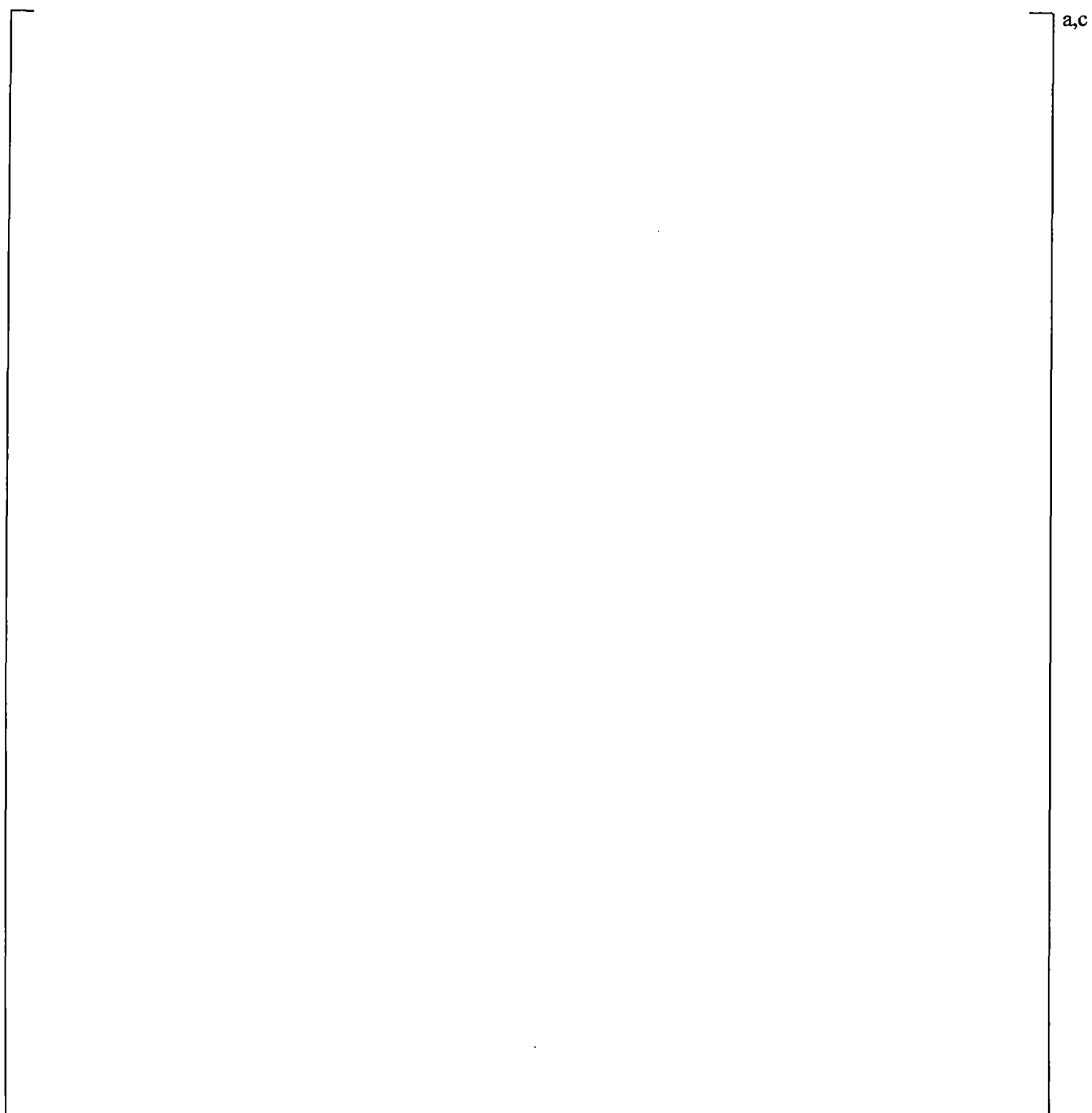
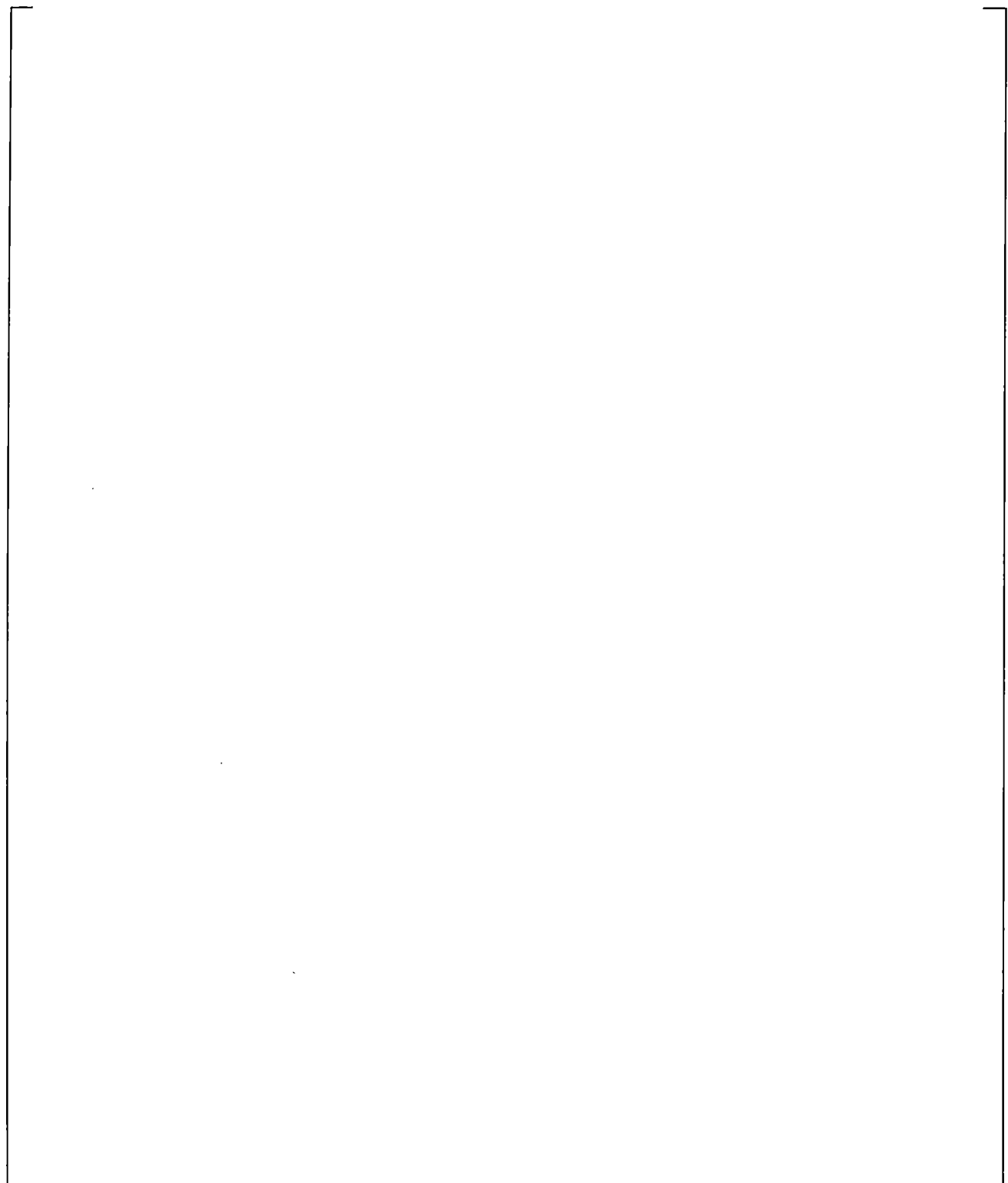


Figure 21.5-6 Pressurizer Pressures



a,c

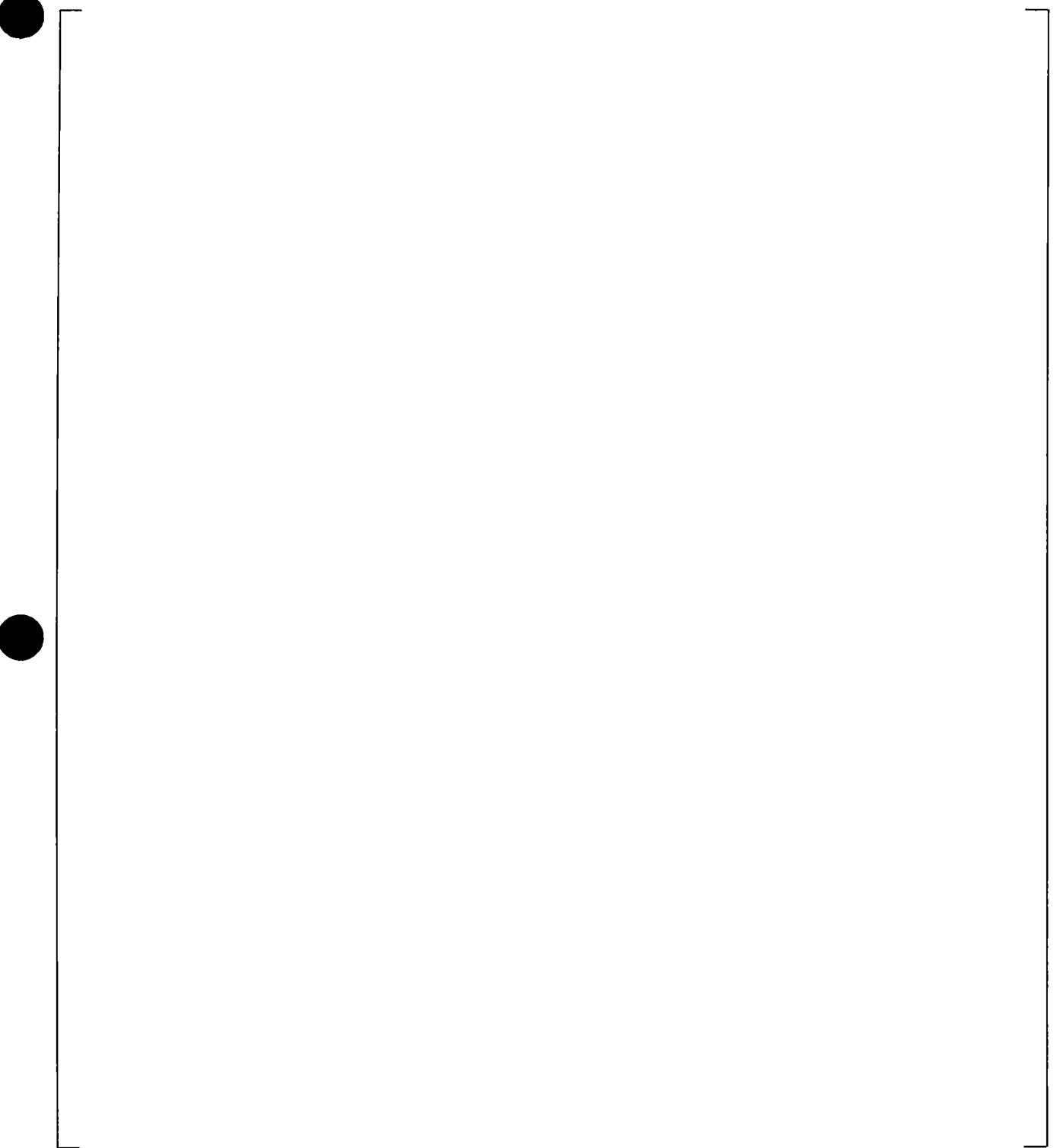
Figure 21.5-7 Steam Generator Secondary Side Pressures

a,c

Figure 21.5-8 Steam Generator A U-tube Differential Pressures

a,c

Figure 21.5-9 Steam Generator B U-tube Differential Pressures



a,c

Figure 21.5-10 Cross-Over Leg A Differential Pressures

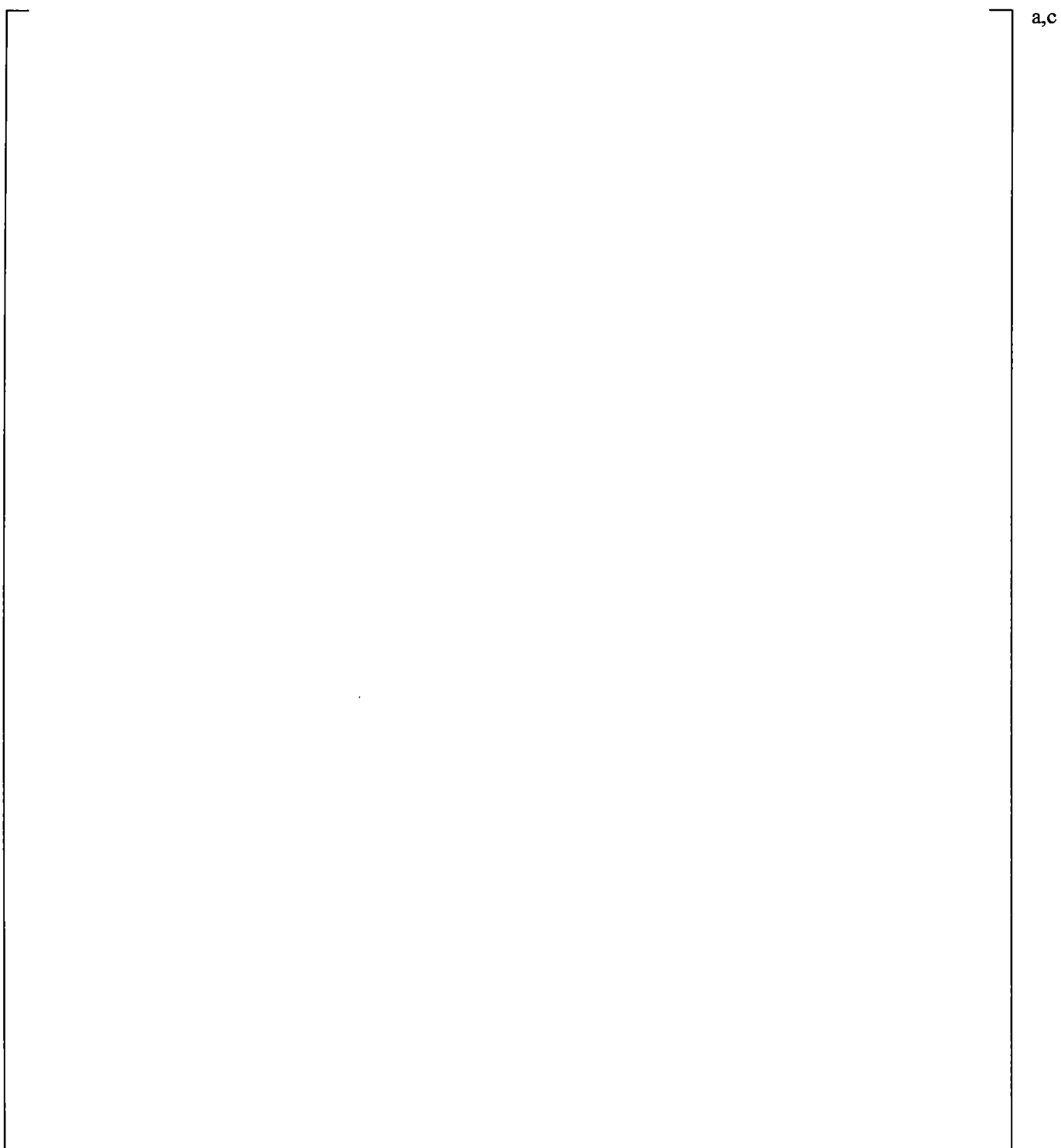


Figure 21.5-11 Cross-Over Leg B Differential Pressures

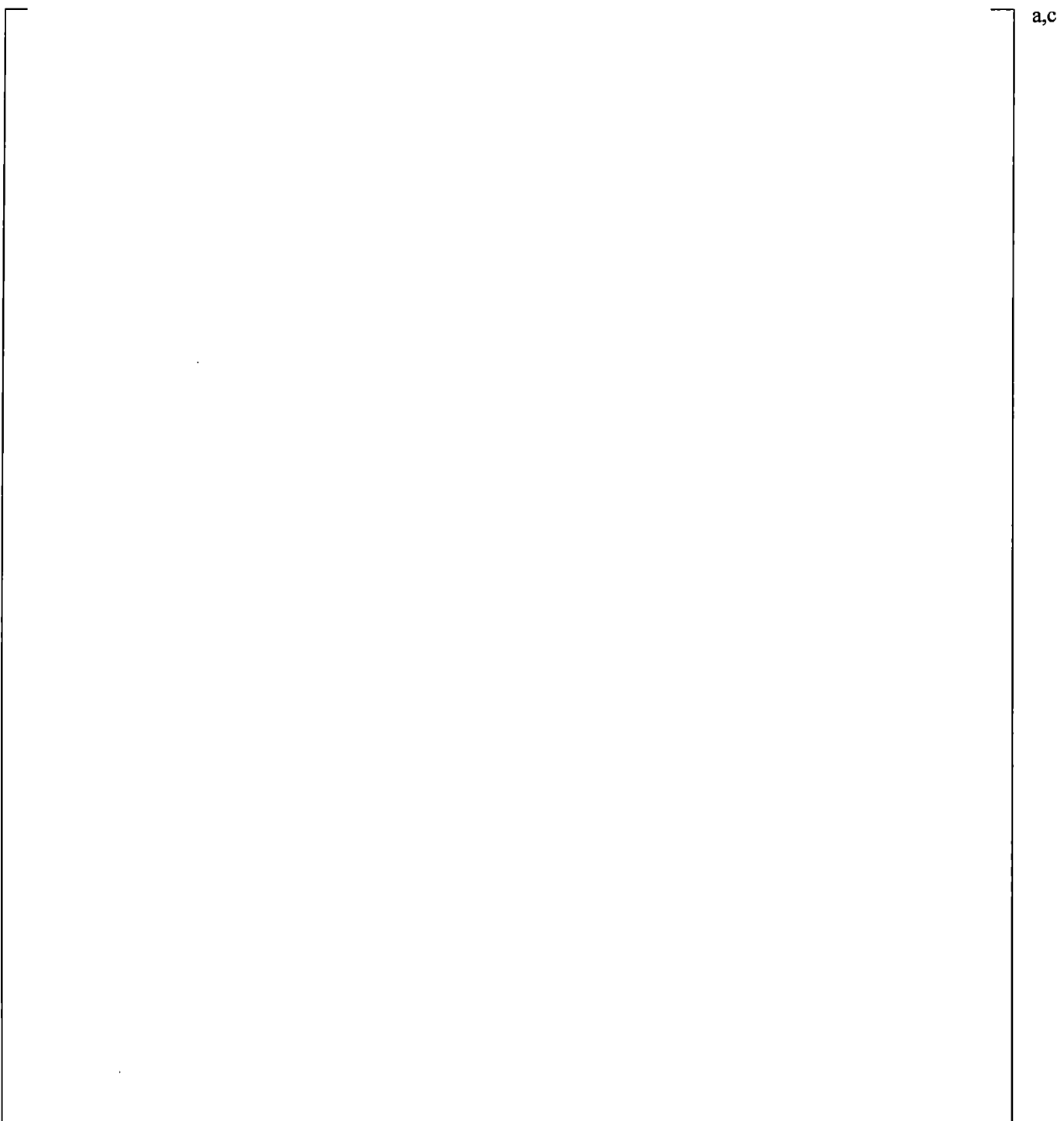
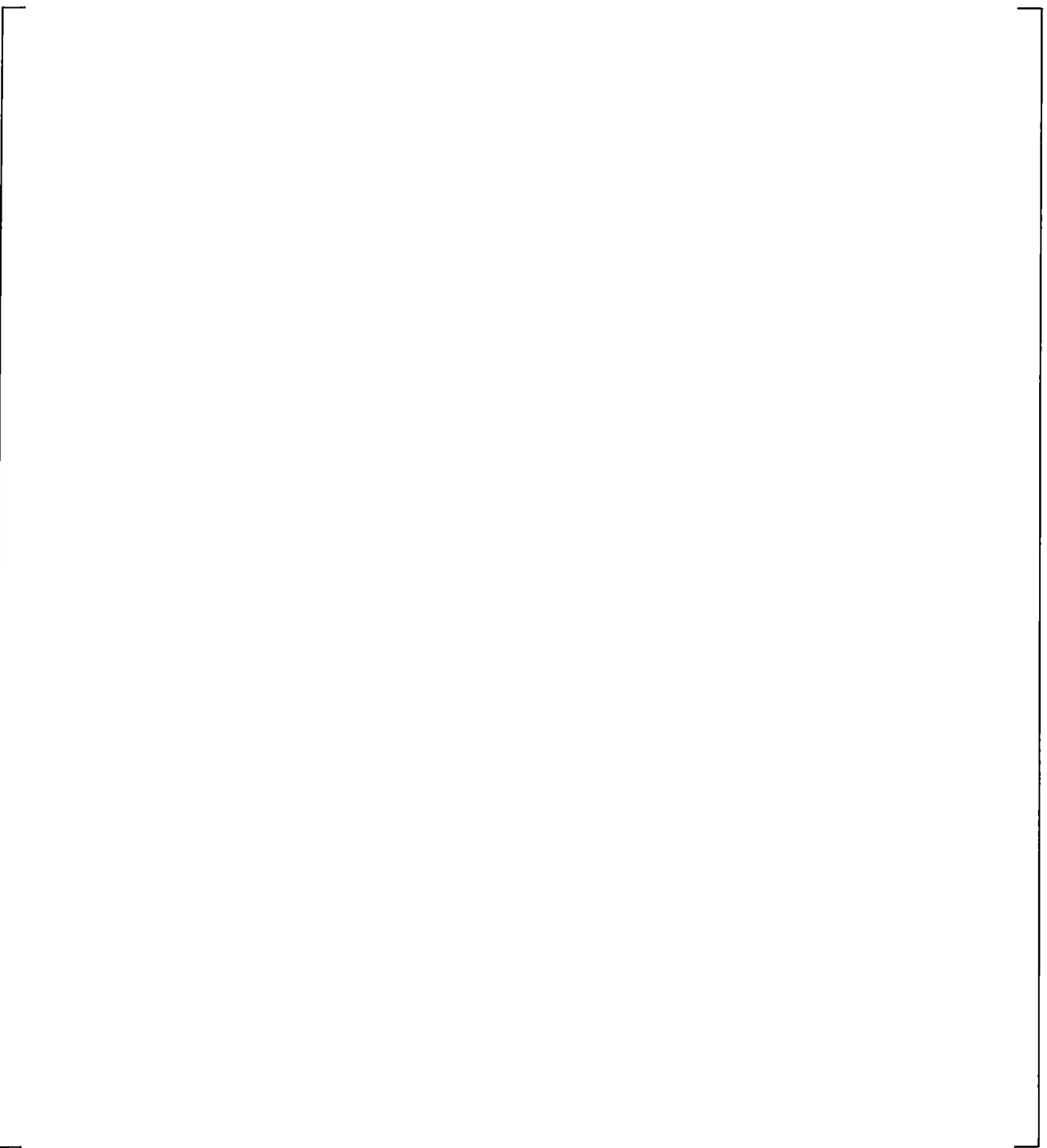
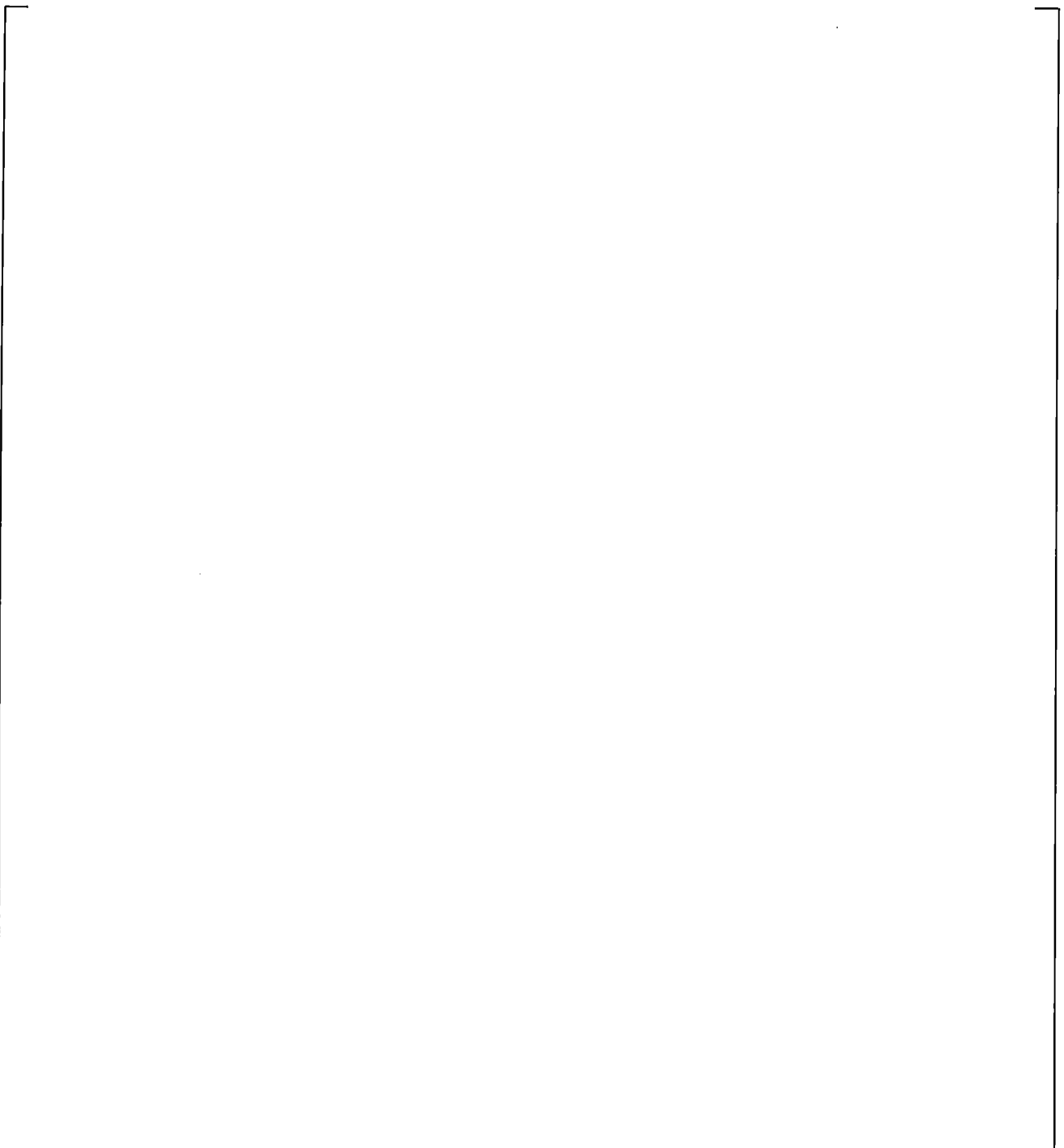


Figure 21.5-12 Upper Plenum Differential Pressures



a,c

| **Figure 21.5-13 Upper Plenum to Steam Generator A Inlet Differential Pressures**



a,c

| **Figure 21.5-14 Upper Plenum to Steam Generator B Inlet Differential Pressures**

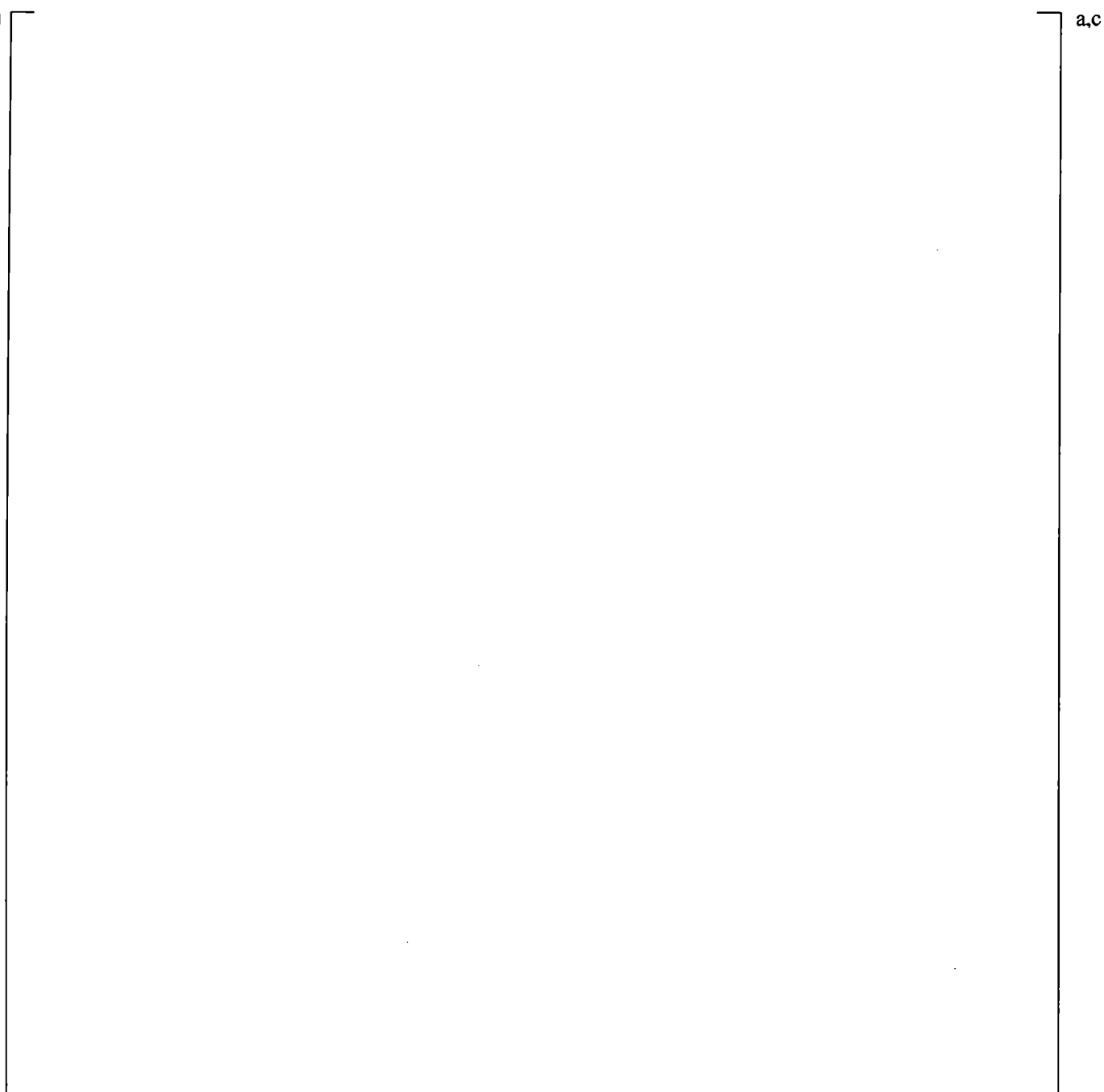


Figure 21.5-15 Downcomer Differential Pressures

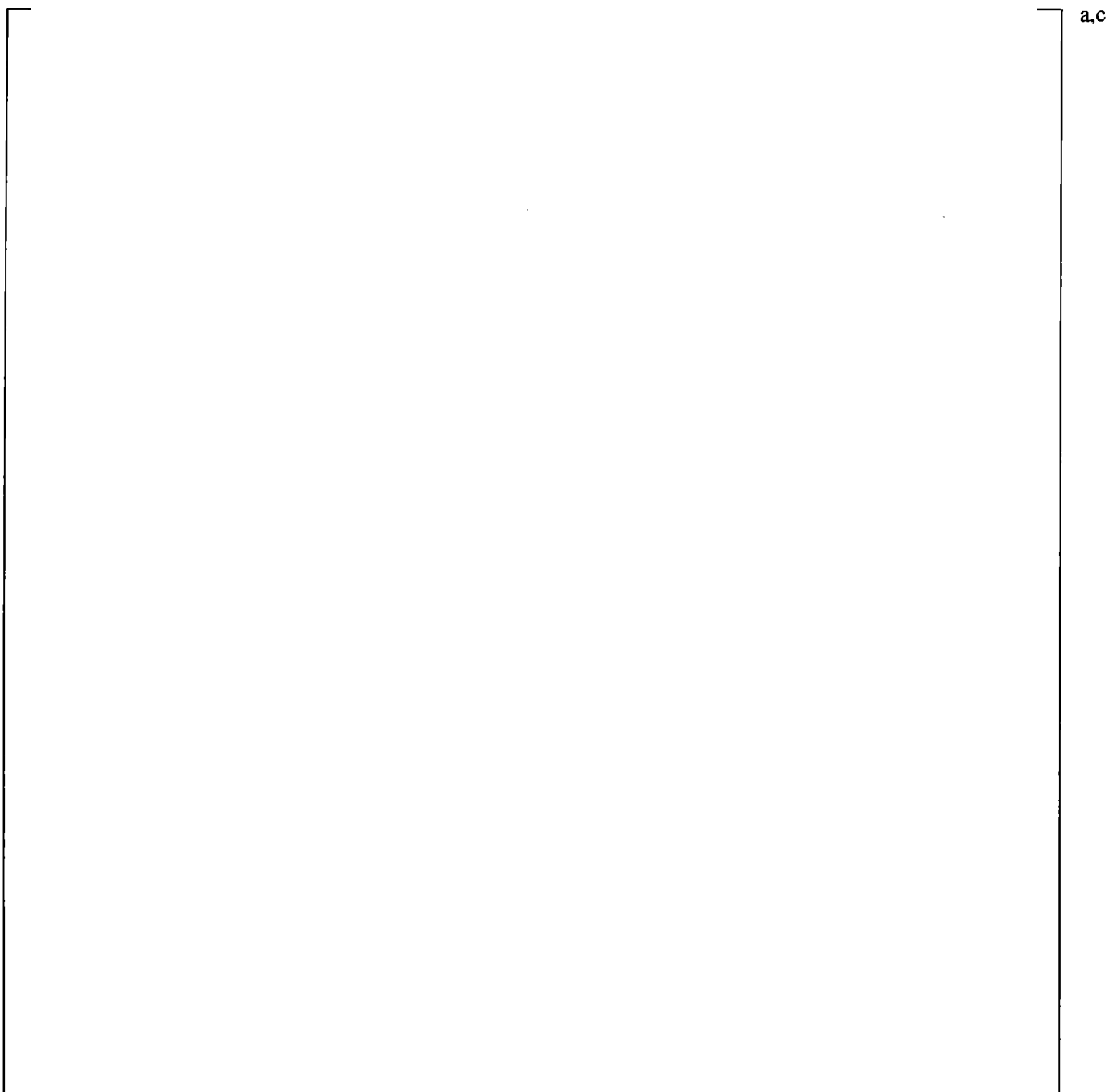


Figure 21.5-16 Core Differential Pressures

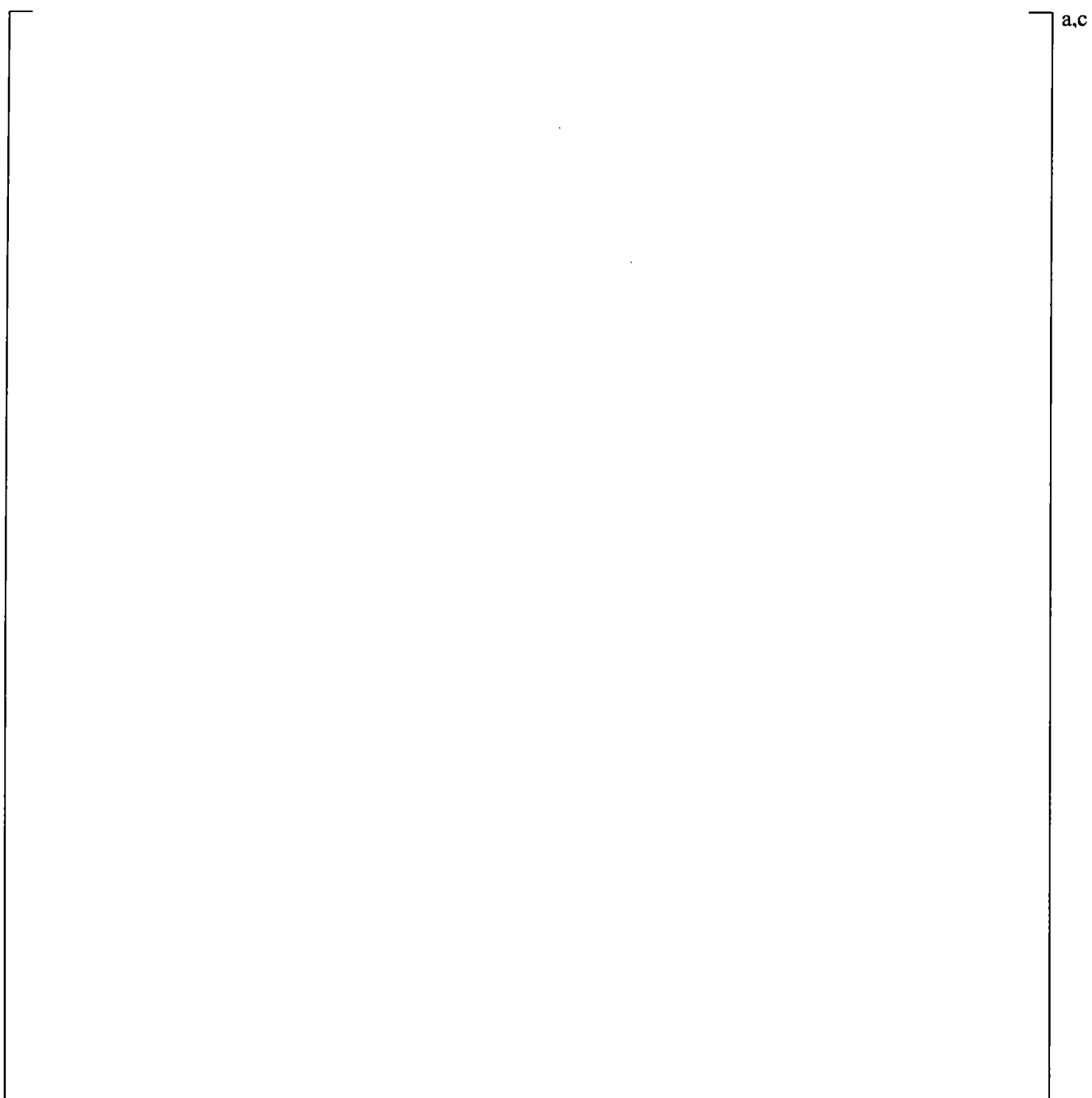
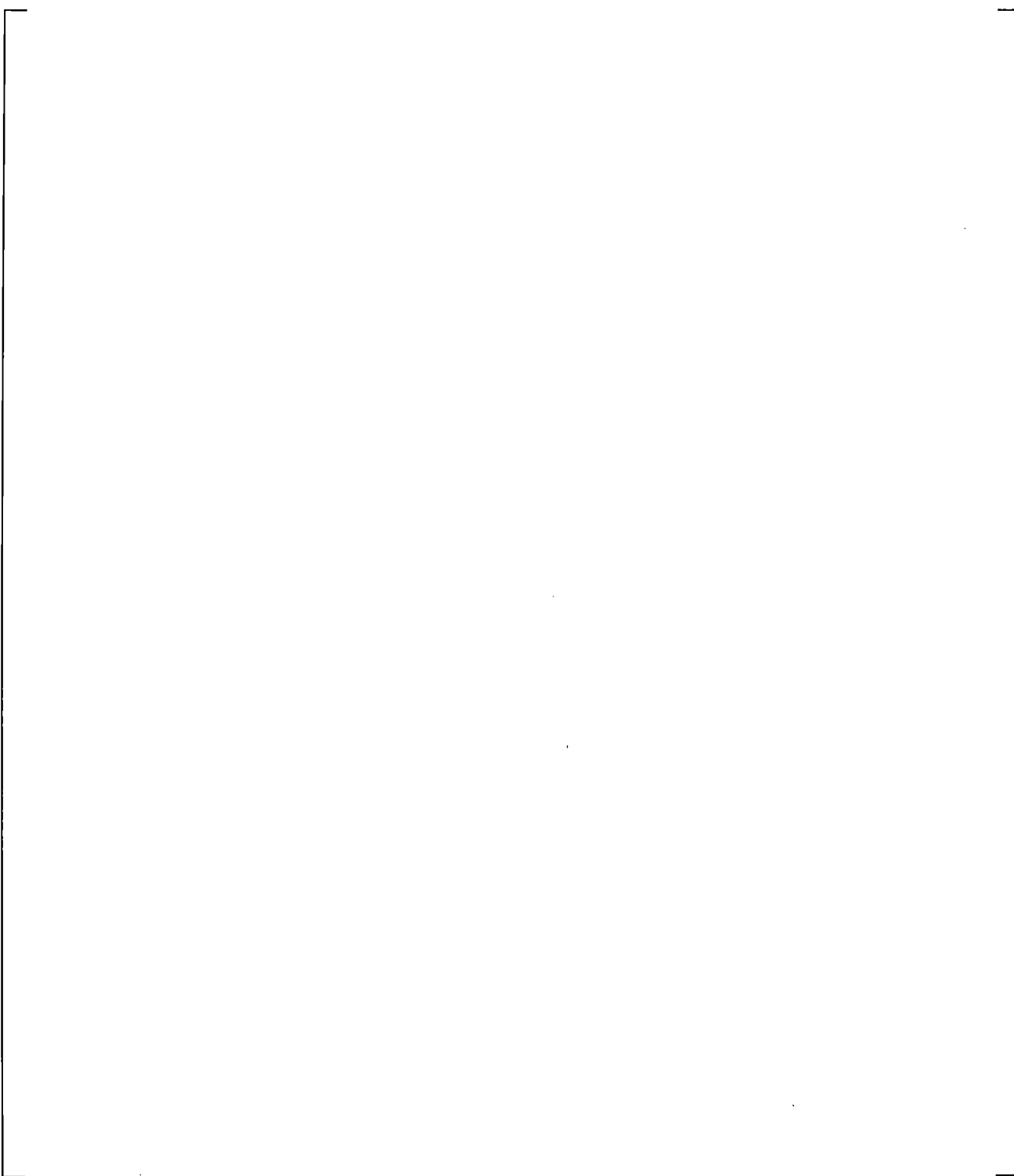


Figure 21.5-17 Core Differential Pressures for SB-CL-05 and SB-CL-18



a,c

Figure 21.5-18 Cold Leg A Pumped ECCS Injection Flows (CLA)

a,c

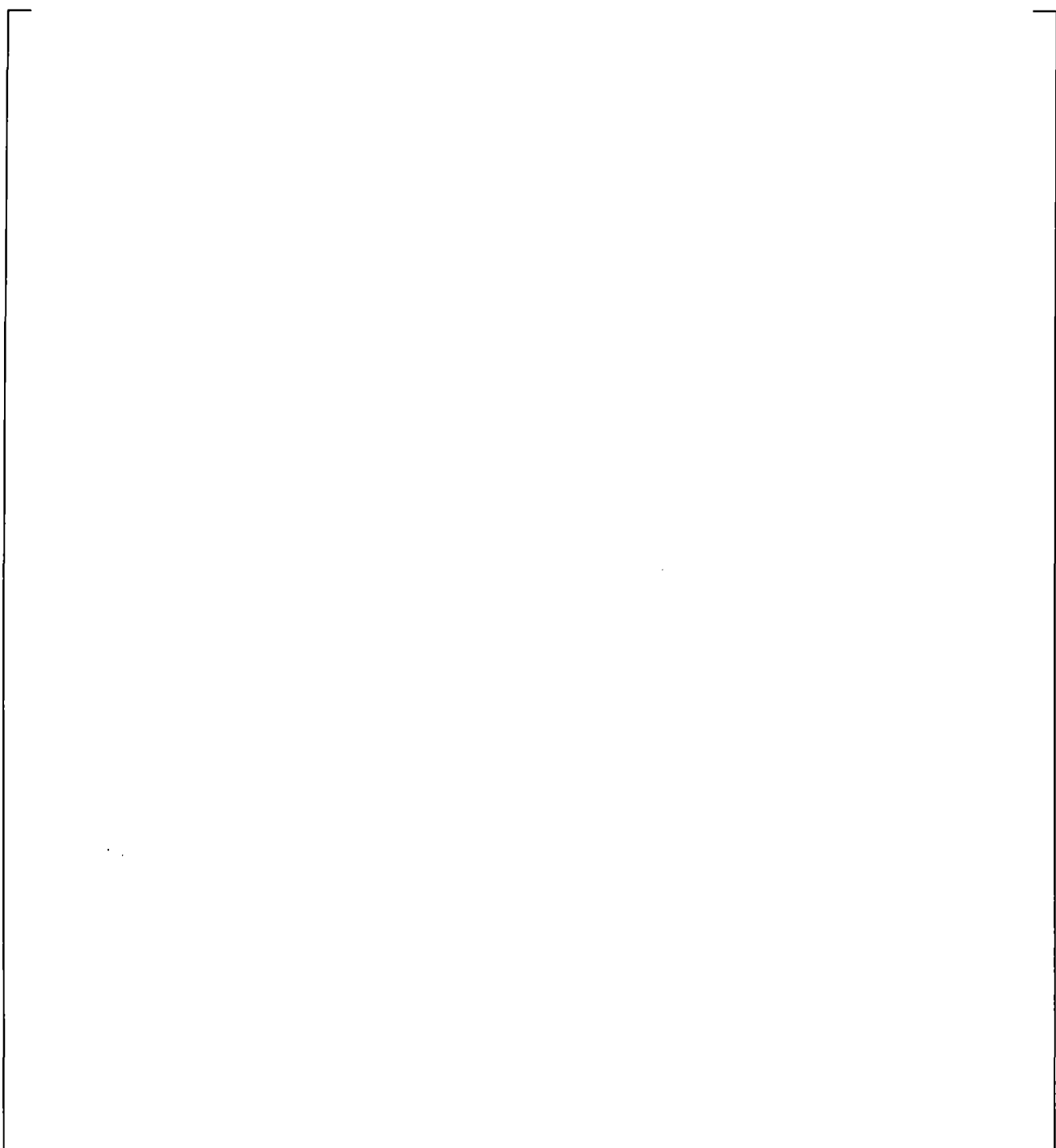


Figure 21.5-19 Total Pumped ECCS Injection Flows (Cold Leg A plus Cold Leg B)

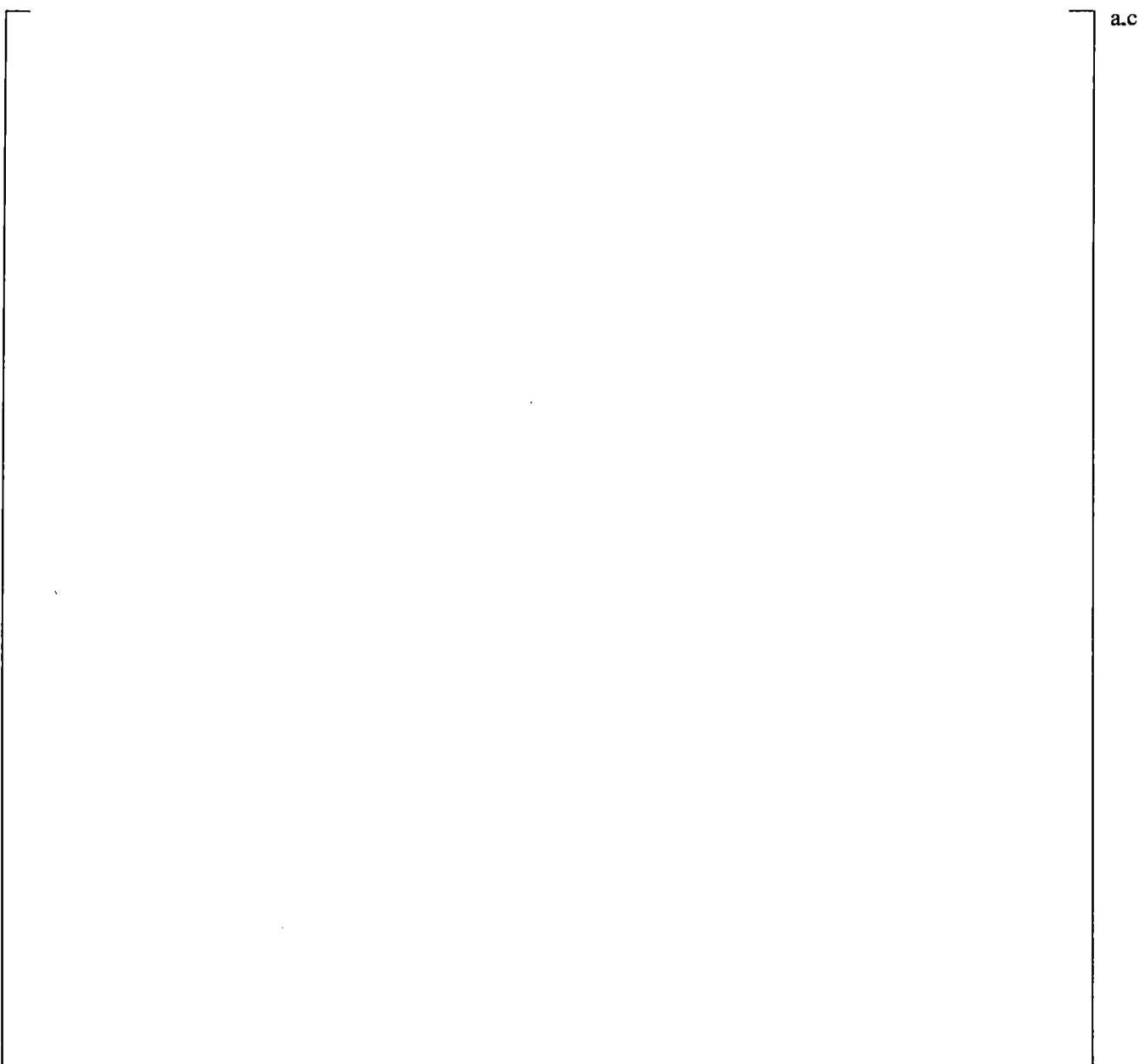


Figure 21.5-20 Accumulator Hot (ACH) Liquid Level

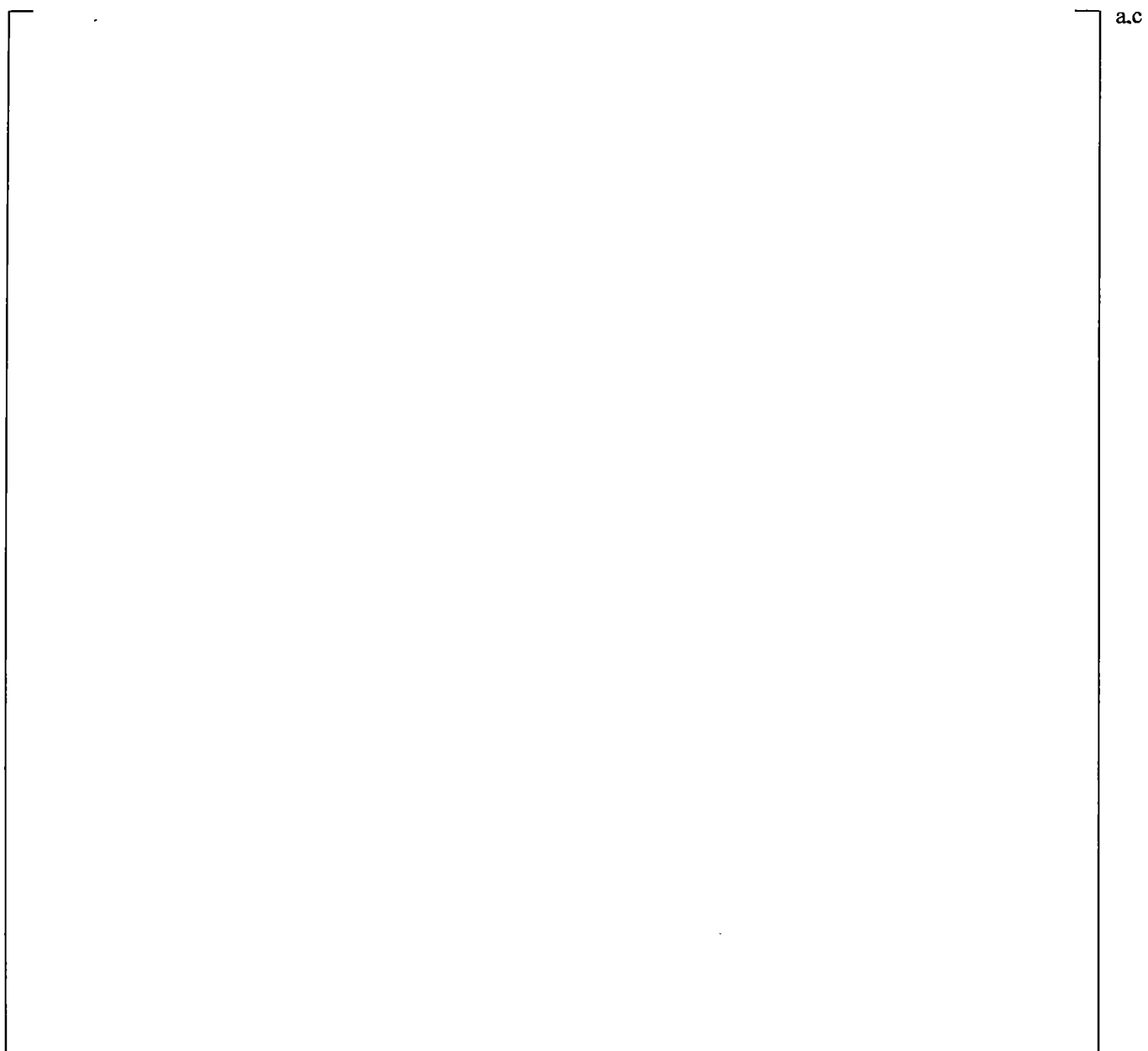


Figure 21.5-21 Calculated and Measured Cladding Temperatures at Mid-Core Elevation

21.6 SIMULATION OF THE 10% SIDE BREAK TEST SB-CL-14

One of the integral shakedown tests performed in the LSTF is a 10-percent cold leg break, which was the maximum break size for the facility design. This is a relatively large break size, corresponding to approximately a 9-inch break in a PWR, which could be considered more of an intermediate break as opposed to a small break LOCA. This break size is considered in order to test the code capabilities and expand the break spectrum to include intermediate break sizes as well.

]^{a,c}

21.6.1 Description of the Boundary and Initial Conditions

The initial conditions for the 10% break test SB-CL-14 are summarized in Table 21.6-2.

The operational setpoints for this 10-percent break are consistent with the standard set used in all ROSA-IV tests, as summarized in Table 21.2-2. The charging and the high-pressure injection were not actuated in this test. The low-pressure injection system was active in this test, but was not modeled in the simulation, since during the test the injection initiated 862 seconds after the break, well beyond the period of interest in this calculation.

The break was located in loop B, the loop without the pressurizer, and was oriented horizontally from the middle of the cold leg. The 10% break size was simulated by using a break orifice with diameter of 31.9 mm (1.256 inch). The break was initiated by opening of a fast acting air operated valve that directed the break flow into the catch tank.

As mentioned earlier, this test used a realistic decay heat curve, as documented in Table 21.6-1. Initiated by the reactor scram signal, the core power was controlled by a test sequence controller according to the curve in Table 21.6-1.

The pump speed was controlled by the sequence controller to follow a preprogrammed coastdown curve. The pump speed was initially increased but then, triggered by the reactor scram signal, a coastdown was initiated at 13.2 seconds which followed a predefined curve.

21.6.2 Results and Conclusions for the SB-CL-14 Simulations

This section presents the results of two SB-CL-14 test transient simulations. Both simulations were performed with break flow discharge coefficients []^{a,c} Consistent with the adopted modeling approach with regards to counter-current flow, one of the simulations was performed with CCFL []^{a,c}

Table 21.6-3 summarizes the predicted and measured chronology of key events for the 10-percent cold leg test. Figures 21.6-1 through 21.6-16 present the SB-CL-14 test simulation results compared to the test measurements. With the exception of Figures 21.6-1 and 21.6-2, these figures show the results of both simulations, with and without CCFL enforced. Figures 21.6-17 through 21.6-20 show counter-current flow conditions at the steam generator U-tube inlet and the hot leg elbow locations, calculated for both test simulations.

Figures 21.6-1 and 21.6-2 show a comparison of the modeled vs. measured pump speed for the two pumps for the simulation with CCFL enforced; it is noted that the same pump coast-down curves were implemented for the simulation without CCFL enforced. As seen, there is a good match between the modeled and measured pump speed. Consequently, the calculated loop flows for the first minute of the transient are fairly consistent with the test measurements, as shown in Figures 21.6-3 and 21.6-4. Due to the two-phase conditions established at the flow meters following the onset of loop seal clearance, the measured (test) flow rates beyond 80 seconds are unreliable and cannot be used for validation of the calculated break flow.

The break flow comparison is shown in Figure 21.6-5, where the predicted break flow is compared against the test break flow as calculated from the measured level in the catch tank. []^{a,c}

[]^{a,c}

]^{a,c}

Table 21.6-1

] a,c

a,c

Table 21.6-2

J^{a,c}

a,c

Table 21.6-3

a,c

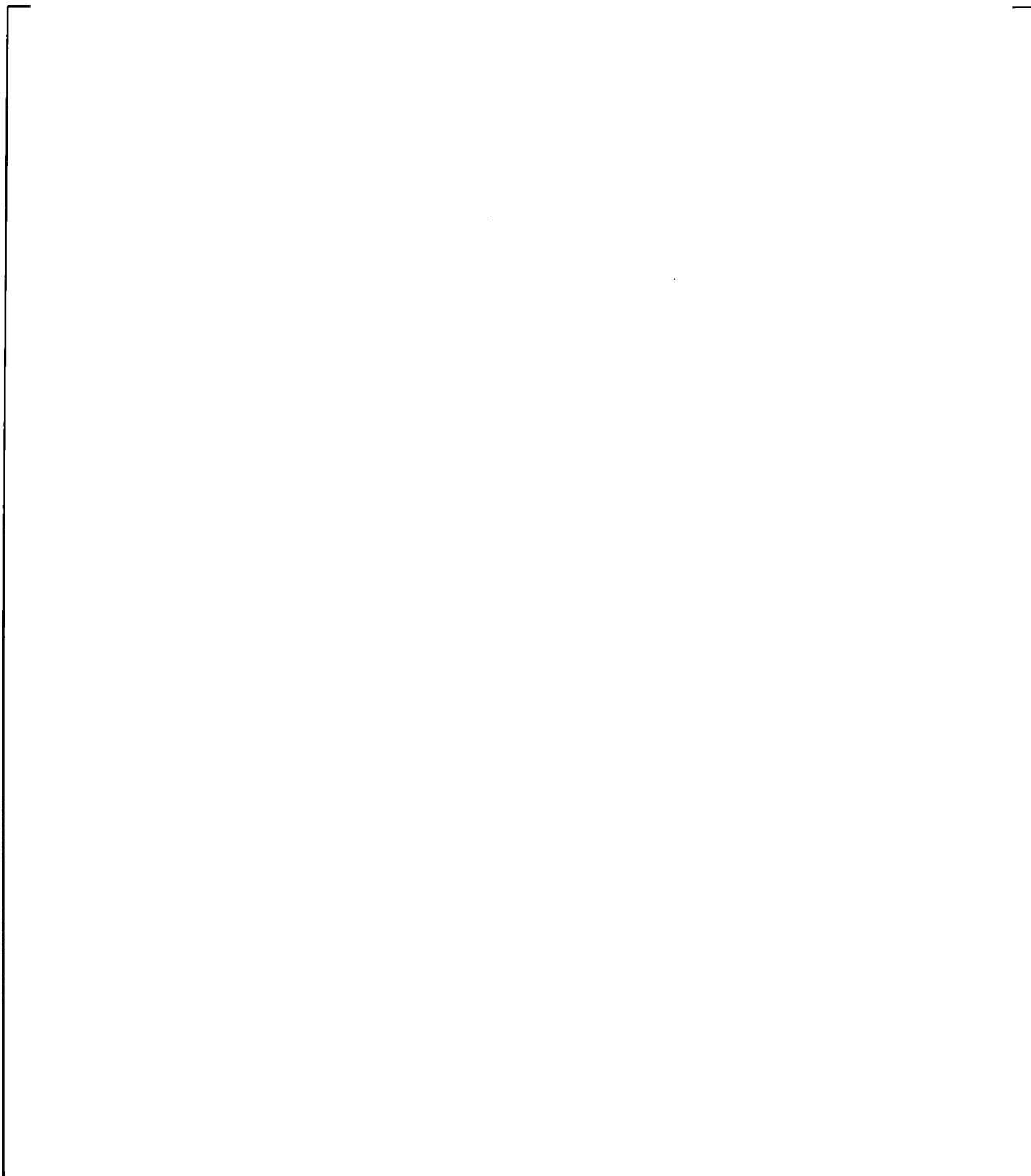


Figure 21.6-2 Loop-B Pump Speed Comparison

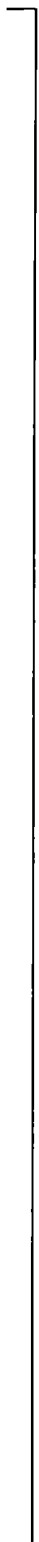
Note: 1 Hz=30 rpm=3.1415 rad/sec

a,c

Figure 21.6-3 Comparison of Loop-A Flow Rates

a,c

Figure 21.6-4 Comparison of Loop-B Flow Rates



a,c

Figure 21.6-5 Comparison of Break Flows

a,c

Figure 21.6-6 Comparison of Fluid Density in the Break Spool

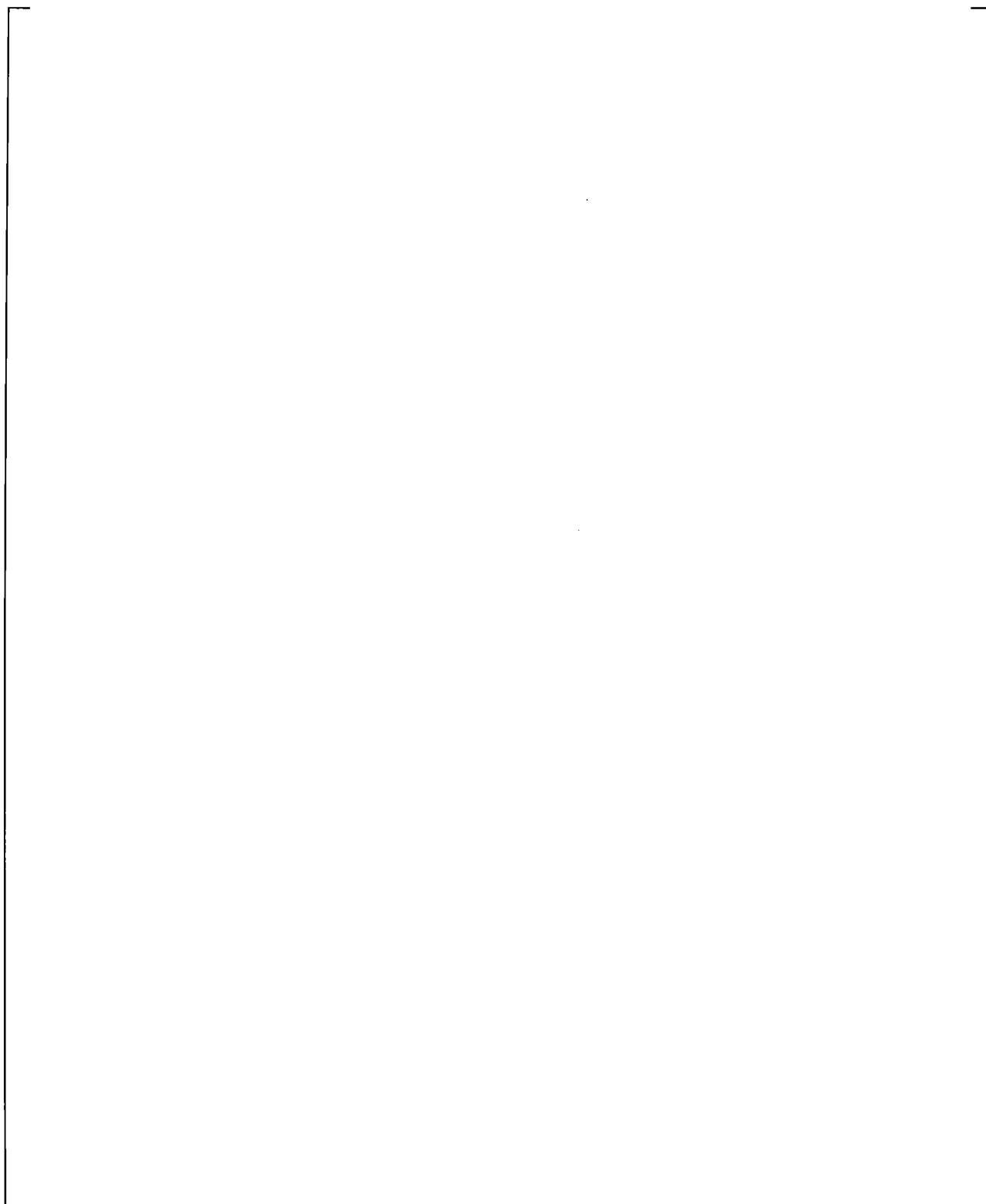


Figure 21.6-7A Comparison of Loop-A Cross-Over Leg Differential Pressures

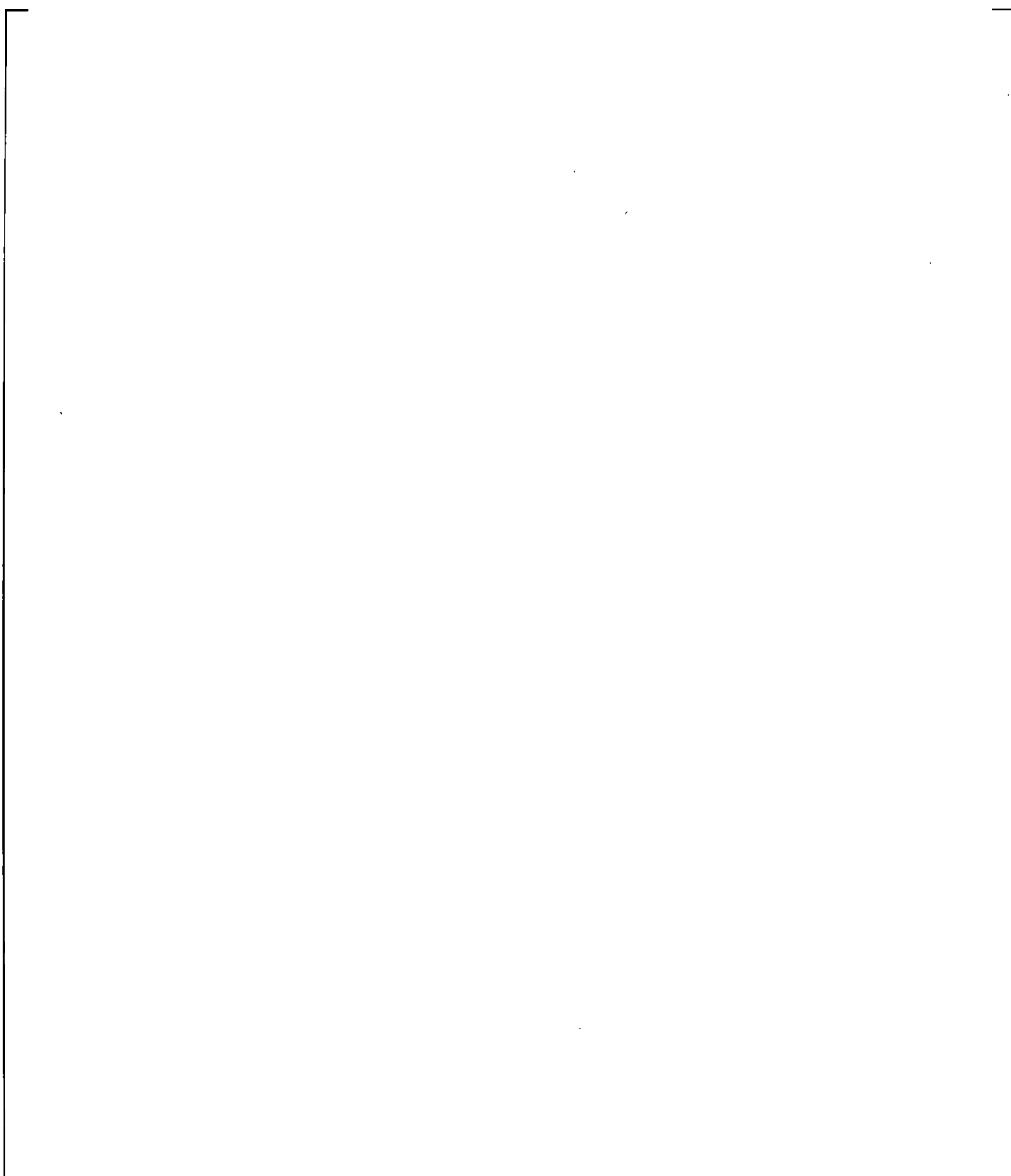
a,c

Figure 21.6-7B Comparison of Loop-B Cross-Over Leg Differential Pressures

a,c

Figure 21.6-8 Comparison of System Pressures

a,c,e



| **Figure 21.6-9 Comparison of Steam Generator A U-tube Inlet-to-top Differential Pressures**

a,c,e

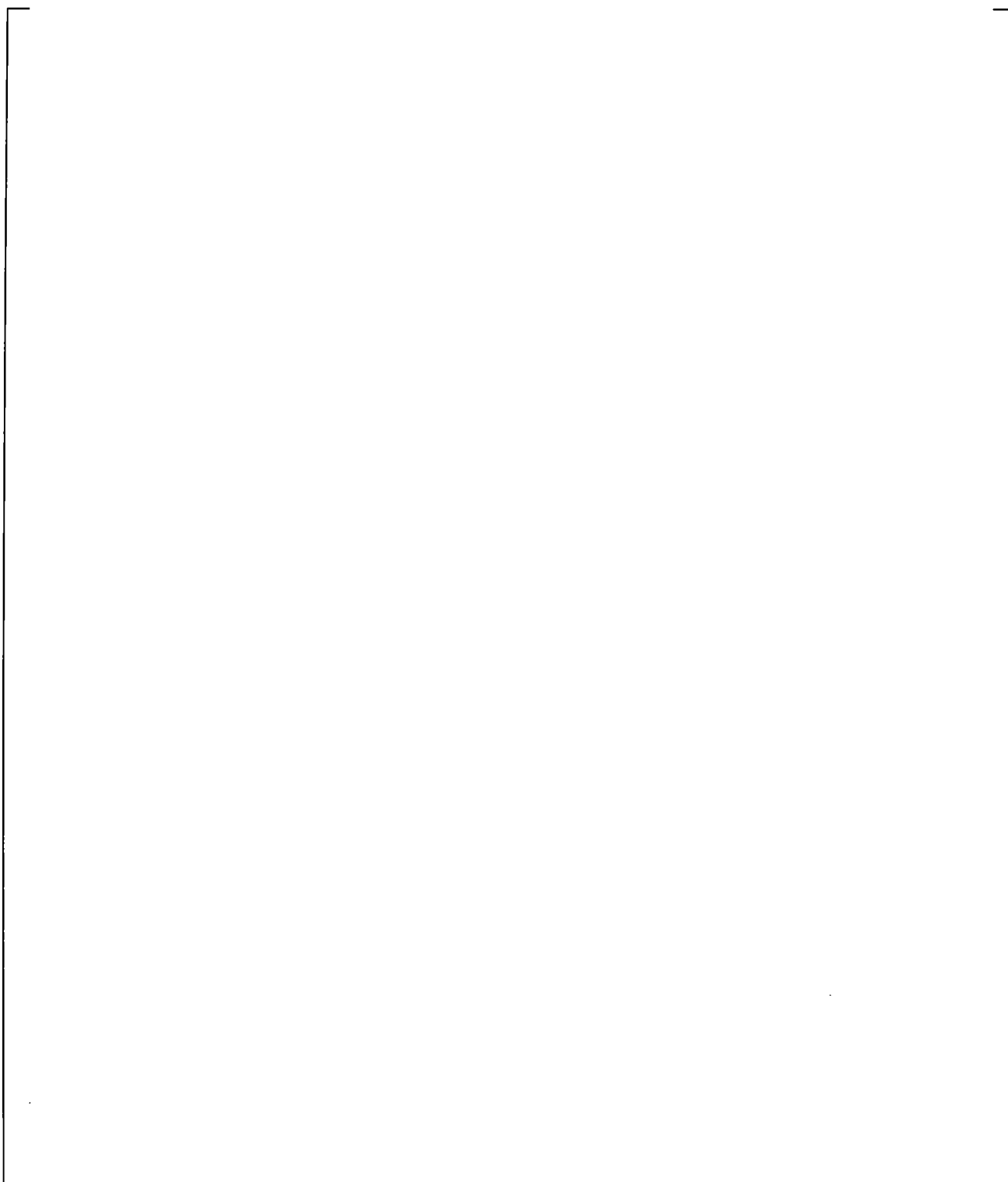


Figure 21.6-10 Comparison of Steam Generator B U-tube Inlet-to-top Differential Pressures

a,c,e

Figure 21.6-11 Comparison of Steam Generator A U-tube Outlet-to-top Differential Pressures

a,c,e

Figure 21.6-12 Comparison of Steam Generator B U-tube Outlet-to-top Differential Pressures

a,c,e

Figure 21.6-13A Comparison of Steam Generator A Inlet Plenum Draining

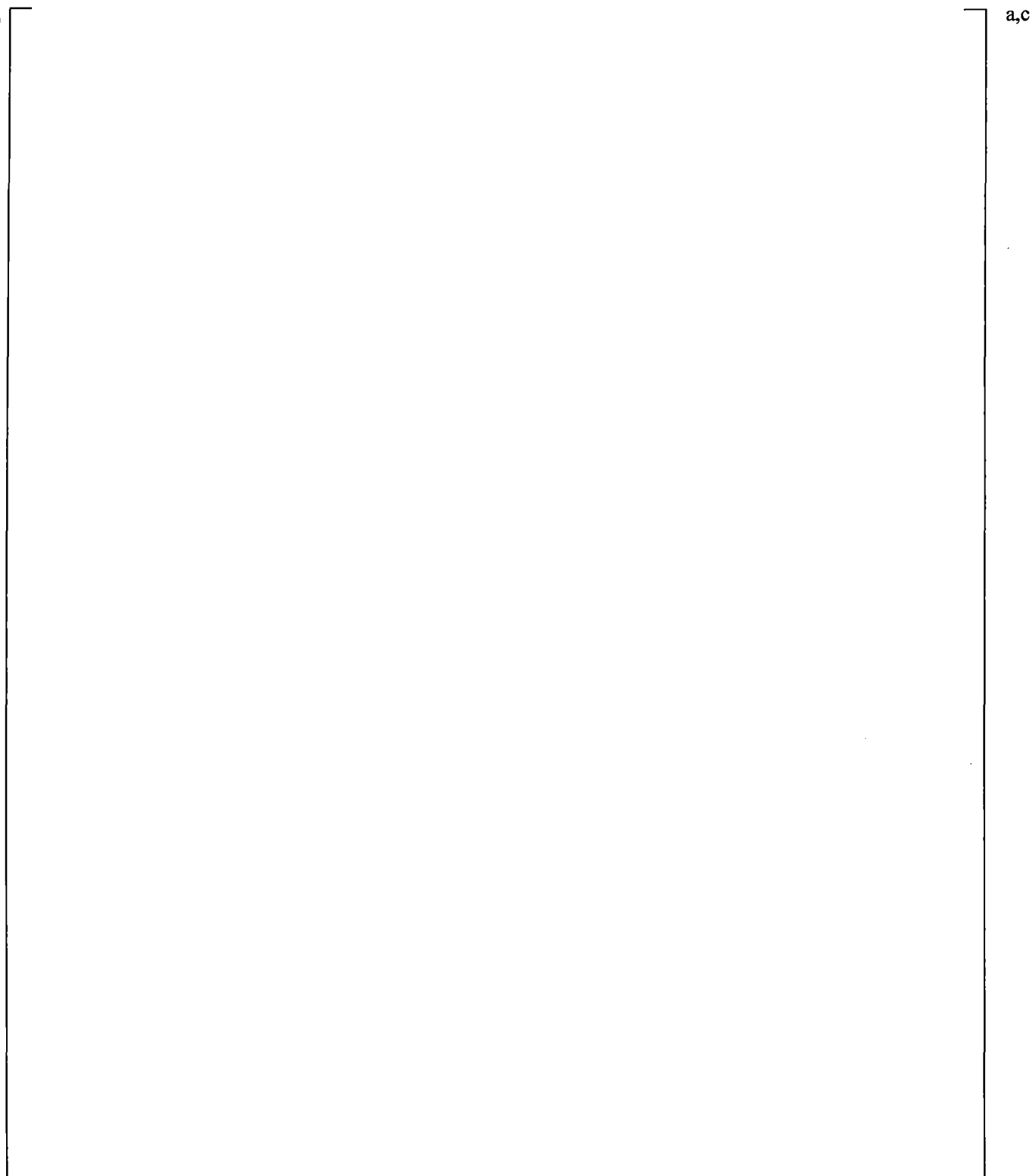


Figure 21.6-13B Comparison of Steam Generator B Inlet Plenum Draining

Figure 21.6-14 Comparison of Core Collapsed Liquid Levels

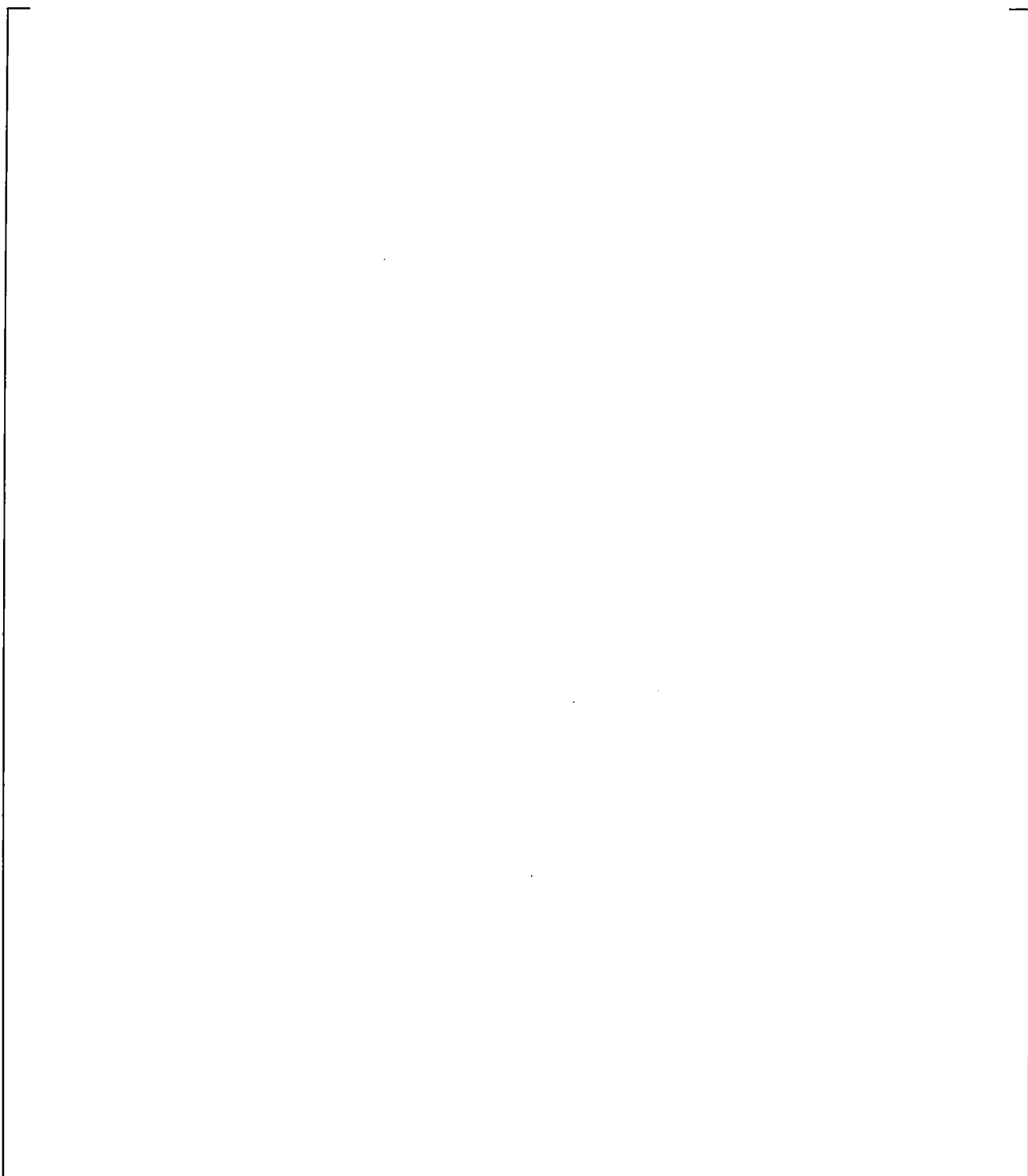
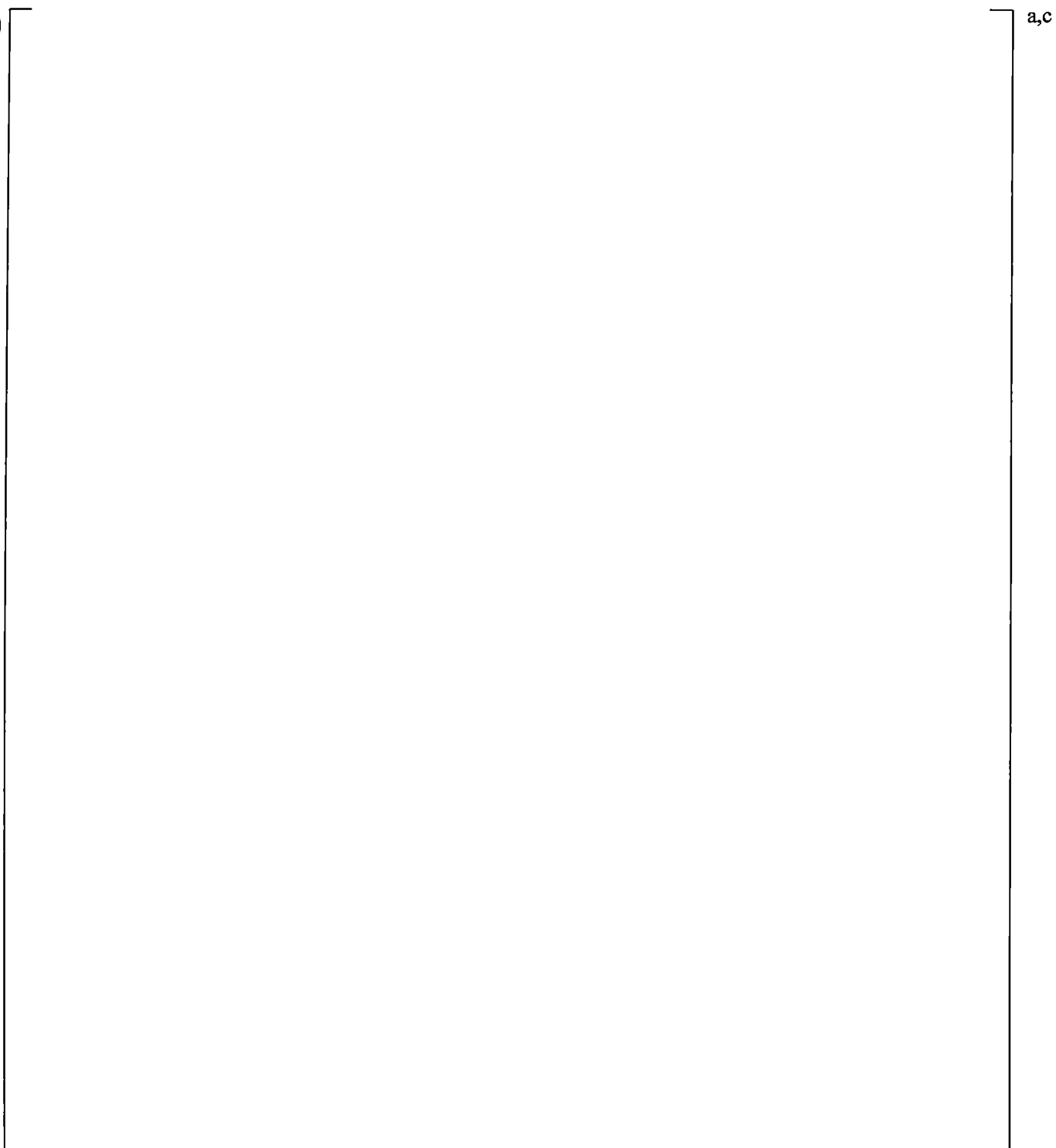


Figure 21.6-15A Calculated Accumulator Injection to Loop A

a,c

Figure 21.6-15B Calculated Accumulator Injection to Loop B



a,c

Figure 21.6-16 High Power Rod (Rod 1) Cladding Temperature at 6-ft (1830 mm) Core Axial Location (Measurement uncertainty is 6.4K)

a,c

Figure 21.6-17 Calculated Counter-current Flow at Steam Generator A U-tube Inlet

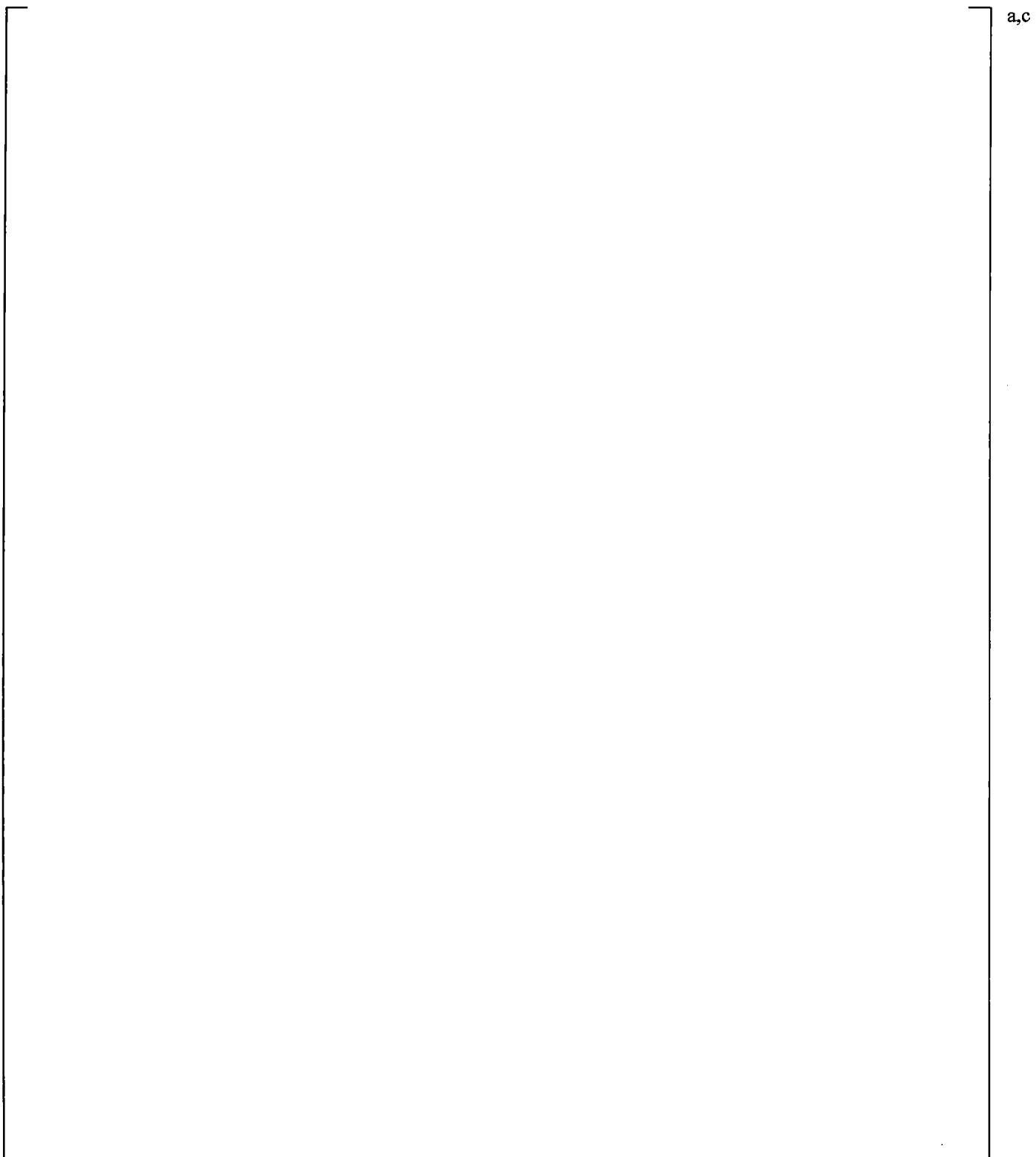


Figure 21.6-18 Calculated Counter-current Flow at Steam Generator B U-tube Inlet

a,c

Figure 21.6-19 Calculated Counter-current Flow at Elbow of Hot Leg A

Figure 21.6-20 Calculated Counter-current Flow at Elbow of Hot Leg B

21.7 BREAK ORIENTATION STUDY: SIMULATION OF TOP/SIDE/BOTTOM 0.5% (SB-CL-16/12/15) AND 2.5% (SB-CL-03/01/02) COLD LEG BREAKS

^{a,c} The purpose of the study, presented in this section, is to assess the ability of the WCOBRA/TRAC-TF2 code to predict break orientation effects.

21.7.1 Description of the Boundary and Initial Conditions

For each of the test simulations presented here a steady-state calculation is performed first to achieve the desired initial conditions according to the particular test being simulated. |

12,0

21.7.2 Discussion of Results

In LSTF, the break unit can be configured such that the break orientation effect can be studied. Two sets of three experiments were conducted in the LSTF to investigate the effect of break orientation. The first three tests (SB-CL-01, -02, and -03; side, bottom and top respectively), simulated a 2.5 % break in the cold leg. The second set of three tests (SB-CL-12, -15 and -16) simulated a 0.5% break in the cold leg. In this section these two sets of break orientation studies will be discussed.

21.7.2.1 2.5% Tests

In these experiments, the break was oriented at the side, bottom, and top of the loop B cold leg. Experimental results are summarized in the data report by Koizumi (Koizumi et al., 1988). The test results showed that break orientation had only a small effect on system parameters such as pressure and core collapsed liquid level. Figure 21.7-1 shows the break geometry and orientation for these tests. Together with 0.5% break orientation tests, which will be discussed later in this section, these tests provide a useful means of evaluating the break flow model in WCOBRA/TRAC-TF2 for the effects of vapor pull through and liquid entrainment near the break orifice.

Boundary Conditions

Operational setpoints for the 2.5 % cold leg break tests were the same as those implemented in all ROSA-IV small break tests, shown in Table 21.2-2, with the following two exceptions. [

1a,c

All three tests were conducted, and modeled, using the same JAERI (full conservative) decay heat curve, Table 21.7-1.

Figure 21.7-2 shows the break modeling approach used in the 2.5 percent cold leg break simulations. Results for the 2.5 percent cold leg break runs are compared to data in Figures 21.7-3 through 21.7-9. Figure 21.7-10 shows just the calculated accumulator flows; no test data was available for comparison.

Pressure

[
]
]^{a,c}

Break Flow

Figure 21.7-4 shows the predicted and measured break flows. The test data for all three orientation breaks show no difference in the break flow rate until 150 seconds. Similar to the experimental data, the break orientation simulations showed only a small effect on the predicted break flow during the first 150 seconds as well. After the transition to two-phase, which occurs around 150 seconds, the flow in the cold legs becomes stratified. When the break flow quality turns to two-phase and the cold leg flow stratifies, the test data shows that the break flows diverge from each other, Figure 21.7-4(b). First, the top break and side break discharge becomes two-phase, and the discharge flow rate reduces abruptly. In the test, the transition of the bottom break to two-phase occurs about 50 seconds later. For the bottom break, it takes longer to become two-phase because the level in the cold leg needs to drop low enough in order for the vapor to be entrained into the break spool. In the simulations, the predicted timing of the break flow transition from single-phase sub-cooled discharge to high void two-phase discharge is predicted

[
]
]^{a,c}

The comparison in Figure 21.7-5 indicates that the WCOBRA/TRAC-TF2 simulations predict relatively well the general two phase level characteristics of the experiments. Similar to the test, after the calculated brief period of 30 seconds instability following the transition to two-phase flow, the top and side breaks tend to maintain a higher mixture level in the broken cold leg compared to the bottom oriented break. However, the calculated mixture level for the bottom break is somewhat higher than that observed in the test. One possible explanation of this inconsistency might be that the code calculates downcomer level

[
]
]^{a,c}

WCAP-16996-NP

June 2015
Revision 1

Core Collapsed Liquid Level

[

|

]^{a,c}**Core Heat-up**

[

|

|

]^{a,c}**21.7.2.2 0.5% Breaks**

Break orientation study was also conducted with the 0.5% break tests SB-CL-12, 15 and 16 (side, bottom and top break respectively). Figure 21.7-11 shows the break unit used in these tests. Unlike the SB-CL-01/02/03 tests, in these tests there is no break offtake pipe and the break hole (orifice) is located right at the cold leg wall.

As the 2.5% break tests, these three tests were conducted, and modeled, using the same JAERI (full conservative) decay heat curve, Table 21.7-1.

Liquid Level in Broken Cold Leg

[

]^{a,c}

Core Collapsed Level

[

|

|

|

]^{a,c}

Break Flow

[

|

]^{a,c}

21.7.3 Conclusions

Comparison between the test data and the simulation runs performed using WCOBRA/TRAC-TF2 show that the break orientation effects exhibit similar trends in terms of the break flow, loop seal clearing timing, core depression, and the beginning of boil-off heat-up. [

I^{a,c}

Table 21.7-1 JAERI (Full Conservative) Decay Heat Curve

Time After Rx Trip	Test Power	Normalized Power
sec	MW	-
(1)	(2)	(3)
-	10.000	1.00000
0	10.000	1.00000
29	10.000	1.00000
40	8.912	0.89120
60	7.344	0.73440
80	6.128	0.61280
100	5.200	0.52000
150	3.632	0.36320
200	2.848	0.28480
400	1.776	0.17760
600	1.568	0.15680
800	1.488	0.14880
1000	1.424	0.14240
1500	1.280	0.12800
2000	1.200	0.12000
4000	0.992	0.09920

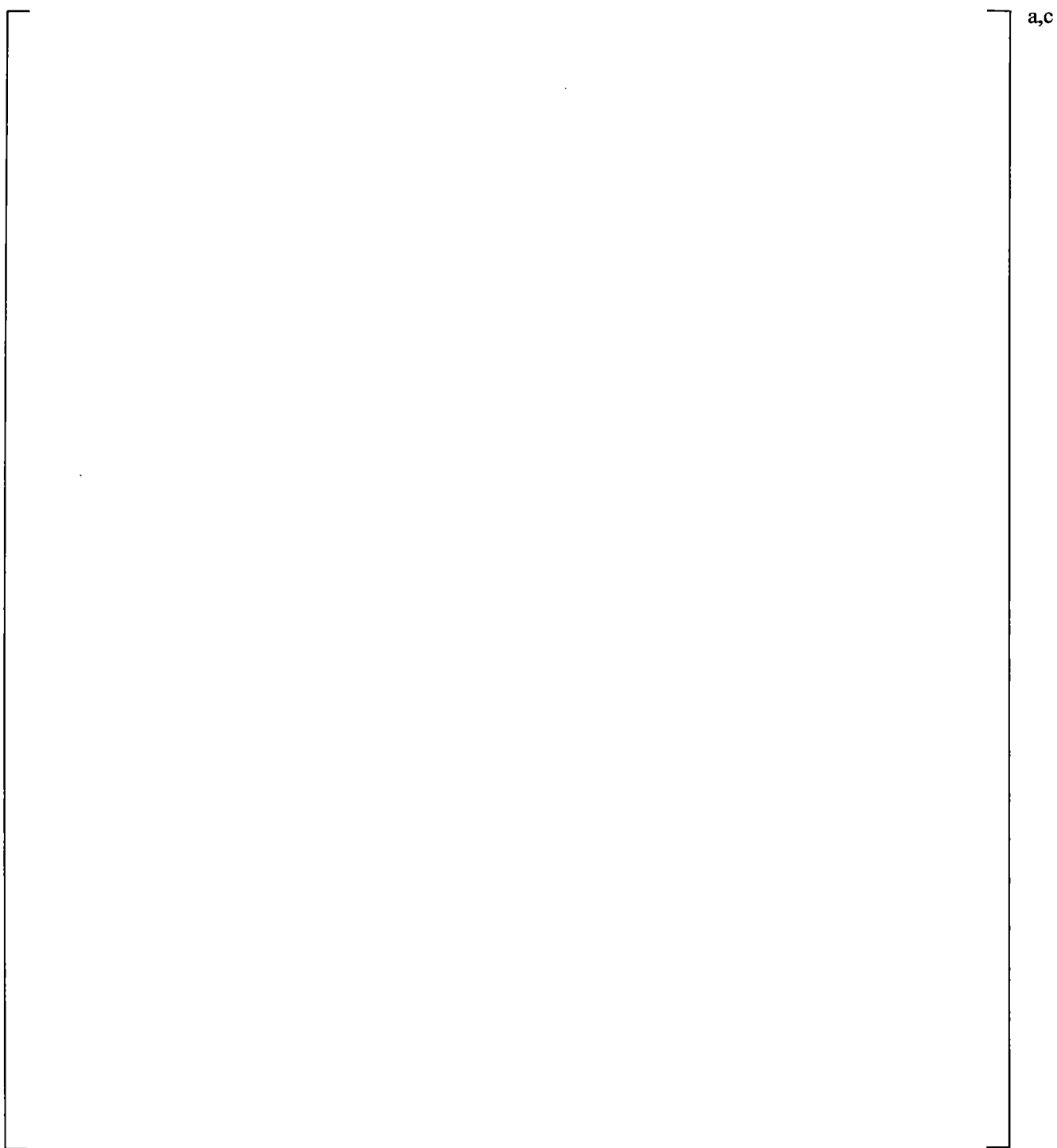


**Figure 21.7-1 Break Unit Configuration used in 2.5% Cold Leg Break Tests, SB-CL-01, 02, and 03
(Koizumi et al., 1987)**

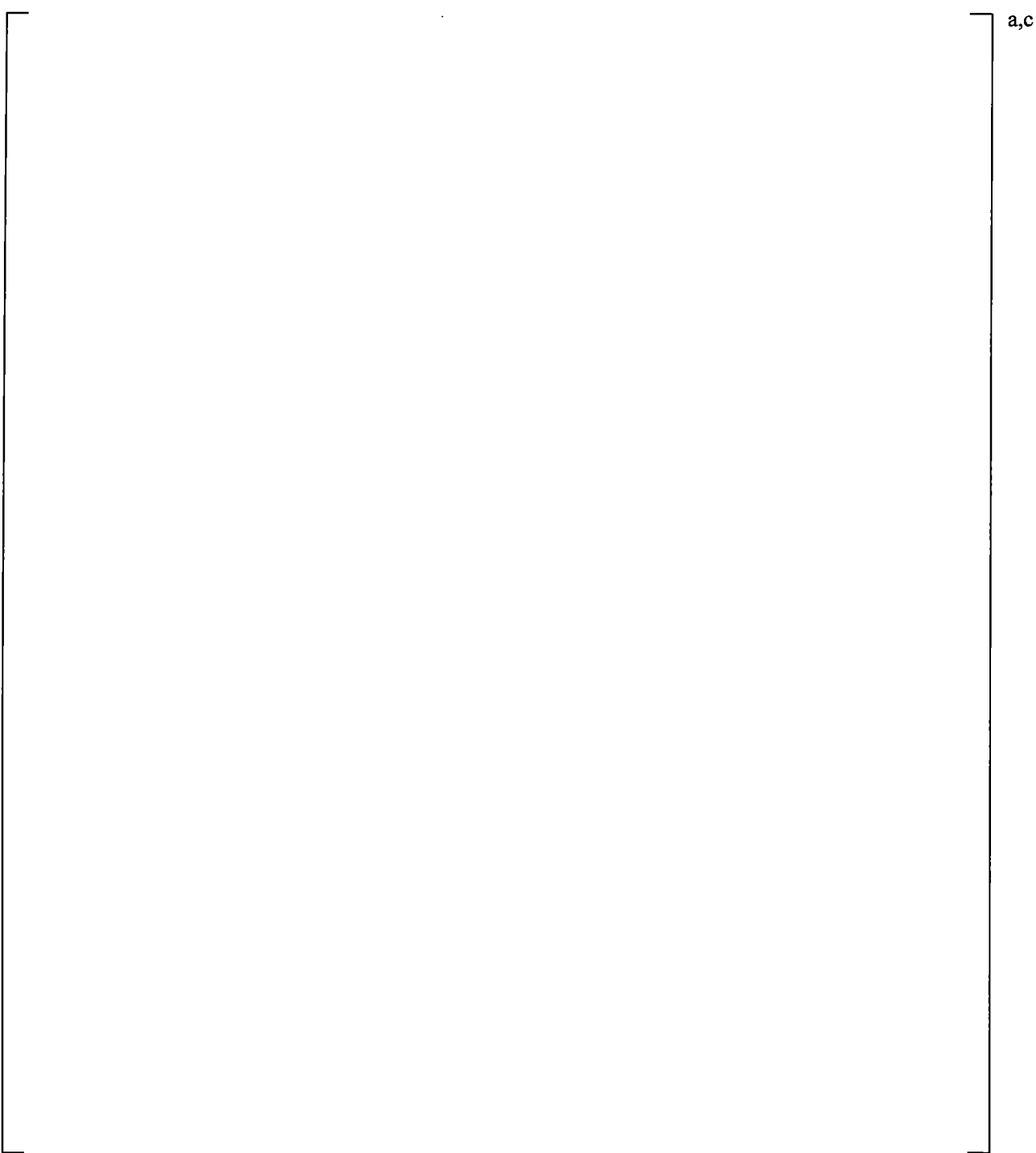
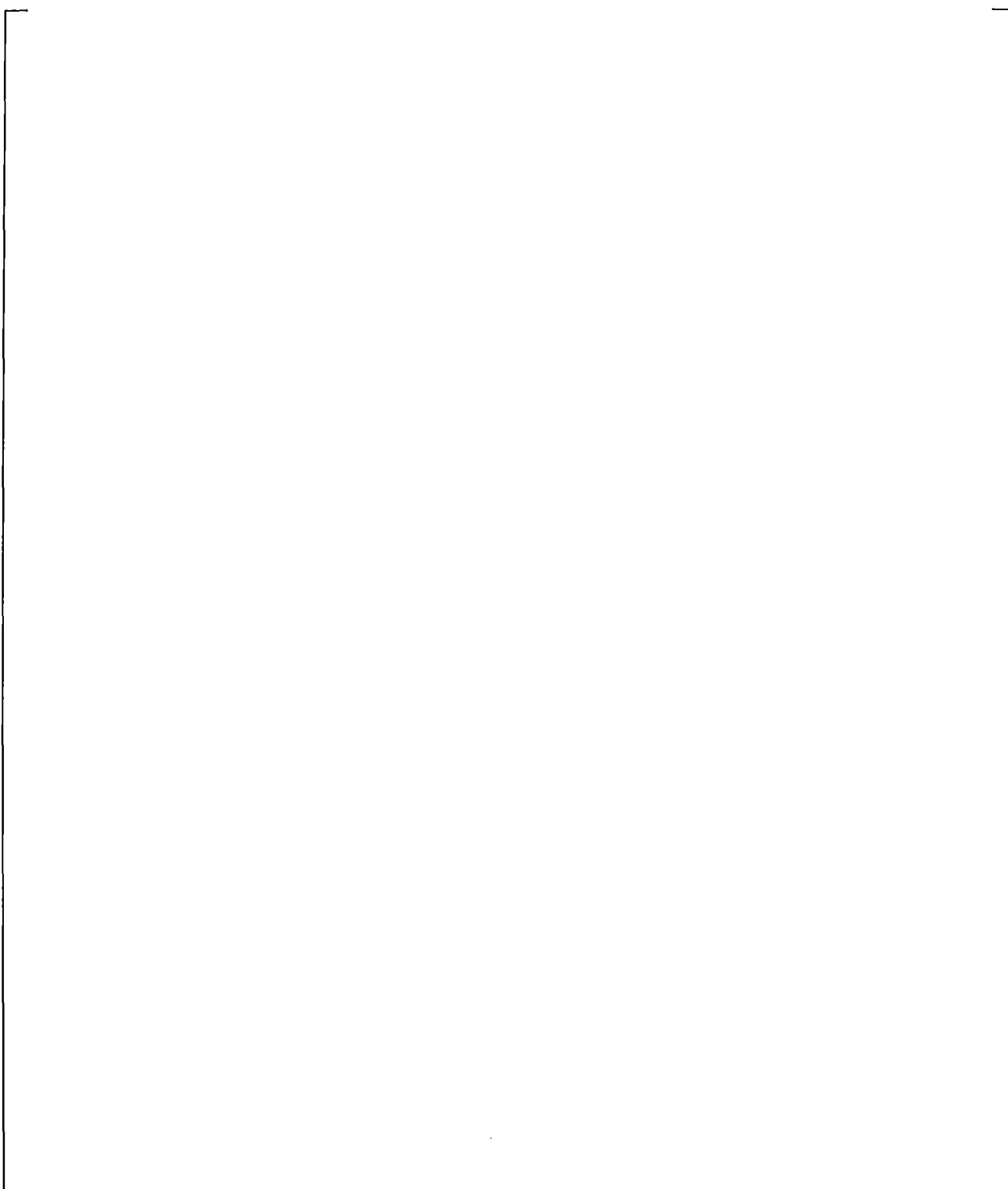


Figure 21.7-2 WCOBRA/TRAC-TF2 Nodalization of LSTF Break Unit

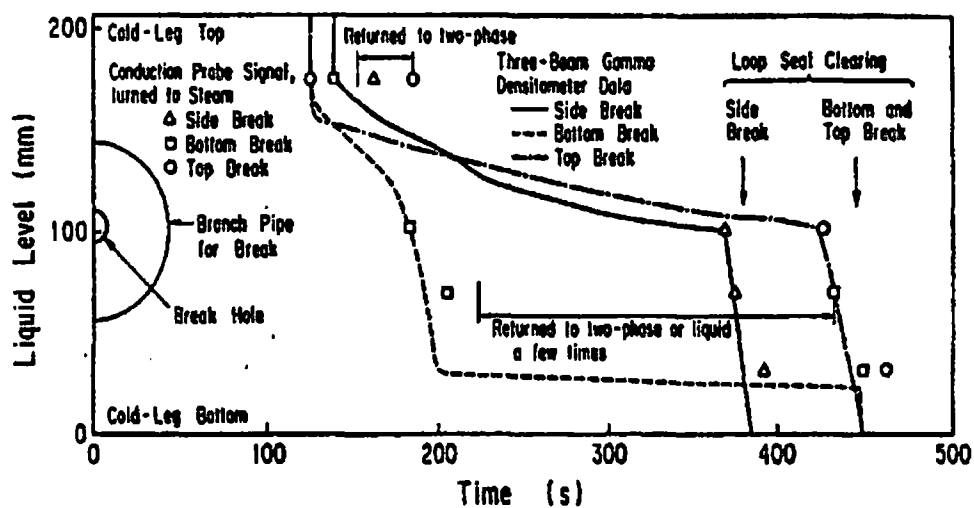
a,c,e



**Figure 21.7-3 Comparison of Predicted and Measured Primary System Pressure
(ROSA-IV 2.5-Percent Cold Leg Break)**

**Figure 21.7-4 Comparison of Predicted and Measured Break Flow Rates
(ROSA-IV 2.5-Percent Cold Leg Break)**

a,c



(b) Reported in (Koizumi et al., 1988)

Figure 21.7-5 Comparison of Predicted and Measured Mixture Levels in Broken Cold Leg (ROSA-IV 2.5-Percent Cold Leg Break Runs)

a,c

**Figure 21.7-6 Comparison of Predicted and Measured Core Collapsed Liquid Levels
(ROSA-IV 2.5-Percent Cold Leg Break Runs)**

a,c,e

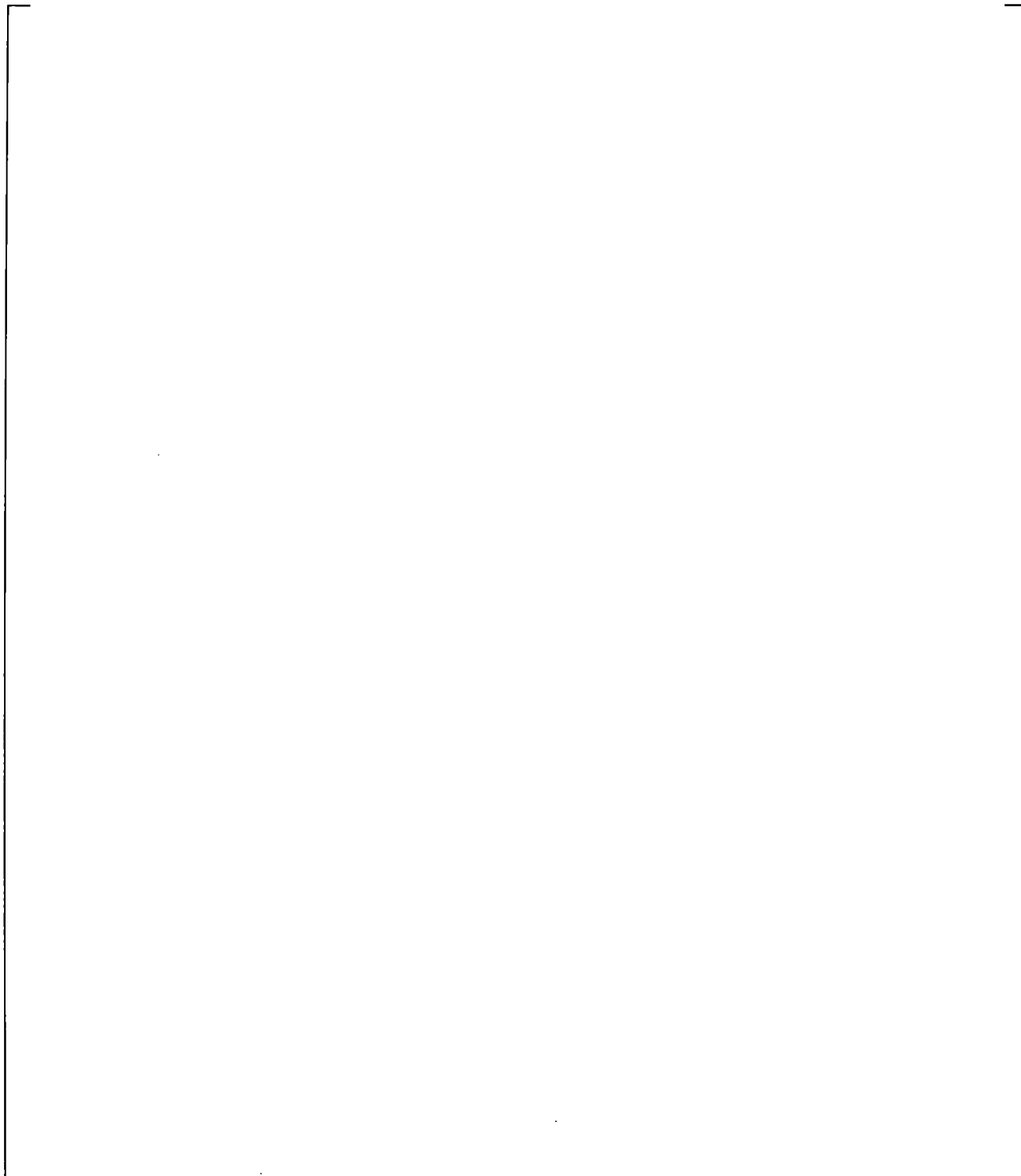


Figure 21.7-7 Cladding Temperature of B-20 Rod at Position 7 (8.67-ft Elevation) for Side, Bottom, and Top Break Experiments

a,c,e

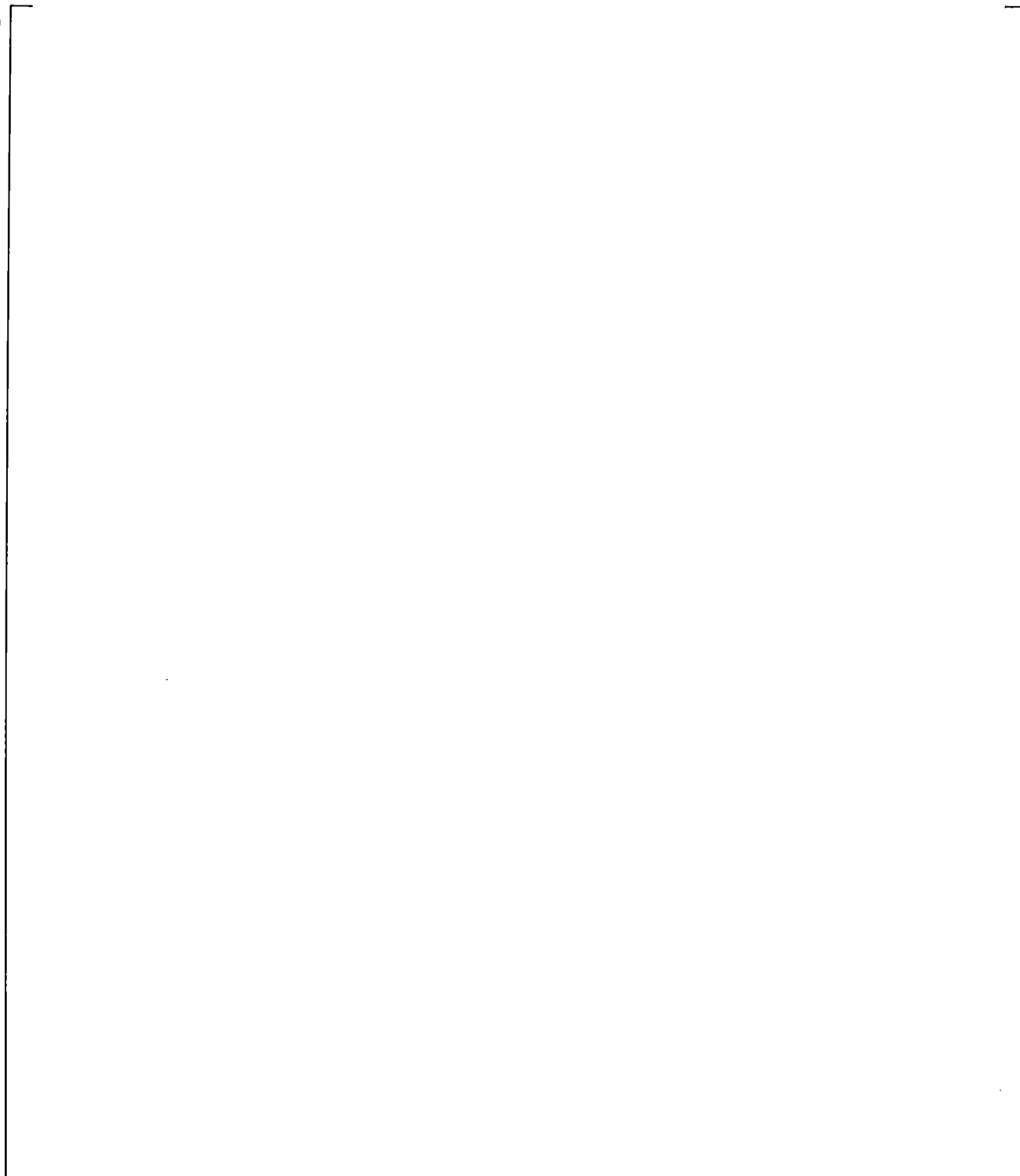


Figure 21.7-8 Predicted and Measured Differential Pressures in Steam Generator A Uphill Side

a,c,e

Figure 21.7-9 Predicted and Measured Differential Pressures in Steam Generator B Uphill Side



a,c

Figure 21.7-10 Calculated Accumulator Injection Flows

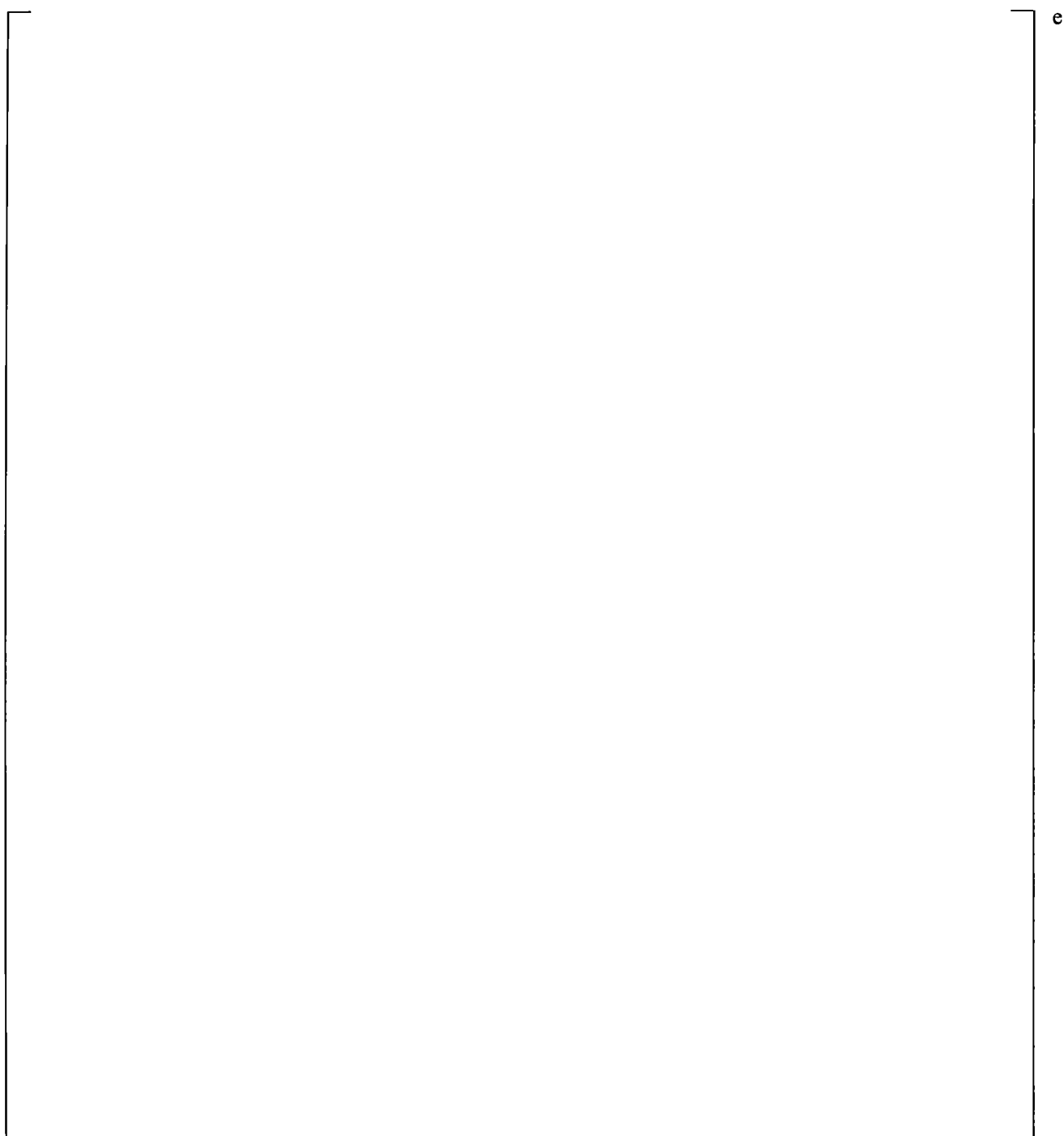


Figure 21.7-11 Break Unit Configuration used in the 0.5% Break Tests, SB-CL-12, -15, and -16

a,c,e

**Figure 21.7-12 Comparison of Predicted and Measured Broken Cold Leg Liquid Levels,
ROSA 0.5-Percent Cold Leg Break Runs**

a,c,e



**Figure 21.7-13 Comparison of Predicted and Measured Core Collapsed Liquid Levels,
ROSA 0.5-Percent Cold Leg Break Runs**

**Figure 21.7-14 Comparison of Predicted and Measured Integrated Break Flows, ROSA 0.5-Percent
Cold Leg Break Runs**

21.8 BREAK SPECTRUM STUDY

The break spectrum study presented herein is compiled from simulations results of cold leg side break tests, documented in the previous sections. These are the 0.5% break (SB-CL-12), 2.5% break (SB-CL-01), 5% break (SB-CL-18), and 10% break test (SB-CL-14). The results of the break spectrum study are presented in Figures 21.8-1 through 21.8-5.

Figure 21.8-1 compares the calculated break flows. As seen from that figure, the initial values of the break flows are proportional to the break size. Larger break size results in a greater inventory loss at the beginning of the transient, and thus the initial depressurization rate is higher for the larger breaks, which is evident on the system pressure comparison provided on Figure 21.8-2. After the initial fast depressurization, a period of primary system pressure hold-up is observed slightly above 8 MPa, which is the secondary side pressure. The length of this holdup period depends on the break size with the smallest break having the longest hold-up period. During this period, the steam generators are a heat sink and remove heat from the primary side by natural circulation. The length of pressure hold-up (and natural circulation) period is decreasing with the increase of the break size, with the 10% size break exhibiting almost no pressure holdup.

Figures 21.8-3(a) and (b) and Figure 22.8-4 show the cross-over leg vapor flows and the core collapsed liquid levels respectively. Results in these figures show a correlation between the clearing of the loop seal (characterized by spike in loop vapor flow, Figure 21.8-3) and the depression of the core collapsed liquid level (Figure 21.8-4). As seen from those figures, the bigger the break size is, the sooner the loop seals are cleared. The smallest break size (0.5%) clears only one of the loop seals very late – about 1750 seconds into the transient.

And finally, Figures 21.8-5(a) and (b) show the calculated differential pressures in the uphill side of the steam generator U-tubes. The calculation results show that the smallest break size, which has the longest natural circulation period, retains liquid in the U-tubes much longer than the larger breaks.

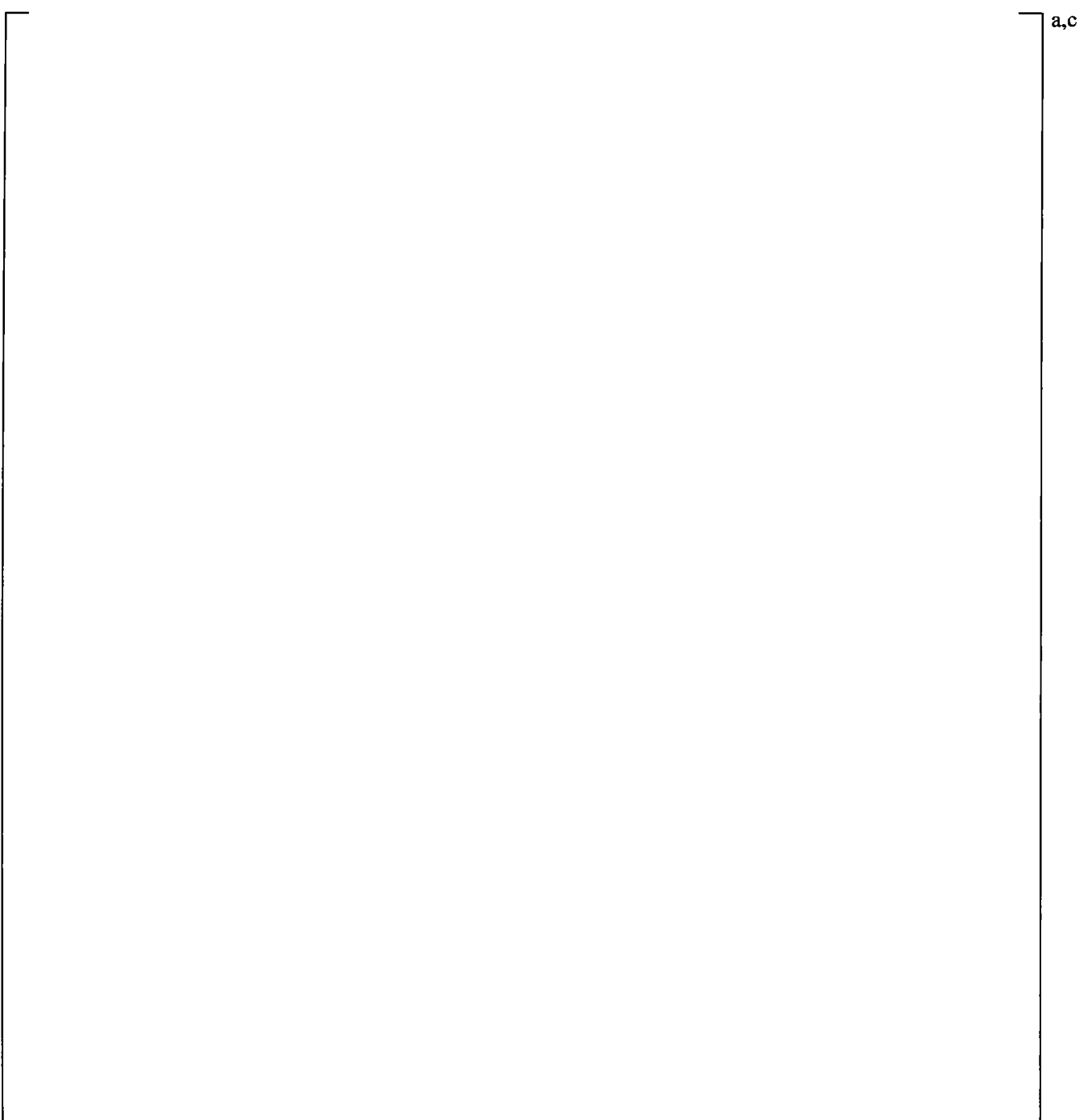


Figure 21.8-1 Break Flow Comparison

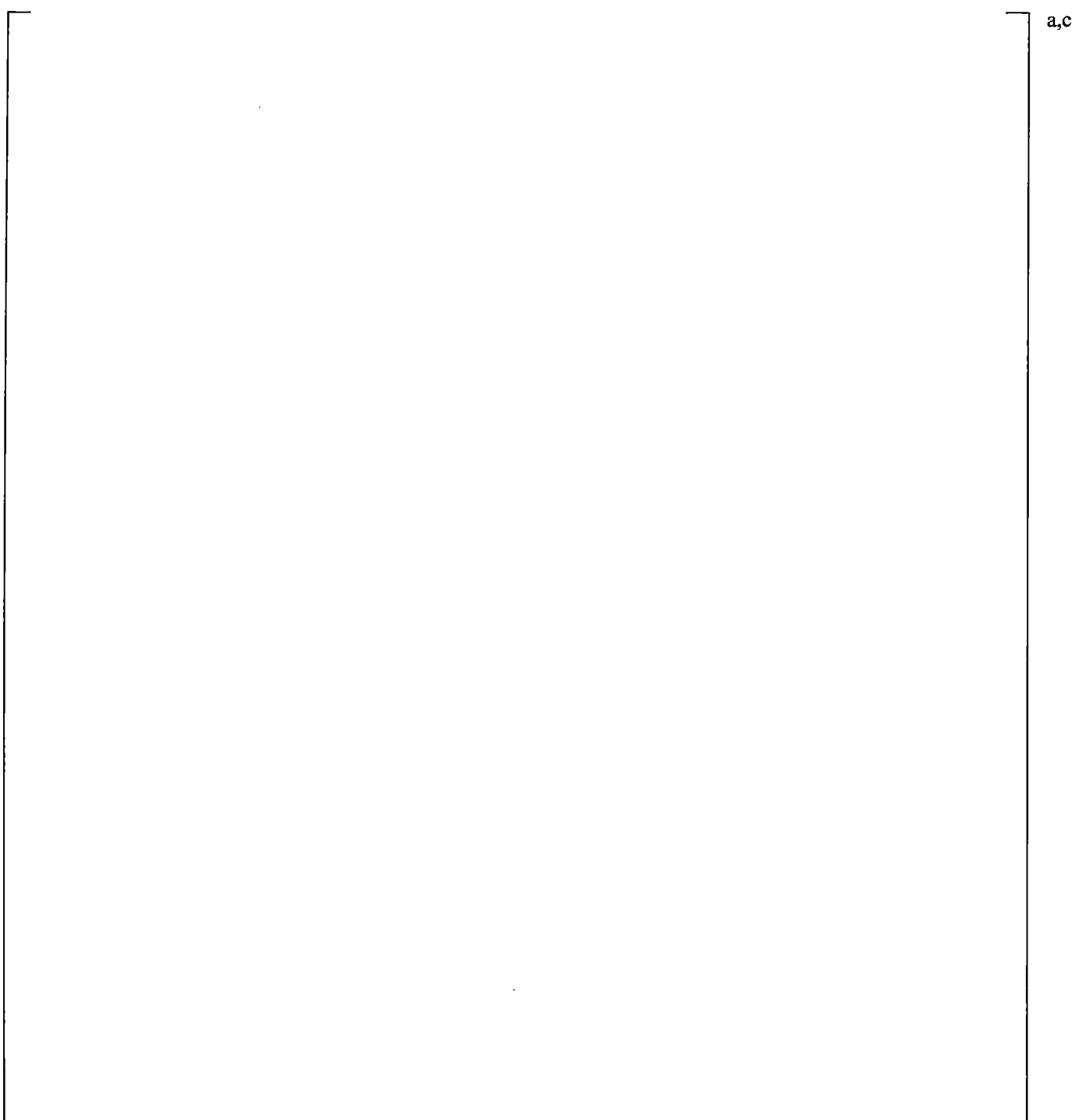


Figure 21.8-2 System Pressure Comparison

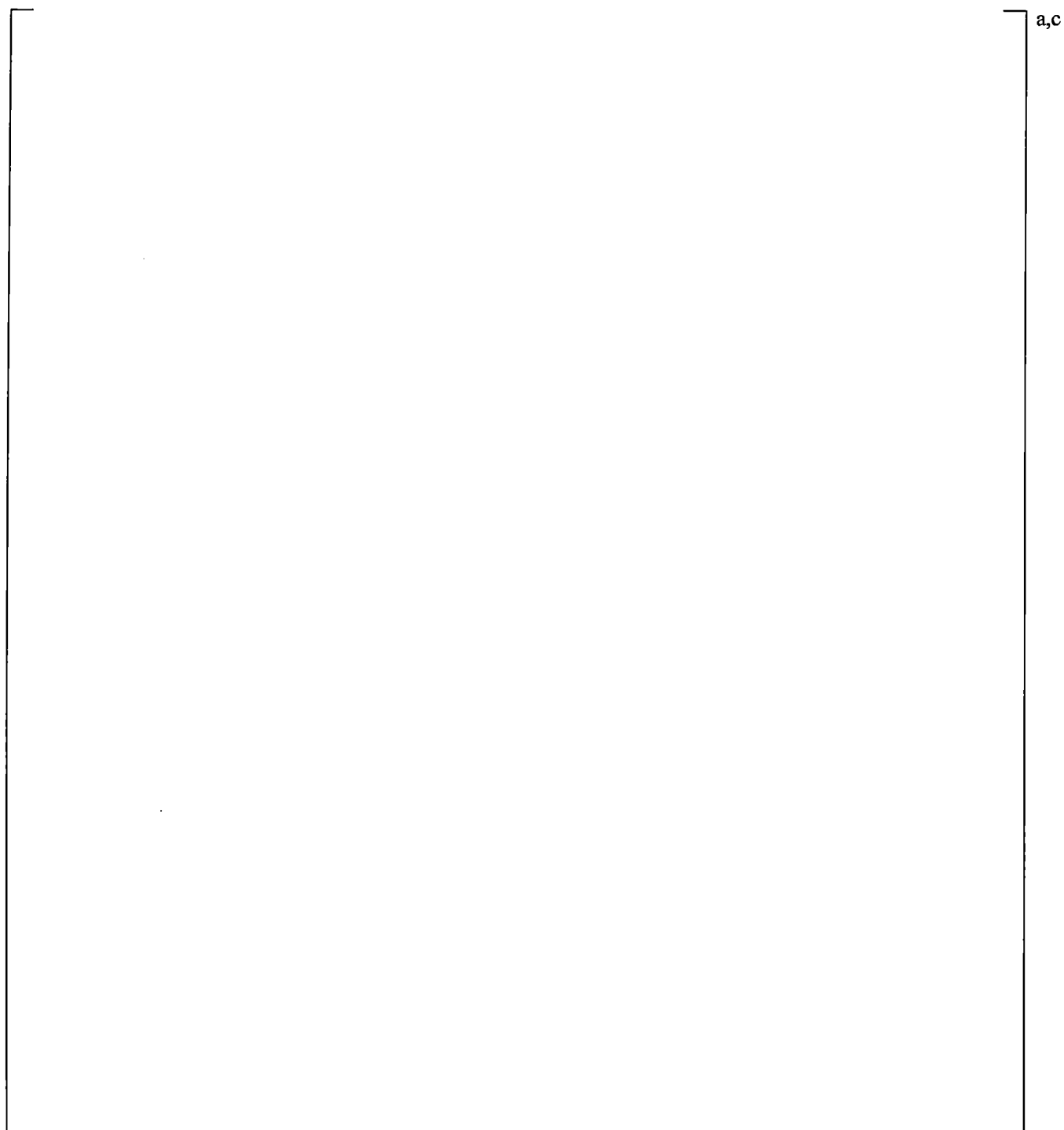


Figure 21.8-3(a) Cross-over Leg A Vapor Flows

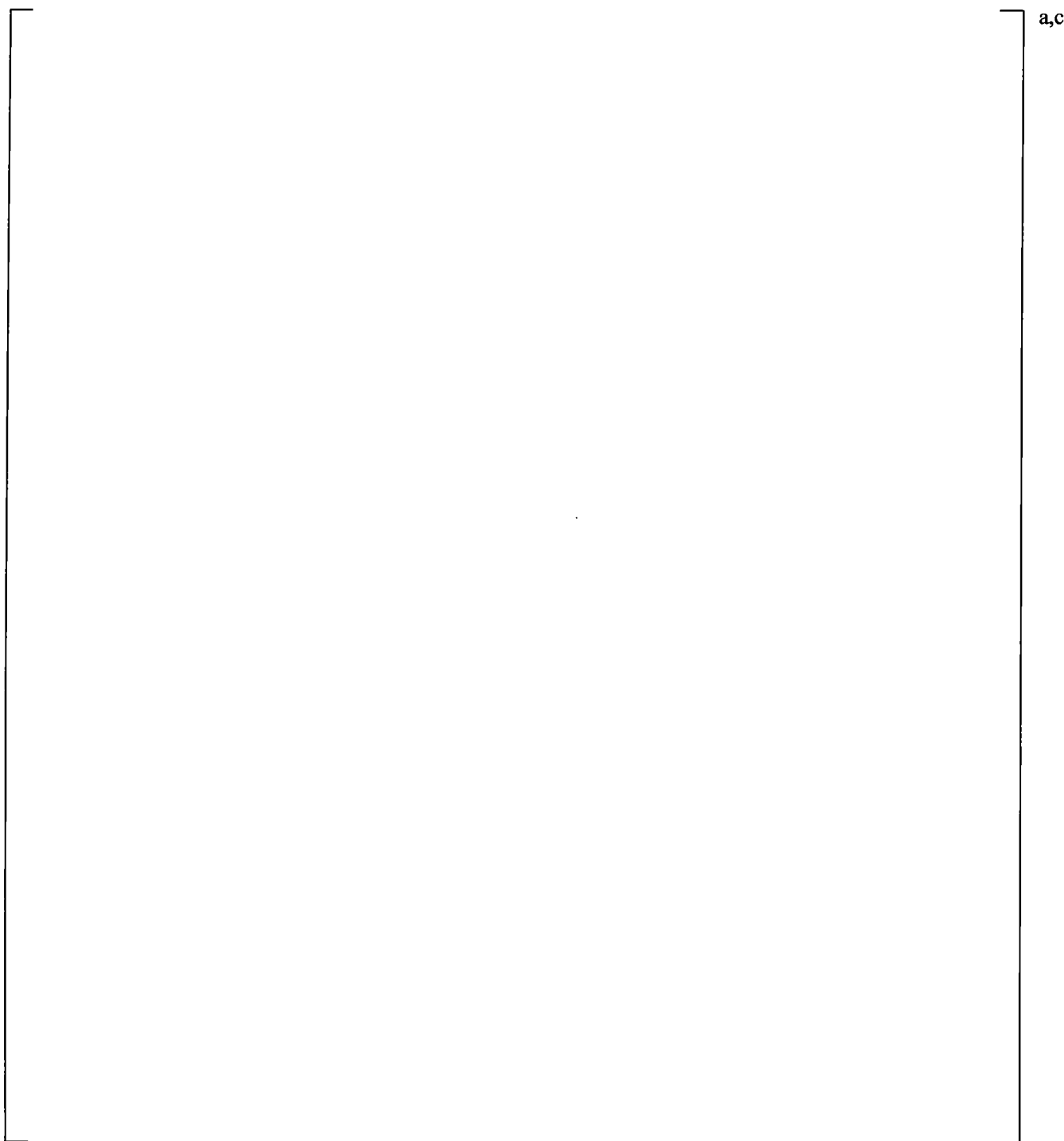


Figure 21.8-3(b) Cross-over Leg B Vapor Flows

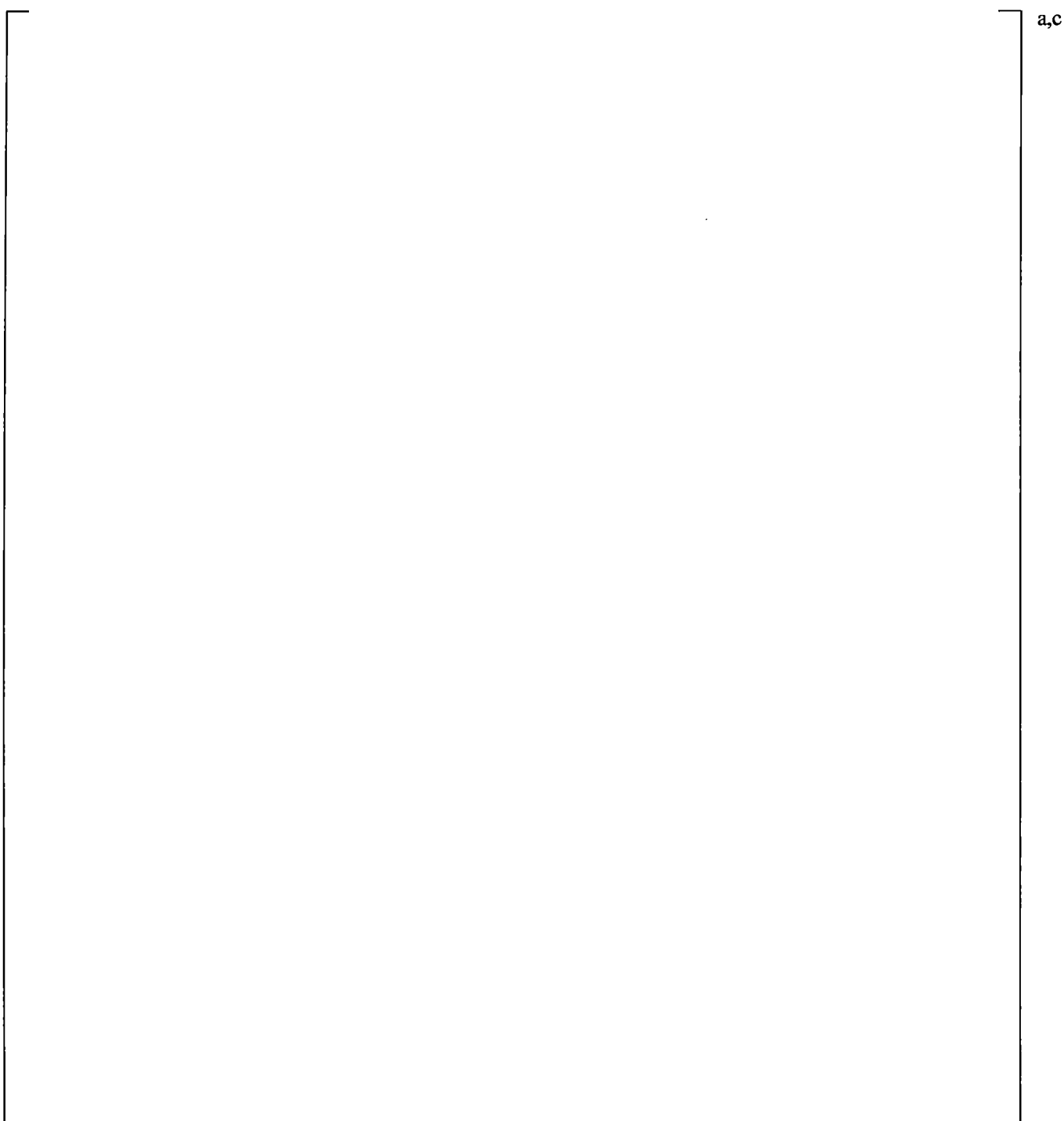
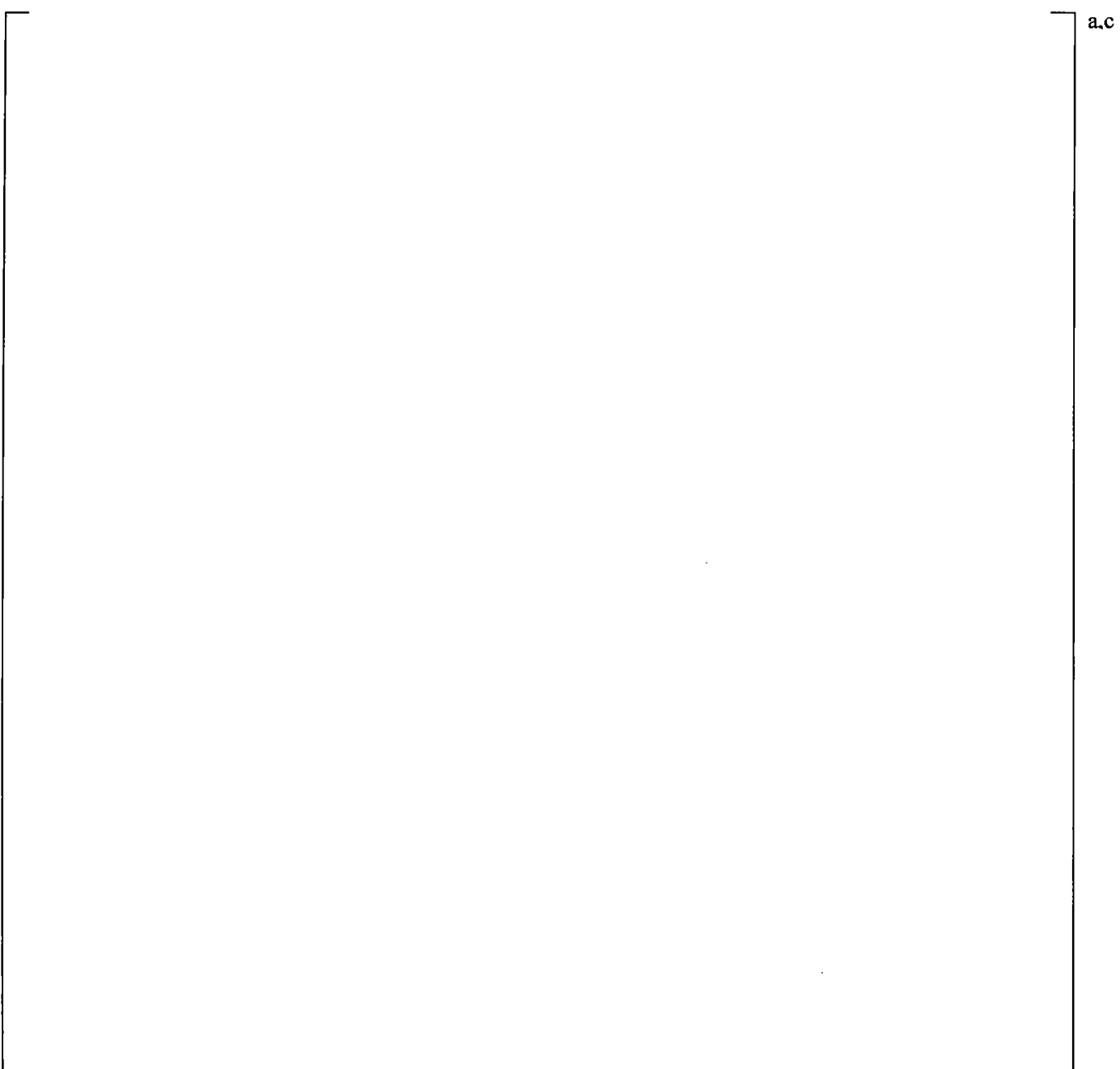
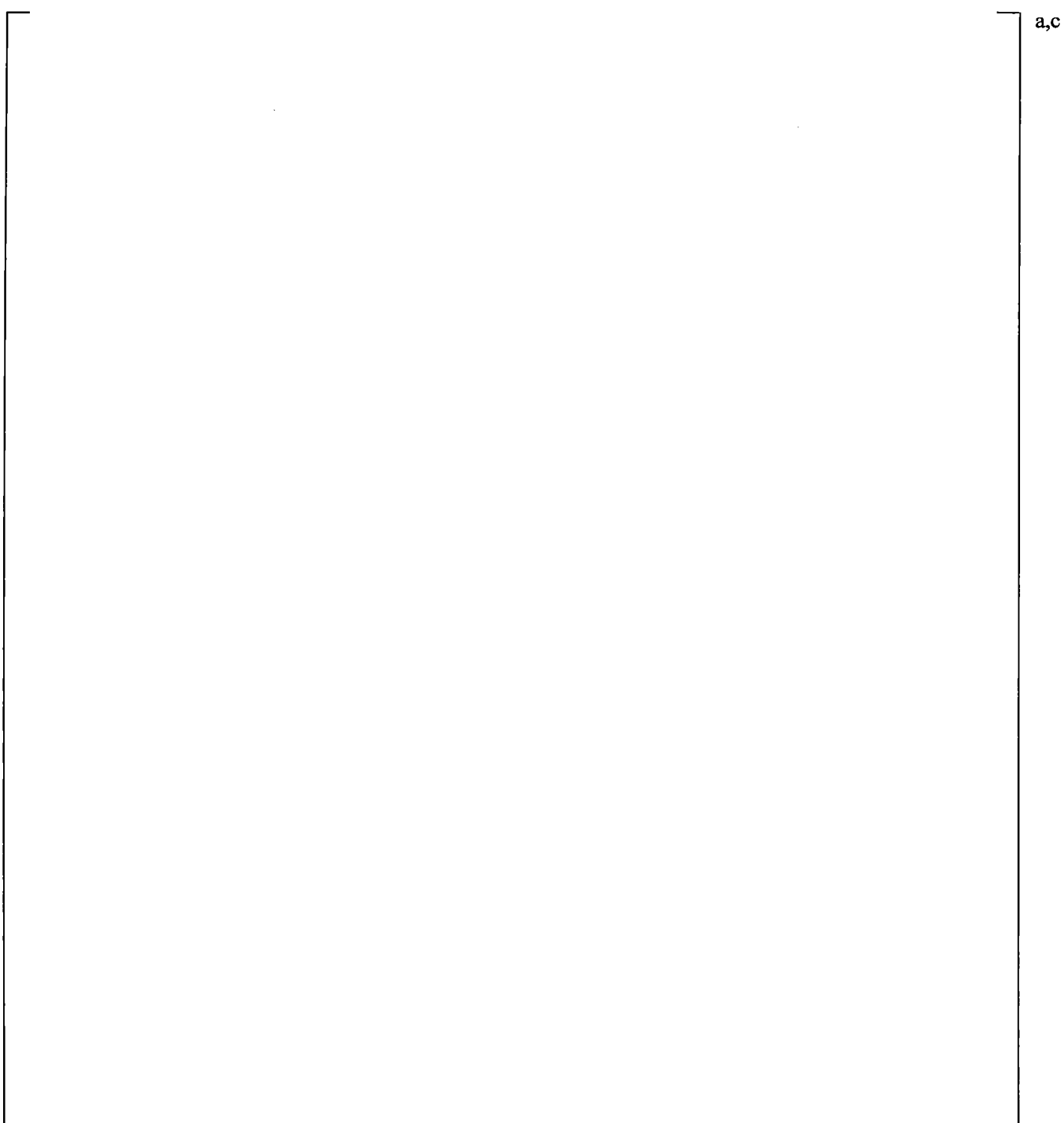


Figure 21.8-4 Core Collapsed Levels



| **Figure 21.8-5(a) Steam Generator A U-tubes Uphill Differential Pressures**



| **Figure 21.8-5(b) Steam Generator B U-tubes Uphill Differential Pressures**

21.9 SIMULATION OF ST-NC-02, 2% POWER NATURAL CIRCULATION TEST

21.9.1 Natural Circulation Phenomena

The natural circulation is an important phenomenon and effective mechanism of heat removal from the primary to the secondary side of the steam generators during a small break LOCA.

One important phenomenon that might influence the severity of small break LOCA transients is liquid holdup in the steam generator U-tubes. This holdup phenomenon was first identified experimentally in the Semiscale small break LOCA experiments (Leonard, 1982a). It has since been duplicated in other facilities such as ROSA (Osakabe et al., 1987) and has been discussed extensively in the open literature (Leonard, 1982b) and (Loomis and Streit, 1985).

The liquid present in the steam generator tubes as a function of total system inventory is an important phenomenon in small break LOCA performance. During the initial phase of natural circulation, the system inventory is sufficient to maintain enough (two-phase bubbly) fluid present in both the uphill and downhill sides the steam generator U-tubes. At this stage, the interfacial drag is big enough to prevent draining of the SG tubes by gravity, and there is a continuous single-phase to bubbly flow established in the entire region of the steam generator tubes. As the primary system inventory is further depleted, voids are first developed at the top of the U-tubes, which then collapse and give way to a cyclic “fill-and-dump” phenomenon. The hydrostatic balance between the uphill and downhill side of the steam generator tubes becomes unstable and the fluid drains from the steam generator tubes – first the downhill side and later the uphill side.

In the later stages of natural circulation, when the inventory is depleted enough to expose the steam generator tubes to steam coming from the core, liquid that is caused by the condensation of that steam – a phenomenon called “reflux condensation,” may be held up in the tubes. This holdup may not be able to drain by gravity back through the hot leg into the upper plenum if it is impeded by high upward steam flow rates; the pressure drop induced by this holdup affects the hydrostatic head balances throughout the RCS.

21.9.2 Description of the ST-NC-02 Natural Circulation Test

JAERI-M-88-215 (Chauliac et al., 1988) documents results of simulations of the ST-NC-02 test with RELAP5/MOD2, and contains a fair amount of detail related to the initialization and execution of the ST-NC-02 natural circulation test and RELAP5/MOD2 simulation results.

Unfortunately, JAERI did not issue the anticipated official Test Report for the ST-NC-02 natural circulation test, listed as Reference [1] in (Chauliac et al., 1988).

(Tasaka et al., 1988), (Kukita et al., 1988) and (Stumpf et al., 1987) present additional analyses of the ST-NC-02 test and provide valuable information that cannot be easily found in (or inferred from) (Chauliac et al., 1988).

As described in Section 2.2 of (Chauliac et al., 1988), the first stage of the experiment was performed at the LSTF nominal conditions: full power (10 MW), pumps on, temperature increase across the core as in the actual plant.

The second stage was designed to study the natural circulation at 100% primary side inventory. The core power was reduced down to 1.42 MW (this is 2% power of the reference PWR) and was kept at that level for the rest of the entire experiment. The pumps were turned off and the secondary side pressure was reduced to 6.6 MPa and kept constant until the end of the experiment. Figure 4 of (Kukita et al., 1988), presented here as Figure 21.9-1, illustrates the measured evolution of the primary side pressure and loop flow and sheds some light on the timing of the different stages of the experiment. As seen from that figure, at the end of the second stage of the experiment, when the pressurizer pressure was established at 12.2 MPa, the pressurizer surge line valve was closed and the pressurizer isolated prior to the drain of the primary side inventory.

During the rest of the experiment, the primary side water inventory was reduced step-wise by bleeding through the drain line at the bottom of the vessel. The drain valve at the bottom was closed when certain inventory reduction was reached and kept closed for some time until intermediate steady state primary pressure and loop flow was achieved at that inventory level.

As described in (Chauliac et al., 1988), constant secondary side water level was maintained throughout the experiment. Unfortunately, there is no ST-NC-02 test report that documents in detail the test execution, and Section 2.2 of (Chauliac et al., 1988) does not explain how the secondary side pressure reduction was achieved and maintained at 6.6 MPa. Most likely, the feed water flow rate was adjusted to keep the constant steam generator level and balance the primary-to-secondary side heat transfer at the reduced secondary side pressure. (Chauliac et al., 1988) (pg. 6) also states that feed water temperature fluctuation of 30K has been observed throughout the drain-down phase of the test as well. Since the test simulated the natural circulation at different primary side inventory levels, safety injection was not modeled by isolating the accumulators.

As seen on Figure 21.9-1, the duration of the experiment was almost 10 hours (35000 sec). Due to computational (CPU) time constraints, it is not reasonable to try and replicate the test in real time length. Moreover, as seen on that figure, the quasi-steady states at different stages could be achieved for time periods shorter than the ones implemented through the experiment, especially those of Stage 1 and 2. Therefore, shorter time periods are used to achieve the desired quasi-steady state conditions at each stage.

21.9.3 Description of the Test Simulation and Boundary and Initial Conditions

The system initial conditions achieved for the ST-NC-02 simulation are presented in Table 21.9-1. The test simulation followed the procedure implemented during the real test, except that shorter time periods were simulated to achieve a quasi-steady state during each drain period. The length of the individual drain periods and the drain flows used in the simulation were estimated from the information in Figure 21.9-1. The accumulators were isolated by closing the accumulator isolation valves. Prior to the beginning of the draining, the pressurizer was isolated by closing the PRZ isolation valve.

The following steps were implemented for the simulation of the natural circulation test ST-NC-02:

[

]^{a,c}

21.9.4 Results and Conclusions

The results of the simulation of the ST-NC-02 natural circulation test (2% core power) are presented in Figure 21.9-2 through Figure 21.9-16.

Figure 21.9-2 compares the measured primary system loop circulation flow against that calculated by the code. During the single-phase natural circulation (primary side inventory from 100% to 90%) the circulation flow is predicted fairly well. [

[

[

]^{a,c}

J^{a,c}

The comparison of the downcomer differential pressures, Figure 21.9-7, shows a good prediction of the amount of liquid in the downcomer.

J^{a,c}

Figures 21.9-11 and 21.9-12 show the calculated void fraction distributions in the uphill and downhill side of the steam generator A U-tubes. The same information is shown for steam generator B in Figures 21.9-13 and 21.9-14. The calculation shows that the downhill sides of the steam generators tends to drain first, while the uphill side retains liquid for a longer period of time; this is consistent with the steam generator draining sequence observed at the rest of the ROSA-IV tests considered here.

Figures 21.9-15 and 21.9-16 show the calculated vapor flows at the inlet and the top of the steam generator U-tube bundles for steam generator A and B respectively. The calculated vapor flow split indicates that the steam condensation would occur predominantly at the uphill section of the U-tubes.

The following major conclusions are made with respect to the ability of the code to calculate primary-to-secondary side heat transfer.

- For purely reflux condensation conditions in the steam generators, the code calculates overall effective heat transfer coefficient (normalized for the outside SG surface area) in the range of []

[]
I^{a,c}

- The power is removed effectively to the steam generator secondary side even though one of the steam generators remains plugged for a prolonged time.

Based on the results documented in this section, it is concluded that when used with WCORBA/TRAC-TF2, the ROSA-IV LSTF model developed for the purpose of the FSLOCA methodology produces simulation results that are in general consistent with those observed at the ST-NC-02 experiment.

Table 21.9-1 Initialization of the SB-CL-02 Natural Circulation Test Simulation

Parameter	End of Stage 1		End of Stage 2 (Prior to Drain)	
	Target		a,c Target	
Core Power, MW	10.0		1.42	
Pressurizer Pressure, MPa	15.47 ±0.06		12.2	
Hot Leg Temperature, K	598 ±5		N/A	
Cold Leg Temperature, K	565 ±5		N/A	
Pump Speed, rad/sec (rpm)	85.8/86.1 (819/822)		0.00/0.00	
Total Loop Flow Rate, kg/sec	51.0 (±0.6)		11.4	
DC-to-UH Bypass Flow Rate, % total loop flow (kg/sec)	0.9% (0.46)		N/A	
Core Inlet Flow Rate, kg/sec	50.54		N/A	
SG Secondary Pressure, MPa	7.38/7.42 (±0.03)		6.5	
SG Steam Flow Rate, kg/sec	2.6 (±0.1)		N/A	

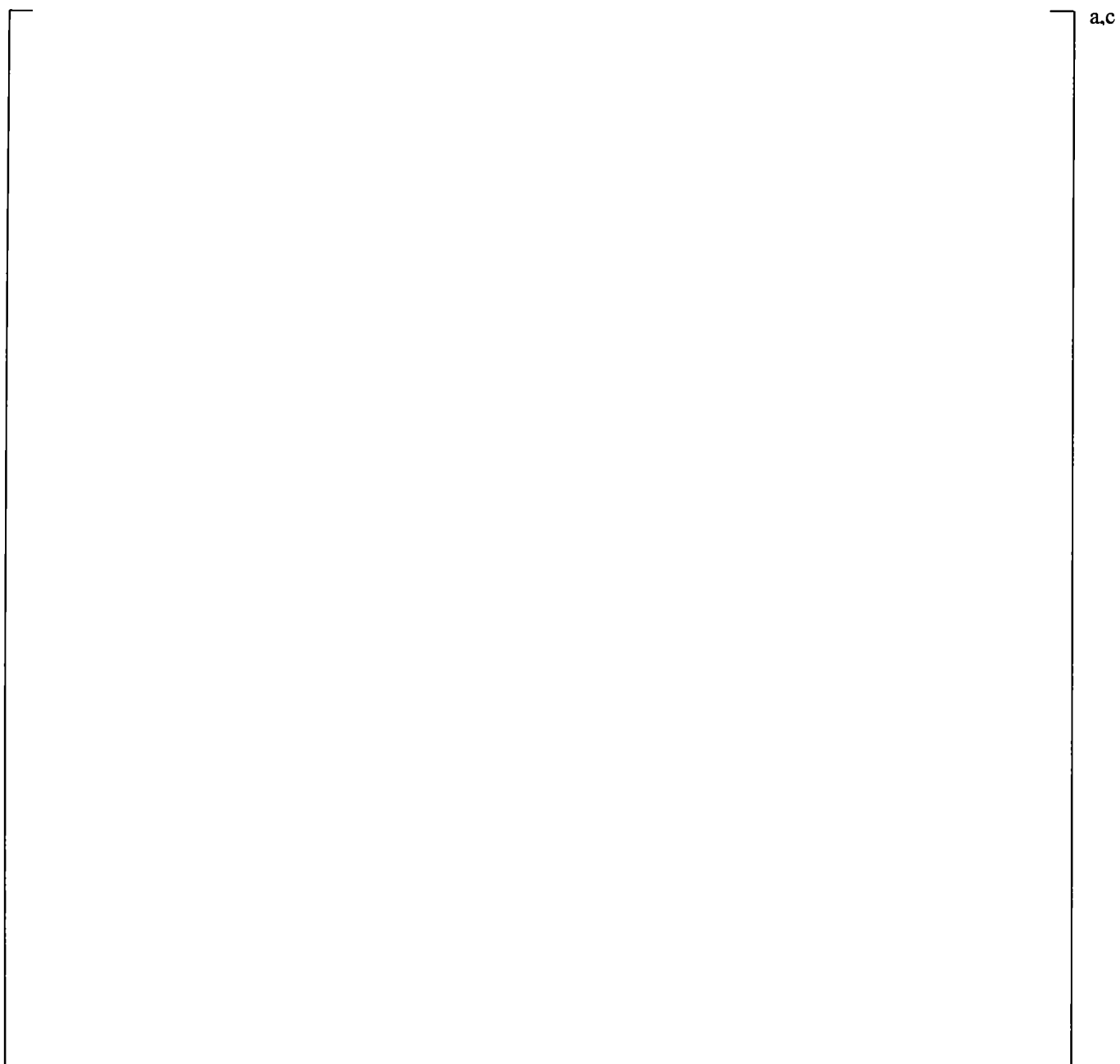


Figure 21.9-1 ST-NC-02 Primary Pressure and Loop Flow Rate (Kukita et al., 1988)

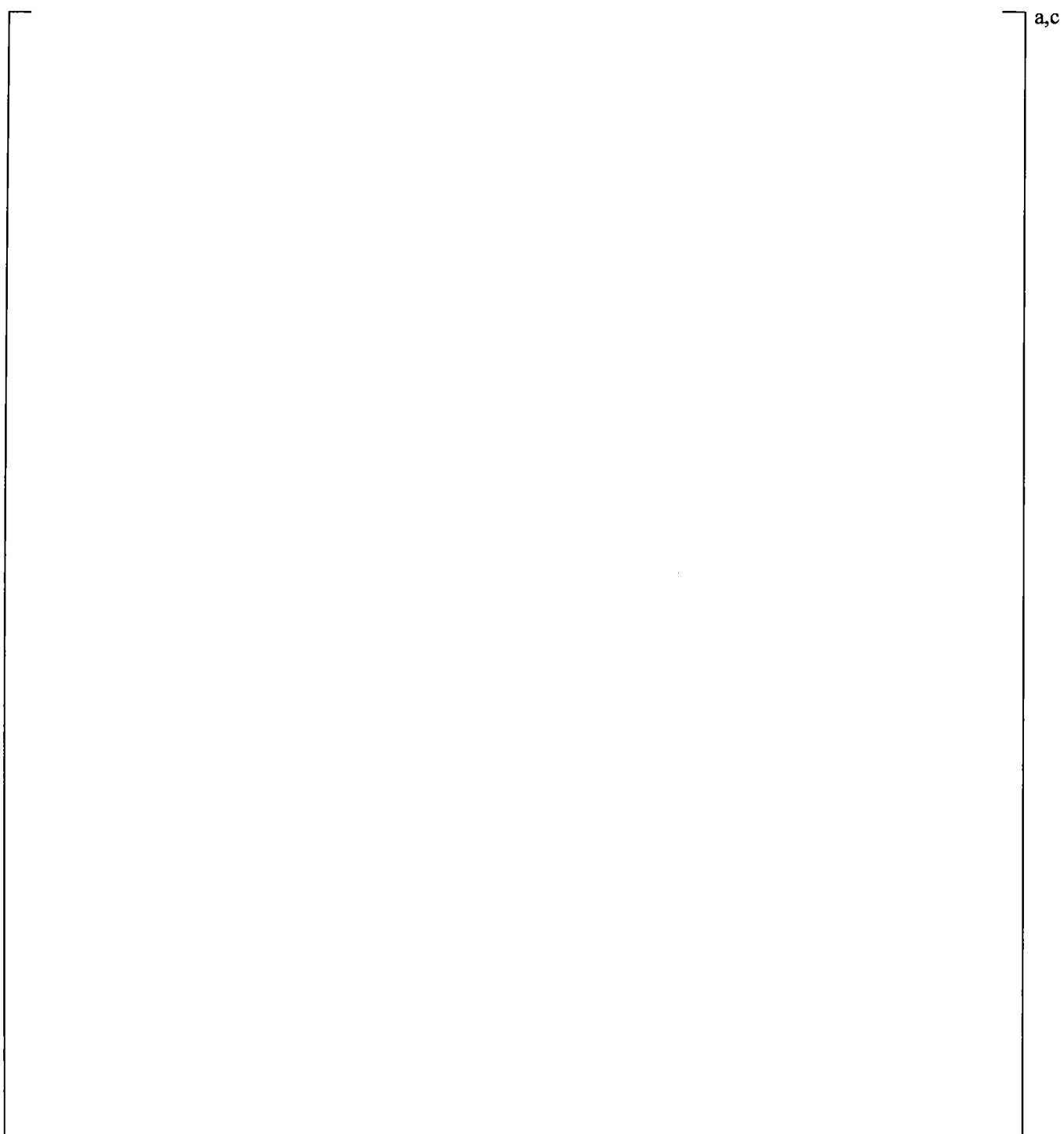


Figure 21.9-2 Primary Side Circulation Flow as a Function of Primary Side Inventory

a,c

Figure 21.9-3 ST-NC-02 Primary and Secondary System Pressures

a,c

Figure 21.9-4 Steam Generator U-tube Uphill Side Differential Pressures

a,c

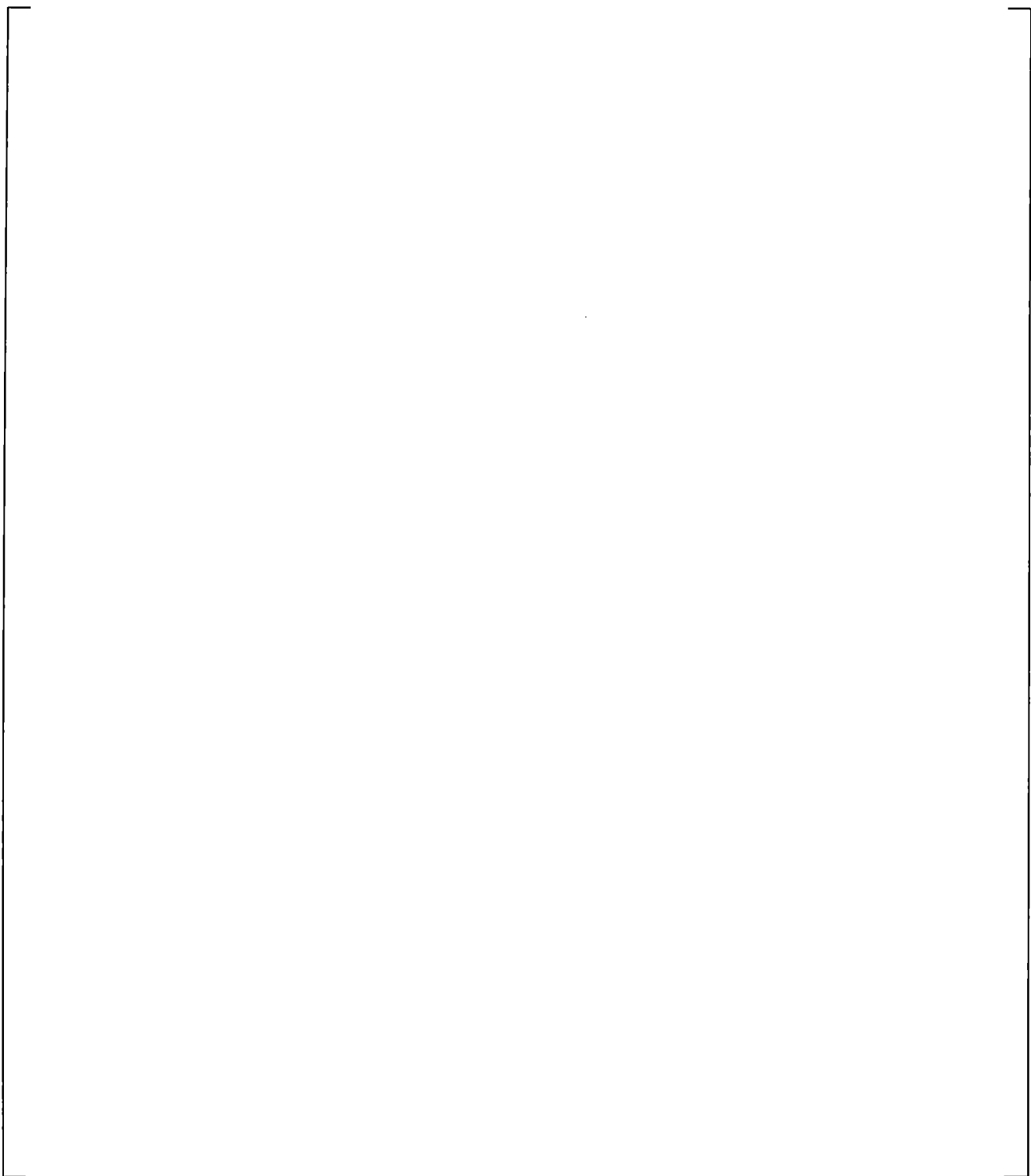
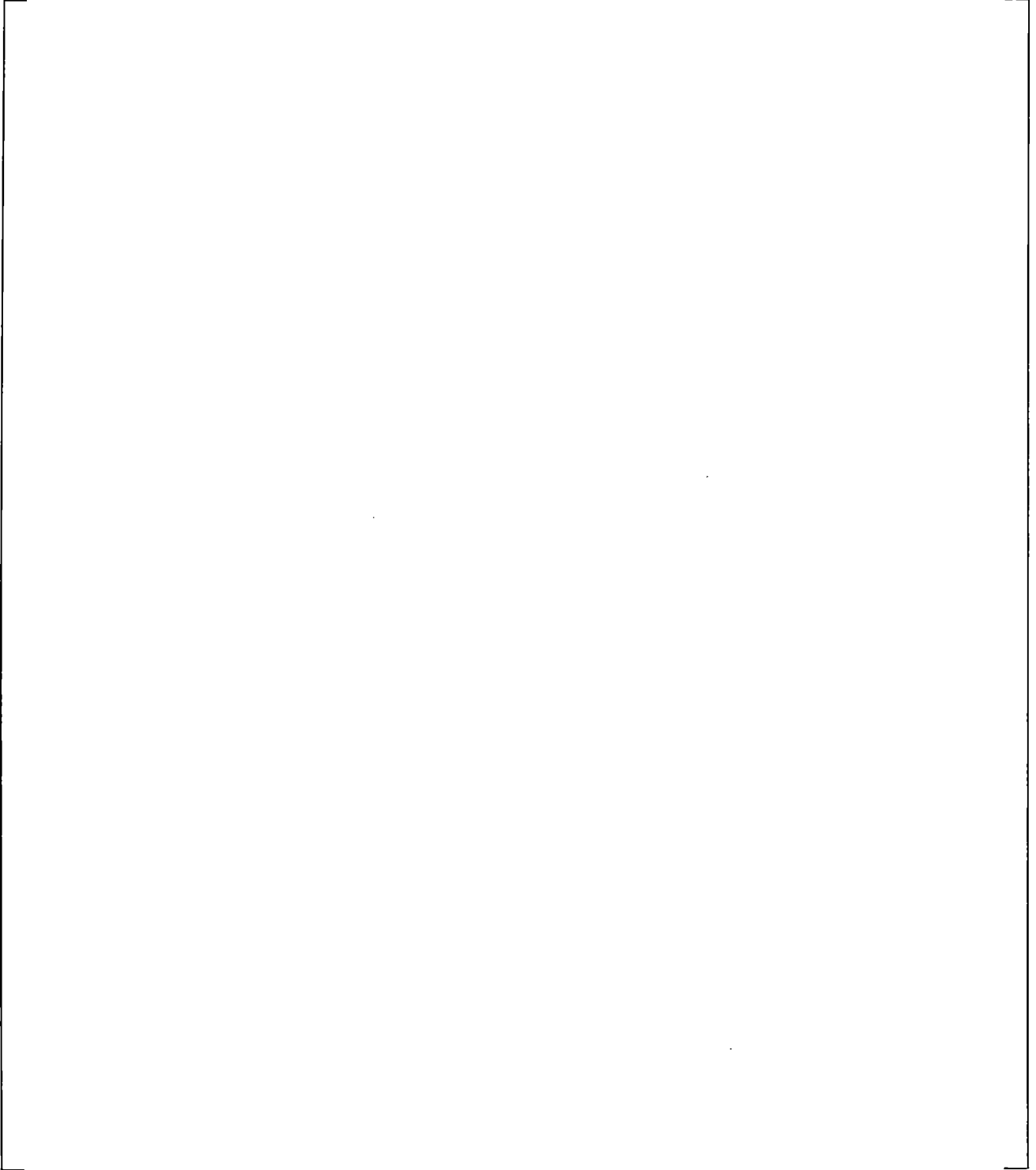


Figure 21.9-5 Core Differential Pressure



a,c

Figure 21.9-6 Upper Plenum Differential Pressure

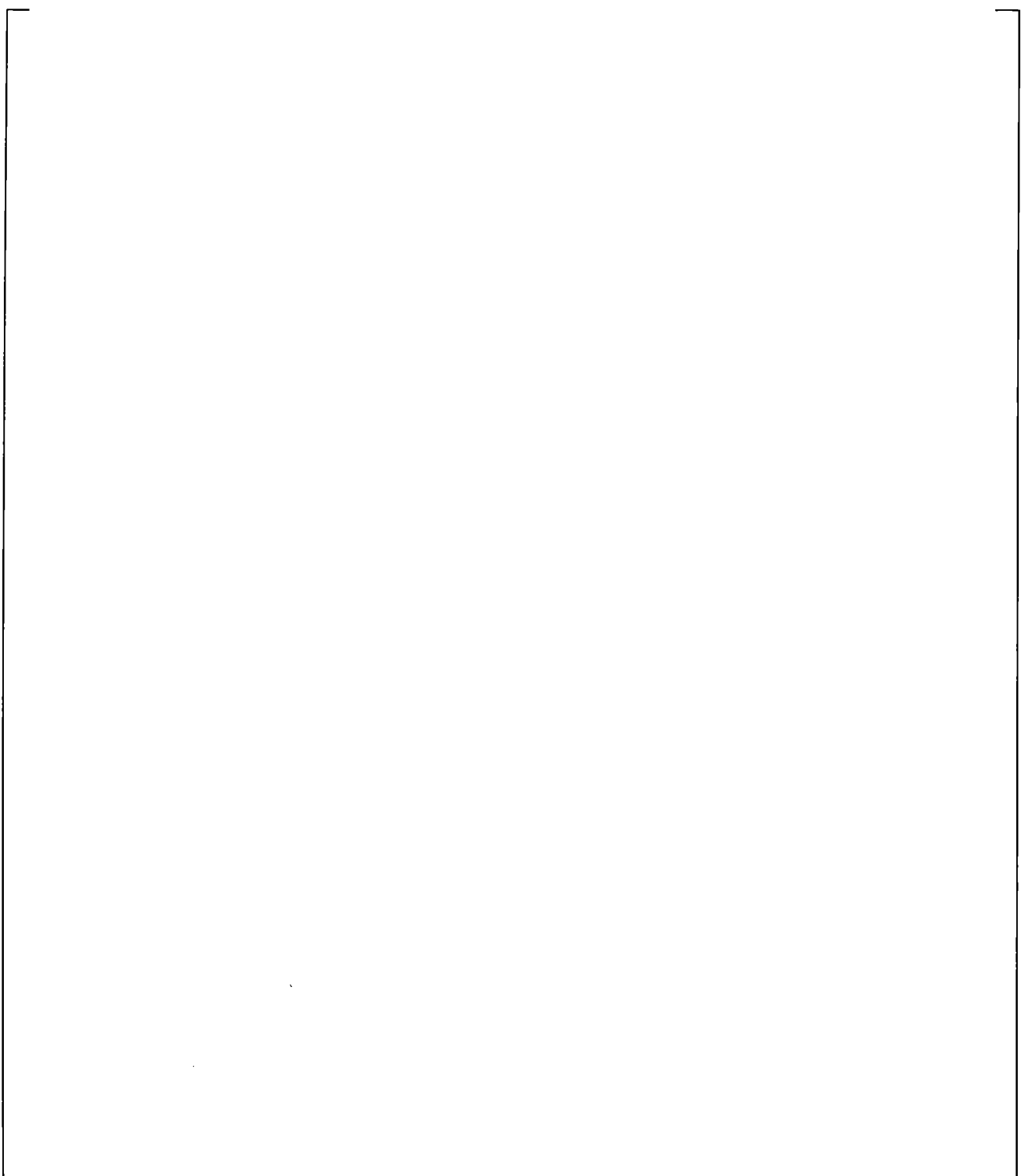


Figure 21.9-7 Downcomer Differential Pressure

a,c

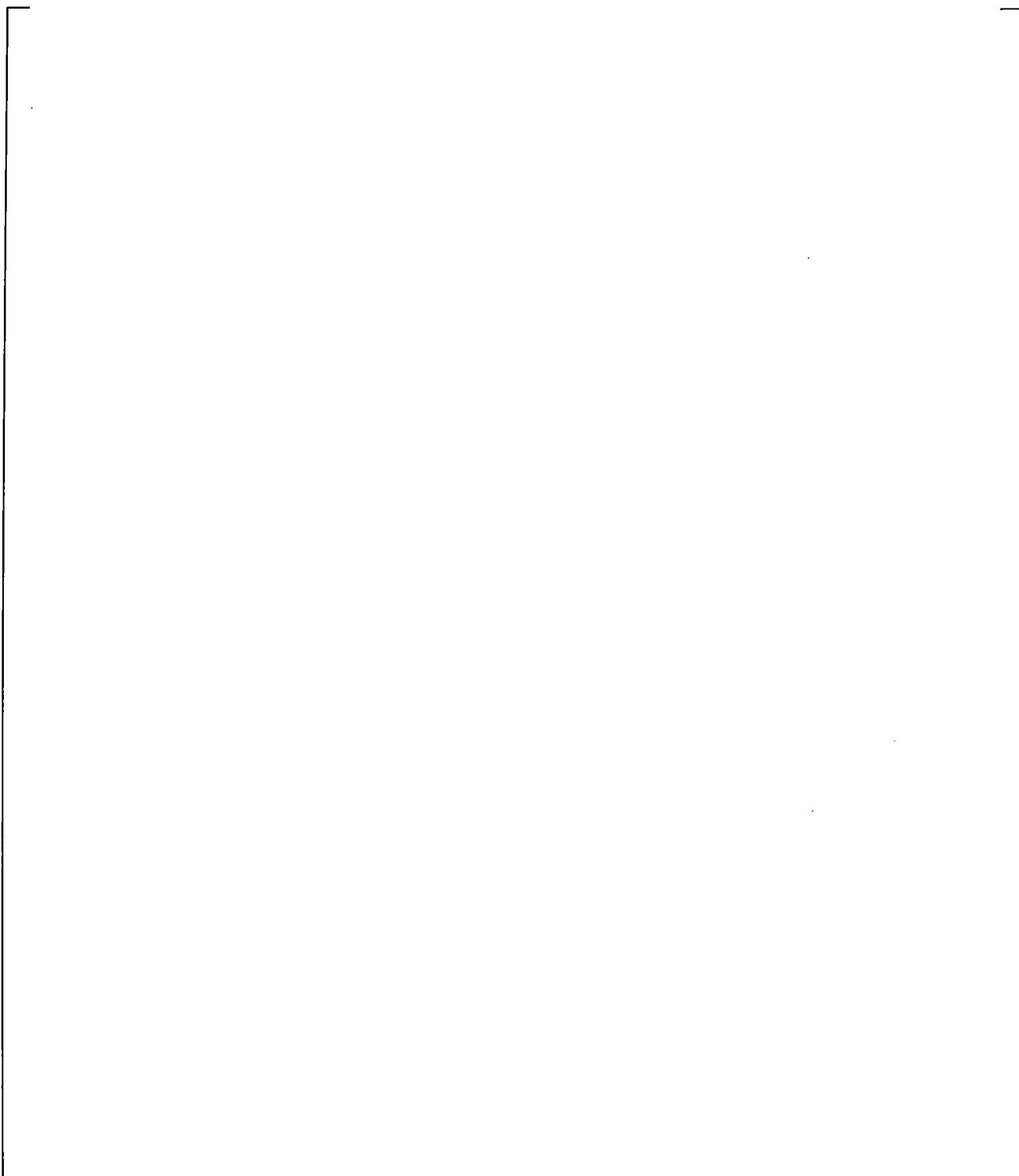
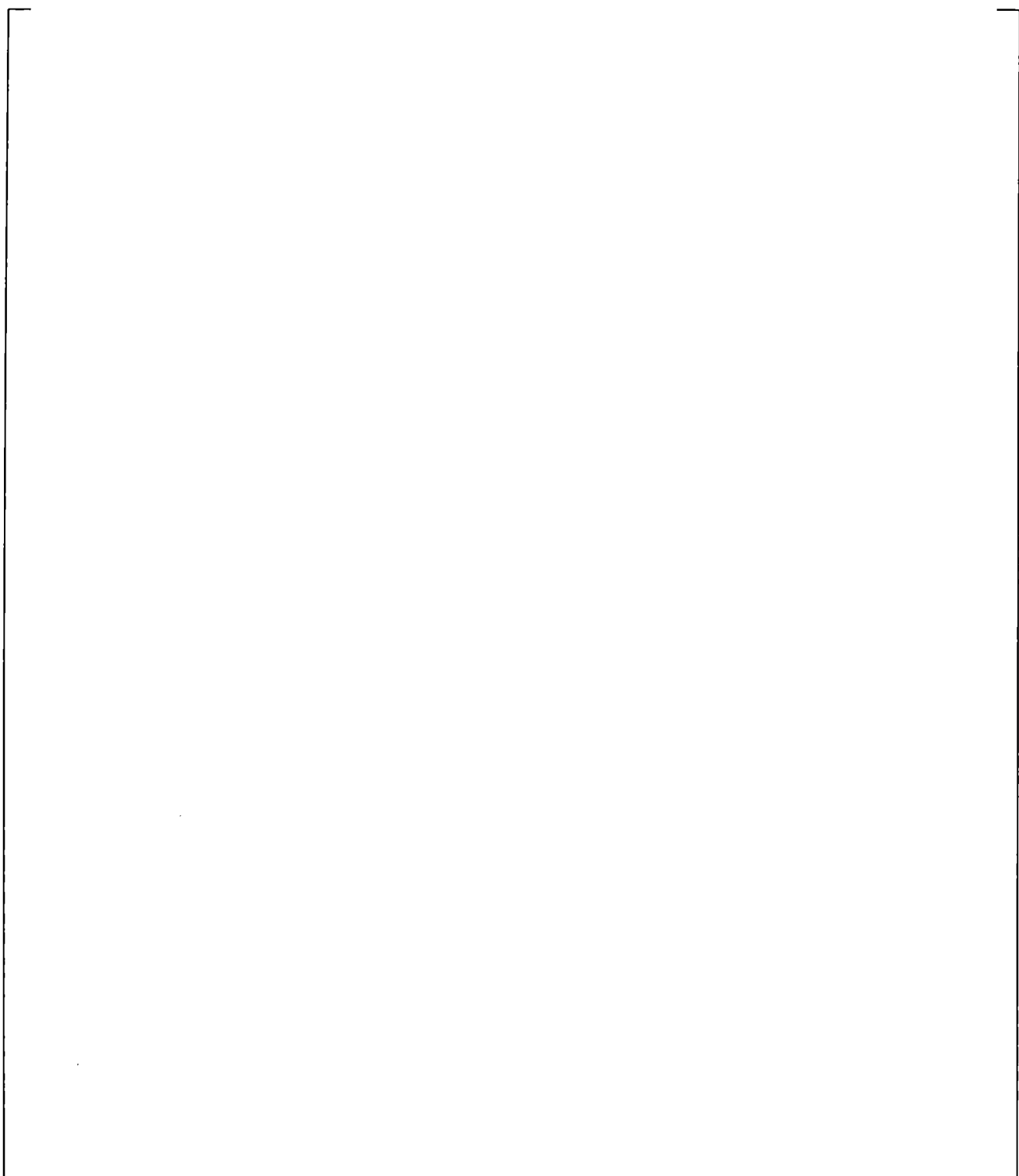


Figure 21.9-8 Downcomer-to-Upper Plenum Differential Pressure

a,c

| **Figure 21.9-9 Calculated SG Primary-to-Secondary Side Heat Transfer Coefficients**

Note: The SG heat transfer coefficient is calculated as $h_{SG} = \frac{Q_{SG,OUT}}{(FA_{SG,OUT} \times \Delta T_{SG})}$



| **Figure 21.9-10 Calculated Steam Generator Primary-to-Secondary Side Temperature Difference**

| **Figure 21.9-11 Calculated Steam Generator SGA U-tube Uphill Void Fraction**

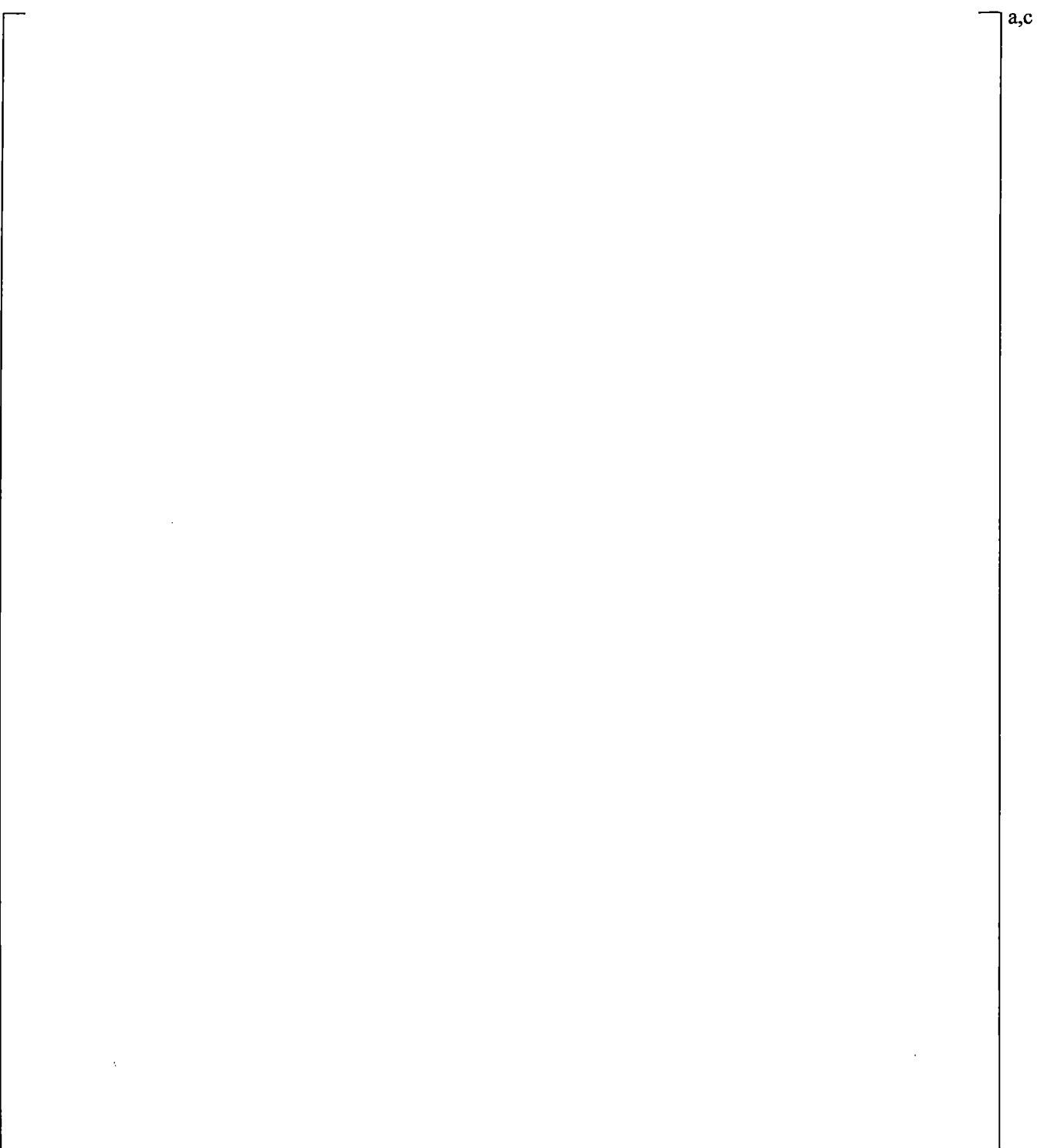


| **Figure 21.9-12 Calculated Steam Generator SGA U-tube Downhill Void Fraction**

a,c

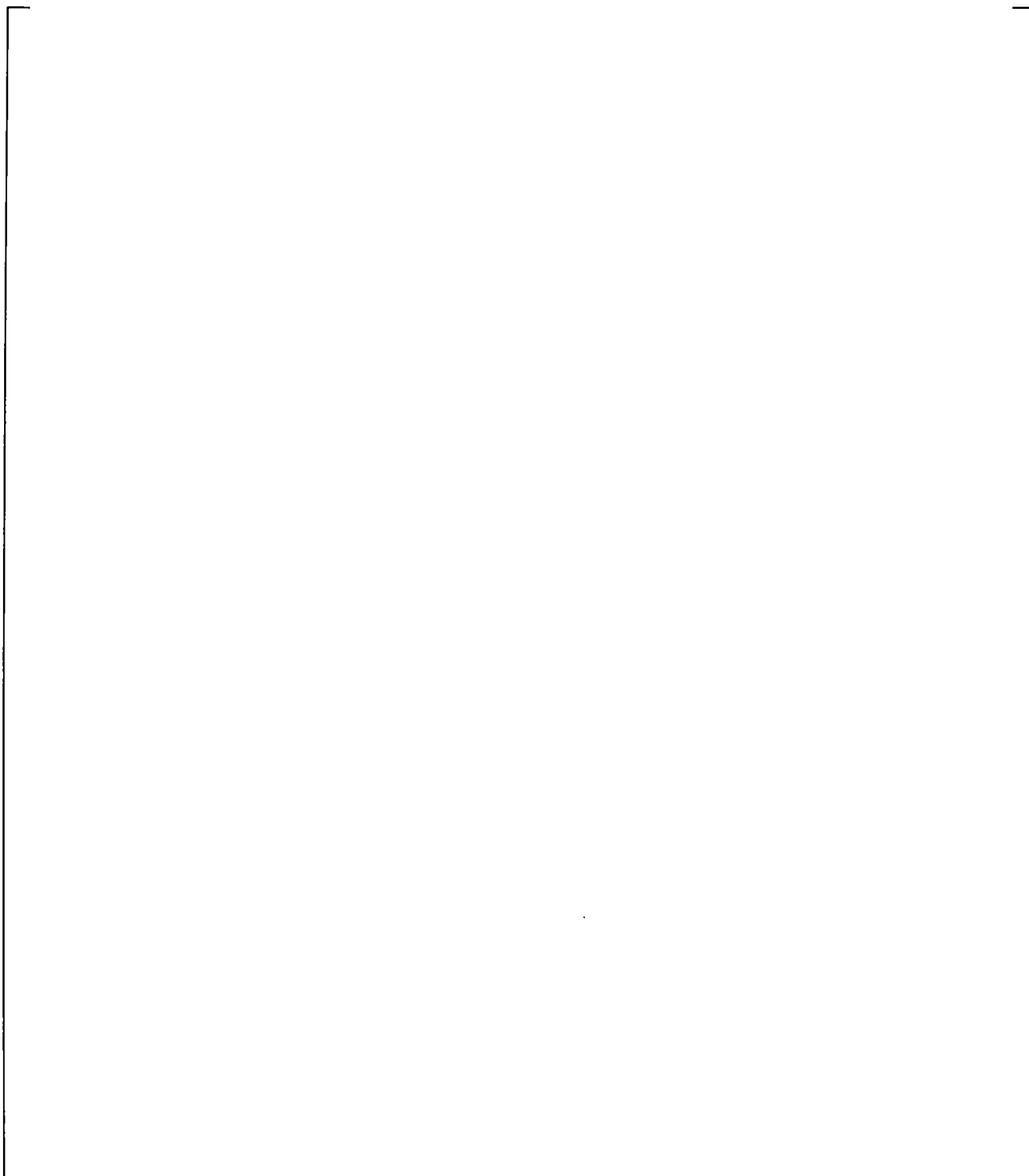


| **Figure 21.9-13 Calculated Steam Generator SGB U-tube Uphill Void Fraction**

a,c

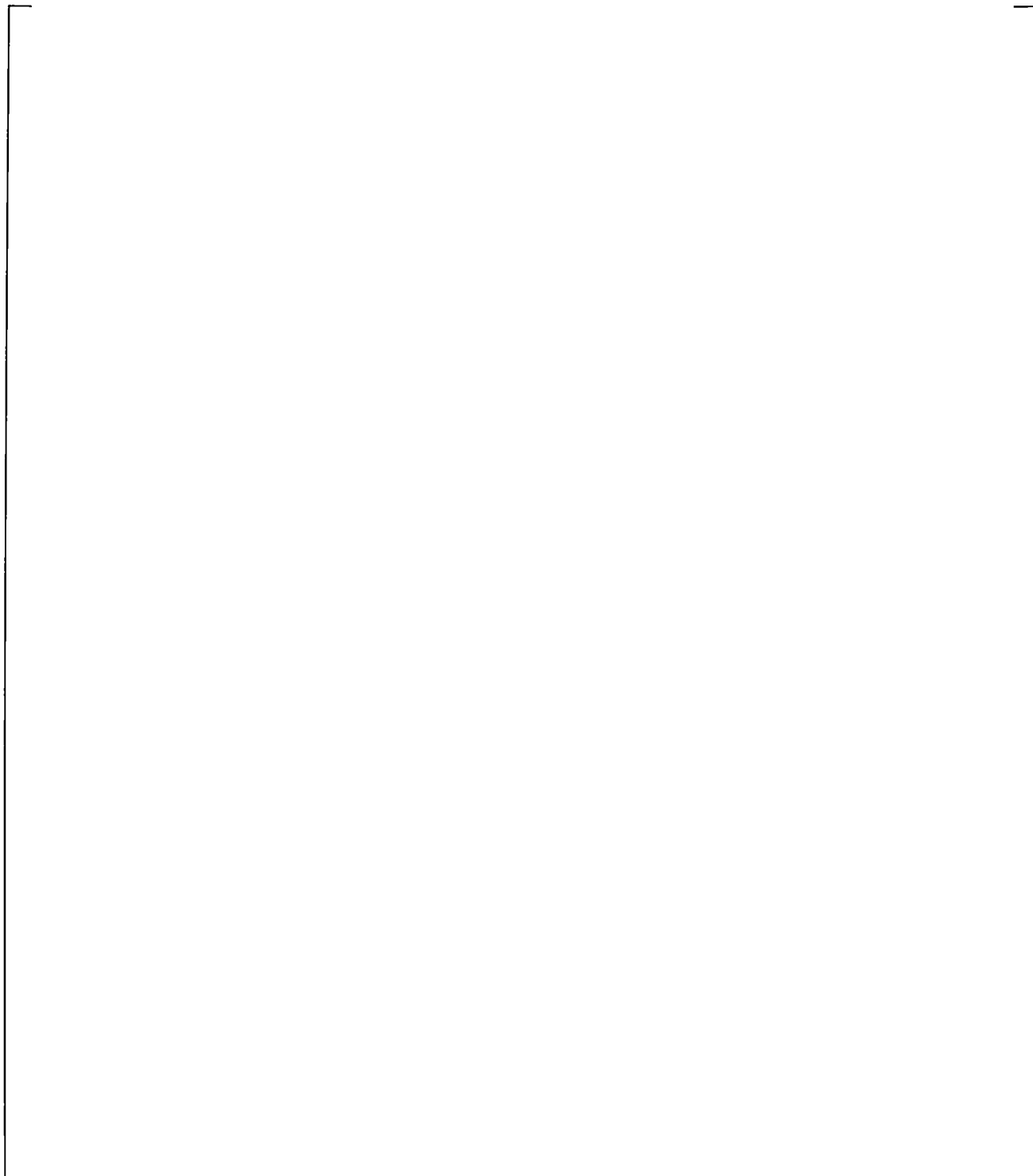


| **Figure 21.9-14 Calculated Steam Generator SGB U-tube Downhill Void Fraction**

a,c

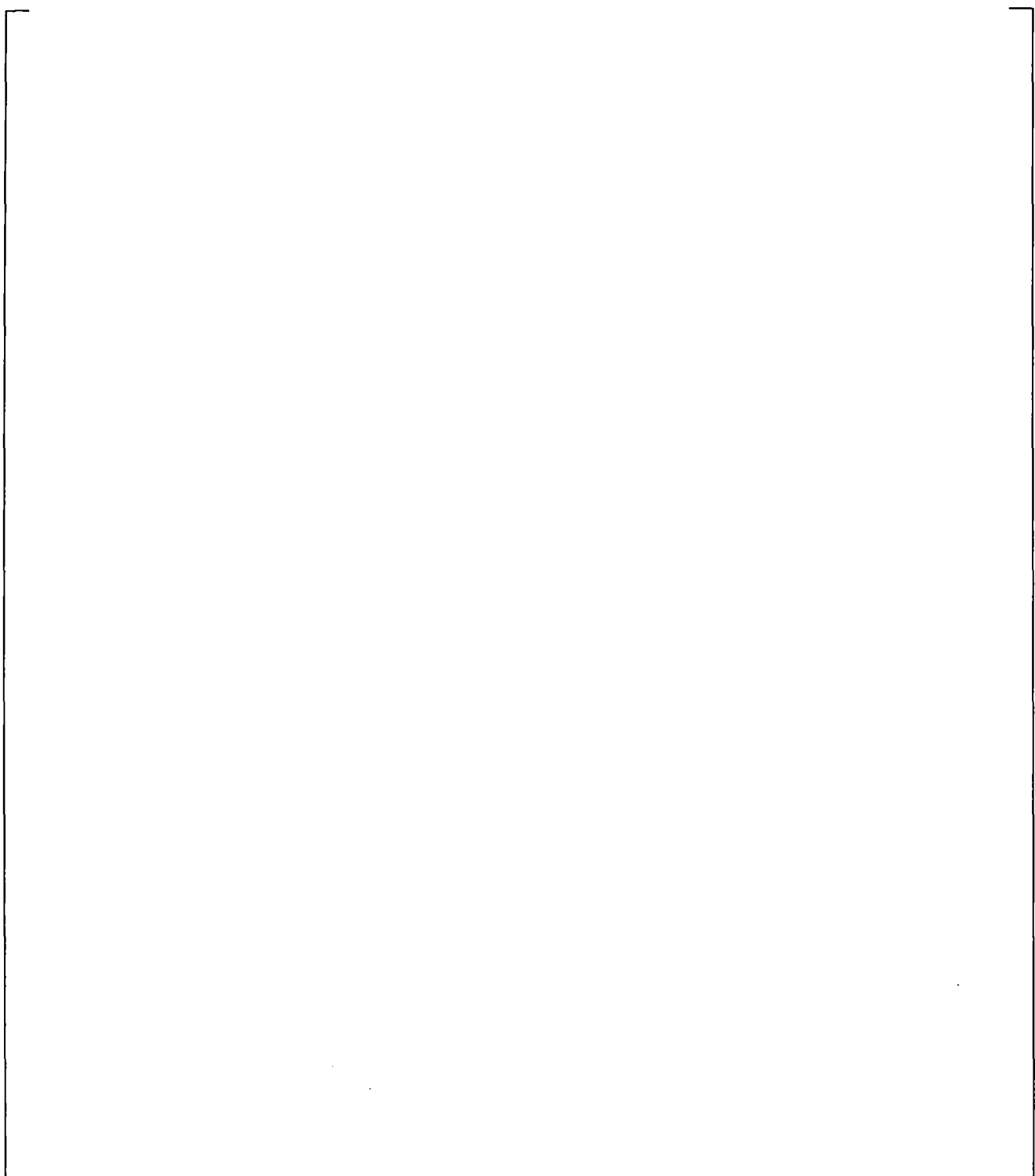


Figure 21.9-15 Calculated Steam Generator SGA Vapor Flows

Figure 21.9-16 Calculated Steam Generator SGB Vapor Flows

21.10 COUNTER-CURRENT FLOW LIMITATION RESULTS AND EVALUATION

The counter-current flow limitation phenomenon is a process where liquid flow, directed downward by the force of gravity, is restricted by vapor flowing in the opposite (upward) direction, due to interfacial drag forces. With increasing vapor velocity, at some point the downward flow of liquid becomes unstable, stagnates and is eventually reversed so that co-current flow is established. The boundary between the stable counter-current flow and the unstable co-current flow configuration is generally recognized as the so called Counter-current Flow Limitation (CCFL).

The importance of CCFL at different locations of the primary side during the different periods of the LOCA transient and its PIRT ranking are discussed in Section 2, Volume 1.

The liquid in the uphill and downhill side of the SG U-tubes drains into the hot leg and loop seal, respectively; CCFL is possible at the U-tube inlet, SG plenum inlet, and in the hot leg elbow. The potential for CCFL in these locations and the impact of CCFL predictions on the transient dictate that a high (H) ranking is assigned for the loop seal clearing period.

During the steam generator reflux phase of the small break LOCA, steam leaving the core enters the SG and condenses forming a liquid film inside the U-tubes. The condensate from the uphill side of the steam generator U-tubes would accumulate at the inlet of tube due to CCFL, and the resultant pressure increase would further depress the core mixture level. The condensate draining in to the SG plenum could again accumulate at the hot leg elbow causing additional pressure loss which would lower the core mixture level.

The liquid draining from the SG through the hot legs and into the upper plenum collects above the upper core plate (UCP). Water draining from the upper plenum region, or falling back after entrainment from the core, can contribute to core cooling. The amount of water that can drain may be limited by CCFL at the upper core plate, if the steam upflow is sufficient to limit or prevent draining.

Validation of the code capability to model CCFL in different regions of the primary system of a PWR is presented in Section 19. However, the large scale experiments considered therein are designed primarily for conditions developing in Large Break LOCA accidents. The purpose of the discussions included in this section is to complement the CCFL discussions in Section 19 and expand the CCFL considerations into the intermediate and small break LOCA space.

21.10.1 CCFL in the Steam Generator U-tubes

Counter-current flow in the steam generator U-tubes develops during the later stage of the two-phase natural circulation and continues into the reflux condensation phase of the Small Break LOCA transient. It is an important phenomenon since it is the major factor that controls the draining of the steam generator tubes especially during the reflux condensation phase of the loop seal clearing period.

One of the most widely used correlations to describe counter-current flow and flooding in U-tubes is a Wallis-type correlation in its general form $(j_g^*)^{1/2} + m \times (j_f^*)^{1/2} = C$, where $m = 0.8-10$ and $C = 0.7 - 1.0$ are empirically determined constants. In the case of turbulent flow m is close to 1.0.

Based on investigation of reflux condensation tests, performed at the ROSA-IV LSTF, it has been suggested by (Kukita et al., 1991) that the steam generator U-tube flooding (CCFL) line can be represented by the following Wallis-type correlation.

$$(j_g^*)^{1/2} + (j_f^*)^{1/2} = 0.88 \quad (21.10-1)$$

It is however important to note that in the $C=0.88$ flooding line suggested in (Kukita et al., 1991) was determined based on the assumption that during reflux condensation phase the vapor entering the steam generator U-tube bundle condenses uniformly along the length of the bundle, so that there is a 1:1 split of the condensation; this is half of the vapor condenses in the uphill and drains back into the hot leg, while the rest condenses in the downhill side of the U-tubes and drains into the SG outlet plenum. However, there is no solid experimental evidence to support this assumption. [

]^{a,c}

The counter-current flow calculation results, presented in Figures 21.10.1-1 through 21.10.1-4, are extracted for the steam generator U-tube inlet locations from different ROSA-IV test simulations documented in the previous subsections. The CCFL results presented in these figures are from test simulations performed with the [

]^{a,c} In each of the figures, (a) shows all the counter-current points calculated at the U-tube inlet of Steam Generator A, and (b) shows the counter-current flow points at the U-tube inlet of Steam Generator B.

I

]^{a,c}

I

]^{a,c}

The counter-current flow calculated in the simulation of the natural circulation test ST-NC-02 is presented in Figure 21.10.1-5. The results show no CCFL points are on the flooding line during reflux conditions in the steam generators. The natural circulation test, ST-NC-02 was conducted at 2% of the nominal power. At this vapor generation level, very little CCFL was expected at the inlet of the U-tubes.

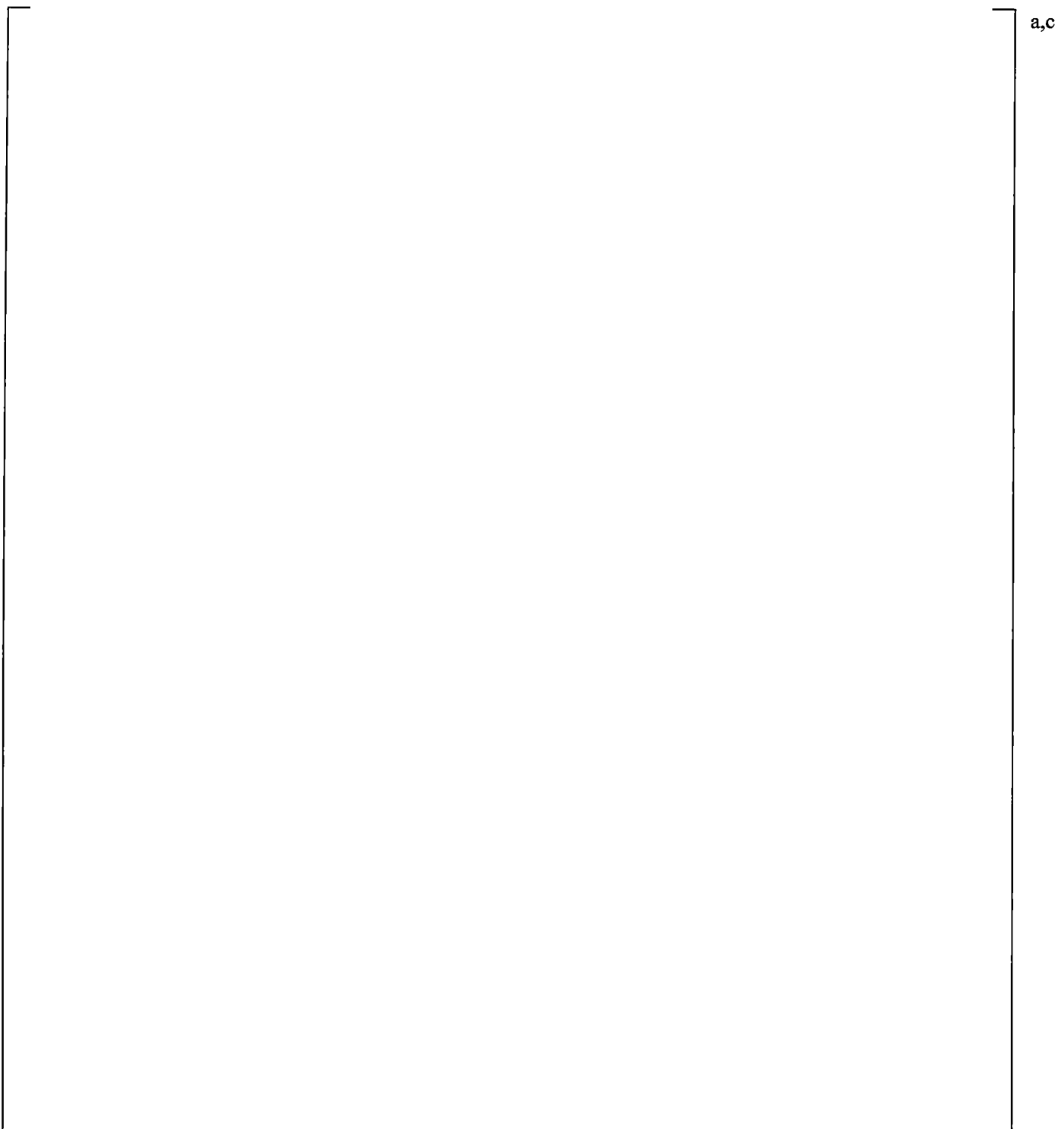
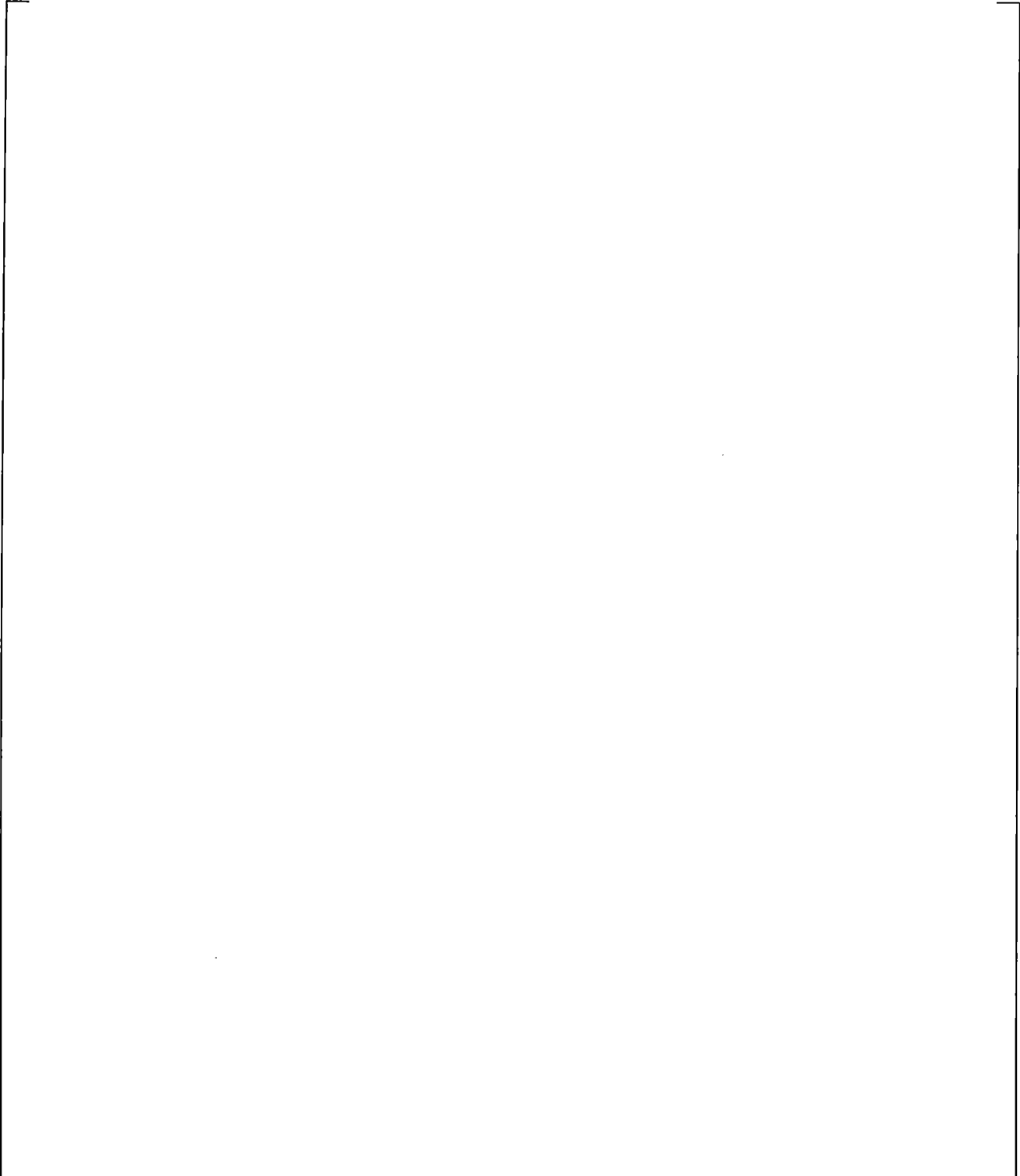


| **Figure 21.10.1-1 Calculated Counter-current Flow at the Inlet of Steam Generator U-tubes
(Simulation of 10% Break Test SB-CL-14)**



a,c

**Figure 21.10.1-2 Calculated Counter-current Flow at the Inlet of Steam Generator U-tubes
(Simulation of 5% Break Test SB-CL-18)**

a,c

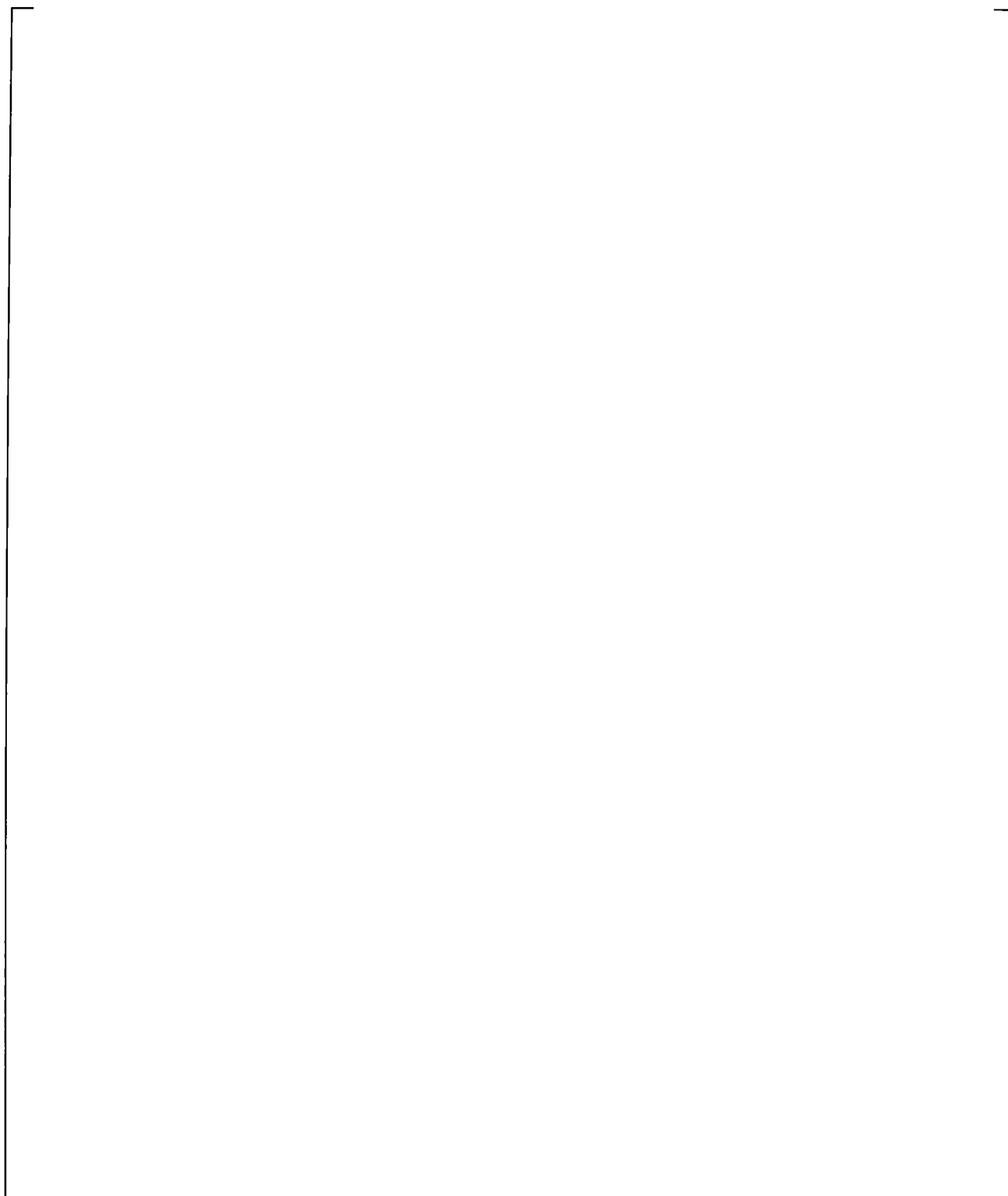


**Figure 21.10.1-3 Calculated Counter-current Flow at the Inlet of Steam Generator U-tubes
(Simulation of 2.5% Break Test SB-CL-01)**

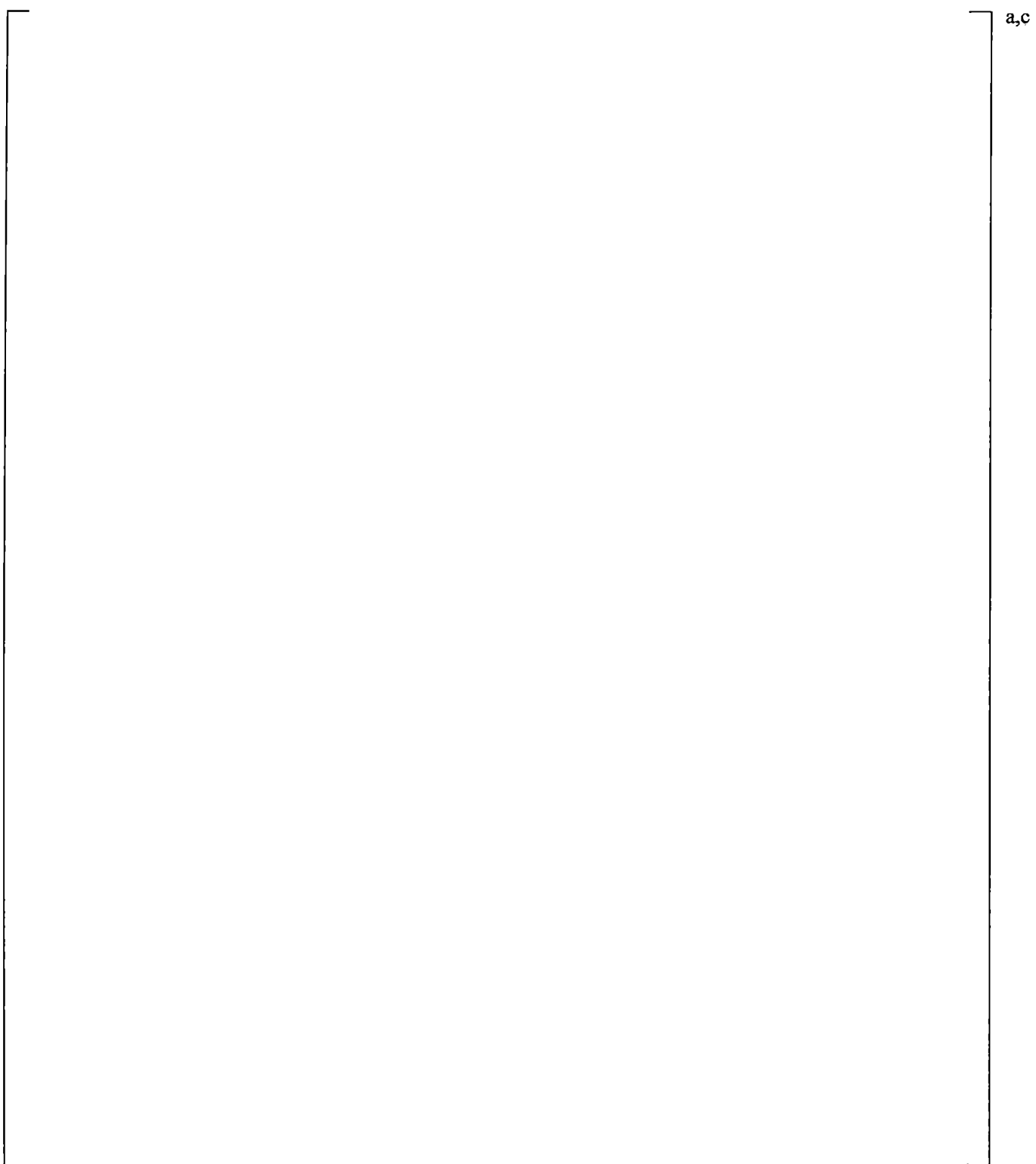


**Figure 21.10.1-4 Calculated Counter-current Flow at the Inlet of Steam Generator U-tubes
(Simulation of 0.5% Break Test SB-CL-12)**

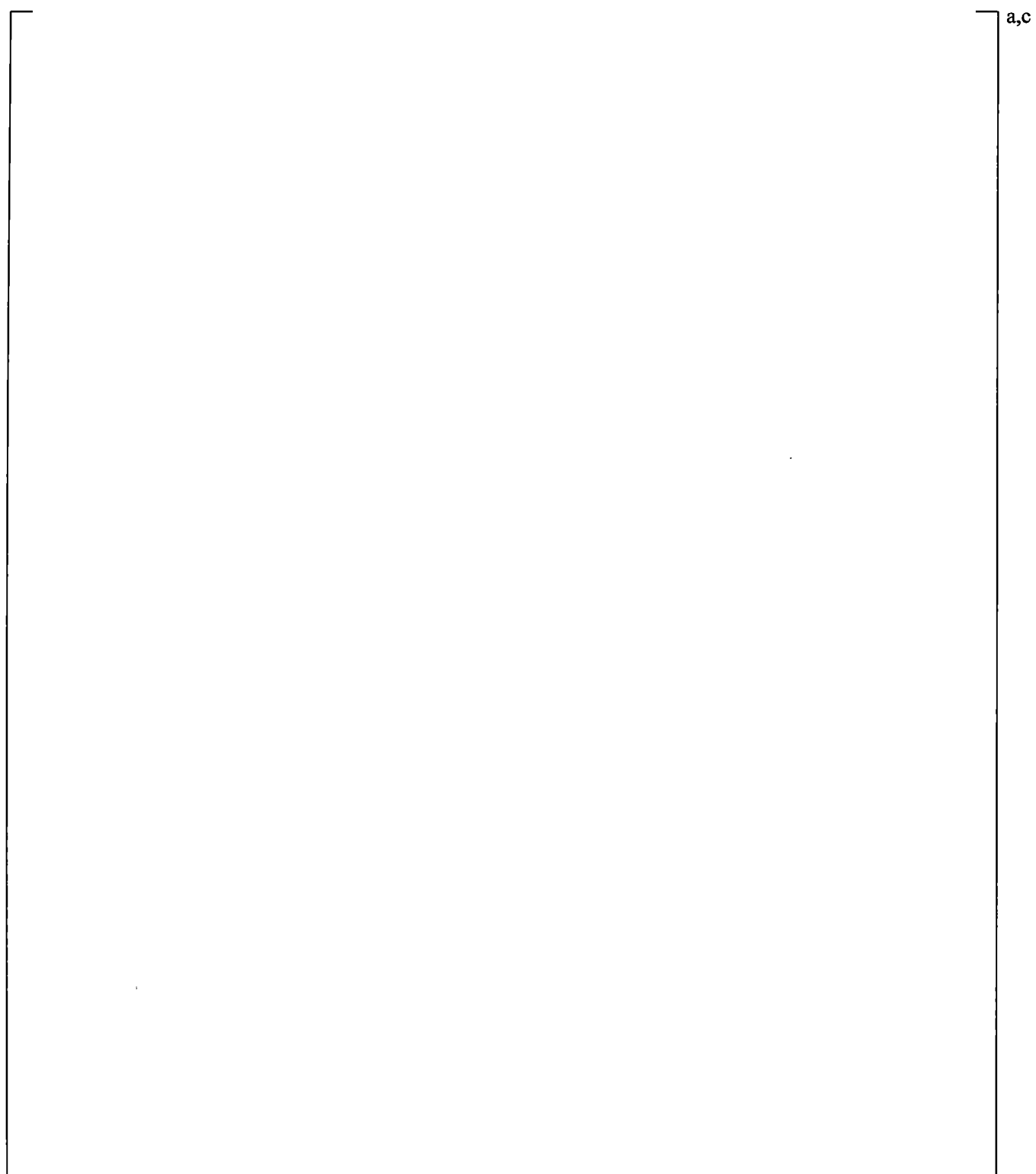


**Figure 21.10.1-5 Calculated Counter-current Flow at the Inlet of Steam Generator U-tubes
(Simulation of the Natural Circulation Test ST-NC-02)**

21.10.2 CCFL in the Vicinity of the Hot Leg Elbow (Steam Generator Inlet)

Counter-current flow in the hot leg (HL), including the vicinity of the elbow and the inlet of the steam generator plenum, can develop during the period of two-phase natural circulation and is especially important during the subsequent reflux condensation phase. The ability of the code to properly calculate the counter-current flow at that location would affect the calculated draining of the SG inlet plenum and subsequently the draining of the U-tubes as well. Acceptable counter-current flow calculation in the hot leg is of critical importance for the correct prediction of the system behavior during the reflux condensation phase of the LOCA transient.

[

 $J^{a,c}$

(21.10-2)

The counter-current flow calculation results, presented in Figures 21.10.2-1 through 21.10.2-4, are extracted for the hot leg elbow and steam generator inlet locations from different ROSA-IV test simulations documented in the previous subsections. All of the simulations considered here were performed with a [$J^{a,c}$]^{a,c}. In these figures, the calculated counter-current conditions (points) are plotted against the two limiting flooding lines, [$J^{a,c}$].

[$J^{a,c}$]^{a,c} In each of the figures, the hot leg elbow counter-current flow points are compared against Equation 21.10-2.

Figure 21.10.2-1 shows results extracted from the simulation of the 10% cold leg side break test SB-CL-14. The calculated counter-current flow points are mostly clustered onto the enforced [$J^{a,c}$]^{a,c} flooding limit without any CCFL violations.

Figure 21.10.2-2 shows the results extracted from the simulation of the 5% cold leg side break test SB-CL-18. [$J^{a,c}$]

 $J^{a,c}$

The counter-current flow points, extracted from the simulations of the 2.5% break test SB-CL-01, Figure 21.10.2-3, and the 0.5% break test SB-CL-12, Figure 21.10.2-4, further confirm the conservative bias of the code with respect to counter-current flow at the hot leg and the steam generator inlet.

[

 $J^{a,c}$

a,c

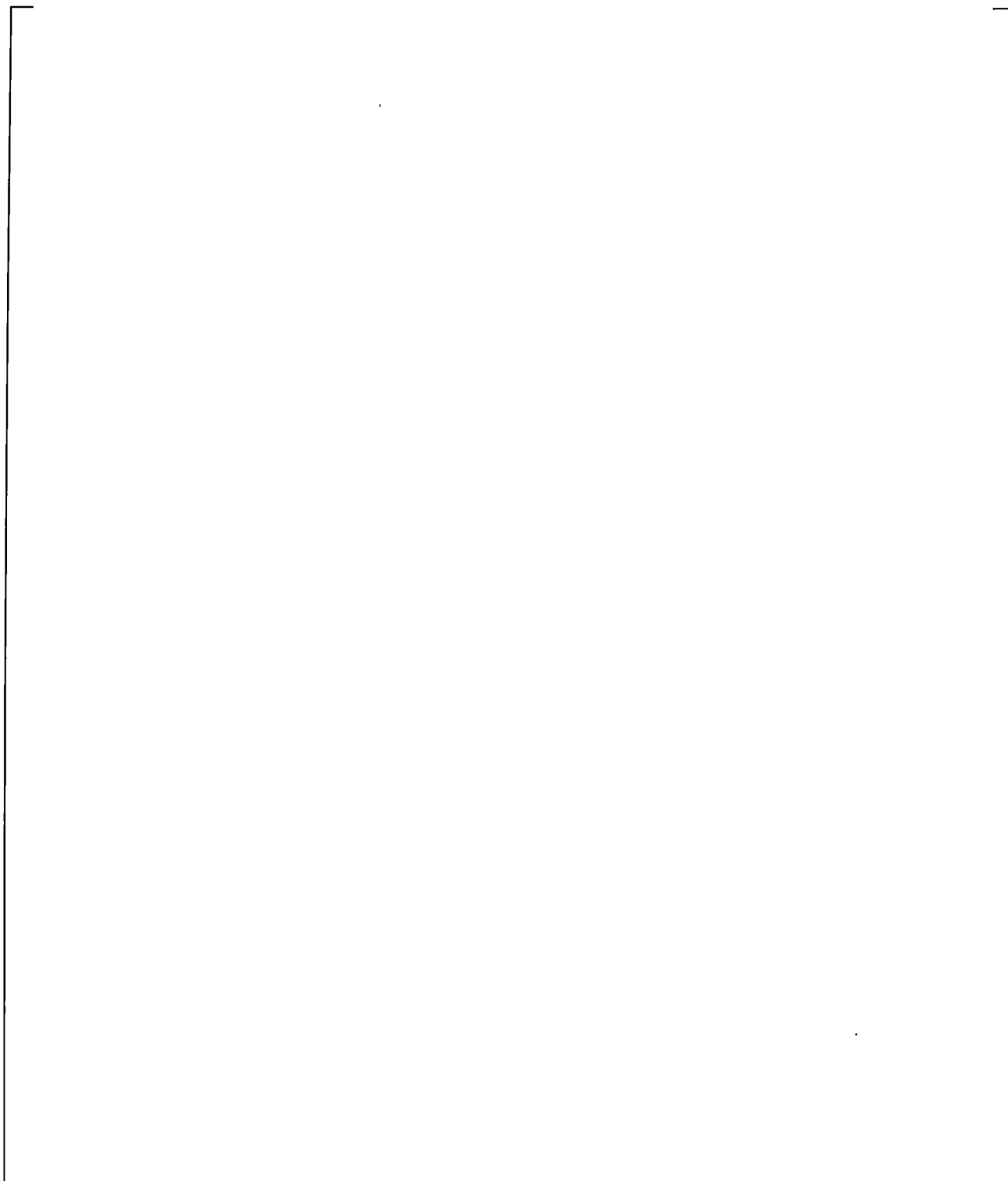


**Figure 21.10.2-1 Calculated Counter-current Flow at the Hot Leg Elbows and SG Inlets
(Simulation of 10% Break Test SB-CL-14)**

a,c

**Figure 21.10.2-2 Calculated Counter-current Flow at the Hot Leg Elbows and SG Inlets
(Simulation of 5% Break Test SB-CL-18)**

a,c

**Figure 21.10.2-3 Calculated Counter-current Flow at the Hot Leg Elbows and SG Inlets
(Simulation of 2.5% Break Test SB-CL-01)**

a,c

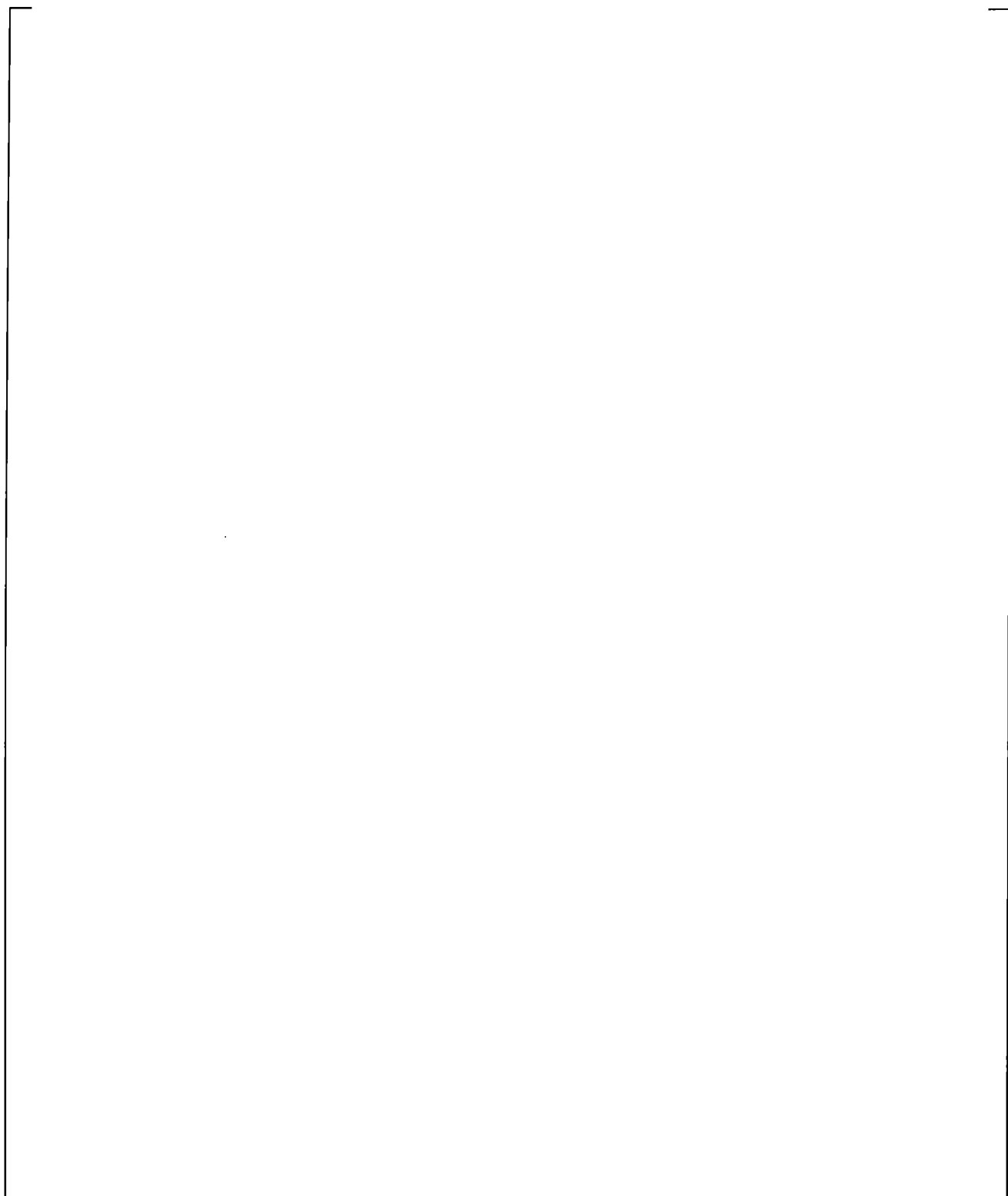


**Figure 21.10.2-4 Calculated Counter-current Flow at the Hot Leg Elbows and SG Inlets
(Simulation of 0.5% Break Test SB-CL-12)**

21.10.3 CCFL at the Upper Core Plate (UCP)

Counter-current flow limitation at the upper core plate is an important phenomenon during both large-break and small-break loss-of coolant accidents. Steam-water counter-current flow condition at the top of UCP might occur during different phases of the LOCA accidents.

In large-break accidents CCFL can occur during the reflood phase when water is accumulated above the UCP as a result of de-entrainment or direct SI injection in the upper plenum. If the flow of vapor generated in the core is high enough, it may impede the penetration of the water accumulated in the upper plenum and reduce the effectiveness of the core cooling. Validation of the capability of the code to calculate CCFL in large break LOCA conditions is presented in Section 19.4, [

]^{a,c}.

In Small-break LOCA, the accumulation of water in the upper plenum occurs primarily as a result of the draining of the hot legs and the uphill side of the steam generators during the later stages of the two-phase natural circulation period. A pool of water accumulated above the UCP can still exist during the reflux condensation period maintained by steam condensing on the surface of the steam generator U-tubes and draining back into the upper plenum. Irrespective of how the pool of water above the UCP is formed and maintained during the accident, the nature of the CCFL phenomenon is in essence similar in both Large-break and Small-break LOCA scenarios.

The results of calculated counter-current flow at the UCP, presented in this section, are extracted from the ROSA-IV LSTF simulations for the individual channels that are modeled in the [

]^{a,c}, see Figures 21.3-1 and 21.3-3. [

]^{a,c}

Figure 21.10.3-1 shows calculated counter-current flow at Channels 73 and 80, located above the peripheral (low-power) core region, extracted from the simulation of the SB-CL-18 test.

Figures 21.10.3-2 and 21.10.3-3 show the counter-current flow calculated at the inner average and inner hot channels respectively.

[

]^{a,c}

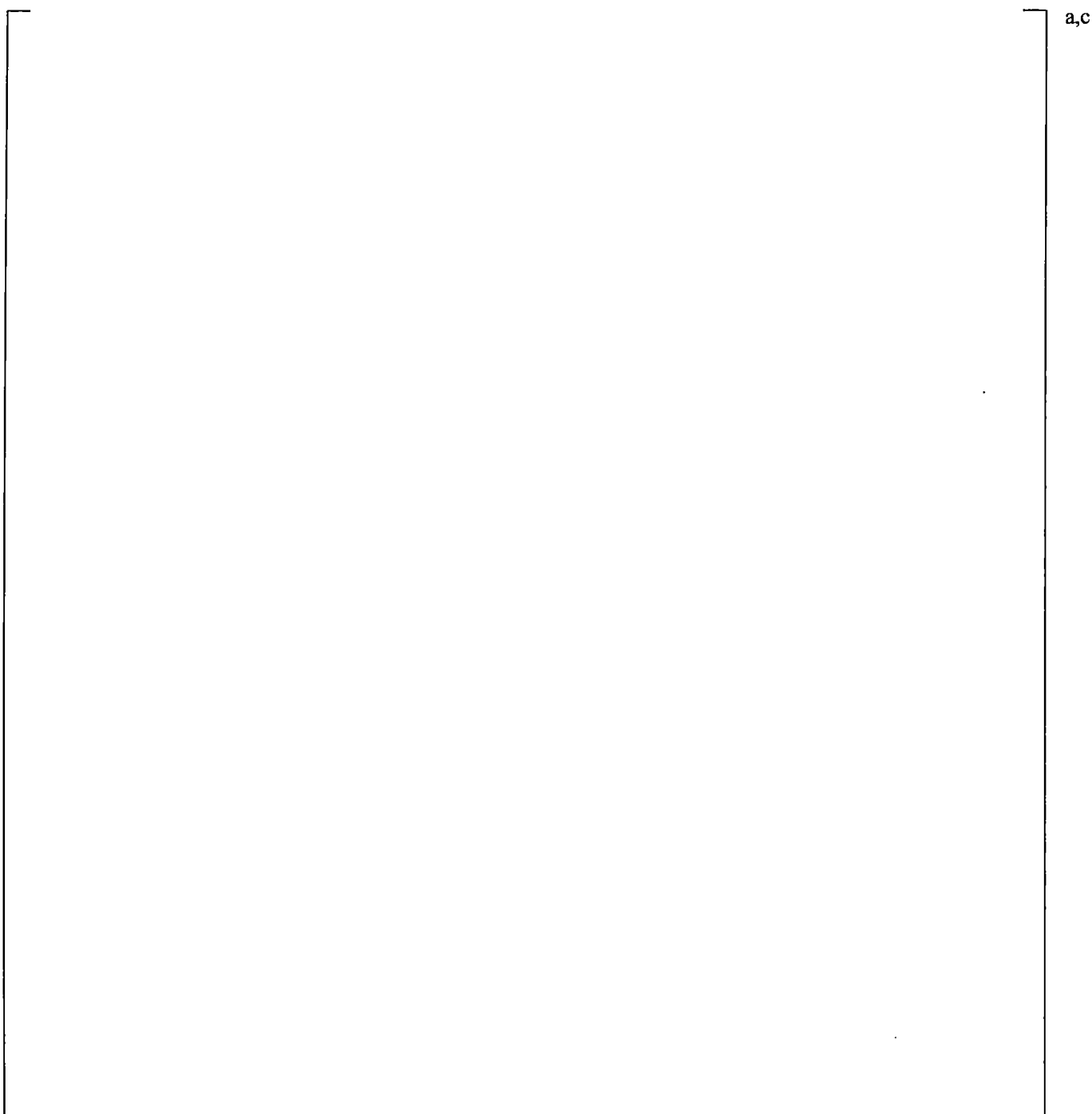
Figures 21.10.3-4 through 21.10.3-6 show counter-current flow results that were extracted from other ROSA-IV test simulations documented in the previous sections. The CCFL results shown in these figures include all instances where counter-current flow is calculated to occur at the UCP location.

Figure 21.10.3-4 shows counter-current flow points extracted from the simulation of the 10% break test SB-CL-14. [

]^{a,c}

The few instances when the NW flooding line is violated (Figures 21.10.3-2, 21.10.3-4 and 21.10.3-5) are of short durations caused by the flow oscillations; they are found to have negligible consequences to the core heat up predictions.

In summary, the results presented in this section show that with the current ROSA-IV LSTF model, the code ([WCOBRA/TRAC-TF2](#)) calculates counter-current flow at the UCP location which is, for the most part, conservative with respect to the draining of the liquid pool that might exist above the upper core plate. This is especially true for the periods of significant core uncover that may be predicted to occur during the loop seal clearance and core boiloff periods of the small-break transient simulations.



| **Figure 21.10.3-1 Calculated Counter-current Flow Conditions at the Bottom of Peripheral CCFL
Channels 73 and 80**

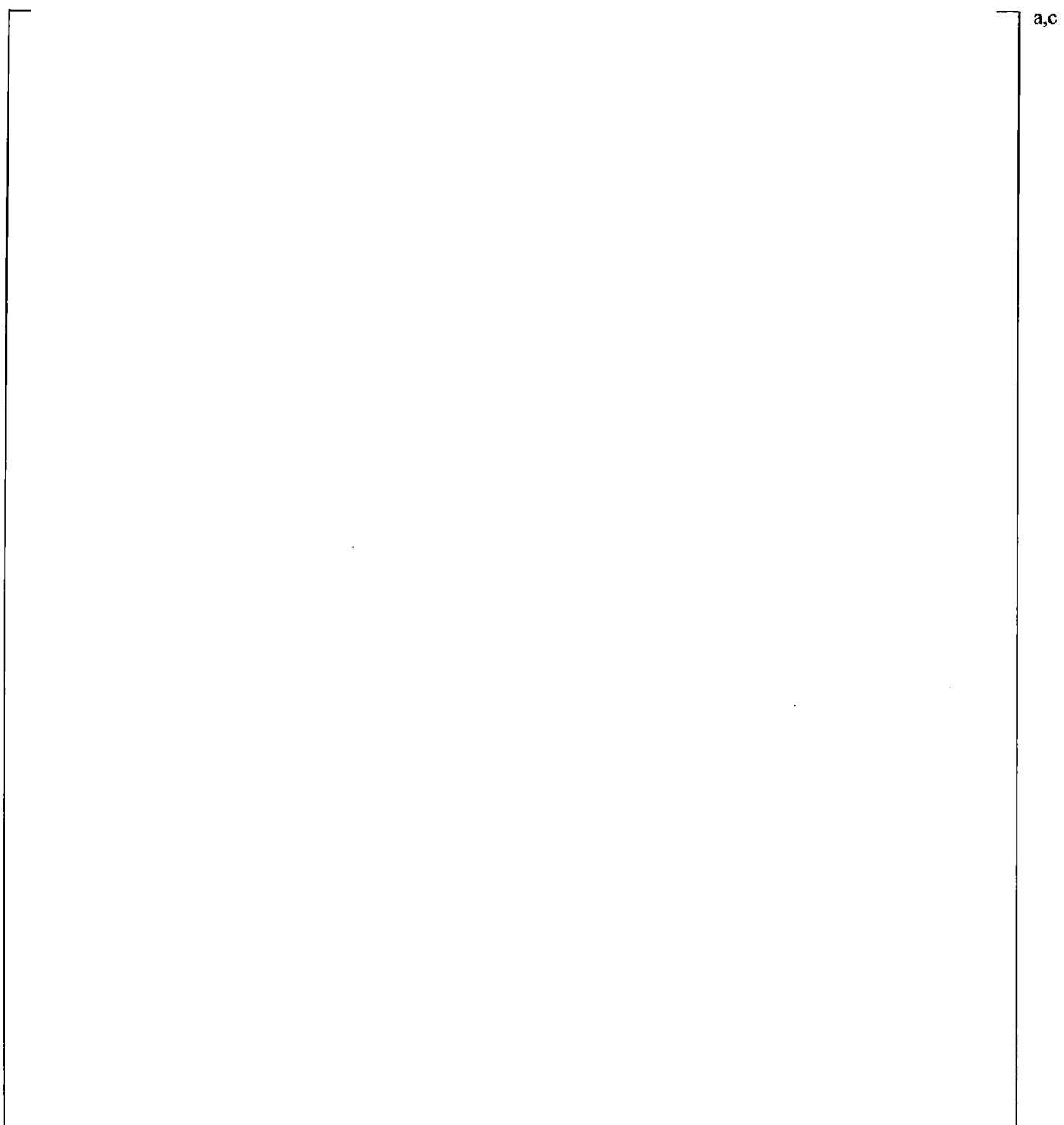
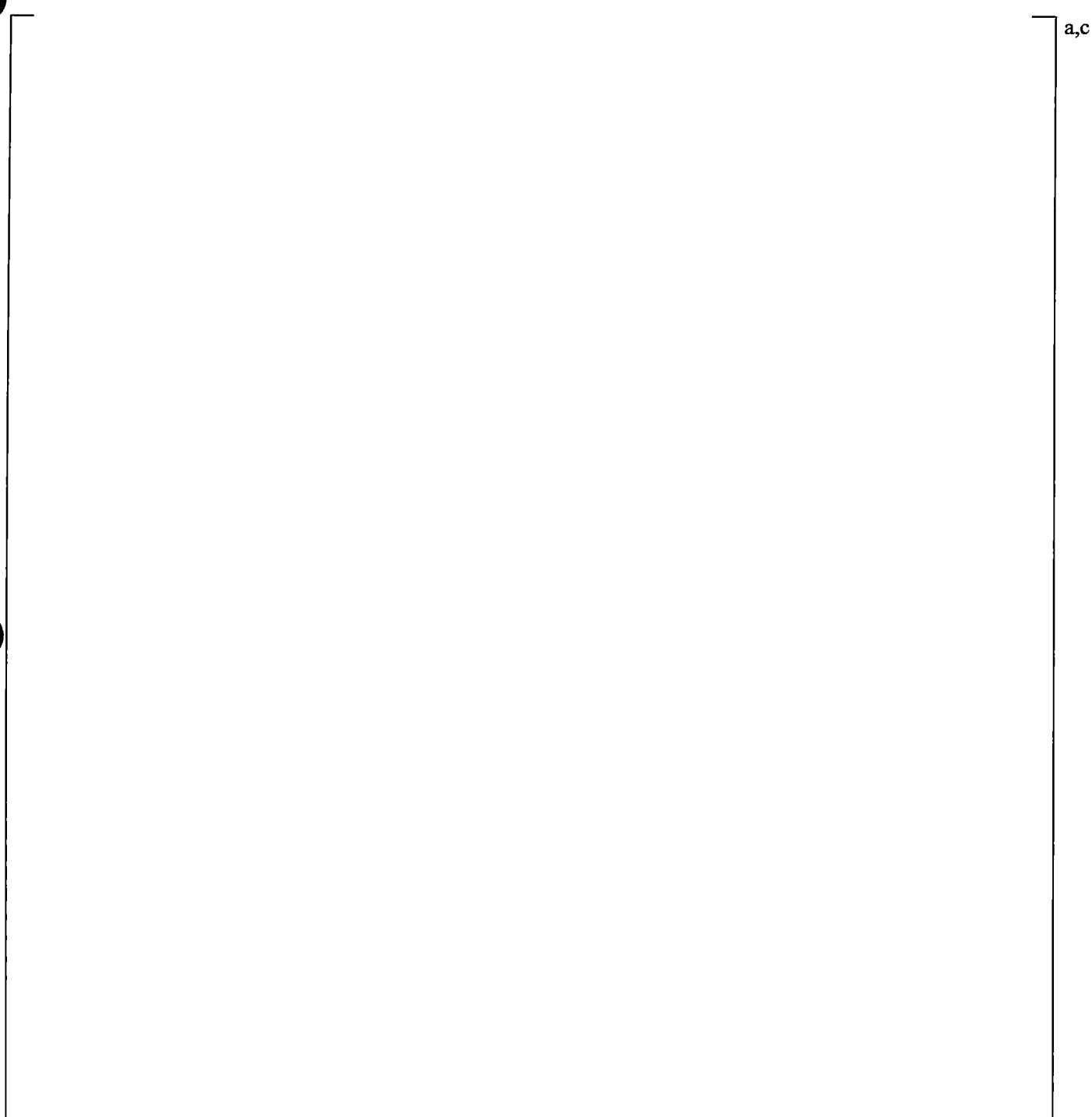


Figure 21.10.3-2 Calculated Counter-current Flow Conditions at the Top of the Inner Average CCFL Channels 13 and 14



**Figure 21.10.3-3 Calculated Counter-current Flow Conditions at the Top of the Inner Hot CCFL
Channels 11 and 12**

a,c

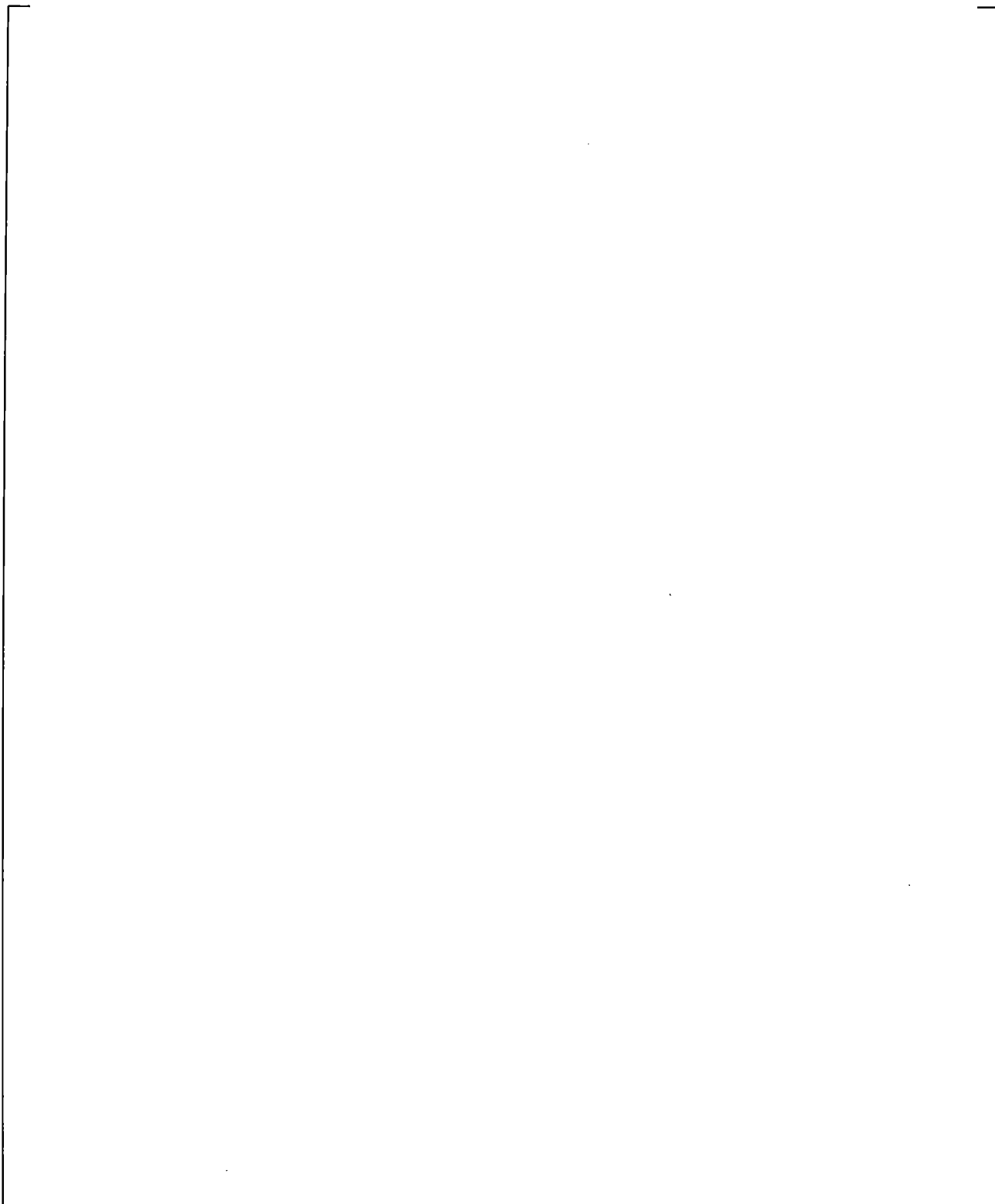


Figure 21.10.3-4 Calculated UCP Counter-current Flow Conditions (10% Break Test SB-CL-14).

a,c

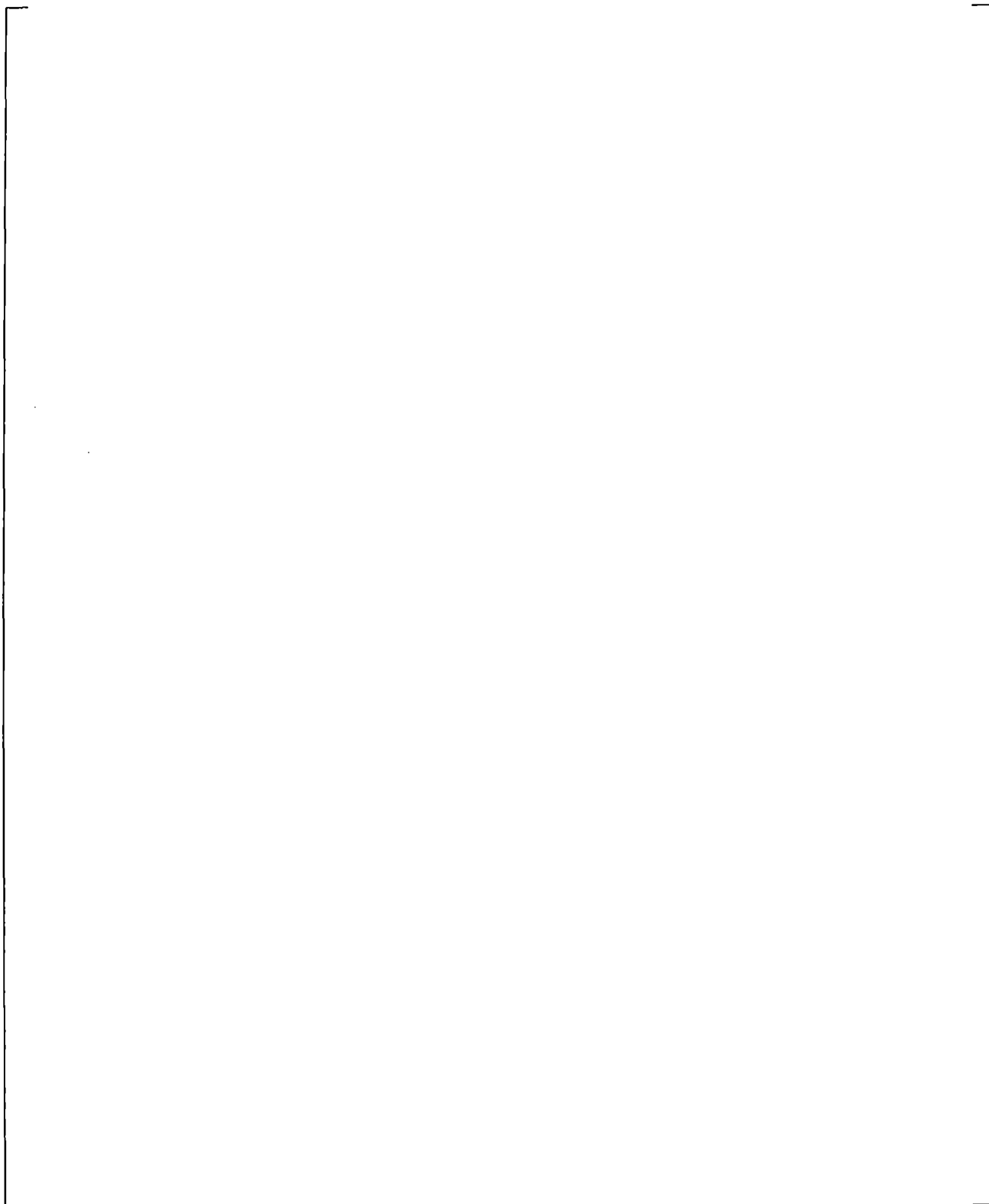


Figure 21.10.3-5 Calculated UCP Counter-current Flow Conditions (2.5% Break Test SB-CL-01)

a,c

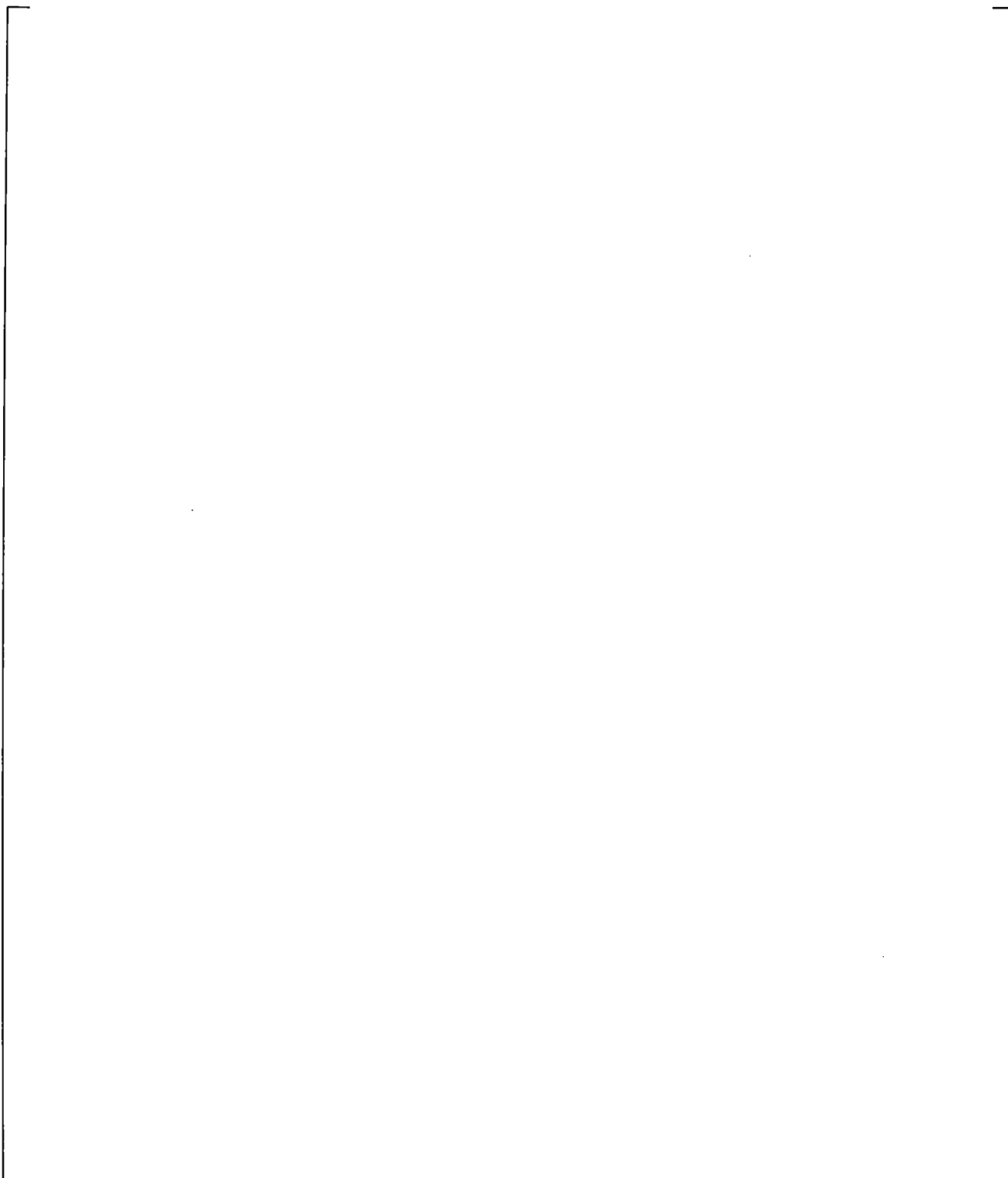


Figure 21.10.3-6 Calculated UCP Counter-current Flow Conditions (0.5% Break Test SB-CL-12)

21.11 BYPASS SENSITIVITY CALCULATIONS

This section documents results from various simulations of ROSA-IV tests performed with different modeling variations. These sensitivity calculations are needed to provide a basis for the treatment of the modeling uncertainty within the FSLOCA Methodology.

21.11.1 Hot Leg Nozzle Gap Modeling Sensitivity with the SB-CL-18 Test

As described in Section 21.3, the ROSA-IV LSTF vessel model used in the different break simulations documented in Section 21 implements a split bypass modeling where the spray nozzle flow path and the line that connects the hot leg outlet nozzles to the downcomer are modeled as separately.

The goal of this sensitivity calculation is to investigate the effect of a modeling approach where the bypass flow through the hot leg nozzle gaps (HL-to-DC) is lumped together with the spray nozzle and the flow link from hot leg nozzles to the downcomer is not explicitly modeled. A calculation with this revised “lumped” bypass modeling is performed with the SB-CL-18 test to investigate the effect of this modeling approach.

Figures 21.11.1-1 through 21.11.1-7 compare the simulation results with the lumped bypass modeling approach against the simulation results of the SB-CL-18 documented in the previous Section 21.4. In each of the figures, the reference SB-CL-18 simulation results (split bypass model) are at the top, while the simulation results obtained with the lumped bypass model are at the bottom.

[

J^{a,c}

a,c

Figure 21.11.1-1 SB-CL-18 Cross-Over Leg A Differential Pressures

a,c

Figure 21.11.1-2 SB-CL-18 Cross-Over Leg B Differential Pressures

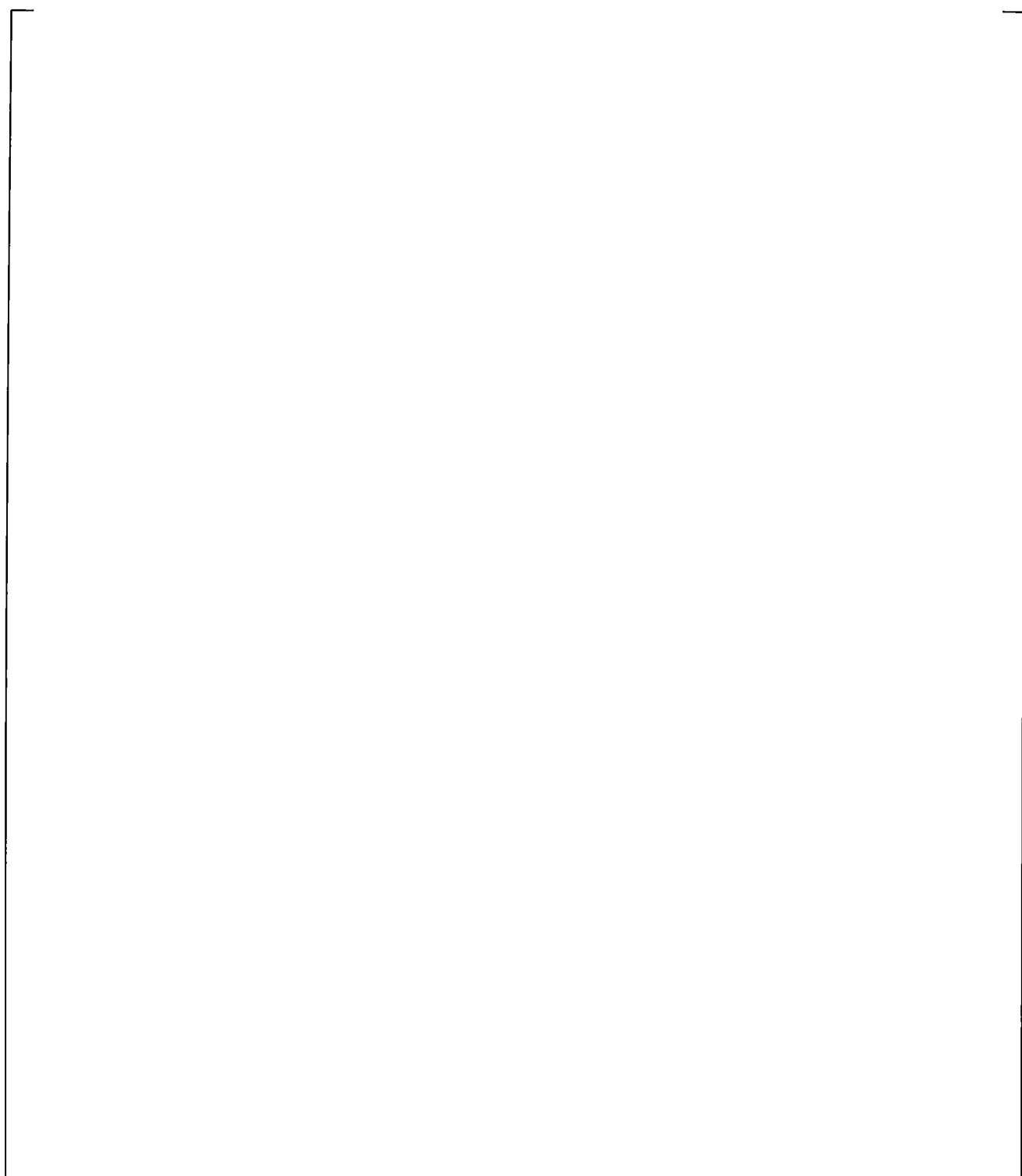


Figure 21.11.1-3 Inner Vessel Differential Pressures (LP+Core+UCP)

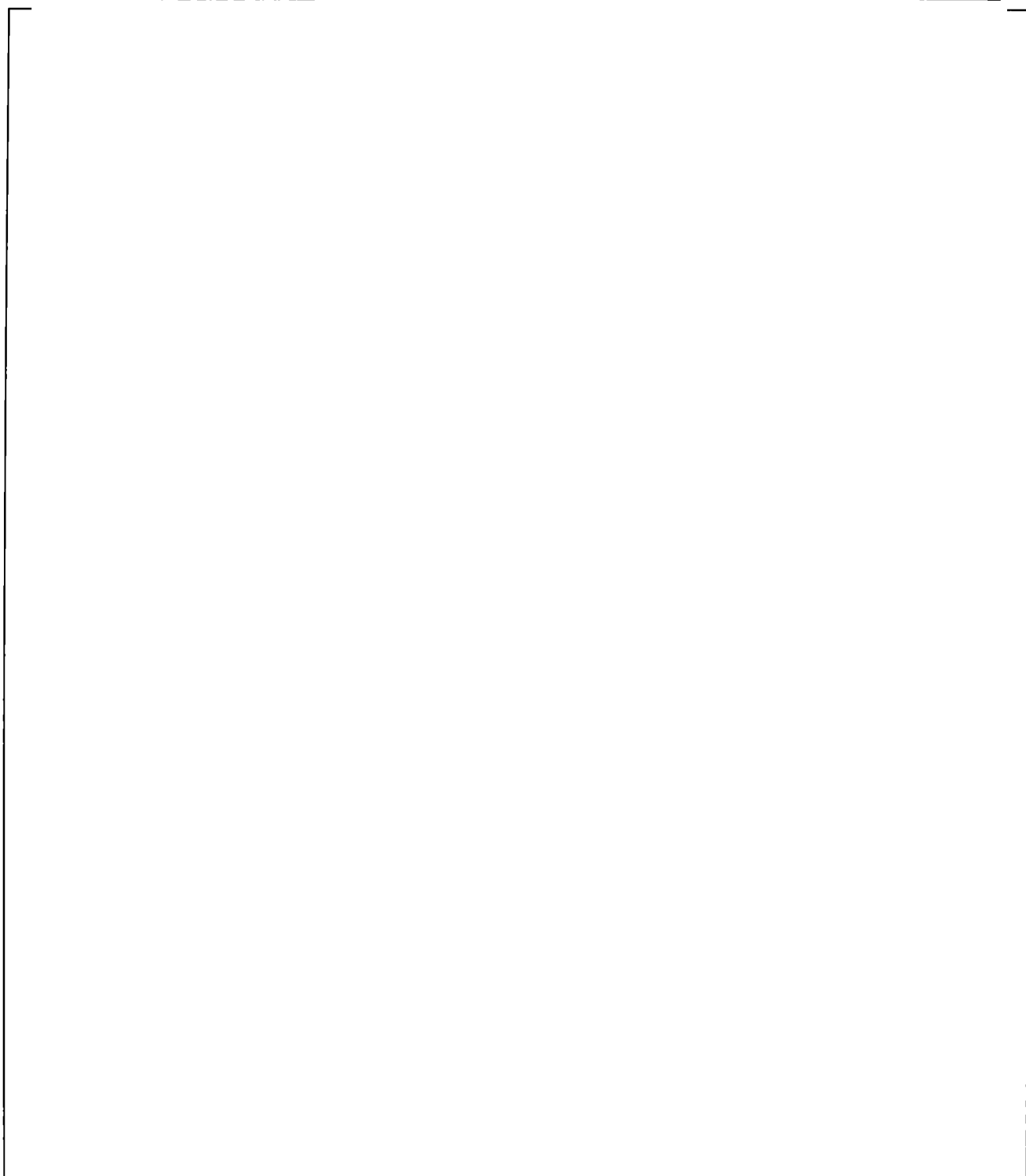


Figure 21.11.1-4 Downcomer Differential Pressures

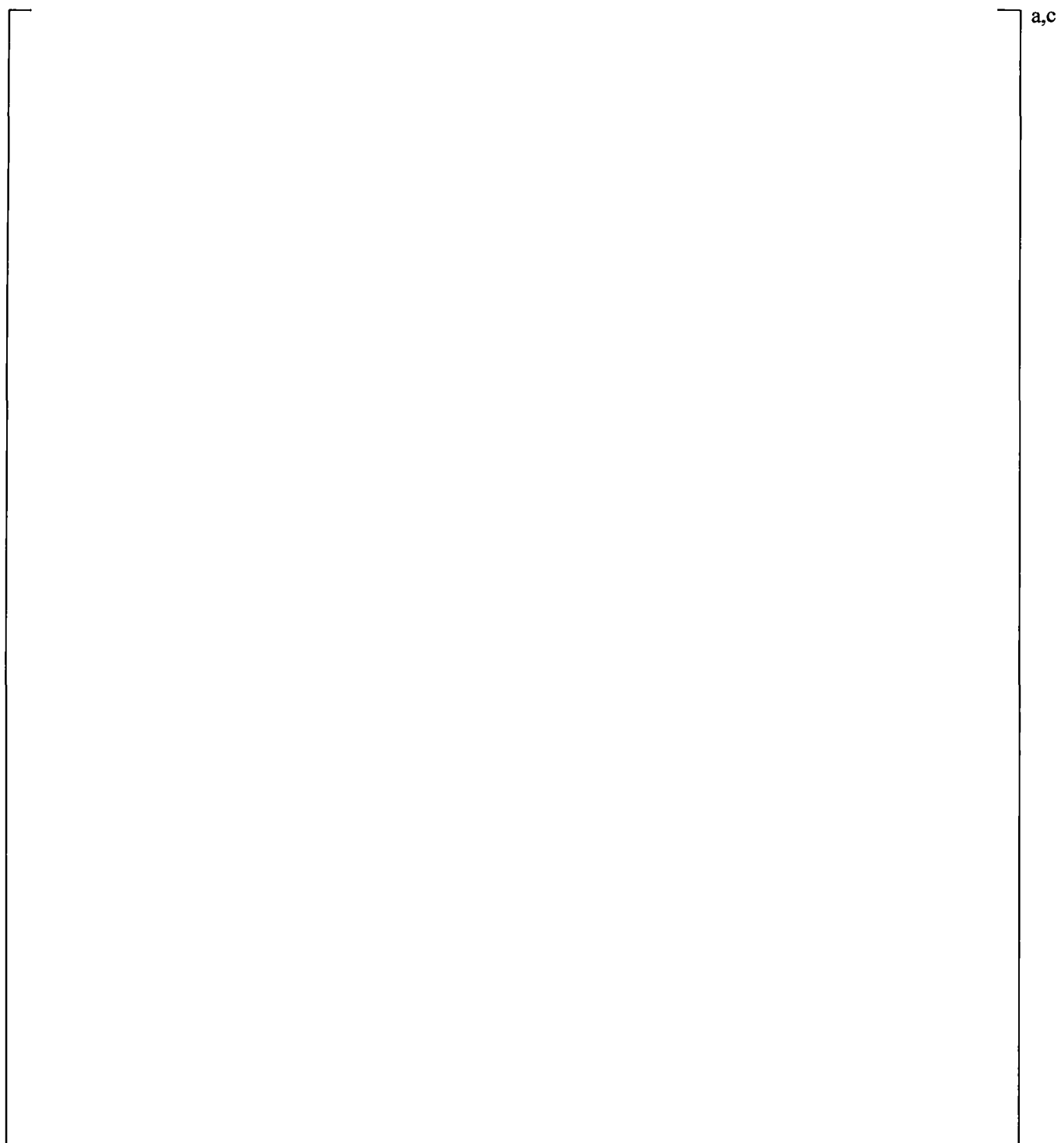


Figure 21.11.1-5 Lower Plenum Differential Pressures

a,c

Figure 21.11.1-6 Upper Plenum Differential Pressures

a,c

Figure 21.11.1-7 Peak Cladding Temperatures

21.11.2 SB-CL-18 Simulation Without Hot Leg Nozzle Bypass Flow

In this calculation, the (spray) bypass flow is tuned to []^{a,c} of the total core flow. This is a case, where the []^{a,c} HL-to-DC gap bypass (modeled in the reference SB-CL-18 simulation in Section 21.4) is eliminated by blocking the HL-to-DC Gaps 21 and 22. The results of this sensitivity calculation are intended to provide a basis for judgment whether modeling HL-to-DC bypass flow has a big effect on the transient calculation. Establishing a direction of conservatism can support making a decision whether to model HL-to-DC bypass in addition to the spray nozzle bypass or not.

[

|

|

|

]^{a,c}

a,c

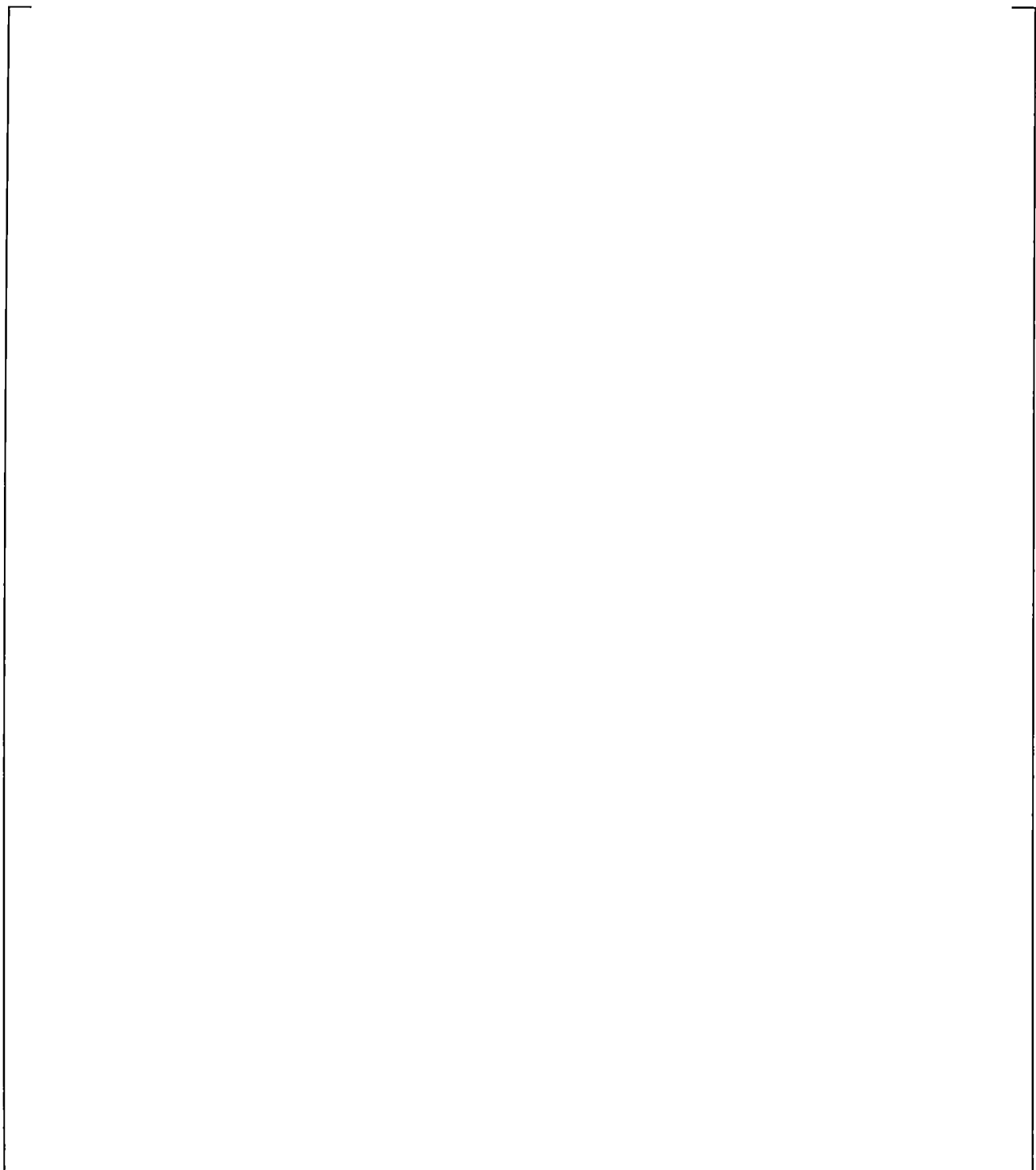


Figure 21.11.2-1 SB-CL-18 Cross-Over Leg A Differential Pressures

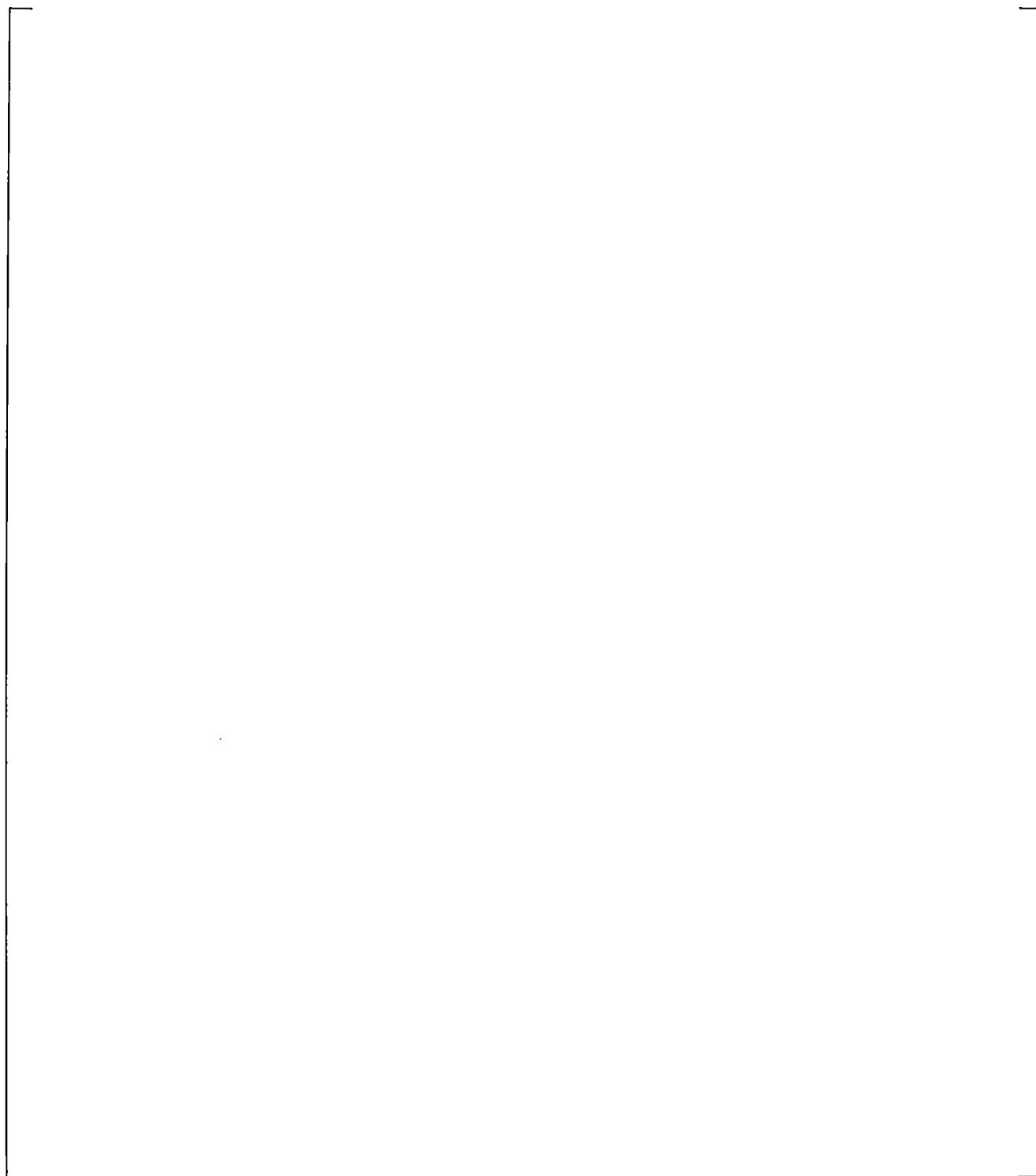


Figure 21.11.2-2 SB-CL-18 Cross-Over Leg B Differential Pressures

Figure 21.11.2-3 Inner Vessel Differential Pressures (LP+Core+UCP)

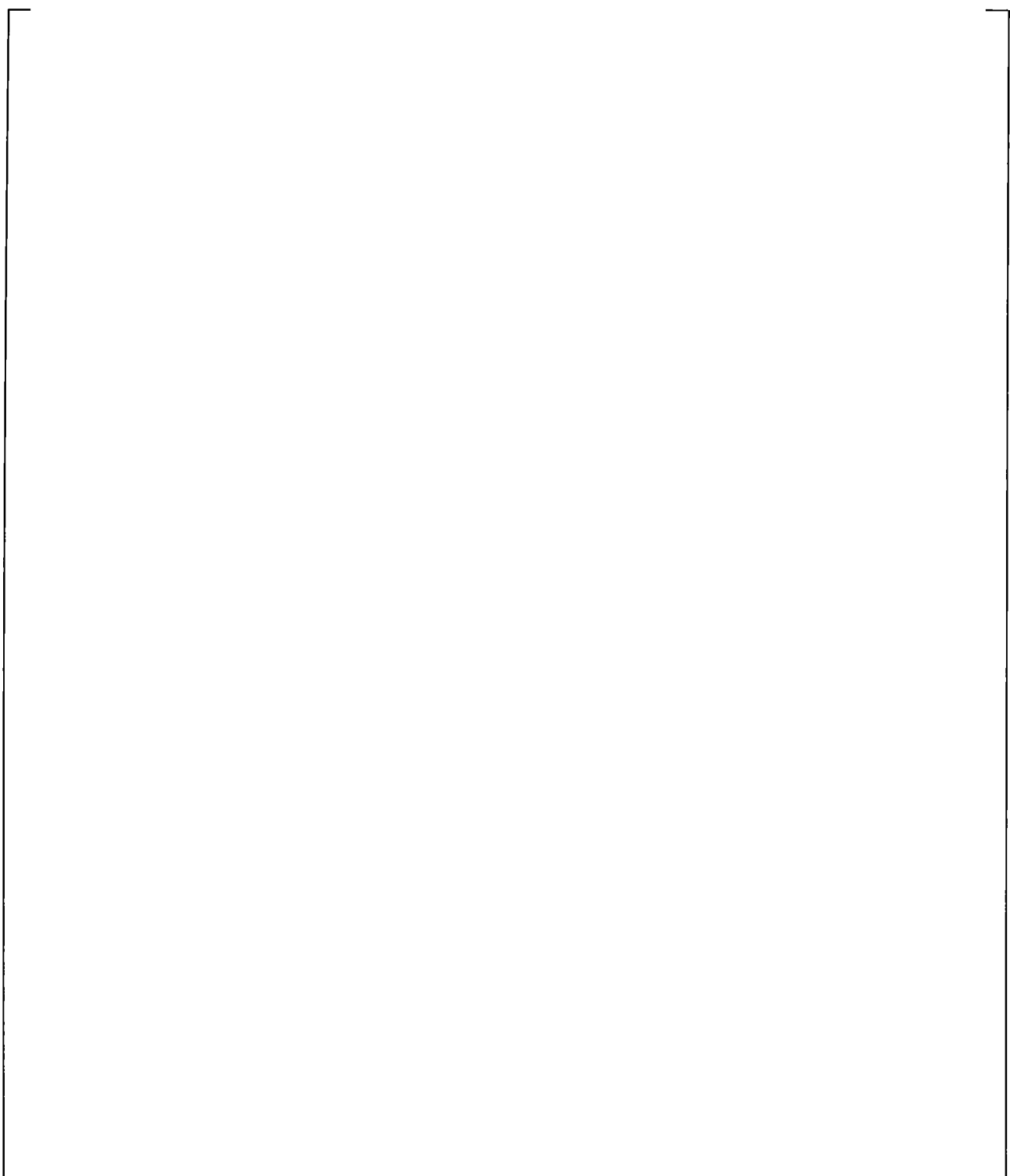


Figure 21.11.2-4 Downcomer Differential Pressures

a,c

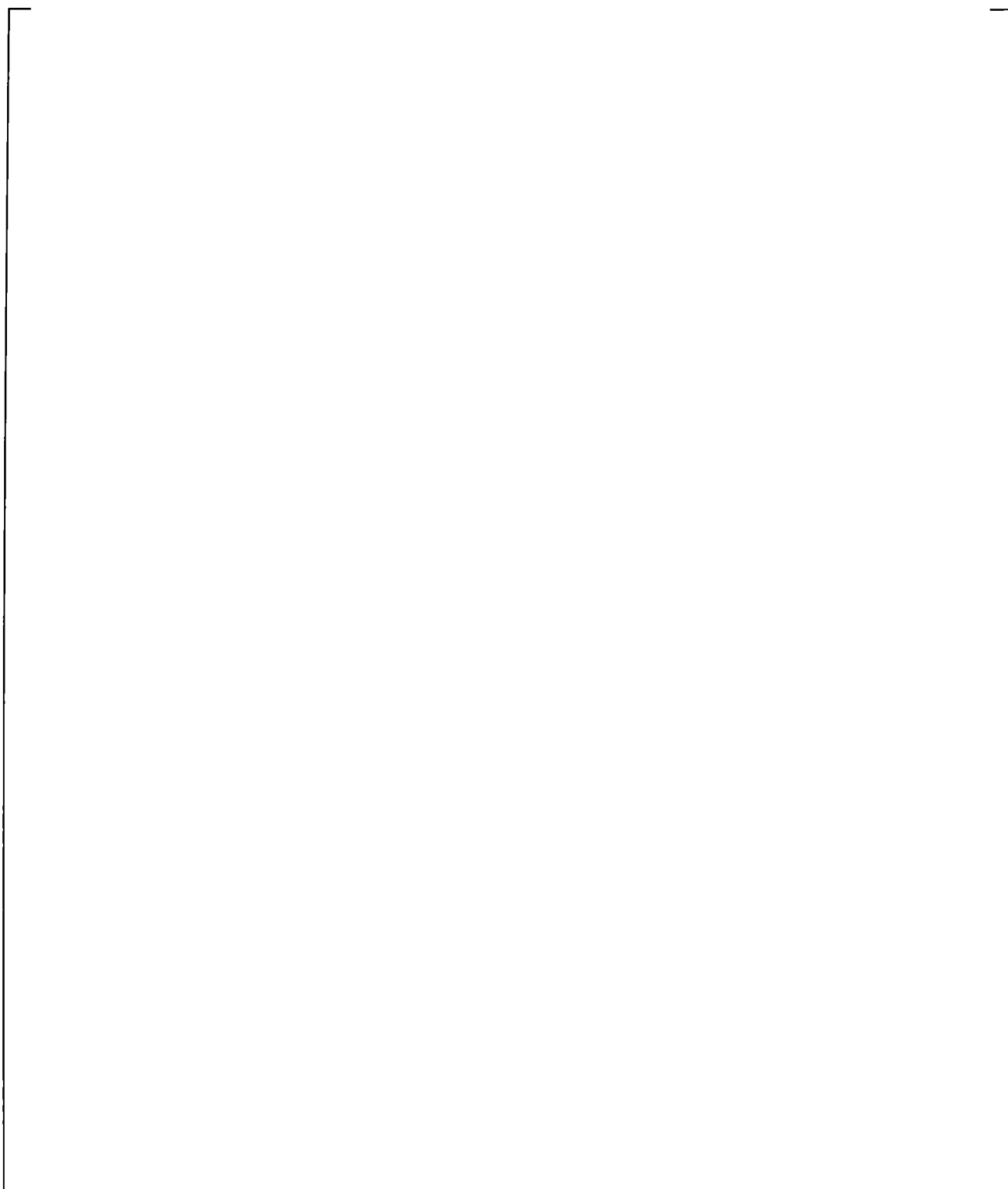
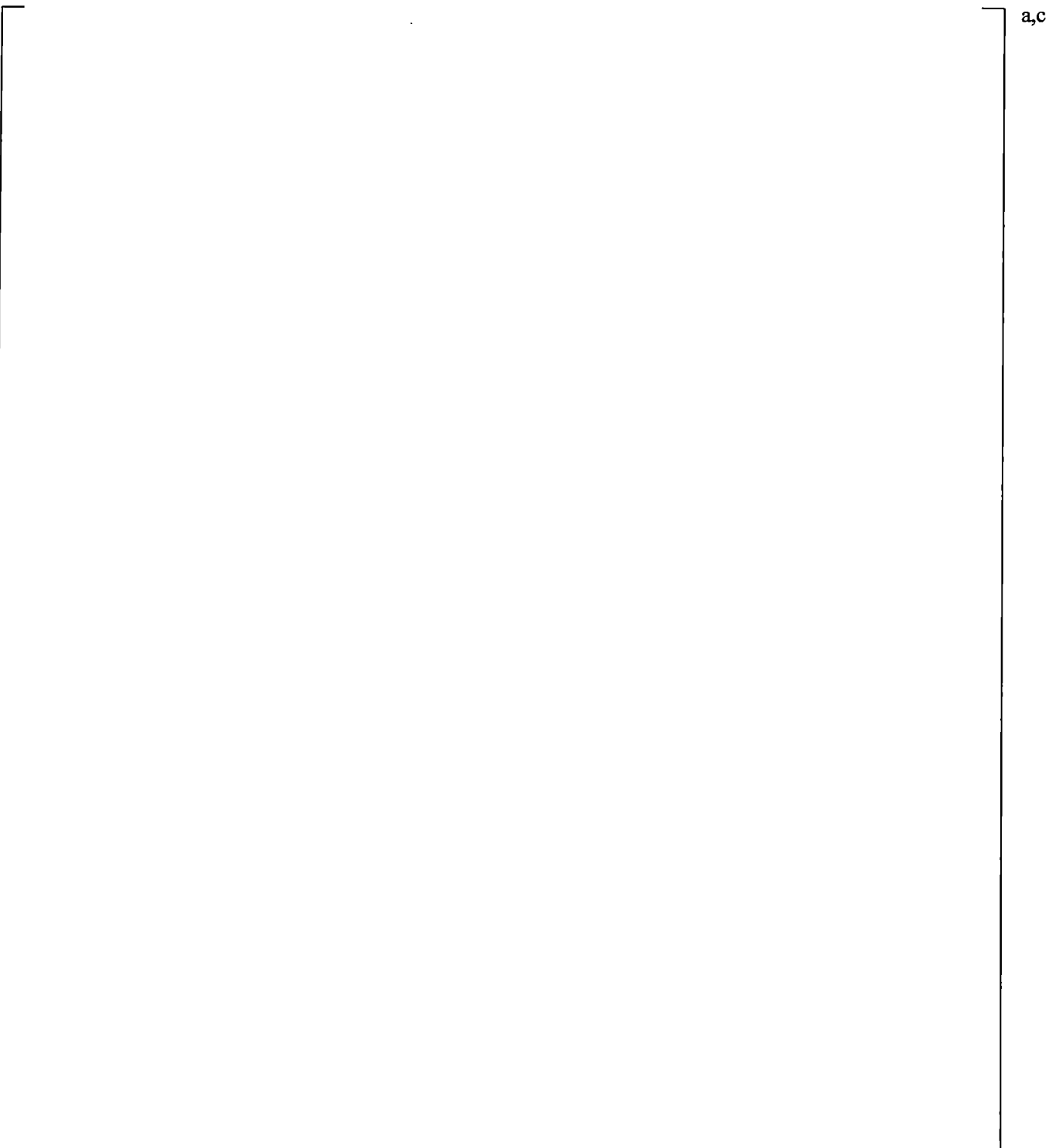


Figure 21.11.2-5 Lower Plenum Differential Pressures



a,c

Figure 21.11.2-6 Upper Plenum Differential Pressures



a,c

Figure 21.11.2-7 Peak Cladding Temperatures

21.11.3 Spray Nozzle Bypass Ranging Sensitivity with the SB-CL-18 Test

The purpose of this sensitivity is to investigate if ranging the spray bypass at []^{a,c} will have a significant effect on the transient.

The results of the sensitivity are presented in Figures 21.11.3-1 through 21.11.3-7. The top figure on each page is the high []^{a,c} bypass case and the bottom is the lower []^{a,c} bypass case. The comparison of the calculation results, provided in this section shows that ranging the spray nozzle bypass []^{a,c} of the desired steady state value has a small effect on the SB-CL-18 transient results.

Consistent with the trend established with the []^{a,c} bypass sensitivity presented in the previous Section 21.11.2, the loop seal clearance PCT is predicted to occur a little earlier with the smaller bypass case and the calculated boiloff PCT excursion is similar, Figure 21.11.3-7. In summary, ranging of the spray bypass []^{a,c} of the desired steady state value does not appear to have significant effect on the SBLOCA transient.



a,c

Figure 21.11.3-1 SB-CL-18 Cross-Over Leg A Differential Pressures

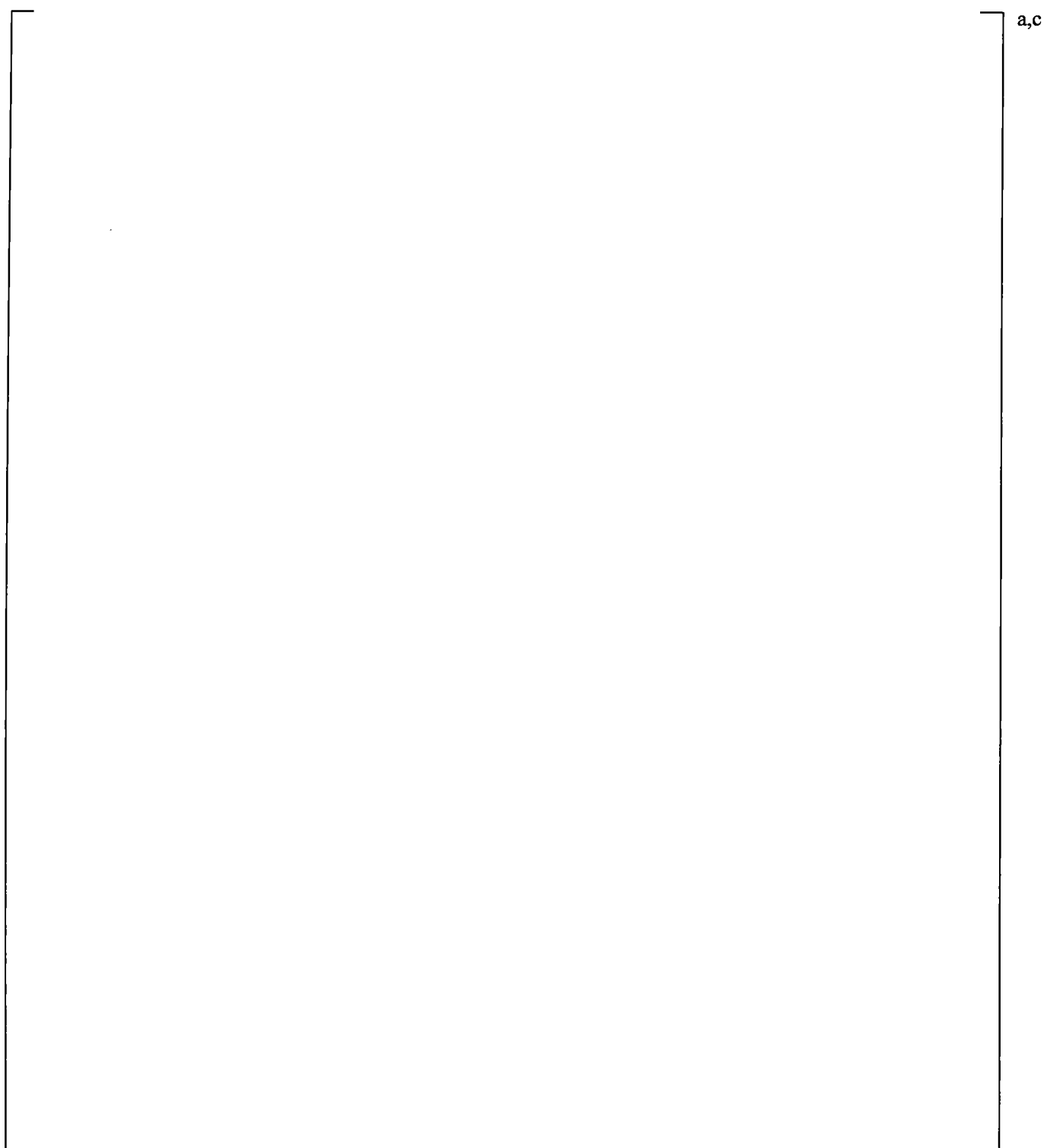


Figure 21.11.3-2 SB-CL-18 Cross-Over Leg B Differential Pressures

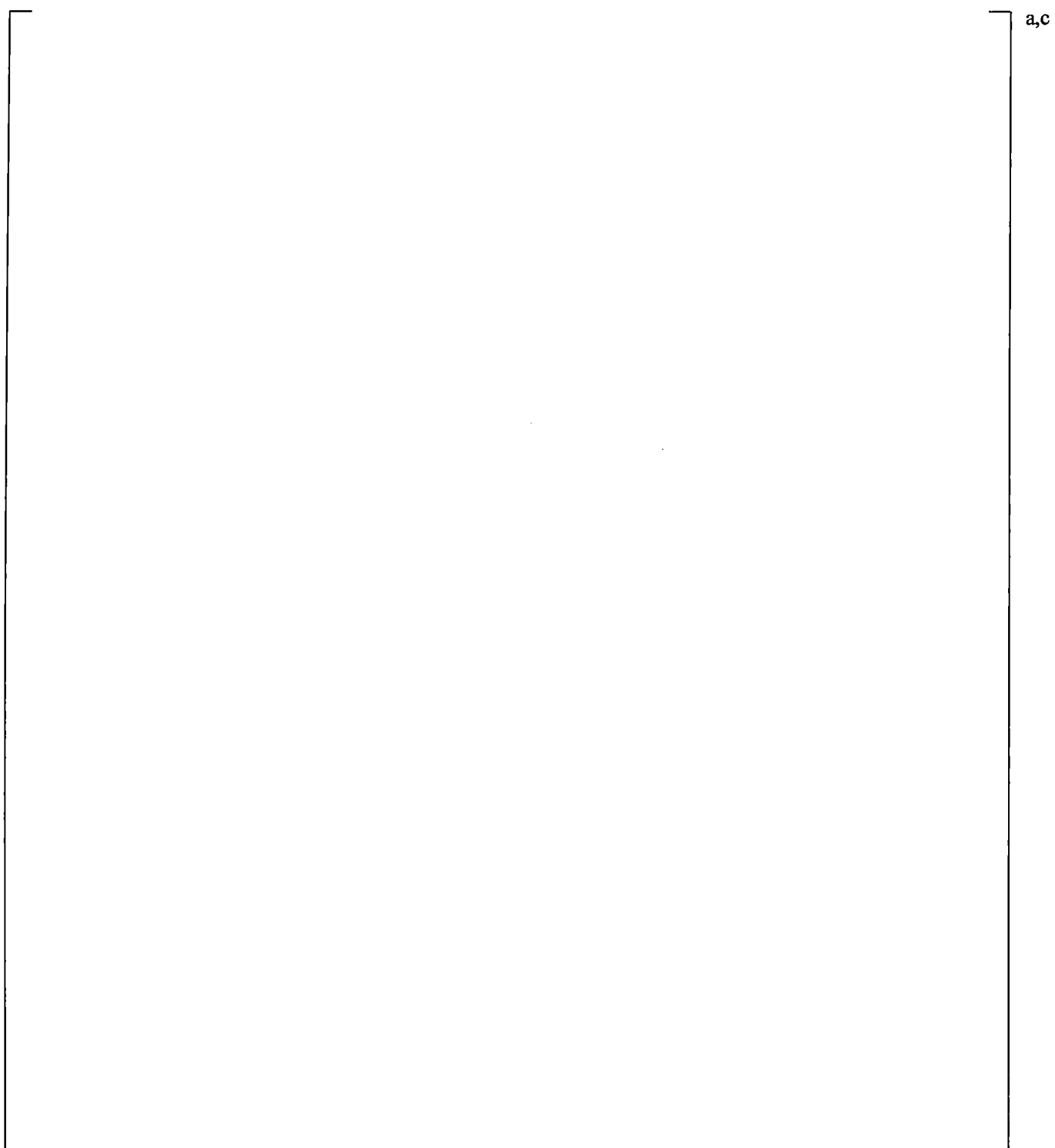


Figure 21.11.3-3 Inner Vessel Differential Pressures (LP+Core+UCP)

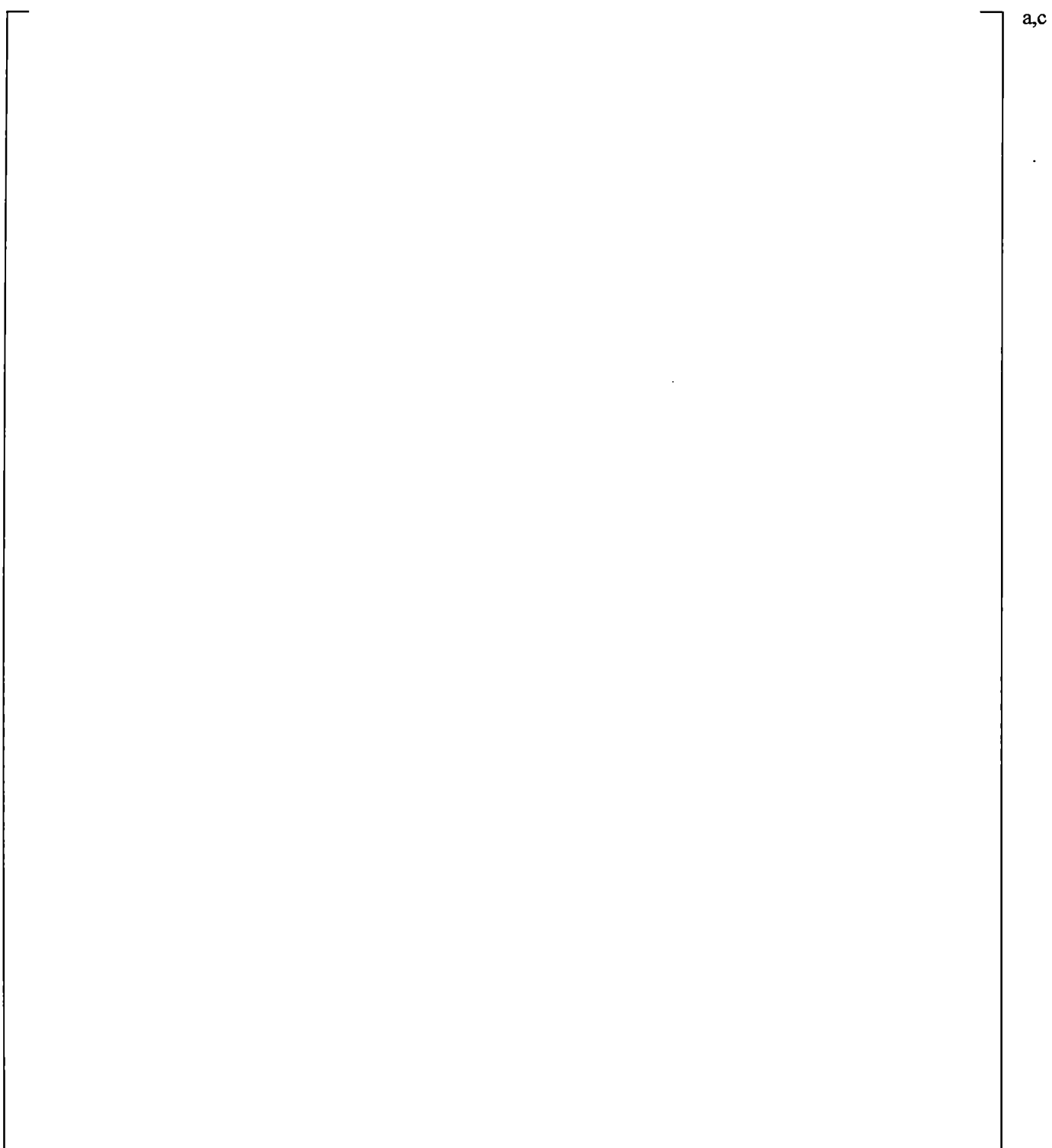


Figure 21.11.3-4 Downcomer Differential Pressures



a,c

Figure 21.11.3-5 Lower Plenum Differential Pressures

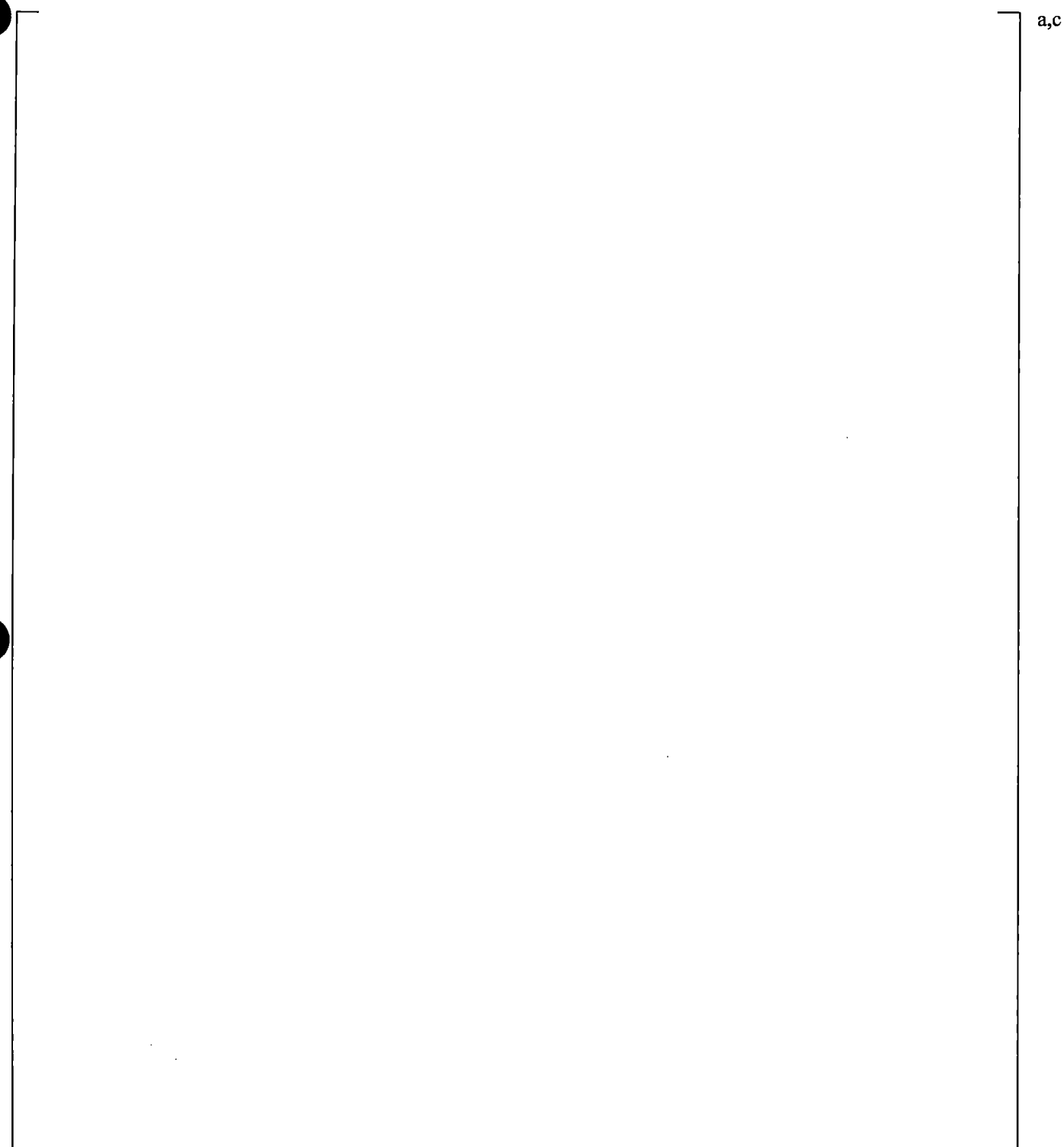


Figure 21.11.3-6 Upper Plenum Differential Pressures



a,c

Figure 21.11.3-7 Peak Cladding Temperatures

21.12 SUB-COOLED BREAK DISCHARGE COEFFICIENT (CD1) SENSITIVITY

Two simulations of the SB-CL-18 test were performed implementing a sub-cooled break discharge coefficients (CD1) at high and low values. The extreme values of CD1 were set at [

]^{a,c}. It is acknowledged that the CD1 range considered in this sensitivity is different from the CD1 uncertainty range established from the validation of the critical flow model in Section 12. However, the range considered here is sufficient to provide sensitivity results to illustrate the importance of this parameter and support the decision on how to address it within the uncertainty treatment approach established for the FSLOCA methodology, Section 29, Volume 3.

Figures 21.12-1 through 21.12-19 show a comparison of the SB-CL-18 simulation results using the two extreme values of CD1. [

]^{a,c} For each of the simulations, the SB-CL-18 test measurements are presented in the figures as well.

Obviously, the effect of the extreme CD1 variation manifests from the very early stages of the transient.

The higher CD1 coefficient results in a visibly higher peak of the break flow, Figure 21.12-1.

The increased loss of inventory with the higher CD1 results in earlier transition to two-phase discharge, Figure 21.12-2, and earlier loop seal clearance, Figures 21.12-3 and 21.12-4. The system depressurization is visibly affected as well, Figure 21.12-5.

The draining of the uphill side of the steam generator tubes occurs visibly earlier in the simulation with the higher CD1 coefficient, Figures 21.12-6 to 21.12-9. With the higher CD1, the draining of the steam generator inlet plenums, Figures 21.12-10 and 21.12-11, and the hot legs, Figures 21.12-12 and 21.12-13, is predicted to occur relatively earlier as well. The calculated differential pressures in the different regions of the test facility is consistent with the expected effect of the inventory lost, which is dependent on the value of CD1, see Figures 21.12-14 through 21.12-17.

[

]^{a,c}

As a result of the greater inventory loss with the higher CD1, the accumulator injection is predicted to occur earlier than the case with low CD1, see Figure 21.12-19.

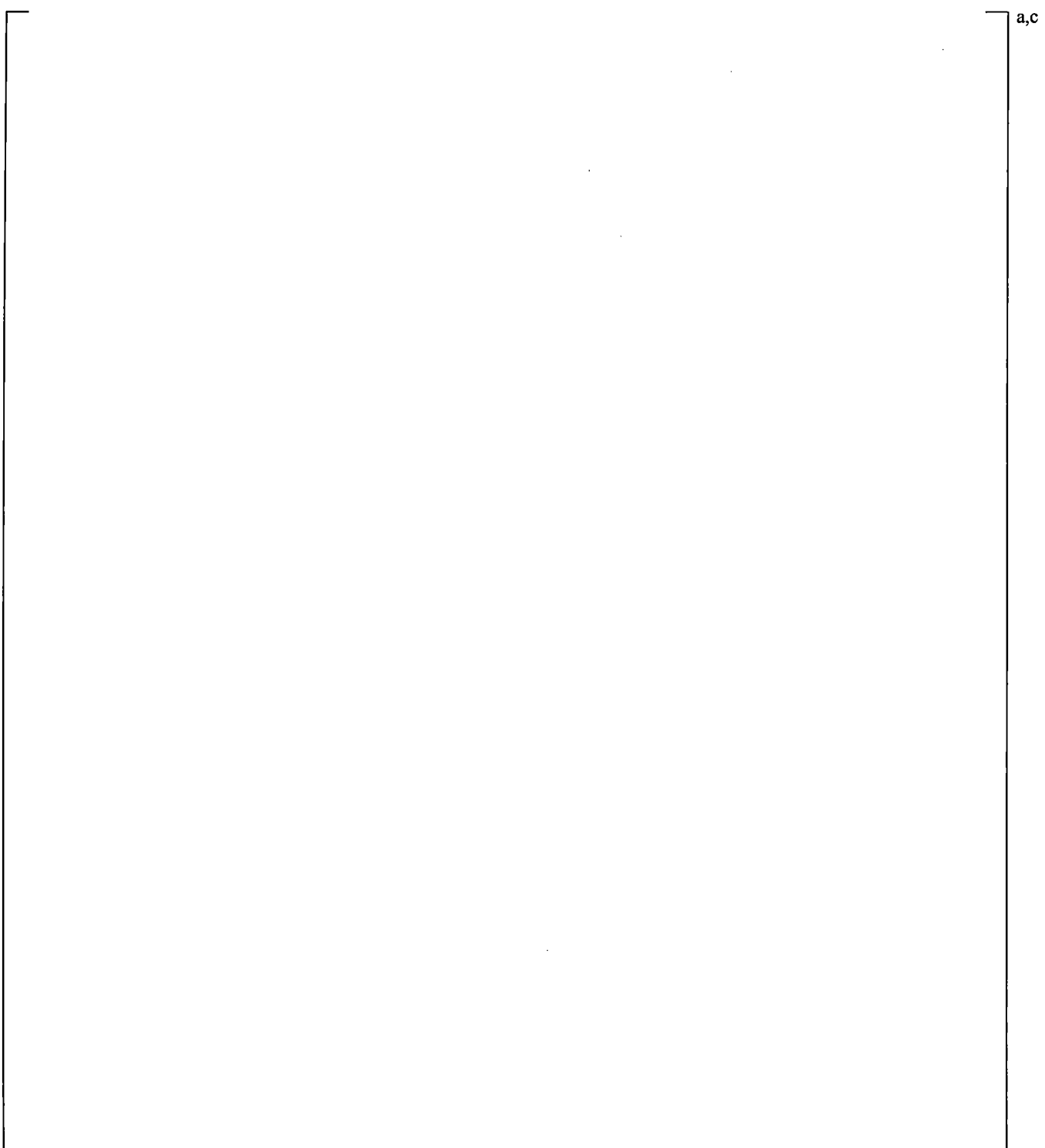


Figure 21.12-1 Break Flows

a,c

Figure 21.12-2 Calculated Break Void Fraction

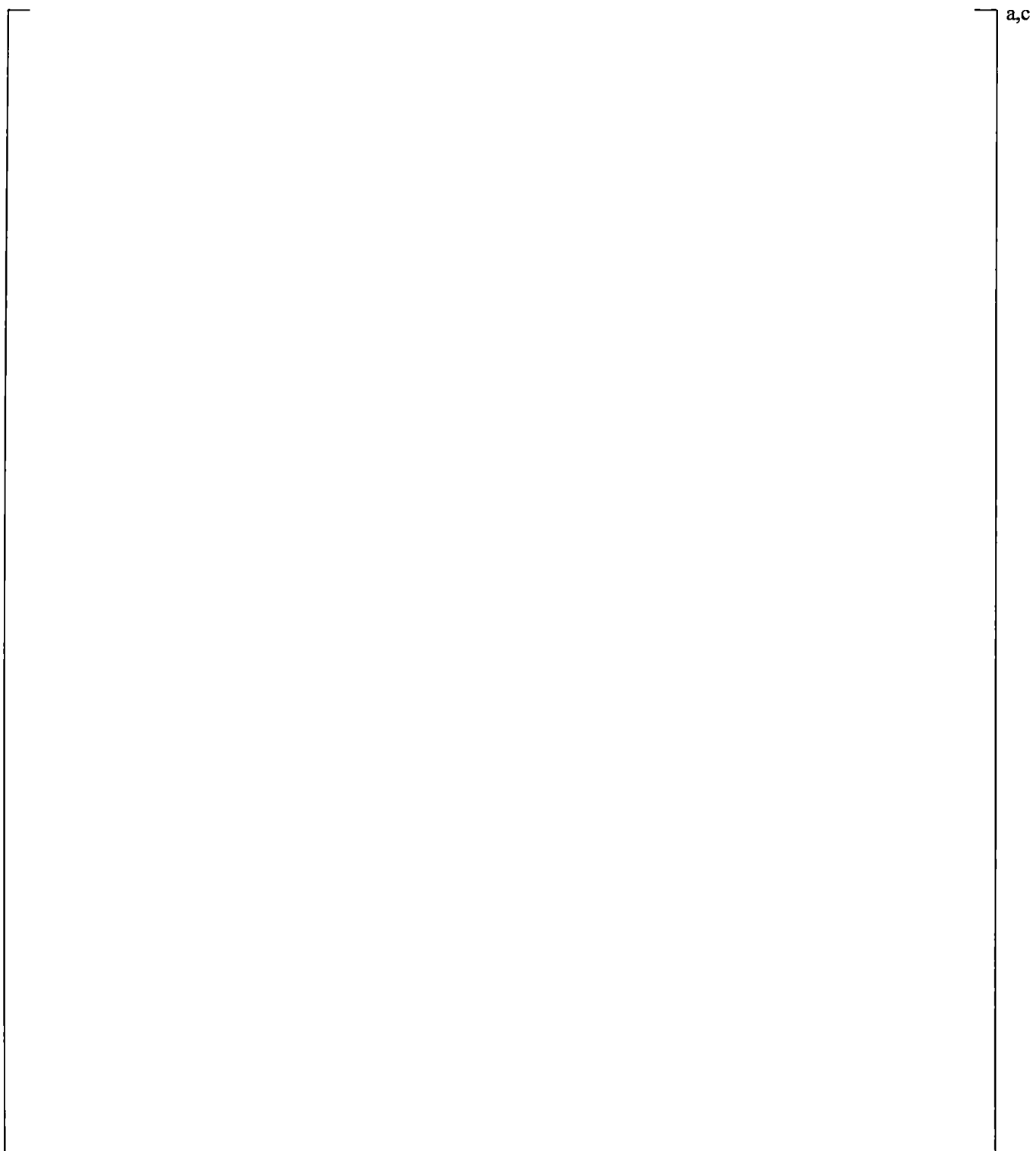


Figure 21.12-3 Cross-Over Leg A Differential Pressures

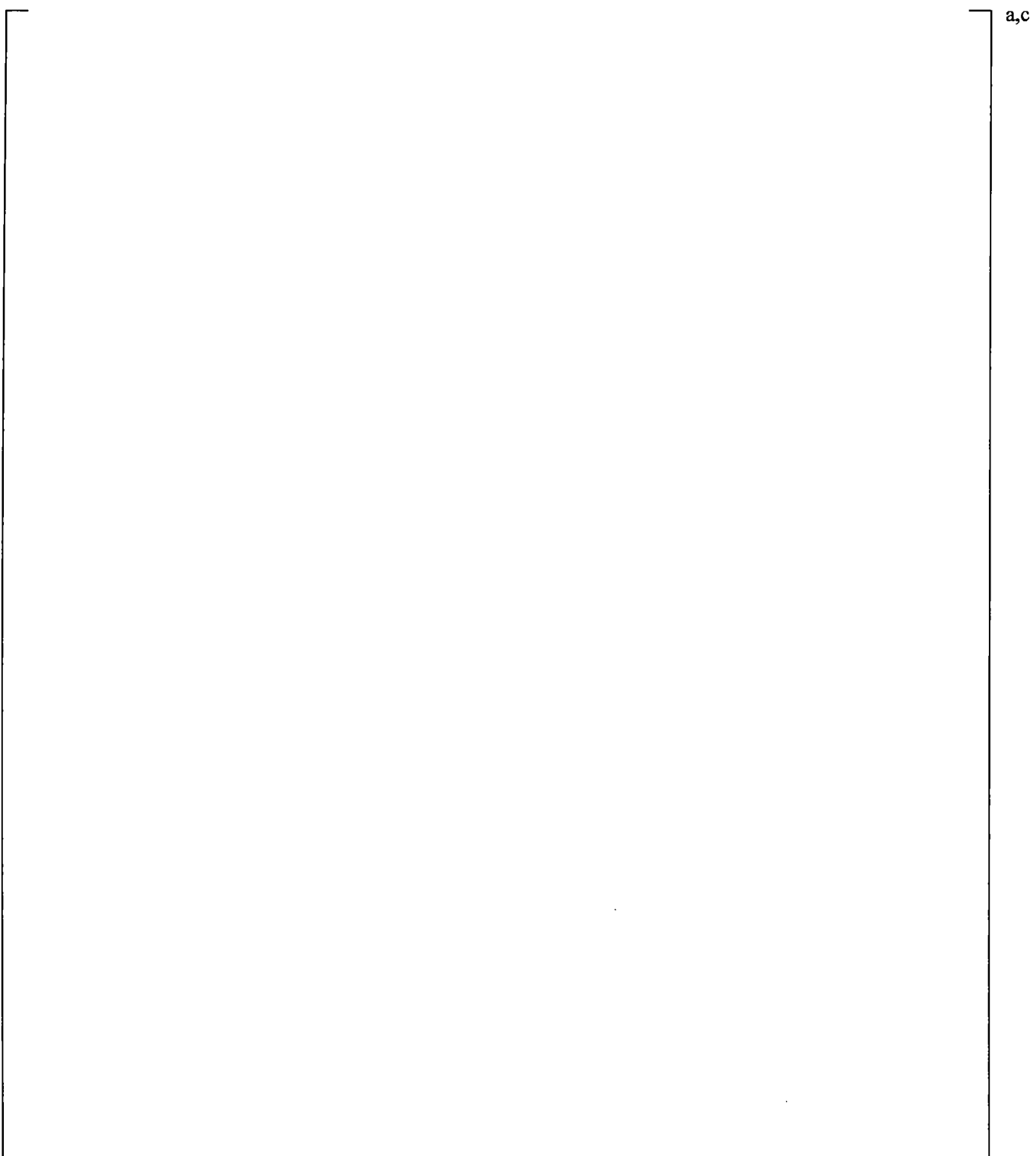


Figure 21.12-4 Cross-Over Leg B Differential Pressures

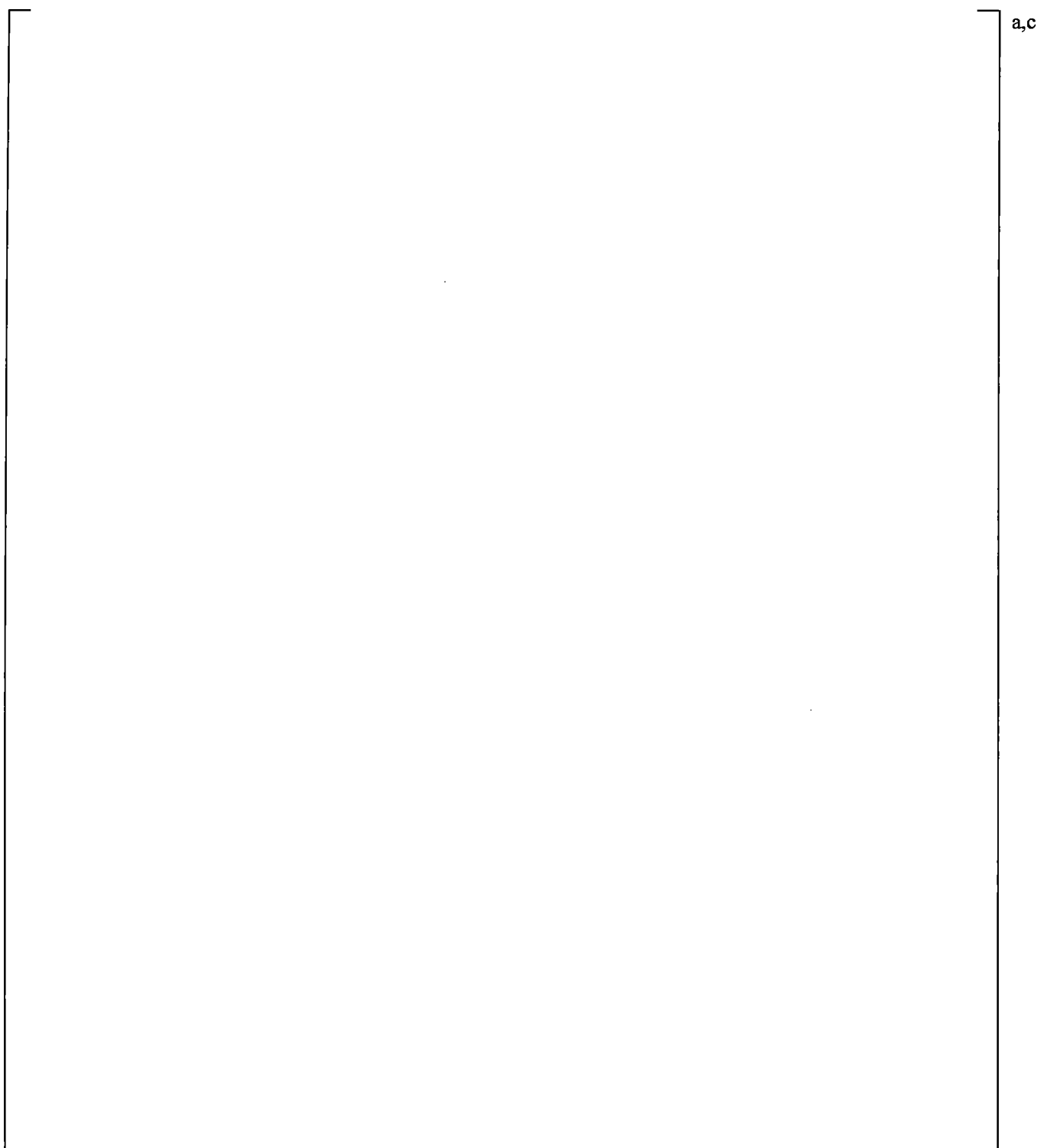
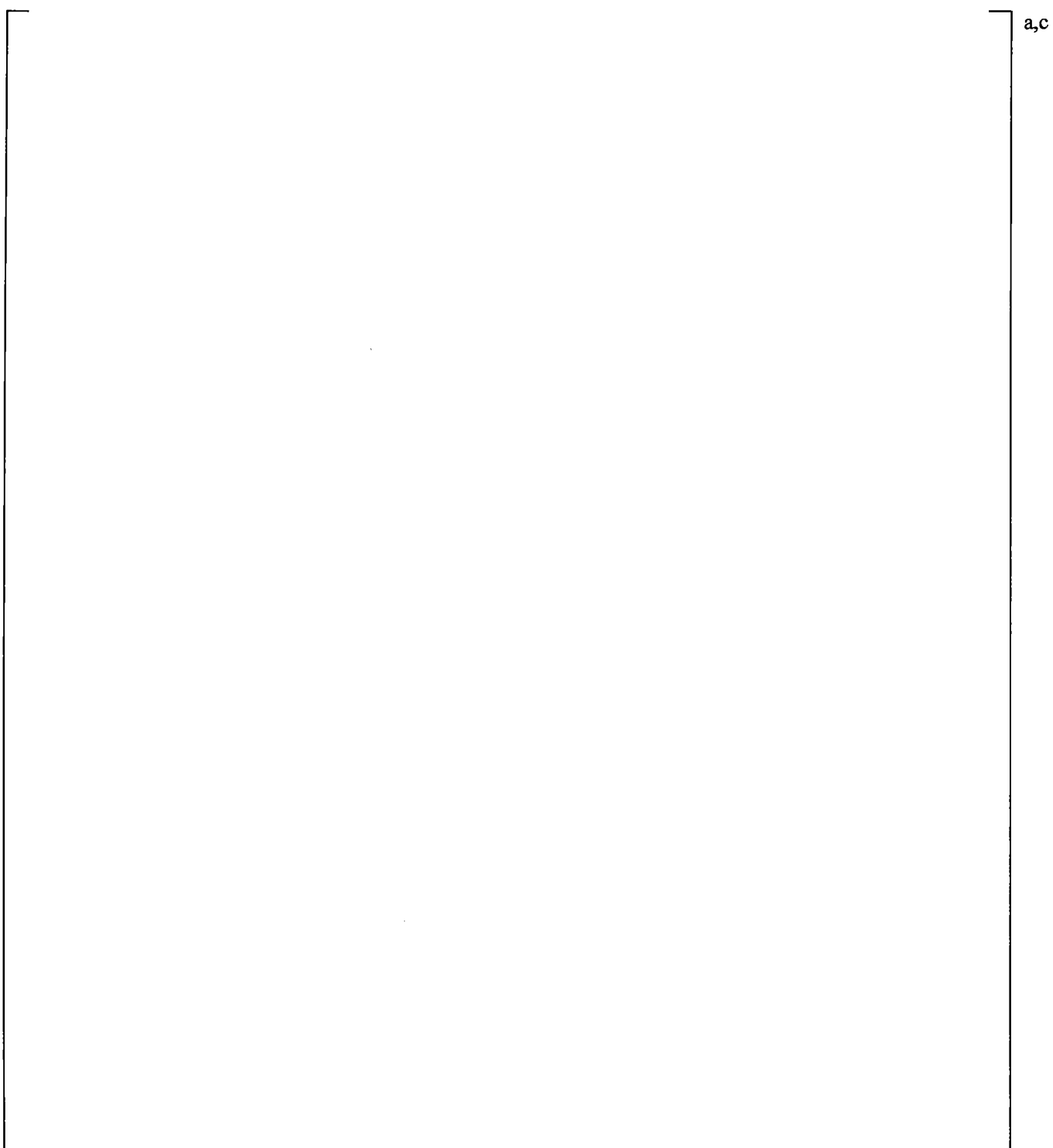
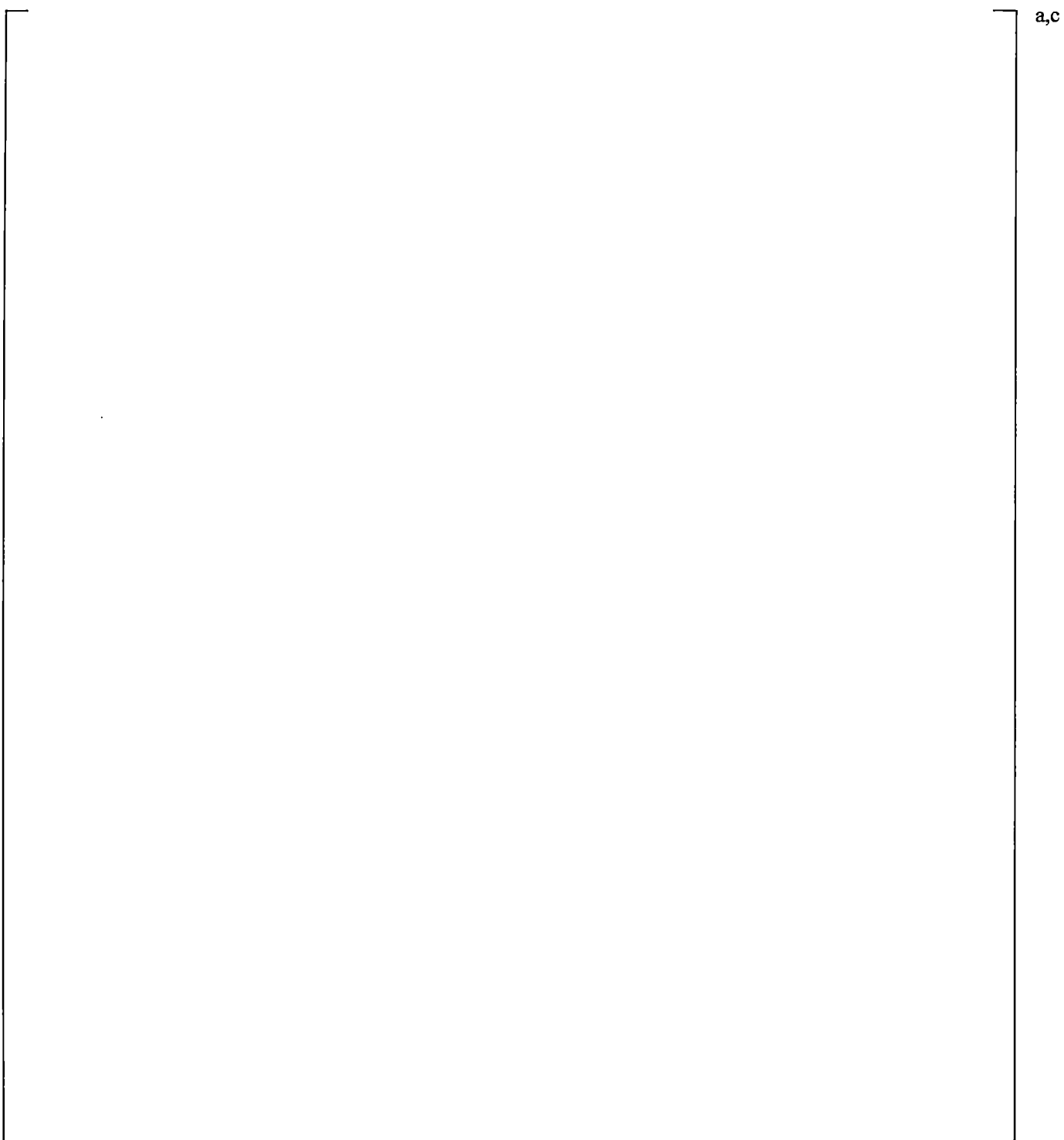


Figure 21.12-5 Pressurizer Pressures



| **Figure 21.12-6 Steam Generator A U-tubes Inlet-to-Top Differential Pressure**



| **Figure 21.12-7 Steam Generator B U-tubes Inlet-to-Top Differential Pressures**

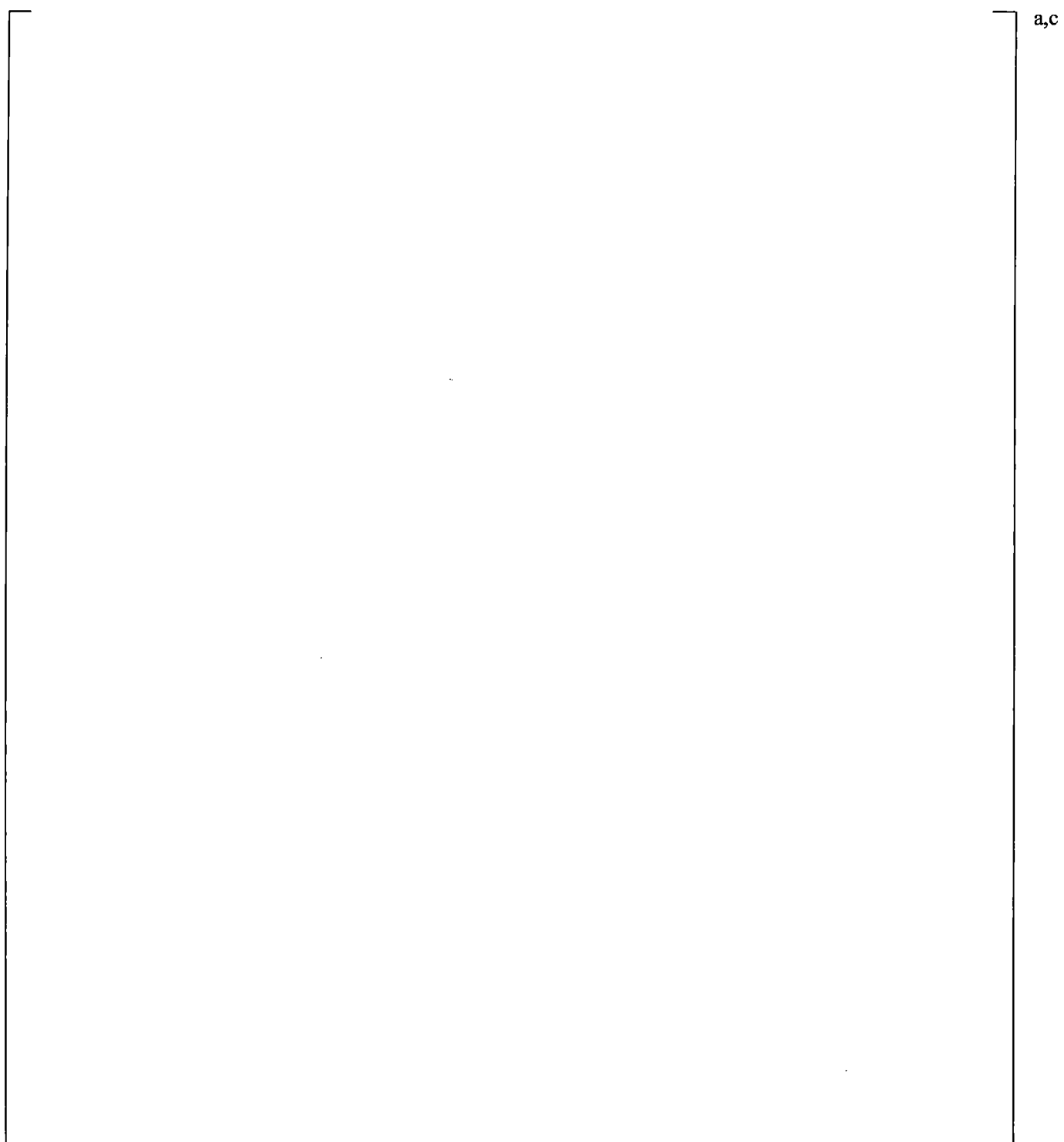


| **Figure 21.12-8 Steam Generator A U-tubes Outlet-to-Top Differential Pressures**

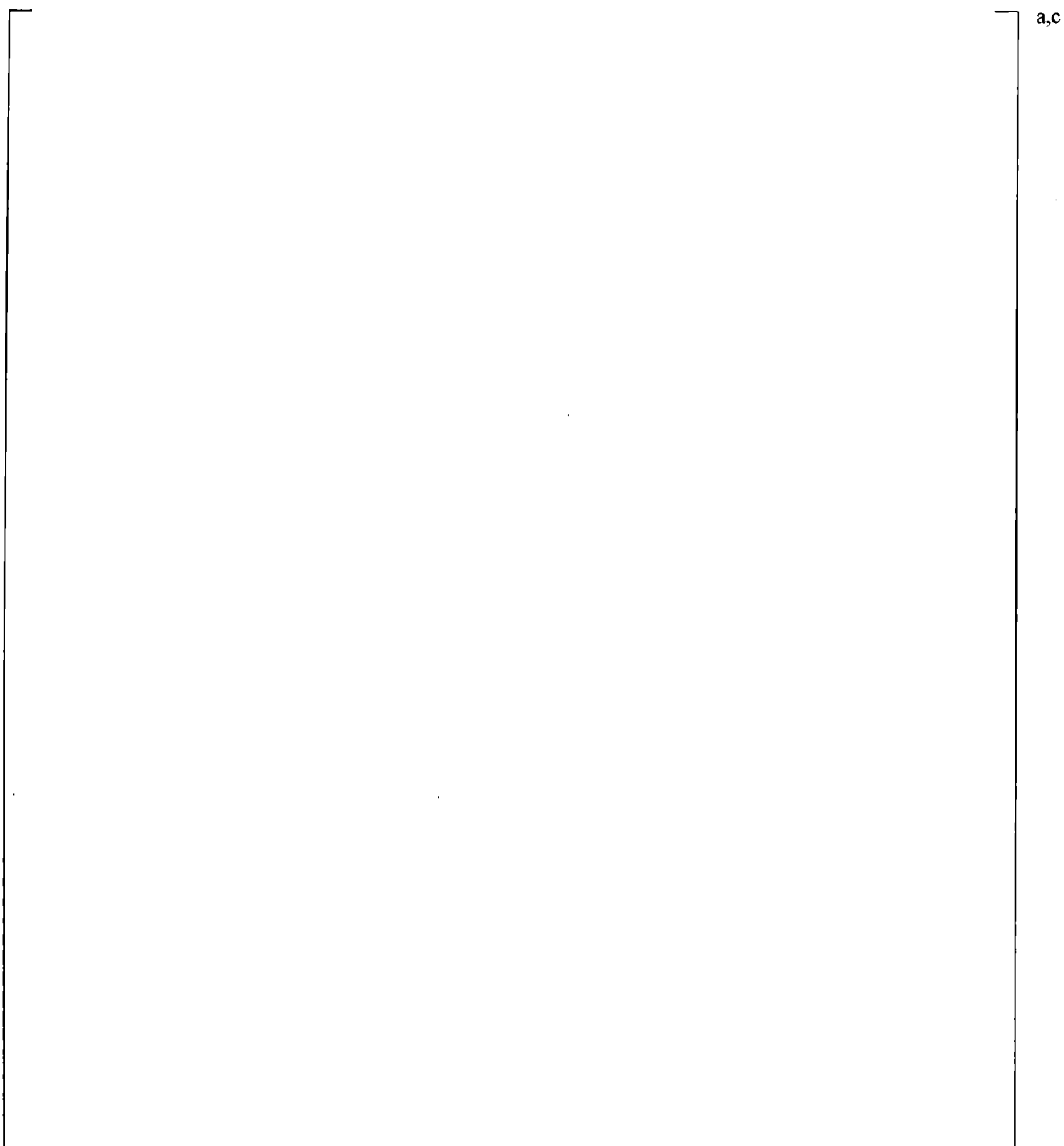


| **Figure 21.12-9 Steam Generator B U-tube Outlet-to-Top Differential Pressures**

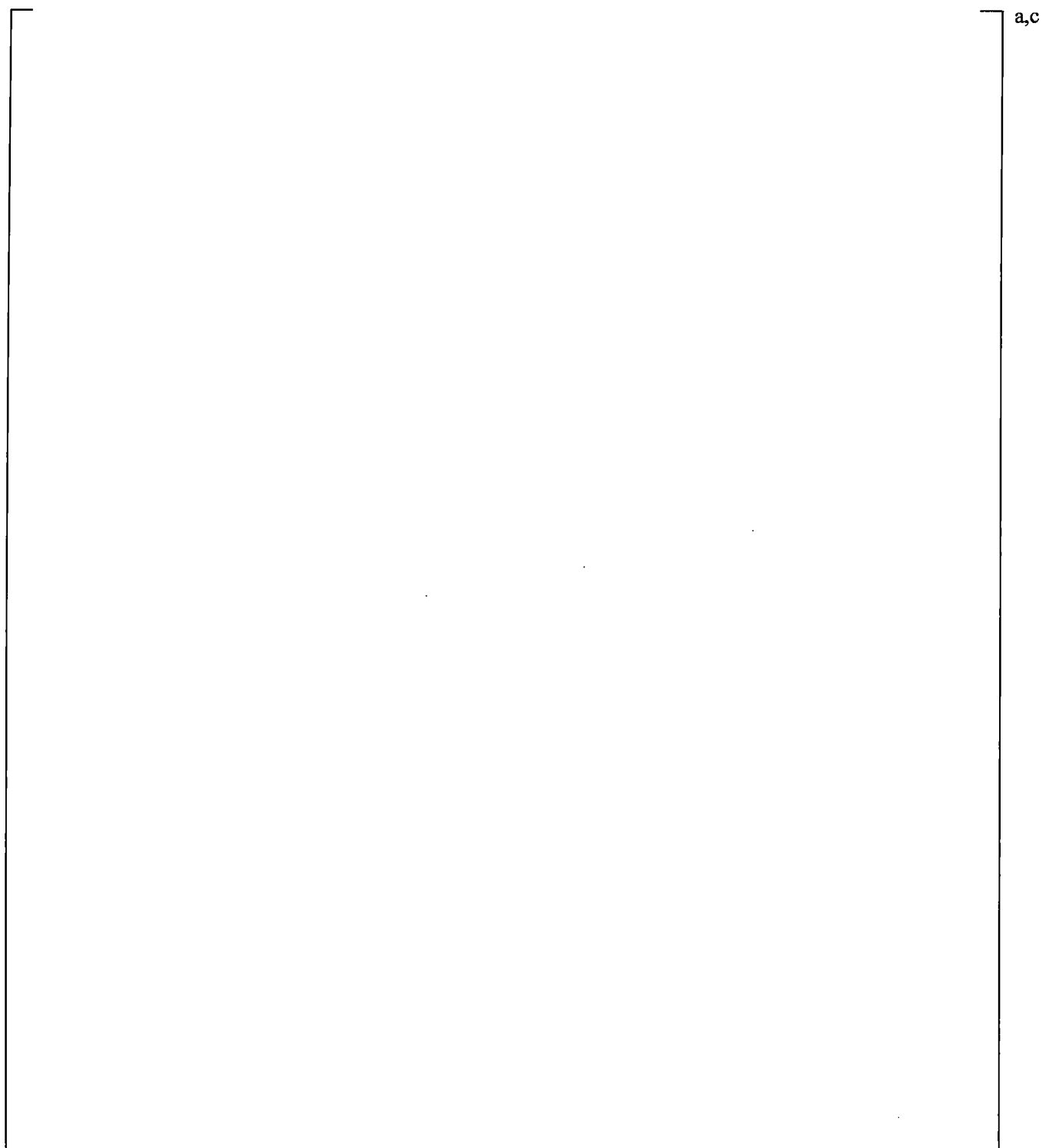
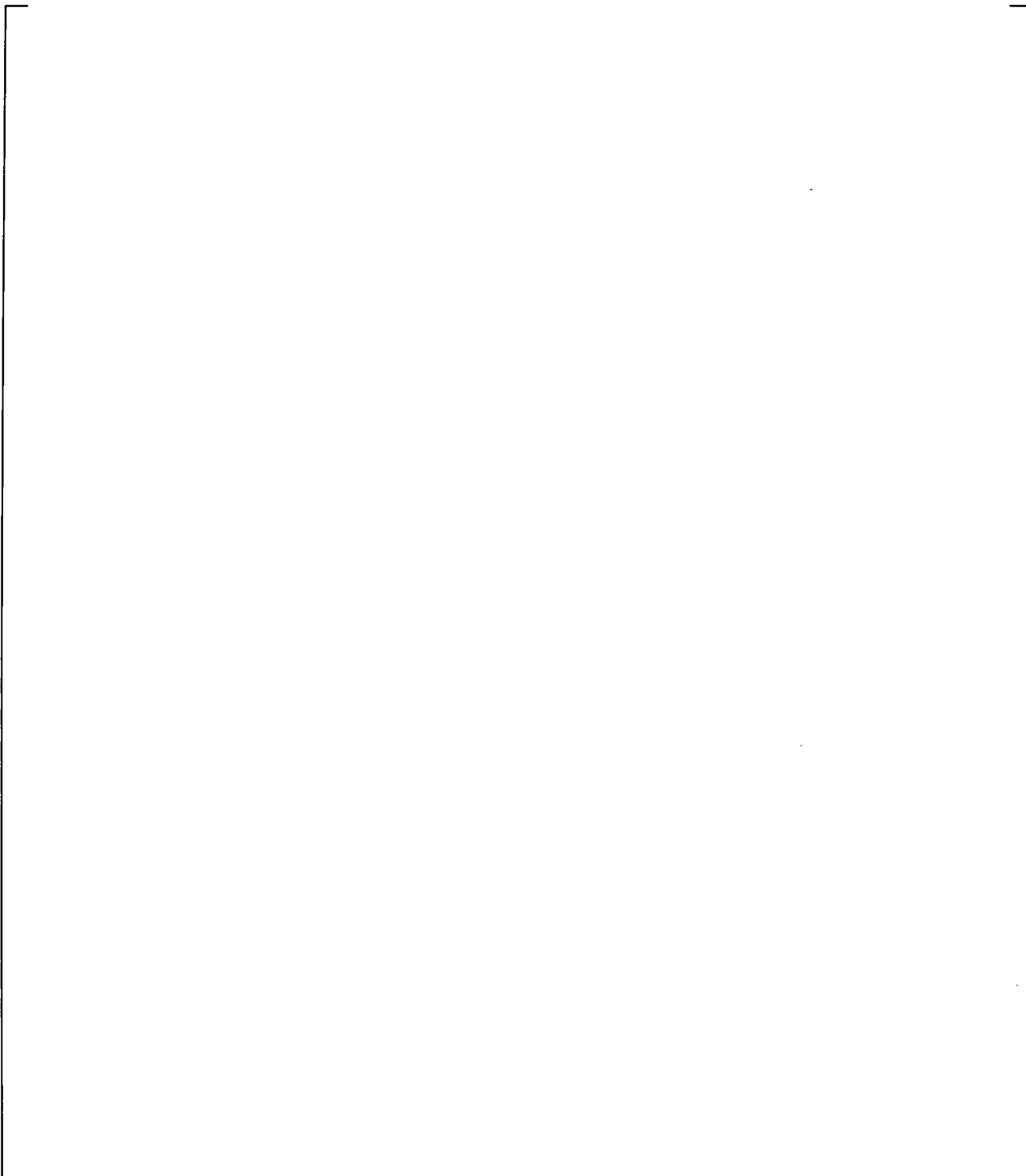
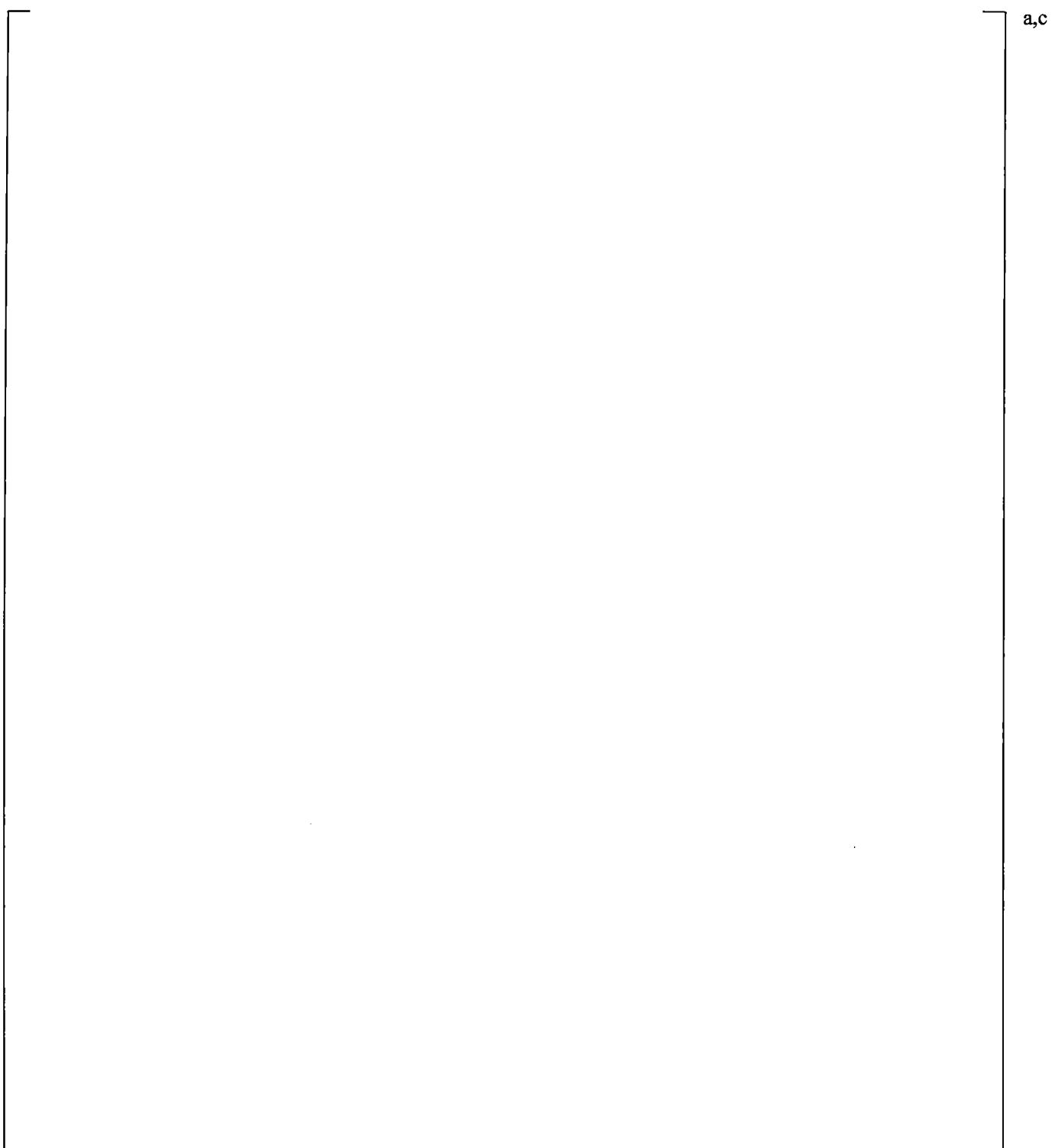


| **Figure 21.12-10 Steam Generator A Inlet Plenum Collapsed Liquid Levels**



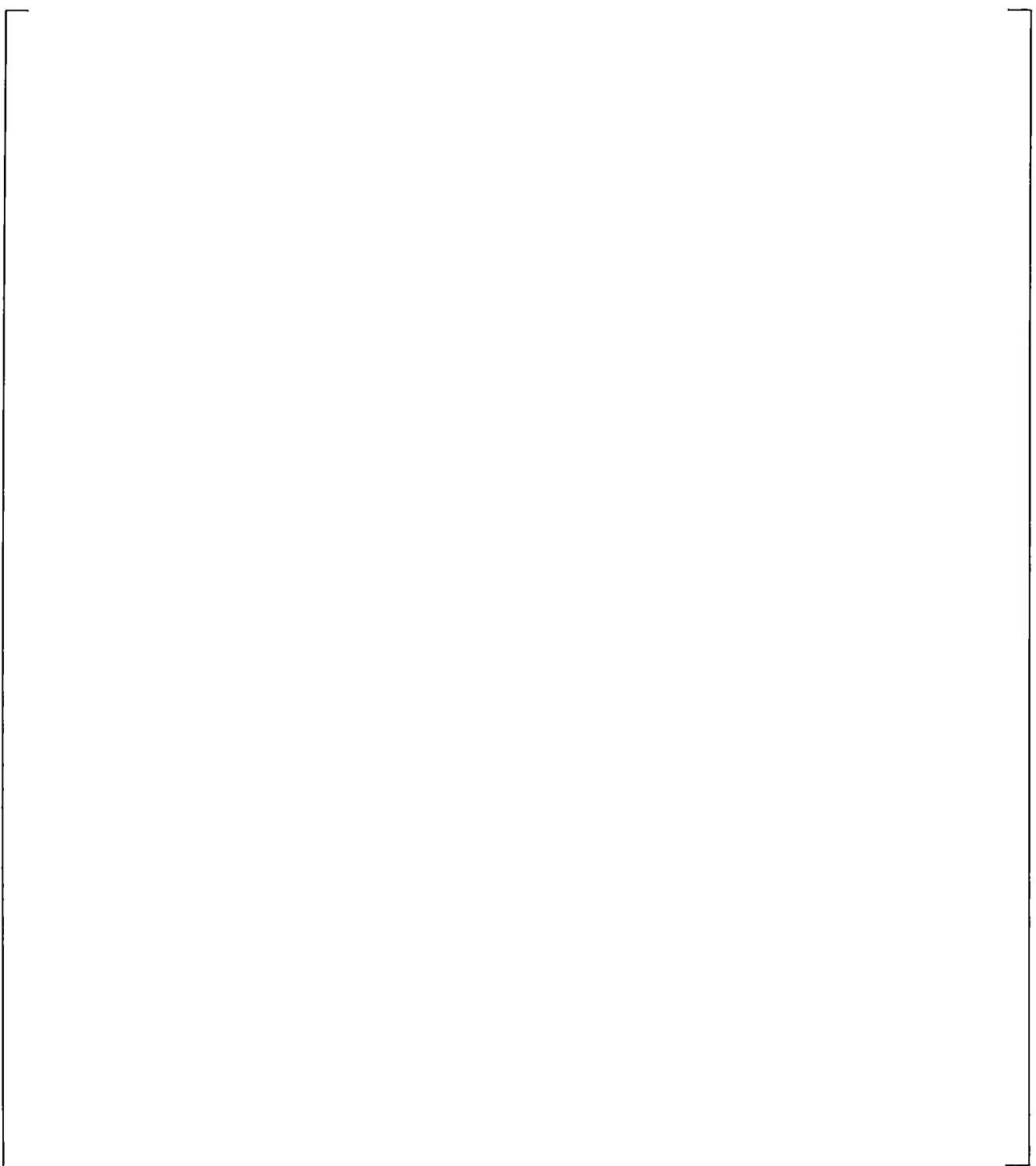
a,c

| **Figure 21.12-11 Steam Generator B Inlet Plenum Collapsed Liquid Levels**



a,c

| **Figure 21.12-12 Upper Plenum to Steam Generator A Inlet Differential Pressures**



a,c

| **Figure 21.12-13 Upper Plenum to Steam Generator B Inlet Differential Pressures**

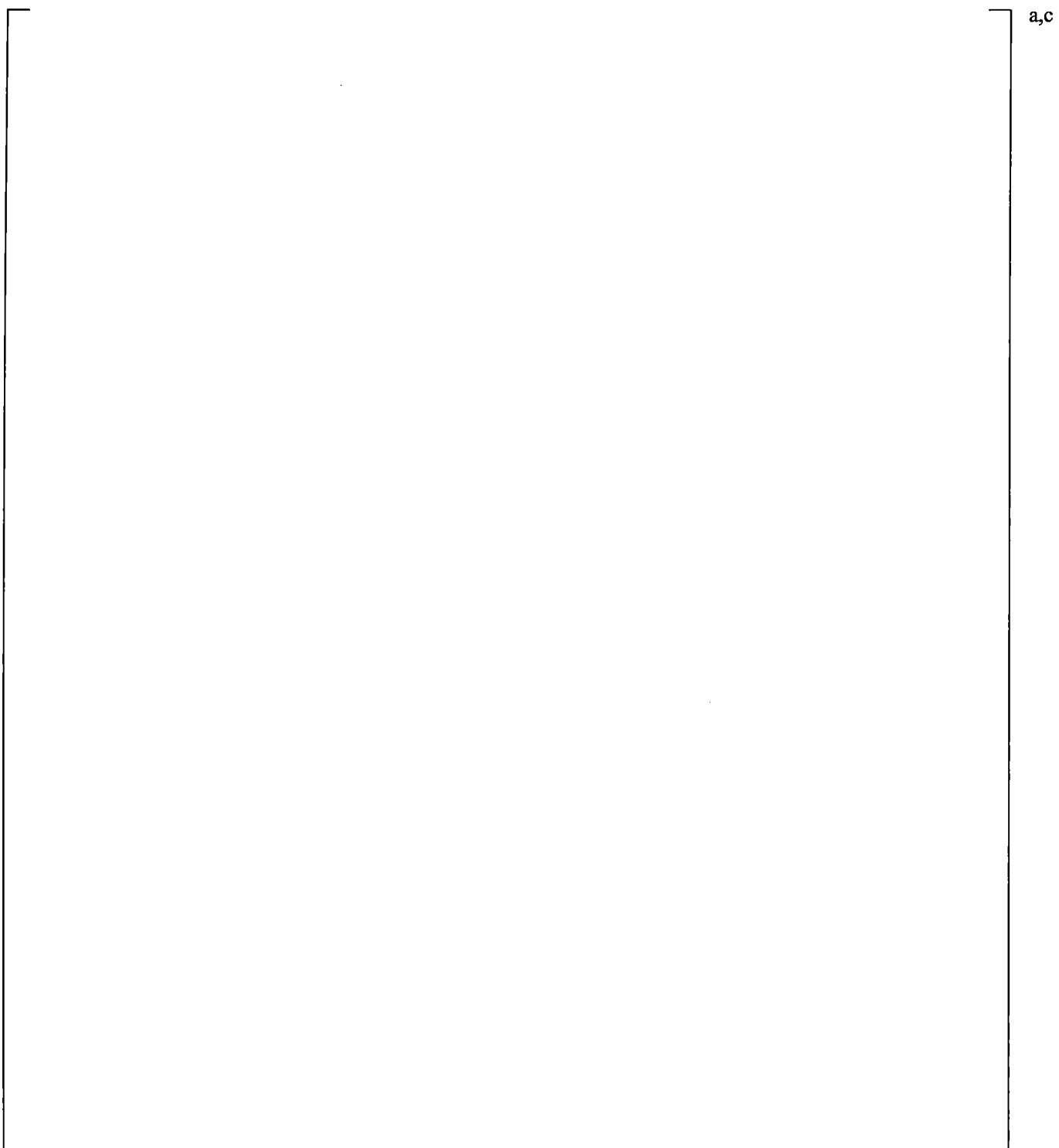


Figure 21.12-14 Downcomer Differential Pressures

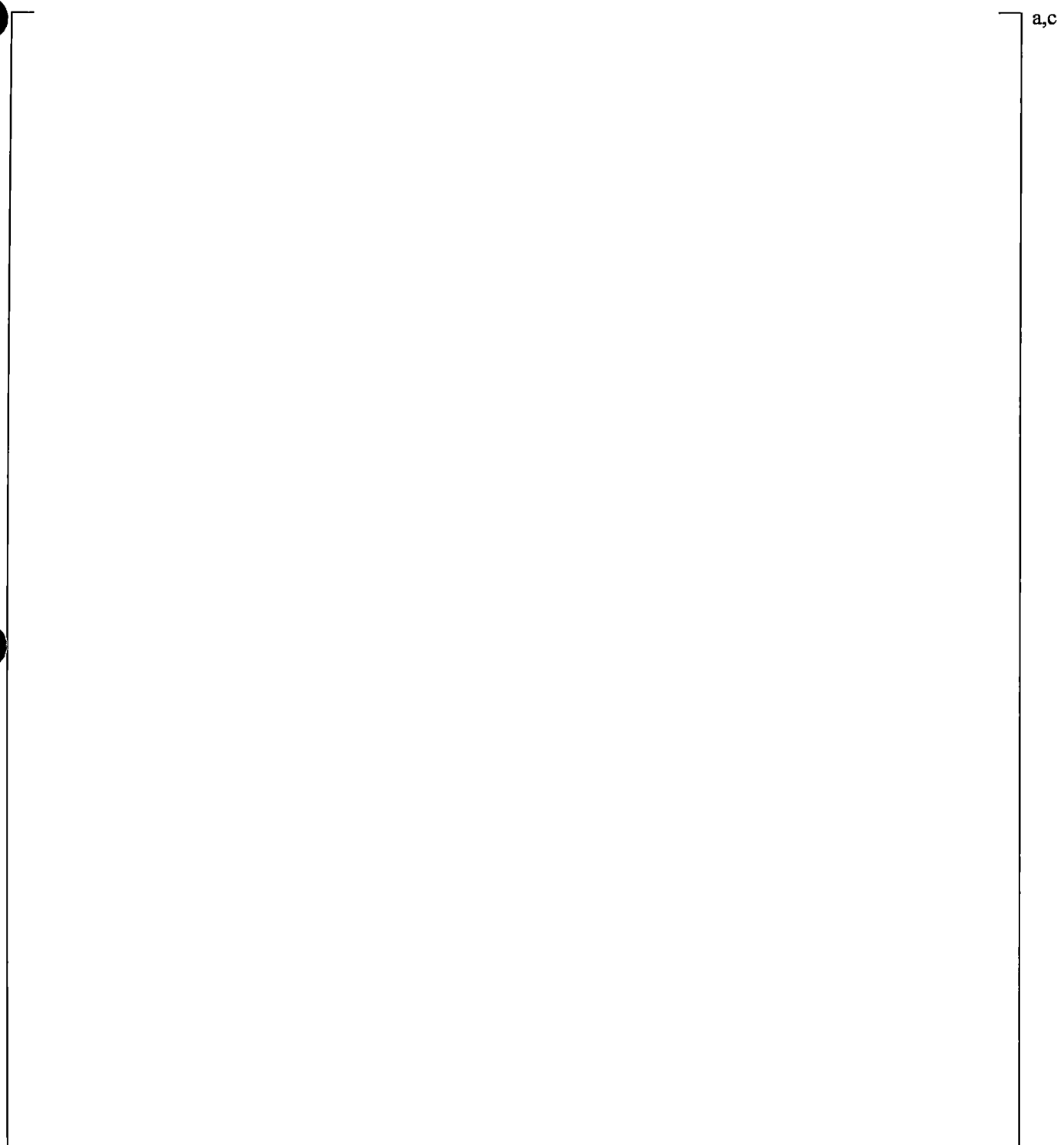


Figure 21.12-15 Upper Plenum Differential Pressures

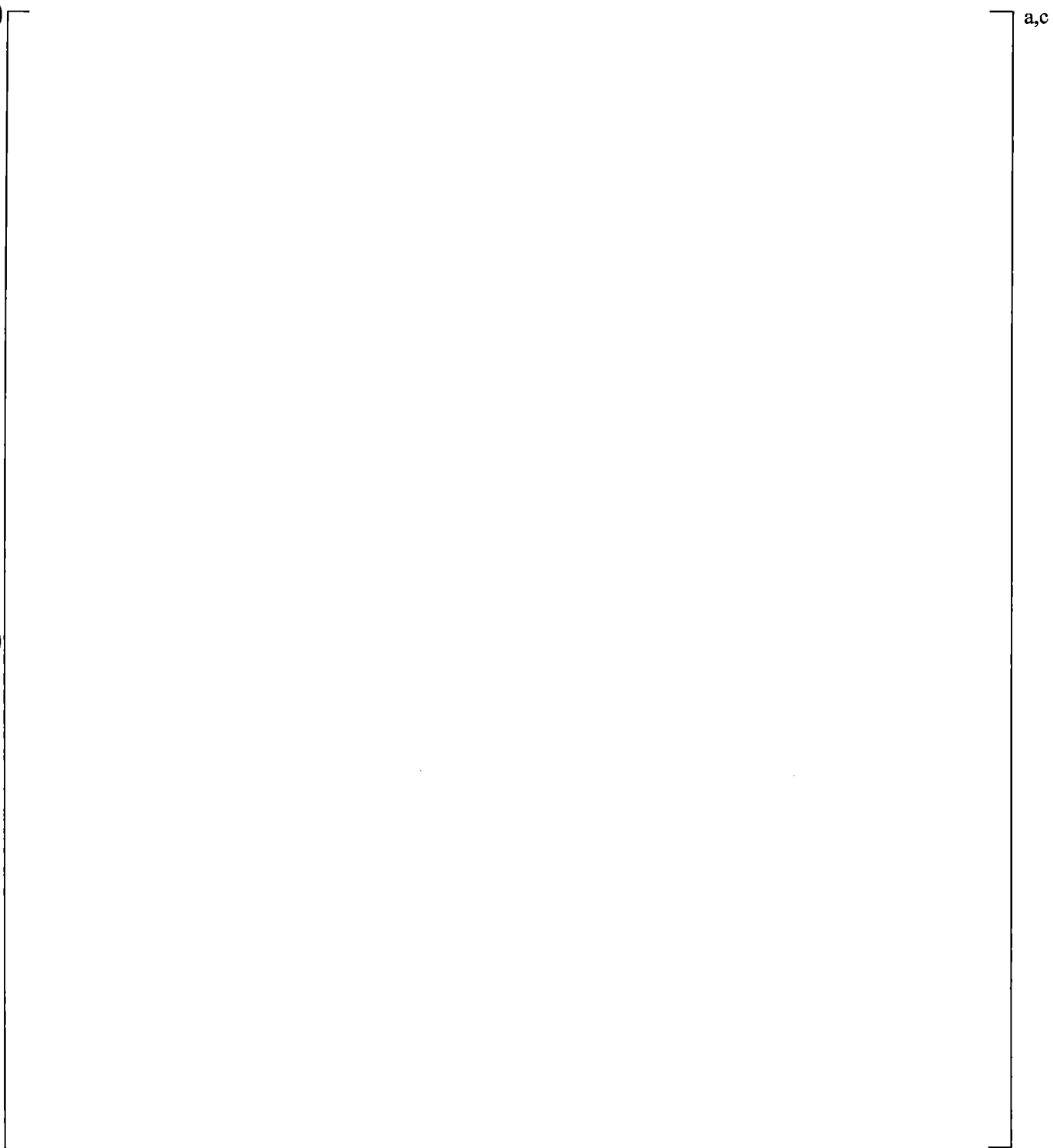


Figure 21.12-16 Inner Vessel (LP+Core+UP) Differential Pressures

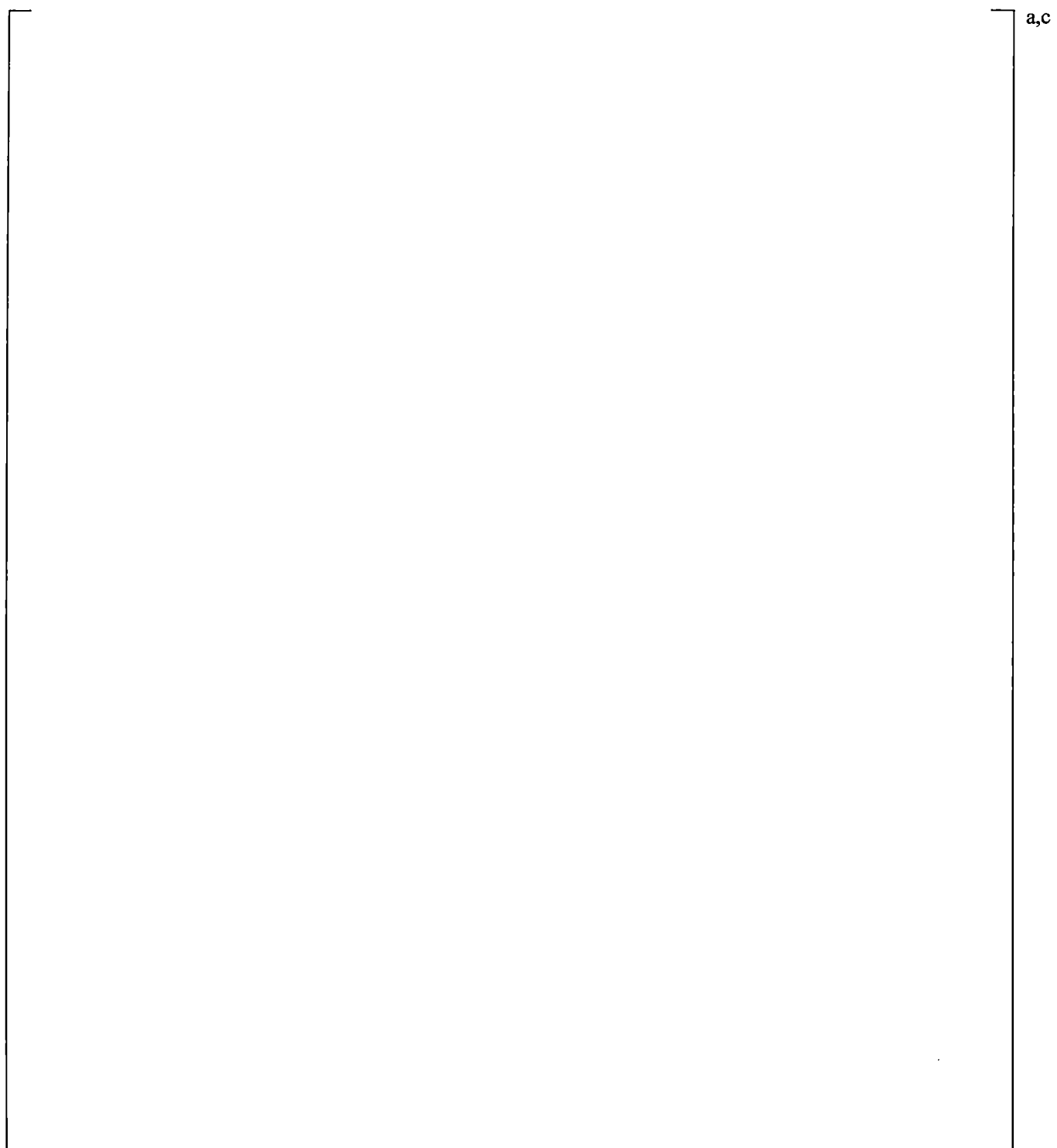


Figure 21.12-17 Lower Plenum Differential Pressures

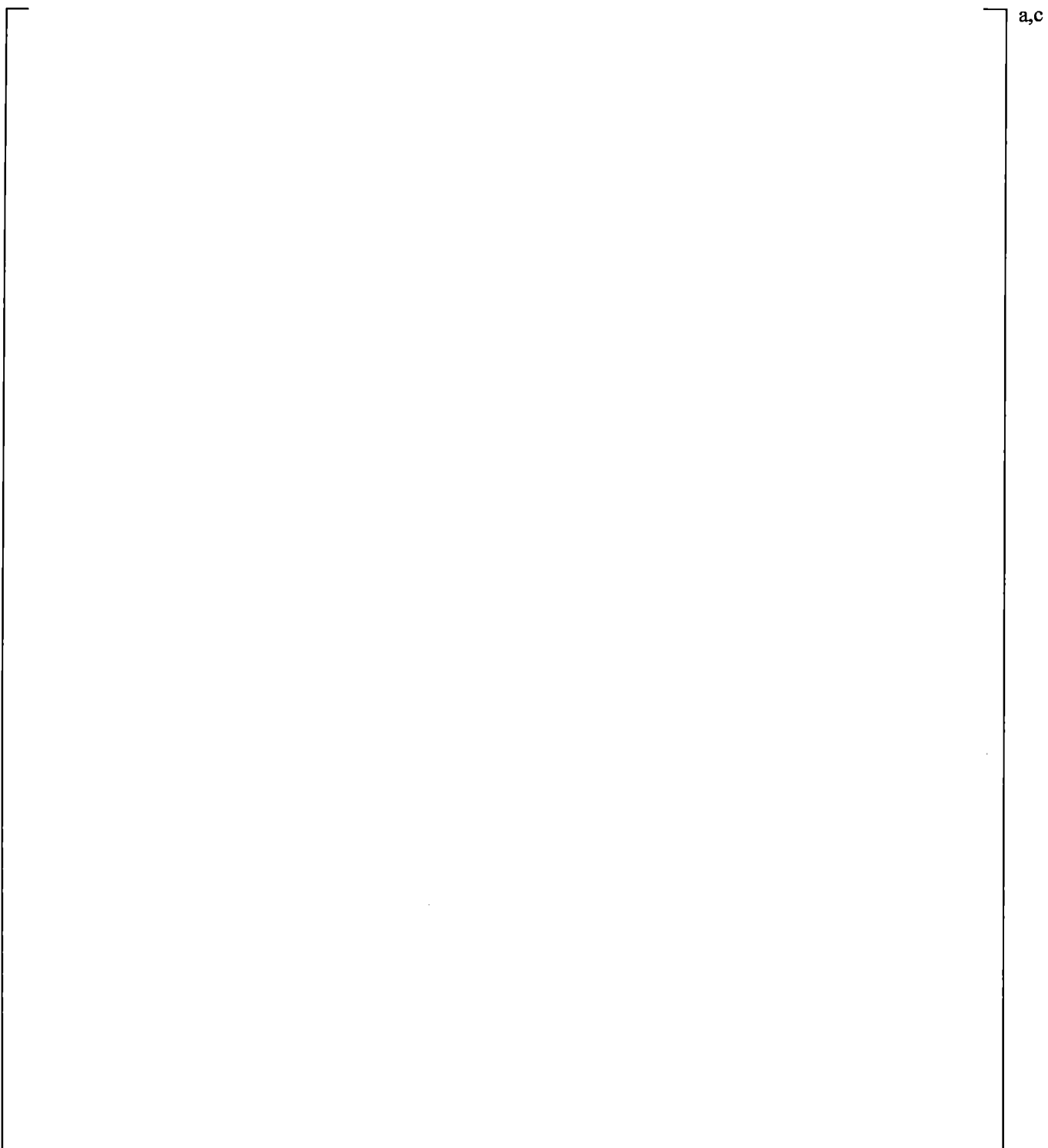


Figure 21.12-18 Peak Cladding Temperatures

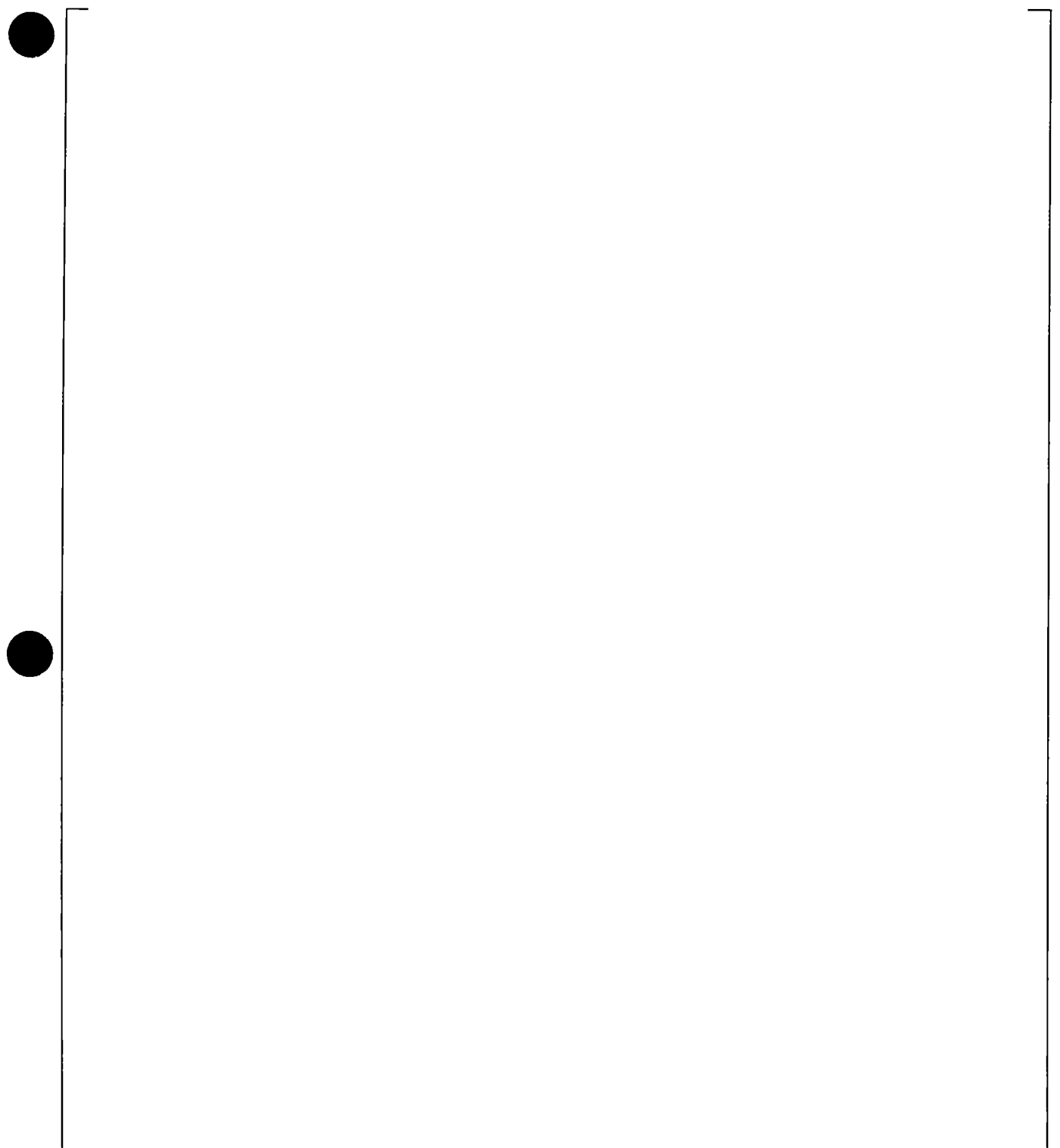


Figure 21.12-19 Accumulator A Injection Flows

21.13 TWO-PHASE BREAK DISCHARGE COEFFICIENT (CD2) SENSITIVITY

The effect of the two-phase break discharge coefficient (CD2) on the small break LOCA transient is shown by comparison of two simulations of the SB-CL-18 test. [

]^{a,c}

The results of the two simulations are presented in Figures 21.13-1 through 21.13-19. [

]^{a,c}

Since the sub-cooled discharge coefficient used in the two simulations was the same, the initial break flow until the time when transition to two-phase flow occurred was not affected, Figure 21.13-1. There is a small difference in the calculated break flow (Figure 21.13-1) during the transition from sub-cooled to two-phase, [

]^{a,c}

The system depressurization rate is visibly affected by the CD2 coefficient during the period of the transient following loop seal clearance, Figure 21.13-5. The case with higher CD2 resulted in faster system depressurization after the loop seals cleared. As a result, the earlier accumulator injection calculated in the simulation with higher CD2 coefficient, Figure 21.13-19.

The draining of the steam generator U-tubes and inlet and outlet plenums is not affected by CD2 as well, Figures 21.13-6 through 21.13-11.

[

]^{a,c}

]^{a,c}

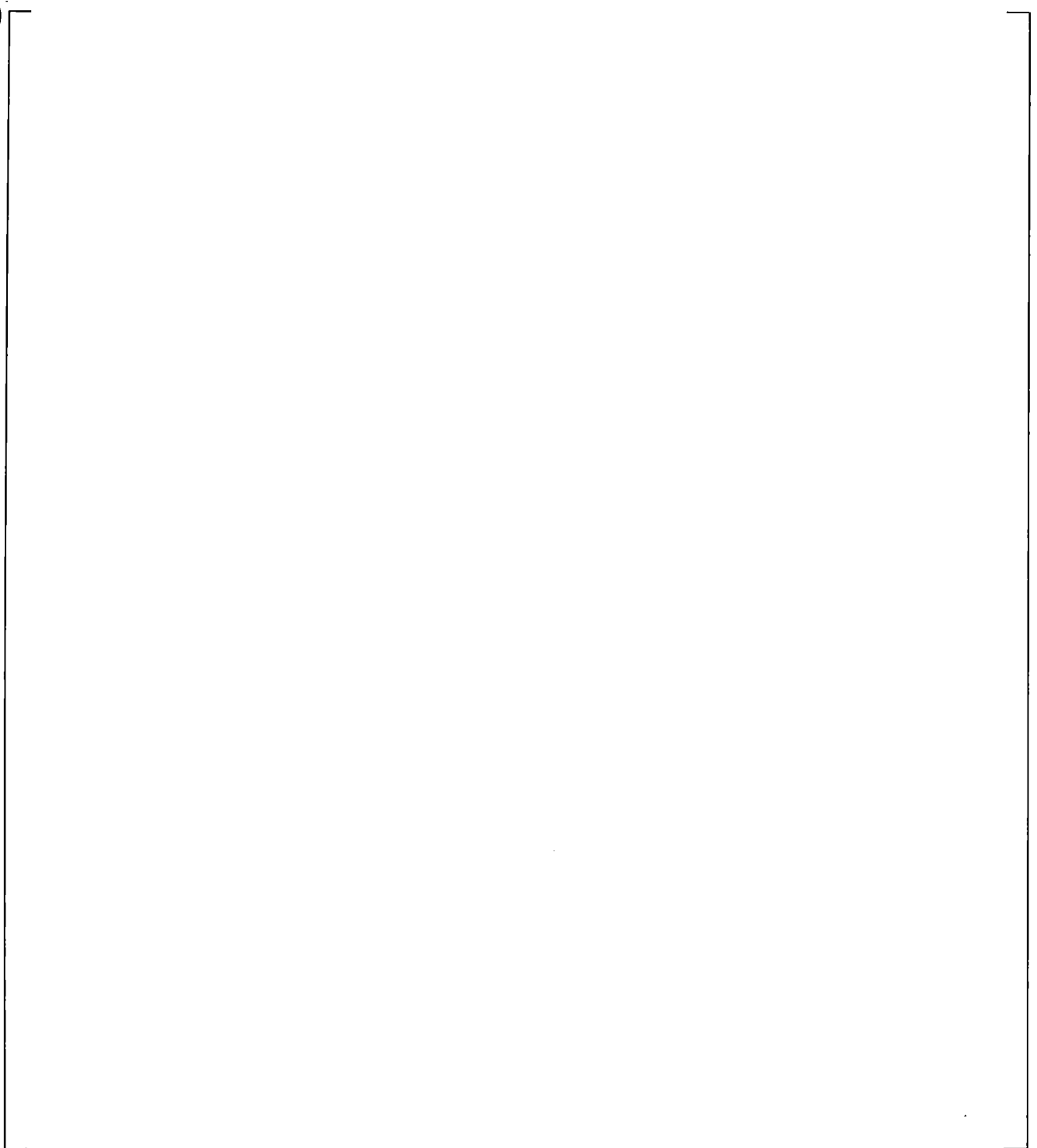


Figure 21.13-1 Break Flows

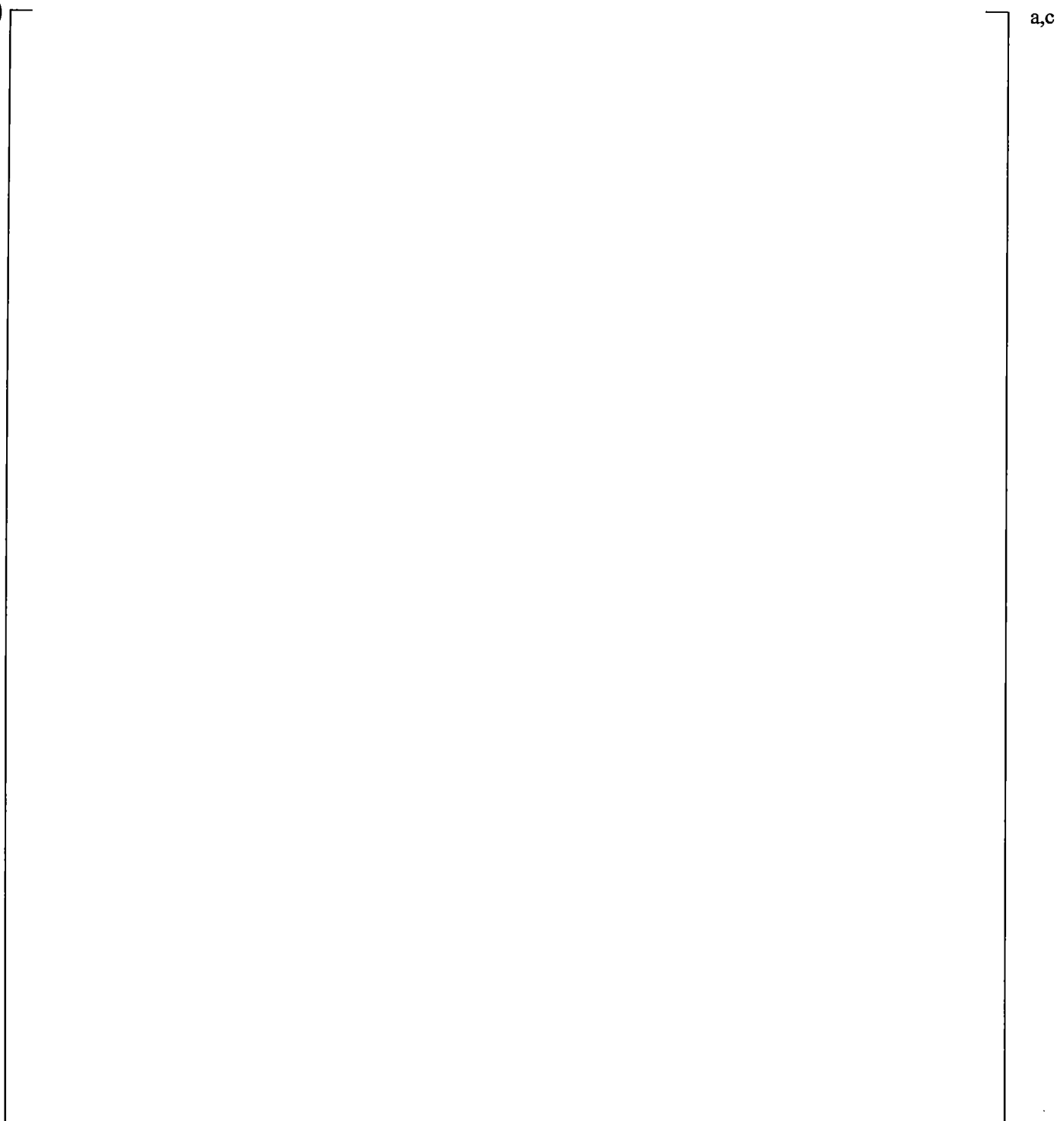


Figure 21.13-2 Calculated Break Void Fraction



a,c

Figure 21.13-3 Cross-Over Leg A Differential Pressures

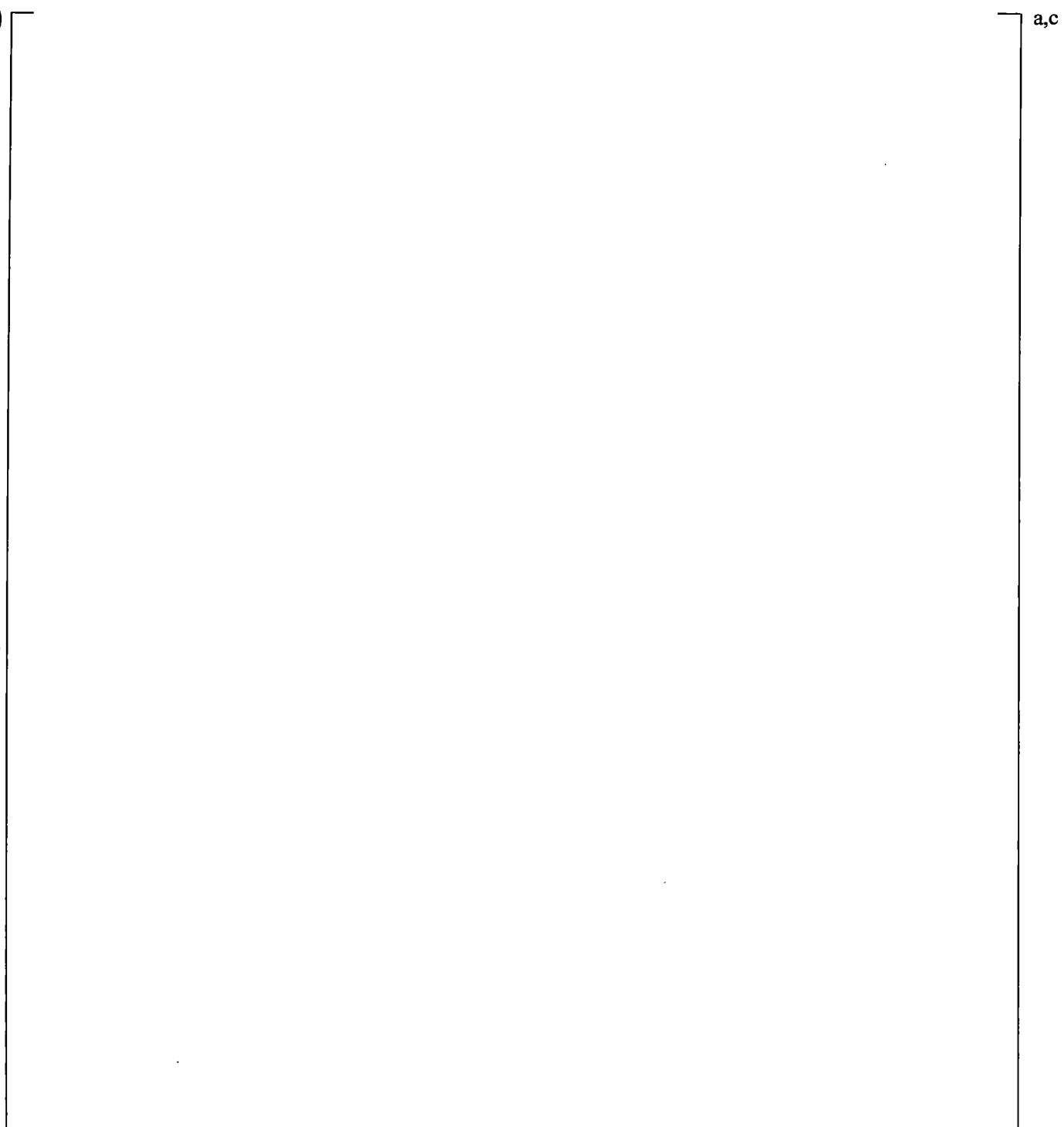
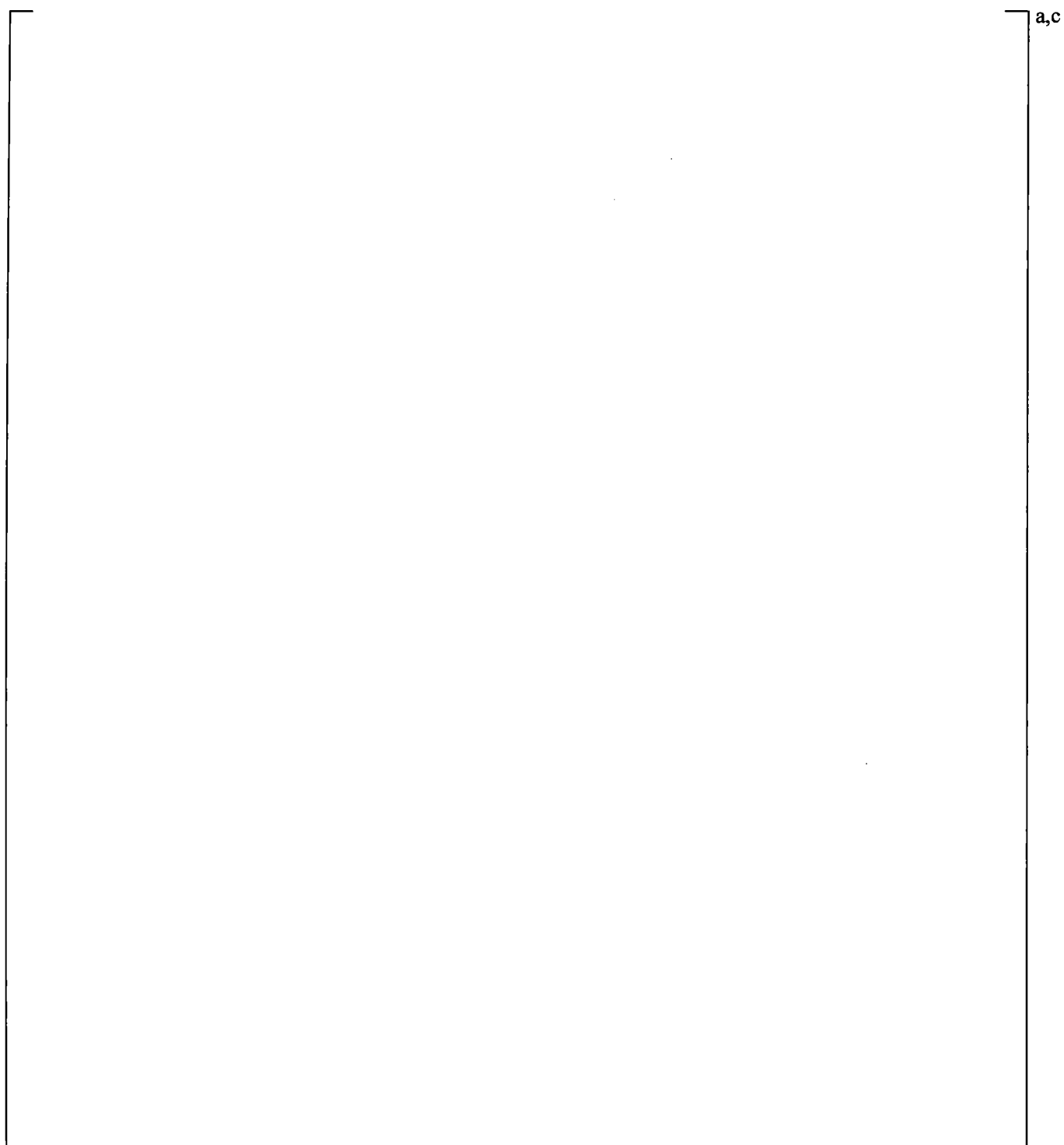


Figure 21.13-4 Cross-Over Leg B Differential Pressures

a,c

Figure 21.13-5 Pressurizer Pressures



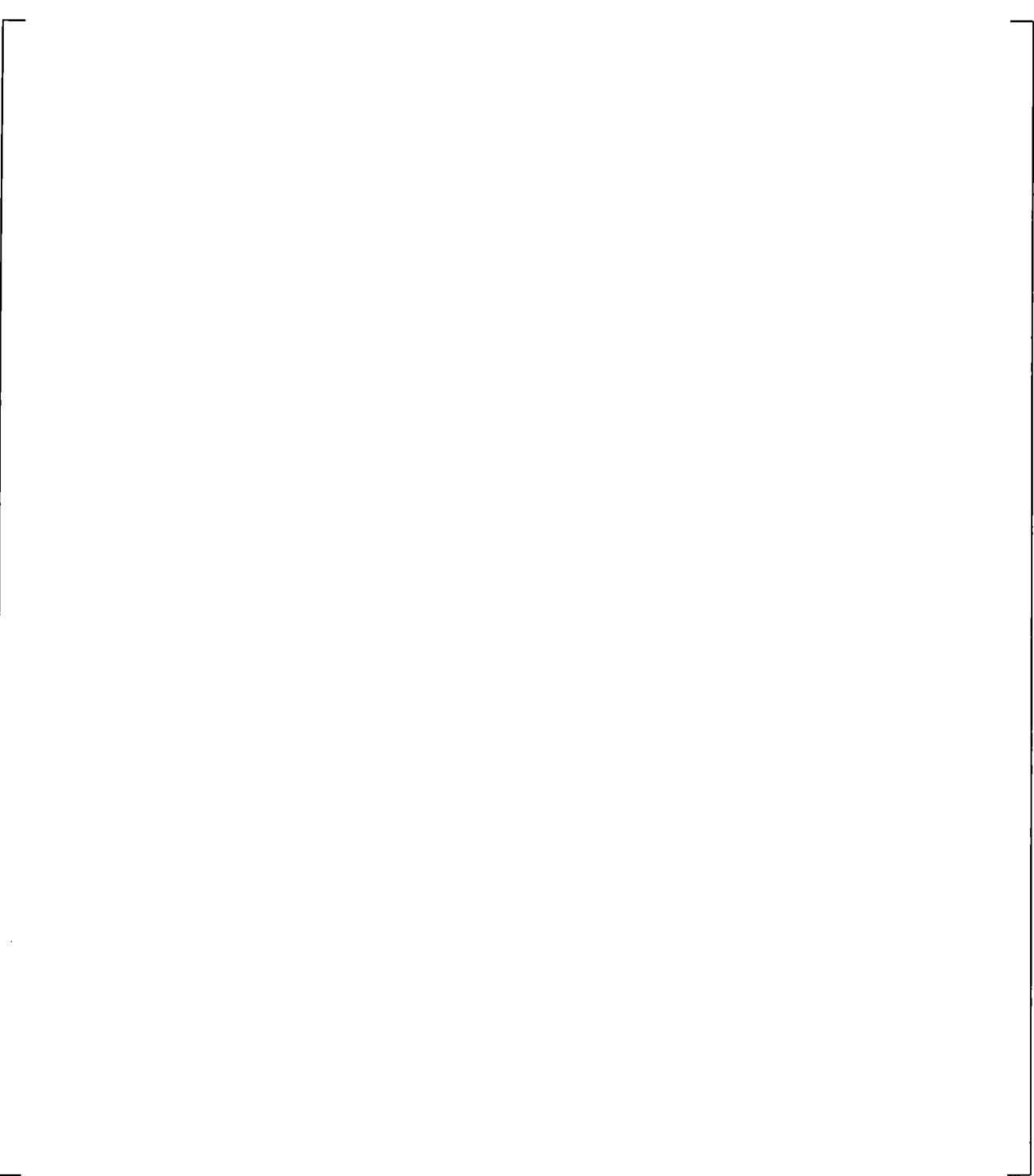
| **Figure 21.13-6 Steam Generator A U-tubes Inlet-to-Top Differential Pressure**



a,c

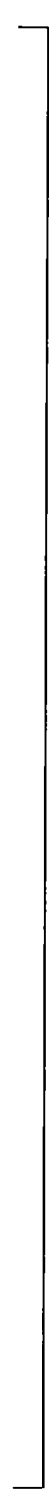


| **Figure 21.13-7 Steam Generator B U-tubes Inlet-to-Top Differential Pressures**



a,c

| **Figure 21.13-8 Steam Generator A U-tubes Outlet-to-Top Differential Pressures**



a,c

| **Figure 21.13-9 Steam Generator B U-tube Outlet-to-Top Differential Pressures**

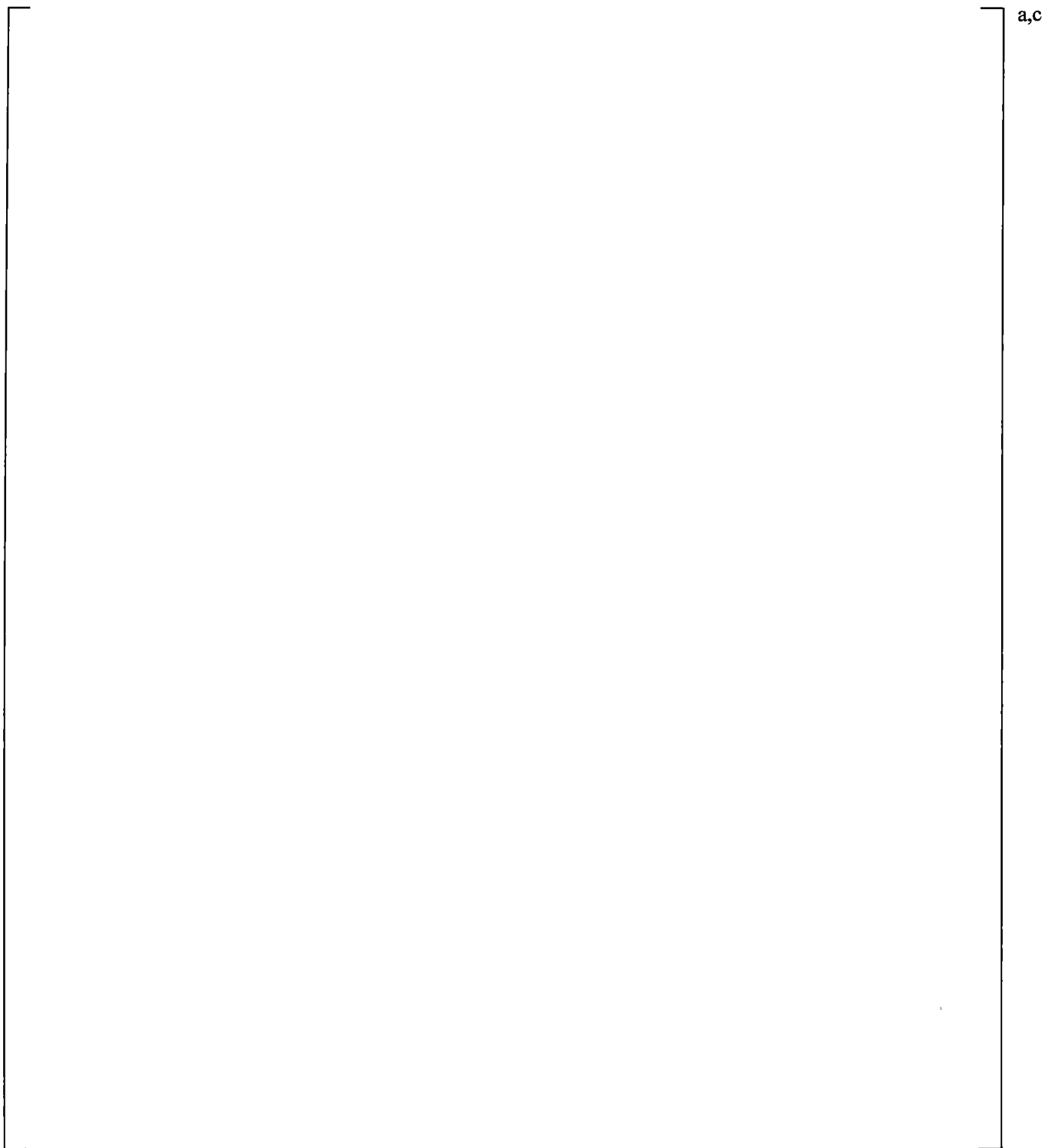
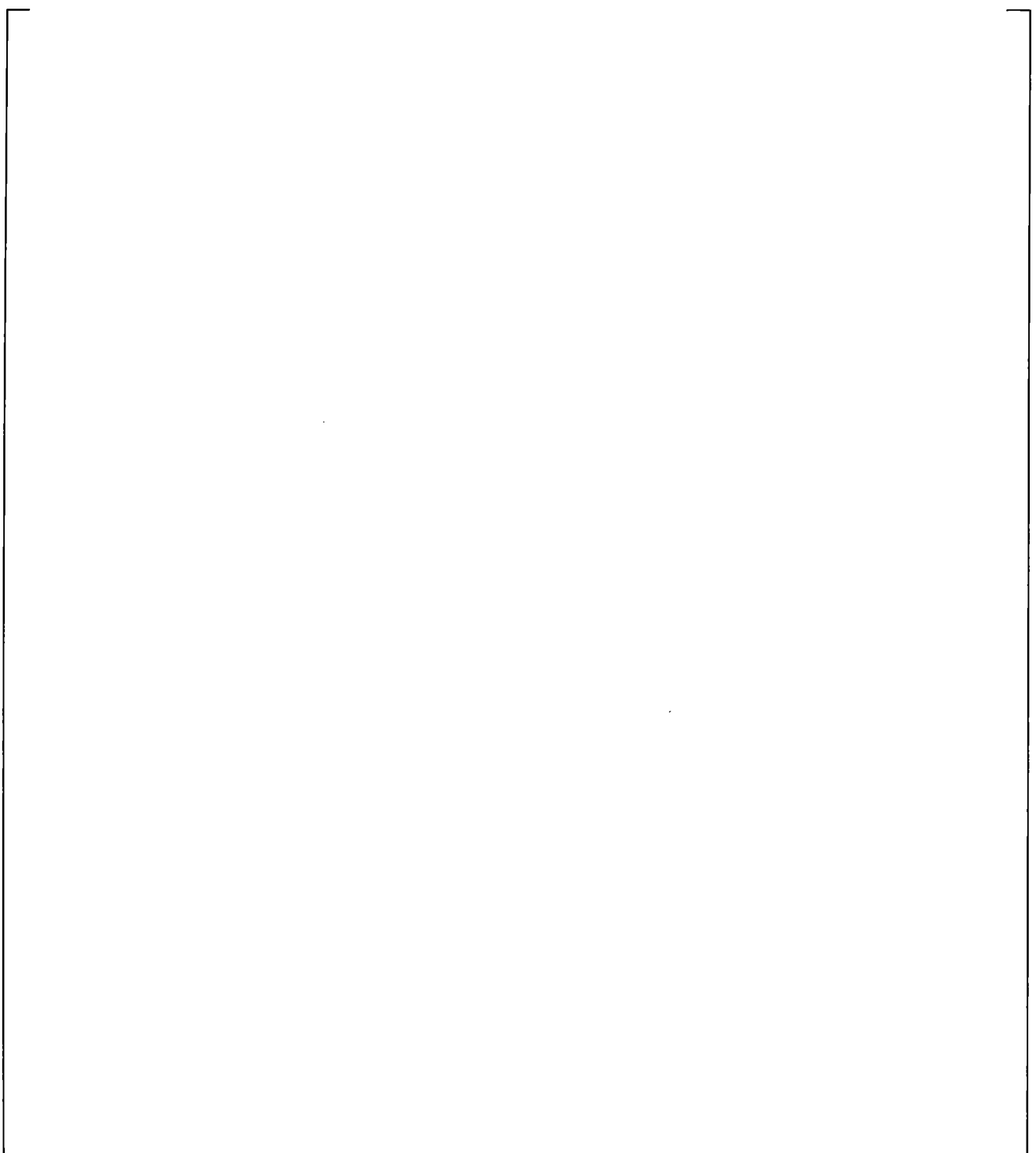
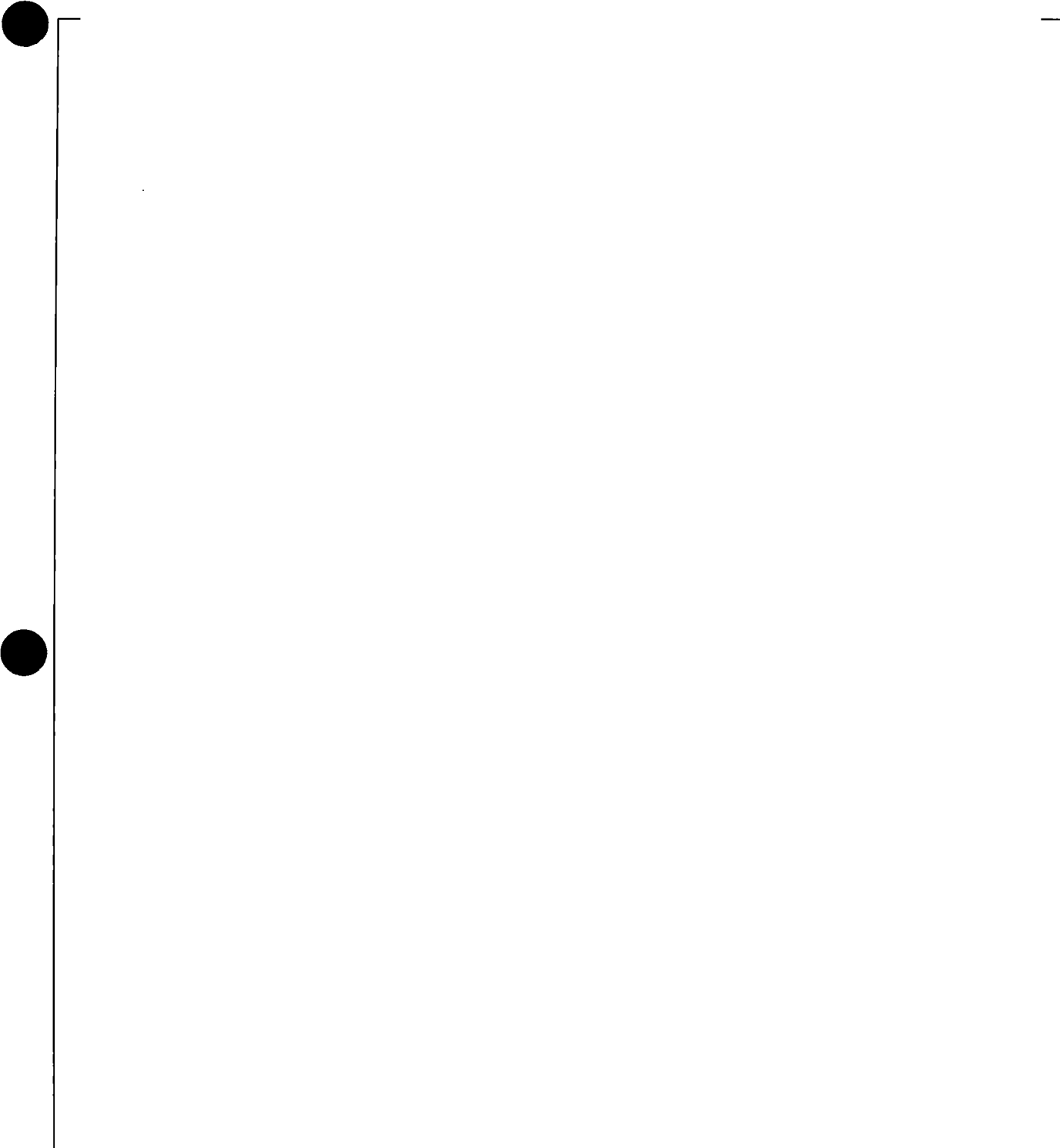


| **Figure 21.13-10 Steam Generator A Inlet Plenum Collapsed Liquid Levels**



a,c

Figure 21.13-11 Steam Generator B Inlet Plenum Collapsed Liquid Levels



a,c

| **Figure 21.13-12 Upper Plenum to Steam Generator A Inlet Differential Pressures**



a,c

Figure 21.13-13 Upper Plenum to Steam Generator B Inlet Differential Pressures

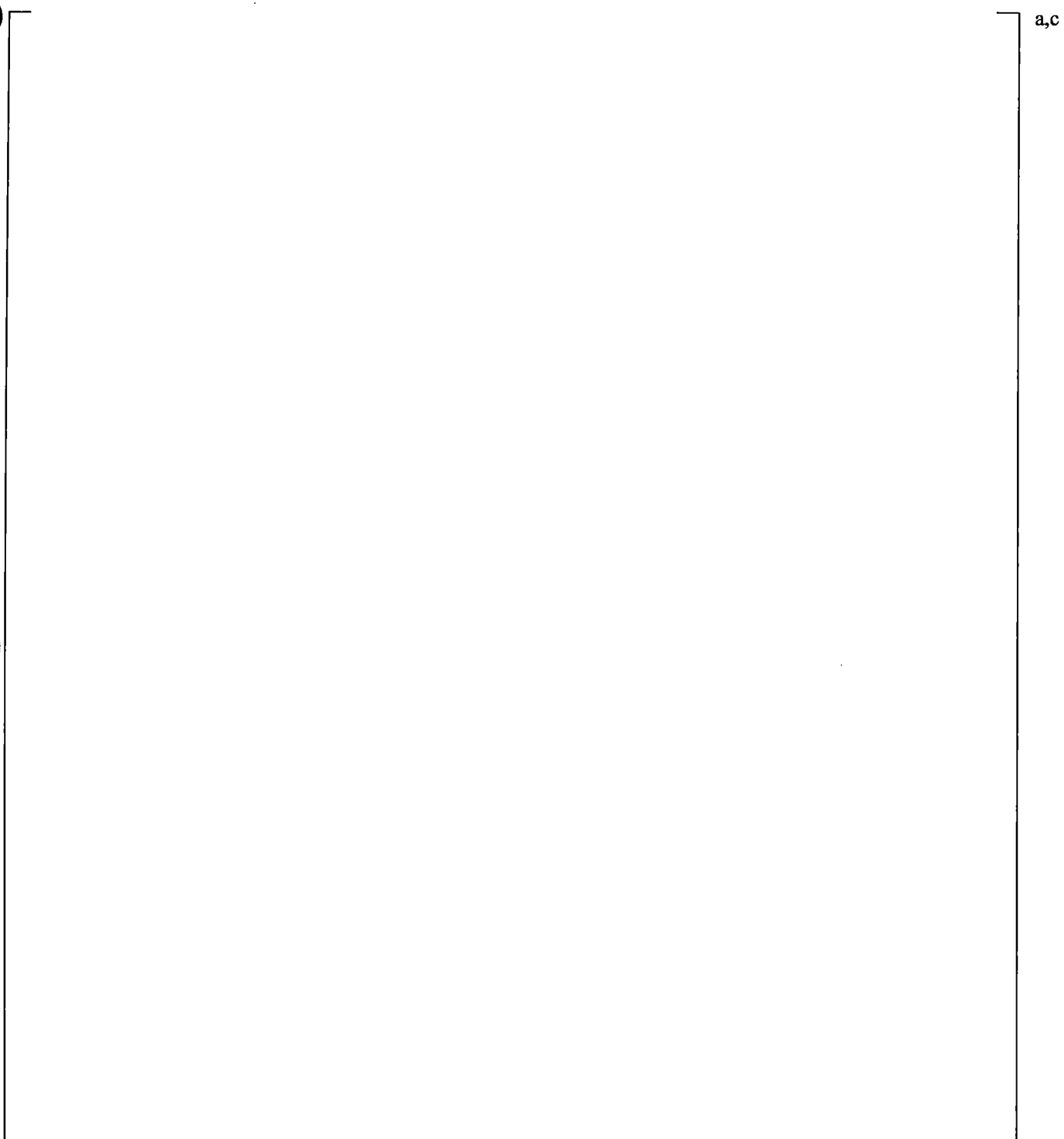


Figure 21.13-14 Downcomer Differential Pressures

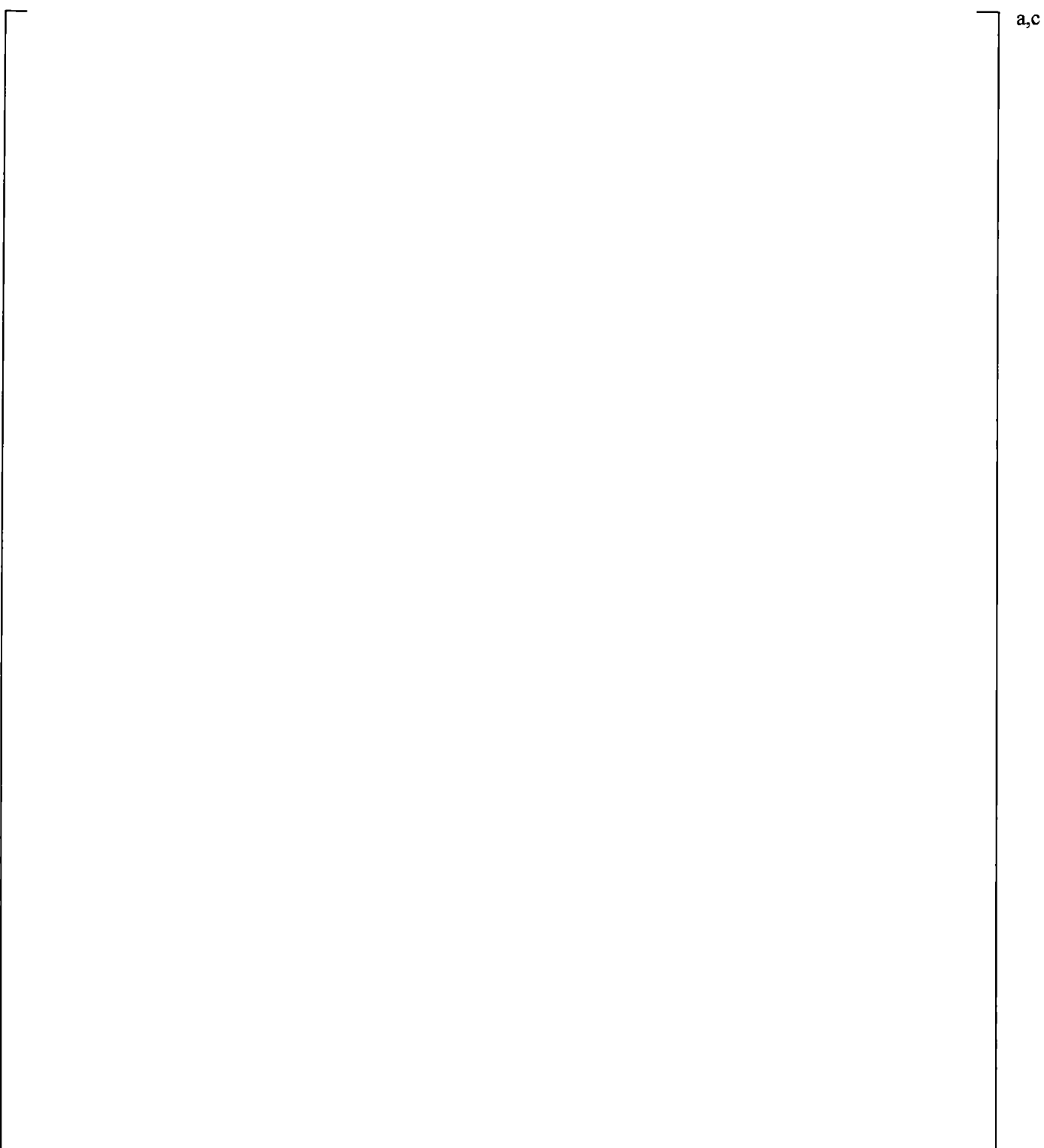


Figure 21.13-15 Upper Plenum Differential Pressures

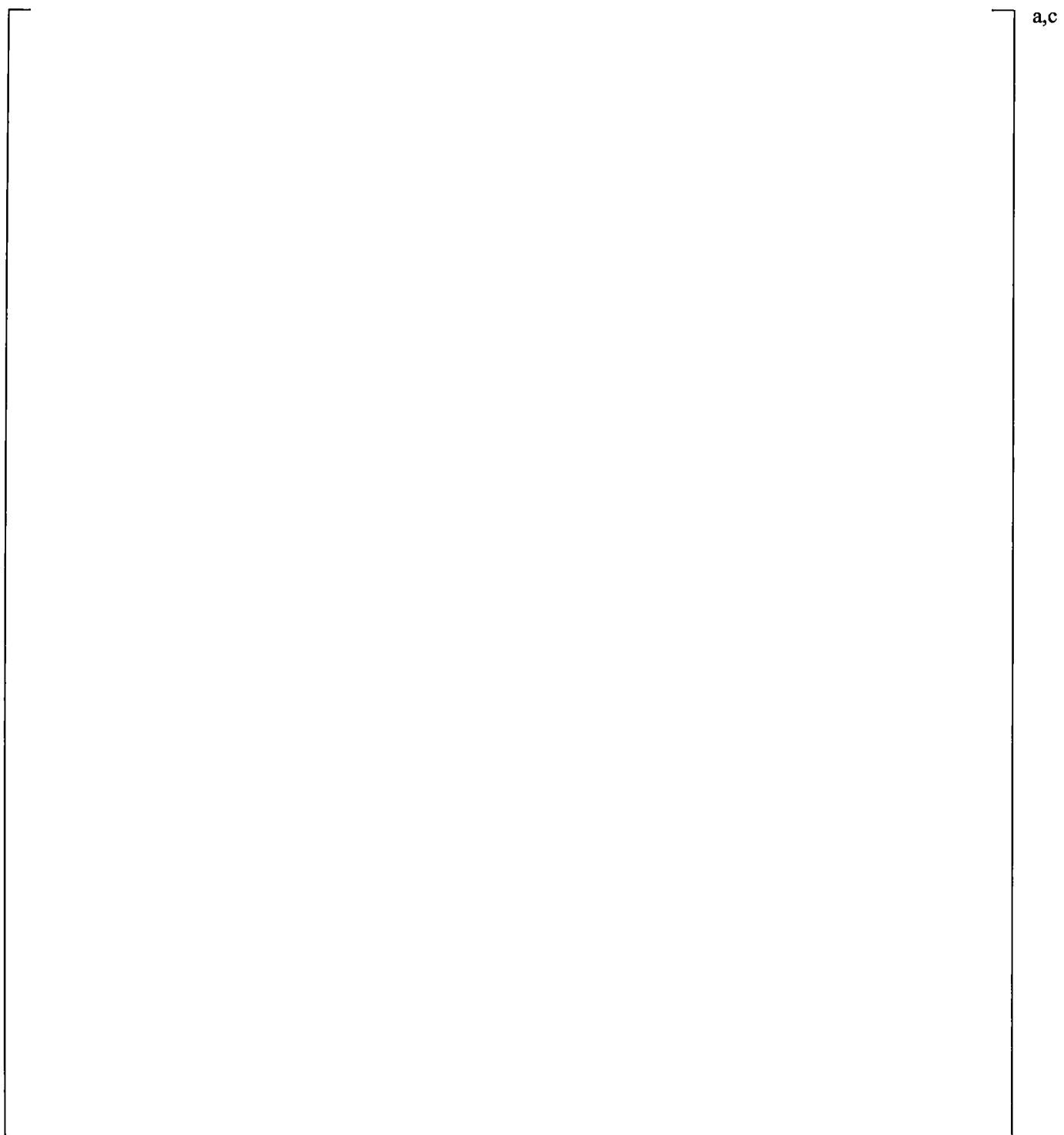
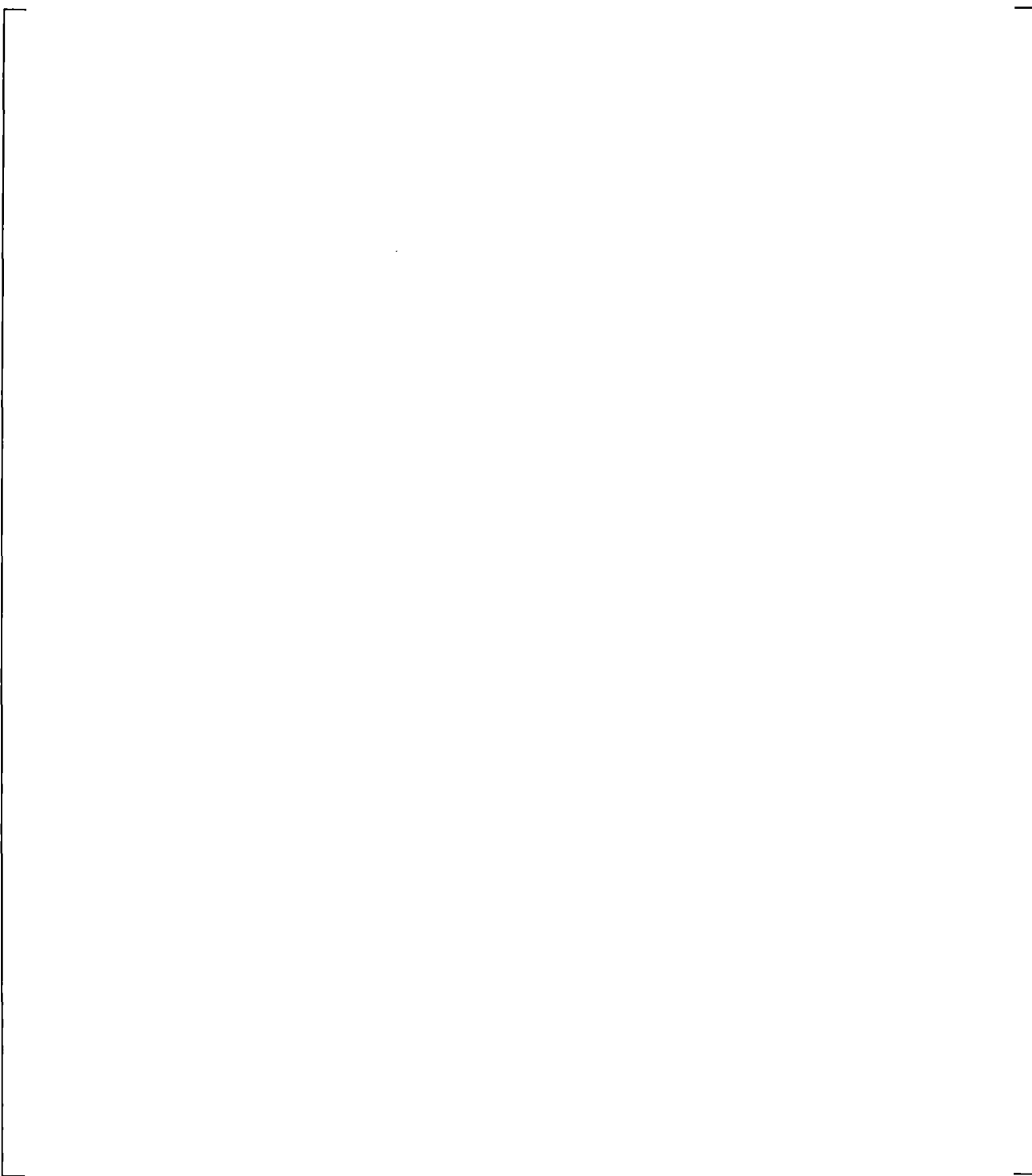


Figure 21.13-16 Inner Vessel (LP+Core+UP) Differential Pressures



a,c

Figure 21.13-17 Lower Plenum Differential Pressures

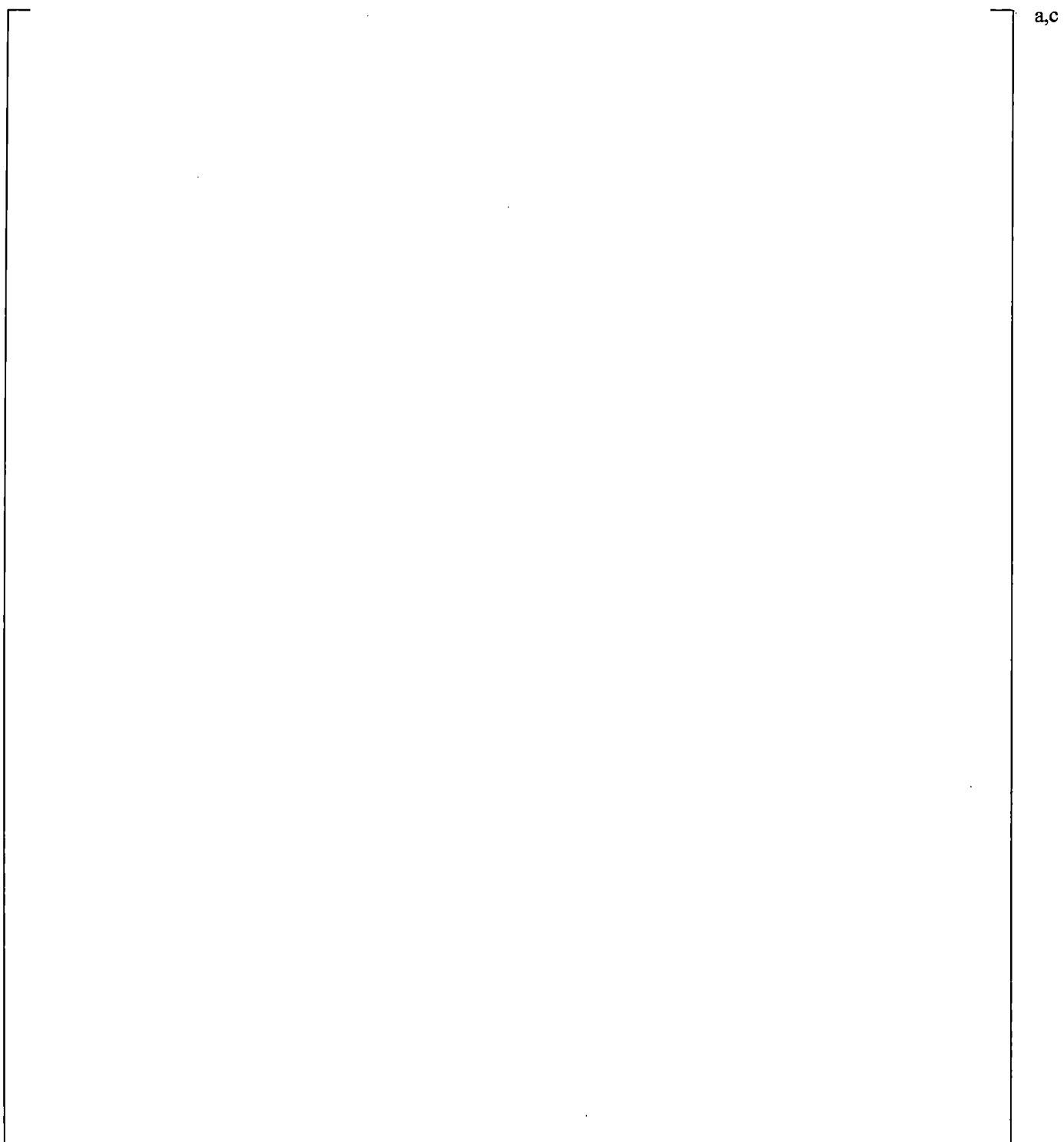
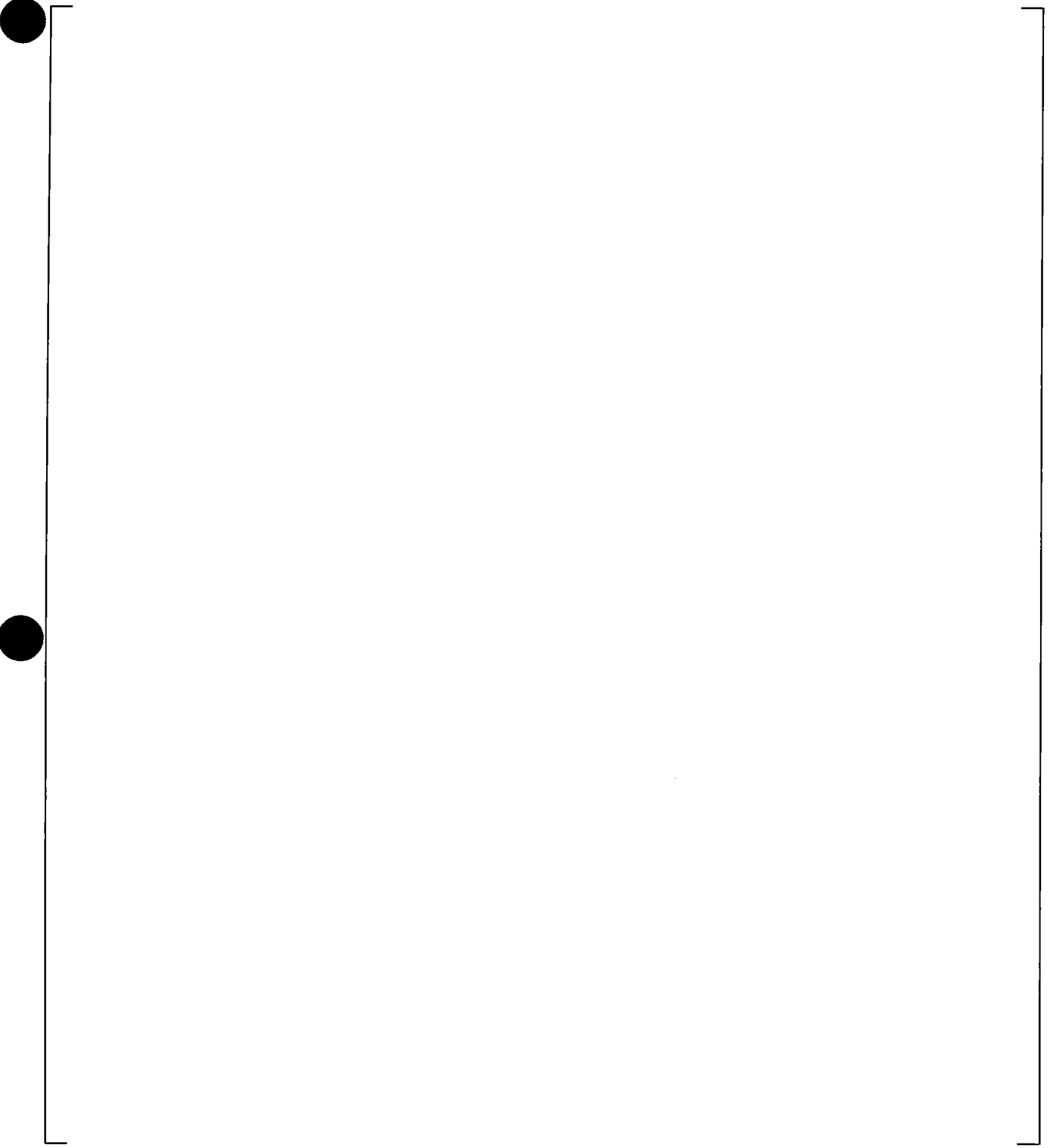


Figure 21.13-18 Peak Cladding Temperatures



a,c

Figure 21.13-19 Accumulator A Injection Flows

21.14 BROKEN LOOP PUMP RESISTANCE SENSITIVITY CALCULATION

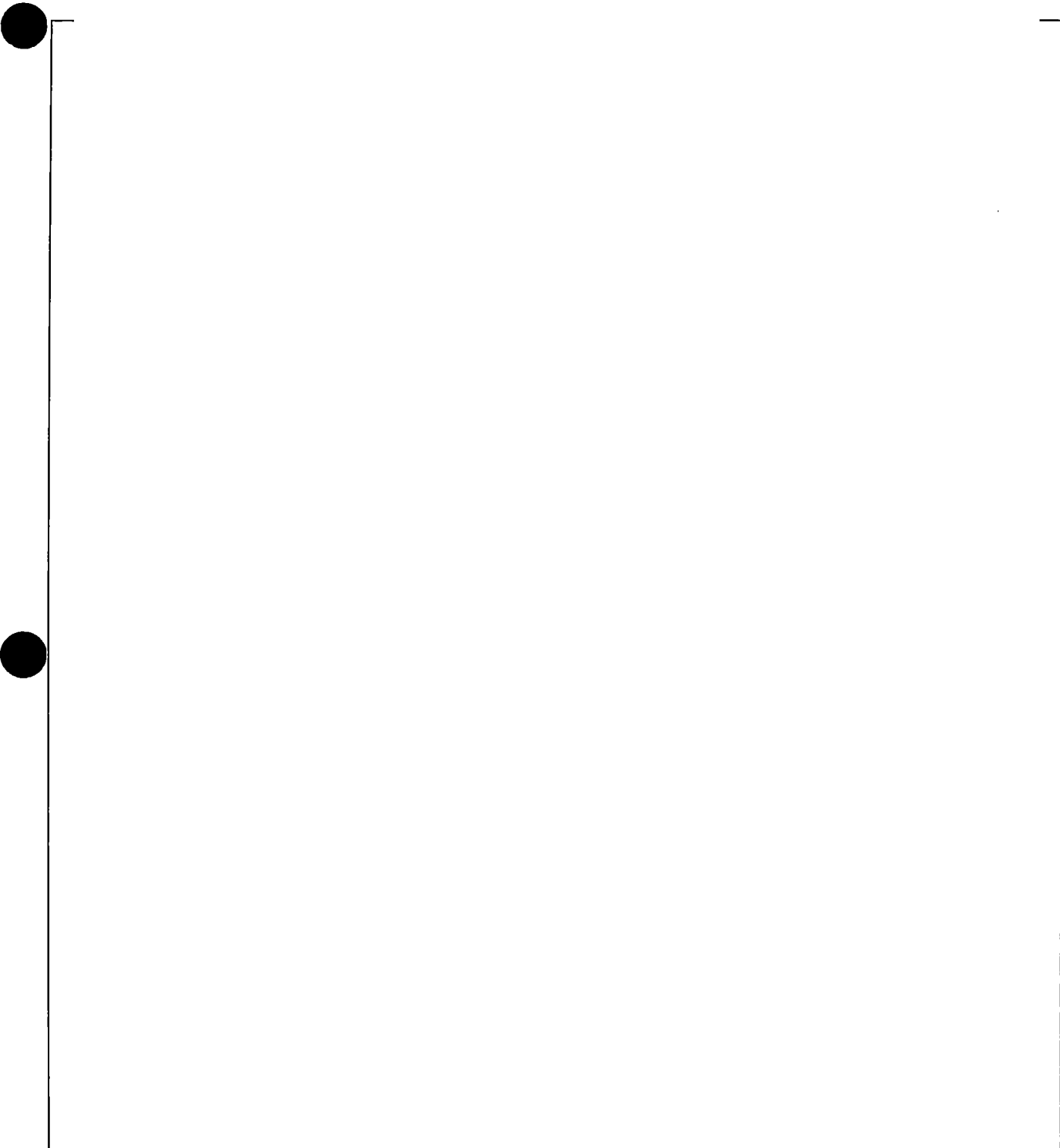
This sensitivity calculation is performed to support a discussion in Section 29, Volume 3, which is related to the ranging of the broken loop pump resistance (KP). The approach on KP ranging is considered to be applicable to both small and large break LOCA scenarios. The sensitivity performed herein is not a sensitivity on KP; it simply looks at the effect on the simulation results when the resistance at zero pump velocity is shifted by a certain amount. In this case, the homologous curve point at zero pump speed is modified so that the resistance for both pumps is reduced by 50% from the one used in the SB-CL-18 simulation in Section 21.4.

Figures 21.14-1 through 21.14-10 show comparison of SB-CL-18 simulation with 50% reduced locked rotor resistance to the SB-CL-18 simulation in Section 21.4. The simulations with the 50% reduced locked rotor resistance are shown in the bottom figures on each page. Except for the slightly different pump differential pressure after the pumps are locked at about 260 seconds, Figure 21.14-1, no major differences are observed in the comparison of the rest of the simulation results.



a,c

Figure 21.14-1 Pump A Differential Pressures



a,c

Figure 21.14-2 SB-CL-18 Cross-Over Leg A Differential Pressures

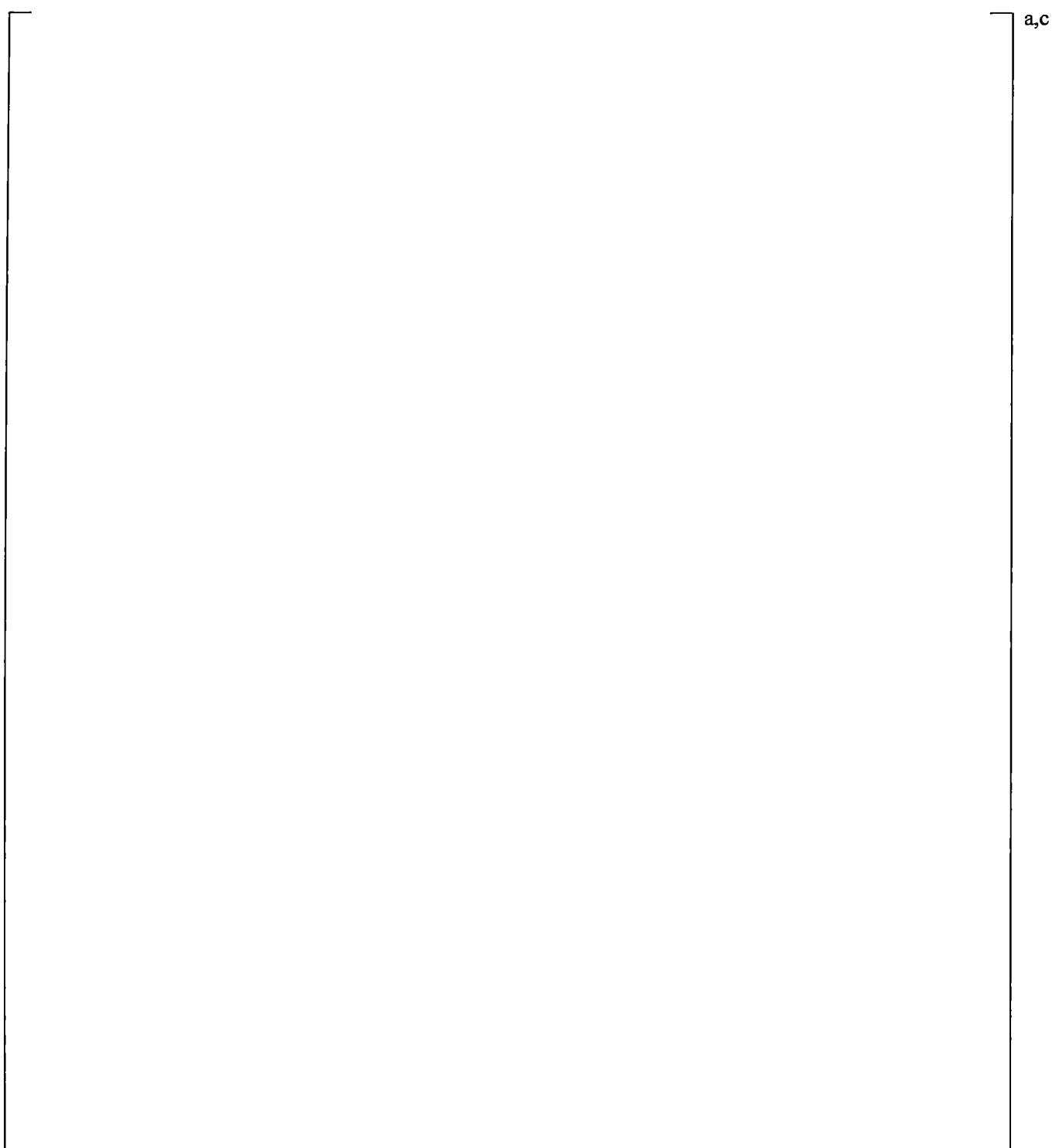


Figure 21.14-3 SB-CL-18 Cross-Over Leg B Differential Pressures

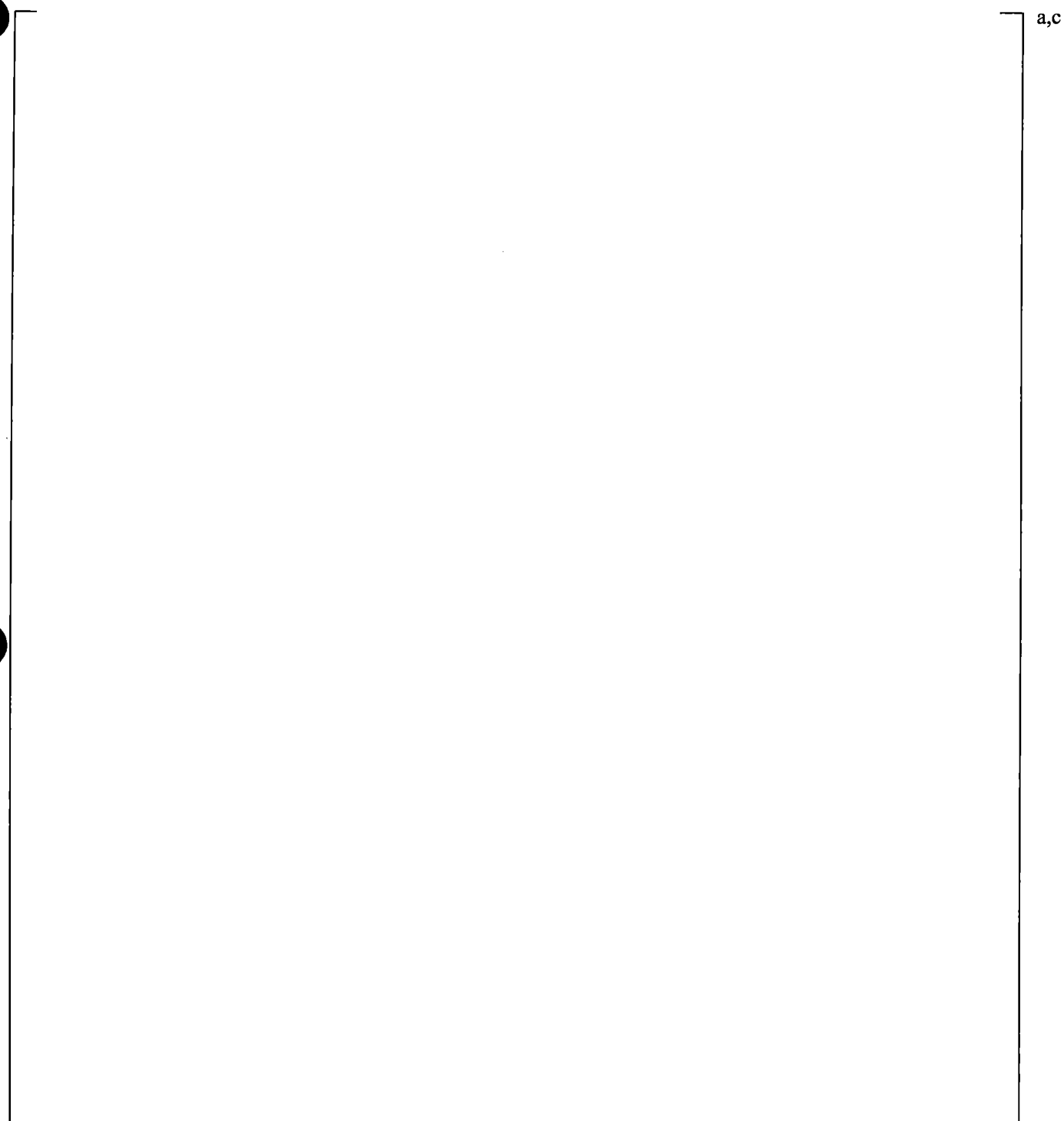


Figure 21.14-4 Inner Vessel Differential Pressures (LP+Core+UCP)

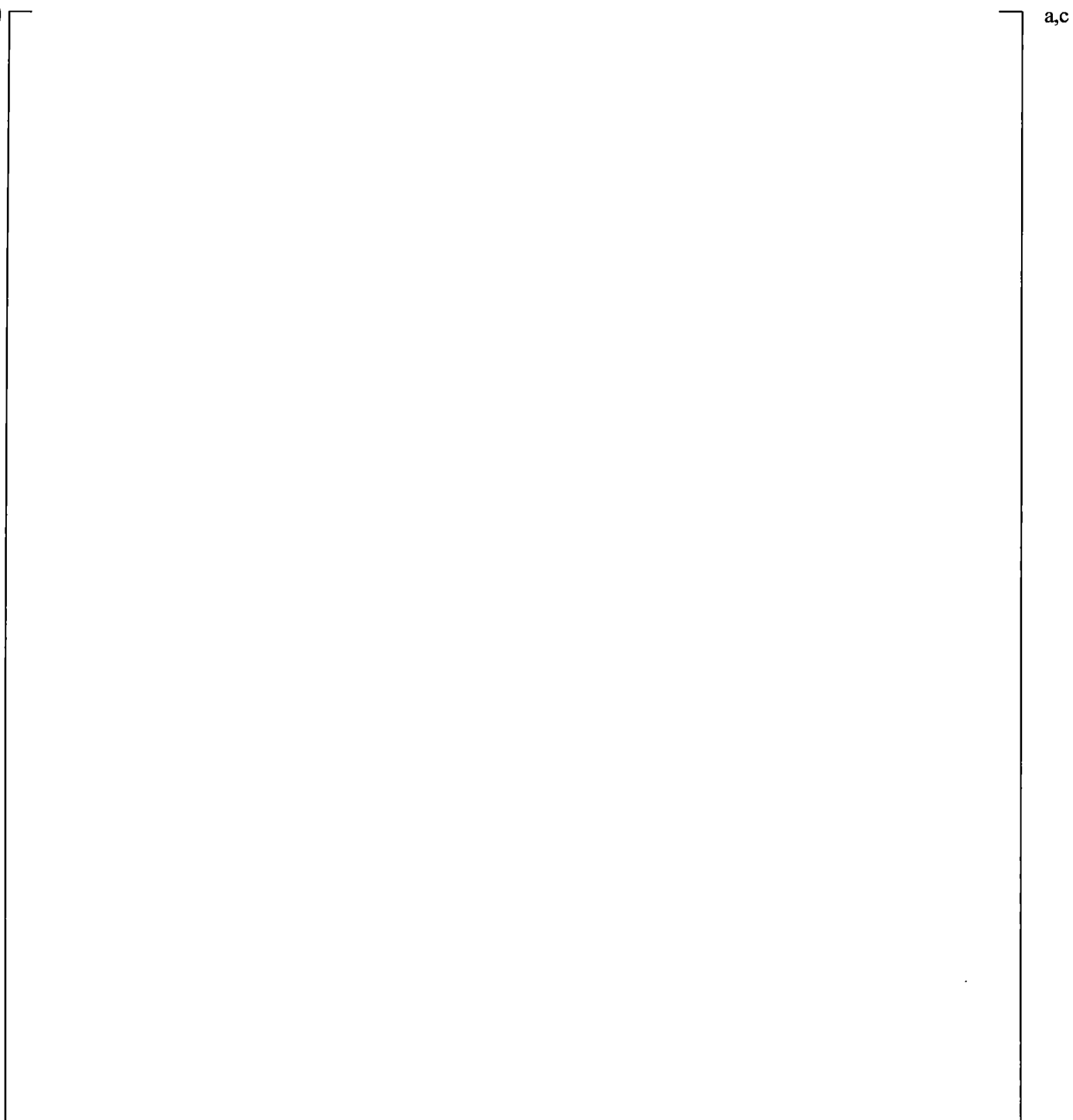


Figure 21.14-5 Downcomer Differential Pressures

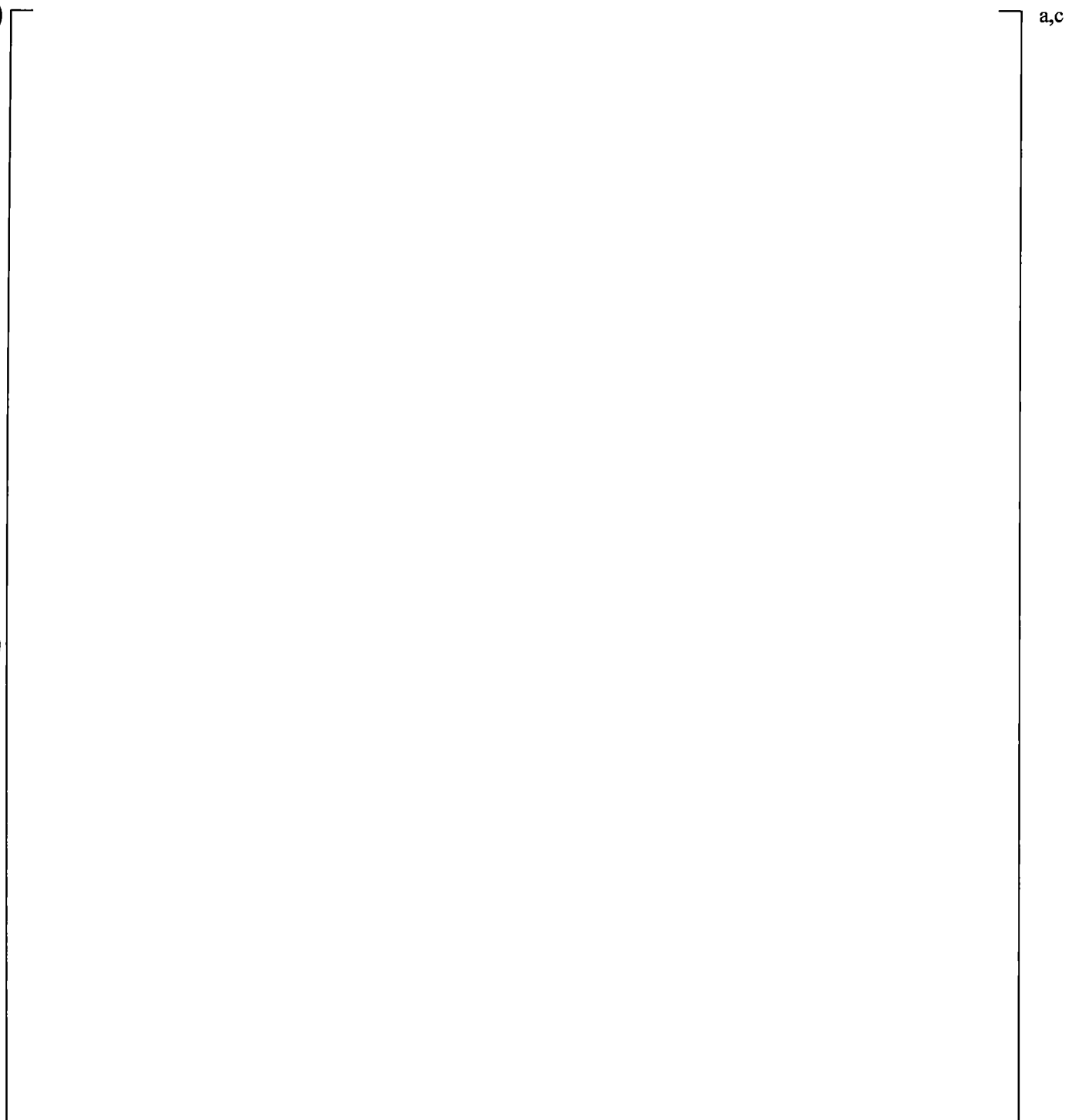


Figure 21.14-6 Lower Plenum Differential Pressures

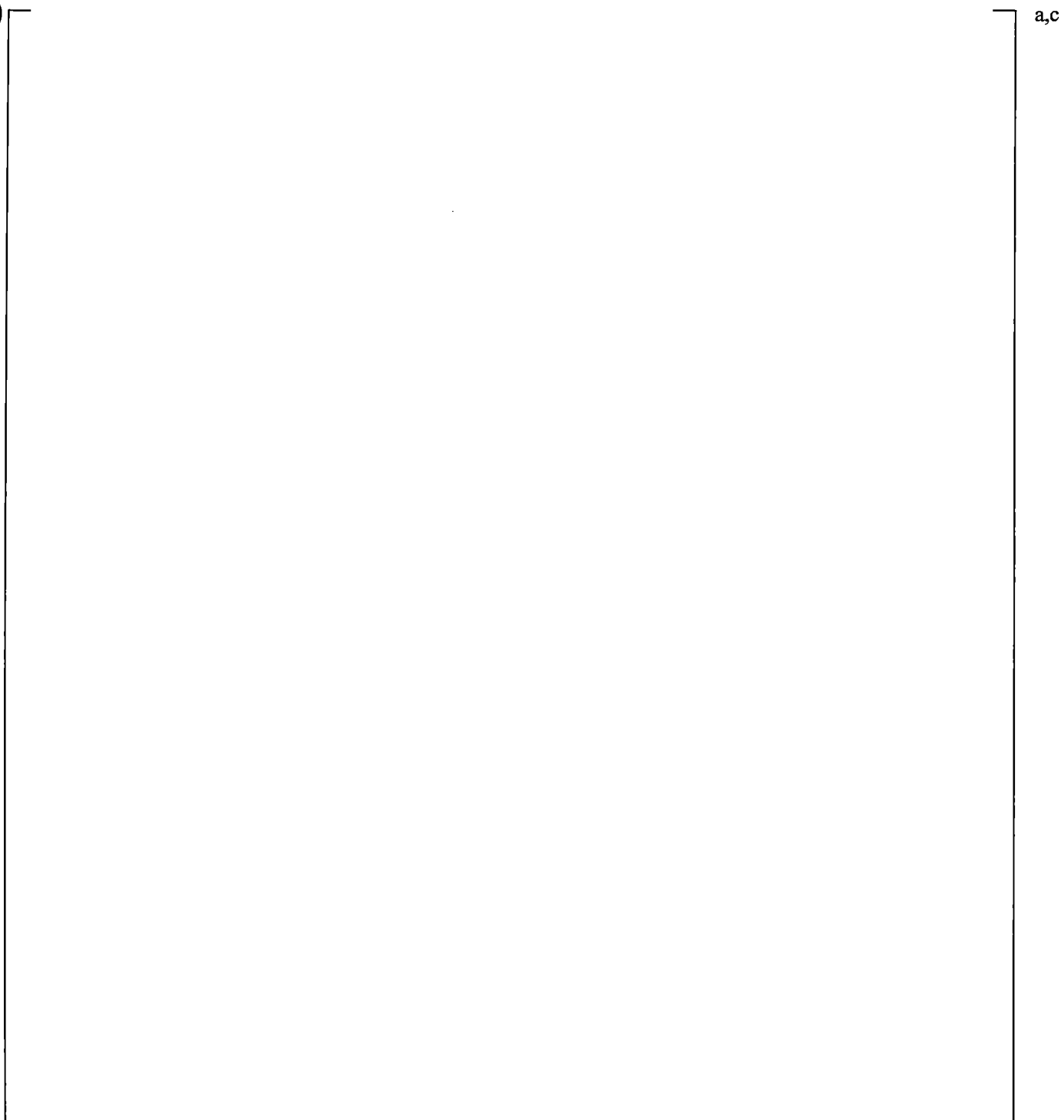


Figure 21.14-7 Upper Plenum Differential Pressures

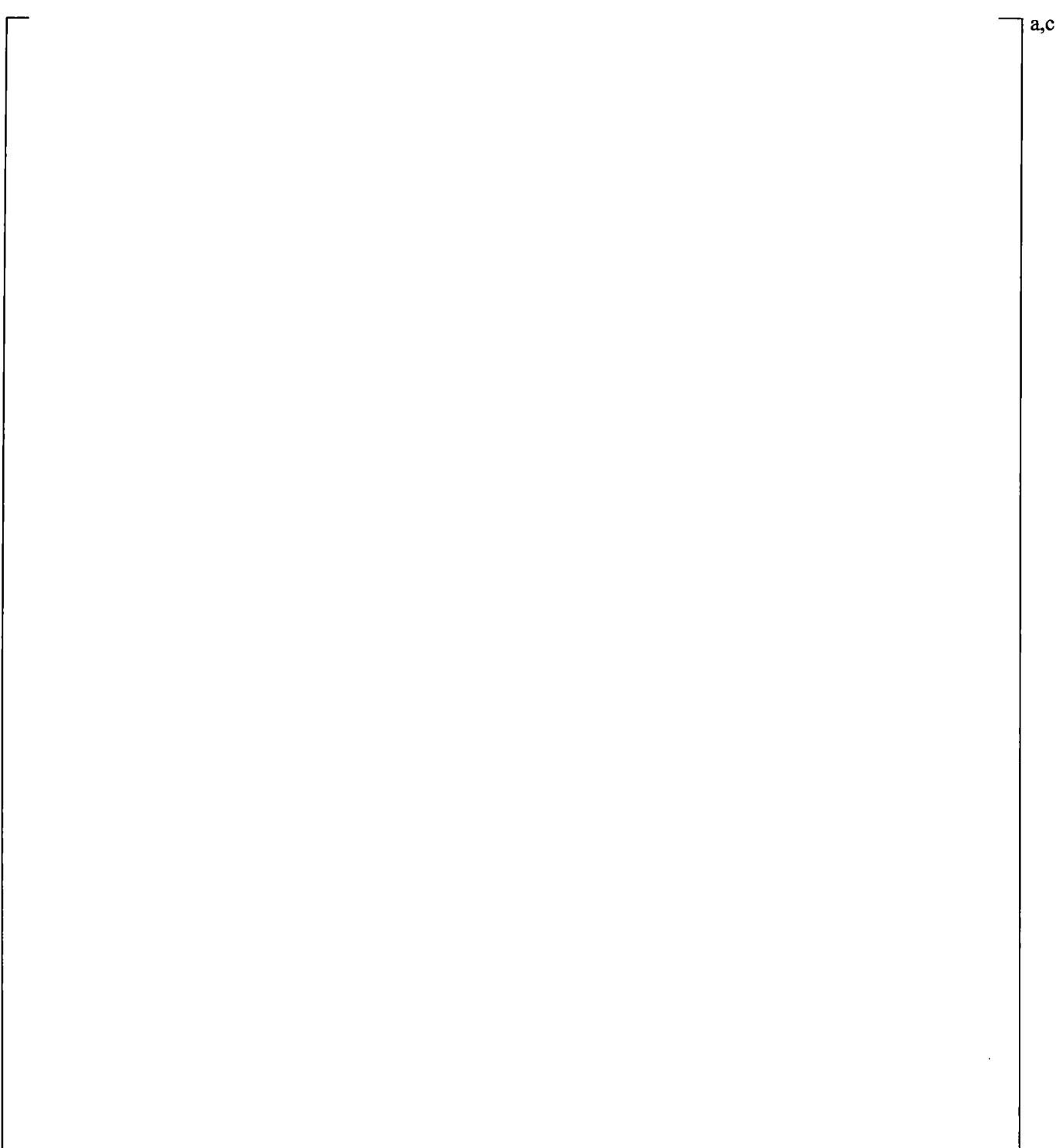
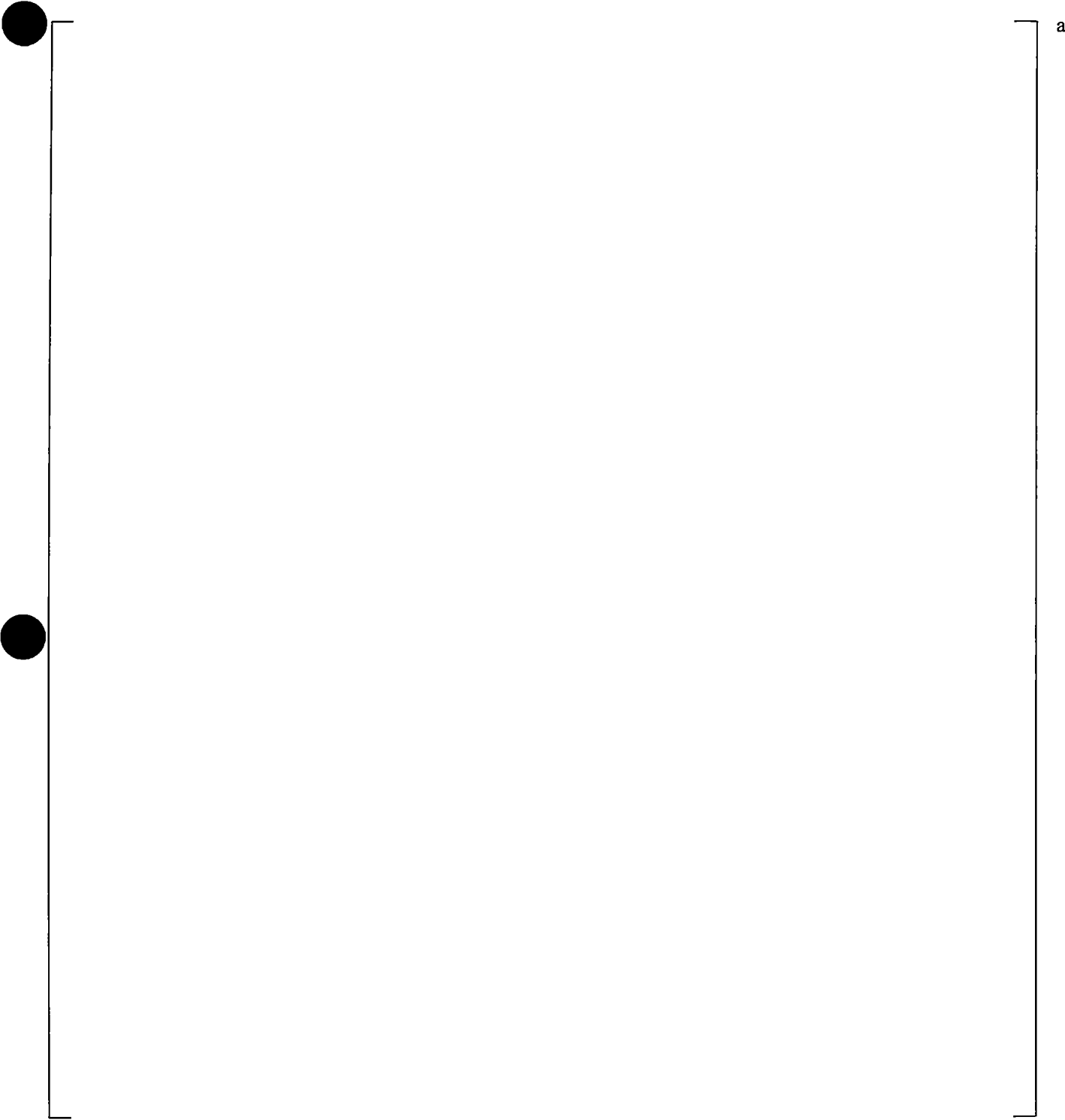


Figure 21.14-8 Hot Leg A Differential Pressures



a,c

Figure 21.14-9 Hot Leg B Differential Pressures

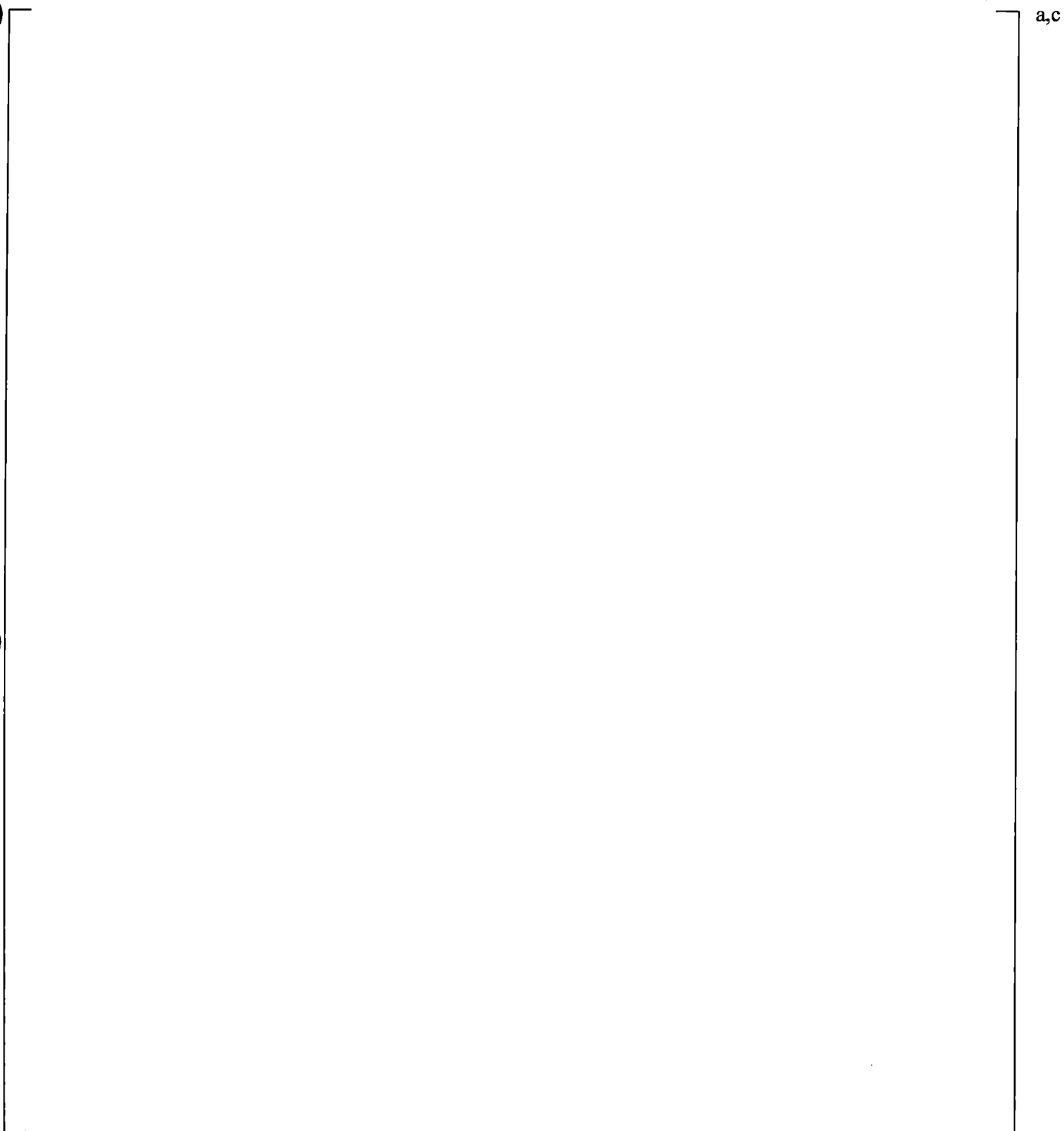


Figure 21.14-10 Peak Cladding Temperatures

21.15 YDRAG SENSITIVITY CALCULATIONS

This sensitivity is performed to investigate the effect of the variation of YDRAG in the core channels on the transient calculation results. The YDRAG multiplier in the core region is set at extreme minimum

[]^{a,c} and maximum []^{a,c} values.

The results of the YDRAG sensitivity are presented in Figures 21.15-1 through 21.15-6.

The loop seal clearance is not affected visibly by the variation of the core YDRAG parameter, Figures 21.15-1 and 21.15-2.

[]

[]^{a,c}

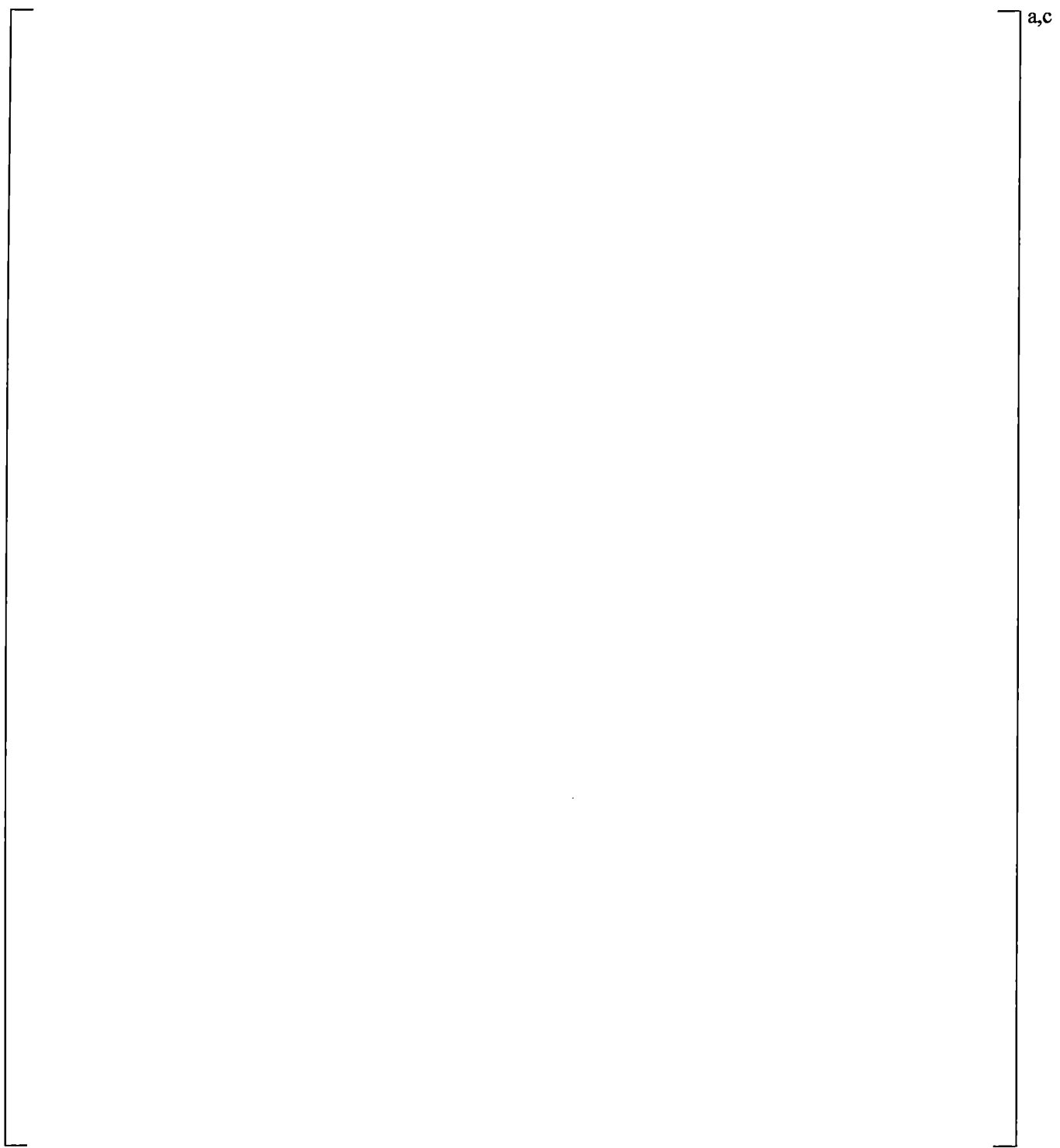


Figure 21.15-1 SB-CL-18 Cross-Over Leg A Differential Pressures

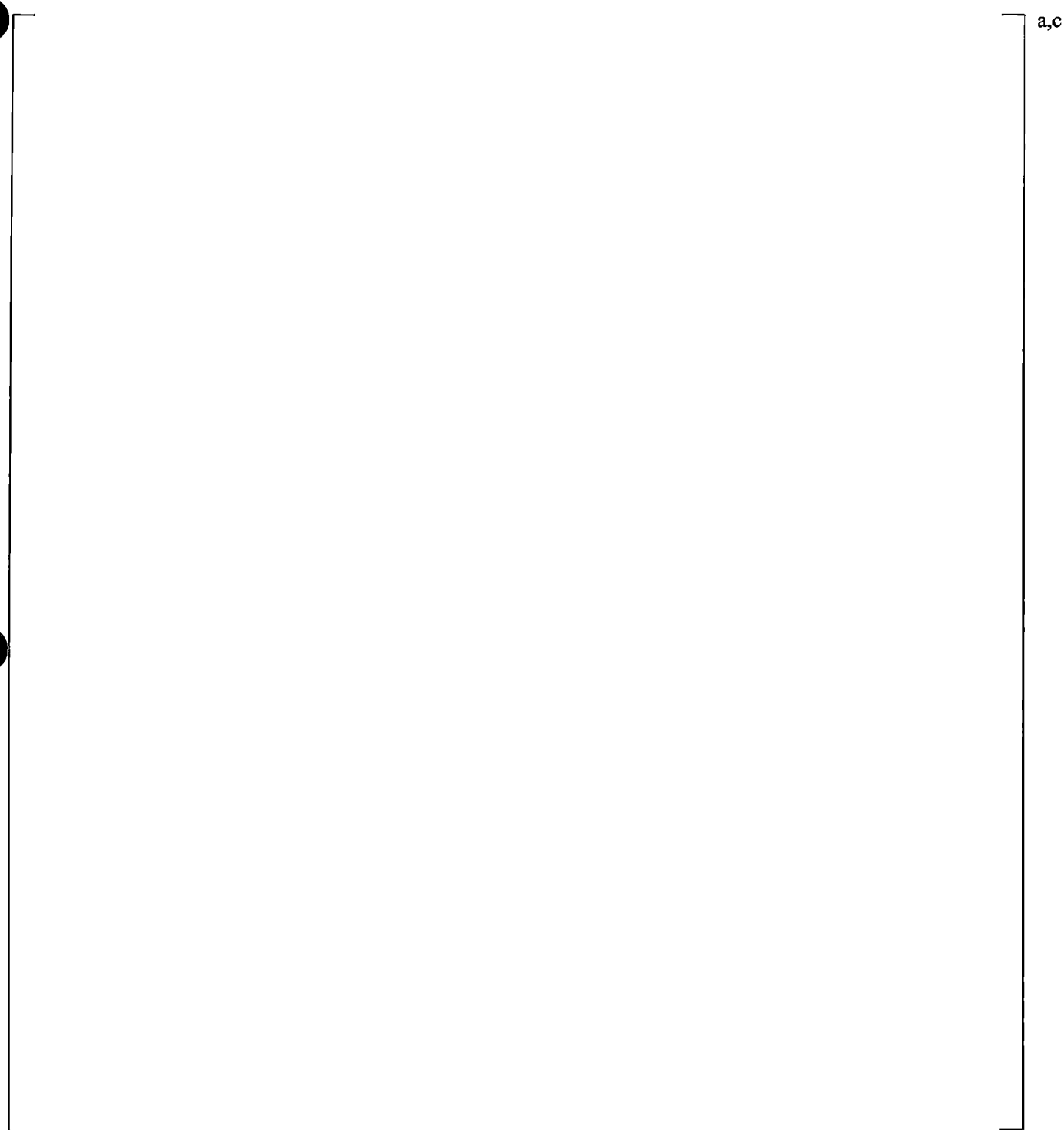


Figure 21.15-2 SB-CL-18 Cross-Over Leg B Differential Pressures

a,c

Figure 21.15-3 Inner Vessel Differential Pressures (LP+Core+UCP)

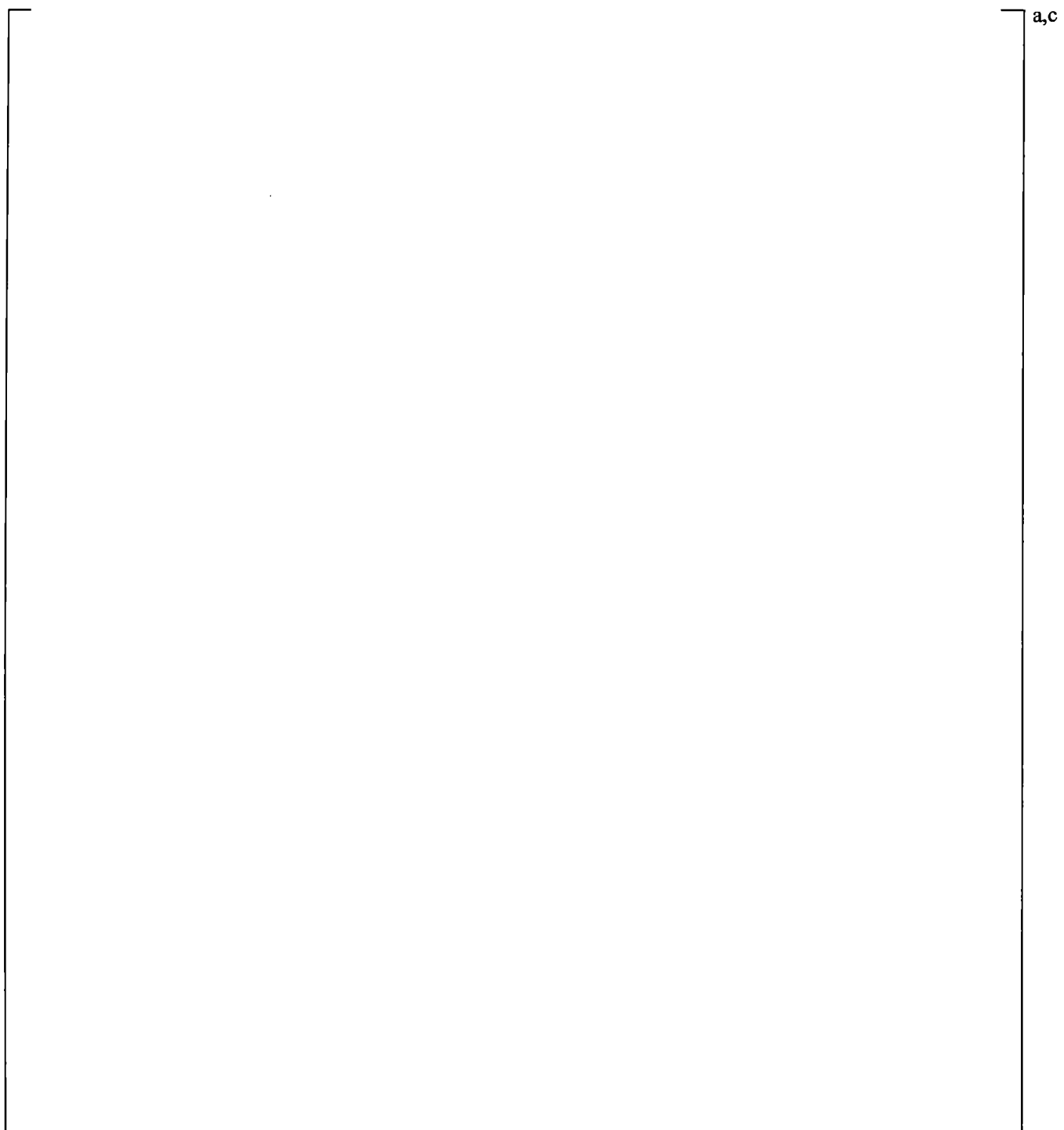


Figure 21.15-4 Upper Plenum Differential Pressures

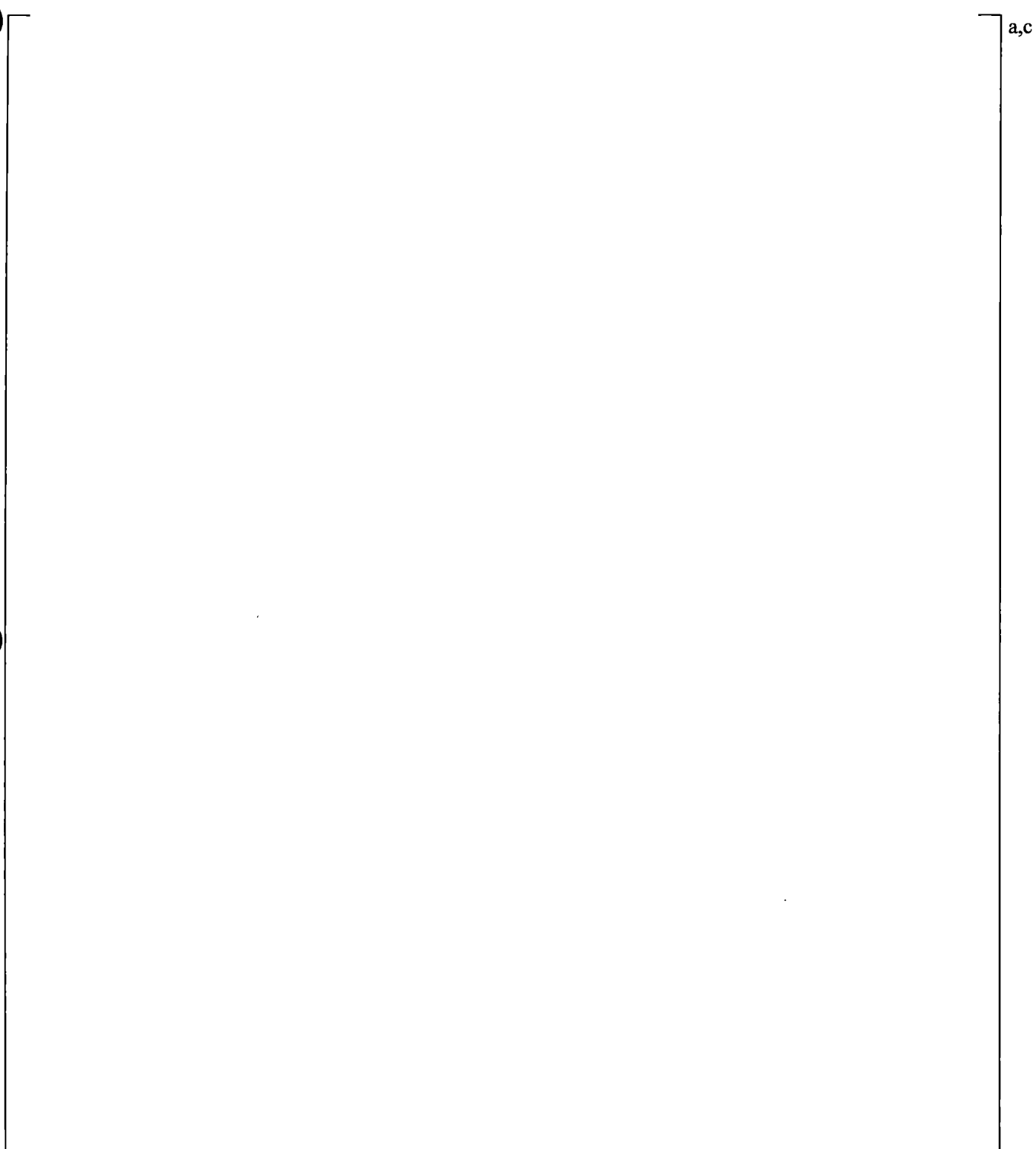


Figure 21.15-5 Downcomer Differential Pressures

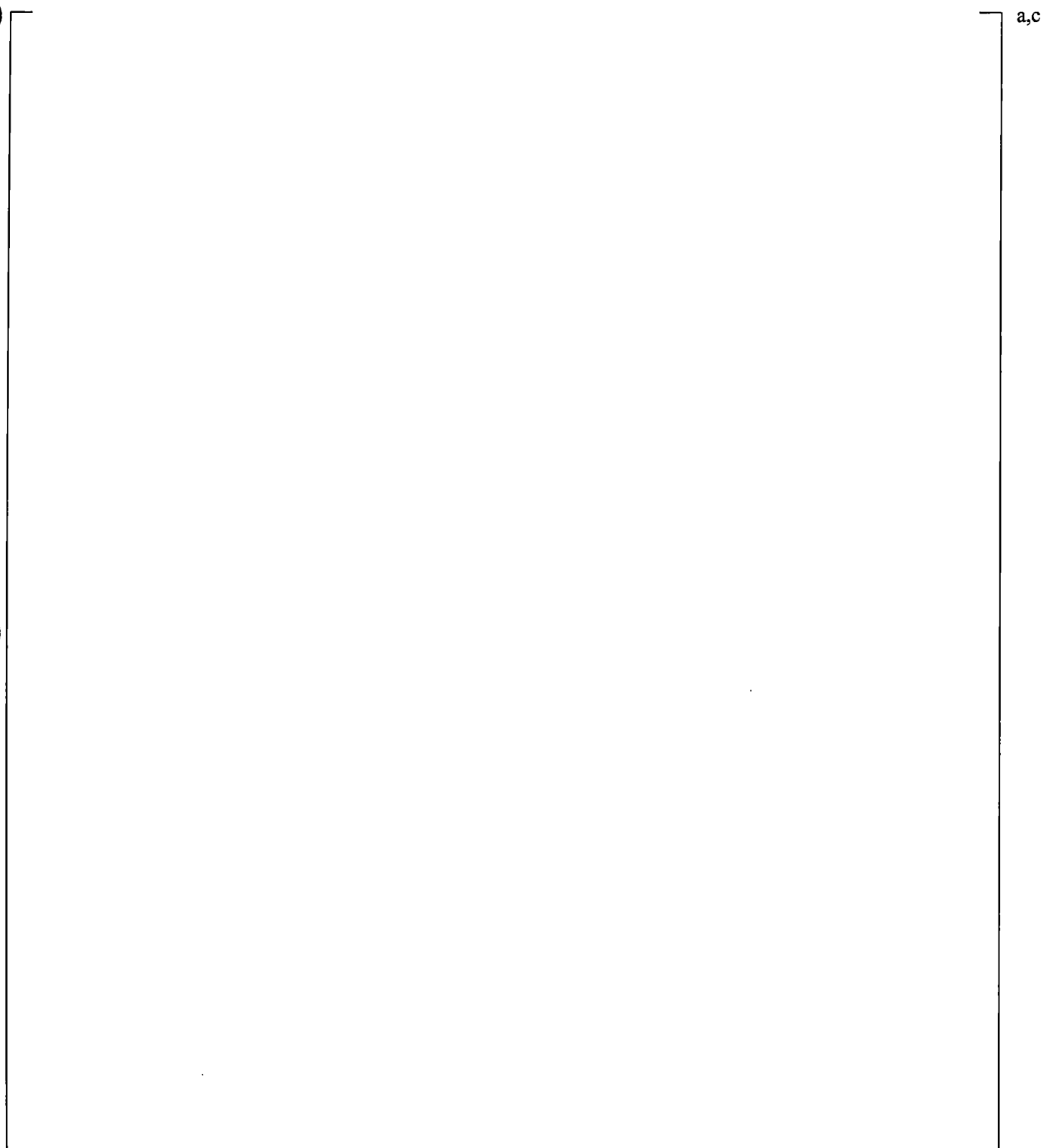


Figure 21.15-6 Peak Cladding Temperatures

21.16 HS_SLUG SENSITIVITY CALCULATIONS

21.16.1 HS_SLUG Sensitivity with 0.5% Side Break Test SB-CL-16

HS_SLUG sensitivity calculations were performed with the 0.5% side cold leg break test SB-CL-16. In these calculations, the HS_SLUG multiplier was set at the maximum []^{a,c} and minimum []^{a,c} values. The results of these calculations are shown in Figures 21.16.1-1 through 21.16.1-10.

| As seen in Figure 21.16.1-1, the break discharge flow was not affected much by the HS_SLUG variation. The timing of the transition from sub-cooled to two-phase and later to pure steam break flow was not affected much as well. As a result, the predicted system pressure response remains unaffected, as seen in Figure 21.16.1-2.

| An asymmetry is observed in the calculated draining of the steam generators, Figure 21.16.1-3. However, if we ignore the asymmetry, the timing when the individual steam generators are completely drained is similar.

The calculated loop seal clearance in the individual cross-over legs, Figures 21.16.1-4 and 21.16.1-5, shows that an asymmetry exists in the calculated differential pressures (SG outlet to bottom), Figures 21.16.1-4(a) and 21.16.1-5(a). This asymmetry can be related to the calculated asymmetry in the steam generator draining, mentioned above.

| The HS_SLUG variation does appear to affect the loop seal clearance. With []^{a,c} loop A does not clear completely, Figure 21.16.1-4, but loop B is predicted to clear, Figure 21.16.1-5. With []^{a,c} loop A clears better, Figure 21.16.1-4, but loop B does not clear, Figure 21.16.1-5. A precursor of this asymmetry appears to be the steam generator draining asymmetry discussed above.

The calculated downcomer differential pressures, Figure 21.16.1-6, and upper plenum differential pressures, Figure 21.16.1-7, are not affected by the HS_SLUG variation as well.

Asymmetry is observed in the calculated hot leg differential pressures, Figure 21.16.1-8, which can be related to the calculated asymmetrical draining of the steam generators, Figure 21.16.1-3.

The asymmetrical steam generator and loop seal clearance behavior, caused by the HS_SLUG variation, does not however affect the calculated core uncover, Figure 21.16.1-9, and the related rod heatup, Figure 21.16.1-10.

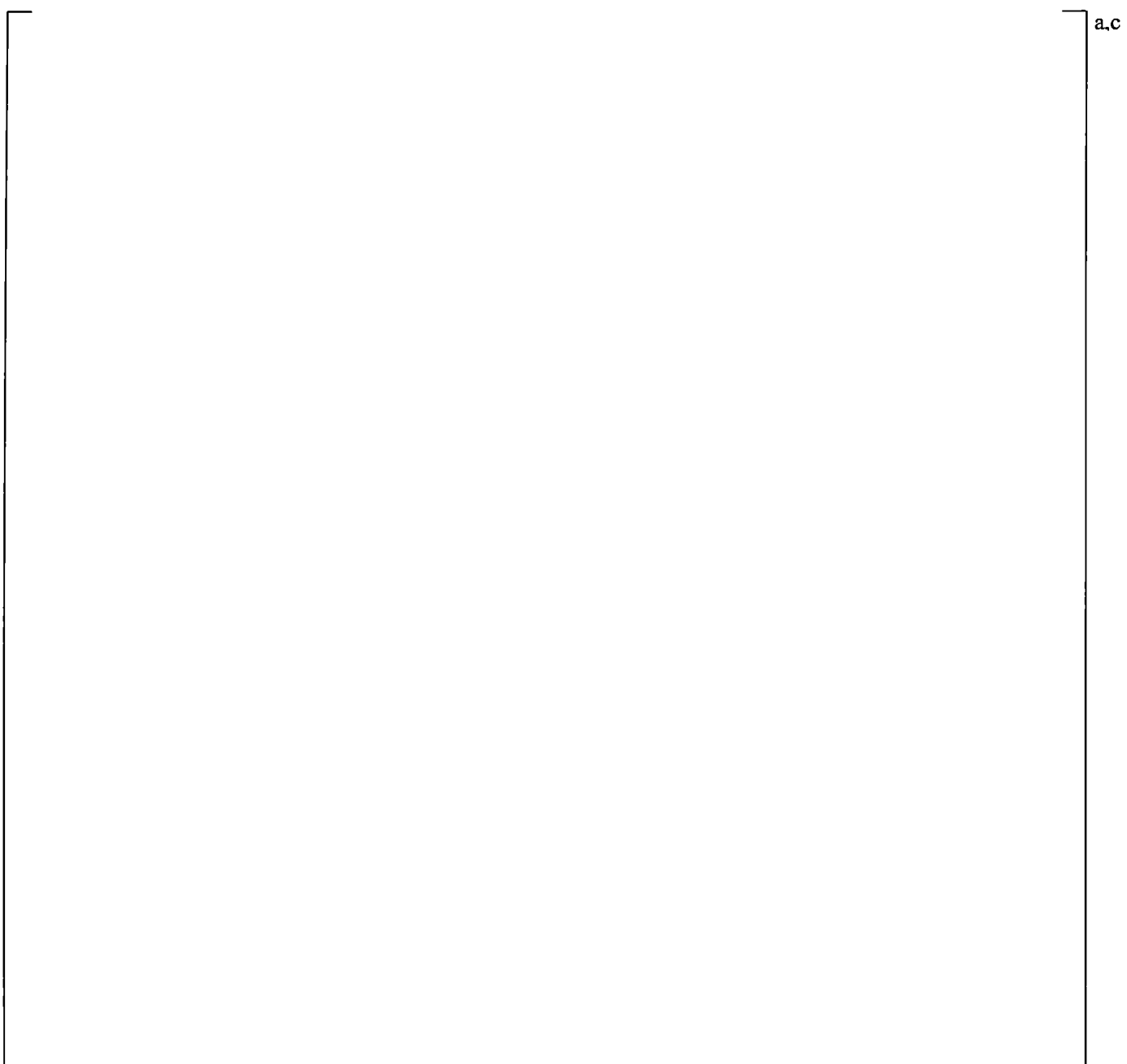
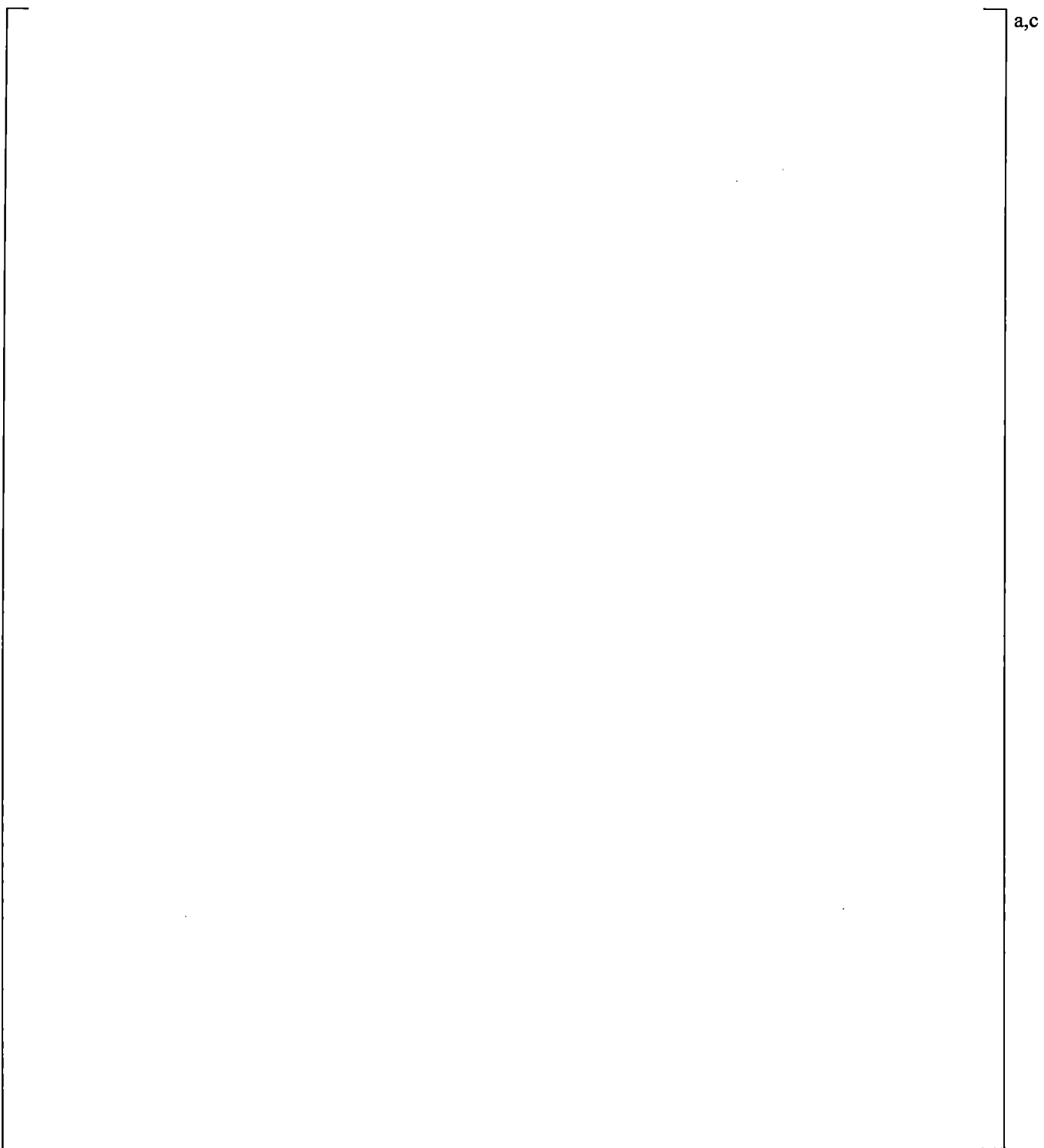


Figure 21.16.1-1 Calculated Break Flow Rates



| **Figure 21.16.1-2 Calculated Pressurizer and Steam Generator Secondary Pressures**

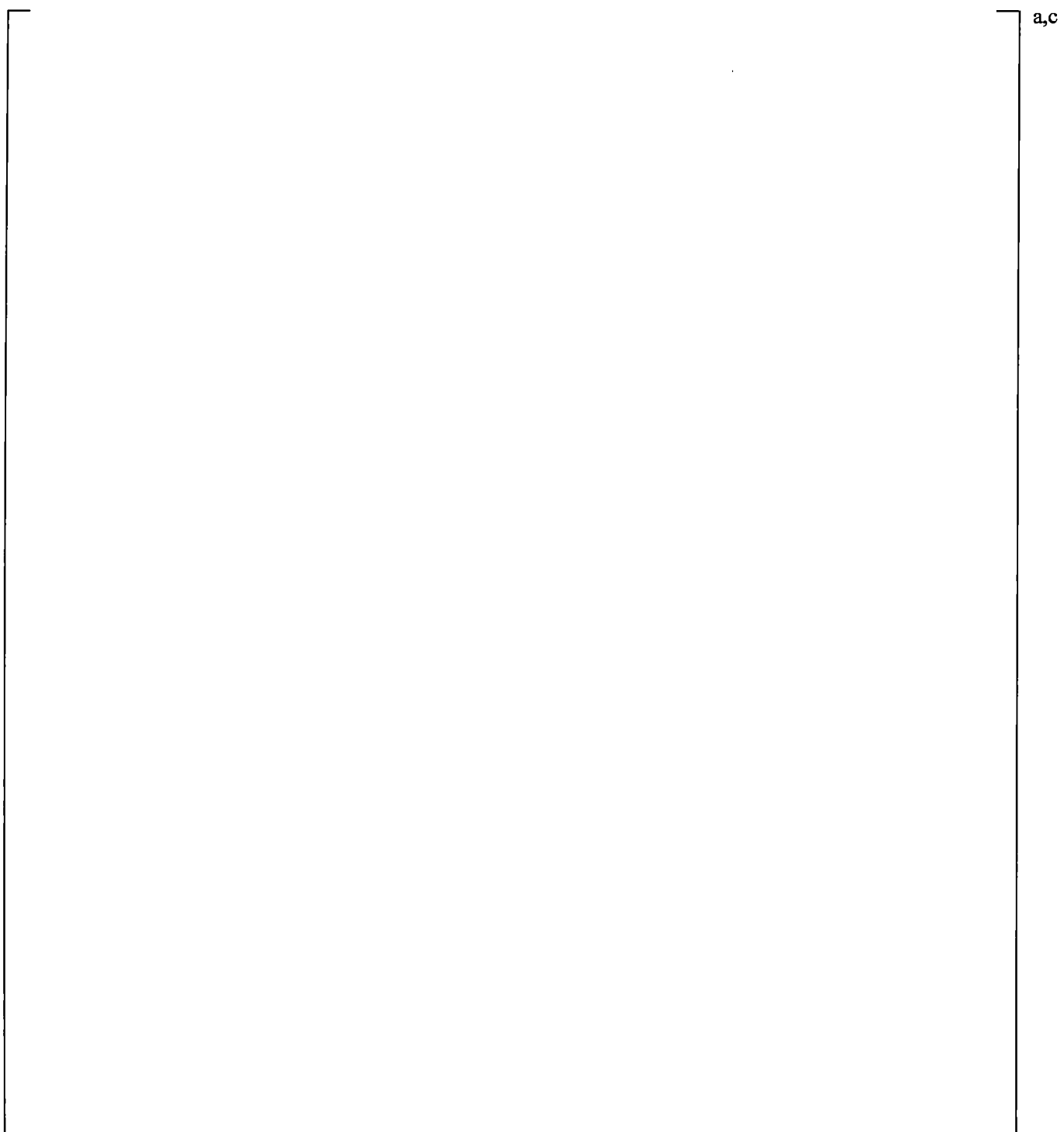


Figure 21.16.1-3 Calculated Steam Generator U-tube Uphill Side Differential Pressures

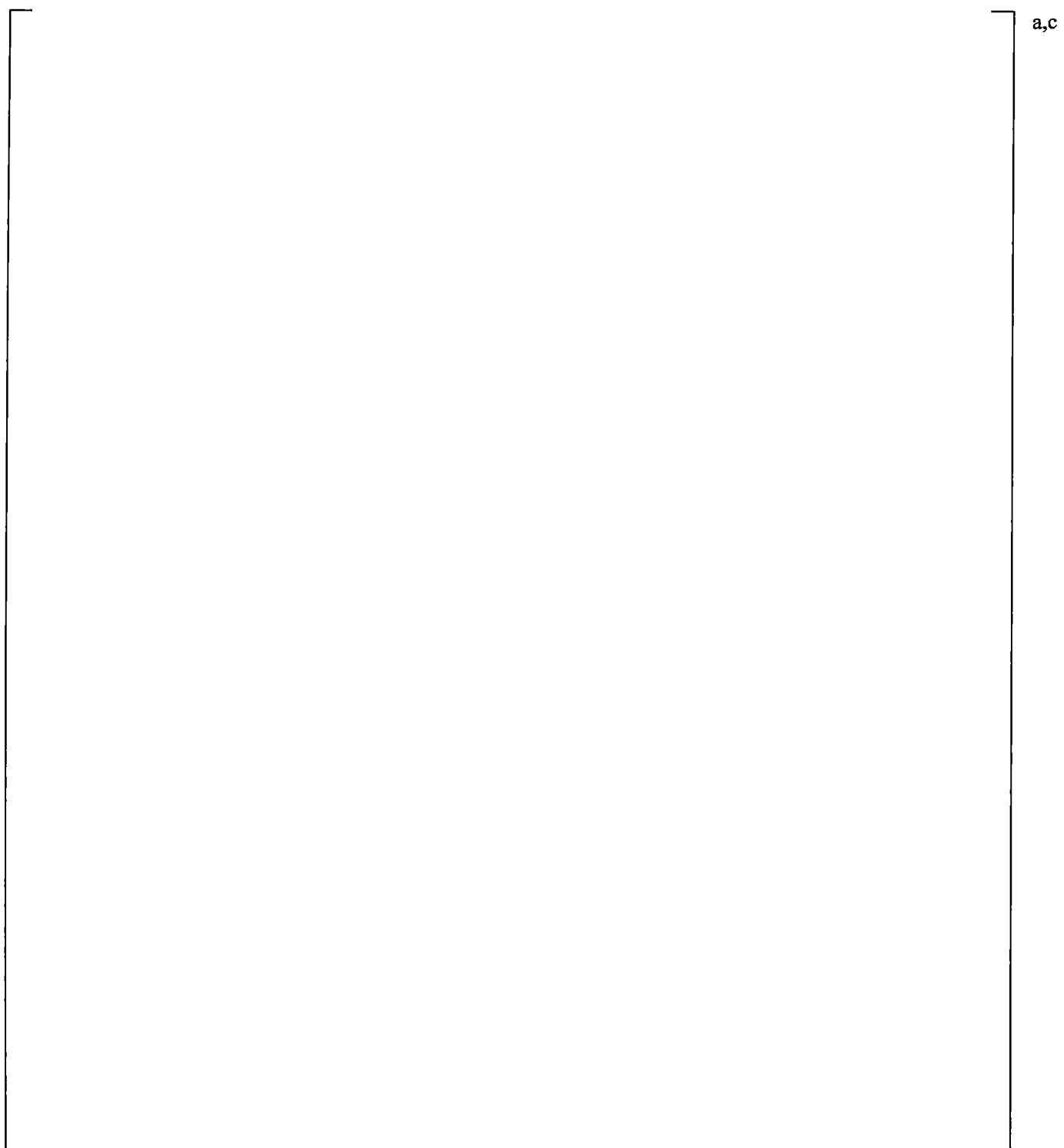


Figure 21.16.1-4 Calculated Cross-Over Leg A Differential Pressures

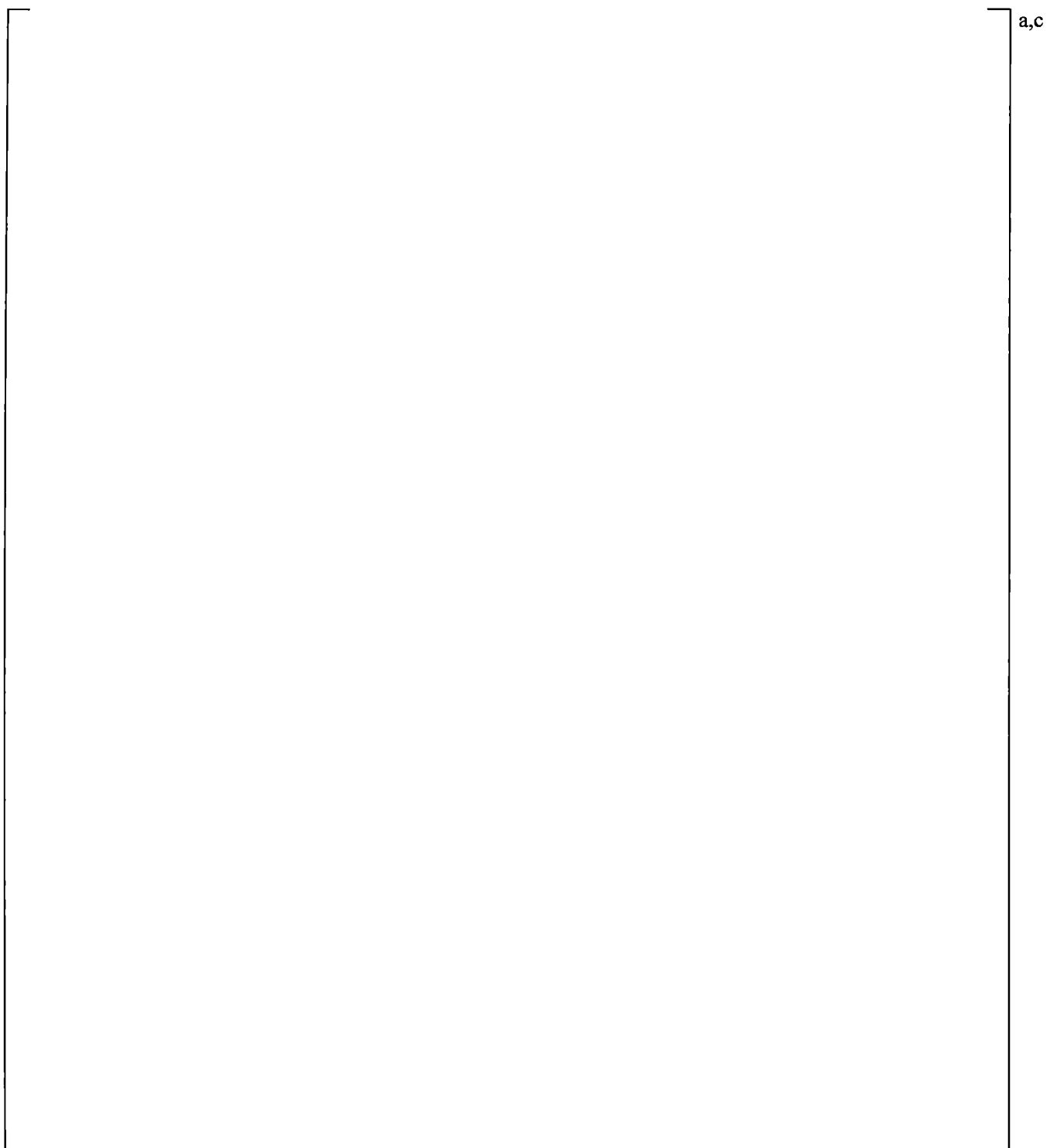


Figure 21.16.1-5 Calculated Cross-Over Leg B Differential Pressures



Figure 21.16.1-6 Calculated Downcomer Differential Pressures



Figure 21.16.1-7 Calculated Upper Plenum Differential Pressures

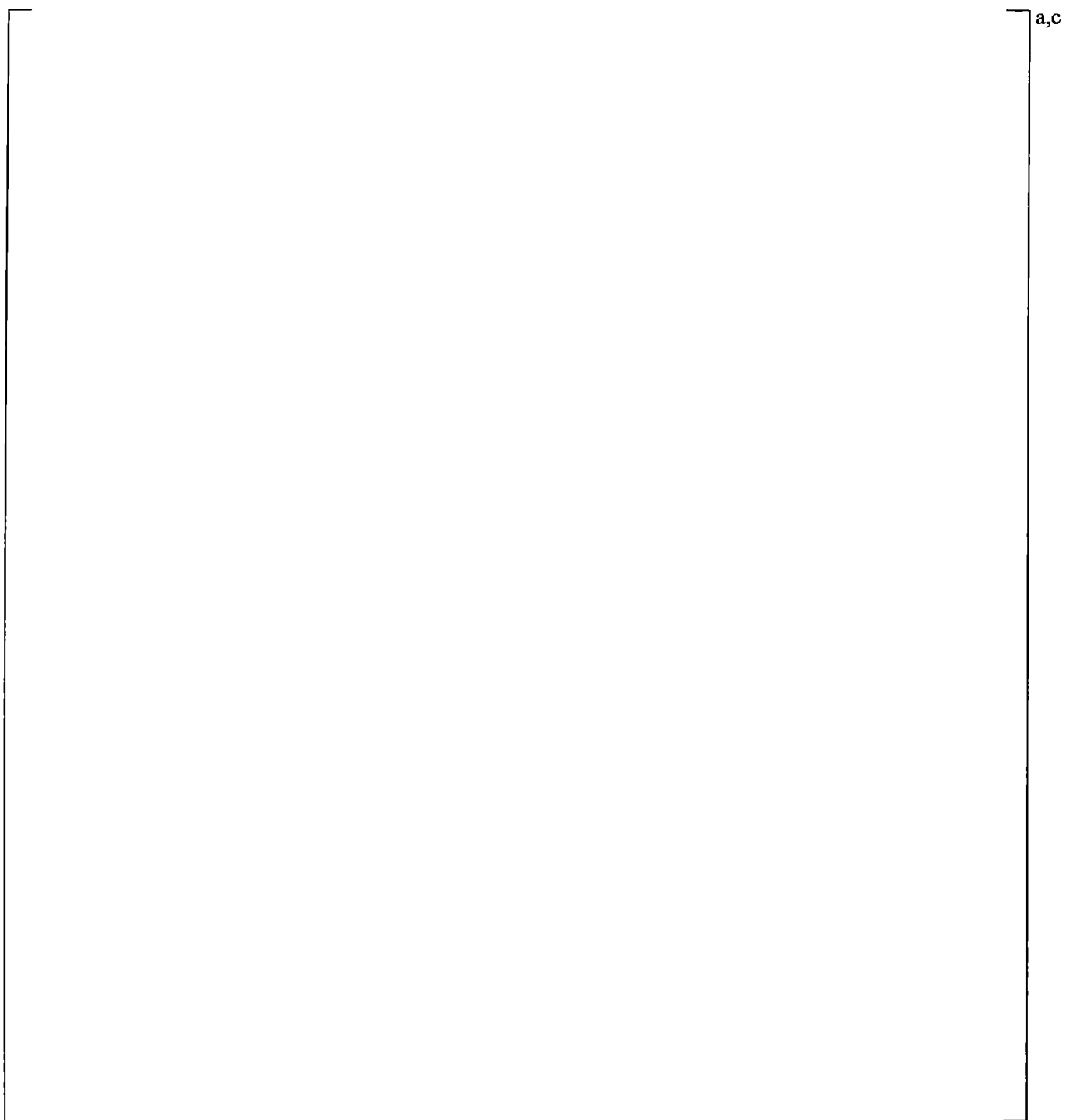


Figure 21.16.1-8 Calculated Hot Leg Differential Pressures



Figure 21.16.1-9 Calculated Core Differential Pressures



Figure 21.16.1-10 Calculated Peak Cladding Temperatures

21.16.2 HS_SLUG Sensitivity with the 5% Top Break test SB-CL-18

Two simulations of the 5% side break test SB-CL-18 test were performed with setting the HS_SLUG multiplier at its maximum []^{a,c} and minimum []^{a,c} values.

The results of these simulations are shown in Figures 21.16.2-1 through 21.16.2-10.

With []^{a,c} the predicted break flow is mostly unaffected, but the transition to two-phase is predicted to occur slightly earlier, Figure 21.16.2-1. The system pressure response, Figure 21.16.2-2, is not significantly affected by the HS_SLUG variation.

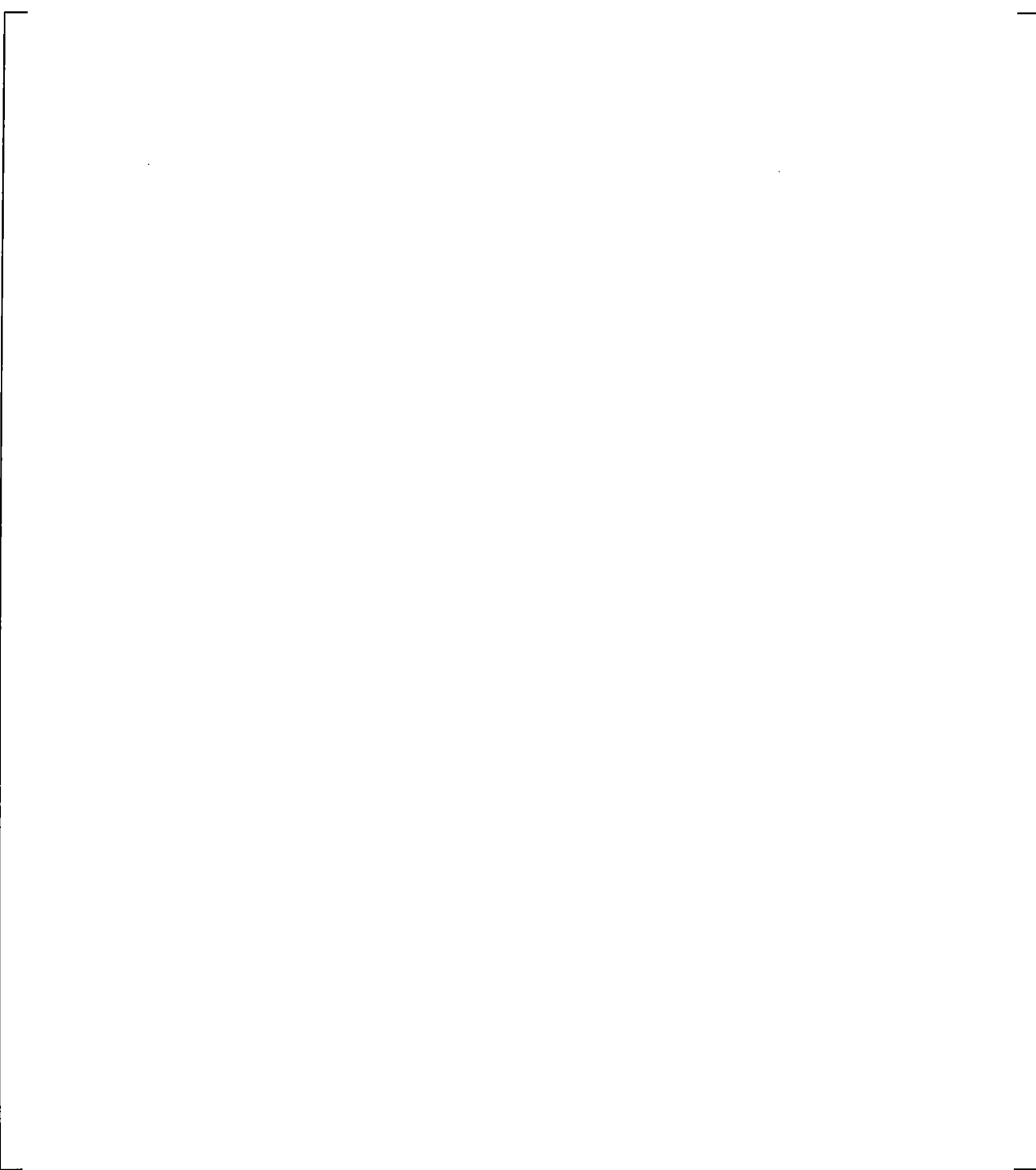
The calculated steam generator draining is very similar as well, Figure 21.16.2-3.

The calculated differential pressures in the cross-over legs (bottom to pump inlet), Figures 21.16.2-4 and 21.16.2-5, do not appear to be affected by the HS_SLUG variation with the timing of the loop seal clearance predicted almost identical.

The calculated upper plenum differential pressures are not affected much by the HS_SLUG variation, Figure 21.16.2-7, as well as the predicted hot leg differential pressures, Figure 21.16.2-8.

The downcomer differential pressure appears to be affected by the HS_SLUG variation, Figure 21.16.2-6. The higher downcomer differential pressure (or level) calculated with []^{a,c} can be attributed to the predicted earlier transition to two-phase break flow; this is less loss of inventory, hence higher downcomer level. As a result, the effect of on the calculated core differential pressures, Figure 21.16.2-9, is a delayed onset of boiloff (due to the higher downcomer driving head) and, as a result, less boiloff heatup with []^{a,c}, Figure 21.16.2-10.

The overall results, however, show that the effect of the HS_SLUG variation on the predicted system behavior in the SB-CL-18 simulation is []^{a,c}



a,c

Figure 21.16.2-1 Calculated Break Flow Rates

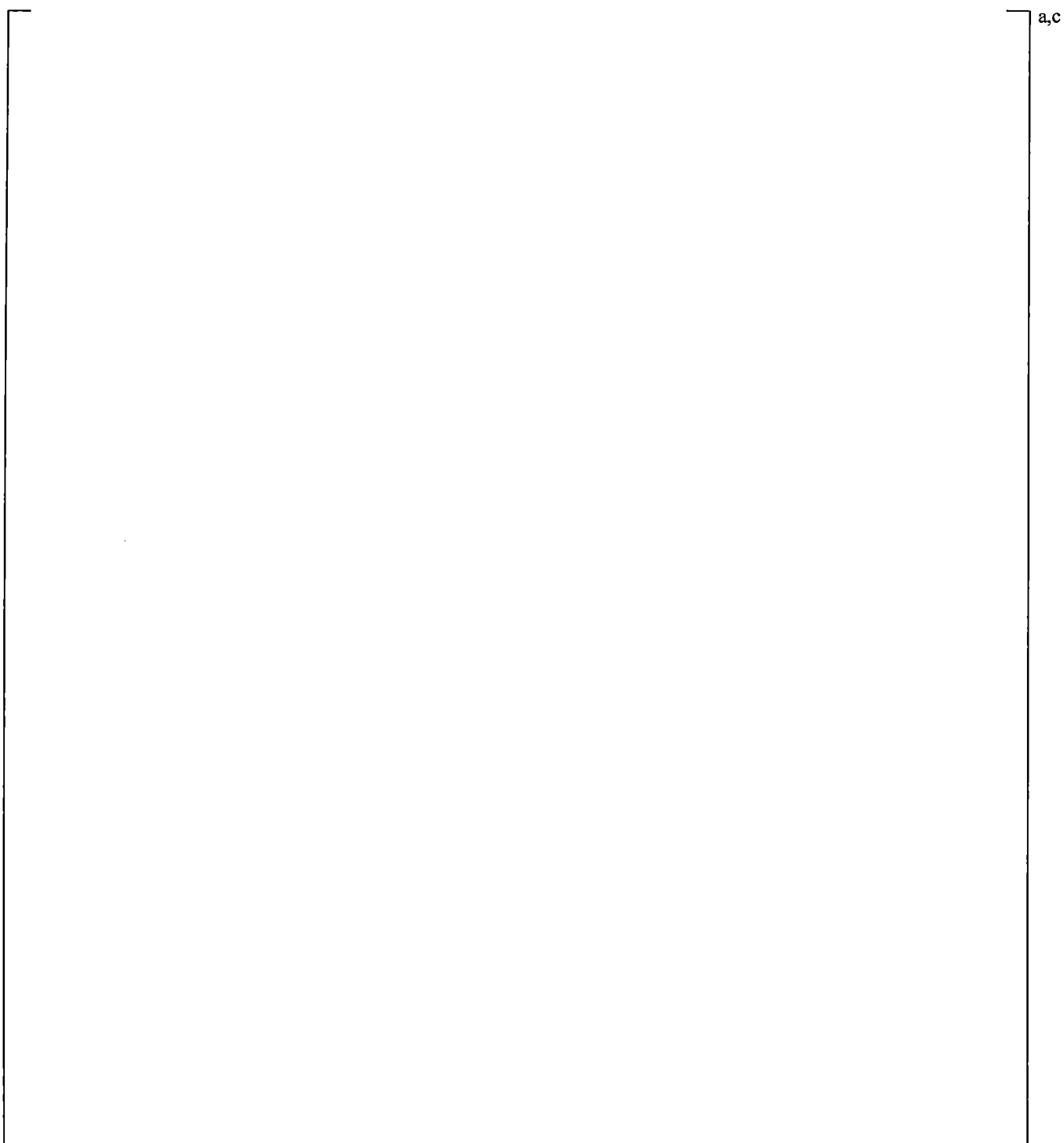
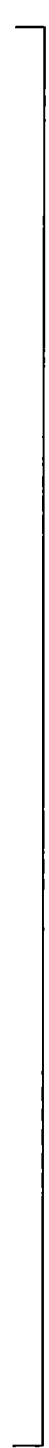


Figure 21.16.2-2 Calculated Pressurizer and Steam Generator Secondary Pressures



a,c

Figure 21.16.2-3 Calculated Steam Generator U-tube Uphill Side Differential Pressures

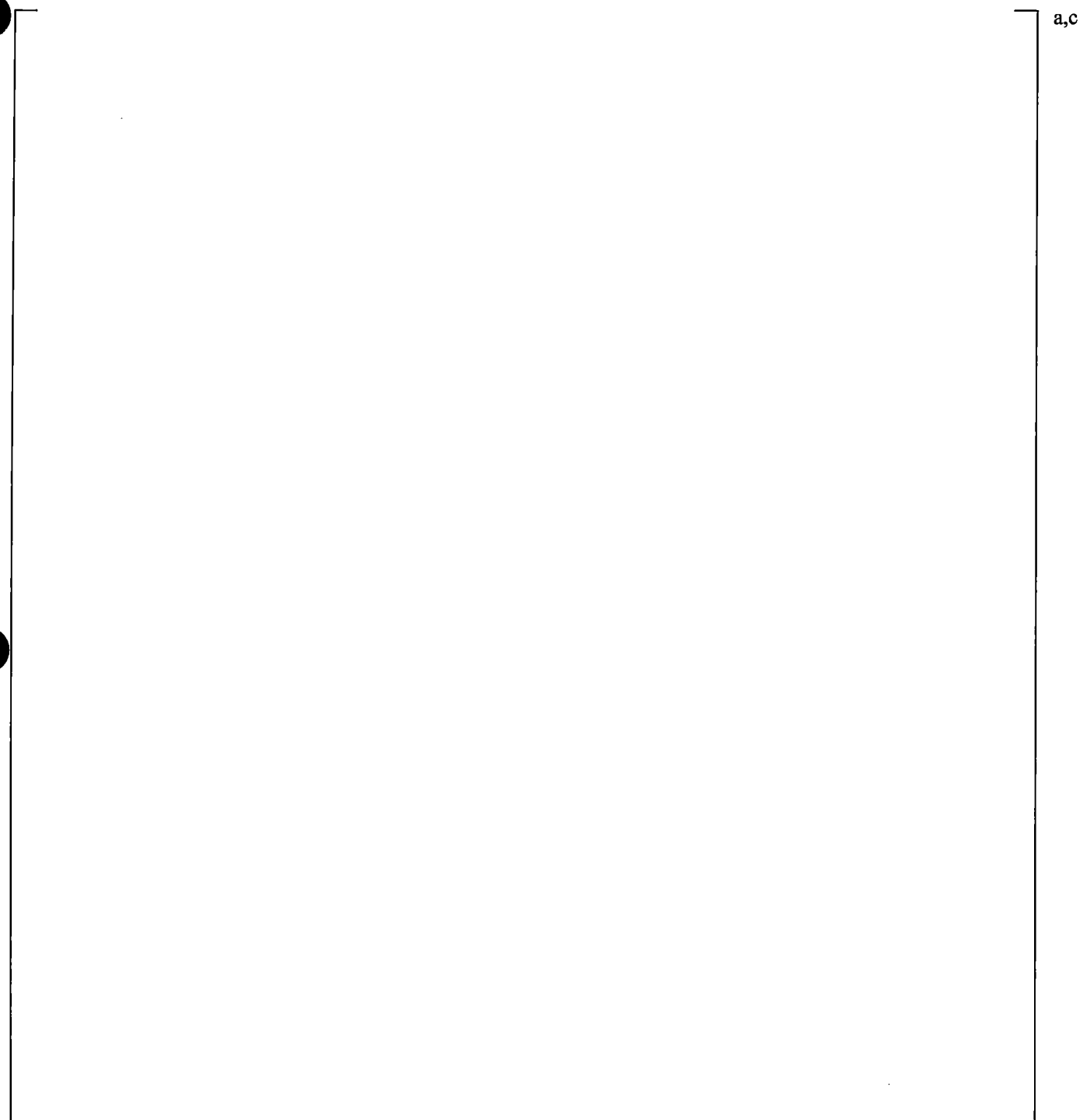


Figure 21.16.2-4 Calculated Cross-Over Leg A Differential Pressures

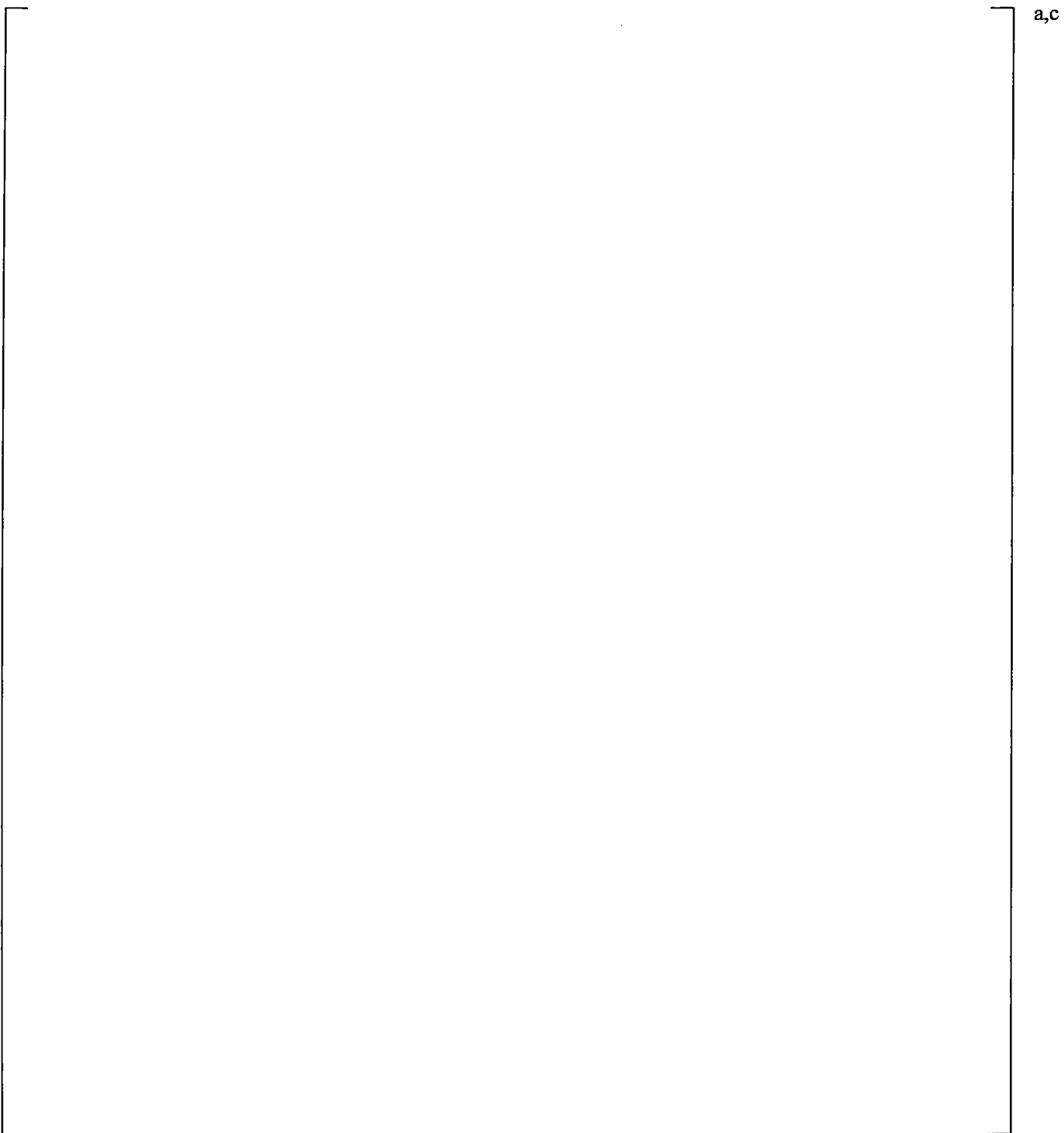


Figure 21.16.2-5 Calculated Cross-Over Leg B Differential Pressures



a,c



Figure 21.16.2-6 Calculated Downcomer Differential Pressures



a,c



Figure 21.16.2-7 Calculated Upper Plenum Differential Pressures

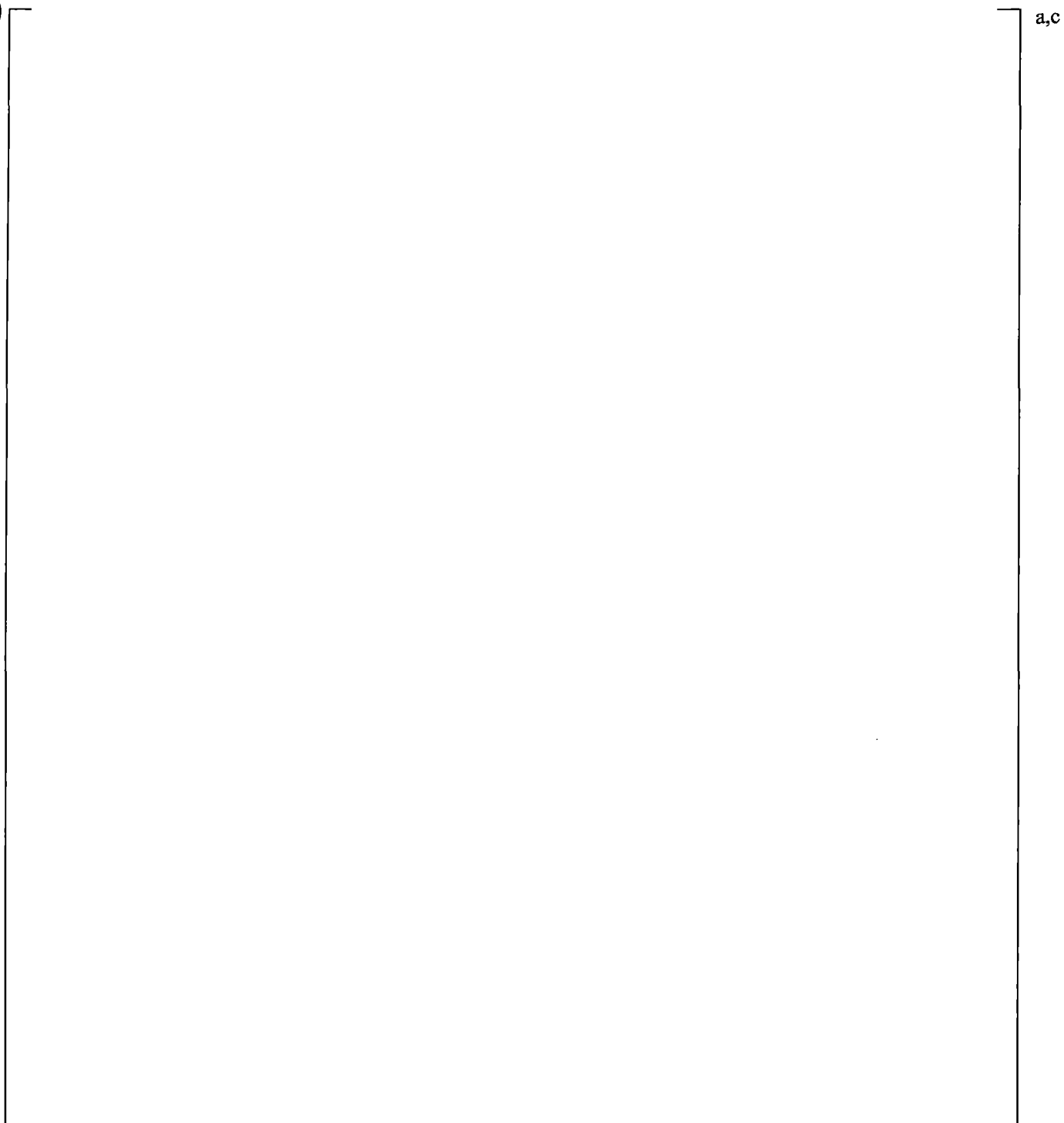
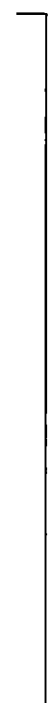
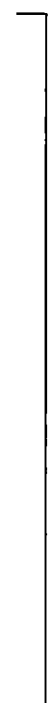


Figure 21.16.2-8 Calculated Hot Leg Differential Pressures



a,c

Figure 21.16.2-9 Calculated Core Differential Pressures



a,c

Figure 21.16.2-10 Calculated Peak Cladding Temperatures

21.16.3 HS_SLUG Sensitivity with 10% Side Break Test SB-CL-14

Two simulations of the 10% side break test SB-CL-14 test were performed with setting the HS_SLUG multiplier at its maximum []^{a,c} and minimum []^{a,c} values.

The results of these simulations are shown in Figures 21.16.3-1 through 21.16.3-10.

The break flow, Figure 21.16.3-1, and system pressure response, Figure 21.16.3-2, are not affected by the HS_SLUG variation. The calculated steam generator draining is almost identical, Figure 21.16.3-3.

The calculated downcomer, upper plenum and hot leg differential pressures are not affected much by the HS_SLUG variation, as shown in Figures 21.16.3-6 through 21.16.3-8.

For the 10% break size the calculated timing of the loop seal clearance is almost identical, Figures 21.16.3-4 and 21.16.3-5. []^{a,c}

[]^{a,c}

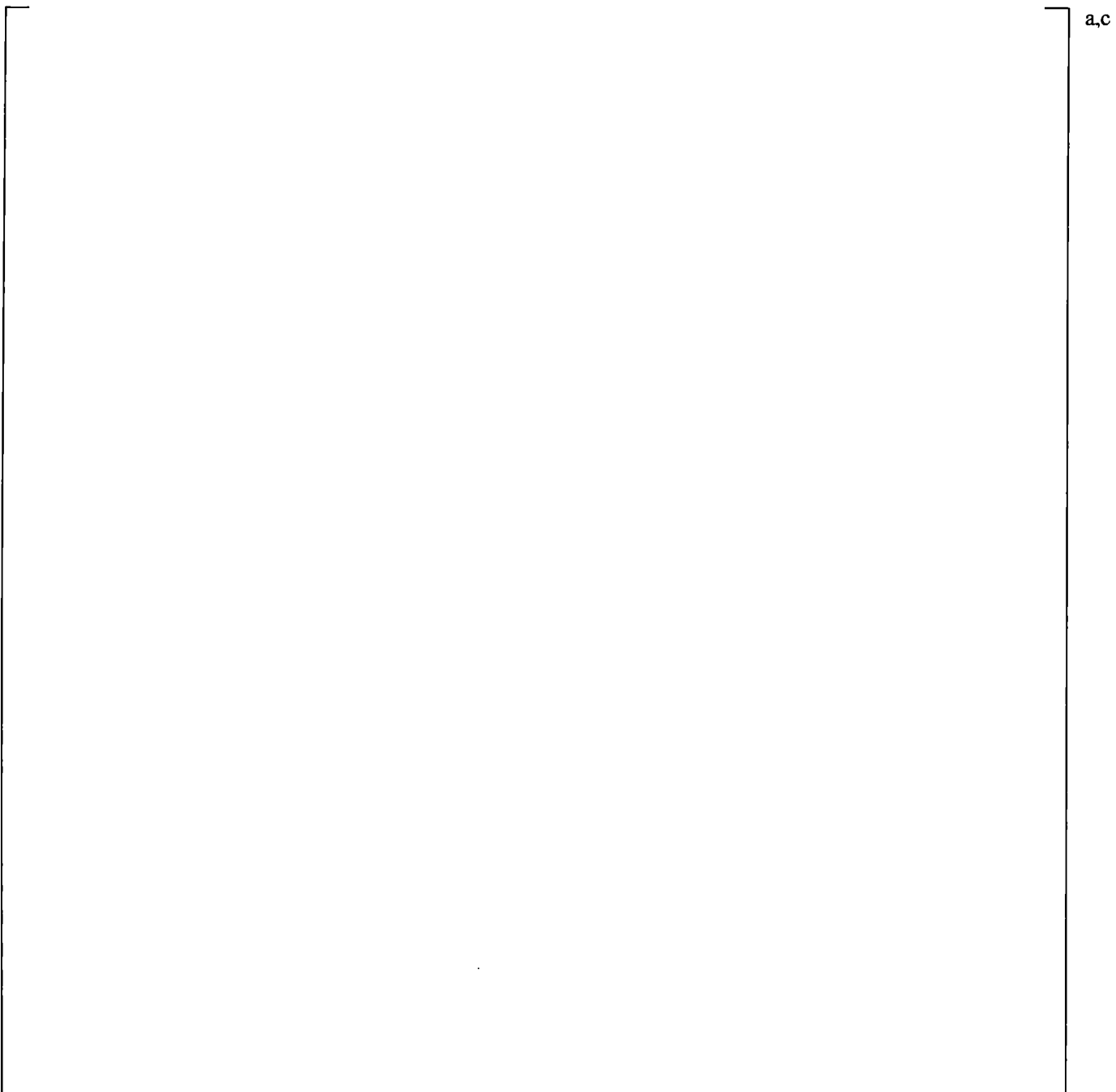


Figure 21.16.3-1 Calculated Break Flow Rates

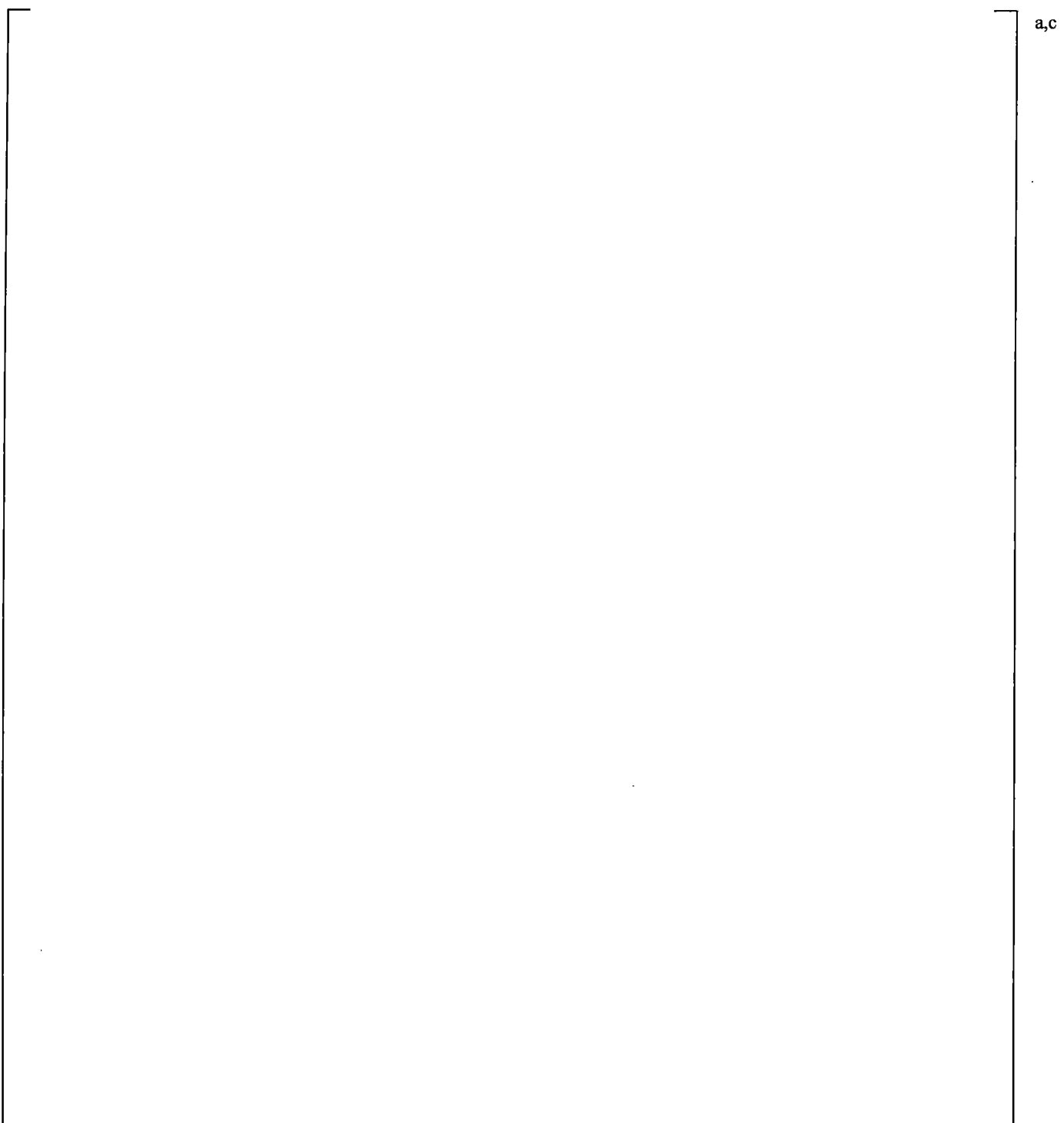


Figure 21.16.3-2 Calculated Pressurizer and Steam Generator Secondary Pressures

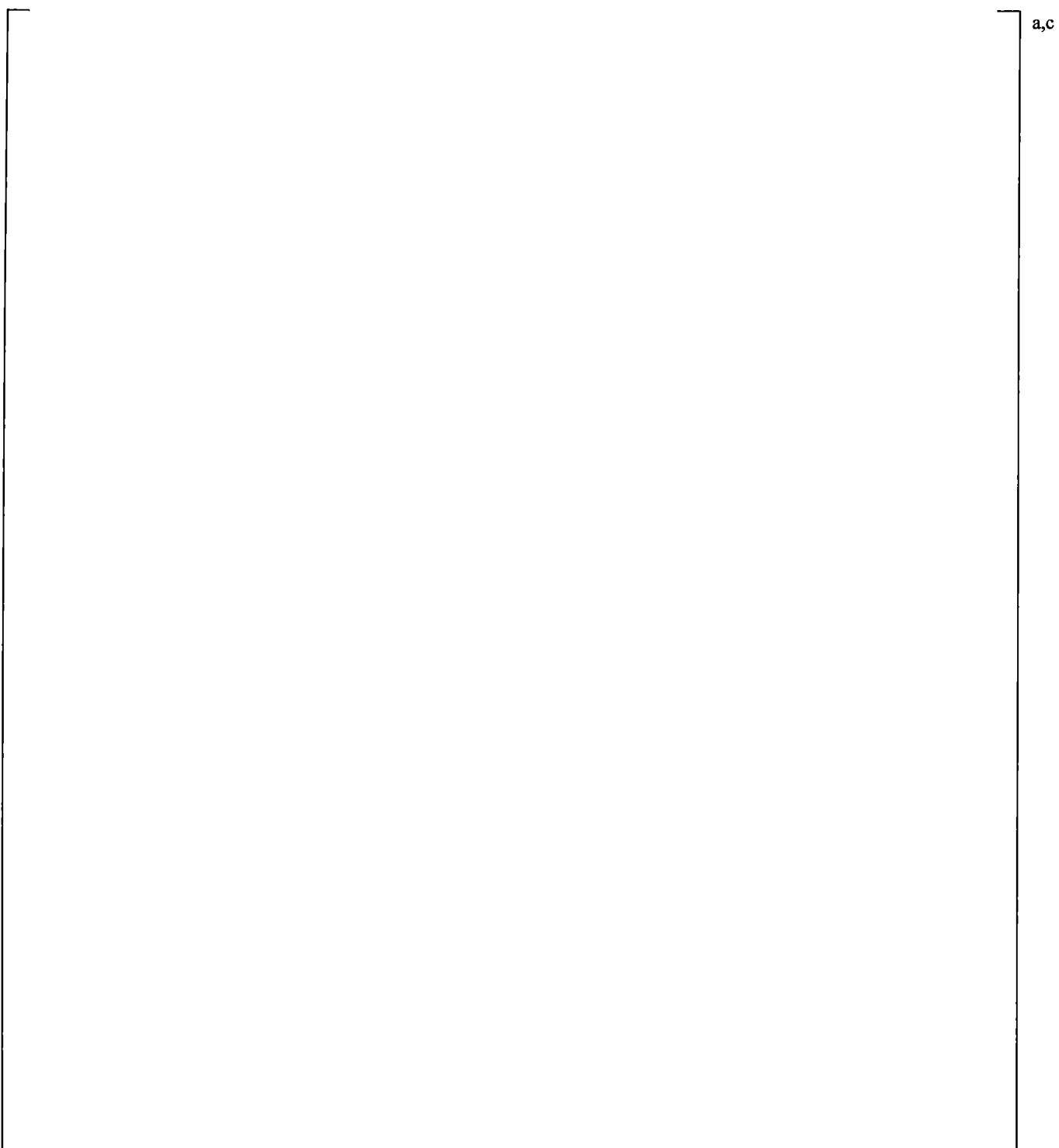
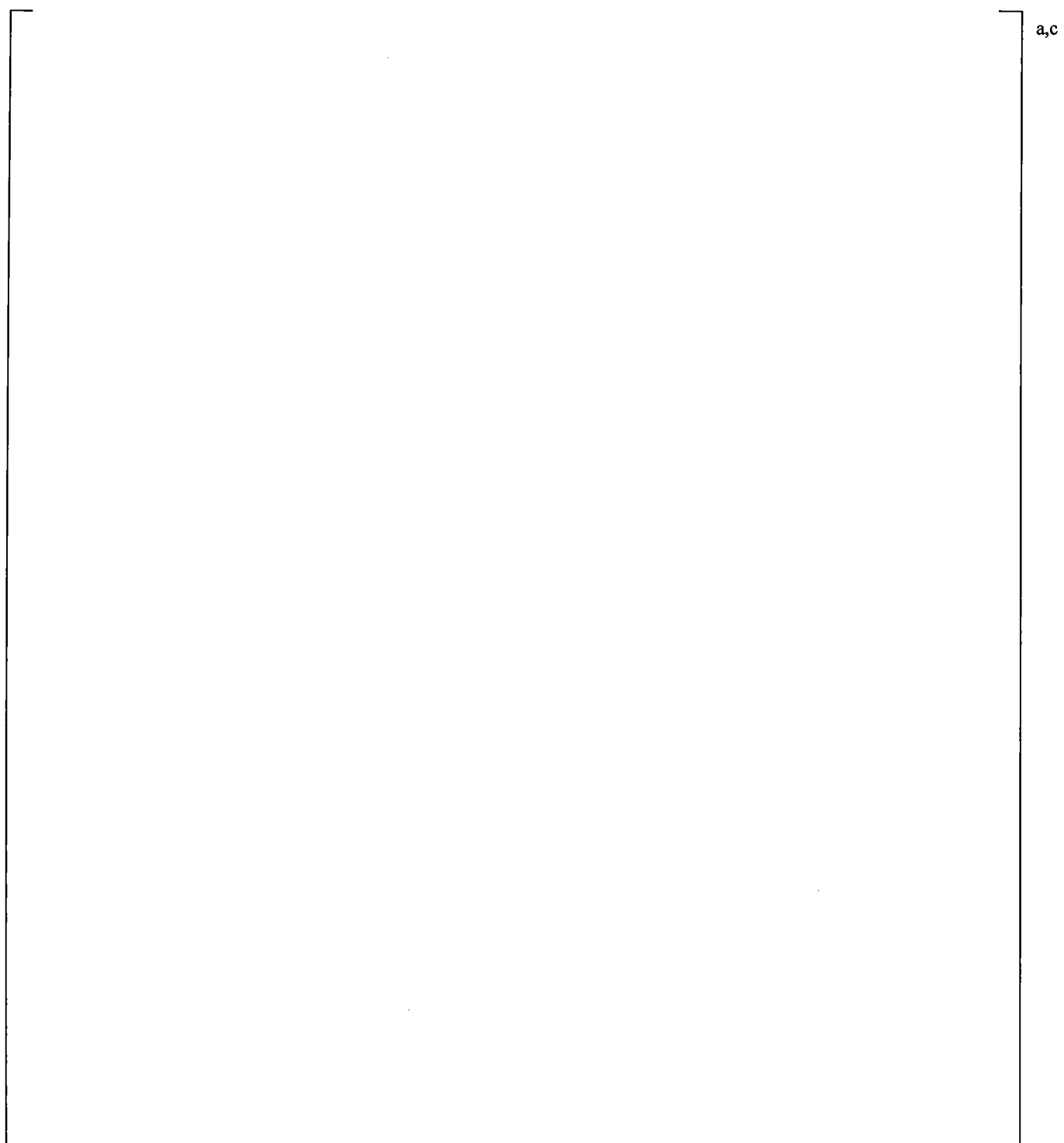


Figure 21.16.3-3 Calculated Steam Generator U-tube Uphill Side Differential Pressures



a,c

Figure 21.16.3-4 Calculated Cross-Over Leg A Differential Pressures

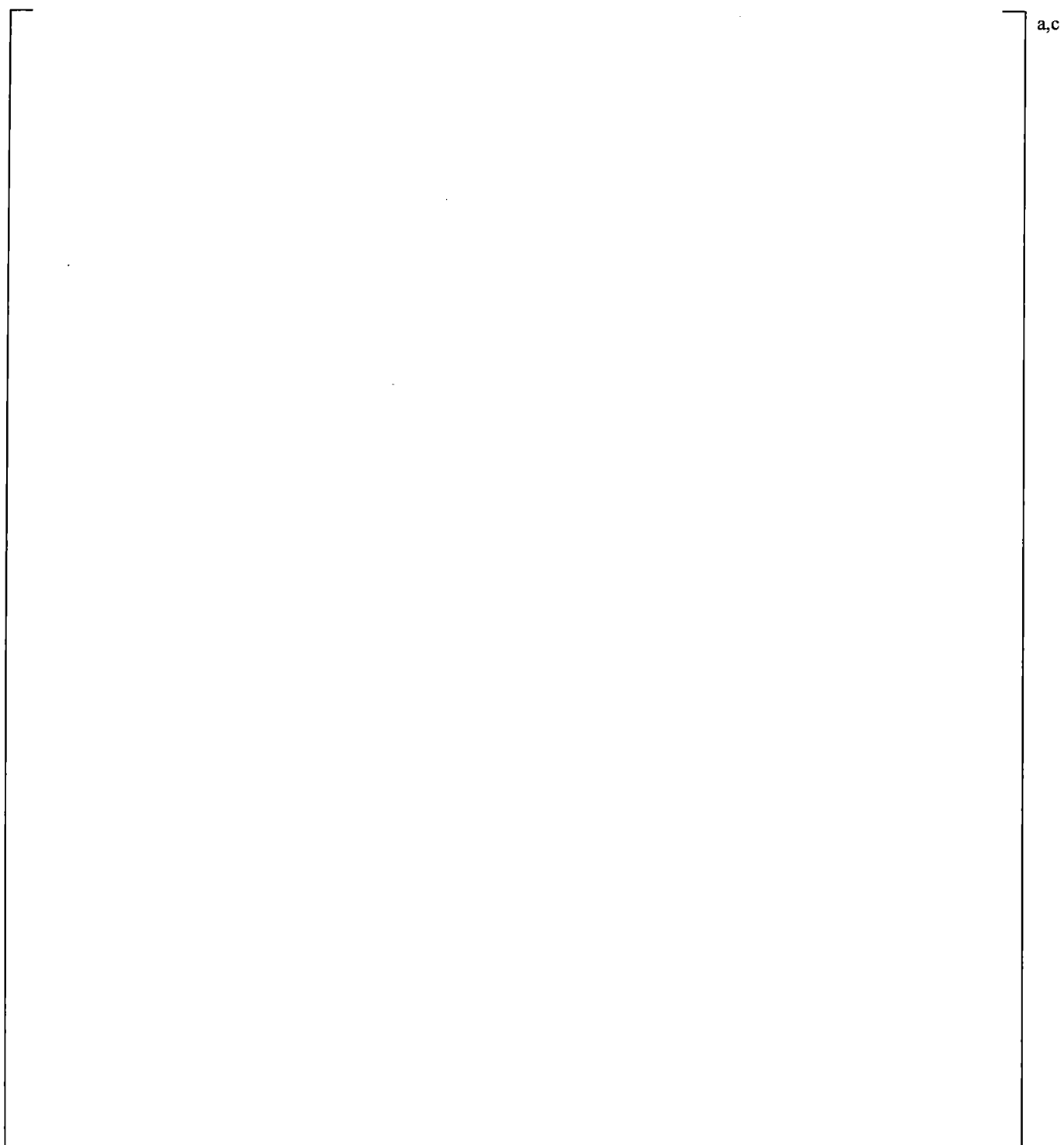


Figure 21.16.3-5 Calculated Cross-Over Leg B Differential Pressures



Figure 21.16.3-6 Calculated Downcomer Differential Pressures



Figure 21.16.3-7 Calculated Upper Plenum Differential Pressures

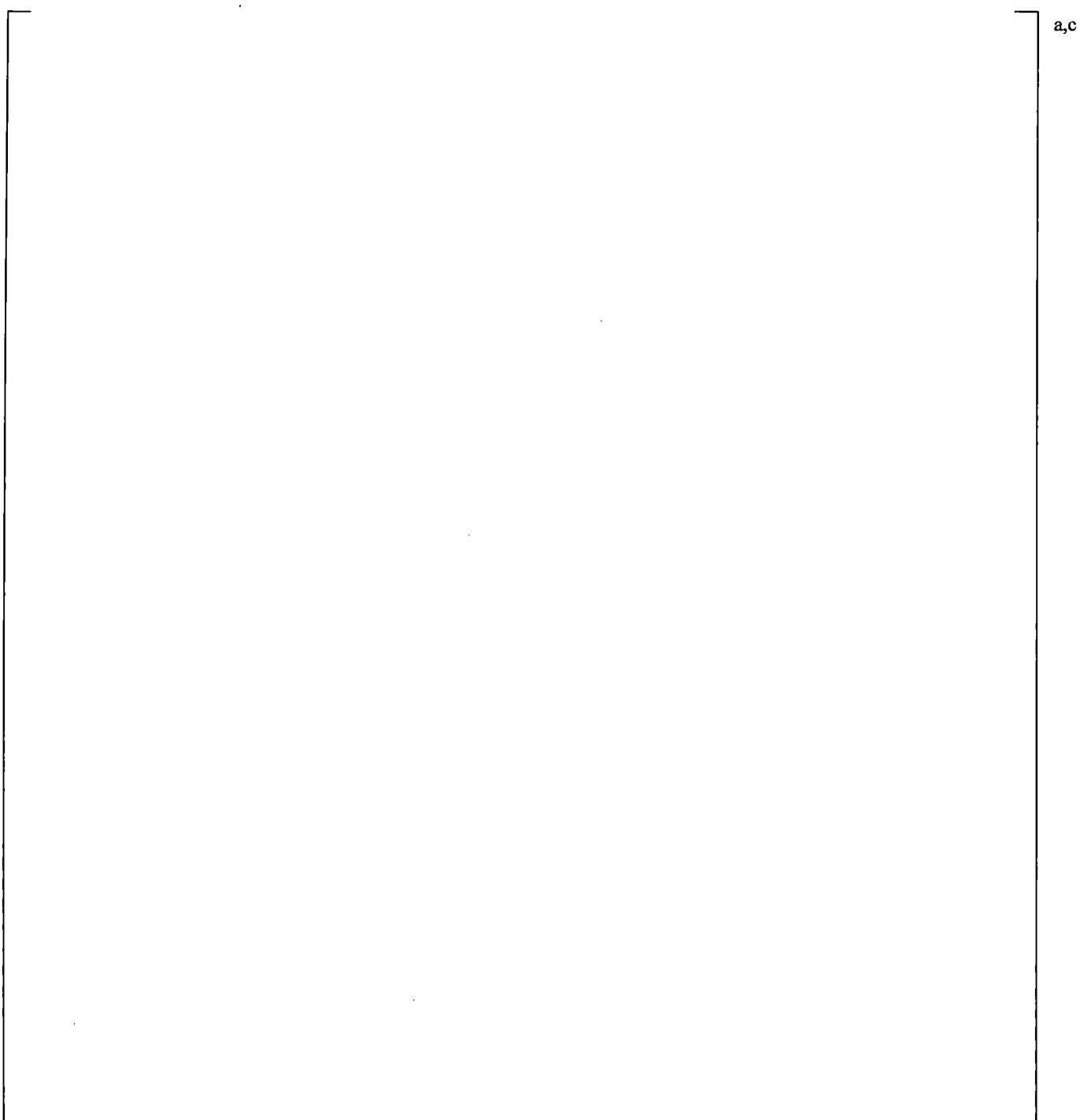


Figure 21.16.3-8 Calculated Hot Leg Differential Pressures



Figure 21.16.3-9 Calculated Core Differential Pressures



Figure 21.16.3-10 Calculated Peak Cladding Temperatures

21.16.4 Conclusion Regarding the HS_SLUG Sensitivity Simulations

Based on the results from the HS_SLUG sensitivity calculations presented herein, it can be concluded that the effect of the HS_SLUG ranging would have minimal effect on the Small Break LOCA transient.

21.17 KCOSI SENSITIVITY CALCULATIONS

This section presents the results of two simulations of the 5% side break test SB-CL-05 (reference case documented in Section 21.5), performed with setting the cold leg condensation multiplier KCOSI at high []^{a,c} and low []^{a,c} values. The results of the sensitivity are presented in Figures 21.17-1 through 21.17-12.

- | With the KCOSI multiplier set at maximum, the code calculates increased liquid present at the SI injection node of the intact cold leg, Figure 21.17-1(a). At the broken cold leg SI injection node the liquid content does not seem to be affected by the KCOSI variation in the intact cold leg, Figure 21.17-1(b).
- | This is explained by the fact that, in this sensitivity, the cold leg condensation model is turned off in the broken cold leg to be consistent with the modeling approach adopted for the PWR simulations, Section 26, Volume 3.

| [

| [

| [

| [

| []^{a,c}

| [

| [

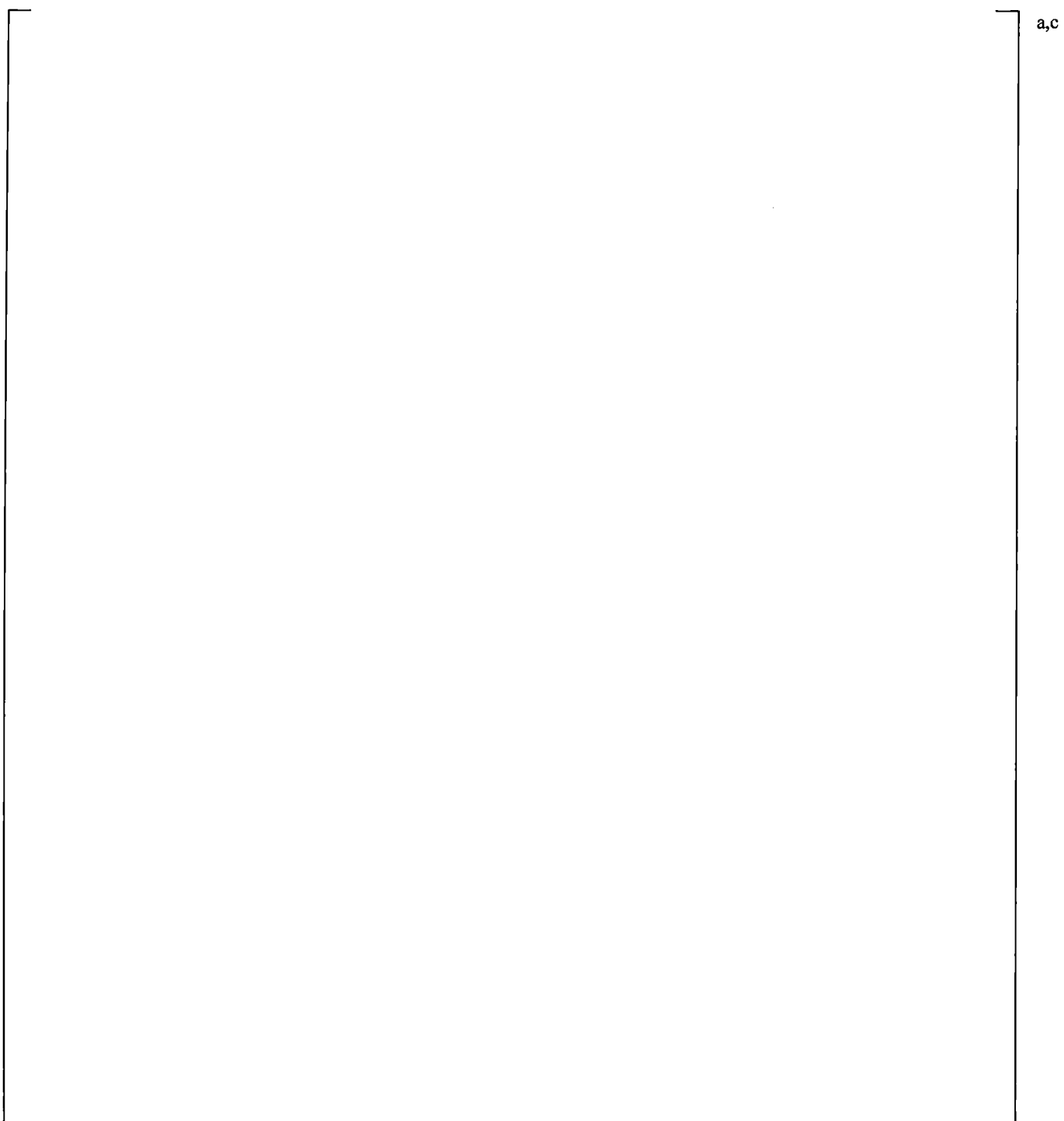


Figure 21.17-1 Cold Leg Void Fractions at the SI Injection Nodes

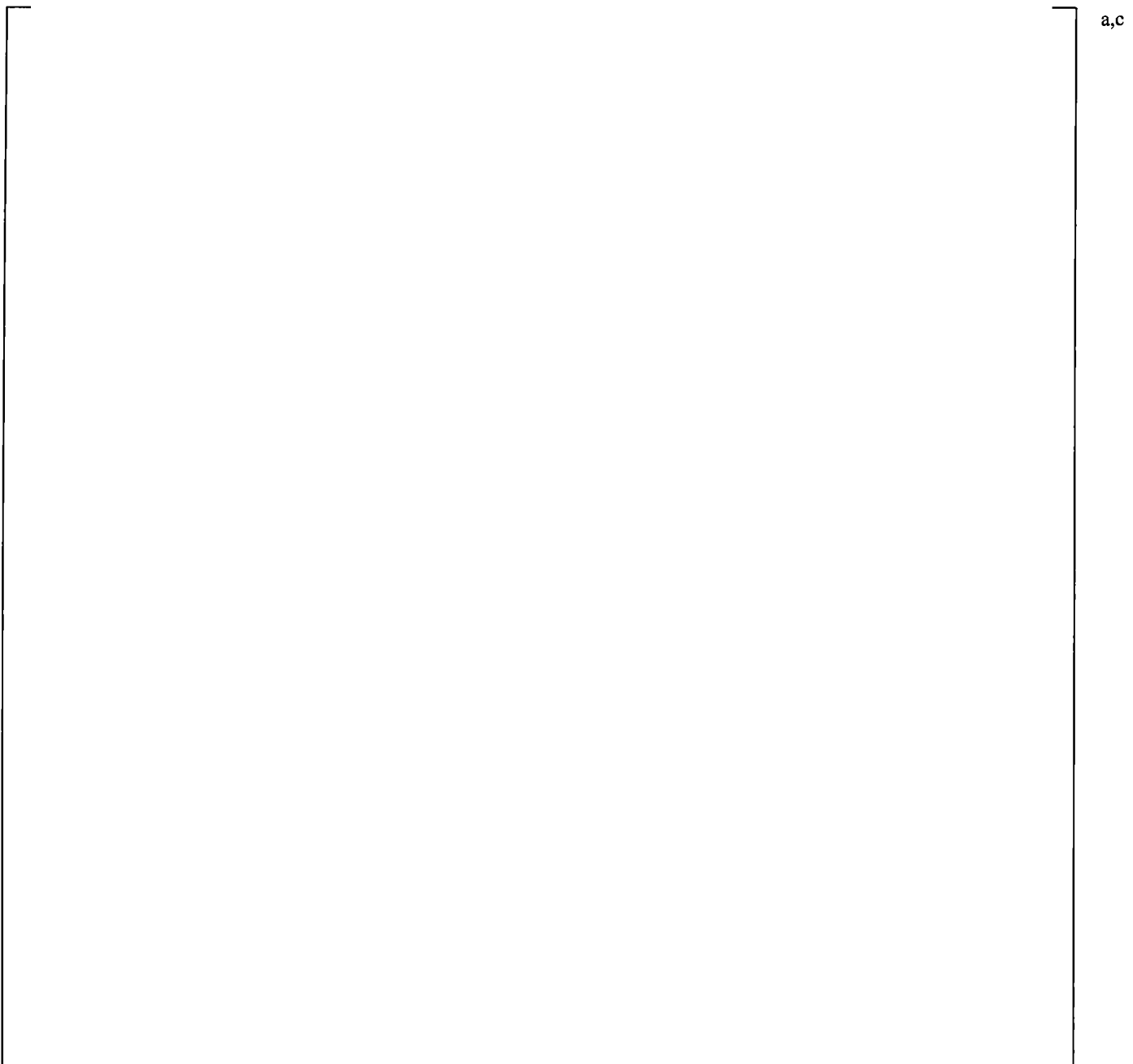


Figure 21.17-2 Mixture Flow at the Broken Cold Leg Nozzle (interface with the vessel)

Note: Negative is flow from the vessel into the cold leg.

a,c



Figure 21.17-3 Total SI Condensation Heat Rate at Cold Leg Injection Node in Cold Leg A

Note: With the cold leg condensation model turned off, CSIQTOT is not calculated in the SI injection node of the broken cold leg.

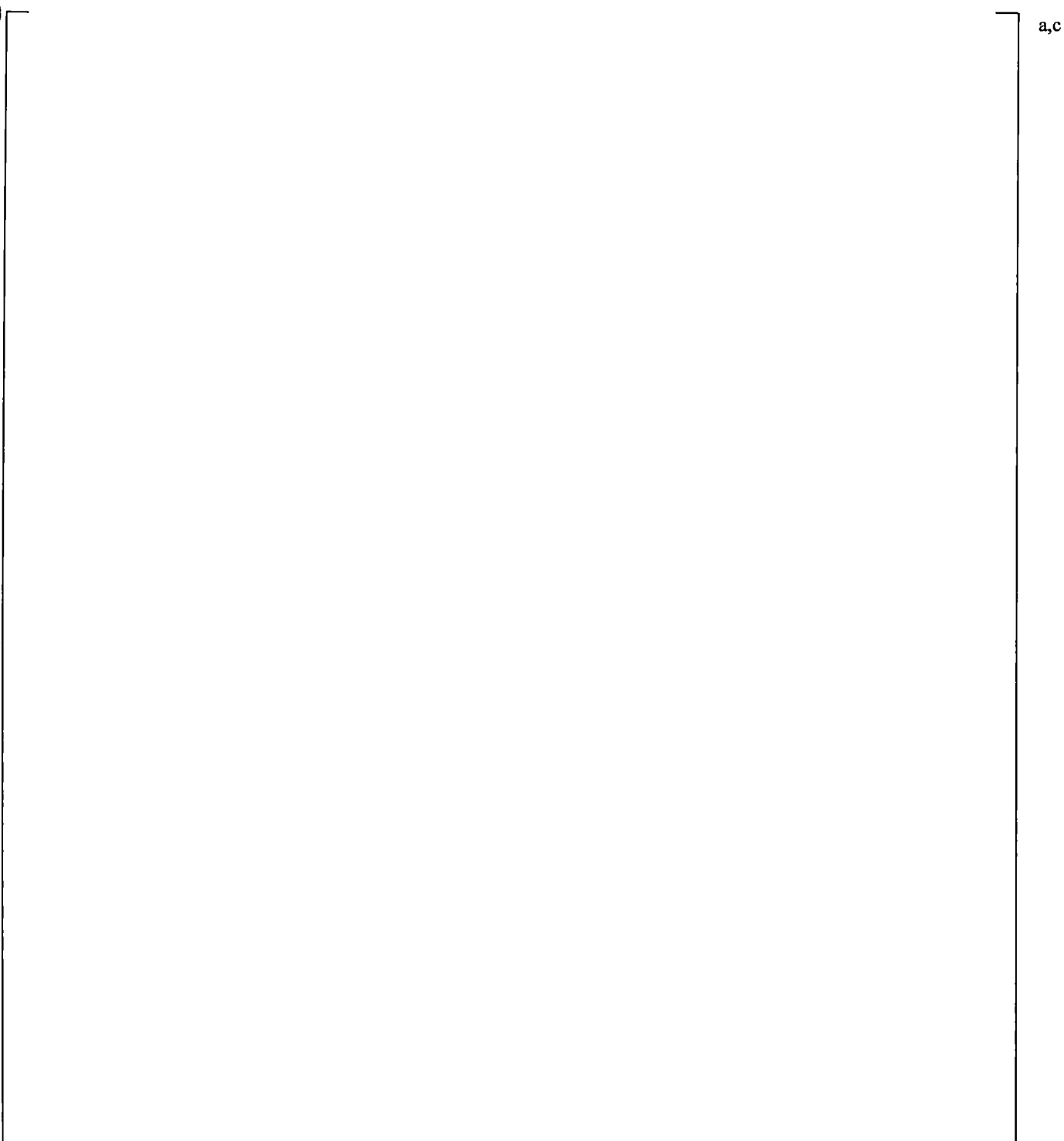


Figure 21.17-4 Cold Leg Fluid Temperatures at SI Injection Nodes

Note: The temperature of the pumped SI delivered into the cold legs is ~310K (98 F)

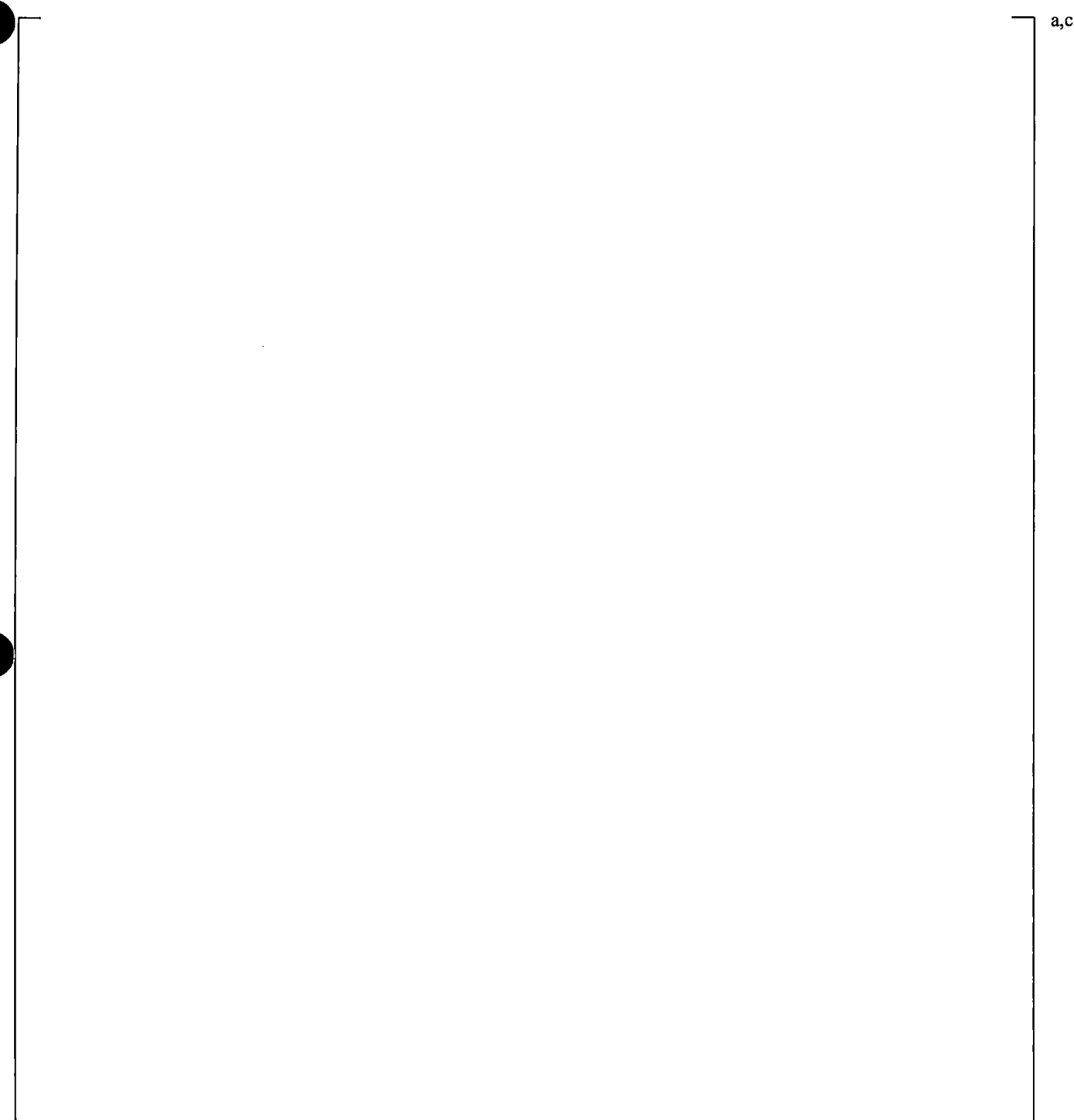
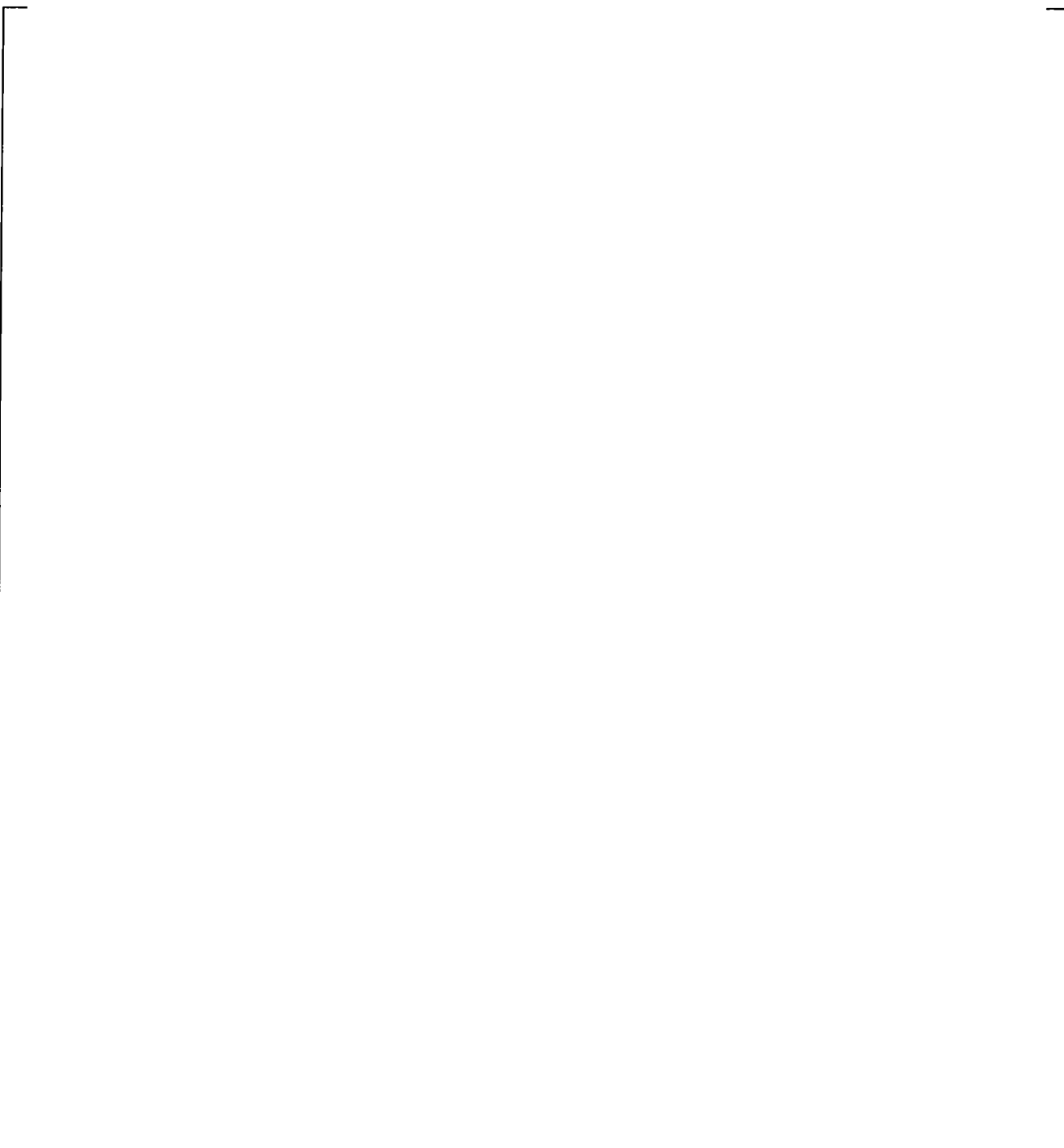


Figure 21.17-5 Cold Leg Pressures at SI Injection Nodes



a,c

| **Figure 21.17-6 Accumulator Injection Flows**



Figure 21.17-7 Broken Cold Leg Void at Break Off-take Node



Figure 21.17-8 Break Void Fractions



Figure 21.17-9 Fluid Temperatures at the Break



Figure 21.17-10 Break Flow Rates



a,c

Figure 21.17-11 Integrated Break Flows



a,c

Figure 21.17-12 Integrated Break Flow Difference (KCOSI_low-KCOSI_high)

21.18 MAIN STEAM SAFETY VALVE SETPOINT SENSITIVITY CALCULATION

A sensitivity calculation is performed with the 0.5% side break test SB-CL-15 to provide a basis for assessing the effect of increased main steam safety valve setpoint on the SBLOCA transient. The 0.5% break was selected for this sensitivity since with this break size the loss of inventory is the lowest, the holdup of the primary system pressure above the secondary side pressure is for a longer period of time, and the effect of the increase of the MSSV setpoint would be greater.

For the purpose of the sensitivity study, the steam generator MSSV pressure setpoints were increased arbitrarily, as follows.

MSSV Open @ 9.37 MPa (old value 8.0 MPa)
MSSV Close @ 8.5 MPa (old value 7.8 MPa)

With the setpoints selected above, the average MSSV setpoint is increased by 1.035 MPa (150 psi).

The calculation results from this sensitivity are compared to the results of the SB-CL-15 simulation, performed for the break orientation studies in Section 21.7.

Figure 21.18-1 compares the calculated pressurizer and steam generator secondary side pressures from the two simulations. As seen, the increase of the MSSV setpoint results in an increased primary system pressure during the prolonged period when the steam generator acts as a heat sink. The cyclical behavior of the secondary side pressure affects the primary side pressure in a similar way, through the primary-to-secondary side heat transfer feedback mechanism. The greater amplitude of the calculated pressure oscillations in the high MSSV setpoint case is due to the greater difference between the Open and Close pressure setpoints of the MSSV, implemented for that case.

The comparison of the calculated break flows, Figure 21.18-2, shows a minor effect on the calculated inventory loss through the break.

With the MSSV setpoint increased, the calculated steam generator draining is asymmetrical, but the steam generators drain at about the same time, Figure 21.18-3. Increased loss of inventory through the break might be the reason for the predicted somewhat earlier draining of the upper plenum, Figure 21.18-4, and the hot legs as well, Figure 21.18-5.

Figure 21.18-6, shows a comparison of the calculated differential pressures from the bottom of the cross-over leg to the pump inlet for the two loops. As seen in that figure, with the increase of the MSSV the loop seal clearance in loop A is predicted to occur a little earlier. The calculated loop flows, Figure 21.18-7, are very similar.

As a result of the calculated greater inventory loss with increased MSSV setpoint, the loop seal clearance uncovering of the core occurs a little earlier, as well as the boiloff, Figure 21.18-8. Consequently, in the case of increased MSSV setpoint the calculated rod heatup is higher, as seen in Figure 21.18-9. The overall effect of the MSSV setpoint, however, does not appear to be significant.



a,c



Figure 21.18-1 Calculated Primary and Steam Generator Secondary Pressures

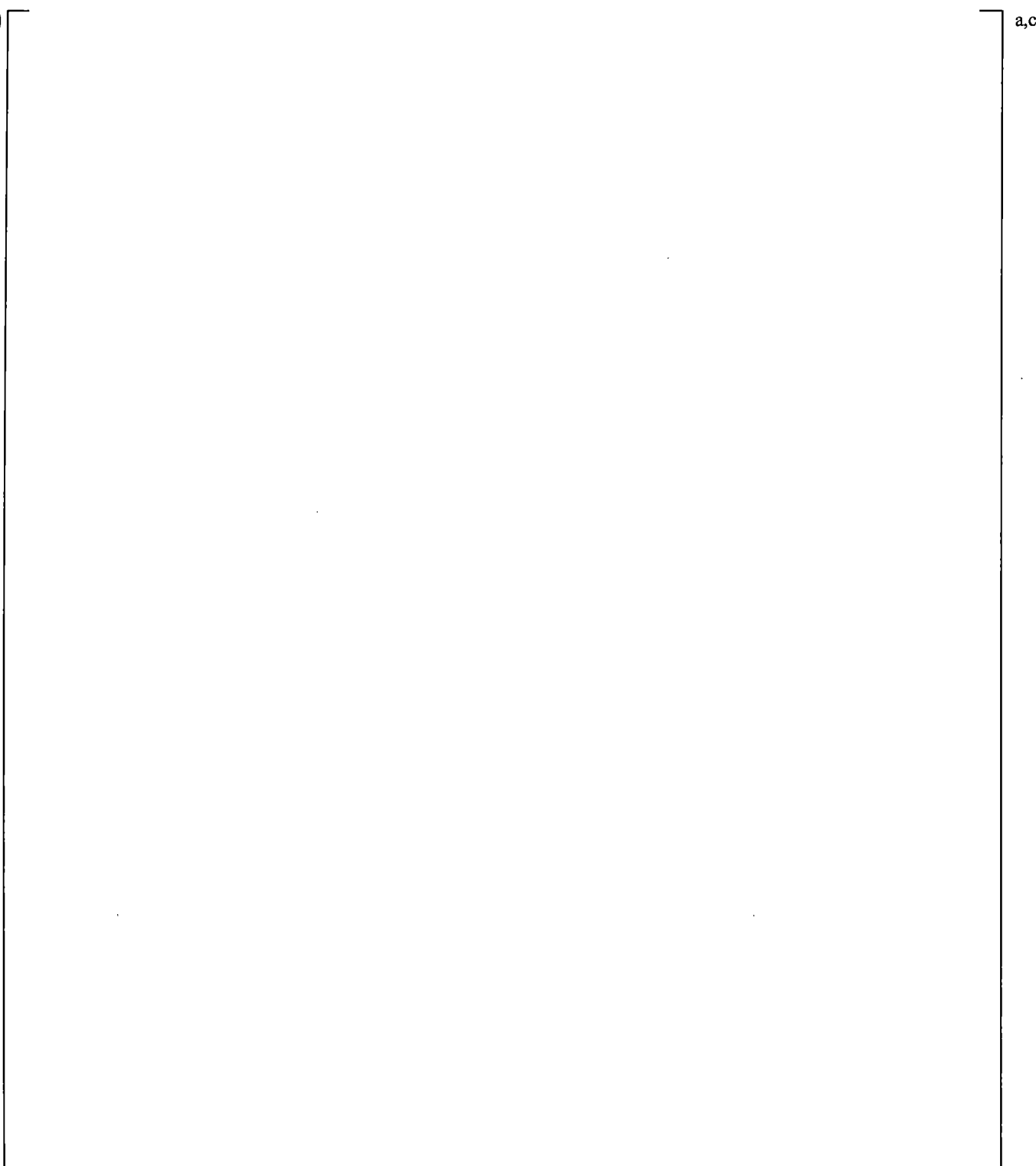


Figure 21.18-2 Calculated Break Flows

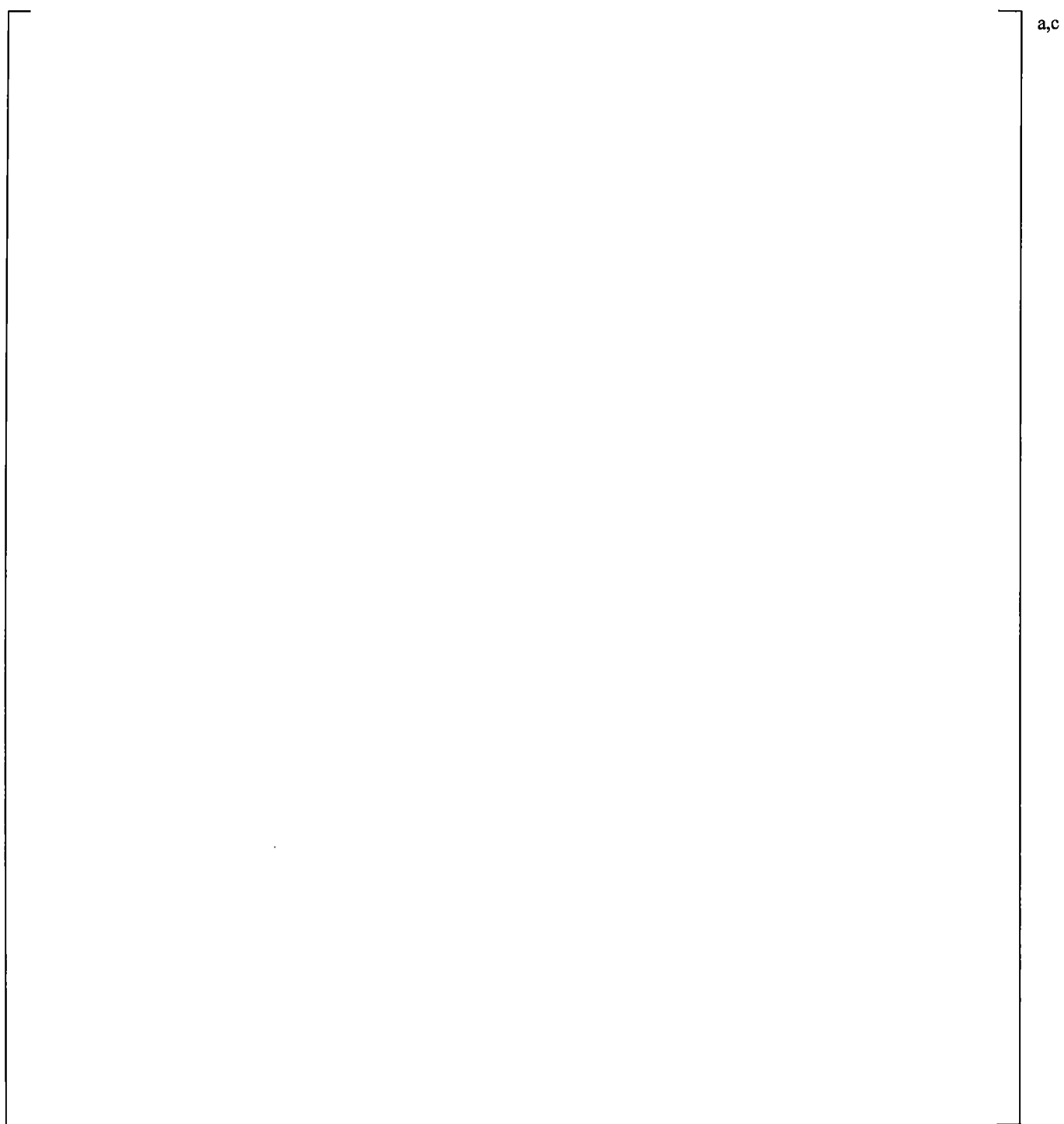


Figure 21.18-3 Calculated Draining of Steam Generator U-tubes Uphill Side

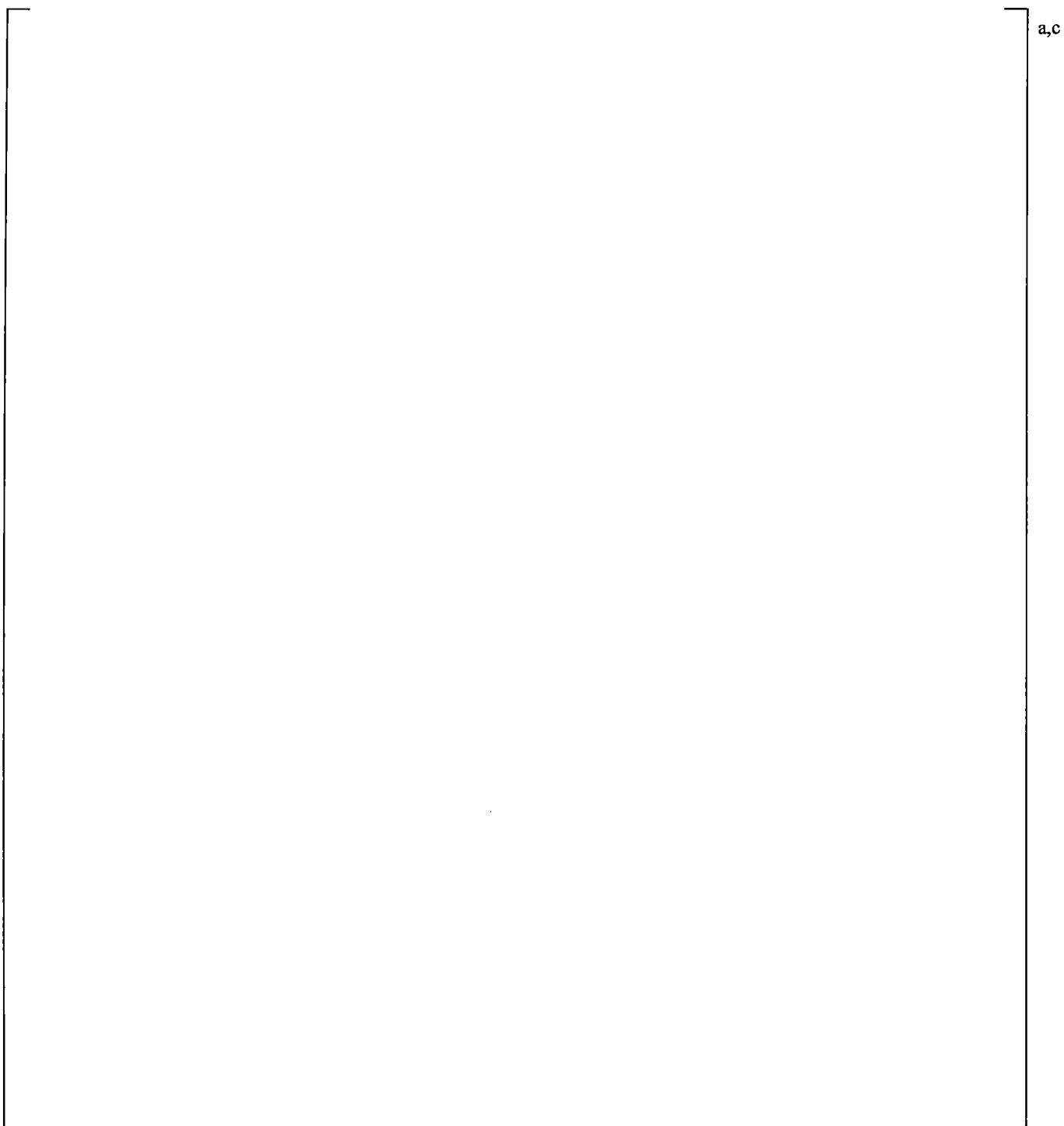
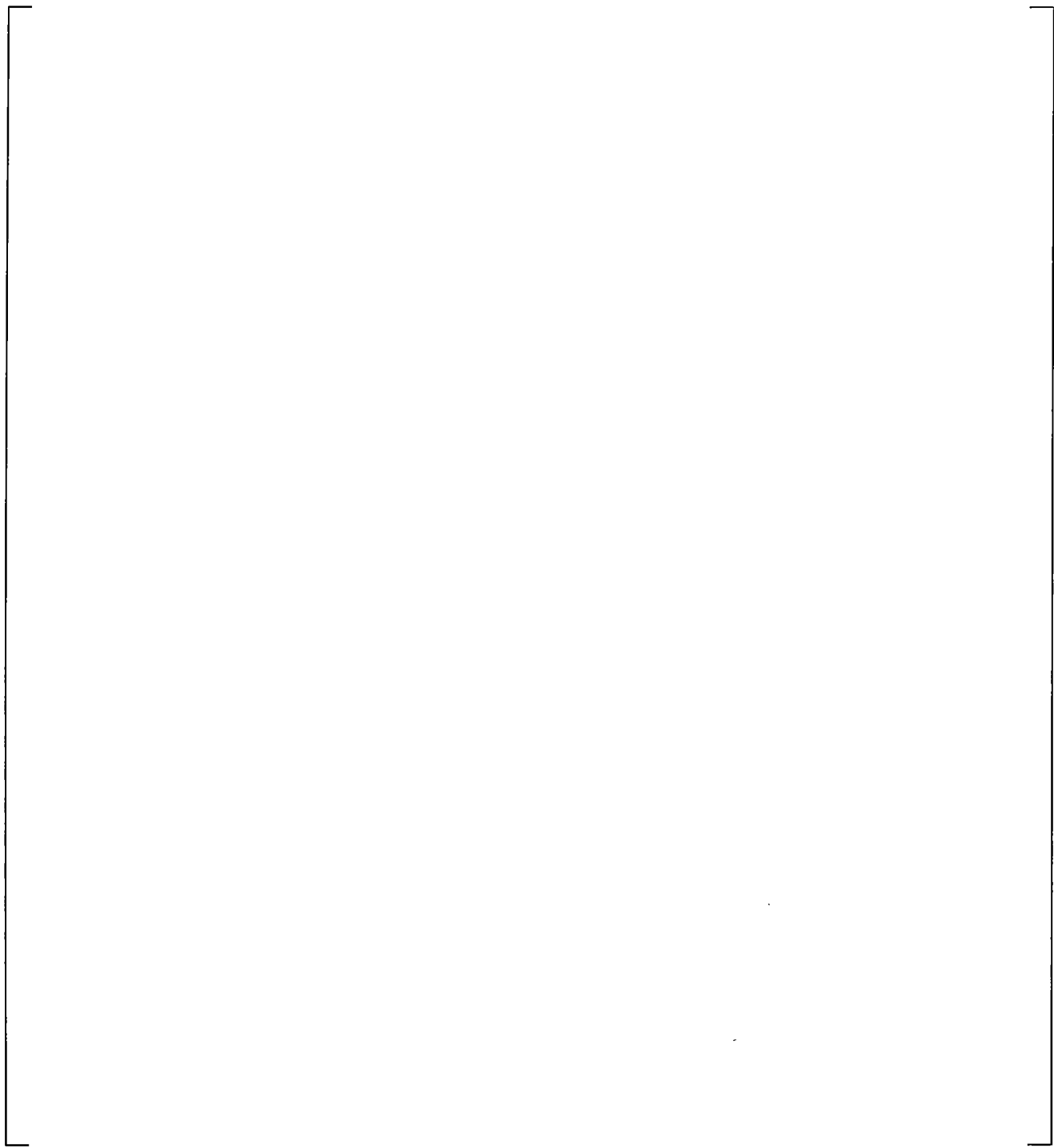


Figure 21.18-4 Calculated Upper Plenum Differential Pressures



a,c

| **Figure 21.18-5 Calculated Upper Plenum to Steam Generator Inlet Differential Pressures**

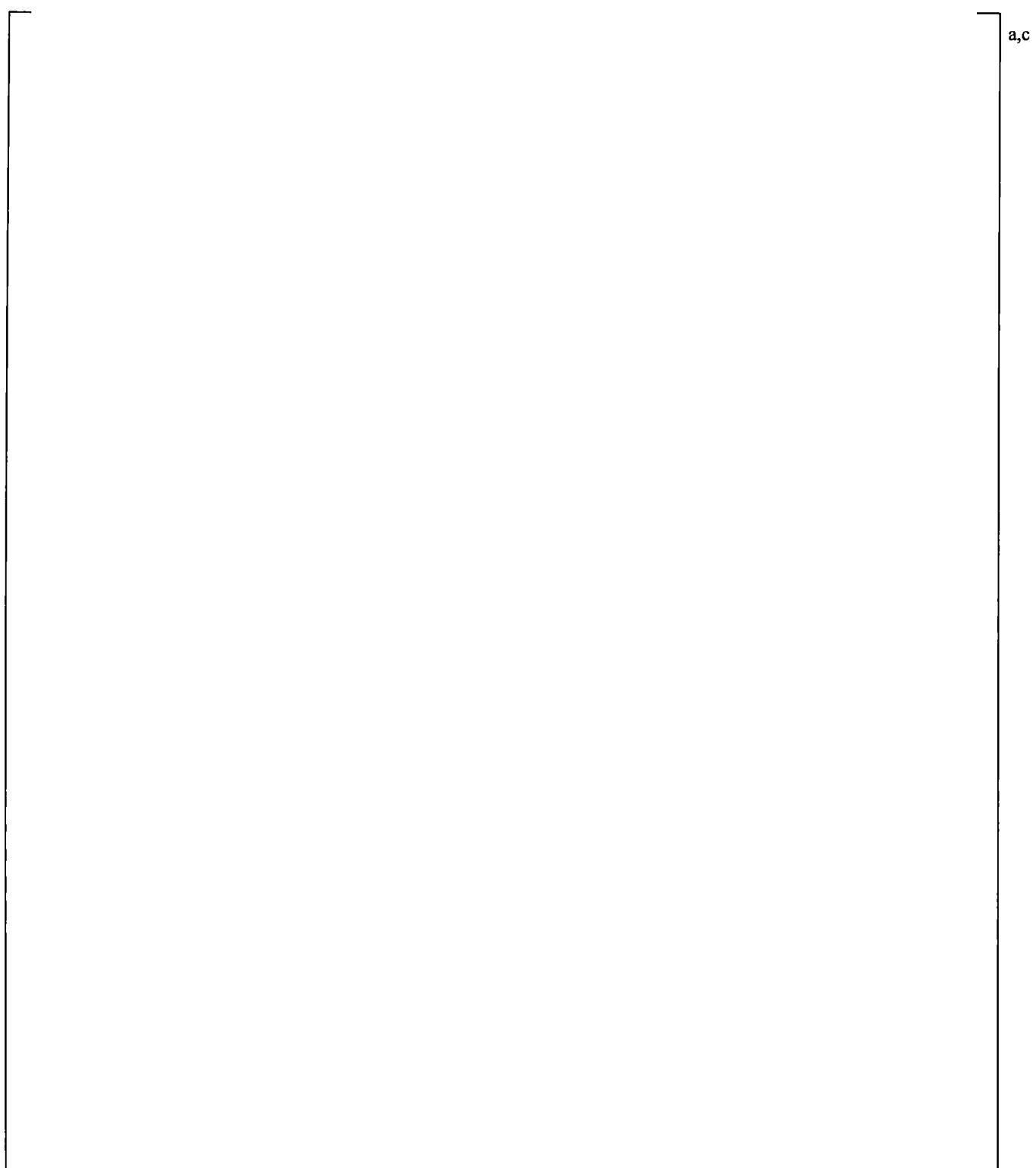


Figure 21.18-6 Calculated Cross-Over Leg Differential Pressures (Bottom-to-Pump Inlet)



a,c



Figure 21.18-7 Calculated Loop Flow Rates



Figure 21.18-8 Calculated Core Differential Pressures



Figure 21.18-9 Calculated Peak Cladding Temperatures

21.19 CONCLUSIONS

The analysis of the results of the various ROSA-IV LSTF test simulations presented in this section demonstrates that WCOBRA-TRAC-TF2 is capable of simulating with sufficient accuracy the key thermal-hydraulic phenomena that might occur during a PWR small break LOCA accident. The major conclusions from the analysis of the test simulations with the ROSA-IV LSTF model presented in this section are summarized below.

- [

a,c

- The simulation of the ST-NC-02 test shows that the code calculates natural circulation phenomena in a manner consistent with the test observations. The transition to reflux condensation is calculated to occur at system inventory consistent with that observed in the test.

1a,c

- The break orientation studies in Section 21.7 show results which are consistent with those observed in the tests. |

12

- The various sensitivity studies show results that are consistent with the expected effect of the parameter being ranged in these small break LOCA test simulations.

21.20 REFERENCES

1. Asaka, et al., 1990, "Results of 0.5% Cold-Leg Small-Break LOCA Experiments at ROSA-IV/LSTF: Effect of Break Orientation," *Experimental Thermal and Fluid Science*, 3, 588-596.
2. Chauliac, C., et al., 1988, "Post-Test Analysis with RELAP5/MOD2 of ROSA-IV/LSTF Natural Circulation Test ST-NC-02," JAERI-M 88-215.
3. Glaeser, H., et al., 1993, "The Contribution of UPPTF Experiments to Resolve Some Scale-up Uncertainties in Counter-current Two Phase Flow," *Nuclear Engineering and Design*, 145 (63-84).
4. Glaeser, H., et al., 2000, "OECD/CSNI Uncertainty Methods Study for "Best Estimate" Analysis," International Meeting on "Best-Estimate" Methods in Nuclear Installation Safety Analysis (BE-2000), Washington, DC.
5. Hsieh, C., et al., 1980, "Counter-current Air/Water and Steam/Water Flow above a Perforated Plate," NUREG/CR-1808.
6. Kawaji, M., et al., 1986, "ROSA-IV/LSTF 5% Cold Leg Break LOCA Experiment Data Report, Run SB-CL-05," JAERI-memo 61-056.
7. Koizumi, Y., et al., 1987, "ROSA-IV/LSTF 2.5% Cold Leg Break LOCA Experiment Data Report for Runs SB-CL-01, 02 and 03," JAERI-memo 62-399.
8. Koizumi, Y., et al., 1988, "Investigation of Break Orientation Effect During Cold Leg Small-Break LOCA at ROSA-IV LSTF," *Journal of Nuclear Science and Technology*, 25.
9. Koizumi, Y. and Tasaka, K., 1988a, "Quick Look Report for ROSA-IV/LSTF 10% Cold Leg Break LOCA Test, SB-CL-14," []^b
10. Koizumi, Y. and Tasaka, K., 1988b, "Quick Look Report for ROSA-IV/LSTF 0.5% Cold Leg Break LOCA Tests, SB-CL-15 and SB-CL-16," []^b
11. Kukita, Y., et al., 1988, "Nonuniform Steam Generator U-Tube Flow Distribution During Natural Circulation Tests in ROSA-IV Large Scale Test Facility," *Nuclear Science and Engineering*, Vol. 99.
12. Kukita, Y., et al., 1989, "Hot Leg Flow Characteristics during Two-phase Natural Circulation in Pressurized Water Reactor," *Proceedings/Fourth International Topical Meeting on Nuclear Reactor Thermal Hydraulics*, NURETH-4, page 465-470.
13. Kukita, Y., et al., 1990a, "Loop Seal Clearing and Refilling During a PWR Small-Break LOCA," *Nuclear Engineering and Design*, 121, pp. 431-440.
14. Kukita, Y., et al., 1990b, "The effect of break location on PWR small break LOCA: Experimental study at the ROSA-IV LSTF," *Nuclear Engineering and Design*, 122, pp. 255-262.

15. Kukita, Y., et al., 1991, "Summary of ROSA-IV LSTF First-phase Test Program – Integral Simulation of PWR Small-break LOAs and Transients," *Nuclear Engineering and Design*, 131 101-111.
16. Kukita, Y., et al., 1992, "OECD/NEA/CSNI International Standard Problem No. 26 (ISP-26) ROSA-IV LSTF Cold-Leg Small-Break LOCA Experiment – Comparison Report."
17. Kumamaru, et al., 1989, "ROSA-IV/LSTF 5% Cold Leg Break LOCA Experiment, Run SB-CL-18 Data Report," JAERI-M 89-027.
18. Leonard, M. T., 1982a, "Vessel Coolant Mass Depletion During a Small Break LOCA," EGG-SEMI-6010.
19. Leonard, M. T., 1982b, "An Analytical Study of a Small Break Loss-Of-Coolant Accident with Upper Head Injection," *Nuclear Technology*, Vol. 62.
20. Loomis, G. G. and Streit, J. E., 1985, "Quick Look Report for Semiscale Mod-2C Experiments S-LH-1 and S-LH-2," EGG-SEMI-6884.
21. Osakabe, M., et al., 1987, "Core Liquid Level Depression due to Manometric Effect during PWR Small Break LOCA – Effect of Break Area," *Journal of Nuclear Science and Technology*, 24, pp. 103-110.
22. Osakabe, M., et al., 1988, "Core Liquid Level Depression due to Manometric Effect during PWR Small Break LOCA – Effect of Core Bypass," *Journal of Nuclear Science and Technology*, 25, pp. 274-282.
23. The ROSA IV Group, 1985, "ROSA-IV Large Scale Test Facility (LSTF) System Description," JAERI-M 84-237.
24. The ROSA-IV Group, 1989, "Supplemental Description of ROSA-IV/LSTF with No.1 Simulated Fuel-Rod Assembly," JAERI-M 89-113.
25. Stumpf, H. et al., 1987, "Reverse Primary-Side Flow in Steam Generators During Natural Circulation Cooling," *ASME Heat Transfer Division (HTD)*, Vol. 92.
26. Tasaka, K., et al., 1988, "The Results of 5% Small Break LOCA Tests and Natural Recirculation Tests at the ROSA-IV LSTF," *Nuclear Engineering and Design*, 108.
27. Yonomoto, T., 2005, "ROSA/LSTF Experiments of PWR Natural Circulation and Validation of RELAP5/MOD3.3," IAEA's 2nd Research Coordination Meeting on the CRP on Natural Circulation Phenomena, Modeling and Reliability of Passive Safety Systems that Utilize Natural Circulation, Corvallis, Oregon (USA).